

Lecture Notes in Mechanical Engineering

G. S. V. L. Narasimham

A. Veeresh Babu

S. Sreenatha Reddy

R. Dhanasekaran *Editors*


# Innovations in Mechanical Engineering

Select Proceedings of ICIME 2021

 Springer


# Lecture Notes in Mechanical Engineering

## Series Editors

Francisco Cavas-Martínez , Departamento de Estructuras, Universidad Politécnica de Cartagena, Cartagena, Murcia, Spain

Fakher Chaari, National School of Engineers, University of Sfax, Sfax, Tunisia

Francesca di Mare, Institute of Energy Technology, Ruhr-Universität Bochum, Bochum, Nordrhein-Westfalen, Germany

Francesco Gherardini , Dipartimento di Ingegneria, Università di Modena e Reggio Emilia, Modena, Italy

Mohamed Haddar, National School of Engineers of Sfax (ENIS), Sfax, Tunisia

Vitalii Ivanov, Department of Manufacturing Engineering, Machines and Tools, Sumy State University, Sumy, Ukraine

Young W. Kwon, Department of Manufacturing Engineering and Aerospace Engineering, Graduate School of Engineering and Applied Science, Monterey, CA, USA

Justyna Trojanowska, Poznan University of Technology, Poznan, Poland

**Lecture Notes in Mechanical Engineering (LNME)** publishes the latest developments in Mechanical Engineering—quickly, informally and with high quality. Original research reported in proceedings and post-proceedings represents the core of LNME. Volumes published in LNME embrace all aspects, subfields and new challenges of mechanical engineering. Topics in the series include:

- Engineering Design
- Machinery and Machine Elements
- Mechanical Structures and Stress Analysis
- Automotive Engineering
- Engine Technology
- Aerospace Technology and Astronautics
- Nanotechnology and Microengineering
- Control, Robotics, Mechatronics
- MEMS
- Theoretical and Applied Mechanics
- Dynamical Systems, Control
- Fluid Mechanics
- Engineering Thermodynamics, Heat and Mass Transfer
- Manufacturing
- Precision Engineering, Instrumentation, Measurement
- Materials Engineering
- Tribology and Surface Technology

To submit a proposal or request further information, please contact the Springer Editor of your location:

**China:** Ms. Ella Zhang at [ella.zhang@springer.com](mailto:ella.zhang@springer.com)

**India:** Priya Vyas at [priya.vyas@springer.com](mailto:priya.vyas@springer.com)

**Rest of Asia, Australia, New Zealand:** Swati Meherishi at [swati.meherishi@springer.com](mailto:swati.meherishi@springer.com)

**All other countries:** Dr. Leontina Di Cecco at [Leontina.dicecco@springer.com](mailto:Leontina.dicecco@springer.com)

To submit a proposal for a monograph, please check our Springer Tracts in Mechanical Engineering at <https://link.springer.com/bookseries/11693> or contact [Leontina.dicecco@springer.com](mailto:Leontina.dicecco@springer.com)

**Indexed by SCOPUS. All books published in the series are submitted for consideration in Web of Science.**

More information about this series at <https://link.springer.com/bookseries/11236>

G. S. V. L. Narasimham · A. Veeresh Babu ·  
S. Sreenatha Reddy · Rajagopal Dhanasekaran  
Editors

# Innovations in Mechanical Engineering

Select Proceedings of ICIME 2021



*Editors*

G. S. V. L. Narasimham  
Department of Mechanical Engineering  
Indian Institute of Science Bangalore  
Bangalore, Karnataka, India

A. Veeresh Babu  
Department of Mechanical Engineering  
National Institute of Technology Warangal  
Warangal, Telangana, India

S. Sreenatha Reddy  
Guru Nanak Institute of Technology  
Ibrahimpattanam, Telangana, India

Rajagopal Dhanasekaran  
Department of Mechanical Engineering  
Guru Nanak Institute of Technology  
Ibrahimpattanam, Telangana, India

ISSN 2195-4356

ISSN 2195-4364 (electronic)

Lecture Notes in Mechanical Engineering

ISBN 978-981-16-7281-1

ISBN 978-981-16-7282-8 (eBook)

<https://doi.org/10.1007/978-981-16-7282-8>

© The Editor(s) (if applicable) and The Author(s), under exclusive license to Springer Nature Singapore Pte Ltd. 2022

This work is subject to copyright. All rights are solely and exclusively licensed by the Publisher, whether the whole or part of the material is concerned, specifically the rights of translation, reprinting, reuse of illustrations, recitation, broadcasting, reproduction on microfilms or in any other physical way, and transmission or information storage and retrieval, electronic adaptation, computer software, or by similar or dissimilar methodology now known or hereafter developed.

The use of general descriptive names, registered names, trademarks, service marks, etc. in this publication does not imply, even in the absence of a specific statement, that such names are exempt from the relevant protective laws and regulations and therefore free for general use.

The publisher, the authors and the editors are safe to assume that the advice and information in this book are believed to be true and accurate at the date of publication. Neither the publisher nor the authors or the editors give a warranty, expressed or implied, with respect to the material contained herein or for any errors or omissions that may have been made. The publisher remains neutral with regard to jurisdictional claims in published maps and institutional affiliations.

This Springer imprint is published by the registered company Springer Nature Singapore Pte Ltd. The registered company address is: 152 Beach Road, #21-01/04 Gateway East, Singapore 189721, Singapore

# Preface

The book contains high-quality papers presented in the Fourth International Conference on Innovations in Mechanical Engineering (ICIME 2021) held at Guru Nanak Institutions, Hyderabad, India, during 26 and 27 February 2021. The objective is provide a platform for researchers, scientists, technocrats, academicians and engineers to exchange their innovative ideas in the field of mechanical engineering, especially the areas like aerospace, alternative fuels, automobile, thermal engineering, renewable energy sources, bio-mechanics, fluid mechanics, MEMS, mechatronics, robotics, CAD/CAM, AE, CFD, design and optimization, tribology, materials engineering and metallurgy, mimics, surface engineering, nanotechnology, polymer science, manufacturing, production management, industrial engineering, rapid prototyping and multidisciplinary areas related to mechanical engineering.

G. S. V. L. Narasimham  
A. Veeresh Babu  
S. Sreenatha Reddy  
Rajagopal Dhanasekaran

# Contents

<b>Design Analysis and Optimization of a Rotating Disc with Variable Thickness</b> .....	1
Prerana D. Rao, Prathamesh Dehadray, Alampally Sainath, Lokavarapu Bhaskara Rao, and Ch. Rajesh	
<b>Design and Analysis of Anti-intrusion Beams for Car Door</b> .....	15
Jaimin Panchal, Keval Bhavsar, and Dharmik Gohel	
<b>Experimental Flow Field Investigation of the Bio-inspired Corrugated Wing and Hybrid Wing for MAV Applications</b> .....	29
Y. D. Dwivedi, Abhishek Mohapatra, and Mohammad Irfan	
<b>Structural Analysis and Topology Optimization of Base of Revolving Chair</b> .....	43
Dharmik Gohel, Keval Bhavsar, and Jaimin Panchal	
<b>Effect of Elliptical Cutout on Buckling Load for Isotropic Thin Plate</b> ...	51
Renuka Gore and Bhaskara Rao Lokavarapu	
<b>Buckling Analysis of Thin Isotropic Square Plate with Rectangular Cut-Out</b> .....	71
Prathamesh Mahesh Dehadray, Sainath Alampally, and Bhaskara Rao Lokavarapu	
<b>Numerical Investigation on Strength of Isotropic and Laminated Composite Pressure Vessel</b> .....	87
Venkata Narayana Yenugula and Raja Shekhar Bhukya	
<b>Experimental Analysis of Hartnell Governor Mechanism in Dynamics of Machinery Laboratory</b> .....	99
Ali Hasan	

<b>Comparative Study and Analysis of Material for Energy Storing Body Panel of an Automobile</b> .....	107
Md. Roshan, Animireddy V. S. S. S. Prasad, Danish Raza, Om Prakash, Md. Shadab, and Sanjeev kumar	
<b>Impact of Diamond-Shaped Cut-Out on Buckling Nature of Isotropic Stainless-Steel Plate</b> .....	119
Vineet Sinha, Rutul Patel, Keval Ghetiya, Mikhil Nair, Tarun Trivedi, and Lokavarapu Bhaskara Rao	
<b>Modelling and Analysis of a Two-Stage Gearbox</b> .....	147
Aditya Sachin Kodolikor, Alahari Venkata Sai Jaswanth, S. Naveen, and Lokavarapu Bhaskara Rao	
<b>Vibrational Analysis of Circular Plates with Square Cutout</b> .....	173
AL. Muthuveerappan, C. Ajay, V. Dhakshain Balaji, Varun Gopalakrishnan, and Lokavarapu Bhaskara Rao	
<b>Vibrational Analysis of Circular Composite Plates with Square Cutout</b> .....	191
Varun Gopalakrishnan, V. Dhakshain Balaji, C. Ajay, AL. Muthuveerappan, and Lokavarapu Bhaskara Rao	
<b>Numerical Analysis of Buckling in Rectangular Plates with Different Cut-Outs</b> .....	209
Mahendhar Kumar, Akash Venkateshwaran, Chamala Vaishnavi, and Lokavarapu Bhaskara Rao	
<b>Analysis of Buckling Behavior on the Thin-Walled Circular Cylinder</b> .....	253
Nayani Uday Ranjan Goud and M. N. V. S. Swethabala	
<b>Design and Analysis of E-Kisan Multi-Tool Machine</b> .....	265
B. Vijaya Kumar	
<b>Effect of NFA on Wear Resistance of Al6063/NFA Composites fabricated through the Stir Casting Method</b> .....	281
Narasa Raju Gosangi and Lingaraju Dumpala	
<b>Formulation Correction of a Lubricant Oils During the Production Process a Case Study</b> .....	287
S Shahab and Shaik Himam Saheb	
<b>Experimental Analysis of Wire Mask Assisted Reverse Micro-EDM (RMEDM) for Fabrication of Arrayed Rods</b> .....	301
S. R. Dharmadhikari, S. A. Mastud, and R. H. Shinde	
<b>Powder Mixed Micro-Electric Discharge Machining—A Review</b> .....	311
R. H. Shinde, D. N. Raut, N. G. Patil, and S. R. Dharmadhikari	

**Effects of MoS<sub>2</sub>-Based Biodegradable Cutting Fluids in MQL During Turning of Stainless Steel** ..... 319  
 N. R. Patil, D. R. Waghole, and A. K. Bewoor

**A Comparison Study between Conventional and Cryogenic Machining** ..... 329  
 Md Zia Arzoo, Mozammil Hassan, and N Gupta

**Effect of Voltage on the Size of Magnetic Nanoparticles Synthesized Using Arc-Discharge Method** ..... 339  
 Shaik Gulam Abul Hasan, A. V. S. S. K. S. Gupta, and B. V. Reddi

**A Review on Biomedical and Mechanical Applications of 3D Printing** ..... 347  
 Ujjwal Purwar, Mohammad Aqib Javed, Ashish Prabhakar, Gaurav Singh, Shrikant Vidya, and K. S. Srikanth

**Experimental Investigation on FTIR Analysis of Produced Biodiesel and Performance and Emission Analysis of Diesel Engine Using Schleicher Oleosa Methyl Ester as Fuel with EGR** ..... 355  
 Ajay Chandravanshi, Ajay Singh Paikra, Shrikant Pandey, and Rakesh Kumar Malviya

**Optimization of Solar Energy Efficiency: A Quadratic Regression Approach** ..... 369  
 Perini PraveenaSri

**Experimental Analysis of Azolla Biodiesel Blends in CI Engine** ..... 379  
 N. Sunil Naik, Dhanunjay Kumar Ammisetti, B. Kishan, and Suresh Chitturi

**Performance Evaluation of Sunflower Oil Biodiesel Before and After Transesterification** ..... 391  
 Surakasi Raviteja, Pujari Satish, Y. R. K. Prasanna, and V. V. Prasanna Kumar

**Evaluation of Heat Transfer Rate in Heat Sink Using FGM** ..... 401  
 N. B. V. L. Kumari, A. Jagadeesh, and Ishrat Meera Mirzana

**Application of Thermoacoustics for Cooling: A Review** ..... 421  
 Rajan Devkota, Atal Babu, Prashant Gupta, Karun Kant, and Shrikant Vidya

**Experimental Investigation on Shell and Tube Exchanger for the Rate of Heat Transfer by Using Ethylene Glycol and Propylene Glycol Fluids** ..... 429  
 Prasanna Kumar Thotakura, Siva Krishna Karnati, Nagoju M. K. Sarath Kumar, and Radha Krishna Gopidesi

<b>Solid Waste Biofuel: An Overview</b> .....	441
N. Srujana, G. Bhanodaya Reddy, and Pinisetty Sai Sampath Aditya	
<b>Effect of Truncated Conic Fins in Distillate of Double Slope Solar Still</b> .....	457
Ajay Kumar Kaviti, Begari Mary, and Akkala Siva Ram	
<b>Experimentation on Pulsating Heat Pipe and CFD Analysis for Performance Enhancement</b> .....	469
J. V. Suresh, P. Bhramara, and K. Hrishikesh	
<b>Performance and Emission Analysis of DI Diesel Engine Fuelled with Magnetic Conditioned Mamey Sapote Biodiesel</b> .....	487
G. Janardhana Raju and A. Raj Kumar	
<b>Comparison of Energy and Exergy Analysis of Parabolic Fin Solar Still with Conventional Solar Still</b> .....	495
V. Raja Ranadher Naike, Shaik Hussain, Ajay Kumar Kaviti, and Akkala Siva Ram	
<b>Suction/Injection Effects on a Stretching Surface of the Stagnation Point Flow Through Porous Medium with Influence of Heat Generation</b> .....	507
B. Shankar Goud, Y. Dharmendar Reddy, B. Praveen Kumar, and M. Anil Kumar	
<b>Effect of ZrB<sub>2</sub> Nano-Ingredient on Uncoated Tool Wear for Aluminum Alloys-Based Metal Matrix Composite</b> .....	515
Seema V. Yerigeri and Shantisagar K. Biradar	
<b>Comparative Study on Dry Sliding Wear Behaviour of TiAlN, ZrAlN and ZrN/Al<sub>2</sub>O<sub>3</sub> Hard Coatings on ZA Alloys</b> .....	533
B. Harish, K. R. Prakash, and R. Suresh	
<b>Failure Load of Jute–Coir Fiber Reinforced Epoxy Matrix Composites Using Micromechanics and Finite Element Method</b> .....	545
Jami Sai Revanth, G. Pavan Kumar, P. Phani Prasanthi, K. Sai Phani Teja, A. Rama Satyanaryana, and G. Ashok Kumar	
<b>Experimental Investigation of Mechanical and Tribological Properties of ABS-Barium Sulfate Polymer Composite by Taguchi Technique</b> .....	557
S. Sreenivasulu and A. Chennakesava Reddy	
<b>Development of Carbon and Glass Fiber-Reinforced Composites with the Addition of Nano-Egg-Shell Powder</b> .....	569
T. Prasad, Barmavatu Praveen, Yalagandala Akshay Kumar, and Kunchala Krishna	

**Investigation on Nitriding and Microstructure Evolution of M50 NiL Steel: A Review** ..... 579  
 B. Venkatesh and C. Anil Kumar Reddy

**Experimental Investigation of Plydrop Behavior in FRP Composites** ... 591  
 G. Likhitha, N. Kiran Kumar, M. Manzoor Hussain, and S. N. S. Sai Hari

**Influence of Coating on Micro Stress Distribution in Cylindrical FRP Composites** ..... 605  
 Namala Kiran Kumar, G. Srinivasa Gupta, K. Ajay Kumar, and M. Manzoor Hussain

**A Review on Carbon Reinforcements in Glass Fiber Polymer Matrix Composites** ..... 627  
 N. Kiran Kumar, B. Chandra Kiran, B. Chennakesava Rao, and M. Manzoor Hussain

**Influences of Functionalized Multiwalled Carbon Nanotube on the Tensile and Flexural Properties of Okra Cellulose Nanofibers/Epoxy Nanocomposites** ..... 639  
 Ajmeera Ramesh, N. V. Srinivasulu, and M. Indira Rani

**Virtual Instrumentation System Design for a Secured Chemical Process Industry Automation** ..... 653  
 S. G. Rahul, R. Chitra, Manasa Madabhushi, M. Kavya, and Sraya

**Multi-robot SLAM: Challenges and Solutions** ..... 663  
 Nishad Kulkarni, Saket Yeolekar, and Prakash Mainkar

**Design and Development of a Prototype Agribot** ..... 675  
 Mohd. Firasath Ali and P. Venkata Ramana

**Analysis of Breathalyzer Effect on a Passenger Vehicle** ..... 689  
 R. Dhanasekaran, S. Sreenatha Reddy, Kandadi Sai Praneeth Reddy, Pathireddy Kowshik Reddy, and Rangaraju Rohan

**Design and Evaluation of a Microsensor for a Bionic Hand with Metamaterials** ..... 699  
 M. Sreedhar and Y. Kalyana Chakravarthy

**Ergonomic Analysis of Mouse Holding Position of Humanoids** ..... 711  
 Chelamban Kalaiselvan and Lokavarapu Bhaskara Rao

**Energy Optimization by Using Low Life Cycle Cost Analysis Method in Split Casing Pump** ..... 723  
 Ramesh. S. Gavade and Suresh M. Sawant

**Identification of Fault Severity of Rolling Element Bearing Using Image Augmentation and Mobile Net V\_2 Convolutional Neural Network** ..... 733  
 P. Akhenia, H. Jamani, and V. Vakharia

**Study of Isomorphism Among Kinematic Chains of Group-IVC** ..... 745  
Ali Hasan

**Flower Pollination Algorithm for Solving Single-Row Facility  
Layout Problems** ..... 761  
R. Sanjeev Kumar, K. Vetrivel Kumar, and M. Francis Luther King

**Microwaves in Healthcare Systems for Cancer Detection** ..... 771  
R. Chitra, G. Srinivasa Sudharsan, S. G. Rahul, Seeram Sai Sudheer,  
and Archakam Amruthavalli

**Virtual Instrumentation Based Graphical User Interface  
for Fermentation Bioprocess Monitoring Using LabVIEW** ..... 783  
S. G. Rahul, R. Chitra, Vulichi Puneeth Kumar,  
Palla Hima Sai Abhishek, and Boggula Obula Reddy

**Analysis of a Multi-channel Closed Loop Green Supply Chain  
Using Modified Particle Swarm Optimization Algorithm** ..... 797  
T. Niranjana, R. Thanigaivelan, and B. Singaravel

**Wireless Electrical Impedance Tomography (EIT)  
Instrumentation: Progress and Limitations** ..... 809  
Tushar Kanti Bera

**Effect of Nano-rice Husk Ash Reinforcement on the Hardness  
of Al6061 Using Taguchi Method** ..... 821  
Subrahmanyam Vasamsetti, Lingaraju Dumpala, and V. V. Subbarao



## About the Editors



**Dr. G. S. V. L. Narasimham** is a Chief Research Scientist in the Department of Mechanical Engineering. He received his M.Tech. from IIT Madras and Ph.D. from IISc, Bangalore, both in Mechanical Engineering. His research interests include CFD, heat and mass transfer HVAC, refrigeration, cryogenics and solar thermal engineering. He has about three decades of experience in teaching, academic and sponsored research and guidance to masters and research students. He works as investigator in the projects sponsored by Air heating system design for erosion studies (CPRI), Airborne liquid cooling system (DRDO) in addition he has undertaken consultancy projects related to cold plate heat exchangers (IMI), automotive air conditioning systems (Mahindra). He is a life member of professional bodies related to heat and mass transfer and cryogenics.



**Dr. A. Veeresh Babu** is an Associate Dean (R&C), and Associate Professor in the Mechanical Engineering Department, NIT Warangal. He did his B.Tech. and M.Tech. in Heat Power Refrigeration from JNTU, Andhra Pradesh, in 1998 and 2000, respectively. He obtained a Ph.D. from Andhra University in 2013. He obtained experience in refrigerator design, clean-room technology, cold room/freezer room design and construction while he was working in the industry. He erected and commissioned cleanrooms at DRDE, Gwalior, RCI, Hyderabad and CRDI, Lucknow. He has research experience of more than 14 years ever since he joined NIT Warangal as an Assistant Professor in the year 2006. He published more than 34 papers

in SCI/SCOPUS/peer-reviewed journals and presented papers at 17 international conferences. He has guided 3 Ph.D. students, and six scholars are working under him for their Ph.D. At present, he has completed two minor research projects and two major projects are under review. He was also appointed as a course writer for the certificate in Power Plant Engineering offered by IGNOU, India.



**Dr. S. Sreenatha Reddy** is a Principal and Professor at Guru Nanak Institute of Technology in Hyderabad, affiliated to JNTUH. He did his B.Tech. in Mechanical Engineering from JNTUH, and M.Tech. in Heat Power, Refrigeration and Air Conditioning and Ph.D. in Mechanical Engineering from JNTUA. He held a variety of administrative positions and contributed to the growth of the institution. Among his honours are the Jawaharlal Nehru Memorial Prize, which was given by the Institution of Engineers on the occasion of the Inauguration of the 27th Indian Engineering Congress in New Delhi in 2012, and the “Bharat Vidya Shiromani Award” and a “Certificate of Education Excellence” given by the International Institute of Education. On the 22nd of December 2014, the International Institute of Education and Management (IIEM) in New Delhi presented the Glory of Education of Excellence Award, and on the 4th of March 2015, the IIEM in New Delhi presented the Glory of Education of Excellence Award. On July 5, 2015, he earned the prize for Best Academic Administrator from the Venus International Foundation’s Centre for Advanced Research and Design On the occasion of the Indo-American Education Summit 2016 in Hyderabad, he won the Indus Foundation’s National Award as an Eminent Educator. From 2018 to 2020, he won a slew of other important accolades. He is a young and energetic technical person with 19 years of experience teaching in the mechanical and aeronautical fields, as well as 3 years of experience in industry, specifically in thermal power plants. He pioneered critical difficulties in the thermal sector such as propulsion, combustion, and heat transfer while working in the automotive industry. He has extensive research and administrative experience. He published 141 papers in prestigious international and national journals, as well as 26 papers at international and national conferences. He is a

member of the governing board of GNIT, a famous institution. He was also a member of the AICTE's Expert Committee, which reviewed project reports internally, as well as the Board of Reviewers for the Institution of Engineers publication. He belongs to a number of professional organisations in the fields of mechanical engineering and technical education.



**Dr. Rajagopal Dhanasekaran** is working as a Professor in Mechanical Engineering, Guru Nanak Institute of Technology, Hyderabad, India, since November 2015. He obtained his B.Tech. in Mechanical and Production Engineering from Annamalai University in 2002, M.E. and Ph.D. from the Department of Mechanical Engineering, Anna University in 2007 and 2013, respectively. He has published more than 40 research papers, presented more than 25 papers at international and national conferences and 7 patent publications; he also received funds from AICTE. He established e-Yantra Lab Initiative Setup collaboration with IIT Bombay and coordinator of NIRF, ARIIA, IIC, IQAC, CII and NISP. He is a member in ISTE and Tribology Society of India. His research interests include tribology, engineering failure, wear characterization and composite materials.

# Design Analysis and Optimization of a Rotating Disc with Variable Thickness



Prerana D. Rao, Prathamesh Dehadray, Alampally Sainath,  
Lokavarapu Bhaskara Rao, and Ch. Rajesh

**Abstract** Rotating disc finds its application in gas turbines. Turbine discs are designed with variable thickness in order to prevent stress concentration, and closed form solutions for stress distribution are not reported extensively in literature. Numerical methods have been developed to provide approximate solution for the problem. In the present study, FEM approach is adopted to obtain a stress distribution in a rotating disc of variable thickness made of NIMONIC 901 and NIMONIC 105 super alloys. The comparison of stress distribution resulted in selecting NIMONIC 105 for the manufacture of disc with minimal induced maximum stress. Further, the optimum cost of production was obtained for NIMONIC 901 which further highlights the complexity of striking balance between the cost of production and stress levels induced in the disc. The study reveals that NIMONIC 901 is the better choice due to its low cost of production.

**Keywords** Rotating disc · Variable thickness · Shrinks fit · Natural frequency · NIMONIC 105

## 1 Introduction

The rotating disc is an important part of any application, ranging from automobiles to aerospace applications. Rotating discs are used extensively in many applications such as flywheels, IC engines, ship propellers, centrifugal compressors and aircrafts. The stress and strain analysis of rotating disc has been investigated by many authors and researchers. The most frequently used is the disc with circular hole. Closed form solutions are available for disc with circular holes and constant thickness. Therefore, variable thickness discs are the areas of current research. In the advancement

---

P. D. Rao (✉) · P. Dehadray (✉) · A. Sainath · L. Bhaskara Rao  
School of Mechanical Engineering, Vellore Institute of Technology, Chennai Campus,  
Vandalur-Kelambakkam Road, Chennai, Tamil Nadu 600127, India

Ch. Rajesh  
Department of Mechanical Engineering, Pragati Engineering College, Chennai Campus,  
Vandalur-Kelambakkam Road, Surampalem, Tamil Nadu 533437, India

© The Author(s), under exclusive license to Springer Nature Singapore Pte Ltd. 2022  
G. S. V. L. Narasimham et al. (eds.), *Innovations in Mechanical Engineering*,  
Lecture Notes in Mechanical Engineering,  
[https://doi.org/10.1007/978-981-16-7282-8\\_1](https://doi.org/10.1007/978-981-16-7282-8_1)

of technology, better tools are available for the analysis of any engineering problem. The stress and strain developed in the elastic plastic region have been studied, and mathematical models have been developed [1]. Attempts have been made to develop analytical solutions for discs with variable thickness. The thickness is varied hyperbolically, parabolically along the radius, and the subsequent parametric study has been carried out subjecting it to different boundary conditions [2–5]. Various aspects of 2D axisymmetric analysis of the disc have been studied. The study is carried out by applying various boundary conditions, and the subsequent stress developed was studied [6–13]. The study gave a more realistic working of a turbine in actual operating conditions. Turbine discs are mounted on shafts. Turbine discs are manufactured with a circular hole for the mounting of the shaft. A design is studied with non-circular bolt clearance hole profile to check the stress distribution and to study the effect of stress by varying the profile of the hole [14]. Optimization of the design is the next important step in the analysis in order to minimize the stress concentration factor in the disc. Various optimisation techniques have been used with ANSYS to minimize the stress distribution [14–16]. Modal analysis has been of utmost importance. Many studies have been undertaken to study the effects of assembled components in the turbine [17–19]. This paper attempts to find out the mode shapes of the disc rotating at high speeds.

## 2 Description of Disc

### 2.1 Disc Geometry

Figures 1 and 2 describe the geometry of the disc. The disc thickness varies from 24 mm at centre to 12 mm at the periphery. The outer diameter is 190 mm. The elliptical hole of major axis of 93 mm and minor axis of 91 mm is considered [6].

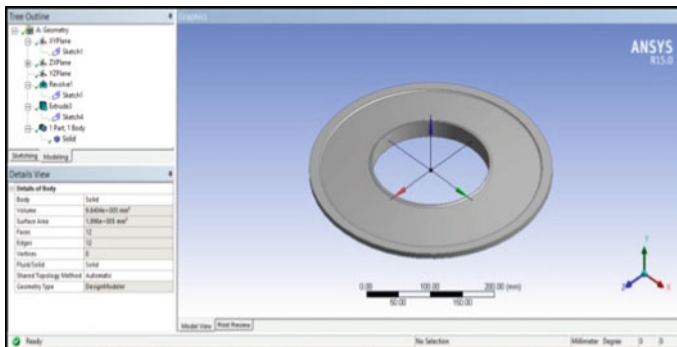
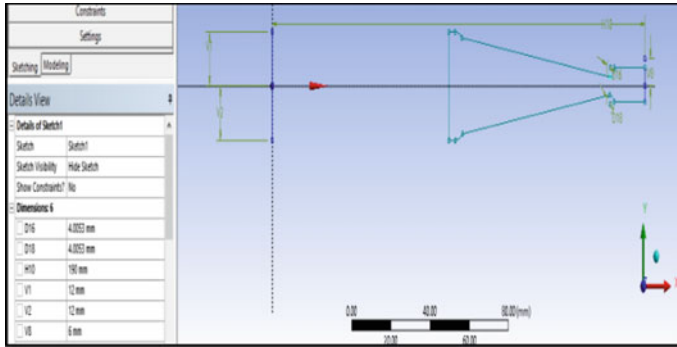


Fig. 1 3D model



**Fig. 2** Dimensions of the disc in mm

## 2.2 *Disc Material*

Two super alloys of nickel NIMONIC 105 and NIMONIC 901 were selected. Young's modulus and Poisson's ratio are assumed to be linear.

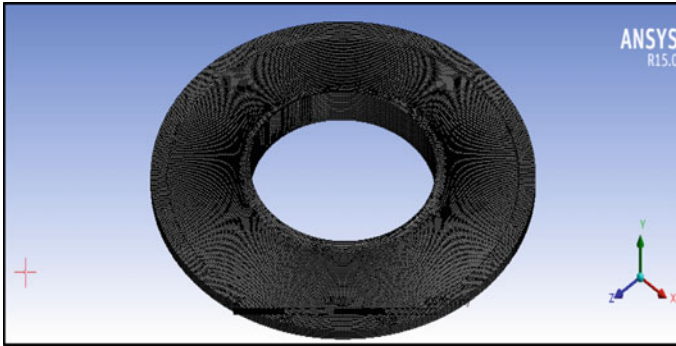
## 2.3 *Disc Operating Parameters*

In the FE simulation, the shrink fit load arising due the mounting of the disc on to the shaft is considered as contact pressure at the inner surface of the disc. Due to the blades being mounted on the periphery of the disc and blades conducting heat to the disc and the shaft, these are also considered in the analysis as blade load and thermal loads.

# 3 **Finite Element Modelling**

## 3.1 *Mesh of Model*

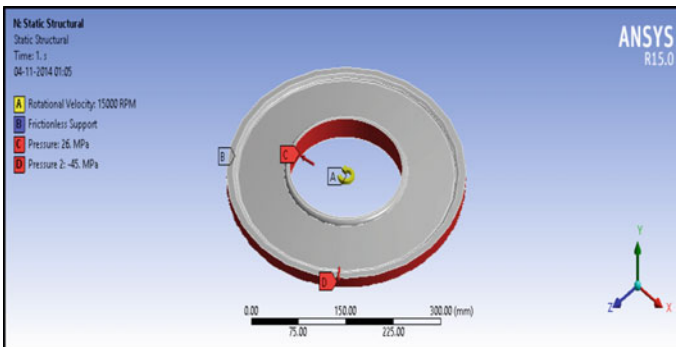
The analysis is carried out using ANSYS Workbench [20]. The disc is modelled as a 3D disc and meshed using SOLID186 which is a 3D six node element exhibiting a quadratic displacement behaviour. Pyr13 is a pyramidal variant of SOLID186 used for interfacing purposes wherever both hexahedral and tetrahedral mesh elements are required (Fig. 3).



**Fig. 3** Meshed model

### 3.2 Loads and Boundary Conditions

The major loads on the disc considered are (a) shrink fit load, (b) blade load, (c) thermal load, (d) rotational load and (e) combined loading (combination of loads a–d). The shrink fit load is represented as a pressure of 26 MPa at the inner surface of the disc and the blade load as a pressure of 45 MPa at the outer surface of the disc [7]. The temperature of 800 °C is applied at the outer surface and 500 °C at the hub. The rotational velocity of 15,000 rpm [6] is applied about Y-axis which results in a centrifugal force equivalent to the rotational load. Perpendicular motion of the disc is constrained by use of frictionless support (Fig. 4).



**Fig. 4** Loads and boundary conditions applied

## 4 Results and Discussions

### 4.1 Analysis

ANSYS 15 was used to obtain stress distribution for the load cases (a)–(d) mentioned earlier. The von Mises and radial stress distribution is obtained considering loading individually and in combination. The following results are for the material NIMONIC 105.

#### **Load case (a) Shrink fit load for NIMONIC 105**

For the shrink fit load, the radial stress developed is 14.78 MPa located at the inner surface, and the equivalent stress found is 106.85 MPa occurring at the hub of the disc. Figure 5a shows the radial stress distribution, and Fig. 5b shows the von Mises stress distribution.

#### **Load case (b) Blade load for NIMONIC 105**

For the blade load, the radial stress developed is 123.25 MPa located at the inner surface, and the equivalent stress found is 166.27 MPa occurring at the hub of the disc. Figure 6a shows the radial stress distribution, and Fig. 6b shows the von Mises stress distribution.

#### **Load case (c) Rotational load for NIMONIC 105**

For the rotational load, the radial stress developed is 118.64 MPa located at the inner surface, and the equivalent stress found is 510.58 MPa occurring at the hub of the disc. Figure 7a shows the radial stress distribution, and Fig. 7b shows the von Mises stress distribution.

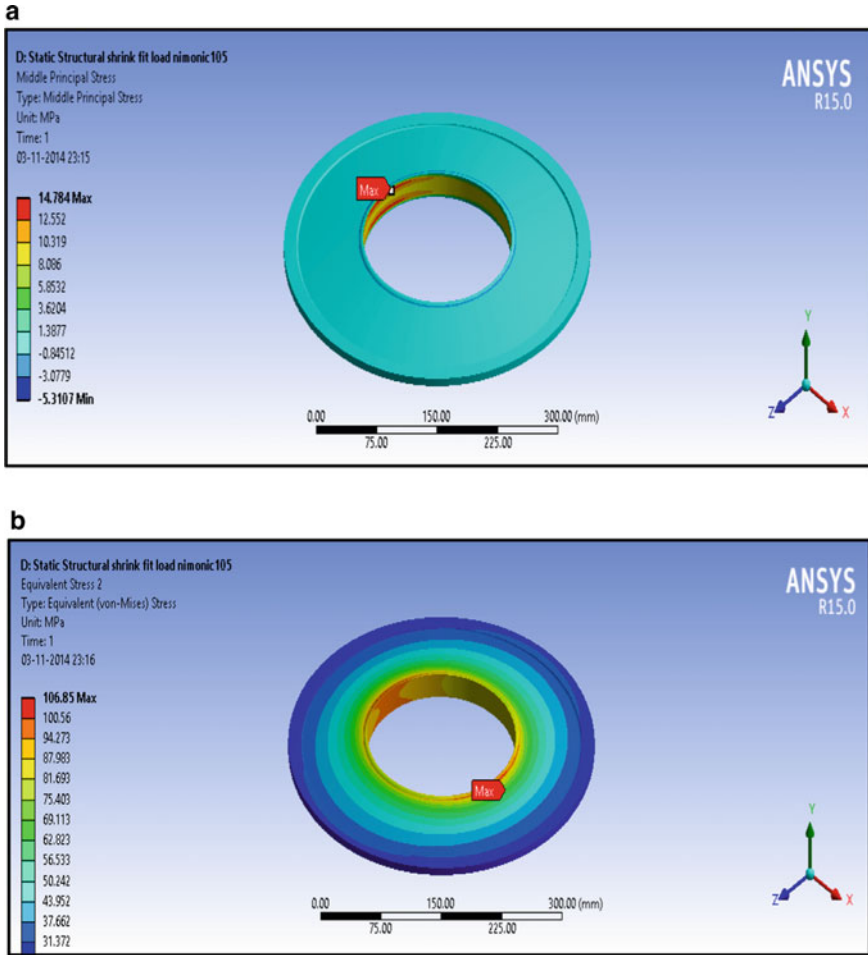
#### **Load case (d) Thermal load for NIMONIC 105**

For the rotational load, the radial stress developed is 66.858 MPa located at the inner surface, and the equivalent stress found is 602.56 MPa occurring at the hub of the disc. Figure 8a shows the radial stress distribution, and Fig. 8b shows the von Mises stress distribution.

#### **Load case (e) Combined load for NIMONIC 901**

For the combined load, the radial stress developed is 264.52 MPa located at the middle, and the equivalent stress found is 1070.7 MPa occurring at the hub of the disc (Fig. 9).





**Fig. 5** a Radial stress distribution for shrink fit load. b Equivalent stress distribution for shrink fit load

### 4.2 Modal Analysis

Modal analysis has been carried out for the frequency range 1000–3000 Hz to find the natural frequencies of the rotating disc to prevent resonance. Figure 10a, b show the natural frequencies at the operating speed of 15,000 rpm for NIMONIC 105 and NIMONIC 901, respectively. The stresses for nimonic 105 under different load cases are presented in Table 1.

From the results presented in Table 1, it can be seen that the maximum load is contributed by the thermal load for NIMONIC105. It contributes 50% of the combined load. From Table 2, it can be seen that maximum load in NIMONIC 901 is

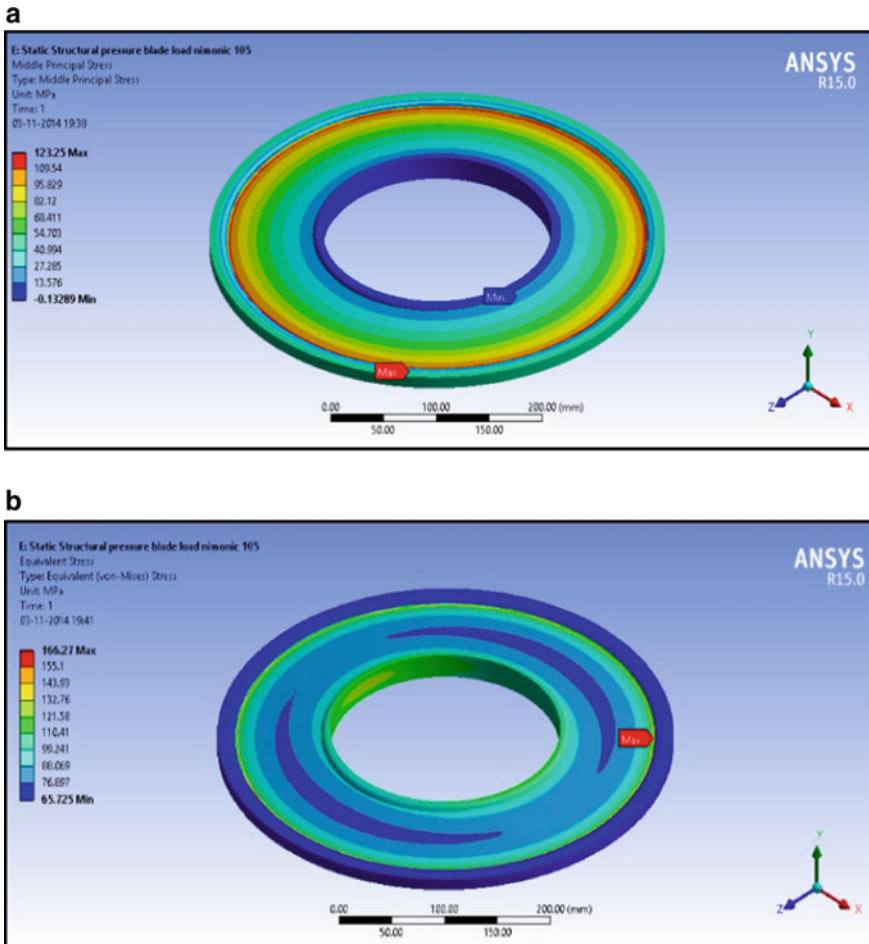
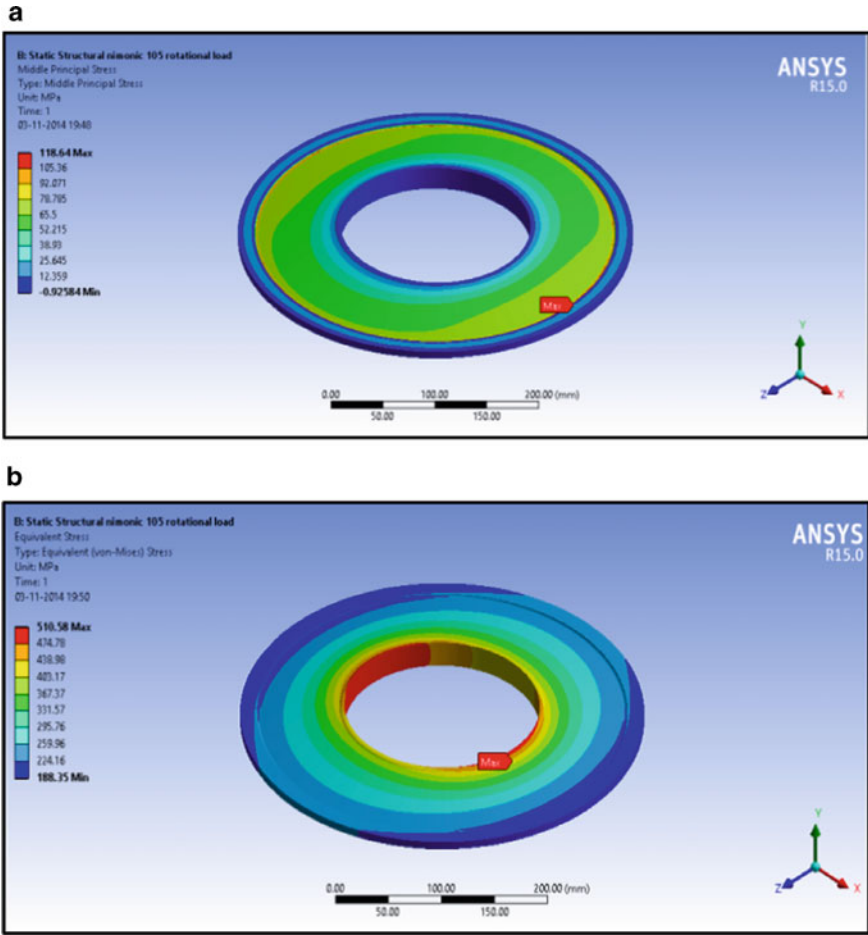


Fig. 6 a Radial stress distribution for blade load. b Equivalent stress distribution for blade load

contributed by the rotational loading. It can be concluded that thermal and rotational loads contribute to most of the stresses in the disc. It can be seen that NIMONIC 901 develops higher stresses when compared to NIMONIC 105. The modal analysis gives the maximum natural frequencies of 2809.2 Hz for NIMONIC 105 and 2493.3 Hz for NIMONIC 901, which helps in avoiding resonance.

### 4.3 Optimization

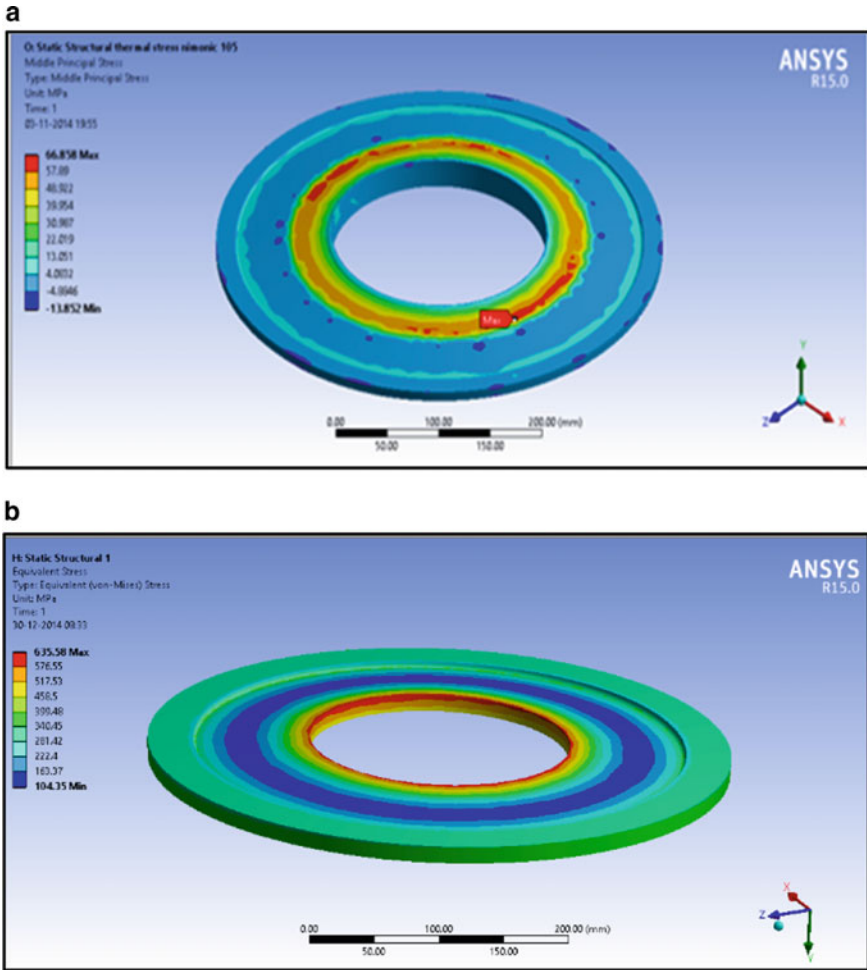
Optimization of elliptical hole geometry (a/b) has been carried out to reduce the stress distribution in the disc. Optimization is done based on a dimensional-less ratio



**Fig. 7 a** Radial stress distribution for rotational load. **b** Equivalent stress distribution for rotational load

$a/b$  of the ellipse in which  $a = 91$  mm is the semi-minor axis and  $b = 93$  mm is the semi-major of the ellipse. In this paper, the optimization is carried out in terms of the non-dimensionless ratio  $a/b$ .

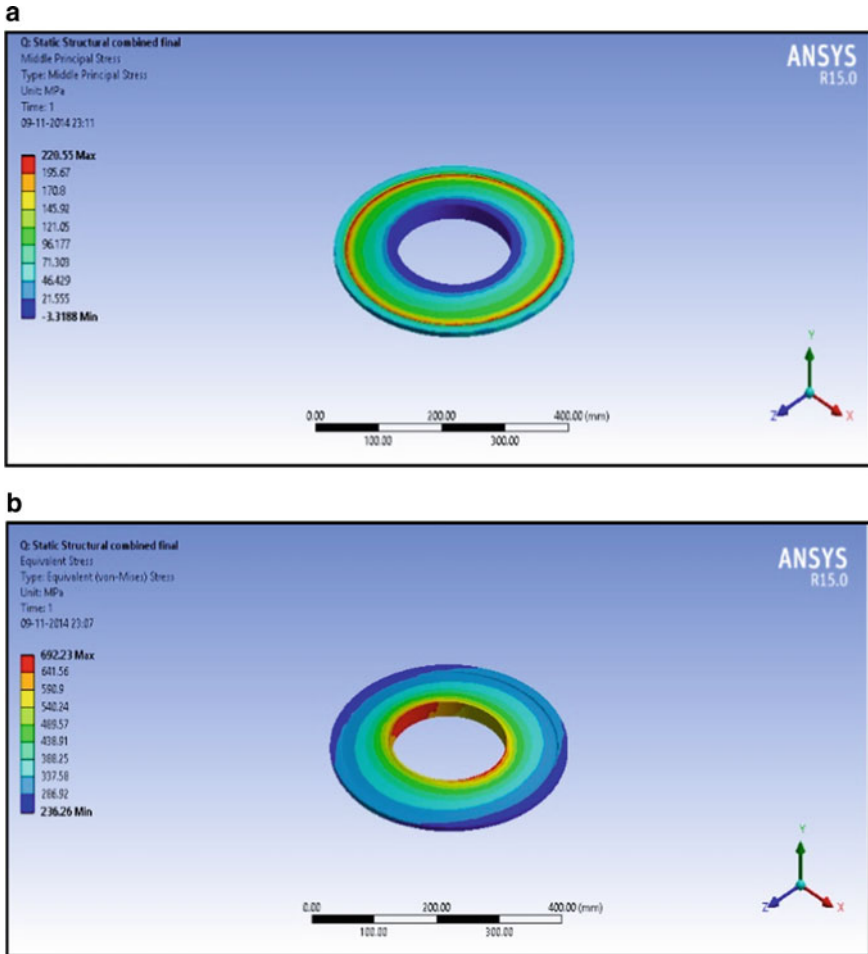
From Fig. 11, it can be seen that as the  $a/b$  ratio decreases, the value of the equivalent stress also decreases and reaches a lowest value at the ratio 1.01, and with further increase in the ratio, the stress value starts to increase. Thus, it can be seen that at the ratio of 1.01, the stresses induced will be less, and hence, the model is optimized at that value. The value of 1.01 is same for both the materials.



**Fig. 8** **a** Radial stress distribution for thermal load. **b** Equivalent stress distribution for thermal load

## 5 Conclusion

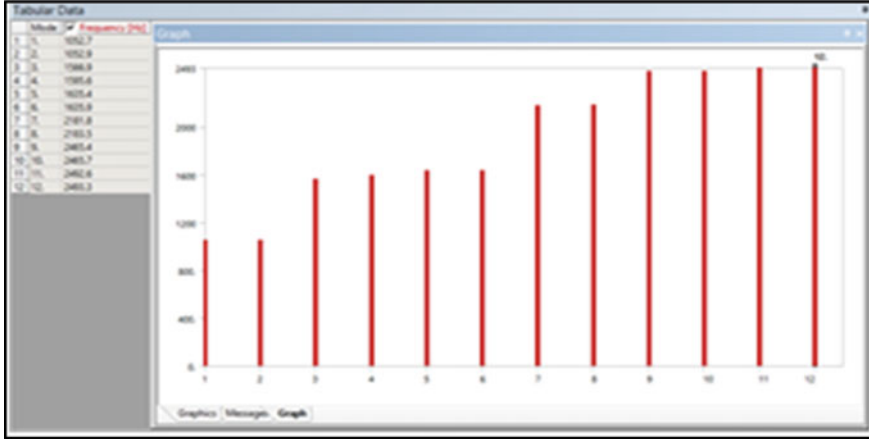
This paper uses FEA as a tool to study the effects of different type of loading on a turbine disc. This method proves to be a very effective method as the closed form solution is not available for complex loadings and geometry. As disc is an integral part of the turbine, necessary precaution should be taken to prevent failure. Various loadings have been taken into account including the shrink fit load, blade load, thermal load and the rotational load. Modal analysis was under taken in order to find out the natural frequencies at the operating speed. Static structural analysis was carried along with modal analysis.



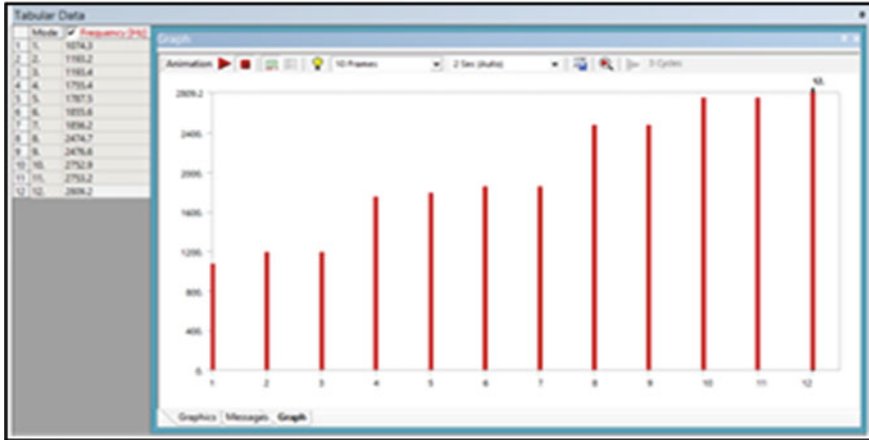
**Fig. 9 a** Radial stress distribution for combined load. **b** Equivalent stress distribution for combined load

It was seen that among the two materials chosen for the study, NIMONIC 105 develops lesser stresses than NIMONIC 901. It can be concluded that NIMONIC 105 is better material for the manufacturing of the disc. The optimization is carried out, and it was found that any ratio around 1.01 is preferable as the stress developed is the least. Hence, an optimal design should be considered keeping in mind the application and the cost.

**a**



**b**



**Fig. 10** a Natural frequencies for NIMONIC 105. b Natural frequencies for NIMONIC 901

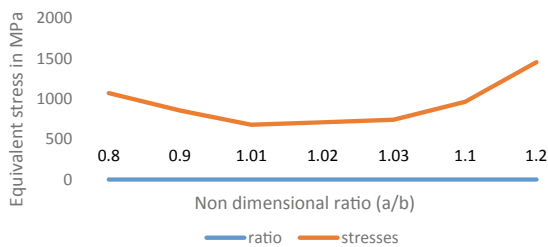
**Table 1** The stresses for nimonic 105 under different load cases

Load case	NIMONIC 105		
	Loading	Stress (MPa)	Radial stress (MPa)
a	Shrink fit	106.85	14.78
b	Blade load	166.27	123.25
c	Rotational load	510.58	118.64
d	Thermal	635.58	66.858
e	Combined	692.23	220.55

**Table 2** Stresses for nimonic 901 under different load cases

Load case	NIMONIC 901		
	Loading	Equivalent stress (MPa)	Radial stress (MPa)
a	Shrink fit	110.83	22.109
b	Blade load	127.77	192.68
c	Rotational load	554.29	182.23
d	Thermal	372.59	81.65
e	Combined	773.39	359.22

**Fig. 11** Variation of stress distribution versus non-dimensional ratio (a/b)



## References

1. Eraslan AN (2003) Elastic–plastic deformations of rotating variable thickness annular disks with free, pressurized and radially constrained boundary conditions. *Int J Mech Sci* 45:643–667
2. Eraslan AN, Orcan Y (2004) A parametric analysis of rotating variable thickness elastoplastic annular disks subjected to pressurized and radially constrained boundary conditions. *Turkish J Eng Environ Sci* 28
3. Zamani SA, Tahmasbpour SR, Asadi OB, Hosseinzadeh M (2014) Numerical simulation and stress analytical solution of rotating disc in high speed. *Indian J Sci Res* 3(1):124–136
4. Maruthi BH, Venkatarama Reddy M, Channakeshavalu K (2012) Finite element formulation for over speed and burst margin limits in aero-engine disc. *Int J Soft Comput Eng (IJSCE)* 2(3). ISSN: 2231-2307
5. Elhefny A, Liang G (2013) Stress and deformation of rocket gas turbine disc under different loads using finite element modelling. *Propul Power Res* 2(1):38–49
6. Rosyid A, Es-Saheb M, Yahia FB (2014) Stress analysis of a non homogeneous rotating disc with arbitrarily varying thickness using FEA. *Res J Appl Sci Eng Technol* 7(15):3114–3125
7. Elhefny A, Guozhu L Stress analysis of rotating disc with non uniform thickness using finite element modelling. In: 2012 international conference on engineering and technology (ICET)
8. Rao LB, Rao CK (2014) Frequency analysis of annular plates with inner and outer edges elastically restrained and resting on Winkler foundation. *Int J Mech Sci* 81(4):184–194
9. Bhaskara Rao L, Kameswara Rao C (2011) Fundamental buckling of annular plates with elastically restrained guided edges against translation. *Mech Des Struct Mach* 39(4):409–419
10. Bhaskara Rao L, Kameswara Rao C (2015) Analysis of vibration natural frequencies of rotationally restrained and simply supported circular plate with weakened interior circle due to an angular crack. *Strength Mater* 47(6):859–869
11. Rao LB, Rao CK (2016) Frequency analysis of annular plates having a small core and guided edges at both inner and outer boundaries. *J Solid Mech* 8(1):168–174
12. Rao LB, Rao CK (2016) An exact frequency analysis of annular plates with small core having elastically restrained outer edge and sliding inner edge. *Appl Acoust* 109:69–81

13. Bhaskara Rao L, Kameswara Rao C (2012) Buckling of circular plates with an internal elastic ring support and outer edge restrained against translation. *J Eng Sci Technol* 7(3):393–407
14. Qiuren C, Haiding G, Chao Z, Xiaogang L (2014) Structural optimization of the uniaxial symmetry non-circular bolt clearance hole on the turbine disk, Jiangsu Province Key Laboratory of Aerospace Power System, Nanjing University of Aeronautics and Astronautics, Nanjing (In press)
15. Jahed BF, Bidabadi J (2005) Minimum weight design of inhomogeneous rotating discs. *Int J Pressure Vessels Piping* 82:35–41
16. Mohan SC, Maiti DK (2013) Structural optimisation of rotating disk using response surface equation and genetic algorithm. *Int J Comput Methods Eng Sci Mech* 14:124–132
17. Srinivasan AV (1984) Vibrations of a bladed disk assemblies—a selected survey (survey paper). *J Vib Acoust* 106(2):165–168
18. Vullo V, Vivio F (2008) Elastic stress analysis of non-linear variable thickness rotating disks subjected to thermal load and having variable density along the radius. *Int J Solids Struct* 45:5337–5355
19. Ewins DJ (1973) Vibration characteristics of bladed disc assemblies. *J Mech Eng Sci* 15(3):165–186
20. ANSYS workbench version 15



# Design and Analysis of Anti-intrusion Beams for Car Door



Jaimin Panchal , Keval Bhavsar , and Dharmik Gohel

**Abstract** Passenger safety is the most important concern while designing an automobile. Most deadly accidents occur when the car gets hit from the front or the side. One of the safety measures to reduce the impact of such accidents is anti-intrusion beams, and they are introduced in the profile of the car door for absorbing the energies when something hits the car door with a huge impact. This work focuses on the design and analysis of anti-intrusion beams. Here, five different types of cross sections of beams and car door models are tested for impact, and all the designs are made in SolidWorks 2017. To check the reliability of different cross sections, an explicit dynamic analysis of these beams is done in ANSYS 2019 R2. The material used for the analysis of beams is aluminum 2024-T3. The effectiveness of the result is then checked on the car door by doing a side impact simulation against the steel column.

**Keywords** Explicit dynamic analysis · Anti-intrusion beams · Side impact · Computer-aided design (CAD) · Safety · Deadly accidents

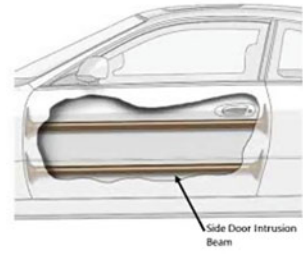
## 1 Introduction

An anti-intrusion beam (Fig. 1) is a beam used for absorbing impact during a collision with another car or a rigid body like a column. During these impacts, it is dangerous for the passenger and drivers if not designed properly. For the best absorption of impact, nonlinear materials are widely used right now due to their high ductility. It also depends upon the type of cross section. Cross sections that are initially used are circular-hollow made up of high-strength steel. Here, five types of cross sections are analyzed (Figs. 2, 3, 4, 5 and 6) and checked via explicit dynamic tests for their safety. Material for beams will be aluminum 2024-T3, the column used for the collision is made up of structural steel, and magnesium alloy is used for the car door (Fig. 7).

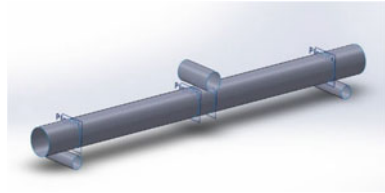
---

J. Panchal (✉) · K. Bhavsar · D. Gohel  
Department of Mechanical Engineering, School of Technology, PDEU, Gandhinagar, Gujarat,  
India

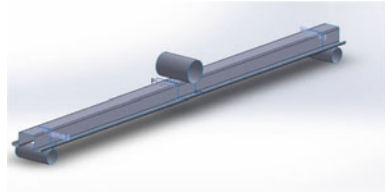
**Fig. 1** Anti-intrusion beam  
[1]



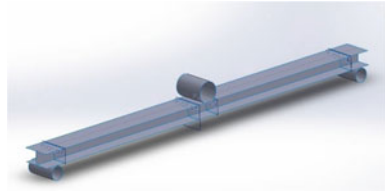
**Fig. 2** O-section



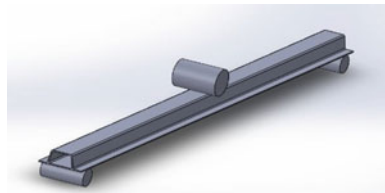
**Fig. 3** N-section



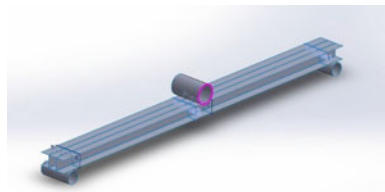
**Fig. 4** I section



**Fig. 5** D section



**Fig. 6** II section



**Fig. 7** Door with pole and beam



Nichit and Battu [1] developed different finite element analysis (FEA) models with varying cross section to perform a three-point bending test on them. The simulation of these models is done using LS-DYNA. All the cross sections are evaluated and compared based on maximum bending force. Lastly, the optimal design of the side intrusion beam which is performing best is selected among them. Nassiopoulos and Njuguna [2] studied dynamic characteristics of the finite element model of a rally car. The model had comprised of the entire vehicle structure and 241 sections including the engines, tires, and the suspension members with four different element types and seven material models. Structural parts are modeled with low carbon steel, and tires are modeled with Blatz-Ko rubber material. They presented that reinforcing the car floor with transverse tubes can reduce the deformation and maintain the weight of the car. After simulations, their studies proved that the side impact of rally cars has a long way from being solved. Teng et al. [3] developed a full-scale finite element model that utilized LS-DYNA for finding the impact energy absorption of side door beams. Simulations are done on displacement analysis, intrusion measurement of the door, and injury analysis of dummy. They concluded that side door beams have the immersive potential for reducing passenger injuries. Patil [4] presented a comparative study of three different cross sections of the anti-intrusion beams with three materials. FEA software has been used to study and compare these cross sections and materials. Lastly, optimal design has been proposed using the Taguchi method which has high absorption capacity and resistance force which is then validated with the experimental setup. Raghuveer [5] modeled a car door in Pro Engineer with five different materials and simulated a dynamic analysis at different speeds. Materials also included composite materials so the overall weight of the car door is reduced. Using composite materials increased the impact of energy absorption but the cost factor is increased. Finally, it is concluded that the FEA results matched with the theoretical calculations. Yoon et al. [6] developed a one-body door impact beam (SPFC1180) with advanced high-strength steel to improve impact energy absorption. A finite element bending model is created to conduct a test on several designs with the same internal area in ANSYS software which is then validated in LS-DYNA software. Results indicate that SPFC1180 can exhibit an equivalent reaction force with reduced cost and weight when compared with a pipe-type door beam. Karagöz [7] studied various optimization techniques to improve the crash performance of thin-walled structures. Objective functions are decided to be weight, and energy absorption is selected to be a constraint. The performance of all recent optimization

techniques is tested to find the optimal thin-walled tube design. Bisagni [8] developed a finite element model using nonlinear, explicit dynamic code LS-DYNA for investigations of side, and steering column impact on formula one race car. The results of the experimental and numerical study indicate that composite materials used for manufacturing F-1 cars show a high value of specific energy absorbed and crash load efficiency. Dhaneesh et al. [9] presented a modified design of a car door impact beam and used high-strength steel with more yield stress than low-strength steel. The modified design performed well enough to reduce intrusion on the side door to protect the passenger. Pavan et al. [10] designed the side impact bars of car door considering various mechanical properties like strength, ductility, hardness, impact resistance, and fracture toughness. The design is done in CREO elements, impacts are analyzed in LS-DYNA, and meshing HyperWorks technology is used. Different cross-sectional views like Hat shape, M-shape are considered among which in results it is concluded that Hat shape cross section had the highest peak crush resistance. Nemani et al. [11] presented three different cross sections of side impact beam. The testing is done with the help of a three-point bending test on FEA developed models. The models are examined with the help of the LS-DYNA element code from which the energy absorption parameter is compared. Based on the Taguchi method, the optimal design is selected among others which are the best performing. Krishana et al. [12] did a study on selecting a better cross section for an SUV vehicle. Comparison is done between an actual beam used and proposed cross section with a pole test as per FMVSS 214. A three-point bending test of proposed rectangular and circular cross sections of the same materials is done with FEA analysis. Finally, a conclusion is made that rectangular cross section is performing significantly better at absorbing the bending force. Pawar et al. [13] to provide high specific strength and high impact energy absorbing as well as reducing the overall weight designed a side impact beam with thermoplastic glass epoxy fiber material. The finite element model is developed to evaluate the design and validate with the FMVSS 214 guidelines for passenger cars. Ponnadai [14] developed side impact beam with various cross sections and with three different materials. FEA model is developed in ANSYS workbench to find displacement, reaction force and absorption energy. After selecting the best beam, it is fitted inside the door and analysis is done with the LS-DYNA PREPOST code.

After doing the literature review, it is found that not many researchers have done the explicit dynamic analysis for testing, as the side impact will be done in the time-variable zone, it will greatly affect the results than static structural analysis. Although total deformation and directional deformation have been performed, the stress concentration factor which will affect side impact test vastly has not been performed widely. Many researchers have used high-strength steels as a material of an anti-intrusion beam, which makes the car door heavy. Instead of which, nonlinear materials like aluminum alloy 2024-T3 should be analyzed as they have a better absorption capacity than them.

This paper shows five different cross sections will be designed in SolidWorks 2017. After that quasi-static analysis of these cross sections will be done as a three-point bending test which gives the best cross section among them. The explicit

dynamic analysis will be done on the best cross section of a beam by putting it inside the actual car door and doing a side impact of the car door with the steel column.

## 2 Bharat New Vehicle Safety Assessment Program

The Bharat New Vehicle Safety Assessment Program or BNVSAP utilizes a star framework to rate the security of a vehicle. It will have the tests in four stages in testing laboratories. The new vehicles that will turn out should experience a frontal impact, back impact, and side impact tests at 56 km/h and common security tests. This program is important as previously car manufacturers are following Global NCAP and FMVSS number 214 for researches [15]. In this study, BNVSAP norms are used for quasi-static analysis.

## 3 Design

The length and thickness of various beams are kept constant so that we can compare them on variable cross sections. Also, three small cylinders are introduced for performing the three-point bending test on the materials. The door is designed by taking actual measurements from the car, and the steel column is placed beside the door for impact testing. The scaled dimension of all the beams remains constant; i.e., the beam has a width of 66 mm, thickness of 2 mm, and length of 900 mm.

### 3.1 Material Properties

- The beam used in cars is made of circular cross section and made up of high-strength steels and some cases stainless steel 304.
- The main purpose of beam is to deform and allow itself to absorb all the load that is transferred to it from the door outer body.
- The material that can sustain high impact and deform freely within the allowable range is nonlinear materials
- The only reason the modulus of elasticity of structural steel is taken so high is to make it rigid because we do not want it to deform or generate more than required stress. The materials used in this project are shown in Table 1.

**Table 1** Material properties

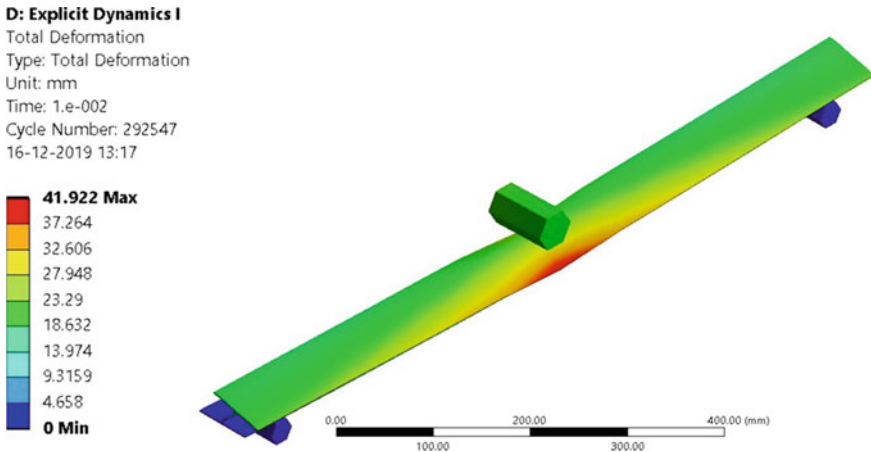
Material/Property	Aluminum 2021—T3	Structural steel	Magnesium alloy
Elastic modulus, N/mm <sup>2</sup>	73,100	2E+08	45,000
Poisson's ratio	0.33	0.30	0.35
Density, Kg/m <sup>3</sup>	2780	7850	1800
Used location	Beam	Rigid column	Door

## 4 Result and Discussion

Here, the reason for using the three-point bending test is to check whether this cross section can withstand the impact at high velocity. Total deformation analysis and von Mises stress analysis are performed on cross sections which are in ANSYS 2019 R2.

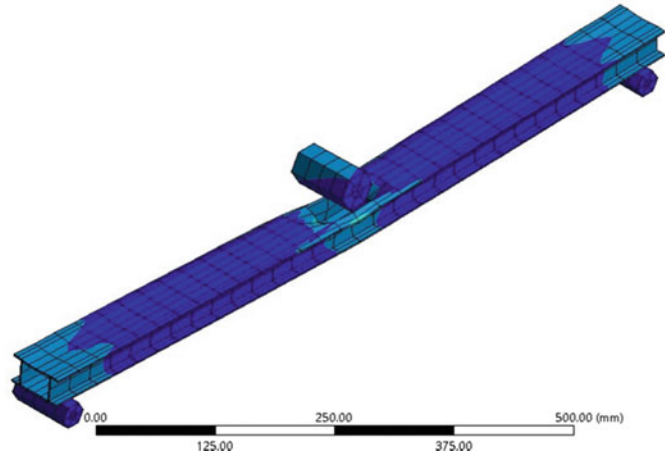
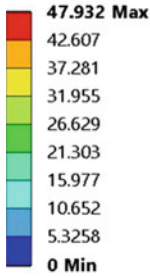
### 4.1 Total Deformation Analysis

The total maximum deformation in order from high to low is as follows: II Section (Fig. 9) > I Section (Fig. 8) > N Section (Fig. 10) > D Section (Fig. 11) > O Section (Fig. 12). The objective this time is different, the deformation should not be that much that it will fail, and it should not be in a rigid state where it is deformed less. As we know the rule of material science, the more deformation will allow the section to absorb more energy at certain prices. The results of the simulation are as below:



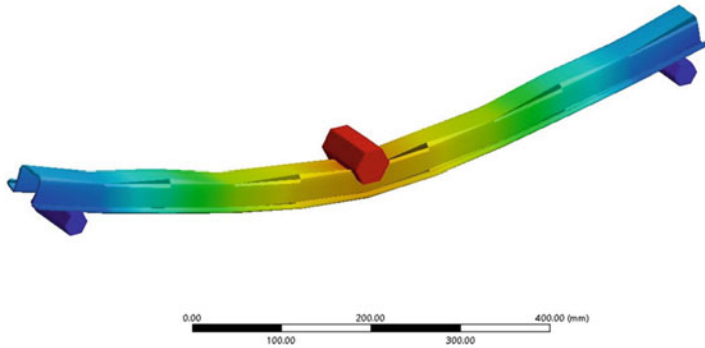
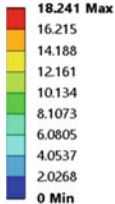
**Fig. 8** I section (41.92 mm) failed

**E: Explicit Dynamics II**  
Total Deformation  
Type: Total Deformation  
Unit: mm  
Time: 1.e-002  
Cycle Number: 94329  
16-12-2019 13:19



**Fig. 9** II section (47.93 mm) failed

**C: Explicit Dynamics \_n**  
Total Deformation  
Type: Total Deformation  
Unit: mm  
Time: 1.e-003  
Cycle Number: 754021  
16-12-2019 13:13



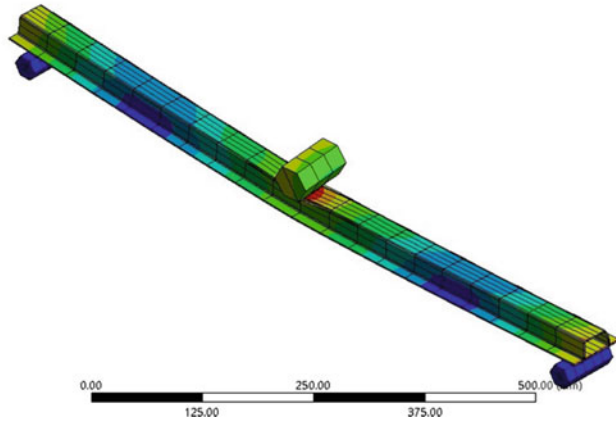
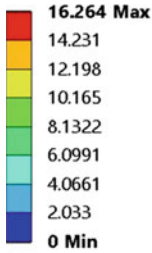
**Fig. 10** N section (18.241 mm)

Here, during testing, it is observed that only three sections are able to withstand high-speed impact and other sections are broken or deformed beyond the acceptable range. Hence, N Section is the better section to be able to absorb so much energy.

### 4.2 Von Mises Stress Analysis

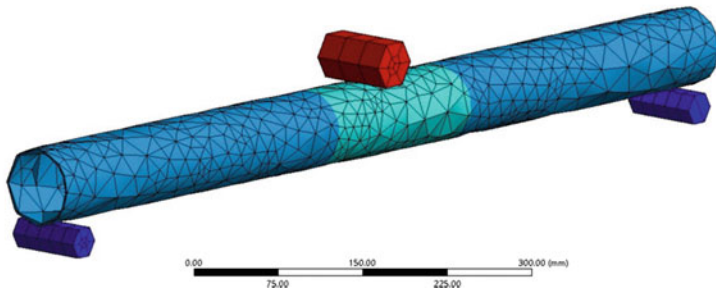
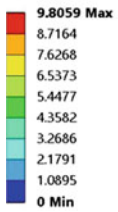
Results of equivalent stress show that total maximum stress induced in descending order is as follows: N Section (Fig. 15) > D Section (Fig. 16) > II Section (Fig. 14) > O Section (Fig. 17) > I Section (Fig. 13). Here the main reason for making a D Section is just because it is able to overcome difficulties that both I and II Sections

**J: new sample experimental**  
Total Deformation  
Type: Total Deformation  
Unit: mm  
Time: 8.e-003  
Cycle Number: 426303  
16-12-2019 13:21



**Fig. 11** D section (16.265 mm)

**I: Explicit DynamicsO**  
Total Deformation  
Type: Total Deformation  
Unit: mm  
Time: 1.e-003  
Cycle Number: 17637  
16-12-2019 13:20



**Fig. 12** O section (9.805 mm)

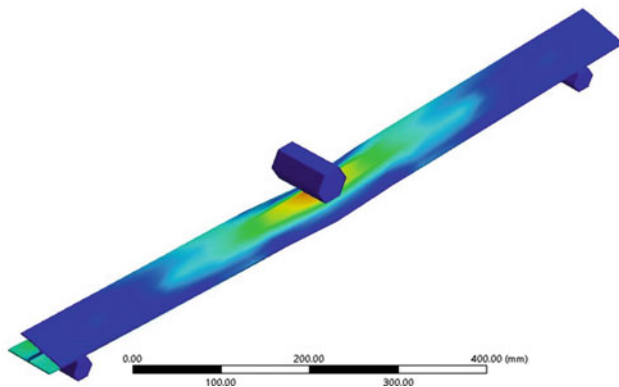
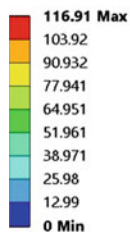
are facing. Also, as we can see N Section can deform well and can generate a large amount of equivalent stress. Still within the fatigue limit of alloy that is used to make this beam.

From Table 2, max deformation is seen in the II Section but, also during the simulation it is seen that design is failing when it collided with a small column of 45 mm radius. Similar results are seen in the D Section. I Section failed and O Section is so rigid, that it deformed only 8 mm which is dangerous. Just from deformation only we can conclude that N Section is suitable for absorbing more load energy. Also, it is safe as 331.31 MPa is well within the limit of failure criteria.



**D: Explicit Dynamics I**

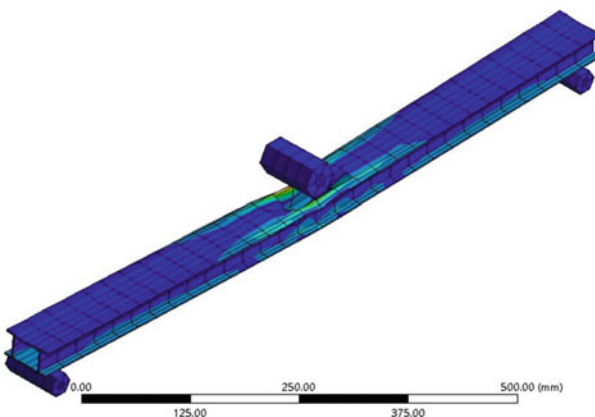
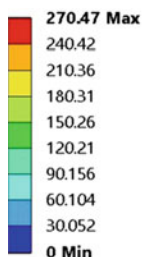
Equivalent Stress  
 Type: Equivalent (von-Mises) Stress  
 Unit: MPa  
 Time: 1.e-002  
 Cycle Number: 292547  
 16-12-2019 13:17



**Fig. 13** I section (116.91 MPa) failed

**E: Explicit Dynamics II**

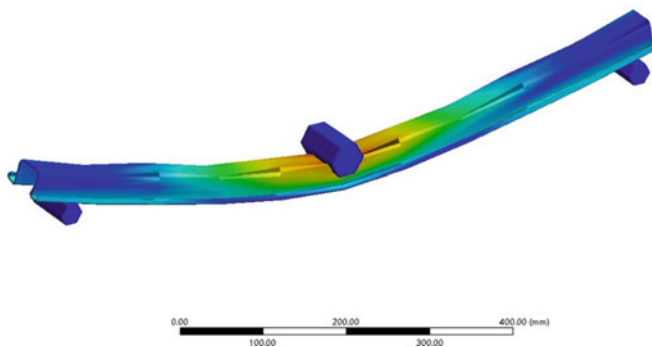
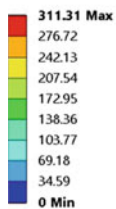
Equivalent Stress  
 Type: Equivalent (von-Mises) Stress  
 Unit: MPa  
 Time: 1.e-002  
 Cycle Number: 94329  
 16-12-2019 13:19



**Fig. 14** II section (270.47 MPa) failed

**C: Explicit Dynamics\_n**

Equivalent Stress  
 Type: Equivalent (von-Mises) Stress  
 Unit: MPa  
 Time: 1.e-003  
 Cycle Number: 754021  
 16-12-2019 13:13



**Fig. 15** N section (311.31 MPa)

**J: new sample experimental**

Equivalent Stress

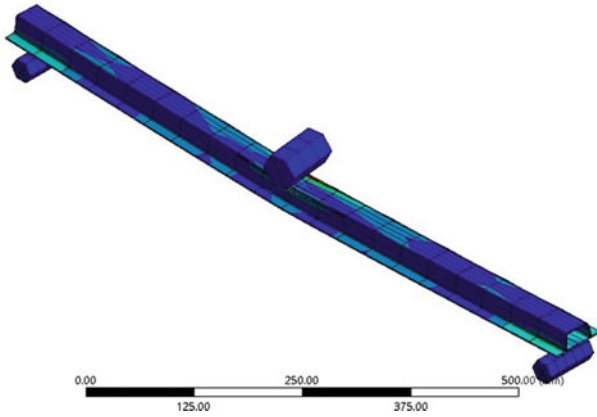
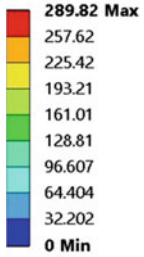
Type: Equivalent (von-Mises) Stress

Unit: MPa

Time: 1.e-002

Cycle Number: 532734

16-12-2019 13:22



**Fig. 16** D section (289.82 MPa)

**I: Explicit DynamicsO**

Equivalent Stress

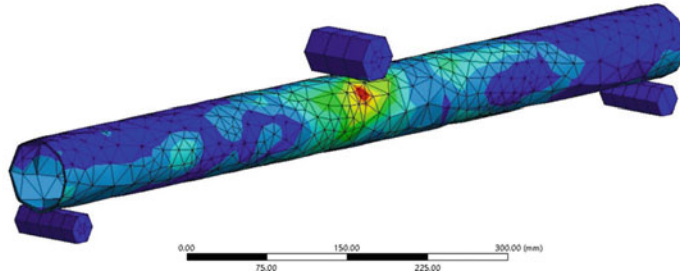
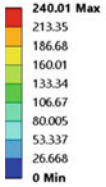
Type: Equivalent (von-Mises) Stress

Unit: MPa

Time: 1.e-003

Cycle Number: 17637

16-12-2019 13:20



**Fig. 17** O section (240.01 MPa)

**Table 2** Comparison of quasi-static results obtained from different cross sections

Cross section	Total deformation (mm)	Equivalent stress (MPa)
N section	18.24	311.31
O section	9.8	240.01
I section	41.92	116.91
II section	47.93	270.47
D section	16.26	289.92

### 4.3 Side Impact on Car Door

Here, after analyzing the different results, N Section is selected as it is performing best it has the allowable amount of deformation and von Mises stress generated is in the limit. After inserting this section inside the car door, impact analysis is done in the explicit dynamic module. To check the extremities, the simulation is performed at 90 m/s which is way higher than the prescribed safety limit, the explicit door collided with the pole of 300 mm diameter made up of modified structural steel [14, 15]. The von Mises stress generation and deformation in the door without beam are shown in Figs. 18, 20 and with beam are shown in Figs. 19, 21.

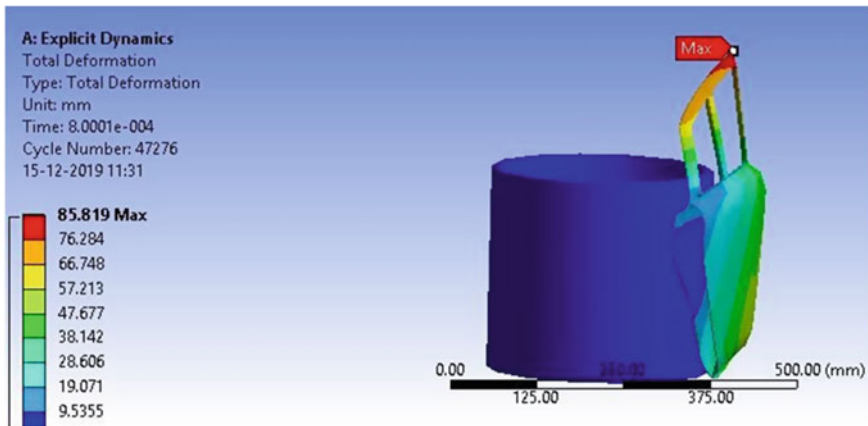


Fig. 18 Door without beam (deformation)

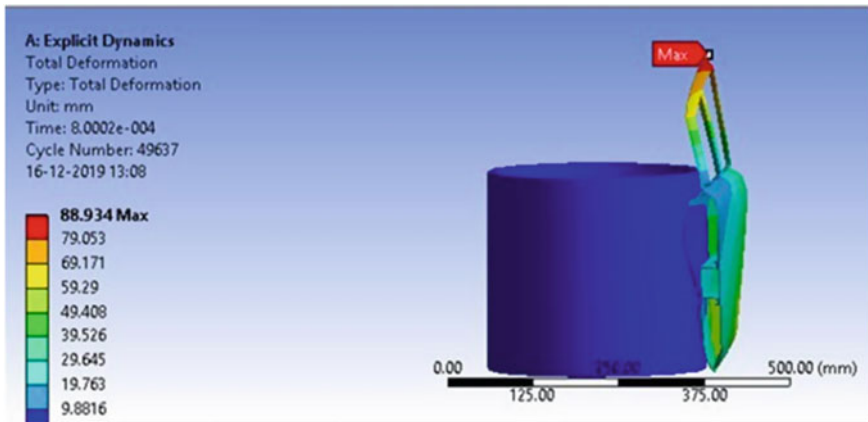


Fig. 19 Door with the beam (deformation)

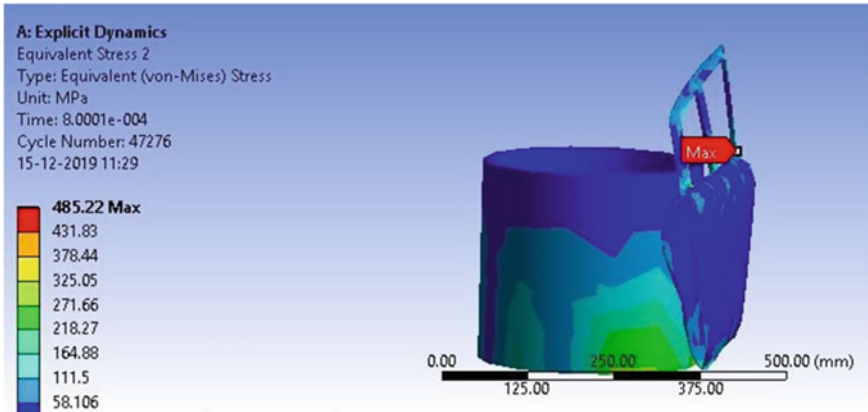


Fig. 20 Door without the beam (von Mises stress)

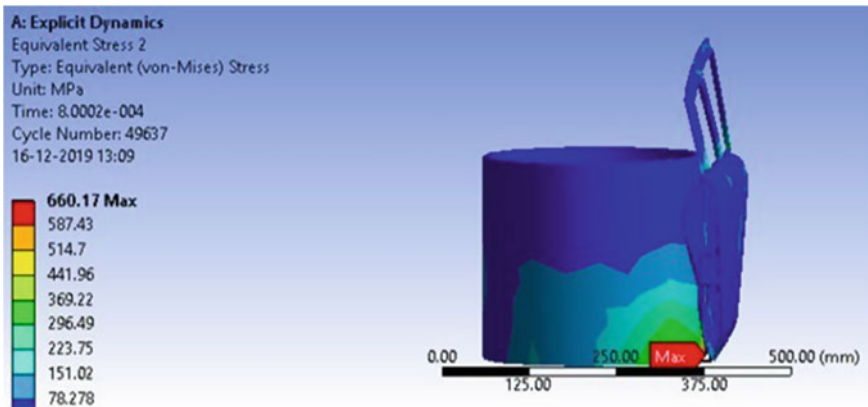


Fig. 21 Door with the beam (von Mises stress)

From the above results, it is observed that, when the car door collided with the steel column, the von Mises stress generated inside the door without beam is 164 MPa while door with beam is roughly around 90 MPa. The deformation of the car door without beam is found to be 85 mm while with beam is 89 mm. Even though the speed of 90 m/s is used, the equivalent stress generated is well within the permissible limit.

## 5 Conclusion

The test is done on five different cross sections: O, I, II, N, D Sections. After doing the analysis, the N Section made of aluminum 2024-T3 is found to be the best. Also, from the results of quasi-static analysis, it is concluded that N Section is better than the other four sections for absorbing the most amount of load. Stress is usually developed in the joints which are within the permissible limit. The results of the explicit dynamic analysis show that there was a 30% decrease in stress concentration level and a 5% increase in deformation level for the door with the anti-intrusion beam of N Section was used.

## References

1. Nichit YK, Battu AK (2017) Development of side door intrusion beam of passenger car for maximum bending load, vol 3, no 8, p 6
2. Nassiopoulous E, Njuguna J (2011) Finite element dynamic simulation of whole rallying car structure: towards better understanding of structural dynamics during side impacts, p 15
3. Teng TL, Chang KC, Nguyen TH Crashworthiness evaluation of side-door beam of vehicle, p 12
4. More KC, Patil GM, Belkhede AA (2020) Design and analysis of side door intrusion beam for automotive safety. *Thin-Walled Struct* 153:106788. <https://doi.org/10.1016/j.tws.2020.106788>
5. Raghuvveer M, Prakash GS Design and impact analysis of a car door, p 8
6. Yoon TH, Kim H, Heo C, Kwon J (2016) An experiment and FE simulation for the development of a SPFC1180 AHSS one-body door impact beam about a car side collision. *Int J Precis Eng Manuf* 17(1):81–89. <https://doi.org/10.1007/s12541-016-0011-2>
7. Karagöz S A comparison of recent metaheuristic algorithms for crashworthiness optimization of vehicle thin-walled tubes considering sheet metal forming effects, p 10
8. Bisagni C, Di Pietro G, Frascini L, Terletti D (2005) Progressive crushing of fiber-reinforced composite structural components of a formula one racing car. *Compos Struct* 68(4):491–503. <https://doi.org/10.1016/j.compstruct.2004.04.015>
9. Dhaneesh P, Prabhakaran B (2016) Study and advanced concept for side impact protection beams to reduce the injury of the occupant using CAE. *Int J Mech Prod Eng* 4(5). Available: [http://www.ijraj.in/journal/journal\\_file/journal\\_pdf/2-257-146536796655-60.pdf](http://www.ijraj.in/journal/journal_file/journal_pdf/2-257-146536796655-60.pdf)
10. Pavan K, Nagarjuna S (2018) Enhancement of car door optimization for crash analysis. *Int J Pure Appl Math* 119(7):1039–1045
11. Nemani RK, Arakerimath DR (2015) Taguchi based design optimization of side impact beam for energy absorption, vol 3, p 6
12. Krishana R, Yadav S, Kumar R, Paliwal HK Development and analysis of side door intrusion beam of SUV, p 8
13. Pawar AP, Mankar SH (1894) Crashworthiness evaluation of low weight recyclable intrusion beam for side impact, p 5
14. Ponnadai S (2018) Analysis of side impact beams in car side door, p 73
15. Federal Motor Vehicle Safety Standards (FMVSS) no. 214 amending side impact dynamic test adding oblique pole test. NHTSA, 2007. Available: <http://www.nhtsa.dot.gov>

# Experimental Flow Field Investigation of the Bio-inspired Corrugated Wing and Hybrid Wing for MAV Applications



Y. D. Dwivedi, Abhishek Mohapatra, and Mohammad Irfan

**Abstract** In this work, the flow behavior of a dragonfly-inspired corrugated wing was undertaken using a subsonic wind tunnel to assess the aerodynamic performance and flow characteristics. The test was performed at Reynolds numbers ( $Re$ ) 46,000 and 67,000, which is the flying regime of micro aerial vehicles. A wing having the same geometrical dimensions as the midsection of the dragonfly forewing known as corrugated wing and another wing having the same geometry as the first wing without corrugations known as hybrid wing were fabricated using 3-D printing machine. The tufts of three different colors were glued at three locations, i.e., 0, 30, and 60% of the semispan of both wings at the trailing edge to visualize the flow separation and reversal phenomenon. The boundary layer rack was used at these three locations to obtain velocity gradient and boundary layer thickness. The result of the tuft flow visualization showed that the flow pattern at all three locations is not the same for the same  $Re$  and angles of attack. At high AOA, the corrugated wing shows lesser velocity gradients than the hybrid wing for both tested Reynolds number. The results clearly demonstrate that the bio-inspired corrugated wing surpassed the hybrid wing by delaying the stall up to 28%.

**Keywords** Bio-inspired wing · Boundary layer · Tuft flow visualization · Stall angle · Flow reversal

## 1 Introduction

For centuries, nature has inspired humans to fly like a bird or wander like an insect in open sky. However, till today humans have not been able to fly like the avians. The primary reason for this issue is the low Reynolds number ( $Re$ ), on which the birds and insects normally fly. Extensive studies have been conducted to understand the flow behavior and aerodynamic characteristics around the wings or airfoils at high  $Re$ , which corresponds to the high speed and large size of the conventional airplanes.

---

Y. D. Dwivedi (✉) · A. Mohapatra · M. Irfan

Department of Aeronautical Engineering, Institute of Aeronautical Engineering, Hyderabad 500043, India

On the other hand, in recent years, small-sized air vehicles like Micro Air Vehicles (MAVs) and small-sized Unmanned Air Vehicles (UAVs) have been developed to undertake tasks like aerial photography, payload delivery, disaster management, and monitoring hazardous places [1–3]. Transportation by automobiles is the main contributor toward the emission of CO<sub>2</sub> which contributes to the emission of greenhouse gases and has posed serious environmental issues [4, 5]. Nowadays, the UAVs, also known as drones, are extensively employed for the delivery of goods and are able to save 90% of the energy while reducing greenhouse emission enormously [6]. It is also observed that the flow field around the wings or airfoils of small aerial vehicles are significantly different from the conventional airplane wings and airfoils [7] because of the low Re of the tiny flights ( $Re < 10^5$ ) [8, 9]. In the high Re range, the inertial force prevails and trailing edge vortices are created, and flow becomes unstable, whereas at low Re, the viscous force is dominant and the flow remains stable as well as smooth. As a result, the performance of the streamlined low Reynolds number wings of MAVs/UAVs/birds/insects, etc. will degrade the performance significantly due to its small size and low velocity [10]. Hence, there is an imperative need to redesign the present conventional airfoils for the application of MAVs/UAVs to obtain better flow characteristics and aerodynamic performance in a low Re regime.

A dragonfly is an insect that fit into the family of *Odonata, anisoptera*, which is significantly fast, agile, and has long endurance. This insect can be classified as low Reynolds number flier as the Re of the dragonfly falls between  $10^2$  and  $10^5$  [11]. It can fly in gliding as well as the flapping mode and also in combination of both [12]. In the flapping mode, the dragonfly is able to move forward, climb, and also hover. However, flapping requires significant energy consumption. So, the insect can not fly for a long duration and switches to the gliding mode of the flight as this mode requires virtually little or no energy consumption at all [13]. The dragonfly is unique in its effective gliding flight as it is proficient of flying 40 chord lengths and up to 30 s without any significant change in its altitude [14]. Unlike other avian wings' cross-section, which is mostly smooth and cambered surface, the dragonfly wings' cross-section is found to be corrugated in the chord as well as in spanwise direction. Several computational and experimental studies were performed to assess the aerodynamic behavior of corrugated wing and most of the investigations revealed that the corrugated wing performed at par and sometimes even better than the smooth conventional airfoils, especially at low Re flow regimes, in which the dragonfly mostly operates [15–24].

Numerous research have been undertaken to understand the important source of the unexpected enhancement in the aerodynamic performance of the corrugated airfoils/wings when compared with existing smooth wings. Kesel [12], Rees [13], and Murphy [19] observed that the corrugated wings function as streamlined airfoil as the Leading Edge Vortices (LEVs) are trapped inside the trough of the valleys. This makes the flow to be streamlined, leading to the delay in separation of the flow [15, 21, 22]. As a result, the lift is increased and drag is reduced thereby resulting in increased aerodynamic performance. Dwivedi et al. [22, 23] has worked extensively on the experimental study of the flow field around the corrugated airfoils at low Re and observed that the spanwise flow and boundary layers were significantly different

from the conventional smooth wings. Luo and Sun [17] have investigated the effect of corrugation on the generation of the aerodynamic forces and Vergas and Mittal [18] have performed the numerical study to assess the aerodynamic efficiency and have established that the corrugation gives better efficiency than the smooth profile wing. Tang et al. [20] have worked computationally for the 3D wing and concluded that spanwise flow direction could promote the lift and decrease the drag. They have also confirmed that the wings are unstable and the same results have been obtained by Dwivedi et al. [21]. Despite different explanations about the flow field mechanism for the improved aerodynamic performance by the different investigators, all studies unanimously agree that the corrugation of the wing works well in the low Re regime, which indicates that the bio-inspired corrugated wings can be potentially used for the wings of future MAVs/UAVs applications.

The flow separation and flow reversal have been experimentally observed by Tamai et al. [25]. The computational result of Skote [26, 27] and Chen and Skote [28] have revealed that the spanwise flow does exist in the corrugated wings and the 3D flow field persists. Flow separation occurs when the thickness of the boundary layer exceeds the critical value which results in the adverse pressure gradient (APG). Most of the earlier investigations only focused on comparing the camber as well as the thickness of corrugated wings with that of either the flat plate or NACA airfoils or both [12, 13, 19, 21]. However, those comparisons are unrealistic. First, the flat plate does not even have the camber; second, NACA airfoil geometry is starkly different from that of bio-inspired corrugated wings. So, the previous results obtained, either computationally or experimentally, may not be corresponding with real bio-inspired corrugated wings.

The present work aims to experimentally investigate the flow behavior of a bio-inspired corrugated wing and to compare the results with another wing having the same thickness, camber, chord, the aspect ratio of the hybrid wing in which all corrugations are filled with the material. In this paper, the model is tested in a wind tunnel by varying AOA and two Reynolds numbers 46,000 and 67,000. The flow phenomena of both the tested wings were visualized by using tufts and boundary layers were measured by using boundary layer rake at three different semispan locations in a low speed wind tunnel at 0.7 chord length (70%) from the leading edge of the wing. The flow visualization and boundary layer study will give the clear understanding of the underlying flow mechanism of the bio-inspired corrugated wing and the wing is assessed for the suitability for future use in the MAVs/UAVs application.

## 2 Methodology

### 2.1 Materials and Methods

Two different wing models were used in the present study: (1) Corrugated wing and (2) Hybrid wing. Both wing models have the same projected planform area ( $S$ ), mean



**Table 1** Coordinates of corrugated wing profile

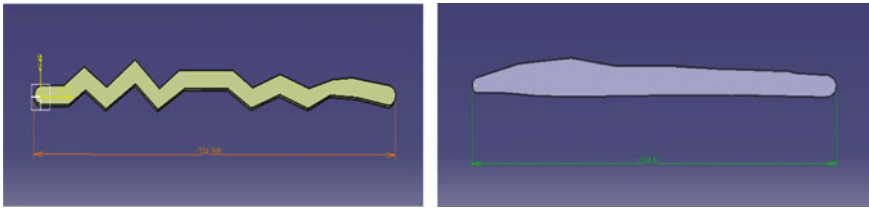
Upper surface		Lower surface	
x/c	y/c	x/c	y/c
0	0.02	0.995	-0.02
0.066	0.02	0.912	-0.005
0.124	0.058	0.833	0
0.189	0.016	0.77	-0.028
0.271	0.073	0.688	0.001
0.341	0.013	0.606	-0.027
0.398	0.051	0.537	0.014
0.553	0.051	0.415	0.014
0.61	0.015	0.337	-0.03
0.689	0.043	0.272	0.023
0.772	0.014	0.187	-0.029
0.839	0.032	0.128	0.01
0.897	0.036	0.08	-0.02
1.005	0.02	0	-0.02

chord length ( $c$ ), and aspect ratio ( $AR$ ). The construction and design of the profile are based on the real-time analysis of the wing structure of the biological dragonfly under microscopic observation and plotting the spatial locations of the elements of the geometry with respect to the mean chord line of the wing. All the coordinates of the points for corrugated and hybrid profile are given in Tables 1 and 2, respectively, for plotting, design, analysis, and fabrication purposes.

The coordinates (Tables 1 and 2) utilized for plotting the wing geometry (Fig. 1) are gathered from various preexisting sources and are spatially multiplied by the

**Table 2** Coordinates of hybrid wing profile

Upper surface		Lower surface	
x/c	y/c	x/c	y/c
0	0.02	0.995	-0.02
0.066	0.02	0.912	-0.005
0.124	0.058	0.833	0
0.271	0.073	0.688	0.001
0.398	0.051	0.537	0.014
0.553	0.051	0.415	0.014
0.689	0.043	0.337	-0.03
0.839	0.032	0.187	-0.029
0.897	0.036	0	-0.02
1.005	0.02		



**Fig. 1** Geometry of corrugated wing and hybrid wing

suitable integral constants (1:100 scale-up) for a noticeable geometry to carryout aerodynamic analysis using the wind tunnel and obtain important results.

**2.1.1 Numerical Adjustments and Curve Fittings**

The profile coordinates were refined for plotting suitable corrugated and hybrid wing models for analysis purposes. The real-time wings of dragonflies are too small and to model accurately to its original dimensions would not yield satisfactory results for the wind tunnel testing. The wing tunnel test section (60 cm × 60 cm × 200 cm) is quite huge in magnitude compared to that of a real corrugated wing model of a dragonfly. Such a relatively small wing model would not induce any noticeable disturbances or any significant changes in the free stream flow in the test section. Hence, geometrical enhancements were made to the miniature real dimensions to scale-up (1:100) the reference model to produce significant variations and flow disturbances in the free stream flow within the test section.

The geometrical aberrations are of magnitudes less than 0.15% error to the total dimensions of the model. These profiles were plotted using the aid of the design and modeling software CATIA V5. The generated models (Fig. 2a, b) were then converted into (.stl) format (stereolithography) and G-Code format (RS-274) under standard ISO 6983 conditions. This data of refined coordinates was then used to produce a 3D printed model of Acrylonitrile Butadiene Styrene (ABS) thermoplastic material as shown in Fig. 3.

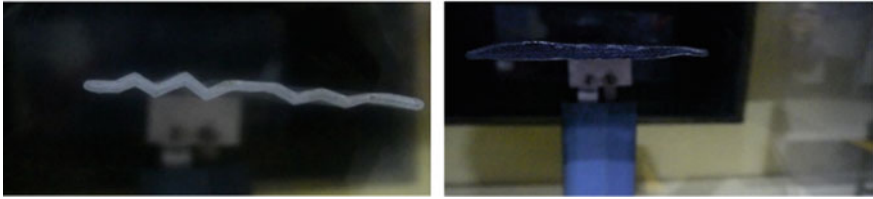
Model specification includes chord length (c) 0.104 m, wing span 0.205 m, effective thickness 4 mm, and camber 0.17 c. The 3D printing machine (Ultimaker S3) was used to fabricate the model as shown in Fig. 3.



**Fig. 2** CATIA 3D model of corrugated (a) and hybrid (b) wings



**Fig. 3** 3D printing of corrugated wings using a Ultimaker S3 3D printer



**Fig. 4** 3D printed wings mounted on six component balance

### 3 Result and Discussion

#### 3.1 Tuft Flow Visualization

Three different colored tufts were used for both wings tuft flow visualization. Black tuft is fixed at the center of the wing (0% of semispan (BT 0)), red tuft at 30% of semispan (RT 30) and a green tuft at 60% of semispan (GT 60), which is near the tip of the wing.

The experiment was carried out at two-chord Reynolds number ( $Re_c$ ) 46,000 and 67,000, the angle of attack (AOA) varied from  $0^\circ$  to  $+20^\circ$  for both the wings. Chord Reynolds number ( $Re_c$ ) calculations are given in Table 3. The green tuft (GT 60) located at 60% of semispan toward the tip showed more fluctuations than that of the other two at AoA  $20^\circ$  and  $Re_c$  46,000, while the remaining two, i.e., BT 0 and RT 30 reacted almost similar to the flow (Figs. 5 and 6). In Figs. 7 and 8 at AoA  $20^\circ$  and  $Re_c$  67,000, the flow shows that the flow reversal happened in the hybrid wing in red

**Table 3** Chord Reynolds number ( $Re_c$ ) calculation

Wind tunnel motor RPM	Chord (m)	Wind tunnel velocity (m/s)	Kinematic viscosity ( $m^2/s$ )	Chord Reynolds no. ( $Re_c$ ) (approx.)
265	0.104	6.9089	$1.562 \times 10^{-5}$	46000
370	0.104	10.0629	$1.562 \times 10^{-5}$	67000

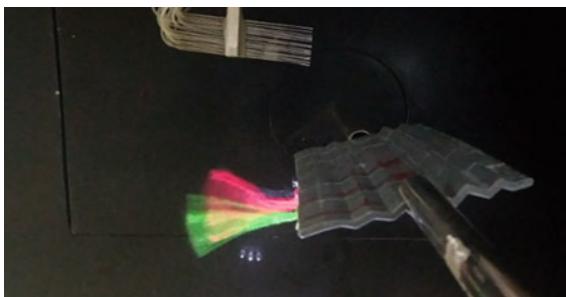
**Fig. 5** Tuft flow visualization for corrugated wing at AOA  $+20^\circ$  and  $Re_c$  46,000



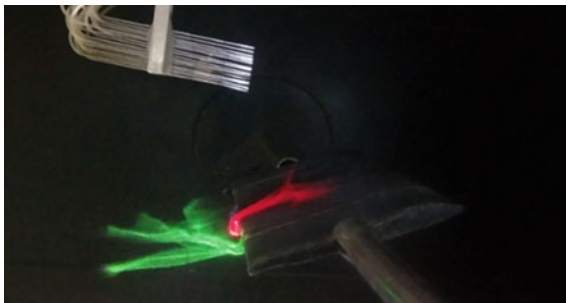
**Fig. 6** Tuft flow visualization for hybrid wing at AOA  $+20^\circ$  and  $Re_c$  46,000



**Fig. 7** Tuft flow visualization for corrugated wing at AOA  $+20^\circ$  and  $Re_c$  67,000



**Fig. 8** Tuft flow visualization for hybrid wing at AOA  $+20^\circ$  and  $Re_c$  67,000



**Fig. 9** Flow reversal for corrugated wing at AOA +18° and  $Re_c$  120,000



**Fig. 10** Flow reversal for hybrid wing at AOA +14° and  $Re_c$  120,000



tuft zone first. At this AoA, there is no indication of flow reversal in the corrugated wing.

To observe the clear flow reversal on both the wings, the  $Re_c$  was increased further to 120,000, and AoA varied from 0° to +18° and it was found that the hybrid wing flow reversal happened at +14° AoA and flow reversal in corrugated wing happened at +18° of AoA (Figs. 9 and 10). This indicates that the flow separation happened first in the hybrid wing. So, the corrugated wing delays the stall 4° which corresponds to nearly 28% gain in in comparison with hybrid wing.

### 3.2 *Boundary Layer Measurements*

In tuft flow visualization, the results were qualitative to find the reversal and separation of the flow for both the wings. However, to find the exact reason which causes flow separation, reversal, and swirling of the flow, a measurement technique was needed. That technique is boundary layer measurement. In boundary layer measurement the target was to obtain the velocity gradients above the two tested wing surfaces at 70% chord length (0.7 c) from the leading edge and at three different semispan

**Table 4** Boundary layer rake device probe numbers and distances

Tube no	Distance (mm)	Tube no	Distance (mm)
1	0	10	14.5
2	1.5	11	16.5
3	2.5	12	20.0
4	4.5	13	22.5
5	5.5	14	24.5
6	7.0	15	27.0
7	8.5	16	31.0
8	10.5	17	34.5
9	12.0		

locations at 0, 30, and 60% from the center of the wing. This location has been taken because the tuft flow visualization was done in the same location.

A 17-probe boundary layer measuring rake is used to measure the velocity profile. The location of the each probes is provided in Table 4. The probes were connected to a manometer filled with methanol and aligned perpendicular to the ground, the perpendicular alignment is verified by two-spirit balances attached to the base of the manometer, perpendicular to each other and parallel to the ground. The velocity field around the wing surface creates the pressure difference between the upper and the lower surfaces. However, the variation in the velocity field was not the same for both corrugated and the hybrid wing. Negative pressure was generated on the upper surface of the corrugated wing. The corrugation present at the lower surface acted as a wing camber. The flow behavior observed is completely governed by parameters like chord length, the thickness of profile, AoA, and the relative velocity across the surface of the profile which is responsible for turbulent flow, flow separation, and flow reversal. The boundary layers measurement results from  $-8^\circ$ ,  $+4^\circ$ , and  $+16^\circ$  angles of attack and  $Re_c$  at 46,000 and 67,000 are given in Figs. 11, 12, 13, 14, 15 and 16.

At AoA  $-8^\circ$  and  $Re_c$  46,000 and 67,000, the boundary layers and velocity gradient of the corrugated wing are lesser than the hybrid wing (Figs. 11 and 12). The same trends observed at AoA  $+4^\circ$  and  $+16^\circ$  (Figs. 13, 14, 15 and 16). At  $+4^\circ$  AoA and chord Reynolds number at 46,000 the corrugated wing velocity gradient at 30% of the semi wing span was observed to be less than and that of the other two positions. The hybrid wing at the  $4^\circ$  AoA and  $Re_c$  46,000 the boundary layer thickness is highest at 60% of semispan, i.e., up to probe number 8, followed by 30% and 0% of the semispan, respectively. It shows that toward the tip of the wing the velocity gradient is higher than the other two locations. However, increasing the  $Re_c$  up to 67,000 resulted in the thickest boundary layer at 60% of the wing semispan up to 14th probe, followed by 30% of semispan and 0% of semispan, respectively (Figs. 13 and 14).

At higher AoA, i.e.,  $+16^\circ$  and  $Re_c$  46,000 and 67,000, the trends of boundary layer velocity gradient and thickness are opposite to the  $-8^\circ$  and  $+4^\circ$  AoA (Figs. 15 and 16). The velocity gradient of the corrugated wing is very less compared to the hybrid

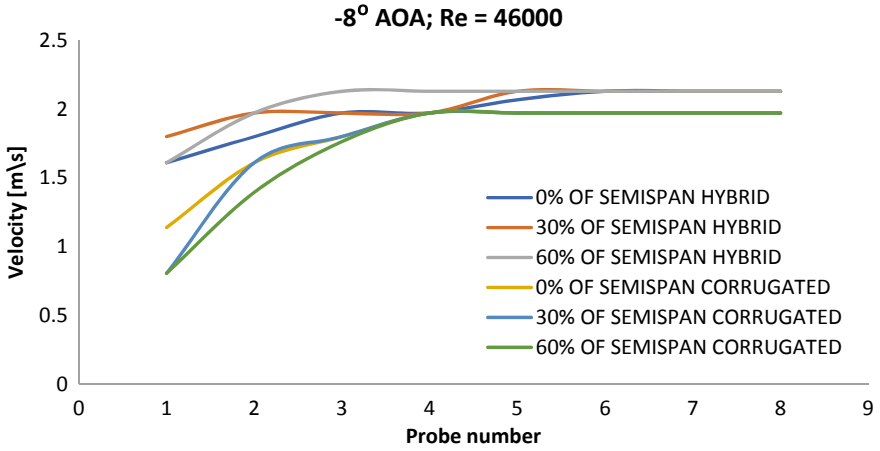


Fig. 11 Comparison of boundary layer velocity at  $-8^\circ$  AOA and  $Re_c = 46,000$

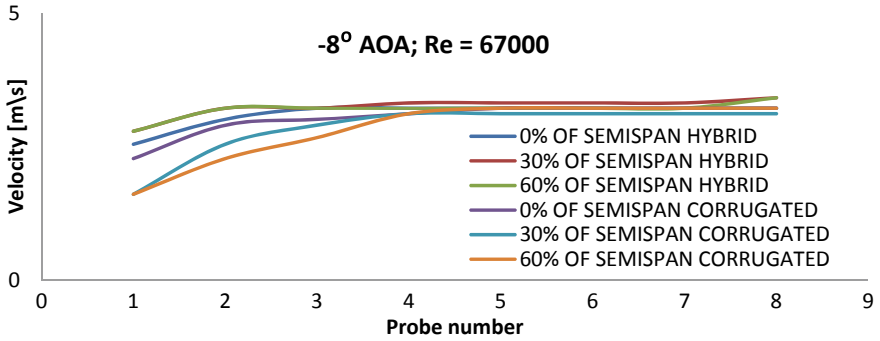


Fig. 12 Comparison of boundary layer velocity at  $0^\circ$  AOA and  $Re_c = 67,000$

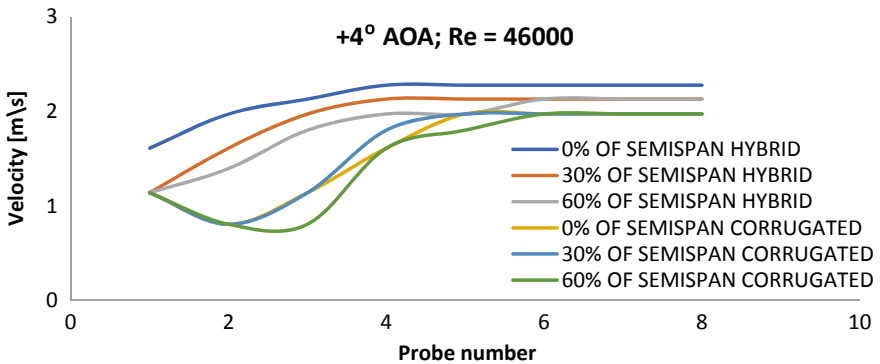


Fig. 13 Comparison of boundary layer velocity at  $+4^\circ$  AOA and  $Re_c = 46,000$

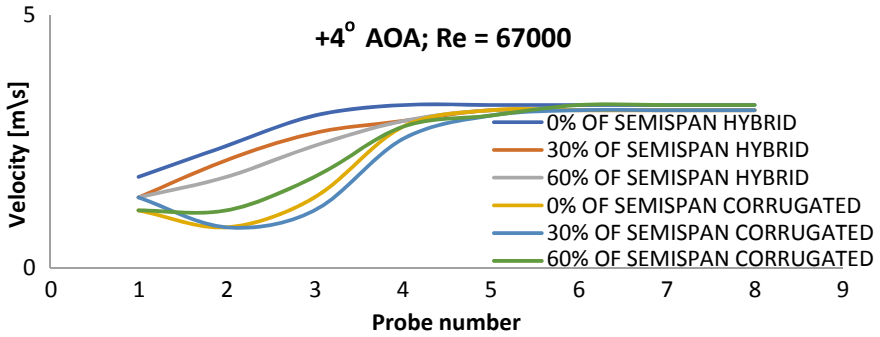


Fig. 14 Comparison of boundary layer velocity at +4° AOA and  $Re_c = 67,000$

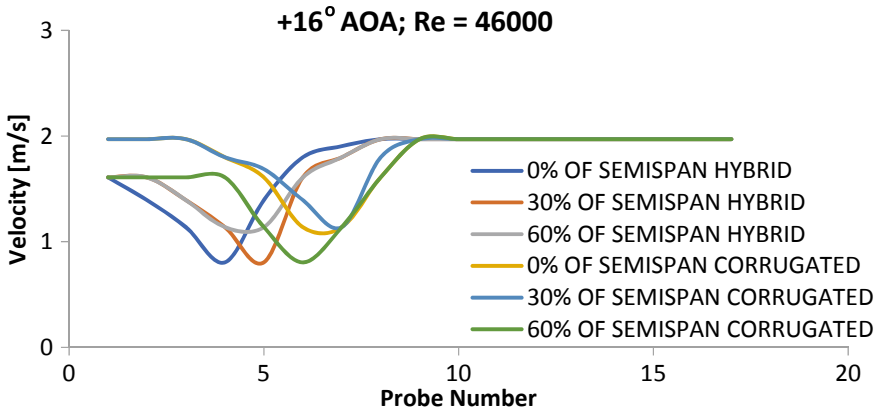


Fig. 15 Comparison of boundary layer velocity at +16° AOA and  $Re_c = 46,000$

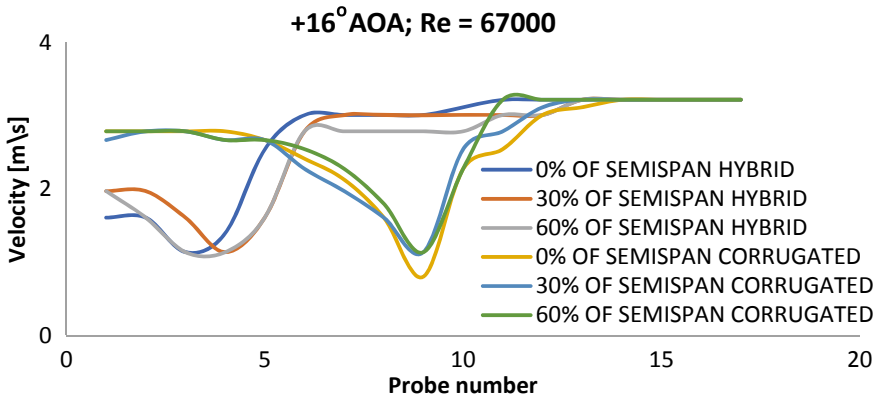


Fig. 16 Comparison of boundary layer velocity at +16° AOA and  $Re_c = 67,000$



wing. This shows that at higher AoA the corrugated wing would perform better than the hybrid wings. The spanwise flow is also almost the same in the corrugated wing in this flow regime, which is not observed in hybrid wing (Fig. 15 and 16).

## 4 Conclusion

No flow reversal and flow separation are observed for the two wings at the  $Re_c$  46,000 or 67,000 and AoA from  $-8^\circ$  to  $+16^\circ$ . However, flow fluctuation in the hybrid wing found more than the corrugated wing.

At chord Reynold number 120,000, the flow reversal occurred in a hybrid wing at  $+14^\circ$  AoA and in corrugated wing it happened at  $+18^\circ$  AoA. This shows that the corrugated wing is 28% more efficient for delaying the stall of the wing.

The boundary layer measurement results also show the same trends, in which at higher AoA, the corrugated wing shows a lesser velocity gradient than the hybrid wing.

The corrugated wing is most suitable for higher AoA (28%) without facing flow separation and flow reversal.

The dragonfly bio-inspired corrugated wing is the most suitable for the future generation low speed micro air vehicle.

## References

1. Estevez J, Lopez-Guede JM, Grana M (2015) Quasi-stationary state transportation of a hose with quadrotors. *Robot Auton Syst* 63:187–194. <https://doi.org/10.1016/j.robot.2014.09.004>;
2. Mohiuddin T, Taha Y, Zweiri D, Gan (2019) UAV payload transportation via RTDP based optimized velocity profiles. *Energies* 12(16):30–49. <https://doi.org/10.3390/en12163049>
3. Wall Street Journal. Google drones can already deliver you coffee in Australia. Available online: <https://www.youtube.com/watch?v=prhDrfUgpB0>. Accessed on 6 Apr 2019
3. Mohiuddin A, Taha T, Zweiri Y, Gan D (2019) UAV payload transportation via RTDP based optimized velocity profiles. *Energies* 12(16):30–49. <https://doi.org/10.3390/en12163049>
4. Stolaroff JK, Samaras C, O'Neill ER, Lubers A, Mitchell AS, Ceperley D (2018) Energy use and life cycle greenhouse gas emissions of drones for commercial package delivery. *Nat Commun* 9:409
5. Liu J, Guan Z, Shang J, Xie X (2018) Analysis of environmental impacts of drone delivery on an online shopping system. *J Syst Sci Inform* 6(4):302–319. <https://doi.org/10.21078/JSSI-2018-302-18>
6. McMasters JH, Henderson ML (1980) Low speed single element airfoil synthesis. *Tech Soaring* 2(2):1–21
7. Carmichael BH (1981) Low Reynolds number airfoil survey, vol 1; NASA CR-165803; NASA, Washington, DC
8. Lissaman PBH (1983) Low-Reynolds-number airfoils. *Annu Rev Fluid Mech* 15:223–239
9. Gad-el-Hak M (2001) Micro-air-vehicles: can they be controlled better? *J Aircr* 38:419–429
10. Wakeling JM, Ellington CP (1997) Dragonfly flight. I. Gliding flight and steady-state aerodynamic forces. *J Exp Biol* 200:543–556

11. Kesel AB (2000) Aerodynamic characteristics of dragonfly wing sections compared with technical aerofoil. *J Exp Biol* 203:3125–3135. [https://doi.org/10.1016/S0010-4825\(98\)01818-3](https://doi.org/10.1016/S0010-4825(98)01818-3)
12. Rees CJC (1975) Aerodynamic properties of an insect wing section and a smooth aerofoil compared. *Nature* 258:141–142
13. Brodsky AK (1994) *The evolution of insect flight*. Oxford University Press, Oxford, UK
14. Rudolph R (1978) Aerodynamic properties of *Libellula quadrimaculata* L. (Anisoptera: Libellulidae), and the flow around smooth and corrugated wing section models during gliding flight. *Odonatologica* 7:49–58
15. Okamoto M, Yasuda K, Azuma A (1996) Aerodynamic characteristics of the wings and body of a dragonfly. *J Exp Biol* 199:281–294
16. Luo G, Sun M (2005) The effects of corrugation and wing planform on the aerodynamic force production of sweeping model insect wings. *Acta Mech Sin* 21:531–541
17. Vargas A, Mittal R (2004) Aerodynamic performance of biological airfoils. In: *Proceedings of 2nd flow control conference*, Portland, Oregon AIAA2004-2319. <https://doi.org/10.2514/6.2004-2319>
18. Murphy J, Hu H (2010) An experimental study of a bio inspired corrugated airfoil for micro air vehicle applications. *Exp Fluids* 49:531–546. <https://doi.org/10.1007/s00348-010-0826-z>
19. Tang H, Lei Y, Li X, Fu Y (2019) Numerical investigation of the aerodynamic characteristics and attitude stability of a bio-inspired corrugated airfoil for MAV or UAV applications. *Energies* 12:4021. <https://doi.org/10.3390/en12204021>
20. Dwivedi YD, Bhargava V, Rao PMV, Jagadeesh D (2019) Aerodynamic performance of micro aerial wing structures at low Reynolds number. *INCAS Bulletin* 11(1):107–120. <https://doi.org/10.13111/2066-8201.2019.11.1.8>
21. Dwivedi YD, Sudhir Sastry YB (2019) An experimental Flow field study of a bio-inspired corrugated wing at low Reynolds number. *INCAS Bulletin* 11(3):55–65. <https://doi.org/10.13111/2066-8201.2019.11.3.5>
22. Dwivedi YD, Ho WH, Rao PMV (2017) Spanwise flow analysis of gliding bio-inspired corrugated wing. *J Adv Res Dyn Control Syst* 12-Special issue
23. Dwivedi YD (2017) Effect of peak shape in bio inspired corrugated wing. In: *International conference on advances in thermal systems, materials and design engineering (ATSMDE2017)*, VJTI, Mumbai
24. Tamai M, Wang Z, Rajagopalan G, Hu H, He G (2007) Aerodynamic performance of a corrugated dragonfly airfoil compared with smooth airfoils at low Reynolds numbers. In: *45th AIAA aerospace sciences meeting and exhibit*, pp 1–12
25. Skote M (2014) Scaling of the velocity profile in strongly drag reduced turbulent flows over an oscillating wall. *I J Heat Fluid Flow* 50:352–358
26. Skote M (2011) Turbulent boundary layer flow subjected to stream wise oscillation of spanwise wall-velocity. *Phys Fluids* 23:1701–1704
27. Chen YH, Skote M (2016) Gliding performance of 3-D corrugated dragonfly wing with spanwise variation. *J Fluids Struct* 62:1–13

# Structural Analysis and Topology Optimization of Base of Revolving Chair



Dharmik Gohel , Keval Bhavsar , and Jaimin Panchal 

**Abstract** The base of the revolving chair is the important part as most of the human load gets transferred to it. Topology optimization is performed to reduce material and get the optimum shape of the chair base which sustains the load transmitted to it. This paper presents the generation and analysis of the optimized design of the revolving chair base. The CAD model is developed using SOLIDWORKS followed by static structural analysis, and topology optimization of the revolving chair is done in Ansys. Then, SpaceClaim is used to enhance the geometry of the optimized model followed by the static structural analysis that is carried out with different materials like polypropylene, aluminum, and stainless steel to check the reliability of the enhanced optimized model. The parameters such as stresses and deformation are used to get the optimal topology and also to validate the enhanced geometry.

**Keywords** Static structural analysis · Polypropylene · Aluminum · Stainless steel · Revolving chair base · Topology optimization · Computer-aided design (CAD) · ANSYS · SOLIDWORKS

## 1 Introduction

The revolving office chair is an assembly of the different parts like chair base, castor wheel, seat, backrest, and foot ring. The chair base is one of the important parts as it provides stability and movement. Also, the majority of the load gets transmitted to chair base. If the chair base gets broke, either it can lead to major injuries (a person lands on the backside) or leads to minor injuries. So, it becomes important to analyze the base of the chair. Chaudhary et al. [1] utilized the BIFMA standard to plan the workplace seat, and it is approved utilizing FEA apparatuses and the procedure comprised of pre-preparing utilizing Hypermesh, Ansys is utilizing LS-Dyna, and post-handling utilizing HyperView. Upon iterative changes and approvals. Brackett et al. [2] perform the topology optimization for additive manufacturing and

---

D. Gohel (✉) · K. Bhavsar · J. Panchal

Department of Mechanical Engineering, School of Technology, PDEU, Gandhinagar, Gujarat, India

workflow for it. Li et al. [3] the optimal structure shape of the mounting bracket of ROV simulator, topology optimization design of it by finite element analysis software Ansys, and the outcomes show that this is a successful improvement strategy and demonstrate that the strategy is right and effective. It has a specific designing application prospect. Cionca [4] done the research to create, develop, and experiment with a scientific method to visualize the concepts and design process for chairs. Bellinger et al. [5] built model and analysis were run, and all major components of chair are analyzed for backrest strength test based on BIFMA by using FEA tool. Zhong et al. [6] performed topology optimization for designing a new cage after it analyzes the stress distribution of the lumbar spine using Ansys. Finite element estimated that an optimized cage reduced to 36% of the volume of the total volume of the original cage, and the optimized model provides more space. Wang and Kang [7] studied the topology optimization for nonlinear magnetostatic systems using the finite element method. Kang and Wang [8] also analyze magnetostatic fields which are developed by the 3D finite element method. Krishna et al. [9] proposed the application of topography and shape optimization techniques for the design of a jounce bumper bracket of a pick-up truck. Gustafsson et al. [10] performed the finite element analysis on chair of wood and verified the data.

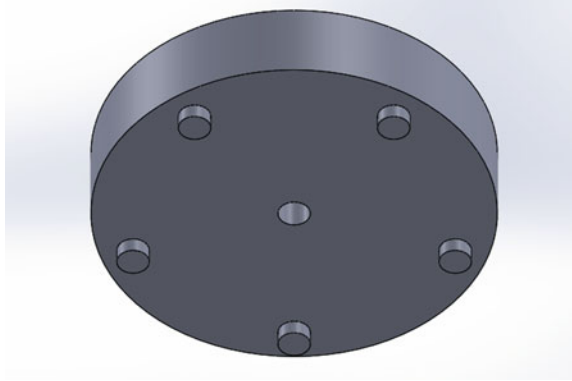
After doing a rigorous literature survey, it is found that not many researchers have not done the topology optimization of the base of the revolving chair base. Also, little research has been done on selection of the material for the chair base. Most researchers have used stainless steel and aluminum.

In this paper, the CAD model of a revolving chair base is designed in SOLIDWORKS, then to do the topology optimization of the model, static structural analysis is performed on the CAD model. To further enhance the geometry of the optimized model, SpaceClaim is used. For checking the strength and stability of an enhanced model, static structural analysis is carried out for materials like polypropylene, aluminum, and stainless steel. Ansys is used to perform the static structural and topology optimization of the chair base.

## 2 Design

As a prerequisite to the finite element model, the physical geometry of the round base of the revolving chair is developed using SOLIDWORKS. The CAD model as seen in Fig. 1 is developed by taking actual measurements from the chair. The model has a center circle which transmits the load from the top assembly to the five extruded cylinders.

**Fig. 1** Solid modeling of the base of revolving chair

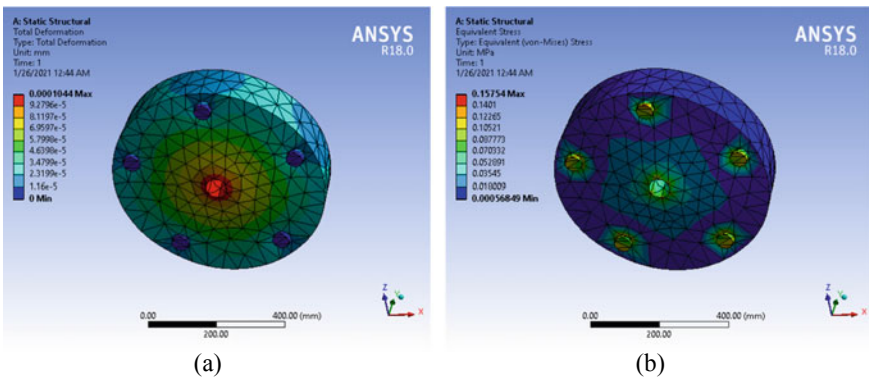


### 3 Result and Discussion

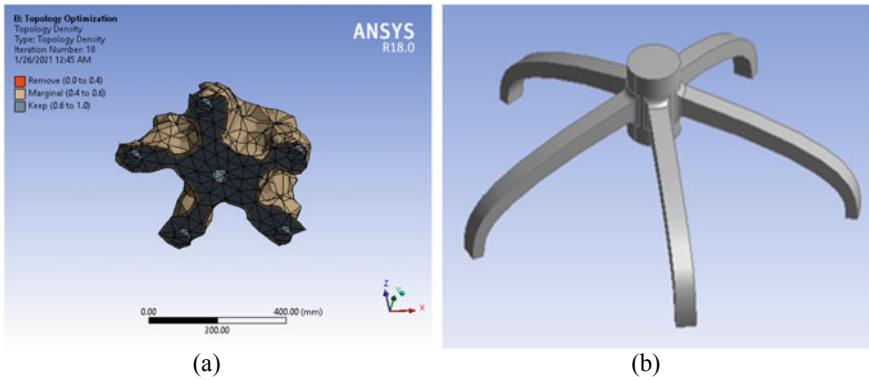
The deformation and equivalent stress analyses is performed in Ansys material as stainless steel of the round base model. After it, the topology optimization performed on it so get 5-star base. The topology-optimized model further enhanced in SpaceClaim. With steel, aluminum, and polypropylene deformation and equivalent stress performed on the enhanced model.

#### 3.1 Static Structural Analysis and Topology Optimization

The static structural analysis is performed on the CAD model with steel as a material in which the load of 1000 N applied in the center circle that generates the total deformation of 0.104  $\mu\text{m}$  and the equivalent stress of 0.15 MPa as in Fig. 2. These



**Fig. 2** Static structural analysis of base **a** total deformation and **b** equivalent stress



**Fig. 3** **a** Topology optimized model. **b** Enhanced model

results are fed for topology optimization for removing the excess material (regions) from the model that has relatively low stress values as seen in Fig. 3a. After that, the model is further enhanced in SpaceClaim to remove uneven shape and edges as seen in Fig. 3b.

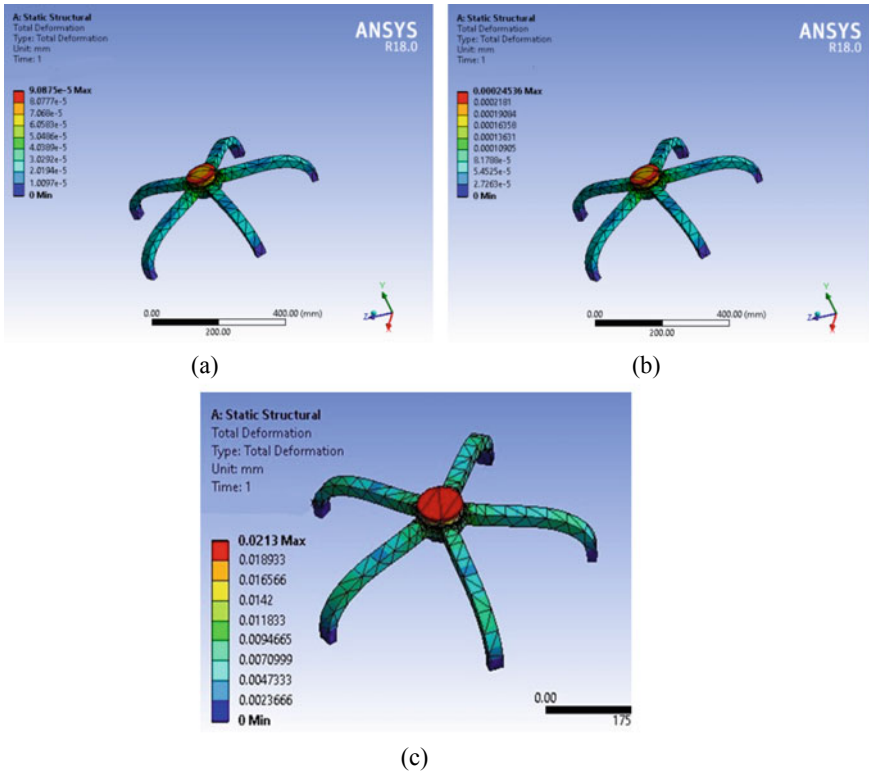
### 3.2 Analysis of Optimized Shape

Parameters such as total deformation and equivalent stress are used from static structural analysis to check the reliability of the enhanced model and to find the optimum material from polypropylene, aluminum, and stainless steel. The total maximum deformation (Fig. 4) and equivalent stress (Fig. 5) in order from high to low is as follows: polypropylene > aluminum > stainless steel.

Here, Table 1 provide all the analysis results of chair base.

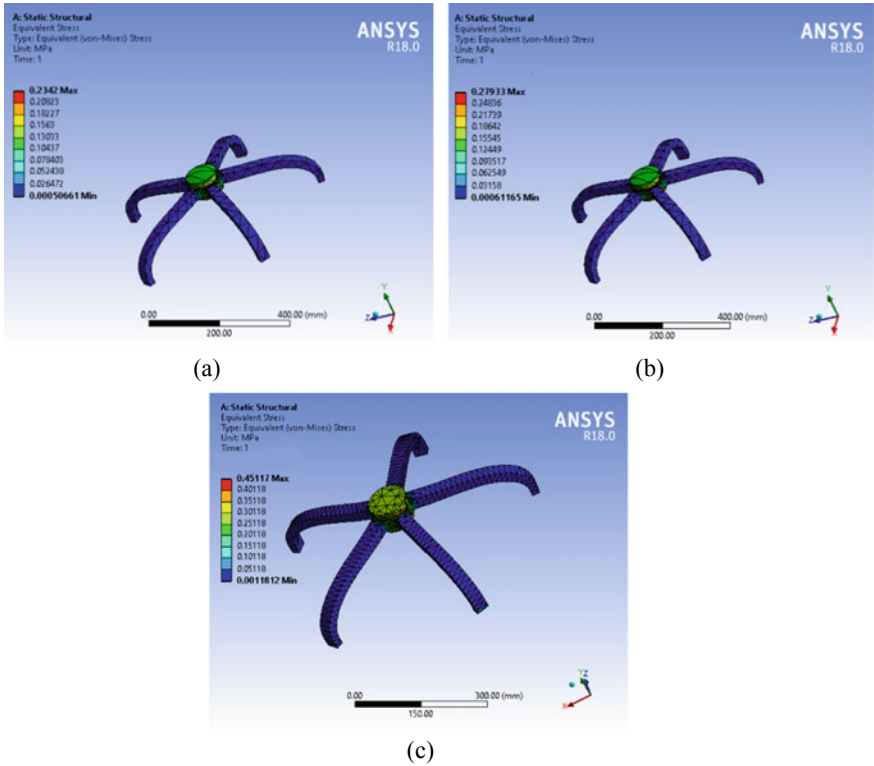
## 4 Conclusion

Here, in this study, the static structural analysis is performed with steel as a material for the round base of revolving chair. Total deformation of  $0.104 \mu\text{m}$  and equivalent stress of  $0.15 \text{ MPa}$  are fed to topology optimization for removing excess material that resulted in 5-star shape of base. The model is then enhanced in SpaceClaim to remove uneven shape and edges which is followed by static structural analysis



**Fig. 4** Results for total deformation in **a** stainless steel, **b** aluminum, **c** polypropylene

by applying steel, aluminum, and polypropylene as materials. The results show that maximum deformation of 21.3  $\mu\text{m}$  and equivalent stress of 0.45 MPa was observed in polypropylene, while minimum deformation of 0.091  $\mu\text{m}$  and equivalent stress of 0.23 MPa was observed in stainless steel. Hence, if high strength is a concern, then stainless steel can be used, and if mobility is a concern, then polypropylene can be used.



**Fig. 5** Results for total equivalent stress in **a** stainless steel, **b** aluminum, **c** polypropylene

**Table 1** Results of total deformation and total equivalent stress

Static structural analysis	Round base (Before optimization)	Enhanced model		
		Stainless steel	Aluminum	Polypropylene
Deformation ( $\mu\text{m}$ )	0.104	0.091	0.24	21.3
Total equivalent stress (MPa)	0.15	0.23	0.28	0.45

## References

1. Chaudhary VD, Taji DSG, Bawiskar HS Validation of office chair for BIFMA standard using FEA tool, p 9
2. Brackett D, Ashcroft I, Hague R Topology optimization for additive manufacturing, p 15
3. Li X, Zhao L, Liu Z (2017) Topological optimization of continuum structure based on ANSYS. MATEC Web Conf 95:07020. <https://doi.org/10.1051/mateconf/20179507020>
4. Cionca M (2013) MID 20TH century innovations in chair design, vol 9, p 10
5. Bellingar TA, Benden ME (2015) New ANSI/BIFMA standard for testing of educational seating. Ergon Des Q Hum Factors Appl 23(2):23–27. <https://doi.org/10.1177/1064804613513899>



6. Zhong Z-C, Wei S-H, Wang J-P, Feng C-K, Chen C-S, Yu C (2006) Finite element analysis of the lumbar spine with a new cage using a topology optimization method. *Med Eng Phys* 28(1):90–98. <https://doi.org/10.1016/j.medengphy.2005.03.007>
7. Wang S, Kang J (2002) Topology optimization of nonlinear magnetostatics. *IEEE Trans Magn* 38(2):1029–1032. <https://doi.org/10.1109/20.996264>
8. Kang J, Wang S (2000) Shape optimization of BLDC motor using 3-D finite element method. *IEEE Trans Magn* 36(4):1119–1123. <https://doi.org/10.1109/20.877637>
9. Krishna MMR (2002) Finite element topography and shape optimization of a Jounce Bumper bracket, pp 2002–01–1468. <https://doi.org/10.4271/2002-01-1468>
10. Gustafsson S-I (1996) Finite element modelling versus reality for birch chairs. *Holz als Roh-und Werkstoff* 54(5):355–359

# Effect of Elliptical Cutout on Buckling Load for Isotropic Thin Plate



Renuka Gore and Bhaskara Rao Lokavarapu

**Abstract** Steel thin plates with cutouts are mainly used in ships, aircrafts and automobile as cutouts provide provision for assessment, service and maintenance. The size of cutout has noteworthy consequence on the buckling load. Plates continue to carry loads even after buckling. Significance of this paper is to study the outcome of material properties and geometrical varying effects on the buckling load carrying capability of the rectangular thin plates with simply supported on both width and length of plates are clamped. Comparison between solid plate and plate with cutout is being done. Changes in orientation of the elliptical cutout and maximum buckling load that can be obtained are studied. The numerical study was done using Kirchhoff's classical plate theory, and simulations were carried out using Ansys 2020R Workbench.

**Keywords** Thin plate · Buckling load · Geometrical parameter · Solid plate · Elliptical cutout

## 1 Introduction

Buckling analysis of plate is a sizzling topic for numerous researchers due to its extensive application prospects in a lot of engineering field such as civil and structure engineering, mechanical engineering, marine and aerospace engineering. Plates are lean structural components commonly used in quite a few manufacturing applications. They are straight and plane, having a geometric configuration where one dimension, referred to as thickness ( $t$ ) is much smaller than the in-plane. A plate can be considered as thin if its transverse shears deformations are negligible compared to its bending deflections [1]. Thin-walled structure is extensively used in aerospace and defence industry applications. Statistical discontinuities are frequently encountered in numerous structural components either as part of the design requirement (in the case of the elliptical cutout) or because of effect of break at some stage in

---

R. Gore (✉) · B. R. Lokavarapu  
School of Mechanical Engineering, Vellore Institute of Technology, Chennai Campus,  
Vandalur-Kelambakkam Road, Chennai, Tamil Nadu 600127, India

© The Author(s), under exclusive license to Springer Nature Singapore Pte Ltd. 2022  
G. S. V. L. Narasimham et al. (eds.), *Innovations in Mechanical Engineering*,  
Lecture Notes in Mechanical Engineering,  
[https://doi.org/10.1007/978-981-16-7282-8\\_5](https://doi.org/10.1007/978-981-16-7282-8_5)

the manufacturing or in check (in the scenario of impact harm). The attendances of these local geometric discontinuities have been revealed the reason for the difficulty of stress redeployment contained by the structural member. Plate buckling is a wavering observable fact with the intention of occurrence when a compressive load generates a dangerous stress intensity that causes a much unexpected deflection inside the out-of-plane transverse way This compressive load is been to produce by unadulterated axial compression, other than it is capable of in addition to generate by shear, bending moment, or local intense loads, otherwise by means of a permutation amongst these.

Komur studied the buckle stress cause on the steel A50 with circular hole, aspect ratio special effects from 1 to 4 [2]. Arif E. Orun et al. studied the effect of the hole fortification on the buckle presentation of thin-walled beams subjected to shared loading [3]. Saumit Kumar Mandal and Pradeep Kumar Mishra studied buckling load effects for Poisson's ratio 0.22, 0.27, 0.3, 0.36 and he studied aspect ratio of 1 and 2 for a circular hole. The plate buckling involves bending in two planes [4].

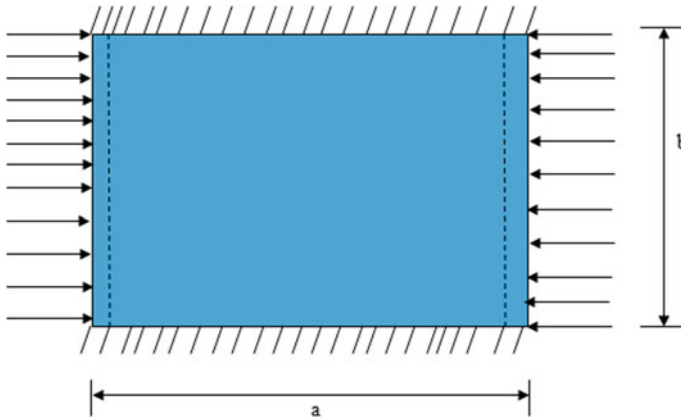
Prasun Jana did linear elastic buckling examination for simply support rectangular plate with sole circular cutout. Iterative move towards selecting of the optimum cutout location by means of the majority favourable algorithm is engaged. Significant load for simply supported rectangular boundary condition and analyzed in Ansys. MATLAB is used to locate the optimum position. Optimum cutout position for maximum buckling load is obtained at centre along longitudinal direction [5]. Emanuele Maiorana et al. studied the effects of localized proportioned load on the behaviour of square plate circular and rectangular hole with rounded corner. For variation in ratio of diameter of hole to width of plate buckling, coefficient is calculated. Critical buckling coefficient increases by four times for localized buckling load, and it is independent of plate thickness [6]. Daniel Helbig et al. considered the effects of buckling on the thin perforate steel plate with dissimilar geometries are analyzed. Best and worst geometric shapes are compared [1]. Mohammad Hossein et al. studied buckling stability of plates with dissimilar size range from stunted to stretch out off-centre crack is calculated using experimental and arithmetical methods. Boundary conditions used are clamped-free with cracks and no cracks are calculated [7]. For plate, width is important and for beam, length is crucial. The elastic buckling loads depend on boundary conditions, geometric parameter and material properties of the plate. The study with different aspect ratio, increasing thickness of plate, orientation and size of cutout effects with different boundary conditions are not yet studied. Buckling of circular and annular plates with guided edges [8–10] and with elastic/rigid ring support [11–14] and elastic edges [15, 16] studied by Rao and Rao.

## 2 Problem Definition

Consider a thin rectangular plate with length ( $a$ ), width ( $b$ ) and thickness ( $t$ ). Buckling load analysis on this isotropic plate with materials considered as stainless steel and aluminium alloy. The properties of the plate considered have Poisson's ratio ( $\mu$ ) and

**Table 1** Properties of material

Material	Young’s modulus (GPa)	Poisson’s ratio	Density (kg/m <sup>3</sup> )
Aluminium alloy	70	0.33	2710
Stainless steel	190	0.31	7750



**Fig. 1** Non-perforated plate

Young’s Modulus ( $E$ ) mentioned in Table 1. A plate shown in Fig. 1 is considered as the problem with boundary condition of simply supported on width and clamped on length in  $x$ - $y$  plane. For simply support, the slope of plate can vary depending on the loading but edge deflection is zero and the clamped edges have both slope and deflection are considered to be zero. The plate is subjected to linear in flat surface weight on the entire edge as shown in the figure. Similarly, study is being done on Fig. 2 which consists of elliptical hole at the centre of the plate that is at width ( $b/2$ ) from sides and length ( $a/2$ ) on both top and bottom of the plate. Orientations from  $0^\circ$  to  $90^\circ$  from the centre are considered as shown in Fig. 2. The major axis ( $d$ ) and minor axis ( $c$ ) are considered as the dimensions of the elliptical cutout. A thin plate with dimensions  $200 * 100 * 2$  in mm is considered for calculations.

### 3 Mathematical Model

Thin plates are the plates that have insignificant thickness compared to length and width of the plate. A thin plate neglects the transverse deformation of the plate, therefore, Kirchhoff’s plate theory is applied [17]. Few assumptions are made whilst following Kirchhoff’s plate theory such as points along normal to the middle plane have the same vertical displacement that means thickness does not change during deformation [18]. The normal stress in  $z$  direction is neglected [19]. A thin plate in

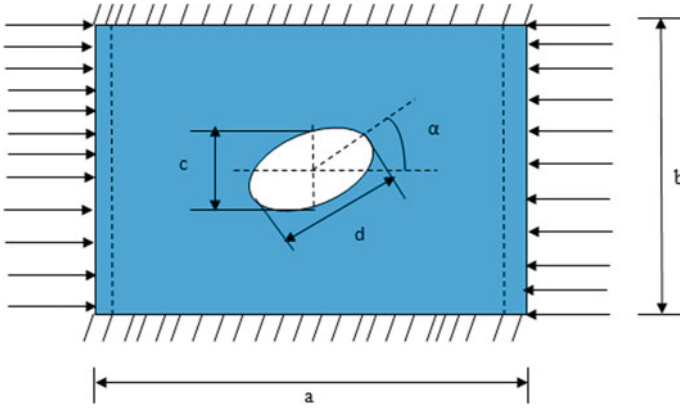


Fig. 2 Perforated plate

$x$ - $y$  plane is considered and compressive linear axial preload is applied on the entire width of the plate. In this plate moment of inertia ( $I$ ) is formed, Young’s Modulus ( $E$ ) and Poisson’s ratio ( $\mu$ ) of the plate of which material the plate is made, here, it would be aluminium or stainless steel depending upon the analysis, and  $P$  is the compressive force on the entire width of the thin plate.

From Kirchhoff’s classical plate theory,

$$D \left( \frac{\partial^4 \omega}{\partial x^4} + 2 * \frac{\partial^4 \omega}{\partial x^2 \partial y^2} + \frac{\partial^4 \omega}{\partial y^4} \right) = - P \frac{\partial^2 \omega}{\partial y^2} \tag{1}$$

$D$  flexural rigidity =  $\frac{EI}{(1-\mu^2)}$ .

$I$  moment of inertia in ( $\text{mm}^4$ ) =  $\frac{bt^3}{12}$ .

For sinusoidal deformation,

$(\omega = \sin(\frac{m\pi y}{a}) \sin(\frac{n\pi x}{b}))$   $m, n$ —number of half waves in  $x$  and  $y$  direction

$$\frac{\partial \omega}{\partial x} = \frac{\partial}{\partial x} \left( \sin\left(\frac{m\pi y}{a}\right) \left(\frac{n\pi x}{b}\right) \sin\left(\frac{m\pi y}{a}\right) \cos \frac{n\pi x}{b} \cdot \left(\frac{n\pi}{b}\right) \right) \tag{2}$$

$$\frac{\partial^2 \omega}{\partial x^2} = \sin\left(\left(\frac{m\pi y}{a}\right)\right) \left(\left(\frac{n\pi}{b}\right)\right)^2 \left(-\sin\left(\frac{n\pi x}{b}\right)\right) \tag{3}$$

$$\frac{\partial^3 \omega}{\partial x^3} = \left(\sin\left(\frac{m\pi y}{a}\right)\right) \left(\frac{n\pi}{b}\right)^3 \left(-\cos\left(\frac{n\pi x}{b}\right)\right) \tag{4}$$

$$\frac{\partial^4 \omega}{\partial x^4} = \sin\left(\frac{m\pi y}{a}\right) \left(\frac{n\pi}{b}\right)^4 \left(\sin \frac{n\pi x}{b}\right) \tag{5}$$

$$\frac{\partial \omega}{\partial y} = \frac{\partial}{\partial y} \left( \sin\left(\frac{m\pi y}{a}\right) \right) \left( \sin\left(\frac{n\pi x}{b}\right) \right) = \sin\left(\frac{m\pi x}{b}\right) \cos\frac{n\pi y}{a} \cdot \left(\frac{n\pi}{a}\right) \quad (6)$$

$$\frac{\partial^2 \omega}{\partial y^2} = \left( \sin\left(\frac{m\pi x}{b}\right) \left(\frac{m\pi}{b}\right)^2 \right) \left( \sin\left(\frac{m\pi y}{a}\right) \right) \quad (7)$$

$$\frac{\partial^3 \omega}{\partial x^3} = \sin\left(\frac{m\pi x}{b}\right) \left(\frac{n\pi}{a}\right)^3 \left(-\cos\left(\frac{n\pi y}{a}\right)\right) \quad (8)$$

$$\frac{\partial^4 \omega}{\partial x^4} = \sin \sin\left(\frac{m\pi y}{b}\right) \left(\frac{n\pi}{a}\right)^4 \left(\sin\left(\frac{n\pi y}{a}\right)\right) \quad (9)$$

$$\frac{\partial^2 \omega}{\partial y^2} = \left( \sin\left(\frac{m\pi x}{b}\right) \left(\frac{m\pi}{b}\right)^2 \right) \left(-\sin\left(\frac{m\pi y}{a}\right)\right) \quad (10)$$

$$\frac{\partial^3 \omega}{\partial x \partial y^2} = \cos\left(\frac{m\pi x}{b}\right) \left(\frac{n\pi}{b}\right) \left(\frac{m\pi}{b}\right)^2 \left(-\sin\left(\frac{m\pi y}{a}\right)\right) \quad (11)$$

$$\frac{\partial^4 \omega}{\partial x^2 \partial y^2} = \left(\frac{n\pi}{b}\right)^2 \left(\frac{m\pi}{b}\right)^2 \sin\left(\frac{m\pi y}{a}\right) \sin\left(\frac{n\pi x}{b}\right) \quad (12)$$

Putting Eqs. (5), (9) and (12) in Eq. (1) we get,

$$P = D \frac{\pi^2}{b^2} \left\{ n^4 \left(\frac{a}{mb}\right)^2 + 2n^2 + \left(\frac{mb}{a}\right)^2 \right\} \quad (13)$$

For critical strength  $n = 1$ ,

$$P = D \frac{\pi^2}{b^2} \left\{ \frac{a}{mb} + \frac{mb}{a} \right\}^2 \quad (14)$$

Let  $K_c = \left\{ \frac{a}{mb} + \frac{mb}{a} \right\}^2$  - Buckling coefficient.

$\sigma_{cr}$  = Critical buckling stress,

$$P = \sigma_{cr} \cdot t \quad (15)$$

$$\sigma_{cr} \cdot t = D \frac{\pi^2}{b^2} * K_c \quad (16)$$

$$\sigma_{cr} t = \frac{EI}{12(1 - \mu^2)} * \frac{\pi^2}{b^2} * K_c \quad (17)$$

$$\sigma_{cr} \cdot t = \frac{E * b * t^3}{12(1 - \mu^2)} * \frac{\pi^2}{b^2} * K_c \quad (18)$$

$$\sigma_{cr} = \frac{Kc(\pi^2 E)}{12(1 - \nu^2)} \left(\frac{t}{b}\right)^2 \quad (19)$$

## 4 Results and Discussion

### 4.1 Non-perforated Plate

Eigen buckling analysis is performed in Ansys Workbench 2020R [20–22] for the thin plate as simply supported on both widths and clamped on both lengths shown in Fig. 1. The buckle mode represents the contour, the structure assumes whilst it buckles in a meticulous mode; however, say nothing about the arithmetical value of the displacements or the stress. The five modes obtained during analysis, we observe different shapes, a thin plate would take during the examination.

#### 4.1.1 Deviation of Buckling Load with Respect to Aspect Ratio

Substantial consequence of aspect ratio has been observed on buckling performance. The plate starts to behave analogous to a column of finite breadth, when the aspect ratio is outsized. In the midst of declining aspect ratio, there is also a limit under which malfunction do not take place by elastic buckling. Aspect ratio is, therefore, a vital consideration for designers in aerospace and other fields of engineering. The effect of boundary condition on buckling load increases with increasing aspect ratio as shown in the Fig. 3. Here, width is varied whereas other parameters are kept same. As the aspect ratio is increasing, we observe that buckling load carrying capacity of stainless steel and aluminium is increasing. Stainless steel has more effect compared to aluminium alloy.

#### 4.1.2 Deviation of Buckle Load with Respect to Thickness of Plate

Thickness of the plate is another parameter which affects the buckle load carrying ability of plates. The lean plates are different from thick plates. The thin plate has absence of transverse deformation, hence, it does not consider shear deformation. The thin plate as mentioned earlier follows Kirchhoff's classical plate theory. The thick plates do consider shear deformation, hence, it follows Mindlin Resser's effect. We can observe the effect of thickness in the Fig. 4.

As the aspect ratio is increasing, we observe that buckling load carrying capacity of stainless steel and aluminium is increasing. Stainless steel has more effect compared to aluminium alloy. We observe in the Fig. 4 that the thickness (mm) of the plate is

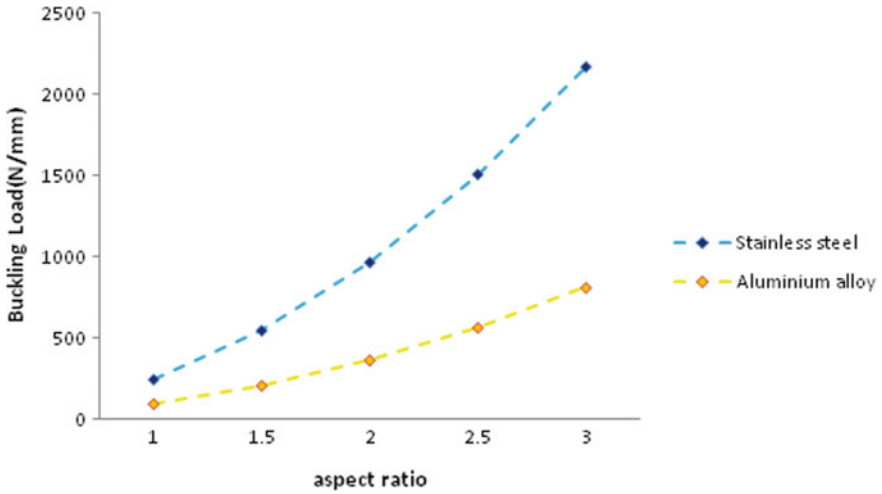


Fig. 3 Deviation of buckle load with respect to aspect ratio

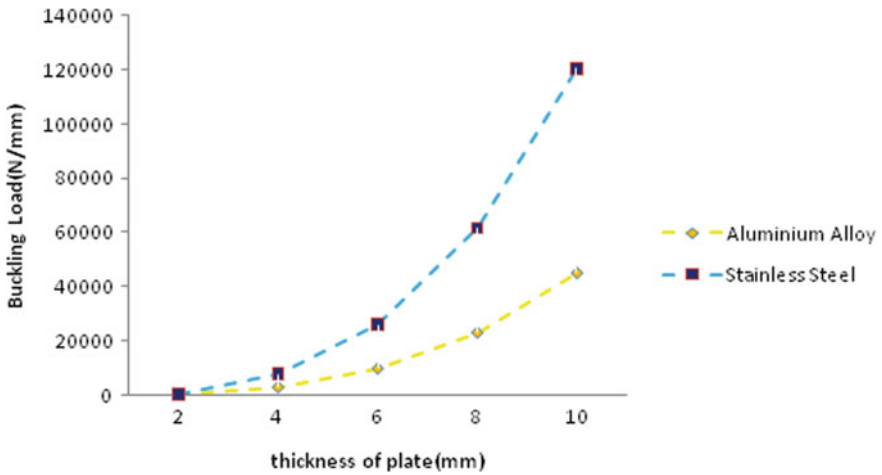


Fig. 4 Deviation of buckle load with respect to thickness

increasing. The buckle load carrying competence of both the materials considered according to Table 1 properties is increasing with thickness.



## 4.2 Perforated Plate

An elliptical cutout considered at the centre of solid plate. Same boundary conditions as that applied for solid plates are applied to the plate. Comparison is done for non-perforated and perforated plate. Changes in parameters of the plate as well as elliptical cutout size and orientations are being done. During plotting of results for comparison between perforations and non-perforation, their ratio is being considered.

### 4.2.1 Orientation of Cutout

Changes of the orientation in elliptical cutout are being done from 0° to 90°. The orientations have consequence on top of the buckle load carrying competence of the plate. Figures 5 and 6 represent the increasing value of buckling load with changing orientations. The maximum buckling load obtained is at 90°. In the Figs. 7 and 8, it represent the evaluation of buckle load with non-perforate and perforated plates for aluminium alloy and stainless steel. Here, the dimensions of plate are 200 \* 100 \* 2 mm (Table 2).

### 4.2.2 Changing Aspect Ratio

The perforated plate length is kept same, and width is changed, and the size of the elliptical area is same. We observe variations in buckling load for both materials at 0° and 90°. Here, decrement in breadth of the plate is made and accordingly comparison with values of non-perforation plate and perforated plate is made and results are plotted by considering the ratio of both quantities. Aspect ratios have effect

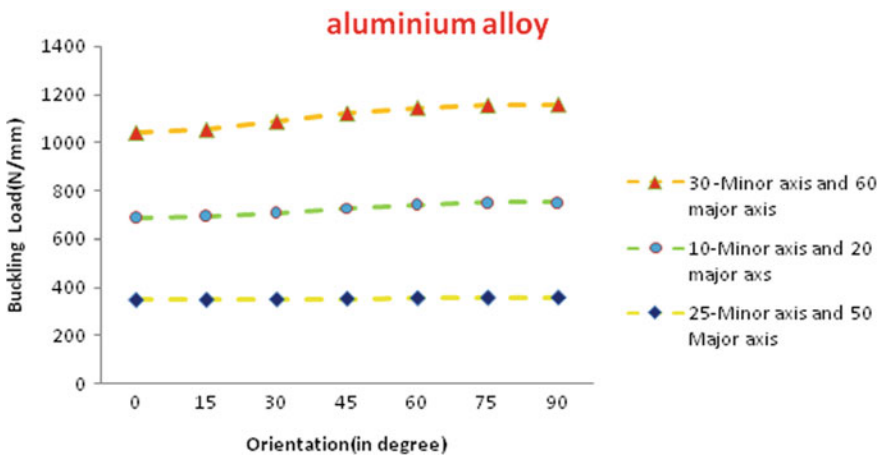


Fig. 5 Deviation of buckling loads with orientation for aluminium alloy

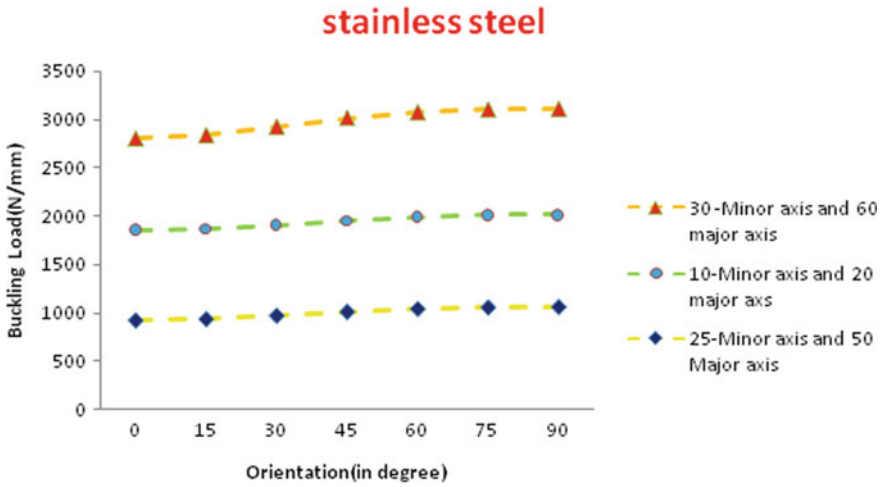


Fig. 6 Deviation of buckling loads with orientation for stainless steel

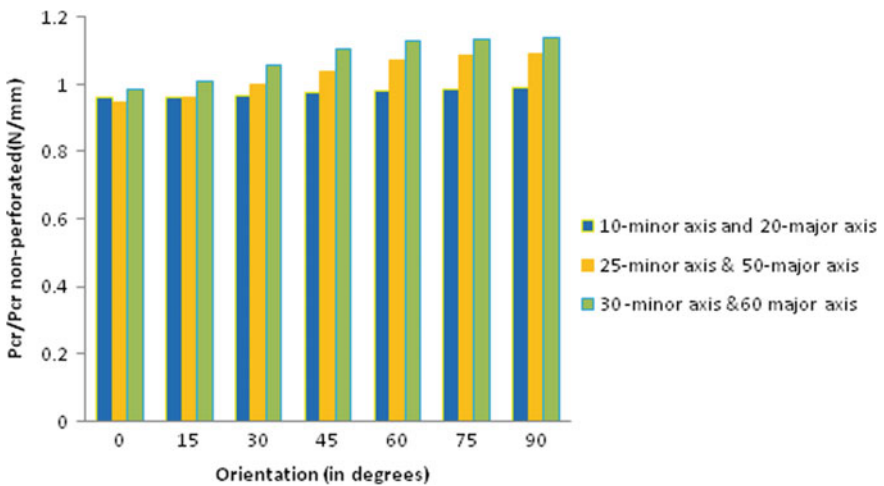
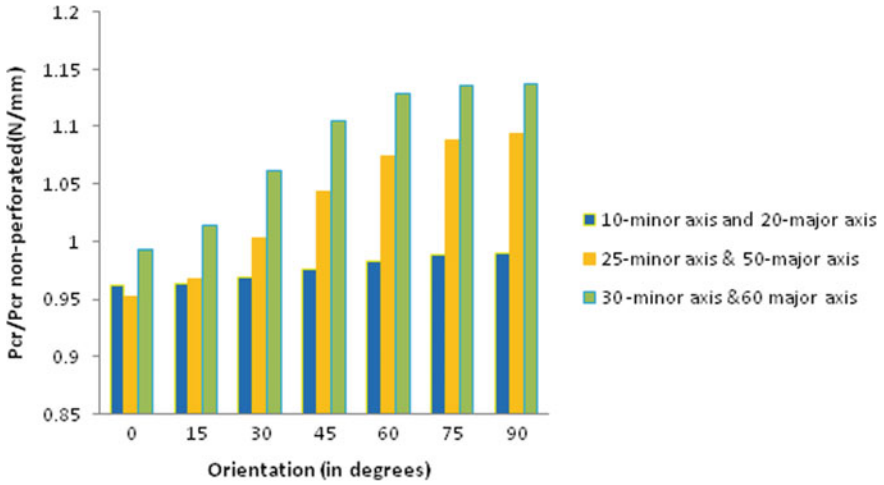


Fig. 7 Comparison of perforated and non-perforated with orientations with aluminium alloy

on buckling load as seen in Figs. 9 and 10. Here, elliptical cutout size is kept same. We observe in Figs. 11 and 12. Comparison of the solid isotropic plate buckling load with same dimensions perforated plate (Table 3; Fig. 13).



**Fig. 8** Comparison of perforated and non-perforated with orientations with stainless steel

**Table 2** Critical buckling load for perforated and non-perforated

Major axis (mm)	Minor axis (mm)	Orientation (°)	Aluminium alloy (N/mm)		Stainless steel (N/mm)	
			Withoutcutout	With cutout	Without cutout	With cutout
20	10	0	360.256	345.81	964.26	928.08
		15	360.256	346.35	964.26	929.58
		30	360.256	348.36	964.26	934.89
		45	360.256	350.82	964.26	941.31
		60	360.256	353.49	964.26	953.01
		75	360.256	355.29	964.26	954.39
		90	360.256	355.26	964.26	952.95
50	25	0	360.256	340.86	964.26	918.57
		15	360.256	346.17	964.26	932.55
		30	360.256	359.25	964.26	966.69
		45	360.256	374.37	964.26	1005.96
		60	360.256	385.71	964.26	1035.24
		75	360.256	391.38	964.26	1049.76
		90	360.256	393.33	964.26	1054.77
60	30	0	360.256	355.35	964.26	957.69
		15	360.256	362.67	964.26	976.89
		30	360.256	380.58	964.26	1023.39
		45	360.256	397.17	964.26	1065.75
		60	360.256	405.99	964.26	1088.16
		75	360.256	408.87	964.26	1095.3
		90	360.256	409.32	964.26	1096.38

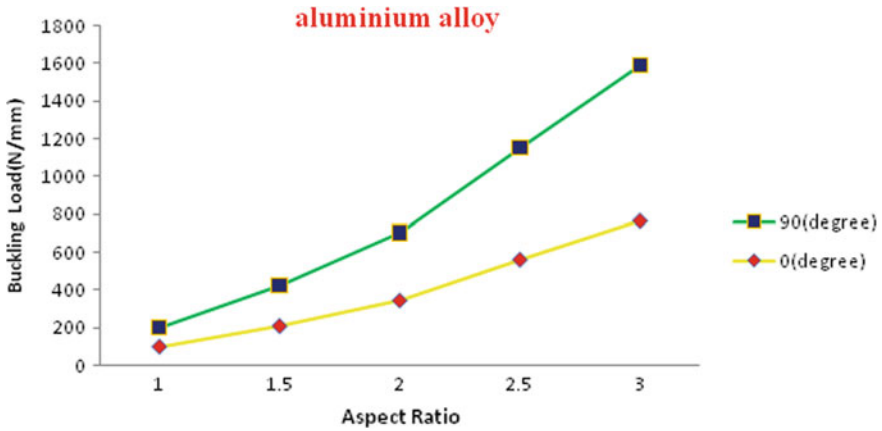


Fig. 9 Deviation of buckling load with perforated plates changing aspect ratio for aluminium alloy

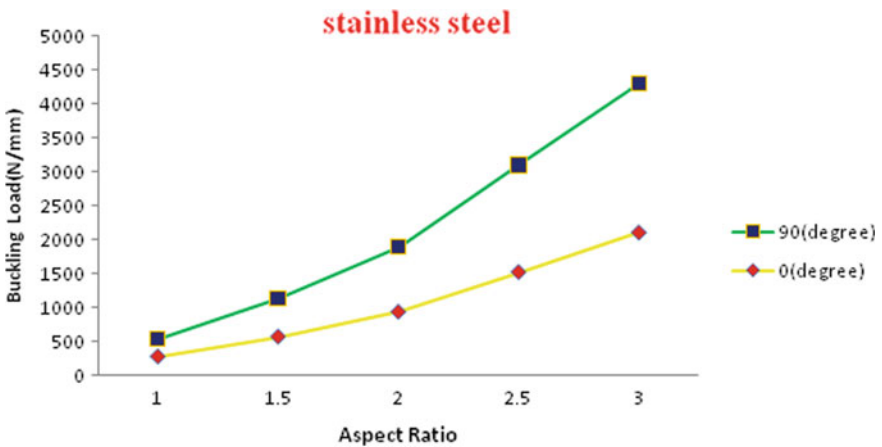


Fig. 10 Deviation of buckling load with perforated plates changing aspect ratio for stainless steel

### 4.2.3 Effect of Changing Area of Elliptical Cutout

The area of elliptical cutout is changed, and different mode shapes are obtained. More effect of changing buckling load is observed as the area of cutout increases. At 0° as the area of cutout increases, the buckling load almost remains constant as shown in Figs. 14 and 15 but further it decreases for both the considered material. Similarly, we observe that at 90° for stainless steel initially, there is increment in buckling load

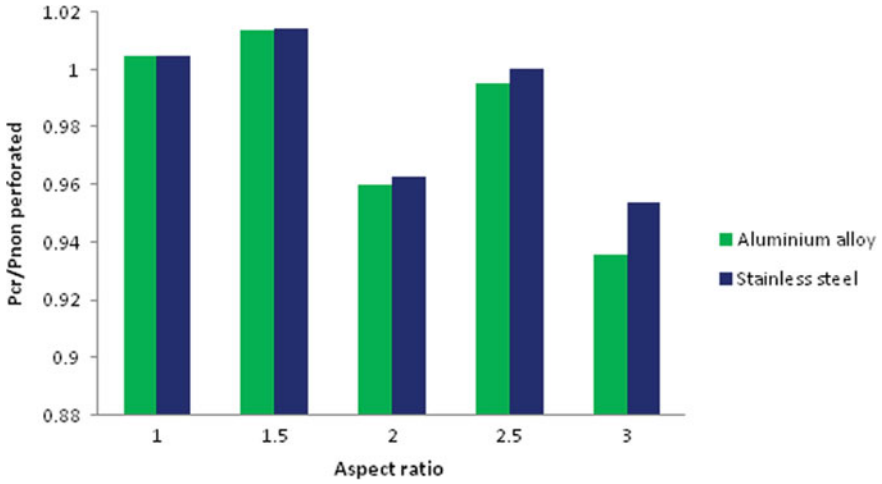


Fig. 11 Comparison of buckling load for non-perforated and perforated at 0°

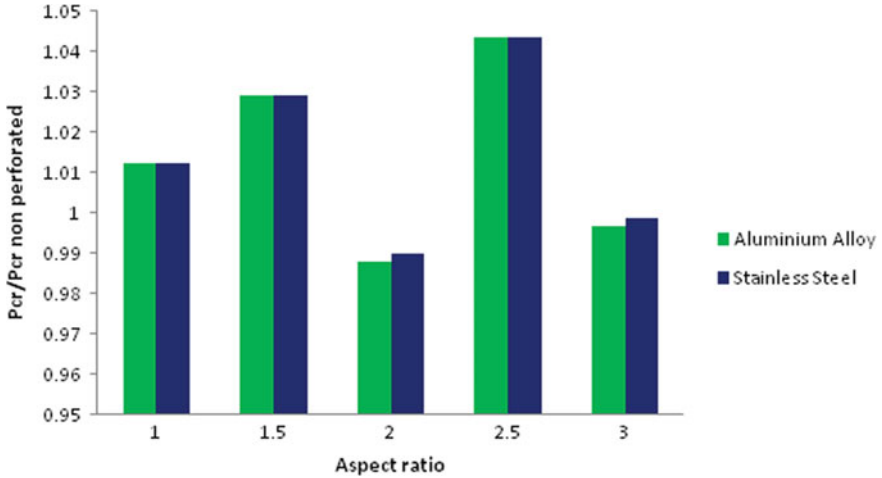
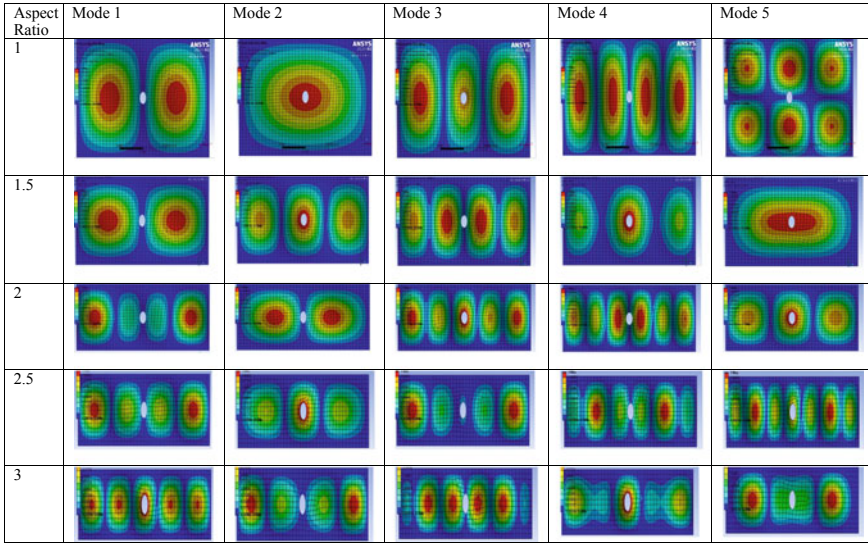


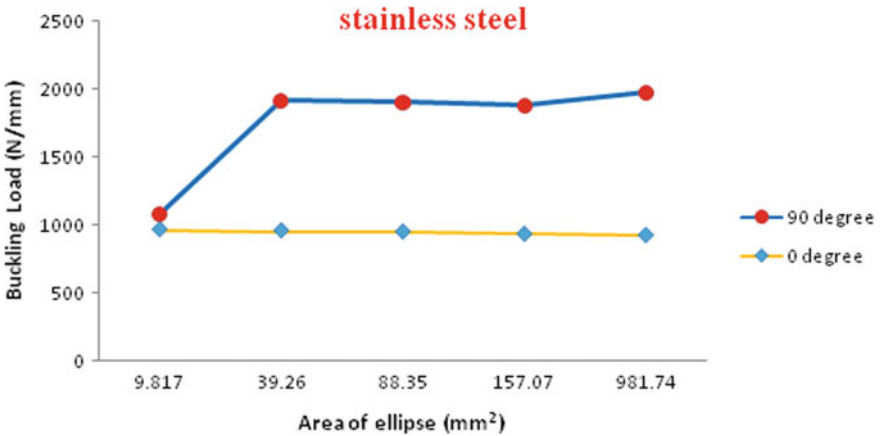
Fig. 12 Comparison of buckling load for non-perforated and perforated at 90°

Table 3 Perforation effect on aspect ratio

Sr. No	Aspect ratio	Aluminium alloy (N/mm)			Stainless steel (N/mm)		
		Without perforation	With perforation		Without perforation	With perforation	
			0°	90°		0°	90°
1	1	99.432	99.915	100.644	266.085	267.39	269.34
2	1.5	206.88	209.79	212.88	553.67	561.479	569.7367
3	2	360.256	345.81	355.86	964.26	928.08	954.45
4	2.5	565.16	562.65	589.6875	1512.862	1513.8	1578.63
5	3	821.02	768.046	818.329	2198.23	2096.22	2195.305



**Fig. 13** Mode shapes for perforated plate with changing aspect ratio of plate at 90°



**Fig. 14** Deviation of buckling load with perforated plates changing elliptical area for stainless steel rectangular plate

carrying capacity; it remains constant for a whilst but further increase in elliptical cut area, the buckling load carrying capacity for rectangular plate increases. For aluminium alloy at 90° as we increase the elliptical cutout area, the buckling load remains constant but further it varies linearly. Ratio of perforated and non-perforated buckling load is compared for both materials and is shown in Figs. 16 and 17 for rectangular plate. Similar process as done for rectangular plate is done for square plate is also carried out and graphs in Figs. 18 and 19 are plotted. For square plate as

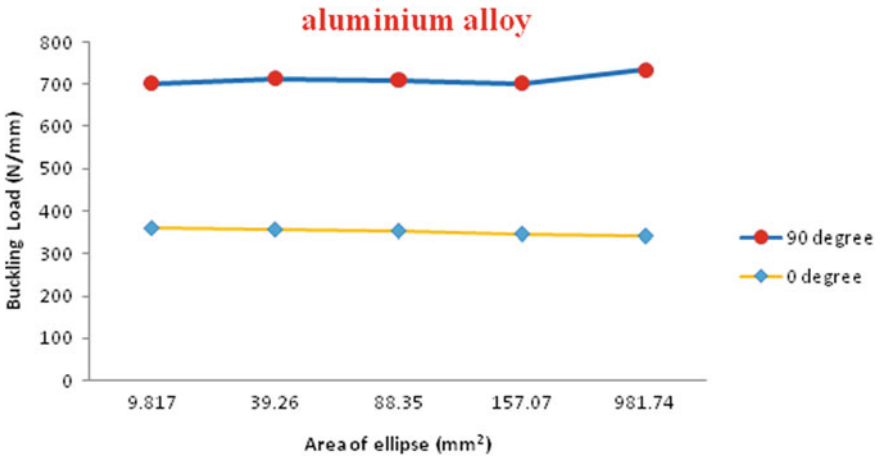


Fig. 15 Deviation of buckling load with perforated plates changing elliptical area for aluminium alloy rectangular plate

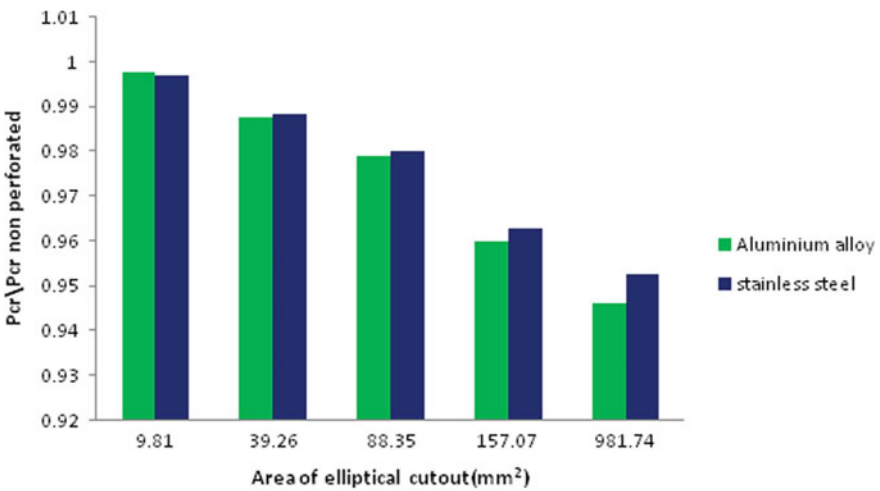


Fig. 16 Comparison of buckling load for non-perforated and perforated at 0° for ellipse cutout area

we increase the elliptical area, the buckling load carrying capacity of plate increases but further increment in elliptical area causes decrement in the buckling load carrying capacity (Tables 4 and 5; Figs. 20 and 21).

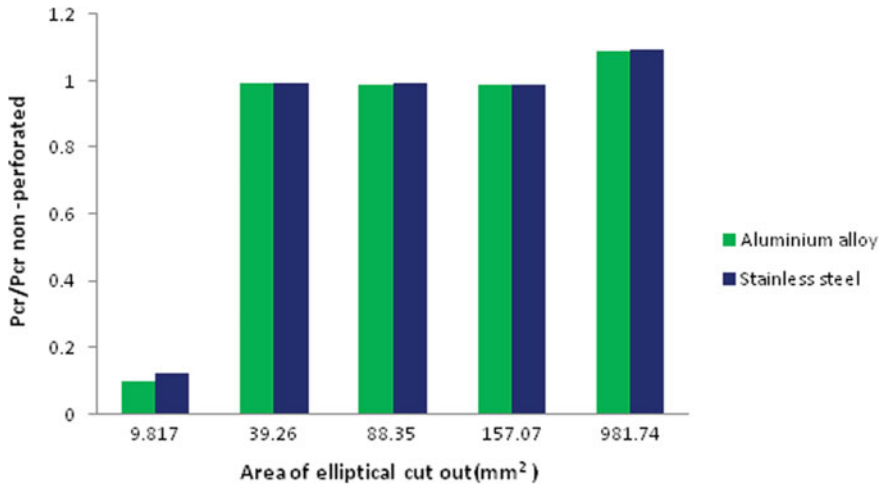
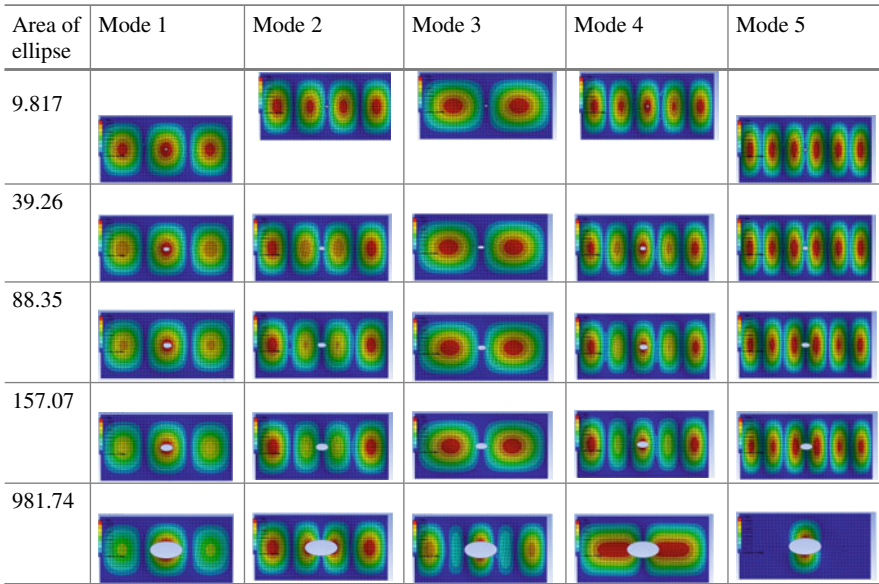


Fig. 17 Comparison of buckling load for non-perforated and perforated at 90° for ellipse cutout area



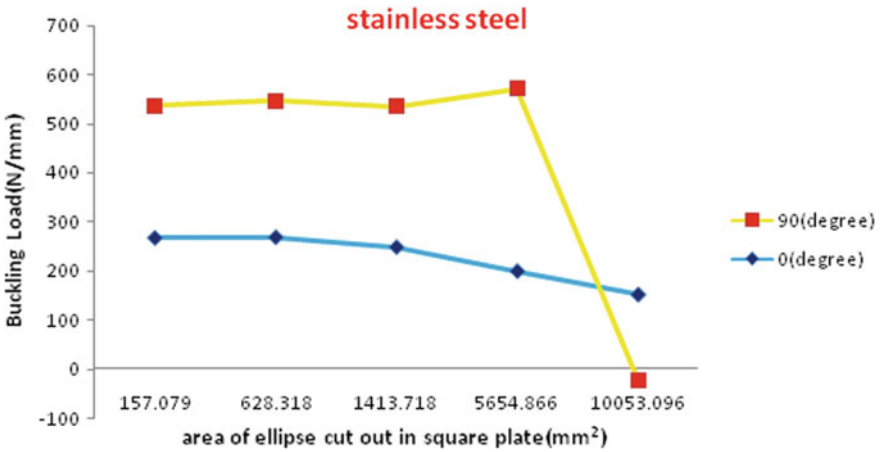


Fig. 18 Deviation of buckling load with perforated plates changing elliptical area for stainless steel square plate

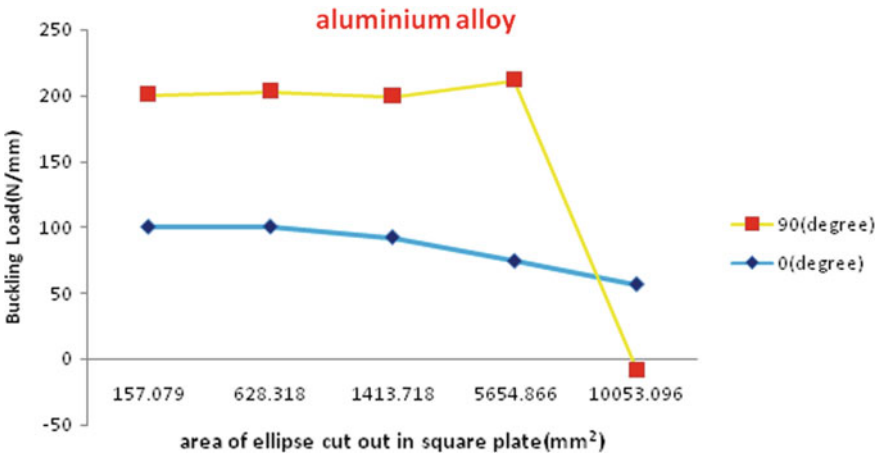


Fig. 19 Deviation of buckling load with perforated plates changing elliptical area for aluminium square plate

### 5 Conclusions

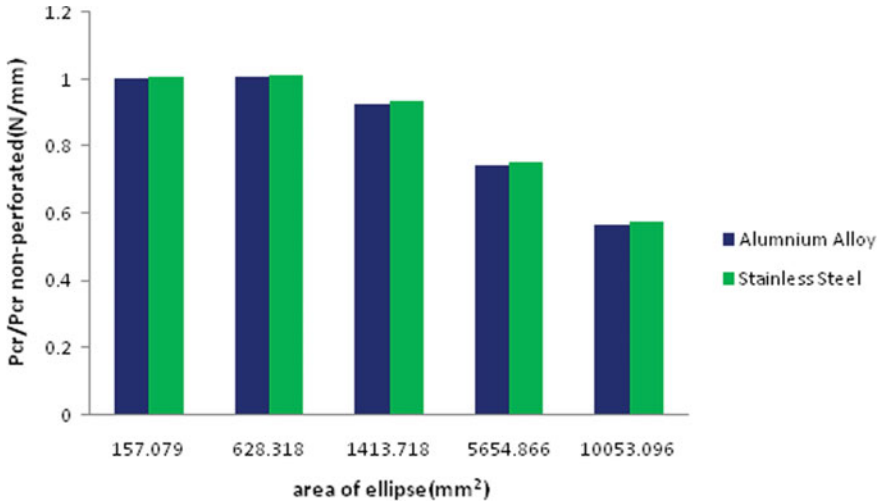
Thin plates are mainly have failure mode due to buckling, hence studying of this phenomena has become an important criteria for design engineers. Edge circumstances affect the buckle load carrying capacity to a very large extent. The Poisson's ratio and Young's Modulus do have effect on the buckling load carrying capacity. The boundary condition for rectangular thin plate used is simply supported on both the

**Table 4** Area of elliptical cutout at 0° and 90° for rectangular plate

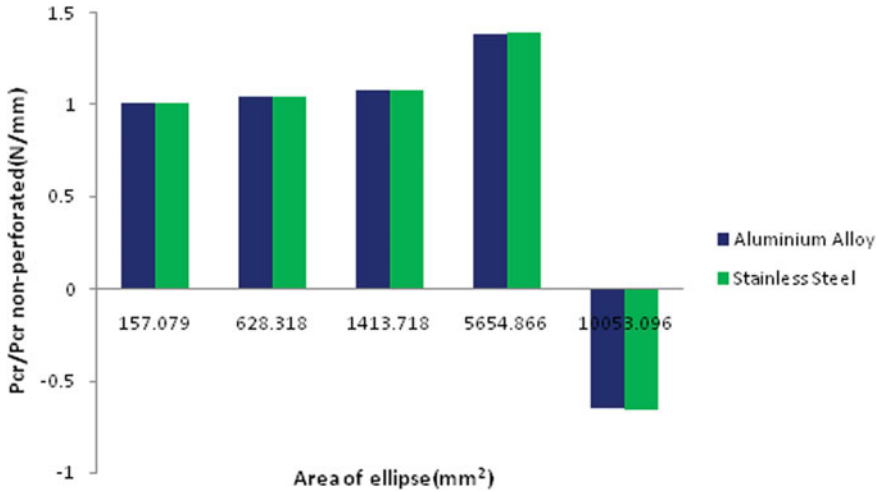
Sr. No	Area of ellipse (mm <sup>2</sup> )	Aluminium alloy (N/mm)		Stainless steel (N/mm)	
		0°	90°	0°	90°
1	9.81	359.1	343.77	961.32	118.2
2	39.26	355.81	358.14	953.1	959.22
3	88.35	352.62	356.67	945.03	955.74
4	157.07	345.81	355.86	928.08	954.45
5	981.74	340.86	393.18	918.57	1054.35

**Table 5** Area of elliptical cutout at 0° and 90° for square plate

Sr. No	Area of ellipse (mm <sup>2</sup> )	Aluminium alloy (N/mm)		Stainless steel (N/mm)	
		0°	90°	0°	90°
1	157.079	99.915	100.64	267.39	269.34
2	628.318	100.0845	103.7985	268.77	277.905
3	1413.718	92.076	107.154	248.85	287.295
4	5654.866	73.9215	137.54	200.37	370.995
5	10,053.096	56.244	-64.464	153.06	-175.8



**Fig. 20** Comparison of buckling load for non-perforated and perforated at 0° for square plate



**Fig. 21** Comparison of buckling load for non-perforated and perforated at 90° for square plate

widths and clamped on the lengths. With increase in thickness and aspect ratio of the plate, buckling load carrying capacity also amplifies. Decrement in width of the plate helped in enhancing the buckling load delivery ability. When comparisons between 0° and 90° orientation of the ellipse shaped cutout are made, we detect increase in buckling load because at 90° more material exists. On comparing results obtained in non-perforated and perforated plates, the plate having aspect ratio of 1 and 2.5, the buckling load capacity of perforated is more as against, this aspect ratio of 2 and 3 plates observe decrement in buckling load carrying capacity upon perforations in plate at centre for the considered boundary condition. When we increase the area of elliptical cutout at 0° and 90°, we observe increment in buckling load carrying capacity initially, but on further amplification, we obtain negative values of buckling load, that is, for the reason that the course of the buckling load carrying of the plate changes to opposite way.

## References

1. Helbig D, da Silva CCC, de Vasconcellos Real M, dos Santos ED, Isoldi LA, Rocha LAO (2016) Study about buckling phenomenon in perforated thin steel plate employing computational modeling and Constructural design method. *Solids Struct* 13:1912–1936
2. Komur MA (2011) Elasto-plastic buckling analysis for perforated steel plates subject to uniform

- a Compression. *Mech Res Commun* 38:117–122
3. Orun AE, Guler MA (2017) Effect of hole reinforcement on the buckling behaviour of thin-walled beams subjected to combined loading. *Thin-Walled Struct* 118:12–22
  4. Mandal SK, Mishra PK (2018) Buckling analysis of rectangular plate element subjected to in-plane loading using finite element method. *Int J Sci Eng Res* 9:2229–5518
  5. Jana P (2015) Optimal design of uniaxially compressed perforated rectangular plate for maximum buckling load. *Thin Walled Structures, Mechanical Engineering, Indian School of Mines, Dhanbad 826004, India, 30 Dec 2015*, pp 0263–8231
  6. Maiorana E, Pellegrino C, Modena C (2008) Linear buckling analysis of perforated plates subjected to localized symmetrical load. Department of Structural and Transportation Engineering, University of Padova, Via Marzolo, 9, 35131 Padova, Italy. *Eng Struct* 30:3151–3158
  7. Taheri MH, Memarzadeh P (2020) “Experimental and numerical study of compressive buckling stability of plates with off-centre crack”, Department of Civil Engineering, Najafabad Branch, Islamic Azad University, Najafabad, Iran. *Theor Appl Fract Mech* 10
  8. Rao LB, Rao CK (2009) Buckling of circular plates with an internal elastic ring support and elastically restrained guided edge against translation. *Adv Vib Eng* 8(1):59–67
  9. Rao LB, Rao CK (2009) Buckling of circular plates with an internal elastic ring support and elastically restrained guided edge against translation. *Mech Based Des Struct Mach* 37(1):60–72
  10. Rao LB, Rao CK (2011) Fundamental buckling of annular plates with elastically restrained guided edges against translation. *Mech Based Des Struct Mach* 39(4):409–419
  11. Rao LB, Rao CK (2010) Buckling analysis of circular plates with elastically restrained edges and resting on internal elastic ring support. *Mech Based Des Struct Mach* 38(4):440–452
  12. Rao LB, Rao CK (2012) Buckling of circular plates with an internal elastic ring support and outer edge restrained against translation. *J Eng Sci Technol* 7(3):393–407
  13. Rao LB, Rao CK (2015) Buckling of elastic circular plates with an elastically restrained edges against rotation and internal elastic ring support. *Int Appl Mech* 51(4):480–488
  14. Rao LB, Rao CK (2013) Fundamental buckling of circular plates with elastically restrained edges and resting on concentric rigid ring support. *Front Mech Eng* 8(3):291–297
  15. Rao LB, Rao CK (2015) Buckling of circular plate with foundation and elastic edge. *Int J Mech Mater Des* 11(2):149–156
  16. Rao LB, Rao CK (2013) Buckling of annular plates with elastically restrained external and internal edges. *Mech Des Struct Mach* 41(2):222–235
  17. Djelosevic M, Tepic J, Tanackov I, Kostelac M (2013) Mathematical identification of influential parameters on the elastic buckling of variable geometry plate. *Sci World J*
  18. Structural analysis with the finite element method linear statics, beams, plates and shells vol 2
  19. Komur MA, Sonmez M (2008) Elastic buckling of rectangular plates under linearly varying in-plane normal load with a circular cutout. *Mech Res Commun* 35:361–371
  20. ANSYS (2015) User’s Manual (version 16.0). Appendix A Eigen value Buckling Analysis
  21. Ventsel E, Krauthammer T (2001) *Thin plates and shells theory, analysis, and applications*. Marcel Dekker, Inc.
  22. Hasan A, Kurgan N (2019) Modeling and buckling analysis of rectangular plates in ANSYS. *Int J Eng Appl Sci*

# Buckling Analysis of Thin Isotropic Square Plate with Rectangular Cut-Out



Prathamesh Mahesh Dehadray, Sainath Alampally,  
and Bhaskara Rao Lokavarapu

**Abstract** This paper investigates the effect of rectangular cut-out on the buckling behaviour of isotropic square plate. Thin plates are used in many complex automobile, aviation and civil structures, and if there are any imperfections, then buckling load highly depends upon cut-out geometry and size. Cut-outs are generally used to lighten the structure and to access for maintenance of structure. This study investigates the critical buckling load for square isotropic plate with rectangular cut-out for simply supported boundary condition. Results for steel and aluminium plate are calculated for variation in thickness of plate, variation in aspect ratio of cut-out and variation in orientation of cut-out. Classical plate theory is used for analytical formulation and finite element analysis is carried out in Ansys software.

**Keywords** Thin plates · Critical buckling load · Cut-outs · Variation of different parameters

## 1 Introduction

Thin plates are extensively used in many structures such as automobiles, ships, aircrafts and missiles. Plates buckle as they subjected to compressive loads more than critical limit; hence, buckling analysis is very important. Various openings and cut-outs are provided for many applications such as ventilation, accessibility for maintenance and damage inspection [1]. Presence of cut-outs in plates changes the behaviour of plate; hence, this study is based on buckling behaviour of plates with rectangular cut-outs. Suneel Kumar et al. [2] studied the effect of rectangular cut-out on the plate. Results are carried out by variation in cut-out dimension, variation in slenderness ratio and variation in area ratio. The effect of the variation of different parameters on the ultimate strength of plate loaded under axial compression is concluded. The results found are validated by Ansys simulation. Djelosevic et al. [3] studied the elastic stability of plates with different geometries of openings.

---

P. M. Dehadray (✉) · S. Alampally · B. R. Lokavarapu  
School of Mechanical Engineering, Vellore Institute of Technology, Chennai Campus, Vandalur-  
Kelambakkam Road, Chennai, Tamil Nadu 600127, India

The effect of different parameters such as shape, size and orientation of holes on the elastic stability of the plate is analysed, and sensitivity factor is obtained for different openings such as square, rectangular and circular. They concluded that the existence of holes reduces the deformation energy. Behzad Mohamazadeh and Noh [4] studied the effect of variation in the thickness of plate with hole on the buckling behaviour of plate. Gerard and Becker equations are used to calculate buckling coefficient and buckling stresses are calculated. They compared the results obtained for plates with holes and plate without holes and concluded that buckling load and stress increase as the thickness of plate increases. Jana [5] analysed the buckling behaviour of rectangular plate with simply supported boundary for uniform axial compression with circular cut-out for various aspect ratios. Eigen value buckling analysis is used for variation in size of cut-out, aspect ratio of plate and thickness of plate. He found out the optimal location of cut-out for maximum buckling load by combining Ansys with MATLAB and concluded that optimal location of cut-out is obtained at centre of the axis on which load is applied. Maiorana et al. [6] studied the effects of holes on the linear buckling behaviour of plates. Circular and square holes are considered, and boundary condition is taken as simply supported all edges under uniaxial compression. Results are obtained for circular and square holes with variation in the location of the holes and graphs are plotted. Ibearugbulem et al. [7] studied the Ritz method and Taylor-McLaurin's series for analysing the buckling behaviour of thin plate with simply supported boundary condition under axial compression. Total potential energy functional for thin plate under buckling load is derived and Taylor-McLaurin's shape function is substituted in it, and after minimization through Ritz method, critical buckling coefficient for different aspect ratios is calculated.

Pouladkhan et al. [8] carried out analysis of buckling behaviour of rectangular plate under uniaxial compression for simply supported all edges and simply supported, fixed, simply supported and free boundary conditions. Equilibrium method is used for finding analytical solution and ABAQUS is used for FEM solution. Study is carried on rectangular steel plate. They concluded that critical buckling load for SSSS boundary condition is more than SFSF boundary condition. Shariati and Dadrasi [9] investigated the behaviour of perforated rectangular steel plates under uniaxial compressive loading for buckling analysis. Circular and square cut-outs are used for various loading bands and numerical as well as experimental results are obtained. ABAQUS software is used for finite element analysis and a set of servo hydraulic INSTRON8802 used for experimental analysis. Results are compared for plate with and without cut-out. They concluded that critical buckling load increases as loading band increases, and buckling load for circular cut-out is more than plate with square cut-out. Mohammadzadeh and Noh [10] studied the effect of holes on the buckling behaviour of thin plate. Simulation is carried out in ABAQUS and critical values for buckling stress as well as buckling load for variation in diameter of hole and variation in thickness of plate are calculated. Banagar et al. [11] carried out the buckling analysis of Aluminium 6061-T6 rectangular plate with rectangular central cut-out. They studied the effect of aspect ratio of plate, boundary conditions, geometry of cut-out and size of cut-out on the buckling behaviour of plate. Experimental study is carried out on UTM and finite element analysis is done in

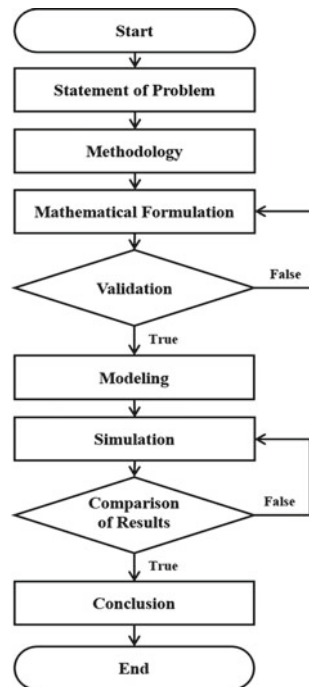
MSC/NASTRAN. Buckling of circular and annular plates with guided edges [1, 12, 13] and with elastic/rigid ring support [14–17] and elastic edges [18, 19] studied by Rao and Rao. However, they have not considered the cut-out in their study. Adah et al. [20] developed a MATLAB program for calculating the critical buckling load for rectangular plate with axially compression load by using Ritz energy equation. They calculated critical buckling coefficient for various boundary conditions and validated with current literature.

Very little literature is available for thin plates with cut-outs and more precisely plates with non-circular cut-outs; hence, this study deals with thin square plate with rectangular cut-out and effect of variation in cut-out aspect ratio and orientation for two different materials.

## 2 Methodology

Research methodology is shown in Fig. 1. Kirchhoff’s thin plate theory is used for mathematical calculations, and simulation is carried out in Ansys Workbench [21]. Analytical and simulation results obtained are validated with previous literature.

Fig. 1 Methodology



### 3 Analytical Formulations

Consider an isotropic thin rectangular plate having length ‘*a*’ mm and width ‘*b*’ mm with thickness ‘*t*’ mm as shown in Fig. 2. Plate is loaded by uniaxial compression load ‘*N<sub>x</sub>*’ N/mm along longitudinal direction with all edges are simply supported.

From Kirchhoff’s classical plate theory [6],

$$D \left( \frac{\partial^4 w}{\partial x^4} + \frac{\partial^4 w}{\partial x^2 \partial y^2} + \frac{\partial^4 w}{\partial y^4} \right) - N_x \frac{\partial^2 w}{\partial x^2} = 0 \tag{1}$$

where *D* is Flexural rigidity given by

$$D = \frac{EI}{(1 - \mu^2)}$$

- E* Young’s Modulus
- I* Moment of inertia
- $\mu$  Poisson’s ratio.

As buckling behaviour is in the form of sinusoidal wave, the function *W* can be taken as,

$$w(x, y) = \sin\left(\frac{m\pi x}{a}\right) * \sin\left(\frac{n\pi y}{b}\right) \tag{2}$$

where *m* and *n* are number of half waves in *x* and *y* direction, respectively.

By solving the governing differential equation, *N<sub>x</sub>* is found as,

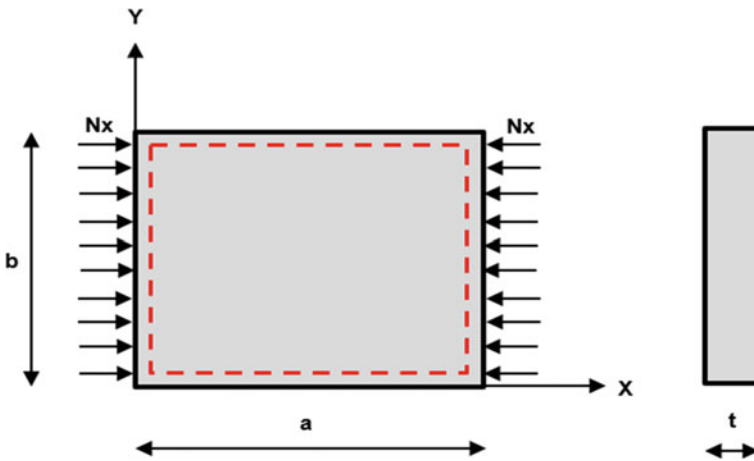


Fig. 2 Thin isotropic plate



$$N_x = D \left( \frac{\pi}{b} \right)^2 \left[ \frac{mb}{a} + \frac{n^2 a}{mb} \right]^2 \quad (3)$$

Critical load is obtained at  $n = 1$ ,  
Hence, critical buckling load is given by,

$$N_x = \frac{K D \pi^2}{b^2} \quad (4)$$

where  $K$  is critical buckling coefficient given by

$$K = \left[ \frac{mb}{a} + \frac{a}{mb} \right]^2 \quad (5)$$

For the square plate,  $a/b = 1$ ; hence,  $K = 4$ .

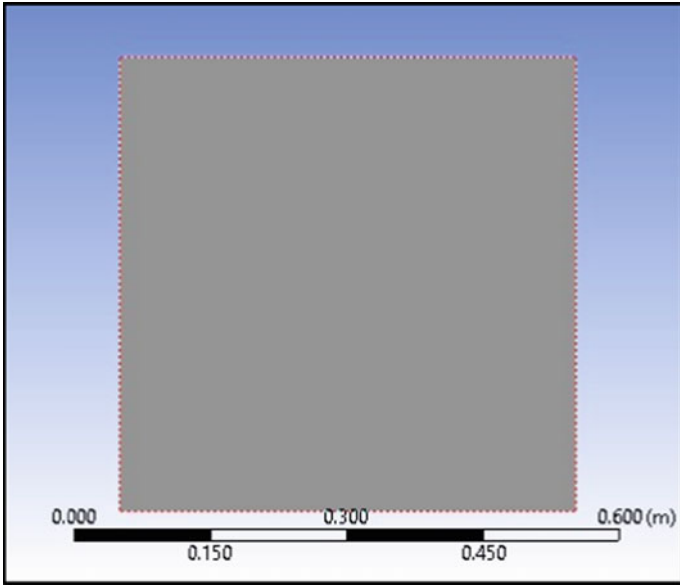
## 4 Fem Model

To find the critical buckling load on a square isotropic plate without cut-out and with rectangular cut-out, eigenvalue buckling analysis is carried out in Ansys 2020 [22, 23]. The eight-noded SHELL 281 elements used in numerical analysis to model the plate. The shell element SHELL281 has 6 degree of freedom at each node (3 displacements and 3 rotations). This study involves analysis of square plate with and without cut-out. Figure 3 shows FEM model of square plate having side 500 mm and thickness 5 mm. For the meshing, element of 5 mm size is taken as shown in Fig. 4, and buckling analysis is carried out. Further, cut-outs are varied for different angles and for various aspect ratios. Initial static structural analysis is done on the model to know the deformations and in the second step, eigenvalue buckling is done to find the load factors for the different modes of the plate.

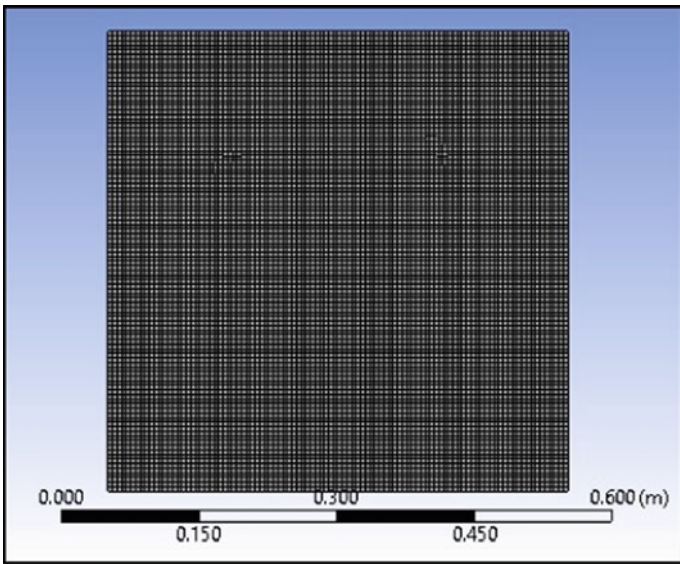
Pouladkhan et al. [8] carried out buckling analysis on rectangular plate having length 200 mm, width 100 mm and height 1 mm. The material is taken as steel having Young's modulus 200 GPa and Poisson's ratio 0.3. Critical buckling load obtained in present study is validated from study carried out by Pouladkhan et al. [8] as shown in Table 1.

## 5 Results and Discussion

In this study, steel and aluminium materials are taken and critical buckling loads are compared for both materials. A square plate of 500 mm length and 5 mm thickness is considered.



**Fig. 3** FEM model of square plate



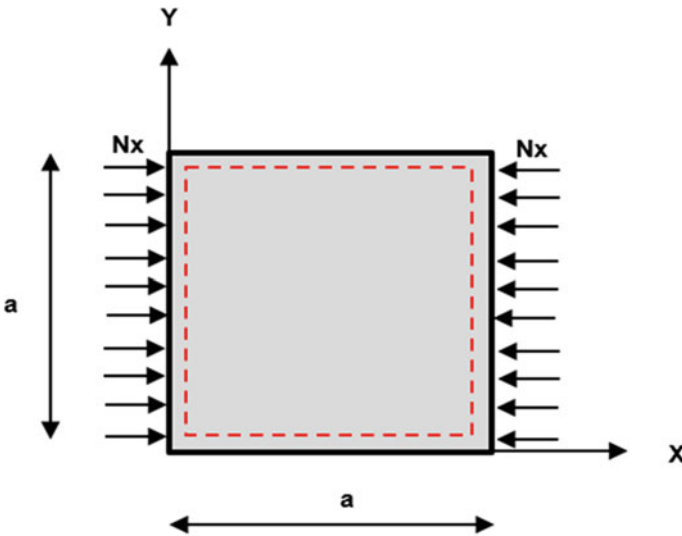
**Fig. 4** Mesh model with element size of 5 mm

**Table 1** Comparison of results with existing work [8]

Pouladkhan et al. [8]		Present study	
Analytical	Ansys	Analytical	Ansys
72.304	71.004	72.32	71.92

### 5.1 Isotropic Plate Without Cut-Out

Figure 5 shows the thin isotropic plate without cut-out with simply supported boundary condition. From Eq. (4), critical buckling load for steel and aluminium square plate having side 500 mm and thickness 5 mm without cut-out is found to be 361.62 N/mm and 131.09 N/mm, respectively, as shown in Table 1. Finite element analysis is carried out in Ansys and obtained values are compared with the values calculated from analytical formulations as shown in Table 2. Error percentage for steel and aluminium are found to be 0.718 and 0.707, respectively.



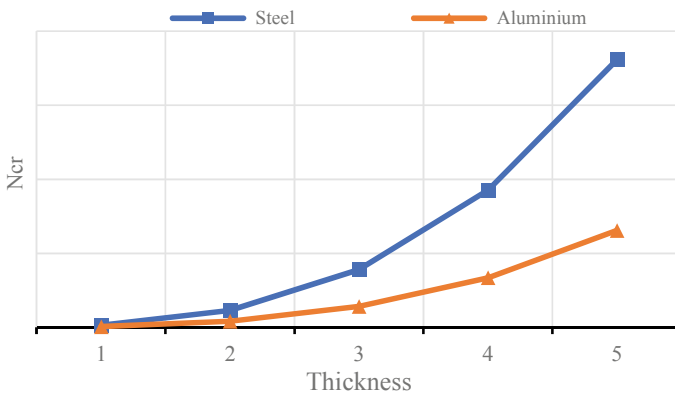
**Fig. 5** Isotropic thin square plate

**Table 2** Critical buckling load (Analytical vs. Ansys)

Steel		Aluminium	
Analytical	Ansys	Analytical	Ansys
361.62	359.02	131.10	130.18

**Table 3** Variation in thickness of plate

Thickness	Steel		Aluminium	
	Analytical	Ansys	Analytical	Ansys
1	2.89	2.89	1.05	1.04
2	23.14	23.11	8.39	8.38
3	78.11	77.86	28.32	28.22
4	185.15	184.2	67.12	66.78
5	361.62	359.02	131.10	130.18



**Fig. 6** Variation in thickness of plate

### 5.2 Effect of Variation in Thickness of Plate

Thickness of plate is varied from 1 to 5 mm to study the buckling behaviour of plate. Results are obtained for steel and aluminium materials analytically as well as by simulation in Ansys are shown in Table 3. As thickness increases, critical buckling load increases as shown in Fig. 6.

### 5.3 Effect of Cut-Out

Plates with cut-outs are generally used for maintenance purpose; hence, analysis of cut-outs is very important. Cut-out of 200 mm length and 100 mm width is made centrally as shown in Fig. 7. Buckling analysis is carried out in Ansys, and results obtained are shown in Table 4. Critical buckling load for steel and aluminium plate with cut-out are obtained as 258.02 N/mm and 91.71 N/mm, respectively. Due to cut-out in the plate, critical buckling load decreases by 29%. FEM model of thin

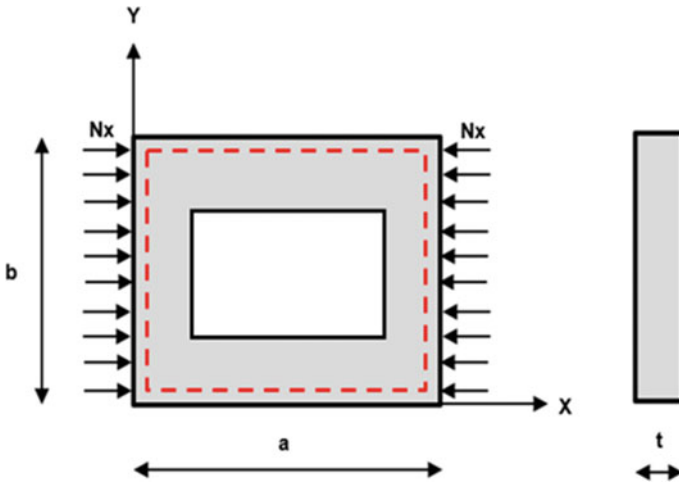


Fig. 7 Thin isotropic plate with cut-out

Table 4 Without versus with cut-out

Steel		Aluminium	
Without cut-out	With cut-out	Without cut-out	With cut-out
361.62	258.02	130.18	91.71

plate with rectangular cut-out is shown in Figs. 8 and 9 shows the mesh model with refinement at the edges of cut-out.

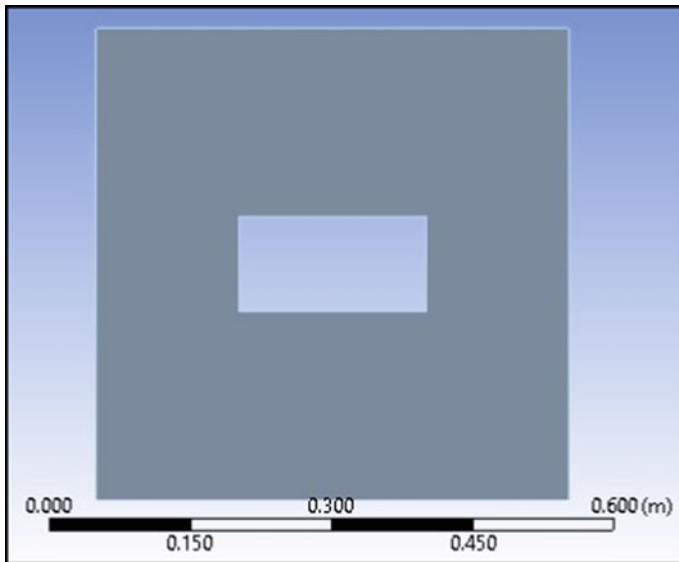


Fig. 8 FEM model of thin plate with cut-out

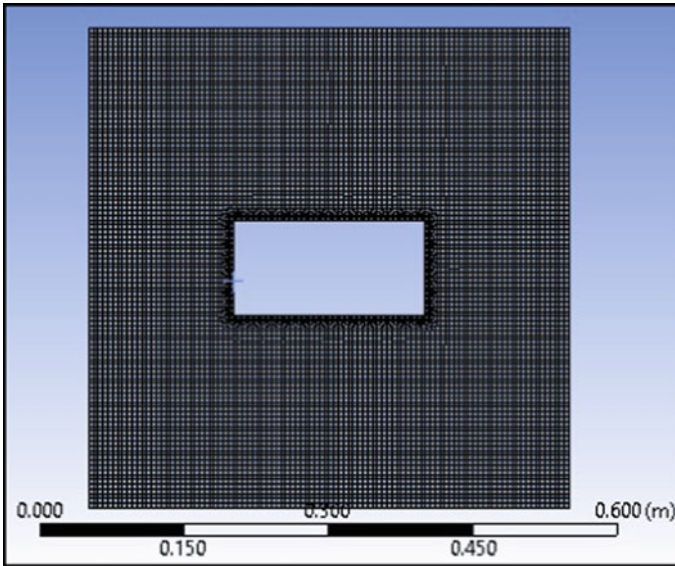


Fig. 9 Mesh model with refinement at edges of cut-out

### 5.4 Effect of Aspect Ratio of Cut-Out

To study the effect of aspect ratio of cut-out, aspect ratio is varied from 1 to 4 horizontally as well as vertically, and results are calculated as shown in Table 5. Critical buckling load is calculated for cut-out dimension 100 \* 100 mm to 400 \* 100 mm for steel as well as aluminium as shown in Table 5. As aspect ratio increases, horizontally, critical buckling load decreases for both materials which is shown in Figs. 10 and 11 shows that as aspect ratio of cut-out increases vertically, buckling load increases up to 3.5 aspect ratio, then decreases.

Table 5 Variation in aspect ratio of cut-out (horizontally and vertically)

Aspect ratio of cut-out	Horizontal orientation			Vertical orientation		
	Cut-out Dimension (mm)	Ncr (N/mm)		Cut-out Dimension (mm)	Ncr (N/mm)	
		Steel	Aluminium		Steel	Aluminium
1	100 * 100	308.53	110.33	100 * 100	308.53	110.33
1.5	150 * 100	282.64	100.51	100 * 150	314.21	111.88
2	200 * 100	258.5	91.71	100 * 200	339.19	120.53
2.5	250 * 100	238.4	84.05	100 * 250	399.69	141.35
3	300 * 100	220.22	77.6	100 * 300	530.75	181.1
3.5	350 * 100	206.37	72.41	100 * 350	625.36	220.61
4	400 * 100	195.38	68.46	100 * 400	444.2	156.31

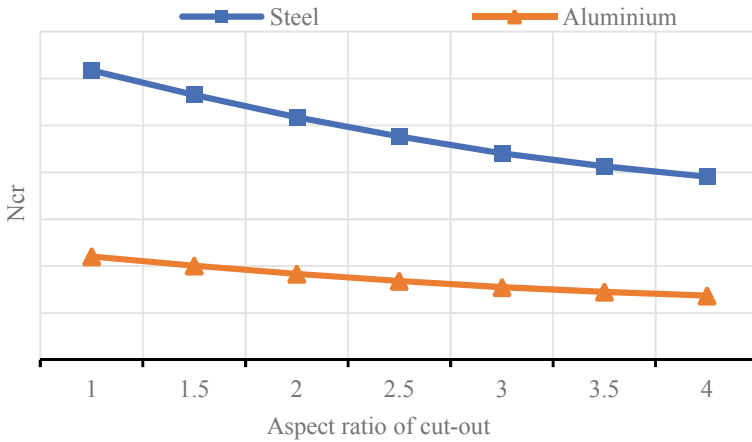


Fig. 10 Variation in aspect ratio of cut-out (horizontally)

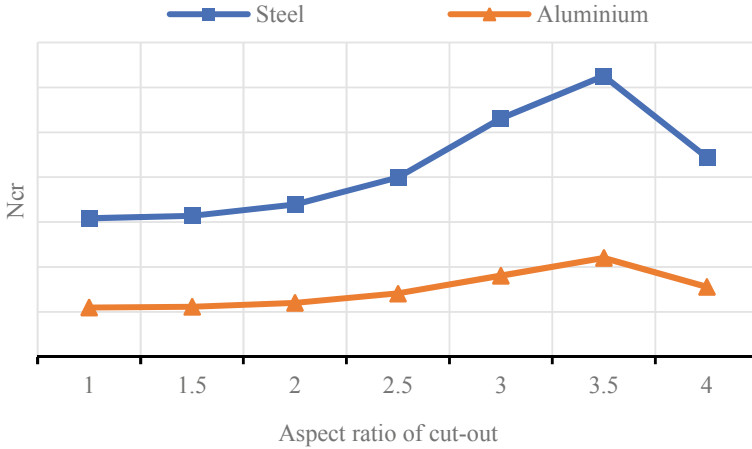


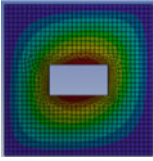
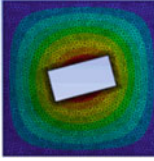
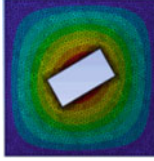

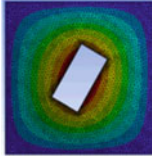
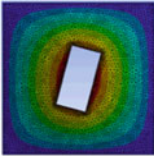
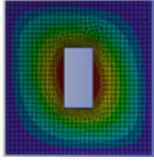
Fig. 11 Variation in aspect ratio of cut-out (vertically)

### 5.5 Effect of Orientation of Cut-Out

To study the effect of orientation of the cut-out on the buckling behaviour of square plate, cut-out of length 200 mm and width 100 mm is made centrally, and the orientation of cut-out is varied from 0 to 90° by increment of 15° as shown in Table 6. The obtained results for steel and aluminium plates are shown in Table 7.

Effect of variation in orientation of cut-out from 0 to 90° is shown in Fig. 12 for steel and in Fig. 13 for aluminium. From the graphs, it can be concluded that with increase in angle of orientation of cut-out, critical buckling load increases up to 60°

**Table 6** Orientation of cut-out

			
0°	15°	30°	45°
			
60°	75°	90°	

for cut-out dimension 350 \* 100 mm then decreases and for all other aspect ratios, critical buckling load decreases after 75°.

Comparison of critical buckling load (Ncr) and weight of steel and aluminium thin square plate with and without cut-out is shown in Table 8. Figures 14 and 15 show comparison of buckling load and weight, respectively, in graphs.

## 6 Conclusion

Buckling behaviour of isotropic thin plates for uniaxial compression loading with and without cut-out is studied. Classical plate theory for thin plate is used, and numerical data for steel and aluminium is generated. Finite element analysis is carried out in Ansys software. Effect of variation in thickness of plate, variation in aspect ratio of cut-out and variation in orientation of cut-out on the buckling behaviour of plate is investigated. The conclusions are,

1. Critical buckling load increases by almost 95% when thickness of plate increases.
2. For horizontal cut-out, critical buckling load decreases gradually with increase in aspect ratio of cut-out.
3. For vertical cut-out, critical buckling load increases gradually with increase in aspect ratio of cut-out up to 3.5, then decreases.
4. As orientation of cut-out increases from 0 to 90°, critical buckling load increases for aspect ratio up to 3 and for aspect ratio 3.5 and 4, critical buckling load increases up to 75°, then decreases.
5. Critical buckling load for aluminium is 65% less than steel, but weight for the same plate of aluminium is also 65% less than steel; hence, aluminium is most widely used to lighten the engineering structures.



**Table 7** Variation orientation of cut-out

Cut-out Orientation	Ncr (Steel)						Ncr (Aluminium)					
	200 * 100	250 * 100	300 * 100	350 * 100	400 * 100	400 * 100	200 * 100	250 * 100	300 * 100	350 * 100	400 * 100	400 * 100
0	258.5	238.4	220.22	206.37	195.38	195.38	91.17	84.05	77.6	72.41	72.41	68.46
15	262.16	241.79	223.61	207.62	193.97	193.97	93.08	85.6	78.98	73.22	73.22	68.33
30	272.54	256.98	241.88	226.51	210.31	210.31	96.81	90.99	85.48	77.93	77.93	74.15
45	291.97	291.69	297.46	310.05	330.64	330.64	103.67	103.31	105.09	109.2	109.2	116.28
60	315.57	341.88	397.35	510.19	519.52	519.52	112.13	121.07	140.25	179.34	179.34	184.38
75	333.78	384.31	493.88	649.63	452.2	452.2	118.6	136.18	174.45	230.83	230.83	160.17
90	339.69	399.69	530.75	625.36	444.2	444.2	120.88	141.74	187.63	221.99	221.99	157.2



Fig. 12 Variation orientation of cut-out (steel)

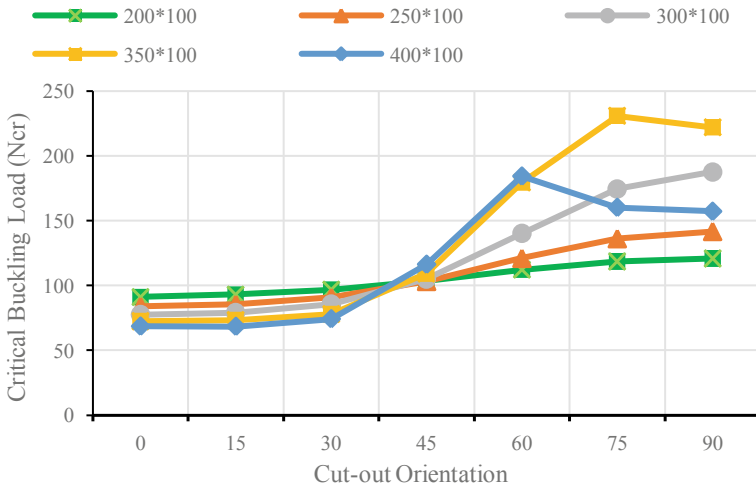


Fig. 13 Variation orientation of cut-out (aluminium)

Table 8 Comparison of Ncr and weight

Parameter	Without Cut-out		With Cut-out	
	Steel	Aluminium	Steel	Aluminium
Ncr (N/mm)	361.62	131.1	258.5	91.17
Weight (N)	96.23	33.94	88.58	31.19



Fig. 14 Comparison of Ncr with and without cut-out

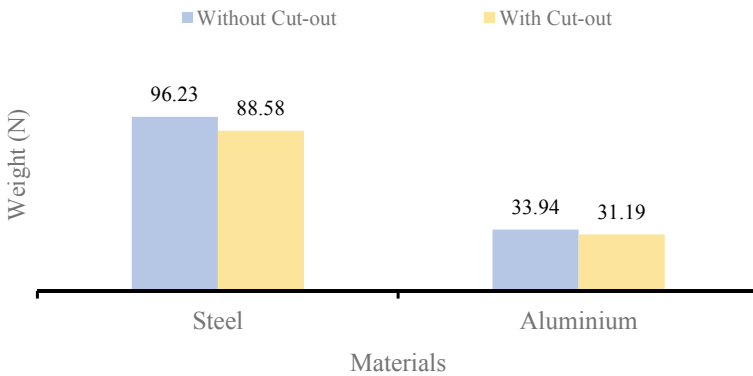


Fig. 15 Comparison of weight with and without cut-out

## References

1. Rao LB, Rao CK (2009) Buckling of circular plates with an internal elastic ring support and elastically restrained guided edge against translation. *Mech Based Des Struct Mach* 37 (1):60–72
2. Suneel Kumar M, Alagusundaramoorthy P, Sundaravadivelu R (2007) Ultimate strength of square plate with rectangular opening under axial compression. *J Naval Architect Mar Eng*
3. Djelosevic M, Tepic J, Tanackov I, Kostelac M (2013) Mathematical Identification of influential parameters on the elastic buckling of variable geometry plate. Hindawi Publishing Corporation, *The Scientific World Journal* Volume 2013
4. Mohamazadeh B, Noh H-C (2014) Use of buckling coefficient in predicting buckling load of plates with and without holes. *J Korean Soc Adv Comp Struc* 5(3):1–7, Sept 2014

5. Jana P (2015) Optimal design of uniaxially compressed perforated rectangular plate for maximum buckling load. *Thin-Walled Structures*
6. Maiorana E, Pellegrino C, Modena C (2008) Linear buckling analysis of perforated plates subjected to localised symmetrical load. *Eng Struct* 30:3151–3158
7. Ibearugbulem OM, Osadebe NN, Ezeh JC, Onwuka DO (2011) Buckling analysis of axially compressed SSSS thin rectangular plate using taylor-mclaurin shape function. *Int J Civil Struct Eng* 2(2)
8. Pouladkhan AR, Emadi J, Safamehr M (2011) Numerical study of buckling of thin plates. *World Acad Sci Eng Technol* 78
9. Shariati M, Dadrasi A (2012) Numerical and experimental investigation of loading band on buckling of perforated rectangular steel plates. *Res J Recent Sci* 10:63–71
10. Mohammadzadeh B, Noh HC (2016) Investigation into buckling coefficients of plates with holes considering variation of hole size and plate thickness. *22(3):167–175*
11. Banagar AR, Ganesh UL, Rampur VV, Srinivas CV (2019) Buckling analysis of plates with rectangular cutouts. *Int J Eng Res Technol (IJERT)*
12. Rao LB, Rao CK (2009) Buckling of circular plates with an internal elastic ring support and elastically restrained guided edge against translation. *Adv Vib Eng* 8(1):59–67
13. Rao LB, Rao CK (2011) Fundamental buckling of annular plates with elastically restrained guided edges against translation. *Mech Based Des Struct Mach* 39(4):409–419
14. Rao LB, Rao CK (2013) Fundamental buckling of circular plates with elastically restrained edges and resting on concentric rigid ring support. *Front Mech Eng* 8(3):291–297
15. Rao LB, Rao CK (2010) Buckling analysis of circular plates with elastically restrained edges and resting on internal elastic ring support. *Mech Based Des Struct Mach* 38 (4):440–452
16. Rao LB, Rao CK (2012) Buckling of circular plates with an internal elastic ring support and outer edge restrained against translation. *J Eng Sci Technol* 7(3):393–407
17. Rao LB, Rao CK (2015) Buckling of elastic circular plates with an elastically restrained edges against rotation and internal elastic ring support. *IntAppl Mech* 51(4):480–488
18. Rao LB, Rao CK (2013) Buckling of annular plates with elastically restrained external and internal edges. *Mech Based Des Struct Mach* 41(2):222–235
19. Rao LB, Rao CK (2015) Buckling of circular plate with foundation and elastic edge. *Int J Mech Mater Des* 11(2):149–156
20. Adah EI, Onwuka DO, Ibearugbulem OM (2019) MATLAB based buckling analysis of thin rectangular flat plates. *Am J Eng Res (AJER)* 8(4):224–228
21. Ventsel E, Krauthammer T (2001) *Thin plates and shells theory: analysis, and applications*
22. Solid works version 19 user manual
23. ANSYS version 19.2 user manual

# Numerical Investigation on Strength of Isotropic and Laminated Composite Pressure Vessel



Venkata Narayana Yenugula and Raja Shekhar Bhukya

**Abstract** Cylindrical pressure vessels are being used in different industrial applications like power plants, chemical and processes plants to store and use fluids and liquids. The thermal, fatigue and static stress analysis has been carried out on cylindrical pressure vessels for a given geometry with different materials. Buckling analysis also carried out to find the satiability of the cylindrical pressure vessel with hemispherical domes. The generalized finite element code with Ansys is used to perform the above analysis. The static analysis is to determine the stress, deformation and strain. Fatigue analysis is performed to determine life, damage and safety factor of the pressure vessel using AISI-1513 steel, carbon fiber and E-glass fiber-reinforced materials. Thermal analysis has been carried out to find the temperature gradients and rate of heat transfer per unit area of the pressure vessel using AISI-1513 steel, carbon fiber and E-glass fiber materials. Buckling analysis of pressure vessel has been carried out with AISI-1513 steel and with the laminated composite material. Comparisons are made after performing static, fatigue and thermal analysis with different materials.

**Keywords** Pressure vessel · Static analysis · Buckling analysis · Factor of safety · Fatigue analysis and carbon fiber

## 1 Introduction

Metals as well as composite pressure vessels were designed for holding gases and liquids at substantially very high pressure. Historically, it was evident that improper design of pressure vessels causes fatal accidents and hazardous environment in plants during development of pressure vessels and their operations. Consequently, design, developments and operations of pressure vessels are controlled and monitored by some accredited engineering departments supported by legislations. Due to this reason, definition and development procedures of pressure vessels vary for different

---

V. N. Yenugula (✉) · R. S. Bhukya  
Department of Mechanical Engineering, Sreenidhi Institute of Science and Technology,  
Ghatkesar, Hyderabad, Telangana 501301, India

© The Author(s), under exclusive license to Springer Nature Singapore Pte Ltd. 2022  
G. S. V. L. Narasimham et al. (eds.), *Innovations in Mechanical Engineering*,  
Lecture Notes in Mechanical Engineering,  
[https://doi.org/10.1007/978-981-16-7282-8\\_7](https://doi.org/10.1007/978-981-16-7282-8_7)

countries. The design parameters which influence the safety of pressure vessels are maximum working pressure, minimum temperature, safety factor and corrosion allowances for metallic pressure vessels. Leak-proof development and manufacturing pressure vessels decrease extensive damage of property, and also physical injuries can be avoided. General theoretical shapes of pressure vessels are cylindrical pressure vessels, spherical and cone-shaped pressure vessels. Spherical vessels are stronger among other shapes, but development and manufacturing are very complicated. Pressure vessels material should consist of more ductility and toughness to withstand different pressure variations during operation [1, 2]. Pressure vessels manufactured with metals are less preferable in automotive, aerospace industries and gas and oil refinery industries because of having more weight to strength factor and more corrosion characteristics. These companies are in demand with lightweight materials (high strength to weight ratio) such as carbon fiber and glass fiber-reinforced materials. Composite materials are used for increasing performance of different structures due to having more strength to weight ratio and replacing conventional metal material [3–5].

Kharat. A et al. [6] carried out literature review on stress analysis of composite pressure vessels and concluded that ASTM and other codes sufficient enough to give solutions for regular-shape pressure vessels with higher factor of safety. But pressure vessels with non-standard shapes with geometric discontinuities with limit loads and stress concentration are not possible to analyze with the above codes. Abdalla et al. [7] studied and formulated analytically optimum shape and thickness of the pressure vessel and observed that the solutions were admitted only for additional constraints. Raja et al. [8] made an attempt to evaluate the bursting pressure of filament wounded pressure vessel with different layup sequences using commercially available finite element software, Ansys. Abdolreza. T et al. [9] done critical review on pressure vessel analysis based on ASTM pressure vessel code and observed that it is essential to choose suitable analytical procedure to design and analysis of different pressure vessels. In industrial applications, fiber-reinforced composite shells and pressure vessels undergo high operating pressure throughout their life cycle. Generally, 15–300 MPa pressure range is used for high pressure vessels

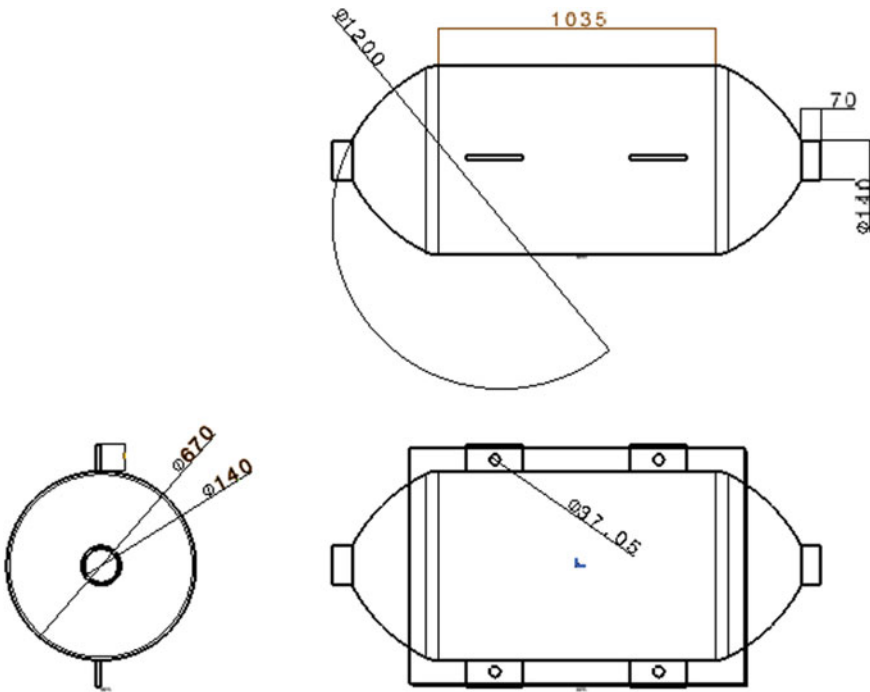
## 2 Methodology of Paper

Based on the radius ( $r$ ) to thickness ratio ( $t$ ), there are two types of approaches in design of pressure vessels analysis. First method: if the  $r/t$  ratio is more than 20, we need to go for structural stability analysis, otherwise elasticity approach need to be followed. The geometry of the pressure vessel is as follows: overall length = 1732 mm, thickness = 15 mm and radius = 335 mm was taken for performing analysis. Buckling analysis is one of the most important collapse modes of the pressure vessel. The first one is that pressure vessel code usually only provided design method by rules to protect against global bulking of shell under conventional loads, such as external pressure or axial compression load.

**Table 1** AISI-1513 steel mechanical properties

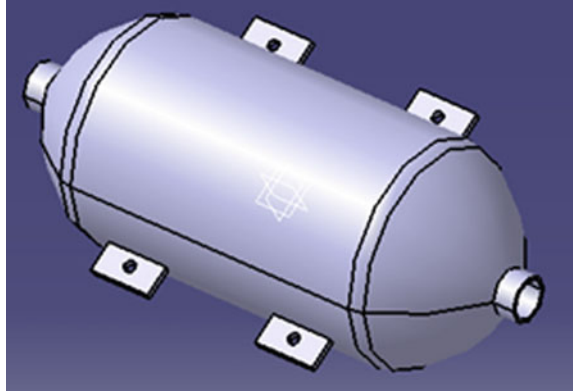
Name of the property	Property value
Modulus of elasticity	$200 \times 10^5 \text{ N/mm}^2$
Poisson's ratio	0.29
Shear modulus	$80 \times 10^5 \text{ N/mm}^2$
Ultimate tensile strength	$36010^5 \text{ N/mm}^2$ – $480 \text{ N/mm}^2$
Tensile strength, yield	$215 \times 10^5 \text{ N/mm}^2$

The material properties of the pressure vessel are as shown in Table 1. The internal pressure used for the above analysis was  $15 \text{ N/mm}^2$  with different boundary conditions. The  $r/t$  ratio of the pressure vessel considered here is 22. In this work, the analysis of geometric failure and material failure was carried out using generalized finite element software, Ansys. The 2D drawing which gives the overall dimensions of the pressure vessel is shown in Fig. 1. To get the overall idea about the pressure vessel, solid modeling was developed by using CATIA as shown in Fig. 2.



**Fig. 1** 2D model of pressure vessel

**Fig. 2** Solid model of pressure vessel



### 2.1 Buckling Analysis of Pressure Vessel Using Ansys

For modeling purpose, a shell 281 element is being selected among the available element library of Ansys. The eight-nodded shell element 281 having six degrees of freedom at each node is used in buckling analysis of pressure vessel. The boundary conditions used for the buckling analysis of isotropic and laminated composite (CFRP) pressure vessel is shown in Fig. 3.

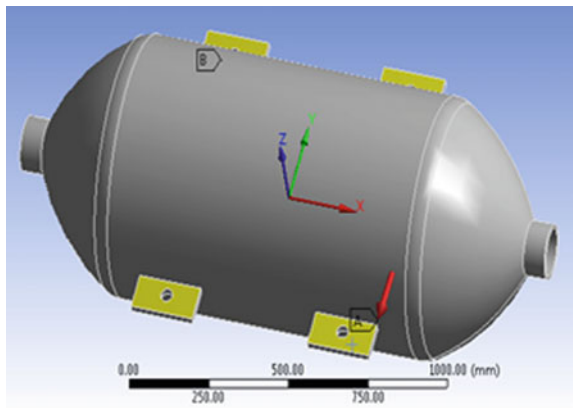
The linear buckling analysis was carried out with different materials (AISI-1513 steel and carbon fiber-reinforced plastics—CFRP) and following boundary conditions as shown in Fig. 3.

1. Both ends of the pressure vessel fixed

$$U_x = U_y = U_z = R_x = R_y = R_z = 0 \tag{1}$$

2. Fixed at four points on cylindrical portion

**Fig. 3** Boundary conditions on cylindrical portion





**Table 2 (a) CFRP mechanical properties, (b) GFRP mechanical properties**

(a)		
Name of the property	Direction	Property value
Modulus of Elasticity in longitudinal direction	$E_1$	$2.7 \times 10^5 \text{ N/mm}^2$
Modulus of Elasticity in transverse direction	$E_2$	$5.2 \times 10^3 \text{ N/mm}^2$
Shear modulus	$G_{12}$	$2.6 \times 10^3 \text{ N/mm}^2$
Poisson's ratio	$\nu_{12}$	0.25
(b)		
Modulus of Elasticity in longitudinal direction	$E_1$	$1.0.64 \times 10^5 \text{ N/mm}^2$
Modulus of Elasticity in transverse direction	$E_2$	$1.27 \times 10^3 \text{ N/mm}^2$
Shear modulus	$G_{12}$	$3.0 \times 10^3 \text{ N/mm}^2$
Poisson's ratio	$\nu_{12}$	0.20

$$U_x = U_y = U_z = R_x = R_y = 0 \tag{2}$$

The above boundary conditions were as per the horizontal pressure vessel realistic conditions. The material properties of the steel (AISI-1513 steel) and the CFRP-laminated composite material is as shown in Tables 1 and 2, respectively. The CFRP-laminated composite material is widely used in civil and offshore applications; generally, it is a quasi-isotropic material having four fundamental elastic constants. Other five elastic constants for this material used to find using empirical formulas in order to convert this in to orthotropic material.

The quasi-isotropic angle-ply  $(\nu/\nu)5_s$ , where  $\nu=45^\circ$ , orientation with 1.5-mm layer thickness of the carbon fiber-reinforced plastic material was used for investigation of the buckling analysis.

The results of linear buckling analysis of pressure vessels using generalized finite element software, Ansys with two different materials (isotropic and laminated composite material) and two different boundary conditions are as shown in Table 3. It is evident that the buckling factors for the steel pressure vessels are more than CFRP material pressure vessel. It is also observed that the critical buckling pressures for the steel pressure vessels are more than the applied pressure than the CFRP pressure for a given boundary condition of the finite element model. Generally, it is also known that if BLF (buckling load factor)  $< 1$  pressure vessel loses its geometry rather than elastic failure. The critical pressures ( $P_{cr}$ ) of the isotropic pressure vessel are observed to

**Table 3** Buckling load factors and critical loads

SN	Material	Lay-up sequence	B.C'S	BLF	$P_{cr}$
1	Steel	–	Fixed-Ends	1.93	20.42
2	Steel	–	Fixed on cylinder	1.36	28.95
3	CFRP	$(45^\circ/-45^\circ)_{5_s}$	Fixed-Ends	0.37	5.59
4	CFRP	$(45^\circ/-45^\circ)_{5_s}$	Fixed on cylinder	0.51	7.63

be more than the applied pressure ( $15 \text{ N/mm}^2$ ). 1705 mm effective length, 15 mm thickness and 15 MPa internal pressure was considered for buckling of isotropic and laminated composite pressure vessels. The buckling factors and critical pressures of laminated pressure vessels were observed to be less than the AISI-1513 steel.

The first fundamental mode shape of CFRP pressure vessel and AISI-1513 steel pressure vessels with fixed end boundary conditions are shown in Fig. 3. Fig. 4a shows the first mode shape and critical buckling load (5.59 MPa) of CFRP material pressure vessel. Fig. 4b shows the first mode shape and critical buckling load (20.42 MPa) of AISI-1513 steel pressure vessel. The buckling analysis was carried out with the effective length of the pressure vessel using Ansys, and other attachments were removed (Fig. 4).

## 2.2 *Static, Fatigue and Thermal Analysis of Pressure Vessel*

The fatigue analysis has been carried out to find out the life, damage and safety factor of the pressure vessel after completing the static analysis. Fatigue analysis has been carried out with three different materials. The fatigue analysis results are shown in Figs. 5 and 6. Thermal analysis was carried out to find the temperature distribution and heat flux of the internal pressure vessel subjected to operating temperature and air convection as boundary conditions. In present work,  $300 \text{ }^\circ\text{C}$  operating temperature, air convection,  $30 \text{ }^\circ\text{C}$  ambient temperature and  $2200 \text{ W/m}^2 \text{ }^\circ\text{C}$  air film coefficient were considered. The results were evaluated for AISI-1513 steel pressure vessel and other two composite materials also.

## 3 Results and Discussions

### 3.1 *Static Analysis*

Buckling analysis of pressure vessel with different boundary conditions and three different materials was carried out using finite element software, Ansys. Table 3 depicts the comparison of critical pressure of both AISI-1513 steel and CFRP pressure vessel. It has been observed that the critical pressure and buckling load factors of AISI-1513 steel are more than the composite pressure vessels.

The static analysis has been carried out on both AISI-1513 steel and composite pressure vessels. It is evident that the results of both AISI-1513 steel and the composite pressure vessel show that the induced stresses are well below the allowable stresses for a given boundary condition and geometry. Table 4 and Fig. 5 present the results of static analysis. E-Glass fiber has major contribution followed by AISI-1513 steel and carbon fiber. Deformation is low at AISI-1513 steel followed by E-Glass fiber and carbon fiber composite.

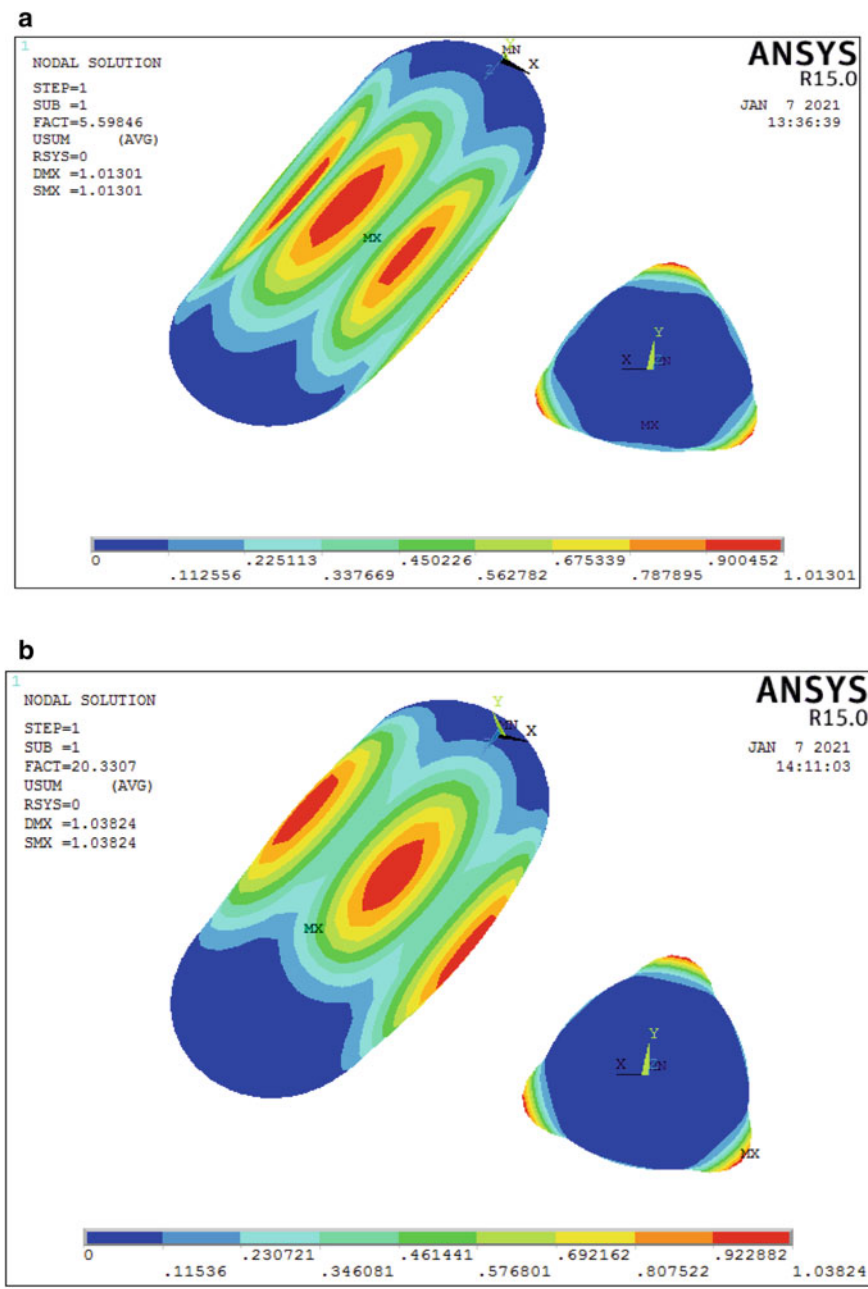
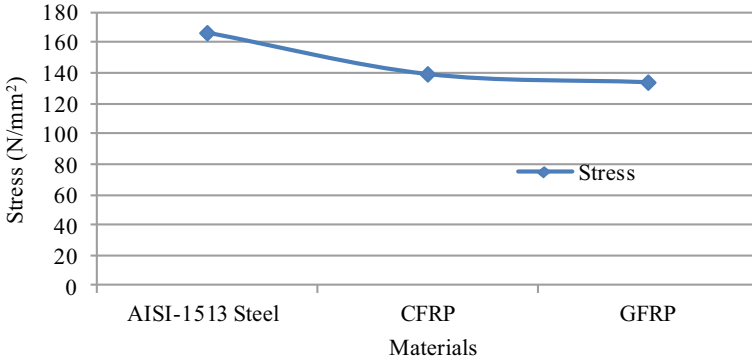
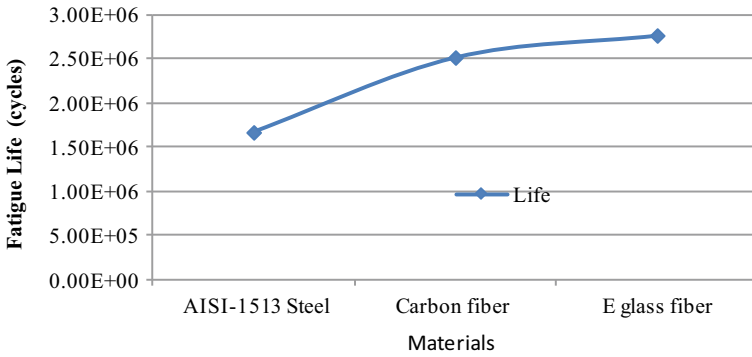


Fig. 4 (a) CFRP-fixed ends, (b) Isotropic (steel)-fixed ends



**Fig. 5** Static analysis stress versus materials



**Fig. 6** Fatigue analysis life and materials

**Table 4** Static analysis results

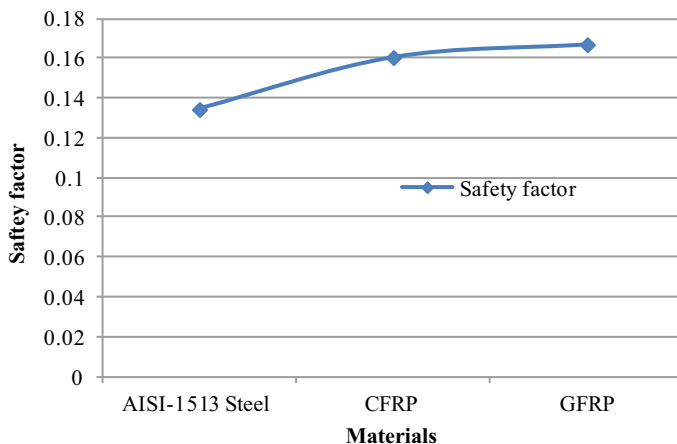
Material	Deformation (mm)	Stress (N/mm <sup>2</sup> )	Strain
Steel	0.23452	166.73	0.00083952
CFRP	0.57623	139.64	0.0020695
GFRP	0.49539	134.21	0.0017375

### 3.2 Fatigue Analysis

Fatigue analysis results were shown in Table 5, Figs. 6 and 7. Life of pressure vessel is good at E-glass fiber composite has major contribution followed by carbon fiber composite material and AISI-1513 steel. Damage is also low for E-glass fiber when compared to carbon fiber and AISI-1513 steel. Safety of pressure vessel is good for E-glass fiber material.

**Table 5** Fatigue analysis results

Material	Temperature distribution (°C)	Heat flux (w/m <sup>2</sup> )
AISI-1513 steel	29.886	0.51658
Carbon fiber	30.00	0.59580
E glass fiber	30.002	0.86702



**Fig. 7** Safety graph

**Table 6** Thermal analysis results

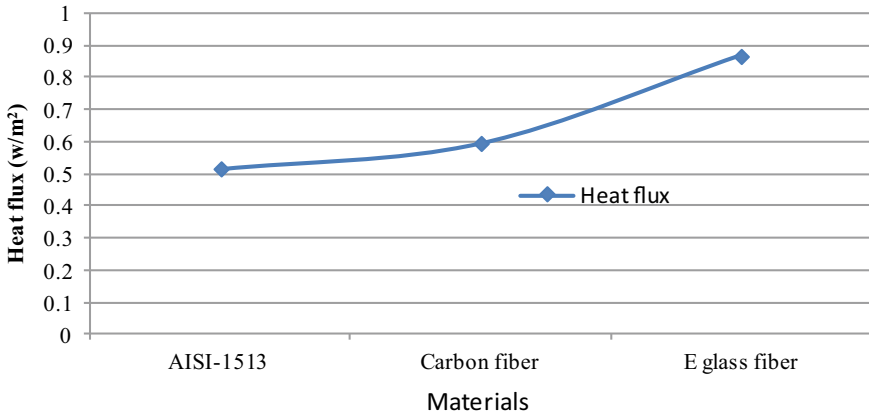
Material	Life	Damage	Safety factor
Steel	1.67e <sup>6</sup>	1323.9	0.13442
CFRP	2.52e <sup>6</sup>	834.72	0.16051
GFRP	2.77e <sup>6</sup>	752.99	0.16699

### 3.3 Thermal Analysis

By observing the thermal analysis results Table 6 and Fig. 8, the heat dissipation is more for E-glass fiber material when compared to AISI-1513 steel and carbon fiber materials.

### 3.4 Linear Layer Analysis

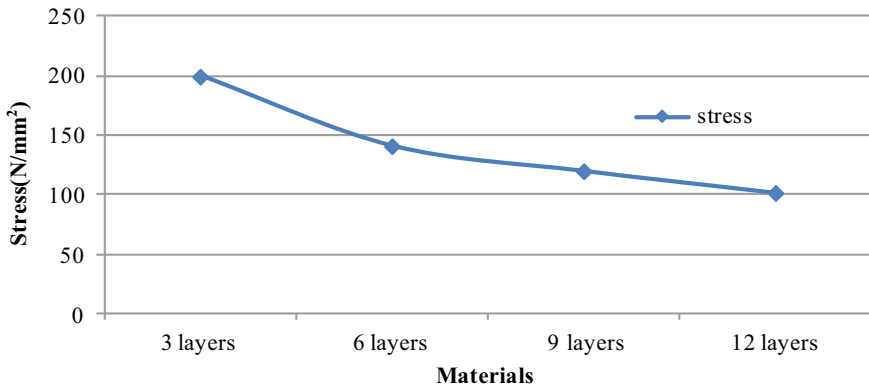
Table 7 and Fig. 9 present the results of linear layer analysis carbon-reinforced plastics material. In the linear layer analysis results, the stress values are less at 12 layers stacking pressure vessel model when compared to conventional model.



**Fig. 8** Heat flux graph

**Table 7** Linear layer analysis results

Layer stacking	Deformation (mm)	Stress (N/mm <sup>2</sup> )	Strain
3 layers	5.2012	199.35	0.01534
6 layers	1.462	141.05	0.032109
9 layers	6.248	138.68	0.01028
12 layers	5.6307	101.8	0.008944



**Fig. 9** Layer analysis graph

## 4 Conclusions

Analysis of pressure vessels subjected to internal pressure has been carried out with different material and different loads for given geometry. The following conclusions are made after performing analysis using generalized finite element software, Ansys.

1. The static analysis has been carried out with different materials for given boundary conditions and pressure, and it has been observed that the induced stress value for E-glass fiber pressure vessel is  $134.21 \text{ N/mm}^2$ , whereas the stress values for AISI-1513 steel and carbon fiber-reinforced plastic pressure vessel are  $166.73 \text{ N/mm}^2$  and  $139.64 \text{ N/mm}^2$ , respectively.
2. After performing fatigue analysis, it is also observed that GFRP (glass fiber-reinforced plastic) pressure vessels has more life ( $2.77e^6$  cycles) than other materials, i.e.,  $2.52e^6$  cycles for CFRP and  $1.67e^6$  cycles for steel pressure vessels.
3. It is also evident from the thermal analysis results that the heat dissipation is more ( $0.86702 \text{ w/m}^2$ ) for E-glass material in comparison with AISI-1513 steel ( $0.51658 \text{ w/m}^2$ ) and carbon fiber ( $0.51658 \text{ w/m}^2$ ) pressure vessels.
4. After observing all above results, it has been concluded that GFRP (glass fiber-reinforced plastic) pressure vessels is more suitable for this radius to thickness ratio and for given load and displacement boundary conditions.

## References

1. Krikanov AA (2000) Composite pressure vessels with higher stiffness. *Compos Struct* 48:119–127, published by Elsevier Science Ltd.
2. Sharifi et al (2016) Numerical and experimental study on mechanical strength of internally pressurized laminated woven composite shells incorporated with surface-bounded sensors. *Compos Part B* 94, published by Elsevier Ltd.
3. Analysis of liquid petroleum gas cylinder using twice elastic slope criteria to calculate the burst pressure of cylinder (2015) *Int J Eng Res Technol* 4(01), Jan 2015
4. Onder A, Sayman O, Dogan T, Tarakcioglu N (2009) Burst failure load of composite pressure vessels. *Compos Struct* 89:159–166, published by Elsevier Ltd.
5. Chang RR (2000) Experimental and theoretical analyses of first-ply failure of laminated composite pressure vessels. *Compos Struct* 237
6. Kharat A, Kamble S (2017) Stress analysis in composite pressure vessels-a review. *Int J Innovative Res Sci Eng Technol* 6(9), Sept 2017
7. Abdalla HMA, Casagrande D, De Bona F (2020) Thin walled pressure vessels of minimum mass or maximum volume. *Struct Multi Optim* 61:111–121
8. Raja SJI, Sivaganesan SGS, Sridhar R (2018) Modeling and analysis of composite pressure vessel. *Int J Adv Eng Res Dev* 5(03):1–11, 1483–1487, Mar 2018
9. Abdolreza T, Hong TW (2019) A critical review and analysis of pressure vessel Structures. In: *IOP Conference series: materials science and engineering*, vol 469, pp 012009

# Experimental Analysis of Hartnell Governor Mechanism in Dynamics of Machinery Laboratory



Ali Hasan

**Abstract** The proposed work is aimed to analyze the performance characteristics of Hartnell governor mechanism available to our UG/PG/Research Scholars in dynamics of machinery laboratory and compare with the theoretical one given by the manufacturer. On the basis of this study, the researchers/scientist/design engineers will be able to select the specific spring length and mass of fly ball to perform the specific task as per specific requirements. The study covers the theoretical as well as practical aspects of the Hartnell governor. This study may be used as a reference guide to researchers/scientists in carrying out their research work in the initial conceptual stage of design.

**Keywords** Hartnell governor · Spindle speed · Sleeve displacement

## 1 Theory and Literature Review

In Hartnell governor, a spring controls the movement of the balls. In the beginning, the spring is kept under compression for the application of force on the sleeve. There are two bell crank levers that connect the fly ball and at one end and sleeve at the other. If we increase the governor spindle speed, then fly balls will go away the governor axis. As a result, the force is applied on the sleeve by the bell crank lever to lift the sleeve upside. But, when the speed decreases, the bell crank lever applies force on the sleeve downwards and the sleeve goes down side. The sleeve upside and downside displacement is directly connected with the throttle valve of the engine. The spring force is kept balanced by screw tightening or loosening. The sleeve displacement information goes to the throttle of the engine with the help of four bar mechanism for sending the fuel supply as per the loading conditions. Truuti

---

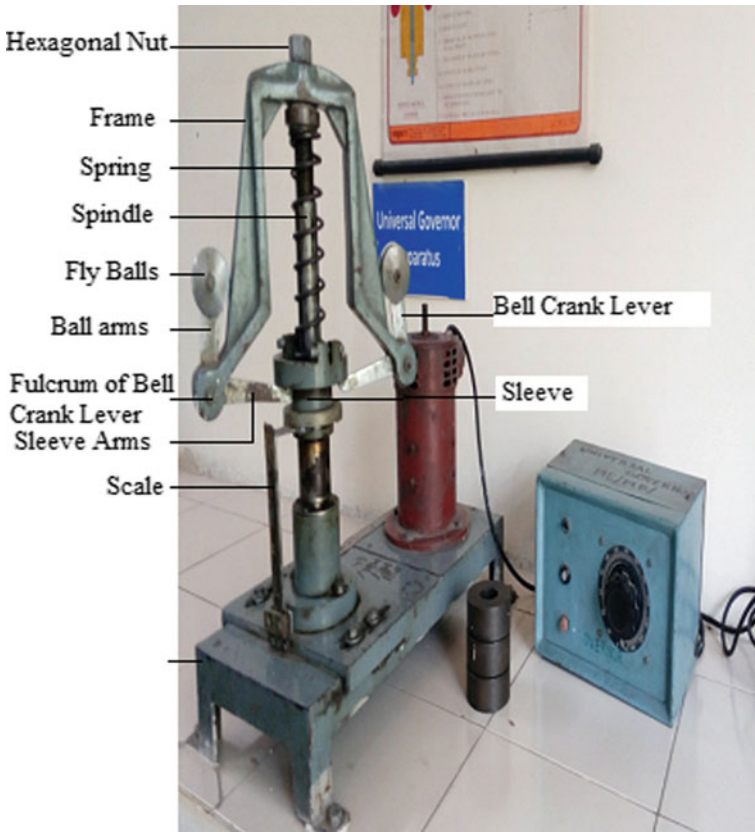
A. Hasan (✉)  
Mechanical Engineering Department, Jamia Millia Islamia, New Delhi, India  
e-mail: [ahasan@jmi.ac.in](mailto:ahasan@jmi.ac.in)



et al. [1] suggested the stress concentration areas that have a tendency to failure if governor speed exceeds some value as the stresses induced in the materials. The main focus was on the mass of the arms. The authors had done stress analysis theoretically. Vanga et al. [2] proposed a study about various components of a centrifugal governor with the help of Catia. The author showed the deformation manner, spring analysis, speed, and shape mode at various frequencies during the analysis. Ravindra et al. [3] worked on stress analysis at a specific position of a governor assembly. Kumar et al. [4] suggested the modification in Watt governor. The author tried to fix the ball at different distances from the intersection of the arms. Raghavendra and Kumarappa [5] suggested the use of electronic governor instead of mechanical governor. Burje et al. [6] gave an idea to opening and closing the throttle by the application of actuators by using microcontrollers. The author justified the use of hardware and software in real-time testing. Ge and Lee [7] investigated about kinematic as well as the dynamic characteristics of mechanical governor connected to external disturbance. Surarapu et al. [8] suggested the modification in Watt governor so that its minimum speed may be increased. They manufactured a watt governor model and performed several experiments on it after changing the length of lower arm. Wankhade et al. [9] suggested an automatic system for opening and closing the dam door with the application of governor. Siddappa et al. [10] studied on sky saver with the application of mechanical centrifugal governor. Kashyap and Mohankrishna [11] studied a collision accident problem for forecasting the possibility of collision sequences in vehicles. Miljic and Popovic [12] presented a mechanical governor model that can adjust various parameters. Sakharov and Tarabarin [13] worked on mechanical governors. They studied the usual problems in governors and their solutions. Srinu et al. [14] invested a proell governor to increase its minimum speed. They change the length of lower arms and positions of the fly ball of the proell governor. Manychkin et al. [15] discuss the collection of centrifugal governors collected at the end of the nineteenth century. Few models were taken from Europe, but most of the models were designed and manufactured in the school (IMTS). The study presents summary of some models and basic principles of their working operation. It also gives information about the history of their creation and production. Zengyao et al. [16] shown that centrifugal governors play a main role in rotating machinery like internal as well as external combustion engines. They studied two impulse excitations of the freewheel. A feedback control method suggested to realize the control objectives of the existence, stability, and the mean radius of cross section of the torus solution. Their criterion did not use Eigen value in their calculations. They use the central manifold theory and the normal form reduction method to study the nonlinear gain of the control torus stability.

## 2 Materials and Methodology

A universal governor experimental setup available in the Machine Dynamics laboratory of Mechanical Engineering Department is shown in Fig. 1, which is a motorized setup having a shaft driven by DC motor. Note down the initial reading of pointer on



**Fig. 1** Experimental setup of Hartnell governor

the vertical scale. Now, switch on the rotary switch and slowly increase the governor speed till the sleeve is lifted from its initial position, and it should be stabilized. Note down the value of sleeve displacement on the scale and spindle speed with the help of tachometer. Repeat the procedure with the increase in the spindle speed. The author has recorded five observations at different speeds of the spindle of the governor.

### 3 Notations Used

- $r_o$  = Initial radius of rotation when the governor is in mid position in mm,
- $r_1$  = Minimum radius of rotation of ball center from spindle axis in mm,
- $r_2$  = Maximum radius of rotation of ball center from spindle axis in mm,

- $S_1$  = Spring force exerted on sleeve at minimum radius in Newton,  
 $S_2$  = Spring force exerted on sleeve at minimum radius in Newton,  
 $m$  = Mass of each fly ball in kg,  
 $M$  = Mass of sleeve in kg,  
 $N_1$  = Minimum speed of governor at minimum radius in RPM,  
 $N_2$  = Minimum speed of governor at minimum radius in RPM,  
 $N$  = Mean speed of governor in RPM,  
 $N_{act}$  = Actual speed of governor in RPM,  
 $N_{tho}$  = Theoretical speed of governor in RPM,  
 $M$  = Dead mass on the central sleeve in kg,  
 $F_{c2}$  = Centrifugal force corresponding to maximum speed in kg =  $m r_2 \omega_2^2$ ,  
 $F_{c1}$  = Centrifugal force corresponding to minimum speed in kg =  $m r_1 \omega_1^2$ ,  
 $\omega_1, \omega_2$  = Corresponding minimum and maximum angular velocities in rad/s,  
 $s$  = spring stiffness in kg/mm,  
 $a$  = Length of ball arm of bell crank lever in mm,  
 $b$  = Length of sleeve arm of bell crank lever in mm,  
 $r$  = Radius of rotation in mm =  $[r_o + x(a/b)]$ ,  
 $F_c$  = Centrifugal force corresponding to minimum speed in Newton =  $m r \omega^2$ ,  
 $S = [(2 * F_c * (a/b))] \text{ kg}$   
 $s = [(2 * (a/b)^2 * F_c / (r - r_o))] \text{ in N/mm.}$

## 4 Observations

Experimental setup manufacturer's data are:  $a = 78 \text{ mm}$ ,  $b = 125 \text{ mm}$ ,  $m = 0.16 \text{ kg}$ ,  $r_o = 155 \text{ mm}$ ,  $M = 1.53 \text{ kg}$ . The observations data and other details are given in Table 1.

**Table 1** Experimental observations for Hartnell governor

S. N.	$N_{act}$ (rpm)	$x$ (mm)	$r$ (mm)	$F_c$ (Newton)	$S$ (Newton)	$s$ (N/mm)
1	330	5	158.12	30.21	37.7	7.41
2	355	10	160.62	35.50	46.1	5.16
3	395	15	164.36	44.99	56.2	3.77
4	454	20	167.48	60.54	75.6	3.81
5	506	23	169.35	76.08	94.9	4.16
Avg						4.86

### 5 Results and Conclusions

In Fig. 2,  $F_c$  versus  $r$  graph is plotted. Controlling force ( $F_c$ ) is on  $y$ -axis and radius ( $r$ ) in  $x$ -axis. If line is going to cut the  $y$ -axis in negative region, it means it is a stable governor. If this line starts from the origin from zero, then it means it is an isochronous governor. If this line intersects  $y$ -axis somewhere in the positive region, then it is unstable governor. Therefore, in our case, the available governor is unstable. From Table 1, it clear that with the change of  $N$  (governor speed) ' $r$ ' also changes. It means this governor is not stable. The actual average sensitivity comes to a value of 11%. From actual spindle speed versus sleeve displacement graph shown in Fig. 3, which is also a straight line. The graph between the sleeve displacement and speed and between the force and radius of rotation came out to be straight line, representing a linear variation of speed and sleeve displacement with radius of rotation. With slight change, i.e., increase in RPM, centrifugal force on the masses (balls) increase, increasing the radius of rotation resulting in increased sleeve displacement. As the speed decreases, the radius of rotation decreases slightly resulting in lowering of the sleeve. This phenomenon is used to regulate the fuel supply into an engine, which ultimately regulates the running speed of the engine.

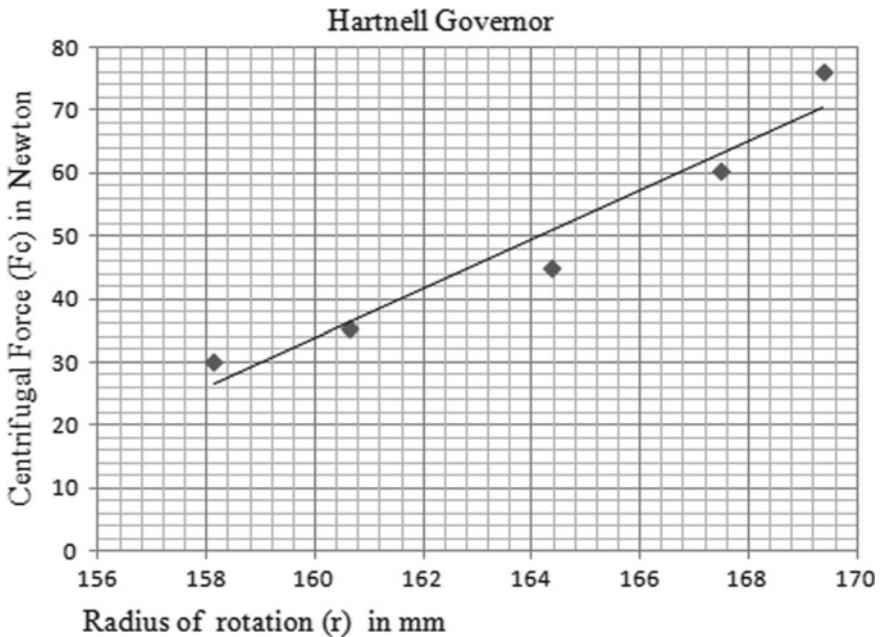
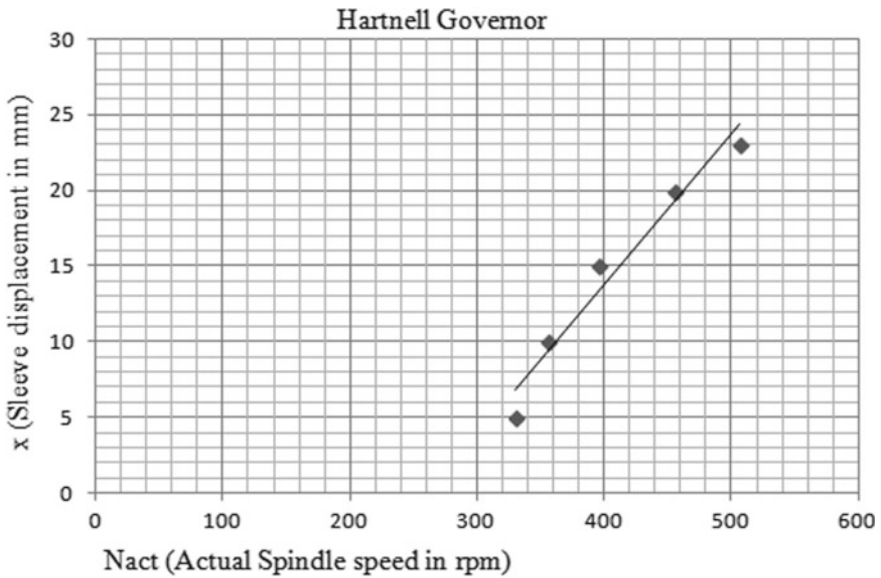


Fig. 2 Effect of radius of rotation ( $r$ ) on centrifugal force ( $F_c$ )



**Fig. 3** Effect of actual spindle speed ( $N_{act}$ ) on sleeve displacement ( $x$ )

**Acknowledgements** The author appreciates and is thankful to Prof. Emran Khan, Head, Department of Mechanical Engineering, F/O-Engineering and Technology, Jamia Millia Islamia (A Central University), New Delhi for granting all the facilities along with the permission to work in the laboratory and all those who participated in the study and helped me to facilitate the research process successfully.

## References

1. Navathale TJ, Paralkar AA, Ghorade VS (2017) Design and analysis of centrifugal governor: a review. *Int J Eng Res Technol (IRJET)* 4(1):1058–1062
2. Rana RS, Purohit R, Singh A (2012) Design and stress analysis of watt and porter governor. *Int J Sci Res Publ* 2(6):1–6
3. Padmasri V, Suresh N, Surendar E, Vidyasagar M (2018) Design multi body dynamics and modal analysis of a centrifugal governor by using ANSYS. *Int J Eng Res Technol (IRJET)* 7(11):73–79
4. Kumar S, Kumar R, Kumar H (2016) Analysis and investigation on watt governor to improve the speed range of the governor. *Int J Res Sci Innov (IJRSI)* 3(6):109–112
5. Raghavendra EH, Kumarappa S (2015) Retrofication of mechanical speed governor with electronic speed governor for heavy duty diesel engines. *Int J Res Appl Sci Eng Technol (IJRASET)* 3(9):383–388
6. Burje SR, Kulkarni SA, Dhande NB (2012) Design and development of microcontroller based electronic speed governor for genset/automotive engine, research invent. *Int J Eng Sci* 1(5):26–33
7. Ge Z-M, Lee C-I (2000) Non-linear dynamics and control of chaos for a rotational machine with a hexagonal centrifugal governor with a spring. *J Sound Vib* 1:845–865

8. Surarapu GB, PeddiReddy S, Uotkuri N (2015) Experimental investigation on watt governor to increase minimum speed. *Int J Sci Res Publ* 5(2):1–4
9. Wankhade MA, Jawale MD, More MD, Chhangani MG (2017) Automatic dam doors control centrifugal governor. *Int J Advan Sci Res Eng Trends* 2(3):27–31
10. Siddesh Siddappa D, Pawan G, Omkar G, Vijay D, Varun C (2019) Sky saver using centrifugal governor. *J Emerg Technol Innovative Res (JETIR)* 6(3):12–18
11. Kashyap AR, Mohankrishna K (2015) Vehicle collision avoidance with dynamic speed governor. *Int J Innov Eng Technol (IJJET)* 5(4):323–331
12. Miljic N, Popovic SJ (2014) Model based tuning of a variable speed governor fuel injection pump. *FME Trans* 42:40–48
13. Sakharov M, Tarabarin V (2012) Centrifugal governors: the story of a mistake'. In: Koetsier T, Ceccarelli M (eds) *Explorations in the history of machines and mechanisms. History of mechanism and machine science*, vol 15. Springer, Dordrecht, pp 323–336. [https://doi.org/10.1007/978-94-007-4132-4\\_22](https://doi.org/10.1007/978-94-007-4132-4_22)
14. Srinu D, Surarapu GB, Rao MN (2016) Experimental investigation of proell governor to increase minimum speed. *Int J Mod Trends Eng Res* 3(2):622–626
15. Manychkin N, Sakharov M, Tarabarin V (2010) The models of centrifugal governors in the collection of Bauman Moscow state technical university. In: Pislá D, Ceccarelli M, Husty M, Corves B (eds) *New trends in mechanism science. Mechanisms and machine science*, vol 5. Springer, Dordrecht. [https://doi.org/10.1007/978-90-481-9689-0\\_59](https://doi.org/10.1007/978-90-481-9689-0_59)
16. Lv Z, Xu H, Bu Z (2021) Control of neimark-sacker bifurcation in a type of weak impulse excited centrifugal governor system. *Int J Non-Linear Mech* 128:1–11, 103624. <https://doi.org/10.1016/j.ijnonlinmec.2020.103624>

# Comparative Study and Analysis of Material for Energy Storing Body Panel of an Automobile



Md. Roshan, Animireddy V. S. S. S. Prasad, Danish Raza, Om Prakash, Md. Shadab, and Sanjeev kumar

**Abstract** This paper compares the structural analysis of various car body panels between materials carbon fiber and aluminum with equivalent stress, displacement magnitude and the total capacitance of 3000F can be achieved to run the car replacing batteries with super capacitor packs in the car body panels and finally achieving the total weight reduction of 487.34 kgs from vehicle.

**Keywords** Super capacitors · Li-ion batteries · 3000F · Power discharge · Storage capacity · Secondary energy storage devices

## 1 Introduction

There is a drastic increase in public demand for new cars, but this rapid growth causes tremendous carbon footprints and impacts on global warming. We have existing methods to avoid the major concern of environmental health in which like Li-ion battery vehicles and some relevant technologies are there, but they reduce room space and adds weight. To get overcome of these drawbacks there is a more effective and efficient technology of “Energy storage panel car” therefore uses super capacitors as the main power unit fabricated with a body in carbon fiber resin as panels attached inside them with super capacitors. This body, which is strong enough to withstand high tensile stress, fatigue property, and reduces its weight throughout a vehicle by 35%. which have enough strength to withstand impact force, and at high temperature.

In this research, we performed the analysis for the body panels of electric vehicle in which the super capacitors replace batteries as an alternative method were used for storing the energy. The research is carried out to clarify the chance of modification in automotive e-vehicles, super capacitor capacitance and battery energy comparison, carbon fiber material used as manufacturing material for automotive e-vehicle’s body panels, comparison between the normal vehicle body panel material and carbon fiber.

---

Md. Roshan (✉) · A. V. S. S. S. Prasad · D. Raza · O. Prakash · Md. Shadab · S. kumar  
Mechanical Engineering, Lovely Professional University, Phagwara, India

## 2 Research Methodology

In this research, we performed the analysis for the body panels of electric vehicle in which the battery was eliminated and the supercapacitors as an alternative method were used for storing the energy. This research is carried out as in the following steps:

1. Study of the different types of electric vehicles, batteries, supercapacitors used in EV and the chances of modifications in it.
2. Calculating the no of supercapacitors can be used in a single-vehicle to provide enough energy storage.
3. Study on the dimensions of the panels and the supercapacitors and compare the energy capacitance between the battery and supercapacitors.
4. Comparing the standard vehicle body panel material with the carbon fiber.
5. Study on different software, which is used for designing and analyzing the various essential parameters.

## 3 Calculation

Comparison with tesla S model; It is specifications are:

Voltage = 350 v; Battery capacity = 40 kwh; Battery weight = 478 kgs

Energy stored in battery is given in KWh, where as in super capacitors we use farads.

So,

$$\begin{aligned} \text{Energy}(W) &= \frac{1}{2} C \times V \\ 40 \times 1000 \times 3600 &= \frac{1}{2} \times C \times 3502 \end{aligned} \quad (1)$$

Tesla's capacitance  $C = 2351.02 \text{ F}$

where

$W$  energy  
 $C$  capacity  
 $V$  voltage  
 $F$  farads.

To replace the battery of the EV with super capacitors, we need to provide the required voltage of 350 v to the motor. We need to find out the no of super capacitors required to match the required voltage and connect them in series.

We consider a super capacitor of HV series (high capacitance type)

$$\begin{aligned} \text{Height} &= 50 \text{ mm}; \text{Dia} = 35 \text{ mm}; \text{Weight} = 61.5 \text{ g} \\ \text{Area of capacitor} &= 35 \times 50 = 1750 \text{ mm}^2 \end{aligned}$$



### 3.1 Calculation for Total Number of Capacitors

#### 3.1.1 Doors

$$\text{Area of door} = 762 \times 590 = 449580 \text{ mm}^2$$

$$\text{Area of capacitor} = 1750 \text{ mm}^2$$

$$\begin{aligned} \text{No of capacitors that can be mounted in 1 door} &= 449580/1750 \\ &= 256 \end{aligned} \quad (2)$$

So, in 4 doors =  $4 \times 256 = 1024$ .

Therefore, 1024 super capacitors in four doors.

#### 3.1.2 Roof

$$\text{Area of roof} = 965 \times 762 = 735330 \text{ mm}^2$$

$$\begin{aligned} \text{Number of capacitors that can be mounted} &= 735330/1750 \\ &= 420.18 \end{aligned} \quad (3)$$

So, 420 capacitors in roof.

#### 3.1.3 Bonnet

$$\text{Area of bonnet} = 1300 \times 600 = 780000 \text{ mm}^2$$

$$\begin{aligned} \text{Number of capacitors that can be fitted} &= 780000/1750 \\ &= 445 \end{aligned} \quad (4)$$

So, 445 capacitors in roof.

$$\begin{aligned} \text{Now total number of super capacitors used in vehicles} &= 4 \text{ doors} + \text{roof} \\ &\quad + \text{bonnet} \\ &\quad \text{(adding equation 2, 3 and 4)} \\ &= 1024 + 420 + 445 \\ \text{Total no. of super capacitors} &= 1889 \end{aligned} \quad (5)$$

- Divide the motor voltage by super capacitor voltage to get no of super capacitors required in series connection =  $350\text{v}/2.7 = 130$ .  
capacitors in series connection will have same capacitance but voltage adds up.
- No of capacitors required for parallel connection in a pack =  $1889/130 = 15$   
capacitors in parallel connection will have same voltage but capacitance adds up.

So,  $200F \times 15 = 3000F$ .

This total super capacitor pack provides **3000F** which is more than standard range tesla battery and near to standard range plus.

### 4 Design and Mesh Details of Cad Models

See Tables 1, 2, 3 and 4 and Figures 1, 2, 3, 4, 5, 6 and 7.

#### Set up of super capacitors on vehicle and its block diagram

**Table 1** Material properties for Aluminum and Carbon fiber for car panels

S. No.	Particulars	Model 1	Model 2
1	Material	Aluminum	Carbon Fiber
2	Density	2491.2 kg/m <sup>3</sup>	1830 kg/m <sup>3</sup>
3	Mesh size	4 mm	4 mm
4	Poisson's ratio	0.33	0.34
5	Pattern	Triangular	Triangular
6	Shear modulus	2.6E + 10	1.3E + 10

**Table 2** Final mesh data for door

S. No.	Particulars	Units
1	Mesh element size	4 mm
2	Number of nodes	1.401E + 06
3	Number of elements	7.093E + 05
4	Element shape	Tetrahedral
5	Type of analysis	Static structural

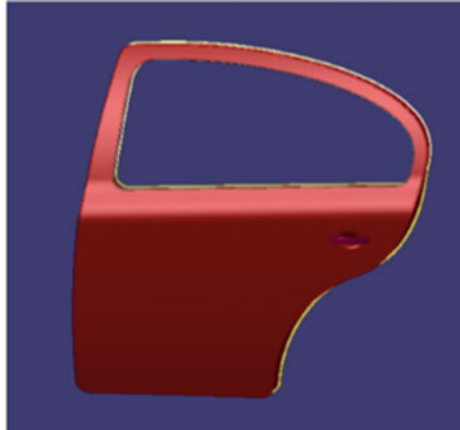
**Table 3** Final mesh data for bonnet

S. No.	Particulars	Units
1	Mesh element size	4 mm
2	Number of nodes	2.175E + 05
3	Number of elements	1.462E + 05
4	Element shape	Tetrahedral
5	Type of analysis	Static structural

**Table 4** Final mesh data for roof

S. No.	Particulars	Units
1	Mesh element size	4 mm
2	Number of nodes	6.918E + 07
3	Number of elements	5.026E + 06
4	Element shape	Tetrahedral
5	Type of analysis	Static structural

**Fig. 1** Car door cad model



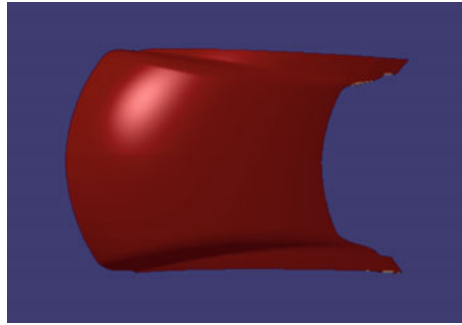
**Fig. 2** Car door meshing



## 5 Structural Analysis

The analysis is carried out by using two well-known applications namely, Catia V5 and Ansys AIM. In this analysis, the car door and bonnet were prepared in Catia v5 software and then analysis is performed for the two body panels with carbon

**Fig. 3** Car bonnet cad model



**Fig. 4** Car bonnet meshing



**Fig. 5** Car roof cad model



fiber composite and compared them with conventional aluminum alloy material. The results are as follows:



Fig. 6 Car roof meshing

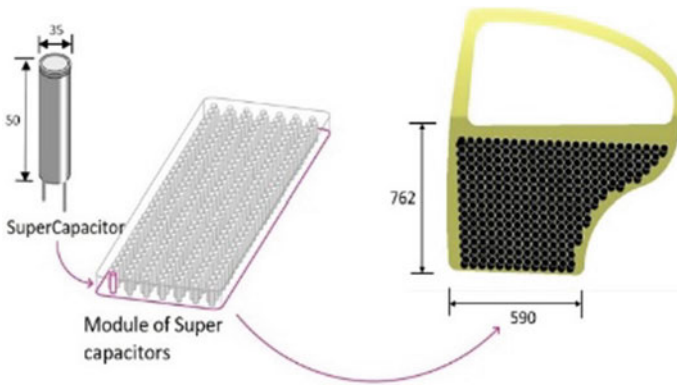


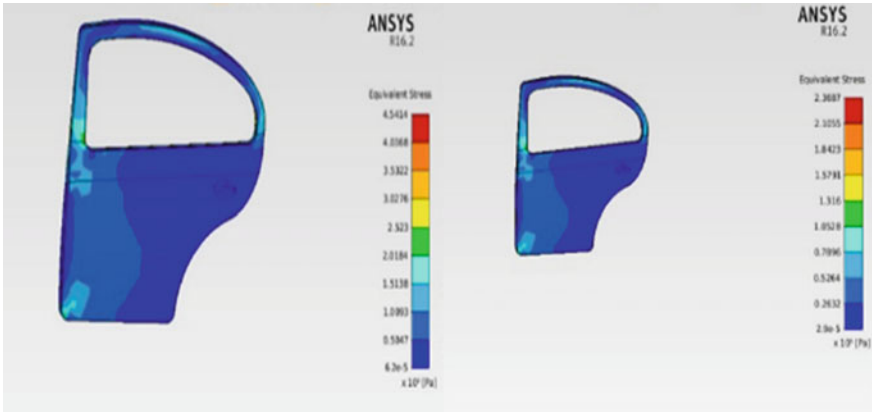
Fig. 7 Block diagram

**5.1 Case: 1 Equivalent Stress and Displacement Magnitude on Door**

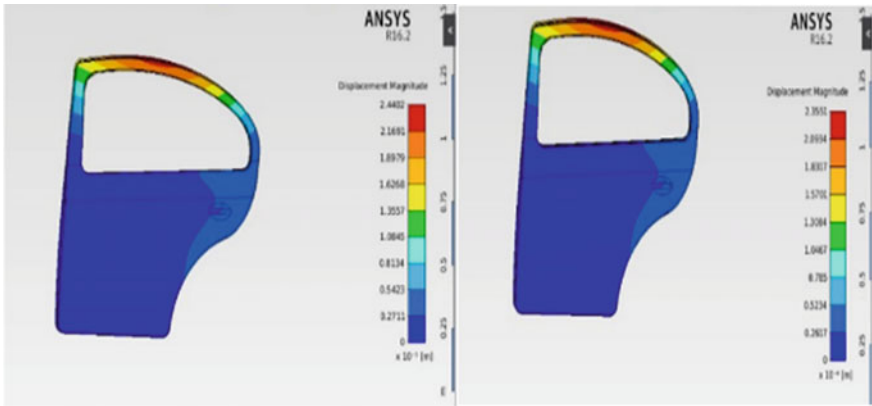
See Figs. 8 and 9, Table 5.

**5.2 Case: 2 Equivalent Stress and Displacement Magnitude on Bonnet**

See Figs. 10 and 11, Table 6.



**Fig. 8** Equivalent stress over the aluminum and carbon fiber panel



**Fig. 9** Displacement magnitude over the aluminum and carbon fiber panel panel

**Table 5** Analysis data for door

	Aluminum	Carbon fiber
Min stress	62.187 Pa	2.9035 Pa
Max stress	4.5454E + 06 Pa	2.3687E + 05 Pa
Min displacement	0 m	0 m
Max displacement	2.4404E-05 m	2.3551E-04 m

### 5.3 Case: 3 Equivalent Stress and Displacement Magnitude on Roof

See Figs. 12 and 13, Table 7.

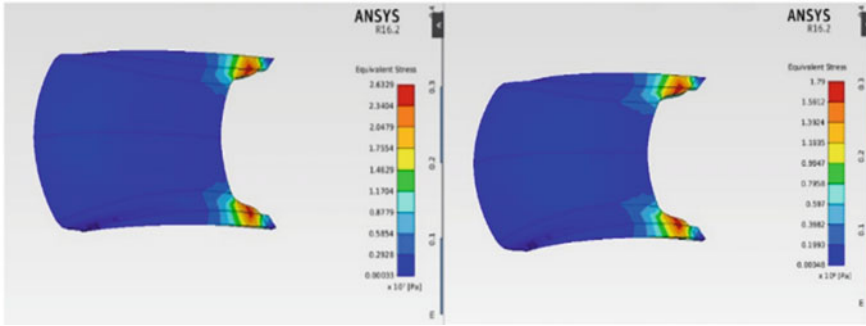


Fig. 10 Equivalent stress over the aluminum and carbon fiber panel

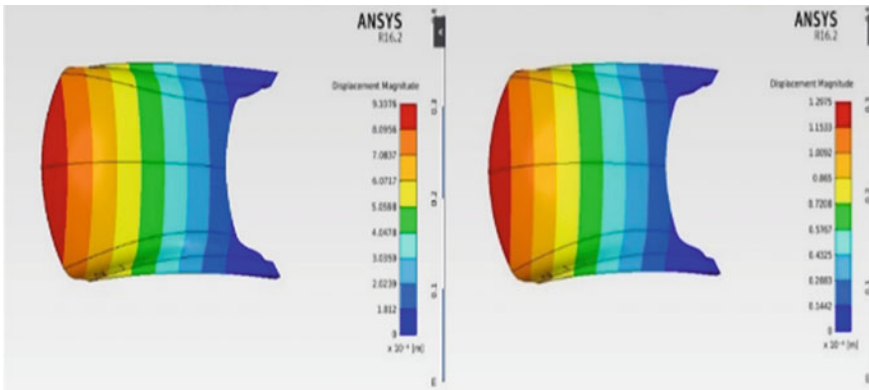


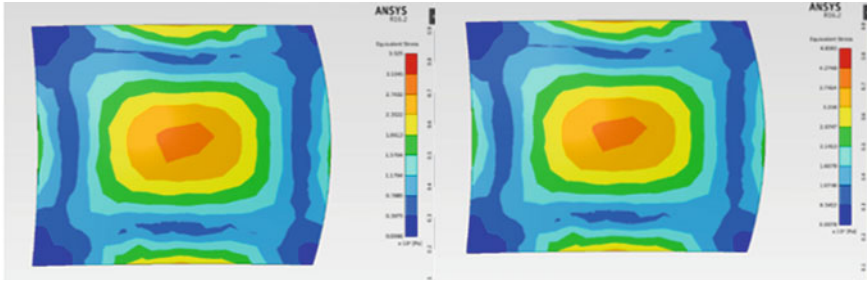
Fig. 11 Displacement magnitude over the aluminum and carbon fiber panel

Table 6 Analysis data for bonnet

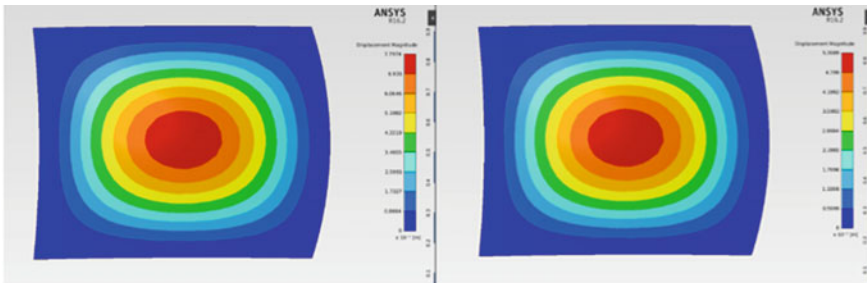
	Aluminum	Carbon fiber
Min stress	3272 Pa	478.767 Pa
Max stress	2.6329E + 07 Pa	1.79E + 06 Pa
Min displacement	0 m	0 m
Max displacement	0.00091076 m	2.3551E-04 m

## 6 Conclusion

- The weight of the tesla battery pack is 540 kg, whereas the super capacitors weigh only 116.17 kg.
- By replacing the regular aluminum with carbon fiber and battery pack with super capacitor pack totally helped in reducing the weight of the car by 28% from 2500 kgs to 1749.96 kgs.



**Fig. 12** Equivalent stress over the aluminum and carbon fiber panel



**Fig. 13** Displacement Magnitude over the aluminum and carbon fiber panel

**Table 7** Analysis data for roof

	Aluminum	Carbon fiber
Min stress	78 Pa	66 Pa
Max stress	4.808E + 04 Pa	3.525E + 04 Pa
Min displacement	0 m	0 m
Max displacement	7.797E-07 m	5.398E-07 m

- The super capacitors pack produces 3000F capacity which is more than standard range tesla battery and near to standard range plus.
- The carbon fiber doors, bonnet and roof produce less stresses and displacement magnitude when compared to aluminum body panels.

**References**

1. Veneri O, Capasso C, Patalano S (2018) Experimental investigation into the effectiveness of a super-capacitor based hybrid energy storage system for urban commercial vehicles. Appl Energy 227:312–323



2. Horn M, MacLeod J, Liu M, Webb J, Motta N (2019) Super capacitors: a new source of power for electric cars? *Econ Anal Policy* 61:93–103
3. Hredzak B, Agelidis VG, Jang M (2013) A model predictive control system for a hybrid battery-ultracapacitor power source. *IEEE Trans Power Electron* 29(3):1469–1479
4. Xiang C, Wang Y, Hu S, Wang W (2014) A new topology and control strategy for a hybrid battery-ultracapacitor energy storage system. *Energies* 7(5):2874–2896
5. Zhao S, Wu F, Yang L, Gao L, Burke AF (2010) A measurement method for determination of dc internal resistance of batteries and super capacitors. *Electrochem Commun* 12(2):242–245
6. Kouchachvili L, Yaïci W, Entchev E (2018) Hybrid battery/supercapacitor energy storage system for the electric vehicles. *J Power Sources* 374:237–248
7. Libich J, Máca J, Vondrák J, Čech O, Sedlářková M (2018) Supercapacitors: properties and applications. *J Energy Storage* 17:224–227
8. Idoni-Matthews JO, Silverman JC, Mosti VA, Manalo J (2016) U.S. patent no. 9,517,388. Washington, DC: U.S. Patent and Trademark Office
9. Yarger EJ, Morrison J, Richardson JG, Spencer DF, Christiansen DW (2010) U.S. patent no. 7,688,036. Washington, DC: U.S. Patent and Trademark Office
10. Shaffer A, Patterson J, Miller R, MacNeille P (2015) U.S. patent no. 8,997,901. Washington, DC: U.S. Patent and Trademark Office

# Impact of Diamond-Shaped Cut-Out on Buckling Nature of Isotropic Stainless-Steel Plate



Vineet Sinha, Rutul Patel, Keval Ghetiya, Mihhil Nair, Tarun Trivedi, and Lokavarapu Bhaskara Rao

**Abstract** Perforated plates are widely used in aerospace and structural engineering where the cut-outs serve as a means of weight reduction, give aesthetic appeal or assist in cooling purposes. By selecting the proper cut-out shape better mechanical properties can be obtained for the same amount of material removed. In this study, a buckling analysis was carried out on stainless-steel plates with and without perforation by using finite element method. Stainless-steel plates having constant width and thickness with varying lengths were analysed to examine the impact of length on buckling load. Plates of constant length and width, with varying thickness were analysed to examine the impact of thickness on buckling load. Plates of constant length and width having diamond-shaped perforation of seven different sizes were analysed to examine the impact of perforation size on the buckling load values. And plates of constant length and width having a diamond-shaped perforation with seven different orientations with the horizontal were analysed to examine the impact of perforation orientation on buckling load. ANSYS 19.2 software was used to perform the finite element analysis.

**Keywords** Buckling · Diamond cut-out · Isotropic · Finite element analysis

## 1 Introduction

Perforated stainless-steel plates are extensively used in structural engineering. The cut-outs serve as a means of weight reduction, as access ports, to serve as doors or windows or simply give aesthetic appeal. Hence, good understanding of buckling of perforated as well as non-perforated plates is needed. Buckling of plates is an instability phenomenon which occurs when there is an abrupt deflection in transverse direction. This happens due to the development of a critical stress level when the plates are being subjected to compressive load. Partial differential equations are used

---

V. Sinha (✉) · R. Patel · K. Ghetiya · M. Nair · T. Trivedi · L. Bhaskara Rao  
School of Mechanical Engineering, Vellore Institute of Technology, Chennai Campus,  
Vandalur-Kelambakkam Road, Chennai, Tamil Nadu 600127, India

© The Author(s), under exclusive license to Springer Nature Singapore Pte Ltd. 2022  
G. S. V. L. Narasimham et al. (eds.), *Innovations in Mechanical Engineering*,  
Lecture Notes in Mechanical Engineering,  
[https://doi.org/10.1007/978-981-16-7282-8\\_10](https://doi.org/10.1007/978-981-16-7282-8_10)

to govern the nature of plates undergoing buckling, which makes the analysis very complex [1].

Many researchers have studied the buckling behaviour of plates. In earlier studies, Blesa Gracia and Rammerstorfer [2] examined the increase in buckling load by the introduction of cut-outs and found out that it is possible to increase the buckling strength of plates along with the reduction of weight with the help of cut-outs. Shariati et al. [3] examined a rectangular plate with circular perforation at different positions of the plate with different boundary conditions and found out that boundary conditions have a considerable impact on buckling nature. Mauro de Vasconcellos Real et al. [4] examined the buckling load of uniaxially loaded rectangular plates with circular cut-outs and found that when plates are thin instability happens much before the yield point, whereas if plates are thick instability happens after the yield point of the plate material. Sandeep Singh et al. [5] examined the impact of partial edge compression along with change in aspect ratio and the presence of perforation on buckling load, finding out partial edge compression profoundly influences square plates as compared to rectangular plates, partial edge compression has higher influence on buckling strength than uniform edge compression and the plates without cut-out have shown higher critical load than plates with cut-out; however, impact of partial edge compression is almost same. Giulio Lorenzini et al. [6] examined the impact of the different types and shapes of cut-out in the plate buckling and discovered that by choosing the proper cut-out type superior performance can be obtained, i.e. by removing the same amount of plate material the performance can be improved by the choosing the correct cut-out type. Caio César Cardoso da Silva et al. [7] studied the impact of geometric configuration of hexagonal hole on the mechanical performance in buckling and found out that lengthwise hexagonal cut-out gives better mechanical performance than the oblique hexagonal cut-out. Fundamental buckling of circular and annular plates with guided edges [8–10] and with elastic/rigid ring support [11–14] and elastic edges [15, 16] studied by Rao and Rao. However, they have not considered the cut-out in their study.

From the above-mentioned literature, it has been observed that buckling analysis of plates having varying perforation shapes, size, orientation and position have been the subject of many researches. The results of their studies indicate that the perforation shape, size and orientation impact the buckling nature of plates. However, there is a lot of scopes to examine the impact of these variables with different combinations. In this study, the impact of diamond-shaped perforation on the buckling nature of a stainless-steel plate is examined. The impact of non-perforated plate's length and thickness is studied. And the impact of perforation size and orientation is also examined. A comparison between the buckling nature of perforated and non-perforated plates is also done.

## 2 Finite Element Model

To perform the buckling analysis, the eigenvalue method is applied [1]. Linear and nonlinear terms are included in the strain formulation being used in the analysis. The total stiffness matrix  $[K]$  is the sum of stiffness matrix for small deformations  $[K_E]$  and the geometric stiffness matrix  $[K_G]$ .  $[K_G]$  depends on geometry as well as the initial stresses existing at the beginning of load step  $\{P_0\}$ . Hence, the total stiffness matrix at load  $\{P_0\}$  is given as:

$$[K] = [K_E] + [K_G] \quad (1)$$

When load reaches the level  $\{P\} = \lambda\{P_0\}$ , here  $\lambda$  is a scalar load multiplier, the stiffness matrix can be defined as:

$$[K] = [K_E] + [K_G] \quad (2)$$

The governing equilibrium equation is:

$$[[K_E] + \lambda[K_G]]\{U\} = \lambda\{P_0\} \quad (3)$$

Here  $\{U\}$  is total displacement vector, which can be defined as:

$$\{U\} = [[K_E] + \lambda[K_G]]^{-1}\lambda\{P_0\} \quad (4)$$

If the load multiplier attains a critical value, there is large displacement with no increase in load. The displacement  $\{U\}$  approaches infinity when:

$$\det[[K_E] + \lambda[K_G]] = 0 \quad (5)$$

This is an eigenvalue problem whose solution gives the minimum eigenvalue corresponding to the critical buckling load.

### 2.1 Finite Element Analysis

Eigenvalue buckling analysis was performed using ANSYS 19.2 finite element program [17]. Table 1 presents the convergence study of load multiplier value. DesignModeler integrated into ANSYS was used to make the models, and ANSYS Mechanical was used to define the boundary conditions and the mesh design. The inbuilt material properties (of stainless steel) were assigned to the model. Figure 1 depicts the boundary conditions of the plate, which is clamped on the right and left edges and free on the top and bottom edges. Figures 2 and 3 show the mesh structure

for perforated and non-perforated plates, respectively. A very fine mesh of element size 0.3 mm was used to get precise results.

Figures 4 and 5 depict the ANSYS model for non-perforated and perforated plates, respectively. The left side of the model was assigned as fixed support, and the right side was subjected to a compressive load of 1 N/mm. The other two sides were free. The eigenvalue buckling analysis was performed on the models, and results

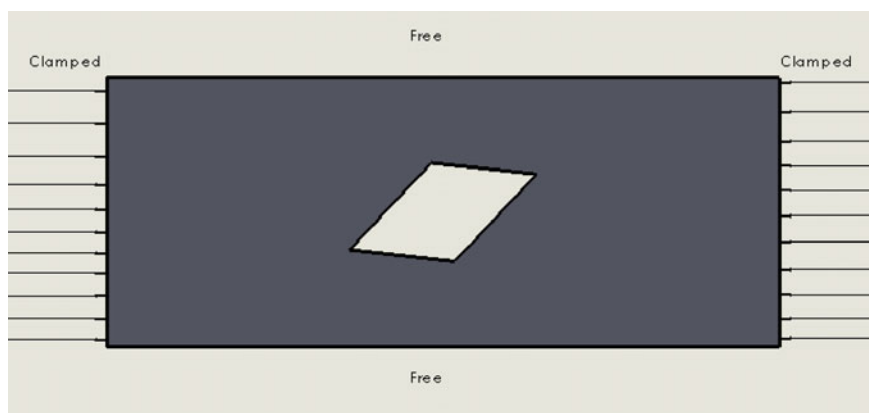
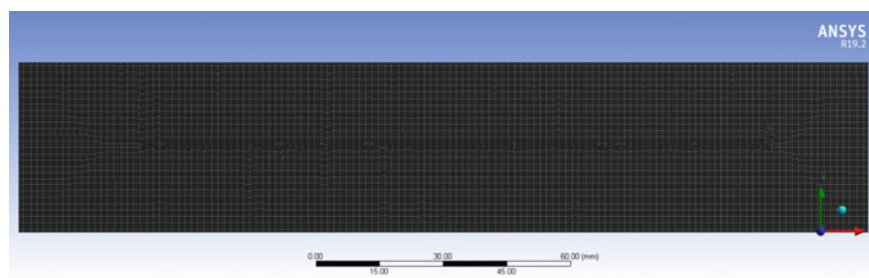
**Table 1** Convergence study of load multiplier value

Aspect ratio (L/t)	Element size (mm)	No. of mesh elements	Load multiplier value
12.5	5	80	25,887
	4	130	25,807
	3	221	25,185
	2	500	24,722
	1	2000	24,427
	0.9	2464	24,407
	0.8	3150	24,390
	0.7	4047	24,377
	0.6	5561	24,364
	0.5	8000	24,353
	0.4	12,500	24,344
	0.30	22,211	24,337
25	5	160	13,128
	4	250	12,885
	3	429	12,702
	2	1000	12,564
	1	4000	12,483
	0.9	4884	12,478
	0.8	6250	12,473
	0.7	8151	12,469
	0.6	11,189	12,465
	0.5	16,000	12,462
	0.4	25,000	12,460
	0.3	44,289	12,458
	0.2	100,000	12,457
50	5	320	5359.7
	4	500	5316.0
	3	871	5821.2
	2	2000	5256.4
	1	8000	5240.9
	0.9	9768	5239.9
	0.8	12,500	5239.0
	0.7	16,302	5238.2
	0.6	22,311	5237.5
	0.5	32,000	5236.9
	0.4	50,000	5236.4
	0.3	89,192	5236.0

(continued)

**Table 1** (continued)

Aspect ratio (L/t)	Element size (mm)	No. of mesh elements	Load multiplier value
100	5	640	1312.3
	4	1000	1309.4
	3	1729	1307.1
	2	4000	1305.3
	1	16,000	1304.1
	0.9	19,829	1304.1
	0.8	25,000	1304
	0.7	32,547	1303.9
	0.6	44,687	1303.9
	0.5	64,000	1303.8
	0.4	100,000	1303.8
	0.3	177,289	1303.8

**Fig. 1** Boundary conditions of the plate**Fig. 2** Mesh of non-perforated plate

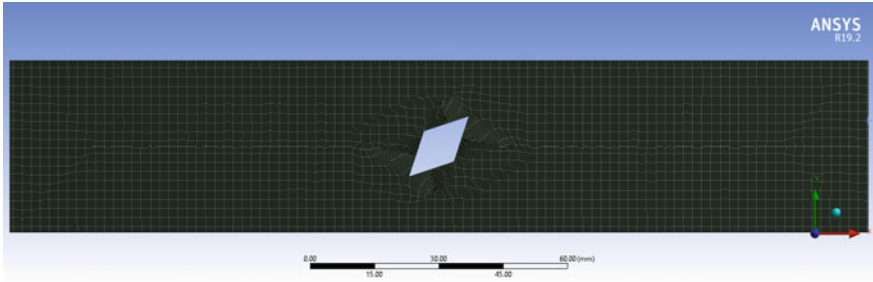


Fig. 3 Mesh of perforated plate

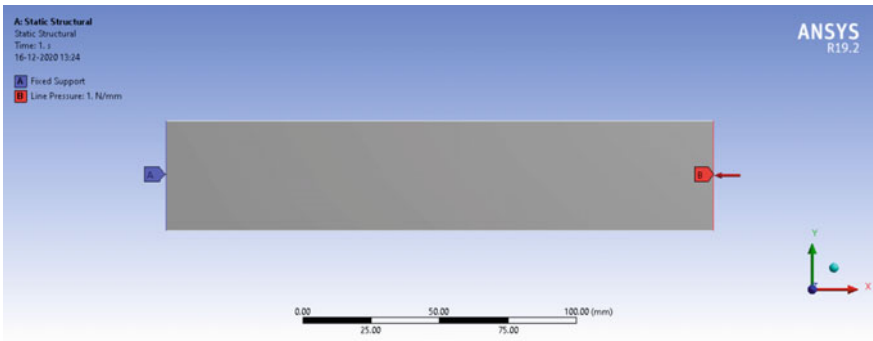


Fig. 4 ANSYS model for non-perforated plate

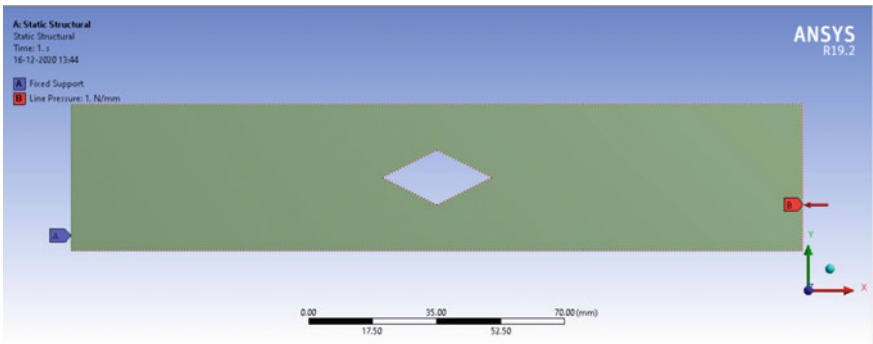
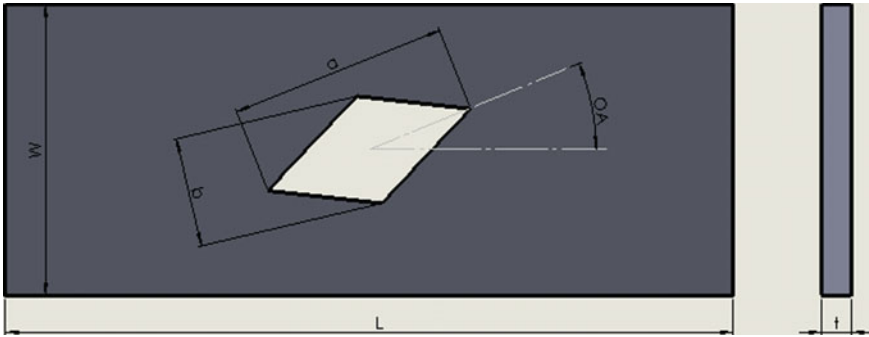


Fig. 5 ANSYS model for perforated plate

were obtained for 5 modes. The critical buckling load was calculated using the load multiplier obtained and multiplying it with the applied load.



**Fig. 6** Geometry of perforated plate

Figure 6 shows the geometry of the plate, where ‘ $L$ ’ depicts the length, ‘ $W$ ’ the width, ‘ $t$ ’ the thickness, ‘ $OA$ ’ the angle of orientation of the cut-out, ‘ $a$ ’ the longer diagonal and ‘ $b$ ’ the shorter diagonal of the cut-out.

To ascertain the impact of length on the magnitude of critical buckling load, rectangular models of constant width of 40 mm and thickness of 4 mm with varying lengths of 50 mm, 100 mm, 200 mm and 400 mm were made and analysis was performed on each to obtain the critical buckling load. To ascertain the impact of thickness models of constant length of 200 mm and width of 40 mm with varying thickness of 2 mm, 4 mm and 6 mm were made and analysed. To ascertain the impact of diamond-shaped perforation models having different perforation sizes ( $a \times b$ ) of  $5 \times 2.5$ ,  $7 \times 3.5$ ,  $10 \times 5$ ,  $15 \times 7.5$ ,  $20 \times 10$ ,  $25 \times 12.5$  and  $30 \times 15$  mm were made with fixed length of 200 mm, width of 40 mm and thickness of 4 mm. To ascertain the impact of cut-out orientation analysis were performed on models of constant length of 200 mm, width 40 mm, thickness 4 mm with varying angles of 0, 15, 30, 45, 60, 75 and 90°.

### 3 Results and Discussion

To verify the finite element model, non-perforated plates of dimensions as specified in Table 3 with thickness 1.6 mm were analysed. The models were based on the work of Ahmet Erkliğ and Eyüp Yeter [18], and the mechanical properties specified by them as given in Table 2 were used in the finite element analysis.

**Table 2** Mechanical properties (Ahmet Erkliğ and Eyüp Yeter [18])

Young’s modulus, E (GPa)	Shear modulus, G (GPa)	Poisson’s ratio, $\nu$
31.610	3.220	0.206



**Table 3** Comparison with results of Ahmet Erklig and Eyüp Yeter [18]

Plate size (mm)	Ahmet Erklig and Eyüp Yeter [18]			Present work (N/mm)	Relative error with respect to experimental
	Theoretical (N/mm)	Numerical (N/mm)	Experimental (N/mm)		
100 × 100	42.94	43.44	40.82	44.416	0.08809
150 × 150	19.13	19.42	18.26	19.872	0.08828
200 × 200	10.82	10.94	10.38	11.204	0.07938
250 × 250	6.870	7.014	6.680	7.1817	0.07510
300 × 300	4.790	4.873	4.670	4.9914	0.06882

The critical buckling load obtained and comparison with the results of [18] are presented in Table 3. It is observed that the results are complying with each other.

Table 4 displays the mode shapes for 0, 15, 30, 45, 60, 75 and 90° orientation of 20 × 10 mm diamond cut-out.

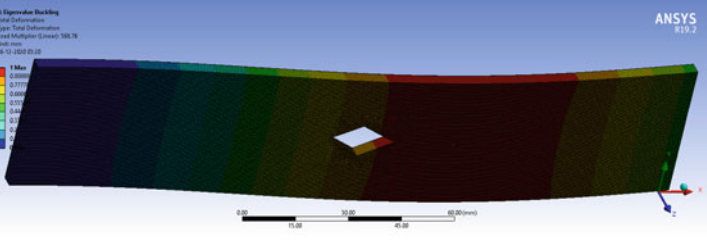
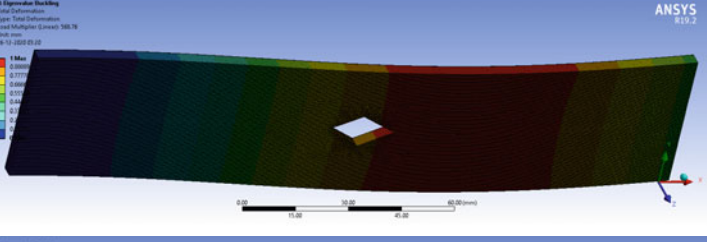
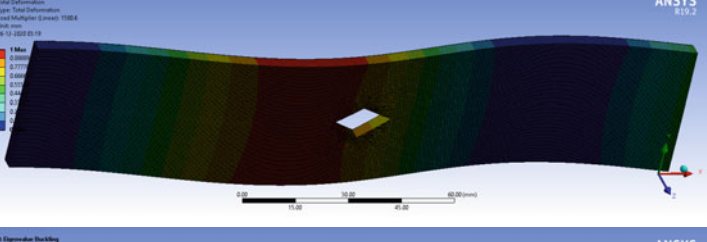
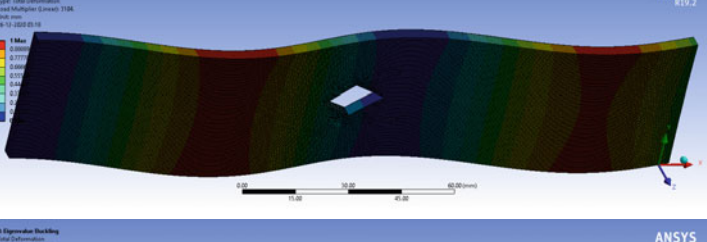
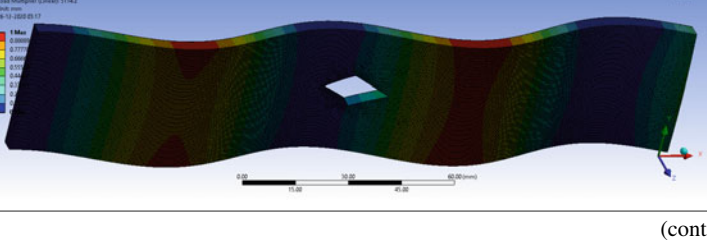
### 3.1 Impact of Length

The change in buckling load with change in length of plate has been presented in Table 5 and Fig. 7. It is observed that buckling load is maximum for shortest aspect ratio (12.5), i.e. shortest plate and minimum for largest aspect ratio (100), i.e. longest plate. It is observed that the buckling load decreases with increase in length. The plate of length 50 mm is about 19 times stronger than the plate of length 400 mm. Hence, we can conclude that the shorter is the length of the plate the stronger the plate is in buckling.

### 3.2 Impact of Thickness

The change in buckling load with change in thickness of plate has been presented in Table 6 and Fig. 8. It is observed that buckling load increases with decrease in aspect ratio. Hence, buckling load increases with increase in thickness of the plate. The plate of thickness 6 mm is 16 times stronger than the plate of thickness 2 mm. So, we can say that the higher the thickness of the plate the stronger the plate is in buckling.

**Table 4** Mode shapes for 20 × 10 mm cut-out

0 deg	
Mode 1	
Mode 2	
Mode 3	
Mode 4	
Mode 5	

(continued)

**Table 4** (continued)

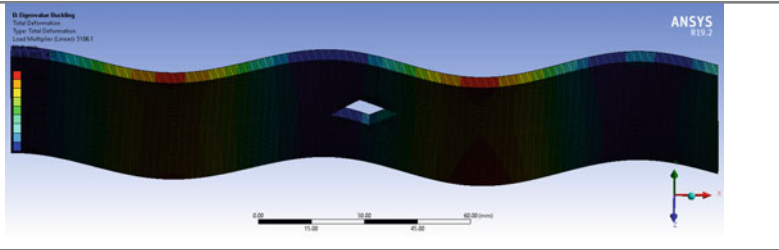
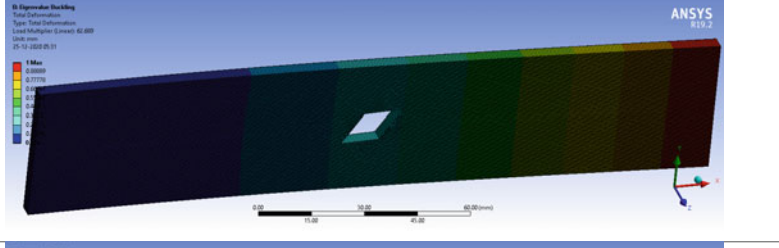
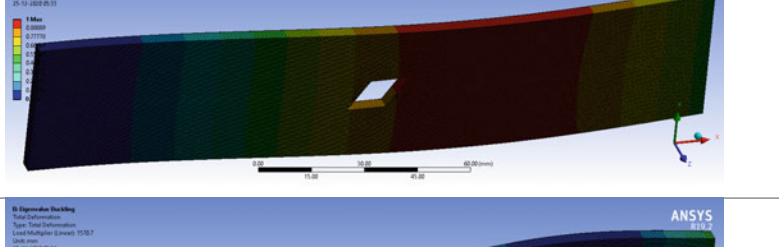
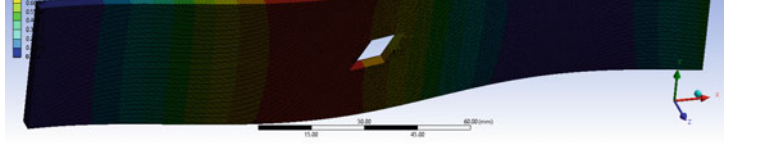
0 deg	
15 deg	
Mode 1	
Mode 2	
Mode 3	
Mode 4	

(continued)

### 3.3 Impact of Cut-Out Size

The change in buckling load with change in diamond perforation dimensions is presented in Table 7 and Figs. 9 and 10. It is observed that buckling load is minimum for largest perforation  $30 \times 15$  mm and maximum for the smallest perforation  $5 \times 2.5$  mm. With increase in perforation size, the buckling load is found to decrease linearly. It is also noticed that the buckling load for perforated plate is lesser than

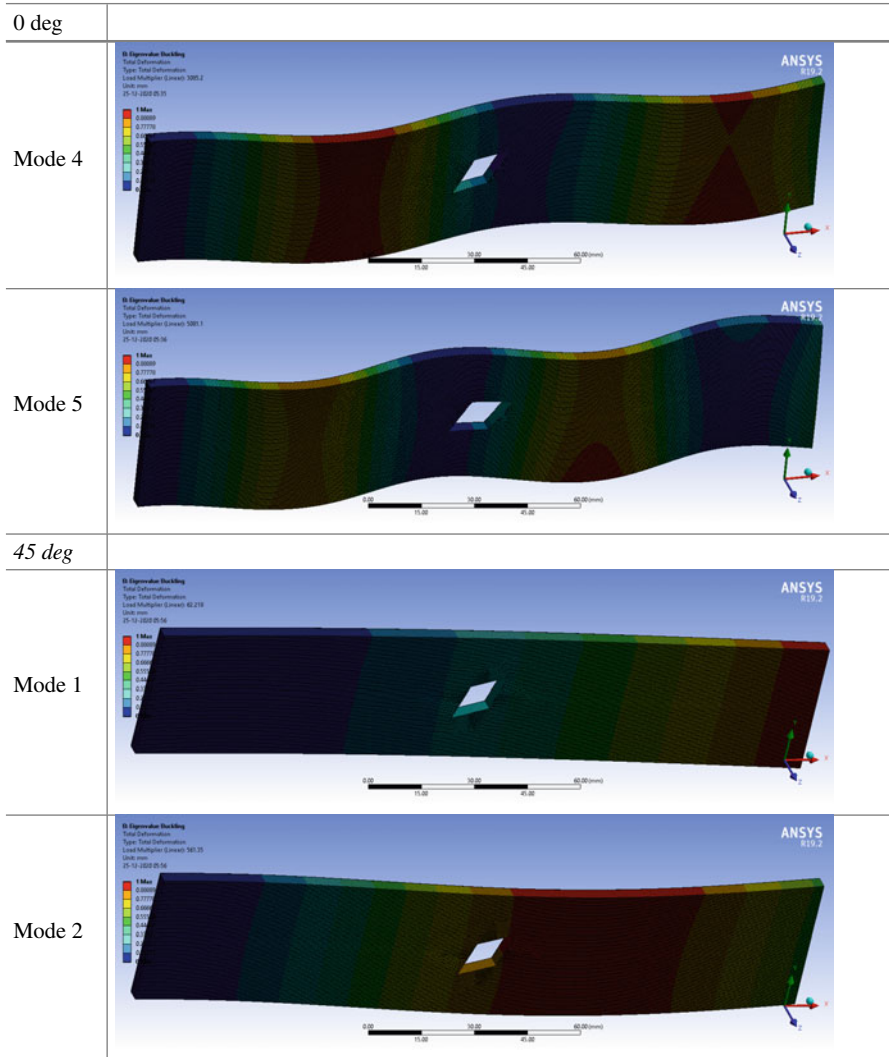
**Table 4** (continued)

0 deg	
30 deg	
Mode 2	
Mode 3	

(continued)

non-perforated plate. The buckling load for perforation  $5 \times 2.5$  mm is just 0.16% lesser than the buckling load of non-perforated plate. Whereas the buckling load of perforation  $30 \times 15$  mm is 5.05% lesser than the buckling load of non-perforated plate. Hence, it is observed that the smaller the perforation size the stronger the plate is in buckling.

**Table 4** (continued)



(continued)

### 3.4 Impact of Cut-Out Orientation

Figure 11 displays the impact of diamond cut-out's orientation for different perforation sizes. It is observed that the buckling load for plates with perforation is lesser than that of non-perforated plate. The decrease in buckling load with orientation angle is not much significant for smaller perforation sizes like  $5 \times 2.5$ ,  $7 \times 3.5$  and  $10 \times 5$  mm while for larger perforation sizes like  $15 \times 7.5$ ,  $20 \times 10$ ,  $25 \times 12.5$  and

**Table 4** (continued)

0 deg	
Mode 4	
Mode 5	
60 deg	

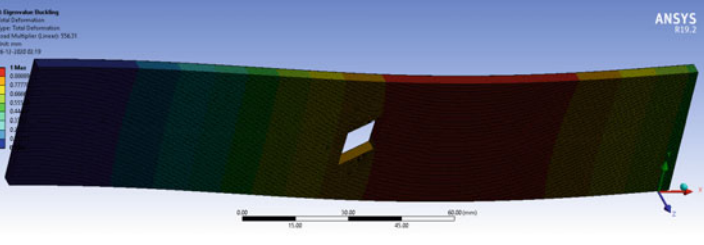
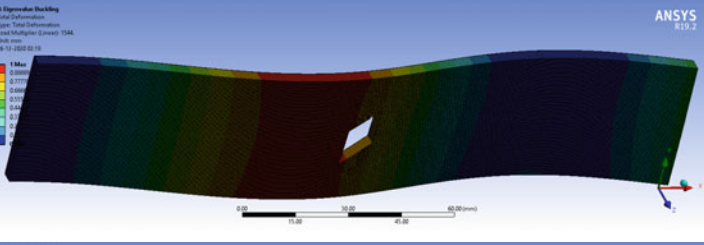
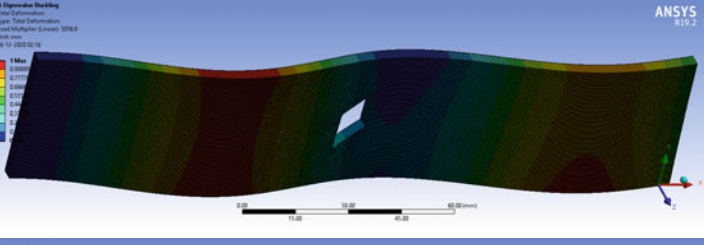
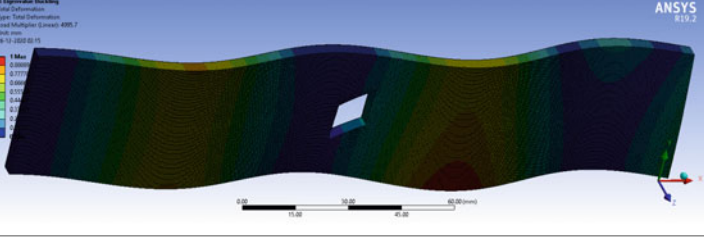
(continued)

30 × 15 mm, the decrease is quite significant. The following sections give a detailed analysis of the impact of perforation orientation.

### 3.4.1 Cut-Out 5 × 2.5 mm

The impact of perforation orientation on buckling load for 5 × 2.5 mm cut-out is shown in Table 8 and Fig. 12. It is observed that the buckling load is highest for

**Table 4** (continued)

0 deg	
Mode 2	
Mode 3	
Mode 4	
Mode 5	
75 deg	

(continued)

orientation of  $0^\circ$  and least for orientation of  $90^\circ$ . The buckling load decreases with incremental inclination with the horizontal. The buckling load for  $0^\circ$  is just 0.16% lesser than the buckling load for non-perforated plate. Whereas the buckling load for  $90^\circ$  is 0.41% lesser than the buckling load for non-perforated plate.



**Table 4** (continued)

0 deg	
Mode 1	
Mode 2	
Mode 3	
Mode 4	
Mode 5	

(continued)



**Table 4** (continued)

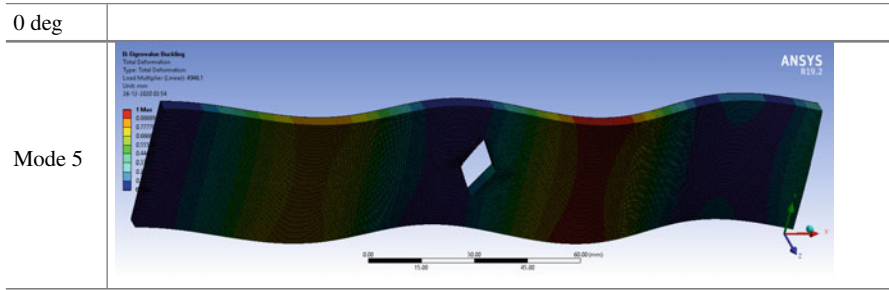
0 deg	
90 deg	
Mode 1	
Mode 2	
Mode 3	
Mode 4	

(continued)

### 3.4.2 Cut-Out 7 × 3.5 mm

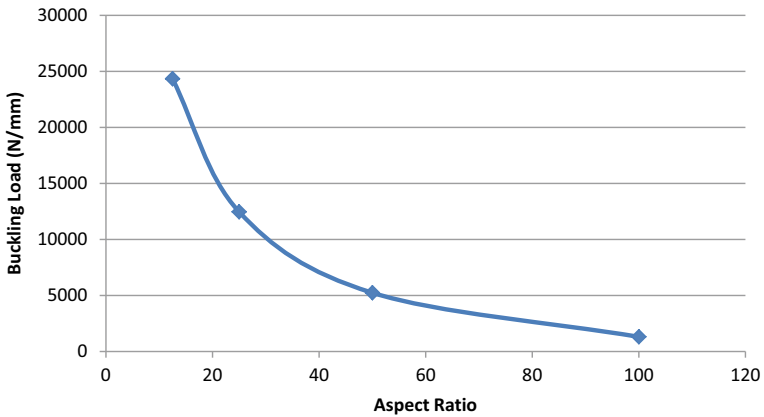
The impact of perforation orientation on buckling load for 7 × 3.5 mm cut-out is shown in Table 9 and Fig. 13. It is observed that the buckling load is highest for orientation of 0° and least for orientation of 90°. The buckling load decreases with incremental inclination with the horizontal. The buckling load for 0° is just 0.29% lesser than the buckling load for non-perforated plate. Whereas the buckling load for 90° is 0.75% lesser than the buckling load for non-perforated plate.

**Table 4** (continued)



**Table 5** Impact of length ( $W = 40$  mm and  $t = 4$  mm)

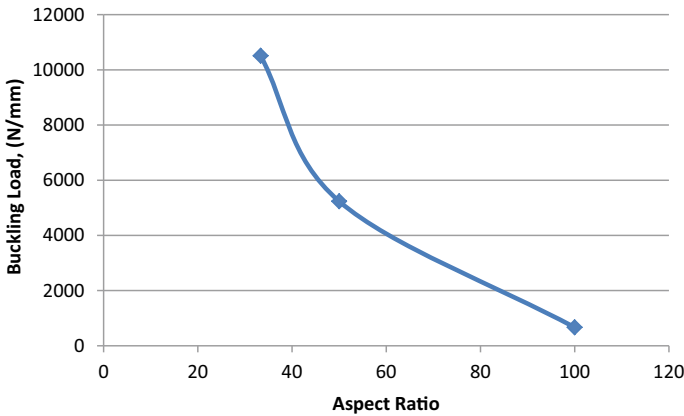
Plate type	Length (mm)	Aspect ratio, (L/t)	Buckling load, (N/mm)
C-C	50	12.5	24,337.0
C-C	100	25	12,458.0
C-C	200	50	5236.0
C-C	400	100	1303.8



**Fig. 7** Impact of length ( $W = 40$  mm,  $t = 4$  mm)

**Table 6** Impact of thickness ( $W = 40$  mm,  $L = 200$  mm)

Plate type	Thickness, (mm)	Aspect ratio, (L/t)	Buckling load, (N/mm)
C-C	2	100	666.97
C-C	4	50	5236
C-C	6	33.33	10,510



**Fig. 8** Impact of thickness ( $W = 40$  mm,  $L = 200$  mm)

**Table 7** Impact of perforation size ( $W = 40$  mm,  $L = 200$  mm,  $t = 4$  mm)

Plate type	Buckling load for non-perforated plate ( $L = 200$ mm, $W = 40$ mm, $t = 4$ mm) (N/mm)	Cut-out size, (mm) $a \times b$	Cut-out area, (mm <sup>2</sup> )	Buckling load for perforated plate, (N/mm)
C-C		$5 \times 2.5$	12.5	5227.70
C-C		$7 \times 3.5$	24.5	5220.80
C-C		$10 \times 5$	50.0	5203.90
C-C	5236.00	$15 \times 7.5$	112.5	5165.80
C-C		$20 \times 10$	200.0	5114.20
C-C		$25 \times 12.5$	312.5	5049.80
C-C		$30 \times 15$	450.0	4971.70

### 3.4.3 Cut-Out $10 \times 5$ mm

The impact of perforation orientation on buckling load for  $10 \times 5$  mm cut-out is depicted in Table 10 and Fig. 14. It is observed that the buckling load is highest for orientation of  $0^\circ$  and least for orientation of  $90^\circ$ . The buckling load decreases with incremental inclination with the horizontal. The buckling load for  $0^\circ$  is 0.61% lesser than the buckling load for non-perforated plate. Whereas the buckling load for  $90^\circ$  is 1.45% lesser than the buckling load for non-perforated plate.

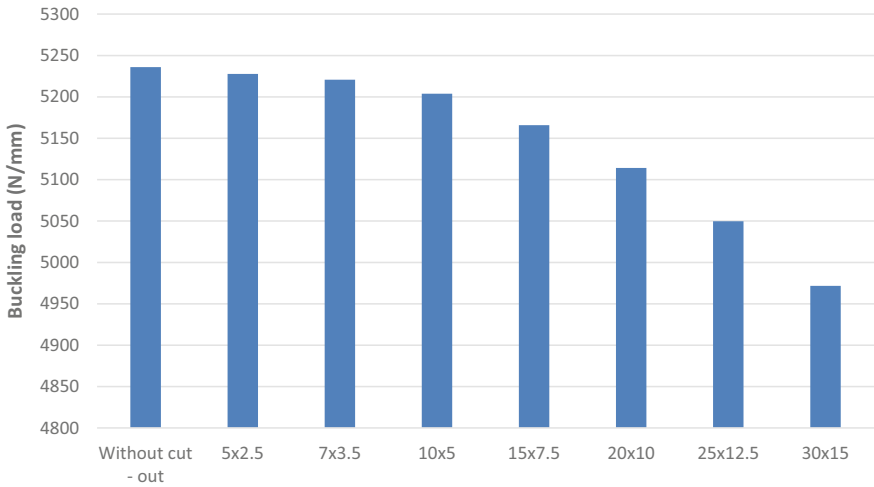


Fig. 9 Impact of perforation size ( $W = 40$  mm,  $L = 200$  mm,  $t = 4$  mm)

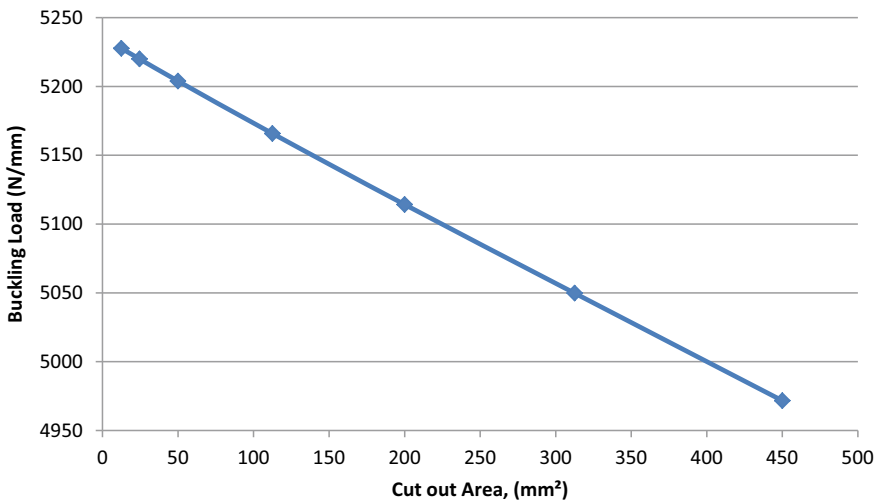


Fig. 10 Impact of perforation area ( $W = 40$  mm,  $L = 200$  mm,  $t = 4$  mm)

### 3.4.4 Cut-Out 15 × 7.5 mm

The impact of perforation orientation on buckling load for 15 × 7.5 mm cut-out is depicted in Table 11 and Fig. 15. It is observed that the buckling load is highest for orientation of 0° and least for orientation of 90°. The buckling load decreases with incremental inclination with the horizontal. The buckling load for 0° is 1.34% lesser



**Fig. 11** Impact of perforation orientation for different perforation sizes

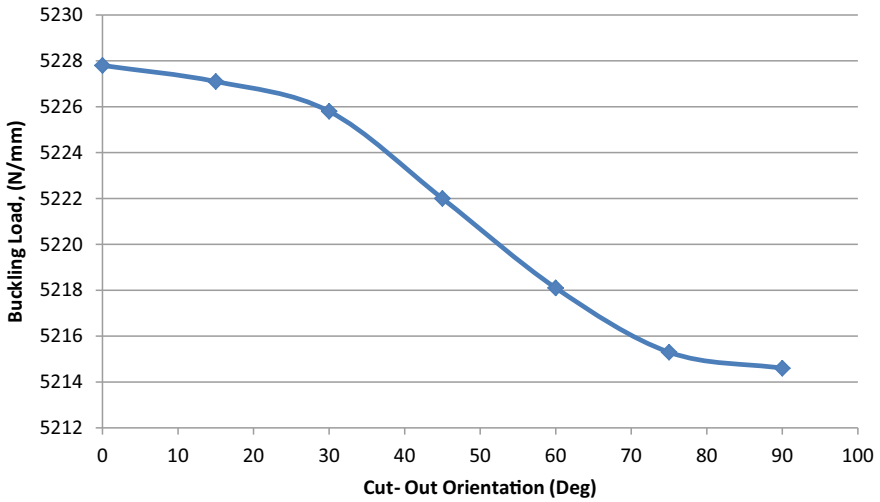
**Table 8** Impact of perforation orientation ( $W = 40$  mm,  $L = 200$  mm,  $t = 4$  mm,  $5 \times 2.5$  mm)

Plate type	Buckling load for non-perforated plate ( $L = 200$ mm, $W = 40$ mm, $t = 4$ mm) (N/mm)	Cut-out ( $5 \times 2.5$ mm) orientation (deg)	Buckling load, (N/mm)
C-C		0	5227.70
C-C		15	5227.10
C-C		30	5225.80
C-C	5236.00	45	5222.00
C-C		60	5218.10
C-C		75	5215.30
C-C		90	5214.60

than the buckling load for non-perforated plate. Whereas the buckling load for  $90^\circ$  is 3.22% lesser than the buckling load for non-perforated plate.

### 3.4.5 Cut-Out $20 \times 10$ mm

The impact of perforation orientation on buckling load for  $20 \times 10$  mm cut-out is depicted in Table 12 and Fig. 16. It is observed that the buckling load is highest for orientation of  $0^\circ$  and least for orientation of  $90^\circ$ . The buckling load decreases with incremental inclination with the horizontal. The buckling load for  $0^\circ$  is 2.32% lesser



**Fig. 12** Impact of perforation orientation ( $W = 40$  mm,  $L = 200$  mm,  $t = 4$  mm,  $5 \times 2.5$  mm)

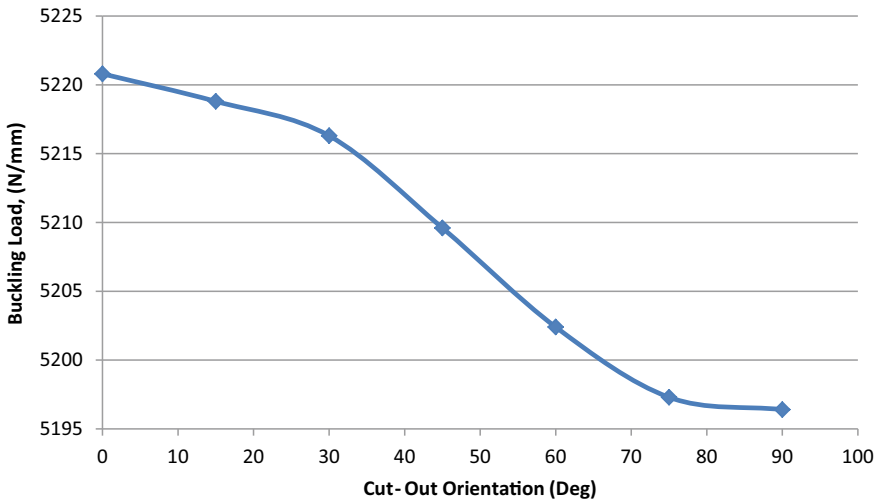
**Table 9** Impact of perforation orientation ( $W = 40$  mm,  $L = 200$  mm,  $t = 4$  mm,  $7 \times 3.5$  mm)

Plate type	Buckling load for non-perforated plate ( $L = 200$ mm, $W = 40$ mm, $t = 4$ mm) (N/mm)	Cut-out ( $7 \times 3.5$ mm) orientation (deg)	Buckling load, (N/mm)
C-C		0	5220.80
C-C		15	5218.80
C-C		30	5216.30
C-C	5236.00	45	5209.60
C-C		60	5202.40
C-C		75	5197.30
C-C		90	5196.40

than the buckling load for non-perforated plate. Whereas the buckling load for  $90^\circ$  is 5.53% lesser than the buckling load for non-perforated plate.

### 3.4.6 Cut-Out $25 \times 12.5$ mm

The impact of perforation orientation on buckling load for  $25 \times 12.5$  mm cut-out is depicted in Table 13 and Fig. 17. It is observed that the buckling load is highest for orientation of  $0^\circ$  and least for orientation of  $90^\circ$ . The buckling load decreases with incremental inclination with the horizontal. The buckling load for  $0^\circ$  is 3.55% lesser



**Fig. 13** Impact of perforation orientation ( $W = 40$  mm,  $L = 200$  mm,  $t = 4$  mm,  $7 \times 3.5$  mm)

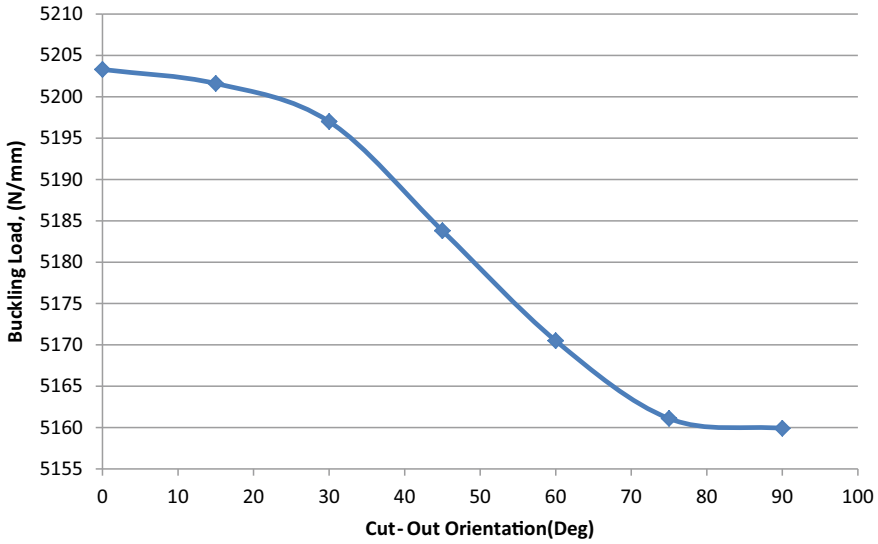
**Table 10** Impact of perforation orientation ( $W = 40$  mm,  $L = 200$  mm,  $t = 4$  mm,  $10 \times 5$  mm)

Plate type	Buckling load for non-perforated plate ( $L = 200$ mm, $W = 40$ mm, $t = 4$ mm) (N/mm)	Cut-out ( $10 \times 5$ mm) orientation (deg)	Buckling load, (N/mm)
C-C		0	5203.90
C-C		15	5201.60
C-C		30	5197.00
C-C	5236.00	45	5183.80
C-C		60	5170.50
C-C		75	5161.10
C-C		90	5159.90

than the buckling load for non-perforated plate. Whereas the buckling load for  $90^\circ$  is 8.54% lesser than the buckling load for non-perforated plate.

### 3.4.7 Cut-Out $30 \times 15$ mm

The impact of perforation orientation on buckling load for  $25 \times 12.5$  mm cut-out is depicted in Table 14 and Fig. 18. It is observed that the buckling load is highest for orientation of  $0^\circ$  and least for orientation of  $90^\circ$ . The buckling load decreases with incremental inclination with the horizontal. The buckling load for  $0^\circ$  is 5.04% lesser than the buckling load for non-perforated plate. Whereas the buckling load for  $90^\circ$  is 12.47% lesser than the buckling load for non-perforated plate.



**Fig. 14** Impact of perforation orientation ( $W = 40$  mm,  $L = 200$  mm,  $t = 4$  mm,  $10 \times 5$  mm)

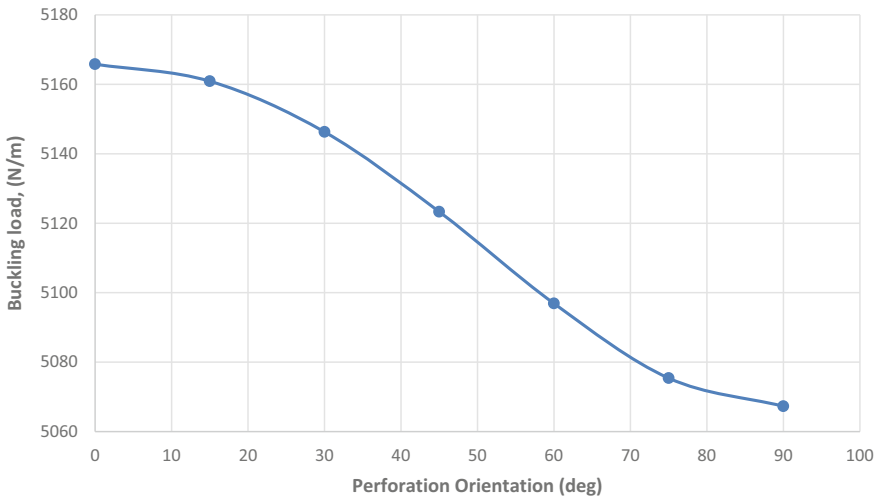
**Table 11** Impact of perforation orientation ( $W = 40$  mm,  $L = 200$  mm,  $t = 4$  mm,  $15 \times 7.5$  mm)

Plate type	Buckling load for non-perforated plate ( $L = 200$ mm, $W = 40$ mm, $t = 4$ mm) (N/mm)	Cut-out ( $15 \times 7.5$ mm) orientation (deg)	Buckling load, (N/mm)
C-C		0	5165.80
C-C		15	5160.90
C-C		30	5146.30
C-C	5236.00	45	5123.30
C-C		60	5096.90
C-C		75	5075.40
C-C		90	5067.30

## 4 Conclusions

In this study, the impact of length and thickness of plate along with the size and orientation of diamond-shaped perforation on the buckling nature of stainless-steel plate was examined. This would aid in selecting the proper cut-out shape, size or orientation needed to give higher buckling strength. The following results are obtained:



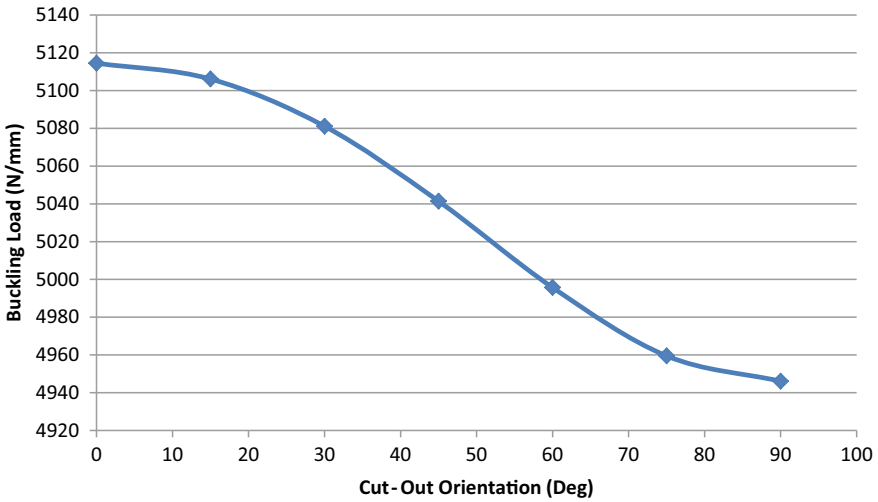


**Fig. 15** Impact of perforation orientation ( $W = 40$  mm,  $L = 200$  mm,  $t = 4$  mm,  $15 \times 7.5$  mm)

**Table 12** Impact of perforation orientation ( $W = 40$  mm,  $L = 200$  mm,  $t = 4$  mm,  $20 \times 10$  mm)

Plate type	Buckling load for non-perforated plate ( $L = 200$ mm, $W = 40$ mm, $t = 4$ mm) (N/mm)	Cut-out ( $20 \times 10$ mm) orientation (deg)	Buckling load, (N/mm)
C-C		0	5114.20
C-C		15	5106.10
C-C		30	5081.10
C-C	5236.00	45	5041.40
C-C		60	4995.70
C-C		75	4959.50
C-C		90	4946.10

- The buckling load of plate decreases by increasing the length of plate. So, the shorter the length of the plate, the stronger it is in buckling.
- The buckling load of plate increases by increasing the thickness of plate. So, the thicker the plate is, the stronger it is in buckling.
- The buckling load of plate decreases by increasing the size of diamond-shaped cut-out. So, the smaller the size of perforation on plate, the stronger the plate is in buckling.
- The buckling load of plate decreases by incrementing the diamond-shaped cut-out's orientation with the horizontal. So, plates with perforation inclined at  $0^\circ$



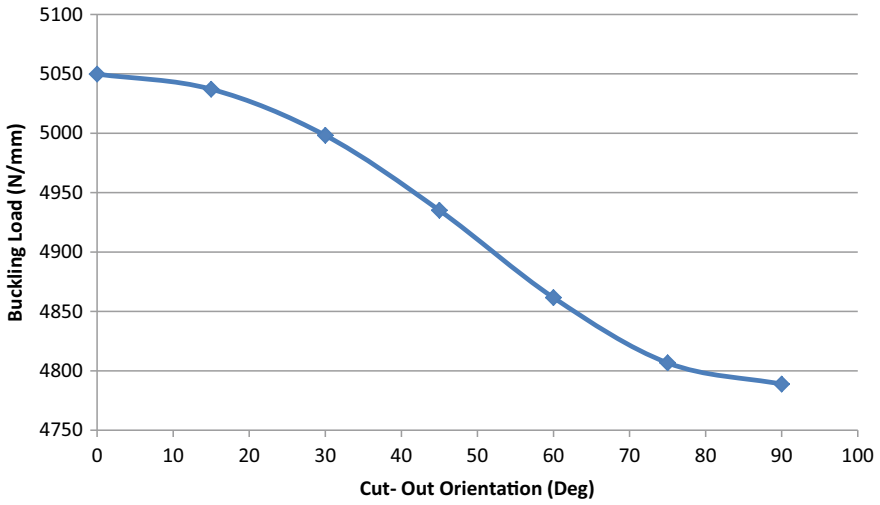
**Fig. 16** Impact of perforation orientation ( $W = 40$  mm,  $L = 200$  mm,  $t = 4$  mm,  $20 \times 10$  mm)

**Table 13** Impact of perforation orientation ( $W = 40$  mm,  $L = 200$  mm,  $t = 4$  mm,  $25 \times 12.5$  mm)

Plate type	Buckling load for non-perforated plate ( $L = 200$ mm, $W = 40$ mm, $t = 4$ mm) (N/mm)	Cut-out ( $25 \times 12.5$ mm) orientation (deg)	Buckling load, (N/mm)
C-C		0	5049.80
C-C		15	5037.10
C-C		30	4998.20
C-C	5236.00	45	4935.10
C-C		60	4861.60
C-C		75	4806.70
C-C		90	4788.80

are the strongest in buckling, whereas plates with perforation inclined at  $90^\circ$  are weakest in buckling.

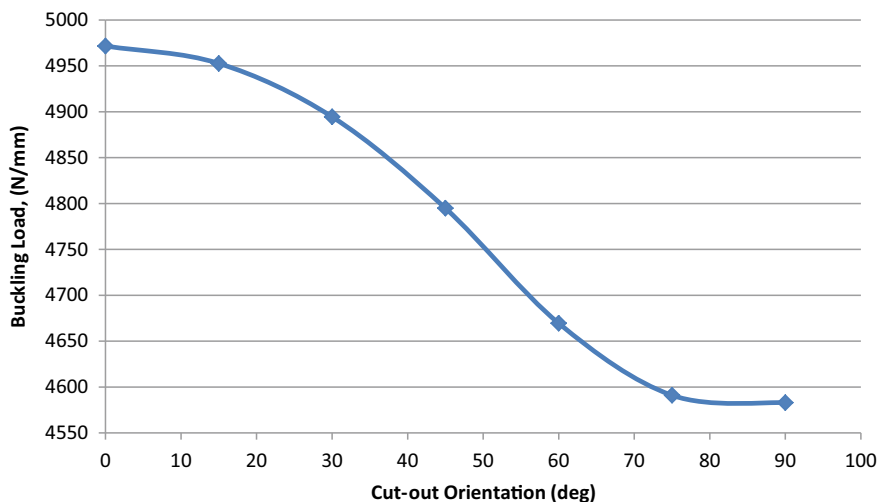
- The decrease in buckling load with orientation angle is not much significant for smaller cut-outs, while for larger cut-outs the decrease is quite significant.
- The buckling load for perforated plates is lesser than the buckling load for non-perforated plate.



**Fig. 17** Impact of perforation orientation ( $W = 40$  mm,  $L = 200$  mm,  $t = 4$  mm,  $25 \times 12.5$  mm)

**Table 14** Impact of perforation orientation ( $W = 40$  mm,  $L = 200$  mm,  $t = 4$  mm,  $30 \times 15$  mm)

Plate type	Buckling load for non-perforated plate ( $L = 200$ mm, $W = 40$ mm, $t = 4$ mm) (N/mm)	Cut-out ( $30 \times 15$ mm) orientation (deg)	Buckling load, (N/mm)
C-C		0	4971.70
C-C		15	4952.70
C-C		30	4894.50
C-C	5236.00	45	4794.90
C-C		60	4669.50
C-C		75	4591.00
C-C		90	4582.90



**Fig. 18** Impact of perforation orientation ( $W = 40$  mm,  $L = 200$  mm,  $t = 4$  mm,  $30 \times 15$  mm)

## References

1. Helbig D, Silva CCCD, Real MV, dos Santos ED, Isoldi LA, Rocha LAO (2016) Study about buckling phenomenon in perforated thin steel plates employing computational modeling and constructal design method. In: Latin American journal of solids and structures, vol 13. pp 1912–1936
2. Gracia JB, Rammerstorfer FG (2019) Increase in buckling loads of plates by introduction of cutouts. *Acta Mech* 230:2873–2889
3. Shariati M, Faradjian Y, Mehrabi H (2016) Numerical and experimental study of buckling of rectangular steel plates with a cut-out. *J Solid Mech* 8(1):116–129
4. Real MDV, Isoldi LA, Damas AP, Helbig D (2013) Elastic and elasto-plastic buckling analysis of perforated steel plates. *Vetor, Rio Grande* 23(2):61–70
5. Singh S, Kulkarni K, Pandey R, Singh H (2012) Buckling analysis of thin rectangular plates with cutouts subjected to partial edge compression using FEM. *J Eng, Design Technol* 10(1):128–142. Emerald Group Publishing Limited
6. Lorenzini G, Helbig D, da Silva CCC, Real MV, dos Santos ED, Isoldi LA, Rocha LAO (2016) Numerical evaluation of the impact of type and shape of perforations on the buckling of thin steel plates by means of the constructal design method. *Int J Heat Technol* 34(1):S9–S20
7. da Silva CCC, Helbig D, Cunha ML, dos Santos ED, Rocha LAO, de Vasconcellos Real M, Isoldi LA (2019) Numerical buckling analysis of thin steel plates with centered hexagonal cut-out through constructal design method. *J Braz Soc Mech Sci Eng* 41:309
8. Rao LB, Rao CK (2009) Buckling of circular plates with an internal elastic ring support and elastically restrained guided edge against translation. *Mech Based Design Struct Mach* 37(1):60–72
9. Rao LB, Rao CK (2009) Buckling of circular plates with an internal elastic ring support and elastically restrained guided edge against translation. *Advan Vibr Eng* 8(1):59–67
10. Rao LB, Rao CK (2011) Fundamental buckling of annular plates with elastically restrained guided edges against translation. *Mech Based Design Struct Mach* 39(4):409–419
11. Rao LB, Rao CK (2013) Fundamental buckling of circular plates with elastically restrained edges and resting on concentric rigid ring support. *Frontiers Mech Eng* 8(3):291–297

12. Rao LB, Rao CK (2010) Buckling analysis of circular plates with elastically restrained edges and resting on internal elastic ring support. *Mech Based Design Struct Mach* 38(4):440–452
13. Rao LB, Rao CK (2012) Buckling of circular plates with an internal elastic ring support and outer edge restrained against translation. *J Eng Sci Technol* 7(3):393–407
14. Rao LB, Rao CK (2015) Buckling of elastic circular plates with an elastically restrained edges against rotation and internal elastic ring support. *Int Appl Mech* 51(4):480–488
15. Rao LB, Rao CK (2013) Buckling of annular plates with elastically restrained external and internal edges. *Mech Based Design Struct Mach* 41(2):222–235
16. Rao LB, Rao CK (2015) Buckling of circular plate with foundation and elastic edge. *Int J Mech Mater Design* 11(2):149–156
17. (Nov 2013) ANSYS fluent user's guide engineering, vol 1, ANSYS, Inc. Southpointe Technology Drive Canonsburg, USA, Release 15.0
18. Erklığ A, Yeter E (2012) The impacts of cut-outs on buckling nature of composite plates. *Sci Eng Compos Mater* 19:323–330

# Modelling and Analysis of a Two-Stage Gearbox



Aditya Sachin Kodollikar, Alahari Venkata Sai Jaswanth, S. Naveen, and Lokavarapu Bhaskara Rao

**Abstract** The world today as we know it is advancing in many factors as per manufacturing and design. One of the key factors during this process is to reduce weight and volume without changing the performance of the required product. This can be achieved by the selection of materials and manufacturing processes. In this study, a two-stage reduction gearbox was designed and analysed for its use on an all-terrain vehicle (ATV). Computer-aided design (CAD) and computer-aided engineering (CAE) software packages are used for designing and analysis of gears and shafts. A similar approach was adopted for designing of gears and shafts, whereas sequential approach thereafter for the design of casing geometry. The product was designed in accordance with the American Gear Manufacturers Association (AGMA) standards and is meant for off-road application.

**Keywords** Powertrain · Gears · All-terrain vehicle (ATV) · GearTraxPRO · SolidWorks · ANSYS

## 1 Introduction

For the all-terrain vehicles (ATV) that are configured for an automatic transmission drive using a continuously variable transmission (CVT), a gearbox has to be coupled with the CVT to get desired speed and torque output. Since the CVT is providing variable transmission ratios, a forward–neutral–reverse (FNR), two-step reduction gearbox can be used for this purpose. The work proposed here is to design a two-stage gearbox consisting of both helical and spur gears. This gearbox is designed for an ATV, made for the BAJA competitions. Here weight reduction is focused upon as the main goal to achieve maximum acceleration and also to get the centre of gravity as low as possible. Thus, factors such as weight, strength and size are optimized

---

A. S. Kodollikar (✉) · A. Venkata Sai Jaswanth · S. Naveen · L. Bhaskara Rao  
School of Mechanical Engineering, Vellore Institute of Technology, Chennai Campus,  
Vandalur-Kelambakkam Road, Chennai, Tamil Nadu 600127, India

**Table 1** Input parameters

Input parameters	Sign	Value
Coefficient of friction	fr	0.16
Mass of vehicle + driver	mf	225 kg
Gradeability angle		30 degree
Air Density	PI	1.199 kg/m <sup>3</sup>
Coefficient of drag	Cw	0.5
Velocity of car	V = Vf	25 km/hr
Acceleration of car	a	2.83 m/s <sup>2</sup>
Efficiency of CVT	E1	0.88

to achieve the best possible gearbox. The analysis operations conducted during the research were done according to Navneet et al. [1], in their study in ‘Analysis and Simulation of Gearless Transmission Mechanism’ and also by Timir Patel et al. [2], in their study ‘Design and Analysis of an Epicyclic Gearbox for an Electric Drivetrain’.

## 2 Vehicle Parameters

Engine power = 10 hp = 7.456 kW @ Max RPM = 3800 rpm

Engine torque = 19.2 Nm @ 2700 rpm

Transmission type = CVT + Gearbox drive

Gearbox type = forward spool two-stage helical gearbox

Overall reduction = 9

Stage 1 reduction = 3, stage 2 reduction = 3

Gear material = 20 MnCr5, Yield strength: 350–550 N/mm<sup>2</sup>, Tensile strength: 650–880 N/mm<sup>2</sup>.

The Table 1 shows the parameters taken into account of an ATV for which the gearbox is being designed.

## 3 Torque Requirements

To determine the required torque, the most important factor that turns in is the total resistance experienced by the vehicle. The driving resistance is an important variable taken into consideration while designing transmission systems. Driving resistance is made up of mainly four resistances:

- Wheel Resistance
- Air Resistance
- Gear Resistance

**Table 2** Resistance calculations

Engine RPM	Total reduction	Engine (N-m)	Torque (N-m)	Traction (N)	Velocity (m/s)	Gradient	Acceleration (m/s <sup>2</sup> )	Total resistance (N)
1800	27	18	487	1498	5.8	32	1.9	932
2000	26.4	18.7	494	1520	6.6	32.1	1.9	943
2200	25.9	18.8	487	1499	7.4	32.1	19	932
2400	24.7	18.9	467	1438	8.5	29.1	2	901
2600	23.4	19	445	1368	9.7	25.8	1.7	867
2800	22.5	19.1	430	1322	10.9	23.6	1.6	844
3000	19.8	18.9	374	1151	15.3	17.4	1.3	759
3200	15.3	18.8	288	887	23.6	12.7	0.9	626
3400	12.6	18.3	231	711	32.5	4.2	0.6	537
3600	11.7	18.2	213	655	40.8	1.5	0.6	510
3800	6.75	17.6	119	366	49.3	1	0.5	502

- Acceleration Resistance.

The Table 2 comprises of the resistance values experienced by the ATV at different RPMs. As the engine increases its RPM, the resistance value changes [3–5].

Taking reference from the Table 2, we determined what is the exact reduction required for our BAJA vehicle [4, 6, 7].

## 4 Design of Gearbox

Design calculations of various parts of gearbox are as follows [4, 6–9].

### 4.1 Design of Gears

Lewis bending equation is.

$$\sigma = \frac{K_v W^t}{FmY} \tag{1}$$

where

$\sigma$  is the bending stress on gear teeth (not considering dynamic loading)

$F$  is the face width

$m$  is the module

$W^t$  is the tangential load



$Y$  is the Lewis form factor

$K_v$  is the velocity factor

AGMA bending stress equation is

$$\sigma = \frac{K_v W^t K_s K_o K_H K_B}{b m_t Y_J} \quad (2)$$

where

$\sigma$  is the bending stress-induced

$K_v$  is the dynamic factor

$W^t$  is the tangential transmitted load

$b$  is the face width of the narrower member

$K_o$  is the overload factor

$K_s$  is the size factor

$K_B$  is the rim thickness factor

$K_H$  is the load distribution factor

$Y_J$  is the geometry factor for bending strength

$m_t$  is the transverse module

AGMA pitting stress equation is

$$\sigma_c = Z_E \sqrt{W^t K_o K_v K_s \frac{K_H}{d_{wl} b} \frac{Z_R}{Z_I}} \quad (3)$$

where

$\sigma_C$  is the pitting stress-induced

$Z_E$  is the elastic coefficient

$d_{wl}$  is the pitch diameter of the pinion

$Z_I$  is the geometry factor of the pitting resistance

$Z_R$  is the surface condition factor

AGMA allowable bending stress equation is

$$\sigma_{all} = \frac{S_t Y_N}{S_F Y_\theta Y_Z} \quad (4)$$

where

$S_t$  is the allowable bending stress

$Y_N$  is the stress cycle factor for bending stress

$Y_Z$  is the reliability factor

$Y_\theta$  is the temperature factor

$S_F$  is the AGMA factor of safety.

**Table 3** For reduction stage 1 pinion and gear

Parameter	Value
Gear type	Spur
Helix angle	Zero
Pressure angle	20 degree
No. of teeth on pinion	18
No. of teeth on gear	54
Max. RPM	1267
Module	2
Face width	15 mm

AGMA allowable pitting stress equation is

$$\sigma_{c,all} = \frac{S_c Z_N Z_W}{S_H Y_\theta Y_Z} \tag{5}$$

where

- $\sigma_{c,all}$  is the allowable pitting stress
- $Z_N$  is the stress cycle factor
- $S_c$  is the allowable contact stress
- $S_H$  is the AGMA factor of safety
- $Z_W$  is the hardness ratio factors for pitting resistance.

To avoid failure in gearing, the following condition must be satisfied:

$\sigma$  (both of Lewis bending equation and AGMA strength equation)  $\ll \sigma_{all}, \sigma_c \ll \sigma_{c,all}$ .

Solving the above equations by inserting the specified vehicle parameters, the above conditions are satisfied. Therefore, the design is safe.

The values obtained by solving the equations in GearTraxPRO (Camnetics Suite) are shown in Table 3 for stage 1 pinion and gear and Table 4 for stage 2 pinion and gear.

The following tables show the parameters taken as for both pinion gears for design [3] (Table 5).

### 4.2 Design of Shafts

Parameters:

- Material: AISI/SAE 4340
- UTS: 925 MPa
- Yield strength: 680 MPa
- Allowable shear stress for shaft: 462.5 MPa

**Table 4** For reduction stage 2 pinion and gear

Parameter	Value
Gear type	Helical
Helix angle	20 degree
Pressure angle	20 degree
No. of teeth on pinion	18
No. of teeth on gear	54
Max. RPM	423
Module	2
Face width	25 mm

**Table 5** Factors for spur and helical gears

Factors	Symbols	Value
Overload factor	Ko	1
Dynamic effect factor	Kv	1.178
Size factor	Ks	1.0029
Load distribution factor	Km	1.149
Rim thickness factor	Kb	1.139
Bending strength factor	Yj	0.317
Geometry factor	I	0.12
Temperature factor	Kt	1
Reliability factor	Kr	1
Hardness factor	Ch	1

Torque transmitted by pinion:

$$T = \frac{P \times 60}{2\pi N_P} \quad (6)$$

Equivalent no. of teeth:

$$T_E = \frac{T_P}{\cos^3 \alpha} \quad (7)$$

Tooth factor:

$$y' = 0.154 - \frac{0.912}{T_E} \quad (8)$$

Tangential tooth load:

$$W_T = \frac{2T}{m \times T_P} \quad (9)$$

$$\frac{1}{n} = \frac{16}{\pi d^3} \left\{ \frac{1}{S_e} \left[ 4(K_f M_a)^2 + 3(K_{fs} T_a)^2 \right]^{1/2} + \frac{1}{S_{ut}} \left[ 4(K_f M_m)^2 + 3(K_{fs} T_m)^2 \right]^{1/2} \right\} \quad (10)$$

where

Factor of safety (FOS) =  $n$

Diameter of the shaft =  $d$

Endurance limit at critical location  $S_e = k_a k_b k_c k_d k_e k_f S'_e$

$k_a$  is the surface condition modification factor

$k_b$  is the size modification factor

$k_c$  is the load modification factor

$k_d$  is the temperature modification factor

$k_e$  is the reliability factor

$k_f$  is the miscellaneous effects modification factor

$S'_e$  = rotary beam test specimen endurance limit

Stress concentration factor for Bending,  $K_f = 1 + q(K_t - 1)$ .

Stress concentration factor for torsion,  $K_{fs} = 1 + q_{\text{shear}}(K_t - 1)$ .

$q$  is the notch sensitivity

$M_e$  is the midrange bending moment

$M_a$  is the maximum bending moment

$T_a$  is the alternating torque

$T_e$  is the maximum torque

$S_{ut}$  is the tensile strength.

By drawing shear force and bending moment diagrams, we are able to find the values of  $M_a$  and  $T_e$ .

Resultant bending moment:  $M_a = \sqrt{(M_1)^2 + (M_2)^2}$ .

Putting the values in Eq. 10, we get  $n = 1.37$ .

From the above equation, we get  $d_p = 17$  mm (standardized according to the availability of support bearing sizes and oil seals).

The value of principal shear stress is equated which is significantly less than the permissible shear stress of the shaft material. Hence, the design is safe.

Repeating the above calculations for the intermediate shaft and the output shaft, we get shaft diameters as **22 mm** and **27 mm**.

### 4.3 Design of Casing

The casing design was aimed at achieving the lowest possible volume, while constraining the shafts with gears mounted on them. The geometry is kept simple for lowering the machining cost.

## 5 CAD Modelling of Gears, Shafts and Casing

SolidWorks 2018–19 modelling software was used to design the various components of the gearbox. Based on the input design parameters from GearTraxPRO software, modelling was done in SolidWorks. The images of the components are shown in the figures below. Gear material was selected as 20MnCr5 [10]. Figures 1 and 2 show the gears of the first stage reduction of the gearbox. Figures 3 and 4 show the gears of the second stage reduction of the gearbox. Figures 5, 6 and 7 show the CAD model of the input shaft, intermediate shaft and output shaft, respectively. Figures 1, 2, 3, 4, 5, 6 and 7 are the gears and shafts designed as per parameters in SolidWorks [11, 12, 17].

**Fig. 1** Spur pinion



**Fig. 2** Spur gear



**Fig. 3** Helical pinion

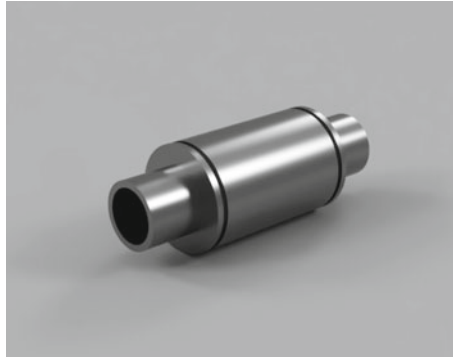


**Fig. 4** Helical gear



**Fig. 5** Input shaft





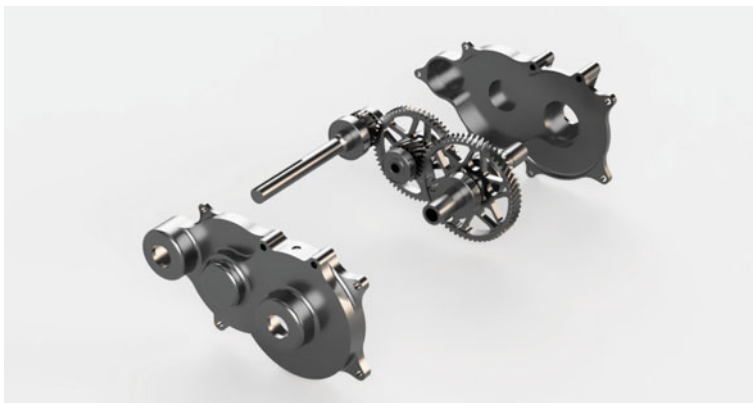
**Fig. 6** Intermediate shaft

**Fig. 7** Output shaft



The CVT is coupled with the input shaft with the help of the keyway in the input shaft. The casing design was optimized for minimum machining cost by reducing the number of contours that were made keeping in mind the weight of the gearbox. Following Figs. 8 and 9 show the final geometry including the left and right casing sides. Aluminium 6061-T6 was chosen as casing material [11].

The final assembly was done using SolidWorks, which included all the gears, shafts, bearings and the shifter. Figures 9 and 10 show the assembled view of the gearbox.



**Fig. 8** Exploded view of complete gearbox

**Fig. 9** Assembled view of gearbox without casing



**Fig. 10** Complete assembly of gearbox





## 6 Static Analysis

### 6.1 Gears

Maximum loading conditions were assumed for checking the gears for maximum safety. It was assumed that the worst loading condition on the gearbox would be when the vehicle is stuck and the engine is working at full power to get out of the obstacle. At this point of time, maximum torque would fall on the intermediate shaft gear 3. In the result, maximum stress-induced under full-loading condition was less than maximum allowable stress for the selected material [1]. The following pictures are of the analysis done on gears on ANSYS software [5, 12–14, 16].

#### Model (A4) > Static Structural (A5) > Solution (A6) > Total Deformation

Time [s]	Minimum [mm]	Maximum [mm]
1.	0. .	5.897e-002

Gear teeth are subjected to both bending and wear. The section where it experiences the maximum stress is the root of the tooth. It is considered that there are three teeth in contact with the mating gear [12]. Tangential force ( $F_t$ ) because of the torque which the gear is transmitting is applied on these three teeth. The total tangential force is distributed amongst the three teeth considering one tooth takes 50% of force and others take 25% each. The radial forces ( $F_r$ ) generated on the gear are acting towards the centre of the gear [12, 13].

Magnitudes of the tangential and radial forces for the application in the analysis are taken from the GearTraxPRO output values in the design of the gears. The analysis result shows that the design is safe, even when the worst loading condition is considered. Figures 11, 12 and 13 show the dimensioning and force calculation outputs for reduction set 1 (for gear 1 and gear 2). The results were obtained by simulation in ANSYS software. Based on the results and analysis, we chose EN24 as our material for gear manufacturing [10] (Fig. 14).

### 6.2 Shafts

Shafts are mainly subjected to bending and torsion. It is considered that the shafts are subjected to maximum torsion at the location of gear through spline. Hence, the torque is applied at that position. Bearing portion where taken as the frictionless support and the fixed support will be the output of the shaft at both ends where the drive shaft through the joints will attach [5, 14, 15] (Figs. 15, 16 and 17).

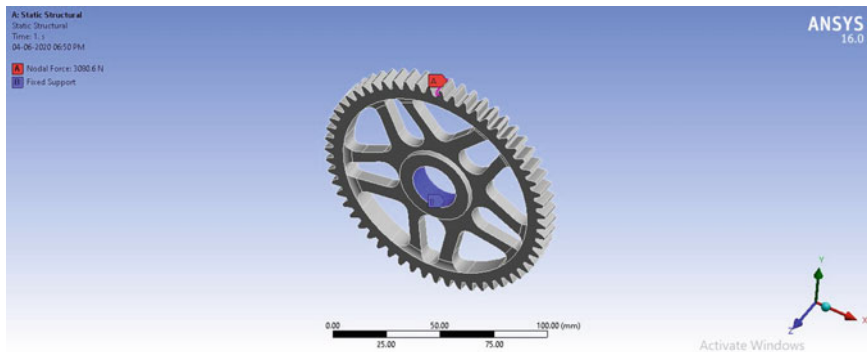


Fig. 11 Force model of gear

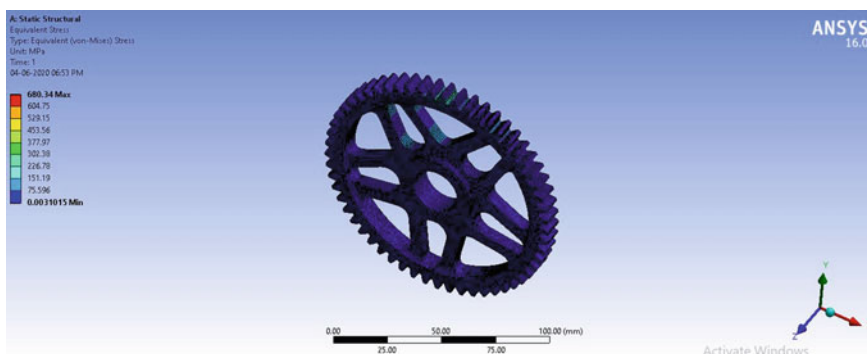


Fig. 12 Equivalent stress of gear

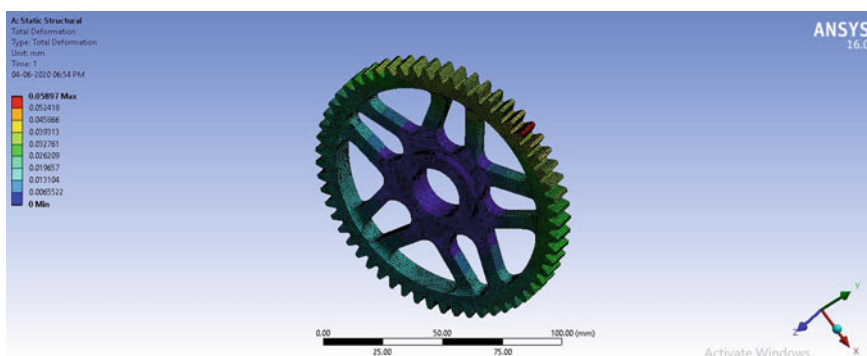


Fig. 13 Total deformation model

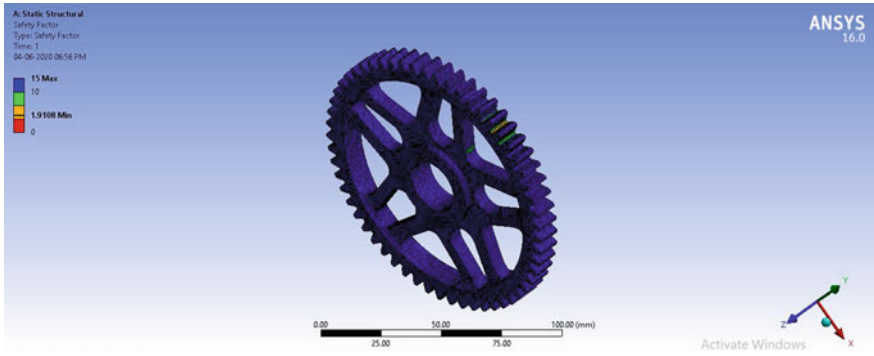


Fig. 14 Factor of safety of gear

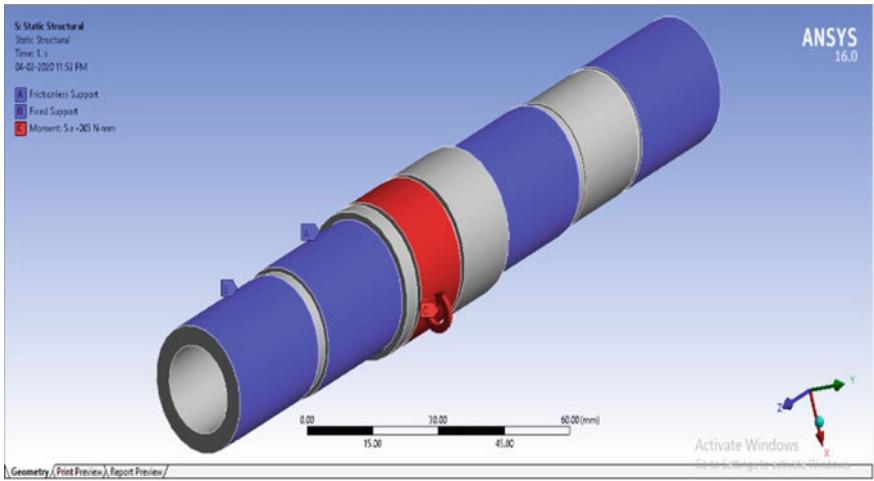


Fig. 15 Force model of output shaft

### 6.3 Casing

See Figs. 18, 19, 20 and 21.

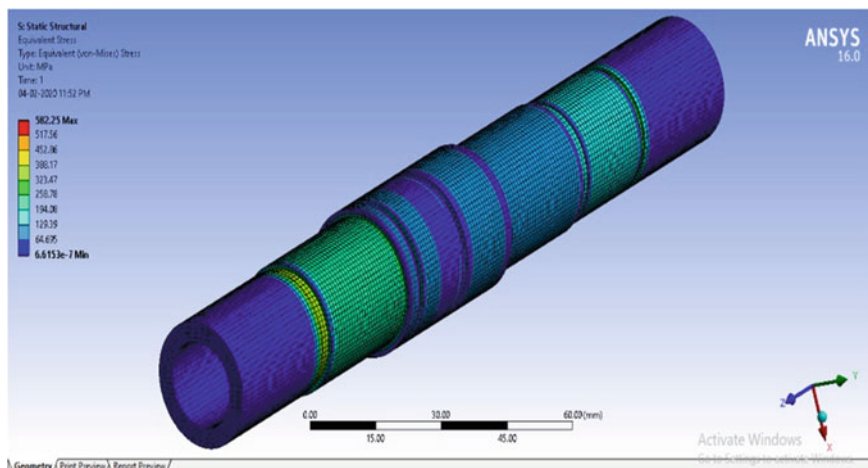


Fig. 16 Equivalent stress of output shaft

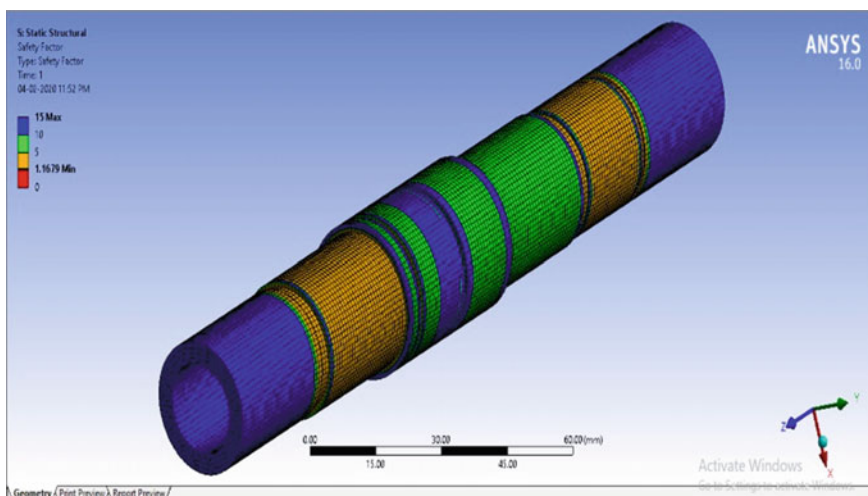


Fig. 17 Factor of safety of output shaft

## 7 Software Results for Gear Design (GearTRAXPRO)

The following pictures are screenshots of the GearTRAXPRO software while obtaining a SolidWorks part file of the gear. It also includes all parameters taken into consideration for designing the gear.

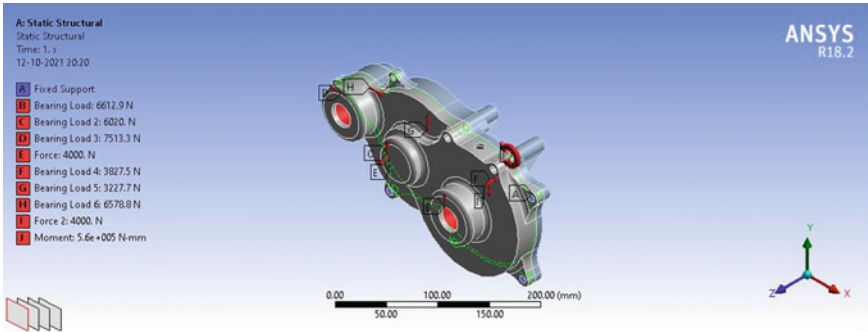


Fig. 18 Force model of casing

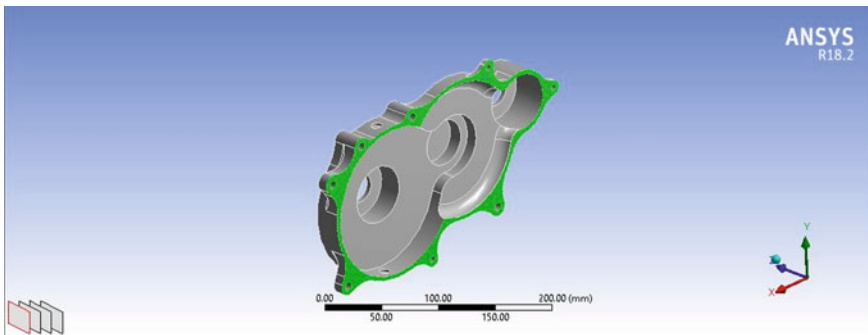


Fig. 19 Contact region

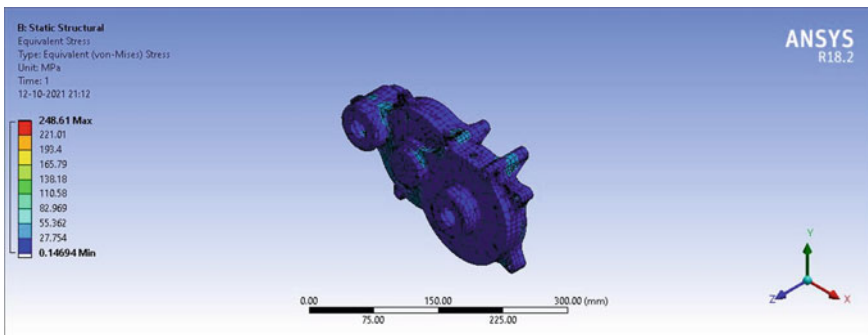


Fig. 20 Equivalent stress of casing

Figures 22 and 23 show the dimensioning and Figs. 24, 25, 26, 27, 28 and 29 force calculation outputs and other parameter calculations for reduction set 1 (for gear 1 and gear 2). The results were obtained by simulation in GearTraxPRO software.

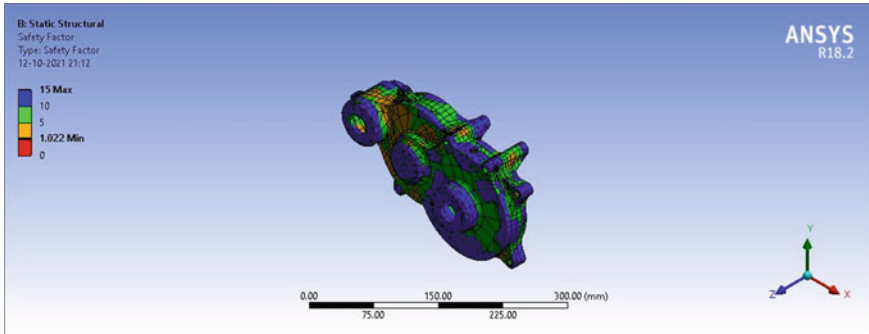


Fig. 21 Factor of safety of casing

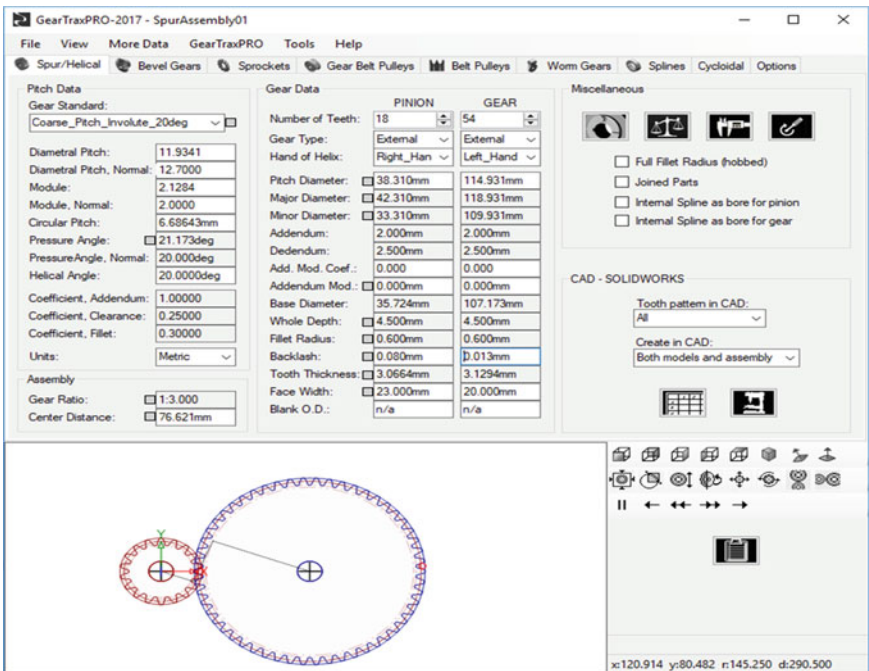
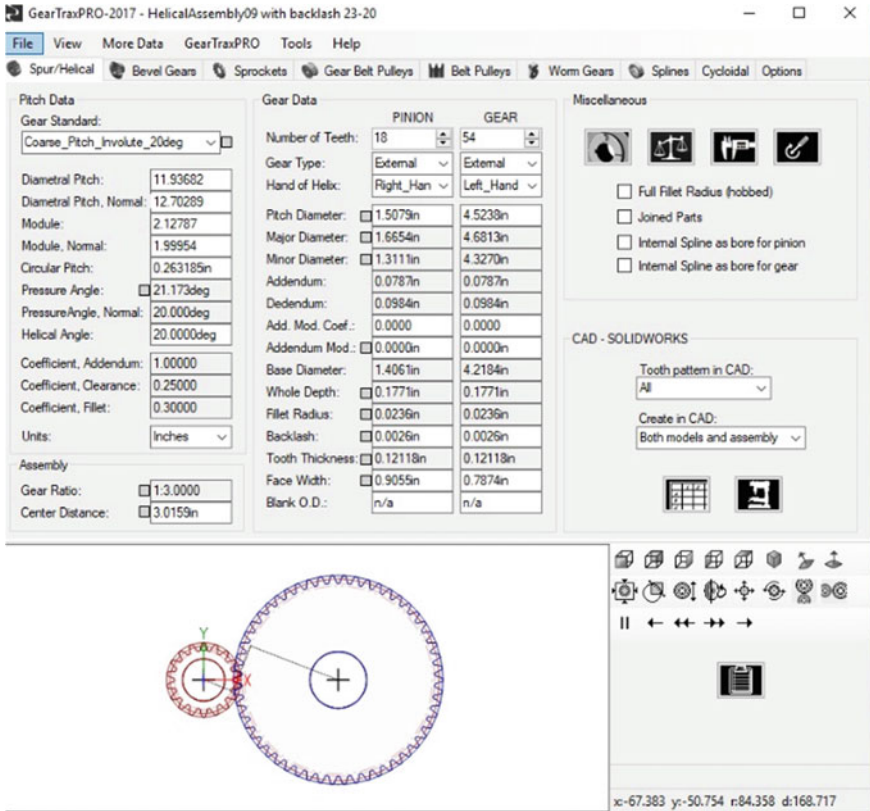


Fig. 22 Gear set 1 dimensioning

## 8 Conclusion

Comparison of existing alternative options in the market and this new design of the gearbox show that there is a significant reduction in weight of the gearbox. This is achieved while keeping the performance parameters as required by the potential



**Fig. 23** Gear set 2 dimensioning

customers. The gearbox design was finalized in geometry and material (in accordance with AGMA standards) and was forwarded to manufacturers [3] for getting a prototype model for testing. Once manufactured, the model will be tested on a BAJA ATV, by replacing the old gearbox with this gearbox. An overall weight reduction of 9.5 kg is expected from the design, when compared with its alternative market option.

External Spur Sizing - Beta 1 - AGMA 908-B89 & 2001-D04
✕

Tools Help
Loading
Bending Strength
Pitting Resistance

Pitting Resistance of Gear Set - for metallic spur gears (1500 FPM max for this formula)

	PINION	GEAR
u = Poisson's Ratio	0.3	0.3
E = Modulus of Elasticity PSI	3,04,57,920.0	3,04,57,920.0
Cp = Elastic Coefficient	2308.02	
Wt = Transmitted Tangential Load, LB	526.9	
Ko = Overload Factor	1.00	
Kv = Dynamic Factor	1.18	
Ks = Size Factor	1.00	
Km = Load Distribution Factor	1.00	
Cf = Surface Condition Factor	1.00	
ZN = Stress Cycle Factor	0.92	
CH = Hardness Ratio Factor	1.00	
SH = Safety Factor	1.00	
KT = Temperature Factor	1.00	
KR = Reliability Factor	0.99	
K = Contact Load Factor PSI	739.69	
CG = Gear Ratio Factor	0.75	
Lmin, Face Width of Narrowest Member	0.63in	
I = Geometry Factor for Pitting Resistance	0.18900	
<b>Kac = Allowable Contact Load Factor PSI</b>	1316.46	
<b>cs = Contact Stress PSI Actual</b>	1,35,833.5	
sac = Allowable Contact Stress, PSI	1,95,000.0	

Show Parabola

Fig. 24 Pitting resistance for gear set 1



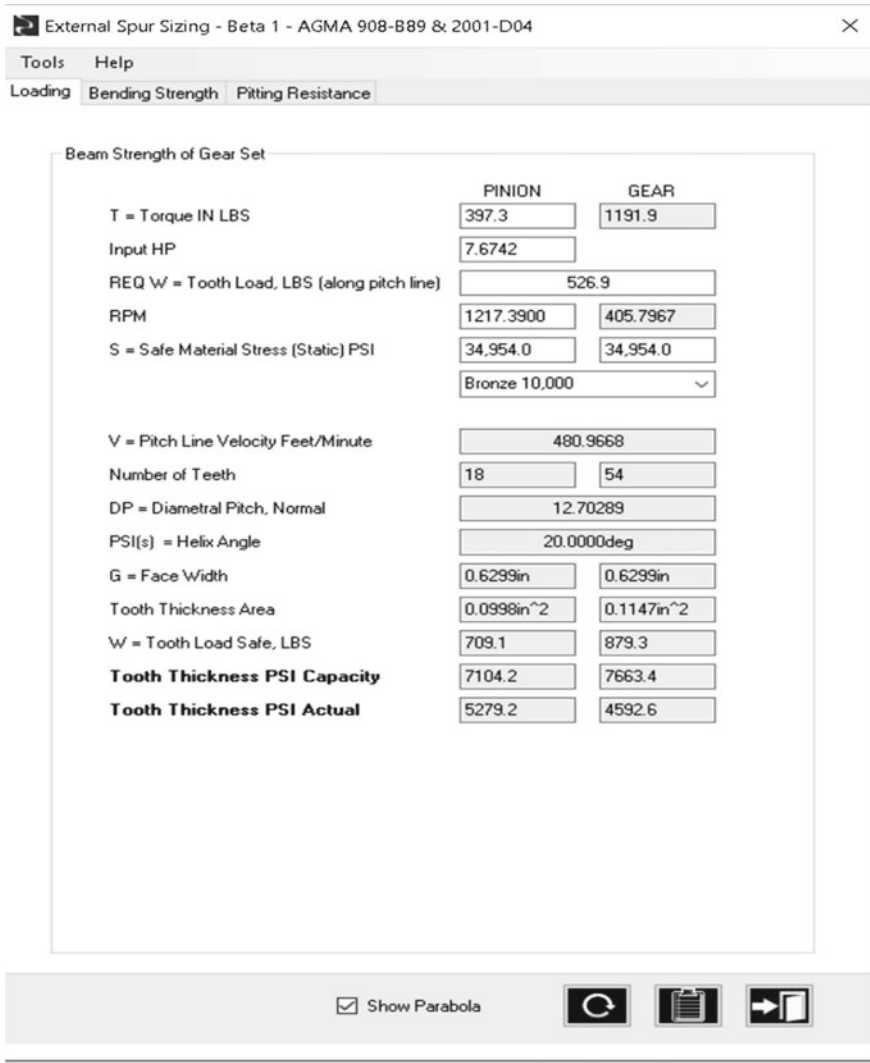


Fig. 25 Force calculations for gear set 1

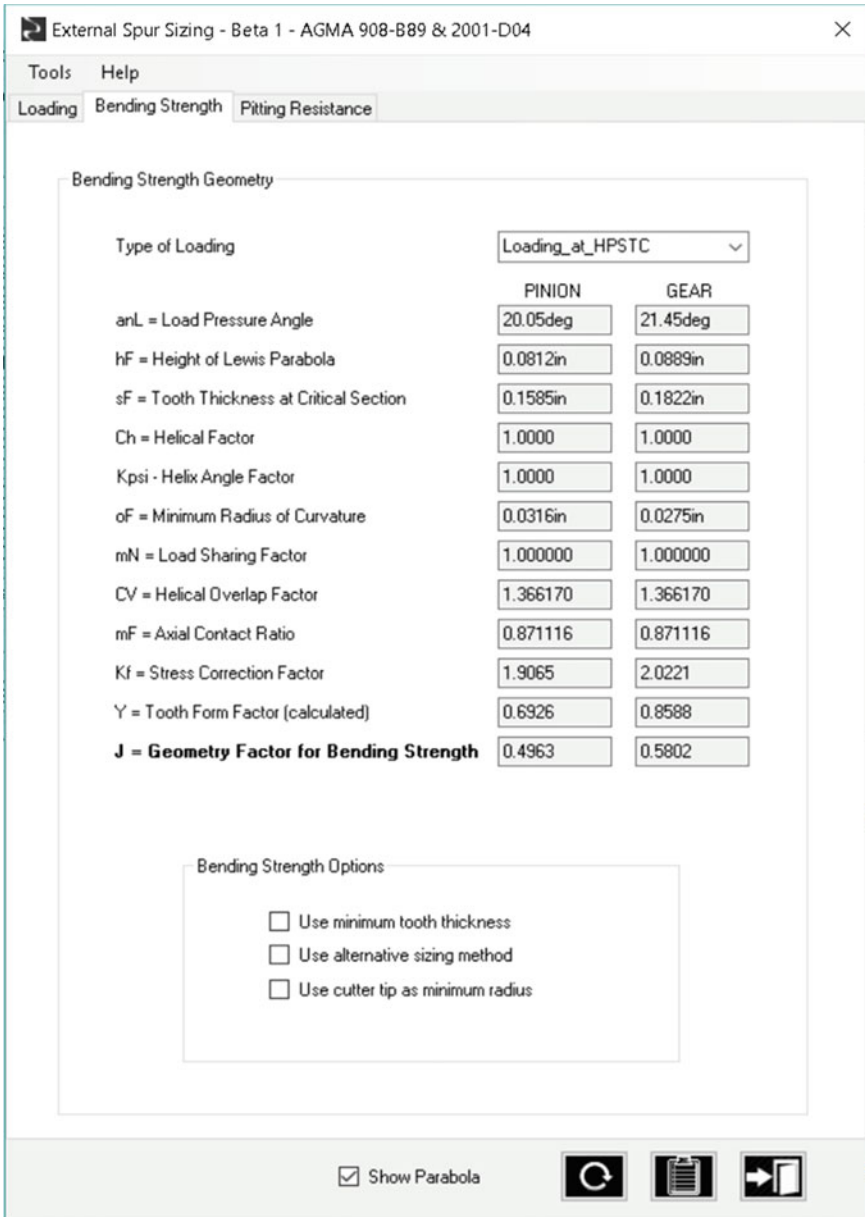


Fig. 26 Bending strength for gear set 1

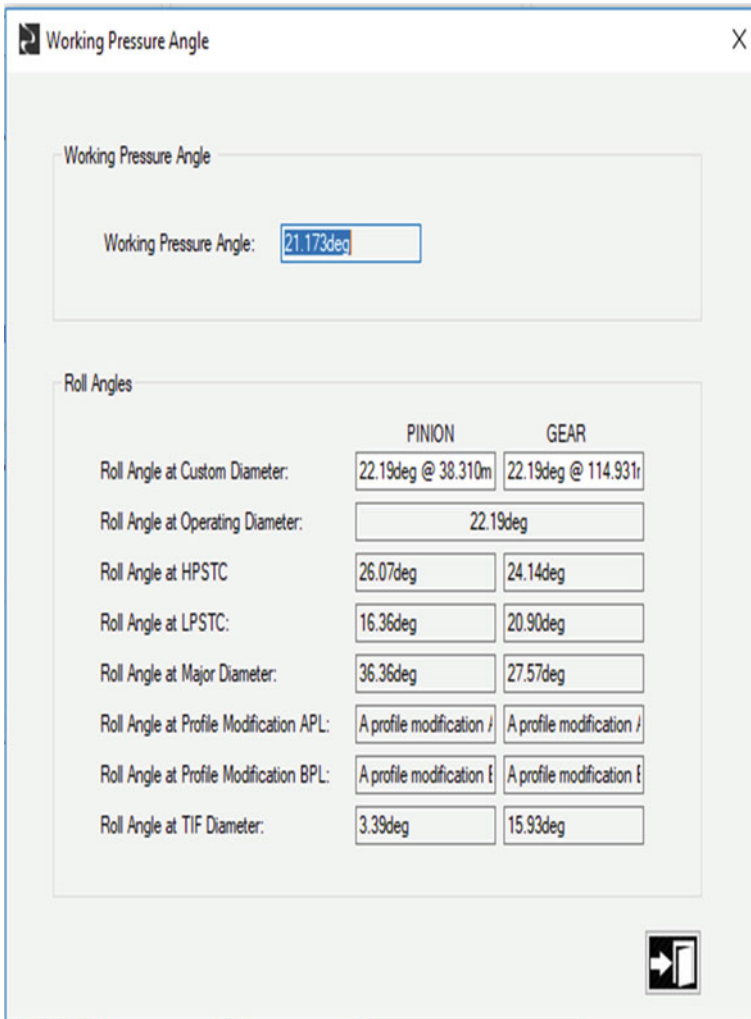


Fig. 27 Pressure angle for first stage reduction

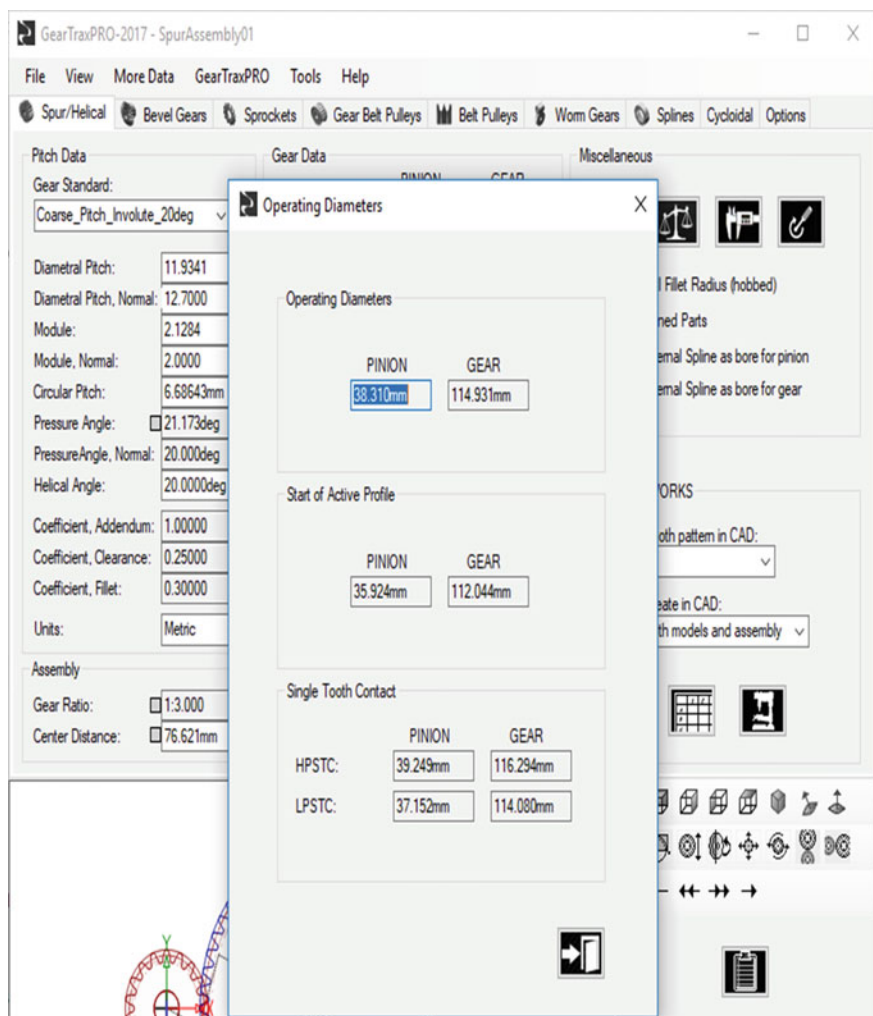


Fig. 28 Operating parameters for reduction gear 1

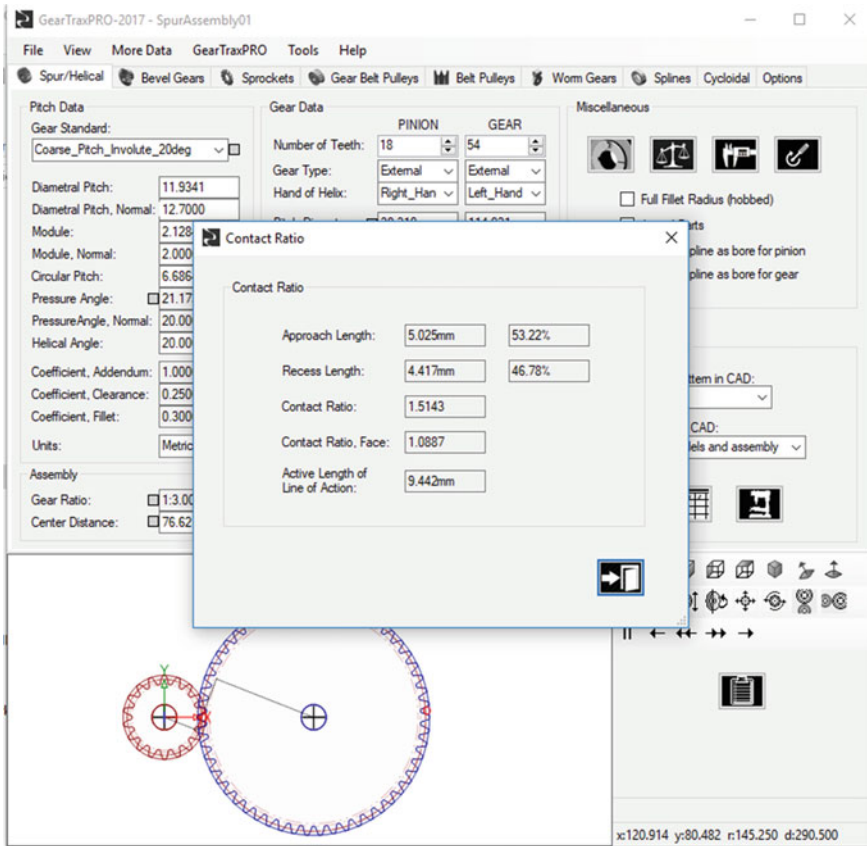


Fig. 29 Contact ratios for gear set 1

**Acknowledgements** The authors would also like to thank ‘The Road Runners’ team and their faculty advisor Dr. Lokavarapu Bhaskara Rao for the support and resources provided through the time of this work.

## References

1. Bardiya N, Karthik T, Rao LB (Sep 2014) Analysis and simulation of gearless transmission mechanism. *Int J Core Eng Manag (IJCEM)* 1(6)
2. Patel T, Dubey A, Rao LB (Sep 2019) Design and analysis of an epicyclic gearbox for an electric drivetrain. *Int J Recent Technol Eng (IJRTE)* 8(3). ISSN: 2277-3878
3. Herring DH, Otto FJ, Specht FR (2013) Gear materials and their heat treatment. BNP Media
4. Payne ET (2015) Design of an SAE baja racing off-road vehicle powertrain. The University of Akron in Akron, Ohio, USA, Spring

5. Sekhar K, Dharmadhikari P, Panchal S, Rao LB (2020) Design and optimization of a two stage gearbox using GEARTRAX. *Recent Trends Mech Eng, Lect Notes Mech Eng* 445–477
6. Ashby M (2001) *Materials and process selection for engineering design*, 3rd ed. Pergamon Press, Ch. 4, pp 110–144
7. Sharma A, Singh J, Kuma A (June 2015) Optimum design and material selection of baja vehicle. *Int J Curr Eng Technol* 5(3)
8. PSG (2006) *PSG design data book*, PSG college of technology. Kalaikathir Achchagam
9. Budynas R, Nisbett K (2006) *Shigley's mechanical engineering design*, 8th edn, Ch 3, sec 14. pp 711–762
10. Gligorijević R (1976) Materials for gears manufacturing their dynamic and structural characteristics and heat-treatment. *J Technol* 5(6):367–379
11. Gupta A, Yashvanth VP, Rao LB (2020) Design of gears using aluminium 6061-T6 alloy for formula SAE steering system. *Recent trends in mechanical engineering, lecture notes in mechanical engineering*. pp 489–505
12. Vara Prasad V, Satish G, Ashok Kumar K (2013) Trade of analysis for helical gear reduction unit. *Int J Eng Res Technol* 2(11):54–63
13. Aru S, Jadhav P, Gajabhiye S, Jadhav V, Angane P (2014) Design and analysis of centrally suspended cage-less differential. *Int J Mech Prod Eng Res Develop* 4(4):49–60
14. Anand S, Sriekshav AD, Sharran B, Rao LB (2020) Design and analysis of helical teeth harmonic drive. *Recent trends in mechanical engineering, lecture notes in mechanical engineering*. pp 507–519
15. Gujaba KP, Parashar S, Rao LB (2020) Design and analysis of permanent magnetic gears. *Recent trends in mechanical engineering, lecture notes in mechanical engineering*. pp 521–530
16. ANSYS user manual, Version 14
17. Solidworks user manual (2020)

# Vibrational Analysis of Circular Plates with Square Cutout



AL. Muthuveerappan, C. Ajay, V. Dhakshain Balaji, Varun Gopalakrishnan, and Lokavarapu Bhaskara Rao

**Abstract** Isotropic materials find wide range of applications in the manufacturing industry. The present work focuses on studying the free vibration analysis in a circular plate made out of isotropic material with and without square cutouts. The system was generated and simulated using CAD modeling software and solved using a finite element method. The variations in the vibrational frequencies of isotropic plates composed of mild steel, cork, and rubber are observed with respect to changes in the height and radius of the plate. The effects of the dimensions of the square cutout on the frequencies of the plates under different modes of vibrations are also tested and tabulated. The frequencies of non-perforated plate increase with increase in height of plate and decrease with increase in radius of plate. In plates with square cutout, the frequencies exhibited a wave-like trend as the cutout dimension was varied.

**Keywords** Circular plate · Cutout · Vibration analysis · Modal diagram · Finite element analysis

## 1 Introduction

Various mechanical structures have circular plates with cutouts [1]. These structures have multiple applications in the fields like aerodynamics, aircraft manufacturing, and weapons manufacturing [2]. Cutouts are used for inserting fasteners, accessing

---

AL. Muthuveerappan (✉) · C. Ajay · V. Dhakshain Balaji · V. Gopalakrishnan · L. Bhaskara Rao  
School of Mechanical Engineering, Vellore Institute of Technology, Chennai Campus, Vandalur,  
Kelambakkam Road, Chennai, Tamil Nadu 600127, India  
e-mail: [al.muthuveerappan2018@vitstudent.ac.in](mailto:al.muthuveerappan2018@vitstudent.ac.in)

C. Ajay  
e-mail: [c.ajay2018@vitstudent.ac.in](mailto:c.ajay2018@vitstudent.ac.in)

V. Dhakshain Balaji  
e-mail: [dhakshain.balaji2018@vitstudent.ac.in](mailto:dhakshain.balaji2018@vitstudent.ac.in)

V. Gopalakrishnan  
e-mail: [varun.g2018@vitstudent.ac.in](mailto:varun.g2018@vitstudent.ac.in)

ports and other internal structures, setting up electrical lines, ventilation, and system weight reduction [3]. Vibration analyses of such components are performed to identify structural parameters and prevent damages [1]. The inclusion of cutouts in plate-like structures changes the frequency response appreciably. Therefore, there is a need to conduct free vibration analysis of plates with cutouts. Literature review suggest several works done in the field of vibrational analysis of plates with cutouts, and a selected list of those studies is briefly reviewed as follows.

Lee et al. [4] deduced the natural frequencies of a rectangular plate with an arbitrarily placed rectangular cutout using the Rayleigh quotient method. This study was performed under different modes, and it was concluded that this method has the potential to serve as an alternative to finite element analysis. Ramakrishna et al. [5] analyzed the free vibrational characteristics of laminates with circular cutouts using the eight-noded hybrid-stress finite element method under different boundary conditions. By varying the orientation of fiber and the dimensions of the cutout, the different frequency responses were studied. Ju et al. [6] employed the finite element method and studied the free vibrational characteristics of circular and square plates with delamination around cutouts. Through this study, the delamination on the natural frequencies of circular and square plates with cutouts and its mode-dependency was established. Boay [7] studied the free vibrational analysis of symmetrically laminated composite plates with a central hole. The materials and the stacking sequence used by Boay in his study are those which find their applications in aircraft structures. His study also validates the accuracy of the results as obtained by the finite element analysis with experimental data. Sivakumar et al. [8] came up with a genetic algorithm that aids in the optimized design of laminated composite plates. This genetic algorithm worked with any number of variables and any type of design constraints. Turvey et al. [9] conducted experiments to determine the mode shapes and free vibrational frequencies of thick pultruded glass reinforced plastic (GRP) square plates with boundary conditions in varied combinations. Their study confirmed that the prediction of free vibrational response of the GRP plates can be modeled based on the thin homogenous orthotropic/anisotropic plate theory.

Liew et al. [10] conducted a three-dimensional free vibration analysis of perforated superelliptical plates by applying elasticity theory and p-Ritz algorithm. Alongside parametric investigations, the approach provided a complete vibration spectrum for the analysis of given structures. Sai Ram et al. [11] studied free vibrations using finite element method based on higher-order deformation theory in a composite spherical shell cap with and without cutout. The frequency trends with respect to number of plies, boundary conditions, radius to thickness ratio, and cutout size of composite spherical shell were analyzed. Cheng et al. [1] studied the effects of eccentricity, hole size, and boundary conditions on vibration modes of annular-like plates using both numerical and experimental approaches. Kwak et al. [12] employed an independent coordinate coupling method to conduct free vibration analysis of a rectangular plate with hole. The results shown by the novel method were verified using the classical Rayleigh–Ritz method. Jhung et al. [13] performed free vibration analysis of a circular plate with an eccentric hole submerged in fluid based on finite



Fourier–Bessel series expansion and Rayleigh–Ritz method. The study threw light on the effect of fluid and eccentric holes on modal characteristics.

Lee et al. [14] used the indirect boundary integral formulation and addition theorem in an analytical model derived as a coupled infinite system of simultaneous linear algebraic equations to conduct free vibration analysis of a circular plate having multiple circular holes. The numerical results agreed with finite element method (FEM) results with good accuracy and a faster rate of convergence. Maziar et al. [15] utilized finite element method to study the free vibration analysis of functionally graded plates with multiple circular and non-circular cutouts. Effects of boundary conditions and cutout size, location and number were obtained through parametric studies. Choudhary et al. [16] performed the vibrational analysis of a square plate with a circular hole at different boundary conditions using finite element method. Parametric study concluded that an increase in hole diameter resulted in decrease of natural frequency. Bhardwaj et al. [3] conducted free vibration analysis of laminated composite plates with triangular cutouts using Ansys software. Their parametric study revealed the effect of various geometric and material properties on natural frequency. Xue et al. [17] conducted free vibration analysis of porous plates with a centrally located circular hole using isogeometric analysis. The porosity distributions were formulated using non-uniform rational B-spline basis functions and described by first-order shear deformation theory. Investigations into the effects of porosity coefficient, geometric parameters, and boundary conditions on the free vibrations were studied. Vibrations of circular plate with concentric ring and rigid ring support have been studied [18–20]. Exact frequency analysis of annular plates with small core has been studied by Rao and Rao [21, 22]. The frequency of restrained circular plates with weakened interior circle has been studied by Rao and Rao [23–25]. The fundamental frequency of circular plate and annular plate with elastic edge has been studied by Rao and Rao [26–30].

A general conclusion from the above-conducted literature survey is the finite element analysis (FEA) is proven to be an efficient and a reliable method to perform vibrational studies of various composite and isotropic plates, irrespective of the geometry of the plate, and the presence of cutouts. Though numerous works have been done over the years in this field, there is a need to understand the vibrational characteristics of cork-made and rubber-made isotropic plates too. Extending this understanding by considering the presence of cutouts in these plates would enhance their scope of applications in various domains. On being able to provide a comparative analysis between mild steel, cork, and rubber plates with square cutouts, the results of this study suggest a holistic understanding of the different vibrational characteristics of each of these plates, in addition to determining the relations between the geometric specifics of the plate and its vibrational frequencies as well.

## 2 Materials and Methods

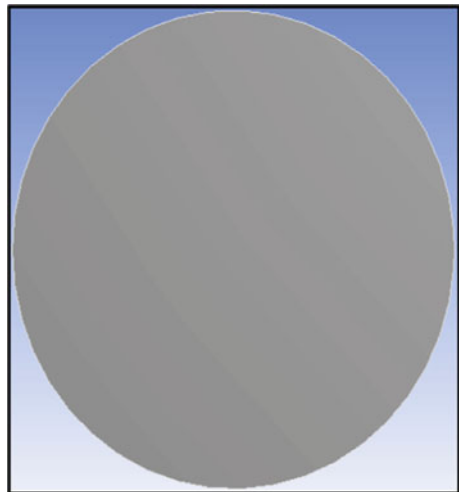
The free vibration analysis of circular plates made of isotropic material with and without square-shaped cutouts was conducted. The materials used in this study are mild steel, cork, and rubber, and their respective properties are given in Table 1. It is to be noted that the materials are selected to cover the spectrum of possible values of Poisson's ratio.

The models were generated using SolidWorks 2020 [31]. Circular plate with different radius values,  $R$ , and different thickness values,  $h$ , with square cutouts of different side lengths,  $a$ , is taken into consideration. The models were imported into Ansys 19.2 [32], where the natural frequencies were obtained using finite element methods. The non-perforated and perforated plates used in this study for the material sample of mild steel are shown in Figs. 1 and 2, respectively.

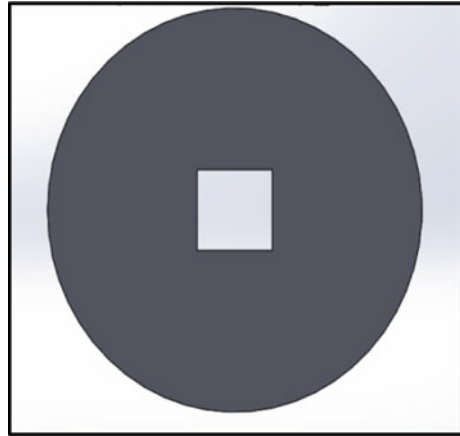
**Table 1** Material properties

Property	Mild Steel	Cork	Rubber
Density ( $\text{g/cm}^3$ )	7.85	0.15	0.95
Thermal expansion ( $\text{K}^{-1}$ )	$12 \times 10^{-6}$	$200 \times 10^{-6}$	6.1
Young's modulus (Pa)	$2 \times 10^{11}$	$2 \times 10^7$	$1 \times 10^6$
Poisson's ratio	0.32	0	0.4999

**Fig. 1** Non- perforated plate



**Fig. 2** Perforated plate



### 3 Validation and Convergence

Free vibrational characteristics of non-perforated mild steel circular plate were analyzed using FEM and compared with the results obtained by Bhatnagar et al. [33]. From Table 2, it is clear that the data as obtained in the present work and Bhatnagar et al. lie within a difference range of 13% which suggests the validity of the method of approach followed us.

Using the same method, the free vibration characteristics of a circular plate composed of cork without any cutouts were studied with the constant parameter being the height of the plate and the variable parameter being the radius of the plate. The results as given in Table 3 suggest the ability of the method to produce converging results. It is also important to note that despite increasing the number of elements analyzed under the method, there is no deviation in the final output obtained in terms of vibrational frequencies under different modes. Thus, the method of approach as followed in the present work is proven to produce reliable converging results, as validated by Bhatnagar et al. [33].

**Table 2** Validation of data with reference to Bhatnagar et al.

Mode	Bhatnagar et al. [33]	Present data	%Difference
1	973.43	975.44	0.21
2	1975.5	1860.3	6
3	1976.3	1861.5	5.98
4	3153.3	2812.4	11.42
5	3154.5	2813.2	11.43
6	3578.8	3145.7	12.88

**Table 3** Analysis of a cork-made circular plate with no cutouts and varying radius

Cork	No. of elements	Frequency mode					
		1	2	3	4	5	6
75	2538	294.43	593.83	593.84	941.85	941.86	1064.9
	4626	294.35	593.55	593.56	941.21	941.22	1064.2
	5370	294.35	593.54	593.55	941.19	941.19	1064.1
	6114	294.35	593.54	593.54	941.16	941.17	1064.1
	7578	294.35	593.53	593.53	941.14	941.14	1064.1
125	4030	108.31	222.66	222.66	360.24	360.24	409.36
	4492	108.31	222.66	222.66	360.23	360.23	409.36
	5190	108.31	222.66	222.66	360.23	360.23	409.35
	5626	108.31	222.66	222.66	360.22	360.23	409.35
	9825	108.29	222.62	222.62	360.13	360.13	409.23
175	4388	55.599	114.97	114.97	187.22	187.22	213.1
	4904	55.599	114.97	114.97	187.22	187.22	213.1
	5788	55.599	114.97	114.97	187.22	187.22	213.1
	6760	55.599	114.97	114.97	187.22	187.22	213.1
	8066	55.599	114.97	114.97	187.22	187.22	213.1
225	5480	33.72	69.903	69.903	114.15	114.15	130.03
	5682	33.72	69.903	69.903	114.15	114.15	130.03
	6652	33.72	69.903	69.903	114.15	114.15	130.03
	7352	33.72	69.903	69.903	114.15	114.15	130.02
	8514	33.72	69.903	69.903	114.15	114.15	130.02
275	3035	22.611	46.947	46.947	76.806	76.806	87.526
	3409	22.611	46.947	46.947	76.806	76.807	87.526
	3510	22.61	46.947	46.947	76.806	76.806	87.526
	8136	22.602	46.915	46.915	76.727	76.727	87.427
	8124	22.603	46.915	46.915	76.727	76.727	87.427

## 4 Results and Discussion

On performing FEM analysis using Ansys on circular plates composed of mild steel, cork, and rubber, the following results were obtained depending on the presence of a centrally located square cutout.

Table 4 provides a collection of modal diagrams observed in perforated and non-perforated plates for height 10 mm, radius 250 mm, and the area of the cutout being  $100 \times 100 \text{ mm}^2$ .

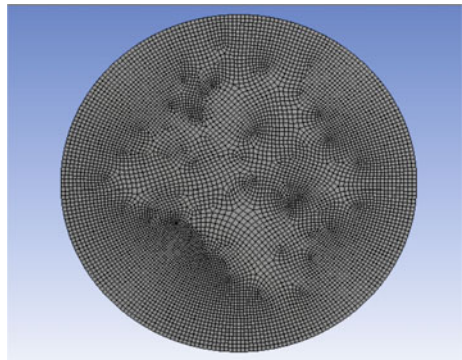
**Table 4** Modal diagrams for plates with and without perforations under all modes of vibrations

Material	Mode 1	Mode 2	Mode 3	Mode 4	Mode 5	Mode 6
Mild steel						
Mild steel with cutout						
Cork						
Cork with cutout						
Rubber						
Rubber with cutout						

### 4.1 Non-Perforated Plate

Non-perforated plate with fine meshing was considered as shown in Fig. 3 for analysis. Having the radius of the plate set at 250 mm, the vibrational frequencies corresponding to the first 6 modes were obtained for mild steel, cork, and rubber, when the height of plate was varied, results of which are shown, respectively, in Tables 5, 6 and 7. In all of the cases, the frequency under a particular mode increases upon increasing the height of the plate as seen, respectively, in Figs. 4, 5 and 6. The aforementioned graphs throw light on the influence of height on the vibrational frequency.

**Fig. 3** Meshed non-perforated plate



**Table 5** Vibration characteristics of mild steel circular plate with no cutouts and a fixed radius of 250 mm

Mild steel	Frequency mode					
Height (mm)	1	2	3	4	5	6
3	120.17	249.99	250	409.94	409.95	467.42
5	200.06	415.91	415.92	681.44	681.46	776.85
10	398.96	826.78	826.78	1349.7	1349.7	1537.3
25	976.72	1983.4	1983.4	3167.5	3167.6	3588.6
50	1822.3	3506.5	3506.7	5336.3	5336.5	5975.4
100	2963.9	5163.6	5163.9	6660.8	6661	7386

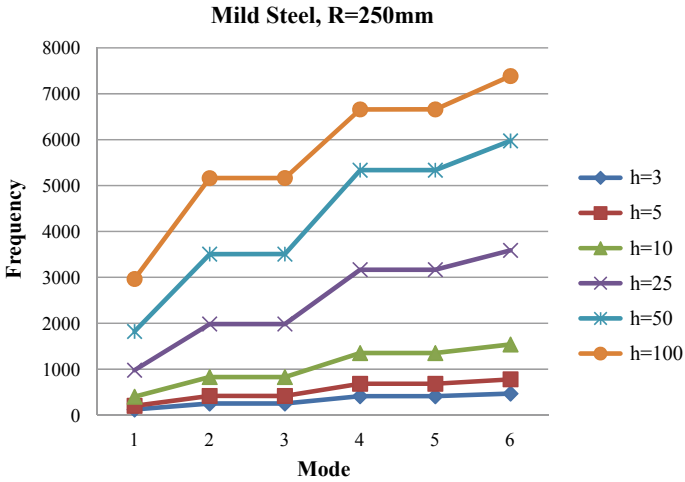
**Table 6** Vibration characteristics of cork-made circular plate with no cutouts and a fixed radius of 250 mm

Cork	Frequency mode					
Height (mm)	1	2	3	4	5	6
3	2.6008	5.4112	5.4112	8.8743	8.8743	10.119
5	4.3327	9.0106	9.0106	14.769	14.769	16.838
10	8.6437	17.932	17.932	29.307	29.307	33.39
25	21.254	43.411	43.411	69.742	69.742	79.113
50	40.263	78.734	78.734	121.4	121.4	136.3
100	68.161	121.73	121.74	152.55	152.55	176.25

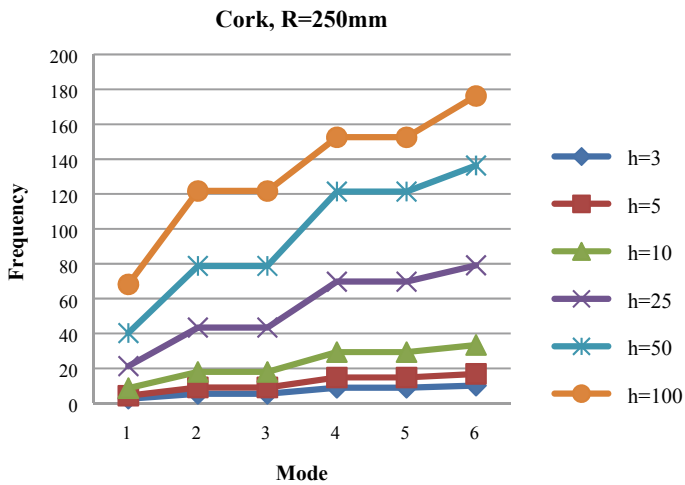
**Table 7** Vibration characteristics of rubber-made circular plate with no cutouts and a fixed radius of 250 mm

Rubber	Frequency mode					
Height (mm)	1	2	3	4	5	6
3	1.205	2.5061	2.5074	4.1097	4.111	4.6866
5	2.0088	4.1751	4.1758	6.8392	6.8399	7.7965
10	4.0091	8.2996	8.3008	13.533	13.535	15.411
25	9.8607	19.879	19.908	31.542	31.555	35.702
50	18.074	34.103	34.136	51.114	51.126	57.114
100	28.2	47.73	47.751	64.622	65.053	65.07

The vibration characteristics were also analyzed by having height fixed at  $h = 10$  mm, while varying the radius of the circular plate without any cutouts. The results show that on increasing the radius of the circular plate, the frequency with which it vibrates decreases, and this has been duly tested under different modes of vibration as well. The results of this test for mild steel, cork, and rubber are shown in Tables 8,

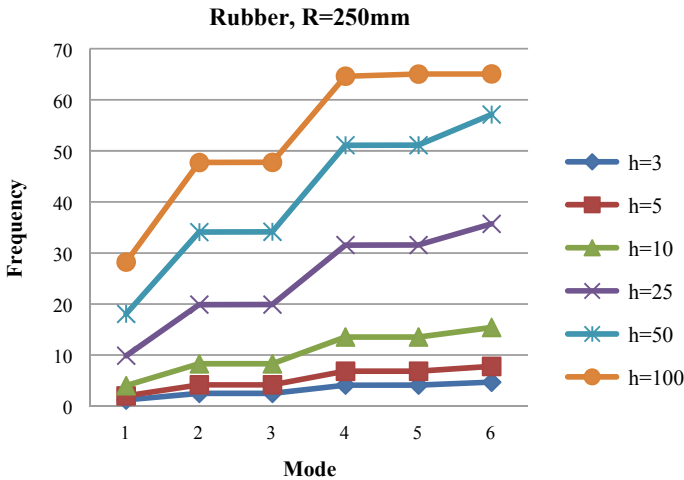


**Fig. 4** Vibration analysis of non-perforated mild steel plate with variable heights and a fixed radius of 250 mm



**Fig. 5** Vibration analysis of non-perforated cork plate of variable heights and a fixed radius of 250 mm

9 and 10, respectively, and also graphically presented, respectively, in Figs. 7, 8 and 9. The trends can be noticed without fail in the graphs.



**Fig. 6** Vibration analysis of non-perforated rubber plate with variable heights and a fixed radius of 250 mm

**Table 8** Vibration characteristics of non-perforated mild steel circular plate and a height of 10 mm

Mild steel Radius (mm)	Frequency mode					
	1	2	3	4	5	6
75	4263.2	8517	8517.7	13,387	13,387	15,108
125	1577.7	3230.7	3230.9	5204.9	5205	5909.4
175	811.62	1674.9	1675	2721.3	2721.3	3095.9
225	492.46	1019.6	1019.6	1662.7	1662.7	1893.3
275	330.18	684.74	684.79	1118.8	1118.8	1274.6

**Table 9** Vibration characteristics of non-perforated cork-made circular plate and a height of 10 mm

Cork Radius (mm)	Frequency mode					
	1	2	3	4	5	6
75	294.35	593.53	593.53	941.14	941.14	1064.1
125	108.29	222.62	222.62	360.13	360.13	409.23
175	55.599	114.97	114.97	187.22	187.22	213.1
225	33.72	69.903	69.903	114.15	114.15	130.02
275	22.603	46.915	46.915	76.727	76.727	87.427

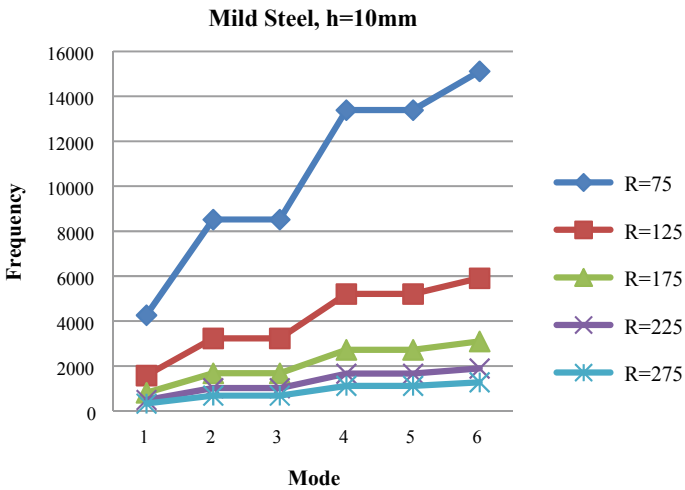
### 4.2 Perforated Plate

Perforated plate with fine meshing was considered as shown in Fig. 10 for analysis. A centrally located square-shaped cutout with variable dimensions was incorporated in



**Table 10** Vibration characteristics of non-perforated rubber-made circular plate and a height of 10 mm

Rubber	Frequency mode					
Radius (mm)	1	2	3	4	5	6
75	30.237	59.732	59.802	92.95	92.97	104.73
125	11.247	22.912	22.952	36.757	36.777	41.707
175	5.7921	11.925	11.932	19.331	19.334	21.984
225	3.5123	7.26	7.2667	11.826	11.828	13.464
275	2.3572	4.882	4.8884	7.9719	7.9771	9.083

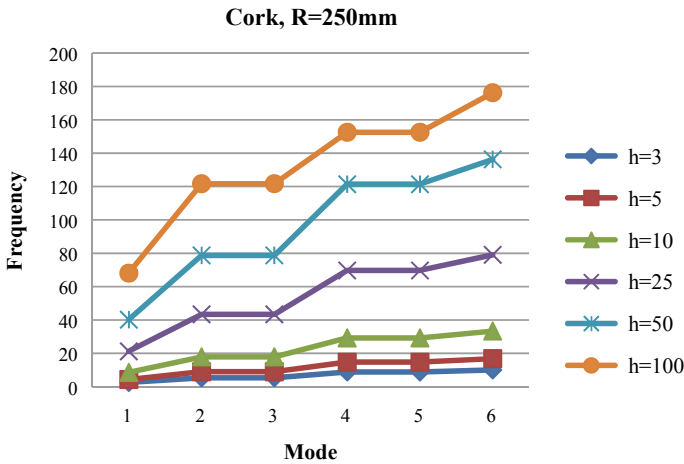


**Fig. 7** Vibration analysis of non-perforated mild steel plate of variable radius and a fixed height of 10 mm

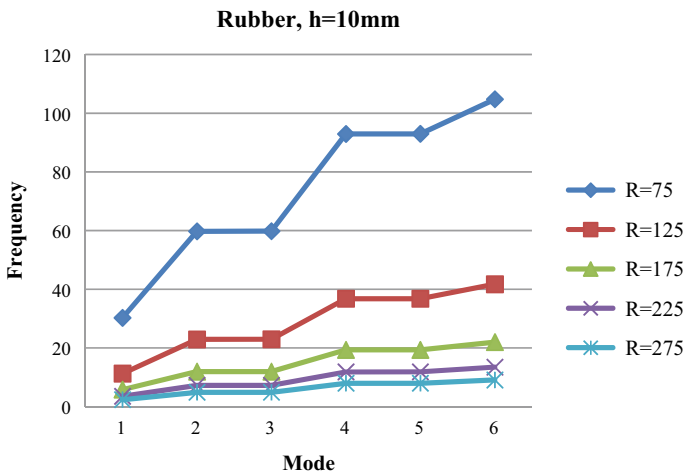
the middle of the plate of radius 250 mm and a height of 10 mm. The dimension of the cutout was varied from 2.5 mm to 100 mm for all mild steel, cork, and rubber plates. The vibrational frequencies at first six modes were calculated and given in Tables 11, 12 and 13. In all materials, different modes of frequencies exhibited wave-like trends when the dimension of cutout was varied. This can be observed in Figs. 11, 12 and 13.

### 5 Conclusion

FEA proved to be an efficient method to perform vibration analysis of three-dimensional isotropic circular plates with and without cutouts. Mild steel, cork, and rubber were the materials used in the study, where the height of the plate as

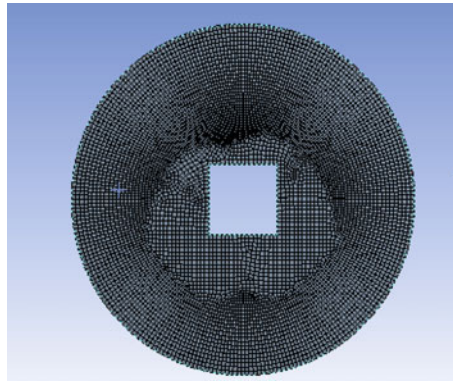


**Fig. 8** Vibration analysis of non-perforated cork plate with variable radius and a fixed height of 10 mm



**Fig. 9** Vibration analysis of non-perforated rubber plate of variable radius and a fixed height of 10 mm

well as its radius was interchangeably used as the variable and the fixed parameters. Irrespective of the material used, a direct relationship was observed between the frequency of vibration of the plate and the height of the plate, whereas an inverse relationship was noted between the frequency of vibration of the plate and its radius; both of which were tested in a solid circular isotropic plate without any cutouts.



**Fig. 10** Meshed perforated plate

**Table 11** Vibration characteristics of perforated mild steel circular plate with a centrally located square cutout

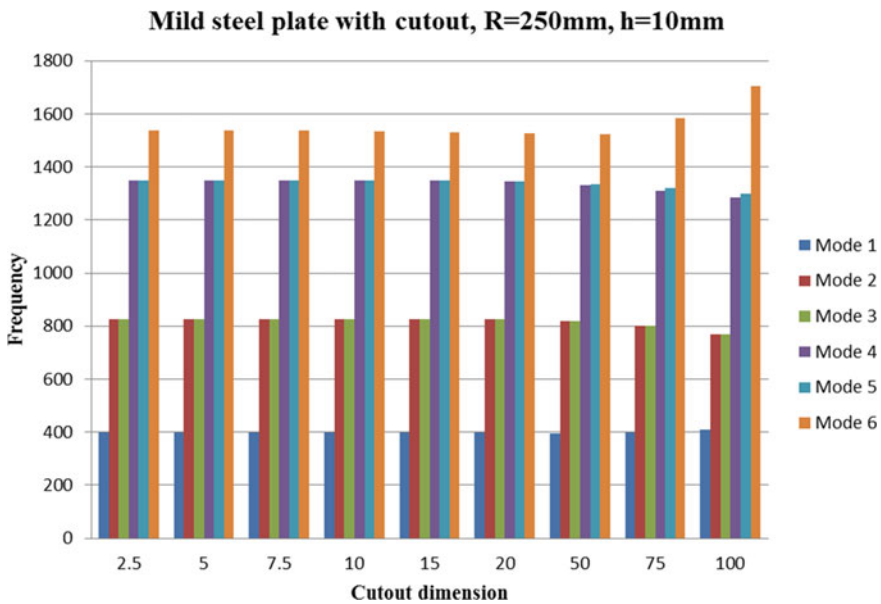
Mild steel Cutout area (mm <sup>2</sup> )	Frequency mode					
	1	2	3	4	5	6
2.5 × 2.5	399.3	827.56	827.56	1350.9	1350.9	1538.6
5 × 5	399.22	827.5	827.5	1350.6	1350.6	1537.9
7.5 × 7.5	399.12	827.49	827.49	1350.3	1350.3	1536.7
10 × 10	398.93	827.47	827.47	1349.8	1349.9	1534.9
15 × 15	398.52	827.39	827.39	1348.6	1348.8	1530.9
20 × 20	397.96	827.2	827.2	1347.1	1347.3	1526.2
50 × 50	395.04	820.47	820.47	1331.4	1334.5	1523.7
75 × 75	397.51	800.72	800.73	1310.3	1320.6	1583.5
100 × 100	408.41	768.58	768.61	1283.6	1299.3	1704.2

**Table 12** Vibration characteristics of perforated rubber circular plate with a centrally located square cutout

Rubber Cutout area (mm <sup>2</sup> )	Frequency mode					
	1	2	3	4	5	6
2.5 × 2.5	2.8497	5.9008	5.9009	9.62	9.62	10.96
5 × 5	2.8425	5.8866	5.8866	9.5974	9.5975	10.922
7.5 × 7.5	2.8399	5.8865	5.8865	9.5956	9.5958	10.899
10 × 10	2.8375	5.8863	5.8863	9.5936	9.5938	10.878
15 × 15	2.8301	5.8854	5.8854	9.5876	9.5884	10.816
20 × 20	2.8208	5.8835	5.8835	9.5802	9.5816	10.745
50 × 50	2.7606	5.8313	5.8313	9.5316	9.5539	10.56
75 × 75	2.7294	5.5978	5.5979	9.3598	9.4324	10.891
100 × 100	2.7735	5.2521	5.2528	9.1098	9.2002	11.722

**Table 13** Vibration characteristics of cork circular plate with a centrally located square cutout

Cork Cutout area (mm <sup>2</sup> )	Frequency mode					
	1	2	3	4	5	6
2.5 × 2.5	27.334	56.705	56.705	92.669	92.669	105.59
5 × 5	27.336	56.705	56.705	92.643	92.644	105.59
7.5 × 7.5	27.338	56.705	56.705	92.604	92.608	105.59
10 × 10	27.34	56.704	56.704	92.544	92.553	105.58
15 × 15	27.348	56.7	56.7	92.413	92.424	105.59
20 × 20	27.36	56.693	56.693	92.243	92.255	105.63
50 × 50	27.629	56.435	56.435	90.608	90.741	107.81
75 × 75	28.252	55.707	55.708	88.83	89.383	113.1
100 × 100	29.398	54.527	54.529	87.204	88.174	121.96



**Fig. 11** Vibration analysis of perforated mild steel plate of radius 250 mm and a height of 10 mm

Irrespective of material used, unique wave-like trends were observed in the frequency of plate when the cutout dimension was varied. Table 14 provides a comparative analysis of the isotropic plates for all materials with and without perforations, with a height of 10 mm, radius of 250 mm, and a cutout area of 50 × 50 mm<sup>2</sup>. The results obtained for each of the materials in both perforated and non-perforated cases are represented graphically in Figs. 14, 15 and 16 for a better understanding of the trends. From Figs. 14, 15 and 16, we note that the effect of including perforation varies

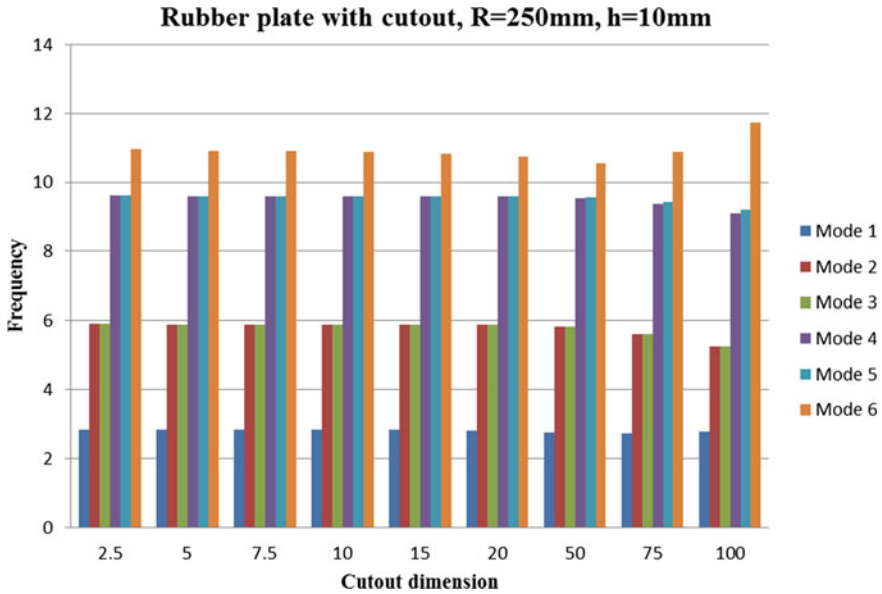


Fig. 12 Vibration analysis of perforated rubber plate of radius 250 mm and a height of 10 mm

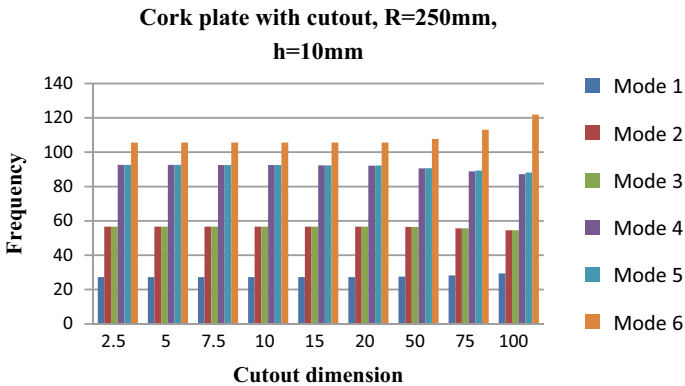
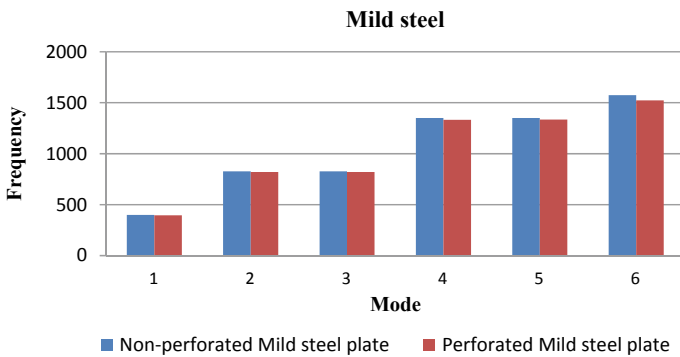


Fig. 13 Vibration analysis of perforated cork plate of radius 250 mm and a height of 10 mm

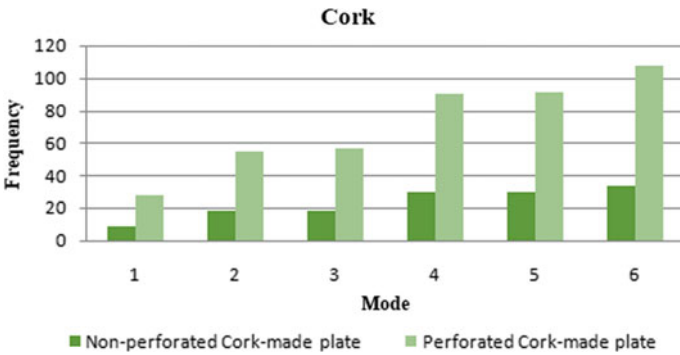
with material. In cork, the inclusion of cutout has significantly raised the frequency, whereas there is no significant change in frequency in case of mild steel. Also, in rubber, the inclusion of perforation has reduced the frequency. As Poisson’s ratio is changed from 0 to 0.5, the effect of inclusion of cutout changes from increasing frequency, producing no considerable change, to decreasing frequency. Hence, it can be concluded that it is essential to improve the number of cases tested in this scenario in order to get a complete understanding of the trends observed and their variations.

**Table 14** Comparative analysis of the vibration characteristics of perforated and non-perforated plates for different materials with a plate of fixed dimensions ( $R = 250$  mm,  $h = 10$  mm,  $a = 50$  mm)

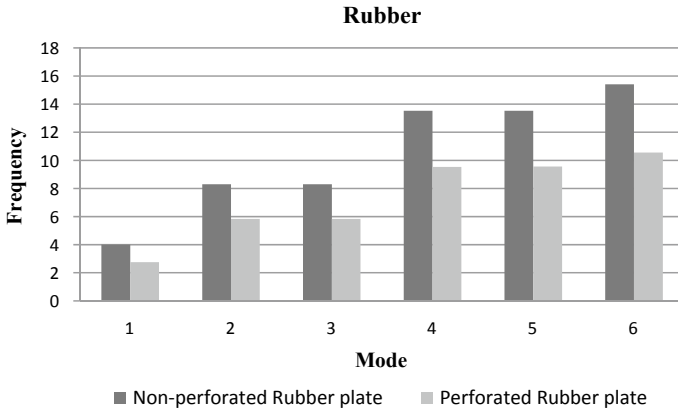
Mode	Frequency					
	Non-perforated mild steel	Perforated mild steel	Non-perforated cork	Perforated cork	Non-perforated rubber	Perforated rubber
1	398.96	395.04	8.6437	27.629	4.0091	2.7606
2	826.78	820.47	17.932	54.435	8.2996	5.8313
3	826.78	820.47	17.932	56.435	8.3008	5.8313
4	1349.7	1331.4	29.307	90.608	13.533	9.5316
5	1349.7	1334.5	29.307	90.741	13.535	9.5539
6	1573.3	1523.7	33.39	107.81	15.411	10.56



**Fig. 14** Comparative analysis of vibration characteristics of non-perforated and perforated mild steel plate



**Fig. 15** Comparative analysis of vibration characteristics of non-perforated and perforated cork plate



**Fig. 16** Comparative analysis of vibration characteristics of non-perforated and perforated rubber plate

## References

- Cheng L, Li YY, Yam LH (2003) Vibration analysis of annular-like plates. *J Sound Vib* 262:1153–1170. [https://doi.org/10.1016/S0022-460X\(02\)01093-3](https://doi.org/10.1016/S0022-460X(02)01093-3)
- Thakare S (2013) Free vibration analysis of circular plates with holes and cutouts. *IOSR J Mech Civ Eng* 8:46–54. <https://doi.org/10.9790/1684-0824654>
- Bhardwaj HK, Vimal J, Sharma AK (2015) Study of free vibration analysis of laminated composite plates with triangular cutouts. *Eng Solid Mech* 3:43–50. <https://doi.org/10.5267/j.esm.2014.11.002>
- Lee HP, Lim SP, Chow ST (1990) Prediction of natural frequencies of rectangular plates with rectangular cutouts. *Comput Struct* 36:861–869. [https://doi.org/10.1016/0045-7949\(90\)90157-W](https://doi.org/10.1016/0045-7949(90)90157-W)
- Ramakrishna S, Rao KM, Rao NS (1992) Free vibration analysis of laminates with circular cutout by hybrid-stress finite element. *Compos Struct* 21:177–185. [https://doi.org/10.1016/0263-8223\(92\)90017-7](https://doi.org/10.1016/0263-8223(92)90017-7)
- Ju F, Lee HP, Lee KH (1995) Free vibration of composite plates with delaminations around cutouts. *Compos Struct* 31:177–183. [https://doi.org/10.1016/0263-8223\(95\)00016-X](https://doi.org/10.1016/0263-8223(95)00016-X)
- Chai GB (1996) Free vibration of laminated composite plates with a central circular hole. *Compos Struct* 35:357–368. [https://doi.org/10.1016/S0263-8223\(96\)00037-2](https://doi.org/10.1016/S0263-8223(96)00037-2)
- Sivakumar K, Iyengar NGR, Deb K (1997) Optimum design of laminated composite rectangular plates with cutouts using genetic algorithm, India. *J Eng Mater Sci* 4:189–195
- Turvey GJ, Mulcahy N, Widdén MB (2000) Experimental and computed natural frequencies of square pultruded GRP plates: effects of anisotropy, hole size ratio and edge support conditions. *Compos Struct* 50:391–403. [https://doi.org/10.1016/S0263-8223\(00\)00116-1](https://doi.org/10.1016/S0263-8223(00)00116-1)
- Liew KM, Feng ZC (2001) Three-dimensional free vibration analysis of perforated super elliptical plates via the p-Ritz method. *Int J Mech Sci* 43:2613–2630. [https://doi.org/10.1016/S0020-7403\(01\)00051-0](https://doi.org/10.1016/S0020-7403(01)00051-0)
- Sai Ram KS, Sreedhar Babu T (2002) Free vibration of composite spherical shell cap with and without a cutout. *Comput Struct* 80:1749–1756. [https://doi.org/10.1016/S0045-7949\(02\)00210-9](https://doi.org/10.1016/S0045-7949(02)00210-9)
- Kwak MK, Han S (2007) Free vibration analysis of rectangular plate with a hole by means of independent coordinate coupling method. *J Sound Vib* 306:12–30. <https://doi.org/10.1016/j.jsv.2007.05.041>

13. Jhung MJ, Choi YH, Ryu YH (2009) Free vibration analysis of circular plate with eccentric hole submerged in fluid. *Nucl Eng Technol* 41:355–364. <https://doi.org/10.5516/NET.2009.41.3.355>
14. Lee WM, Chen JT (2011) Free vibration analysis of a circular plate with multiple circular holes by using indirect BIEM and addition theorem. *J Appl Mech Trans ASME* 78:0110151–01101510. <https://doi.org/10.1115/1.4001993>
15. Janghorban M, Rostamsowlat I (2012) Free vibration analysis of functionally graded plates with multiple circular and non-circular cutouts. *Chin J Mech Eng (English ed)* 25:277–284. <https://doi.org/10.3901/CJME.2012.02.277>
16. Choudhary T, Kumar A (2015) Vibration analysis of stiff plate with cutout. *Int J Tech Res Appl* 3:135–140
17. Xue Y, Jin G, Ma X, Chen H, Ye T, Chen M, Zhang Y (2019) Free vibration analysis of porous plates with porosity distributions in the thickness and in-plane directions using isogeometric approach. *Int J Mech Sci* 152:346–362. <https://doi.org/10.1016/j.ijmecsci.2019.01.004>
18. Rao LB, Rao CK (2014) Frequencies of circular plate with concentric ring and elastic edge support. *Front Mech Eng* 9(2):168–176
19. Rao LB, Rao CK (2015) Vibrations of a rotationally restrained circular plate resting on a concentric rigid ring support. *Int J Acoust Vibr* 20(4):220–225
20. Rao LB, Rao CK (2016) Vibrations of circular plate supported on a rigid concentric ring with translational restraint boundary. *Eng Trans* 64(3):259–269
21. Rao LB, Rao CK (2016) Frequency analysis of annular plates having a small core and guided edges at both inner and outer boundaries. *J Solid Mech* 8(1):168–174
22. Rao LB, Rao CK (2016) An exact frequency analysis of annular plates with small core having elastically restrained outer edge and sliding inner edge. *Appl Acoust* 109:69–81
23. Rao LB, Rao CK (2013) Frequencies of circular plates weakened along an internal concentric circle and elastically restrained edge against translation. *J Appl Mech Trans ASME* 80/011005–1. Published online Jan 2013
24. Rao LB, Rao CK (2015) Analysis of vibration natural frequencies of rotationally restrained and simply supported circular plate with weakened interior circle due to an angular crack. *Strength Mater* 47(6):859–869
25. Rao LB, Rao CK (2017) Exact closed-form solution of vibrations of a generally restrained circular plate with crack and weakened along an internal concentric circle. *Int J Acoust Vibr* 22(3):334–347
26. Rao LB, Rao CK (2012) Free vibration of circular plate with elastic edge support and resting on elastic foundation. *Int J Acoust Vibr* 17(4):204–207
27. Rao LB, Rao CK (2012) Vibrations of circular plates with guided edge and resting on elastic foundation. *J Solid Mech* 4(3):307–312
28. Rao LB, Rao CK (2013) Vibrations of elastically restrained circular plates resting on Winkler foundation. *Arab J Sci Eng* 38(11):3171–3180
29. Rao LB, Rao CK (20014) Frequency analysis of annular plates with inner and outer edges elastically restrained and resting on Winkler foundation. *Int J Mech Sci* 81(4):184–194
30. Rao LB, Rao CK (2016) Vibrations of circular plates with elastically restrained edge against translation and resting on elastic foundation. *J Eng Res* 13(2):187–196
31. Lombard M (2018) Introducing SolidWorks, mastering SolidWorks. 3–24. <https://doi.org/10.1002/9781119516743.ch1>
32. Launder BE, SD B. (2013) MAN—ANSYS fluent user’s guide release. *Knowl Creat Diffus Util* 15317:724–746
33. Bhatnagar V, Mamaduri PK, Sreenivasulu B (2019) Comparative study for modal analysis of circular plates with various cutouts and end conditions. *Vibroengineering Procedia* 29:87–93. <https://doi.org/10.21595/vp.2019.21162>



# Vibrational Analysis of Circular Composite Plates with Square Cutout



Varun Gopalakrishnan, V. Dhakshain Balaji, C. Ajay, AL. Muthuveerappan, and Lokavarapu Bhaskara Rao

**Abstract** Composite materials find wide range of applications in the aerospace and automobile industry. This paper is aimed at studying the free vibration characteristics of circular carbon-epoxy composite plates with and without square cutouts. Finite element method is the primary mode of study followed through the paper which was achieved by using the respective CAD modeling software. The influence of height, radius, and the fiber orientation angles of the non-perforated composite plate on its vibrational behavior is observed. The effects of the dimensions of the square cutout on the frequencies of the plates under different modes of vibrations are also tested and tabulated. It is found that frequency of the plate increases with increase in height and decrease in radius.

**Keywords** Circular plate · Composite · Cutout · Vibration analysis · Modal diagram · Finite element analysis

## 1 Introduction

Owing to the potentially beneficial structural and thermal efficiencies [1, 2] and the weight-reducing nature [3, 4] of laminated composite elements, the aerospace industry has always considered this domain of research to be of great value. Cutouts

---

V. Gopalakrishnan (✉) · V. Dhakshain Balaji · C. Ajay · AL. Muthuveerappan · L. Bhaskara Rao  
School of Mechanical Engineering, Vellore Institute of Technology, Chennai Campus,  
Vandalur-Kelambakkam Road, Chennai, Tamil Nadu 600127, India  
e-mail: [varun.g2018@vitstudent.ac.in](mailto:varun.g2018@vitstudent.ac.in)

V. Dhakshain Balaji  
e-mail: [dhakshain.balaji2018@vitstudent.ac.in](mailto:dhakshain.balaji2018@vitstudent.ac.in)

C. Ajay  
e-mail: [c.ajay2018@vitstudent.ac.in](mailto:c.ajay2018@vitstudent.ac.in)

AL. Muthuveerappan  
e-mail: [al.muthuveerappan2018@vitstudent.ac.in](mailto:al.muthuveerappan2018@vitstudent.ac.in)

are used for including fasteners, accessing ports, and other internal features. A significant decrement in the performance of aerospace structures is because of the undesirable vibrations that occur in flight, and this might lead to severe damage to the components and accidents as well. It is thus crucial to study the vibrational behaviors of perforated and non-perforated composite elements for use in different aeronautical and other engineering applications. Over the years, several research groups have taken up different cases of modal analysis of composite plates, each leading to a distinctive understanding of the theory of using perforated and non-perforated elements. Rao and Rao studied the vibrations of circular plates with concentric ring and rigid ring support [5–7]. They further went on to perform frequency analysis on annular plates with small core and different boundary conditions [8, 9]. The frequency of restrained circular plates with weakening along interior circle has also been studied by Rao and Rao [10–12]. The fundamental frequencies of circular plate and annular plate with elastic edges have also been analyzed by Rao and Rao [13]; however, their studies in this field did not include isotropic materials or perforated composite plates.

Rajamani et al. [14] studied the effect of square cutouts on natural frequencies of symmetrically laminated, simply supported, square composite plates, assuming the effect equivalent to external loading on the plate. Large amplitude flexural vibrations of rectangular composite plate possessing rectangular cutouts were analyzed by Reddy [15] using the Reissner–Mindlin type shear deformation theory and von Karman theory. The natural frequency of simply supported rectangular composite plates with rectangular cutout was predicted by Lee et al. [16] using a numerical method based on Rayleigh’s principle and the method validated with previous literature. A study conducted on rectangular composites under various boundary conditions by Reddy et al. [17] proved that the accurate prediction of the natural frequencies of composite laminates is achieved by the shear deformation theory, whereas over-prediction of the values happens with the classical laminate theory. Bicos et al. [18] analyzed the free damped vibration characteristics in composite plates with centrally located circular cutouts using computer code.

The dynamic behavior in laminated composite plates with elliptical cutouts was analyzed by Ramakrishna et al. [19], employing an eight-noded hybrid-stress finite element. The effect of varying parameters like hole size, fiber orientation, major to minor axes ratio, and width to thickness ratio on the natural frequency of perforated plates was studied. Levraea et al. [20] conducted vibration analysis of circular and cylindrical composite panels with eccentrically located square cutouts and obtained natural frequencies using a video holographic interferometry technique which also agreed with predictions from finite element method with less than 10% difference in all cases. Free vibrations of circular and square composite plates having delamination at internal cutouts were investigated by Ju et al. [21] using finite element method. They established the mode dependency of effect of delamination on natural frequencies. Boay [22] subjected a symmetrically laminated composite plate with a central hole to free vibrational studies using finite element method, where the values agreed with experimental results. The trends of natural frequencies by varying hole sizes, aspect ratio, and boundary conditions were also studied. A genetic algorithm was utilized by Sivakumar et al. [23] to find the optimal design of a square composite plate with

varied boundary conditions and an elliptical cutout, where the natural frequencies studied by first-order shear deformation (FSDT) theory were a constraint.

Turvey et al. [24] studied the free vibrational behaviors of pultruded glass reinforced plastic (GRP) plates subjected to different boundary conditions. The experiments were also extended to GRP plates with central circular cutouts where the finite element frequencies and mode shapes were obtained. Using Hamilton's principle and higher-order shear deformation theory (HSDT), Kumar et al. [25] understood the free vibration behavior of thick composite plates with cutouts. The study also conducted a comparative analysis of the results obtained using HSDT and first-order shear deformation theory. The attempt made by Anil et al. [26] on the stability analysis of composite plates with cutouts under in-plane compressive loading helped the scientific community to understand the effect of pre-buckled stress on the modal studies of such plates. Using higher-order shear deformation theory (HSDT) and four unknown displacement functions, the changes in critical buckling response of rectangular symmetric laminates to fiber orientation angle were studied with the help of finite element method. A finite element approach toward studying the vibrational characteristics of composite skew laminates was carried out by Park et al. [27]. The higher-order shear deformation theory was applied to understand the effect of a quadrilateral cutout located in the center of the composite plate.

Based on Reddy's third-order theory, a nonlinear vibrational study of composite laminated plates was carried out by Chandrashekar et al. [28]. On varying the oscillation amplitude ratio, stacking sequence, and aspect ratio, different numerical results were obtained. A Latin hypercube sampling technique combined with Monte Carlo simulation was used to understand the different natural frequencies of the plate caused by random material properties. The first-order shear deformation theory (FSDT) was used to study the free vibration of laminated composite plates with a new effective radial basis function (RBF) collocation technique by Ngo-Cong et al. [29]. Variations in aspect ratios, material properties, and boundary conditions lead to different results, obtained by modeling the plates as Cartesian grids. Lei et al. [30] conducted free vibrational studies on nanocomposite plates, reinforced with single-walled carbon nanotubes. The element-free kp-Ritz method was used to analyze the effects of the aspect ratio, change in temperature, and also volume fraction of carbon nanotubes on the natural frequencies of the nanocomposite plate.

With the help of a support vector regression (SVR) model, Dey et al. [31] were able to investigate the stochastic natural frequency of composite plates with cutouts. In addition to the SVR model, this study has been validated by the finite element method and Monte Carlo simulations as well. An independent coordinate coupling method was employed by Huang et al. [32] to perform vibrational analysis of orthotropic composite laminated plates possessing a rectangular cutout. On imposing a displacement matching condition near the cutout, the team was able to understand the effect of aspect and modulus ratio, and the effect of boundary conditions on the natural frequency of the plate. The static and the free vibrational analysis of laminated composite plates using the polygonal finite element method in combination with higher-order shear deformation theory was conducted by Nguyen et al. [33]. Timoshenko's beam model was applied to attend to shear-locking problems. Fallah et al.

[34] proposed to use a novel meshless finite volume method to study the vibrational characteristics of laminated composite plates. Delaunay triangulation scheme was used to obtain control volumes after which the first-order shear deformation theory was used to arrive at the necessary equilibrium equations. This method proved to be more accurate with a shear-locking free property that was validated with other data from the available literature. The vibrational behavior of plates subjected to bending was tested by Dai et al. [35]. Changes in the eigen pairs of the plate on increasing the area of the cutout and also on increasing the number of cutouts were observed and presented. The entire study was based on primitive cell plates with double cutouts.

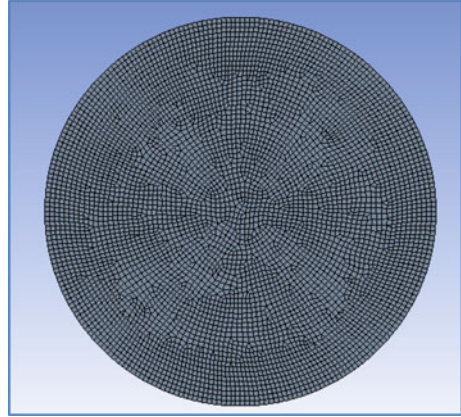
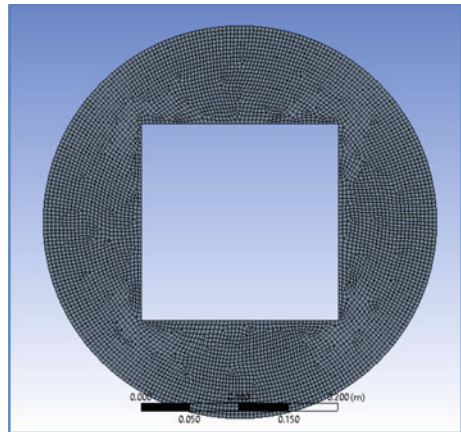
Despite the various innovative methods adopted to analyze the vibrational characteristics of perforated and non-perforated composite plates, the finite element method proves to be the most important theory used in practical engineering applications. In this study, a proper understanding of the relationship between the height, radius, and fiber orientation angles is established. In case of the composite plate with a square cutout of varying dimensions, the effect of the area of cross-section of the cutout on the overall vibrational characteristics of the composite plate is also analyzed. The effective use of the finite element method can be seen throughout the study as the conclusions drawn are primarily based on the observations made through the Ansys finite element software. The numerical reliability of the results published here has been verified, and the accuracy of the study is validated through an extensive literature survey over the years.

## 2 Materials and Methods

In order to understand the free vibrational behaviors of carbon-epoxy circular plates with and without cutouts, a finite element analysis was performed. Solidworks 2020 [36] was used to generate the composite circular plate model of radius ' $R$ ' and height ' $h$ ' with and without cutouts of dimension ' $a$ ', and they were analyzed using Ansys 19.2 [37]. The models generated using Solidworks 2020 (meshed in Ansys 19.2) have been shown in Figs. 1 and 2, respectively, and the corresponding properties of the carbon-epoxy composite of density  $1540 \text{ kgm}^{-3}$  are presented in Tables 1 and 2, respectively.

## 3 Validation and Convergence

The results obtained by Bhatnagar et al. [38] were used to compare and validate the results obtained by the finite element analysis of perforated and non-perforated carbon-epoxy composite plates. With reference to Table 3, it can be seen that the difference limits between the results obtained by Bhatnagar et al. and present study stands to be less than 10% which proves this method to be validated and an

**Fig. 1** Non-perforated plate**Fig. 2** Perforated plate

appropriate alternative to perform modal analysis on composite plates with or without cutouts.

By varying parameters like the radius and the height of the plate, and the dimension of the cutout too, this study looks forward to understanding the behavior of carbon-epoxy composite plates with and without perforations. With regards to this procedure, the orientation of the fiber is also varied to get an even better understanding of the behavior of carbon-epoxy composite plate under different modes of vibration. Tables 4 and 5 present the results obtained on analyzing a carbon-epoxy circular plate of radius 200 mm and height of 3 mm, without cutout and with a cutout of dimension  $200 \times 200 \text{ mm}^2$ , respectively. This has been carried out in the [0/90/0/90] fiber orientation scheme. These results convey the ability of the method followed to produce converging results. It is also important to note that despite increasing the number of elements analyzed under the finite element method, there is no major

**Table 1** Axial properties of carbon-epoxy composite

Property	Axis	Value	Units
Coefficient of thermal expansion	X	$-4.00 \times 10^{-7}$	$^{\circ}\text{C}^{-1}$
	Y	$3.00 \times 10^{-5}$	$^{\circ}\text{C}^{-1}$
	Z	$3.00 \times 10^{-5}$	$^{\circ}\text{C}^{-1}$
Young's modulus	X	$2.09 \times 10^{11}$	Pa
	Y	$9.45 \times 10^9$	Pa
	Z	$9.45 \times 10^9$	Pa
Orthotropic stress-tensile	X	$1.98 \times 10^9$	Pa
	Y	$2.60 \times 10^7$	Pa
	Z	$2.60 \times 10^7$	Pa
Orthotropic stress-compressive	X	$-8.93 \times 10^8$	Pa
	Y	$-1.39 \times 10^8$	Pa
	Z	$-1.39 \times 10^8$	Pa
Orthotropic strain-tensile	X	$9.20 \times 10^{-3}$	–
	Y	$3.10 \times 10^{-3}$	–
	Z	$3.10 \times 10^{-3}$	–
Orthotropic strain-compressive	X	$-5.30 \times 10^{-3}$	–
	Y	$-1.72 \times 10^{-2}$	–
	Z	$-1.72 \times 10^{-2}$	–

**Table 2** Planar properties of carbon-epoxy composite

Property	Plane	Value	Units
Poisson's ratio	XY	0.27	–
	YZ	0.4	–
	XZ	0.27	–
Shear modulus	XY	$5.5 \times 10^9$	Pa
	YZ	$3.90 \times 10^9$	Pa
	XZ	$5.50 \times 10^9$	Pa
Orthotropic stress-shear	XY	$1.00 \times 10^8$	Pa
	YZ	$5.00 \times 10^7$	Pa
	XZ	$1.00 \times 10^8$	Pa
Orthotropic strain-shear	XY	$1.60 \times 10^{-2}$	–
	YZ	$1.40 \times 10^{-2}$	–
	XZ	$1.60 \times 10^{-2}$	–

**Table 3** Validation of data with reference to Bhatnagar et al.

Mode	Bhatnagar et al. [38]	Present data	Difference %
1	629.59	600.25	4.771
2	1224.8	1168.72	4.685
3	1238.1	1175.4	5.195
4	1898.8	1752.4	8.01
5	1935	1806.3	6.879
6	2191.1	2088.6	4.79

**Table 4** Analysis of carbon-epoxy composite plate without cutout and a fixed dimension of  $R = 200$  mm,  $h = 3$  mm under the [0/90/0/90] fiber orientation

No. of elements	Frequency mode					
	1	2	3	4	5	6
6005	261.51	522.66	560.79	823.72	920.7	1027.7
7370	261.49	522.55	560.67	823.43	920.45	1027.3
9509	261.47	522.43	560.53	823.18	920.06	1026.8
11,947	261.45	522.34	560.43	823.01	919.79	1026.5

**Table 5** Analysis of carbon-epoxy composite plate of  $R = 200$  mm,  $h = 3$  mm having a cutout of dimension  $200 \times 200$  mm<sup>2</sup> under [0/90/0/90] fiber orientation

No. of elements	Frequency mode					
	1	2	3	4	5	6
7752	537.35	577.94	598.4	663.89	925.98	1107.7
5980	537.39	578.08	598.53	664.25	926.19	1108.4
9509	540.16	575.26	598.52	663.6	926.77	1108.3
10,638	540.1	574.95	598.24	662.79	926.27	1106.9

deviation in the final output obtained in terms of vibrational frequencies observed under different modes.

Following the same procedure with composite plates with fiber orientation scheme being [0/45/-45/0], the results obtained for the solid plate of  $R = 200$  mm,  $h = 3$  mm, and the plate with cutout of dimension  $200 \times 200$  mm<sup>2</sup> are shown in Tables 6 and 7, respectively.

**Table 6** Analysis of carbon-epoxy composite plate with cutout and a fixed dimension of  $R = 200$  mm,  $h = 3$  mm under [0/45/-45/0] fiber orientation

With perforation	Frequency mode					
	No. of elements	1	2	3	4	5
3883	520.46	538.73	635.31	674.83	962.41	1085.6
4707	520.4	538.62	635.22	674.65	962.03	1085.1
6044	520.2	538.24	635.04	674.15	961.58	1084.1
7873	520.11	538.08	634.89	673.85	961.21	1083.4
10,651	519.99	537.83	634.77	673.51	960.88	1082.7

**Table 7** Analysis of carbon-epoxy composite plate without cutout of dimension,  $R = 200$  mm and  $h = 3$  mm under [0/45/-45/0] fiber orientation

No perforation	Frequency mode					
	No. of elements	1	2	3	4	5
4230	260.74	452.27	616.12	713.37	879.45	1044.6
5013	260.71	452.13	615.95	713.03	879.12	1043.8
6005	260.68	452.01	615.79	712.73	878.8	1043.1
7370	260.66	451.9	615.65	712.47	878.49	1042.5
9509	260.64	451.81	615.51	712.16	878.25	1041.9

## 4 Results and Discussion

FEM analysis was performed on composite circular plates using ANSYS; the following results were obtained depending on the presence of a centrally located square cutout. Table 8 shows a set of modal diagrams of composite circular plate with and without cutouts, of varying radius, thickness, and size of cutout. The fiber orientation scheme is [0/90/0/90].

### 4.1 Non-Perforated Plate

A non-perforated composite circular plate of radius 200 mm was taken. The vibrational frequencies for six modes were obtained in both [0/90/0/90] and [0/45/-45/0] fiber orientations when the height of plate was varied between 2 mm, 3 mm, and 4 mm. The vibrational frequencies are shown in Tables 9 and 10. At all conditions, the frequency increases with increase in mode number. From the graphs in Figs. 3 and 4, it is also evident that when height of plate is increased, the frequencies also increase. No significant change of trend or frequency values observed with respect to change in fiber orientation.

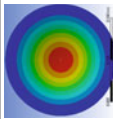
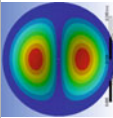
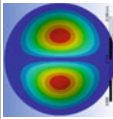
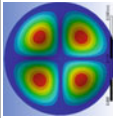
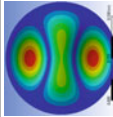
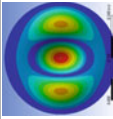
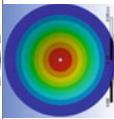
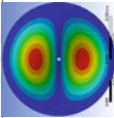
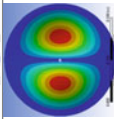
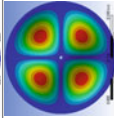
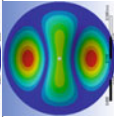
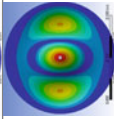
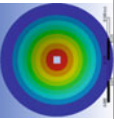
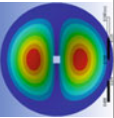
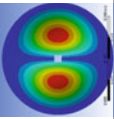
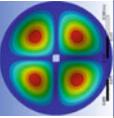
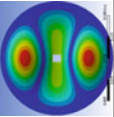
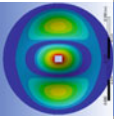
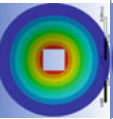
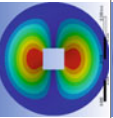
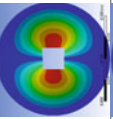
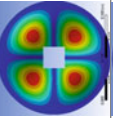
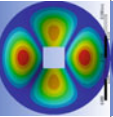
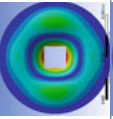
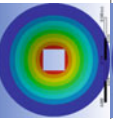
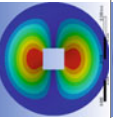
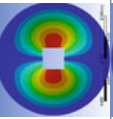
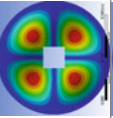
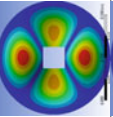
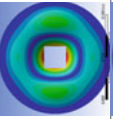
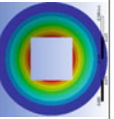
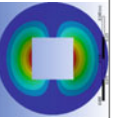
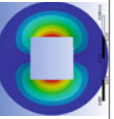
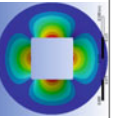
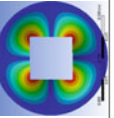
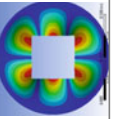


**Table 8** Modal diagrams obtained for perforated and non-perforated plates on varying the radius of the plate, the height of the plate, and the dimension of the cutout

	Mode 1	Mode 2	Mode 3	Mode 4	Mode 5	Mode 6
R_h_a						
200_2_0						
200_3_0						
200_4_0						
50_3_0						
100_3_0						

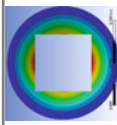
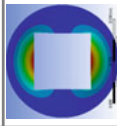
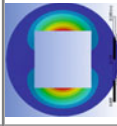
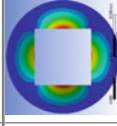
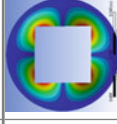
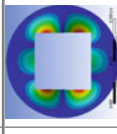
(continued)

Table 8 (continued)

	Mode 1	Mode 2	Mode 3	Mode 4	Mode 5	Mode 6
R_h_a						
200_3_2.5						
200_3_10						
200_3_25						
200_3_75						
200_3_150						

(continued)

**Table 8** (continued)

R_h_a	Mode 1	Mode 2	Mode 3	Mode 4	Mode 5	Mode 6
200_3_200						

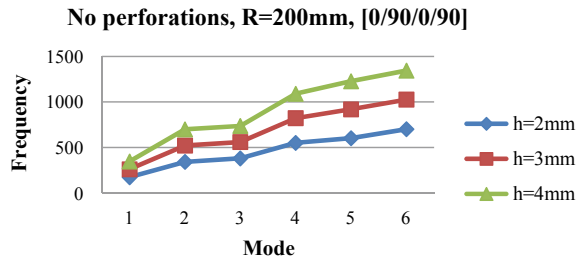
**Table 9** Vibrational characteristics of non-perforated composite circular plate of fixed radius, 200 mm and [0/90/0/90] fiber orientation

Height (mm)	Frequency mode					
	1	2	3	4	5	6
2	174.65	342.76	381.42	551.41	603.11	701.96
3	261.45	522.34	560.43	823.01	919.79	1026.5
4	347.63	699.42	736.78	1089.7	1227.4	1344.4

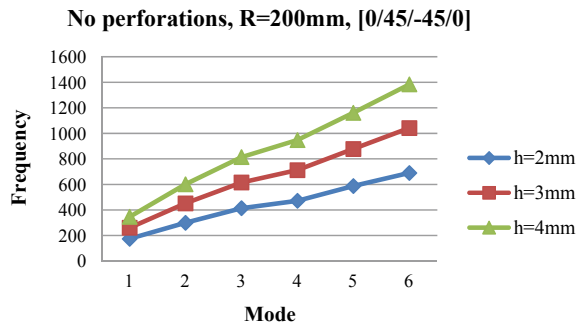
**Table 10** Vibrational characteristics of non-perforated composite circular plate of fixed radius, 200 mm and [0/45/-45/0] fiber orientation

Height (mm)	Frequency mode					
	1	2	3	4	5	6
2	174.13	299.86	413.96	471.7	588.03	690.04
3	260.64	451.81	615.51	712.16	878.25	1041.9
4	346.41	601.28	813.78	947.27	1161.3	1383.8

**Fig. 3** Vibrational characteristics of a non-perforated composite circular plate of fixed radius, 200 mm and [0/90/0/90] fiber orientation



**Fig. 4** Vibrational characteristics of a non-perforated composite circular plate of fixed radius, 200 mm and [0/45/-45/0] fiber orientation



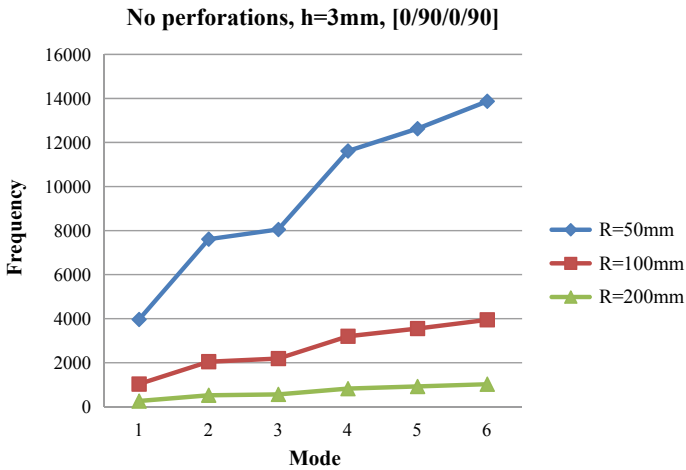
The vibrational frequencies were also analyzed with the height of circular composite plate fixed at 3 mm. The radius of the plate was varied between 50 mm, 100 mm, and 200 mm. The tabulated frequencies can be found in Tables 11 and 12. From the graphs as shown in Figs. 5 and 6, we observe a general trend of increase

**Table 11** Vibrational characteristics of non-perforated composite circular plate of fixed height, 3 mm and [0/90/0/90] fiber orientation

Radius (mm)	Frequency mode					
	1	2	3	4	5	6
50	3963.9	7612	8052	11,614	12,629	13,871
100	1034.1	2047.7	2189.5	3201.7	3553.2	3948.8
200	261.45	522.34	560.43	823.01	919.79	1026.5

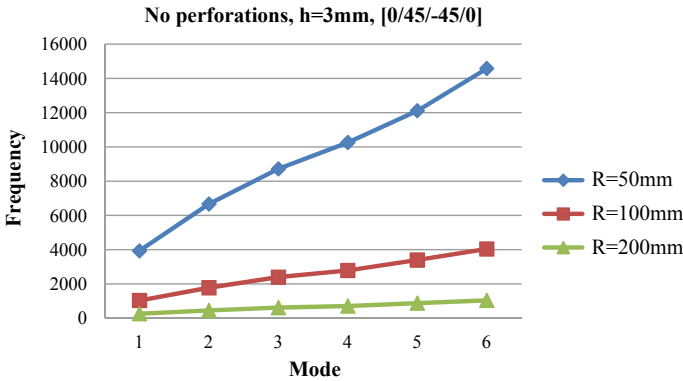
**Table 12** Vibrational characteristics of non-perforated composite circular plate of fixed height, 3 mm and [0/45/-45/0] fiber orientation

Radius (mm)	Frequency mode					
	1	2	3	4	5	6
50	3929.7	6669.2	8718.1	10,258	12,110	14,578
100	1029.6	1776	2396.4	2783.2	3395.4	4042.7
200	260.64	451.81	615.51	712.16	878.25	1041.9



**Fig. 5** Vibrational characteristics of non-perforated composite circular plate of fixed height, 3 mm and [0/90/0/90] fiber orientation

in frequency with increase in mode number. We also observe significant increase in frequency with decrease in radius. No significant change in trend or frequency values is observed between the different fiber orientation schemes.



**Fig. 6** Vibrational characteristics of non-perforated composite circular plate of fixed height, 3 mm and [0/45/-45/0] fiber orientation

### 4.2 Perforated Plate

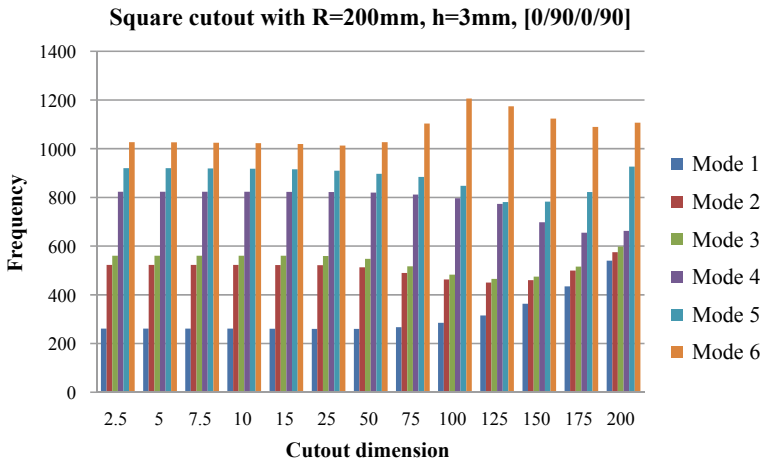
A square cutout of varying dimensions was made at the center of a composite circular plate of radius 200 mm and height 3 mm. The vibrational characteristics of the plate with both [0/90/0/90] and [0/45/-45/0] fiber orientation schemes were observed, and the values are shown in Tables 13 and 14, respectively. For all values, the frequency increases with increase in mode number. From the graphs as shown in Figs. 7 and 8,

**Table 13** Vibrational characteristics of composite circular plate of radius 200 mm, height 3 mm, [0/90/0/90] fiber orientation, and a centrally located square cutout

Cutout Dimension (mm)	Frequency mode					
	1	2	3	4	5	6
2.5	261.47	522.44	560.55	823.16	920.03	1026.8
5	261.44	522.44	560.53	823.15	919.62	1026.3
7.5	261.3	522.42	560.52	823.11	918.81	1024.9
10	261.12	522.41	560.5	823.06	917.77	1023.1
15	260.75	522.29	560.34	822.86	915.35	1019.4
25	259.94	521.62	559.44	822.36	909.72	1013.1
50	259.95	512.94	547.83	819.47	897.23	1026.7
75	267.1	489.85	517.42	811.68	884.1	1103.2
100	284.65	463.14	482.91	796.35	847.66	1205.8
125	315.31	449.95	465.12	773.69	780.52	1174.3
150	363.13	460.37	474.44	697.99	782.2	1123.9
175	434.75	499.91	516.22	655.11	822.45	1089.4
200	540.1	574.95	598.24	662.79	926.27	1106.9

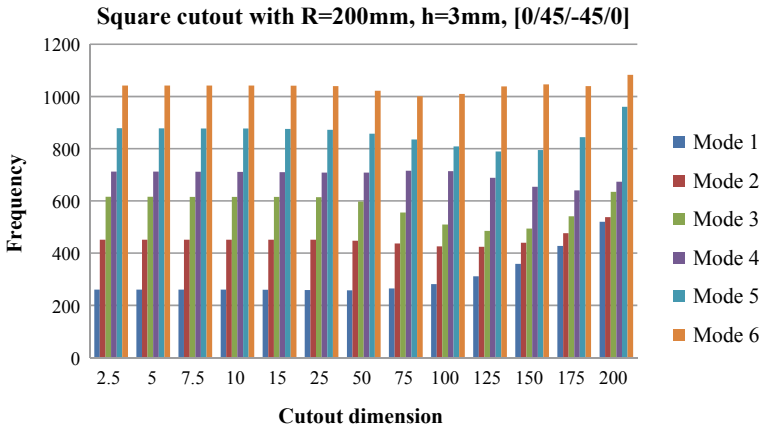
**Table 14** Vibrational characteristics of composite circular plate of radius 200 mm, height 3 mm, [0/45/-45/0] fiber orientation, and a centrally located square cutout

Cutout dimension (mm)	Frequency mode					
	1	2	3	4	5	6
2.5	260.63	451.8	615.52	712.15	878.19	1041.9
5	260.61	451.8	615.51	712.02	878	1041.8
7.5	260.46	451.8	615.47	711.72	877.55	1041.9
10	260.29	451.79	615.44	711.29	877.13	1041.7
15	259.84	451.74	615.25	710.3	875.9	1041.5
25	258.79	451.43	613.95	708.29	872.36	1039.8
50	257.98	447.42	597.45	708.48	857.3	1022.4
75	264.42	437.2	555.39	715.61	834.91	1001
100	281.43	426.27	509.44	714.03	808.59	1009.5
125	311.65	424.47	485.4	688.8	789.44	1038.3
150	358.73	439.6	494.1	654.48	795.14	1046.3
175	427.56	476.43	541.03	640.35	844.01	1040.1
200	519.99	537.83	634.77	673.51	960.88	1082.7



**Fig. 7** Vibrational characteristics of composite circular plate of radius 200 mm, height 3 mm, [0/90/0/90] fiber orientation, and a centrally located square cutout

we observe wave-like trends in frequency with change in cutout size. At first mode of frequency, the value is stagnant up to side of cutout size, 50 mm after which we notice an upward trend. Similarly, at second and third modes of frequency, we observe a stagnation at first, a temporary dip, and then an increase in trend. The wave-like nature of the trend is noted. As the modes of frequency are increased, the wave trend



**Fig. 8** Vibrational characteristics of composite circular plate of radius 200 mm, height 3 mm, [0/45/-45/0] fiber orientation, and a centrally located square cutout

is more prominently observed. No significant differences resulted in the vibrational characteristics due to the fiber orientation scheme in the composite material.

## 5 Conclusion

Based on the study conducted and the numerous references cited, FEA can be concluded as a methodical technique for the systematic analysis of modal frequencies of circular composite plates with and without cutout. Carbon-epoxy composite with different fiber orientation schemes was used in this study where the vibrational characteristics under the first six modes were analyzed by altering the radius of the plate, the height of the plate, and the dimensions of the cutout as well. Throughout the study, the modal frequencies of both perforated and non-perforated plate showed an increasing trend through the first six modes irrespective of the constant and the variable parameters. However, certain specific trends were observed in some particular scenarios like:

1. Frequency of plate increases with increase in height of plate.
2. Frequency of plate increases with decrease in radius of plate.
3. Frequency of plate has a wave-like structure as it varies with cutout size.

It is also noted that the fiber orientation scheme of the composite material did not affect the frequency of plate. Hence, it can be concluded that it is essential to improve the number of cases tested in this scenario to obtain a complete understanding of the trends observed and their variations.



## References

1. Yan C, Yin Z, Shen X, Mi D, Guo F, Long D (2020) Surrogate-based optimization with improved support vector regression for non-circular vent hole on aero-engine turbine disk. *Aerosp Sci Technol* 96:105332. <https://doi.org/10.1016/j.ast.2019.105332>
2. Wen Z, Zhang Y, Li Z, Yue Z (2018) Equivalent and simplification of nickel-based single crystal plates with film cooling holes. *Aerosp Sci Technol* 82–83:119–139. <https://doi.org/10.1016/j.ast.2018.09.011>
3. Tsuchima N, Yokozeki T, Su W, Arizono H (2019) Geometrically nonlinear static aeroelastic analysis of composite morphing wing with corrugated structures. *Aerosp Sci Technol* 88:244–257. <https://doi.org/10.1016/j.ast.2019.03.025>
4. Nicassio F, Scarselli G, Pinto F, Ciampa F, Iervolino O, Meo M (2018) Low energy actuation technique of bistable composites for aircraft morphing. *Aerosp Sci Technol* 75:35–46. <https://doi.org/10.1016/j.ast.2017.12.040>
5. Rao LB, Rao CK (2014) Frequencies of circular plate with concentric ring and elastic edge support. *Front Mech Eng* 9:168–176. <https://doi.org/10.1007/s11465-014-0299-5>
6. Rao L, Chellapilla KR (2015) Vibrations of a rotationally restrained circular plate resting on a concentric rigid ring support. *Int J Acoust Vib* 20:220–225
7. Rao L, Chellapilla KR (2016) Rao, vibrations of a circular plate supported on a rigid concentric ring with translational restraint boundary. *Eng Trans* 64:259–269
8. Rao L, Chellapilla KR (2016) Frequency analysis of annular plates having a small core and guided edges at both inner and outer boundaries. *J Solid Mech* 8:168–174
9. Rao LB, Rao CK (2016) An exact frequency analysis of annular plates with small core having elastically restrained outer edge and sliding inner edge. *Appl Acoust* 109:69–81. <https://doi.org/10.1016/j.apacoust.2016.03.006>
10. Rao LB, Rao CK (2012) Frequencies of circular plates weakened along an internal concentric circle and elastically restrained edge against translation. *J Appl Mech* 80. <https://doi.org/10.1115/1.4006938>
11. Rao L, Chellapilla KR (2015) Analysis of vibration natural frequencies of rotationally restrained and simply supported circular plate with weakened interior circle due to an angular crack. *Strength Mater* 47. <https://doi.org/10.1007/s11223-015-9723-2>
12. Rao LB, Chellapilla KR (2017) Exact closed-form solution of vibrations of a generally restrained circular plate with crack and weakened along an internal concentric circle. *Int J Acoust Vib* 22:334–347. <https://doi.org/10.20855/ijav.2017.22.3479>
13. Rao LB, Chellapilla KR (2012) Free vibration of circular plates with elastic edge support and resting on an elastic foundation. *Int J Acoust Vib* 17:204–207. <https://doi.org/10.20855/ijav.2012.17.4311>
14. Rajamani A, Prabhakaran R (1977) Dynamic response of composite plates with cut-outs, part I: simply-supported plates. *J Sound Vib* 54:549–564. [https://doi.org/10.1016/0022-460X\(77\)90612-5](https://doi.org/10.1016/0022-460X(77)90612-5)
15. Reddy JN (1982) Large amplitude flexural vibration of layered composite plates with cutouts. *J Sound Vib* 83:1–10. [https://doi.org/10.1016/S0022-460X\(82\)80071-0](https://doi.org/10.1016/S0022-460X(82)80071-0)
16. Lee HP, Lim SP, Chow ST (1987) Free vibration of composite rectangular plates with rectangular cutouts. *Compos Struct* 8:63–81. [https://doi.org/10.1016/0263-8223\(87\)90016-X](https://doi.org/10.1016/0263-8223(87)90016-X)
17. Reddy JN, Khdeir AA (1989) Buckling and vibration of laminated composite plates using various plate theories. *AIAA J* 27:1808–1817. <https://doi.org/10.2514/3.10338>
18. Bicos AS, Springer GS (1989) Vibrational characteristics of composite panels with cutouts. *AIAA J* 27:1116–1122. <https://doi.org/10.2514/3.10230>
19. Ramakrishna S, Rao KM, Rao NS (1993) Dynamic analysis of laminates with elliptical cutouts using the hybrid-stress finite element. *Comput Struct* 47:281–287. [https://doi.org/10.1016/0045-7949\(93\)90378-Q](https://doi.org/10.1016/0045-7949(93)90378-Q)
20. Levraea VJ, Palazotto AN, Maddux GE (1993) The effect of cutout positioning on the dynamic characteristics of a curved composite panel. *Compos Struct* 23:263–272. [https://doi.org/10.1016/0263-8223\(93\)90227-H](https://doi.org/10.1016/0263-8223(93)90227-H)

21. Ju F, Lee HP, Lee KH (1995) Free vibration of composite plates with delaminations around cutouts. *Compos Struct* 31:177–183. [https://doi.org/10.1016/0263-8223\(95\)00016-X](https://doi.org/10.1016/0263-8223(95)00016-X)
22. Chai GB (1996) Free vibration of laminated composite plates with a central circular hole. *Compos Struct* 35:357–368. [https://doi.org/10.1016/S0263-8223\(96\)00037-2](https://doi.org/10.1016/S0263-8223(96)00037-2)
23. Sivakumar K, Iyengar NGR, Deb K (1997) Optimum design of laminated composite rectangular plates with cutouts using genetic algorithm, *Indian. J Eng Mater Sci* 4:189–195
24. Turvey GJ, Mulcahy N, Widden MB (2000) Experimental and computed natural frequencies of square pultruded GRP plates: effects of anisotropy, hole size ratio and edge support conditions. *Compos Struct* 50:391–403. [https://doi.org/10.1016/S0263-8223\(00\)00116-1](https://doi.org/10.1016/S0263-8223(00)00116-1)
25. Kumar A, Shrivastava RP (2005) Free vibration of square laminates with delamination around a central cutout using HSDT. *Compos Struct* 70:317–333. <https://doi.org/10.1016/j.compstruct.2004.08.040>
26. Anil V, Upadhyay CS, Iyengar NGR (2007) Stability analysis of composite laminate with and without rectangular cutout under biaxial loading. *Compos Struct* 80:92–104. <https://doi.org/10.1016/j.compstruct.2006.04.088>
27. Park T, Lee SY, Voyiadjis GZ (2009) Finite element vibration analysis of composite skew laminates containing delaminations around quadrilateral cutouts. *Compos Part B Eng* 40:225–236. <https://doi.org/10.1016/j.compositesb.2008.11.004>
28. Chandrashekhar M, Ganguli R (2010) Nonlinear vibration analysis of composite laminated and sandwich plates with random material properties. *Int J Mech Sci* 52:874–891. <https://doi.org/10.1016/j.ijmecsci.2010.03.002>
29. Ngo-Cong D, Mai-Duy N, Karunasena W, Tran-Cong T (2011) Free vibration analysis of laminated composite plates based on FSDT using one-dimensional IRBFN method. *Comput Struct* 89:1–13. <https://doi.org/10.1016/j.compstruc.2010.07.012>
30. Lei ZX, Liew KM, Yu JL (2013) Free vibration analysis of functionally graded carbon nanotube-reinforced composite plates using the element-free kp-Ritz method in thermal environment. *Compos Struct* 106:128–138. <https://doi.org/10.1016/j.compstruct.2013.06.003>
31. Dey S, Mukhopadhyay T, Sahu SK, Adhikari S (2016) Effect of cutout on stochastic natural frequency of composite curved panels. *Compos Part B Eng* 105:188–202. <https://doi.org/10.1016/j.compositesb.2016.08.028>
32. Huang B, Wang J, Du J, Ma T, Guo Y, Qian Z (2016) Vibration analysis of a specially orthotropic composite laminate with rectangular cutout using independent coordinate coupling method. *Compos Struct* 150:53–61. <https://doi.org/10.1016/j.compstruct.2016.05.010>
33. Nguyen NV, Nguyen HX, Phan DH, Nguyen-Xuan H (2017) A polygonal finite element method for laminated composite plates. *Int J Mech Sci* 133:863–882. <https://doi.org/10.1016/j.ijmecsci.2017.09.032>
34. Fallah N, Delzendeh M (2018) Free vibration analysis of laminated composite plates using meshless finite volume method. *Eng Anal Bound Elem* 88:132–144. <https://doi.org/10.1016/j.enganabound.2017.12.011>
35. Dai L, Chen Y, Wang Y, Lin Y (2020) Experimental and numerical analysis on vibration of plate with multiple cutouts based on primitive cell plate with double cutouts. *Int J Mech Sci* 183:105758. <https://doi.org/10.1016/j.ijmecsci.2020.105758>
36. Lombard M (2018) *Introducing SolidWorks, mastering SolidWorks*. 3–24. <https://doi.org/10.1002/9781119516743.ch1>
37. I. ANSYS, *Ansys 19.2 Capabilities*, (n.d.)
38. Bhatnagar V, Mamaduri PK, Sreenivasulu B (2019) Comparative study for modal analysis of circular plates with various cutouts and end conditions. *Vibroengineering Procedia* 29:87–93. <https://doi.org/10.21595/vp.2019.21162>

# Numerical Analysis of Buckling in Rectangular Plates with Different Cut-Outs



Mahendhar Kumar, Akash Venkateshwaran, Chamala Vaishnavi, and Lokavarapu Bhaskara Rao

**Abstract** This article examines the impact of boundary conditions on the buckling load for rectangular uniform isotropic plates of different aspect ratios and cut-out shapes. Plates with cut-outs have been extensively used in many applications like an aircraft fuselage, wings, etc. So proper understanding of their buckling is a crucial step before implementing them in various applications. Tests have been completed on aluminium alloy plates with circular holes and notches under different boundary conditions comprising of clamped, fixed and their combinations are considered. For complex geometries like such, analytical methods are tiresome and time-consuming, hence numerical methods are enforced to obtain very close results to what is expected from an analytical solution. Analysis by the numerical method is led and the effect of aspect ratio, boundary conditions, and cut-out shape on the buckling behaviour of isotropic plates under in-plane axial compression load is investigated and discussed. Buckling analysis is performed by employing finite element analysis software ANSYS. The numerical results received are in true agreement with the formerly posted data.

**Keywords** Finite element analysis · Buckling · Ansys · Circular holes · Notches

---

M. Kumar (✉) · A. Venkateshwaran · C. Vaishnavi · L. B. Rao  
Vellore Institute of Technology, Chennai Campus, Vandalur Kelambakkam Road, Chennai  
600127, Tamil Nadu, India  
e-mail: [mahendharkumar.k2018@vitstudent.ac.in](mailto:mahendharkumar.k2018@vitstudent.ac.in)

A. Venkateshwaran  
e-mail: [akash.v2018@vitstudent.ac.in](mailto:akash.v2018@vitstudent.ac.in)

C. Vaishnavi  
e-mail: [chamalavaishnavi.j2018@vitstudent.ac.in](mailto:chamalavaishnavi.j2018@vitstudent.ac.in)

# 1 Introduction

Reddy defines a plate as: “A plate is a structural element with plan form dimensions that are large compared to its thickness and is subjected to loads that cause bending deformation in addition to stretching [1]”. These thin structural elements are predominantly used in automobiles, ships, planes, bridges and buildings. When these slender components are subjected to axial compressive loads, they fail suddenly due to a phenomenon known as buckling instability [2]. Buckling of a plate is defined as the loss of its stability under compressive loading [3].

Buckling of plates is an imperative topic in structural engineering, be it mechanical, civil, marine, or aircraft structures. The prediction of buckling of structural members restrained laterally is crucial for designing numerous engineering components [4]. An important feature of this elastic buckling is that the instability may also occur at a stress degree that is extensively lower than the yield strength of the material.

Too often, it is almost inevitable to have holes in these plate elements due to their practical requirements like maintenance, inspection and service and also to produce lighter and more efficient structures. These perforations cause a redistribution of the plate membrane stresses accompanied by changes within the mechanical behaviour of the plate with notable modification in their stability [5, 6]. Loss of stability implies that shape of the buckled structure vagaries into a different configuration when the loads reach a critical value. At a certain given critical load, the plate will all of a sudden present a large deflection in the out-of-plane transverse direction [7]. Buckling occurrence relies on the shape of the structure, properties of the material, loading configuration and boundary conditions. Different bodies buckle in different ways. Flat plates experience bifurcation buckling, aka classical buckling [8].

A large number of researches have been done to study the buckling behaviours of perforated plates in the last decade. The first theoretical examination of buckling of plates was attributed to Bryan. Using the energy criterion of stability, he was able to perform the buckling analysis of rectangular plates subjected to uniaxial and uniform compression loads [9, 10]. The analysis methods espoused in the published articles can be segregated into two classes, i.e. linear elastic buckling and nonlinear elastoplastic buckling. Amongst the elastic buckling studies category, El-Sawy and Nazmy explored how aspect ratio affected the critical buckling loads of rectangular plate with rectangular and eccentric circular holes under uniaxial and uniform compression load [11].

El-Sawy and Martini used the FEM techniques to find the elastic buckling stresses of biaxial loaded perforated rectangular plates with circular holes located in the longitudinal axis [12]. Finite element analysis (FEA) is by far the most effective and widely used numerical method in structural engineering. That is due to its profound theory and its ability to analyze complicated geometries and include nonlinearities. ANSYS® [27] provides ready-to-use general-purpose FEA software that has the capability of coupling different analysis fields. Most of the known exact buckling loads of plates have been summarized in the text by Timoshenko and Gere [13]. On

the other hand, Moen and Schafer formulated and authorized analytical expressions for assessing the impact of single or multiple holes on the elastic buckling critical stress of plates on compression [14]. Subsequently, Paik examined the ultimate strength properties of perforated plates under edge shear loading, axial compressive loading, and the combined edge shear loads and biaxial compression, and put forward empirical formulae to speculate the ultimate strength of the same, derived from the regression analysis of the nonlinear FEA results [15–17]. Rao and Rao explored the buckling load responses of circular plates with internal elastic ring support and extended their study by restraining the edges against any translational and rotational movements [18].

Buckling of circular and annular plates with guided edges [19–21] and with elastic/rigid ring support [22] and elastic edges [23, 24] studied by Rao and Rao. However, they have not considered the cut-out in their study. In the pool of studies devoted to the problem of elasto-plastic buckling, El-Sawy et al. studied the elasto-plastic buckling of uniaxially loaded square and rectangular plates with circular cut-outs by using FEM techniques [25].

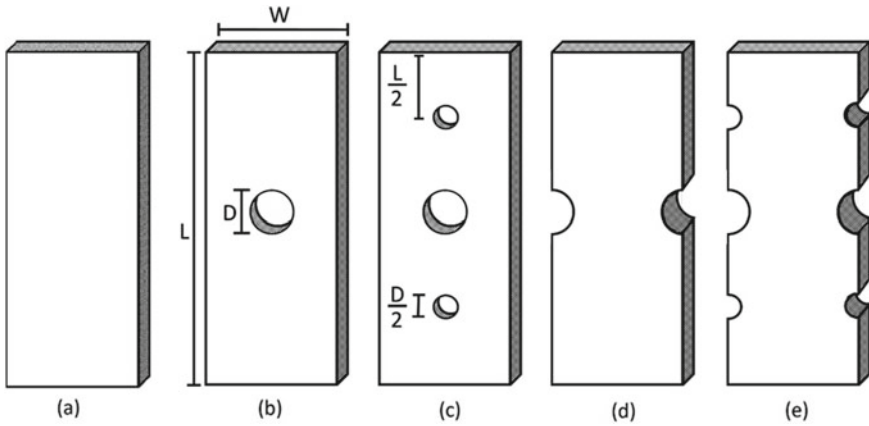
This article deals with buckling analysis of uniform isotropic aluminium plates under diverse boundary conditions. The effects on critical buckling load by the number of cut-outs, aspect ratio and specific boundary conditions are studied. First, the problem statement is described. Next, the test specimens and final element model are presented. Then, the consequences of different parameters are discussed in the light of the results.

## 2 Problem Statement

In this study, buckling loads of aluminium alloy have been determined numerically; effects of different parameters like boundary conditions, length to thickness ratio, and cut-out shape were studied. The rectangular plates made of aluminium alloy with and without cut-outs chosen for study are shown in Fig. 1. The elastic properties of aluminium alloy used in this study are given in Table 1. The cut-out chosen are central hole, central notch, 3 holes and 6 notches with diameter  $D$ . The diameter  $D$  of the cut-outs are 2.5 mm, 5 mm, 10 mm, 15 mm, and other dimensional parameters chosen for this study are given in Table 2.

## 3 Finite Element Model

In this investigation, the commercial finite element code ANSYS was used as a tool for performing numerical analysis. The investigation included five different types of rectangular plates (with and without cut-outs as seen in Fig. 1), four different lengths, 2 different thicknesses which contributed to eight different  $L/T$  ratios, four different



**Fig. 1** a Simple plate b plate with central hole c plate with 3 holes d plate with central notch e plate with 6 notch

**Table 1** Material property of aluminium alloy

Elastic properties		Values
Density	kg m <sup>-3</sup>	2770
Young's modulus	Pa	7.10E + 10
Poisson's ratio		0.33
Bulk modulus	Pa	6.90E + 10

**Table 2** Plates considered in this study

Width (mm)	Thickness (mm)	Length (mm)	Length/thickness ratio
30, 40	3, 4.5	75, 150, 250, 300	16.66, 25, 33.33, 50, 55.55, 66.66, 83.33, 100

radii of cut-outs and finally 2 sets of boundary conditions. The boundary conditions implemented in this study were as follows:

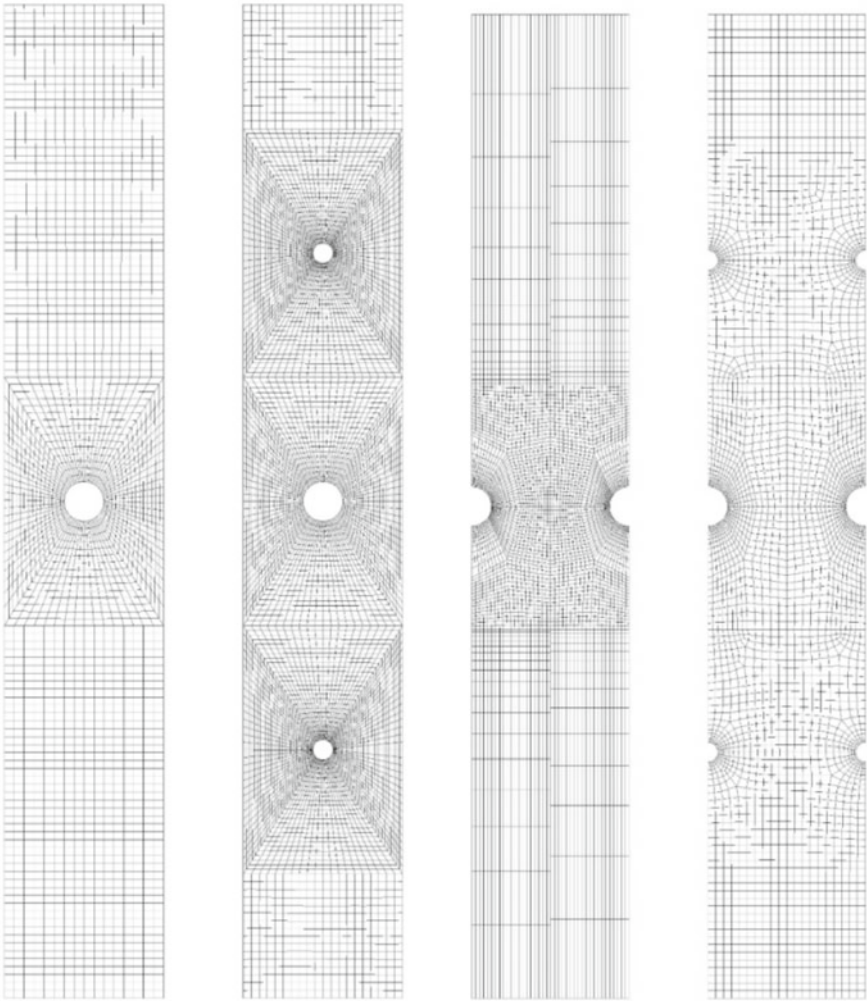
- Both opposite edge of the plates is clamped, whilst the remaining edges are free (CC)
- Lower end of the plate is clamped, whilst all the remaining three edges are free (CF).

Figure 2 represents the boundary conditions, and Fig. 3 shows a typical finite element mesh used for plates with cut-outs. The element used in this study is eight-noded SHELL 91 multi-layered shell elements which pose 3 rotational degrees of freedom and 3 displacement degree of freedom. In the presence of cut-outs, large numbers of nodes were used around the vicinity of cut-outs for proper results. From Fig. 2, it can be noticed that a compressive load was applied to the rectangular plates in the y-direction.





$$\text{Percentage error} = (\text{Pmodel buck} - \text{Preference buck}) \times 100 / \text{Preference buck}$$



**Fig. 3** Finite element mesh incorporated in the buckling analysis

**Table 3** Buckling loads for validation and material properties

	Plate without hole		Plate with circular hole		Plate with semi-circular hole	
	CC	CP	CC	CP	CC	CP
Buckling load [17]	234.81	118.64	228.78	116.65	229.25	116.81
Buckling load (FEA model)	235.82	120.79	230.92	119.18	228.26	119.17
Percentage error %	0.43	1.81	0.93	2.16	0.43	2.02



provides buckling load for all three types of plates which are simple plates, a plate with a central hole and a plate with semi-circular holes. The composite material property used in the study are shown in Table 3 as well.

Mechanical properties	Unit	Values
E1	GPa	39
E2 = E3	GPa	8.2
G12 = G13 = G23	GPa	2.9
V12 = v13 = v23	GPa	0.29
t	mm	0.1875

Buckling load for the stacking sequence 8 [0/45/-45/90] as with two boundary conditions (CC, CP) for all types of plates was calculated using the present FEA model. The validation process shown in Table 3 has an average percentage error of 1.29%. Thus, it can be observed there is a good agreement between the present study and the values available in the literature.

$$\text{Percentage error} = (\text{Pmodel buck} - \text{Preference buck}) \times 100 / \text{Preference buck}$$

## 5 Result and Discussion

This study aims to understand the effect of cut-outs, boundary conditions and  $L/T$  ratio on the buckling load under compression loading. The buckling loads (2 Modes) for different aluminium alloy plates are tabulated below. Buckling loads with 2 Modes for a plate of chosen length  $L = 75$  mm is tabulated in Table 4. Whilst the 2 Modes of buckling loads for a plate of length  $L = 150$  mm are compiled in Table 5. Similarly, Tables 6 and 7 speak for the buckling load of a plate of length  $L = 250$  mm and 300 mm respectively. Graphs are used in this study to compare the effects of different dimensions of cut-outs and  $L/T$  ratio. In Fig. 4, Mode 1 buckling loads for a plate of  $L = 75$  mm are plotted against the different diameter of cut-outs, and graphs for Mode 2 buckling loads can be found in Fig. 5, the graphs are plotted after considering the possible  $L/T$  ratio which can be found above each plot. Similarly, Figs. 6, 7, 8, 9, 10 and 11 represent Mode 1-Mode 2 buckling loads of a rectangular plate of length  $L = 150$  mm, 250 mm, 300 mm, respectively. To study the effect of the  $L/T$  ratio, buckling loads from simple plates have been used. Figure 12 (Mode 1) and Fig. 13 (Mode 2) show the influence of the  $L/T$  ratio on buckling loads for different boundary conditions considering both widths  $W = 30$  mm, 40 mm into consideration. A particular sample model was chosen and the visualization of buckling of the sample model for both modes is presented in Fig. 14. The following section deals with the buckling results of aluminium alloy plates.

**Table 4** Buckling load for all aluminium alloy plates with length  $L = 75$  mm

Mode 1																	
Height = 3, Width = 40																	
Simple plate	Plate with centre hole			Plate with 3 holes			Plate with 2 notch			Plate with 6 notch							
	d = 2.5	d = 5	d = 10	d = 15	d = 2.5	d = 5	d = 10	d = 15	d = 2.5	d = 5	d = 10	d = 15					
CC	47,092	46,437	45,496	42,472	38,749	46,439	45,469	42,309	38,297	46,486	40,547	38,330	35,151	46,498	45,654	38,059	36,683
CF	2923.8	2915	2884.1	2764.4	2565.8	2909.8	2863.8	2694.5	2445.2	2914.7	2889	2770.1	2573	2908.7	2861.8	2698.2	2443.8
Height = 4.5, Width = 40																	
CC	1.56E + 05	1.52E + 05	1.42E + 05	1.29E + 05	1.28E + 05	1.55E + 05	1.52E + 05	1.41E + 05	1.28E + 05	1.55E + 05	1.53E + 05	1.44E + 05	1.31E + 05	1.55E + 05	1.52E + 05	1.42E + 05	1.29E + 05
CF	9843.3	9805.4	9695.9	9282.5	8603.8	9787.5	9624.5	9040.6	8194.4	9803.6	9693.6	9281.9	8608.2	9782.8	9616.7	9030.3	8186.3
Height = 3, Width = 30																	
CC	34,899	34,636	33,420	30,595	26,601	34,551	33,390	30,441	26,171	34,601	33,806	27,544	24,245	34,640	33,742	30,769	23,775
CF	2170.4	2161.4	2130.5	2006.7	1794.4	2153.7	2110.6	1939.4	1685.1	2159	2128.1	2013	1800.1	2159.5	2106.2	1937.2	1687.1
Height = 4.5, Width = 30																	
CC	1.16E + 05	1.15E + 05	1.11E + 05	1.01E + 05	88,746	1.15E + 05	1.11E + 05	1.01E + 05	87,096	1.15E + 05	1.12E + 05	1.03E + 05	90,401	1.15E + 05	1.12E + 05	1.02E + 05	88,065
CF	7305.7	7262.3	7158.7	6736.3	6003.7	7243.2	7089.2	6504.4	5631	7261.4	7157.8	6736.4	6008.2	7240.4	7082.8	6495.9	5623.2
Mode 2																	
Height = 3, Width = 40																	
CC	67,529	67,210	66,044	60,911	51,711	67,032	65,330	58,622	48,369	67,840	68,991	71,156	73,640	67,951	68,958	72,077	73,901
CF	26,266	26,188	25,904	24,846	23,216	26,139	25,709	24,188	22,058	26,205	26,048	25,126	23,574	26,156	25,792	24,511	22,379

(continued)

**Table 4** (continued)

Mode 1																	
Height = 3, Width = 40																	
Simple plate	Plate with centre hole			Plate with 3 holes			Plate with 2 notch			Plate with 6 notch							
	d = 2.5	d = 5	d = 10	d = 15	d = 2.5	d = 5	d = 10	d = 15	d = 2.5	d = 5	d = 10	d = 15					
Height = 4.5, Width = 40																	
CC	2.20E + 05	2.19E + 05	2.15E + 05	1.98E + 05	1.68E + 05	2.18E + 05	2.13E + 05	1.90E + 05	1.56E + 05	2.21E + 05	2.23E + 05	2.30E + 05	2.37E + 05	2.21E + 05	2.24E + 05	2.32E + 05	2.39E + 05
CF	87,852	87,516	86,527	82,902	77,354	87,345	85,854	80,639	73,434	87,558	86,724	83,478	78,119	87,389	86,083	81,328	74,342
Height = 3, Width = 30																	
CC	71,004	71,124	70,045	67,454	52,733	70,691	69,181	64,799	49,199	70,941	70,534	61,037	55,524	69,955	69,738	65,251	51,800
CF	19,536	19,462	19,183	18,122	16,494	19,385	18,994	17,492	15,420	19,445	19,195	18,283	16,627	19,473	19,007	17,597	15,582
Height = 4.5, Width = 30																	
CC	2.31E + 05	2.29E + 05	2.18E + 05	1.68E + 05	2.31E + 05	2.26E + 05	2.10E + 05	1.55E + 05	2.31E + 05	2.29E + 05	2.18E + 05	1.95E + 05	2.31E + 05	2.26E + 05	2.10E + 05	1.83E + 05	
CF	65,318	64,940	64,033	60,461	54,855	64,760	63,380	58,310	51,210	64,958	64,118	60,665	55,000	64,779	63,477	58,575	51,439

**Table 5** Buckling load for all aluminium alloy plates with length  $L = 150$  mm

Mode 1																	
Height = 3, Width = 40																	
Simple plate	Plate with centre hole			Plate with 3 holes			Plate with 2 notch			Plate with 6 notch							
	d = 2.5	d = 5	d = 10	d = 15	d = 2.5	d = 5	d = 10	d = 15	d = 2.5	d = 5	d = 10	d = 15	d = 2.5	d = 5	d = 10	d = 15	
CC	11,537	11,384	10,936	10,246	11,505	11,383	10,927	10,221	11,507	10,702	10,339	9745.6	11,507	11,395	10,313	10,301	
CF	717.14	715.81	712.06	697.3	671.42	715.17	709.52	687.93	715.79	712.7	698.01	672.32	715.14	709.37	688.48	652.19	
Height = 4.5, Width = 40																	
CC	38,863	38,730	38,308	36,768	34,422	38,729	38,302	36,734	34,329	38,741	38,364	34,793	38,741	38,344	36,894	34,594	
CF	2416.5	2411.9	2398.5	2347.1	2258.1	2409.6	2389.5	2314.1	2191.7	2411.7	2398.3	2347.1	2258.4	2409.4	2388.9	2190.5	
Height = 3, Width = 30																	
CC	8565.3	8530.9	8412.1	7957.7	7219.4	8530.7	8410.7	7951.2	7196.9	8002.4	7906	7523.1	6875.5	8038.3	7900.9	7506.7	6834.6
CF	534.1	533.19	529.44	514.09	484.89	532.54	526.89	504.91	466.87	533.62	529.9	514.65	485.65	533.04	527.31	505.43	467.51
Height = 4.5, Width = 30																	
CC	26,655	28,716	28,298	26,731	24,218	28,695	28,292	26,705	24,131	28,724	28,337	26,881	24,472	28,725	28,321	26,807	24,296
CF	1802.9	1796.5	1783.1	1729.6	1628.9	1793.6	1774.1	1697	1565.8	1796.3	1783	1729.5	1629.1	1794.1	1773.7	1696.6	1565.4
Mode 2																	
Height = 3, Width = 40																	
CC	23,725	23,740	23,718	23,579	23,192	23,712	23,605	23,150	22,324	23,738	22,351	22,193	21,795	23,716	23,608	22,816	22,356
CF	6481.7	6470.2	6437.2	6307.9	6088.1	6464.1	6413.2	6220.2	5912.4	6470.4	6446.5	6321.8	6106.5	6464.6	6414.9	6237.4	5926.2
Height = 4.5, Width = 40																	
CC	79,519	79,528	79,444	78,926	77,513	79,433	79,055	77,451	74,558	79,525	79,410	78,737	77,131	79,447	79,048	77,426	74,496
CF	21,800	21,760	21,643	21,195	20,441	21,739	21,560	20,887	19,830	21,760	21,646	21,209	20,466	21,739	21,562	20,907	19,865

(continued)

**Table 5** (continued)

Mode 1																
Height = 3, Width = 40																
Simple plate	Plate with centre hole			Plate with 3 holes			Plate with 2 notch			Plate with 6 notch						
	d = 2.5	d = 5	d = 10	d = 15	d = 2.5	d = 5	d = 10	d = 15	d = 2.5	d = 5	d = 10	d = 15				
Height = 3, Width = 30																
CC	17,585	17,597	17,582	17,473	17,126	17,570	17,471	17,055	16,281	16,585	16,395	16,011	16,624	16,455	16,026	15,244
CF	4825	4813.5	4780.6	4647.4	4405	4807.5	4757.1	4563.2	4241.6	4819	4786.9	4416.4	4813.6	4763.6	4573.4	4254.3
Height = 4.5, Width = 30																
CC	54,939	58,944	58,887	58,472	57,188	58,816	58,505	57,027	54,309	58,932	58,813	56,559	58,853	58,450	56,831	53,936
CF	16,253	16,186	16,070	15,606	14,773	16,160	15,987	15,310	14,204	16,185	16,070	14,784	16,165	15,987	15,316	14,215

**Table 6** Buckling load for all aluminium alloy plates with length  $L = 250$  mm

Mode 1																	
Height = 3, Width = 40																	
Simple plate	Plate with centre hole			Plate with 3 holes			Plate with 2 notch			Plate with 6 notch							
	d = 2.5	d = 5	d = 10	d = 15	d = 2.5	d = 5	d = 10	d = 15	d = 2.5	d = 5	d = 10	d = 15	d = 2.5	d = 5	d = 10	d = 15	
CC	4118.5	4098.9	4073.4	3974.3	3807.5	4098.9	4073.3	3973.7	3805.5	4099	4075	3981.7	3822.9	4099.8	4074.3	3978.9	3816.4
CF	256.24	255.93	255.09	252	246.38	255.74	254.49	249.89	242.04	255.91	255.16	252.04	246.52	255.87	254.56	250	242.19
Height = 4.5, Width = 40																	
CC	13,868	13,823	13,732	13,389	12,816	13,823	13,732	13,386	12,808	13,824	13,738	13,414	12,870	13,825	13,736	13,404	12,845
CF	864.94	863.75	860.84	849.65	830.5	863.26	858.89	842.44	815.37	863.72	861.04	850.09	831.17	862.62	858.35	842	814.97
Height = 3, Width = 30																	
CC	3068.5	3051.7	3026.2	2924	2738.7	3051.7	3063.3	2923.5	2736.7	3052.1	3027.1	2928.6	2748.5	3051.9	3027.9	2926.6	2743.3
CF	191.15	190.84	190.04	186.73	180.22	190.7	189.49	184.68	176	190.84	190.03	186.72	180.24	190.7	189.48	184.67	176
Height = 4.5, Width = 30																	
CC	10,332	10,201	9845.1	9208.2	10,292	10,201	9843.3	9200.3	10,292	10,205	9861.4	9242.3	10,293	10,203	9853.8	9222.8	10,292
CF	644.54	640.6	629.03	606.54	642.97	638.66	621.77	591.67	643.44	640.57	629	606.54	642.95	638.58	621.69	591.59	643.46
Mode 2																	
Height = 3, Width = 40																	
CC	8466	8443.4	8442	8432.2	8403.5	8437.6	8418.3	8341	8205.3	8442.4	8438.4	8417.4	8369.4	8438.5	8415.5	8332.1	8186
CF	2314.7	2312	2304.6	2277.5	2228.7	2310.2	2298.9	2258	2189.2	2311.8	2305.3	2278.2	2230.7	2311.5	2299.9	2259.7	2191.8
Height = 4.5, Width = 40																	
CC	28,450	28,421	28,415	28,379	28,272	28,400	28,333	28,058	27,583	28,419	28,404	28,323	28,143	28,402	28,323	28,021	27,500
CF	7810.5	7799.7	7774	7676.6	7510.6	7794.3	7755.5	7609.6	7372.3	7799.5	7776.5	7681.3	7518.7	7787.6	7749.8	7605.9	7370.4

(continued)

**Table 6** (continued)

Mode 1																	
Height = 3, Width = 40																	
Simple plate	Plate with centre hole			Plate with 3 holes			Plate with 2 notch			Plate with 6 notch							
	d = 2.5	d = 5	d = 10	d = 15	d = 2.5	d = 5	d = 10	d = 15	d = 2.5	d = 5	d = 10	d = 15					
Height = 3, Width = 30																	
CC	6295.4	6278.7	6277.8	6270.4	6245.3	6273	6270.8	6180.6	6048.8	6278.7	6274.5	6257.2	6216	6272.7	6254.4	6170.8	6028.8
CF	1723.3	1720.6	1713.5	1684.4	1628.4	1719.3	1708.5	1665.9	1590.6	1720.7	1713.4	1684.5	1629	1719.3	1708.4	1666.1	1591.3
Height = 4.5, Width = 30																	
CC	21,156	21,136	21,132	21,104	21,010	21,116	21,051	20,787	20,323	21,134	21,121	21,054	20,899	21,117	21,040	20,748	20,244
CF	5806.3	5796.8	5772.4	5669.7	5476.1	5792.4	5753.9	5604.5	5344.2	5796.8	5771.4	5670.2	5477.8	5792.2	5753.4	5604.4	5345.1

**Table 7** Buckling load for all aluminium alloy plates with length  $L = 300$  mm

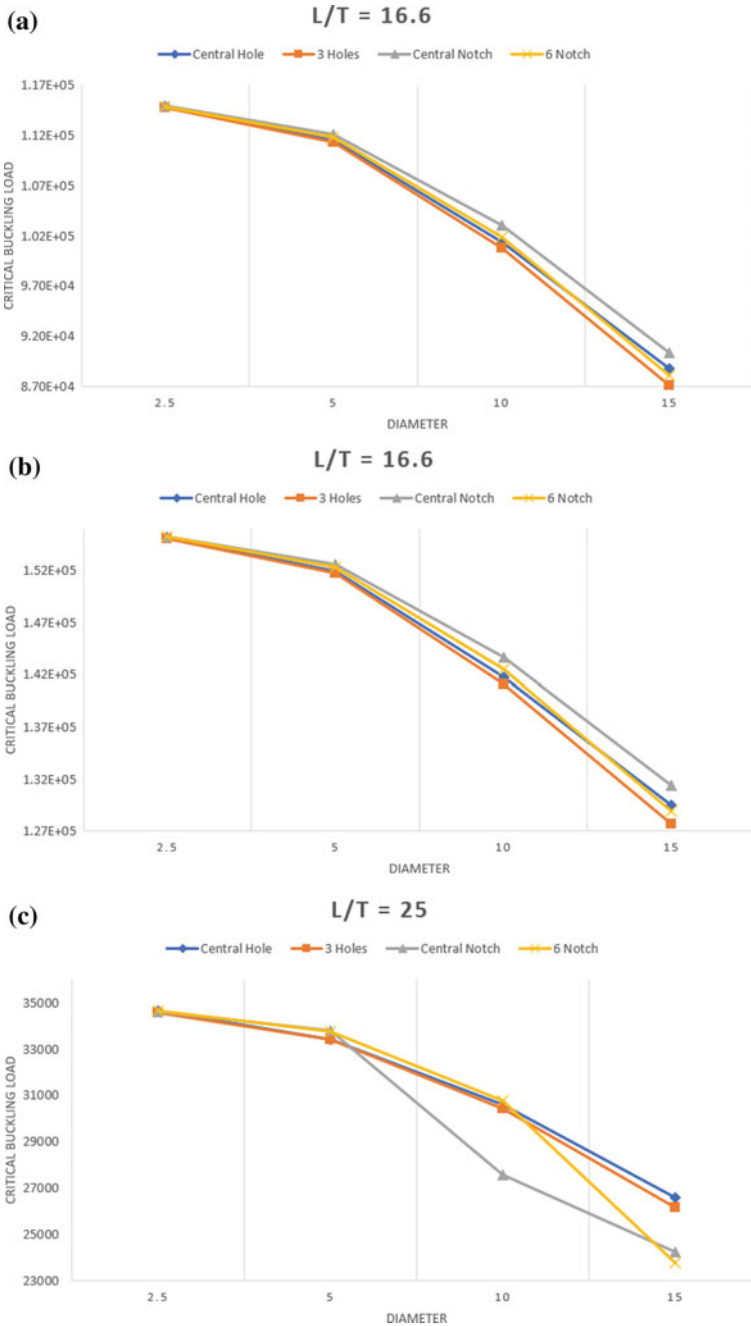
Mode 1																	
Height = 3, Width = 40																	
Simple plate	Plate with centre hole			Plate with 3 holes			Plate with 2 notch			Plate with 6 notch							
	d = 2.5	d = 5	d = 10	d = 15	d = 2.5	d = 5	d = 10	d = 15	d = 2.5	d = 5	d = 10	d = 15					
CC	2842	2700.5	2690.1	2634.9	2543.9	2701.6	2685	2635.3	2543.7	2706.8	2690.1	2638.9	2552.6	2706.7	2700.1	2636.6	2548.9
CF	177.22	177.21	176.76	174.95	171.68	177.14	177.55	173.79	169.19	177.21	176.75	174.95	171.7	177.13	176.45	173.77	169.2
Height = 4.5, Width = 40																	
CC	9590.1	9090.8	9056	8865.1	8553.9	9087.6	9040.4	8857.6	8547.4	9554.2	9497.5	8867.1	8567.2	9551.4	9503.6	8863	8556.3
CF	597.68	597.64	595.61	589.73	578.48	597.39	594.98	585.64	569.72	597.27	595.58	589.71	578.48	597	594.54	585.53	569.7
Height = 3, Width = 30																	
CC	2119.9	2015.8	2002.4	1948	1927.7	2022	2002.5	1957.8	1845.3	2047.9	2034.3	1942.4	1876.9	2056.4	2034.4	1978.6	1874.6
CF	132.5	132.44	131.99	130.08	126.19	132.26	131.69	128.79	123.85	132.39	131.93	129.95	126.26	132.31	131.61	128.84	123.77
Height = 4.5, Width = 30																	
CC	7154.2	6786	6739.5	6546.9	6196.5	6784	6721	6545	6192.2	6820	6740.1	6552.9	6210.4	6820.7	6773.2	6545	6201.3
CF	446.85	446.66	445.07	438.4	425.34	446.42	443.54	434.3	416.69	446.67	445.03	438.37	425.35	446.4	443.97	434.23	416.72
Mode 2																	
Height = 3, Width = 40																	
CC	5837.3	5572.2	5571.5	5566.8	5554	5571.3	5564.4	5517.5	5442.8	5583.2	5574.1	5562.3	5543.2	5580.1	5580.7	5511.7	5435.6
CF	1599.2	1598.8	1594.9	1579	1550.5	1598.2	1602.8	1568.4	1527.9	1598.8	1594.8	1579.1	1551	1598.1	1592.2	1568.4	1528.5
Height = 4.5, Width = 40																	
CC	19,670	19,740	19,619	18,725	18,679	18,724	18,685	18,535	18,281	19,630	19,612	18,686	18,606	19,615	19,578	18,515	17,256.1

(continued)



**Table 7** (continued)

Mode 1																	
Height = 3, Width = 40																	
Simple plate	Plate with centre hole			Plate with 3 holes			Plate with 2 notch			Plate with 6 notch							
	d = 2.5	d = 5	d = 10	d = 15	d = 2.5	d = 5	d = 10	d = 15	d = 2.5	d = 5	d = 10	d = 15					
CF	5389.8	5389.5	5370.6	5320	5221.9	5387.2	5365.7	5282.7	5142.9	5385.2	5370.4	5320.3	5223	5382.7	5360.9	5282.5	5144.1
Height = 3, Width = 30																	
CC	4339.4	4154.6	4153.5	4150.1	4128.5	4337.6	4286.3	4141.2	4026.8	4214.3	4212.6	4201.5	4187.9	4227.6	4200	4154.8	4077.2
CF	1194	1193.7	1189.7	1172.9	1138.9	1191.9	1187	1161	1118.2	1193.2	1189.2	1171.7	1139.8	1192.5	1186.3	1161.8	1117.8
Height = 4.5, Width = 30																	
CC	14,649	13,974	13,971	13,951	13,910	13,960	13,915	13,773	13,512	14,035	13,967	13,932	13,868	14,026	13,985	13,750	13,484
CF	4024.8	4023.8	4009.8	3951.1	3837.7	4021.6	3995.2	3914.3	3760.9	4023.9	4009.5	3951.1	3838.5	4021.6	3999.9	3913.8	3761.9



**Fig. 4** Variation of buckling load for a plate of length 75 mm-mode 1 **a** CC condition width 30 **b** CC condition width 40 **c** CC condition width 30 **d** CC condition width 40 **e** CF condition width 30 **f** CF condition width 40 **g** CF condition width 30 **h** CF condition width 40

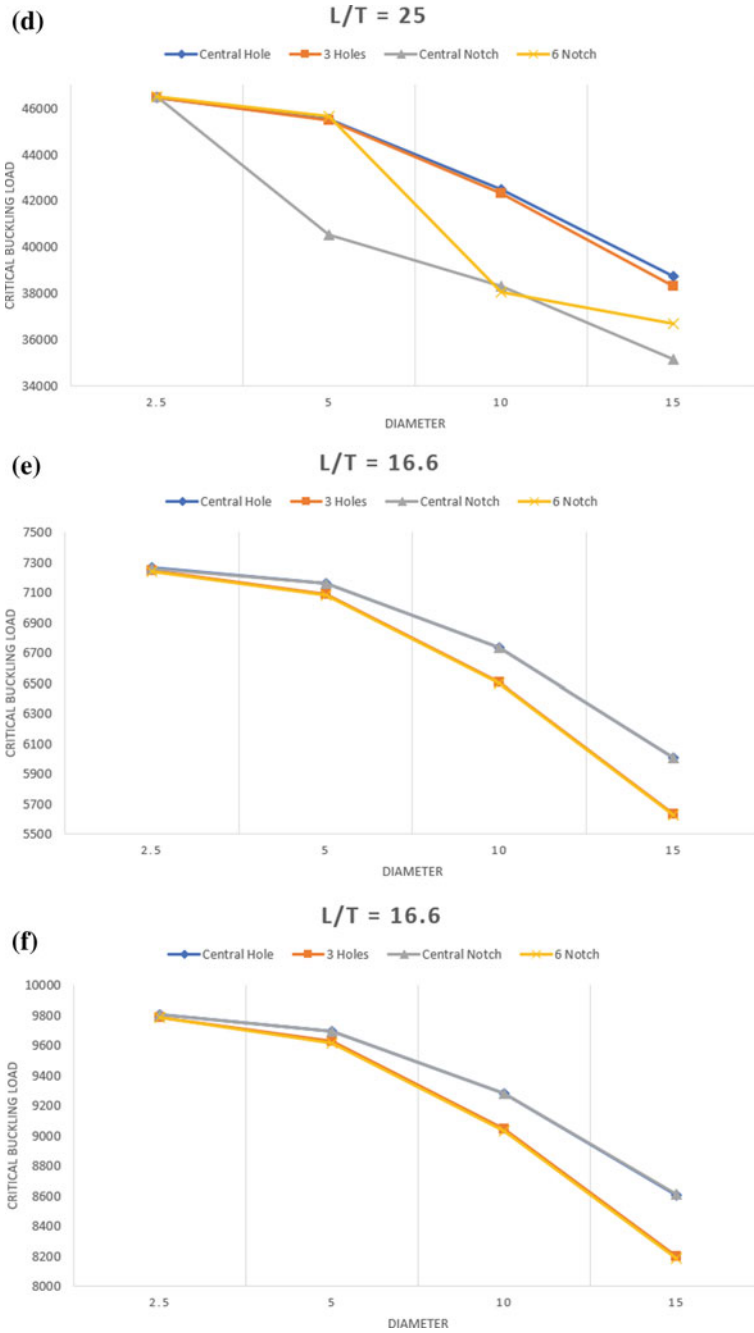


Fig. 4 (continued)

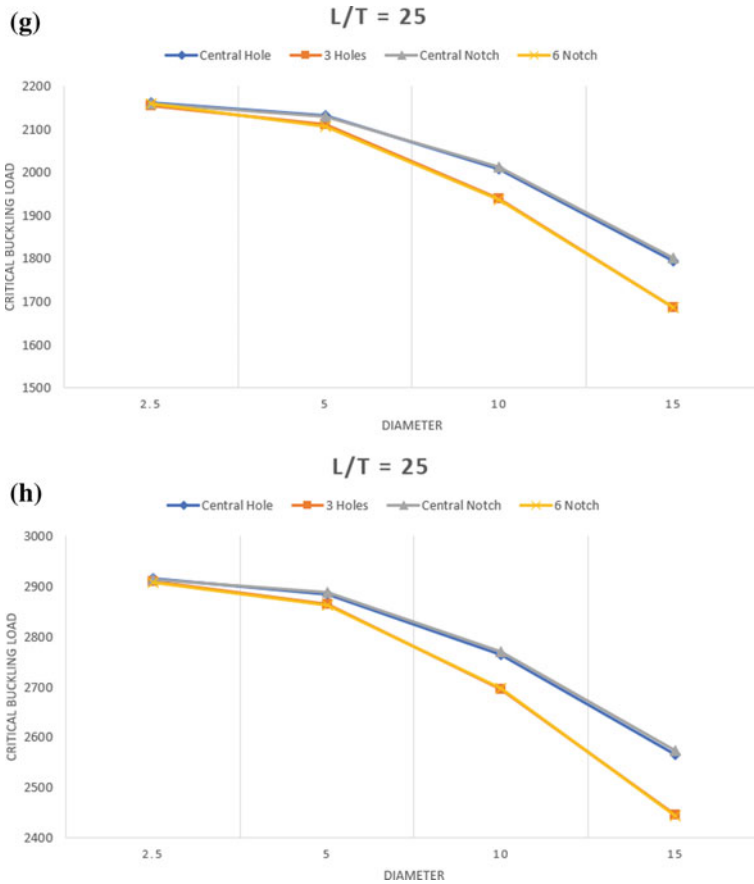
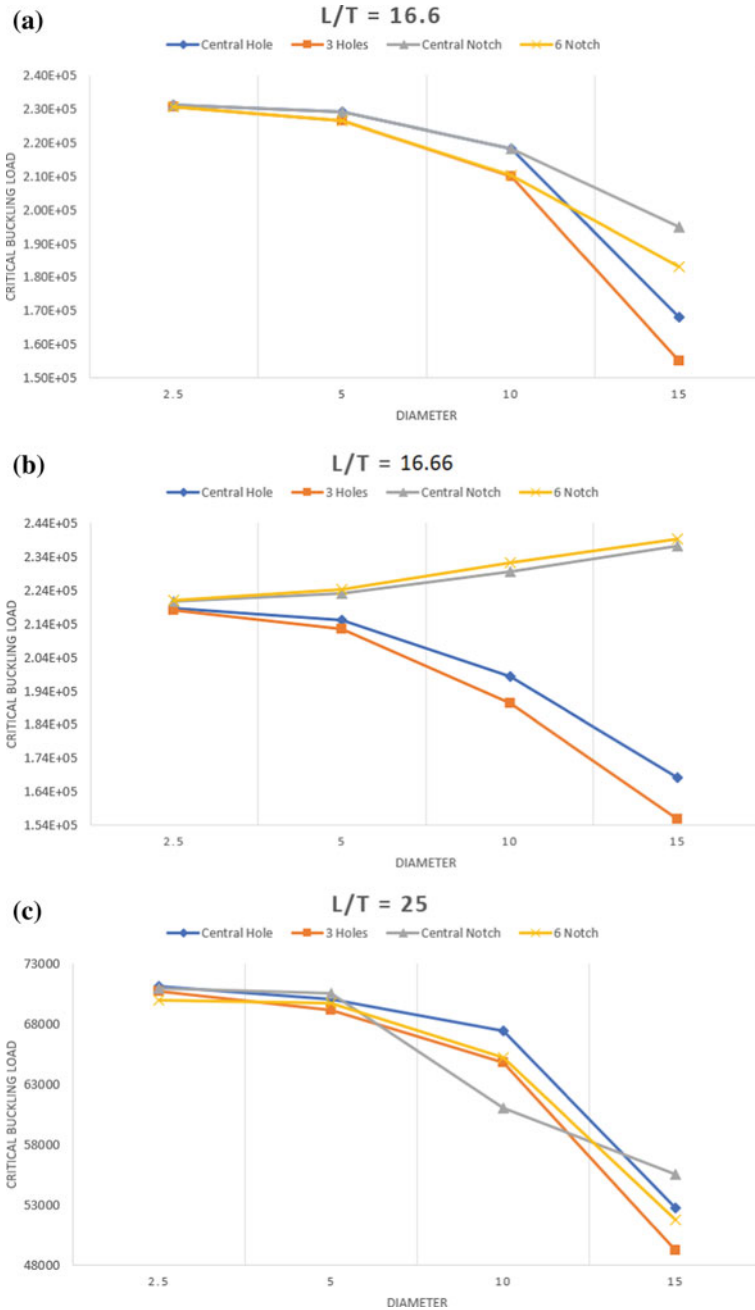


Fig. 4 (continued)

### 5.1 Effect of Cut-Outs

Aluminium alloy plates with and without cut-outs are extensively used in industries for their easy manufacturability and low-cost purposes. To meet the design requirement, it is important to understand the buckling response of such plates. In this section, the effect of the central hole, 3 holes along with the central notch, and 6 notches are taken into account.

It can be seen that the buckling load gradually decreases with the introduction of holes and notches into the simple geometry (Figs. 4 and 5). Comparing the result obtained for the plate of length  $L = 75$  mm in Mode 1, we can notice that as the diameter of the cut-out increased there's a drop of about 17% in buckling load for a plate with a central hole, 18% drop for a plate with 3 holes, 25% drop for a plate with central notch and 22% drop for a plate with 6 notches in the CC boundary



**Fig. 5** Variation of buckling load for a plate of length 75 mm-mode 2 **a** CC condition width 30 **b** CC condition width 40 **c** CF condition width 30 **d** CC condition width 40 **e** CF condition width 30 **f** CF condition width 40 **g** CF condition width 30 **h** CF condition width 40

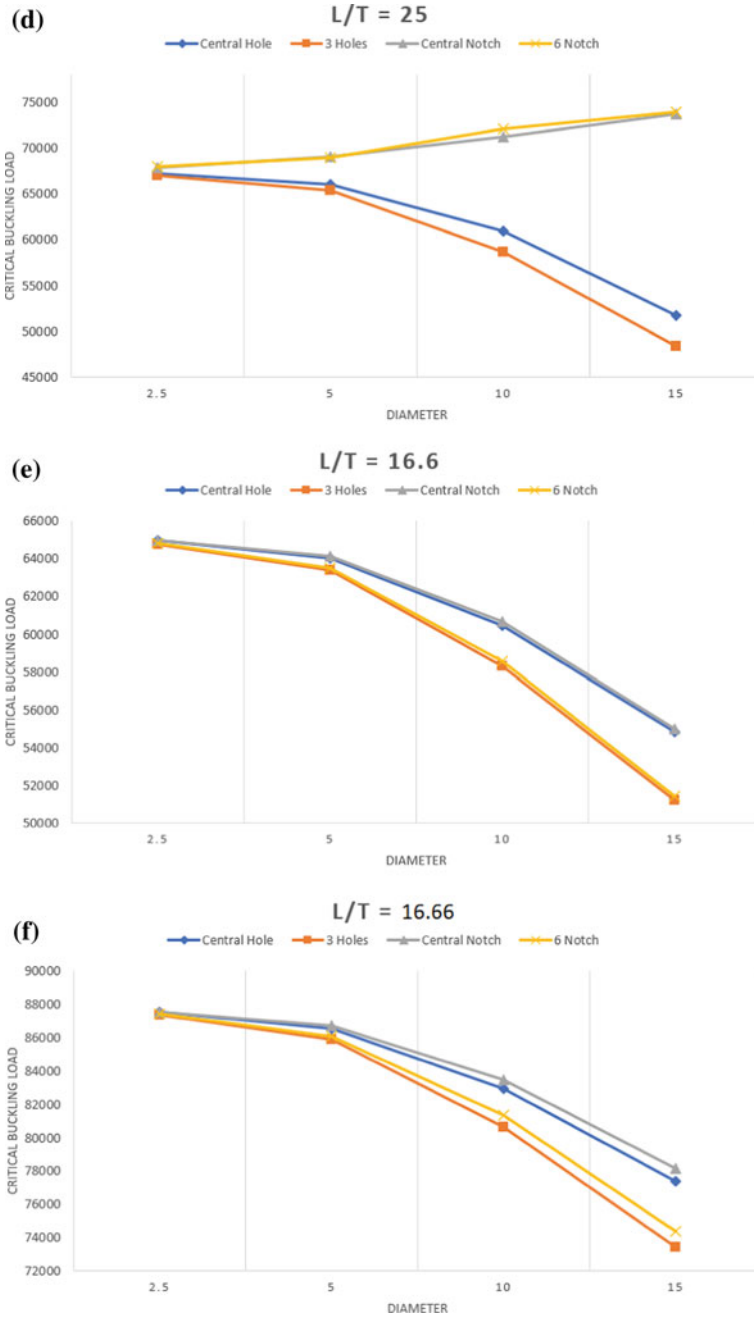


Fig. 5 (continued)

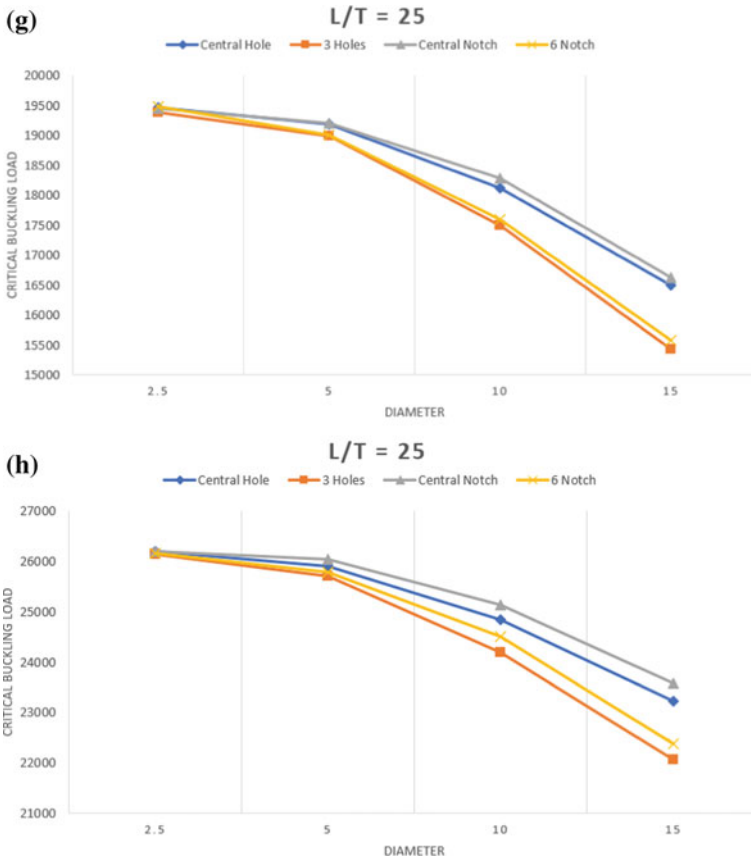
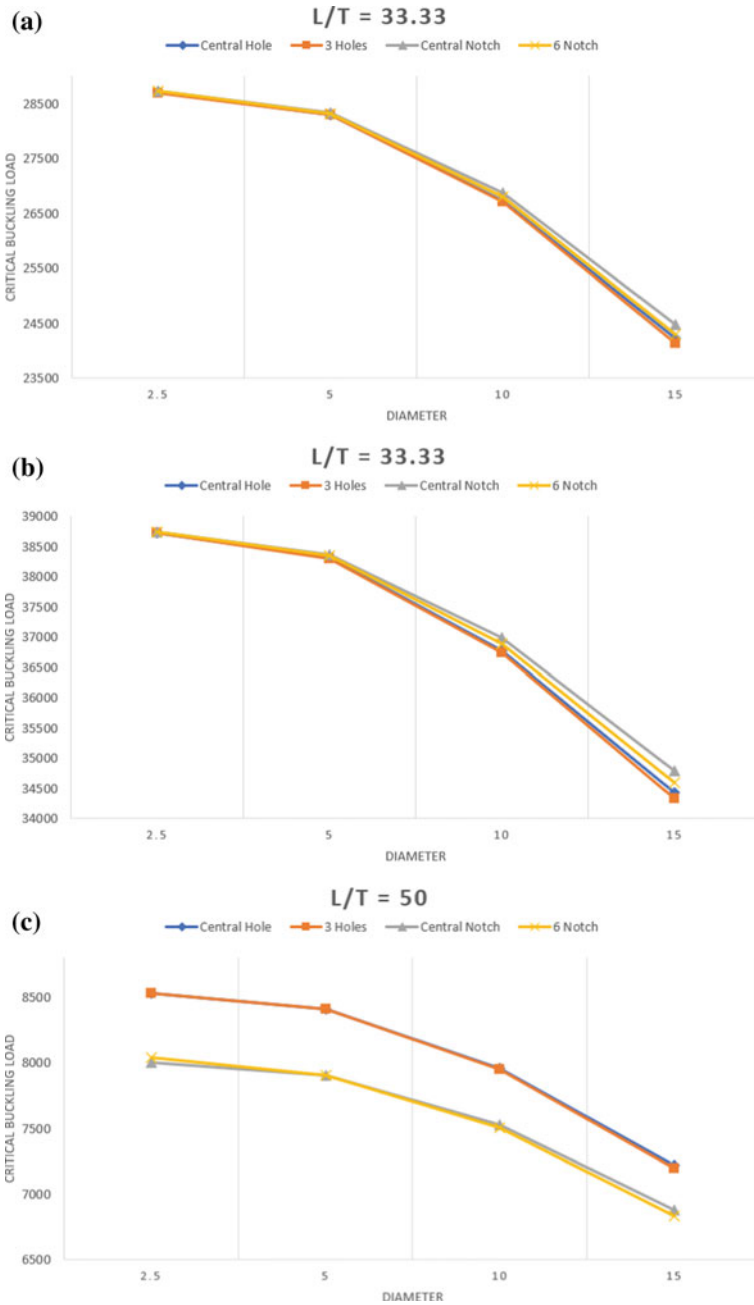


Fig. 5 (continued)

conditions. A similar decrease in buckling load for increasing diameter of cut-outs can be observed in all other cases of varying lengths and other boundary conditions (CF), especially in Mode 1 buckling analysis (Figs. 6, 8 and 10). As the investigation is carried out with all possible  $L/T$  ratios it has become easy to compare the effect of different cut-outs with varying  $L/T$  ratios.

With the increase in the  $L/T$  ratio, the influences of cut-outs on buckling loads are boosted. There is a drastic drop in buckling load under CC boundary conditions for different cut-outs as the  $L/T$  ratio increased. This can be noticeably seen in the Mode 1 table for a plate of Length  $L = 75$  mm (Table 5).

Similar trends are followed in all cases of varying lengths. After tabulating all the buckling loads, it merits referencing that even though plates with central hole patterns have somewhat less buckling load than those with a central notch pattern at a lesser diameter range, but the diameter increased the buckling load of holes was a little higher than the notches. The conduct of plates with holes and notch patterns is



**Fig. 6** Variation of buckling load for a plate of length 150 mm-mode 1 **a** CC condition width 30 **b** CC condition width 40 **c** CC condition width 30 **d** CC condition width 40 **e** CF condition width 30 **f** CF condition width 40 **g** CF condition width 30 **h** CF condition width 40



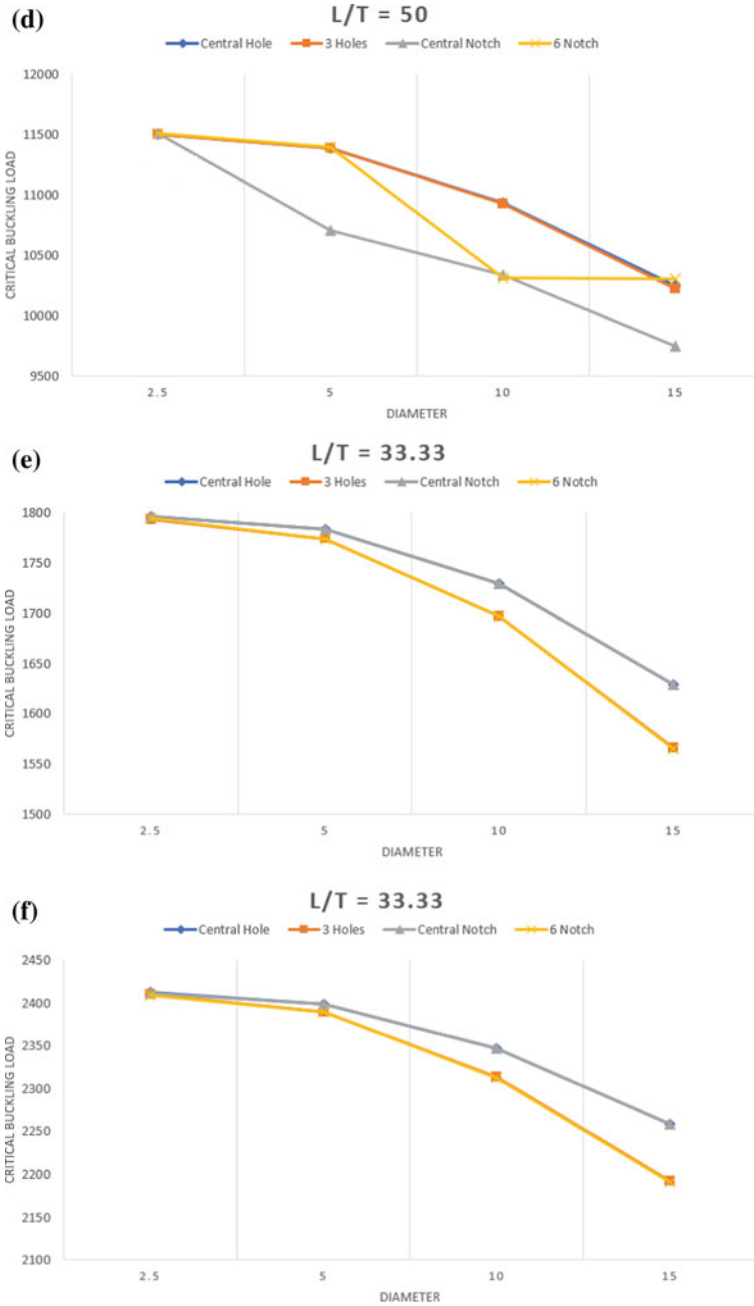


Fig. 6 (continued)

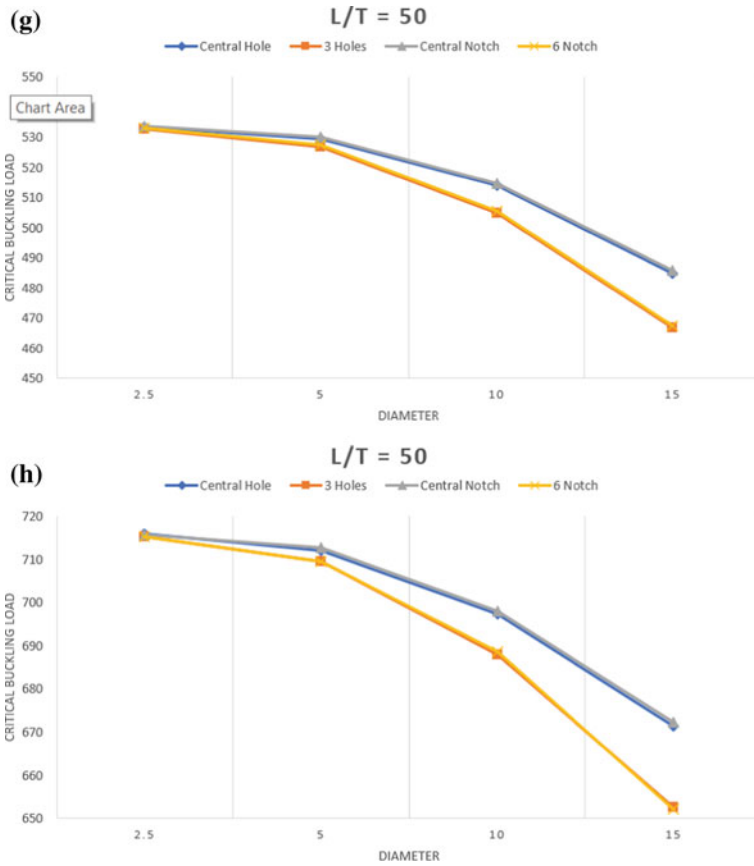
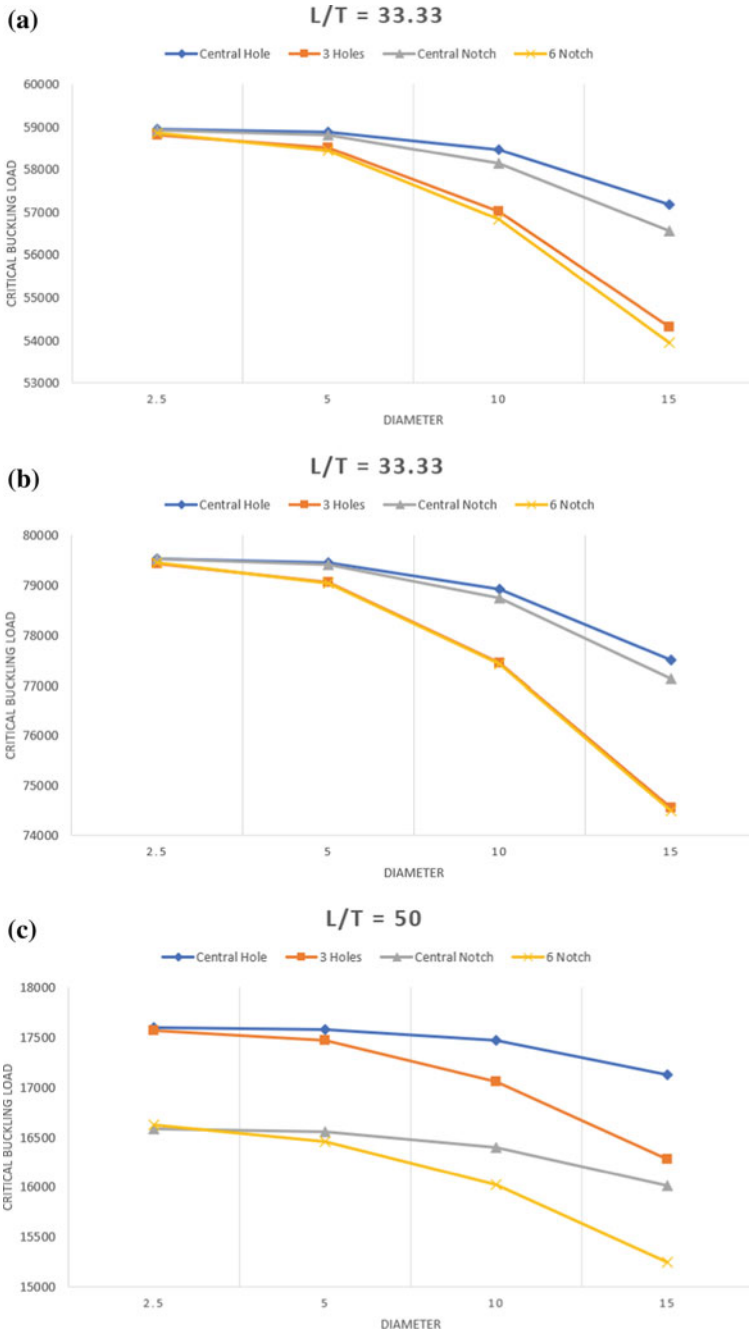


Fig. 6 (continued)

very much alike, regarding buckling load. This can be clarified by the way that the regions of holes and notch patterns are equivalent.

When the Mode 2 buckling analysis is considered, the same decrease in buckling load has been noticed for increasing diameters of cut-outs for nearly all cases of varying length, width and  $L/T$  ratio. However, at one special case, the buckling loads increased as the diameter of the cut-out increased, these special cases were noticed under the plate of length  $L = 75$  mm, width  $W = 40$  (Fig. 5). This increase in buckling load was only observed in this case and all other types of the plate had their buckling load decreasing for an increase in diameter of cut-outs (Figs. 7, 9 and 11).



**Fig. 7** Variation of buckling load for a plate of length 150 mm-mode 2 **a** CC condition width 30 **b** CC condition width 40 **c** CC condition width 30 **d** CC condition width 40 **e** CF condition width 30 **f** CF condition width 40 **g** CF condition width 30 **h** CF condition width 40

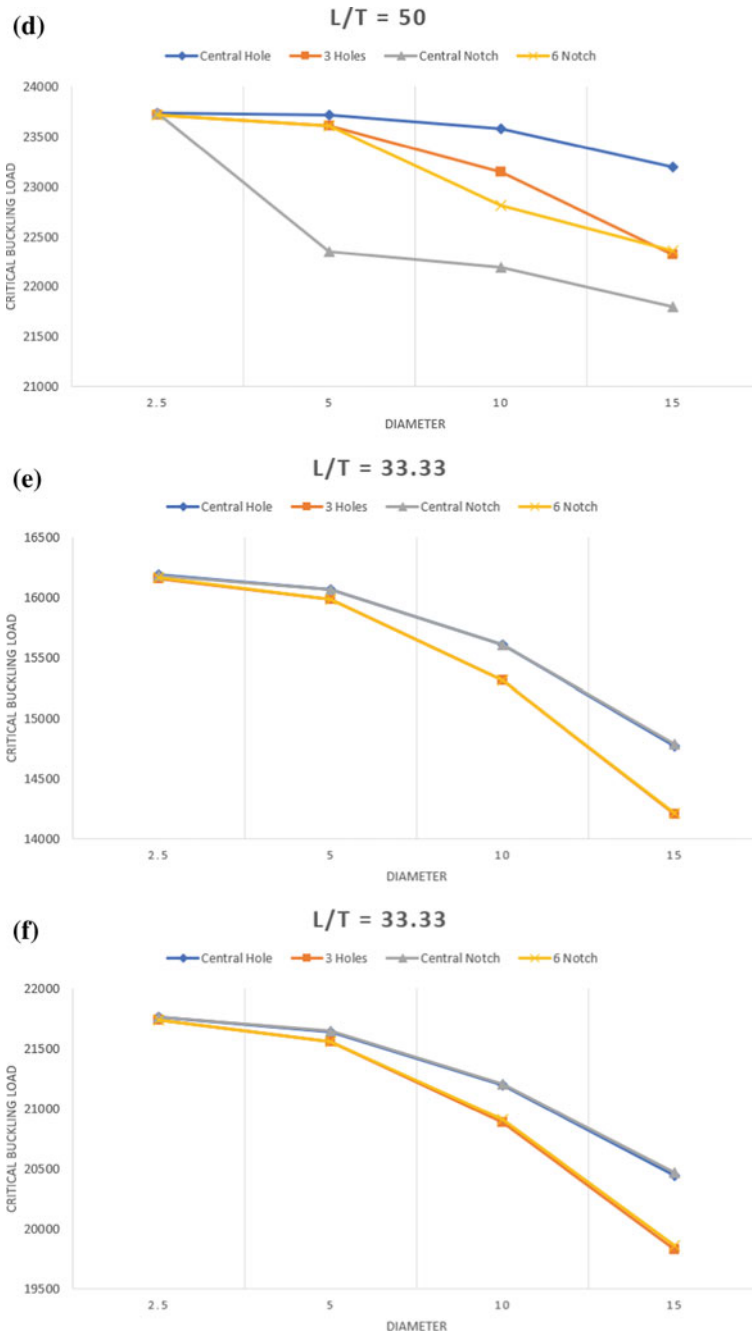


Fig. 7 (continued)

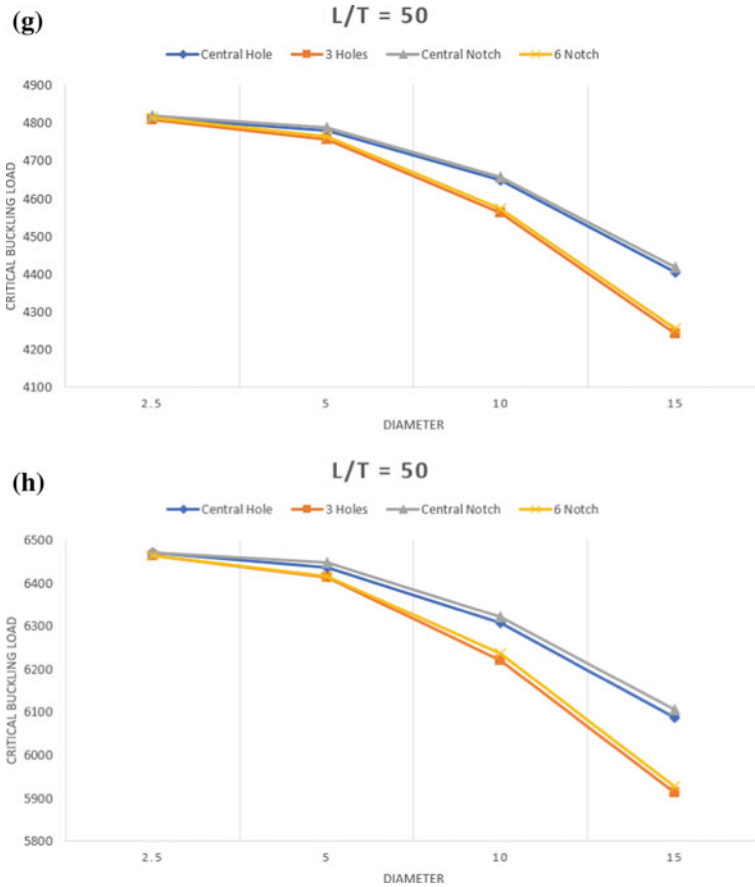
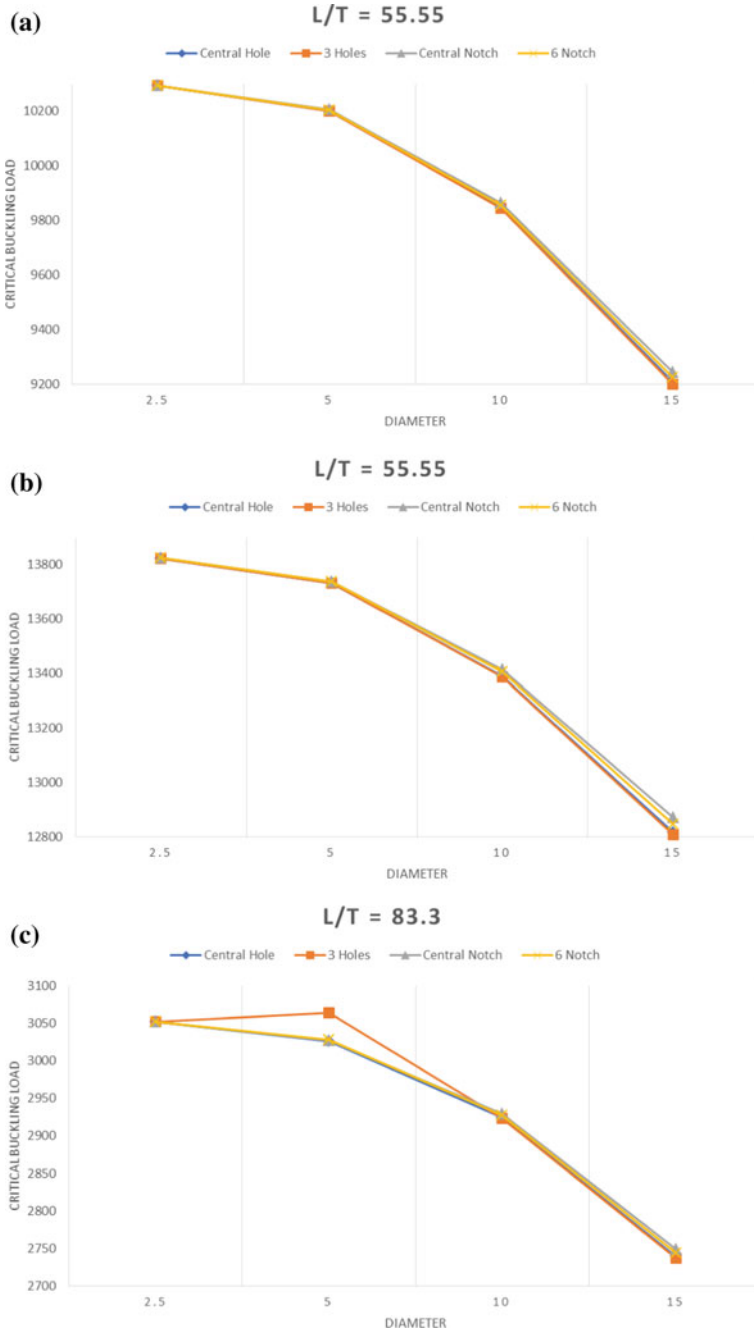


Fig. 7 (continued)

### 5.2 Effect of Length to Thickness Ratio

This part of the paper deals with the effect of length to thickness ratio on buckling load for different plate dimensions. As mentioned earlier in Table 2, totally eight different  $L/T$  ratios were used in this study. All the possible buckling loads in both Mode 1 and Mode 2 for different  $L/T$  ratios were tabulated in Tables 4, 5, 6, and 7. As mentioned earlier, buckling loads from simple plates are used to study the effect of the  $L/T$  ratio. As expected, the numerical analysis showed the reduction in buckling load for increasing  $L/T$  ratio which can be noticed in both Fig. 12 for Mode 1 and Fig. 13 for Mode 2. The reduction in buckling load as the  $L/T$  ratio increased from 16.66 to 100 was about 98% in all the cases on which the buckling analysis is studied. This drop has to be considered, whilst design components which include



**Fig. 8** Variation of buckling load for a plate of length 250 mm-mode 1 **a** CC condition width 30 **b** CC condition width 40 **c** CC condition width 30 **d** CC condition width 40 **e** CF condition width 30 **f** CF condition width 40 **g** CF condition width 30 **h** CF condition width 40

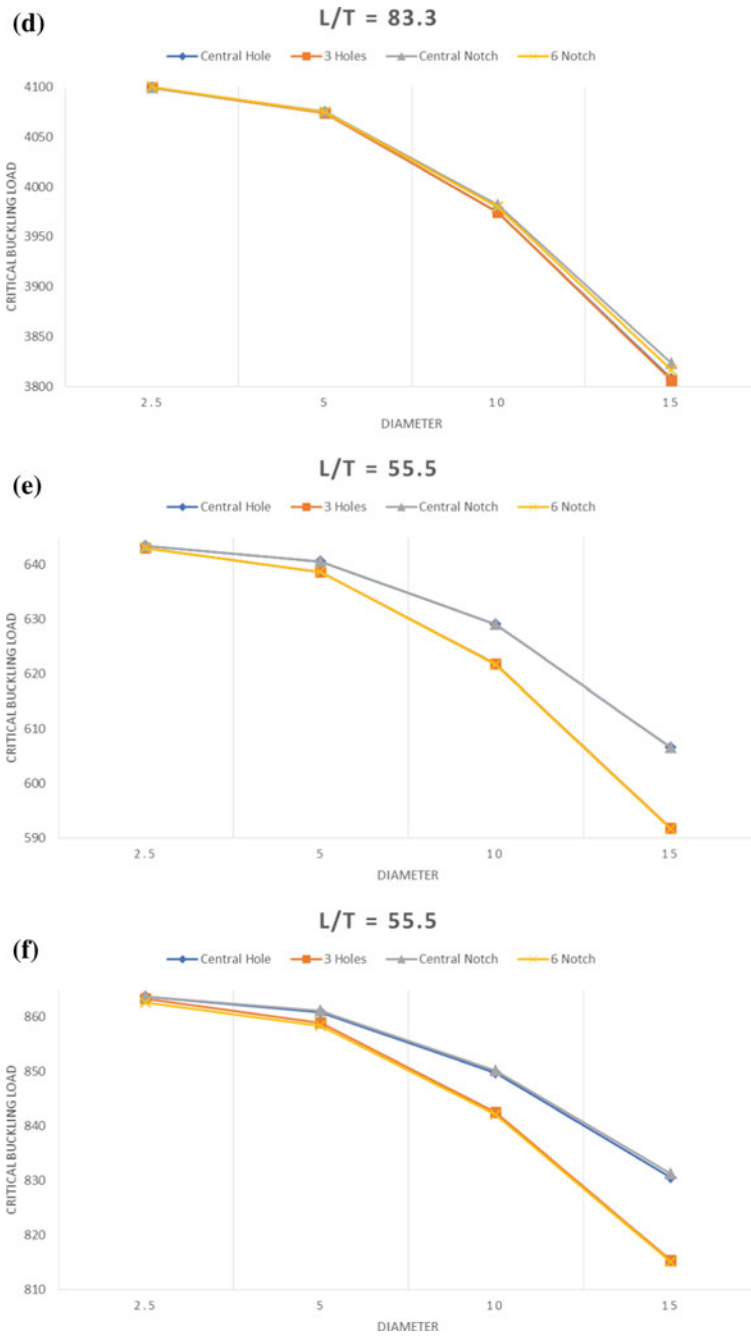


Fig. 8 (continued)

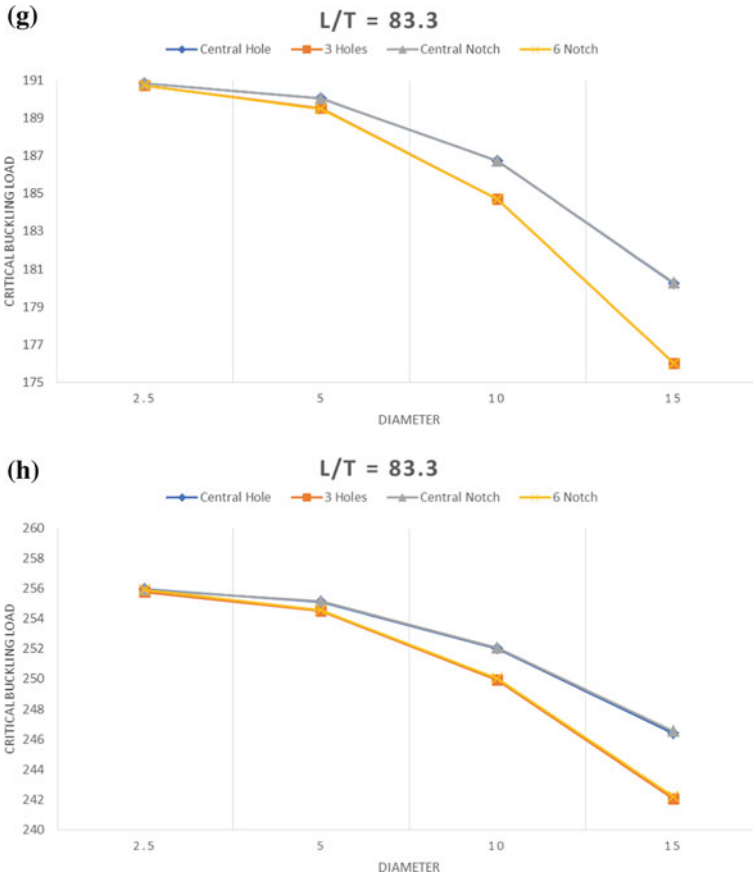
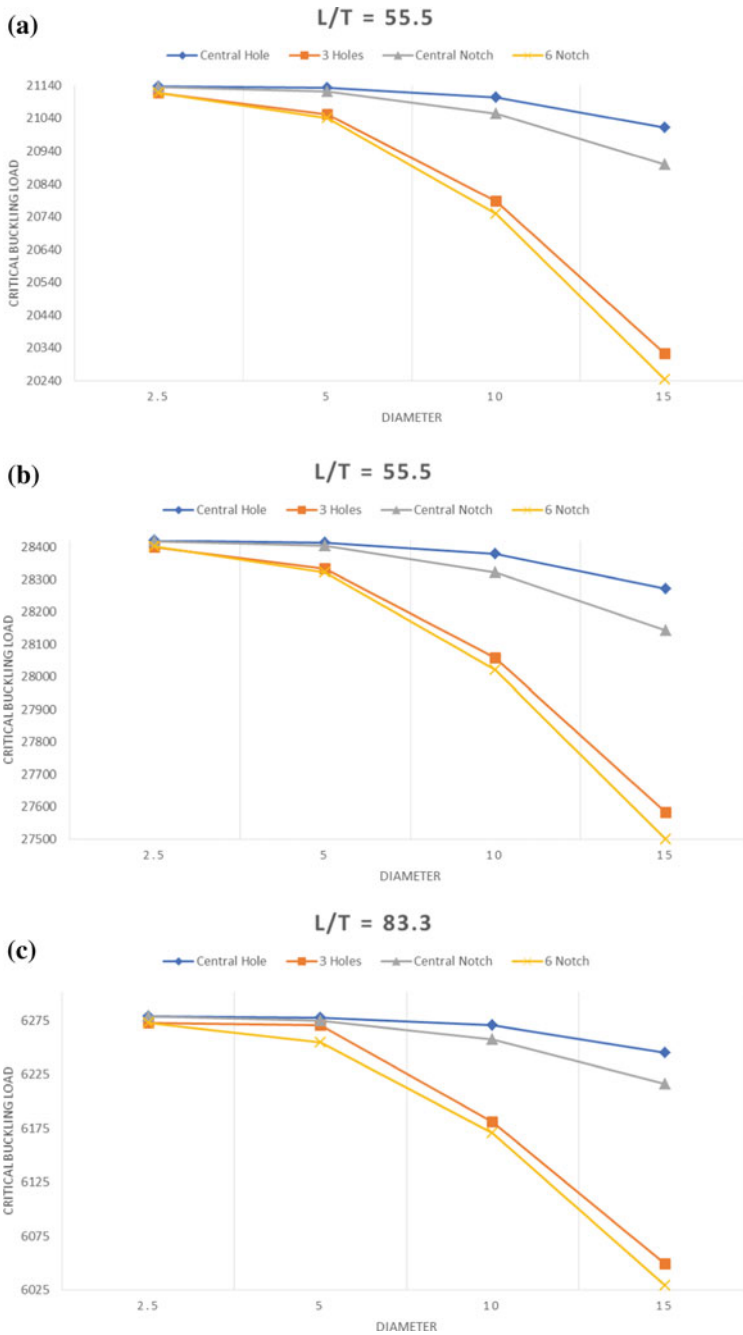


Fig. 8 (continued)

plates because the  $L/T$  ratio plays a major role in buckling load and an optimum  $L/T$  ratio must be picked in any case.

In many cases, the buckling loads of different cut-outs of the same diameter have very similar values under the same  $L/T$  ratio. Another special case can be noticed from Figs. 12 and 13, i.e. the buckling load slightly increased for all boundary conditions despite the width, when the  $L/T$  ratio was around 55.5 and then decreased gradually as the  $L/T$  ratio increased further.





**Fig. 9** Variation of buckling load for a plate of length 250 mm-mode 2 **a** CC condition width 30 **b** CC condition width 40 **c** CC condition width 30 **d** CC condition width 40 **e** CF condition width 30 **f** CF condition width 40 **g** CF condition width 30 **h** CF condition width 40

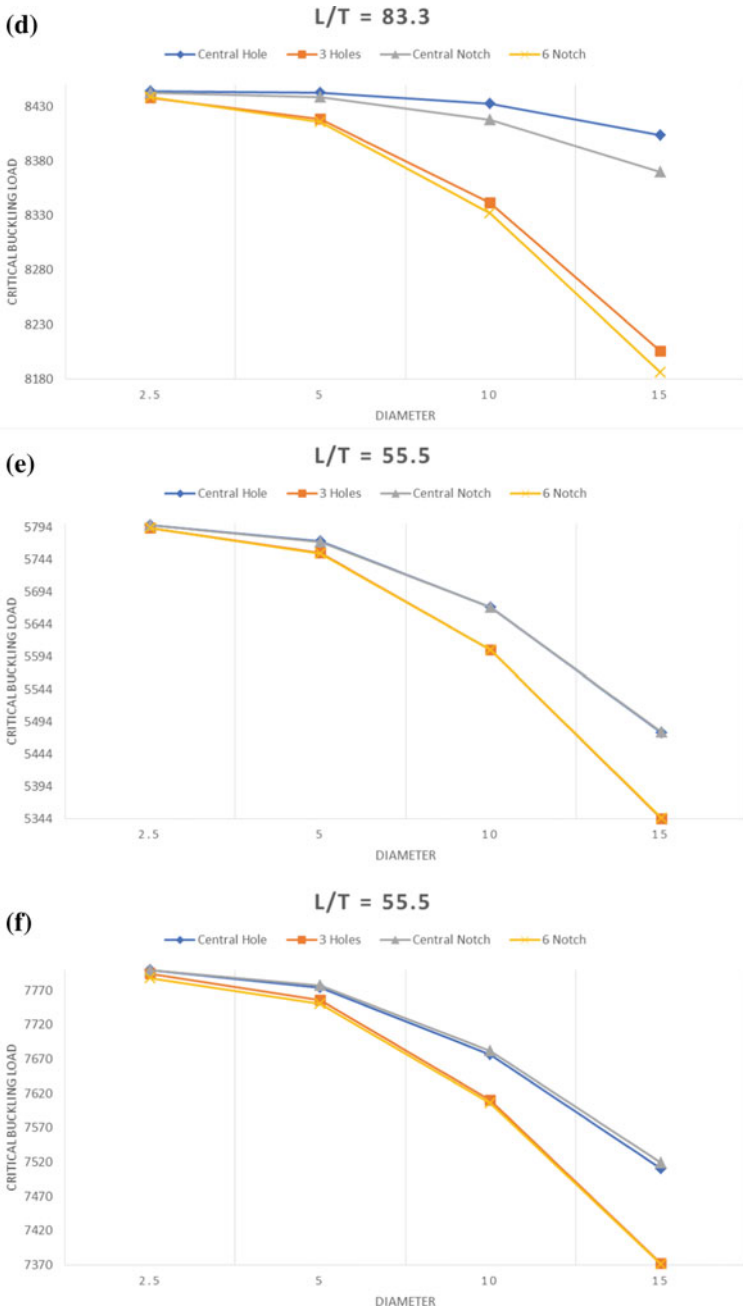


Fig. 9 (continued)

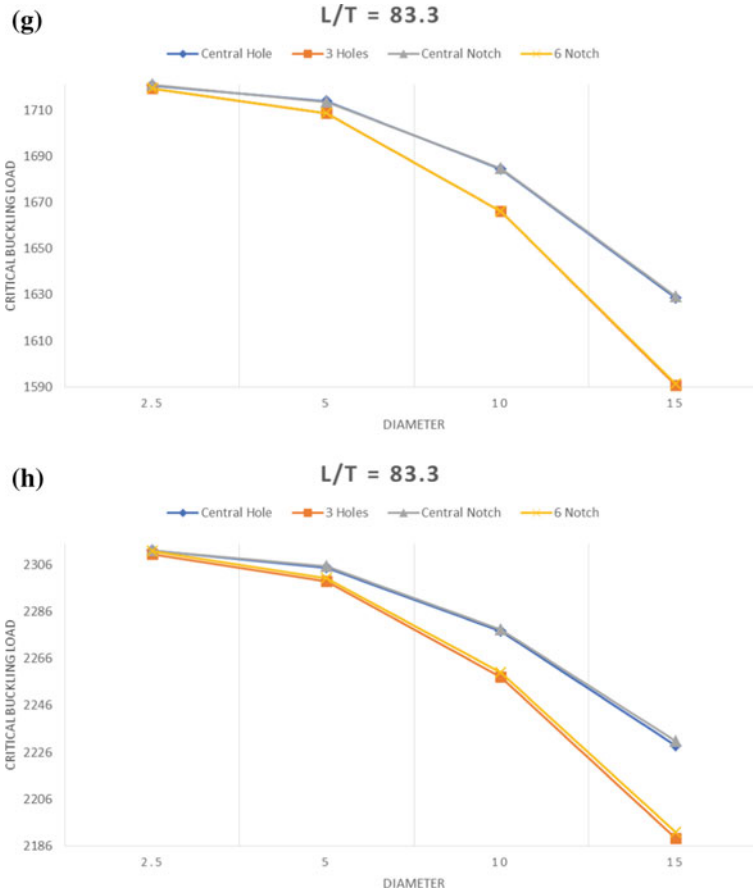
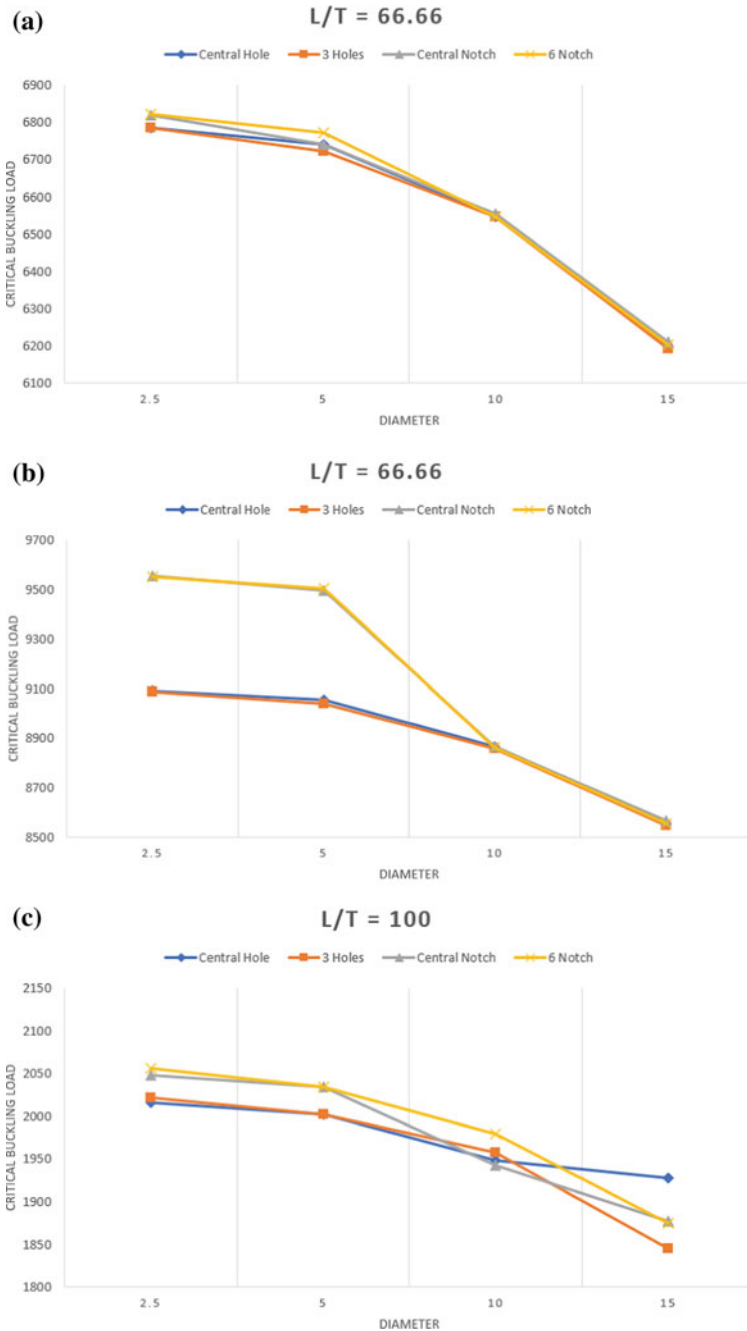


Fig. 9 (continued)

### 5.3 Effect of Boundary Conditions

In this study, the aluminium alloy plates are investigated with 2 different boundary conditions to exhibit different characteristics under buckling load. Boundary conditions have the highest effect on buckling load when compared to other parameters like cut-outs and  $L/T$  ratio. Tables 4, 5, 6, and 7 tabulates the buckling load of different plates under both CC and CF boundary conditions.

Figures 4, 5, 6, 7, 8, 9, 10 and 11 show the effect of boundary condition on rectangular plates under compression loads. It can be noticed from both table and figure that different boundary condition has a different influence on buckling load. In general, it can also be observed that the buckling loads under CC boundary conditions are much higher than the CF boundary conditions in all studied cases.



**Fig. 10** Variation of buckling load for a plate of length 300 mm-mode 1 **a** CC condition width 30 **b** CC condition width 40 **c** CC condition width 30 **d** CC condition width 40 **e** CF condition width 30 **f** CF condition width 40 **g** CF condition width 30 **h** CF condition width 40

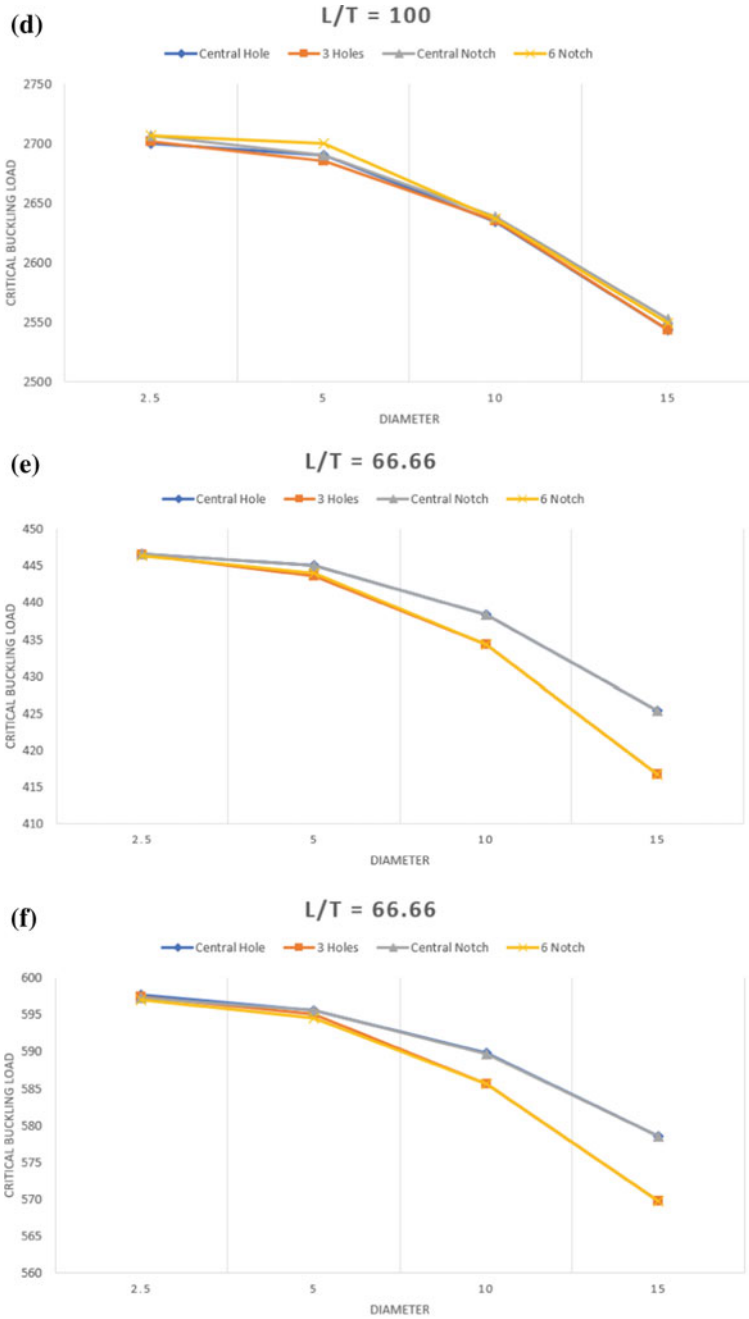


Fig. 10 (continued)

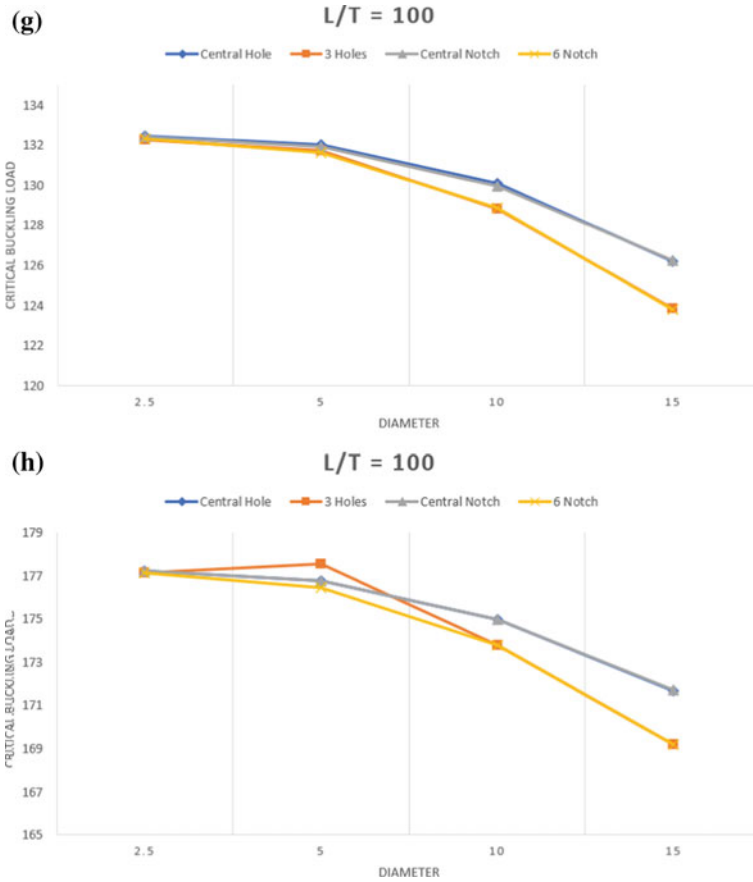
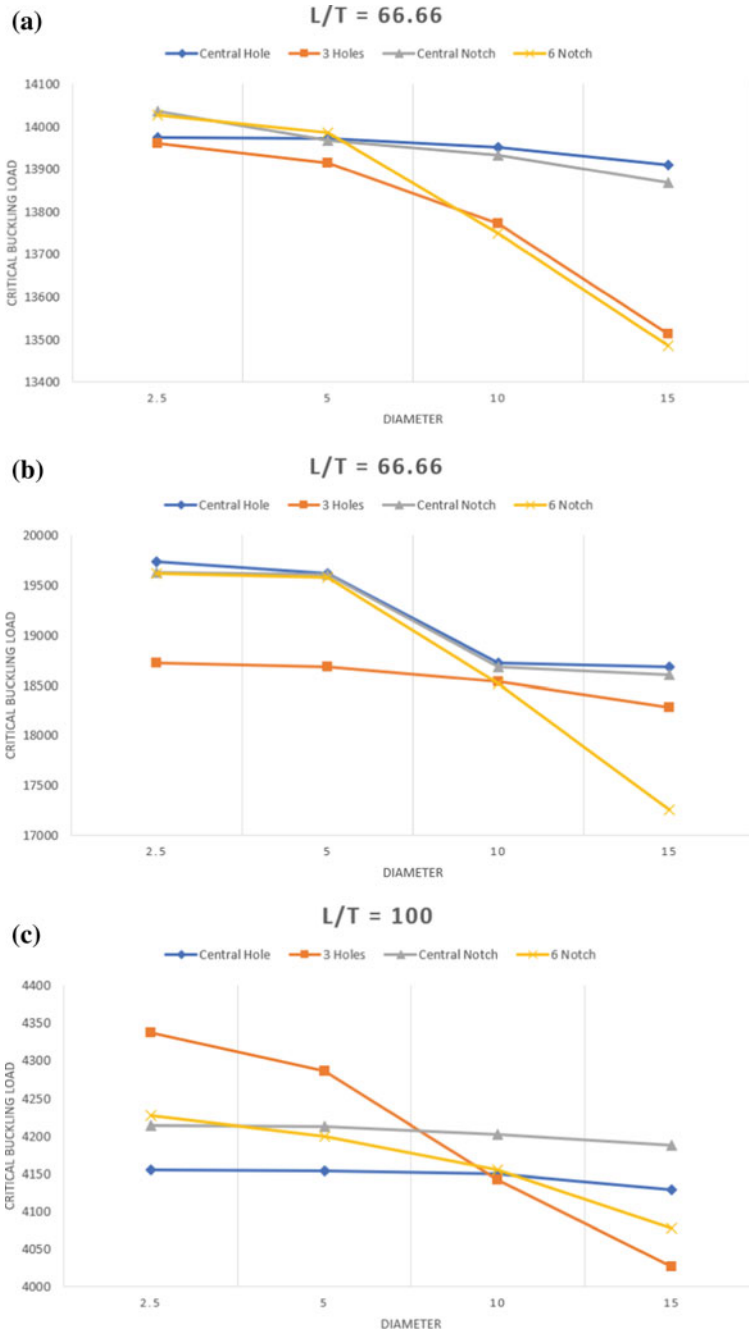


Fig. 10 (continued)

Results show that the buckling load of the plates impressively increased under all boundary conditions as the  $L/T$  proportion diminished. The distinction in buckling load brought about by the changing of  $L/T$  proportion is almost the equivalent for every one of the boundary conditions. The test results likewise foresee essentially a similar pattern. Due to the rigidity of the CC boundary condition, they usually possess a higher buckling load than the CF boundary condition despite the influence of other effects of cut-outs and  $L/T$  ratio.

From Fig. 12 and Fig. 13, we can notice that the buckling load for CC conditions is much greater than the CF conditions for chosen width and a similar trend is followed in both Modes of buckling analysis. When compared, there is a constant drop of about 70–75% in buckling load from CC boundary condition to CF boundary conditions for all  $L/T$  ratios.



**Fig. 11** Variation of buckling load for a plate of length 300 mm-mode 2 **a** CC condition width 30 **b** CC condition width 40 **c** CC condition width 30 **d** CC condition width 40 **e** CF condition width 30 **f** CF condition width 40 **g** CF condition width 30 **h** CF condition width 40

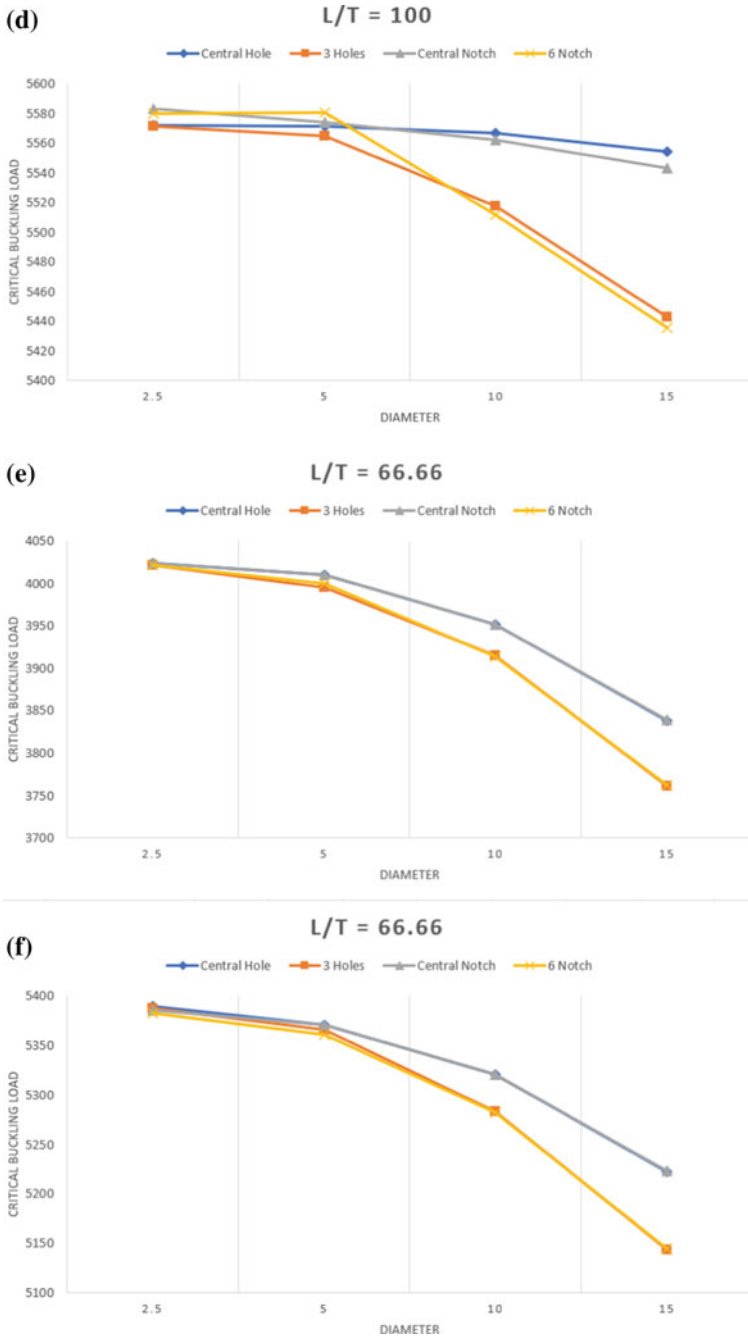


Fig. 11 (continued)



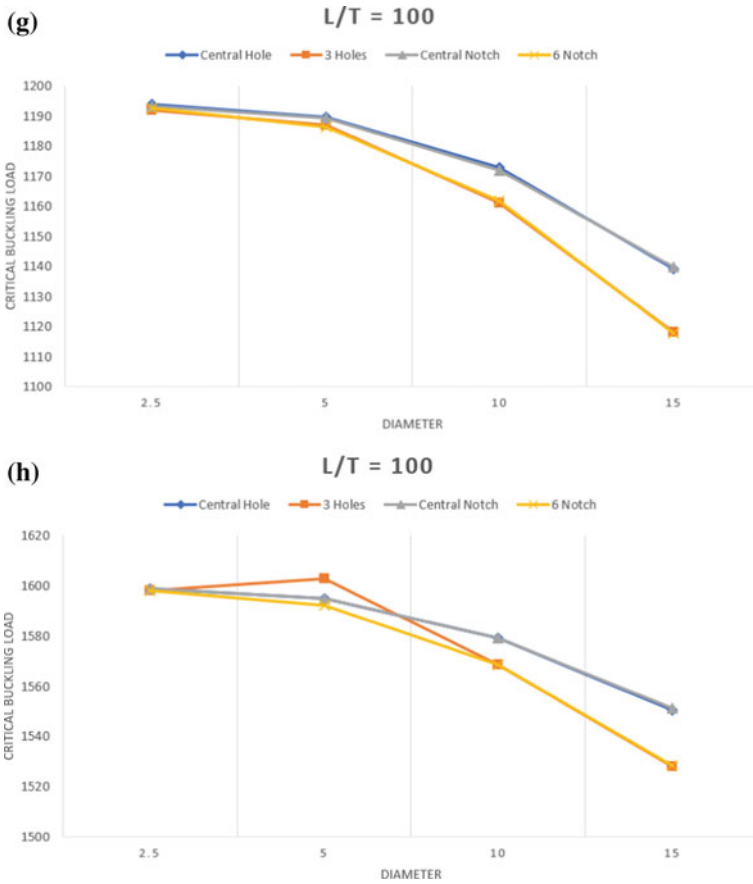


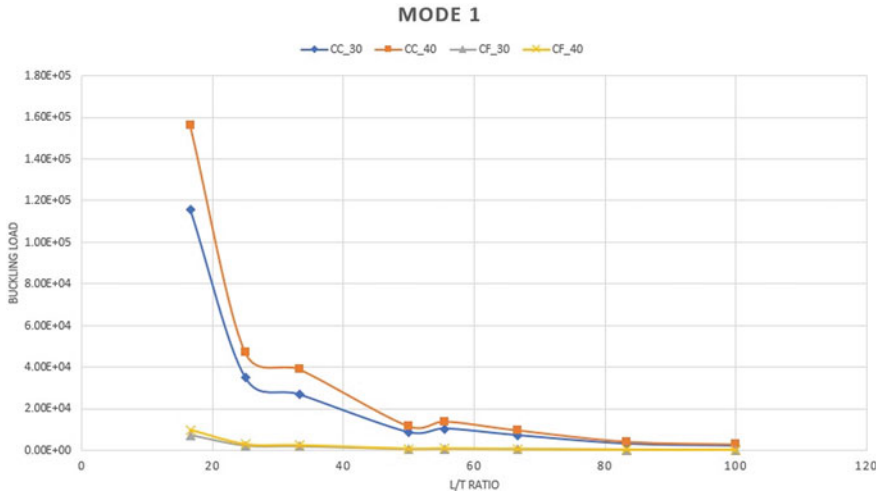
Fig. 11 (continued)

## 6 Conclusion

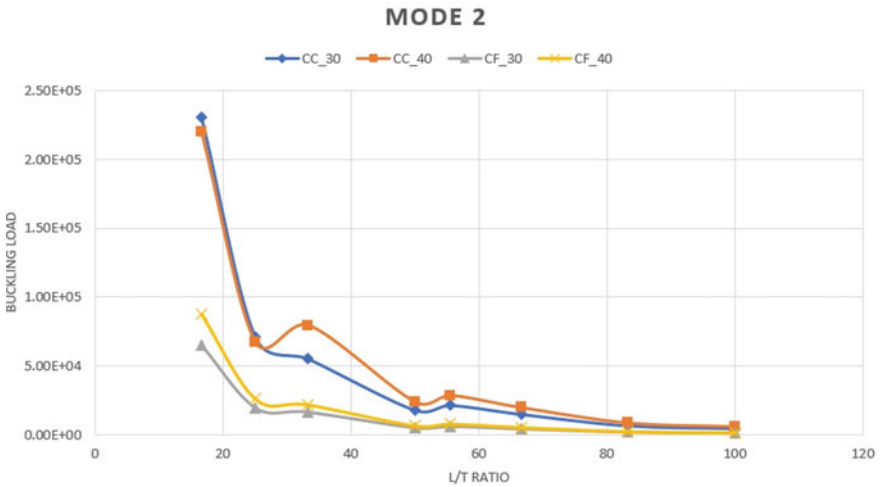
In this article, the buckling reaction of aluminium alloy rectangular plates with two different boundary conditions is considered. The considered rectangular plates have changed the aspect ratio, cut-out shape. The test results for the numerical analysis are obtained from ANSYS finite element code after proper validation of the integrity of this tool.

From the present numerical analysis study, the following conclusions can be made.

1. The diminishing buckling load for both Mode 1 and Mode 2 due to the presence of cut-outs was found to be prominent. With the increase in diameter of the various cut-outs, the buckling load was found to be dropping exponentially. This proves that the presence of cut-outs lowers the buckling load. From the



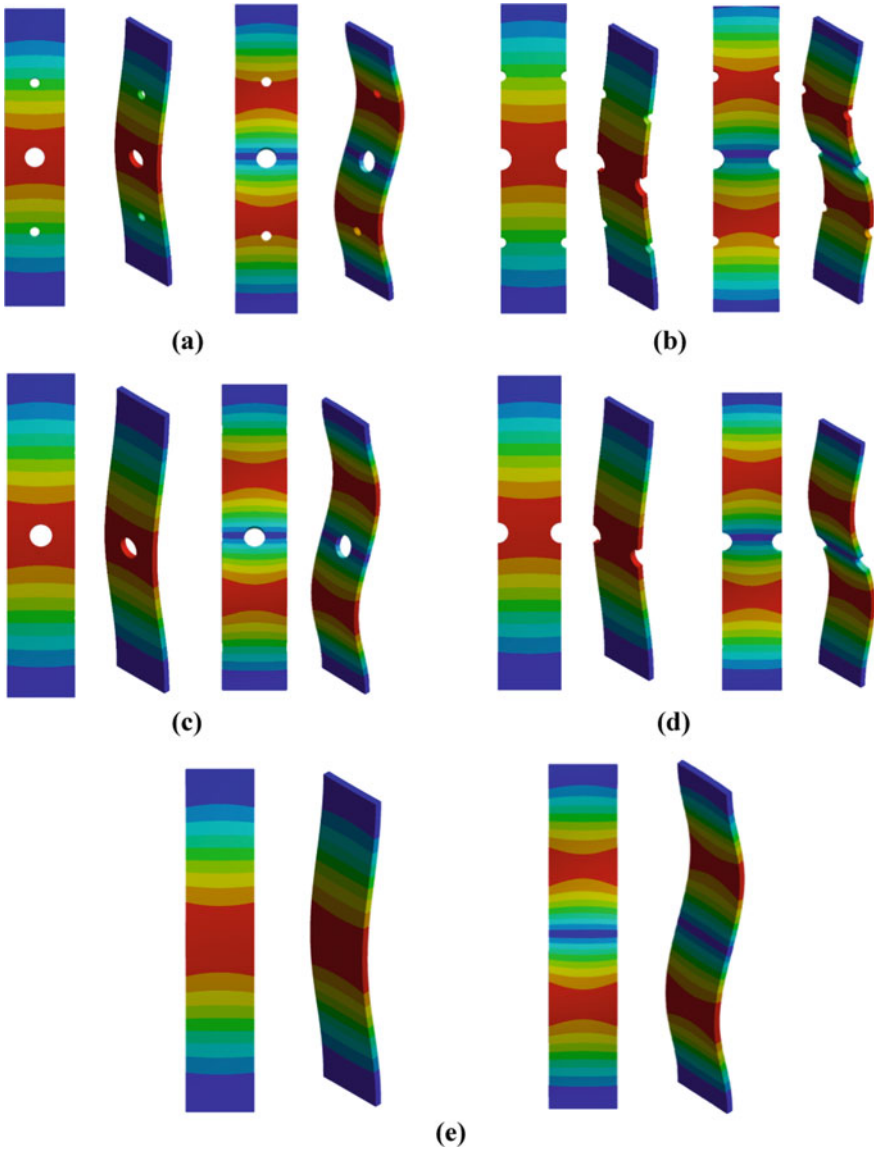
**Fig. 12** Effect of  $L/T$  ratio on the rectangular plate for different boundary condition and widths (Mode 1)



**Fig. 13** Effect of  $L/T$  ratio on the rectangular plate for different boundary condition and widths (Mode 2)

discussion on the effect of cut-outs, we can also conclude that the effect of both holes and notches behaves similarly.

2. The increase in buckling load in Mode 2 for  $L = 75$  mm and  $W = 40$  mm in CC boundary condition was noticed because of the close dimensional parameters, as the length and width dimensions are close to each other and also the rigidity



**Fig. 14** Visualization of both mode 1 and mode 2 buckling in a rectangular plate with different cut-outs **a** cut-out with 3 holes **b** cut-out with 6 notches **c** cut-out with central hole **d** cut-out with central notch **e** simple plate with no cut-outs

increase for smaller plates in CC boundary conditions, combined effect of these two reasons are the conclusion behind the increase in buckling load.

3. As the  $L/T$  ratio increased, the buckling load in both Modes decreased drastically. From the earlier discussion, we can conclude that the buckling load decreased about 98% when the  $L/T$  ratio increased from 16.66 to 100.
4. The clamped boundary condition showed the highest buckling load amongst the other boundary conditions. As already mentioned, it is only because of the rigidity that arises when components are clamped at ends. The buckling loads of CF conditions are much smaller when compared to CC boundary conditions. We can notice a drop of the buckling load of about 70–75% from CC to CF boundary condition for all widths despite the change in  $L/T$  ratio.

## References

1. Reddy JN (2006) Theory and analysis of elastic plates and shells, 2nd edn. CRC press
2. Megson THG (2005) Structural and stress analysis, Ed. Elsevier Butterworth-Heinemann
3. Yoo CH, Lee S (2011) Stability of structures: principles and applications. Elsevier
4. Rao LB, Rao CK (2010) Buckling analysis of circular plates with elastically restrained edges and resting on internal elastic ring support. *Mech Based Des Struct Mach* 38(4):440–452
5. Cheng B, Zhao J (2010) Strengthening of perforated plates under uniaxial compression: buckling analysis. *Thin-Walled Struct* 48(12):905–914
6. Rocha L, Isoldi L (Sep 2013) Constructal design applied to the elastic buckling of thin plates with holes
7. Åkesson B (2007) Plate buckling in bridges and other structures. Taylor, Francis
8. Eslami MR, Eslami J (2018) Buckling and postbuckling of beams, plates, and shells. Springer
9. Bryan GH (1891) On the stability of a plane plate under thrust in its own plane with application to the buckling of the side of a ship. *Proc Lond Math Soc* 22(1):54–67
10. Rao LB, Rao CK (2013) Fundamental buckling of circular plates with elastically restrained edges and resting on concentric rigid ring support. *Front Mech Eng* 8(3):291–297
11. El-Sawy KM, Nazmy AS (2001) Effect of aspect ratio on the elastic buckling of uniaxially loaded plates with eccentric holes. *Thin-Walled Struct* 39(12):983–998
12. El-Sawy KM, Martini MI (2007) Elastic stability of biaxially loaded rectangular plates with a single circular hole. *Thin-Walled Struct* 45(1):122–133
13. Timoshenko SV, Gere JM (1961) Theory of elastic stability. McGraw-Hill, New York
14. Moen D, Schafer BW (2009) Elastic buckling of thin plates with holes in compression or bending. *Thin-Walled Struct* 47(12):1597–1607
15. Paik JK (2007) Ultimate strength of perforated steel plates under edge shear loading. *Thin-Walled Struct* 45(3):301–306
16. Paik JK (2007) Ultimate strength of perforated steel plates under axial compressive loading along short edges. *Ships Offshore Struct* 2(4):355–360
17. Paik JK (2008) Ultimate strength of perforated steel plates under combined biaxial compression and edge shear loads. *Thin-Walled Struct* 46(2):207–213
18. Rao LB, Rao CK (2012) Buckling of circular plates with an internal elastic ring support and outer edge restrained against translation. *J Eng Sci Technol* 7(3):393–407
19. Rao LB, Rao CK (2009) Buckling of circular plates with an internal elastic ring support and elastically restrained guided edge against translation. *Advan Vibr Eng* 8(1):59–67
20. Rao LB, Rao CK (2009) Buckling of circular plates with an internal elastic ring support and elastically restrained guided edge against translation. *Mech Based Des Struct Mach* 37(1):60–72

21. Rao LB, Rao CK (2011) Fundamental buckling of annular plates with elastically restrained guided edges against translation. *Mech Based Des Struct Mach* 39(4):409–419
22. Rao LB, Rao CK (2015) Buckling of elastic circular plates with an elastically restrained edges against rotation and internal elastic ring support. *Int Appl Mech* 51(4):480–488
23. Rao LB, Rao CK (2015) Buckling of circular plate with foundation and elastic edge. *Int J Mech Mater Des* 11(2):149–156
24. Rao LB, Rao CK (2013) Buckling of annular plates with elastically restrained external and internal edges. *Mech Based Des Struct Mach* 41(2):222–235
25. El-Sawy KM, Nazmy AS, Martini MI (2004) Elastoplastic buckling of perforated plates under uniaxial compression. *Thin-Walled Struct* 42(8):1083–1101
26. Baba B (2007) Buckling behavior of laminated composite plates. *J Reinf Plast Compos—J Reinf Plast Compos* 26:1637–1655. <https://doi.org/10.1177/0731684407079515>
27. Ansys® Academic research mechanical, Release 19.1

# Analysis of Buckling Behavior on the Thin-Walled Circular Cylinder



Nayani Uday Ranjan Goud and M. N. V. S. Swethabala

**Abstract** Buckling is a critical phenomenon in structural failure under compression load. Buckling strength of the structures depends on many parameters like supports, linear material, composite material, or nonlinear material. Buckling behavior is also influenced by thermal loads and imperfections. Analyzing all these conditions is essential, few parameters are considered for the present work. Due to the advances in the finite element techniques, analysis of these problems is possible which is difficult in earlier days. In the present work, buckling behavior of thin-walled cylinders is to be analyzed in terms of buckling load factor for various thicknesses using Ansys and the results are compared with the theoretical values for validation.

**Keywords** Buckling load factor · Buckling strength · Finite element technique · Thin-walled cylinder

## 1 Introduction

Thin cylindrical shell structures are highly efficient structures widely employed in the fields of mechanical engineering, civil engineering, aerospace engineering, marine engineering, etc. The elastic critical stress is determined by using the following equation and is given by, where  $E$  is the modulus of elasticity [1].

$$\sigma_{cr} = \frac{E}{\sqrt{3(1 - \nu^2)}} \left( \frac{t}{r} \right)$$

Axially compressed cylindrical shells and pressurized shells have high sensitivity due to which prediction of critical loads is a challenging task. Owing to the difficulties

---

N. U. R. Goud (✉) · M. N. V. S. Swethabala  
Department of Aeronautical Engineering, MLR Institute of Technology, Hyderabad, Telangana, India  
e-mail: [uday.goud@mlrinstitutions.ac.in](mailto:uday.goud@mlrinstitutions.ac.in)

M. N. V. S. Swethabala  
e-mail: [swethabala@mlrinstitutions.ac.in](mailto:swethabala@mlrinstitutions.ac.in)

© The Author(s), under exclusive license to Springer Nature Singapore Pte Ltd. 2022  
G. S. V. L. Narasimham et al. (eds.), *Innovations in Mechanical Engineering*,  
Lecture Notes in Mechanical Engineering,  
[https://doi.org/10.1007/978-981-16-7282-8\\_15](https://doi.org/10.1007/978-981-16-7282-8_15)

253

in manufacturing, thin shells structures are subjected to numerous imperfections. This in turn effects the load carrying capacity of the shells. It is very important to effectively prognosticate the buckling strength, or it may result in a catastrophic failure of the entire structure. This is the crux of the issue which the structural engineers have to focus on, i.e., developing necessary skills to carry out stability tests and perform necessary calculations [2].

The complex phenomenon starts with initial buckling stages as global and local buckling. There are many methods to foresee the buckling behavior of thin-walled cylinders out of which finite element method can be able to solve complex geometries, load, and support conditions [3]. The load-bearing capacity of any structure is determined by the buckling phenomenon, and the imperfections in the geometries of any structure with loading are of practical importance as the external pressure and cylindrical shells under axial compression are very sensitive. A very small change in the geometry and imperfection or material nonlinearity can lead to considerable reduction in limit loads for the cylindrical shells [4]. The analysis of imperfection sensitivity is one of the theoretical analysis is used to determine the effect of initial imperfections on the buckling of thin-walled circular cylinders [5]. Batikha et al. [6] conducted investigations on strengthening of cylindrical shells which increase buckling strength by the addition of small amounts of fiber reinforced polymer composites. Many studies in the literature show the study of both theoretical and experimental analysis of buckling of thin-walled circular cylinders. When the effects of thin-walled cylindrical shells subjected to external pressures were investigated, experiments showed that there was a slight increase in buckling of the tested models [7]. The pressure forces due to vortex-induced vibrations when the splitter plate was introduced were altered and therefore the drag forces also changed. It is observed that as the length of the splitter plate is increases, the drag on the cylinder decreases [8]. When the fibers are parallel to the laminar surface, there exists maximum stress concentration. The change in the ply angle orientation due to increase in diameter of the hole alters the stress distribution. The stress concentration depends on the hole size in the transverse direction [9]. As the gap between the cylinder and the leading edge of the splitter plate increases, drag force decreases [10]. As the thickness of the material directly effects the critical moment of the section. The effect of change in length of the section on the critical moment can be neglected [11]. Change in the material properties lead to enhance factors of safety. Al alloy 2024 T4 and 6061 T6, for bulkheads carbon fiber 90° and 45°, Carbon fibers with 45° orientations perform better in terms of factor of safety when compared to using 90° orientation fibers [12]. Analytically proven, computational results for eigen buckling obtained using ANSYS and modal behavior pattern of the structures using ANSYS tool [13] were taken as the boundary conditions in this paper. The natural frequencies of the structures are observed to be the function of compression loads applied axially [13].

It is observed that when the theoretical predictions of critical loads and the experimental results of buckling loads are compared, and there is a significant magnitude of deviation exists, which is highly unacceptable. This discrepancy was effortlessly

explained in both analytical and experimental point of views. In the analytical explanation, the assumptions made at the start of the problem were re-evaluated and modified or removed. This led the way to accredit the discrepancies related to different factors, viz., effects of pre-buckling deformations, in-plane boundary conditions, or the imperfections in geometry in the initial stages.

## 2 Methodology

The thin-walled cylinders or shells have wide applications in various areas, which marks the importance of the study of induced stresses in them. They are used as boiler shells, pressure tanks, pipes, etc.

In general, there are three types of stresses are developed in pressure shells:

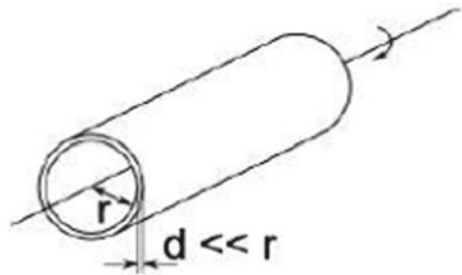
- Circumferential or ring stresses ( $\sigma_\theta$ )
- Longitudinal or axial stresses ( $\sigma_L$ )
- Radial stresses ( $\sigma_r$ ) (Fig. 1).

**Buckling of Thin Cylinder under Axial Compression:** Thin-walled cylindrical shells are highly efficient structures with wide applications in variety of industries including aerospace, petrol, and mechanical engineering. When they are subjected to compressive loads, they tend to buckle which often results in catastrophe; it is very important to predict the buckling strength. This area offers a wide scope for engineers to work in.

In addition to this, thin shells in civil engineering applications are subjected to nonuniform compressive loads along the axis, and it is observed that very few people worked in the direction for estimating failure criteria to get design optimization. A plenty of literature is available on the thin shells under uniform axial compressive loads. It is also observed that very little research is carried on the buckling and post-buckling behavior wind-loaded cylinders as well.

This section bridges this narrow gap of elastic buckling of thin shells subjected to both uniform and nonuniform axial compressive loading.

**Fig. 1** Thin-walled cylinder under pressure [14]





### 3 Experimental Details

**Experimental determination of buckling load factor using Ansys:** SHELL181 is apt for carrying out structural analysis of thin to moderately-thick shell structures. It is identified as four-node element with each node having six degrees of freedom, viz.,: translations in the  $x$ ,  $y$ , and  $z$  directions, and rotations about the  $x$ ,  $y$ , and  $z$  axes. Care should be taken that we use only the degenerate triangular option as filler element in mesh generation (Fig. 2).

The buckling load factors are determined theoretically for the thin-walled cylindrical shell with thicknesses of 1.5 mm and 2 mm, respectively. A uniformly distributed load of 300 KN/mm is applied to the top shell through nodes.

Considering a thin cylindrical shell with end supports is subjected to uniform compression along its axis. We can estimate the buckling load factor (BLF) through general method (Fig. 3).

$$N_x = \text{Axial load.}$$

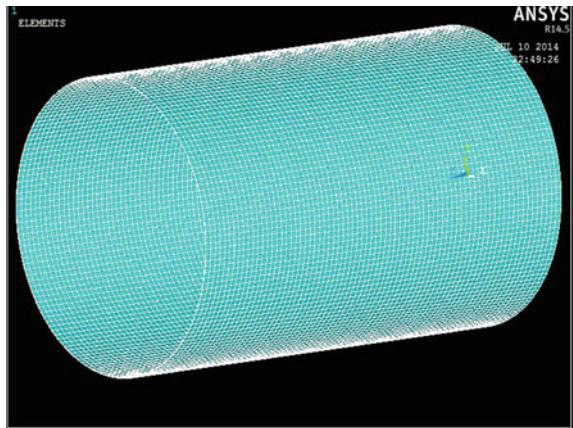
**Formula Used:**

$$F_{cr/n} = \frac{Kc\pi^2 E}{12(1 - \nu^2)} \left(\frac{t}{L}\right)^2 \tag{1}$$

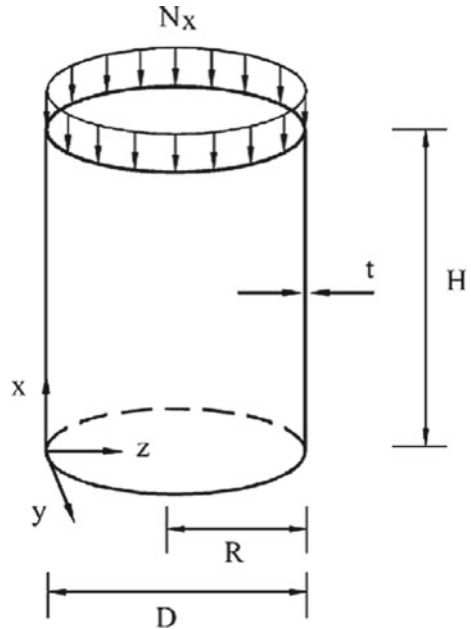
$$K_c = \left(\frac{4\sqrt{3}}{\pi^2}\right) * Z \tag{2}$$

$$Z = \frac{L^2}{rt} \sqrt{1 - \nu^2} \tag{3}$$

**Fig. 2** Mesh generation of thin-walled cylindrical shell



**Fig. 3** Cylindrical shell subjected to axial load.  $D$  = diameter of cylinder,  $R$  = radius of cylinder,  $H$  = height of the cylinder



$$F_{cr} = CE \left( \frac{t}{r} \right) \tag{4}$$

$$C = \frac{1}{\sqrt{3(1 - \nu^2)}} \tag{5}$$

$$\text{Buckling load factor} = \frac{F_{cr/n}}{\sigma}$$

where

- $L$  length of the cylinder.
- $E$  Young's modulus of elasticity.
- $\nu$  poisson's ratio.
- $Z$  curvature parameter for isotropic cylinder.
- $F_{cr}$  compressive buckling Stresses.

To analyze the theoretical results for the thin circular cylinder, we use the two materials as the reference; the theoretical results (i.e., the buckling load factors) are calculated.

To analyze the experimental results for the thin circular cylinder, we use 'ANSYS 14.5' version, and the buckling load factor is calculated. Thus, the two buckling load factors values obtained from theoretical and experimental results are compared with each other.

**Theoretical calculations for determination buckling load factor:**

The following data are considered for the analysis:

Length of the cylinder,  $L = 1500$  mm

Radius of the cylinder,  $r = 500$  mm.

Poisson's ratio,  $\nu = 0.32$ .

And Young's modulus,  $E = 10 \times 10^3$  N/mm<sup>2</sup>.

**Calculation when the thickness of the cylinder,  $t = 1.5$  mm.**

$$Z = \frac{1500^2}{500 * 1.5} \sqrt{1 - 0.32^2}$$

$$Z = 2842.50$$

Substituting the value of  $Z$  in equation for  $K_c$

$$K_c = \left( \frac{4\sqrt{3}}{\pi^2} \right) * 2842.50$$

$$K_c = 1995.18$$

Substituting the value of  $K_c$  in Eq. (1).

We will get critical load as

$$F_{cr/n} = \frac{1995.18\pi^2 \times 69 \times 10^3}{12(1 - 0.32^2)} \left( \frac{1.5}{1500} \right)^2$$

$$F_{cr/n} = 126.144 \text{ N/mm}^2$$

Now, as we know the value of  $F = 300$  kN.

Since,

$$A = \pi(r_o^2 - r_i^2)$$

$$A = \pi(500^2 - 498.5^2) = 4705.32 \text{ mm}^2$$

$$\sigma = \frac{300 \times 10^3}{4705.32}$$

$$\sigma = 63.75 \text{ N/mm}^2$$

Substitute the value of  $F_{cr/n}$  and  $\sigma$  in Eq. (7) to get the buckling load factor.

$$\text{Buckling load factor} = \frac{F_{cr/n}}{\sigma}$$

$$\text{Buckling load factor} = \frac{126.144 \text{ N/mm}^2}{63.75 \text{ N/mm}^2}$$

$$\text{Buckling load factor} = 1.978.$$

**Calculation is for thickness of the cylinder,  $t = 2$  mm.**

$$Z = \frac{1500^2}{500 \times 2} \sqrt{1 - 0.32^2}$$

$$Z = 2131.6894$$

Substituting the value of  $Z$  in Eq. (2)

$$K_c = \left( \frac{4\sqrt{3}}{\pi^2} \right) \times 2131.6894.$$

$$K_c = 1496.39.$$

Substituting the value of  $K_c$  in Eq. (1).

We will get critical load as

$$F_{cr/n} = \frac{1496.39\pi^2 \times 69 \times 10^3}{12(1 - 0.32^2)} \left( \frac{2}{1500} \right)^2$$

$$F_{cr/n} = 168.198 \text{ N/mm}^2$$

Now, as we know the value of  $F = 300$  kN.

Since,

$$A = \pi(r_o^2 - r_i^2)$$

$$A = \pi(500^2 - 498^2) = 6270.6189 \text{ mm}^2$$

$$\sigma = \frac{300 \times 10^3}{6270.6189}$$

$$\sigma = 47.84 \text{ N/mm}^2$$

Substitute the value of  $F_{cr/n}$  and  $\sigma$  in Eq. (7) to get the buckling load factor.

$$\text{Buckling load factor} = \frac{F_{cr/n}}{\sigma}$$

$$\text{Buckling load factor} = \frac{168.198 \text{ N/mm}^2}{47.84 \text{ N/mm}^2}$$

$$\text{Buckling load factor} = 3.514.$$

### 4 Results and Discussion

When the thickness of the cylindrical shell is 1.5 mm, its critical stress obtained from theoretical results as 63.75 N/mm<sup>2</sup>, and the corresponding buckling load factor is estimated to be 1.978.

Similarly, when the thickness of the cylindrical shell is 2 mm, its critical stress obtained from theoretical results as 47.84 N/mm<sup>2</sup>, and the corresponding buckling load factor is estimated to be 3.514.

The critical stresses are then determined analytically by using Ansys shell 181 element. For this, the static linear and nonlinear analyses are used to determine the values of critical stresses in elastic and plastic zones.

Figure 4 Nodal solution of thin-walled cylindrical shell.

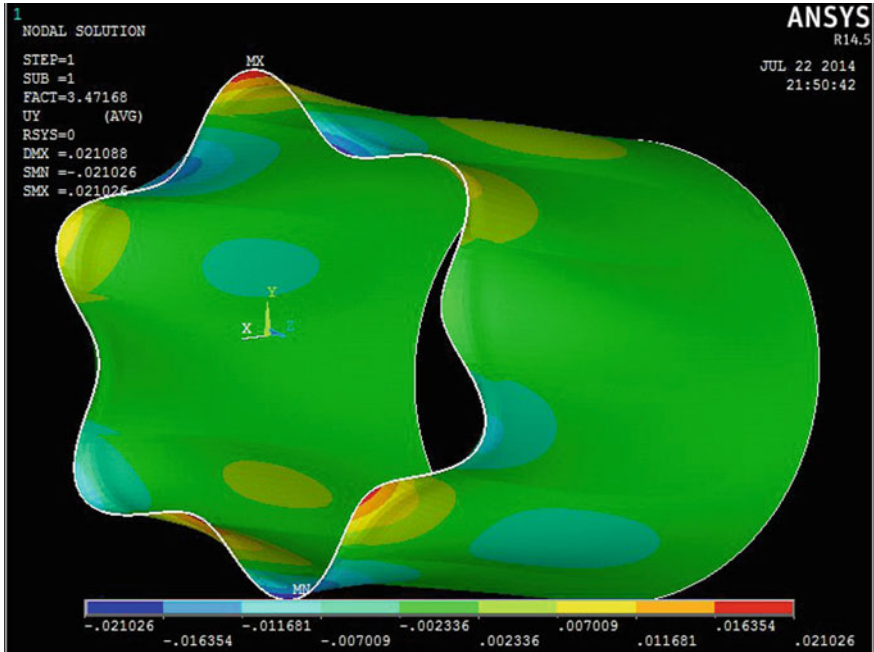


Fig. 4 Main effects plot for SN ratios

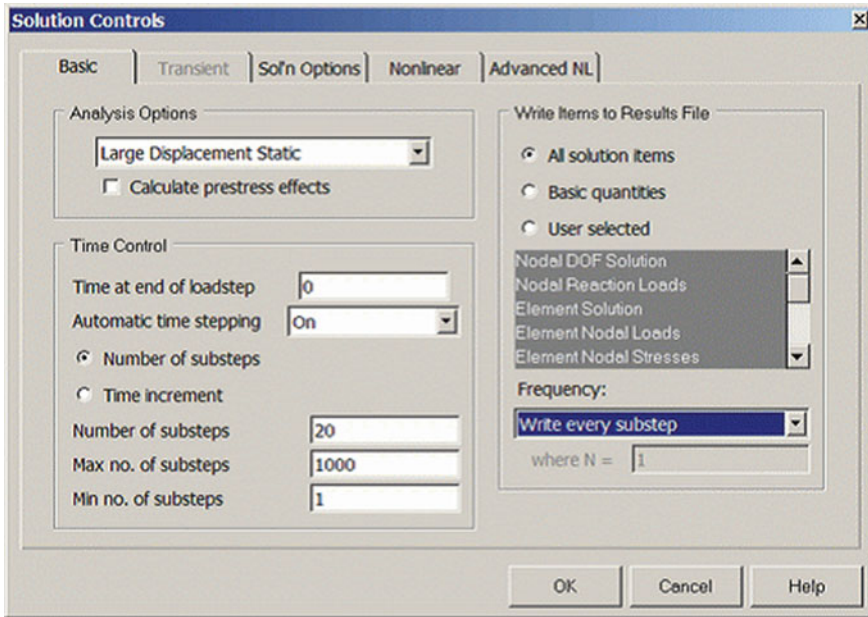


Fig. 5 Load steps

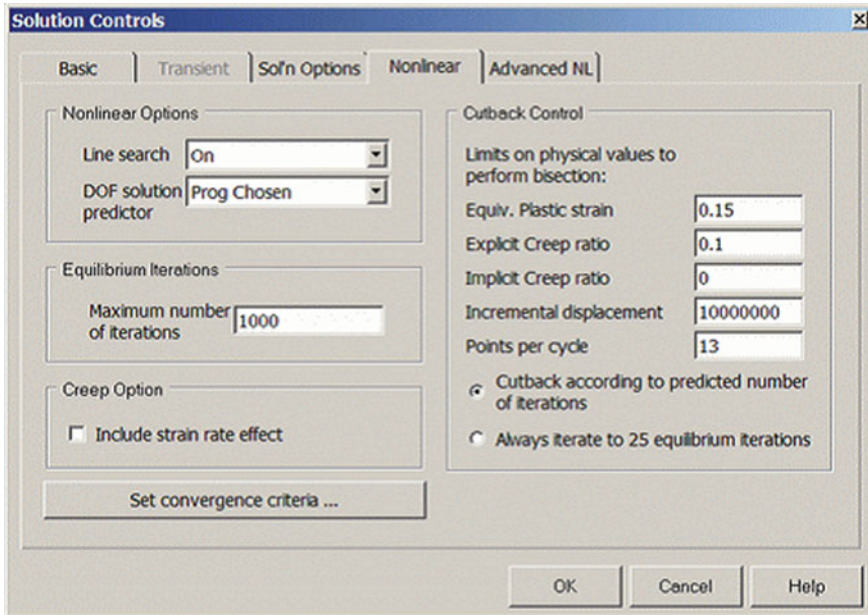
### Nonlinear analysis:

Automatic time stepping allows ANSYS to determine appropriate sizes to break the load steps (Fig. 5).

Before performing this operation, ensure the following:

- A. Permit the large static displacements (to include the effects of higher values deflection).
- B. Automatic time stepping should be turned on. This allows the software to break the load steps into suitable intervals. Lesser the step size, greater is the accuracy though it consumes time. Enabling automatic time step ensures appropriate balance along with activating bisection feature in the software leading to recovery of the file in case of failure of convergence.
- C. The number of sub-steps are 20. This will set the sub-steps to 1/20th of the total load.
- D. The number of maximum sub-steps = 1000. This step enables to halt the iterations if the convergence doesn't appear after the said number.
- E. Minimum number of sub-steps = 1.
- F. The solution is scripted to the results file.

Furthermore, make sure of selecting the items as shown in below in the figure of 'Non Linear'



**Fig. 6** Load steps for maximum iterations

- A. Keep the line search 'On'. This allows the convergence of Newton–Raphson solver.
- B. Maximum number of iterations = 1000 (Fig. 6).

Select all nodes on other end and apply the force with respective of all nodes = total applied force/No. of nodes selected. Apply in the FZ-direction (Fig. 7).

Solution > Solve > Current LS

The above figures show the deformation pattern of the thin cylinder after being subjected to buckling. By applying the load axially the deformation starts from a point where the force is applied and it transfer along the shell.

## 5 Conclusion

The shell is going to buckle when the buckling load factor is less than 1. When knockdown factor is multiplied with B.L.F if the result is greater 1.5 then structure can withstand buckling load. For  $t = 1.5$  mm, the B.L.F is less than 1.5, i.e., it cannot resist the buckling load. For  $t = 2$  mm, deformation does not exists on the bottom part of the shell. Buckling load factor depends on thickness of the cylindrical shell and

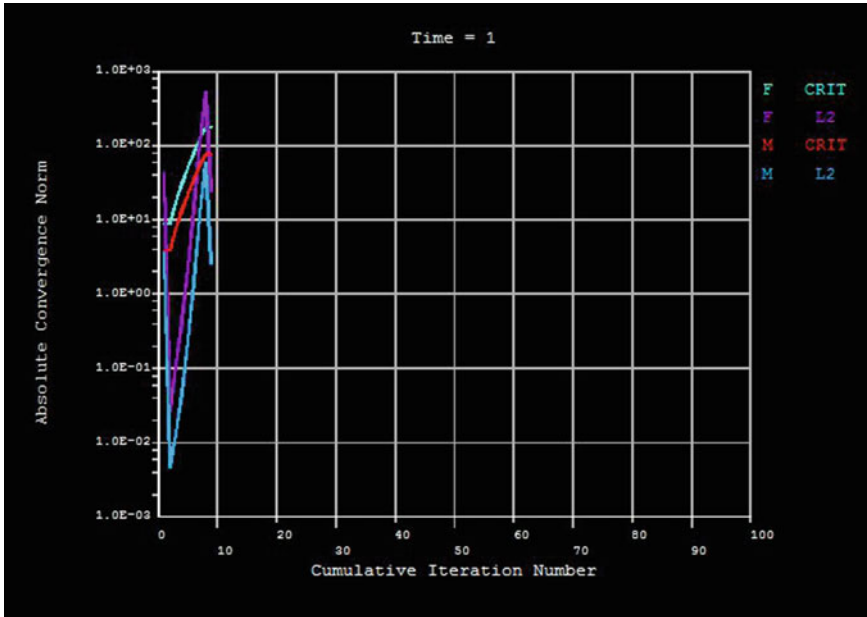


Fig. 7 Deformation pattern of thin cylinder

also at the point where it is applied. Based on the theoretical analysis and analytical results derived from Ansys, we came to conclude that the buckling load factors are 3.514 and 3.714, respectively, which is approximately same for the thickness 2 mm. Thus, the thickness of the circular cylinder is predicted as 2 mm to carry the loads safely. The shell is going to buckle when the buckling load factor is less than 1. If the B.L.F is more than 1.5 then the cylinder has the ability to resist the buckling load.

## References

1. Houliara S, Karamanos SA (2011) Buckling of thin-walled long steel cylinders subjected to bending. *J Pressure Vessel Technol* 133(1). <https://doi.org/10.1115/1.4002902>
2. Fan H (2019) Critical buckling load prediction of axially compressed cylindrical shell based on non-destructive probing method. *J Thin Walled Struct* 139:91–104. <https://doi.org/10.1016/j.tws.2019.02.034>
3. Nedelcu M, Cucu HL (2014) Buckling modes identification from Fea of thin-walled members using only GBT cross-sectional deformation modes. *J Thin Walled Struct* 81:150–158. <https://doi.org/10.1016/J.Tws.2013.06.007>
4. Estekanchi HE, Avafai (1999) On the buckling of cylindrical shells with through cracks under axial load. *J Thin Walled Struct* 35(4):255–274. [https://doi.org/10.1016/S0263-8231\(99\)00028](https://doi.org/10.1016/S0263-8231(99)00028)
5. Tennyson RC, Booton M, Caswell RD (1971) buckling of imperfect elliptical cylindrical shells under axial compression. *AIAA J* 9(2). <https://doi.org/10.2514/3.6159>
6. Batikha M, Chen JF, Rotter JM, Teng JG (2009) Strengthening metallic cylindrical shells against elephant's foot buckling with FRP. *Thin-Walled Struct* 47:1078–1091



7. Merve F et al (2019) Experimental analysis of the effect of dent variation on the buckling capacity of thin-walled cylindrical shells. *J Thin Walled Struct* 143:106259. <https://doi.org/10.1016/j.tws.2019.10625>
8. Kumar PD, Kumar A, Praveen NB (2017) Flow analysis experiment around a circular cylinder with splitter plate. *Int J Mech Product Eng Res Dev* 7(22496890):83–94
9. Sreelakshmi K, Madhavi N, Satyanarayana Gupta M (2017) Analysis of Interlaminar stresses in a composite material with a circular hole by using finite element method. *Int J Civ Eng Technol (IJCIET)* 8(0976–6316):500–508
10. Kumar NE, Anil Kumar PD, Nagaraj Goud B (2017) Drag reduction over a circular cylinder. *Int J Civ Eng Technol (IJCIET)* 8(0976–6316):1334–1345
11. Naidu KS (2015) Analysis on thin walled aircraft structure. 2(5):1–4. ISSN 2395-0056, IRJET
12. Satyanarayana Gupta M (2015) Factor of safety and stress analysis of fuselage bulkhead using composite materials. 04(32):6390–6396, ISSN 2319-8885, IJSETR
13. Goud NUR et al (2019) Buckling load predictions of panel and shell using vibration correlation technique. *Int J Eng Adv Technol (IJEAT)* 9(2). ISSN: 2249-8958
14. Sudhir Kumar et al V (2019) Experimental and numerical investigation of thin cylindrical shell subjected to axial compression loading. In: AIP conference proceedings, vol 2128, p 050012. <https://doi.org/10.1063/1.5117984>

# Design and Analysis of E-Kisan Multi-Tool Machine



**B. Vijaya Kumar**

**Abstract** The aim of this work is to design and analysis of e-kisan multi-tool machine to operate and handle manually by farmers. The objective of this machine is to extract soil effectively from dry land pits which are used to estate plants. In this, the design of earth auger tool, plowing tool, saw cutter tool, and grass cutting tools is designed, and assembly of these tools is done to the machine. Battery and geared motor design are also done by using the same software. As per the design calculations, the induced stresses because of the axial load is  $2.69 \text{ N/mm}^2$ , and the deflection is around  $0.0006 \text{ mm}$ . Then, analysis operations are performed on the tools to check the effect on the tool because of the axial loading and its functional deflections, and it is found that has with-stand ability when forces are applied. This evaluation helps in practical implementation of the tool.

**Keywords** Earth auger · Plowing · Geared motor · Deflection

## 1 Introduction

Fruit farming has become one of the profitable crop to farmers, In ancient days, all human beings are followed the different lifestyle like hunter-gatherer [1, 2]. Now a day, we have well established technologies [3, 4] and sophisticated cultivation; we are getting fruits throughout the year without depending on season due to hybrid culture, but in olden days they got fruits only few months per year on seasonal basis. Harvesting totally depends on labor intensive operation due to soft nature of fruits. Fruit farming and harvesting would manually to be continue; there are many mechanical harvesters [5] for fruits harvesting can be used where fruits need to be sent immediately to industries for different requirements processing. Now a days, the living standard of the people in country is increased is just by the per capita consumption of fruits and production; there are many traditional methods of tools

---

B. V. Kumar (✉)

Head of the Department, Mechanical, Gurunanak Institute of Technology, Ibrahimpatnam, Hyderabad, Telangana, India

e-mail: [hodme.gnit@gniindia.org](mailto:hodme.gnit@gniindia.org)

used in farming based on the investment, but all farmers are not having financial ability to invest money on most advanced tools, for them an economic farming tools to be manufactured and cost should be within their budget in order to use for small yields.

In most of the villages, still farmers are not using tools in harvesting and farming because of lack of awareness on how to use mechanically and manually operated tools. For creating awareness on usage of power tools, they can start using small and easily operated tools based on their farming area and yield capacity within their budget, for that at low cost more useful tools has been developed and e-kisan multi-tool machine will be one of economical machine.

## 2 Material Used

### 2.1 *LiFePO<sub>4</sub> Battery*

LiFePO<sub>4</sub> cells have an ostensible voltage of about 3.2 or 3.3 V. In this design, various cells in succession (frequently 4) to make up a lithium iron phosphate battery pack are utilized. Using four lithium iron phosphate cells in succession, offers us generally ~12.8–14.2 V pack when full. That is the nearest factor we will look out to a standard lead corrosive or AGM battery. Lithium iron phosphate cells have higher cell thickness than lead corrosive, for a portion of the heap. Lithium iron phosphate cells have significantly less cell thickness than lithium particle [6]. This makes them substantially less flimsy, more secure to utilize, a moderate almost up to a balanced substitute for AGM packs. To prevail in the indistinguishable thickness as lithium-particle cells, we need to stack lithium iron phosphate cells in corresponding to expand their capacity. So, lithium iron phosphate battery loads with the indistinguishable 25 capacity of a lithium-particle cell, will probably be greater, in light of the fact that it requires additional cells in corresponding to achieve the indistinguishable ability. Lithium iron phosphate cells can be used in high-temperature conditions, the spot lithium-particle cells should in no way, shape or form be utilized over + 60 °C. The regular assessed lifetime of a lithium iron phosphate battery is 1500–2000 expense cycles for as much as 10 years. In some cases, a lithium iron phosphate pack will keep up with its expense for 350 days. Lithium iron phosphate cells have 4 cases (4x) the ability of lead corrosive batteries (Fig. 1).

#### **Specifications:**

- Specific energy: 90–160 Wh/kg
- Energy density: 325 Wh/L
- Specific power: 200 W/kg
- Time durability: >10 years

**Fig. 1** Lithium iron phosphate battery (LiFePO4)



- Cycle durability: 4000–8000 cycles
- Number of cells: 4
- Battery voltage: 12.8–14.2 V.

## 2.2 DC-Geared Motor

E-bike MY1016Z3 24 V 350 W 324 geared DC motor total with a nine teeth sprocket having 1/2" (12.7 mm) pitch [7] is used. This motor is incredible for lightweight machines which can be easily handle during operation and to make their comfort for while digging holes. This electrical motor accompanies gear lower which delivers extra low-end torque than common plate machine. We can alter machine course to left or right by simply turning around wires. We can likewise utilize the accompanying other tools with this machine (Fig. 2).

**Fig. 2** DC-geared motor



**Specifications:**

- Voltage: 24 V DC
- Power: 350 W
- Speed (after reduction): 324 RPM
- Torque: 11 N-m (110 kg cm)
- Stall torque: 55 N-m (550 kg cm)
- Weight: 2.98 kg
- Current: 19.2 A.

**3 Design Calculations****3.1 Axial Load Calculations**

$$\text{Stress, } \sigma = F/A$$

where  $F$  = Force (Newton or pounds).

$A$  = Inches<sup>2</sup> or meters<sup>2</sup>.

We also know that  $F = ma$

$$\sigma = ma/A$$

( $a = g$ , gravitational acceleration).

$g = 9.81 \text{ m/s}^2$

$$\sigma = m.g/A$$

Let,  $m$  = force applied on the machine by the farmer. (Consider  $m = 50 \text{ kg}$ ).

And,  $A = \pi/4.d^2$  and  $d$  = diameter of hollow rod = 6 Inch =  $6 \times 2.54 = 152.4 \text{ mm}^2$ .

Now,  $\sigma = m.g/A$

$$\sigma = (50 \times 9.81)/(0.785 \times 152.4 \times 152.4)$$

$$\sigma = 2.69029200 \text{ N/mm}^2 \text{ (Shear Stress)}$$

The material we used in the manufacture of tool is low carbon steel (1045).

So, let's find out deflection in the tool when axial load is applied

$$\delta = FL/AE$$

Density,  $\rho = 7.87 \text{ g/cm}^3$

Shear modulus = 80 GPa

Modulus of elasticity = 200 GPa

Poisons ratio,  $\mu = 0.290$

Tensile strength (ultimate) = 565 MPa

Tensile strength (yield) = 310 MPa.

$$\delta = (50 \times 480)/(18232.22 \times 200)$$

$$\delta = 0.00658175 \text{ mm (deflection)}$$

### 3.2 *Battery Power and Time Calculations*

$$\text{Power} = \text{work}/\text{time}$$

By using mass, height and time power are determined.

$$P = \text{mass} * \text{height}/\text{time}$$

$$\text{Power} = \text{work}/\text{time} = \text{force} \times \text{displacement}/\text{time} = \text{force} \times \text{Velocity}$$

$$\text{From motor } P = 350 \text{ W}$$

$$350 = (15 \times 480 \times 9810)/(\text{Thr} \times 3600)$$

$$\text{Thr} = 5.6 \text{ h (Time)}$$

$$P = V \times \text{ah}$$

$$P = 24 \text{ V} \times 15 \text{ ah}$$

$$P = 360 \text{ W.}$$

### 3.3 *Factor of Safety*

FOS = yield stress/working stress

$$\text{FOS} = 310/565$$

$$\text{FOS} = \mathbf{0.5486}$$

$$\text{Margin of safety} = \text{FOS} - 1 = -0.4514 \text{ mm.}$$

### 3.4 Taylor's Equation

$V_c$  Cutting speed

$T$  Tool life

$D$  Depth of cut

Tool life

$$V_c(\pi \times D_c \times n)/1000$$

$$V_c = 15.504$$

Here,  $n = \text{Speed} = 324$ .

$D_c = \text{Drill dia} = 6 \text{ Inches} = 15.24 \text{ cm}$ .

### 3.5 Drilling Time ( $T_c$ )

$$T_c = (I_d \times i)/(n \cdot \text{fr})$$

where  $I_d$  hole depth (30 cm).

$i$  No. of holes

$n$  speed

$\text{fr}$  feed per revolution = 0.2 IS (standard).

$$T_c = (30 \times 30)/(64.8 \times 0.2)$$

$$T_c = 694.44 \text{ mins} = 41640 \text{ s}$$

### 3.6 Feed of Main Spindle

$$V_f = \text{fr} \cdot n$$

$$V_f = 0.2 \times 324 \text{ IS}$$

$$\text{Spindle feed} = 64.9 \text{ mm/min}$$

Number of holes:

In this number of hole that can be dig per hour and in total battery life is discussed. The below data will be purely based on the assumptions from the previous results.

No. of holes per hour,

A machine usually takes 5 min to dig a hole

$$\text{No. of holes} = 5 \times 60 \text{ mins} = 12 \text{ holes/h}$$

$$\begin{aligned} \text{No. of holes} &= 12 \times 5.6 \text{ h} \\ &= 67 \text{ holes/battery life} \end{aligned}$$

Draining of battery also depends upon the type of soil in which the hole is done and the depth of the hole to be done. Based on these conditions above values can be slightly changed.

## 4 Design of Multi-tools

### 4.1 Design of Soil Digging Tool

SolidWorks software was employed to carry out the designing operations of the e-kisan multi-tool machine (Fig. 3).

It is digging tool of a earth auger machine by using SolidWorks software tools (with help of these tool line, offset, helical curve, revolve, rectangle, lift, filter, and

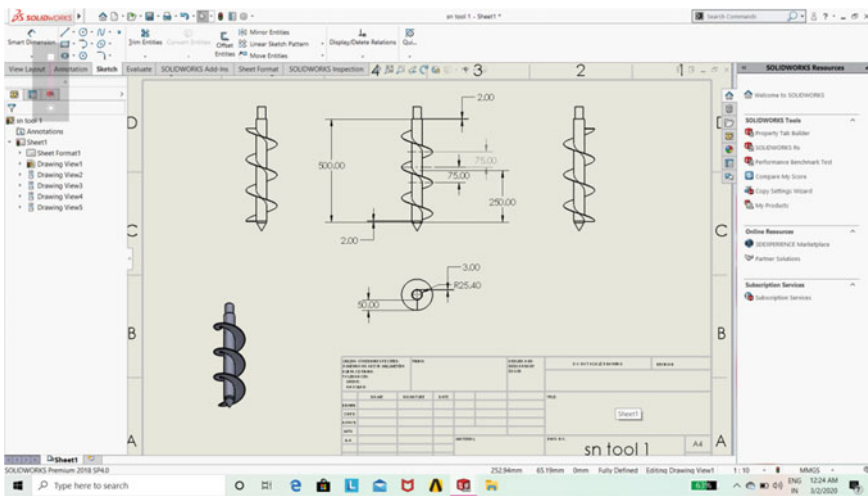


Fig. 3 Digging tool



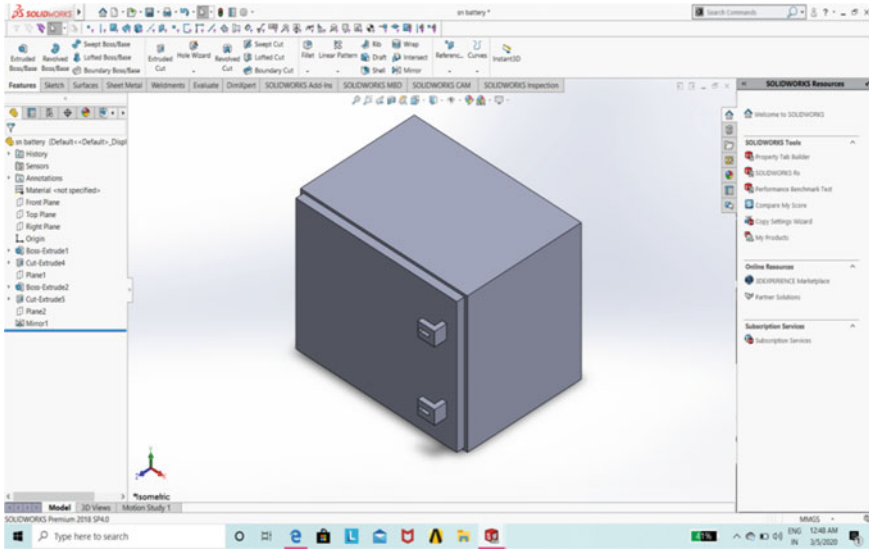


Fig. 4 Design of battery

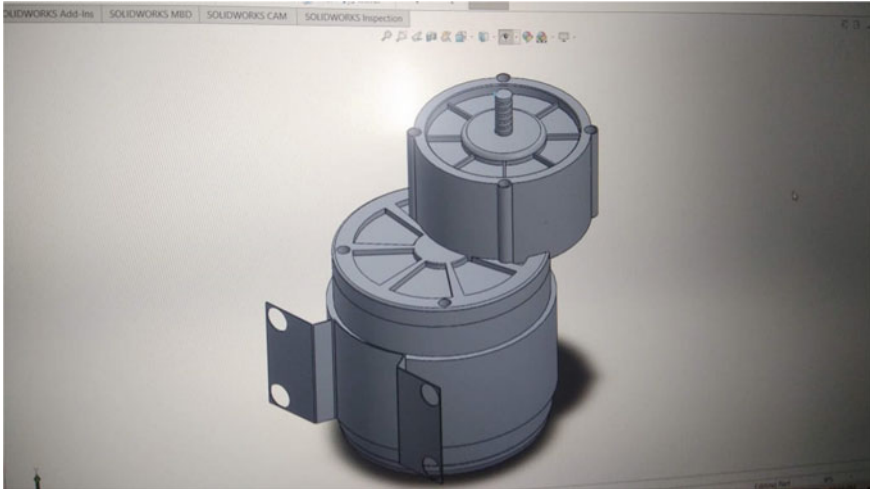
extrude) for thickness of helical plate 3 mm, seamless hollow pipe 5 mm thickness pitch of the helical tool 110 mm, diameter of the tool 152.4 mm, and height of the tool 500 mm [8] (Fig. 4).

### 4.2 Design of Battery

It is lithium ion battery, the design by using mechanical software (SolidWorks) with the help of suitable tools (rectangle, line, mirror, shell, extrude and filter). First open solid work window in that select part design and sketch, before starting the design check dimensions in mm. Select the front plane in rectangle tool choose select the first point and second point than click ok. Choose extrude tool add material of sketch 1. Select the top surface of a boss extrude 1 and sketch draw the shape remove material [9].

### 4.3 Design of Geared DC Motor

The electrical motor with geared produces extra low-end torque than any customary motor. These design is designed in mechanical software (SolidWork) by using the tools circle, line, extrude, shall, add material, remove material, circle pattern, mirror, reference plane, helical curve, and filter first select front plane draw a circle and



**Fig. 5** Design of e-vehicle DC motor

extrude. Select the top surface draw a shape choose circle pattern click ok and remove material, draw circle extrude shaft with threads as for dimensions (Fig. 5).

#### ***4.4 Design of Body Frame***

It is a frame one of the major component in the machine assembly; all components are placed in a frame; then, it is easy to carry [10]. The components are designed using SolidWorks software (line, circle, rectangle, add material, and remove material. Select the front plane draw rectangle add material, choose slide plane draw circle, and extrude) (Fig. 6).

#### ***4.5 Soil Weeder Tool***

It is the extra arrangement done on the shaft so that it acts as a multi-tool earth auger machine. It is used to plow the land for the agriculture purpose. Use of this machine can reduce lot of efforts of the farmers and saves huge amount of investments in big machines (Fig. 7).

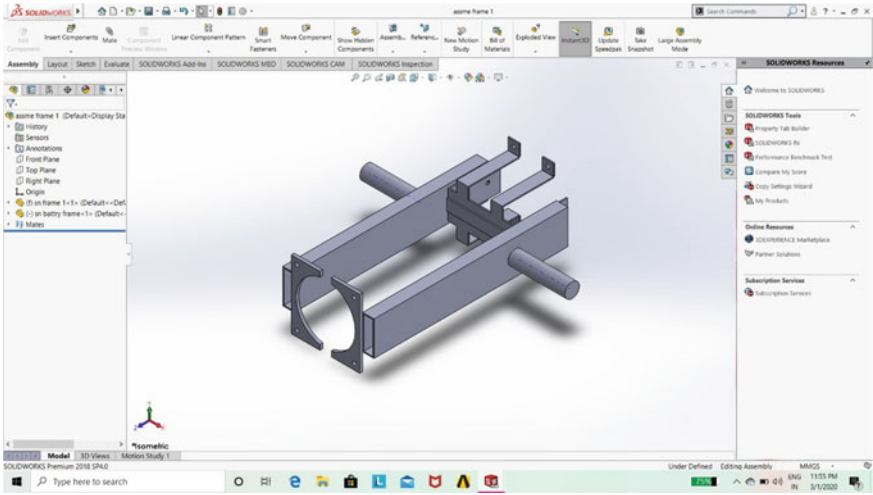


Fig. 6 Design of body frame

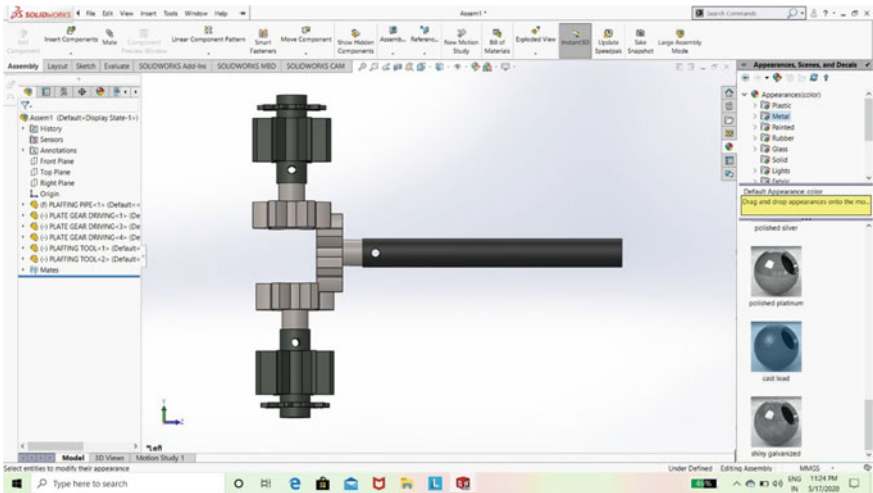


Fig. 7 Design of plowing tool

### 4.6 Saw Cutter Tool

A round noticed is a power-saw utilizing a toothed or abrasive disk or blade to chop completely different supplies utilizing a rotary movement spinning round an arbor. A hole saw and ring saw additionally use a rotary movement however are completely different from a round noticed. *Round saws* can also be loosely used for the blade itself. It is also used by aligning it to the shaft powered by the motor.

Here, saw cutter tool is an extra tool. The purpose of designing this tool is with the sole intention of reducing the efforts of farmers and to minimize their working cost on field. As it is used in as a tool in multipurpose machine, it reduces cost of farmers to the far extent (Figs. 8 and 9).

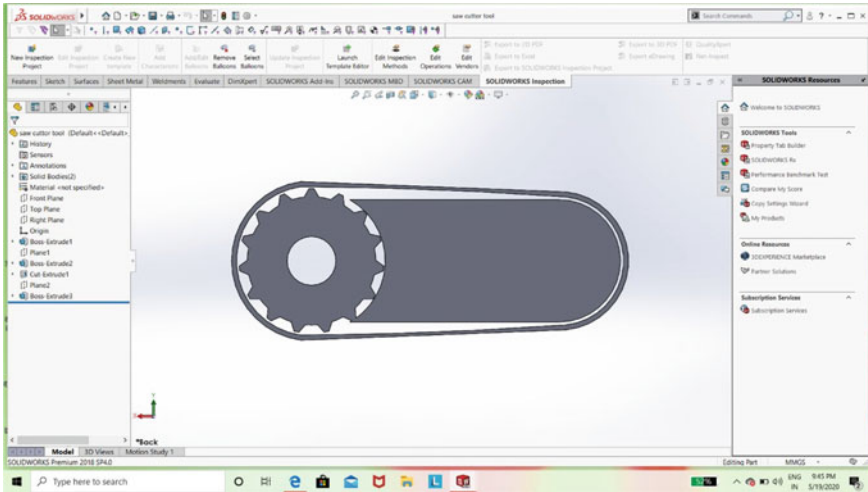


Fig. 8 Design of saw cutter tool

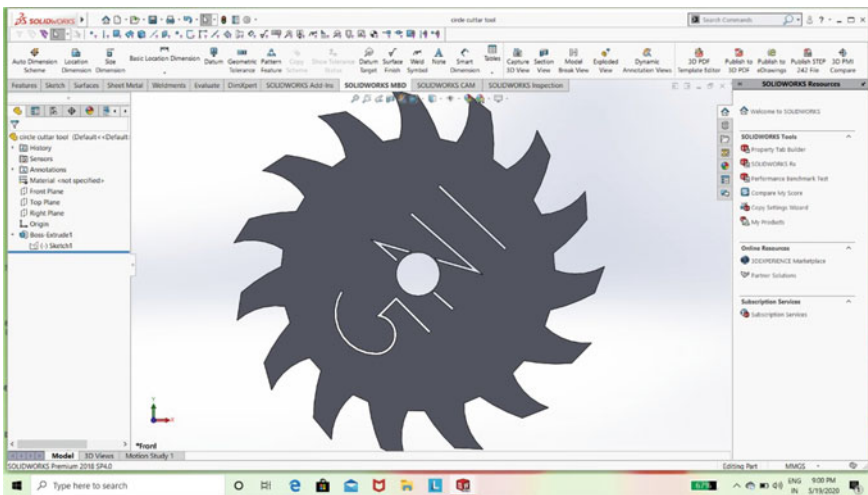


Fig. 9 Grass cutter tool

### 4.7 Grass Cutter Tool

The design of grass cutter tool is done. It also adds extra benefit for the farmers in terms of machine maintenance and machine costs (Figs. 10, 11 and 12).

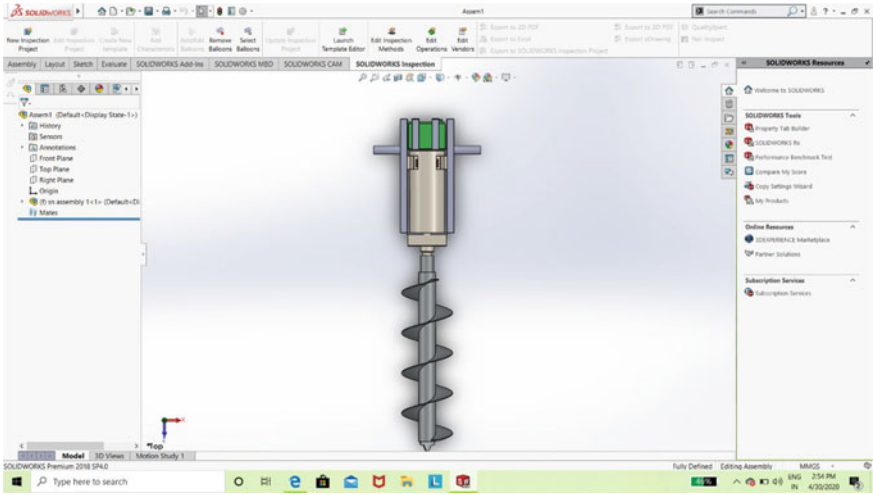


Fig. 10 Assembly of earth auger machine

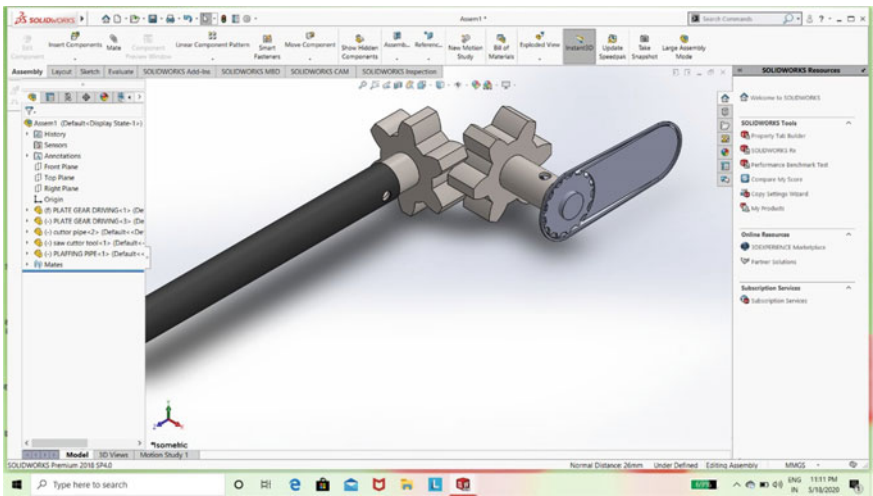


Fig. 11 Assembly of saw cutter tool

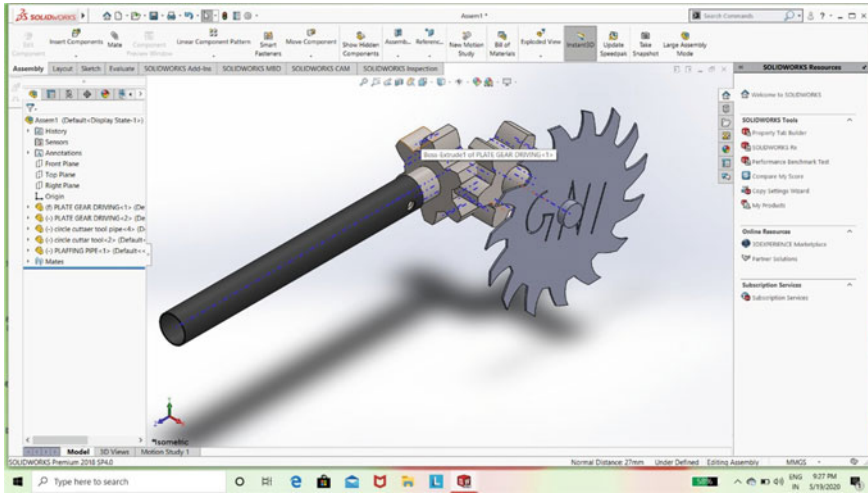


Fig. 12 Design of grass cutter tool

### 4.8 Assembly of Machine Components

Above images represent the assembly part of the different tool designed in the e-kisan multi tool machine. This assembly part is done in the SolidWorks software.

### 4.9 Analysis of Machine Tool

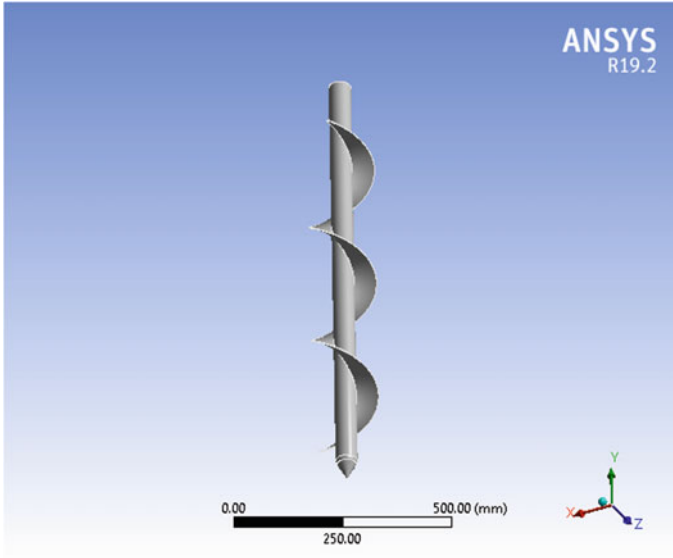
Analysis of the machine tool is done by the Ansys software. As Ansys software user interface is world class and it is recommended by the top designers, we performed our analysis work in the Ansys software [11] (Fig. 13).

The static structural evaluation and modal evaluation did on digging device. In these analysis, one fixed support given top of the digging tool hollow pipe and shear stress and shear strain force applied along the Y-axis direction. The tool working effectively without damage working up to below result.

$$\text{Maximum shear stress} = 0$$

$$\text{Minimum shear strain} = 3.8704e - 002$$

$$\text{Total deformation (average)} = 1.5942e - 002$$



**Fig. 13** Analysis on digging tool

## 5 Conclusion

Based on the problem statement, the design and analysis of the e-kisan multi-tool machine have been done. In this, the design of earth auger tool, plowing tool, saw cutter tool, and grass cutting tools are design, and assembly of these tools is done to the machine. Battery and motor design are also done by using the same software. As per the design calculations, the induced stresses because of the axial load is  $2.69 \text{ N/mm}^2$ , and the deflection is around  $0.0006 \text{ mm}$ . Then, analysis operations are performed on the tools to check the effect on the tool because of the axial loading and its functional deflections, and it is found that has with-stand ability when forces are applied. This evaluation helps in practical implementation of the tool. The auger is able to drill, to dig a bunch of small holes for gardening or landscaping. This one-man earth augers make them sensible choice for single initiatives with cheaper and lightweight of  $11 \text{ kg}$ .

## References

1. Tractor operated auger. IJSRD. [www.ijsrd.com](http://www.ijsrd.com)
2. Solar powered soil digging machine. IJTRE. [www.ijtre.com](http://www.ijtre.com)
3. Development of a mobile operated hole digger for cultivation using a slider-wrench feed mechanism. J Agric Bio Eng

4. Research on design and manufacture of a machine to drill holes for tree planting. IJAITE. [www.ijaite.com](http://www.ijaite.com)
5. Journal of material science springer—the journal of materials science issues articles which report original research results on study techniques
6. Lithium ion battery system to charging/Discharging characteristics supported circuit model. Int J Online Biomed Eng
7. Structural analysis of planetary geared winch—IJSR. [www.ijsr.com](http://www.ijsr.com)
8. Modeling and finite element analysis of post hole digger. IJSRD. [www.ijsrd.com](http://www.ijsrd.com)
9. Digital engineering 24/7, this article gives the review of Solid works. [www.wikipedia.com](http://www.wikipedia.com). Geo-mechanical earth modeling( GMEM). [www.shodhganga.inflibnet.ac.in](http://www.shodhganga.inflibnet.ac.in)
10. Samal Multipurpose farm machine. [www.irjet.com](http://www.irjet.com)
11. Analysis of drilling tool life. [www.ijear.com](http://www.ijear.com)



# Effect of NFA on Wear Resistance of Al6063/NFA Composites fabricated through the Stir Casting Method



Narasa Raju Gosangi  and Lingaraju Dumpala

**Abstract** The aluminum metal matrix composites (AMCs) are the most reasonable materials for various applications and have altogether improved properties. The interest for low-density AMCs containing economical fortifications expanded. The fly ash (FA) in nanoscale definitely improved the properties of the AMCs and is manufactured effectively through ultrasonic-assisted stir casting. In this work, Al6063 combination is built up with nano fly ash (NFA) particles by ultrasonic-assisted stir casting to fabricate Al6063/NFA composites. Distinctive weight portions 0, 1, 2, and 3%wt. of NFA were reinforced into the melt under steady stirring speed. The impact of %wt. of NFA was examined on cast samples to set up fabricated composites' wear behavior. It was discovered that wear resistance of Al6063/NFA composites expanded with increase in %wt. of NFA content. However, increase in sliding speed and wear load decreases the wear resistance.

**Keywords** NFA · Composites · Stir casting · Wear loss

## 1 Introduction

The solid materials have inadequacies concerning potential combinations of density, strength, and stiffness. Metal matrix composites (MMCs) have advanced to conquer these limitations and meet increasing demands of present day innovation. Recently, particulate-reinforced aluminum-based MMCs attracted the world due to their potential replacement to monolithic counterparts mostly in power and automobile sectors [1]. The consistent fiber-reinforced composites have improved strength; however, their manufacturing strategies are cost effective, which ruins their adoption. And those are not allow secondary manufacturing process of forming like forging, rolling,

---

N. R. Gosangi (✉)

Department of Mechanical Engineering, JNTUK, Kakinada, Andhra Pradesh 533003, India

L. Dumpala

Department of Mechanical Engineering, University College of Engineering, JNTUK, Kakinada, Andhra Pradesh 533003, India

and extrusion. Because of such limitations, the research has been focused on particulate reinforcements. The particulate-reinforced aluminum matrix composites are acquiring significance on account of their minimal effort with benefits like isotropic properties [2].

The AMCs are developed either by liquid casting or powder metallurgy. The casting has the benefits of producing the larger composites at low cost. Stir casting employed to fabricate composites materials is mixing dispersed phase with matrix phase in a liquid state through mechanical stirring [3]. Stirring speed and time were most influencing process parameters affecting particles' distribution in the molten matrix. An increase in these parameters improves the homogeneous dispersion of particulate reinforcement particles in the composites' matrix material [4]. However, the liquid casting's inherent difficulties are ceramic particles low wettability in liquid aluminum, segregation of particulates, high porosity levels, and reaction at interfacial due to elevated processing temperature [5].

The waste FA utilization can be improved by uniformly dispersing in the aluminum matrix material to fabricate composites [6]. The FA mainly consists of refractory oxides like alumina, iron, and silica used as the reinforcing phase [7]. Composites can be produced with different percentages of reinforcing phases [8]. The FA converted to rough irregular NFA and most suitable for aluminum metal matrix composites as reinforcement material. The clustered particles separated and dispersed through cavitations generated by ultrasonic waves, leading to the uniform distribution of NFA in the primary aluminum [9]. Higher percentage of FA reinforcement material leads to agglomeration and blow holes in the composites [10]. The FA reinforcement influenced the sliding wear and slurry erosive wear behavior of AMCs [11].

The sliding wear resistance increased in the composites due to fracture and debonding of FA particles at lower loads and sliding velocities [12]. Wear resistance increased with increased inclusion of FA particles [13]. The wear loss of the composite reduced due to the effect of FA particles, which influencing wear resistance [14]. In the present work, the NFA particles were reinforced into the Al6063 alloy with different weight proportions through an ultrasonic-assisted stir casting route. The Al6063/NFA composites were examined to establish the wear behavior by considering different sliding speeds and wear loads.

## 2 Experimentation

The matrix materials used in the experimentation were aluminum alloy (Al6063) and NFA as reinforcement material [5–7]. The AMC-reinforced with NFA was fabricated using ultrasonic-assisted stir casting. The Al6063 alloy ingots were heated and melted in electrical furnace. The molten metal temperature raised to 680 °C, and argon gas focused on the melt to avoid atmosphere contaminations.

Desired amount of FA based on %wt. NFA was added to the molten metal. Hence, the melt was stirred with stirrer for 4–5 min at a speed of 400 rpm [1–4]. The temperature of melt maintained at 680 °C which is above the melting point during inclusion

of FA particles. The distribution of reinforcing particles was carried by the vortex method. The FA-reinforced melt was poured into the permanent metallic preheated mold. The temperature was maintained at 670 °C during pouring. A vibrating probe at 20 kHz was inserted in molten metal to distribute the NFA particles uniformly in the melt to achieve the uniform distribution of reinforcement material in the primary aluminum. The molten metal was allowed for solidification. The %wt. of NFA was considered 0, 1, 2, and 3% by weight for fabricating individual separate castings [8, 9].

### 3 Results and Discussion

The tribological property wear is the resistance offered by the surface of the material against scratching. The Al6063/NFA composite specimens were tested on pin on disk wear resistance testing machine. Various process parameters were considered for testing on the pin on disk machine, and NFA was the most dominating parameter, reducing wear resistance drastically. Further, reduction in wear resistance was achieved with an increase in NFA in Al6063/NFA composites. The wear test was conducted at different wear loads, i.e., 20, 30, 40 and 50 N, and sliding speeds, i.e., 200, 300, 400, and 500 rpm for all specimens Al6063/NFA composites. Wear resistance was considered in weight loss/kg and obtained for all Al6063/NFA composites with 0, 1, 2, and 3%wt. of reinforcement material. The results were presented in the graphs shown in Fig. 1 based on testing parameters considered for the wear test.

#### 3.1 *Effect of NFA on Wear Resistance*

The wear resistance on Al6063/NFA composites at different loads, speeds, and different %wt. of NFA was recorded. It could be seen from Fig. 1 that the increase in %wt. of NFA added to the primary Al6063 alloy leads to decrease in wear resistance on Al6063/NFA composite irrespective of increasing load and sliding speed. Higher volume fractions of FA reinforcement improve the composites' grain refinement, which leads to the enhanced wear resistance in the composites, and increased wear rate in the composite materials was observed compared to pure aluminum alloys [10, 14].

Figure 1a shows the variation in wear loss of Al6063/NFA composites with enhanced %wt. of NFA at 200 rpm speed of disk. The reduced wear loss was observed with an increase in NFA reinforcement on the Al6063/NFA composites due to the effect of NFA particles. The nanoparticles were pushed to interdendritic locations, adhere to primary aluminum during the solidification. It leads to the improved wear resistance in the resulting composites with increase in the %wt. of nanoparticles [11, 12].

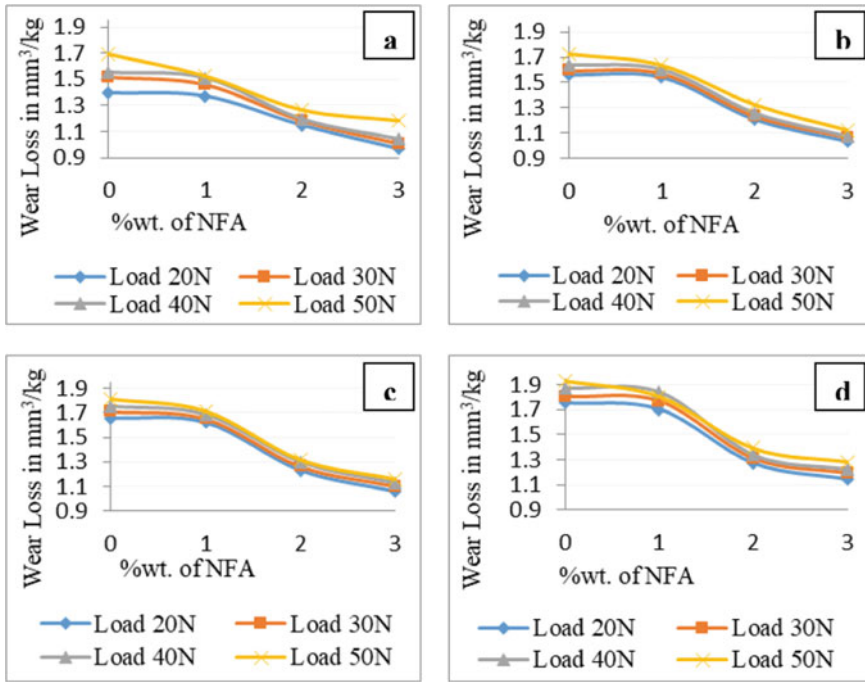


Fig. 1 Wear loss of Al6063/NFA composites at 200, 300, 400, and 500 rpm sliding speed

Figure 1b, d show variation of wear loss in Al6063/NFA composites with enhanced %wt. of NFA at 300, 400, and 500 rpm disk speeds. An increase in wear loss was obtained on Al6063/NFA composites with decreased disc speed of pin-on-disc machine. The wear resistance was low for the Al6063/NFA composites containing 3% NFA. And for the same percentage of NFA reinforcement, an increased wear rate was observed with an increased frictional load. Perhaps, due to tough and hard NFA particles distributed in the Al6063 alloy material, there was rapid attainment of stability in the wear resistance of Al6063/NFA composites was achieved. Increased wear resistance was observed by Zahi and Daud [13] with the inclusion of FA particulates in the AMCs.

### 3.2 Worn Surface Morphology

Figure 2 shows the SEM photographs of worn surface on Al6063/NFA composites.

The wear loss was high in the composites due to debonding and fracture of FA particles at lower loads and sliding velocities. The wear debris accumulation and consequent wear mechanism during abrasion were responsible for the increase in frictional resistance. Micro cutting, delamination, and abrasion were observed in

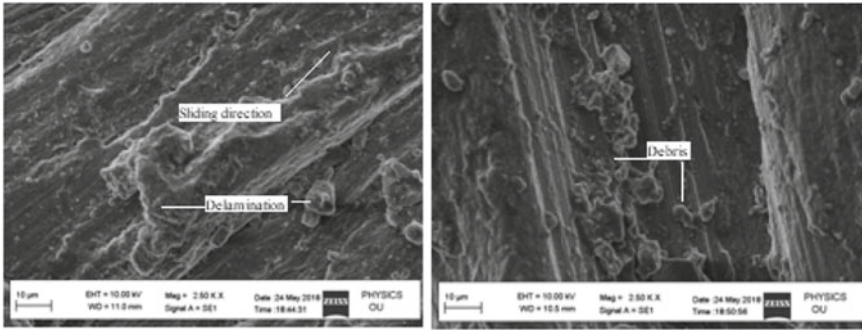


Fig. 2 SEM photographs of worn surface on Al6063/NFA composites

the composites due to crack propagation from rubbing surfaces [11]. The increased frictional force at elevated load leads to increased debonding and resulted in easy removal of surface material. Hence, the wear resistance was increased with increased normal load.

## 4 Conclusions

Following conclusions drawn from the effect of NFA on the wear behavior of Al6063/NFA composites.

1. The percentage weight of NFA included in the Al6063 alloy as reinforcement material decreases the wear loss of the Al6063/NFA composite irrespective of increasing load and sliding speed.
2. The wear loss decreased with an increase in NFA content and minimum for the Al6063/NFA composites containing 3% NFA.
3. The wear loss increases as the load increases and is almost constant at lower loads and increases with an increased sliding speed for all Al6063/NFA composites.
4. Abrasive wear was observed in the composites due to crack propagation from the rubbing surfaces.
5. Wear debris accumulation increases the wear loss due to debonding and fracture of FA particles at higher sliding speeds and wear loads.

### Future Scope:

1. NFA-reinforced composites could be developed by considering other aluminum alloys as matrix material.
2. Al6063/NFA composites could be developed by considering other manufacturing techniques like powder metallurgy.
3. TEM investigations could be carried to understand the detailed bonding nature of the matrix and reinforcement materials.

## References

1. Rohatgi PK, Guo RQ (1997) Low cost cast aluminium–FA composites for ultra light automotive applications TMS annual meeting. *Automot Alloys* 157–68
2. Sobczak J (1993) Metal matrix composites fabricated by the squeeze casting process. *Trans Foundry Res Inst* 415:1–99
3. Uvaraja VC, Natarajan N (2012) Optimization of friction and wear behaviour in hybrid metal matrix composites using Taguchi technique. *J Miner Mater Charact Eng* (11):757–768
4. Prabu SB, Karanamooty L, Kathiresan S, Mohan B, Influence of stirring speed and stirring time on distribution of particulates in cast metal matrix composite. *J Mater Process Technol* 171(2):268–273
5. Ezatpour HR, Sajjadi SA (2013) Microstructure and mechanical properties of extruded Al/Al<sub>2</sub>O<sub>3</sub> composites fabricated by stir-casting process. *Trans Nonferrous Met Soc China* 23(5):1262–1268
6. Narayana Swami P, Nooka Raju B, Venkata Rao D, Babu Rao J (2010) Synthesis and characterization of nano-structured FA: a waste from thermal power plant. *Proc Inst Mech Eng Part N J Nanoeng Nanosyst* 223(2):35–44
7. Tiwari M, Sahu MS, Bhangare RC, Ajmal PY, Pandit GG (2014) Elemental characterization of coal, FA, and bottom ash using an energy dispersive X-ray fluorescence technique. *Appl Radiat Isot* 90:53–57
8. Arun Kumar MB, Swamy RP (2011) Evaluation of mechanical properties of al6061, FA and e-glass fibre reinforced hybrid metal matrix composites. *ARPN* 6(5)
9. Narasimha Murthy, I. Venkata Rao, D and Babu Rao, J.: Microstructure and mechanical properties of aluminum – FA nanocomposites made by ultrasonic method. *Mater. Des.*, vol. 35, pp. 55–65, doi:<https://doi.org/10.1016/j.matdes.2011.10.019> (2012).
10. Vijaya Ramnath B, Elanchezian C, Naveen E, Nagarajakrishnan P, Chezian T, Saleem A, Srivalsan M (2018) Mechanical and wear behavior of aluminium-zircon sand-flyash metal matrix composite. *IOP Conf Ser Mater Sci Eng* 390:012018. <https://doi.org/10.1088/1757-899X/390/1/012018>
11. Ramachandra M, Radhakrishna K (2007) Effect of reinforcement of FA on sliding wear, slurry erosive wear and corrosive behavior of aluminium matrix composite. 262:1450–1462
12. Rohatgi PK, Guo RQ, Huang P, Ray S (1997) Friction and abrasion resistance of cast aluminum alloy–FA composites. *Met Mat Trans A* 28A:245–250
13. Zahi S, Daud AR (2011) FA characterization and application in Al-based Mg alloys. *Mater Des* 32(3):1337–1346. <https://doi.org/10.1016/j.matdes.2010.09.021>
14. Srinivasa Prasad K, Swami Naidu G (2016) WEAR behaviour of NFA reinforced aluminium-10 magnesium alloy matrix composites. *IEEE*. 978-1-4673-9939-5/16

# Formulation Correction of a Lubricant Oils During the Production Process a Case Study



S Shahab and Shaik Himam Saheb

**Abstract** Mostly base oil and additives and some dye are used for desired lubricants product. These two raw materials are widely divided into formulation on 9:1 ratio according to the different product classifications following the American Petroleum Institute (API) and Society of Automotive Engineers (SAE). As the testing of total manufactured components is impossible the sampling of the product is tested for quality results. Globally most of industries the sampling process carried out as per ASTM standards. The large scale manufacturing industries there are some errors which can lead to failing the proper product before testing on the equipment. While taking the sample there are human errors, sample test equipment errors, sampling quantity errors, raw material receiving errors, and formulation calculation errors. These errors leads to in accurate results of the products, In this article, the errors of sampling is taken as case study and three test samples were tested in three batches, and the laboratory results are presented.

**Keywords** Lubricants · Raw materials · Lube oil processing · Lube oil formulation category · Sampling extraction · Sampling errors

## 1 Introduction

Lubrication whether it is lubricant oil or greases it is focused on the same principle: the main function of a lubricant is to build a film between the two surfaces relative to two surfaces mating each other. To separate the surfaces and to avoid it from preventing touching are with each other. This helps to achieve a goal to reduce the frictional contact between the surfaces. Now selecting right viscosity oil is always

---

S Shahab (✉)

Department of Mechatronics, Faculty of Science and Technology, The ICFAI Foundation for Higher Education, Hyderabad, India

*Present Address:*

S. H. Saheb

Department of Mechatronics Engineering, Faculty of Science and Technology, The ICFAI Foundation for Higher Education, Hyderabad, India

a critical job to prevent is from surface to surface contacting and this oil is known as lubrication. The main property of this oil is to reduce the wear and friction and observe the amount of heat generated when heat is generated when the metal comes into contact.

When it comes about the science behind this is called boundary oil film. The oil whether it is grease oil or greases it is focused on a similar rule: the primary capacity of oil is to manufacture a film between the two surfaces comparative with two surfaces mating one another [1]. To isolate the surfaces and to stay away from it from forestalling to impact are with each other. This assists with accomplishing an objective to diminish the frictional contact between the surfaces. Now choosing a correct consistency oil is always a basic activity to forestall is from surface to surface reaching and this oil is known as grease [2]. The fundamental property of this oil is to lessen the wear and erosion and watch the measure of warmth produced when warmth is generated when the metal comes into contact [3].

Oil whether it is oil or grease it is focused on a comparable principle the essential limit of oil is to fabricate a film between the two surfaces similar with two surfaces mating each other is shown in Fig. 1. To confine the surfaces and to avoid it from thwarting are to affect with one another. This helps with achieving a goal to lessen the frictional contact between the surfaces. Presently picking right consistency oil is consistently an essential movement to thwart is from surface to surface coming to and this oil is known as oil. The principal property of this oil is to decrease the wear and disintegration and watch the proportion of warmth created when warmth is produced when the metal comes into contact. Oil whether it is oil or oils it is focused on a comparable principle: the essential limit of an oil is to produce a film between the two surfaces near with two surfaces mating each other [5, 6]. To disconnect the surfaces and to avoid it from hindering are to affect with one another. This helps with achieving a target to lessen the frictional contact between the surfaces [7]. Presently

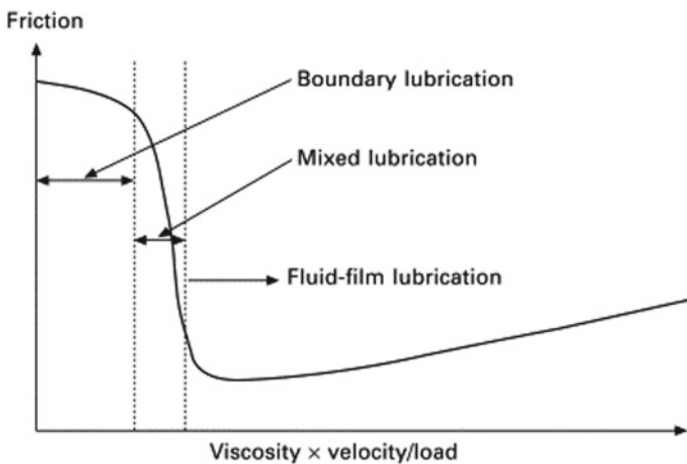


Fig. 1 Lubricant film [4]



picking right consistency oil is consistently an essential action to prevent is from surface to surface coming to and this oil is known as oil. The basic property of this oil is to diminish the wear and disintegration and watch the proportion of warmth created when warmth is produced when the metal comes into contact [8].

### ***1.1 Blending of Lube Oil***

The lubricant blending ratio depends on the acceptable or target viscosity of the product. However, the percentage of peroxide treated oil in terms of weight percentage of 77–99% for different products and the dependency ratio of additives in it. A mixed mineral oil is made having a higher consistency file than anticipated by ascertaining the thickness file from an ASTM standard technique assigned D 341-87 or by figuring the normal of the genuine VI dependent on the extent of every segment of the mix. The additive is treated with peroxide compound, ideally natural peroxide, for example, di-tertiary butyl peroxide to expand the thickness file. The treated additive is mixed with an oil of lower thickness list to accomplish mixed grease having an improved consistency list. The grease charge stock and mixing part can be a wax-inferred additive division or an ordinary light unbiased or overwhelming nonpartisan mineral oil.

As the formulae are decided on the product it is finally divided into a percentage of the weight of the raw material required. Then the raw material goes into the blending tank where the recipe is added and the product is heat-treated and performs many other activities in a mean time of 40–60 min maximum as shown in Fig. 2. If the sample is passed by the laboratory then the finished product is transferred into the finished product tank it is then distributed into the number batches of cans according to the requirement of the customers.

## **2 Methodology**

### ***2.1 Properties of a Lubricant***

A lubricant is basically tested for the following of its properties in the laboratory. Where the best lubricant is the one which exceedingly passes its properties and according to the American Society of testing materials (ASTM) method this below are the sequential process.

- I. **Viscosity:** It is the measure of a fluid of its resistance to deformation by its shear stress or tensile stress.
- II. **Pour point:** In pour point test the liquid is set at a temperature at which the liquid gets semi solid and losses its flow characteristics.

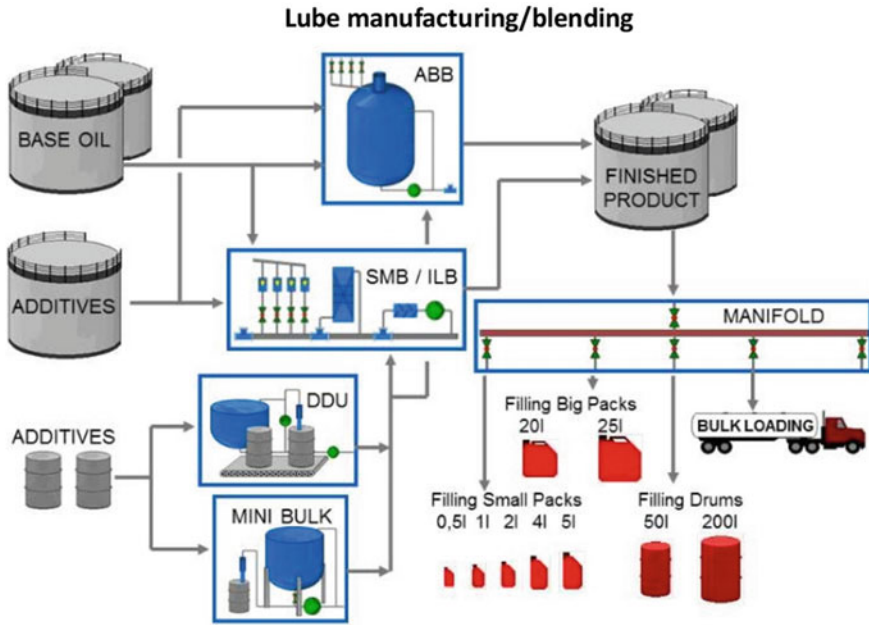


Fig. 2 Lubricant oil manufacturing process [9]

- III. **Flash point:** The flash point of the liquid is the minimum temperature at which there is more flammable vapour which ignites the air fuel mixture when an ignition source is taken place.
- IV. **Viscosity index:** VI is the arbitrary measure for the change of viscosity of a fluid with variation in temperature.
- V. **Oxidation stability:** This test shows the resistance shown by the oil to oxidation.
- VI. **Demulsibility:** In these tests the oil is separate from water its formation.
- VII. **Foaming:** Foaming is a collection of the minute bubbles formed on the surface of the liquid.
- VIII. **Air release:** It is the ability of the lubricants to release entrapped air.

This above definition is the basic knowledge of a testing for the finished product which will be helpful to understand the upcoming data in results.

## 2.2 Sampling Extraction

Extraction of the sample of any product is one of the most essential and the important job to be taken care off, otherwise this small mistakes can lead to failure of the product

in the laboratory and lead to waste a time, which is very precious in a manufacturing industry where a small delay in the approval of batch turn to lose the market.

There are some errors in any steps which is always needed to be corrected if there is a chance. In the lubrication industry after every production of a batch, the sample is to be tested up from the pipeline, drain line, above the kettle, and with the direct line to the laboratory. As a result, there are chances of an error that may fail the sample in the first attempt. The errors are human errors, equipment functioning errors, sampling errors, raw material error.

Now, considering each of the errors, I will elaborate it with the failed product sample and make a corrective act to find out the issue by comparing it to the results before and after from the laboratory.

### 3 Experimental Work: Case Study 1

#### 3.1 Human Error

In a human error in lubricants industry, when a new batch is created in an automation system like ABB batch production and simultaneously metered blending (SMB) the operator in a control room should keep a straight eye on the screen to monitor each and every steps which is already assigned according to the formulae of the product.

The steps for blending in the automation is of the following,

- i. Dosing of a raw material 1 from point A to B.
- ii. Dosing of raw material 2 from point A to B.
- iii. Stirring both the raw material in assigned time
- iv. Manual entry of any product
- v. Timer
- vi. Hot oil system to transfer an energy to the loss the viscosity of the product to mix it with minimum bubble formation.
- vii. QC evaluation
- viii. End.

Low calcium in a complete batch product of quantity 13000 Kg. According to its density 0.8624 g/ml the product actual size is 15,072 l, where the product specification is 20 W 50 with following to SAE standards.

When the product results come out the sample was failed due to less calcium in this product by 100 ppm (range was 2000–2500 ppm) following to the formulation of this product the requirement was 8.5% wt. of calcium-based additive equals to  $13000 * 8.5 = 1105$  kg.

Now, in the investigation it was found that the calcium value entered into the software by the operator 1005 kg instead of 1105 kg which made the difference of 100 kg of calcium.

**Table 1** Product sample result before correction

S. No.	Test name	Method	Units	Minimum	Type	Maximum
1	Density @ 15c, relative	ASTM D4052	g/ml	0.861	0.863	0.865
2	Appearance	Visual	Clear and bright			
3	Viscosity, kinematic 100c	ASTM D445	mm <sup>2</sup> /s	16.5	24	21.2
4	Viscosity, CCS –15C (20 W)	ASTM D5293	m pas (cp)	–	6100	7000
5	Zinc, % wt	ASTM D4951	% wt	0.101	0.106	0.119
6	Calcium, % wt	ASTM D4951	% wt	0.84	0.60	0.87
7	Phosphorus	ASTM D4951	% wt	0.09	0.093	0.109
8	Foaming	ASTM D892	MI	–	0	50
9	Molybdenum, %	ASTM D4951	% wt	0.01	0.011	0.012
10	Sodium, % wt	ASTM D4951	% wt	0.037	0.038	0.041
11	Flash point	ASTM D93	°C	–	260	–
12	Pour point	ASTM D97	°C	–	–24	–27

Later, we tried to correct the portion which was to be adding remaining 100 kg of calcium-based additive to balance its chemical properties. Below are the laboratory results with marks the difference before and after the correction.

After the 1st results which are shown in Table 1 where the calcium was less, the calcium-based additive was added to the product which was about 100 kg and then again after mixing of additive the new sample was taken and tested again shown in Table 2, where the calcium was found in the range with the present formulation of a product.

### 3.2 Case Study 2 (Equipment Functioning Error)

In this case equipment which is used lubricant industry which is called manifold is considered as shown in Fig. 3. The main principle of this system is to transfer a finished product to another tank or a filling machine at a time. The manifold is designed in two pipelines vertical and horizontal. When the vertical and horizontal line meet it is called a cross-sectional point, where at every intersection point a valve is fixed.

While transferring of raw material base oil from its originated located tank to the blending kettle the manifold is used, as the operating command was given correctly but due to some malfunction of the pressure line, it transferred 1000 plus to the tank adding 31000 kg equals to 35776 l of oil instead of 34770 l quantity into the tank.

**Table 2** Product sample\* result after correct in formulae

S. No	Test name	Method	Units	Minimum	Type	Maximum
1	Density @ 15c, relative	ASTM D4052	g/ml	0.8666	0.869	0.871
2	Appearance	Visual	Clear and bright			
3	Viscosity, kinematic 100c	ASTM D445	mm <sup>2</sup> /s	16.5	21	21.2
4	Viscosity, CCS –15C (20 W)	ASTM D5293	mpa.s (cp)	-	6600	7000
5	Zinc, % wt	ASTM D4951	% wt	0.101	0.111	0.119
6	Calcium, % wt	ASTM D4951	% wt	0.84	0.85	0.87
7	Phosphorus	ASTM D4951	% wt	0.09	0.106	0.109
8	Foaming	ASTM D892	MI	-	0	50
9	Molybdenum, %	ASTM D4951	% wt	0.01	0.002	0.012
10	Sodium, % wt	ASTM D4951	% wt	0.037	0.34	0.041
11	Flash point	ASTM D93	°C	-	260	-
12	Pour Point	ASTM D97	°C	-	-24	-27

\*0.5 ml of tube + 10 ml white spirit

**Fig. 3** Manifold used in industry



**Fig. 4** Manifold valve with added sensor

The pressure in the manifold pipeline helps the gear pump to have a smooth flow of oil, but if the pressure is build up more than maximum either it can burst the pipeline, destroy the valves or at last, it can open any other valve with pressure and goes in any other line which is dangerous. To avoid this mistake in future an additional conventional sensor and an air solenoid valve is attached to the opening or closing of a valve which act accordingly at the time of the same issue as shown in Fig. 4. This malfunction could have spoiled the product but with correction from formulae the base oil viscous improver and main additive was added which results to improve the viscosity of the hydraulic oil as shown in Table 3.

### **3.3 Case Study 3 (Sampling Error)**

Sampling process is an important and very responsible job for a sample man to transfer a sample from finished blending kettle to the laboratory for performing to get approval for the batch. A sample man is given an instruction on the procedure to be followed for getting a sample from a sampling line.

A sample man is trained from the standards of the international organization of standardizations (ISO). But there are some minor mistakes which are unseen to rectify. Also, the sample man should know the history of which product was blended before this product.

For example, a hydraulic oil is been blended in the kettle, after approval of the product it is been transferred to the finished tanks. Now the new product is been made but the colour of this product is more darken than the old one because the colour

**Table 3** Product sample\* result after correct in formulae

S. No	Test name	Method	Units	Minimum	Type	Maximum
1	Density @ 15c, relative	ASTM D4052	g/ml	0.8666	0.8678	0.871
2	Appearance	Visual	–	Clear		
3	Viscosity, kinematic 100c	ASTM D445	mm <sup>2</sup> /s	16.5	21	21.2
4	Viscosity, CCS –15C (0 W)	ASTM D5293	mpa.s (cp)	–	6600	7000
5	Zinc, % wt	ASTM D4951	% wt	0.101	0.111	0.119
6	Calcium, % wt	ASTM D4951	% wt	0.84	0.87	0.87
7	Phosphorus	ASTM D4951	% wt	0.09	0.106	0.109
8	Foaming	ASTM D892	ml	–	0	50
9	Molybdenum, %	ASTM D4951	% wt	0.01	0.002	0.012
10	Sodium, % wt	ASTM D4951	% wt	0.037	0.34	0.041
11	Flash point	ASTM D93	°C		250	
12	Pour Point	ASTM D97	°C		–30	–30

\*0.5 ml of tube + 10 ml white spirit

of the hydraulic oil is crystal clear with some haziness. In Fig. 5 is a perfect visual example to be understood.

Flushing is an important job for the operator who is making this oil and for the sample man is collecting the sample.

In Fig. 5, we can see: 1st sample from the right which is collected directly from sample line without flushing. 2nd sample from the middle is collected without flushing after 1st sample was taken 3rd sample, 1st from left is collected after flushing 20 l of oil into the bucket. The difference in these 3 samples makes us justify that the old blended oil whose colour was crystal clear was still in the pipeline, where the

**Fig. 5** Colour difference with and without flushing



**Table 4** Product sample before flushing

S. No	Test name	Method	Units	Minimum	Type	Maximum
1	Density @ 15c, relative	ASTM D4052	g/ml	0.861	0.820	0.889
2	Appearance	Visual			Very light brown	Not acceptable
3	Viscosity, kinematic 100c	ASTM D445	mm <sup>2</sup> /s	16.5	16	21.2
4	Viscosity, CCS – 15C (20 W)	ASTM D5293	mpa.s (cp)		6600	7000
5	Zinc, % wt	ASTM D4951	% wt	0.101	0.106	0.119
6	Calcium, % wt	ASTM D4951	% wt	0.84	0.87	0.87
7	Phosphorus	ASTM D4951	% wt	0.09	0.106	0.109
8	Foaming	ASTM D892	MI		0	50
9	Molybdenum, %	ASTM D4951	% wt	0.01	0.0012	0.012
10	Sodium, % wt	ASTM D4951	% wt	0.037	0.038	0.041
11	Flash point	ASTM D93	°C		260	
12	Pour point	ASTM D97	°C		–25	–27

\*0.5 ml of tube + 10 ml white spirit

dark brown colour from the present product makes it light brown and flushing and removing complete oil from the pipeline 4mtr gives us a good result. The result in Tables 4, 5, and 6 represent the data which is collected from this three samples show how it affects its properties.

Now, by comparing the results from Tables 4, 5, and 6 and Fig. 1 we can see there are major changes in the density, viscosity, and sodium from the three samples. As mentioned earlier the engine lubricant oil has more viscosity, density, and the zinc then hydraulic oil. If we keep Table 4 the sample without flushing as a reference for the following other results it can be noticed that the density rapidly increases and the colour changes comparing to Tables 5 and 6.

Also, the % wt of the zinc increase slightly in the second sample and more third sample as seen in Fig. 6 because the engine oil has more zinc then hydraulic oil. The number of CCS directly increases when the flushing of 20ltr which results in getting a purer form of current product sample.

From these results (visual and tabular data) it can be clearly seen that by following this method the ratio of sample rejection can be decrease and, in another way, it also smoothens the process of blending products.



**Table 5** Product sample before flushing for second time

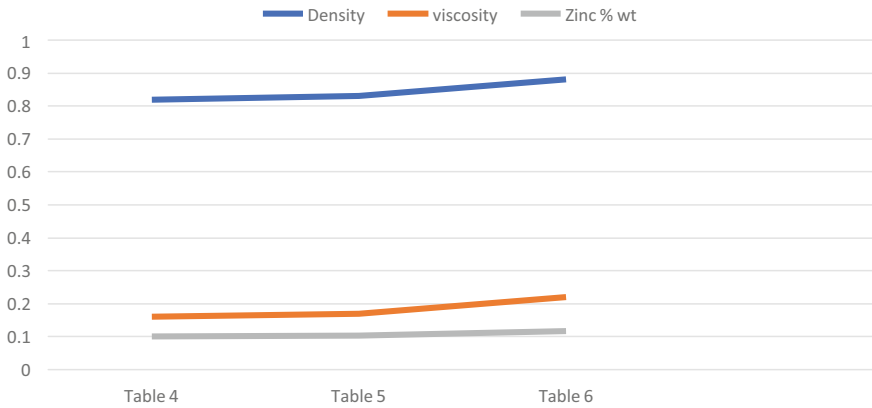
S. No	Test name	Method	Units	Minimum	Type	Maximum
1	Density @ 15c, relative	ASTM D4052	g/ml	0.861	0.859	0.889
2	Appearance	Visual			Light brown	Not acceptable
3	Viscosity, kinematic 100c	ASTM D445	mm <sup>2</sup> /s	16.5	19.2	21.2
4	Viscosity, CCS –15C (20 W)	ASTM D5293	mpa.s (cp)		6665	7000
5	Zinc, % wt	ASTM D4951	% wt	0.101	0.101	0.119
6	Calcium, % wt	ASTM D4951	% wt	0.84	0.87	0.87
7	Phosphorus	ASTM D4951	% wt	0.09	0.106	0.109
8	Foaming	ASTM D892	MI		0	50
9	Molybdenum, %	ASTM D4951	% wt	0.01	0.001	0.012
10	Sodium, % wt	ASTM D4951	% wt	0.037	0.042	0.041
11	Flash point	ASTM D93	°C		260	
12	Pour point	ASTM D97	°C		–25	–27

\*0.5 ml of tube + 10 ml white spirit

**Table 6** Product sample after flushing

S. No	Test name	Method	Units	Minimum	Type	Maximum
1	Density @ 15c, relative	ASTM D4052	g/ml	0.861	0.888	0.889
2	Appearance	Visual			Brown	
3	Viscosity, kinematic 100c	ASTM D445	mm <sup>2</sup> /s	16.5	20.1	21.2
4	Viscosity, CCS –15C (20 W)	ASTM D5293	mpa.s (cp)		6772	7000
5	Zinc, % wt	ASTM D4951	% wt	0.101	0.117	0.119
6	Calcium, % wt	ASTM D4951	% wt	0.84	0.87	0.87
7	Phosphorus	ASTM D4951	% wt	0.09	0.106	0.109
8	Foaming	ASTM D892	MI		0	50
9	Molybdenum, %	ASTM D4951	% wt	0.01	0.009	0.012
10	Sodium, % wt	ASTM D4951	% wt	0.037	0.038	0.041
11	Flash point	ASTM D93	°C		260	
12	Pour Point	ASTM D97	°C		–25	–27

\*0.5 ml of tube + 10 ml white spirit



**Fig. 6** Trend of value changes

### 3.4 Raw Material Error

In this industry, there are many additives which ordered around the world especially from the European countries. There are some additives in which it needs to be always hot on temperature to maintain its viscosity, carbon capture, and storage (CCS) at some temperature oil the time. But ones this treatment is overheated or the temperature does not heat to its limit then it releases its carbon emission when cause the failure of this additive. If this additive is used in the product this can cause damage to the total product and big loss.

**Concluding Remarks:** This paper, mainly focused on how sampling can be given importance especially for a fluid industry and save a lot of time also a losses in production, majorly for a company which does a mass production of 200 ton of lubricants product in a week. As we discussed about human error, equipment functioning error, sampling error, and raw material error in this paper with all the examples which we have faced in real-time while studying and performing the test for this paper. The data provided from Tables 1, 2, 3, 4, 5 and 6 are a result which is performed in this case study. The method which is tried to follow for human error, equipment error, and sampling errors can be fixed with taking the corrective action. This analysis is useful to the quality department to know the importance of sampling in the fluid industries.

## References

1. Gustavsson B, Luthbom K, Lagerkvist A (2006) Comparison of analytical error and sampling error for contaminated soil. *J Hazard Mater* 138:252–260. <https://doi.org/10.1016/j.jhazmat.2006.01.082>
2. Hansen MH, Waksberg J (1970) Research on non-sampling errors in censuses and surveys. *Revue de l'Institut International de Statistique/Rev Int Stat Inst* 38(3):317–332
3. Karanovic V, Mitar J, Wakiru J, Orošnjak M (2018) Benefits of lubricant oil analysis for maintenance decision support: a case study. *IOP Conf Ser Mater Sci Eng* 393:012013. <https://doi.org/10.1088/1757-899X/393/1/012013>
4. Burstein L (2011) 3—Lubrication and roughness, tribology for engineers. Woodhead Publishing, pp 65–120. ISBN 9780857091147. <https://doi.org/10.1533/9780857091444.65>
5. Fitch J, Troyer D (2000) Sampling methods for used oil analysis. *Lubr Eng* 56(11):39
6. Saheb SH (2015) Performance test on diesel engine using alternative fuels like B5 and B10. *Int J Mech Eng Rob Res*
7. Hisham S, Kadirgama K, Devarajan R, Noor MM, Amiruddin AK, Najafi G, Rahman MM (2017) Waste cooking oil blended with the engine oil for reduction of friction and wear on piston skirt. *Fuel* 205. <https://doi.org/10.1016/j.fuel.2017.05.068>
8. Higgins LR, Wikoff DJ (2008) *Maintenance engineer handbook*, 7th edn
9. <https://www.edl.poerner.de/en/areas-edl/lube-oil-blending/>

# Experimental Analysis of Wire Mask Assisted Reverse Micro-EDM (RMEDM) for Fabrication of Arrayed Rods



S. R. Dharmadhikari, S. A. Mastud, and R. H. Shinde

**Abstract** Arrayed micro rod has many applications in current technology like, printer heads, medical devices, micro heat sinks, etc. Many studies highlighted capability of RMEDM for fabrication of these features. From exhaustive literature it has been found that in every variant of RMEDM the pre-processed tool has prime requirement as the process is a replication of electrode features on work piece. Hence, pre-processing of tooling has direct influence on costing and time. In the present study, the feasibility of readily available micro wire masks has been studied. The array of square rods of 200  $\mu\text{m}$  side and 600  $\mu\text{m}$  lengths were successfully generated on 4 mm bulk rod of brass. The effect of process parameters like Voltage, Capacitance and feed rate on machining time is investigated. L 18 full factorial design is used for the experimentation. Analysis of variance (ANOVA) results were used to observe the influence of factors on overall machining and found the highest influence of Voltage followed by Capacitance. Scanning electron microscope (SEM) has been used to characterize the fabricated surface.

**Keywords** LIGA · Micro · MRR · Reverse micro—EDM · Micro—sieves · Surface roughness

## 1 Introduction

Current technological development, demands the miniaturization of mechanical parts within the range of 1–500  $\mu\text{m}$  with efficient utilization of space, energy and material. Arrayed micro features has wide applications in fields like electrical contacts, printer heads, medical devices, micro heat sinks, etc. [1–7]. Among many manufacturing methods MEDM has proven its suitability for fabricating arrayed features with high

---

S. R. Dharmadhikari (✉) · R. H. Shinde  
Department of Production Engineering, VJTI, Mumbai, India

S. A. Mastud  
Department of Mechanical Engineering, VJTI, Mumbai, India  
e-mail: [samastud@vjti.org.in](mailto:samastud@vjti.org.in)

aspect ratios also producing the replica of tool electrode on the work piece of any shape. The micro electrical discharge machining (MEDM) is capable of producing any complex shapes and arrayed features with high aspect ratios its use is limited to machine only electrically conductive materials.

RMEDM a process variant of MEDM has proven its suitability for creations of arrayed structures on metallic surfaces of any shape with accurate dimensions. Reverse micro electrical discharge machining (RMEDM) has shown its competency over the other process like LIGA and wire electrical discharge machining (WEDM) economically. The thin foils or plates that are pre-machined with required arrayed features cavity works as cathode and the work piece to be machine in larger surface area compared to tool is use as anode. The metal removal phenomenon is similar to that of conventional EDM process, but variation in electrode geometries results in positive features generation on the surfaces instead of negative features. Since last decades few studies has been cited towards the development of micro electrical discharge machining and its variant for efficient use for arrayed features fabrication and improving the productivity.

Kim et al. has studied the feasibility of process for fabrication of three micro pins with the dimensions of diameter  $35\ \mu\text{m}$  and length of  $1.5\ \text{mm}$  on tungsten carbide rod which were used as tool electrode for ECM process for improving the productivity. They also reported optimal process parameters for stable machining and minimum tool wear also, effect of debris resulting short circuiting disturbing the stable machining [1]. An array of  $40 \times 40$  micro pins array with average diameter below  $30\ \mu\text{m}$ , length of  $625\ \mu\text{m}$  and pitch of  $100\ \mu\text{m}$  with  $0.6\ \text{mm}$  thick brass plate predrilled using vibration assisted mechanical peck drill (VAMPD) was successfully fabricated by H-Wang et al. The variety of debris removal process also studied and suggested their suitability. Yi et al. has studied fabrication of  $3 \times 3$  and  $4 \times 4$  arrayed features on AISI 304  $100\ \mu\text{m}$  thick steel plate followed by utilization of those as an electrode for drilling  $6 \times 6$  and  $16 \times 16$  array of micro holes and results shows five times improvement in productivity over use of single electrode fabrication process [3]. Mastud et al. has studied the process mechanics using Voltage and current signals. They depict the influence of normal discharge condition on erosion rate also the process of RMEDM is stable at Capacitance of  $100\ \text{nF}$  and voltage of  $120\ \text{V}$  [8]. Majumdar et al. has studied the process characteristics and effects of processing parameters experimentally and found the stability of the process at  $100\ \text{V}$  but the features fabricated with the taper and reduction in side error compared to  $80\ \text{V}$  due reduced machining time for  $100\ \text{V}$  [9]. Tapas et al. fabricated array of  $25 \times 25$  micro fins using Wire EDM with an average height of  $820\ \mu\text{m}$  and investigated the effects of parameters on the features fabricated [10]. Singh et al. analysed the effects of process parameters to machine anisotropic brittle material, i.e. pyrolytic carbon using MEDM which depicted the increase MRR value and good surface characteristics obtained at  $110\ \text{V}$ . Increase in voltage and capacitance leads to increase the tool wear drastically and the formation of taper rods [11]. Gangadharudu et al. has experimentally investigated the feasibility of the REDM process to macro scale and studied the effects of process parameters. The peak current plays significant role towards the surface roughness, taper and cylindricity errors [12]. T Roy et al.

has developed variant of REMDM for fabrication of various shapes micro features and experimentally investigated the effect of flat bottom and taper bottom holes on fabrication of hemispherical structures [13]. Though, the reverse micro EDM (RMEDM) has proven its capability for fabrication of arrayed structures but due to non-rotational movement of tool electrode accumulation of debris between tool and work piece makes the process unstable. To eliminate the accumulation of debris particles and carbon particles Zeng et al. provided the vibration in axial direction and found very good surface finish and high aspect ratio of features compared to normal RMEDM process [14]. Mastud et al. fabricated 1.5 mm long micro rods with sizes 80 and 200  $\mu\text{m}$  of WC with studying the effect of various thickness of plate electrode on erosion rate and surface finish and found that the surface roughness improves by 20% and 11% respectively [15]. Mastud et al. with the help of vibration fabricated the textures in the form of pillars of 40–50  $\mu\text{m}$  with approximate spacing of 35  $\mu\text{m}$ . They have found the dimensional inaccuracies of machined structures varying from 20 to 45  $\mu\text{m}$  also the rods fabricated at centre were smaller in diameter compared to the pillars at periphery of work piece [16]. H-Wang et al. experimentally investigated the feasibility of multi stage micro holes electrodes and three different kinds of debris flushing mechanisms for fabricating 1600 micro pins array with average diameter below 30  $\mu\text{m}$ , length of 625  $\mu\text{m}$  and pitch of 100  $\mu\text{m}$ . The use of working fluid spraying, vibration assisted tool electrode and shake down type work piece enhances the stability of the process by expelling the debris from the interelectrode gap efficiently results in reduction of machining time as well as wear of tool [2]. Based on these studies it is found that the RMEDM process requires the pre-process tool electrodes as it is a process of replication of tool on the work piece. Therefore, the main objective of this study is to check the feasibility of wire mesh screen for fabrication of arrayed micro pillars and eliminate the process of pre-fabricated tool.

## 2 Experimental Setup and Method

The present study, investigate the feasibility of wire screen for fabrication of arrayed micro pillars, experiments have been conducted using Synergy Nano systems Hyper—15 (table top) micro EDM setup. Brass rod of 4 mm diameter is used as work piece and 200  $\mu\text{m}$  wire mesh used as a tool to eliminate the pre-processing of tool. The preliminary experiments were performed using one factor at a time. From the preliminary experiments it was observed that the higher and lower levels of parameters setting produces frequent short sparking between the tool and work piece due to accumulation of debris. Also, tool wear and machining time is more due to frequent pull out of work piece increasing the idle machining time. Also, while in trial experiments normal and reverse polarity is also analysed. The use of normal polarity results in more tool electrode wear and machining time compared to reverse polarity. The work piece of 4 dia and 10 mm in length is cut from bulk copper rods using CNC machine and the surface polished to make it flatten.

Voltage (V) and Capacitance (C) plays vital role in the process mechanics of MEDM and RMEDM which relates the spark energy as follows:

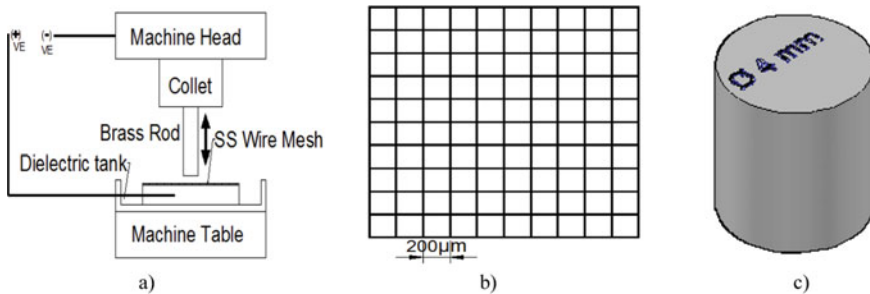
$$E = \frac{1}{2}CV^2 \quad (1)$$

Stability of MEDM process depends on the flushing of debris from the gap which depends on the spark energy, hence adequate amount of spark energy is playing a vital role. The occurrence of short circuiting was quite often at lower spark energies and goes on decreasing with increase in increase spark energy. Higher spark energies also not accepted as it produces higher size craters also higher amount of debris which are difficult to flush resulting short circuiting quite often.

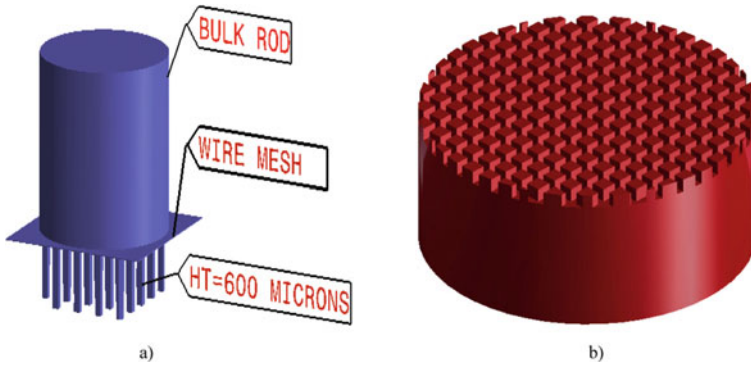
The work piece is attached to the spindle head using collet and the wire mesh is placed stationary on to the worktable. The work piece connected to negative terminal and the tool is connected to positive terminal as shown in (Fig. 1a). The to and fro motion is provided to the spindle for machining the arrayed rods. The process started as soon as the interelectrode gap between tool and work piece reaches too few microns producing the sparks with the help of dielectric fluid which removes the material from the surface with melting and evaporation phenomenon. The array of solid micro pillars is generated from the surface is in contact with the hollow portion of square mesh. Figure 2. a show arrayed micro rod.

The main objective of this study is to study the effects of process parameters, i.e. Voltage (V), Capacitance (C) and Feed rate (F) presented in Table 1 on the machining time.

In this context, L 18 full factorial based design of experiment was used to evaluate all possible combinations of parameters. For each parameter settings the machining time were recorded at every interval of 100  $\mu\text{m}$  machining. The machining length was fixed to 600  $\mu\text{m}$ . Minitab 17 a statistical tool is used to understand and analysed the recorded data and analysis of variance (ANOVA) was performed.



**Fig. 1** Schematic of **a** RMEDM process, **b** Tool electrode SS316 wire mesh of 200  $\mu\text{m}$  and **c** 4 mm dia brass rod



**Fig. 2** a Electrode positions while machining, b Array of micro rods after machining

**Table 1** Experimental conditions

<i>Details of work piece and tool material</i>			
Work piece:—brass rod of 4 mm diameter			
Tool:—SS316 Wire mesh of 200 μm			
<i>Processing parameters and their levels</i>			
Parameter	Level—1	Level—2	Level—3
Voltage (V)	80	100	120
Capacitance (pF)	100	1000	10,000
Feed rate (μm/s)	10	15	- -
Dielectric:—EDM oil			
Polarity:—reverse [tool (+) & work piece (-)]			
Objective:—machining time			

### 3 Result and Discussion

An array of square rods of 200 μm was fabricated successfully on brass rod using micro sieves. The sample images have been shown in Fig. 3a, b for easy view using higher magnification.

Analysis of variance is used to investigate the significance of the processing parameters on the response variable statistically. Estimation of variance in ANOVA is performed by calculating the degree of freedom for each term and sum of squares between the group and sum of square within the group for estimation of mean square values. The F value calculated using the factor mean square and error mean square then compared with critical F value identified from the statistical test tables. Values of P is estimated for each parameter using the percentage of contribution of factor in sum of squares and F values.



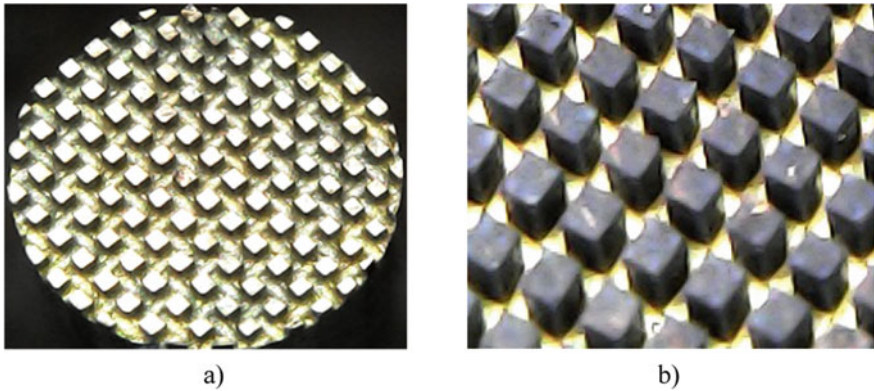


Fig. 3 Microscopic images of fabricated micro rods

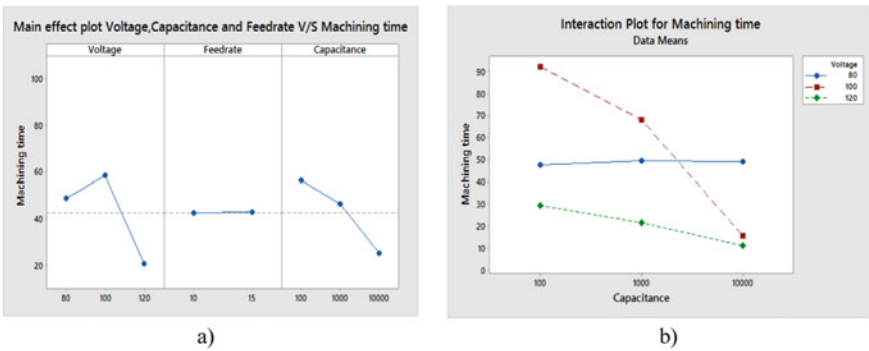


Fig. 4 a Main effect plot of voltage, capacitance and federate. b Interaction effect of voltage and capacitance

### 3.1 Effect of Processing Parameters on Machining Time

The time required for the machining depends upon the spark energy generated for the erosion and the craters developed on the surface of work piece. In RC circuit, frequent charging of capacitor results in difference of pulse energies for every individual spark. Also, the pulse energy shows the dependency upon Voltage, with increase in voltage the pulse energy gets increase but has zero effect on duration of sparks stated by cho et al. At lower voltage values the frequency of short circuiting is higher due to lower spark energies and accumulation of large amount of debris between tool and work piece. Based upon the combinations of process parameters the machining time required to machine the array of square rods varies from 11 min (120 V, 10,000 pF, 10  $\mu\text{m/s}$ ) to 96 min (100 V, 100 pF, 15  $\mu\text{m/s}$ ). From Table 2, it has been observed that Voltage has significant effect on the process followed by Capacitance and Feederate

has negligible effect on the machining time. Figure 4 represents the main effect plot of Voltage, capacitance and feed rate.

It has been seen from the main effect plot; the machining time was increasing as the voltage was increased from 80 to 100 V and decreasing further increasing of voltage to 120 V. Kim et al. [1] had also reported the significance of voltage to increase the erosion rate and minimize the machining time.

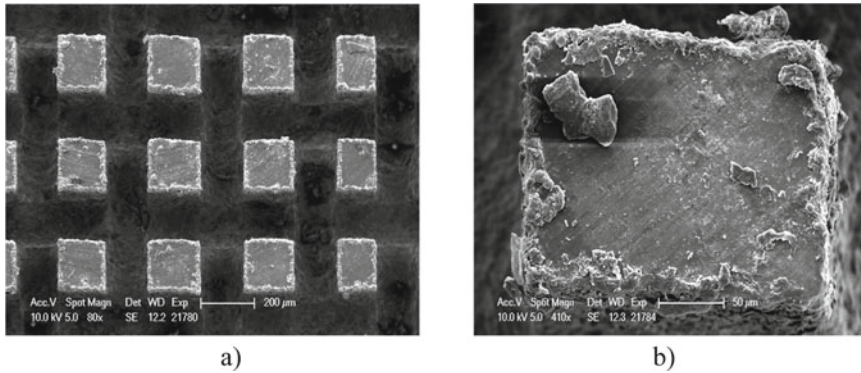
**Effect of Voltage:** According, the spark energy equation Voltage has square effect. At, lower values of voltage the short circuiting happen quite often due to smaller spark energies resulting pull out of electrode to several microns of height which stabilize the process and remove the debris entrap. This, results in increase of idol time of machining and overall machining time. With the traversal of tool electrode deeper into the work piece short circuiting happens quite often. When 120 V was applied the machining, time shows the least value which was the results of sufficient spark energy generation and pressure of discharging explosions for flushing out debris effectively. Hence, from analysis of variance (ANOVA) voltage was found the significant factor at 95% confidence level.

**Effect of Capacitance:** Capacitance was second most influential parameter which sets the charging time in RC circuit. Combined effect of capacitance with voltage decides the intensity of energy and crater formed. At higher capacitances due to large machining gap the frequency of short bridge was very rear. From main effect plot of Capacitance with machining time shows that continuous reduction in machining time with an increase of capacitance as indicated in Fig. 4a. Better debris evacuation was observed during the machining with 10,000 pF capacitance which can be a result of large machining gap.

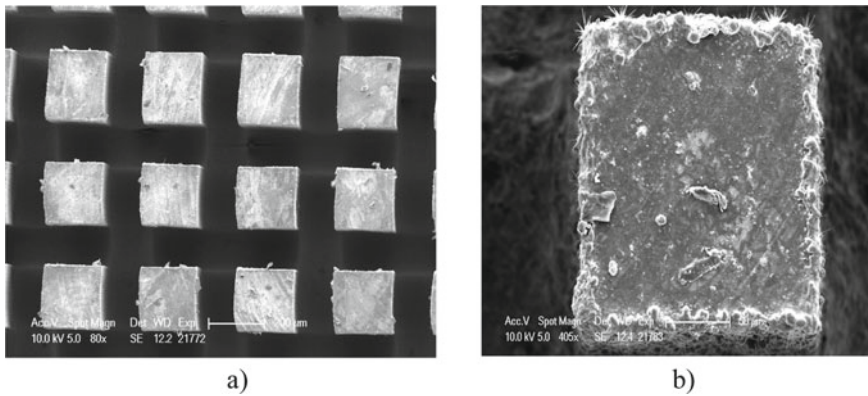
**Effect of Feedrate:** Feedrate is a parameter which has direct effect on idol time of machining during short circuiting. The accumulation of debris in the gap results in formation of short bridge and pullout of electrode until the elimination of short circuiting phenomenon. The feedrate results in quicker movement of electrode towards the work piece after elimination of short bridge. From main effect plot it was observed that feed rate has almost constant variation at every condition having negligible effect compared to other two factors.

To investigate the interaction, Voltage (V) kept constant at 80 V and capacitances was varied from 100 to 10,000 pF and it shows the negligible variation in machining time further at 120 V constant Voltage and varying capacitances machining time shown slight variation represented in Fig. 4b. Unlike 80 and 120 V at 100 V machining time shows large variation over the range of varying capacitances. This should be an effect of higher current exertion at the time of discharge.

Figures 5 and 6 shows different parts of arrayed rods at different magnification. The readdressence of large amount of debris particles can be clearly observed in Fig. 5b, also the globules formation is bigger and larger in size due to improper flushing of debris. Whereas in Fig. 6b, same scenario is observed at higher parameter settings but the amount of readdressence of debris particles and formation of globules is less. Increase in discharge pressure improves the surface finish of arrayed rods is clearly observed from Fig. 6a.



**Fig. 5** SEM images of Specimen fabricated at lower parameter settings



**Fig. 6** SEM images of Specimen fabricated at higher parameter settings

## 4 Conclusion

The feasibility of micro sieves to fabricate the array of square rods was studied using RMEDM. The experimental and statistical result clearly shows the Voltage (V) has prominent factor followed by Capacitance (C). The feed rate is insignificant factor for all combinations. Overall dimensions of micro rods varies from 175 to 195 μm. Very small amount of readherence of debris and globules formation on the machine surface is observed at 120 V and 10,000 pF levels and surface produce is very smooth. Finally, using RMEDM and micro sieves the arrayed of square micro rods were fabricated on brass rod successfully. The overall quality of pillars is very much acceptable.

## References

1. Kim B, Park B, Chu C (2006) Fabrication of multiple electrodes by reverse EDM and their application in micro-ECM. *J Micromech Micro Eng* 16(4):843–850
2. Hwang YL, Kuo CL, Hwang SF (2010) Fabrication of a micro pin array with high density and high hardness by combining mechanical peck-drilling and reverse EDM. *J Mater Process Technol* 210(9):24–27
3. Yi SM, Park MS, Lee YS, Chu CN (2008) Fabrication of a stainless-steel shadow mask using batch mode micro-EDM. *Microsyst Technol* 14(3):411–417
4. Mastud SA, Garg M, Singh R, Joshi SS (2012) Recent developments in the reverse micro-electrical discharge machining in the fabrication of arrayed micro-features. *Proc Inst Mech Eng C J Mech Eng Sci* 226(2):367–384
5. Singh SK, Chourasia A, Agarwal P (2014) Reverse EDM of collective electrodes in micro ECM. *Int J Appl Innov Eng Manage* 31(10):342–346
6. Takahata K, Gianchandani YB (2002) Batch mode micro electro discharge machining. *J Micro Electromech Syst* 11(2):102–110
7. Singh AK, Patowari PK, Deshpande NV (2016) Experimental analysis of reverse micro-EDM for machining microtool. *Mater Manuf Processes* 31(4):530–540
8. Mastud SA, Singh RK, Joshi SS, Johnson S (2011) Comparative study of the process mechanics in micro electrical discharge machining (EDM) and Reverse micro-EDM. In: *Proceedings of ASME 2011 international manufacturing science and engineering conference*, June 13–17, 2011, Corvallis, Oregon, USA
9. Mujumdar SS, Mastud SA, Singh RK, Joshi SS (2009) Experimental characterization of reverse micro- electric discharge machining process for machining of aspect ratio micro rod array. *Proc Inst Mech Eng Part B J Eng Manuf* 224(5):778–794
10. Tapas D, Patowari P, Fabrication of an array of micro-fins using Wire-EDM and its parametric analysis. *Mater Manuf Processes*, 1–10
11. Singh R (2008) Characterization of micro-EDM process for pyrolytic carbon. In: *Proceedings of the world congress on engineering*, London, U.K., 2–4 July 2008
12. Gangadharudu T, Gangopadhyay S, Nageendra B, Experimental investigation and optimization during the fabrication of arrayed structures using reverse EDM. *Mater Manuf Processes* 32(9):958–969
13. Roy T, Balasubramaniam R Effect of various factors influencing the generation of hemispherical micro features using nonconformal RMEDM, *J Micromanufacturing* 1–13
14. Zeng WL, Gong YP, Liu Y, Wang ZL (2008) Experimental study of microelectrode array and micro-hole array fabricated by ultrasonic enhanced micro-EDM. *Key Eng Mater* 364:482–487
15. Mastud S, Singh RK, Joshi SS (2012) Analysis of fabrication of arrayed micro-rods on tungsten carbide using reverse micro-EDM. *Int J Manuf Technol Manage* 26(1–4):176–195
16. Mastud SA, Singh RK, Joshi SS, Johnson S, Garg M (2012) Experimental characterization of vibration assisted reverse micro electrical discharge machining (EDM) for surface texturing. In: *International manufacturing science and engineering conference (MSEC)*, 4-8 June 2012, University of Notre Dame, South Bend, USA

# Powder Mixed Micro-Electric Discharge Machining—A Review



R. H. Shinde , D. N. Raut, N. G. Patil, and S. R. Dharmadhikari

**Abstract** Powder mixed micro-electric discharge machining ( $\mu$ PMEDM) is trending today in manufacturing industry because of its capability of creating complex three-dimensional shapes, high aspect ratio micro-holes and micro-machining of very hard materials like ceramics, tool steel and super alloy with dimensional accuracy as well as good surface finish. So there is need and scope for more research to be undertaken in this area to identify the influencing parameters to optimize the machining process. This paper aims to study the impact of technological and electrical input parameters such as voltage, current, capacitance, feed rate, rotational speed, powder mixed at different concentration levels on the output measures such as tool wear rate, material removal rate, surface roughness and surface integrity of the machined surface defining the performance of  $\mu$ PMEDM of advanced engineering materials, as it could open the possibility of its use in more innovative applications.

**Keywords** Powder mixed micro-electric discharge machining ( $\mu$ PMEDM) · Material removal rate · Tool wear rate

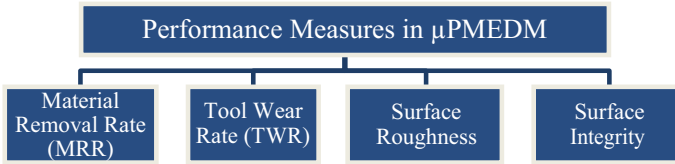
## 1 Introduction

$\mu$ EDM works on the same principle of macro-electric discharge machine, differing only with the tool dimensions, sparking energy and the size of the plasma at micro-level developed for its use in precision and accurate machining of micro-structures. Owing to its machining capability with good surface finish, in last few years,  $\mu$ PMEDM has gained popularity due to enhance process capabilities. This is an attempt of presenting effect of added powder in dielectric and the study of various methodology used by different researchers for optimizing the process, viz. material

---

R. H. Shinde (✉) · D. N. Raut · S. R. Dharmadhikari  
VJTI, Mumbai, M.S. 400019, India

N. G. Patil  
MIT, Aurangabad, M.S. 431005, India



**Fig. 1** Classification of response measures in micro-PMEDM

removal rate (MRR), tool wear rate (TWR), surface roughness (SR) and surface integrity to enhance the quality of micro-machining.

**Process Parameters:** The process parameters in  $\mu$ PMEDM which decides machining condition and affecting machining performance.

- Electrical parameters: Current, gap voltage, discharge voltage, capacitance, polarity, pulse frequency, pulse waveform, electrode gap.
- Powder-based parameters: Powder material, powder size, powder conductivity, powder concentration, powder density.
- Non-electrical parameters: Type of dielectric, working time, electrode feed rate, nozzle flushing, gain.
- Electrode-based parameter: Electrode material, electrode size, electrode shape.

**Response variable:** These variables measure the various process performances of EDM results.

- Material removal rate (MRR)/material erosion
- Tool wear rate (TWR)/electrode wear rate (EWR)
- Surface roughness
- Surface integrity (Fig. 1).

## 2 Material Removal Rate

The powder particle size, particle concentration, density, thermal and electrical conductivity of powder are found to be the most important characteristics that affect the machining process in  $\mu$ PMEDM [1]. Chow et al. [2] studied that mixing of silicon carbide and aluminum powders in kerosene increases the inter-electrode gap resulting in increased material removal rate and improved flushing efficiency. Kibria et al. [3] performed the experiment on titanium alloy Ti-6Al-4V using boron carbide (B<sub>4</sub>C) mixed kerosene, pure kerosene and de-ionized water as a dielectric and observed that de-ionized water gives more material removal rate, whereas higher value of MRR is achieved with rise in pulse interval in the boron carbide mixed kerosene than pure kerosene. Han et al. [4] presented the comparison between transistor type and traditional type pulse generator in  $\mu$ EDM. Where in the transistor type pulse generator shown better results in machining speed. Qian et al. [5] observed that in RC pulse generator, the reverse current is flowing due to the resonance capacitance

in the discharging circuit which increases MRR to a greater extent. Wong et al. [6] observed the eight times higher erosion efficiency of material removal at low energy discharges compared to that of higher energy discharges while investigating the material removal characteristics using single RC pulse discharges. They also observed consistency in the size and volume of micro-craters at lower energy discharge than that of higher energy discharge. Mustafizur Rahman et al. [7] demonstrated the effectiveness of de-ionized water as a dielectric in  $\mu$ EDM offering higher MRR as well as low tool wear than other dielectric media. At the same time, small pulse interval with higher value of frequency decreases material erosion.

### 3 Tool Wear Rate

Jahan et al. [8] have used nanopowders mixed in dielectric, e.g., graphite, aluminum and alumina in the  $\mu$ EDM of tool steel and tungsten carbide. Due to the presence of a conductive and semi-conductive nanopowder, there was uniform discharging and increased spark gap resulting the improved topography and surface finish significantly. In addition, increased spark gap contributed to higher MRR, lower tool wear. Ali et al. [9] have experimentally presented the effect of SiC powder mixed at different concentration along with range of discharge energy on  $\mu$ EDM of titanium alloy. They have observed remarkably reduced electrode wear as well as low surface roughness and better material removal. Kibria et al. [3] that during  $\mu$ EDM machining of titanium alloy. The de-ionized water gives more TWR than kerosene. Whereas use of B4C dielectrics gives higher value of MRR, but TWR reduces. Suzuki et al. [10] worked on the influence of size of (carbon nanotubes) CNT used on the wear characteristic of copper-based CNT composite tool. The reduction up to 72% in tool wear ration has been observed compared to electrolytic copper tools. Liew et al. [11] put up the study on effect of carbon nanofiber of diameter 150 nm and length 6–8  $\mu$ m added in dielectric, and their experimental results proposed that it not only improves the electrode gap, discharge frequency, material erosion rate but also reduces the electrode tip concavity and its wear. It also supports bidirectional material transfer among the electrodes. Cho et al. [12] observed the micro-hole produced in  $\mu$ EDM. They concluded higher value of electrode wear and machining time due to discharge inductance. They also observed that machining time rises with improvement in charging resistance. Wang et al. [13] adopted a pulse counting method to analyze the alternating current run during discharge to see the effect of reverse current. The reverse current flow helps to polish the edges and to form the crater. By passing the reverse current by connecting the diode between the spark tracks of the discharging circuit enhances the tool wear with respect to the workpiece removal. D'Urso et al. [14] performed the through micro-holes on stainless steel plates using three different tubular electrodes. They observed that brass and copper electrodes are best suited for high speed drilling than the tungsten one. But for best surface finish, dimensional accuracy and geometrical precision tungsten carbide electrodes proved to be best suited.



## 4 Surface Roughness

Although a number of researches are being carried out to improve the quality of surface of EDMed and micro-EDMed material in most of the cases, super finishing operations like lapping, diamond grinding and polishing are used after EDM [15]. However, in most of the cases, polishing or lapping is difficult to perform in micro-holes, small components, micro-molds and dies, as there is a chance of destroying the structures. At this point, for finishing processes, a novel approach in the form of uniformly dispersed suspended powder in the dielectric medium found to be most effective [16]. Jahan et al. [17] studied the surface characteristics improvement of  $\mu$ EDM and  $\mu$ EDM milling of cemented tungsten carbide using graphite nanoparticles mixed in dielectric. The results shown enhanced surface finish, material erosion rate and reduced the EWR. The powder mixed  $\mu$ EDM milling exhibited even and perfect surface because of good flushing condition compared to sinking  $\mu$ EDM. Tong et al. [18] have achieved accuracy of  $\pm 1 \mu\text{m}$ , Ra of  $0.38 \mu\text{m}$  and increased efficiency of 2.4 times during roughing and finishing boundaries by using online measurement method of micro-electrodes for the transformation of roughing and finishing operations by intersecting point electrical contact method between the micro-electrode and a standard thin rod. Chow et al. [19] checked the feasibility of using SiC mixed water as a dielectric, and as a result, he found better electrical conductivity, increased inter-electrode gap, improved material removal rate, flushing efficiency and considerably reduced surface roughness. Jahan et al. [20] experimented the effect of various added nanopowder such as alumina, graphite, aluminum to improve surface finish of  $\mu$ EDM of WC and reported that powder characteristics such as particle size, their concentration and density, thermal and electrical conductivity were found to be influencing one.

## 5 Surface Integrity

Dielectric mixed with conductive powder can increase the micro-hardness and reduces surface cracks; smaller the particle size, better the surface finish of the machined surface; the machining performance improves with excellent thermal and electrical conductivity of powder material; also, the lower density of it improves the machining performance in the EDM process [21]. Chen et al. [22] investigated study of  $\mu$ EDM using titanium powder mixed dielectric to analyze the modification of machined surface. The powder concentration of 3–6 g/l resulted in low to almost no surface cracks with increase concentration gradually. Mai et al. [23] proposed the novel technique of mixing CNTs with dielectric to attain a very fine finish. With the concentration of 0.4 g/l, the defects of recast layer and micro-cracks on the machined surface were considerably reduced, and the average surface roughness of  $0.09 \mu\text{m}$  was achieved within 1.2 h. The surface finish had been improved by almost 70%, and the machining time had improved up to 60%, respectively. Mustafizur



Rahman et al. [7] stated that machined surface with de-ionized water shows minor result from material movement as the smaller amount debris observed in the  $\mu$ EDM machining. Kibria et al. [3] stated that lower white layer thickness on EDMed surface is observed using de-ionized water compared to kerosene as dielectric fluid and also observed that the taper of the micro-hole was improved. Yeo et al. [24] presented systematic study of influence of mixed powder in dielectric on crater characteristics of  $\mu$ EDMed surface. It was observed during single spark investigations that the craters produced on the surface are smaller in diameter and depth also with the less circularity errors compared to craters produced without powder additives dielectric. Murali et al. [25] investigated the parameters affecting the micro-EDM and micro-structure. They identified that the Machining depth is inversely proportional to the feed rate.

## 6 Conclusions

The authors have tried to put brief summary of research work done so far in the area of powder mixed micro-EDM using different conductive and semi-conductive powder on different tool and workpiece material. It has been observed that much of the research works were conducted on the transistor type electric discharge machining. But the effect of important RC circuit process parameters such as capacitance and voltage and interaction effect of powder concentration on machining rate, tool wear and machined surface can be undertaken. Very little work has been reported on use of CNTs for micro-EDM process improvement, and almost no work is reported on effect of different powder particle shapes on machining parameters and output measures.

## References

1. Tzeng Y-F, Lee C-Y (2001) Effects of powder characteristics on electrodischarge machining efficiency. *Int J Adv Manuf Technol* 17(8):586–592. <https://doi.org/10.1007/s001700170142>
2. Chow H-M, Yan B-H, Huang F-Y, Hung J-C (2000) Study of added powder in kerosene for the micro-slit machining of titanium alloy using electro-discharge machining. *J Mater Process Technol* 101(1–3):95–103. [https://doi.org/10.1016/s0924-0136\(99\)00458-6](https://doi.org/10.1016/s0924-0136(99)00458-6)
3. Kibria G, Sarkar BR, Pradhan BB, Bhattacharyya B (2009) Comparative study of different dielectrics for micro-EDM performance during microhole machining of Ti-6Al-4V alloy. *Int J Adv Manuf Technol* 48(5–8):557–570. <https://doi.org/10.1007/s00170-009-2298-y>
4. Han F, Chen L, Yu D, Zhou X (2006) Basic study on pulse generator for micro-EDM. *Int J Adv Manuf Technol* 33(5–6):474–479. <https://doi.org/10.1007/s00170-006-0483-9>
5. Qian J, Yang F, Wang J, Lauwers B, Reynaerts D (2015) Material removal mechanism in low-energy micro-EDM process. *CIRP Ann* 64(1):225–228. <https://doi.org/10.1016/j.cirp.2015.04.040>
6. Wong Y, Rahman M, Lim H, Han H, Ravi N (2003) Investigation of micro-EDM material removal characteristics using single RC-pulse discharges. *J Mater Process Technol* 140(1–3):303–307. [https://doi.org/10.1016/s0924-0136\(03\)00771-4](https://doi.org/10.1016/s0924-0136(03)00771-4)

7. Nguyen MD, Rahman M, Wong YS (2011) An experimental study on micro- EDM in low-resistivity deionized water using short voltage pulses. *Int J Adv Manuf Technol* 58(5–8):533–544. <https://doi.org/10.1007/s00170-011-3397-0>
8. Jahan MP, Anwar MM, Wong YS, Rahman M (2009) Nanofinishing of hard materials using micro-electrodischarge machining. *Proc Inst Mech Eng Part B J Eng Manuf* 223(9):1127–1142. <https://doi.org/10.1243/09544054jem1470>
9. Ali MY, Adesta EYT, Rahman NABA, Aris EBM (2011) Powder mixed micro electro discharge milling of titanium alloy: analysis of surface roughness. *Adv Mater Res* 341–342:142–146. <https://doi.org/10.4028/www.scientific.net/amr.341-342.142>
10. Suzuki T, Kato M, Saito H, Iizuka H (2011) Effect of carbon nanotube (CNT) size on wear properties of Cu-based CNT composite electrodes in electrical discharge machining. *J Solid Mech Mater Eng* 5(7):348–359. <https://doi.org/10.1299/jmmp.5.348>
11. Liew PJ, Yan J, Kuriyagawa T (2013) Carbon nanofiber assisted micro electro discharge machining of reaction-bonded silicon carbide. *J Mater Process Technol* 213(7):1076–1087. <https://doi.org/10.1016/j.jmatprotec.2013.02.004>
12. Cho PJ, Kim BH, Choi DK, Chu CN (2008) Characteristics of MEDM for micro-holes with respect to circuit elements. *J Mech Sci Technol* 22(2):300–307. <https://doi.org/10.1007/s12206-007-1039-0>
13. Wang J, Yang F, Qian J, Reynaerts D (2016) Study of alternating current flow in micro-EDM through real-time pulse counting. *J Mater Process Technol* 231:179–188. <https://doi.org/10.1016/j.jmatprotec.2015.12.010>
14. D'Urso G, Maccarini G, Quarto M, Ravasio C (2015) Investigation on power discharge in micro-EDM stainless steel drilling using different electrodes. *J Mech Sci Technol* 29(10):4341–4349. <https://doi.org/10.1007/s12206-015-0932-1>
15. Koshy P, Jain V, Lal G (1997) Grinding of cemented carbide with electrical spark assistance. *J Mater Process Technol* 72(1):61–68. [https://doi.org/10.1016/s0924-0136\(97\)00130-1](https://doi.org/10.1016/s0924-0136(97)00130-1)
16. Wong Y, Lim L, Rahuman I, Tee W (1998) Near-mirror-finish phenomenon in EDM using powder-mixed dielectric. *J Mater Process Technol* 79(1–3):30–40. [https://doi.org/10.1016/s0924-0136\(97\)00450-0](https://doi.org/10.1016/s0924-0136(97)00450-0)
17. Jahan MP, Rahman M, Wong YS (2010) Study on the nano-powder-mixed sinking and milling micro-EDM of WC-Co. *Int J Adv Manuf Technol* 53(1–4):167–180. <https://doi.org/10.1007/s00170-010-2826-9>
18. Tong H, Li Y, Zhang L (2015) On-machine process of rough-and-finishing servo scanning EDM for 3D micro cavities. *Int J Adv Manuf Technol* 82(5–8):1007–1015. <https://doi.org/10.1007/s00170-015-7416-4>
19. Chow H-M, Yang L-D, Lin C-T, Chen Y-F (2008) The use of SiC powder in water as dielectric for micro-slit EDM machining. *J Mater Process Technol* 195(1–3):160–170. <https://doi.org/10.1016/j.jmatprotec.2007.04.130>
20. Jahan MP, Rahman M, Wong YS (2010) Modelling and experimental investigation on the effect of nanopowder-mixed dielectric in micro-electrodischarge machining of tungsten carbide. *Proc Inst Mech Eng Part B J Eng Manuf* 224(11):1725–1739. <https://doi.org/10.1243/09544054jem1878>
21. Yih-fong T, Fu-chen C (2005) Investigation into some surface characteristics of electrical discharge machined SKD-11 using powder-suspension dielectric oil. *J Mater Process Technol* 170(1–2):385–391. <https://doi.org/10.1016/j.jmatprotec.2005.06.006>
22. Chen S-L, Lin M-H, Huang G-X, Wang C-C (2014) Research of the recast layer on implant surface modified by micro-current electrical discharge machining using deionized water mixed with titanium powder as dielectric solvent. *Appl Surf Sci* 311:47–53. <https://doi.org/10.1016/j.apsusc.2014.04.204>
23. Mai C, Hocheng H, Huang S (2011) Advantages of carbon nanotubes in electrical discharge machining. *Int J Adv Manuf Technol* 59(1–4):111–117. <https://doi.org/10.1007/s00170-011-3476-2>

24. Yeo SH, Tan PC, Kurnia W (2007) Effects of powder additives suspended in dielectric on crater characteristics for micro electrical discharge machining. *J Micromech Microeng* 17(11):91–98. <https://doi.org/10.1088/0960-1317/17/11/n01>
25. Murali M, Yeo SH (2004) Rapid biocompatible micro device fabrication by micro electro-discharge machining. *Biomed Microdevice* 6(1):41–45. <https://doi.org/10.1023/b:bmmnd.0000013364.71148.51>

# Effects of MoS<sub>2</sub>-Based Biodegradable Cutting Fluids in MQL During Turning of Stainless Steel



N. R. Patil , D. R. Waghole , and A. K. Bewoor 

**Abstract** Cutting fluids are meant to reduce the frictional wear and to dissipate the heat generated at the tool–workpiece interface, during machining operations. Conventionally applied cutting fluids are mineral-based oils, which pose grave environmental and health hazards. The traditional flood cooling systems result in cleaning and disposal issues apart from a lot of water consumption. In recent years, research work is focused on exploring sustainable techniques with the use of biodegradable oils as cutting fluids and the supply concepts like minimum quantity lubrication (MQL). Vegetable oils, apart from being bio degradable, have strong potential by virtue of their superior lubrication properties. Moreover, addition of nanoparticles in vegetable oils exhibits better performance. The present work conducts experimental-based investigations of machining SS410 for minimum quantity lubrication (MQL) condition. Molybdenum disulfide (MoS<sub>2</sub>) nanoparticles with palm oil and coconut oil are used as cutting fluids. The experimentations are carried out under selected conditions, and machining performance is measured. Analysis is done to identify the combination for optimum machining performance.

**Keywords** Biodegradable · Nanofluid · MQL

---

N. R. Patil (✉) · D. R. Waghole  
Dr. Vishwanath Karad M.I.T. World Peace University, Pune, India  
e-mail: [nitin.patil@cumminscollege.in](mailto:nitin.patil@cumminscollege.in)

D. R. Waghole  
e-mail: [dnyaneshwar.waghole@mitwpu.edu.in](mailto:dnyaneshwar.waghole@mitwpu.edu.in)

A. K. Bewoor  
Cummins College of Engineering for Women, S.P.P.U., Pune, India  
e-mail: [anand.bewoor@cumminscollege.in](mailto:anand.bewoor@cumminscollege.in)

## 1 Introduction

During machining operations, the tool–workpiece interface is subjected to considerable friction and the resulting heat generation. The cutting fluid ensures reduction in friction and dissipation of heat generated.

Commonly used cutting fluids consist of oil–water emulsions, gels, pastes, aerosols, air or gases, etc. These are generally petroleum-based or made from plant oils, animal fats, air, water, and other ingredients. Traditionally, flood cooling technique is used to deliver the cutting fluid at the tool–workpiece interface. This involves abundant use of cutting fluid thereby causing very high consumption rate as high as 1200 l/h [1]. The cost related to the use of cutting fluids range from 7 to 17% of total cost of manufactured workpiece. As conventional cutting fluids are mineral-based oils, their disposal causes soil and water contamination, thereby posing severe environmental hazards [1].

Moreover, traditional cutting fluids contain constituents like chlorinated paraffin in extreme pressures (EPs) and other chemical additives. Exposure to these cutting fluids causes irritation to eyes, nose, skin, lungs and throat and respiratory diseases such as acne, dermatitis, hypersensitivity pneumonitis, asthma, chronic bronchitis. Cutting fluid degrades in quality after number of uses since it is contaminated by hazardous chemical constituents and metal carry off, oil content oxygen depletion, and nutrient loading. Mist generated from evaporation of cutting fluid can also be the reason of serious health issues.

To overcome these issues, it is necessary to switch toward sustainable machining techniques. Minimum quantity lubrication (MQL), also known as near dry machining, has emerged as a significant alternative as it involves very small quantity of cutting fluid to be applied exactly tool-workpiece interface, with the aid of compressed air. MQL enhances the machining performance, eliminates the disposal issues, and ensures cost reduction. There is variation in the quantity or amount of lubricant used in MQL according to various studies. According to review by Boswell Islam et al., Tschatsch and Reichelt reported that consumption rate of cutting fluid is 50 ml/h–2 l/h where according to other studies it is 10–100 ml/h [1].

Vegetable oils can be applied in MQL by virtue of its better lubrication and high-pressure performance. Also in terms of resource renewability, biodegradability, and performance efficiency vegetable oils are environment friendly [2]. But vegetable oils suffer from some drawbacks, in particular they have high pour point and low oxidation stability. Recent developments indicate that MQL combinations with various additives, nanoparticles, ionic liquids, cryogenic MQL, cooled air and supercritical carbon dioxide can improve the performance of vegetable oil. MQL containing nanofluids is effective in reducing friction, tool wear and to improving surface quality and the tool life. Nanofluids are potential heat transfer fluids owing to their better tribological and thermal properties. Nanofluids used while machining yields better lubrication due to its inherent properties of rolling, sliding, filming and better surface finish due to mending and polishing characteristics [3].

Lawal et al. [4] reviewed available literature on lubrication techniques like high-pressure coolant, cryogenic cooling, solid lubricant, air/vapor/gas as coolant, and minimum quantity lubrication during metal cutting processes including case study for MQL using vegetable oil-based lubricant. MQL with rapeseed oil has only a small lubricating effect and MQL with synthetic ester without water shows a better lubrication effect. MQL with palm oil produced lower tool wear as compared to MQL with synthetic oil during drilling of titanium alloys.

Kumar Gajrani et al. [5] focused on finding the use of vegetable-based oils as cutting fluid with the intention that machining processes become eco-friendly and less lethal for operators. Vegetable oils mostly consist of triglycerides which are long-chain fatty acids having number of unsaturated double bonds. Higher biodegradability, high viscosity index, higher boiling point, high molecular weight, and homogeneous nature make these oils to be used as metal working fluids. Reduction in tool wear, surface roughness, and metal cutting temperature was obtained in turning of AISI 1060 using MQL with vegetable oil. Different oils like sunflower, canola, semi-synthetic and mineral-based cutting fluids were used, and their experimental performance was compared in turning of AISI 304 stainless steel. Coconut oil was able to perform best in terms of reducing temperature, cutting forces, tool wear, and better surface finish during turning of AISI 304 stainless steel as compared to an emulsion and neat cutting oil. In high-speed drilling of Ti-6Al-4 V, lower tool rate was measured during MQL with palm oil than MQL with synthetic ester. MQL with palm oil has outperformed others (synthetic ester MQL, dry air machining, and flood cooling) in terms of wear rate. Due to its high viscosity, palm oil resulted in reduction of friction and tool wear.

Nanoparticles can be used for improving the heat transfer capability of cutting fluids. Nanofluids are colloidal suspensions of nanoparticles in base fluid [6]. Amrita et al. [7] have evaluated the performance of nanographite-based cutting fluid in machining process in turning of AISI 1040 Steel using MQL. Comparison is done between dry, flood, and MQL cooling by using conventional cutting fluids and MQL used with nanofluid. Nanofluid has shown better wear preventive properties as compared to flood cooling. MQL application as compared to flood cooling showed decrease in the cutting forces by 54%, cutting temperature by 25%, tool wear by 71%, and surface roughness by 30%. Chip morphology was also found to be improved. This is due to the penetration of droplets of nanofluid into the interface. Minute droplets formed due to mist application convicts heat generated at interfaces efficiently than flood cooling due to increased surface area of each drop reducing cutting temperature. The MQL application with nanofluid showed better results as compared to MQL with conventional fluids. It decreased cutting forces by 50%, cutting temperature by 40%, tool wear by 37%, and surface roughness by 28%. The nanoparticles addition decreased the temperature and friction at interfaces slowing down the wearing process of tool and reducing flank wear.

MoS<sub>2</sub> nano particles are used along with paraffin oil and soyabean oil. The results were compared with flood cooling. Results indicated lowering in losses due to friction thereby exhibiting 53% lesser energy consumption. Enhanced performance

**Table 1** Orthogonal array (L9) for the design of experiment

Exp. No	Speed (m/min)	Feed (mm/rev)	Pressure (bar)	Concentration (wt%)
1	250	0.1	3	0
2	250	0.15	4	0.25
3	250	0.2	5	0.5
4	400	0.1	4	0.5
5	400	0.15	5	0
6	400	0.2	3	0.25
7	530	0.1	5	0.25
8	530	0.15	3	0.5
9	530	0.2	4	0

was achieved with higher nano particle concentration. Also there was boost of 50% in G-ratio leading to higher wheel life.

## 2 Design of Experiments

For each combination of oil and nanoparticle, variation of control parameters, viz. cutting speed, feed, concentration of nanoparticles and pressure each in three levels result in  $3^4$ , i.e., 81 experiments. Taguchi method gives optimum solution with reduced set of experiments. The array presented by Taguchi with number of control factors and number of levels for each factor placed orthogonally is used to find optimum number of experiments. In this experiment, 4 control factors with 3 levels require minimum 9 experiments as shown in Table 1.

It is desirable to obtain performance parameters to be lower as possible in value, smaller the better approach is adopted while computing the S/N ratio.

## 3 Experimental Setup and Data Acquisition

See Fig. 1 and Table 2.

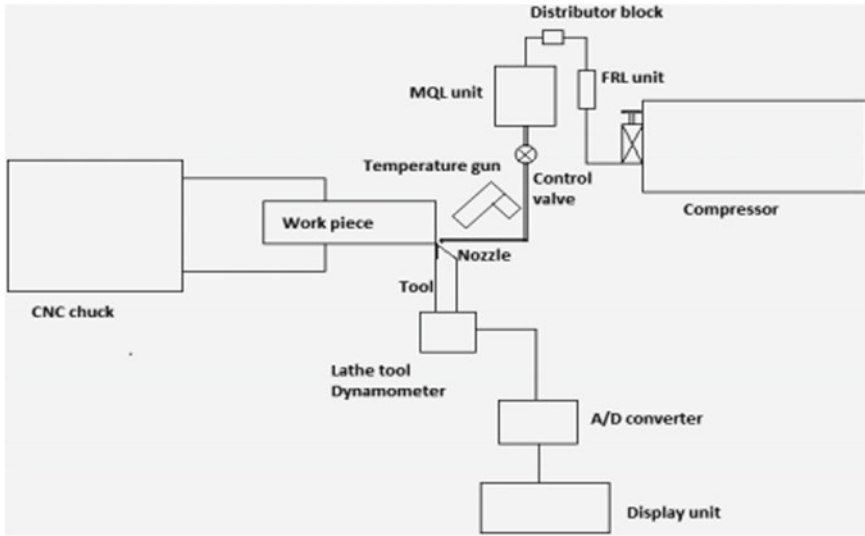
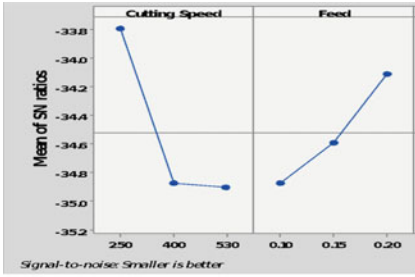


Fig. 1 MQL experimental setup

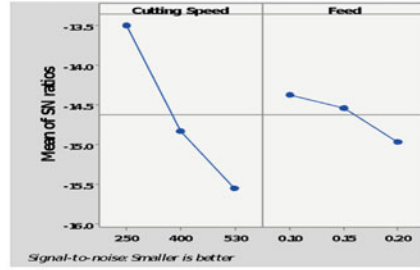
Table 2 Parameters for experimentation

<i>Machine tool and materials</i>	
Machine tool	CNC machine tool (texcellence)
Workpiece material	SS410 bars (Ø50)
Cutting tool insert	TNMG inserts (nose radius = 0.8 mm)
<i>Process parameters</i>	
Feed rate	0.1, 0.15, 0.2 mm/rev
Cutting speed	250, 400, 530 rpm
Depth of cut	0.2 mm
Cutting environment	Dry cooling, minimum quantity lubrication
MQL supply	Pressure: 3, 4, 5 bar Supply rate: 600 ml/h (Nozzle angle 45° and at 50 mm from rake face)
<i>Coolant parameters</i>	
Lubricants	Coconut oil <ul style="list-style-type: none"> <li>• Thermal conductivity—0.321 W/mK</li> <li>• Viscosity—29 cP</li> <li>• Density—924.27 kg/m<sup>3</sup></li> </ul> Palm oil <ul style="list-style-type: none"> <li>• Thermal conductivity—0.1721 W/mK</li> <li>• Viscosity—43 cP</li> <li>• Density—887.5 kg/m<sup>3</sup></li> </ul>
Nanoparticles	Molybdenum disulfide (50 nm, purity: 99.90%) Spherical shape
Mixture concentration	0, 0.25, 0.5% wt./vol. nanoparticles in oil

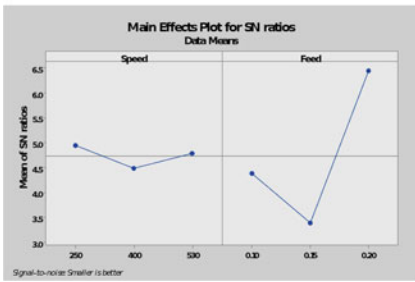




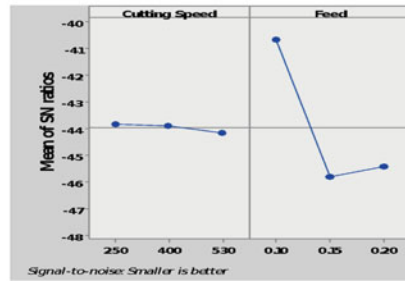
a) Temperature



b) Surface roughness



c) Tool Wear



d) Cutting forces

Fig. 2 Plots for dry machining

## 4 Results and Discussion

### 4.1 Dry Cutting

- In the absence of cutting fluid, there is increase in surface roughness with feed and speed.
- Optimum cutting forces are obtained at speed of 250 rpm speed and feed of 0.1 mm/rev (Fig. 2).

### 4.2 MoS<sub>2</sub> + Coconut Oil

See Fig. 3.

### 4.3 MoS<sub>2</sub> + Palm Oil

See Fig. 4 and Table 3.

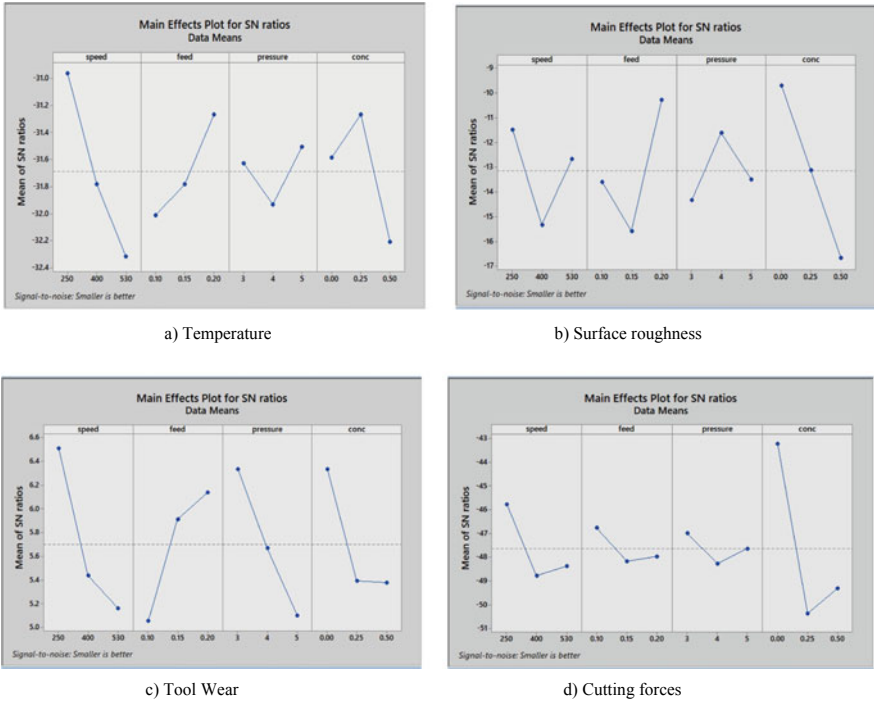


Fig. 3 Plots for MoS<sub>2</sub> + coconut oil

- At low concentration of nanoparticles, viscosity of cutting fluid is low forming thin lubricating film at tool workpiece interface. Also at low concentration of nanoparticles, thermal conductivity of cutting fluid is low. Thus, high temperature has been observed.
- At high concentration of nanoparticles, viscosity of cutting fluid is high forming thicker film layer thus not able to penetrate efficiently. Thus, high cutting force is observed.
- Built-up edge wear decreases at higher cutting speed, thus improvement in surface roughness has been observed. Whereas surface roughness increases at higher concentration of nanoparticles as it begins to agglomerate resulting in ineffective lubrication.
- Cutting edge of tool is not in contact with workpiece for long time at higher feed value which results in lower tool wear. At high pressure, chips are carried away efficiently thus resulting in reduction in tool wear.
- Temperature rise at cutting zone is observed at higher speeds as tool contact with workpiece increases. Whereas, at higher feed value cutting edge of tool is not in contact with workpiece for long time resulting in lower temperatures.
- Coconut oil lubricating film breaks at high speed, and thus, tool wear increases with increasing speed. Cutting edge of tool is not in contact with workpiece for

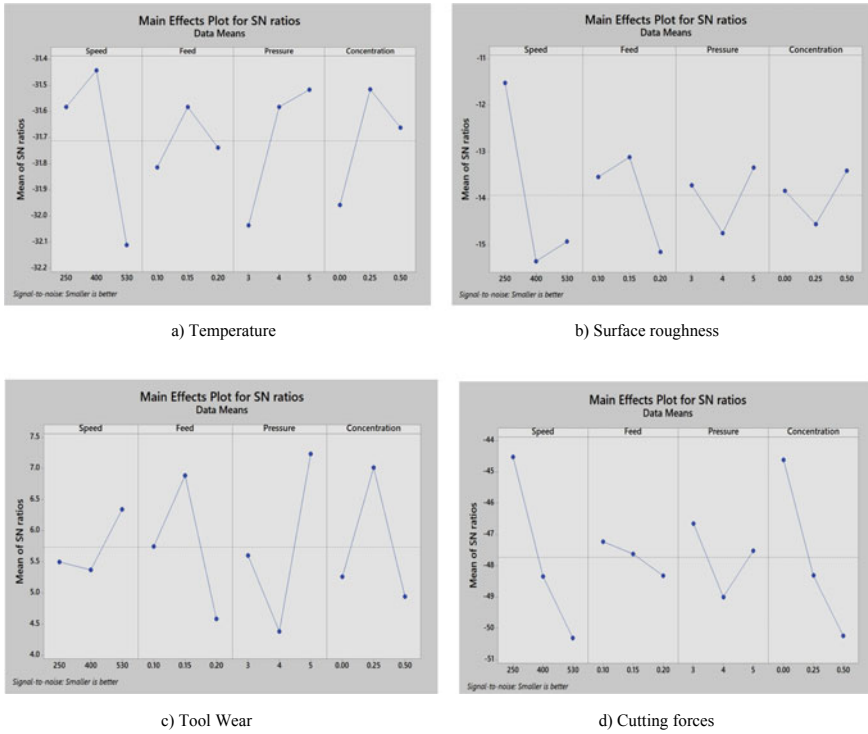


Fig. 4 Plots for MoS<sub>2</sub> + palm oil

Table 3 Variation in measured attributes as compared to dry machining

Cutting fluid	Surface roughness (%)	Tool wear (%)	Temperature (%)
MoS <sub>2</sub> -coconut	6.9	11.82	29.47
MoS <sub>2</sub> -Palm	6.17	10.89	27.85

long time at higher feed rates, and thus, lower tool wear is observed at the highest feed value.

- Frequency of tool contact increases at high speed. Hence, better surface finish is observed. Low tool wear is noted at high pressure of MQL supply because chips are carried away efficiently.
- Low concentration of nanoparticles is insufficient to induce rolling effect, and thin lubricating film of nanofluid is formed. Therefore, high tool wear and higher surface roughness are observed at low concentration is observed.
- MoS<sub>2</sub>-coconut oil outperforms the MoS<sub>2</sub>-palm oil in terms of surface roughness, tool wear, and temperature. This is because of lower viscosity, and higher thermal conductivity of coconut oil as compared to palm oil.

- The optimum solution for MoS<sub>2</sub>-coconut oil is obtained for 250 rpm speed, 0.2 mm/rev feed, 3 bar pressure, and 0 concentration.

The optimum solution for MoS<sub>2</sub>-palm oil is obtained for 250 rpm speed, 0.2 mm/rev feed, 5 bar pressure, and 0 concentration.

## 5 Conclusions

In this paper, experimental-based investigations are carried out using molybdenum disulfide (MoS<sub>2</sub>) nanoparticles with palm oil and coconut oil as cutting fluids with minimum quantity lubrication (MQL) for turning SS410. The investigations suggest that the use of biodegradable nanofluids applied with MQL exhibit good cooling and lubrication effects, thereby overcoming the limitations of conventional mineral-based cutting fluids with flood cooling. Significant reduction in tool wear, surface roughness, and interface temperature is observed. MoS<sub>2</sub>-coconut oil outperforms the MoS<sub>2</sub>-palm oil in terms of surface roughness, tool wear, and temperature. This is by virtue of lower viscosity and higher thermal conductivity of coconut oil as compared to palm oil.

## References

1. Boswell B et al (2017) A review identifying the effectiveness of minimum quantity lubrication (MQL) during conventional machining. *Int J Adv Manuf Technol* 92(1–4):321–340. <https://doi.org/10.1007/s00170-017-0142-3>
2. Uysal A, Demiren F, Altan E (2015) Applying minimum quantity lubrication (MQL) method on milling of martensitic stainless steel by using nano MoS<sub>2</sub> reinforced vegetable cutting fluid. *Proc Soc Behav Sci* 195:2742–2747. <https://doi.org/10.1016/j.sbspro.2015.06.384>
3. Mao C et al (2014) The tribological properties of nanofluid used in minimum quantity lubrication grinding. *Int J Adv Manuf Technol* 71(5–8):1221–1228. <https://doi.org/10.1007/s00170-013-5576-7>
4. Lawal SA, Choudhury IA, Nukman Y (2013) A critical assessment of lubrication techniques in machining processes: a case for minimum quantity lubrication using vegetable oil-based lubricant. *J Clean Prod* 41:210–221. <https://doi.org/10.1016/j.jclepro.2012.10.016>
5. Kumar Gajrani K, Ravi Sankar M (2017) Past and current status of eco-friendly vegetable oil based metal cutting fluids. *Mater Today Proc* 4(2):3786–3795. <https://doi.org/10.1016/j.matpr.2017.02.275>
6. Srikant R et al (2013) Nanofluids as a potential solution for minimum quantity lubrication: a review. *Proc Inst Mech Eng Part B J Eng Manuf* 228(1):3–20. <https://doi.org/10.1177/0954405413497939>
7. Amrita M et al (2014) Experimental investigation on application of emulsifier oil based nano cutting fluids in metal cutting process. *Proc Eng* 97:115–124. Available at: <http://dx.doi.org/10.1016/j.proeng.2014.12.231>
8. Su Y et al (2015) Performance evaluation of nanofluid MQL with vegetable-based oil and ester oil as base fluids in turning. *Int J Adv Manuf Technol* 83(9–12):2083–2089. <https://doi.org/10.1007/s00170-015-7730-x>

9. Kalita P et al (2012) Study of specific energy and friction coefficient in minimum quantity lubrication grinding using oil-based nanolubricants. *J Manuf Process* 14(2):160–166. <https://doi.org/10.1016/j.jmapro.2012.01.001>

# A Comparison Study between Conventional and Cryogenic Machining



Md Zia Arzoo, Mozammil Hassan, and N Gupta

**Abstract** Machining is one of the highly important manufacturing processes. The global machining market is currently estimated to be worth \$341.91 billion. As per Beroe's machining industry analysis reports, the global market size is expected to reach \$414.24 billion by 2022. So as the market so vast and big and the use of machining is so high in manufacturing industries, therefore, there is a lot of research going on various machining techniques to get more efficient, economical and environment-friendly machining process. One such technique is cryogenic machining in which we replace the traditional machining fluid with cryogenic coolant which is very low temperature coolant as there are several disadvantages of traditional cutting fluids in various domain which has been discussed in the paper briefly. Therefore, in this paper, we will be talking about both of these techniques over various factors such as tool wear, surface roughness and hardness and environmental aspects, and we will find out how application of cryogenics affects these machining factors and final machined product.

**Keywords** Cryogenic machining · Tool wear · Chip formation · Eco-friendly · Tool life · Surface finish · Liquid nitrogen · Cutting forces

## 1 Introduction

Traditional machining is one of the earliest machining techniques. It is mainly a subtractive machining process. It mainly uses tools, such as lathes, milling machines, boring machines and presses, to achieve desired dimension with the use of various cutting tools to get the final desired shape; normally, a direct contact between the tool and the workpiece is formed.

Usually, there is a lot of heat generation during contact of tool and workpiece material. And heat generation influences machinability and tool life especially for

---

M. Z. Arzoo · M. Hassan · N. Gupta (✉)  
Delhi Technological University, Delhi, India

superalloys and very hard materials. So to decrease the heat generation, cutting fluids are introduced during machining in traditional machining.

Cutting fluids help in cooling and lubricating the workpiece and tool interface. But cutting fluids have various limitations as it deteriorates our environment, and the cooling action is not that efficient at higher temperatures. So to overcome these problems, we use various alternative methods which will help in minimizing the various impacts on the environment and increase productivity simultaneously, and hence, one of the techniques is cryogenic machining in which we replace traditional cutting fluids in extremely low temperature and even lower than  $-150\text{ }^{\circ}\text{C}$  which is the sub-zero temperature at tool and workpiece interface. Carbon dioxide ( $\text{CO}_2$ ), ( $\text{N}_2$ ) nitrogen, helium (He), etc., are usually used in compressed liquid form. Most of these gases are abundant in atmosphere and can be changed to a fluid form. Cryogenic remove heat more efficiently from the cutting zone.

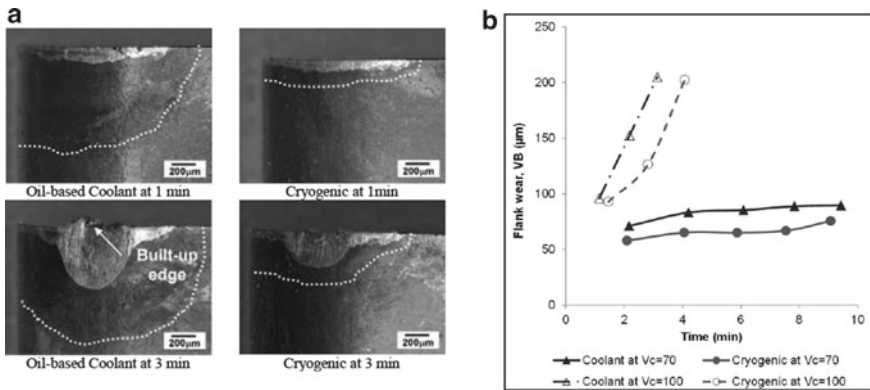
The boiling point of liquid nitrogen is less than that of carbon dioxide, and it might aggregate at lower levels or floor of machining, and it can lead to breathing problems due to its higher density; therefore, liquid nitrogen is usually preferred over liquid carbon dioxide. Thus, liquid  $\text{CO}_2$  is less suggested for its use as a cutting liquid in machining operations.

The major application of cryogenic machining is in machining of superalloys (titanium alloy, Inconel alloys, etc.), ferrous materials and elastomers. But in general, better results are seen irrespective of material of the working material.

## 2 Discussion

### 2.1 Tool Wear

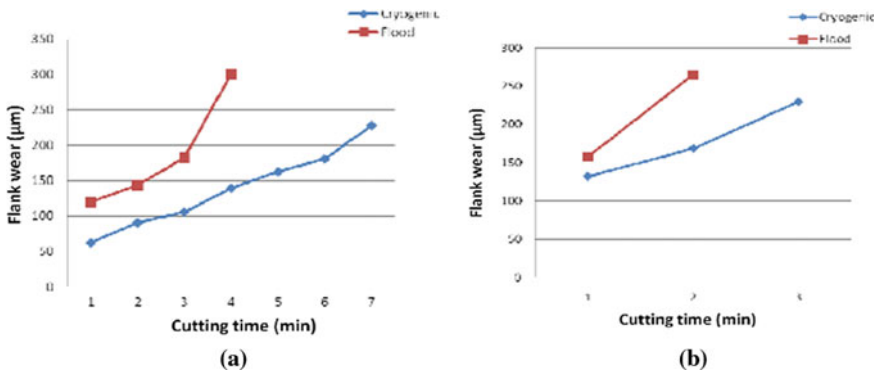
The zone of heat-influenced zone was a lot bigger in oil-related coolant when contrasted with cryogenics and furthermore developed or built-up edge was seen after some time under oil-based coolant while no development or built-up edge in cryogenics case. We can derive from this explanation that the impact of heat gets more grounded with cutting time and causes developed edge and chips on tool surface. Furthermore, it was seen that cryogenics lessens the wear rate contrasted with oil-related coolant at both cutting velocities. It was noticed that tools chip contact lengths at rake face was much less in case of cryogenics, and as it brought about less rubbing between rake face and chip at secondary deformation zone which brought about less possibility of advancing developed edge and bond wear. Thus, this shows that cryogenic coolant gives better availability and lubricity when contrasted with oil-related coolant, so it will bring better tool durability as announced Ampara with Ti alloy [1] (Fig. 1).



**Fig. 1** a Wearing of tool [1] at cutting velocity of 100 m/minutes. b Tool wear trend [1] when using oil-based and cryogenic cooling at cutting speed (Vc) of 70 and 100 m/min

Better surface finish was observed with the reduction of tool wear under cryogenic machining. Besides, the decrease in cutting temperature was much clear at a lesser feed and lesser cutting speed, as revealed by Dhar [2, 3]. Sivaiah and Chakradhar directed examination between cryogenic, wet, dry and MQL machining condition in turning of 17–4 pH tempered steel, and it was found that the cryogenics-based machining operation beats others regarding surface completion, tools wear and chip morphology [4].

Similar results were seen by Arun in the machining of SS304 steel with cryogenic coolant and oil-based coolant with same tool material [5] (Fig. 2).



**Fig. 2** Flank wear [1] at a 200 m/min and b 250 m/min



**Table 1** Surface roughness measurements of SS304 machined surface [5]

Test Parameters	Surface Roughness-Ra ( $\mu\text{m}$ )	
	Cryogenic	Flood
200–0.2–1.5	1.17	2.59
250–0.2–1.5	1.22	3.38

## 2.2 Surface Roughness

As investigated by Yap et al. [6] for dry, oil-based and cryogenic machining of carbon steel, it is inferred that at low cutting speeds, the surface finish difference is not significant between all three machining's but as the cutting speed was increased, conventional cutting fluid outperformed all other processes which are cryogenic and dry machining. In the case of SS304, after some time, interval roughness value increased for the traditional machined surface in comparison to the cryogenic machined surface as reported by Arun [5] (Table 1).

Cryogenic coolant performed better than the traditional coolant in terms of surface roughness, tool wear and cutting forces. When conducted by Dhananchezian and Kumar [7] in machining operations of Ti–6Al–4 V with an adjusted cutting supplement utilized for penetrating an opening at rake surface of the addition with utilization of fluid nitrogen to the opening.

Similar things were reported by Wang and Rajurkar [8]. They reported a delay in tool wear and improvement of surface roughness of Inconel 718 with LN<sub>2</sub> cooling.

## 2.3 Surface Hardness

The microhardness of surface of workpiece was increased after cryogenic cooling, and martensite was also detected on the surface after cryogenic turning which can show us that cryogenic turning can help us in surface hardness improvements in manufacturing as reported by Kirsch et al. [9].

Cryogenics hardened the workpiece which in turn increased the machining ability of SS304 workpiece because of the decrease in ductile power and fracture toughness of the workpiece as investigated by Wang and Rajurkar [7].

The result of cryogenics to the corrosion behaviour and surface finish of AISI 316L stainless steel was conducted by Bruschi [10], and it was reported that the cryogenics changed the inner structure of the machined segment, mainly the outermost surface of it. Furthermore, when stainless steel gets machined in cryogenics, it showed better handling power to corrosion (Table 2).

**Table 2** Hardness (HRC) measurement of the SS304 material [5]

Before Machining	After Machining	
	Cryogenic	Flood
30	32.5	29

## 2.4 Chip

### 2.4.1 Chip Formation

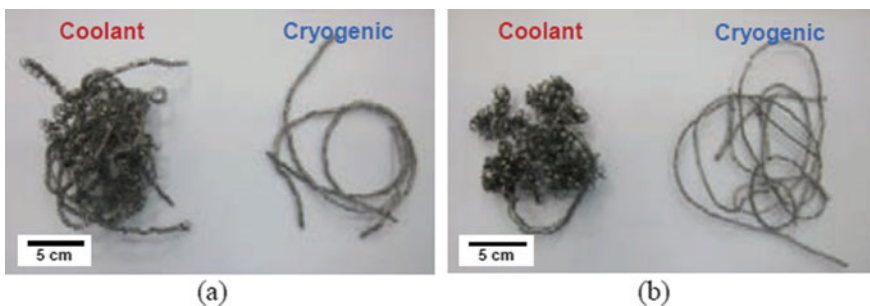
As investigated by Aramcharoen [1] on titanium alloy helical chips were produced while cryogenic coolant is applied and snarled chips were produced on the application of oil-based coolant because of the deeper penetration of cryogenic coolant in between tool–chip interfaces. Growned chips ordinarily collect close to cutting zones and harm machine surface segments; therefore, helical chips are preferred over snarled because they are easily manageable (Fig. 3).

### 2.4.2 Chip Morphology

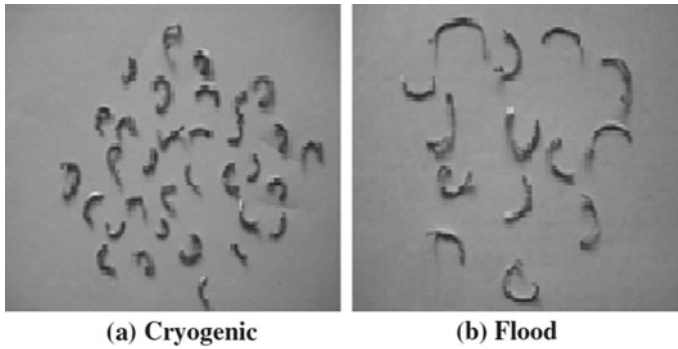
Longer chips were found to be formed in wet machining in comparison to cryogenics related machining and this decreases the cutting forces in cryogenic machining by decrease in the temperature around chip- tool contact as reported by Arun [5] (Fig. 4).

As investigated by Aramcharoen [1], the overall shapes were identical with both cryogenic coolant and oil-related as divided and serrated form of chip in case of titanium.

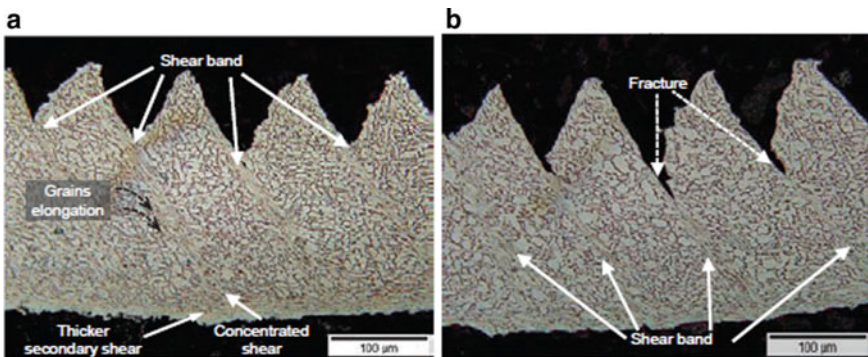
Thicker shear bands were seen in oil-related coolants which helped in accumulating more heat at the primary shear zone and result in a contribution of localization of shears and therefore, influenced the secondary shearing zone. In case of cryogenics, more fracture between the chips took place which was caused by perpendicular load instead of thermoplastic strain from high temperature. Misshaping of grain inside shear groups and encompassed by shear groups indicated prolongation in use of



**Fig. 3** Chips formed [1] at cut velocity of: **a** 70 m/min and **b** 100 m/min



**Fig. 4** Shapes of chips [5] in **a** cryogenic and **b** flood machining



**Fig. 5** **a** Chip morphology [1] in oil-based coolant. **b** Chip morphology in cryogenic coolant

oil-based coolants, which implies the inefficiency of cooling in case of oil-related coolants. And as a fact, cryogenic coolant resultant temperature was 200 °C lower than oil-related coolant as per their report (Fig. 5).

## 2.5 Cutting Forces

The tangential cutting force increases for both conventional coolant and cryogenic coolant with time, but the force was less in case of cryogenic than conventional coolant.

A decrease in cutting force led to the in chip contact length as cryogenic coolant produces shorter chip lengths and also no built-up edge is found in cryogenic machining. As its presence increases the tool wear which in turn increases the cutting forces. Therefore, in case of cryogenic coolant, cutting forces are less than that of traditional machining as reported by Arun [5] (Fig. 6).

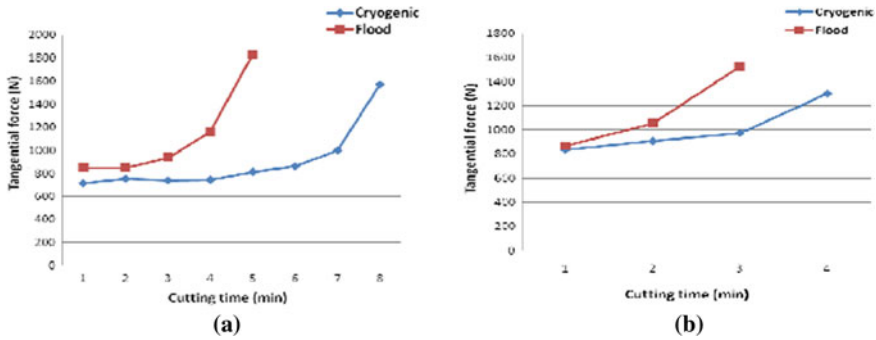


Fig. 6 Force versus cutting speed [5] at a 200 m/min, b 250 m/min

### 2.6 Environmental Aspect

Maintainability in machining has been embraced through use of effective assets, reusable materials, multiuse of machines instruments, to make least generation of waste products, minimization of power required, improvement in tools life, extending administrative scope of the use of metal-working liquids, taking of life cycle appraisal methods, and greasing up oil [11, 12]. Solvent oils are one of the most widely recognized machining cooling fluid utilized in machining in current situation. These are the combination of oil, limit greases, emulsifiers and biocides [13].

In metal cutting coolant frameworks, microorganisms and microbial life forms feed on the coolants oil, rust inhibitors and lubricators due to the oils and different impurities that become a constituent of framework. Microorganisms might make the coolant incapable by parting the emulsions. Accordingly, the coolants' lubricating power is diminished, and therefore, instrument's ability to work decreases. Biocide might be utilized to restrict coolant microscopic organisms and microbial action and broaden helpful coolants life. Nonetheless, these biocides are exorbitant and very dangerous added substances.

Biocides are hard to regulate securely and can cause last coolant removal much more exorbitant. And for environment, biocides are a worry since biocides neutralize the central operation in garbage removal. In the event that biocides is inadvertently spilled or is being added extra to coolant framework, there is a danger of obstructing the normal deterioration measure needed by sewage frameworks for emanating. A few regions of municipal departments have restricted the utilization of biocides thus [13].

Several wellbeing-related perils being accounted for, while cutting liquid is utilized in various machining tasks. Exposed skin is the simplest method of exposing to these hazards, and it is accepted that about 80% of all word-related perils are brought about by skin contact with liquids. When there is a contact between water mixed fluids and workers skin irritant dermatitis and allergic dermatitis are usually

reported. Non-water miscible liquids may cause skin problems, for example, folliculitis, oil skin inflammation, keratosis and carcinomas. Other than eye, inward breath is likewise one of the routes [14].

The cost of fluid usually varies the overall machining cost from 15 to 17%. The tools wear have a major part in choosing the expense of machining titanium alloy [15]. Another major cost is expounded to the energy consumption of machining process. The cryogenic machining burned through 22.8% less energy in examination with the traditional cooling measure. Ozone harming substance transmitted were practically half less for the cryogenics-helped machining. Moreover, no fluid waste was created by the cryogenics measure in view of the dissipation of liquid nitrogen into the air that leaves no build-up [12]. The complete cost was decreased by 26% for machining one element of a workpiece utilizing cryogenic helped machining measure. It has been accounted for 39% cost decrease by cryogenic machines than ordinary in a study [16]. Therefore, through the contextual investigation, the expected advantages of the machining cycle as far as monetary and environmental perspective were shown.

### 3 Conclusion

The above work is utmost effort to discuss and compare between cryogenic and traditional machining onto various thermal, economical, material, mechanical and environmental aspects. As we can clearly see through the various studies that cryogenic was way better than the traditional machining in almost every aspect of machining discussed in the paper. All the studies have shown that how cryogenic machining has less environmental impact, better manageable chips, less amount of cutting forces and relatively very small heat effective zone and cryogenic machined parts have less tool wear, lower surface roughness and higher surface hardness as comparable to traditional machining.

As we can infer from above data about how cryogenic machining is better than traditional machining, there is a huge scope in future for cryogenic machining as a sustainable machining method with higher productivity and efficiency as an overall process. Simultaneously, it can be combined with some of the evolving techniques by using cryogenic-added CNC machines, so there is a huge possibility for cryogenic machining in future.

### References

1. Aramcharoen A (2016) Influence of cryogenic cooling on tool wear and chip formation in turning of Titanium alloy. *Procedia CIRP* 46:83–86
2. Dhar N, Kamruzzaman M (2007) Cutting temperature, tool wear, surface roughness and dimensional deviation in turning AISI-4037 steel under cryogenic condition. *Int J Mach Tools Manuf* 47(5):754–759

3. Dhar NR, Paul S, Chattopadhyay AB (2001) The influence of cryogenic cooling on tool wear, dimensional accuracy and surface finish in turning AISI 1040 and E4340C steels. *Wear* 249:932–942
4. Sivaiah P, Chakradhar D (2018) Effect of cryogenic coolant on turning performance characteristics during machining of 17–4 PH stainless steel: A comparison with MQL, wet, dry machining. *CIRP J Manuf Sci Technol* 21:86–96
5. Magadum S, Kumar A, Yoganath VG, Srinivasa CK (2014) Cryogenic machining of SS304 steel
6. Yap TC, Sivaraos CS, Lim CS, Leau JW (2015) Surface roughness and cutting forces in cryogenic turning of carbon steel
7. Dhananchezian M, Pradeep Kumar M (2011) Cryogenic turning of the Ti–6Al–4V alloy with modified cutting tool inserts. *Cryogenics* 51(1):34–40
8. Wang Z, Rajurkar K (2000) Cryogenic machining of hard-to-cut materials. *Wear* 239(2):168–175
9. Kirsch B, Hotz H, Müller R, Becker S, Boemke A, Smaga M, Beck T, Aurich J (2019) Generation of deformation-induced martensite when cryogenic turning various batches of the metastable austenitic steel AISI 347. *Prod Eng Res Devel* 13(3–4):343–350
10. Bruschi S, Pezzato L, Ghiotti A, Dabalà M, Bertolini R (2019) Effectiveness of using low-temperature coolants in machining to enhance durability of AISI 316L stainless steel for reusable biomedical devices. *J Manuf Process* 39:295–304
11. Benedicto E, Carou D, Rubio E (2017) Technical, economic and environmental review of the lubrication/cooling systems used in machining processes. *Procedia Engineering* 184:99–116
12. Zindani D, Kumar K (2020) A brief review on cryogenics in machining process. *SN Appl Sci* 2(6)
13. Hong S, Broomer M (2000) Economical and ecological cryogenic machining of AISI 304 austenitic stainless steel. *Clean Prod Process* 2(3):0157–0166
14. Bennett EO, Bennett DL (1987) Minimizing human exposure to chemicals in metalworking fluids. *Lubr Eng* 43(3):167–175
15. Shokrani A, Dhokia V, Newman S (2012) Environmentally conscious machining of difficult-to-machine materials with regard to cutting fluids. *Int J Mach Tools Manuf* 57:83–101
16. Lu T, Kudaravalli R, Georgiou G (2018) Cryogenic machining through the spindle and tool for improved machining process performance and sustainability: Pt. II, sustainability performance study. *Procedia Manuf* 21:273–280

# Effect of Voltage on the Size of Magnetic Nanoparticles Synthesized Using Arc-Discharge Method



Shaik Gulam Abul Hasan, A. V. S. S. K. S. Gupta, and B. V. Reddi

**Abstract** Nowadays, researchers started to invest their efforts and ideas in finding out the most economical and efficient method by which magnetic nanoparticles of different sizes can be synthesized. In this paper, the formation of nanoparticles using the arc-discharge is clearly explained. LiCl electrolyte and ER70S-2 electrode were used in the experiment for the formation of magnetic nanoparticles of different sizes based on the requirement. Using this method, magnetic nanoparticles were obtained in good quantity as well as in quality. A very interesting observation was noticed while conducting the experiment, as the voltage applied is altered; the size of the nanoparticles varies continuously. There is an indirect proportionality between size of the nanoparticles and applied voltage. This paper helps to select a particular method by which magnetic nanoparticles of different sizes can be generated by altering the voltage. These obtained nanoparticles were characterized using XRD and particle size analyzer and SEM analysis. Using this analysis, one can come to a conclusion regarding the size, structure and phases obtained of the magnetic nanoparticles using arc-discharge method.

**Keywords** Magnetic nanoparticles · Voltage · XRD · SEM

## 1 Introduction

Nanotechnology is one of the most rapidly growing and powerful technologies in recent times which has collaborated with all fields of science and technology. Human activity and approach regarding nanotechnology have been changed, and now, it has become a common technical daily used term. Nowadays, nanotechnology is referred as one of the key technologies that triggered the third industrial revolution, and it

---

S. G. A. Hasan (✉) · B. V. Reddi  
Department of Mechanical Engineering, V.J.I.T, JNTU-H, Hyderabad, India  
e-mail: [hasan@vjit.ac.in](mailto:hasan@vjit.ac.in)

A. V. S. S. K. S. Gupta  
Department of Mechanical Engineering, JNTU-H, Hyderabad, India  
e-mail: [avs\\_gupta@jntuh.ac.in](mailto:avs_gupta@jntuh.ac.in)

© The Author(s), under exclusive license to Springer Nature Singapore Pte Ltd. 2022  
G. S. V. L. Narasimham et al. (eds.), *Innovations in Mechanical Engineering*,  
Lecture Notes in Mechanical Engineering,  
[https://doi.org/10.1007/978-981-16-7282-8\\_23](https://doi.org/10.1007/978-981-16-7282-8_23)

339

will also impact the future in many areas related to environment, manufacturing, nanoelectronics, biotechnology, health and medicine. We unknowingly use many nanopowders in our daily lifestyle in many medicines and also in cosmetics [1]. Nanoscience and nanotechnology [2] come across many scientific fields such as in chemistry, physics, biology, material science [3] and also in many engineering fields. Out of these nanoparticles, magnetic nanoparticle plays a very important role in the future work. Magnetite and hematite are the popular iron oxide phases among magnetic nanoparticles due to their unique magnetic and electrical properties. The magnetism of these magnetic nanoparticles plays an important role in electronic, electrical and mechanical engineering [4] because without the use of magnet, many components such as motors, headphones computers, biosensors, loud speakers [5], generators, transformers, electricity meters, inductors, coils will not function. Also, it has many applications in wastewater treatments, magnetic resonance imaging [6], cancer therapy [7], tissue repair [8], color imaging, magnetic coatings, ferrofluids, tissue engineering, hyperthermia [9] and also used in many other drug industries [10]. A matter is controlled at an atomic and molecular scale using many methods. There are many physical and chemical methods [11] and techniques for preparing magnetic nanoparticles with specified size and shape like co-precipitation [12], thermal decomposition, nanodispersion, hydrothermal synthesis, solvothermal [13], sol-gel method [14], decomposition of metals, polyol method, laser pyrolysis, carbon arc, micro-emulsion, arc-discharge method [15]. Out of these methods, we need to select a particular method by which both the quantity and quality of the nanoparticles should increase in very less time. The current paper gives us the information regarding the best method to be used to produce magnetic nanoparticles with required less size. Magnetically and dimensionally controlled synthesis of magnetic nanoparticles has acquired a notable attention due to their exceptional properties. The physicochemical properties of magnetic nanoparticles such as morphology, magnetization, structure and size distribution strongly depend upon the synthesis method.

## 2 Experimental Details

In the synthesis of magnetic  $\text{Fe}_3\text{O}_4$  nanoparticles using arc-discharge method [16], many different steps are to be followed by which the required size of the nanoparticles can be obtained. In this electrolysis process, we prepare  $\text{Fe}_3\text{O}_4$  magnetic nanoparticles using a welding rod (ER70S-2) as electrode and  $\text{LiCl}$  salt as electrolyte. The diameter of the electrode used in this experiment is of 1.6 mm. After electrolysis for 15 min at a voltage of 50 V and 70 V, red and black color precipitates are formed in the solution which can be separated easily using filter paper. These obtained precipitates were washed with water and converted to powder form by heating them in a furnace at 50 °C for nearly 24 h. Both the samples were studied later using different characterizing techniques to confirm their phases and size (Fig. 1).



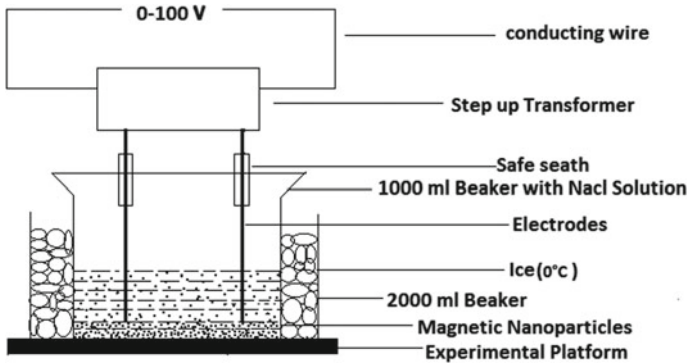


Fig. 1 Experimental setup

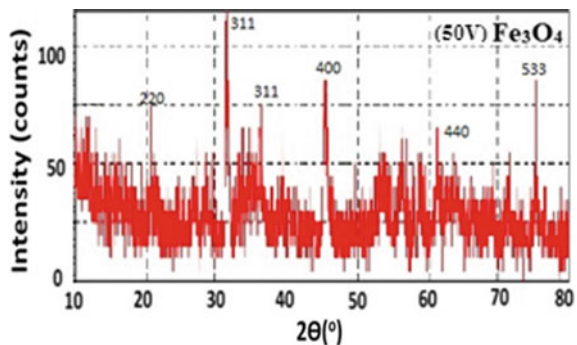
### 3 Characterization

The magnetic nanoparticles obtained are characterized using XRD, particle size analyzer techniques and SEM techniques. XRD data gives information regarding particles size and chemical composition of the elements. The peaks obtained in the XRD graphs help us to calculate the size of nanoparticles which also confirms the existence of magnetic nanoparticles in the experiment. Particle size analyzer technique is useful to know the mean size of nanoparticles obtained, and this data helps us to confirm the results with XRD. SEM analysis data reveals the clarity regarding the size of the nanoparticles obtained at different voltages.

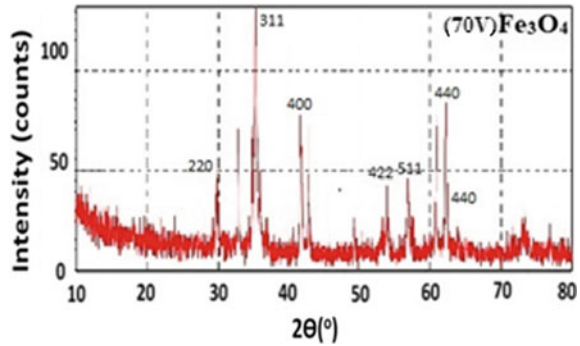
### 4 Results and Discussion

The X-ray diffraction pattern of the  $Fe_3O_4$  nanoparticles [17] is shown in Figs. 2 and 3 which reveals the formation of magnetite nanoparticles with well-defined crystallinity using arc-discharge method under 50 V and 70 V. All the diffraction

Fig. 2 XRD analysis under 50 V



**Fig. 3** XRD analysis under 70 V



**Table 1** Nanoparticles mean size obtained using Debye–Scherrer formula

Electrolyte	Minimum size (nm)	Maximum size (nm)	Average size (nm)
LiCl at 50 V	40.5	108.76	77.0
LiCl at 70 V	14.48	28.78	20.85

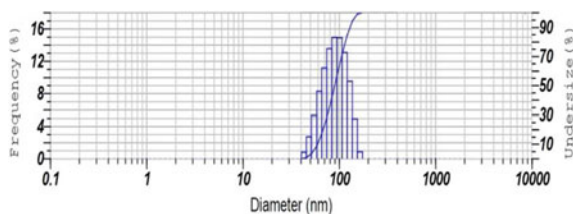
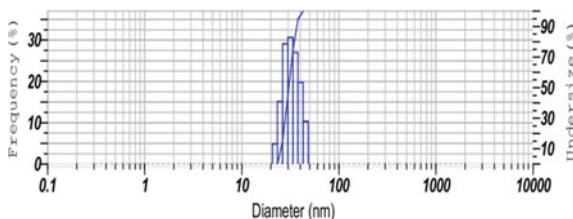
peaks match with the normal characteristics diffractions of the  $Fe_3O_4$ . Based on the Debye–Scherrer equation, the average particle size obtained under 50 V is 80 nm and under 70 V is 30 nm, so this result gives an idea on the effect of voltage on the particle size obtained using the arc-discharge method.

#### 4.1 XRD Result Analysis Based on LiCl Electrolyte at 50 V and 70 V

See Figs. 2 and 3 and Table 1.

#### 4.2 Particle Analyzer Results of Magnetic Nanoparticles Using KCl Electrolyte at 50 V and 70 V

Particle size analyzer [18] is a technique which gives the information regarding the particle size of nanoparticles obtained. This analysis helps to know the maximum nanoparticles obtained in a particular range. The graph drawn between the frequency and diameter in nm in Figs. 4 and 5 confirms that the average size of nanoparticles obtained using 50 V and 70 V is around 75 nm and 35 nm, respectively (Table 2).

**Fig. 4** Particle analyzer at 50 V**Fig. 5** Particle analyzer at 70 V**Table 2** Nanoparticles mean size obtained using particle size analyzer

Electrolyte	Minimum size (nm)	Maximum size (nm)	Average size (nm)
LiCl at 50 V	40	110	75
LiCl at 70 V	20	50	35

### 4.3 SEM Images of Magnetic Nanoparticles Using KCl Electrolyte at 50 V and 70 V

SEM images reveal [19] the size of the obtained magnetic nanoparticles. Figures 6 and 7 indicate the difference in sizes obtained. When observed properly, the minimum size obtained in Fig. 6 is 56 nm and the maximum is around 135 nm. Similarly, for the nanoparticles obtained under 70 V, the minimum size is around 18 nm and the maximum is 32.5 nm. When the average is considered for both, the average nanoparticle size obtained under 50 V is 95 nm and the average nanoparticle size obtained under 70 V is 28 nm. The data obtained using SEM matches with both XRD and particle size analyzer's data which gives us the clarity that as the voltage increases, the size of the nanoparticles decreases using the arc-discharge method.

## 5 Conclusion

This paper gives a clarity of using a particular voltage at which nanoparticles with minimum or maximum sizes around 30 nm and 80 nm can be obtained which are less than 100 nm using the arc-discharge method. To obtain different sizes of magnetic nanoparticles, different voltages can be applied. Many unique techniques are known

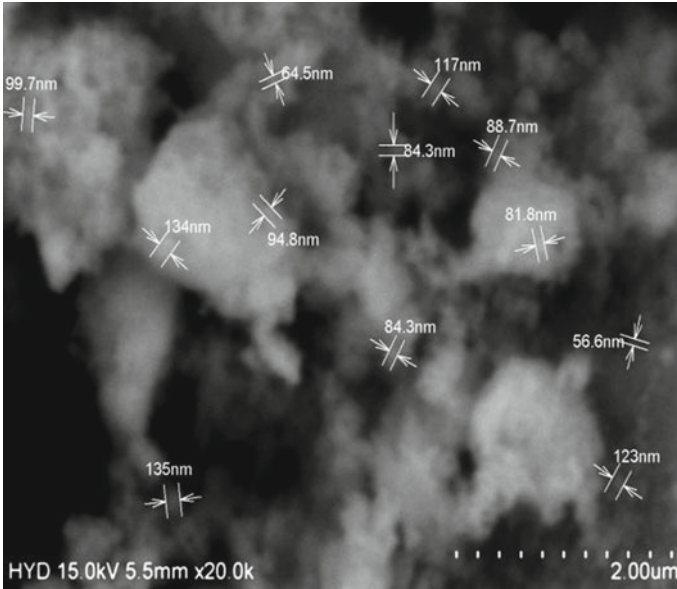


Fig. 6 SEM image obtained at 50 V

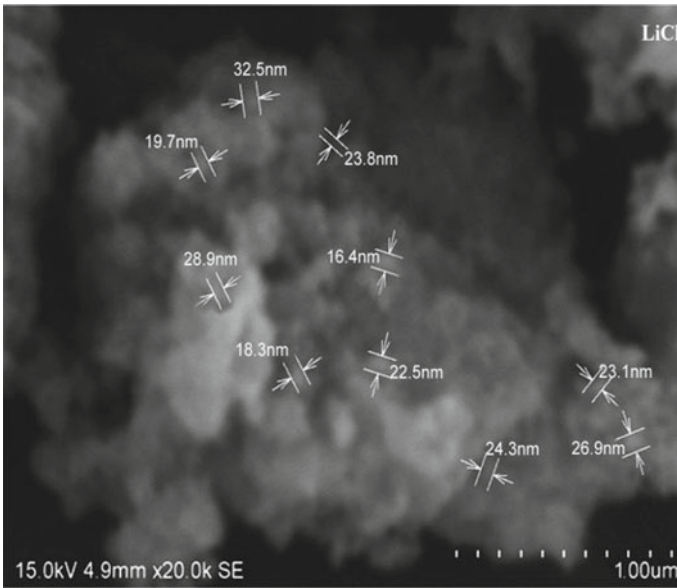


Fig. 7 SEM image obtained at 70 V

to us but we are generating magnetic nanoparticles using the arc-discharge method because it is the most economical, effective and fastest techniques by which magnetic nanoparticles are synthesized. In summary, we conclude the successful synthesis of  $\text{Fe}_3\text{O}_4$  nanoparticles very economically based on our requirement by altering the voltage using the arc-discharge method.

## References

1. Lin X-M, Samia AC (2006) Synthesis assembly and physical properties of magnetic nanoparticles. *J Magn Magn Mater* 305:100–109
2. Thapa D, Palkar VR, Kurup MB, Malik SK (2004) Properties of magnetite nanoparticles synthesized through a novel chemical route. Tata Institute of Fundamental Research, Mumbai, vol 1, pp 1–10
3. Wei Y, Han B, Xiaoyang H, Lin Y, Wang X, Deng X (2012) Synthesis of  $\text{Fe}_3\text{O}_4$  nanoparticles and their magnetic properties. *Procedia Eng* 27:632–637
4. Dulinska-Litewka J, Lazarczyk A, Szafranski PHO, Karnas K, Karewicz A (2019) Superparamagnetic iron oxide nanoparticles current and prospective medical applications. *Materials* 12:1–26
5. Zhang JH, Kong QH, Lu WL, Liu H (2009) Synthesis, characterization and magnetic properties of near monodisperse,  $\text{Fe}_3\text{O}_4$  sub-micron spheres. *Chin Sci Bull* 54:2433–2439
6. Chertok B, Moffat BA, David AE, Yu F, Bergemann C, Ross BD, Yang VC (2008) Iron oxide nanoparticles as a drug delivery vehicle for MRI monitored magnetic targeting of brain tumors, vol 29, pp 487–496
7. Hasan SGA, Gupta AVSSKS, Reddi BV (2021) Comparison of ER70S-2 with ER309L in synthesis of magnetic nanoparticles using arc-discharge method. *Int J Curr Eng Technol* 11:322–325
8. Thomas R, Park I-K, Jeong YY (2013) Magnetic iron oxide nanoparticles for multimodal imaging and therapy of cancer. *Int J Mol Sci* 4:1–12
9. Hedayatnasab Z, Abnisa F, Daud WMAW (2017) Review on magnetic nanoparticles for magnetic nanofluid hyperthermia applications. *Mater Des* 123:174–196
10. Gupta AK, Gupta M (2004) Synthesis and surface engineering of iron oxide nanoparticles for biomedical applications. *Biomaterials* 26:3995–4021
11. Hasan SGA, Gupta AVSSKS, Reddi BV, Sreeram Reddy G (2018) A critical review on preparation of  $\text{Fe}_3\text{O}_4$  magnetic nano-particles and their potential application. *Int J Curr Eng Technol* 8:1613–1618
12. Kandpal ND, Sah N, Loshali R, Joshni R, Prasad J (2014) Co-precipitation method of synthesis and characterization of iron oxide nanoparticles. *J Sci Ind Res* 73:87–90
13. Mishra D, Arora R, Lahiri S, Amritphale SS, Chandra N (2014) Synthesis and characterization of iron oxide nanoparticles by solvothermal method. *Prot Metals Phys Chem Surf* 50:628–631
14. Kashif M, Hashim U, Ali ME, Foo KL, Usman Ali SM (2012) Morphological, Structural, and Electrical Characterization of Sol-Gel-Synthesized ZnO Nanorods (INEE). *UniMAP* 16:1–7
15. Hasan SGA, Gupta AVSSKS, Reddi BV (2020) Synthesis and characterization of magnetic nanocrystallites using ARC-discharge method. *Solid State Technol* 63:578–587
16. Wang CY, Zhou Y, Mo X, Jiang WQ, Chen B, Chen ZY (2000) Synthesis of  $\text{Fe}_3\text{O}_4$  powder by a novel ARC discharge method. *Mater Res Bull* 35:755–759
17. Theivasanthi T, Alagar M (2011) Electrolytic synthesis and characterizations of silver nanopowder. *Nano Biomed Eng* 11:1–13

18. Prabhu YT, Venkateshwara Rao K, Siva Kumara B, Kumar VSS, Pavani T (2015) Synthesis of Fe<sub>3</sub>O<sub>4</sub> nanoparticles and its antibacterial applications, vol 5. Springer, pp 85–92
19. Ang BC, Yaacob II, Nurdin I (2000) Investigation of Fe<sub>2</sub>O<sub>3</sub>/SiO<sub>2</sub> nano composite by FESEM and TEM. Hindawi 2013:1–6

# A Review on Biomedical and Mechanical Applications of 3D Printing



Ujjwal Purwar, Mohammad Aqib Javed, Ashish Prabhakar, Gaurav Singh, Shrikant Vidya, and K. S. Srikanth

**Abstract** This is a survey on 3D printing which is an added substance fabricating measure that was created at the Massachusetts Institute of Technology, Boston, USA, by Emanuel Sachs and co-researchers during the last part of the 1980s. It is been forty years yet still; this technology is amazingly useful in both mechanical and biomedical fields. This technology allows us to produce 3D designs by increasing material a covering premise, and this cycle could be accomplished by using assorted sorts of materials, for example, pottery, metals, plastics, and polymers. The development of 3D printing has seen fast development in the numerous areas grasping the innovation. Through this investigation, we will perceive how 3D printing is pushing forward of the limits of speedy prototyping.

**Keywords** 3D printing · Biomedical · FDM · Health care

## 1 Introduction

There 3D printing or added substance fabricating is a cycle of making three-dimensional strong articles from an advanced document the plan of 3D printed objects which is achieved utilizing added substance measures. 3D printing encourages you to get mind-boggling shapes utilizing not many materials than traditional manufacturing techniques. 3D printing for fast prototyping is utilized for being speedy and moderately modest. Emphases are simpler and less expensive to make and you don't peruse pricy shells or instruments. In the event that we examine the product, there are numerous from modern evaluation to open a few. Despite the fact that for amateurs to start Tinker creep is typically suggested in light of the fact that it is free and works in your program and with that need no establishment in your PC. Nowadays, tissue designing examinations are going down on a boundless balance in the regions of recovery, repair, or substitution defective or wounded effective living organs and tissues. In this examination, we will portray normal AM creation strategies, BioMed

---

U. Purwar · M. A. Javed · A. Prabhakar · G. Singh · S. Vidya (✉) · K. S. Srikanth  
School of Mechanical Engineering, Galgotias University, Greater Noida, Uttar Pradesh, India

pertinent printing materials, and their utilization inside the medical care area. There are different 3D printing techniques which were set up to construct 3D designs and items. A number of them are overflowing these days and some have fallen by the wayside.

## 2 The Distinctive Assortment of 3D Printers

- Fused deposition modeling (FDM)—FDM is the solitary 3D printing technology which utilizes creation grade thermoplastics, so things printed have phenomenal mechanical, warm, and synthetic ascribes. 3D printers which use FDM innovation assemble objects layer by layer from the incredibly base up by warming and ousting thermoplastic fiber. The whole cycle looks like stereolithography. Explicit activities or Slicers “cut” computer-aided design models into layers and cycles the way printer’s extruder would accumulate each layer. Despite thermoplastic, a printer may oust maintain materials also. By then, the printer warms thermoplastic until its conditioning point and ousts everything through the spout on a printing bed, which you may know as a built stage or a work zone, on a destined model directed by the 3D model and slicer programming.
- Stereolithography (SLA)—The thought and usage of this procedure are astounding. Whether or not you are a mechanical modeler, who needs to affirm whether the part can suit your arrangement or innovative individual who wishes to print a plastic model for a fresh approaching endeavor. Stereolithography can truly restore your 3D models. SLA printing machines do not work like common work territory printers that remove some measure of ink to the surface [1]. SLA 3D printers work with a wealth of liquid plastic that sometimes cements and designs to a solid article.
- Digital Light Preparing (DLP)—DLP is another 3D printing measure particularly similar stereolithography. The DLP innovation was made in 1987 by Larry Hornbeck of Texas Instruments and has gotten notable for its utilization inside creation of projectors. It utilizes progressed micro-mirrors spread out on a semiconductor chip. The development is found in phones, film projectors, and, clearly, in 3D printing.
- Selective Laser Sintering (SLS)—SLS is such a strategy that uses a laser considering the way that the power supply to shape strong 3D printed objects. This strategy was made through Carl Deckard, an oil of Texas College, and his instructor Joe Beaman in the last piece of the 1980s. SLS is more dissipated among produces rather than of 3D fledglings gathering since this development requires using incredible lasers, inciting these printers being to some degree expensive. Another mind-blowing model is the Center SLS printer which can be viably used at home and at first was presented at Thingiverse.
- Selective Laser melting (SLM)
- Laminated item producing (LOM)
- Digital Shaft Liquefying.



The last three sorts of 3D printing advances are specific laser softening (SLM), overlaid object manufacturing (LOM), and digital beam melting (EBM). Through the last 20 years, these technologies have either dropped outdated or end up being financially unreliable. As such, you won't find the 3D printers of nowadays using SLM, LOM, or EBM advancements, or referenced in any amateurs' manual for 3D printing. Some of the best 3D printing applications to use are Thingiverse, Tinkercard, Autodesk, Onshape, Sculpteo, and MakerBot.

### 3 Biocompatible 3D Printing Materials [1–10]

In the district of biofabrication, there is an away from between direct printing of a cell-developed material, named as “bio-ink,” and in this way the printing of a without cell structure from a “biomaterial ink,” which may therefore be developed with cells or clearly implanted. Ink determination is obsessed by both a definitive capacity of the fraction and in this way the print method to be there utilized. Bio-material inks are for the most part used to deliver a hard framework for the perpetual or moderate debasing adjustment of construction, while bio-inks produce a milder platform that can be all the more immediately supplanted by the statement of another extracellular network (ECM) by the inserted cell populace Biotin k-It is the material accustomed to create designed (counterfeit) live tissue utilizing 3D printing innovation. It very well may be made only of cells, yet in the greater part of the cases, an extra transporter material that wraps the cells is additionally added. This transporter material is for the most part a bio-polymer gel, which goes about as a 3D subatomic framework. Cells joined to this gel, and this empowers them to spread, develop, and multiply. Significantly, the gel can likewise give protecting to the phones during the printing cycle. Its significance is such a lot of high that the expression “bio-ink” is frequently generally used to depict the transporter material alone, regardless of what the cells that may develop on it.

**Biomaterial Inks**—This kind of inks frequently necessitates distributing under conditions that are toxicity, for example, cutoff of temperature or the utilization of solvents; however, they can be stacked with restorative atoms that can withstand these preparing conditions. Synthetic hydrogel—Engineered hydrogels are frequently not befitting for the straight cultivating of cell and however have comparable non-Newtonian property to bio-polymeric hydrogels, letting them to be printed by expulsion.

Thermoplastic and tars thermoplastics be basic materials for 3D printing across numerous specialized enterprises and are additionally benefited by specialists. In bio-printing, the key preferred position is that they be able to be refined and go through various warm cycles for the joining of variables, and to shape fibers for expulsion, gums for photolithography or polymer liquefies for electrospinning.

Earthenware production terminated materials are a mix of inorganic salts, including calcium and phosphate, which are used for bone and dental applications

because of their superconductivity. All alone, pottery is extremely weak, which makes them hard to deal with and embed; subsequently, in bio-fabrication, ceramics are gotten together with a polymeric clasp for ejection bioprinting or 3D powder printing.

**Metal Inserts-**Metallic inserts for muscular, dental, and craniofacial applications have commonly been created from solidified steel, cobalt-chromium molybdenum, and titanium combinations by strategies like projecting, fashioning, and machining.

**Biomedical Applications of 3D Printing:** The Nider methodologies have edges with respect to the shapes and fine reasons for made things that are expected to change the tissue stages, models, duplicates, embeds, and prosthetic articles using the accumulated biometric information of patients. This is to some degree thing that forefront AM can handle, making ultra-present day and changed things and contraptions from getting CT and X-beam checks, and conceivably overriding standard procedures.

## 4 Healthcare and Medical Applications [11–17]

**Tissue engineering:** For the replacements of non-functional and damaged tissues, tissue designing assumes a significant part in fabrications of compatible implants. Principle of tissue engineering is mixing of biocompatible materials, live cells and alongside that development variables to make embeds that guide ordinary tissue development all through the cycle.

3D models and organoids: implants, tissue regeneration, implant tissue interface, dentistry, orthopedics.

**Drug delivery:** The role of advance machining and 3D printing in the pharmaceutical sector exceptionally various. Growing new strategies for the restricted arrival of medications from divergent courses of organization keeps on being a territory of premium for research. Customary courses of medication association are ingestible tablets and implantable contraptions that offer a prearranged speed of medicine release. Here we depict some novel ways where AM is being utilized for improving drug conveyance delivery: tablets, transdermal delivery, and drug retesting implant.

**Surgical tools:** Headways in radiological imaging have permitted the production of computer-aided design recreations of patient life structures, giving the possibility to planning and manufacturing tolerant explicit, redid careful instruments. Most surgical tools are designed to work with most patients. Nonetheless, one of a kind anatomical highlights or complex methods could profit by redid instruments that take into account a more-controlled and enhanced employable experience, thus diminishing the danger of complications. All the more all things considered, the expense adequacy of utilizing 3D-printed careful devices or projects in low-pay nations and organizations has high feasibility.

**Operative planning:** Perhaps one out of everything about generally settled and advertised utilizations of AM in a medical procedure is its utilization in employable

arranging. From end-to-end imaging modalities like CT, exact CAD reproductions of patient life structures can be made utilizing high-goal AM procedures like SLA. These models furnish specialists with the unrivaled visual and material enthusiasm for complex harms and distortions that would else be hard to completely evaluate with 2D radiological imaging. These models can be utilized intra-operatively just as the following sanitization.

Bioprinting has been fruitful in making little useful units of organs called organoids. Notwithstanding, the best open entryway for bio printing lies in its potential for printing a totally working organ that can be migrated into a patient. This would discard the necessity for wait lists or exhaustive testing for histocompatibility, as the patient's cells can be used in the bioprinting cycle.

Bioprinting innovation should conquer issues, for example, miniature vascularization and bio-ink lifespan, prior to endeavoring to print a full organ. Nonetheless, with the current pace of improvement, it is energizing to perceive what the not so distant upcoming holds.

## 5 3D Printing Applications for Mechanical Sectors [18–22]

From building up your model to the improvement of your plans and the advancement of your stock, additive manufacturing could offer you extraordinary advantages with your mechanical parts. 3D printing is helpful in various ways:

- **Optimizes your design:** Additive manufacturing opens a great deal of potential outcomes with regard to plan and geography improvement allowing you to find the best compromise between strength, weight, and creation cost for your mechanical parts. From a 3D record, we can print your parts paying little notice to their eccentricism. In any endeavor, the arrangement is the key, and especially for particular assignments, with complex computations.
- **Saves your time:** Additive manufacturing will accelerate your assembling cycle. Without a doubt, verification of ideas or models can be enhanced utilizing 3D printing innovation. 3D printing is the ideal assembling strategy to utilize on the off chance that you require to do several fast prototyping. Utilizing 3D displaying programming, the formation and trial of your plans will be essentially quickened.

**Aeronautics using 3D printing:** The aviation and guard (A&D) industry is maybe the soonest adopter of 3D print, with the essential usage of the advancement getting back to 1989. Presently, after thirty years, A&D speaks to a 6.8% portion of the \$ 10.4 billion added substance fabricating markets and vigorously adds to progressing research endeavors inside the business.

The advantages of 3D printing for aviation & defense:

- Low volume production
- Weight reduction
- Material efficiency

- Part consolidation
- Maintenance and repair.

**Automotive using 3D printing:** The automotive industry is a developing client of added substance producing: In 2019 alone, worldwide car AM incomes reached \$1.4 billion. This outline simply looks lay down to augment, as salaries concerning to AM in vehicle part creation are depended upon to accomplish \$5.8 billion by 2025, according to a SmarTech testimony. In zones reminiscent of motor sports and execution hustling, plan devices like generative plan and geography streamlining are gradually changing customary ways to deal with planning parts. Whereas prototyping by and by stays the essential use of 3D engraving in the vehicle business, associations are continuously finding other use cases, for instance, tooling. Additionally, a couple of vehicle associations are beginning to find advance end-use applications for 3D printing, hailing an invigorating improvement for the zone.

Advantage of 3D printing for automotive:

- Faster product development
- Greater design flexibility
- Customization
- Create complex geometries.

## 6 Conclusion

3D printing innovation has upset the biomedical designing district offering adaptabilities commonly as far as usefulness notwithstanding plan. Moving from straightforward confound designed platform structure and impersonating the genuine structure of the transfer can likewise be explored into. Significantly there is a great deal of extent of progress in the plan of 3D printer themselves to loan flexibility to its applications. From a comprehensive viewpoint, 3D printing innovation can be created to cover the whole scope of clinical application starting from finding finishing with anticipation. This audit zeroed in on the up-to-date biomedical livelihoods of AM and the focal centers it gives over standard creation methods. As AM headway progresses, in addition to the fact that we would have the alternative to imagine that the expense of the equipment should diminish, yet we can in like way anticipate that new and remarkable materials ought to build up that can improve its biomedical and tissue arranging applications. Thermoplastics for immaterial effort 3D printing have nearly gotten the standard, with their use clear in different emergency offices and examination foundations. New and translational materials are being made at a high rate, which may consider clinical use in tissue-fix applications very soon.

## References

1. Beg SW, Almalki WH, Malik A, Mohd Farhan M, Aatif M, Rahman Z, Alruwaili NK, Alrobaian M, Tarique M, Rahman M (2020) 3D printing for drug delivery and biomedical applications. *Drug Discov Today* 25(9):1668–1681
2. Roy A, Kumar R, Dadhich P (2018) 3D printing in biomedical applications. Chemical engineering world edition. Jasubhai Media Pvt. Ltd
3. Paul G, Rezaenia MA, Condoor S (2018) Medical applications for 3D printing: recent developments. *Mo Med* 115(1):75–81
4. Ahangar P, Cooke ME, Weber MH, Rosenzweig DH (2019) Current biomedical applications of 3D printing and additive manufacturing. *Appl Sci* 9(8):1713
5. Siderits R, Neyman G (2014) Experimental 3D printed 4-port ventilator manifold for potential use in disaster surges. *Open J Emerg Med* 2(3)
6. Pranzo D, Larizza P, Filippini D, Percoco G (2018) Extrusion-based 3D printing of microfluidic devices for chemical and biomedical applications. *Micromachines* 9(8):374
7. Takenaga S, Schneider B, Erbay E, Biselli M, Schnitzler T, Schoning MJ, Wagner T (2015) Fabrication of biocompatible lab-on-chip devices for biomedical applications by means of a 3D-printing process. *Phys Status Solidi A* 212(6):1347–1352
8. Yu C, Schimelman J, Wang P, Miller KL, Ma X, You S, Guan J, Sun B, Zhu W, Chen S (2020) Photopolymerizable biomaterials and light-based 3D printing strategies for biomedical applications. *Chem Rev* 120(19):10695–10743
9. Singh S, Prakash C, Ramakrishna S (2019) 3D printing of polyether-ether-ketone for biomedical applications. *Eur Polymer J* 114:234–248
10. Al-Dulimi Z, Wallis M, Tan DK, Maniruzzaman M, Nokhodchi A (2020) 3D printing technology as innovative solutions for biomedical applications. *Drug Discov Today*. <https://doi.org/10.1016/j.drudis.2020.11.013>
11. George M, Aroom KR, Hawes HG, Gill BS, Love J (2017) 3D printed surgical instruments: the design and fabrication process. *World J Surg* 41:314–319
12. Alhnan MA, Okwuosa TC, Sadia M, Wan KW, Ahmed W, Arafat B (2016) Emergence of 3D printed dosage forms: opportunities and challenges. *Pharm Res* 33:1817–1832
13. Bartikian M, Ferreira A, Goncalves-Ferreira A, Neto LL (2019) 3D printing anatomical models of head bones. *Surg Radiol Anat* 41:1205–1209
14. Berginann C, Lindner M, Zhang W, Koczur K, Kirsten A, Telle R, Fischer H (2010) 3D printing of bone substitute implants using calcium phosphate and bioactive glasses. *J Eur Ceram Soc* 30(12):2563–2567
15. Zhang YS, Yue K, Aleman J, Mollazadeh-Moghaddam K, Bakht SM, Yang J, Jia W, Erba VD, Assawes P, Shin SR, Dokmeci MR, Oklu R, Khademhosseini A (2017) 3D bioprinting for tissue and organ fabrication. *Ann Biomed Eng* 45:148–163
16. Ventola CL (2014) Medical applications for 3D printing: current and projected uses. *PT* 39(10):704–711
17. Ho CMB, Ng SH, Yoon YN (2015) A review on 3D printed bioimplants. *Int J Precis Eng Manuf* 16(5):1035–1046
18. Abduo J, Lyons K, Bennamoun M (2014) Trends in computer-aided manufacturing in prosthodontics: a review of the available streams. *Int J Dent*. <https://doi.org/10.1155/2014/783948>
19. Shiblee NI, Ahmed K, Khosla A, Masaru Kawakamia M, Furukawa H (2018) 3D printing of shape memory hydrogels with tunable mechanical properties. *Soft Matter* 38
20. Al Khawaja H, Alabdouli H, Alqaydi H, Mansour A, Ahmed W, Al Jassmi H (2020) Investigating the mechanical properties of 3D printed components. In: *Advances in science and engineering technology international conferences (ASET)*, Dubai, United Arab Emirates, pp. 1–7. <https://doi.org/10.1109/ASET48392.2020.9118307>
21. Ma G, Li Z, Wang L, Wang F, Jay S (2019) Mechanical anisotropy of aligned fiber reinforced composite for extrusion-based 3D printing. *Constr Build Mater* 202:770–783. <https://doi.org/10.1016/j.conbuildmat.2019.01.008>

22. Grasso M, Azzouz L, Ruiz-Hincapie P, Zarrelli M, Ren G (2018) Effect of temperature on the mechanical properties of 3D-printed PLA tensile specimens. *Rapid Prototyping J* 24(8):1337–1346. <https://doi.org/10.1108/RPJ-04-2017-0055>

# Experimental Investigation on FTIR Analysis of Produced Biodiesel and Performance and Emission Analysis of Diesel Engine Using Schleicher Oleosa Methyl Ester as Fuel with EGR



Ajay Chandravanshi, Ajay Singh Paikra, Shrikant Pandey,  
and Rakesh Kumar Malviya

**Abstract** The current work manages the Fourier Transform Infrared (FTIR) Spectroscopy of created biodiesel. It also deals with the execution and outflow tests with different blends of biodiesel with convectional diesel as fuel on 662 cc water-cooled, single-cylinder four stroke combined with swirl flow dynamometer. All observations were taken with and without 10% Exhaust Gas Recirculation (EGR). Maximum properties of Schleicher Oleosa Methyl Ester (Kusum Oil Methyl Ester/KME) were discovered to be matched approximately with diesel engine fuel and as per ASTM (American Society for Testing and Materials) principles. Biodiesel shows strength against oxidation. Blends with a lower level of biodiesel indicated better properties with better performance parameters and lower emissions. Thus, KME can be a likely elective fuel in the present time for diesel engines. The brake thermal efficiency marginally diminishes with 10% EGR, while brake specific fuel consumption and brake specific energy consumption slightly increases with 10% EGR. Discharges of Oxides of Nitrogen ( $\text{NO}_x$ ) were discovered to be lower with 10% EGR, while other emissions are marginally higher.

**Keywords** KME · FTIR · EGR ·  $\text{NO}_x$  · Biodiesel · Diesel engine · Performance parameters

---

A. Chandravanshi (✉) · S. Pandey · R. K. Malviya  
Department of Mechanical Engineering, Shri Vaishnav Vidhyapeeth Viswavidyalaya, Indore,  
Madhya Pradesh 453111, India

A. S. Paikra  
Department of Mechanical Engineering, Government Engineering College, Jagdalpur, Bastar,  
Chhattisgarh 494001, India  
e-mail: [aspaikra@gecjd.ac.in](mailto:aspaikra@gecjd.ac.in)

## 1 Introduction

The expanding industrialization and mechanization of the world have prompted a precarious ascent for the interest of oil-based fuels. Oil-based fuels are acquired from restricted stores. These limited stores are profoundly moved in specific locales of the world. Subsequently, those nations not having these assets are confronting an energy trade emergency, for the most part, because of the import of rough oil. Thus, it is important to search for elective powers which can be created from assets accessible locally inside the nation, for example, alcohol, biodiesel, vegetable oils, and so forth. Biodiesel is a non-conventional, locally delivered fuel that has been appeared to diminish particulate, hydrocarbon, and carbon monoxide emanations from the ignition.

Yuan et al. (2014) developed an online monitoring system of biodiesel transesterification using mid Fourier Transform Infrared spectrometer. It was found that online FTIR monitoring is feasible to be used, advantageous in form of simplicity and better than other methods. FTIR analysis provides real-time reaction data and the ability to adjust the process if required. FTIR also allows for optimization for improving product consistency and yield [1].

Rabelo et al. (2015) produced soyabean biodiesel with the use of microwave-assisted transesterification using methanol as esterifying agent and sodium methoxide as catalyst. FTIR spectroscopy was utilized for the quantification of fatty acid methyl ester (FAME) content in the produced biodiesel. Results implied that reaction time can be reduced with the use of microwave irradiation as compared to conventional methods. FTIR spectroscopy also demonstrated the feasibility for multi-variation statistics for quantification of FAME content in biodiesel [2].

Rosset and Lopez (2019) utilized FTIR and Gas Chromatography (GC) for the analysis of produced biodiesel. It was noted that Calcium-based catalyst showed higher activity for methyl transesterification than magnesium based catalyst. It was also notified that pure oxides are more active than mixed oxides. Results obtained from FTIR and GC were similar, but FTIR was advantageous in terms of simplicity to use, economically and speed [3].

Química et al. (2017) coupled FTIR with column chromatography to differentiate and notify the molecule functional groups, which are responsible for biodiesel fluorescence compounds [4].

Jindal et al. (2010) used jatropha methyl ester blends with diesel on single-cylinder four stroke, water cooled variable compression ratio diesel engine with speed of 1600 rpm. It was observed that BSFC has been reduced by 10%, while HC and EGT showed increments, with decrease in CO and smoke [5].

Ramadhas et al. (2005) utilized rubber seed biodiesel blends with diesel on single-cylinder four stroke compression ignition diesel engine with speed of 1500 rpm. It was observed that maximum BTE was obtained about 28% for B10. The BTE obtained, while using B50, B75, B100 were 25%, 25%, and 24%, respectively. BSFC was found to decrease with increased in load as compared with diesel. Emission of CO and CO<sub>2</sub> was increased as engine load increased but lower than that with diesel [6].

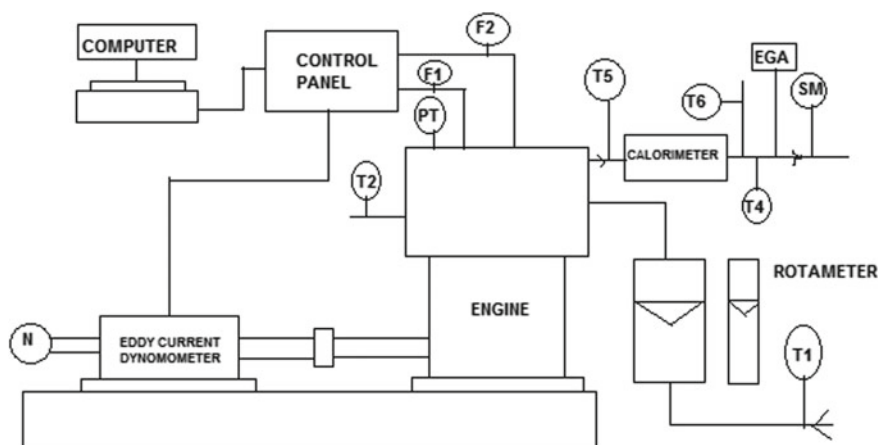


Kumar et al. (2009) used cotton seed methyl ester blends with diesel on single-cylinder four stroke, compression ignition, water cooled diesel engine with 1500 rpm having compression ratio 17.5. It was notified that, 10% BD mixtures reduced PM, smoke emission by 24% and 14%, respectively, as compared to the neat diesel fuel. Biodiesel mixtures (30%) reduced CO emission by 24%, while 10% increase was found in the  $\text{NO}_x$  emission with the same blend [7].

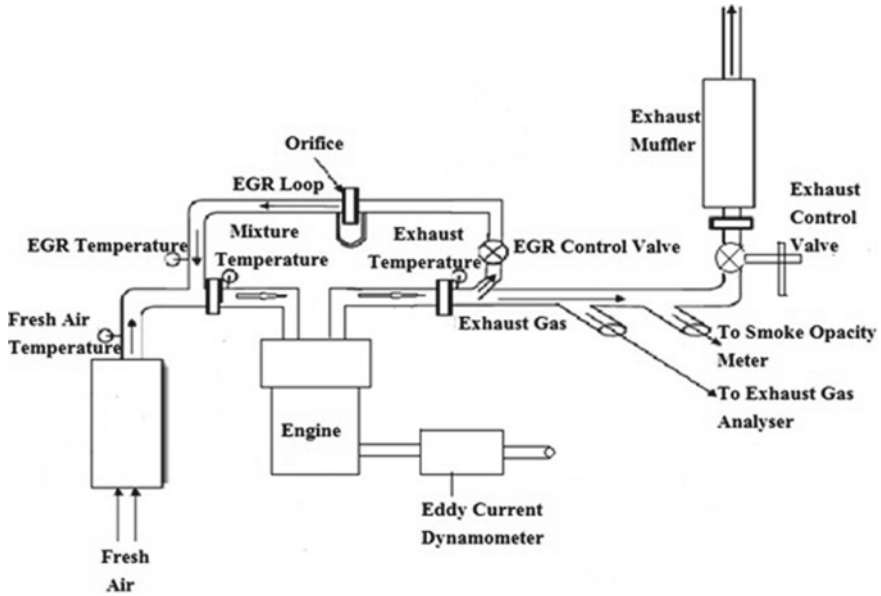
The expanding center around the ecological effects of the petroleum derivative-based force age has prompted expanded exploration with the point of lessening outflows and improving burning effectiveness. A lot of this work is driven by the expanding interest in elective fills, for example, biodiesel, alcohol, artificially stored power in chemical form, hydrogen, non-fossil methane, non-fossil petroleum gas, oil, and different biomass sources. Fumes gas distribution (EGR) is one more method to decrease unsafe discharges, explicitly for diminishing the emanation of oxides of nitrogen ( $\text{NO}_x$ ) [8–13]. In fumes gas distribution, some part of the fumes gas is sent back to the inlet, which blends in with channel air, and oxygen contained in it has been utilized for complete ignition of fuel. At the point, when EGR was utilized with ethanol as an added substance and biodiesel blends as fuel, at that point, BTE was discovered to be lower and BSFC was discovered to be higher relatively [8–12].

## 2 Experimental Setup

The schematic diagrams of the experimental setups are shown in Figs. 1 and 2. Performance tests were carried out on a single-cylinder, water-cooled, compression ignition, diesel engine using various blends of biodiesel and diesel as fuel.



**Fig. 1** Schematic diagram of experimental setup



**Fig. 2** Line diagram of single-cylinder four stroke diesel engines with exhaust gas recirculation system EGR system

Here T1-Inlet water temperature, T2-Outlet engine jacket water temperature, T4-Outlet calorimeter water temperature, T5-Exhaust gas temperature before calorimeter, T6-Exhaust gas temperature after calorimeter, N-RPM decoder, F1-Fuel flow difference pressure unit, F2-Air intake difference pressure unit, EGA-Exhaust Gas Analyzer, SM-AVL Smoke meter.

The technical details of the engine used are mentioned in the following Table 1.

### 3 Methodology

Various properties of the biodiesel have been found by laboratory tests. In addition to this, FTIR spectroscopy of produced biodiesel was also done.

In order to find out the performance and emission parameters of diesel engine using biodiesel as fuel with EGR, various observations were taken. The engine tests were conducted at different loads (0, 3, 6, 9, 12, 15, and 18 kg) using diesel and KME blends of 25% biodiesel + 75% diesel, 50% biodiesel + 50% diesel, 75% biodiesel + 25% diesel, 100% biodiesel + 0% diesel, and 0% biodiesel + 100% diesel (B25, B50, B75, B100 and D100, respectively) as fuel, with and without 10% EGR.

The dynamometer used to quantify brake load was eddy current type. The stacking sensor of this dynamometer has a limit of 0–50 kg. The Piezo sensor of this dynamometer with 5000 psi range has treated steel type and airtight scaled

**Table 1** Technical details of CI engine

Engine	Kirloskar tv 1
Bore x stroke	87.5 mm × 110mm
Cubic capacity	661 cm <sup>3</sup>
Compression ratio:	17.5:1
Rated output:	5.2 kw at 1500 rpm
Fuel injector pressure	20–25Mpa
Injection timing	23 degree before TDC
No. of valves	2
Valve timing	4.5°
Inlet valve opens BTDC	35.5°
Inlet valve opens ABDC	35.5°
Exhaust valve opens BBDC	4.5°
Governor type	Mechanical, centrifugal
Class of governing	B1
Fuel injection type	Mechanical individual pump

diagram. The Rotameter utilized for estimating the stream pace of cooling water for the dynamometer has a scope of 10–100 lph.

AVL 437 smoke meter had been utilized for estimation of smoke with exactness and reproducibility of  $\pm 1\%$  (full-scale perusing) and estimating the scope of 0–100% (Opacity in %) with the precision of 100% for simple yield. Five gas analyzer had been utilized to quantify the level of different fumes gases, intended to work with a motor speed of 250–8000 rpm. With this gas analyzer, CO can be estimated in a limit from 0 to 10% by volume, CO<sub>2</sub> can be estimated in a limit from 0 to 20% by volume, HC can be estimated in a limit from 0 to 20,000 ppm volume and NO<sub>x</sub> can be estimated in a limit from 0 to 4000 ppm volume.

## 4 Results and Discussion

In this part, results of all the tests performed with diesel and biodiesel are discussed here. Yields of bio-diesel, the performance testing on single-cylinder four stroke CI engine with or without EGR are discussed.

**Table 2** Properties of diesel and Schleichera Oleosa methyl ester

Properties	KME	Diesel
Density @ 15 °C (kg/m <sup>3</sup> )	857.60	850
Flash point (°C)	52	65
Pour point (°C)	-2	-5
Calorific value (kJ/kg)	37,595.50	43,400

#### 4.1 Comparison of Various Properties of Schleichera Oleosa Methyl Ester with Diesel

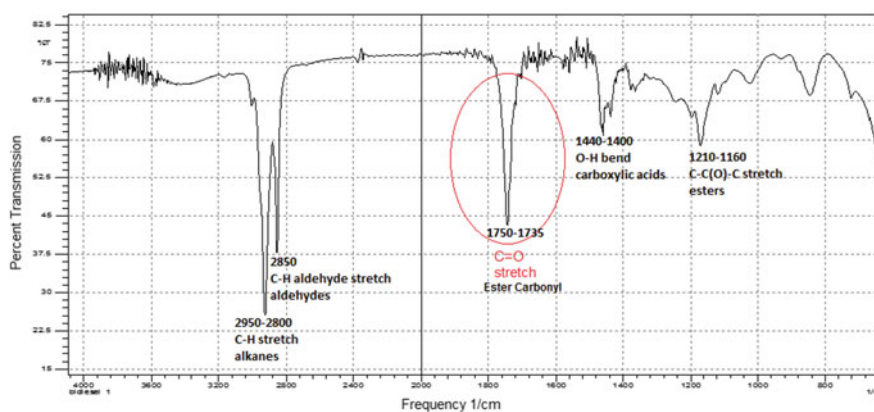
The properties of the biodiesel have been tested and the majority of values are found to be under ASTM standard (Table 2).

- Density of biodiesel is higher than mineral diesel.
- Flashpoint falls under the ASTM standard for biodiesel.
- Pour point also falls under ASTM standards with much lesser value.
- Calorific value of mineral diesel is higher than that of bio-diesel.

#### 4.2 FTIR Analysis of Schleichera Oleosa Methyl Ester

After performing FT-IR absorption measurements over both near-infrared (NIR) and mid-infrared ranges, we found the mid-infrared range is more promising. Figure 3 clearly shows evidence of the spectra range of the ester group. The first stretch ester absorption band appears from 1160 cm<sup>-1</sup> to 1210 cm<sup>-1</sup>, where biodiesel presents.

The second stretch ester carbonyl absorption band appears from 1735 cm<sup>-1</sup> to 1750 cm<sup>-1</sup>, where biodiesel presents a prominent peak, which corresponds to the

**Fig. 3** FTIR spectrum of Kusum oil biodiesel

carbonyl group (C = O) absorption, known as the carbonyl peak, which is the typical property of esters. This absorption peak is connected to the stretching vibration of ester groups and is known by its relatively constant position and freedom from interfering bond.

### 4.3 Engine Tests Using Diesel and Various Blends of *Schleichera Oleosa* Oil Methyl Esters, with and Without 10% EGR

The engine tests were conducted on Kirloskar engine at different loads (0, 3, 6, 9, 12, 15, and 18 kg) using B25, B50, B75, B100, and D100 as fuel, with and without 10% EGR. The results found out when tests conducted on the engine are as follows. Variations in performance parameters (BTE, BSFC, and BSEC) and emission parameters (CO<sub>2</sub>, CO, HC, and NO<sub>x</sub>) with different fuel blends and different EGR concentrations have been discussed below.

#### 4.3.1 Brake Thermal Efficiency

Figure 4 shows the variations in brake thermal efficiencies of diesel engine with different blends of fuels, with and without EGR. It is observed from the figure that, the brake thermal efficiencies increase with increase in load with EGR. The brake thermal efficiencies are improved with increasing concentration of biodiesel and its diesel blends due to the higher oxygen present in the biodiesel. B100 KME with

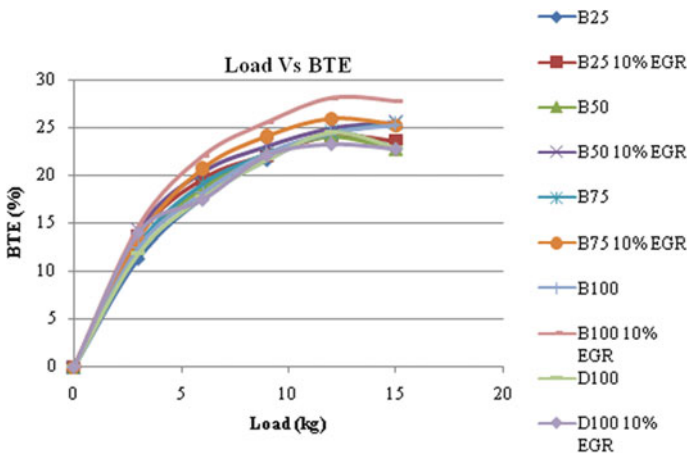


Fig. 4 Load versus brake thermal efficiency with 10% EGR and without EGR

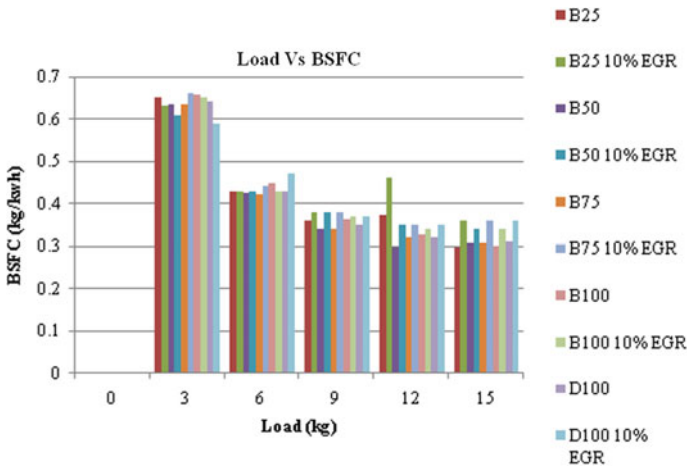


Fig. 5 Load versus brake specific fuel consumption with 10% EGR and without EGR

10% EGR shows a 4% increase in brake thermal efficiency at peak load compared to diesel without EGR.

### 4.3.2 Brake Specific Fuel Consumption

For diesel engines with various fuel blends, the variation of specific fuel consumption with brake power is shown in Fig. 5. Specific fuel consumption without EGR, under full load was found to be 0.2985 kg/kW-hr for B25 and 0.3067 kg/kW-hr for B75 and B50, 0.2998 kg/kW-hr for B100 and 0.31 kg/kW-hr for diesel. Full load values for D100, B25, B50, B75, B100 with 10% EGR are 0.36, 0.36, 0.34, 0.36, and 0.34 kg/kW-hr, respectively. With 10% EGR, at higher and medium load, specific fuel consumption increases for all fuel blends. Some of the reasons for higher BSFC are lower calorific values, higher viscosity and higher density.

### 4.3.3 Brake Specific Energy Consumption

Figure 6 shows the variations of brake specific energy consumption of diesel engine with KME and diesel fuel blends, with and without EGR.

Under full load BSEC were found to be 14,459.74, 14,072.96, 12,842.43, 12,432.83, and 15,419.12 kJ/kW-hr for B25, B50, B75, B100, and D100, respectively without EGR. Full load values of BSEC for D100, B100, B75, B50, and B25 with EGR are obtained as 15,843.34, 12,962.92, 14,255.92, 14,048.66, and 15,101.59 kJ/kW-hr, respectively. It is clear that BSEC increasing with EGR compare to without EGR.

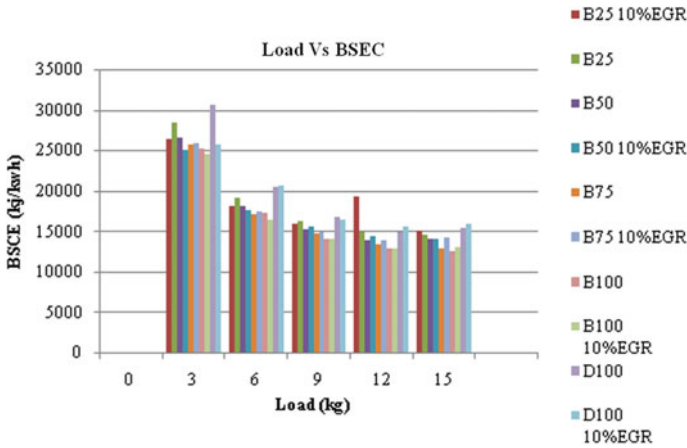


Fig. 6 Load versus brake specific energy consumption with 10% EGR and without EGR

### 4.3.4 Carbon Dioxide Emissions (CO<sub>2</sub>)

Figure 7 shows the variations in emission of CO<sub>2</sub> with different fuel blends of KME and diesel with and without EGR. CO<sub>2</sub> emission increases with the increase of brake power with and without EGR. The present graph shows that with the use of biodiesel and EGR, CO<sub>2</sub> emission decreases due to poor combustion.

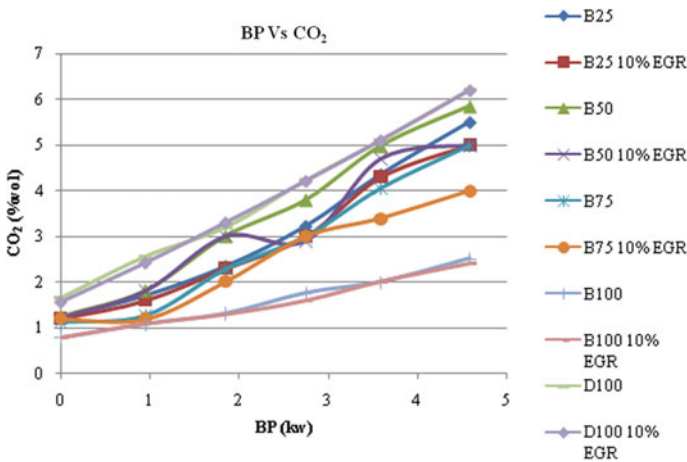


Fig. 7 Brake power versus carbon dioxide emissions with 10% EGR and without EGR

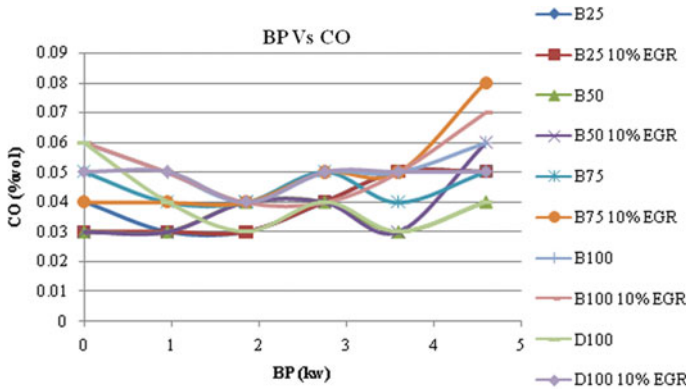


Fig. 8 Brake Power vs Carbon Mono-oxide emissions with 10% EGR and without EGR

### 4.3.5 Carbon Mono-Oxide Emissions (CO)

Figure 8 shows the variations in the emission of CO from diesel engine with KME and diesel fuel blends, with EGR and without EGR. CO emission increases with the use of EGR and KME. Higher values of CO were observed at full load for biodiesel fuels with EGR. For biodiesel, the excess of oxygen content is accepted to have partially compensated for the oxygen-insufficient activity under EGR. Separation of CO<sub>2</sub> to CO at top loads where high-ignition temperatures and nearly fuel-rich activity exists can also add to higher CO discharges. All the increase is under safe level that is why the same can be considered.

### 4.3.6 Unburnt Hydrocarbon Emissions (UBHC)

Figure 9 shows the variations in the emission of UBHC from diesel engine with KME and diesel fuel blends, with and without EGR. The emission of UBHC increases with the use of EGR. Because of lower oxygen content available for combustion that is lower excess oxygen concentration results rich mixture, which results in incomplete combustion and results in higher hydrocarbon emission. It is also observed from the graph the B25 and B75 biodiesel blend with 10% EGR gives higher UBHC emissions with full load compared to a diesel with EGR.

### 4.3.7 Nitrogen Oxides Emission (NO<sub>x</sub>)

Figure 10 shows the variations in the emission of NO<sub>x</sub> from diesel engine using KME and diesel fuel blends with and without EGR. The level of decrease in NO<sub>x</sub> is higher at higher loads. The fundamental explanations behind the decrease in NO<sub>x</sub> emanations utilizing EGR in diesel engines are decreased oxygen level and lower



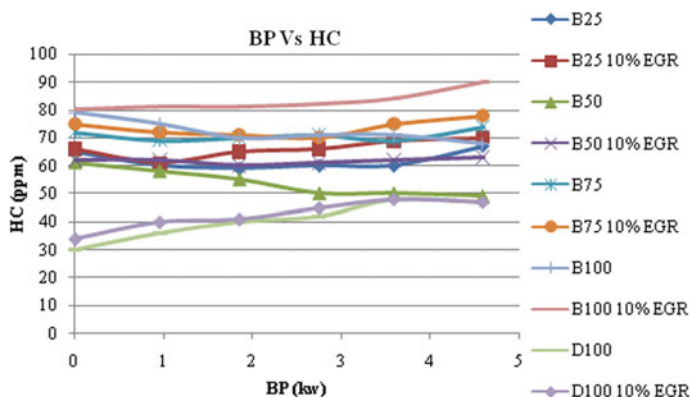


Fig. 9 Brake power versus unburnt hydrocarbon emissions with 10% EGR and without EGR

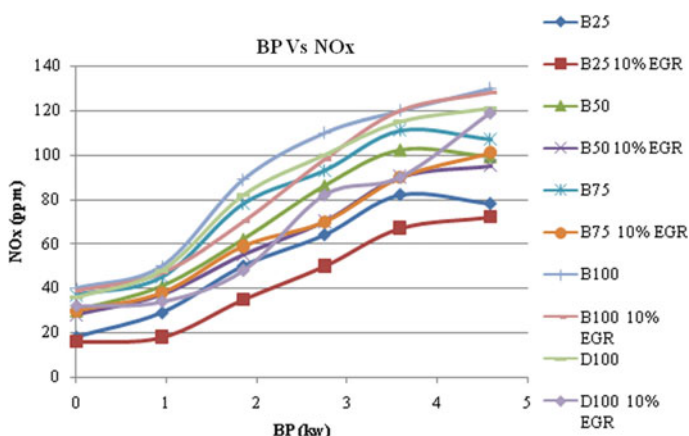


Fig. 10 Brake power versus nitrogen oxides emissions with 10% EGR and without EGR

temperatures of flame in the ignition chamber. However,  $\text{NO}_x$  emissions on account of biodiesel blends, without EGR are higher than diesel because of higher temperatures predominant in the ignition chamber. It is also observed from the graph that all fuel blends with EGR have lower  $\text{NO}_x$  emissions, respectively, when compared to diesel fuel without EGR.

## 5 Conclusion

Different properties, for example, viscosity, calorific value, flash point and pour point, all are discovered as per the ASTM standard for diesel. From the FTIR spectroscopy, it is also clear that the fuel which has been used for investigation belongs to the ester

group and the ester group also represents biodiesel, so the KME can be used as fuel in diesel engines. According to the investigation, the current examination approves the utilization of Schleicher oleosa methyl ester (Kusum methyl ester) for diesel engines. KME and diesel blend with a lower percentage of biodiesel (B25, B50) can be a potential alternative fuel for diesel engines.

The outcomes of utilizing EGR with 10% on compression ignition engine are expanding of BTE, BSFC, BSEC, CO, CO<sub>2</sub>, HC marginally, and diminishing NO<sub>x</sub>. As the quantity or rate of EGR increases, it diminishes the engine performance parameters. Since more recycled fumes gas is going into the inlet manifold of the engine. Poor combustion will take place due to a decreased amount of oxygen.

## References

1. Yuan T, Koble EA, Pinchuk D, Voort FRVD (2014) FTIR on-line monitoring of biodiesel transesterification. *Int J Renew Energy Biofuels* 2014, Article ID 178474. <https://doi.org/10.5171/2014.178474>
2. Rabelo SN, Ferraz VP, Oliveira LS, Franca AS (2015) FTIR analysis for quantification of fatty acid methyl. *Int J Environ Sci Dev* 6(12). <https://doi.org/10.7763/IJESD.2015.V6.730>
3. Rosset M, Lopez OWP (2019) FTIR spectroscopy analysis for monitoring biodiesel production by heterogeneous catalyst. *Vib Spectrosc* 105:102990. <https://doi.org/10.1016/j.vibspec.2019.102990>
4. Silva HRGD, Quintella CM, Meirab M (2017) Separation and identification of functional groups of molecules responsible for fluorescence of biodiesel using FTIR spectroscopy and principal component analysis. *J Braz Chem Soc* 28(12):2348–2356. <https://doi.org/10.21577/0103-5053.20170088>
5. Jindal S, Nandwana BP, Rathore NS, Vashistha V (2010) Experimental investigation of the effect of compression ratio and injection pressure in a direct injection diesel engine running on Jatropha methyl ester. *Appl Therm Eng* 30:442–448. <https://doi.org/10.1016/j.applthermaleng.2009.10.004>
6. Kumar AS, Maheswar D, Reddy KVK (2009) Comparison of diesel engine performance and emissions from neat and transesterified cotton seed Oil. *Jordan J Mech Industrial Eng* 3(3):190–197. ISSN 1995-6665
7. Ramadhas AS, Muraleedharan C, Jayaraj S (2005) Performance and emission evaluation of a diesel engine fueled with methyl esters of rubber seed oil. *Renew Energy* 30:1789–1800. <https://doi.org/10.1016/j.renene.2005.01.009>
8. Yasin MHM, Mamat R, Yusop AF, Paruka P, Yusaf T, Najafi G (2015) Effects of exhaust gas recirculation (EGR) on a diesel engine fuelled with palm-biodiesel. *Energy Procedia* 75:30–36. <https://doi.org/10.1016/j.egypro.2015.07.131>
9. Sakhare NM, Shelke PS, Lahane S (2016) Experimental investigation of effect of exhaust gas recirculation and cottonseed B20 biodiesel fuel on diesel engine. *Procedia Technol* 25:869–876. <https://doi.org/10.1016/j.protcy.2016.08.195>
10. Can O, Ozturk E, Solmaz H, Aksoy F, Cinar C, Yucesu HS (2016) Combined effects of soybean biodiesel fuel addition and EGR application on the combustion and exhaust emissions in a diesel engine. *Appl Therm Eng* 95:115–124. <https://doi.org/10.1016/j.applthermaleng.2015.11.056>
11. Solaimuthu C, Ganesan V, Senthilkumar D, Ramasamy KK (2015) Emission reductions studies of a biodiesel engine using EGR and SCR for agriculture operations in developing countries. *Appl Energy* 138:91–98. <https://doi.org/10.1016/j.apenergy.2014.04.023>

12. Shehata MS, Razek SMA (2011) Experimental investigation of diesel engine performance and emission characteristics using jojoba/diesel blend and sunflower oil. *Fuel* 90:886–897. <https://doi.org/10.1016/j.fuel.2010.09.011>
13. Shi X, Liu B, Chao Z, Hu J, Zeng Q (2017) A study on combined effect of high EGR rate and biodiesel on combustion and emission performance of a diesel engine. *Appl Therm Eng* 125:1272–1279. <https://doi.org/10.1016/j.applthermaleng.2017.07.083>

# Optimization of Solar Energy Efficiency: A Quadratic Regression Approach



Perini PraveenaSri

**Abstract** The well-established premise about intensified transformational shifts toward cleaner renewable sources of electric energy generation was evidently reflected over the past one decade. At global level, the solar generation targets for adding 1270.5 GW by 2022 along with India un-daunting task of its predetermined time frame of 100 GW appears to be pioneering using new technological breakthroughs. The optimal standard norm of 20% efficiency of solar panel will have the technical ability of producing more electric energy output. This paper examines the statistical impact of two technical parameters such as high solar efficiency and temperature coefficient for top notch (upgraded technology) using quadratic polynomial regression techniques. By employing Kruskal–Wallis test, the study gauges at the sample medium efficient solar panels to evaluate its quality perception. The replica of sophisticated cell technology by developing nations maximizes the plausibility of increasing solar panel efficiency for wider applications in a robust manner.

**Keywords** Solar PV module · Efficiency · Temperature coefficient · Solar electric output

## 1 Introduction

The rationale for renewables emanates from climate disrupting and energy insecurity anomalies of the economy. The commercialization of this viable source of energy dates back to 10 decades with positioning of three generations of renewable energy (RE). The main feedstock for first generation technologies comprises of biomass, hydro power, heat, and geothermal. This research study emphasizes on second-generation technologies that includes solar power generation, a modern form of energy. At global level, with an approximation of 319 countries, concerted efforts were continually onset till date with an affixed target of 30 percent electric production

---

P. PraveenaSri (✉)  
Atria Institute of Technology, Bengaluru, India

by 2030 [1, 2]. Recognizing the imperative need for upscaling the RE generation of electricity and efficiency improvements for decarbonization of world energy system, viable impartation of technological upheavals has become compulsory. By this, there will be drastic reduction of CO<sub>2</sub> emissions by 3.5% per year with desirable socio-economic benefits. Moreover, it articulates the re-shaping of the global economy with a boost of 2.5% of gross domestic product amidst Covid-19 pandemic. It also opens enhanced avenues for employment prospects of 0.2% by 2050 [3, 4]. Out of the total installed clean energy amounting to 2563.8 GW for the year 2019, 580.1 GW was contributed by global solar photovoltaic grid interconnectedness. In India as of June 30th, 2020 the solar power generation capacity was added to the level of 351 MW.

## 2 Prologue of Solar Photovoltaic (PV) Technologies

The most prevalent solar PV modules of different types such as mono-crystalline, polycrystalline, thin solar cells play a vital role for generating electric current by utilizing solar energy [5]. This paper reviews the advancements made in recent years most preferably for the year 2019 and 2020 in the field of solar energy technologies. For selection of solar manufacturers, with diversified design of models, random sampling techniques are deployed. In this study, the efficient performance of solar PV cell is excellently defined as maximum power output produced by taking in to account quality panels with lower temperature coefficients as the main proxy [6, 7]. The PV efficiency is influenced greatly by varying temperature coefficient of  $P_{max}$ .

The technically conversant fact of the rated or designed power of solar panel can be empirically estimated in watts (W). It is operationally made functional at normal trial settings with an estimated cell temperature of 25 °C. In reality when solar PV module cells were used for live application, the temperature cell boosts extremely above it, contingent on surrounding air temperature, wind speed, time, and sun powered irradiance. In reality in fact, expanding cell temperature limits power yield or electric flow by a particular sum for each degree overhead 25 °C. This is known as power temperature coefficient assessed in %/°C. The added up to sun-based board adequacy is moreover established on sun-based irradiance of 1000 W/m<sup>2</sup> and air mass of 1.5. The efficiency in percentage terms can be calculated using the following formula as:

$$\text{Efficiency}(\%) = \frac{P_{\max} \text{ multiplied with } 100}{\text{Area} \times 100 \text{ w/m}^2}$$

$$P_{\max} = \text{Max panel power (w) and Area} = \text{panel area(m}^2\text{)}$$

A higher sun-based board productivity rating implies a board that will create more kilowatt long stretches of energy per watt of intensity limit.

### 2.1 Comparative Analysis of Different Solar PV Cell Types

The collected research works of tracking solar panel efficiency are related to module efficiency. The article presents startling facts that need to be pondered over from past to contemporary times with an escalating trend as shown in Fig. 1.

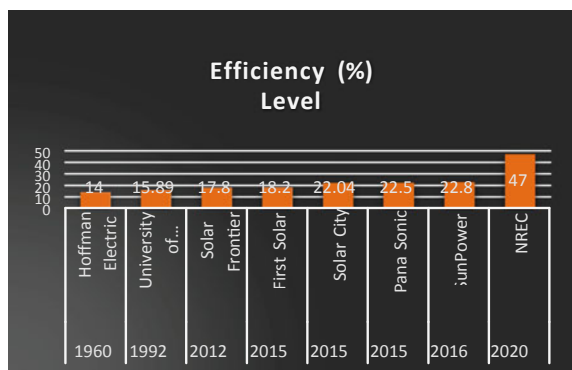
Figure 1 clearly displays the changing role of technological upgrade in solar energy to increase its efficiency and power output to the highest levels. The first and foremost solar panel has started at a minimal efficiency of 14% and geared up its pace to more than 20% for the year 2015 with a remarkable increase to the level of 47% during the year 2020.

An extensive variety of solar PV technologies are available currently which vary in their technical specifications and manufacturing processes such as material, area need, appropriateness, performance, energy produce per unit area, temperature coefficients, and fill factor as shown in Table 1.

### 3 Methods

The goal of this study is to assess the comparative analysis of various technological breakthroughs of solar PV modules from a technical efficiency perspective. For this purpose, the paper assessed the various scenarios of most efficient solar panels of 60–66 cell size to achieve greater electric power production for the year 2020. This electric outcome is utilized for end-use residential customers. Various econometric techniques such as quadratic regression and non-parametric statistical tools have been utilized to assess the real-life performance of the best to medium quality solar panels at global levels.

**Fig. 1** Past to present times changes in technological breakthroughs in solar PV systems



**Table 1** Common versus innovative solar PV technologies (in percentage)

Parameters	Mono-Si	Poly-Si	Thin film	Mono-PERC	Poly-PERC	Mono N type	Mono HJT
Solar productivity	18–22	14–18	10–12	17–20	17–19.5	19–20.5	20–23
Manufacturing process	From only Si crystal	By blending Si crystal	Numerous coatings of PV material	Know-how combines rear wafer surface Passivation and local rear contact	Adding of dielectric passivation layer on the rear of the cell	Solar cells are meddled with phosphorous to reduce maximally metallic impurities of silicon	Best qualities of crystalline silicon are mixed with amorphous silicon thin film to generate high power hybrid cell
Relevance For	Standard Temp	Moderately High Temp	Max temp	Both little and more temp	Both low and high temp	Small temp	Greater temp
Area need per KW	Fewer	Less	Huge	More	Huge	Less	Less
Energy requirement for unit area	Apex owing to high silicon matter	Pinnacle due to high Si content	Low due to meager Si material	High	Elevated	Sky scraping	Peak
Performance at modest sunlight	Low	Low	Moderate	Short and high	Low and high	Low-slung	Meager
Temperature coefficients	Profuse	Abundant	Inadequate	Short	Small	Near to the ground	Low
Fill factor (%)	70–80	70–80	60–68	80–90	80–90	80–90	80–90
Life span	25	25	20	25	25	30	30

## 4 Results

### 4.1 Application of Quadratic Regression Model

The polynomial or curved relationship between dependent  $Y$  variable (solar efficiency) increases or decreases at varying rate as the value of  $X$  temperature coefficient changes. Figure 2 as exemplary of curvilinear relationship exhibits the quadratic association between  $X$  and  $Y$ .

The model can be stated as follows:

$$Y_i = \beta_0 + \beta_1 X_1^2 + \beta_2 X_2 + e_i$$

$\beta_0 = Y$  intercept

$\beta_1 =$  Coefficient of the straight impact on  $Y$

$\beta_2 =$  Coefficient of quadratic impact on  $Y$

$e_i =$  arbitrary blunder in  $Y$  for perception  $I$ .

This sort of quadratic regression is like multiple regression model with double autonomous variable amount. By and by, in a quadratic model, the second free factor called quadratic term is the square of the primary autonomous variable. The condition for this model can be communicated as:

$$Y^i = b_0 + b_1 X_{1i} + b_2 X_{1i}^2$$

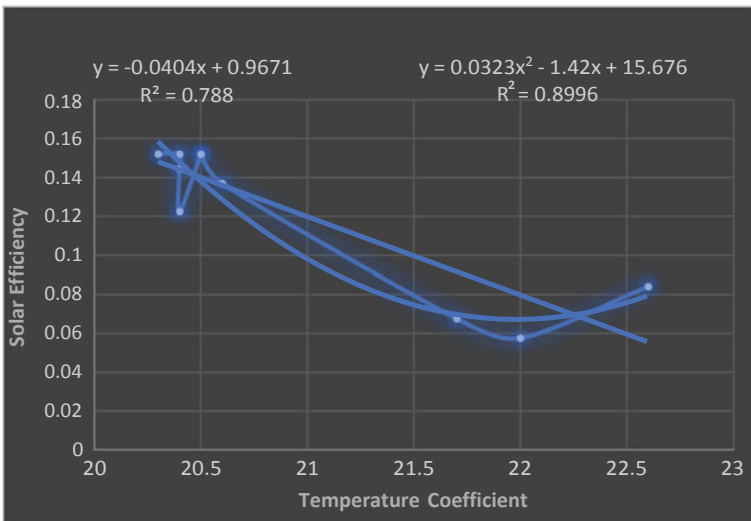


Fig. 2 Scatter plot of solar panel efficiency and temperature coefficient



**Table 2** Solar PV efficiency and temperature coefficients

Manufacturer	Model	Max power (W)	Solar efficiency	Temp coefficient ( $P_{max}$ ) (X)
SunPower	Maxeon 3	400	22.6	-0.29
LG	Neon R	380	22	-0.3
REC	Alpha	380	21.7	-0.26
Longi Solar	Hi-Mo-4	375	20.6	-0.37
Trina Solar	Honey M Deo 8	375	20.5	0.39
Solaria	Power XT	370	20.5	0.39
Jinko Solar	Tiger Pro 6 R 13	390	20.4	-0.35
Canadian Solar	Hi DM CS 1H-MS	345	20.4	-0.38
Phono Solar	Twin Plus M4-9B-R	375	20.4	-0.39
Q cells	Q Peak Duo G8+	360	20.3	-0.39

Note Global Level Solar Power Manufacturers Company Reports

The aforementioned equation clearly connotes with  $b_0$  characterizes as  $Y$  intercept,  $b_1$  as the linear effect, and third base regression coefficient  $b_2$  symbolizes the quadratic effect.

### 4.1.1 Inference the Regression Coefficients and Forecasting Y

To demonstrate the quadratic regression model, the research study considers and examines as how solar panel efficiency ( $Y$ ) being a dependent variable is influenced by temperature coefficient ( $X$ ), (independent variable) as shown in Table 2. Data were collected from a sample of 10 solar manufacturers and organized by application of econometric techniques.

By making the scatter plot in Figure 2 to envisage the data, the study selects proper model for expressing the relationship between the solar efficiency percentage and temperature coefficient.

The trend lines of linear fit and polynomial quadratic fit clearly indicate the association of these two variables that have an association of good fit to the level of 78 and 89%. The graph depicts that with the decrease in temperature coefficients the efficiency of the solar panel increases and vice versa. The nonlinear relationship is further con- firmed by predicting the solar efficiency and temperature coefficient percentages.

The application of advanced data analytics yields the following results, and the regression coefficients are as follows:

$b_0 = 22.92477575$ ,  $b_1 = 0.310299767$ , and  $b_2 = -16.72806583$ . Therefore, the quadratic equation can be represented as  $Y^i = 22.92477575 + 0.310299767X1i - 16.72806583 X1i^2$ , wherein  $Y^i =$  Predicted solar efficiency for sample  $i$  and  $X1i =$  percentage of temperature coefficient for sample  $i$ . To infer the two coefficients

$b_1$  and  $b_2$ , it can be practically observed that after an increase, temperature coefficient decreases as solar efficiency percentage increases. This nonlinear relationship is further proved by envisaging the temperature coefficient for solar efficiency percentages within the range above 20.

Testing for significance of the quadratic model (Table 3).

The study tests whether there is a significant over all relationship between solar efficiency ( $Y$ ) and temperature coefficient ( $X$ ). The null and alternative hypothesis are as follows:

Ho:  $\beta_1=\beta_2=0$  (There is no connectivity between  $X$  and  $Y$ ).

H1:  $\beta_1$  and for  $\beta_2 \neq 0$  (There is an overall relationship between  $X$  and  $Y$ . The overall  $F_{STAT} = MSR/MSE = 1.503320884/0.029263409 = 51.37$ .

The study considers choosing the level of significance of 0.05 from the table and the typical value of F distribution with two and six degrees of freedom as 5.14. As  $F_{STAT} = 51.37 > 5.14$  or because the p value is  $5.4345E-05 < 0.05$ , the study rejects the null hypothesis (Ho) and concludes that there is over all significant relationship with excellent goodness of fit to the level of 94 percent between solar panel efficiency and temperature coefficient.

#### 4.2 Application of Krushal–Wallis Test of H Test for Medium Efficiency Solar Panels

The examination incorporates this test at five percent level of noteworthiness to test the theory that an expert solar panel manufacturers with medium efficiency less than 20% performs equally well with the four solar sample solar PV panels. The following are the given results for the year (Table 4).

The H test is applied by positioning all the figures from most noteworthy to the least, demonstrating other than each the name of the sun-powered board as under

For finding the estimations of R (Ranking 1, 2, 3, 4), we orchestrate the above table as under:

$$H = \frac{12}{n(n + 1)} = \sum_{i=1}^k \frac{R_i^2}{n_i} - 3(n + 1)$$

$$= 12/20(20 + 1) \{50^2/5 + 36^2/5 + 80^2/5 + 44^2/5\} - 3(20 + 1) = 6.3$$

As per Tables 5 and 6, the four examples have five things each the inspecting dispersion of H approximates intimately with X2 Chi-squared test = 7.815 or  $k-1$  or  $4 - 1 = 3$  levels of opportunity at five percent level of noteworthiness. Since the determined estimation of H is just 6.3 and doesn't surpass X2 esteem, we acknowledge the invalid speculation and infer that the tested sun powered producers performed similarly well with the four distinct makers sunlight based boards.

**Table 3** Quadratic regression model of solar PV panels

Summary output									
<i>Regression statistics</i>									
Multiple R	0.972020873								
R square	0.944824578								
Adjusted R square	0.926432771								
Standard error	0.171065511								
Observations	9								
Anova									
	<i>df</i>	<i>SS</i>	<i>MS</i>	<i>F</i>	<i>Significance F</i>				
Regression	2	3.006641768	1.503320884	51.37203537	0.000167972				
Residual	6	0.175580454	0.029263409						
Total	8	3.182222222							
	<i>Coefficients</i>	<i>Standard error</i>	<i>This t stat</i>	<i>P-value</i>	<i>Lower 95%</i>	<i>Upper 95%</i>	<i>Lower 95.0%</i>	<i>Upper 95.0%</i>	
Intercept	22.92477575	0.226562587	101.1851783	6.27964E-11	22.37039707	23.47915	22.3704	23.47915	
-0.29	0.310299767	0.190253183	1.630983317	0.154015179	-0.155233001	0.775833	-0.15523	0.775833	
0.0841	-16.72806583	1.654231918	-10.11228574	5.4345E-05	-20.77582552	-12.6803	-20.7758	-12.6803	
Residual output									
<i>Observation</i>	<i>Predicted 2.6</i>	<i>Balances</i>	<i>Standard remainders</i>						
1	21.88676721	0.113232791	0.76432686						
2	21.71328056	-0.013280555	-0.089644395						
3	20.51989262	0.080107381	0.540728729						

Note Author Own Estimates

**Table 4** Solar panel efficiency (in percentage) results of five solar manufacturers

With SunPower A	16.51	18.5	19.9	20.6	22.5
With solaris B	19.7	19.5	20.9	21.5	20.5
With silfab C	18.6	17.6	19.4	16.7	17.9
With LG solar D	18.4	19.8	21.7	21	18.9

*Note* High efficient solar panel efficiency reports of global manufacturers (Table 4)

**Table 5** Estimated solar panel efficiency outcome

Solar panel efficiency results	Rank	Name of the solar panel associated
22.5	1	A
21.7	2	D
21.5	3	B
21	4	B
20.9	5	D
20.6	6	A
20.5	7	B
19.9	8	A
19.8	9	D
19.7	10	B
19.5	11	B
19.4	12	C
18.9	13	D
18.6	14	C
18.5	15	A
18.4	16	D
17.9	17	C
17.6	18	C
16.7	19	C
16.5	20	A

**Table 6** Solar panel efficiency results with various producers and corresponding ranks

SunPower A	Ranking	Solaris B	Grading	Silfab C	Positioning	LG So lar D	Scaling
16.5	20	19.7	10	18.6	14	18.4	16
18.5	15	19.5	11	17.6	18	19.8	9
19.9	8	20.9	5	19.4	12	21.7	2
20.6	6	21.5	3	16.7	19	18.9	13
22.5	1	20.5	7	17.9	17	21	4
$N1 = 5$	$R = 50$	$N2 = 5$	$= 36$	$N3 = 5$	$= 80$	$N4 = 5$	$=44$

*Note* Author own empirical estimates We can estimate the H statistic as under  $N1 + N2 + N3 + N4 = 20$

## 5 Conclusion

At global level, top most efficient solar experts in their manufacturing process imbibed innovation technological upgradations that have led to upheaval in solar renewable energy capacities. India is still in crawling stage to introduce indigenous technology more commendably for sophisticated hybrid solar component chips. Through collaborative effort of Indian Ministry of National Renewable Energy with developed countries universities and solar expertise of United States of America, United Kingdom and Australia can abridge the technological lacunae. Indian economy needs to foster conducive decision-making to have a blend of massive scale dual wind technology along with hydrogen promotion of green energy initiatives for making renewable energy highly indispensable by 2030 with very least cost options. This enables the Indian economy to realize its dream of renewable energy capacity addition of 175 GW by 2022.

## References

1. Snapshot of Global Photovoltaic Markets—IEA PVPS, International energy agency report IEA PVPS T1–29:2016
2. IEA (International Energy Agency) (2019) World energy balances 2019 (database), IEA, Paris. [www.iea.org/statistics/](http://www.iea.org/statistics/)
3. IRENA (2019) Global energy transformation: a roadmap to 2050 (2019 edition). International Renewable Energy Agency, Abu Dhabi
4. REN21 (2019) Renewables 2019 global status report, REN21 Secretariat, Paris
5. Solar PV, renewable energy technologies: cost analysis series. International Renewable Energy Agency vol 1, no. 4/5, June 2012
6. NREL (2020) Solar panel efficiency technological breakthroughs national renewable energy laboratory. Golden, Colorado
7. US DOE (2018) Solar photovoltaic systems in hurricanes and other severe weather. US department of energy—office of energy efficiency & renewable energy
8. Grid-connected PV systems: design and installation, GSES India sustainable energy Pvt. Ltd., Dec. 2015

# Experimental Analysis of Azolla Biodiesel Blends in CI Engine



N. Sunil Naik, Dhanunjay Kumar Ammisetti, B. Kishan, and Suresh Chitturi

**Abstract** The main aim of the work is an attempt to evaluate the performance of non-edible feedstock known as Azolla (water fern) methyl ester in a CI test rig. At first, oil is extracted from Azolla which is further trans-esterified to Azolla methyl ester oil. The physical properties of esterified oil are evaluated and compared with ASTM standards of biodiesel. Based upon the oil yield rate blends are prepared in proportions of AME10, AME20, and AME30 concerning diesel fuel. These blends are tested in a standard diesel engine to evaluate the performance and emission characteristics at varied load conditions. From the obtained results, it was observed that AME10 blend shown closer behavior with the pure diesel fuel in terms of performance parameters. Whereas, on the other hand in terms of emission parameters such as  $\text{NO}_x$  and HC, AME10 shown significant reduction rate compared with that of diesel fuel. So, based upon the experimental evaluation, it is concluded that AME10 blend can be a potential source of fuel in a diesel engine without any modifications.

**Keywords** Non-edible feedstock · Azolla methyl ester · Transesterification · Diesel engine · Performance · Emissions parameters

## 1 Introduction

There is a rapid increase in the number of vehicles across the world for two or three decades. The fossil fuel requirements of the global community are rising year by year. These fossil fuels or petroleum sources are the major stakeholders in fueling the

---

N. S. Naik (✉) · D. K. Ammisetti  
Department of Mechanical Engineering, Lakireddy Bali Reddy College of Engineering (A),  
Mylavaram, India

B. Kishan  
Department of Mechanical Engineering, JNTUH, Hyderabad, India

S. Chitturi  
Department of Mechanical Engineering, Vignans Institute of Engineering for Women,  
Vishakapatnam, India

transportation sector. There will be a shortage of petroleum sources in the upcoming future. Because of increasing oil demand and also due to the adverse effect of gas emissions of these fuels on global climate change, there is a necessity of going for alternative oil sources. Rudolf Diesel in the 1890s was the first person who made biodiesel from vegetable oil. In search of his vision, more research is being done in the area of alternate fuels majorly using vegetable oils. The biodiesel source should not displace the agricultural land which should not impact on food production. Hence, there is a need for another biomass source.

Biodiesel has gotten the main focus which is the main existing energy source that can be utilized in a CI engine with an almost no or with no adjustment. Additionally, it burns more cleanly than fossil or mineral diesel. Biodiesel becomes the best wellspring of option sustainable power source among the potential choices for diminishing the outflows around the world. Green growth is distinguished as a potential source which is utilized to create biofuels. *Azolla* macroalgae have been developed and their assessment of development was done, and it is utilized for creating biofuels through the trans-esterification process.

Many investigations have been carried out by using algae species oil as biodiesel blends and have indicated that these non-edible algae species shown significant performance while tested in test rigs [1]. Experimentally investigated using novel biodiesel from algae species and found that shorter ignition delay period shown a significant effect on performance and combustion parameters. Whereas, on the other hand,  $\text{NO}_x$  emissions have shown a significant increase compared with overall emission parameters [2]. Studied the potentiality of *Azolla* using anaerobic digestion trials and concluded that the load and temperature are much dependent on energy recovery for biogas production [3]. Evaluated the growth rate and fatty acid profile of *Azolla* Pinnata and found that the lipid content and free fatty acid profile of *Azolla* Pinnata are predominant [4]. Extracted ethanol from *Azolla* using different yeasts and identified that the ethanol yield is relatively higher for *Azolla* using both acid and heat treatment [5]. Carried out exploratory research to sequence the *Azolla* genome and stated that the recent crowdfunding efforts shown a massive green potential toward *Azolla* Pinnata [6]. Evaluated the emission parameters by using *Azolla* biodiesel blended with nonadditive dosages and concluded that NO emissions have significant enhance rate compared with other emission parameters [7]. Analyzed the productivity of *Azolla* in terms of lipid content and fatty acid profile and identified that the fraction step is required to produce high-quality biodiesel from *Azolla* Pinnata [8]. Reviewed regarding next-generation aquatic weeds profiles for bioenergy production and stated that much attention is drawn by the aquatic weeds grown in wastewater due to its high production rates [9]. Studied the oil extraction process from *Azolla* and revealed that biodiesel extraction is technically achievable due to its rich oil content and its chemical constituents [10]. Reviewed regarding *Azolla* offerings on the environment and stated that the aquatic species can sustain the ecosystem, nitrogen-fixing potential and mitigates the greenhouse emissions [11]. Carried intense research for next-generation biodiesel production resource and stated that the *Azolla* species are the rapidly colonize plants yielding high productivity even growing on the natural ecosystem [12]. Analyzed the contribution of *Azolla* organs for their high yield rate

and identified that due to the presence of triacylglycerol lipid droplets results toward significant higher total yield rates [13]. Extracted oil from Azolla algae and analyzed the performance with  $\text{TiO}_2$  nano additives and found that Azolla biodiesel can be effectively used in a CI engine without any modifications [14, 15]. Carried pyrolysis of Azolla at varied temperature range using different catalysts and found a significant decrease in acid content with an increase in area percentage. Ana used aquatic plants as bio-converters to extract biofuel from wastewater and stated that Azolla can be used as potential feedstock which treats the different wastewaters as well as the source for biodiesel production [16]. Carried pyrolysis of Azolla at a varied range of temperature and understood that a maximum lipid content yield of 38.5% which can be the potential source for biodiesel production [17]. Intensively studied about the cultivation and application of Azolla and stated that it is one the fastest growing aquatic plants which doubles its weight within every two days. Further, it has the potentiality to neutralize nitrogen compounds acting as chemical fertilizer [18]. Assessed the potentiality of biodiesel production from the water fern using solvent extraction method and identified that the presence of rich fatty acid profile indicates as an economical source for biodiesel production [19]. Studied regarding the second-generation biofuel resources in developing countries and concluded that renewable energy from second-generation fuels can be potential source mitigating the environmental impacts [20]. Evaluated the effects of CI engine using microalgae with nano additives and revealed that the addition of these additives exhibited better reduction rate in terms of emission parameters [21]. Converted waste to energy from microalgae as feedstock grown in wastewater and stated that it consists of higher FAME content. So, thus confirming its better yield rate.

This work focuses mainly on the feasibility of Azolla blends in a diesel engine test rig. The variation in physicochemical properties of blends proportions was analyzed and compared with the ASTM standards. The performance of Azolla methyl ester as biodiesel blends (AME10, AME20, and AME30) is evaluated on the diesel test rig and compared with diesel fuel D100.

## 2 Materials and Methods

### 2.1 Procedure

Azolla (water fern) is a rapidly colonize plant species as shown in Fig. 1 which exhibits rich lipid content due to presence of free fatty acids yielding up to 38–44% Bijoy et. al (2017). The extracted lipid content has the feasibility to test run in diesel engine test rigs [1]. The way of oil extraction from the kernels was the same extraction process carried by [22].



**Fig. 1** Azolla (water fern)**Table 1** Physical properties

Parameters	D100	AME	AME10	AME20	AME30
Calorific value (kJ/kg)	42,500	38,200	42,073	41,643	41,219
Specific gravity	0.830	0.840	0.831	0.832	0.833
Kinematic viscosity (mm <sup>2</sup> /s)	3.05	6.32	3.377	3.704	4.031
Flash point (°C)	56	108	61.2	66.4	71.6
Cetane number	43	58	44.5	46	47.5

### 2.1.1 Blends Preparation and Testing Fuel Properties

Three test fuel blends were considered that is 10% biodiesel + 90% diesel (AME10), 20% biodiesel + 80% diesel (AME20), and 30% biodiesel + 70% diesel (AME30). These test fuel blends were compared with pure diesel D100. The physicochemical properties of test fuel blends and pure diesel are shown in Table 1.

## 2.2 Experimental Setup

The experiments were carried on a single chamber, four-stroke, water-cooled diesel engine test rig. The specifications of engine test rig are shown in Table 2. The performance and emission parameters such as BTE, ME, BSFC and CO, NO<sub>x</sub>, HC were measured at varied load conditions, respectively.

**Table 2** Test rig specifications

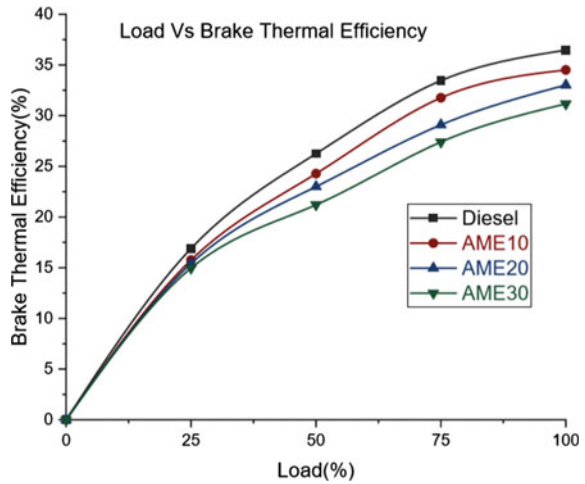
Engine type	Kirloskar model
Power	5 H. P
Speed	1500 rpm
Compression ratio	16.5: 1
Bore	18 mm
Type of ignition	Compression ignition
Stroke	110 mm
Orifice diameter	20 mm
Method of loading	Rope brake
Method of starting	Crankshaft
Method of cooling	Water

### 2.3 Auto-Exhaust Analyzer

The gas analyzer is mostly used to know the emissions is shown in Fig. 2. AVL DI GAS 444 N five gas analyzer quantifies the concentration of emission parameters based on volume rates and the concentration of HC and NO<sub>x</sub> in parts per million (ppm). The framework utilizes a non-dispersive infrared framework for deciding the fixation CO, CO<sub>2</sub>, and HC, and plays out the estimation of O<sub>2</sub> and NO<sub>x</sub> by electro synthetic cells.

**Fig. 2** Exhaust gas analyzer

**Fig. 3** Comparison of BTE with load



### 3 Results and Discussion

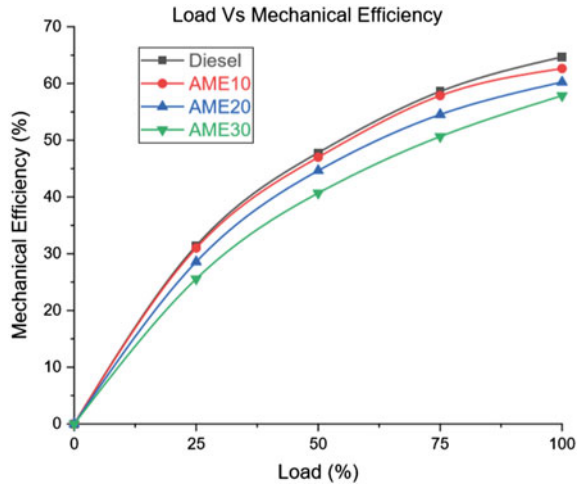
#### 3.1 Brake Thermal Efficiency

Figure 3 illustrates the variation of BTE of test fuel blends with pure diesel fuel at varied load conditions. It can be seen that BTE is steadily decreasing concerning increase in blending percentage. This slightly lower BTE value of test fuel blends compared with the base fuel is mainly due to variation in physical properties such as lower calorific value, high viscosity, and density parameters [1]. Test fuel blends AME10, AME20, and AME30 showed 5.3%, 9.4%, and 14.5% reduction rate in terms of BTE, respectively. The results signify that AME10 closer behavior compared with pure diesel D100.

#### 3.2 Mechanical Efficiency

Figure 4 shows the effects of test fuel blends concerning pure diesel fuel in terms of mechanical efficiency. It can be seen from the results that ME of all test fuel blends are lower compared to that of diesel fuel. This is because of poor atomization behavior of test fuel blends inside the combustion chamber which retards the combustion phenomena [21]. At peak load conditions, test fuel blends AME10, AME20, and AME30 shown significant reduction rate of 3.1%, 6.8%, and 10.5% concerning D100, respectively. This reduction rate can be mainly attributed due to higher viscosity values and slow combustion rates.

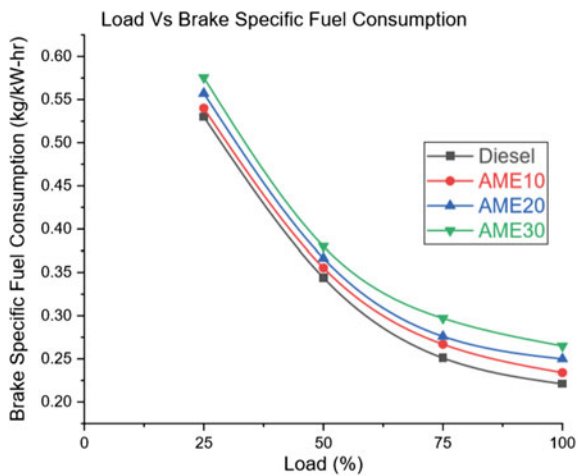
**Fig. 4** Comparison of mechanical efficiency



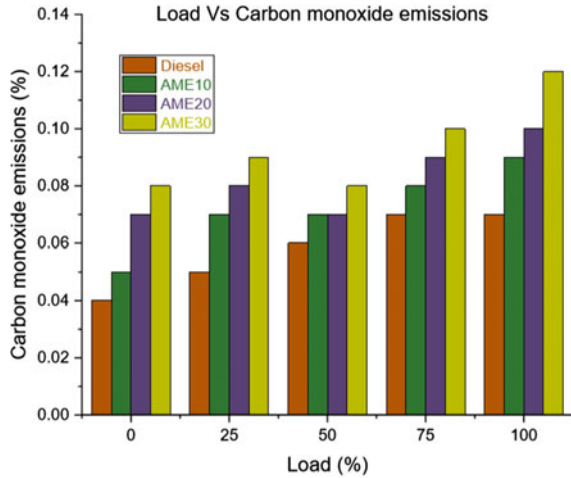
### 3.3 Brake Specific Fuel Consumption

Figure 5 illustrates the function of BSFC concerning varied load conditions. In general, test fuel blends exhibit more fuel consumption rate compared with diesel fuel. As shown in the figure, the BSFC rate of test fuel blends increased steadily concerning the increase of blending percentage. Test fuel blends such as AME10, AME20, and AME30 shown a significant increase of 1.8%, 5.01%, and 7.01% BSFC rate compared with D100 at peak load conditions, respectively. This higher BSFC rate of test fuel blends is due to the variation of physical properties [13]. Among all the test fuel blends, AME10 shown very closer value with that of base diesel fuel.

**Fig. 5** Variation of BSFC with load



**Fig. 6** Comparison of carbon monoxide emissions with load



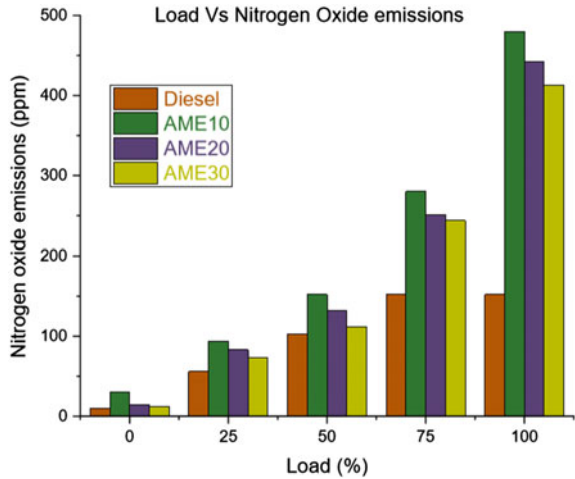
### 3.4 CO

The CO emission rate against the varied load conditions for test fuel blends and diesel fuel are shown in Fig. 6. This emission parameter is mainly dependent on cylinder temperature and air-fuel mixture ratio. It is clearly shown from the figure that the CO emission rate first declines at partial loads and steadily increased concerning rising in load. This is eventually due to lack of in-cylinder temperature inside the combustion chamber which prevents converting CO emissions into carbon dioxide [6]. On the other side, sudden rise of CO emissions at peak load conditions is due to shortage of oxygen content for complete combustion. The variation of CO emission rate at peak load conditions for test fuel blends AME10, AME20, AME30, and D100 are 0.09%, 0.1%, 0.12%, and 0.07%, respectively.

### 3.5 NO<sub>x</sub>

The discrepancy of the NO<sub>x</sub> emission rate of test fuel blends concerning pure diesel fuel at varied load conditions is shown in Fig. 7. This NO<sub>x</sub> formation rate is majorly dependent on the amount of oxygen content and in-cylinder temperature. It can be seen from the figure increase in blend percentage exhibits maximum NO<sub>x</sub> emission rate compared with diesel fuel. This can be attributed mainly due to the presence of rich oxygen content in the test fuel blends which enhanced the combustion rate [1]. So, this improved combustion process raises the cylinder temperature which ultimately resulting in terms of higher NO<sub>x</sub> emission rate. Even the higher cetane no values of test fuel blends are also responsible for higher NO<sub>x</sub> emission rates. The

**Fig. 7** Comparison of nitrogen oxide emissions with load

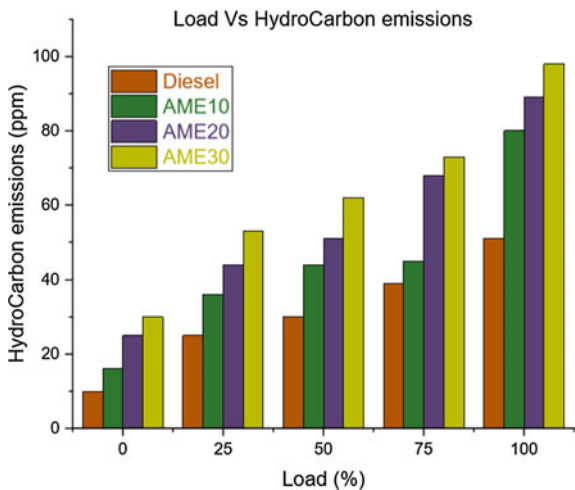


NO<sub>x</sub> emission rates of AME10, AME20, AME30, and D100 at peak load conditions are 480 ppm, 442 ppm, 413 ppm, and 152 ppm, respectively.

### 3.6 HC

Figure 8 represents the variation of HC rate of AME10, AME20, and AME30 blends with pure diesel at measured load conditions. This emission parameter formation is mainly due to the shortage of oxygen atom for complete combustion. The figure clearly states that the HC emission rate for test fuel blends shown significant higher

**Fig. 8** Comparison of hydro carbon emissions with load



rate compared with the diesel fuel. This is because of the lower temperature conditions inside which retards the combustion resulting in incomplete combustion [21]. The HC emission rates of AME10, AME20, AME30, and D100 at peak load conditions are 80 ppm, 89 ppm, 98 ppm, and 51 ppm, respectively.

## 4 Conclusion

The performance and emission parameters of Azolla test fuel blends are evaluated in a diesel engine test rig at the measured load conditions. These obtained results of test fuel blend AME10, AME20, and AME30 are compared with D100 and conclusions drawn as follows:

- With the increase of blending percentage in test fuel blends, there is a significant reduction in terms of physical properties compared with that of diesel.
- Test fuel blends AME10, AME20, and AME30 showed 5.3%, 9.4%, and 14.5% reduction rate in terms of BTE, respectively. The results signify that AME10 closer behavior compared with pure diesel D100.
- At peak load conditions, test fuel blends AME10, AME20, and AME30 shown significant reduction rate of 3.1%, 6.8%, and 10.5% in terms of ME concerning D100, respectively.
- Test fuel blends shown a significant increase of 1.8%, 5.01%, and 7.01% BSFC rate compared with D100 at peak load conditions, respectively. This higher BSFC rate of test fuel blends is due to the variation of physical properties. Among all the test fuel blends, AME10 shown very closer value with that of base diesel fuel.
- The variation of CO emission rate at peak load conditions for test fuel blends AME10, AME20, AME30, and D100 are 0.09%, 0.1%, 0.12%, and 0.07%, respectively.
- The NO<sub>x</sub> emission rates of AME10, AME20, AME30, and D100 at peak load conditions are 480 ppm, 442 ppm, 413 ppm, and 152 ppm, respectively.
- The HC emission rates of AME10, AME20, AME30, and D100 at peak load conditions are 80 ppm, 89 ppm, 98 ppm, and 51 ppm, respectively. This is because of the lower temperature conditions inside the cylinder which retards the combustion resulting in incomplete combustion.

The outcome from the above results suggests that Azolla test blends have the potentiality to be used as a source of alternative fuel in CI engine application without much modifications for improved engine performance and emission parameters.

## References

1. Nautiyal P, Subramanian KA, Dastidar MG, Kumar A (2020) Experimental assessment of performance, combustion and emissions of a compression ignition engine fuelled with *Spirulina platensis* biodiesel. *Energy* 193:116861
2. Kumar V, Kumar P, Kumar P, Singh J (2020) Anaerobic digestion of *Azolla pinnata* biomass grown in integrated industrial effluent for enhanced biogas production and COD reduction: optimization and kinetics studies. *Environ Technol Innov* 100627
3. Kösesakal T, Yıldız M (2019) Growth performance and biochemical profile of *Azolla pinnata* and *Azolla caroliniana* grown under greenhouse conditions. *Arch Biol Sci* 71(3):475–482
4. Hossain R, Chowdhury MK, Yeasmin S, Hoq MM (2010) Production of ethanol using yeast isolates on water hyacinth and *Azolla*. *Bangladesh J Microbiol* 27(2):56–60
5. Li FW, Pryer KM (2014) Crowdfunding the *Azolla* fern genome project: a grassroots approach. *GigaScience* 3(1):2047–2217
6. Kannan D, Chrstraj W (2018) Emission analysis of *Azolla* methyl ester with BaO nano additives for the IC engine. *Energy Sources, Part A: Recovery, Utilization, Environ Eff* 40(10):1234–1241
7. Brouwer P, van der Werf A, Schlupepmann H, Reichart GJ, Nierop KG (2016) Lipid yield and composition of *Azolla filiculoides* and the implications for biodiesel production. *BioEnergy Res* 9(1):369–377
8. Kaur M, Kumar M, Sachdeva S, Puri SK (2018) Aquatic weeds as the next generation feedstock for sustainable bioenergy production. *Biores Technol* 251:390–402
9. Salehzadeh A, Naeemi AS (2017) Biodiesel production from *Anabaena variabilis* cyanobacterium
10. Kollah B, Patra AK, Mohanty SR (2016) Aquatic microphylla *Azolla*: a perspective paradigm for sustainable agriculture, environment and global climate change. *Environ Sci Pollut Res* 23(5):4358–4369
11. Miranda AF, Biswas B, Ramkumar N, Singh R, Kumar J, James A, Mouradov A et al (2016) Aquatic plant *Azolla* as the universal feedstock for biofuel production. *Biotechnol Biofuels* 9(1):221
12. Miranda AF, Liu Z, Rochfort S, Mouradov A (2018) Lipid production in aquatic plant *Azolla* at vegetative and reproductive stages and in response to abiotic stress. *Plant Physiol Biochem* 124:117–125
13. Narayanasamy B, Jeyakumar N (2019) Performance and emission analysis of methyl ester of *Azolla* algae with TiO<sub>2</sub> Nano additive for a diesel engine. *Energy Sources, Part A: Recovery, Utilization, Environ Eff* 41(12):1434–1445
14. Pirbazari SM, Norouzi O, Kohansal K, Tavasoli A (2019) Experimental studies on high-quality bio-oil production via pyrolysis of *Azolla* by the use of a three metallic/modified pyrochar catalyst. *Bioresour Technol* 291:121802
15. Miranda AF, Kumar NR, Spangenberg G, Subudhi S, Lal B, Mouradov A (2020) Aquatic plants, *Landoltia punctata*, and *Azolla filiculoides* as bio-converters of wastewater to biofuel. *Plants* 9(4):437
16. Biswas B, Singh R, Krishna BB, Kumar J, Bhaskar T (2017) Pyrolysis of *Azolla*, *sargassum tenerrimum* and water hyacinth for production of bio-oil. *Biores Technol* 242:139–145
17. Golzary A, Abdoli MA, Yoshikawa K, Khodadadi A, Karbassi A (2016) *Azolla* as a feedstock for bio-refinery: cultivation, conversion and application. In: Qatar foundation annual research conference proceedings, vol 2016 issue 1. Hamad bin Khalifa University Press (HBKU Press), p EESP2082
18. Salehzadeh A, Naeemi AS, Arasteh A (2014) Biodiesel production from *Azolla filiculoides* (water fern). *Trop J Pharm Res* 13(6):957–960
19. Nikkhah A, Bagheri I, Psomopoulos C, Payman SH, Zareiforoush H, El Haj Assad M, Ghnimi S et al (2019) Sustainable second-generation biofuel production potential in a developing country case study. *Energy Sources, Part A: Recovery, Utilization, Environ Eff* 1–14



20. Venkatraman V, Sugumar S, Sekar S, Viswanathan S (2019) Environmental effect of CI engine using microalgae biofuel with nano-additives. *Energy Sources, Part A: Recovery, Utilization, Environ Eff* 41(20):2429–2438
21. Bindra S, Kulshrestha S (2019) Converting waste to energy: production and characterization of biodiesel from *Chlorella pyrenoidosa* grown in a medium designed from waste. *Renew Energy* 142:415–425
22. Zhang L, Wu H-T, Yang F-X, Zhang J-H (2015) Evaluation of Soxhlet extractor for one-step biodiesel production from *Zanthoxylum bungeanum* seeds. *Fuel Process Technol* 131:452–457

# Performance Evaluation of Sunflower Oil Biodiesel Before and After Transesterification



Surakasi Raviteja, Pujari Satish, Y. R. K. Prasanna,  
and V. V. Prasanna Kumar

**Abstract** Chemical and physical attributes of some pressure start powers got from vegetable oils are recorded and a few connections between them set up. From thought of the literature identifying with spark ignition engine execution and its reliance upon hydrocarbon fuel structure, rules are proposed for the chemical structure necessities of pressure start motor fills got from plant seed oils. The way toward trading the natural gathering  $R''$  of an ester with the natural gathering  $R'$  of a liquor is called transesterification. These responses are frequently catalyzed by the expansion of acid or base impetus. The response can likewise be refined with the assistance of chemicals (biocatalysts) especially lipases. In this paper, we will lead execution test on sunflower oils taken in various arrangements when transesterification and contrast the efficiencies all together with pick the best among them.

**Keywords** Biodiesel · Transesterification · Spark ignition engine · Biocatalysts

## 1 Introduction

Expanding vulnerability about worldwide energy creation and flexibly, natural worries because of the utilization of petroleum products and the excessive cost of oil-based goods are the significant motivations to look for options in contrast to petroleum/diesel. Researchers asserted that the worldwide oil supply and flammable gas from the ordinary sources are probably not going to meet the development in energy interest throughout the following 25 years. In this point of view, impressive consideration has been given toward biodiesel which was the creation of a diesel substitute. In addition, biodiesel fuel has become more appealing on account of its ecological advantages because of the way that plants and vegetable oils and animal fats are inexhaustible biomass sources. Biodiesel speaks to a great extent

---

S. Raviteja (✉) · P. Satish · V. V. P. Kumar  
Department of Mechanical, Lendi Institute of Engineering and Technology, Jonnada, India

Y. R. K. Prasanna  
Department of Mechanical, Avanthi Engineering College, Makavarapalem, India

shut carbon dioxide cycle (around 78%), as it is gotten from sustainable biomass sources. Contrasted with oil diesel, biodiesel has lower discharge of contaminations; it is biodegradable and improves the motor lubricity and adds to maintainability. Biodiesel has a higher Cetane number than diesel fuel, no aromatics, no sulfur, and contains 10–11% oxygen by weight.

## 1.1 Sunflower

Sunflower is one of just a small bunch not many yield creature assortments that started in North America. Sunflower was apparently initially familiar with Europe through Spain and spread through Europe as a peculiarity until it showed up at Russia where it was quickly changed. Assurance for high oil in Russia began in 1860 and was generally obligated for extending oil content from 28% to basically half. The high-oil lines from Russia were by and by brought into the U.S. after World War II, which resuscitated interest in the yield [1–5].

## 2 Literature Survey

- [1] D. Yordanov [6] in the paper titled “Biodiesel production by sunflower oil transesterification” explained about the methodology for the optimization of properties like temperature conditions, reactants proportion, and methods of purification with an intention to produce high-quality biodiesel and later tested the properties from the obtained biodiesel.
- [2] Sales [7] in “Production of biodiesel from sunflower oil and ethanol by base catalysed transesterification” elaborated the effect of ethanol and amount of catalyst used on the yield, and properties of biodiesel are studied. It was clearly studied that how ethanol influences the biodiesel production and how ethanol–oil ratio influences the yield improvement.
- [3] Cruz et al. [8] in the paper “Qualitative characteristics of Biodiesel obtained from Sunflower oil” illustrated about the properties of the sunflower oil which are obtained after preparation of biodiesel after various processes.
- [4] Sivakumar [9] in the paper entitled “Preparation of Biodiesel from sunflower oil by Transesterification” demonstrated about how to improve the percentage of yield by varying different parameters and their compositions and in this paper the yield from sunflower oil was about 80%.

## 2.1 Basic Methods of Preparing Biodiesel

For transesterification of vegetable oil in research center

1. Oil was heated in a level base cone like carafe up to 45 °C.
2. To guarantee the anticipation of methanol to arrive at its limit (57 °C), the ideal response temperature was set to be 45 °C.
3. Now, 1 L of separated vegetable oil is filled the response vessel and is mixed, all the while warmed with the assistance of attractive stirrer mechanical assembly.
4. The response items were filled an isolating channel and saved for approx. 6 h for gravity detachment of glycerol with vegetable oil and methyl esters.
5. The glycerol shapes a lower layer because of higher thickness, which is isolated out.
6. This oil recuperated from the isolating channel was again exposed to same method with 80 ml of solution to eliminate the hints of glycerol and recover better nature of biodiesel from the vegetable oil.
7. This biodiesel is then mixed with diesel and different mixes, for example, 10BD, 20BD and 30BD, 40BD are ready for directing CI motor investigation for execution and outflow qualities.
8. Proper portrayal of biodiesel mixes and oil diesel is additionally done in research center according to ASTM standards. Explicit gravity of mixes and kinematic consistency is estimated utilizing Red Wood Viscometer.
9. First, the methanol (MeOH) and the catalyst (NaOH) are blended. After the methanol and catalyst are blended, they go into a reactor, where the vegetable oil is added to the blend.
10. Used oil is initially gone through a channel to eliminate the unsaturated fats.
11. This combination is disturbed constantly for 1–4 h and may likewise be heated.
12. The fat or oil utilized is changed over to esters during this stage.
13. Glycerin and methyl esters are the two significant items made after the response is finished and the abundance methanol has been eliminated from the blend.
14. The glycerin is then drawn off the lower part of the tank and can be sold either as unrefined glycerin which is valuable in cleanser creation, or it very well may be utilized for making composts.

## 3 Experimental Set-Up

The arrangement comprises of single-chamber, four-stroke, multi-fuel, research engine associated with eddy current type dynamometer for stacking. The activity method of the motor can be changed from diesel to petrol or from petrol to diesel with some essential changes. In the two modes, the pressure proportion can be fluctuated ceaselessly by the motor and without adjusting the ignition chamber calculation by uniquely planned inclining chamber block course of action. These signs are interfaced with PC for pressure crank angle outlines. Instruments are given to interface air

**Fig. 1** Diesel engine test rig

flow, fuel flow, temperatures, and load estimations. The setup has independent board box comprising of air box, two fuel tanks for duel fuel test, manometer, fuel estimating unit, transmitters for air and fuel flow estimations, process indicator, and equipment interface. Rotameters are accommodated cooling water and calorimeter water flow estimation. A battery, starter, and battery charger are accommodated motor electric turn over plan. Diesel motor test rig utilized for examinations involved a single cylinder, water cooled, steady speed, four strokes, and variable pressure proportion diesel motor associated with a vortex flow dynamometer for stacking (Fig. 1).

## 4 Experimental Procedure

Prior to turning over the engine, the state of the engine oil was checked and furthermore, the accessibility of water was guaranteed. At first, engine was permitted to run with diesel fuel at no load till engine condition settles. The engine was then tried for various loads at CR set by manufacturer. For each load, the engine was run for 4–5 min till engine boundaries balances out. At each load was rehashed for multiple times and readings were arrived at the midpoint. The engine was then tested with blends of diesel and biodiesel at same setting to obtain base line data. The compression ratio at which the experiment was conducted was 18. The performance of the engine at different loads was evaluated in terms of brake power (BP), indicated power (IP), brake thermal efficiency (BTE), indicated thermal efficiency (ITE), and mechanical efficiency.

### 4.1 Performance Parameters

**10 BD Before Transesterification:**

See Table 1; Fig. 2.

**10 BD After Transesterification:**

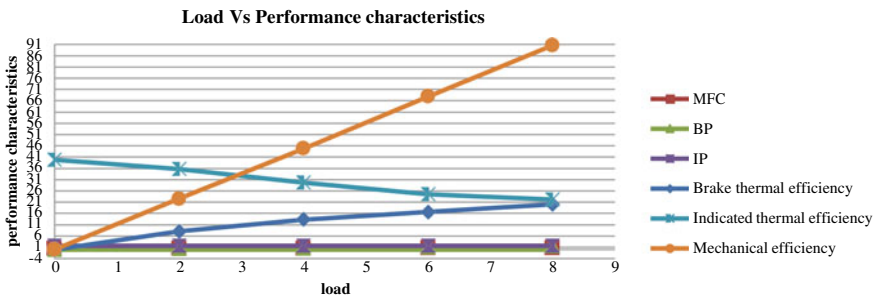
See Table 2; Fig. 3.

**20 BD Before Transesterification:**

See Table 3; Fig. 4.

**Table 1** Performance characteristics of sunflower oil 10BD before T.E

S. No.	Load	Speed	MFC	BP	IP	$\eta_{B.Th}$	$\eta_{I.Th}$	$\eta_{Mech}$
1	0	1445	0.37	0	1.74	0	39.83	0
2	2	1435	0.44	0.39	1.71	7.5	32.92	22.81
3	4	1430	0.56	0.77	1.70	11.65	25.71	45.29
4	6	1425	0.63	1.15	1.69	15.46	22.72	68.04
5	8	1420	0.74	1.53	1.68	17.51	19.23	91.07



**Fig. 2** Load versus performance characteristics for 10BD before TE

**Table 2** Performance characteristics of sunflower oil 10BD after T.E

S. No.	Load	Speed	MFC	BP	IP	$\eta_{B.Th}$	$\eta_{I.Th}$	$\eta_{Mech}$
1	0	1444	0.37	0	1.74	0	39.83	0
2	2	1440	0.41	0.39	1.73	8.06	35.74	22.54
3	4	1436	0.49	0.77	1.72	13.31	29.73	44.77
4	6	1431	0.59	1.16	1.71	16.65	24.55	67.83
5	8	1427	0.65	1.54	1.7	20.1	22.15	90.59

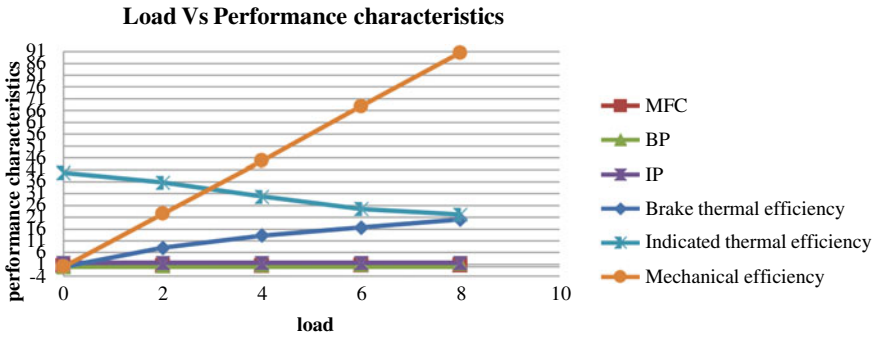


Fig. 3 Load versus performance characteristics for 10BD after TE

Table 3 Performance characteristics of sunflower oil 20BD before T.E

S. No.	Load	Speed	MFC	BP	IP	$\eta_{B,Th}$	$\eta_{I,Th}$	$\eta_{Mech}$
1	0	1445	0.41	0	1.75	0	36.15	0
2	2	1435	0.44	0.39	1.73	7.51	33.31	22.54
3	4	1425	0.54	0.77	1.70	12.08	26.67	45.29
4	6	1415	0.61	1.15	1.68	15.97	23.33	68.45
5	8	1410	0.71	1.53	1.67	18.25	19.92	91.62

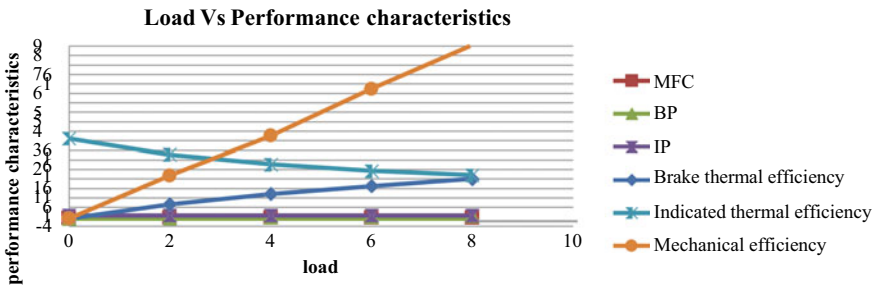


Fig. 4 Load versus performance characteristics for 20BD before TE

**20 BD After Transesterification:**

See Table 4, Fig. 5.

**30 BD Before Transesterification:**

See Table 5; Fig. 6.

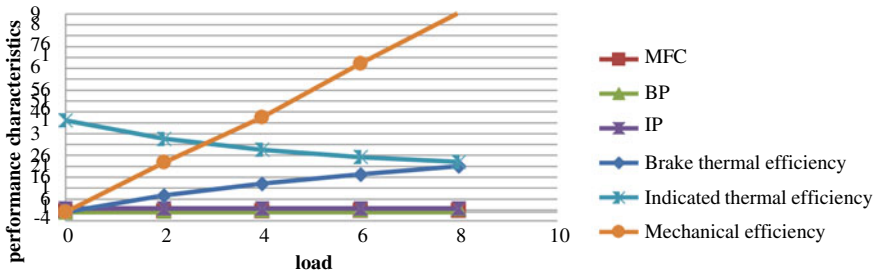
**30 BD After Transesterification:**

See Table 6; Fig. 7.

**Table 4** Performance characteristics of sunflower oil 20BD after T.E

S. No.	Load	Speed	MFC	BP	IP	$\eta_{B,Th}$	$\eta_{I,Th}$	$\eta_{Mech}$
1	0	1448	0.41	0	1.75	0	36.15	0
2	2	1430	0.44	0.39	1.70	0.39	32.72	22.94
3	4	1425	0.52	0.77	1.69	0.78	27.53	45.56
4	6	1420	0.62	1.15	1.68	1.16	22.95	68.45
5	8	1415	0.70	1.52	1.67	1.54	20.21	91.02

**Load Vs Performance characteristics**

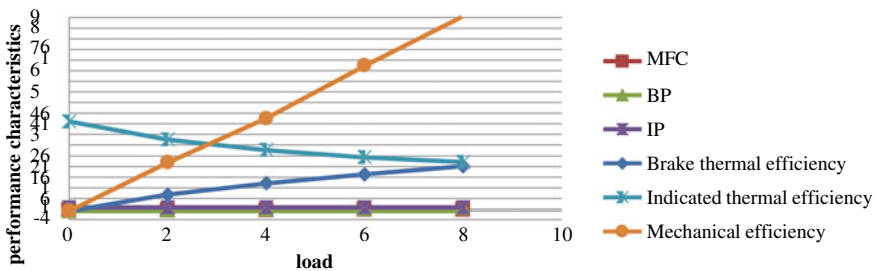


**Fig. 5** Load versus performance characteristics for 20BD after TE

**Table 5** Performance characteristics of sunflower oil 30BD before T.E

S. No.	Load	Speed	MFC	BP	IP	$\eta_{B,Th}$	$\eta_{I,Th}$	$\eta_{Mech}$
1	0	1445	0.36	0	1.74	0	40.94	0
2	2	1435	0.43	0.39	1.71	7.68	33.69	22.8
3	4	1425	0.52	0.77	1.69	12.54	27.53	45.56
4	6	1415	0.61	1.14	1.67	15.83	23.19	68.26
5	8	1410	0.71	1.52	1.66	18.13	19.8	91.57

**Load Vs Performance characteristics**

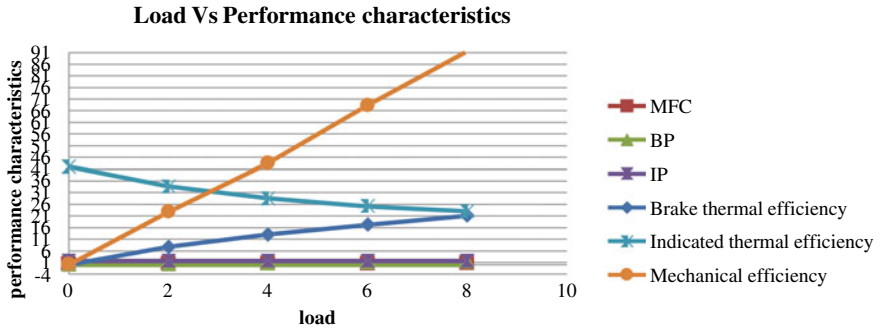


**Fig. 6** Load versus performance characteristics for 30BD before TE



**Table 6** Performance characteristics of sunflower oil 30BD after T.E

S. No.	Load	Speed	MFC	BP	IP	$\eta_{B.Th}$	$\eta_{I.Th}$	$\eta_{Mech}$
1	0	1430	0.4	0	1.75	0	37.06	0
2	2	1425	0.43	0.39	1.747	7.68	34.41	22.32
3	4	1420	0.52	0.78	1.74	12.7	28.34	43.68
4	6	1415	0.60	1.16	1.73	16.37	24.42	67.05
5	8	1400	0.70	1.54	1.7	18.65	20.57	90.59



**Fig. 7** Load versus performance characteristics for 30BD after TE

**40 BD Before Transesterification:**

See Table 7; Fig. 8.

**40 BD After Transesterification:**

See Table 8; Fig. 9.

**Table 7** Performance characteristics of sunflower oil 40BD before T.E

S. No.	Load	Speed	MFC	BP	IP	$\eta_{B.Th}$	$\eta_{I.Th}$	$\eta_{Mech}$
1	0	1445	0.35	0	1.74	0	42.11	0
2	2	1435	0.43	0.39	1.71	7.68	33.69	22.8
3	4	1425	0.5	0.77	1.69	13.04	28.63	43.56
4	6	1415	0.56	1.14	1.67	17.24	25.26	68.26
5	8	1410	0.61	1.53	1.66	21.1	23.05	91.57

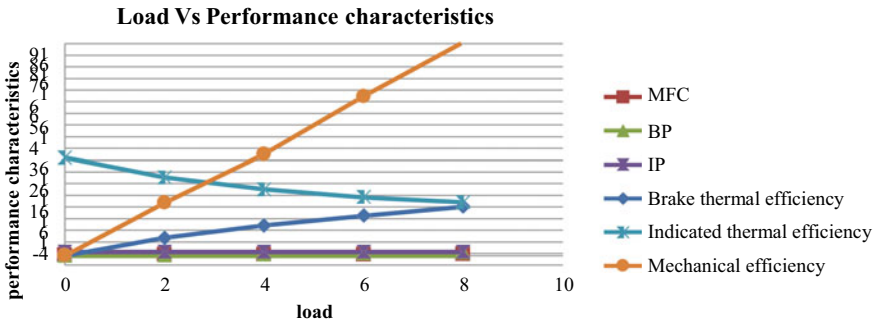


Fig. 8 Load versus performance characteristics for 40BD before TE

Table 8 Performance characteristics of sunflower oil 40BD after T.E

S. No.	Load	Speed	MFC	BP	IP	$\eta_{B.Th}$	$\eta_{I.Th}$	$\eta_{Mech}$
1	0	1445	0.40	0	1.7	0	36	0
2	2	1435	0.45	0.38	1.69	7.15	31.8	22.49
3	4	1430	0.53	0.77	1.68	12.31	26.85	45.83
4	6	1425	0.6	1.14	1.67	16.1	23.58	68.26
5	8	1420	0.7	1.51	1.63	18.27	20.57	92.64

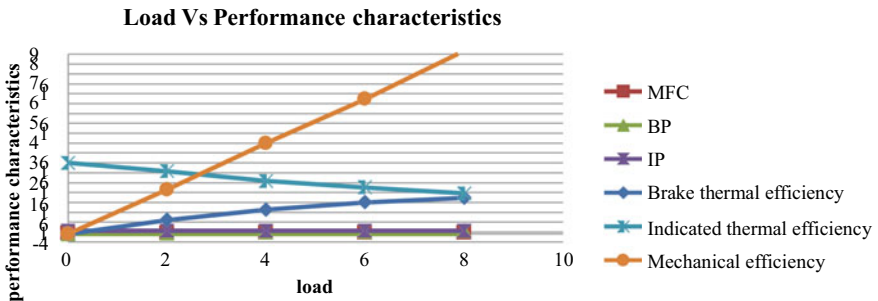


Fig. 9 Load versus performance characteristics for 40BD after TE

## 5 Conclusion

1. It is finished up from this exploration work that by utilizing mixes of biodiesel of sunflower oil after transesterification, 40 BD has shown good results
2. There is an increase in the mechanical efficiency, and the maximum mechanical efficiency is found to be 92%
3. Both indicated and brake thermal efficiency is found to be decreasing by around 2–5%

4. The results are compared for before and after transesterification, and it can be concluded that the results after transesterification are more promising.

## References

1. Rauf S, Jamil N, Tariq SA, Khan M, Kausar M, Kaya Y (2017) Progress in modification of sunflower oil to expand its industrial value. *J Sci Food Agric* 97(7):1997–2006. <https://doi.org/10.1002/jsfa8214>. PMID28093767
2. Christov M (2012) Contribution of interspecific hybridization to sunflower breeding (PDF). *Helia* 35(57):37–46. <https://doi.org/10.2298/hel1257037c.S2CID85351878>
3. Gotor AA, Rhazi L (2016) Effects of refining process on sunflower oil minor components: a review. *Oilseeds Fats, Crops Lipids* 23(2): D207. <https://doi.org/10.1051/ocl/201600>
4. Skorić D, Jocić S, Sakac Z, Lecić N (2008) Genetic possibilities for altering sunflower oil quality to obtain novel oils. *Can J Physiol Pharmacol* 86(4):215–221. <https://doi.org/10.1139/Y08-008>. PMID18418432
5. Nita I, Neagu A, Geacai S, Dumitru A, Sterpu A (2010) Study of the behavior of some vegetable oils during the thermal treatment. Technology and Chemical Engineering Department, Ovidius University, bd. Mamaia 124, Constanta, 900527, Romania. Archived 2011-06-28 at the wayback machine. [http://www.univ-ovidius.ro/anale-chimie/chemistry/2010-1/full/1\\_nita.pdf](http://www.univ-ovidius.ro/anale-chimie/chemistry/2010-1/full/1_nita.pdf)
6. Yordanov D (2007) Biodiesel production by sunflower oil transesterification. *Oxid Commun* 30(2)
7. Sales A (2011) Production of biodiesel from sunflower oil and ethanol by base catalyzed transesterification
8. Portillo ER, Cruz C, Romero R, Amaya A (2015) Qualitative characteristics of biodiesel obtained from sunflower oil. *Peer Rev*. <https://doi.org/10.5772/59673>
9. Sivakumar VM, Merly Xavier A, Prabhakaran D, Thirumarimurugan M Preparation of biodiesel from sunflower oil by Transesterification. *Int J Biosci Biochem Bioinf* 2(6):443–446 <https://doi.org/10.7763/IJBBB.2012.V2.151>
10. Badouin H, Gouzy J, Grassa CJ, Murat F, Staton SE, Cottret L, Lelandais-Brière C, Owens GL, Carrère S, Mayjonade B, Legrand L, Gill N, Kane NC, Bowers JE, Hubner S, Bellec A, Bérard A, Bergès H, Blanchet N, Boniface MC, Brunel D, Catrice O, Chaidir N, Claudel C, Donnadiou C, Faraut T, Fievet G, Helmstetter N, King M et al. (2017) The sunflower genome provides insights into oil metabolism, flowering and asterid evolution. *Nature* 546(7656):148–152. Bibcode: 2017Natur.546..148B. <https://doi.org/10.1038/nature22380>. PMID 28538728

# Evaluation of Heat Transfer Rate in Heat Sink Using FGM



N. B. V. L. Kumari, A. Jagadeesh, and Ishrat Meera Mirzana

**Abstract** In most of the electronic devices, heat transfer is one of the major criteria which affects the performance of the devices for an application. As efficient cooling of the electronic devices becomes a challenging task in thermal fields, these systems should be self-indulge to improve its reliability and failure. Heat sink is an element for heat exchange that cools a device by its extended surfaces. Heat sink is made of metal such as copper or aluminium alloys or a mixture of different materials such as FGM. These are attached on the top of processor. Functionally graded materials (FGMs) are inhomogeneous materials, consisting of two or more different types of material, tailored to have a continuously varying spatial composition profile. These materials are generally made from a mixture of ceramics and metal or it can be a combination of different types of materials. In this paper, evaluation of heat sink is carried to determine the thermal efficiency and thermal analysis is carried out using Ansys software. Latter, obtained experimental data are compared with the analytical data and the performance of the heat sink is validated.

**Keywords** Heat sink · Heat transfer rate · FGM · Ansys

## 1 Introduction

### 1.1 Heat Sink

A heat sink is a thermal conductive metal device designed to absorb and disperse heat away from a high temperature object such as a computer processor. Usually, heat sinks are installed within fans to help dissipate heat and keeping both CPM and heat at appropriate/desired temperature. Heat sink is made of metal such as copper or aluminium alloys or a mixture of different materials such as FGM. These are attached on the top of processor.

---

N. B. V. L. Kumari (✉) · A. Jagadeesh · Ishrat Meera Mirzana  
MED, MJCET, Hyderabad, India

## 1.2 Introduction of FGMs

Functionally graded materials (FGMs) are inhomogeneous materials, consisting of two or more different types of material, tailored to have a continuously varying spatial composition profile. These materials are generally made from a mixture of ceramics and metal or it can be a combination of different types of materials. The main feature of FGM is that its properties change gradually with position used as coatings and interfacial zones as they assist to reduce stresses mechanically and thermally which are caused by the property of the material and also to improve the bonding strength [1, 2].

## 2 Literature Review

- Hassanzadeh et al. [1] carried out their studies on improvement of thermal efficiency in the heat dissipation process from electrical components by replacing the conventional heat sink material with functionally graded materials.
- Mahamood et al. [2] have explained the over view of FGMs, where functionally graded material (FGM) belongs to a class of advanced material characterized by variation in properties as the dimension varies.
- El-Wazery et al. [3] carried out a research on functionally graded ceramic-metal materials. FGMs can be used to avoid problems associated with the presence of an interface in a material: stress singularities due to elastic or thermal property mismatch, poor adhesion, or unwanted reflections at the interface
- Kasaeian et al. [4] have studied FGM materials to find an appropriate model for thermal conductivity. In this study, a précised investigation of the whole available production methods was done and then with considering the field of every special application, a suitable FGM combination was selected.
- Chimielewski et al. [5] investigated metal-ceramic FGM. In this paper, selected results of works carried out by the authors and relating to the application of the developed metal-ceramic composites were presented in order to manufacture functionally graded materials for target purposes
- Saiyathibrahim et al. [6] have discussed the processing techniques of FGM.
- Kieback et al. [7] explained the processing techniques of ‘functionally graded materials (FGM)’ in the field of processing are given.
- Mitomoto et al. [8] conducted a research on FGM and presented in a form of a book called as functionally graded materials: design, processing and application.
- Lasagni et al. [9] carried out a research on enhanced Young’s Modulus of Al-Si alloys and reinforced matrix by co-continuous structures.
- Cem Okumus et al. [10] explained thermal expansion and conductivity behaviours of Al-Si/SiC material matrix.
- You et al. [11] discussed thermal and mechanical properties of infiltrated CuCrZr/W-cu composite materials for FGM heat sink application.

- Jeong-Ha [12] carried out a research on copper matrix composite as a heat sink material.
- Bukhari et al. [13] explained the application of metal matrix composite of Cu-SiC and Al-SiC as electronics building materials, conventional materials such as Al and Cu are normally used in heat sink which is now replaced by Al-SiC and Cu-SiC which are more suitable for heat application.
- Richard Culhan, et al. [14] discussed the influence of material properties and spreading resistance in the thermal design of heat sink.
- Kim et al. [15] carried out a study on analytical heat diffusion models for different heat sink cross-sectional geometries. This study explores heat diffusion effects in micro-channel heat sinks intended for electronic cooling applications.

### 3 Applications of FGM in Industry

- Aerospace—space plane body, rocket engine component, etc.
- Medicine—dental and orthopaedic applications for teeth and bone replacement.
- Nuclear projects—fuel pallets and plasma wall of fusion reactor.
- Energy sector—energy conversion devices.
- Communication field—lenses and semiconductors.
- Defence—a penetration resistant material used for armour plates and bullet-proof vests.

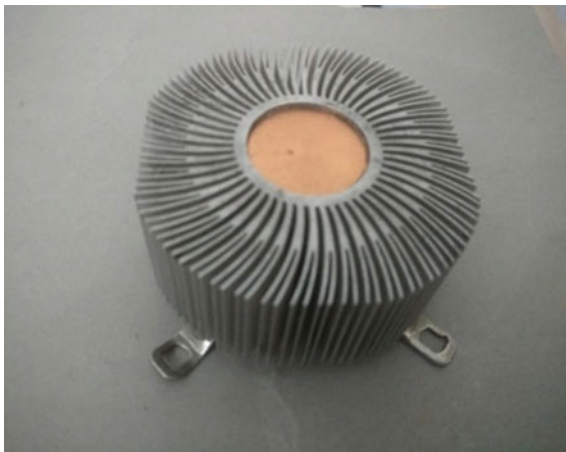
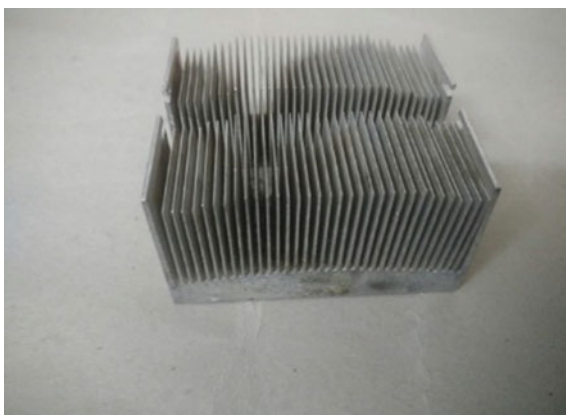
### 4 Methodology

The steps involved in the experimentation are.

1. Heat sink profiles selection
2. Modelling
3. Ansys
4. Experimentation.

#### 4.1 Selection of Heat Sink Profiles

Two different profiles of different cross-sectional areas and different combination of materials are considered for Ansys and experimentation [1, 2] (Figs. 1, 2; Tables 1, 2).

**Fig. 1** Circular profile**Fig. 2** Rectangular profile**Table 1** Specification of circular profile

S. No.	Specification	Measurement
1	Fin height	32 mm
2	Fin material	Aluminium and copper
3	Each fin thickness	1 mm
4	Fin pitch	2.5–2.7 (mm)
5	No. of fins	104
6	Base thickness	5 mm
7	Inner diameter	32 mm
8	Outer diameter	88 mm
9	Fin base thickness	3 mm
10	Fin length	26 mm
11	Inner cylinder length	35 mm
12	Outer cylinder length	32 mm

**Table 2** Specification of the rectangular profile

S. No.	Specifications	Measurements
1	Fin height	28 mm
2	Profile height	42 mm
3	Fin thickness	0.8 mm
4	Fin pitch	2.3 mm
5	Fin material	Aluminium
6	Base thickness	14 mm
7	Profile width	77*68 mm
8	Grove height	29 mm
9	Grove width	11 mm

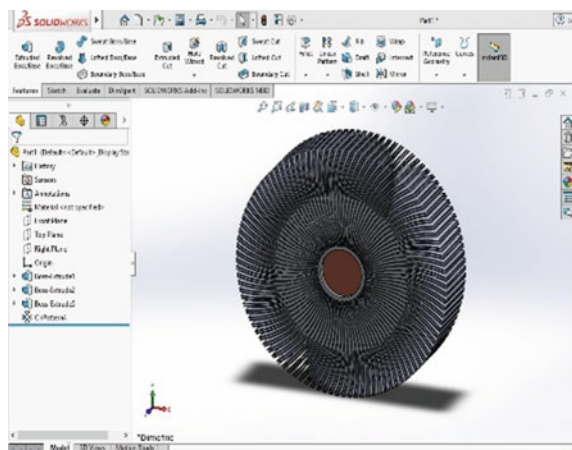
### 4.2 Modelling of Heat Sink Profiles: The Heat Sink Profiles Are Developed Using CAD Software

See Figs. 3, 4.

### 4.3 FE Analysis of Circular Heat Sink (Natural Convection)

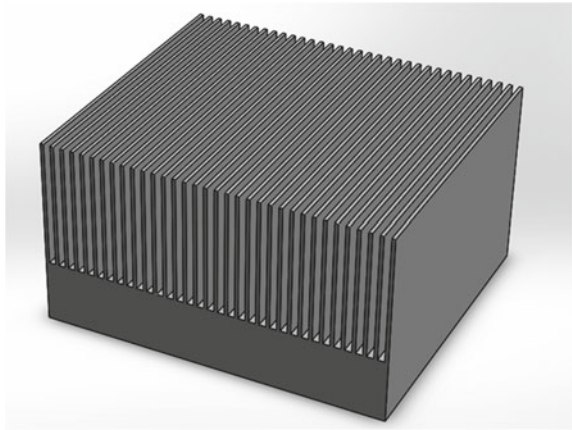
Analysis of a circular heat sink is carried out in Ansys 18 workbench. Initial temperature of 23 °C is provided to the profile, and a heat flux of 92 °C is provided to the bottom of heat sink, and a natural convection of 10 °C temperature is provided on the whole profile except bottom of heat sink, and the solution is carried out [3–5] (Table 3).

**Fig. 3** Model of circular type heat sink





**Fig. 4** Model of rectangular type heat sink



**Table 3** Properties of materials

S. No.	Properties	Al-SiC	CuCrZr	Cu-Si	W-Cu
1	Density [g/cm <sup>3</sup> ]	2.8–3.1	8–9	3–4	14
2	Specific heat [J/kg*K]	768	380	300	298
3	Thermal conductivity [w/(m*k)]	200	320	176	235
4	Young's Modulus [GPa]	167	128	–	170
5	Poisson's ratio [GPa]	0.251	0.3	–	1.1

## 4.4 Experimentation

In order to study the thermal behaviour and to measure the heat transfer rate and heat dissipation, a thermocouple experimental setup is used. The thermocouple is connected at different points on a heat sink with both natural and forced convection, and the results are noted at a time interval of 30 s. The processor which is used in the experimentation is a AMD processor model no AMD FX™-4100, it is a quad core processor and a motherboard of giga byte model no DX-10 [6–8] (Figs. 5, 6; Tables 4, 5, 6, 7).

### 4.4.1 FE Analysis of Circular Heat Sink (Natural Convection)

Analysis of a circular heat sink is carried out in Ansys 18 workbench. A circular heat sink profile is selected from the geometry, and meshing is done on it. Initial temperature of 23 °C is provided to the profile, and a heat flux of 92 °C is provided to the bottom of heat sink, and a natural convection of 10 °C temperature is provided on the whole profile except bottom of heat sink, and the solution is carried out.

**Fig. 5** Thermocouple experimental setup



**Fig. 6** Installation of profile with thermocouples attached



#### **4.4.2 FE Analysis of Circular Heat Sink (Forced Convection)**

Analysis of a circular heat sink is carried out in Ansys 18 workbench. A circular heat sink profile is selected from the geometry, and meshing is done on it. Initial temperature of 23 °C is provided to the profile, and a heat flux of 63 °C is provided to the bottom of heat sink, and forced convection temperature is provided on the whole profile except bottom of heat sink, and then, the solution is carried out (Figs. 7, 8).

#### **4.4.3 FE Analysis of Rectangular Heat Sink (Natural Convection)**

Ansys 18 workbench is implemented for analyzing of rectangular heat sink profile. Heat sink is selected from the geometry, and meshing is done to the profile. Initial temperature of 23 °C is applied to the profile. Heat flux of 92 °C is applied to the bottom of the heat sink, and a natural convection of 10 °C temperature is provided to the whole sink except bottom of heat sink, and solution is carried out.

**Table 4** Experimental values of circular heat sink natural convection

Time (sec)	Temperature of heat sink at bottom °C	Temperature of heat sink at top °C
0	46	46
30	51	51
1	55	55
1.30	57	57
2	59	60
2.30	60	61
3	61	62
3.30	62	63
4	64	64
4.30	65	66
5	67	67
5.30	67	68
6	69	69
6.30	70	71
7	72	72
7.30	74	75
8	77	78
8.30	80	81
9	83	84
9.30	85	86
10	86	88
10.30	89	90
11	90	91
11.30	92	92

#### 4.4.4 FE Analysis of Rectangular Heat Sink (Forced Convection)

Analysis of a rectangular heat sink is carried out in Ansys 18 workbench. A rectangular heat sink profile is selected from the geometry, and meshing is done on it. Initial temperature of 23 °C is provided to the profile, and a heat flux of 61 °C is provided to the bottom of heat sink, and forced convection temperature is provided on the whole profile except bottom of heat sink, and the solution is carried out (Figs. 9, 10).

#### 4.4.5 FE Analysis on FGM Circular Heat Sink (Natural Convection)

Finite element analysis is carried out on a circular heat sink which is made up of Al-SiC. Properties of this material are added manually in Ansys workbench. Similar parameters are used to analyze this FGM profile. Circular profile is chosen from the

**Table 5** Experimental values of circular heat sink forced convection

Time (sec)	Temperature of heat sink at bottom °C	Temperature of heat sink at top °C
0	46	46
30	51	51
1	55	55
1.30	57	57
2	59	60
2.30	60	61
3	61	62
3.30	62	63
4	62	63
4.30	65	66
5	67	67
5.30	67	68
6	69	69
6.30	70	71
7	72	72
7.30	74	75
8	77	78
8.30	80	81
9	83	84
9.30	85	86
10	86	86
10.30	89	90
11	90	91
11.30	91	92
12	92	92

geometry, and meshing is done on it. Initial temperature of 23 °C is provided to the profile, and a heat flux of 93 °C is provided to the bottom of heat sink, and forced convection temperature is provided on the whole profile except bottom of heat sink, and the solution is carried out.

**4.4.6 FE Analysis on FGM Circular Heat Sink (Forced Convection)**

Circular heat sink profile is chosen as it has high heat dissipation compared to rectangular heat sink. FEA is carried out on circular heat sink with FGM material such as Al-SiC, properties of FGM materials are added manually to Ansys workbench 18, and solution is carried out (Figs. 11, 12).

**Table 6** Experimental values of rectangular heat sink natural convection

Time(sec)	Temperature of heat sink at bottom °C	Temperature of heat sink at top °C
0	46	46
30	49	48
1	50	48
1.30	50	48
2	50	49
2.30	51	49
3	50	49
3.30	50	49
4	49–50	48
4.30	48–49	48
5	49	48
5.30	48	48
6	48	48
6.30	50	48
7	49–50	49
7.30	49–50	49
8	49	49
8.30	50	49
9	51	50
9.30	53–54	51
10	56	53
10.30	58	54
11	60	55
11.30	60	55
12	61	56
12.30	62	56
14	62	56
14.30	62	55
15	61–62	56
15.30	62	55
16	63	57
16.30	62	56
17	62	56
17.30	63	57
18	63	56

(continued)

**Table 6** (continued)

Time(sec)	Temperature of heat sink at bottom °C	Temperature of heat sink at top °C
18.30	62	56
19	63	56
19.30	63	57
20	63	57

**Table 7** Experimental values of rectangular heat sink forced convection

Time (sec)	Temperature of heat sink at bottom °C	Temperature of heat sink at top °C
0	46	45
30	54	52
1	53	50
1.30	54	52
2	54	52
2.30	59	56
3	60	59
3.30	61	60
4	60	58
4.30	60	58
5	60	59
5.30	60	59
6	59	59
6.30	62	59
7	60	59
7.30	60	58
8	57	56
8.30	59	56
9	55	55
9.30	59	55
10	60	56
10.30	61	56

#### ***4.5 Graphs Plotted Based on the Experimental Results***

Based on the experimental values, graphs are plotted with time and temperature and the models of both circular heat sink and circular heat sink with natural and forced convection are evaluated. It is observed that in case of circular heat sink, the heat dissipation rate is good compared to rectangular heat sink (Graph 1).

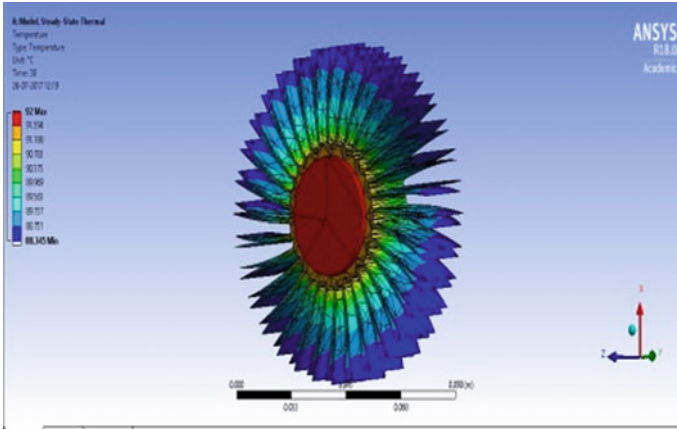


Fig. 7 Results of circular profile natural convection

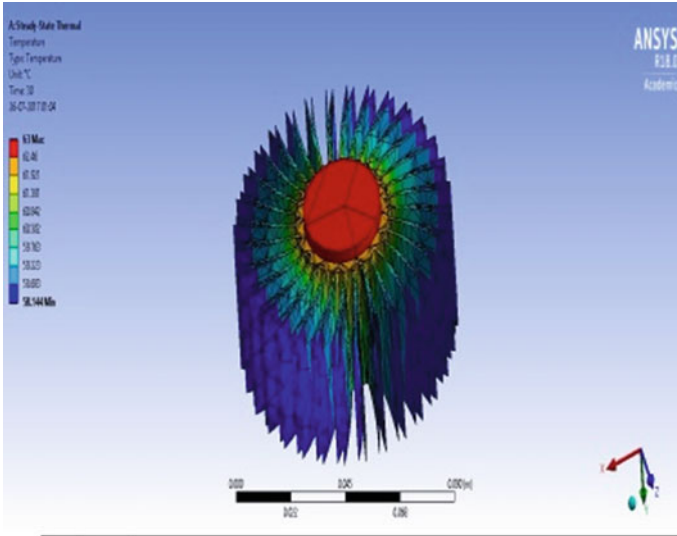


Fig. 8 Results of circular profile forced convection

The above graph is plotted for circular heat sink under natural convection process, and it is observed that the temperature at the bottom and the temperature at the top are same resulting in the better heat dissipation (Graph 2).

The above graph is plotted for circular heat sink under forced convection process, and it is observed that the temperature at the bottom is higher, and the temperature at the top surface of heat sink is reduced resulting in the better heat dissipation (Graph 3).

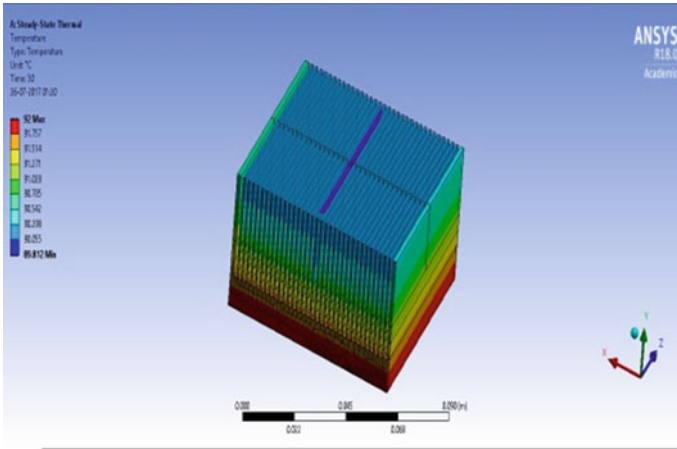


Fig. 9 Results of rectangular profile natural convection

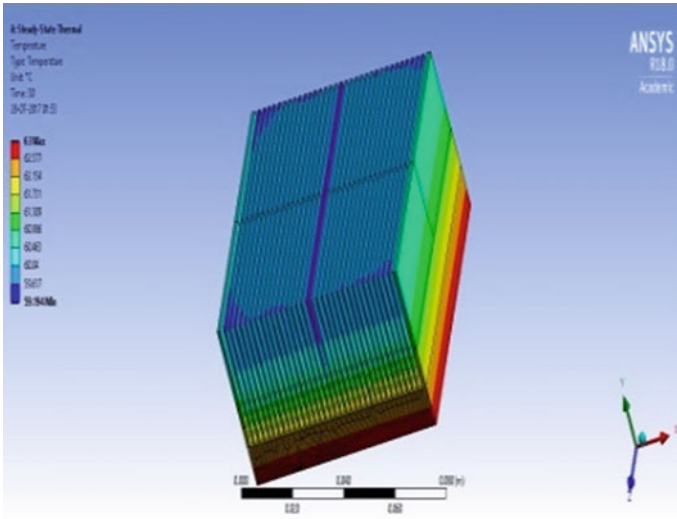


Fig. 10 Results of rectangular profile forced convection

The above graph is plotted for rectangular heat sink under natural convection process, and it is observed that the temperature at the bottom is same as the temperature at the top surface of heat sink (Graph 4).

The above graph is plotted for rectangular heat sink under forced convection process, and it is observed that the temperature at the bottom is higher, and the temperature at the top surface of heat sink is reduced resulting in the better heat dissipation.



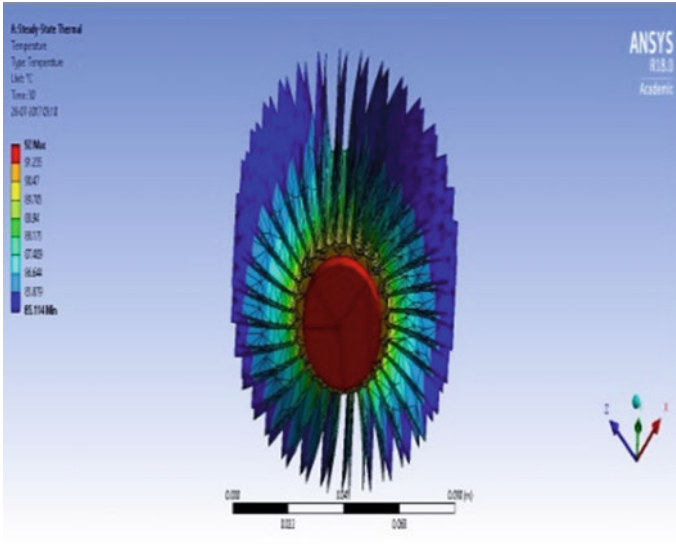


Fig. 11 Results of FGM circular profile circular natural convection

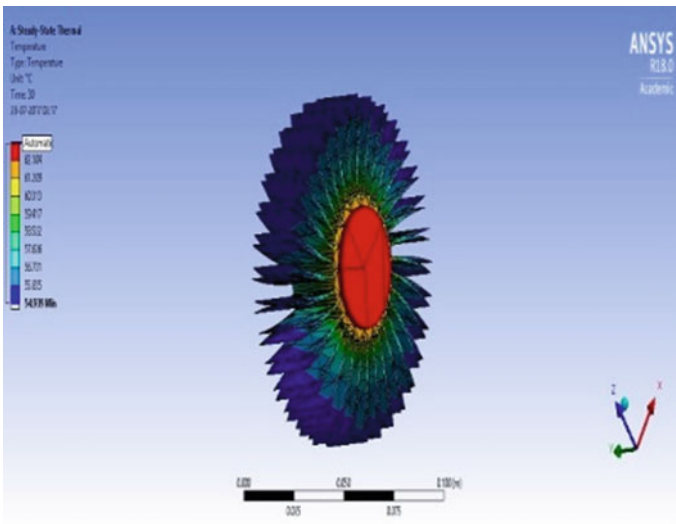
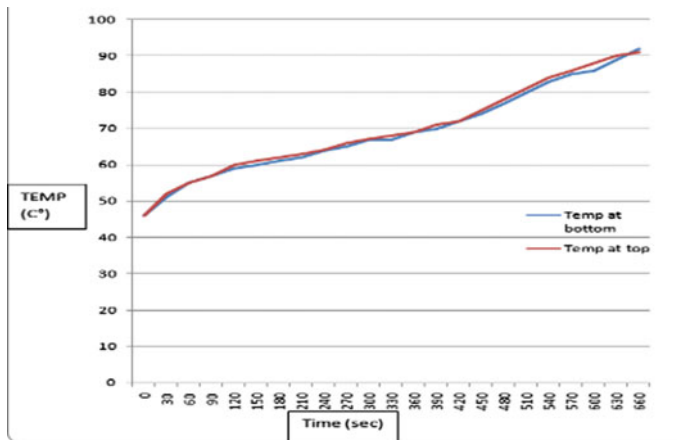
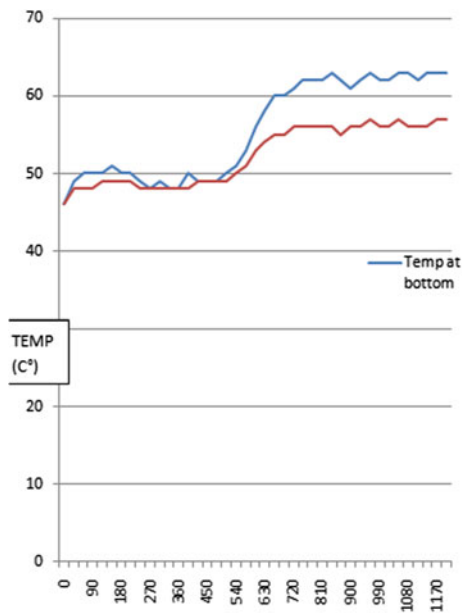


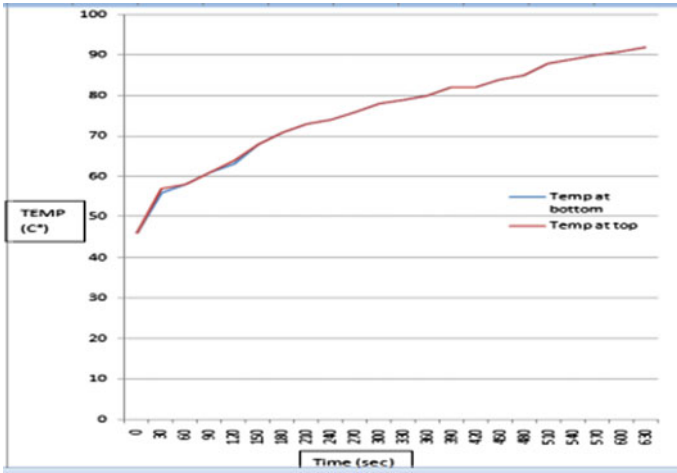
Fig. 12 Results of FGM profile forced convection



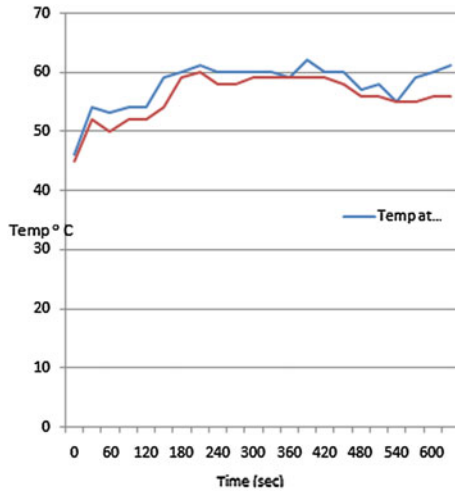
**Graph 1** Circular heat sink natural convection



**Graph 2** Circular heat sink forced convection



**Graph 3** Rectangular heat sink natural convection



**Graph 4** Rectangular heat sink forced convection

### 4.6 Comparison of Results Both Ansys and Experimental Work

#### 4.6.1 Ansys Results

See Table 8.

#### 4.6.2 Experimental Results

See Table 9.

**Table 8** Consolidated results of Ansys

S. No.	Heat sink type	Minimum temperature (°C)	Maximum temperature (°C)	Temperature difference (°C)	Time (sec)
1	Circular heat sink (Al, Cu) natural convection	88.35	92	3.65	30
2	Circular heat sink (Al, Cu) forced convection	58.15	63	4.8	30
3	FGM circular heat sink natural convection	85.11	92	6.8	30
4	FGM circular heat sink forced convection	54.93	63	8	30

**Table 9** Experimental values of circular and rectangular heat sink

S. No.	Heat sink type	Minimum temperature (°C)	Maximum temperature (°C)	Temperature difference (°C)	Time (sec)
1	Circular heat sink (Al, Cu) natural convection	46	45	1	30
2	Circular heat sink (Al, Cu) forced convection	63	57	6	30
3	Rectangular heat sink natural convection	46	45	1	30
4	Rectangular heat sink forced convection	61	56	5	30

## 5 Conclusions

1. Analysis is carried out on rectangular heat sink and circular heat sink in natural convection process, and it has been observed that there is a 1.5 °C difference of heat dissipation when compared.
2. Similarly, both heat sinks are analyzed in forced convection process where an external medium such as a fan is used which is mounted on the top of heat sink. It has been observed that the temperature difference between two heat sink is 1.2 °C
3. It is observed that the minimum temperature attained by FGM is 54.93 °C. In aluminium copper, heat sink temperature attains around 58.15 °C. The temperature difference between two heat sinks is 3.22 °C. Maximum temperature reaches around 63 °C which can be observed in both sinks.
4. From this present study, it is observed that for an FGM heat sink made up of Al-SiC provides a better performance when compared to conventional materials with less cost and high performance and durability.

## References

1. Hassanzadeh R, Bilgili M (2014) Improvement of thermal efficiency in computer heat sink using functionally graded materials. *Int Sci Publ Consul Serv (ISPACS)* 4(3):1–13
2. Mahmood RM, Esther T (2012) Functionally graded material: an overview. In: *Proceeding of the world congress on engineering*, vol 3. 4 July 2012, pp 1–5
3. El-Wazery MS, El-Desouky AR (2015) A review on functionally graded ceramic-metal materials 6(5):1369–1376
4. Kasaeian AB, Nasirivatan SH, Daneshmand S (2011) FGM materials and finding an appropriate model for the thermal conductivity 14(1):3199–3204
5. Chmielewski M, Pietrazak K (2016) Metal-ceramic FGM's- Manufacturing, characterization, application. *Pol Acad Sci Tech Sci* 64(1):151–160
6. Saiyathibrahim A, Mohammed Nazirudeen SS, Dhanapal P (2015) Processing techniques of FGM-A review. *ICSSCET* 01(1):98–105
7. Kieback B, Neubrand A, Riedel H (2003) Processing techniques for functionally graded materials. *Elsevier Publications* 1(2):81–105
8. Myamoto Y, Kaysser WA, Rabin BH (1999) Functionally graded materials, design, processing and application. *Sci Bus Media* 1(1):1–339
9. Lasangni F, Peter H (2010) Enhanced young's modulus of Al-si alloys and reinforced matrices by co-continuous structure 44(6):740–755
10. Okumus SC, Aslan S, Karlioglu R (2012) Thermal expansion and thermal conductivity behaviour of Al-si/ sic/ graphite hybrid metal matrix composites. *Mater Sci (medziagotyra)* 18(4):341–346
11. You JH, Brenel A, Nawka S, Schubert T (2014) Thermal and mechanical properties of omfoltrated W/cucrzr composite materials for functionally graded heat sink application. *J Nucl Mater* 438(1–3):1–6
12. Jeong-Ha (2016) Copper matrix composites as heat sink materials for mater cooled divertor target. *Nucl Mater Energy* 5(1–3):1–6

13. Bukhari MZ, Brabazon D, Hashmi MSJ (2015) Application of metal matrix composite of Cusic and Alsic as electronics packing materials. In: The 28th international manufacturing conference, vol 1, pp 1–8
14. Richard Chlham J, Khan WA (2008) The influence of material properties and spreading resistance in the thermal design of plate fin heat sink 129(4):75–81
15. Kim S-M, Mudawar I (2011) Analytical heat diffusion modals for different micro-channel heat sink cross-sectional geometries. Elsevier Int J Heat Mass Transfer 10(2):4001–4016

# Application of Thermoacoustics for Cooling: A Review



Rajan Devkota, Atal Babu, Prashant Gupta, Karun Kant, and Shrikant Vidya

**Abstract** From the name itself, we can know that thermoacoustics means getting the thermodynamic effect with the application of acoustic medium (i.e., sound). Here, in this project, thermodynamic effect means getting the cooling effect with the help of high-frequency sound. Because it is using sound to get the desired effect, it becomes very much environment friendly as compared to modern days cooling system since it does not emit any environment-unfriendly gases like CFCs, Freons and other hydrocarbons. The hardware-based model can be either designed using the Tijani's model or by simply using the resonator tube. Here we will be more focused on resonator tube method.

**Keywords** Thermoacoustics · Thermoacoustic cooling · Thermoacoustic refrigeration

## 1 Introduction

The refrigeration process means cooling a desired space and maintaining the temperature below the ambient temperature. Acoustics is the study of sound production, transmission. Thermoacoustic is a device which uses high frequency of transducer as its main working components. Thermoacoustic cooling device can be very suitable alternative for the conventional and classical cooling devices. Because of its sustainability, it is being widely used in different arenas as of now. It is used in space, ice cream parlor, and even for household cooling purposes, i.e., cooling of vegetables, fruits, and different edible things. Different mechanisms have been carried out to fabricate the model: Rijke tube model, Tijanis model, resonating tube model, and many more. Besides that, some of them have even found out the model that is not using the stack, which is one of the most important and crucial component of the thermoacoustic.

---

R. Devkota · A. Babu · P. Gupta · K. Kant · S. Vidya (✉)  
School of Mechanical Engineering, Galgotias University, Greater Noida, Uttar Pradesh, India

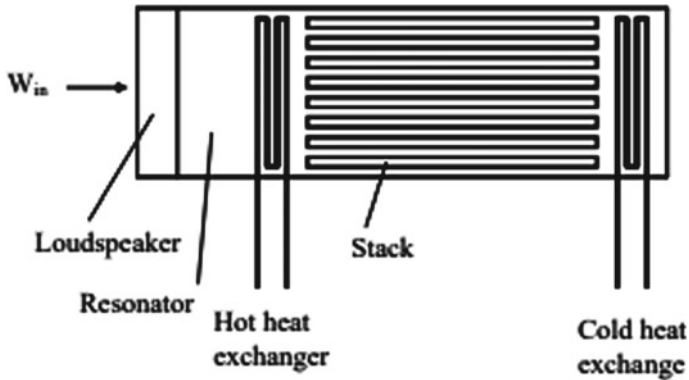


Fig. 1 Basic principle of thermoacoustic refrigeration [1]

## 2 Principle of Thermoacoustics

When the high-frequency sound propagates through the resonating tube, there occurs interference as a result there occurs resonant in the gas (Fig. 1). Because of standing sound waves, the air molecule too starts moving back and forth creating a temperature difference along the length of the stack. While these sound waves propagate through the air medium it creates disturbance which results in the creation of constructive and destructive interference. The air molecules are compressed at the constructive interference, whereas expansion occurs at the destructive interference. Because of this, there occurs change in the temperature and which is used to remove heat from the cold side to the hotter side of the model.

## 3 Components of Thermoacoustic Refrigeration (TAR)

The major components of TAR are:

- **Loudspeaker:** A loudspeaker is electroacoustic transducer that produces sound when given an electrical input. When an electrical power is transferred to the coil, it creates a magnetic field which in turn interacts with the permanent magnet in the speaker which then generates a force pushing the cone outward.

Because of the nature of alternating current, the magnetic field produced by the coil gets reversed repeatedly which again produces the force, but this time pulling the cone back toward it. This repeating process makes the cone vibrate in and out which creates pressure variation in the air, known as sound waves.

- **Resonating Tube:** A resonating tube is simply known as an organ pipe which when subjected to a pressurized air and produces sound of specific pitch and wavelength.

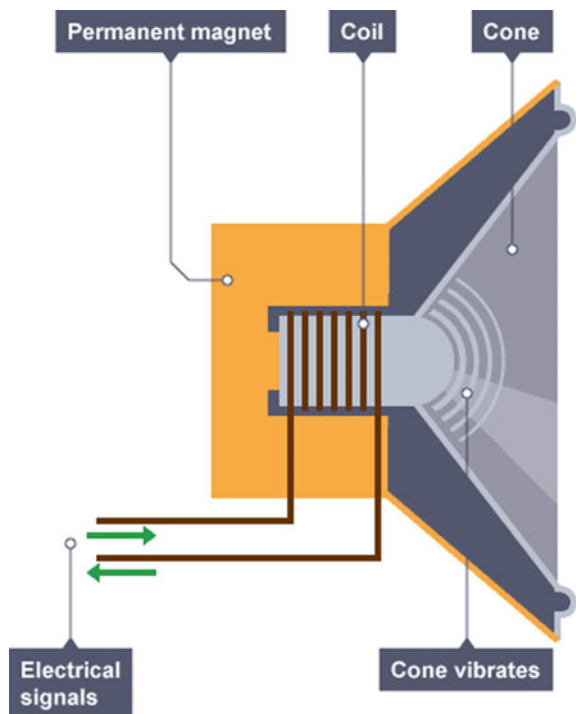


Different types of resonator can be found depending upon the wavelength induced in the tube as in half wavelength resonator, quarter wavelength resonator.

- **Heat exchangers:** Heat exchanger, it is a device that is used to heat transfer between two or more fluids. These fluids can be separated by use of the solid walls in order to prevent the mixing of those fluids. So heat exchangers can be used for both the purposes means for heating and cooling of the liquid.
- **Stack:** Stack is the main component of thermoacoustics device where the thermoacoustic phenomenon occurs. In these characteristics, stacks have a significant impact on the performance of the thermoacoustic device. The stack material should have good heat capacity but low thermal conductivity in extension, its material should not maximum the effect of viscous.
- **Temperature Sensor:** Temperature sensor is the device that can be used to record the temperature of its surrounding and converts the obtained result to monitor the temperature. LM35 temperature sensor based on Arduino display can be used to track the temperature of the desired surrounding.

The basic layout of thermoacoustic devices is represented in Fig. 2

Fig. 2 Basic layout of thermoacoustics



## 4 Reviews on Thermoacoustic Cooling

Tijani [2] discussed the fabrication and performance of the thermoacoustics. They also studied the Prandtl number using the mixture of the gases. Besides that, they have also discussed the positioning of the stack, which is one of the most important components in the fabrication of the thermoacoustics refrigerator. They have achieved the outstanding result of  $-65^{\circ}\text{C}$ .

Pedagogu [3] also discussed the fabrication of the thermoacoustics but he has also talked about the different component of thermoacoustics like speaker, heat exchanger, resonance tube, and especially about the stack. This paper has taken certain defined parameter like the tube diameter to be 5 cm, the stack diameter to be 4 cm, the stack length 8 cm, and many more. The theoretical COP was measured finally, and at  $8^{\circ}\text{C}$  COP of 7 was achieved.

Tijani et al. [4] elaborated the design of the thermoacoustics cooler using the linear theory of the thermoacoustics, thus using some of the dimensionless parameters to reduce the large number of the parameters, therefore discussing the optimization of several components of the thermoacoustics.

Kumar et al. [5] reported a bit different methodology apart from the old classical method; that is, they have incorporated the electrical control unit in their thermoacoustics cooling device. They have also managed to drop the temperature by  $5^{\circ}\text{C}$ .

Jose et al. [6] also incorporated the electrical control unit but they especially focused on the material of the stack and their performance. During the experiment, they kept the position of the stack constant. After the experiment, they found that the aluminum foil rolled with plastic fishnet gave more cooling effect than the steel scrap.

Swift [7] concluded that the refrigeration process means cooling and desired space and maintain the temperature below the ambient temperature. Acoustics is the study of sound production, transmission, and in recent era, the use of thermoacoustic in engines and pumps is fairly.

Jonathan [8] stated that thermoacoustics device utilizes initial force (simply heat generator) and the heat pump. The initial force creates work from the heat, whereas a heat pump moves the work to heat. The thermoacoustic devices involve in resonator, heat exchangers, and stack or regenerator (continuously traveling wave devices).

Symko et al. [9] defined that the longitudinal acoustic wave generated results in the compression/gas medium development/condense of gas related to the crest of sine wave and extension related to troughs of sine wave. Stack material should decrease the effects of viscous.

Pedagogu et al. [10] stated that the burning of natural gas in a thermoacoustic engine develops acoustic energy. Its energy is used in a thermoacoustic liquefy natural gas from the heat pump, on naval ships for cooling electronic equipment: In this project, a speaker generated sound waves and again a thermoacoustic pump is used to provide the cooling.

Brown et al. [11] mentioned that four out of five alternative technologies (but all thermoacoustic) use solid refrigerant that allows directly connection of heat transfer at evaporator and condenser. This effect the present temperature by about 50% is compared to vapor compression technology because refrigerant-side resistance to heat transfer is eliminated.

Babaei et al. [12] illustrated that the thermoacoustic device is simple in design and well-founded. Thermoacoustic is environmental-friendly as no unpredictable gases are to be used in the system, the compression and absorption refrigeration systems currently used in the tri-generation systems that are opposed to thermoacoustic refrigeration.

Poese et al. [13] stated that the thermoacoustic refrigerator as described meets prescribed specifications of efficiency and size. This is able to maintain ice cream at the proper serving temperature in a standard 200-L sales/storage cabinet.

Garrett et al. [14] discussed thermoacoustic heat transport and described the implementation of this new technology in an autonomous, space-qualified refrigerator. STAR is the first attempt to define the advantages of the thermoacoustic heat pump cycle for cryogenic cooler in space.

Vijayaraj et al. [15] reported that there are no moving parts in these thermoacoustic refrigeration devices. Hence, the maintenance cost is also low. It does not use any refrigerant and hence has no polluting effects. From the case study, it is observed that cooling power is dependent on working frequency, pressure, and cooling load. Thermoacoustic refrigerator can be used as a reference for design, improvement, and understanding in this refrigeration system.

Wheatley et al. [16] discussed the different topics like ‘thermoacoustic couple (TAC)’ and some of its model along with the existence of entropy flow in the TAC. They have also discussed some related mathematical relations too. Besides thermoacoustics they have also discussed heat pump engines, critical temperature gradient, and prime moving engines too.

Sarpotdar et al. [17] described a different model than any other model discussed below. They have discussed the Rijke tube thermoacoustics device, in which both the end has open and the heat source has been placed inside it. In this experiment, the source of heat used was the commercial 2.3 kg LPG cylinder with the tube, open at the both end, diameter of 2.5 inches, and 15 to 50 inches in length.

Wakeland et al. [18] also discussed a bit different model than others. They have removed the stack from the thermoacoustics and have used idealized heat exchangers. In place of the stack, they have simply left the gap in between the two heat exchangers. For particular geometry, they found that no-stack-based thermoacoustics exceed the stack-based thermoacoustics in terms of efficiency.

Hariharan et al. [19] studied the geometry of stack and the length of resonating tube which determines the performance of thermoacoustics engine. They found that increase in plate spacing and length of resonating tube leads to decrease in working frequency and increases the onset temperature difference.

Garrett et al. [20] reported about the applications of thermoacoustic engines which depend on refrigerator, which is powered by heat or electricity. However,

the heat-driven thermoacoustic cryocoolers and refrigerators are attractive for applications when there is overflowing heat at the time of present and the only two thermoacoustically driven refrigerators have been demonstrated.

Bansal et al. [21] have discussed the thermoacoustic refrigerator model and vapor compression refrigerator model. And later they have given the brief comparison between the two stating that for small heat loads of household, thermoacoustic refrigerator match well with that of vapor compression system but not for heavy loads. Therefore, they are ideal for cooling low heat loads such as electrical equipments.

## 5 Conclusion

This paper illustrates a brief review of emerging trends in the field of thermoacoustic technologies cooling and refrigeration technologies that have the capability to reduce the environmental impacts of refrigeration especially in the food industry. Thermoacoustics are the simple cooling device that operates with the application of sound. Thermoacoustic devices are very much environmental-friendly and can be used for cooling purpose without hindering the environmental factor. Quarter wavelength resonating tube can be used also instead of half wavelength resonating tube. Also, additional cooling system can be used to minimize the negative heating effect due to speaker. Selection of stack material and its placing position can also alter the performance of the model. Today, thermoacoustic refrigerator remains an eye-catching substitute toward a global agenda of a more sustainable future.

## References

1. Somasekhar T, Kishore N (2017) Thermo Acoustic Refrigeration. *IOSR J Mech Civil Eng* 5:58–63
2. Tijani MEH (2001) M. E. I.: Loudspeaker driven thermo-acoustic refrigeration. Eindhoven, Netherlands: Technische Universiteit Eindhoven
3. Pedagogu VM (2013) A novel approach to design and fabrication of thermo acoustic using high amplitude sound waves. *IOSR J Mech Civil Eng* 8(6):15–24
4. Tijani MEH, Zeegers JCH, deWaele ATAM (2002) The optimal stack spacing for thermoacoustic refrigeration. *J Acoust Soc Am* 112:128–133
5. Kumar MLSD, Kiranmayee T (2017) Design and fabrication of thermoacoustic refrigeration. *J Emerg Technol Res* 4(10):407–410
6. Jose A, Chacko F, Jose JK, Joseph J, Paliakkara K, Sreejith K (2018) Design and fabrication of thermo acoustic refrigerator. *Int Res J Eng Tech* 5 (3)
7. Swift GW (2004) What is thermoacoustics? A brief description. Condensed matter and thermal physics group. Los Alamos National Laboratory, Los Alamos, New Mexico
8. Jonathan N (2006) Thermoacoustic refrigeration. *GSET Res J*
9. Symko OG, Abdel Rahman E, Kwon YS, Emmi M, Behunin R (2004) Design and development of high frequency thermoacoustic engines for thermal management in microelectronics. *Microelectron J* 35(2):185–191
10. Pedagogu VM, Pattapu K (2013) A novel approach to design and fabrication of thermo-acoustic refrigerator using high amplitude sound waves. *IOSR J Mech Civil Eng* 8(6):15–24

11. Brown DR, Dirks JA, Fernandez N, Stout TB (2012) The prospects of alternatives to vapor compression technology for space cooling and food refrigeration applications. *Energy* 43:7–20
12. Babaei H, Siddiqui K, Chishty WA (2017) Sustainable thermoacoustic refrigeration system for gas turbine power plants. In: 17th symposium of industrial application of gas turbines (IGAT), Banff, Canada
13. Poesse ME, Smith RWM, Garrett SL, Gerwen RV, Gosselin P (2004) Thermoacoustic refrigeration for ice cream sales. In: Proceedings of the 6th IIR Gustav Lorentzen conference, The Penn State University Applied Research Laboratory
14. Garrett SL, Aeff JA, Hofler TJ (1993) Thermoacoustic Refrigerator for Space Applications. *J Thermophys Heat Transfer* 7(4):595–599
15. Vijayaraj T, Swathika M, Vinithrabanu T, Durga M (2017) Application of the thermoacoustic effect to cooling of air using acoustic waves. *Int J Adv Res Innovative Ideas Educ* 3(5):67–72
16. Wheatley J, Hofler T, Swift GW, Migliori A (1985) Understanding some simple phenomena in thermoacoustics with applications to acoustical heat engines. *Am J Phys* 53:147–162
17. Sarpotdar SM, Ananthkrishnan N, Sharma SD (2003) The Rijke Tube—A Thermo-acoustic device. *Resonance* 59–71
18. Wakeland RS, Keolian RM (2002) Influence of velocity profile nonuniformity on minor losses for flow exiting thermoacoustic heat exchangers (L). *J Acoust Soc Am* 112(4):1249–1252
19. Hariharan NM, Sivashanmugam P, Kasthuri S (2012) Influence of stack geometry and resonator length on the performance of thermo acoustic engine. *Appl Acoustics* 73(10):1052–1058
20. Garrett SL, Hofler TJ, Perkins DK (1993) Thermoacoustic refrigeration. Alternative fluorocarbons environmental acceptability study, refrigeration and air conditioning technology workshop. Breckenridge Hilton, Breckenridge, CO, 23–25 June
21. Starr R, Bansal PK, Jones RW, Mace BR (1996) The reality of a small household Thermoacoustic Refrigerator. In: International refrigeration and air conditioning conference. The University of Auckland, Auckland, New Zealand

# Experimental Investigation on Shell and Tube Exchanger for the Rate of Heat Transfer by Using Ethylene Glycol and Propylene Glycol Fluids



Prasanna Kumar Thotakura, Siva Krishna Karnati,  
Nagoju M. K. Sarath Kumar, and Radha Krishna Gopidesi

**Abstract** The present experimental work was carried out on shell and tube heat exchanger (SHTE). First phase of experiments was carried out with pure distilled water as working fluid at various flow rates of 60, 120, 180, 240 L per hour (LPH), and hot fluid was kept constant at flow rate of 250 (LPH). The heat transfers rate of SHTE is calculated. It is noted as 3576.2 W for 240 (LPH) 80 °C with, respectively. From the above experimental results observed the higher heat transfer rate at a flow rate of 240 LPH when compared with other flow rates. So, 80 °C is taken as optimal temperature and carried out the second phase experimentation with the working fluid of ethylene glycol (EG)/water and propylene glycol (PG)/water with different volume concentrations such as EG 10%, EG 20%, PG 10%, and PG 20%. We concluded that higher heat transfer rate at PG 20% 3934.2 W was higher when compared with the other fluids.

**Keywords** Shell and tube heat exchanger · Water · Ethylene glycol · Propylene glycol

## 1 Introduction

Now a days, many engineering process mostly used to the heat exchangers are multi-purposes and applications used it is essential component of process of industries. These devices are used to exchange energy in form of heat. Many engineering applications mostly used in, power generation plants, chemical process, oil refineries, etc [1–3].

The name heat exchanger is used, exactly when with at any rate two fluid streams are worked. General models are vehicle radiators, steam boilers arranged in power plants, condensers abused for the coolers. Radeep [4] nanofluids science and technology. Niwalkar et al. [5] estimation of helically coiled tube heat exchanger heat transfer enhancement utilized SiO<sub>2</sub> nanofluids experimentally. The results are

---

P. K. Thotakura · S. K. Karnati · N. M. K. Sarath Kumar · R. K. Gopidesi (✉)  
Department of Mechanical Engineering, Vignan's Lara Institute of Technology and Science,  
Vadlamudi, Guntur, India

© The Author(s), under exclusive license to Springer Nature Singapore Pte Ltd. 2022  
G. S. V. L. Narasimham et al. (eds.), *Innovations in Mechanical Engineering*,  
Lecture Notes in Mechanical Engineering,  
[https://doi.org/10.1007/978-981-16-7282-8\\_31](https://doi.org/10.1007/978-981-16-7282-8_31)

429

showed improve the overall heat transfer coefficient adding to particle concentration ratio.

Alasadi et al. [6] investigated heat exchanger using  $\text{Al}_2\text{O}_3$  nanofluid at different concentrations higher heat transfer rate 2% concentration, and Nusslet number is higher than the base fluid. The Nanoparticles were added to the distilled water to improve thermal conductivity and viscosity at the particle volume concentration.

Duangthongsuk et al. [7] enhancement of counter flow heat exchanger pressure drop and heat transfer and pressure drop of  $\text{TiO}_2$  nanofluid. The results are  $\text{TiO}_2$  nanofluid. The heat transfer coefficient is higher than that of base fluid. Whenever increasing the mass flow rate, it increasing the Reynolds number and also improve the convective heat transfer coefficient of the heat exchanger. Farajollahi et al. [8] shell and tube heat exchanger nanofluids comparison of the heat transfer behavior of two nanofluids  $\gamma\text{-Al}_2\text{O}_3/\text{water}$  and  $\text{TiO}_2/\text{water}$ . Experimentally, results are the nanofluid higher volume concentration to the both nanofluids  $\gamma\text{-Al}_2\text{O}_3$  is better heat transfer rate than the  $\text{TiO}_2$ . In base fluids improve the heat transfer performance whenever addition of nanoparticles are used large heat transfer coefficient compared to the primary fluid.

Mohammed et al. [9] using a nanofluids in rectangular micro-channels heat sink from that increase the pressure drop whenever increase the Reynolds number. Compared with pure water, nanofluid little amount of improvements the pressure drop.

Rao et al. [10] forced convective heat transfer coefficient by using the  $\text{Al}_2\text{O}_3$  of a nanofluid. Nanofluid increases the volume concentrations as well as improves the density and thermal conductivity. An  $\text{Al}_2\text{O}_3/\text{water}$  nanofluid at 2.5% improved heat transfer rate.

Mellal [11] evaluation of shell and tube heat exchanger arrangement and orientation of baffles in this study changing baffle spacing.

The highest heat transfer coefficient is obtained  $180^\circ$ , its' creates fluid flow direction zigzag mode in short by pass. This is an advantage to improve turbulence of fluid particles.

Kushwaha et al. [12] the performance analysis of the shell and tube heat exchangers with various design aspects in this paper was demonstrated. Its value is maximum for triangular pattern and minimum for square pattern tube. Maximum heat transfer efficiency for the square tube pattern the overall heat transfer coefficient higher for rotated square pattern design in all the three different hot fluid inlet temperature.

Ameur [13] heat exchangers in thermal fields inclination of baffle findings of this baffle negative orientation placed improvement of rate of heat transfer. In front of baffle creates more vortex yields this impact to the fluids creating the more turbulent kinetic energy. Bichkar et al. [14] study the baffle impact various types of the results are by using the different type of baffles. Helical baffles are decrease the pressure drops as well as the less pumping power dead zones are eliminated compared to other types of baffles. Helical baffle is working as the higher mass flow rate over other two baffles.

El-Saida et al. [15] a comparative experimental investigation of new segmental baffles configurations they found that the hybrid segmental baffle (HSB) configuration enhances overall heat transfer coefficient, effectiveness, respectively, compared with other types of baffles. Enhancement of CSSB and HSB is the heat exchanger 185%–248%, 134%–149%, and 148.9%–189%, respectively.

Saidura et al. [16] a review on applications and challenges of nanofluids observed heat exchanging devices are more compact and energy efficient by using the nanofluids.

Nanofluids are mainly based on the temperature and thermal conductivity of materials to be used low concentration volume. Still many researchers can't be finding the exact mechanism of the heat transfer for the nanofluids.

Serrano et al. [17] nanotechnology for sustainable energy. All things are taken into consideration, the energy transformation has several constrains, due to significant expense of fabricating cost versus effectiveness and the suggestions on the climate (natural life cost, unsafe squanders, cooling water, and so on) makes these cycles unsatisfactory. Nanotechnology offers, unexpectedly, devices to grow new enterprises dependent on save and cost-productive economies, consequently truly adding to a feasible monetary development.

Srinivasan et al. [18] compact heat exchanger using ZnO and TiO<sub>2</sub> nanofluids in ethylene glycol/water are heat transfer coefficient increases while increase the Nusslet number may be caused by the increase in thermal conductivity. ZnO and TiO<sub>2</sub> nanoparticles dispersed in 70:30 (W:EG) with 0.6 vol.% concentration of ZnO and 0.8 vol.% concentration of TiO<sub>2</sub> give maximum increase in the Nusslet number.

Patil et al. [19] thermal design and optimization of heat exchanger the guidelines for TEMA type selection gives the better options to choose the TEMA configuration required in petrochemical application. It is observed that on varying baffle cut from 15 to 45, 25% baffle cut gives the maximum heat transfer coefficient, better main cross-flow stream fractions, and effective utilization of allowable pressure drop.

Deshpande et al. [20] examination of shell and tube heat exchanger with baffle having along to axis and similar to axis cuts and orientation. In this paper observed that the critical drop in the Reynolds number relating to vertical stream which thus directly affects to the heat transfer coefficient is discovered to be lower than that for flat stream.

Razzaq et al. [21] heat transfer analysis of propylene glycol and water mixture-based TiO<sub>2</sub> nanofluids using maximum enhancement of the heat transfer rate of TiO<sub>2</sub>/PGW nanofluid was 44.39% compared to the base fluid added particle concentration 0.3%. Flow rate 12 L/min of nanofluid at the same flow rate maximum enhancement of the overall heat transfer coefficient was 48.13% when nanoparticle volume concentration and nanofluid flow rate were 0.3%, respectively.

Pawar et al. [22] different types of baffles investigated on shell and tube heat exchanger. We observed the results are overall heat transfer coefficient is FB-STHX higher than SG-STHX at same operating conditions. Helical baffles are manufacturing difficult to the flower baffles are easily fabricated.



Crook et al. [23] Heat transfer performance of PG/EG coolant solutions. The results are observed the maintain the cooling concentration at 50:50 PG:W and EG:W raising the concentration reduces the heat transfer performance of the system.

Gollin and Bjork et al. [24] comparative performance of EG:W and PG:W coolants in automobile radiators. The recent trend as follows as propylene glycol base coolants are accurate thermal performance of automobile radiators.

Sohel Mushred et al. [25] heat transfer characteristics of ethylene glycol-based nanofluids some of the researchers are find to improve the thermal conductivity of the fluids; in this paper, different types of nanofluid suspend are the EG solution slightly improves the thermal performed compared to the base fluid.

It was identified from the literature that ethylene glycol is a viable heat transfer fluid because of its thermal characteristics, but it was noticed that only limited studies were performed with ethylene glycol as a base fluid.

## 2 Experimental Details

The test section is based on the fluid flow rates are varies with the help of the rotameter constrained primary stream line flowing to cold fluid; second one is flowing to the hot fluid. Four thermocouples are arranged the heat exchanger inlet and outlets of fluid flowing conditions.

Two of the thermocouples, 1 and 2, measure the hot fluid temperatures, other two thermocouples, 3 and 4, cold fluid temperatures.

The hot water flow rate and hot fluid inlet temperature is kept constant. The cold water flow rate was controlled by using the control valve of rotameter. It was located at the bottom of the supply tube. Stream rate between cold water like this 60–240 LPH the hot water inner tube temperature 60–80 °C. The experimental setup was shown in Fig. 1.

**Fig. 1** Experimentation setup



The experimental investigation was carried out in two phases. In the first phase, run the experiment at various flow rates with water as working fluid and calculated the performance characteristics and found the optimal flow rate.

The optimal flow rate is noted as 240 LPH and carried out the second phase of investigation at flow rate varying the fluid by mixing of water of ethylene glycol the mixing ratio in between 10% and 20%. From the obtained result, found the better results for 20%. The same procedure applied for propylene glycol compare to the enhancement of heat transfer coefficient and identified.

The results are observed that the enhancement of heat exchanger 240 (LPH) and 80 °C temperature is best performance. Choose better performance mixed together water to binary fluids. Water and ethylene glycol and water and propylene glycol are by mixing ratio is 10%, and 20%. Both results are compared which one gives better improvements in heat exchanger.

### 3 Methodology

From the results, the following conditions are calculated.

It can be expressed as heat transfer rate of the system

$$Q = \frac{Q_h + Q_c}{2}$$

$Q_h$  is heat loss by the hot water;  $Q_c$  is heat gained by the cold water.

Overall heat transfer coefficient of heat exchanger can be expressed as

$$U = \frac{Q}{A_0 \Delta T_m}$$

where  $A_0$  is heat transfer area in  $m^2$ ,  $\Delta T_m$  logarithmic temperature difference (LMTD).  $Q$  as average heat transfer rate of the system.

$$\Delta T_m = \frac{(\Delta T1 - \Delta T2)}{\ln\left(\frac{\Delta T1}{\Delta T2}\right)}$$

$$\Delta T1 = Th1, in - Tc3, in$$

$$\Delta T2 = Th2, out - Tc4, out$$

Here, Th1 is inlet temp tube side; Th2 is outlet temp tube side, Tc3, Tc4 shell side fluid inlet and outlet temp.

These standard equations are using identified by the Reynolds and Prandtl numbers  $Re = \rho UD/\mu$  where  $\rho$  is density of fluid,  $kg/m^3$ .  $\mu$  is viscosity  $N.S/m^2$ .  $D$  is diameter of the pipe (mm).  $U$  is velocity  $m^2/s$ .

Dittus-Boelter equation is using the turbulent flow for the fluids in this equation identified by Nusselt number is related to the Reynolds (Re) and Prandtl (Pr) numbers by the  $Nu = 0.023 * (Re)^{0.8} * (Pr)^{0.4}$

## 4 Results and Discussion

The experimental investigation was carried out on shell and tube heat exchanger with water as base fluid at various temperatures of 60°, 70°, and 80 °C at various flow rates of 60, 120, 180, 240 LPH. From the obtained results observed the optimum temperature as 80 °C with 240 LPH.

In the second phase, the experiments were conducted with propylene glycol and ethylene glycol solutions at constant temperature of 80 °C with flow rate as 240 LPH. In this, present section deliberates performance characteristics of overall heat transfer coefficient, Reynolds number, Nusslet number, and heat transfer rate.

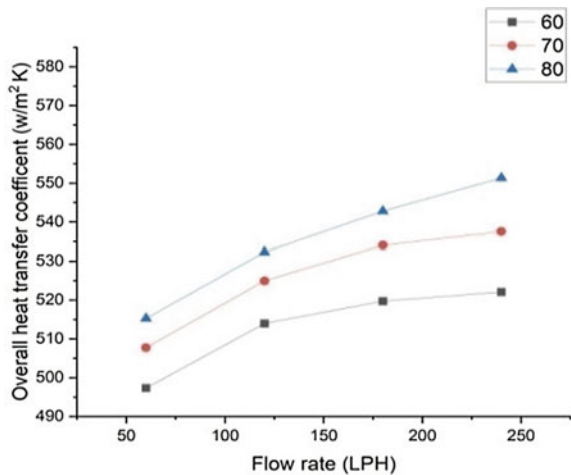
These results are justified by niwalkar.

### 4.1 Overall Heat Transfer Coefficient

See Fig. 2.

We improve the fluid flow rate as well as enhancement to overall heat transfer the fluid flow rate at various conditions. The maximum overall heat transfer coefficient 576.35 W/m<sup>2</sup> K at 80 °C temperature compared to the 60°C using the water.

**Fig. 2** Overall heat transfer coefficient with flow rate



**Fig. 3** Flow rate with overall heat transfer coefficient

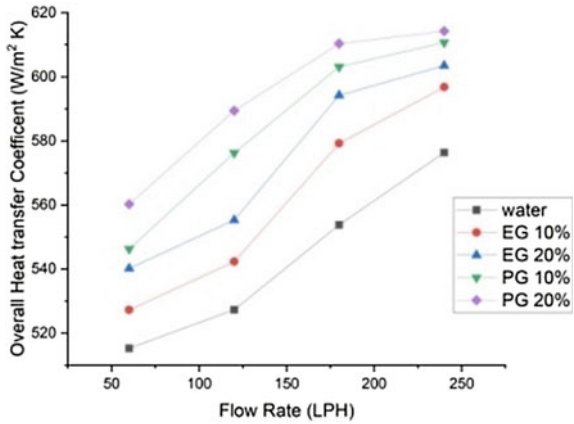
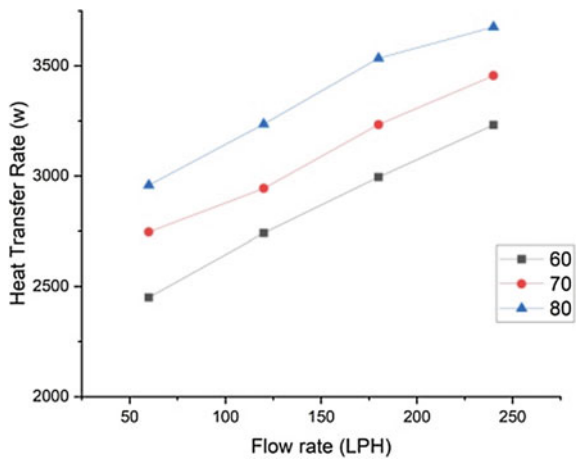


Figure 3 represents the heat transfer coefficient. It appears that there is the same time improves heat transfer coefficient whenever adding to particle volume concentration. Whenever the fluid flow rates are increase, the water boundary layers are moderate to the laminar to turbulent flow creates the increasing heat transfer coefficient. The higher overall heat transfer coefficient 614.3 W/m<sup>2</sup>K was observed PG: W 20%.

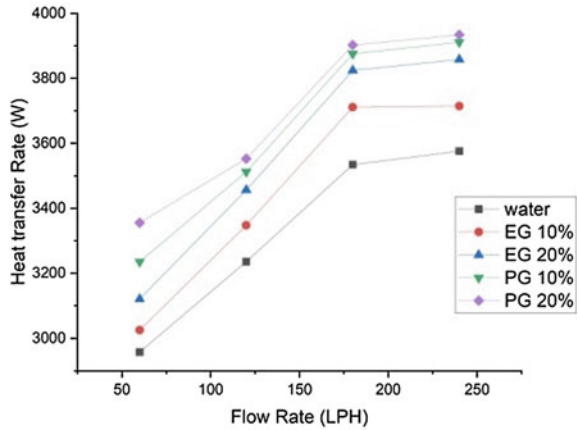
### 4.2 Heat Transfer Rate

Figure 4 represents the heat transfer rate; it appears that there is the same behavior with the different mass flow rates with variation of heat transfer rate. Heat transfer

**Fig. 4** Flow rate versus heat transfer rate



**Fig. 5** Heat transfer rate with different fluids



rate increases with an increase inlet temperature of the fluid. The heat transfer rate was observed from water 3576.2 W.

Experiment results are finding the base fluid by mixing water particular compositions EG and PG 10–20%. Figure 5 heat transfer tare versus for flow rates, respectively. We observed from the result dissolving the solution with the water at different proportions of the EG and PG increases heat transfer rate compared to the base fluid. Higher heat transfer rate PG: W 3934.2 W at composition of 20% PG has specific heat, and thermal conductivity is slightly high heat transfer performance improving by varying the input temperatures binary fluids [26]. In this, results are observed that the inlet temperature 80 °C better results are finding.

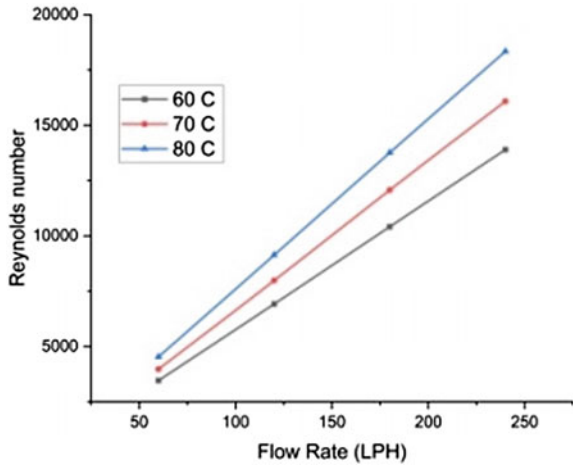
### 4.3 Effect on Flow Rate

See Fig. 6.

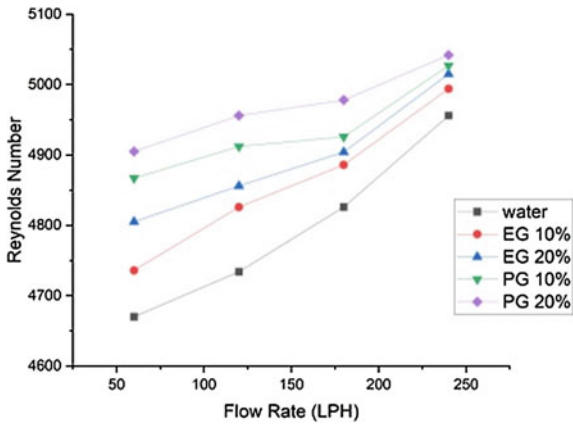
Represents the Reynolds number versus for mass flow rates, respectively. Fluid flow rate increases which improve the Reynolds number. The fluid density depends on the mass flow rate. The Reynolds number with water 4820 to 4950.

Mass flow rates are varied with the binary fluid the heat transfer improving affect of the fluid contains. When ever increasing the flow rate, it also increasing the heat transfers [27]. From Fig. 7, it is observed that laminar flow is low while compared to turbulent flow. Whenever adding to the particles increase as the thermal conductivity, viscosity of brine fluid. Highest the Reynolds number as well as increase the Nusslet number whenever improve the heat transfer coefficient. Reynolds number is 5015–5042, respectively.

**Fig. 6** Variation of RE with flow rate



**Fig. 7** Variation of Reynolds number with flow rate

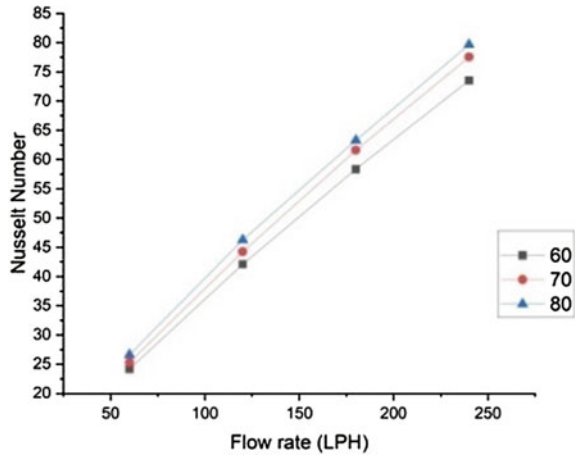


### 4.4 Effect on Nusslet Number

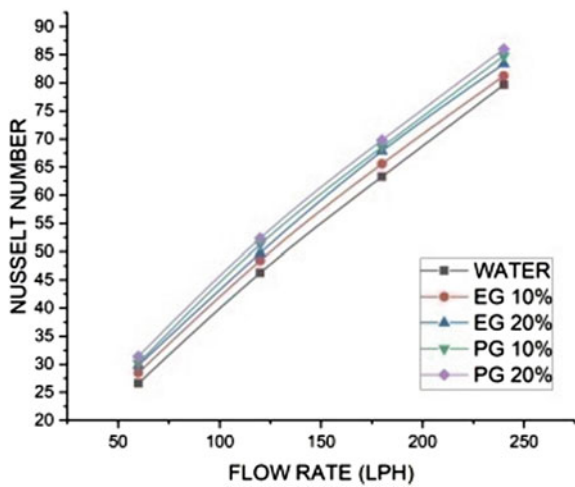
Figure 8 represents the Nusslet number versus for mass flow rates, respectively. Nusslet number characteristics with respect to the fluid flow rate and Reynolds number. Nusslet number increases by increasing the Reynolds number. The both conditions are improved increase the thermal performance of heat exchanger (Fig. 9).

Heat transfer coefficient estimated base fluid mixing with the different composition to the water adding to the binary fluids was EG 10–20%. And PG 10–20% above figure shows the Nusslet number was identified as PG 20% higher than that of EG 20%. By increasing the volume concentration of binary fluids shown the increase in Nusselt number for both the fluids. The specific heat capacity and viscosity are higher PG/base fluid combination Reynolds number and Nusslet number is higher than that of the EG/water combination.

**Fig. 8** Variation of NU with flow rate



**Fig. 9** Variation of Nusslet number with Flow rate



### 5 Conclusion

In the present study ethylene glycol, propylene glycol, these fluids are mixed with base fluid at different composition used. From this study, the following conclusions were made. Experiments indicate overall heat transfer coefficient, and rate of heat transfer Reynolds number and Nusslet number increase the binary fluids. Experimental results showed that the maximum heat transfer rate is water/PG 20% compared to the water/EG20% and base fluid.

The results showed that the heat transfer performance of binary fluids was better than that of base fluid.

- The maximum value of the heat transfer coefficient of EG/W20% is  $603.5 \text{ W/m}^2\text{k}$  at PG/W 20% minimum value  $614.3 \text{ W/m}^2\text{k}$ .
- Whenever increase the Reynolds number and also enhancement the Nusslet number.
- The experimental results are binary fluids are using to the improvising heat transfer rate as compared with water. Heat transfer rate is 3934.2 W PG/W increase up to 2–5% than EG/W.
- In conclusion, PG/W20% is give maximum heat transfer rate and Reynolds number and Nusslet number also compared with other fluids.

## References

1. Gopidesi RK, Premkartikkumar SR (2019) Evaluating the characteristics of a diesel engine fuelled with water in diesel emulsion and hythane gas in a dual-fuel mode. *Int J Ambient Energy* 1–5. <https://doi.org/10.1080/01430750.2019.1670258>
2. Gopidesi RK, Premkartikkumar SR (2021) Abating environmental pollutants of a diesel engine by using emulsified fuel. *Int J Ambient Energy* 42(15):1708–1711. <https://doi.org/10.1080/01430750.2019.1614983>
3. Gopidesi RK, Premkartikkumar SR (2019) Performance, emission and combustion analysis of diesel engine fuelled with emulsified biodiesel. *Prog Ind Ecol* 13(3):292–301
4. Pradeep T, Stephen U, Choi S, Das SK Nano fluids science and technology. John Wiley & Sons, Inc., Publications
5. Niwalkar AF, Kshirsagar JM, Kulkarni K (2019) Heat transfer enhancement of a shell and helically coiled tube heat exchanger using  $\text{SiO}_2/\text{water}$  nano fluids. *Mater Today Proc* 947–962
6. Albadr J, Tayal S, Alasad M (2013) Heat transfer through heat exchanger using  $\text{Al}_2\text{O}_3$  Nano fluid at different concentrations. *Case Stud* 1:38–44
7. Duangthongsuk W, Wongwises S (2009) Heat transfer enhancement and pressure drop characteristics of  $\text{TiO}_2$ –water nano fluid in a double-tube counter flow heat exchanger. *Int J Heat Mass Trans* 52:2059–2067
8. Farajollahi B, Etemad SG, Hojjat M (2010) Heat transfer of nanofluids in a shell and tube heat exchanger. *Int J Heat Mass Transf* 53:12–17
9. Mohammed HA, Gunasegaram P, Shuaib NH (2010) Heat transfer in rectangular micro channels heat sink using nano fluid. *Int Commun Heat Mass Transf* 37:1496–1503
10. Rao MSE, Sreeramulub D, Raoc CJ, Ramanad MV (2017) Experimental investigation on forced convective heat transfer coefficient of a nano fluid. *Mater Today Proc* 4:8717–8723
11. Mellal M, Benzeguir R, Sahel D, Ameer H (2017) Hydro-thermal shell-side performance evaluation of a shell and tube heat exchanger under different baffle arrangement and orientation. *Int J Therm Sci* 121:138–149
12. Kushwaha NK, Kureel V (2018) Performance analysis of the shell-and-tube heat exchangers with various design aspects. *IJIRT* 5:2349–6002
13. Ameer H (2019) Effect of the baffle inclination on the flow and Thermal Fields in channel heat exchangers. *Results Eng* 3:100021
14. Bichkar P, Dandgaval O, Dalvi P, Godase R, Dey T (2018) Study of shell and tube heat exchanger with the effect of types of baffles. *Procedia Manuf* 20:195–200
15. El-Saida EMS, Abou Al-Soodb MM Shell and tube heat exchanger with new segmental baffles configurations: A comparative experimental investigation. *Appl Therm Eng* 150:803–810
16. Saidura R, Leongb KY, Mohammadc HA (2011) A review on applications and challenges of nano fluids. *Renew Sustain Energy Rev* 15:1646–1668



17. Serrano E, Rus G, Garcia-Martinez J (2009) Nanotechnology for sustainable energy. *Renew Sustain Energy Rev* 13:2373–2384
18. Srinivasan PM, Baskar R (2018) Heat transfer studies in compact heat exchanger using ZnO and TiO<sub>2</sub> nanofluids in ethylene glycol/water. *Chem Ind Chem Eng* 4:309–318
19. Patil S, Gulhane NP (2015) shell and tube heat exchanger design and selection based on TEMA type. *JMSME* 2:18–22
20. Deshpande SS, Hinge SA (2014) Study of shell and tube heat exchanger with design and performances of a single segmental baffle having perpendicular & parallel-cut orientation. *IJERT* 3
21. Das UD, Razzaq MEA, Sajib MK, Ahamed JU (2019) Heat transfer analysis of propylene glycol and water mixture based TiO<sub>2</sub> nanofluids. In: *International conference on mechanical engineering and renewable energy (ICMERE)*, pp 11–13
22. Pawar PJ, Yadav RJ (2016) Different types of baffles are used in shell-and-tube heat exchanger by experimentally. *IJCET*
23. Joseph J, Crook RF Heat transfer performance of PG:W Versus EG:W coolant solutions in laboratory testing. SP-1456
24. Gollin M, Bjork D Comparative performance of EG:W nad PG:W coolants in automobile radiators. SP-1175
25. Soheli Mushred SM, de Neto Castro CA (2016) Heat transfer characteristics of EG based Nano Fluids. *Appl Energy*
26. Gopidesi RK, Sankar GR, Pavan Kumar AD, Kumar AS, Srimal B (2019) Evaluating the performance and emission characteristics of ci engine with waste plastic oil. *Int J Mech Prod Eng Res Develop* 9(3):1015–1020
27. Gopidesi RK et al (2017) Development of polymer of matrix composites reinforcing with Al CuMg. *Int J Mech Eng Technol* 8(6):190–199

# Solid Waste Biofuel: An Overview



N. Srujana , G. Bhanodaya Reddy , and Pinisetty Sai Sampath Aditya 

**Abstract** Gradually mounting pollution and temperature levels that are associated with the widespread dependency on fossil fuels are of major concern. This can be avoided by increasing the renewable and bio-energy usage. Waste that is generated from different industrial sectors especially solid waste has the potential to compete in energy industry. This paper focuses on the available technologies for processing of solid waste into biofuels and utilisation of these in internal combustion engines. The processing techniques, nature of fuel, emission and efficiency characteristics are presented in this paper.

**Keywords** Solid waste · Biofuel production · Emissions · Brake thermal efficiency · Break-specific fuel consumption

## 1 Introduction

One of the most important reformation needed in current generation is the policies of climate change. Fossil fuel contributes to at least 75% of global energy needs currently. There are various potentially unwanted chemical compounds emitted from automobiles which are even after being treated with catalytic converters are still hazardous. Even depletion of resources like fossil fuels can show significant negative effects on future generations.

There are various alternate energy options available like the wind, hydro and solar energies but these cannot be made substantially available due to geographical limitations. Bio-energy derived from solid waste is promising as many of them readily produce liquid state fuels unlike renewable sources. These fuels are categorised into various generations that are first-, second- and third-generation fuels along with the

---

N. Srujana · G. Bhanodaya Reddy  
Department of Mechanical Engineering, College of Engineering, Sri Venkateswara University,  
Tirupati, India

P. Sai Sampath Aditya (✉)  
Department of Mechanical Engineering, Vemana Institute of Technology, Bangalore, India

types of raw materials such as agricultural wastes, domestic and urban wastes. This work summarises the recent efforts in producing energy from various wastes through novel and known technologies. This paper reviews the most recent work conducted on methods used for extraction, waste type and its performance analysis in internal combustion engines. Therefore, this manuscript is tailored to fit all the peer-reviewed work in the field of biofuel generation from solid waste.

## 2 Solid Waste

By-products that are in solid state which cannot be reused or recycled are considered to be solid wastes. Agricultural and municipal wastes contribute to most of the solid waste that can be used for biofuel generation. Carbon waste from industries also contributes to the solid waste but in smaller quantities. These wastes are discussed briefly in the following sections.

### 2.1 *Agricultural Waste*

Lignocellulosic fuels are derived from agricultural waste which is abundantly available in many nations across the globe. Fourteen percent of the global energy needs are met by lignocellulosic-based fuels, and if this lignocellulosic fuel usage is not regulated, then the demand for fuel cannot be satisfied by agricultural waste.

Biofuel production techniques from agro-waste need pre-treatment of lignocellulosic mass by physical methods such as mechanical reduction in size, pyrolysis and then followed by physiochemical treatment methods of steam explosion, liquid hot water method and ammonia fibre explosion. These methods require far lesser technological and investment needs but are far away from current biofuel exploration techniques. As a result, lignocellulosic base promises to be a better approach for future energy needs [1].

Transesterification of lipids from biological products such as food waste while the catalyst was lipase and methanol as base Karmee et al. 2015 produced 100% yield of biodiesel. They also found that changing the lipid-to-ethanol ratio from 1:3 to 1:10 significantly changed the yield. Reusability of lipase of needed as the reaction time is low as well as the prices of lipase has substantial impacts on the economic system. This would be damaging if much more efficient production techniques are met [2].

Apart from the conventional approaches such as the production and utilisation of bio-energy from biomass-related sectors, the land-intensive energy approach can be considered as one of the feasible ways to deal with non-heavy-duty transportation category and storage of harvested energy. Walter Reid et al. highlighted this kind of approach which is limited by the amount of land that is available. This is not only difficult to achieve but also it is more of a temporary solution for half a decade But, by taking into account the substantial carbon emissions, the policymakers restrict this

approach to the local energy needs rather than considering global parameters which are quite difficult to manage. As a result, any concept of bio-energy alternatives should be able to significantly reduce the carbon emission impact on the environment with less investment on production scales [3].

Wai-Hong Leong et al. found that using oleaginous micro-organisms will help in the generation of high amount of biomass by yielding high lipid quantities. Even though most algae do better in cultivating the micro-organisms, when they are cultivated using the mixotrophic methodology it produces better yield quantities compared to the autotrophic and heterotrophic methods. Modification of nutrients by manipulating the carbon-to-nitrogen ratio also helped increasing the yield of biomass and composition of oleaginous micro-organisms [4].

Most of the bio-energy-related fuels come from these vital sources such as agricultural crops, industrial biowastes, energy crops, forest residues and animal manure. Many model assumptions were made which helped us to see the possible biofuel transformation. The land availability and biomass energy production are predicted to be 18,833 and 24,901 Peta Joules in two decades after 2030 [5].

Most of the renewable energy sources in Turkey are derived from the fuelwood and animal waste biomass which are mostly used for domestic energy needs. Munzir Ozturk et al. have highlighted that the production of 1.5 million tonnes of biodiesel, 4 billion tonnes of biogas that is produced per year. The authors had shown that much more can be achieved with other waste resource but there needs to be proper policy which can alter the numbers in production [6].

Second-generation biofuels will have positive effects compared to first-generation fuels as the first generation would require 85% of harvest around the globe to serve as the need for replacing fossil fuels. The cellulose biomass which is second generation is naturally available and consists of more than 60% of terrestrial biomass [7].

Second-generation biofuels that are derived from lignocellulosic waste that is derived from agricultural base prove to be one of the best possible alternative to petroleum-based fuels. The metabolic engineering, production of enzymes, pre-treatment and yeast development from the waste will show potential that is available in biofuels [8].

Lack of porous nature in synthetic mixture for biofuel production did not facilitate the volatile release of cellulose for the chemical reaction unlike the lignocellulosic biomass which hindered the pyrolysis distribution in mixture. This behaviour led to the production of unwanted gas and char by repolymerisation at temperature between 350 and 400 °C [9].

## ***2.2 Municipal Waste***

Production of an alternative fuel source from biodiesel is possible through utilising solid waste collected by municipal department, and this has major benefits from manufactures of paper production waste particularly from major cities across the globe [10].

Most of the current biodiesel approaches include the usage of second-generation methods which are actually a by-product of first-generation usage like vegetable oils which are extracted from the plants and the used for cooking. Waste biomass to cellulose ethanol efficiencies was calculated where the lowest to the scale of ligno-cellulosic MSW to ethanol. The total production accounted for 92% of mainly paper-based waste. The global production of 83 billion litres of cardboard and papers waste is accounted for ethanol production, with increase in ethanol-based technology the ability for the biodiesel production will be increased when compared with vegetable oil and agro-based waste recovery techniques.

Allen Zihao S H I et al. concluded that it is possible to replace about 5.36% of the gasoline consumption worldwide with the available of up to 82.9 billion litres of ethanol derived from waste-paper products. This would not only reduce the consumption of petroleum products but as well as greenhouse emissions around 29% worldwide. The technology available to convert the paper-waste products into usable fuel needs to take new approaches, thus increasing the conversion efficiencies and making the cellulose-based products a better possible alternative for future in place of fossil fuels [11].

Anaerobic digestion of floral waste is hugely limited by the literature on biogas production. Higher quantities of biogas production are achieved by implementing new techniques like alkaline pre-treatment, solar heating and co-digestion with food. An output increment of 106% was observed along with a savings of 96% over chemical treatment methods [12].

By employing the dark fermentation and anaerobic technologies, food waste can be used for generation of much more biogas than other approaches. This will not only reduce the waste disposal issues but also will reduce the greenhouse gases (GHG) emissions with immediate effect. Biorefineries need to be developed with some new technologies [13].

Smart food waste recycle bin can be an effective method to deal with surplus food waste which is being generated. This method also helps in dealing with moisture content and lower heating value (LHV) of the waste. The food waste can be converted into an energy source using wooden biochips which contain naturally occurring fermentation micro-organisms using smart food waste recycling system (S-FRB) [14].

Lipids are extracted by using Soxhlet extraction method from micro-cystis bloom samples collected from Biesa Lake, Sri Lanka. The properties of lipids are similar to grade 02 auto-diesel at 15 °C with respect to ASTM standard [15].

### ***2.3 Algae and Micro-organisms Use***

Algae can be used as a biofuel as it possesses a property of storing biogas, which can be extracted through various temperature facilities that help algae to survive. But the process of extraction clearly shows that it is economically and ecologically difficult

to deal with. Much more research is needed to understand the effect because this concept lacks literature [16].

Bio-hydrogen generation is a new and actively prototyped method along with carbon-based biofuels. Kuan-Yeowshowa et al. conducted experiments by performing photosynthesis on the algae. They found that smaller chlorophyll antenna shape can provide high intensity of light which resulted in threefold hydrogen production improvement [17].

Aerobic process is where the solar energy and the interaction of photosynthesis organisms generate biogas upon some exposure time. This can be used for various purposes that need the availability of conventional fuels. Micro-algae have better yield percentage than the terrestrial plants. The aerobic process is hindered by the biomass composition, digestion and the methods of pre-treatment. The production efficiency increased when biohydrogen and biogas process were coupled together [18].

Pre-treatment of microalgae by ohmic heating process helped in lipid secretion from the cells. The extraction fluid is suspended on water which then resulted in the separation of various unwanted chemicals. Taguchi method was used for modification which increased the biomass yield. Transesterification at 40 °C for 24 h increased the transesterification by two times with an incubation time of 120 s [19].

## ***2.4 Current Technological Trends***

Along with the production of biofuel-related energies, process followed to extract the biofuel from solid waste is also an important factor. The biochemical strategies employed are much more effective than the thermochemical strategies. Thermal processes use heat as the primary reaction mechanism which is not sensitive to biomass-related waste generation. Processing of biomass material to extract energy requires much more study on the material handling, conversion efficiencies, transportation and not but not the least economics of production [20].

The work conducted by Pursiheimo et al. shows that the drastic usage of biomass for fuel generation by 2050 is needed. This can be achieved by making the industries run primarily on bioenergy. Global coverage of solar energy is primarily up to 39–44% and the rest is in electric generation sectors. This will help in the generation of synthetic fuels through usage of photovoltaic technology which can be used for the industries and the transportation sectors. They found that such a transition rather than the usage of biofuels for transportation purposes directly will reduce carbon emissions by 90% by the year 2050 [21].

Mustafa reviewed that biomass is a fuel source which can produce all three types of fuel energy matter by various thermochemical processes. Biodiesel and charcoal that were produced were analysed for their performance characteristics. This proved that there is still more room for the development of the machinery to consume less energy and at the same time be economical [22].

Many materials are serving in the energy storage applications like porous carbon, graphene, carbon nanotubes, etc., but there is a scope for the development of biomass-derived materials. Lili Jiang et al. observed that even the biomass materials contain the microstructures similar to the above-mentioned materials like oculus dexter (OD) spherical, 1D fibrous structure. These materials also exhibit porous nature that can work as supercapacitors [23].

The substitute material that is obtained from the conversion of activated carbon- and carbon-based materials is biochar. If this material is treated thermochemically and hydro-thermally, then it has the potential to be used as catalyst in pyrolysis which can be used to remove the pollutants and heavy metals. Then it can be used as an energy storage material for electric transportation issues [24].

Algae use in biofuel generation is a very effective substitute compared to other methods due to their evolving nature with respect to the atmosphere around them. However, it is still difficult to produce the amount of fuel needed for global use and the pricing of the methods and fuels need to be improved for a better reach [25].

Swati et al. showed that mild reaction conditions and optimum molar ratio of alcohol are required for economical production of biodiesel. Nano-porous material is effective in this process as it increases the feedstock reaction area of the catalyst for absorbing the oil and methanol. Solid-based catalysts possess a challenge in reusing them for the following process but the carbon-based nanoporous material mitigated that [26].

Ralph et al. compared the GHG emission characteristics of first and second stage biofuels where they found that second stage has very less emissions than first stage fuels. Moreover, the second stage fuels are more sustainable as they have the better land-use opportunities and these produce much more liquid-based fuels readily than the first stage fuels [27].

Municipal Solid Waste (MSW) wastes were subject to pyrolysis gasification at temperature between 700 and 900 °C, the increase in yield and the LCV gas of synthesis gas was observed whenever the reaction temperatures were increased. The quality of the gas improved after optimum amounts of water vapour was introduced into the system which resulted in tar cracking [28].

The process of producing second-generation fuel using lignocellulosic biomass is a short-term solution. More research needs to be carried in optimising the pace of pyrolysis and sync gas gasification. Hydrogen generation process and bio-oil generation can be clubbed to increase the quality of oil produced [29].

According to Zabed et al., the lignocellulosic base (LCB) has greater potential for ethanol production as they consist of third category waste and cannot be recycled further. The availability along with low pricing of LCB makes it favourable to deal with them. The fermentation and sugars such as pentose and hexose have major knowledge gap technically. But without the help of micro-organisms and carrying the process synthetically is a challenge [30].

### 3 Vegetable Oils

#### 3.1 Seed Oil Extraction Technique

The techniques available in the world oil extraction are compared with each other. Out of the four available options that are chemical, distillation through steam, mechanical and supercritical extraction, mechanical extraction process is found to be the most pocket-friendly to the operator, since it ensures high quality of the oil delivered for the mechanical screw-based fits. However, when compared to the method of solvent extraction, some disadvantages are associated like the higher residual oil quantity from the cake and others [31].

Cottonseed oil provides an opportunity to explore the alternative fuel segment. Purification of the oil with activated charcoal followed by transesterification proved to be beneficial. The purification and analysis methods include purification of the crude cottonseed oil, determination of free fatty acids concentration, molecular weight through gas chromatography, biodiesel synthesis of transesterification determines the biodiesel yield. The purification revealed that the charcoal removes the unnecessary plant-related pigments and the coloured bodies absorption is proportional to temperature increase and mass of absorbents. Intensity of free fatty acids present in the oil depends on the concentration of charcoal and charcoal exposed time. The hot neutralisation technique proved beneficial as the oil colour and quality with respect to the ASTM standards were respectful compared to cold neutralisation technique. The energy evaluation test showed that the oil contains 38 MJ/kg of energy which is closer to 42 MJ/kg when compared to gasoline [32].

#### 3.2 Vegetable Waste

Hoffmann et al. conducted a compatibility test for various oils that emerged from both vegetables and solid wastes. The deterioration rate of oil was measured. These oils were found to be holding well under 300 °C but after which the chemical transformation occurs with the ageing of oil. This proved a bit unstable for internal combustion engine operations [33].

Bio-ethanol has been a viable alternate as a transportation fuel. The presence of starch is vital for the fermentation stage. Kumar et al. considered this product of kitchen waste that can be renewed by exposing the potato peel waste to microwave radiations. With an exposure time of 15 min, they were able to extract 60 wt. % of glucose-based material [34].

Methods involved in the conversion of raw and untreated disposal into ethanol for energy conversion were studied by Dhiman et al. using the anaerobic bacteria called thermophilic. They concluded that around 94% of carbon recovery was achieved particularly when the bacteria were grown at 65 °C. These results proved that commercial production of ethanol can be supported by this method [35].



This study conducted focuses on the zero-waste generation from potato processing industries. The waste is mostly comprised of starch-based products. The process involves the usage of *Aspergillus Niger* and *Saccharomyces* with different incubation times of 12–24 h in place of enzymes. The material that was leftover as a by-product after the process can be later used for the ethanol production through fermentation [36].

An integrated approach to generate biofuels and manures thus reducing the usage of conventional fuels and fertilisers in agriculture by using simultaneous saccharification and fermentation technique (SSF) was used to produce bio-ethanol from pineapple leaves. The by-products of the process were mixed with blue-green algae which resulted in increase in nitrogen, phosphorus and potassium element that can act as manure. So, two stages of pollution are reduced simultaneously [37].

### **3.3 Current Technological Trends**

The study conducted by Spyridon et al. shows that there are many current trends followed by various industries in production of biochemical ethanol, moreover much more promising methodologies are currently under development phase. Government funding was even approved in countries like USA and Europe to develop the yeast and bacteria responsible for the fermentation of ethanol [38].

There are several technologies like anaerobic digestion (AD), anaerobic co-digestion (AcoD) process which are a promising and effective current day methods to extract biogas. The research review conducted by Hagos et al., the AcoD technology is problematic when the demand increases as the production stages increase exponentially. These methods need a tool like ADM1 and biochemical methane potential testing which calculates the biodegradability of the organic materials used. Further, inclusion of nanomaterials can improve the production pace of the standard systems [39].

Gonzalez et al., 2018 have described the current scenarios of biomass liquefaction for transport fuel needs. Thermochemical process that converts lignocellulosic biomass conversion to liquid substances. To achieve better conversion efficiencies, finally, many systematic methodologies and process system engineering which will help the main synthesis process [40].

The production of biofuel or other fuels related to internal combustion engine use does have synergic effects on both positive and negative sides. Merdun et al., 2018 conducted an analysis on the generation of biofuels from vegetable feedstock waste. Greenhouse vegetable waste (GVW) and lignite coal were taken for the experiments with different particle sizes and pyrolysis temperatures along with some naturally occurring catalysts. They found out that a positive synergic effect was noticed for biochar yield while an opposite effect was observed for the bio-oil and fuel yield [41].

Ethanol and butanol compounds provide the chemical energy required for biofuels that can be used as an alternative fuel for transportation needs. Shao et al., 2015

increased the fermentation process of carbohydrates by using *amorphophallus konjac* waste with the help of ATCC 824. They found that the ABE yielding increased as the fermentation time reduced because of the alkaloid effect. This proved that using *amorphophallus* in the fermentation produced low-cost high yield strategy [42].

Experiments were conducted to increase the yield of quality biodiesel according to the ASTM standards. They used palm oil and waste cooking oil following transesterification methods. The ratio of methanol to palm and cooking oil is 4:1 and 11:1 with contact time varying from 2 to 4 h. Biodiesel production yield from 90 to 70% was obtained from the above-mentioned ratios at reaction temperature of 60 °C [43].

Hydrogen production from biomass has been a long-term research due to the complexity in hydrogen interaction at molecular levels as well as its metabolic network. The metabolic flux of hydrogen will have substantial impact on enzymatic metabolism and synthesis of hydrogen gas [44].

## 4 Engine Testing

### 4.1 Waste Oil Usage

Muddineni et al. worked towards the usage of natural-based oils that are capable of generating combustion-related pressures. A single cylinder four-stroke engine was used for the experiments to analyse the smoke emissions of oil from coconut, cottonseed and rice bran against the convectional fuels. The fuel consumption analysis proved that the rice bran is better performing than the other compounds of natural occurrence, as well as the rice bran products, are similar in properties of diesel like brake-specific fuel consumption (BSFC), total fuel consumption, fewer emission levels of carbon monoxide, carbon dioxide and nitrogen dioxides [45].

The recycled engine oil can be a potential fuel for blending the standard diesel fuel for use in compression ignition engines. Prabakaran et al. conducted various experiments by blending the standard diesel fuel with recycled engine oil which resulted in reduced brake-specific fuel consumption (BSFC), NO<sub>x</sub> (oxides of nitrogen) and hydrocarbons (HC) emissions. The brake thermal efficiency (BTE) of fuel for blends such as D95R5 (blend containing 95% diesel and 5% recycled oil), D85R15 (blend containing 85% diesel and 15% recycled oil) and D80R20 (blend containing 80% diesel and 20% recycled oil) proved effective by 2, 4 and 5% of the total energy output compared to diesel fuel [46].

There are many alternatives for producing unconventional fuels not only from used engine oils but also from cooking oils and plastics that can also be worked out. Concentration of carbon emissions is higher when compared to the standard diesel; the recycled oils have 18.51 g/kWh at 25% of rated power to 14.14 g/kWh. Even the NO<sub>x</sub> emissions even increased by the use of recycled oils compared to diesel fuel [47].

The process of pyrolysis has the ability to guide the recycled fuels without any modification. Properties of the fuels produced by pyrolysis were observed to be similar to that of standard diesel and gasoline [48].

#### ***4.2 Micro-organisms and Algae-Based Fuels***

The experiments conducted by Karmakar et al. used biodiesel that was generated by unused algae that are produced by two-step esterification of bio-acids and then followed by the transesterification process which reduced the emissions from petrol- or diesel-based internal combustion engines. Particularly, the  $\text{NO}_x$ , CO and  $\text{CO}_2$  were drastically reduced. The production methodology of biodiesel was altered by using the Taguchi's method with the help of L25 array. The oil molar ratio of 6:1 to ethanol, reaction time of ninety minutes, reaction temperature of fifty degrees Celsius and potassium hydroxide concentration of 2.5 wt. % were the altered conditions of the transesterification process, thus generating biodiesel of 89.7% with free fatty acid of 0.25% only [49].

The reduction in peak pressure within the cylinder of 3.28% and with an 8.21% reduction in BTE was noticed by Kamarulzaman et al., when black soldier fly larvae oil (BSFL) oil was investigated. The shorter (ignition delay) ID period of BSFL oils improved when blended with diesel fuels by 30% along with higher oxygen content. They concluded that BSFL oil is a good substitute for biodiesel blending with standard fuel with respect to emissions and power variation [50].

#### ***4.3 Other Category Fuels and Technical Advancements***

Apart from extraction and using of solely, the biofuels mixing of some naturally generated oils with standard diesel are a better approach as it mitigates the process of production. When the blending ratios were of 6:1, then the maximum thermal efficiency was achieved. This blend produced fewer quantities of carbon emissions as well as hydrocarbons. The toxicity of the pollutants was significantly low compared to standard diesel [51].

Testing an internal combustion engine with three biofuels (chocolate waste, methyl ester and algae) for the performance and emission analysis, they found out that methyl ester reduced the emissions significantly while the chocolate waste emissions increased rapidly with increments in ignition timing. However,  $\text{NO}_x$  emissions remained of a concern even with all three fuels which were of minimum 20% increase compared to standard diesel [52].

Lemon oil was used in a four-stroke diesel engine with the help of steam distillation for extraction. It was observed that lemon oil performance was good compared to diesel in terms of slight improved BTE and reduced fuel consumption. When tested

with in cylinder coating then the thermal efficiency improved which better in cylinder temperatures [53].

Thermally coated engines when used with biofuels are 11% higher in temperatures which resulted in faster combustion speeds. Masera et al. also noticed improved torque and power output along with increase in 10.17 percent in BTE, 13.4% reduction in BSFC reduced CO and HC emissions when compared to standard diesel [54].

Combustion delay is a major concern when it comes to internal combustion engine efficiency. Mateusz et al. conducted experiments with liquid biofuel in a standard diesel engine without any modifications. They found that there is a delay of more than 5° at tested speeds from idling to cruising. This showed that there is a need for the modification of engines in order to retain more heat from the combustion cycle [55].

The mixed and premixed conditions of the biofuels were investigated by Asadi et al. where they concluded that increased premixing of biodiesel led to reduction in flame propagation speeds which is opposite to diesel fuel. With B10 and B20 blends of biodiesel, the soot emission reduction was noticed as these fuels contained higher oxygen molecules. Even the chamber temperature increased with these fuels but it did not trigger the NO<sub>x</sub> emissions rapidly to rise [56].

Kurczynski et al. used a 1.3 L Fiat diesel engine and tested blends of diesel with (fatty acid methyl ester) FAME acids known as B20 and B30. They concluded that by the addition of 7% biodiesel by volume, the effective power was reduced by 4KW at 1750 RPM. As the feed ratio was increased the power and torque figures distinctly fell. The B20 fuel is helped in reducing the ignition characteristics when compared with B30 [57].

Sugarcane diesel and sugarcane biodiesel –LS-9 were tested for emissions on a four-stroke diesel engine. Soto et al. found that the LS-9 variant produced the least THC which is basically due to the rich oxygen and absence of aromatic compounds in the fuel. The NO<sub>x</sub> emissions of LS-9 are, however, higher than the sugarcane diesel—farnesane but with fewer margins. Even the BSFC increased for the LS-9 fuel with higher HC ratio [58].

The boosting characteristics of prenil biofuel with gasoline blends were discovered and the rated octane number (RON) of the prenil was found to be exceeding the blending agent and the stock due to the low water solubility and high density of energy close to petrol [59].

Patel et al. investigated the combustion and emission variable of an engine using the rapeseed and soyabean biodiesels where they observed lower cylinder pressures than the standard diesel. The effective combustion noise was reduced by a range of 0.25–8 Db and the duration increased. However, the CO emissions were high which is mostly due to the trouble associated with atomising the fuels [60].

## 5 Discussion

Agricultural wastes show potential in the generation of the required liquid or gaseous fuels. In order to meet the demands of local or global transportation energy needs pre-treatment of this waste to achieve a better yield, many such techniques were tested but most of them need more development in terms of efficiency, the energy needed for the pre-treatment and the quality analysis of the fuels after extraction.

- Generation of biofuel by using micro-organisms produced different results as they were treated with different approaches like anaerobic, consideration of shorter antennas and ohmic heating produced appreciable results but there is a need for combing all these approaches here the maximum possible quality and quantity of the fuel can be obtained.
- Mechanical extraction techniques of seed oils were generating low qualities of biofuels, and these methods need to be clubbed with chemical treatments where the char is removed from the waste and not transferred to the oils as mentioned by Djomdi et al.

## 6 Conclusion

The solid waste is of better option as they are the most aggressively generated wastes across the globe. Wastes that are starch-based can be a viable option due to their readiness in fermentation process with efficiency of over 70% than other conversion techniques. Fuel quality is dependent on the reaction time and exposed temperatures but as the temperature rises the fermentation bacteria is killed resulting in reduced quantities of fuel that is generated with optimum time and temperature being 12 h and 60 °C, respectively. The testing of biofuels in internal combustion engines is mostly resulted in delay ignition, increased combustion duration which resulted in increase of emissions by 4.37 g/kWh carbon emissions even at lower loading conditions according to Naima et al., When the micro-organism-based fuels were tested, there was a noticeable reduction in BTE of 8.27% and cylinder pressure by 3.28 and increased BSFC except for lemon oil extract which showed percent 0.423 kg/kWh, 0.392 kg/kWh, 0.357 kg/kWh, 0.321 kg/kWh and 0.295 kg/kWh as per Karthick-eyan et al., which improved with the addition of lemon oil composition and thermal insulation coating of the surfaces exposed to combustion. Thus, it can be said that biofuels have the potential to significantly reduce the dependency on fossil fuels and result in reduced emission but this result can be achieved with further research and improvement in biofuel generation, waste tackling systems and the fuel consuming technologies.

## 7 Future work

- More work needs to be carried out regarding the reduction of biofuel generation time by improving the efficiencies of waste to fuel conversion systems which will help in meeting the fuel demand.
- Biofuel quality can be improved to meet the fuel rating and the molecular blending ratios if needed.
- Focus on designing new engine heads according to the biofuel characteristics can help in dealing with the combustion-related issues of biofuels.

## References

1. Panpatte D, Jhala Y (2019) Agricultural waste: a suitable source for biofuel production. *Biofuel and Biorefinery Technologies*, 337–355
2. Karmee S, Linardi D, Lee J, Lin C (2015) Conversion of lipid from food waste to biodiesel. *Waste Manage* 41:169–173
3. Reid W, Ali M, Field C (2015) The future of bioenergy. *Glob Change Biol* 26(1):274–286
4. Leong W, Lim J, Lam M, Uemura Y, Ho Y (2018) Third generation biofuels: a nutritional perspective in enhancing microbial lipid production. *Renew Sustain Energy Rev* 91:950–961
5. Zhao G (2016) Assessment of potential biomass energy production in China towards 2030 and 2050. *Int J Sustain Energy* 37(1):47–66
6. Ozturk M, Saba N, Altay V, Iqbal R, Hakeem K, Jawaid M, Ibrahim F (2017) Biomass and bioenergy: an overview of the development potential in Turkey and Malaysia. *Renew Sustain Energy Rev* 79:1285–1302
7. Raghavendra H, Mishra S, Upashe S, Floriano J (2019) Research and production of second-generation biofuels. In: *Bioprocessing for Biomolecules Production*, pp 383–400
8. Saini J, Saini R, Tewari L (2014) Lignocellulosic agriculture wastes as biomass feedstock's for second-generation bio ethanol production: concepts and recent developments. *3 Biotech* 5(4):337–353
9. Yu J, Paterson N, Blamey J, Millan M (2017) Cellulose, xylan and lignin interactions during pyrolysis of lignocellulosic biomass. *Fuel* 191:140–149
10. Murtaza G (2015) The biofuel potential of municipal solid waste. <https://doi.org/10.13140/RG.2.2.18518.24647>
11. Shi A, Koh L, Tan H (2009) The biofuel potential of municipal solid waste. *GCB Bioenergy* 1(5):317–320
12. Kulkarni MB, Ghanegaonkar PM (2019) Biogas generation from floral waste using different techniques. *Glob J Environ Sci Manage* 5:17–30
13. Sen B, Aravind J, Kanmani P, Lay C (2016) State of the art and future concept of food waste fermentation to bioenergy. *Renew Sustain Energy Rev* 53:547–557
14. Yeo J, Oh J, Cheung H, Lee P, An A (2019) Smart food waste recycling bin (S-FRB) to turn food waste into green energy resources. *J Environ Manage* 234:290–296
15. Madusanka T, Manage P (2018) Potential utilization of microcystis sp. for biodiesel production: green solution for future energy crisis. *Asian J Microbiol Biotechnol Environ Sci* 19(2):143–148
16. Behrendt D, Schreiber C, Pfaff C, Müller A, Grobbelaar J, Nedbal L (2018) Algae as a potential source of biokerosene and diesel—opportunities and challenges. *Biokerosene* 303–324
17. Show KY, Yan Y, Ling M, Ye G, Li T, Lee D (2018) Hydrogen production from algal biomass—advances, challenges and prospects. *Biores Technol* 257:290–300

18. Roland W, Lakatos G, Bojti T, Maroti G, Bagi Z, Rakhely G, Kovacs KL (2018) Anaerobic gaseous biofuel production using microalgal biomass—a review. *Anaerobe* 52:1–8
19. Yodsuwan N, Kamonpatana P, Chisti Y, Sirisansaneeyakul S (2017) Ohmic heating pre-treatment of algal slurry for production of biodiesel. *J Biotechnol* 267:71–78
20. Lee SY, Sankaran R, Chew KW et al (2019) Waste to bioenergy: a review on the recent conversion technologies. *BMC Energy* 1:4
21. Pursiheimo E, Holttinen H, Koljonen T (2019) Inter-sectoral effects of high renewable energy share in global energy system. *Renew Energy* 136:1119–1129
22. Mustafa Omer A (2019) Environment and development: bioenergy for future. *F Chem J* 2:19–50
23. Jiang L, Sheng L, Fan Z (2018) Biomass-derived carbon materials with structural diversities and their applications in energy storage. *Sci China Mater* 61:133–158
24. Lee HW, Kim YM, Kim S, Ryu C, Park SH, Park Y-K (2018) Review of the use of activated bio char for energy and environmental applications. *Carbon Lett* 26(1)
25. KS Rajmohan, CRamya and Varjani S., Trends and advances in bioenergy production and sustainable solid waste management. *Energy & Environment*, Nov 2019. DOI <https://doi.org/10.1177/0958305X1988241>.
26. Sharma S, Saxena V, Baranwal A, Chandra P, Pandey L.M (2018) Engineered nano porous materials mediated heterogeneous catalysts and their implications in biodiesel production. *Mater Sci Energy Technol* 1(1):11–21
27. Sims RE, Mabee W, Saddler JN, Taylor M. An overview of second generation biofuel technologies. *Bioresour Technol*. 2010 Mar;101(6):1570-80. doi: 10.1016/j.biortech.2009.11.046. Epub 2009 Dec 5. PMID: 19963372.
28. Zeng R, Wang S, Cai J, Kuang C (2018) A review of pyrolysis gasification of MSW. <https://doi.org/10.2991/iceesd-18.2018.27>
29. Zhang, XL (2018) Essential scientific mapping of the value chain of thermo chemical converted second-generation bio-fuels. *Green Chem*. <https://doi.org/10.1002/chin.201648298>
30. Zabed H, Sahu JN, Boyce AN, Faruq G (2016) Fuel ethanol production from lignocellulosic biomass: an overview on feedstocks and technological approaches. *Renew Sustain Energy Rev* 66:751–774
31. Mariana I, Nicoleta U, Sorin-Ştefan B, Gheorghe V, Mirela D (2013) Actual methods for obtaining vegetable oil from oilseeds
32. Djomdi D, Leku M, Djoulde R, Delattre C, Michaud P (2020) Purification and valorization of waste cotton seed oil as an alternative feedstock for biodiesel production. *Bioengineering* 7(41)
33. Hoffmann JF, Fasquelle T, Vaitilingom G, Olives R, Py X, Goetz V (2019) Compatibility of vegetable oils with solid filler materials for thermocline thermal energy storage systems. *Sol Energy Mater Sol Cells* 200:109932
34. Kumar Vijay P, Aharon G (2016) Glucose production from potato peel waste under microwave irradiation. *J Mol Catal A Chem* 417:163–167
35. Dhiman SS, David A, Shrestha N, Johnson GR, Benjamin KM, Gadhamshetty V, Sani RK (2017) simultaneous hydrolysis and fermentation of unprocessed food waste into ethanol using thermophilic anaerobic Bacteria. *Biosource Technol* 244:733–740
36. Chintagunta AD, Jacob S, Banerjee R (2016) Integrated bioethanol and bio manure production from potato waste. *Waste Manage (New York, N.Y.)* 49:320–325
37. Chintagunta AD, Ray S, Banerjee R (2017) An integrated bioprocess for bioethanol and bio manure production from pineapple leaf waste. *J Cleaner Prod* 165:1508–1516
38. Achinas S, Euverink G J W (2016) Consolidated briefing of biochemical ethanol production from lignocellulosic biomass. *Electron J Biotechnol* 23(2016):44–53
39. Hagos K, Zong J, Li D, Liu C, Lu X (2017) Anaerobic co-digestion process for biogas production: progress, challenges and perspectives. *Renew Sustain Energy Rev* 76:1485–1496
40. Ibarra-Gonzalez P, Rong BG (2019) A review of the current state of biofuels production from lignocellulosic biomass using thermochemical conversion routes. *Chin J Chem Eng* 27:1523–1535

41. Merdun H, Sezgin IV (2018) Products distribution of catalytic co-pyrolysis of greenhouse vegetable wastes and coal. *Energy* 162:953–963
42. Shao M, Chen, H (2015) Feasibility of acetone-butanol-ethanol (ABE) fermentation from *Amorphophallus konjac* waste by *Clostridium acetobutylicum* ATCC 824. *Process Biochem* 50:1301–1307
43. Kadapure A, Santosh, Subhaya S, Prasanna S, Sagar K (2017) Studies on process optimization of biodiesel production from waste cooking and palm oil. *Int J Sustain Eng* 11:167–172
44. Zhang Z, O'Hara I, Mundree S, Gao B, Ball A, Zhu N (2016) Biofuels from food processing wastes. *Curr Opin Biotechnol* 38:97–105
45. Muddineni N, Reddy BA, Dhruvjyoti B, Liril S (2017) Preparation and performance analysis of biofuels on ci engine. *Int J Mech Eng Technol* 8:447–455
46. Prabakaran B, Zachariah ZT (2016) Production of fuel from waste engine oil and study of performance and emission characteristics in a diesel engine. *Int J Chem Tech Res* 9:474–481
47. Naima K, Liaqid A (2013) Waste oils as alternative fuel for diesel engine: a review. *J Petrol Technol Altern Fuels* 4(3):30–43
48. Ahire CM, Lawankar SM (2017) Waste automotive oil as alternative fuel for IC engine. *Int Res Journal Of Eng Technol (IRJET)* 4(6):934–939
49. Karmakar R, Kundu, K, Rajor, A (2017) Fuel properties and emission characteristics of biodiesel produced from unused algae grown in India. *Petrol Sci* 15(15):385–395
50. Kamarulzaman MK, Hafiz M, Abdullah A, Chen AF, Awad OI (2019) Combustion, performances and emissions characteristics of black soldier fly larvae oil and diesel blends in compression ignition engine. *Renew Energy* 142:569–580
51. Dinesh K, Tamilvanan A, Vaishnavi S, Gopinath M, Lion R (2016) Biodiesel production using *Calophyllum inophyllum* (Tamanu) seed oil and its compatibility test in a CI engine. *Biofuels* 10:347–353
52. Ospina G, Selim MY, Al Omari SA, Ali MI, Hussien AM (2019) Engine roughness and exhaust emissions of a diesel engine fuelled with three biofuels. *Renew Energy* 134:1465–1472
53. Karthickeyan V, Thiyagarajan S, Geo VE, Ashok B, Nanthagopal K, Chyuan OH, Vignesh R (2019) Simultaneous reduction of NO<sub>x</sub> and smoke emissions with low viscous biofuel in low heat rejection engine using selective catalytic reduction technique. *Fuel* 255:115854
54. Masera K, Hossain AK (2018) Biofuels and thermal barrier: a review on compression ignition engine performance, combustion and exhaust gas emission. *J Energy Inst* 92(3)
55. Mateusz B, Piotr O, Marcin W, Mieczysław S (2019) Evaluation of methods for determining the combustion ignition delay in a Diesel engine powered by liquid biofuel. *J Energy Inst* 92:1107–1114
56. Asadi A, Zhang Y, Mohammadi H, Khorand H, Rui Z, Doranehgard MH, Bozorg MV (2019) Combustion and emission characteristics of biomass derived biofuel, premixed in a diesel engine: a CFD study. *Renew Energy* 138: 79–89
57. Kurczynski D, Lagowski P (2019) Performance indices of a common rail-system CI engine powered by diesel oil and biofuel blends. *J Energy Inst* 92:1897–1913
58. Soto F, Marques G, Torres-Jiménez E, Vieira B, Lacerda A, Armas O, Guerrero-Villar F (2019) A comparative study of performance and regulated emissions in a medium-duty diesel engine fuelled with sugarcane diesel-farnesane and sugarcane biodiesel-LS9. *Energy* 176:392–409
59. Monroe E, Gladden J, Albrecht KO, Bays JT, McCormick R, Davis RW, George A (2019) Discovery of novel octane hyper boosting phenomenon in prenil biofuel/gasoline blends. *Fuel* 239:1143–1148
60. Patel C, Tiwari N, Agarwal AK (2019) Experimental investigations of soyabean and rapeseed SVO and biodiesels on engine noise, vibrations, and engine characteristics. *Fuel* 238:86–97



# Effect of Truncated Conic Fins in Distillate of Double Slope Solar Still



Ajay Kumar Kaviti, Begari Mary, and Akkala Siva Ram

**Abstract** Performance exploration of Aluminum truncated conic fins in single basin double slope solar still compared with traditional still. A dual incline single basin solar still is made of wooden box outside and Aluminum on the inside  $1 \times 0.5 \times 0.2$  m. Still with truncated conic fins of 50 mm height and 20 mm diameter. Experimentation was carried out under the same climatic conditions of Hyderabad ( $17.3850^\circ$  N,  $78.4867^\circ$  E) by varying 3 depths of water (1 cm, 2 cm, and 3 cm). Truncated conic fins are compared with traditional still. Experimental results portray that the maximum amount of distillate output has been obtained for the minimum depth of water at 1 cm. Fins play a vital role at higher depths compared to conventional still. Variance in the output of finned stills compared to conventional still progressively increases as the depth of water increases. The optimum depth of evaporation is at 4 cm for both the fin geometries. The distillate output for truncated conic finned basin still has got 4.40, 26.73, and 29.06% higher than conventional still.

**Keywords** Truncated conic fins · Distillate · Depth of water · Solar still · Aluminum

## 1 Introduction

Solar distillation is one of the water refinement processes viewed as the most challenging task and the main possible answer for determining crisp or consumable water from the accessible brackish water and saline water assets everywhere throughout the world [1]. The expulsion of the detachment of salts from the water can not be accomplished consequently yet it is done in desalination frameworks by the guide of some energy source [2].

As we as a whole realize that water is a significant component to control body so drinking water ought to be unadulterated and sterile. Something else, individuals may experience the ill effects of different water-borne illnesses [3]. Water is an

---

A. K. Kaviti (✉) · B. Mary · A. S. Ram  
VNRVJIET, Hyderabad 500090, India

elementary human compulsion. Apiece on Globe essentials at least 20 to 50 lit of crisp, safe water a day to drink, cook, and merely stay dry. Water is the most essential element of human life and its importance [4]. Humanity needs clean water to survive, and only a few have access to adequate and affordable supplies for around 1.1 billion people in the world [5]. Today we can produce clean new water through the utilization of sustainable power source frameworks, for example, wind control, solar energy, and other such inexhaustible advancements to control different water treatment forms for a freshwater generation [6].

El-Sebaai et al. [7] Experimental and theoretic exploration of the thermal effectiveness of a solar fins single basin still by finned absorber plate made of dissimilar materials with 7 circular fins made of copper are used. Average productivity is found to be 1467.4 and 1898.8 (L/m<sup>2</sup>) for traditional stills and still with fins. For stills without and with copper fins. Manokar et al. [8] In order to minimize the solar heat loss, experiments were carried out using an acrylic piece with rounded Aluminum fins attached to the basin to improve yield. A single slope single finned acrylic solar still has daily productivity of 660 ml/0.25m<sup>2</sup>/day.

Hardik et al. [9] Experiments were performed on circular hollow fins made of mild steel. The variations in water depth (10, 20, and 30 mm) in the basin were evaluated for productivity. The highest purified water yield was obtained for 10 mm of water depth, the lowermost for 20 mm of water depth, and intermediary for 30 mm of depth. Rupinder et al. [10] A novel fin concept for a thermal storage device for high-temperature solar cooling that effectively utilizes natural convection. For fast heat absorption, various fin erections are examined and their thermal efficiency is compared to (TES) based on carbon nanoparticles. With pooled fins and nanoparticles, the thermal energy storage system decreases the melting time by up to 43%.

El-Sebaai et al. [11] Experiments directed on a solar fin plate were studied to increase productivity and heat transfer rate. It was found that with an escalation in fin elevation and a reduction in fin thickness and no fins, performance and productivity improved. With  $N_f = 7$ ,  $H_f = 0.04$  m and  $X_f = 0.001$  m. 13.7% better efficiency is obtained by incorporating rectangular fins. Appadurai et al. [12] Hypothetical efficiency and experimental research are being studied for a traditional solar still, finned solar still, fin-type solar pond combined with fin-type solar. The heat transmission rate from basin to water was boosted when fins were connected to the basin. Fin-type single basin solar still and fin-type miniature solar pond combined with fin kind single basin solar still have amplified the benefit in the water pool, which is calculated at about 47%, 45.5%, and 50%, respectively.

Velmurugan et al. [13] Experimentation was performed with an ordinary solar-type of basin still combined with fins on the basin plate. Three chambers of the effluent relaxing tank are made, containing stone, coal, and sand to settle the contaminations and eliminate the bacteria in the effluents. Squeegees, stones, black elastic, and sand are also used to increase the yield in the fin style single solar basin. The usual desertion rate in traditional solar still is 1.66 l per 8 h, it is observed. As fins were inserted into the basin plate, the desertion rate amplified by around 53% (2.54 l per 8 h). Hardik et al. [9] Two separate mild steel absorber plates were welded on mild steel

hollow fins of square geometry (25 mm side length, 20 mm height and 2 mm thick) The maximum distilled water production of  $0.9672 \text{ kg/m}^2\text{-day}$  for still achieved by square finned solar. Because of the thin layer of water for the 10 mm, depth of water has more productivity.

Manokar et al. [14] Comparative analysis of single slope and solar still Aluminum finned acrylic and solar still of made of GI. The daily yield of single basin single slope acrylic solar still is  $660 \text{ ml}/0.25\text{m}^2/\text{day}$  and GI solar still is  $585 \text{ ml}/0.25\text{m}^2/\text{day}$ . In comparison to galvanized iron solar still acrylic still gives 11.36% higher output. Rajaseenivasan et al. [15] Output enhancement on a single solar basin still with incorporated circular and tetragonal fins at the basin. The presentation of the system investigated varies between 1, 2, 3, and 4 cm in depth. Square fins were found to have a maximum of  $4.55 \text{ kg/m}^3$  days and conventional fins to have a maximum of  $3.16 \text{ kg/m}^3$  days. For square fins, overall efficiency is still improved by 36.7% and for fins filled with wick materials, it changes to 36 and 45.8%. Velmurugan et al. [16] At the bottom of the still, fins were incorporated. The production rate has therefore accelerated. Besides, sponges were used to further increase the region of exposure. When fins were used at the bottom of the still, production increased by 45.5% the maximum variance was around 10% between theoretical and experimental. The performance improved from 1.88 to  $2.8 \text{ kg/m}^2$ .

Ayuthaya et al. [17] Developed a calculated model intended for forecasting the output of an ethanol solar still basin type, indoor experiments were performed. It was investigated that fin incorporation into the solar basin could still increase effectiveness and also reduce the preheating time needed to evaporate in the still basin. Compared to traditional still, modified solar productivity of still increased by 15.5%. Kambel et al. [18] Compared with other designs, the thermal behavior and water yield effectiveness of the modified solar still with pin fins absorber and condenser were studied. It originates that for the still employing condenser and simple pin fins absorber, a gain in water effectiveness of 32.18% is just 14.53% compared to traditional stills. The result of the exterior condenser on the output of water is so leading concerning the impact of the absorber of the pin fins.

Alaian et al. [19] The analysis of two similar solar stills is traditional and the other is pin-finned wick surface evaporation. When the pin-finned wick is applied in the still, temperatures at the glass surface, water still, wick surface, and air vapor mixture enhancing the still productivity are demonstrated and found that more than 23% of the device productivity is achieved when the pin-finned wick is applied. Qiu et al. [20] Finned-tube evaporators have been usually used in heat pumps from air sources. An efficient approach to enhancing the heat transfer possessions of finned-tube evaporators using solar energy. Maximum solar energy loss interpretations for approximately 12.7% of the entire solar energy and only 60% of the total heat transfer power is increased by twice the fin height.

Omara et al. [21] Increasing the apparent area of the absorber and heat transfer rate amid brackish water and the absorber to increase the efficiency of basin solar stills. The efficiency of purified water with finned solar still of 40% on average and a corrugated surface of 21% on average, relative to traditional water with the same volume of water. Srivastava et al. [22] In the basin water, porous fins of darkened old

cotton cloths were partially dipped, while the remainder of the portion extended above the surface of the basin water. In the case of the modified still made of expanded polystyrene foam with good insulation property, an extreme distillation yield of approximately  $7.5 \text{ kg/m}^2$  was attained.

According to literature the effect of various fin geometries like circular fins, rectangular fins, square fins, pin fins, and so on are employed in solar stills to advance the efficiency of the water. Fins are surfaces that are prolonged from an object to magnify the pace of heat transmission to or from the earth by expanding convection. Heat transmission is a basic constraint while structuring any cosmological bids. Fin is a direct means which can be exploited in the solar still to build the apparent area. Augmentation of the apparent region stimulates heat transmission. Analysts have utilized fins in the solar stills to expand the exterior area of water and thus enhancement of water temperature. In this paper, the novel geometry of fin that is truncated conic fin with 50 mm height and 20 mm diameter as shown in Fig. 1 was designed and tested to augment the act of the solar still and it is compared with the traditional still by varying the depth of water.

**Fig. 1** Truncated conic fin



## 2 Experimental Setup

An investigational setup contains two double slope solar stills. The traditional solar still and the still integrated with finned basin liner. Modified still is integrated with truncated conic fin geometry. A solar still is made of the wooden box outside and Aluminum on the inside  $1 \times 0.5 \times 0.2$  m. Insulation of 5 cm on the sides and 10 cm in the bottom is made with thermocol between inner still and wooden box to elude the loss of heat from the solar still as shown in Fig. 3. The still is enclosed with a glass of 4 mm thick with a leaning angle of  $17^\circ$ . Still, with a truncated conic profile of 50 mm height and 20 mm diameter, 18 fins were attached on the base plate maintaining the equal pitch of 200 mm with a rectangular  $3 \times 6$  Array was integrated as depicted in Fig. 2 in the dual-slope solar still as portrayed in Fig. 3. The complete setup of Aluminum still, base plate, and fins are treated with black paint with powder layer to intensification the absorptivity and to avoid corrosion. The thermocouples incorporated with a temperature indicator are connected to the basin, glass inside and outside, and the thermocouples placed in water are used to measure the temperatures for both the stills. A beaker of the 1 L volume is used to measure the hourly yield on the east and west side as shown in Fig. 3. Anemometer is to measure the wind velocity and solar power meter to measure solar radiation. Wind velocity, solar power, ambient temperature, and the heats of the basin, glass in glass out are recorded for every 30 min from 9:30 AM to 5:00 PM.

An experiment is carried out simultaneously with traditional still and the still included with fins by varying the depth of water from 1 to 3 cm. Three depths (i.e., 1, 2, and 3 cm) for both the traditional and the still with truncated conic finned basin liner to equate the performance of the system in the same conditions. All the tests were conducted in the genuine solar conditions in November 2020.

**Fig. 2** Array of fins



**Fig. 3** Experimental setup

### 3 Results and Discussion

The experimentations were directed by two single basin double slope solar stills. One with a truncated conic fins absorber plate and the other is conventional still. Temperatures, solar radiation, and yield are noted from 9:30 AM to 5:00 PM for three days that are 17/11/2020, 18/11/2020, and 19/11/2020 at Hyderabad (17.3850° N, 78.4867° E) by changing the water depths from 1 to 3 cm. The results obtained from the experiments are discussed below;

#### 3.1 Solar Intensity

The evolutions of solar radiations have schemed in Fig. 4 for 3 days. The extreme values of solar radiations were at 12:30 pm. Solar emissions of 1000 W/m<sup>2</sup>, 980 W/m<sup>2</sup>, 980 W/m<sup>2</sup> were recorded. It was perfect that the restrained solar emission has a parabolic affinity. This is estimated subsequently the path designated by the locations of the sun from sunrise to sunset is parabolic. The graph shown in Fig. 4 depicts that the solar emission strength increases, achieve the extreme value, and then concentrates in the evening.

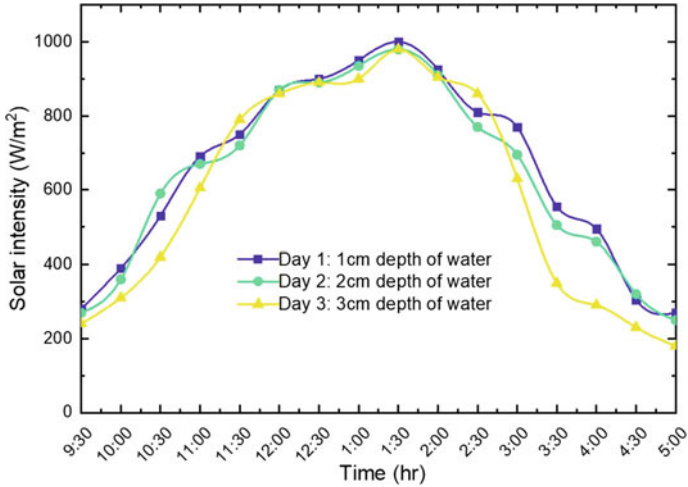


Fig. 4 Solar intensities

### 3.2 Temperatures

The temperatures of the basin, inside the glass, outside glass, water, and ambient temperatures are recorded for three days for both conventional still and truncated conic finned basin still. Figures 5, 6 and 7 shows the difference in temperatures

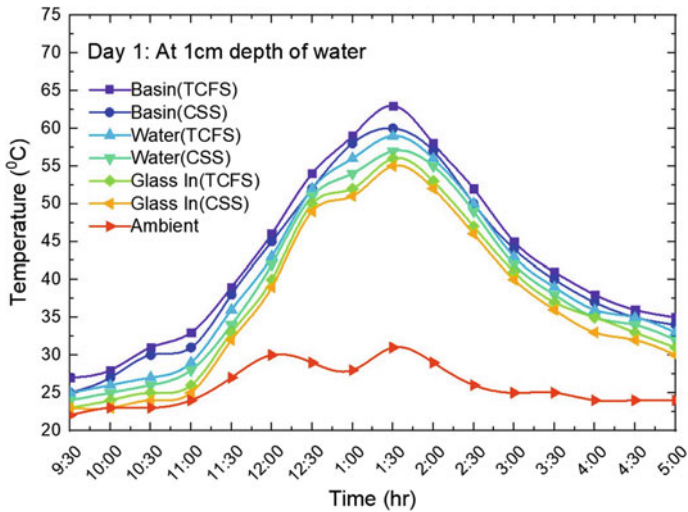


Fig. 5 Temperatures at 1 cm depth of water



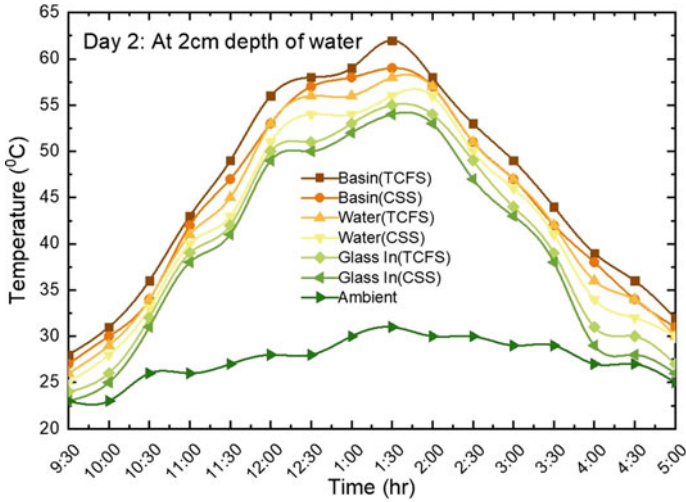


Fig. 6 Temperatures at 2 cm depth of water

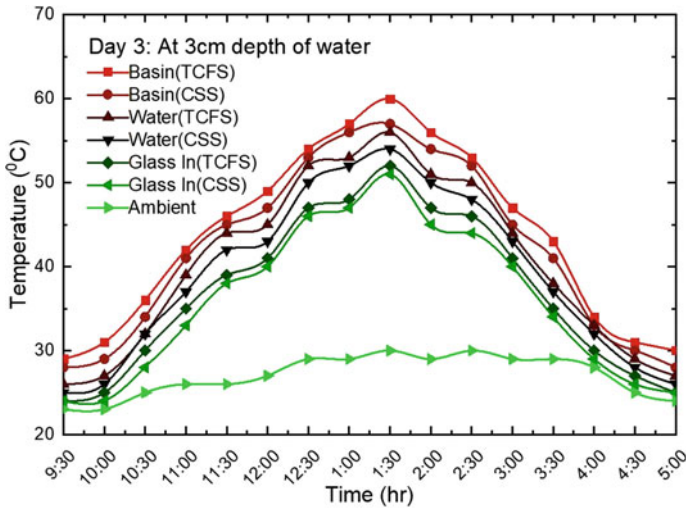


Fig. 7 Temperatures at 3 cm depth of water

in various components. The maximum temperatures were obtained at 13:30 of 56–63 °C. The value of ambient temperature varies between 22 and 35 °C below graph shows that the highest temperature of 63 °C has been attained for the finned basin. A temperature of 64 has been attained for the conventional basin. Maximum temperature of 56 °C for inner glass temperature of truncated conic finned still has obtained. 55 °C for inner glass temperature of conventional still. Experimental remarks depict



that the temperature of the absorber plate and briny water of the finned basin remains greater compared to traditional still as the truncated conic fins have a higher rate of heat transfer. Temperatures of three days with 1, 2, and 3 cm depth of water has been described in the graphs below. Figure 5 day 1 temperature variations at 1 cm depth of water, Fig. 6 day 2 temperature variations at 2 cm depth of water, Fig. 7 shows the temperature differences at 3 cm depth of water.

### 3.3 Distillate Output

The distilled water from both the stills are collected with the beakers of 1 L capacity on both sides of the still. The maximum amount of water was collected at 13:00 h where the solar intensity and temperatures are higher. Through the experimental observations amount of distillate, water output is maximum for finned basin still at 1 cm depth of water due to higher rate of heat transfer through parabolic fins. As the depth of water increases the amount of distillate output is reduced as it is taking more time to reach a higher temperature. The truncated conic finned basin still attained 830, 640, and 555 ml per day, and the conventional still attained 795, 505, and 430 ml per day, respectively, as depicted in Fig. 8 the hourly yield is shown in Fig. 9, hence it is concluded that truncated conic finned basin still has got 4.40, 26.73, and 29.06% higher than conventional still. The percentage intensification in the amount of distilled water is increasing gradually as the depth of water increases. This behavior shows that fins play a crucial role at higher depths.

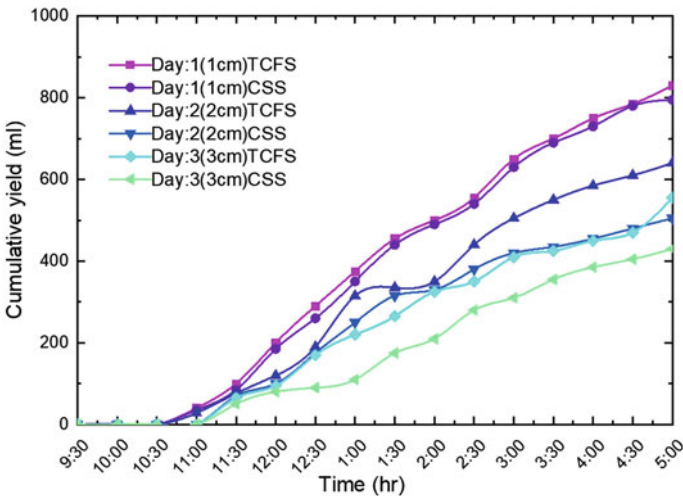


Fig. 8 Cumulative yield

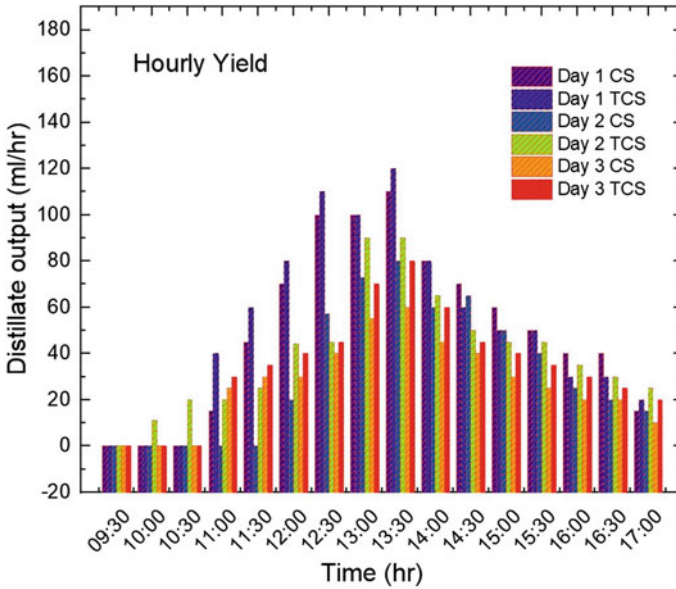


Fig. 9 Hourly yield

### 4 Conclusions

Two identical double slope solar stills were tested in the similar climatic conditions of Hyderabad (17.3850° N, 78.4867° E). One of the still is incorporated with truncated conic and is compared with traditional still. According to the experimental interpretations, it is concluded that the still with truncated conic finned basin accomplished maximum temperatures due to a higher rate of heat transfer. The truncated conic finned basin still attained 830, 640, and 555 ml per day, and the conventional still accomplished 795, 505, and 430 ml per day, hence it is concluded that truncated conic finned basin still has got 4.40, 26.73, and 29.06% greater than conventional still. The percentage intensification in the amount of distilled water is increasing progressively as the depth of water increases. This behavior shows that the desalinated water yield was extreme when the contact area amid the water and absorber plate was augmented, henceforth the fins affixed on the absorber plate increases the output without any intensification in the basin area. But the advanced element of the heat was transmitted from the base plate to basin water because of the tinny level of water at 1 cm depth of water which results in greater efficiency of desalinated water output.

## References

1. Vishwanath Kumar P, Kumar A, Prakash O, Kaviti AK (2015) Solar stills system design: a review. *Renew Sustain Energy Rev* 51:153–181
2. Kaviti AK, Yadav A, Shukla A (2016) Inclined solar still designs: a review. *Renew Sustain Energy Rev* 54:429–451
3. Kaviti AK, Yadav A, Shukla A (2019) Experimental investigation of solar still with opaque north triangular face. *Int J Green Energy* 0:1–8
4. Kumar A, Siva A, Kumari AA, Hussain S (2020) A brief review on high-performance nano materials in solar desalination. *Mater Today Proc*
5. Kumar A, Siva A, Kumari AA, Hussain S (2020) Development of hierarchical structures for enhanced solar desalination. *Mater Today Proc*
6. Ram AS, Kaviti AK (2020) Effect of glass cover angles on the performance of double slope solar still, a CFD simulation analysis. *Int J Mech Prod Eng Res Dev* 10:14019–14028
7. Ei-Sebaili AA, El-Naggar M (2017) Year round performance and cost analysis of a finned single basin solar still. *Appl Therm Eng* 110:787–794
8. Manokar AM, Winston DP (2017) Experimental analysis of single basin single slope finned acrylic solar still. *Mater Today Proc* 4:7234–7239
9. Jani HK, Modi KV (2019) Experimental performance evaluation of single basin dual slope solar still with circular and square cross-sectional hollow fins. *Sol Energy* 179:186–194
10. Singh RP, Xu H, Kaushik SC, Rakshit D, Romagnoli A (2019) Effective utilization of natural convection via novel fin design & influence of enhanced viscosity due to carbon nano-particles in a solar cooling thermal storage system. *Sol Energy* 183:105–119
11. El-Sebaili AA, Ramadan MRI, Aboul-Enein, S El-Naggar M (2015) Effect of fin configuration parameters on single basin solar still performance. *Desalination* 365:15–24
12. Appadurai M, Velmurugan V (2015) Performance analysis of fin type solar still integrated with fin type mini solar pond. *Sustain Energy Technol Assessments* 9:30–36
13. Velmurugan V, Gopalakrishnan M, Raghu R, Srithar K (2008) Single basin solar still with fin for enhancing productivity 49:2602–2608
14. Manokar AM, Winston DP (2017) Comparative study of finned acrylic solar still and galvanised iron solar still. *Mater Today Proc* 4:8323–8327
15. Rajaseenivasan T, Srithar K (2016) Performance investigation on solar still with circular and square fins in basin with CO<sub>2</sub> mitigation and economic analysis. *Desalination* 380:66–74
16. Velmurugan V, Deenadayalan CK, Vinod H, Srithar K (2008) Desalination of effluent using fin type solar still. *Energy* 33:1719–1727
17. Panomwan R, Ayuthaya N, Namprakai P, Ampun W (2013) The thermal performance of an ethanol solar still with fin plate to increase productivity. *Renew Energy* 54:227–234
18. Rabhi K, Nciri R, Nasri F, Ali C, Ben BH (2017) Experimental performance analysis of a modified single-basin single-slope solar still with pin fins absorber and condenser. *Desalination* 416:86–93
19. Alaian WM, Elnegiry EA, Hamed AM (2016) Experimental investigation on the performance of solar still augmented with pin-finned wick. *Desalination* 379:10–15
20. Qiu G, Sun J, Ma Y, Qu J, Cai W (2018) Theoretical study on the heat transfer characteristics of a plain fin in the finned-tube evaporator assisted by solar energy. *Int J Heat Mass Transf* 127:847–855
21. Omara ZM, Hamed MH, Kabeel AE (2011) Performance of finned and corrugated absorbers solar stills under Egyptian conditions. *Desalination* 277:281–287
22. Srivastava PK, Agrawal SK (2013) Winter and summer performance of single sloped basin type solar still integrated with extended porous fins. *Desalination* 319:73–78

# Experimentation on Pulsating Heat Pipe and CFD Analysis for Performance Enhancement



J. V. Suresh, P. Bhramara, and K. Hrishikesh

**Abstract** Heat transport from source to sink is one of the important aspects served by conventional heat pipes, metallic surface fins and heat exchangers, etc. Miniaturization of electronic components and increased performance capabilities of electronic devices required a compact, efficient heat transfer device unlike conventional heat pipes. Closed-loop pulsating heat pipes serve this purpose. This work is focused on experimental analysis of CLPHP of 2 mm internal diameter and 3.6 mm outer diameter, 5 turns, bottom heating mode and 50% filling ratio for calculation of heat transfer performance. The working fluids used are water, acetone pure fluids and water–acetone (1:1 by volume) binary fluid. The CFD analysis for heat transfer is performed so as to compare the experimental results with CFD results on same geometry. It is observed that CFD results are in close agreement with experimental results. Acetone is found to have better heat transfer performance for CLPHP.

**Keywords** CLPHP · CFD · Filling-ratio

## 1 Introduction

Effective heat transport devices to handle increasing power levels due to electronic miniaturization is of major significance. Unlike, traditional cooling approaches such as surface extended metal fins and heat pipes, contemporary approaches such as pulsating heat pipes (which lies in between heat pipes and metal fins as defined in

---

J. V. Suresh

Department of Mechanical Engineering, Gokaraju Rangaraju Institute of Engineering and Technology, Hyderabad, Telangana, India

P. Bhramara

Department of Mechanical Engineering, JNTU College of Engineering, Hyderabad, Telangana, India

e-mail: [bhramara74@jntuh.ac.in](mailto:bhramara74@jntuh.ac.in)

K. Hrishikesh (✉)

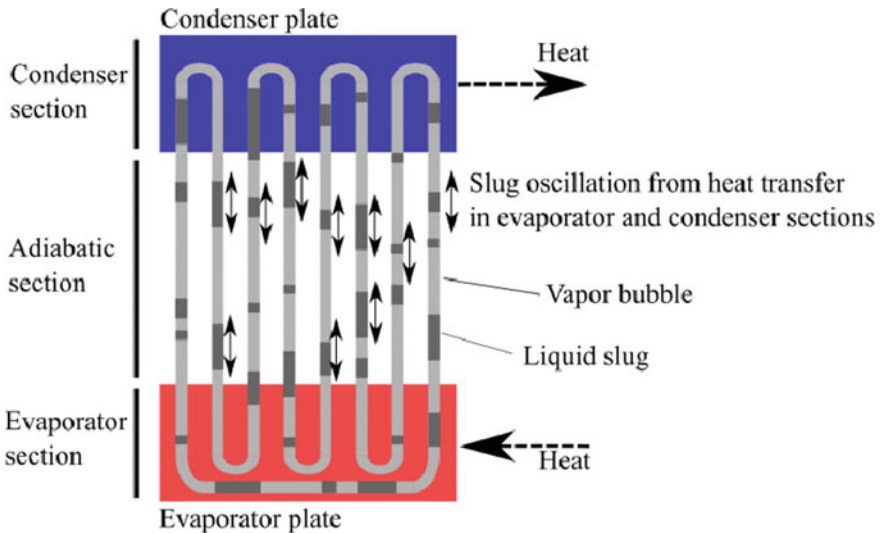
Department of Thermal Engineering, Gokaraju Rangaraju Institute of Engineering and Technology, Hyderabad, Telangana, India

[1]) patented and proposed by Akachi [2] in 1990 has received attention in various spatial applications and cooling of electronics. Pulsating heat pipes or oscillating heat pipes comes under the category of wickless heat pipes, wherein the uniform temperature at heat source is maintained by removal of heat through pulsating or oscillating action of working fluid. Like traditional wicked heat pipes, pulsating heat pipes also consists of evaporator section (where fluid is heated), condenser section (where fluid is condensed) and an adiabatic section except for thin capillary tube bent into few turns with liquid (working fluid) filled in it as shown in figure below. “When difference in temperature between evaporator and condenser hits certain threshold value the slugs of liquid and bubbles of gas start oscillating, which results in transfer of heat from the source.” In the process of transporting heat, an oscillating heat pipe goes through three states namely steady, transient and new-steady state as described in [3] (Fig. 1).

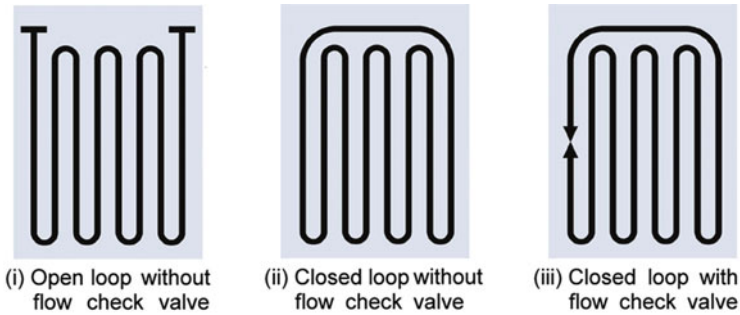
Oscillating heat pipes can be in three forms, i.e., open-loop PHP, closed-loop PHP and closed-loop PHP with check valve. But, due to better liquid flow probability CLPHP is preferred over OLPHP. Closed-loop PHP with check valve can be used when flow is to be regulated (Fig. 2).

Though, the design of pulsating heat pipe appears to be simple-but the heat transfer and thermo- hydrodynamic characteristics are quite complex. In order to predict complex heat transfer performance, a conclusion was given by Shafii et al. [4] through this mathematical model that sensible heat accounts for majority heat transfer (which is 95%) and oscillating flow is driven by latent heat.

Accounting to its intriguing thermo-hydrodynamic performance of OHP, visualization of flow was done by Tong et al. [5] recording that oscillation amplitude



**Fig. 1** Pulsating heat pipe working



**Fig. 2** Types of heat pipe

is high at starting conditions, but when working fluid attains steadiness-consistent circulation can be observed (depending on experimental run).

## 2 Parameters Affecting Pulsating Heat Pipe

With regard to various parameters affecting pulsating heat pipe performance, experiments conducted by Khandekar [6–8], signifies that capability of heat transfer is mainly affected by selection of working fluids, evaporating tube length, condensing tube length, inner diameter, number of turns and variation of thermal resistance with heat input. Desirable thermo-physical properties of working fluids include high  $k$ ,  $C_p$ , and low vaporization LH, (surface tension),  $\nu$  (dynamic viscosity). Though binary fluids are studied along with pure fluids as a working fluid for pulsating HP, Pachghare [9, 10] observed that there is no significant difference in performance of binary fluids over pure fluids. But in pure fluids, acetone has given desired performance and variation of thermal resistances with heat inputs are given, i.e., with increase in heat input thermal resistance decreases.

Though there can be many orientations of pulsating heat pipes for heating, few standard orientations are represented above. Regarding heating mode of evaporator, experiments by Yang [1] resulted that for 2 mm ID tubes bottom heating mode gives best results. With respect to filling ratios Yang [1] states that 50% fill ratio gives required thermal performance under any orientation. Whereas Pachghare [11] conducted experimentation on 2 mm ID and 3 mm OD, better heat transfer and least thermal resistance characteristics are observed at 60% fill ratio.

### 3 Experimental Setup

The experimental setup shown in Fig. 3 is fabricated and tested with respect to the dimensions as in [10] but with 5 turns. The experiment setup consists of pulsating heat pipe with evaporator and condenser with copper tubes of 2 mm inner diameter and 3.6 mm outer diameter. The tubes in adiabatic section are made of borosilicate glass. The adiabatic section is covered with transparent glass for flow visualization. To maintain vacuum inside the tubes, a vacuum pump is incorporated. To measure pressure inside tubes, a manometer is used.

The water in condenser section is continuously supplied through a pump to extract heat from condenser section. Heat input is given to the evaporator through heat variac. Data logger and laptop are used to draw and store experimental data. The details of thermocouples for reading temperature values are shown in Table 1.

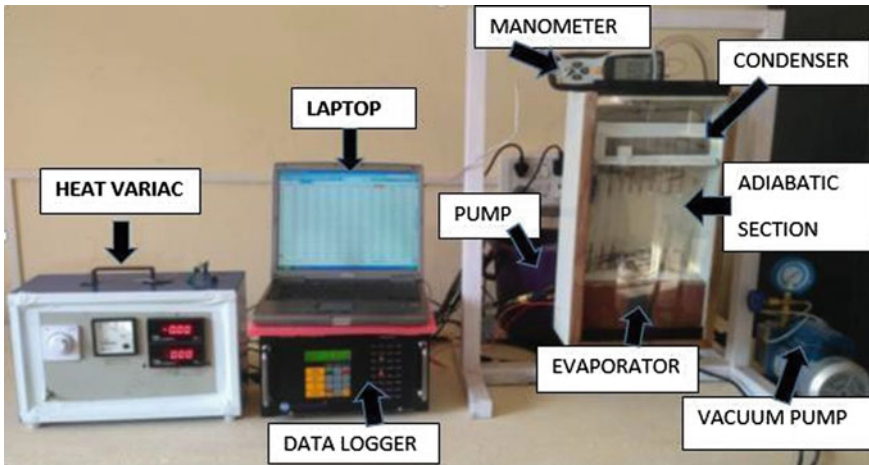


Fig. 3 Experimental setup

Table 1 Thermocouple placements

Thermocouple's	Placement of thermocouple
T1–T10	Symmetric arrangement in condenser
T13–T22	Symmetric arrangement in evaporator
T11 and T12	Water inlet and outlet
T23–T26, T27–T30	Evenly attached on evaporator, condenser

### 3.1 Sample Calculation

The variation of thermal resistance of PHP is calculated by equation below.

$$R_{th} = (T_e - T_c)/Q \tag{1}$$

Where  $Q$  = heat flux in (w)

$T_e$  = Evaporator Temperature in (K)

$T_c$  = Condenser Temperature in (K).

Say for water at 20 W, the average evaporator temperature is calculated as follows,

$$T_e = (T_1 + T_2 + \dots + T_{10})/10. \tag{2}$$

where ( $T_1-T_{10}$ ) are thermocouple readings from evaporator as follows, (Table 2).

The average condenser temperature is calculated as follows,

$$T_c = (T_{13} + T_{14} + \dots + T_{22})/10. \tag{3}$$

where ( $T_{13}-T_{22}$ ) from experiment are, (Table 3).

$T_{11} = 27.6, T_{12} = 28.1.$

From Eqs. (2) and (3),  $T_e = 63.06, T_c = 38.35.$

Therefore, from equation (1),

$R_{th} = (63.06-38.35)/20 = 1.23.$

**Table 2** Average evaporator temperatures

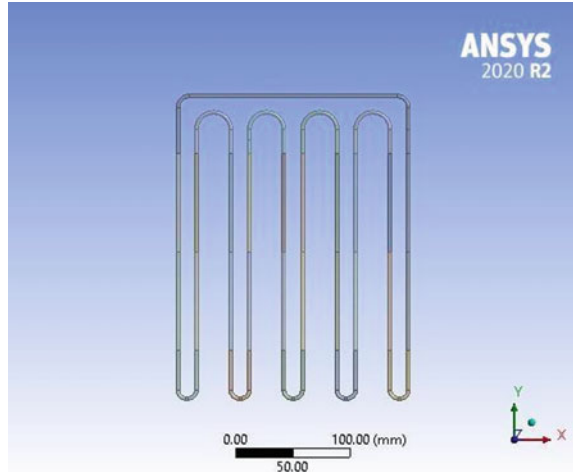
$T_1$	$T_2$	$T_3$	$T_4$	$T_5$	$T_6$	$T_7$	$T_8$	$T_9$	$T_{10}$
71	63.4	76.1	74.2	69.1	66.4	73.2	81.2	61.4	73.6

**Table 3** Average condenser temperatures water inlet and outlet temperatures being

$T_{13}$	$T_{14}$	$T_{15}$	$T_{16}$	$T_{17}$	$T_{18}$	$T_{19}$	$T_{20}$	$T_{21}$	$T_{22}$
41.8	34.1	33.4	32.4	42.4	36.1	37.4	32.4	37.1	36.4



**Fig. 4** Geometry of 5-turn CLPHP



## 4 CFD Modeling

The CFD analysis is performed in **ANSYS-FLUENT R2020**, with volume of fluid model.

### 4.1 Geometry

The geometry is modeled in ANSYS design modeler, with below mentioned dimensions (Fig. 4).

Evaporator length = 42 mm

Condenser length = 50 mm

Adiabatic length = 170 mm

Inner diameter = 2 mm

Outer diameter = 3.6 mm.

### 4.2 Meshing the Geometry

Before meshing, the geometry is divided into named selections (evaporator, condenser, adiabatic, symmetric plane-named selections and air, working fluid-body selection) to apply boundary conditions in setup. The mesh settings used were default for the geometry. The statistics of meshing are as follows,

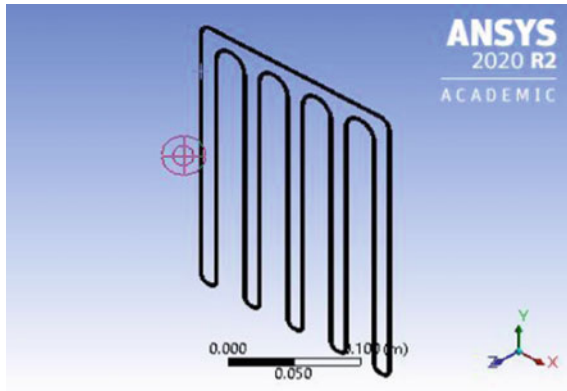


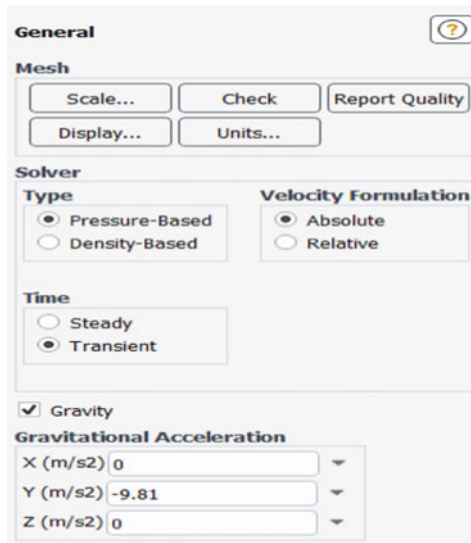
Fig. 5 Mesh

Number of nodes: 137493

Number of elements: 94702 (Fig. 5)

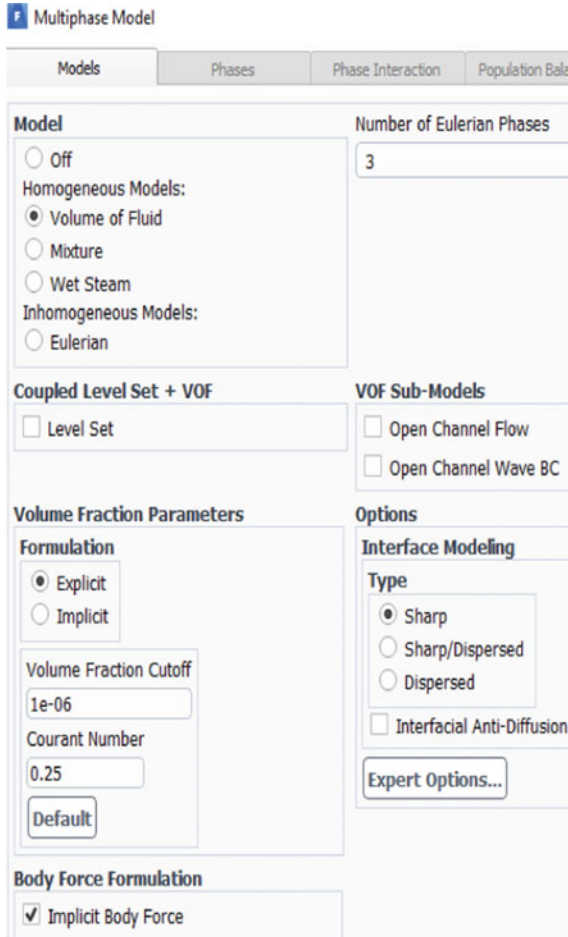
### 4.3 Analysis Setup

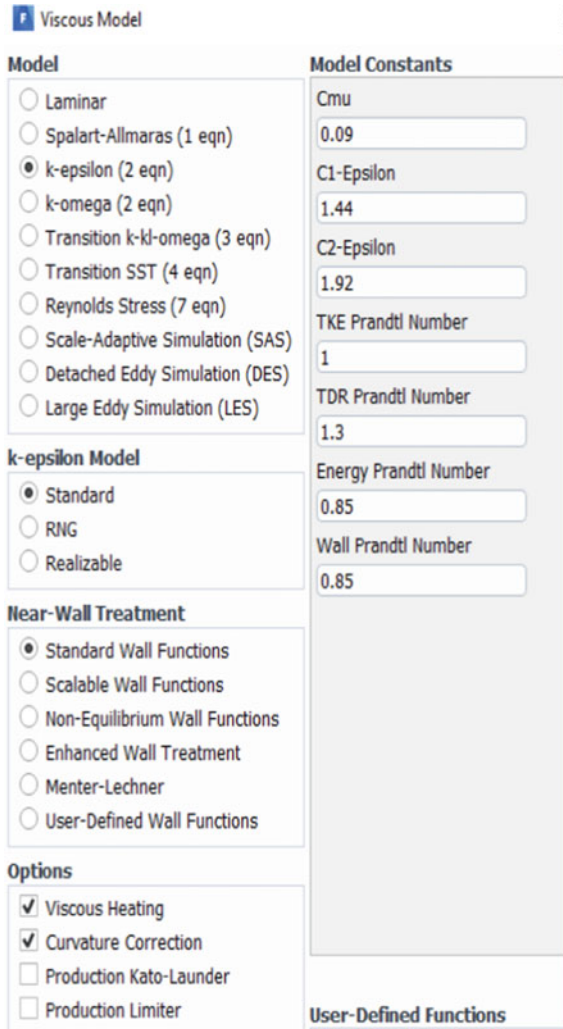
#### In General Settings



The pressure based solver is selected and as pulsating heat pipes is a transient state is selected with gravity in “-y direction” (based on geometry) marked.

**In Models**, Multi-phase modeling with volume of fluid model with number of phases as three is selected. The energy equation is marked for analysis.





**In Materials**, fluent database is used to add materials if available or materials are created with all the properties mentioned. The properties are obtained from table below as obtained in [10] (Table 4).

**Phase's setup** is done once the materials are added with air as primary fluid and selected fluid liquid and vapor as secondary fluids. Surface tension modeling is activated with number of mass transfer mechanism as one, i.e., from liquid to vapor. The mass transfer mechanism is evaporation–condensation model with saturation temperature depending on operating pressure (30 kPa) for water, acetone, water + acetone.

**Table 4** Thermo-physical properties of working fluids

Properties	Water	Acetone	Water + Acet one
Boiling point (°C)	100	56.2	78.1
$H_{fg}$ (KJ/kg)	2251.20	520.56	1385.88
Liquid density (kg/m <sup>3</sup> )	958.7	748.5	853.6
vapor density (kg/m <sup>3</sup> )	0.597	2.123	1.360
Liquid viscosity ( $\times 10^{-7}$ N-s/m <sup>2</sup> )	2790	2340.6	2565.3
Vapor viscosity ( $\times 10^{-7}$ N-s/m <sup>2</sup> )	121	89.25	105.13
Liquid thermal conductivity (W/m-K)	0.680	0.169	0.425
Vapor thermal conductivity (W/m-K)	0.0248	0.0140	0.0194
Surface tension ( $\times 10^{-3}$ N/m)	58.91	19.09	39
CP of liquid (KJ/kgK)	4.22	2.28	3.25
CP of vapor (KJ/kgK)	2.034	1.385	1.709

### Boundary Conditions

#### Evaporator section:

Momentum > no-slip wall type Heat Flux >

At 20 W HI = 9031 W/m<sup>2</sup>

At 40 W HI = 18,062 W/m<sup>2</sup>

At 60 W HI = 27094 W/m<sup>2</sup>

At 80 W HI = 36124 W/m<sup>2</sup>

And wall thickness is 0.0005 m.

#### Condenser section:

Momentum > no-slip wall type

Heat Flux > Free-convection environment with free- stream temperature of 302.5 and wall thickness is 0.0005 m.

#### Adiabatic section:

Momentum > no-slip wall type

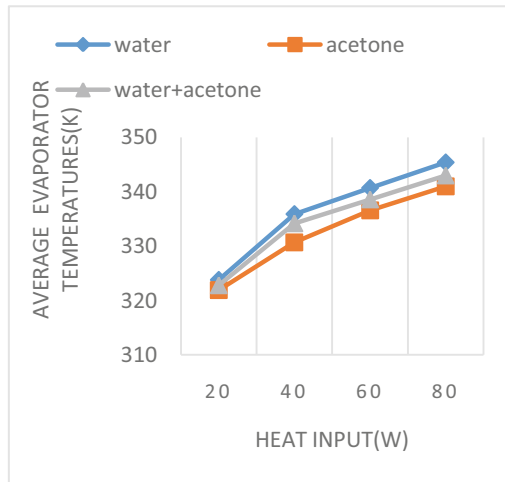
Heat Flux > 0 W/m<sup>2</sup> and wall thickness is 0.0005 m.

**Initialization and Patching**, of fluids with evaporator and condenser region is done, followed by calculation activities. The number of time steps taken are 2500 with time-step size as 0.0005.

## 5 Results and Discussion

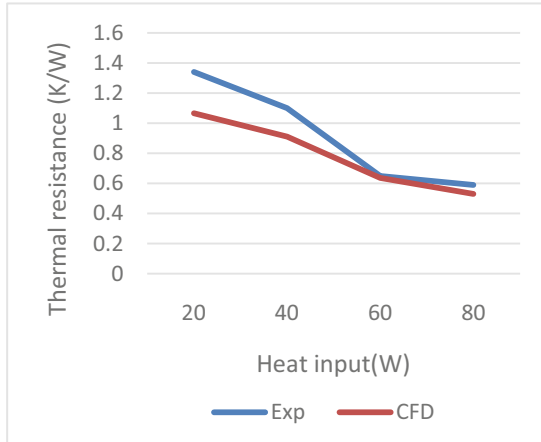
The experimental results obtained are compared with CFD thermal resistance data of the same CLPHP under 50% fill ratio and vertical heating mode.

### 5.1 Graphs



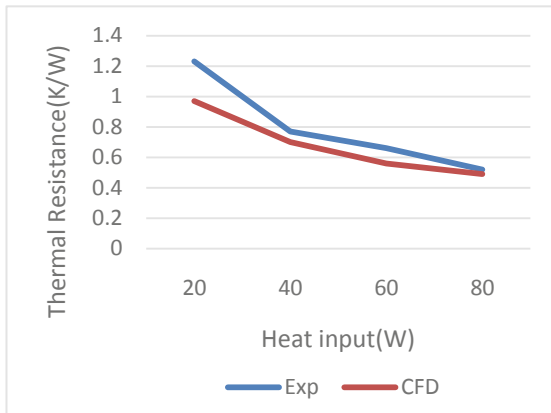
Heat input versus average evaporator temperatures of CFD for water, acetone, water + acetone

The graph above shows variation of average evaporator temperature with heat input. It is observed that average evaporator temperature increases continuously with heat input for all working fluids in CFD analysis.



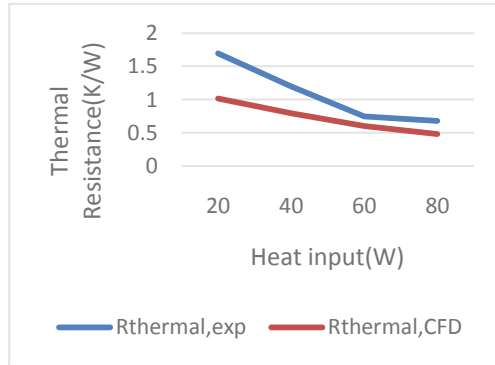
Heat input versus experimental and CFD thermal resistance for water

The graph above infers that with increase in heat input, thermal resistance decreases for water. The experimental thermal resistance is higher than CFD thermal resistance.



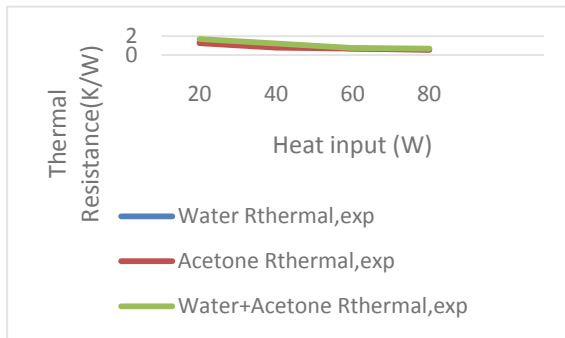
Heat input versus experimental and CFD thermal resistance for acetone

The graph above infers that thermal resistance of acetone decreases with increase in heat input (but decrease is more than water). The experimental thermal resistance is more than CFD thermal resistance.



Heat input versus experimental and CFD thermal resistance for water + acetone

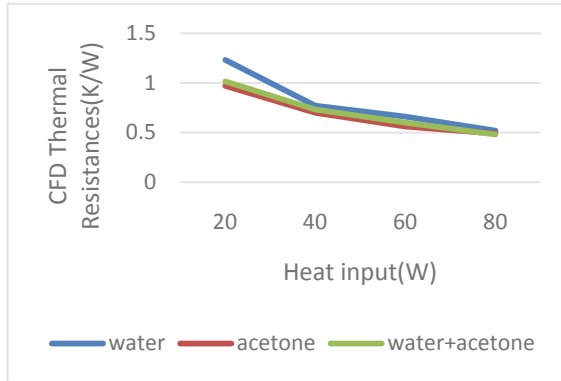
The graph above infers that with increase in heat input, thermal resistance decreases and experimental thermal resistance are more than CFD thermal resistance.



Heat input versus experimental thermal resistance of water, acetone, water + acetone

The comparison of experimental thermal resistances for water, acetone, water + acetone show that thermal resistance increase with increase in heat input and thermal resistance of water + acetone is higher.

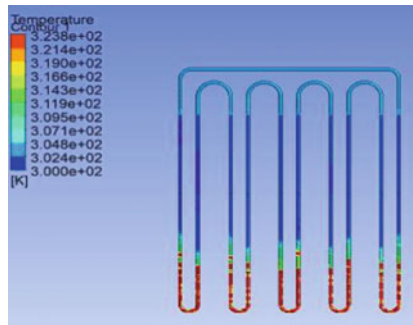




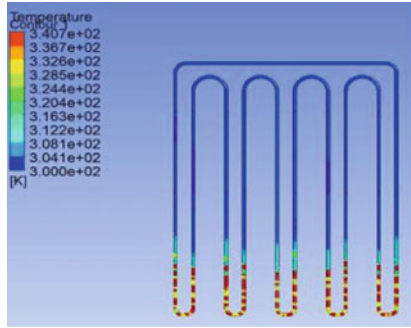
Heat input versus CFD thermal resistances of water, acetone, water + acetone

The graph above implies that thermal resistances of working fluids decrease with increase in heat input. The thermal of water is highest and acetone is least for given heat input.

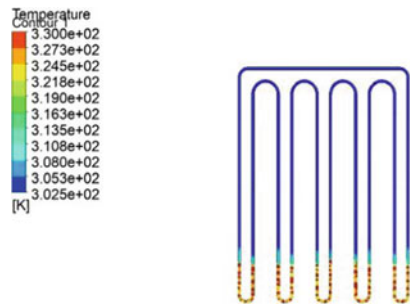
### 5.2 CFD Temperature Contours



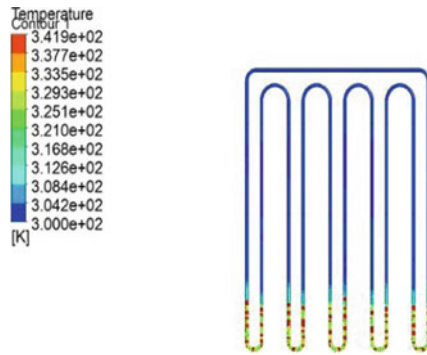
Water at 20 W, 50fr, VH



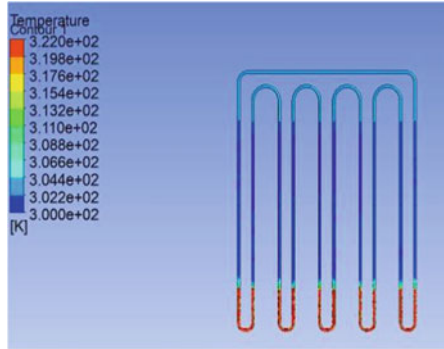
Water at 60 W, 50 fr, VH



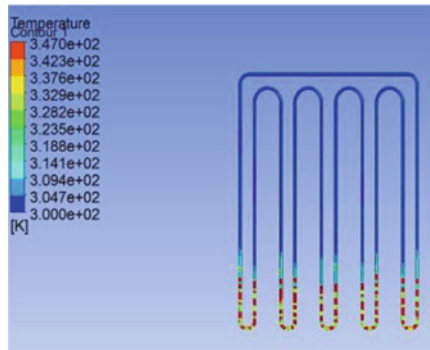
Acetone at 40 W, 50 fr, VH



Acetone at 80 W, 50 fr, VH



Water + Acetone at 20 W, 50% fill ratio, VH



Water + Acetone at 20 W, 50% fill ratio, VH

## 6 Conclusions

The presented work involves CFD validation of experimental results of closed-loop pulsating heat pipes. The obtained experimental and CFD results for water, acetone and water-acetone with 50% filling ratio and for heat input range of 20–80W with bottom heating mode are compared. The conclusions drawn from this work are as follows,

1. Multi-phase flow has been visualized successfully.
2. The CFD thermal resistance's is in close agreement with experimental thermal resistances for water and acetone and water + acetone.
3. It is observed that thermal resistance decreases as heat input increases, irrespective of working fluid.
4. During start-up of CLPHP, water + acetone is observed to have high thermal resistance.

5. Acetone is observed to have low thermal resistance among water, acetone and water + acetone in both CFD and Experimental results. Thus, contributing to better heat transfer of CLPHP.
6. It is found that CFD results of water + acetone binary mixture (1:1 by volume) is higher than water and acetone, i.e., thermal resistances of water + acetone mixture is in between water and acetone.
7. Acetone, water, water + acetone (1:1 by volume) is the order observed for better CLPHP's performance.

## References

1. Yang H, Khandekar S, Groll M (2008) Operational limit of closed loop pulsating heat pipes. *Appl Therm Eng* 28:49–59
2. Akachi H (1990) Structure of a heat pipe. U. S. Patent 4921041
3. Jiao AJ, Maa HB, Critser JK (2009) Experimental investigation of cryogenic oscillating heat pipes. *Int J Heat Mass Trans* 52:3504–3509
4. Shafii M, Faghri A, Yuwen Z (2002) Analysis of heat transfer in unlooped and looped pulsating heat pipes. *Int J Numer Meth Heat Fluid Flow* 12(5):585–609
5. Tong B, Wong T, Ooi K (2001) Closed loop pulsating heat pipe. *Appl Therm Eng* 21(18):1845–1862
6. Khandekar S, Groll M (2004) An insight into thermohydrodynamic coupling in closed loop pulsating heat pipes. *Int J Therm Sci* 43(1):13–20
7. Khandekar S, Charoensawan P, Groll M, Terdtoon P (2003) Closed loop pulsating heat pipes part B: visualization and semi-empirical modeling. *Appl Therm Eng* 23(16):2021–2033
8. Khandekar S, Dollinger N, Groll M (2003) Understanding operational regimes of closed loop pulsating heat pipes: an experimental study. *Appl Therm Eng* 23:707–719
9. Pachghare P, Mahalle M (2013) Effect of pure and binary fluids on closed loop pulsating heat pipe thermal performance. *Int J Procidia Eng* 51:624–629
10. Pachghare P, Mahalle A (2012) Thermal performance of closed loop pulsating heat pipe using pure and binary working fluid. *Front Heat Pipes* 3:033002
11. Pachghare PR, Mahalle AM (2014) Thermo-hydrodynamics of closed loop pulsating heat pipe: an experimental study. *528 (8):3387–3394*

# Performance and Emission Analysis of DI Diesel Engine Fuelled with Magnetic Conditioned Mamey Sapote Biodiesel



G. Janardhana Raju and A. Raj Kumar

**Abstract** Magnetic conditioning has a significant effect on performance and emission characteristics of compression ignition engines. In the present work, B20 (20% of Mamey Sapote biodiesel + 80% of diesel) was conditioned with 10,000 and 12,000 Gauss intensity Neodymium N52 permanent magnets by placing on the fuel lines in between the fuel pump and fuel injector. Due to the magnetic conditioning, the complete combustion and rapid burning of the hydrocarbon fuel can be achieved. The experiments were conducted at different magnetic intensities to find the performance and emissions with base line engine and B20 with and without magnetic conditioning. From the experimental results, it is understood that magnetic conditioned B20 fuel with 12,000 Gauss has improved performance when compared to baseline engine.

**Keywords** Magnetic conditioning · Performance · CI engine · Biodiesel

## 1 Introduction

It was noticed that vegetable oils were the capable alternative to conventional diesel fuel, because their properties are very close to diesel fuel. They are renewable and can be produced easily. Rudolf Diesel demonstrated the diesel engine with peanut oil and hinted that vegetable oils would be the future alternative fuel for diesel engines [1]. Many researchers investigated the performance of vegetable oils as a fuel for CI engines, and arrived performance was poor due to high viscosity and low volatility [1–5]. Improved fuel injection pressure also effects the engine performance in the CI engines [6–8]. Experiments were conducted on SI engine with permanent magnetic intensities from 2000 to 9000 gauss. They found that the fuel consumption is reduced to 14% for 9000 gauss intensity, and the emissions of CO and HC were lowered by 30% and 40%, respectively, whereas CO<sub>2</sub> improved up to 10% [9].

---

G. Janardhana Raju

Nalla Narasimha Reddy Education Society's Group of Institutions, Hyderabad, India

A. Raj Kumar (✉)

Guru Nanak Institutions Technical Campus, Hyderabad, India

Tests were conducted on DI diesel engine at different injection pressures to evaluate the performance of with semi-adiabatic diesel engine with crude vegetable oil conditioned with magnetic induction [10]. Research was carried out on the performance of magnetic conditioned fuel in four-stroke diesel engine and reported that 2% thermal efficiency, and 5% emissions improvement was achieved [11]. The magnetic conditioning allows rapid bonding with the oxidizing medium, which result complete and rapid burning of hydrocarbon fuel [12, 13]. Experiments were conducted on CI engine with magnetic conditioned turmeric leaf oil on four-stroke single cylinder water cooled computerized engine and found that B20 fuel blend has shown brake power and indicated thermal efficiency [14].

## 2 Methodology

The evaluation of performance and emission characteristics of magnetic conditioned B20 Mamey Sapote biodiesel in single cylinder DI diesel engine with Neodymium N52 permanent magnets by placing on the fuel lines in between the fuel pump and fuel injector.

### 2.1 Experimental Procedure

Experiments were conducted on single cylinder, four-stroke water cooled with eddy current dynamometer loading computerized DI diesel engine. It is used for the investigation of performance and emission characteristics of Mamey Sapote biodiesel blend with diesel which can be used as substitute fuel. Figure 1 shows a photograph of fuel conditioning unit, and Fig. 2 represents the experimental setup. Fuel supply is assisted by exterior permanent N52 magnets with various intensities. The performances of Mamey Sapote biodiesel with magnetizer and without magnetizer at various loads are estimated. Table 1 shows the comparison properties of Mamey Sapote biodiesel blend.

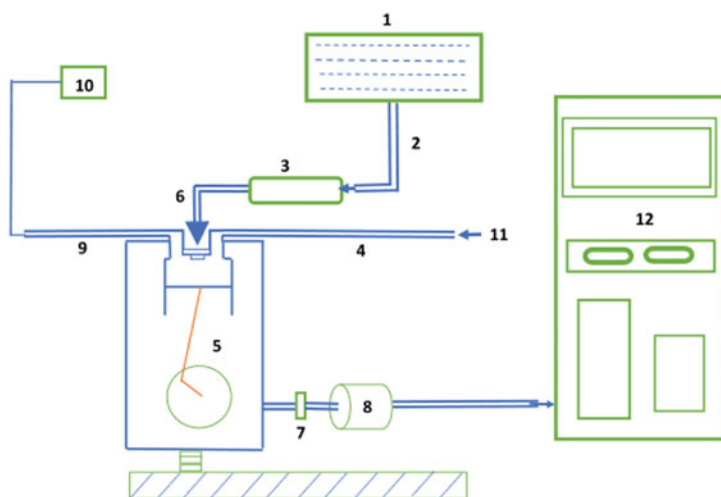
## 3 Result and Discussion

### 3.1 Effect of Magnetic Field on Performance

Figure 3 shows the increase of the brake thermal efficiency of with and without the magnetic conditioning of Mamey sapote biodiesel (B20). The BTE percentage was ranged between (3.7 and 5.6%) depending on the magnetic intensity. Figure 4



Fig. 1 Photograph of Neodymium N52 Magnets fixed on diesel engine fuel line

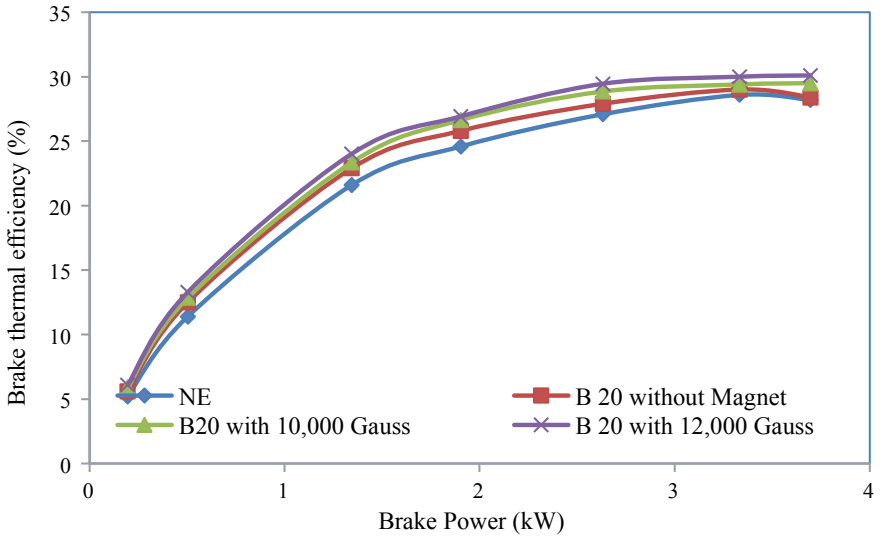


- |                      |              |                              |                               |                             |
|----------------------|--------------|------------------------------|-------------------------------|-----------------------------|
| 1. Primary Fuel Tank | 2. Fuel Line | 3. Magnetic fuel conditioner | 4. Atmospheric Air inlet pipe | 5. Engine                   |
| 6. Fuel Injector     | 7. Coupling  | 8. Eddy current Dynamometer. | 9. Exhaust pipe               | 10. Exhaust gas analyser    |
| 11. Air Inlet        |              |                              |                               | 12. Data acquisition system |

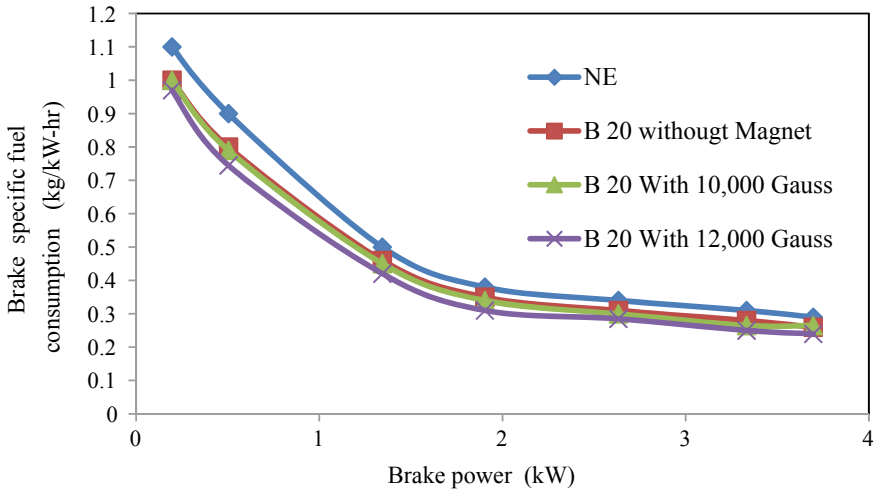
Fig. 2 Experimental setup

**Table 1** Comparison of properties of Mamey Sapote biodiesel blend with diesel

Properties	Diesel	B100	B20
Density Kg/mm <sup>3</sup>	0.842	0.875	0.853
Kinematic viscosity mm <sup>2</sup> /sec	2.5	4.25	3.32
Calorific value MJ/Kg	44	37.12	41.78
Flash point	70 °C	171	77.2



**Fig. 3** Increased brake thermal efficiency with increased magnetic intensities



**Fig. 4** Decreased BSFC with increased magnetic intensities



indicates the decrease of brake-specific fuel consumption for magnetic intensities. The BSFC was ranged between (8.6 and 17.2%). The percentage was the highest for B20, 12,000 gauss magnetic conditioned fuel.

### 3.2 Effect of Magnetic Field on Emissions

The percentages the exhaust emissions were recorded during the experimentation of the engine for Mamey Sapote biodiesel (B20) before and after magnetic conditioning with 10,000 and 12,000 gauss intensities was presented in Figs. 5, 6, 7 and 8. It was obtained that the lowering percentages of exhaust emissions (HC, CO, and smoke number) up to (8.6, 17.2, and 14.89%), respectively. But, the percentage of nitrogen oxides was increased up to 3.21%.

Magnetic conditioning of fuel breaks the hydrocarbon chains which effects the density and surface tension of the fuel, thus forms tiny droplets during atomization. These tiny droplets cause high rate of evaporation better mixing of fuel and oxygen and promotes improved oxidation. The ultimate effect is an improved rate of combustion, an improvement in brake power and reduction in emissions.

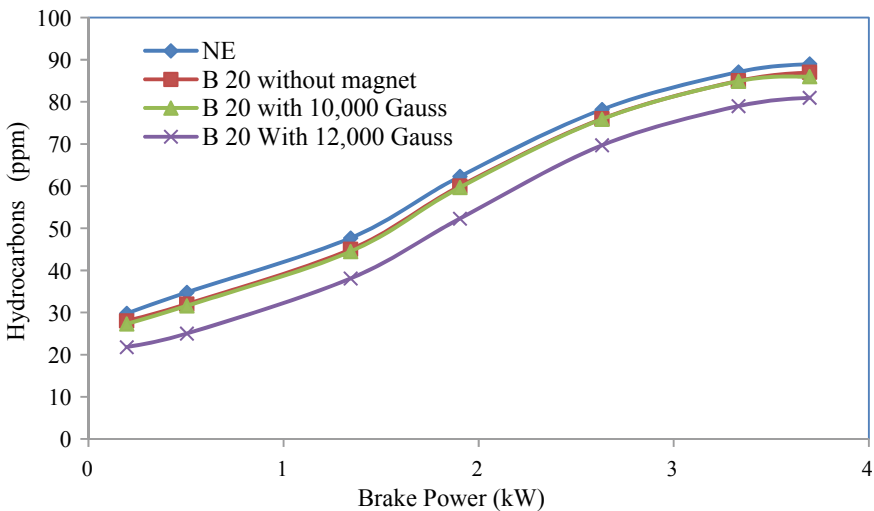


Fig. 5 Decreased hydrocarbon emissions with increased magnetic intensities

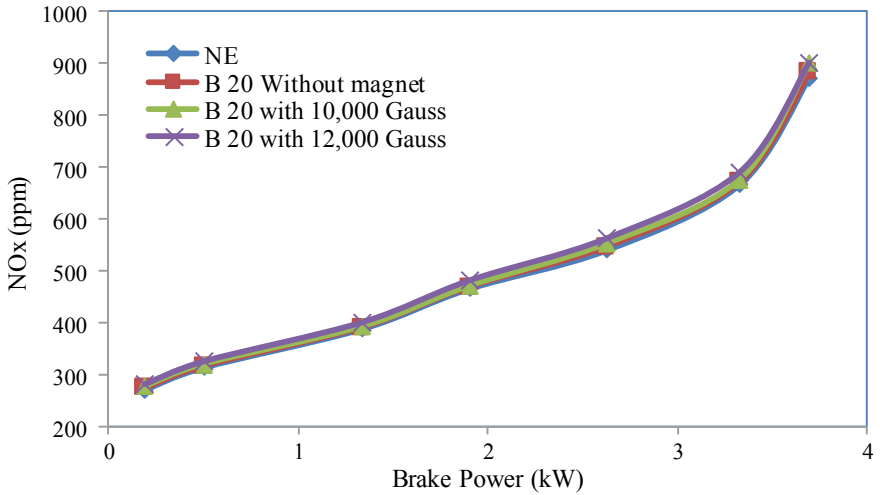


Fig. 6 Increased NOx emissions with increased magnetic intensities

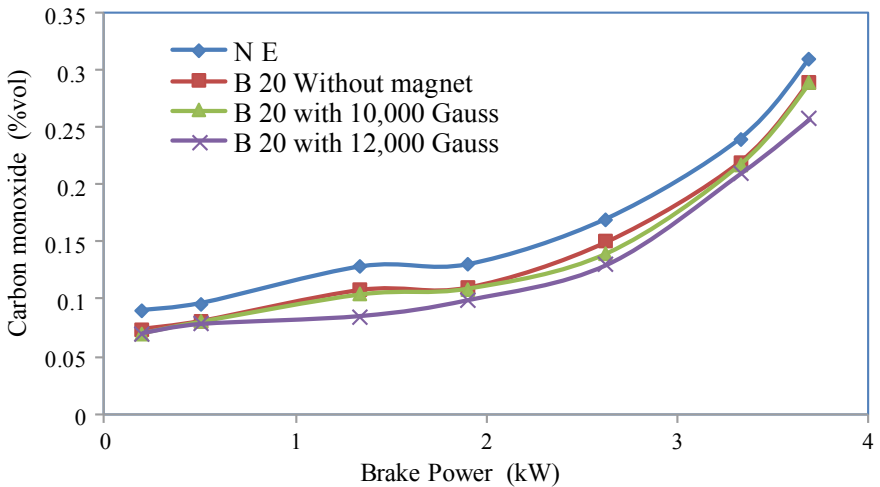
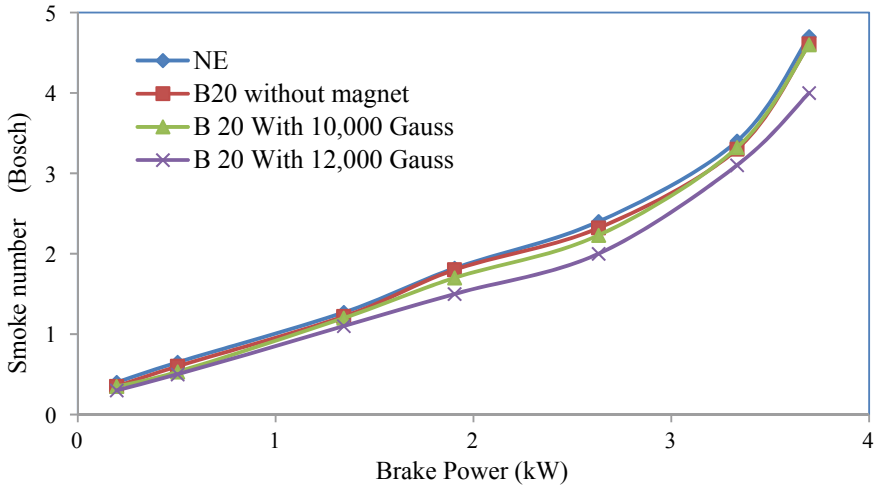


Fig. 7 Decreased carbon monoxide emissions with increased magnetic intensities

### 4 Conclusion

From the obtained experimental results, it was observed that with magnetic conditioning of Mamey Sapote biodiesel (B20) blend with two intensities the brake thermal efficiency was increased (3.7–5.6%), whereas the brake-specific fuel consumption was decreased (8.6–17.2%). The exhaust emissions (HC, CO, and smoke number) up to (8.6, 17.2, and 14.89%), respectively. But, the percentage of nitrogen oxides



**Fig. 8** Decreased smoke intensity emissions with increased magnetic intensities

was increased up to 3.21%. Hence, it is concluded the magnetic treatment of fuel improves combustion rate, performance, and reduction in emissions.

**Acknowledgements** Authors thank JNTU Hyderabad for funding the project under Collaborative Research Scheme, TEQIP-III on “Experimental investigation of a novel magnetic fuel ionization method in a DI diesel engine to improve the performance and emissions” the bearing file no: JNTUH/TEQIP-III/CRS/2019/MECH/13.

## References

1. Acharya SK, Swain RK, Mohanti MK (2009) The use of rice bran oil as a fuel for a small horse-power diesel engine. *Energy Sources Part A Recovery Utilization Environ Eff* 33(1):80–88
2. Venkanna BK, Venkataramana Reddy C, Wadawadagi SB (2009) Performance, emission and combustion characteristics of direct injection diesel engine running on rice bran oil/diesel fuel blend. *Int J Chem Biol Eng* 2(3):131–137
3. Misra RD, Murthy MS (2010) Straight vegetable oils usage in a compression ignition engine—a review. *Renew Sustain Energy Rev* 14:3005–3013
4. No SY (2011) Inedible vegetable oils and their derivatives for alternative diesel fuels in CI engines: a review. *Renew Sustain Energy Rev* 15:131–149
5. Agarwal AK, Dhar A (2013) Experimental investigations of performance, emission and combustion characteristics of Karanja oil blends fuelled DIC engine. *Renew Energy* 52:283–291
6. Jindal S, Nandwana BP, Rathore NS, Vashistha V (2010) Experimental investigation of the effect of compression ratio and injector opening pressure in a direct injection diesel engine running on Jatropha methyl ester. *Appl Therm Eng* 30:442–448

7. Agarwal AK, Srivastava DK, Dhar A, et al (2013) Effect of fuel injection timing and pressure on combustion, emissions and performance characteristics of a single cylinder diesel engine. *Fuel* 111:374–83
8. Murali Krishna MVS, Chowdary RP, Kishen Kumar Reddy T, Murthy PVK (2012) Performance evaluation of waste fried vegetable oil in a low grade low heat rejection diesel engine, *Int Res Mech Eng Technol* 2(2):35–43
9. Ali S (2014) Faris effects of magnetic field on fuel consumption and exhaust emissions in two-stroke engine. *Energy Procedia* 18(2012):327–338
10. Murali Krishna MVS (2017) Influence of injection pressure on performance parameters of semi adiabatic diesel engine with crude vegetable oil with magnetic induction. *IJRSET* 4(7):62–71
11. Jain S et al (2012) Experimental investigation of Magnetic Fuel Conditioner (MFC) in I.C. engine, *IOSR J Eng* 2:27–31
12. Mingdong S et al (1984) Combustion efficiency of magnetized petroleum Fuels, *Chinese science bulletin*
13. Cummins JCL (1976) Early IC and Automotive Engine" SAE paper 760604. Society of Automotive Engineers, Warrendale, Pennsylvania, USA, pp 18–26
14. Halli G Performance analysis of CI engine fuelled with turmeric leaf oil assisted by magnetic fuel energizer. Project reference No. 41S\_B\_BE\_031

# Comparison of Energy and Exergy Analysis of Parabolic Fin Solar Still with Conventional Solar Still



V. Raja Ranadher Naike, Shaik Hussain, Ajay Kumar Kaviti,  
and Akkala Siva Ram

**Abstract** Potable water is essential for different purposes for every living entity to live healthily on earth. This water is a critical need of every human for various applications such as drinking, cooking food, agriculture, and industrial purposes. In this experimental study, parabolic fin's influence on the energy and exergy of basin still performance was obtained with three different water depths such as 1, 2, and 3 cm, compared with conventional still. Aluminum parabolic fin with 50-mm height and 30-mm diameter was fixed on the bottom basin liner. The experimental study was conducted in the climatic conditions of Hyderabad, Telangana, India (17.3850 °N, 78.486 °E). The calculated data shows that the energy efficiency obtained for the parabolic fin-assisted still are 65%, 56%, and 53%, respectively. The exergy efficiency obtained for the modified still was improved by 6.06%, 3.57%, and 3.07%, respectively, over conventional still for different depths of water. The cumulative water yield obtained from the parabolic fin-assisted still is 1250 ml, 1115 ml, and 1015 ml at the 1-cm, 2-cm, and 3-cm water depths. The 1-cm level of basin salt water gave the optimum energy and exergy values to other water depths for both parabolic fin still and conventional still.

**Keywords** Parabolic fins · Energy · Exergy · Efficiency · Solar still

## 1 Introduction

Naturally available water on the earth is a vital tool to the human being. It is an essential human's need to lead life. The Earth is the only planet to live comfortably in our solar system. It is covered with three-fourth part of natural water resources, in that only 1% of the water is available for our utility [1].

---

V. Raja Ranadher Naike · S. Hussain  
Department of Mechanical Engineering, MREC, Hyderabad, India

A. K. Kaviti (✉) · A. S. Ram  
Department of Mechanical Engineering, VNRVJIET, Hyderabad, India

About 97% of the amount is unusable ocean saltwater, and 2% is in the form of ice [2]. Since the living organisms also relies on water, absence of it could cause a water crisis and food crisis. This lack of food and water can cause a food chain imbalance [3]. The drinkable water crisis can solve by solar still. It is a desalination device to make pure water from brackish [4].

The device solar still is mainly used in solar desalination because of its low fabrication cost, simple operation, and eco-friendliness [5]. Two methods can obtain the performance of the still system, which are energy and exergy analysis. Depending on first law of thermodynamics, energy analysis represents conservation of energy and the quantitative element of energy transfer [6]. The second law of thermodynamics exergy analysis represents the energy quality and involves the uncertainty while analyzing the system. It can also give information on how the performance of the system is degraded, where, and how much [7].

Several experimental studies have been conducted to investigate still system's performance analysis of energy and exergy. Layek [8] improved the single-slope stills energy and exergy efficiency using black-colored ink, solution of black color dye in saltwater, and photocopier on the surface of basin water. These absorbing materials can receive more radiation from the Sun, which can help more water evaporation. The final data obtained showed that the energy and exergy efficiencies for these absorbing materials are about 41.3%, 43.42%, and 45.79% and 5.9%, 6.34%, and 7.10%, respectively.

Rajaseenivasan et al. [9] experimented on a single- and double-glazing stills to obtain how exergy efficiency affected with wick materials and mild steel pieces. From the result data, the mild steel pieces gave higher efficiency values of exergy, for these two stills are 1.412% and 2.072%, respectively. Yousef et al. [10] investigated the effect of absorbing material such as steel mesh fibers and pin fins with hollow cylindrical on efficiency of energy and exergy of the single glass-covered still. In this work, three cases of still have been carried out, which are (i) standard still, (ii) pin fins (hollow cylindrical) used still, and (iii) still with steel wool fibers. Their results reveal that the greater energy efficiencies for cases (i), (ii), and (iii) are obtained to be 42%, 45.5%, and 52.5%, respectively. The efficiency values of exergy for case (ii) and (iii) are improved by 14% and 23%, respectively.

Appadurai and Velmurugan [11] used rectangular fins in the single-slope solar still to provide more heat transfer area and receive more radiation energy from the Sun. This study confirmed that due to the fin's effect, still's thermal performance was improved. Velmurugan et al. [12] tested still productivity with absorber materials such as rectangular fins and sponges. These fins improve the water temperature, and sponges provide more evaporation area to solar radiation. Results revealed that due to fins and sponges, productivity was improved by 45.5% and 15.3%.

El-Sebaai et al. [13] assisted strip fins to solar still to improve the transfer rate of heat from still absorber plate to the saline water. They concluded that the efficiency and water yield of still device was enhanced with rise in fin's height and reduced with grow in fin's number and thickness. Alaian et al. [14] examined the influence of pin fin's wick material plane on the basin still with single slope performance and found the efficiency of still about 55% along with 23% improved water output. Sebaai and

Naggar [15] performed experiments on solar stills using fins with various fin materials such as stainless steel, glass, iron, copper, mica, aluminum, and brass. Further, evaluated the thermal performance of the still.

Hardik and Modi [16] conducted experiments on two double-sloped glass cover stills (one with circular hollow fins and another with square hollow fins) to evaluate the still's productivity and efficiency. Their results revealed that the obtained productivity for circular-finned still is 54.22%, 38.49%, and 43.86% higher than square-finned still. The efficiency obtained for circular-finned still is 54.19%, 34.81%, and 62.24% higher over circular-finned still for 1-cm, 2-cm, and 3-cm depth of salty water.

According to the above literature, a limited number of experiments have been conducted on double-sloped still system thermal performance, still device utilizing the parabolic fins to improve its energy and exergy performance. Hence, this experimental study's main aim is to obtain the energy and exergy performance using parabolic fins as a performance enhancer in the still and compared to conventional still at 1-cm, 2-cm, and 3-cm depth of brackish water.

## 2 Experimental Setup

Two similar stills with a double slope were fabricated for this work as shown in Fig. 1. One is normal still, and parabolic fins modify another. The solar still basin having its length, width, and heights 1 m, 0.5 m, and 0.2 m, respectively. This basin is constructed with 2-mm thick aluminum sheets for its better heat transfer rate and lower price. It is painted with black-colored paint to enhance solar radiation



**Fig. 1** Photograph of the experimental setup

absorption feature. For providing more heat transfer area, 18 parabolic fins with 50-mm height and 30-mm diameter are attached to the basin's base plate.

The still basin sides and bottom are insulated by 5-cm and 10-cm thickness of Thermocol sheets and enclosed by a wooden box. The upper side of the still is protected with two glasses of 4-mm thick with an inclination angle of  $17^\circ$  [17]. Thermocouple wires are used to obtain the temps at basin liner, covered glasses, and saltwater of basin. These thermocouples are connected to a data logger. A solar power meter is used for solar intensity measurements. An electronic anemometer is used to check the velocity of the wind. The beakers of 1000-ml quantity are used to collect half an hourly water output on the colored eastern side and western side of both still. The temperatures of still basin, water, glazing, and ambient and this solar intensity and wind velocity are also noted down for every 30 min of time intervals from 9:30 AM–5:00 PM. An exploratory research is carried out simultaneously with normal still device, and parabolic fin-assisted solar still by increasing the water from a depth of 1 cm to 3 cm to analyses both the stills' energy and exergy performance in the same climatic conditions. All of the tests are conducted in the average solar conditions during the time span of November 2020.

### 3 Results and Discussion

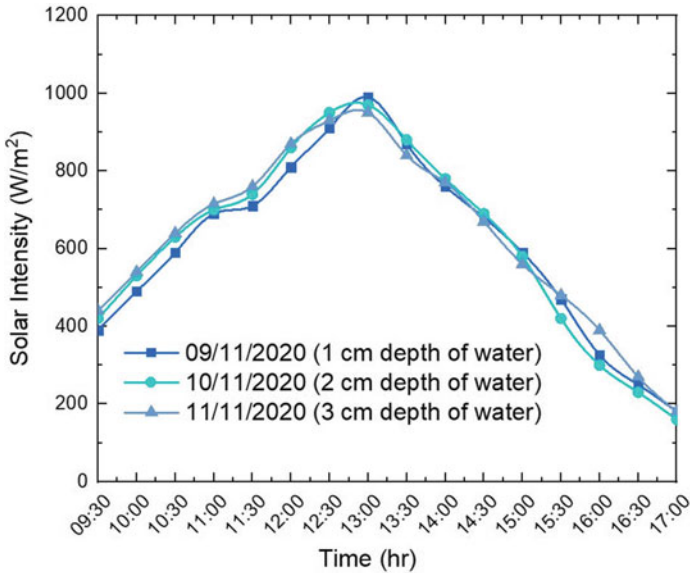
The influence of parabolic fins on the energy and exergy performance of a double-slope still device is performed in this experimental work and compared with normal still device. The tests were conducted with these two stills for the different levels of salt water. The tests were conducted for different water quantities are 1 cm, 2 cm, and 3 cm in the month of November 2020.

The variations of solar radiation intensity concerning local time for three test days 9th, 10th, and 11th November. The maximum intensities of solar radiation are  $990 \text{ W/m}^2$ ,  $970 \text{ W/m}^2$ , and  $950 \text{ W/m}^2$  obtained at noon, and gradually solar intensity values decrease in the evening time are shown in Fig. 2.

The temperature changes with time of the basin liner, basin water, glazing cover, and atmosphere for the parabolic fin-assisted solar still and standard solar still at the 1, 2, and 3 cm water levels as shown in Fig. 3. The still parts temperature increases as the intensity of sunrays increases, obtain the greater value, and then reduced until sunset. The fins contained basin liner receive the additional radiation heat energy that results in higher salt water temperature due to the reason of uniform heating of basin water by the parabolic fins. Experimental results depict that the temperature of basin liner and basin water of the parabolic fin-assisted still system remains greater than usual still for the different water levels (like 1, 2, and 3 cm).

The variation of cumulative pure water yield with time for the parabolic fin-assisted solar still and normal still and for different water levels like 1, 2, and 3 cm are shown in Fig. 4. The cumulative pure water yield values obtained from the parabolic fin-assisted still are 1250 ml, 1115 ml, and 1015 ml, and the conventional still values are 1180 ml,  $1050 \text{ ml/m}^2$ , and 940 ml for different levels of water. The



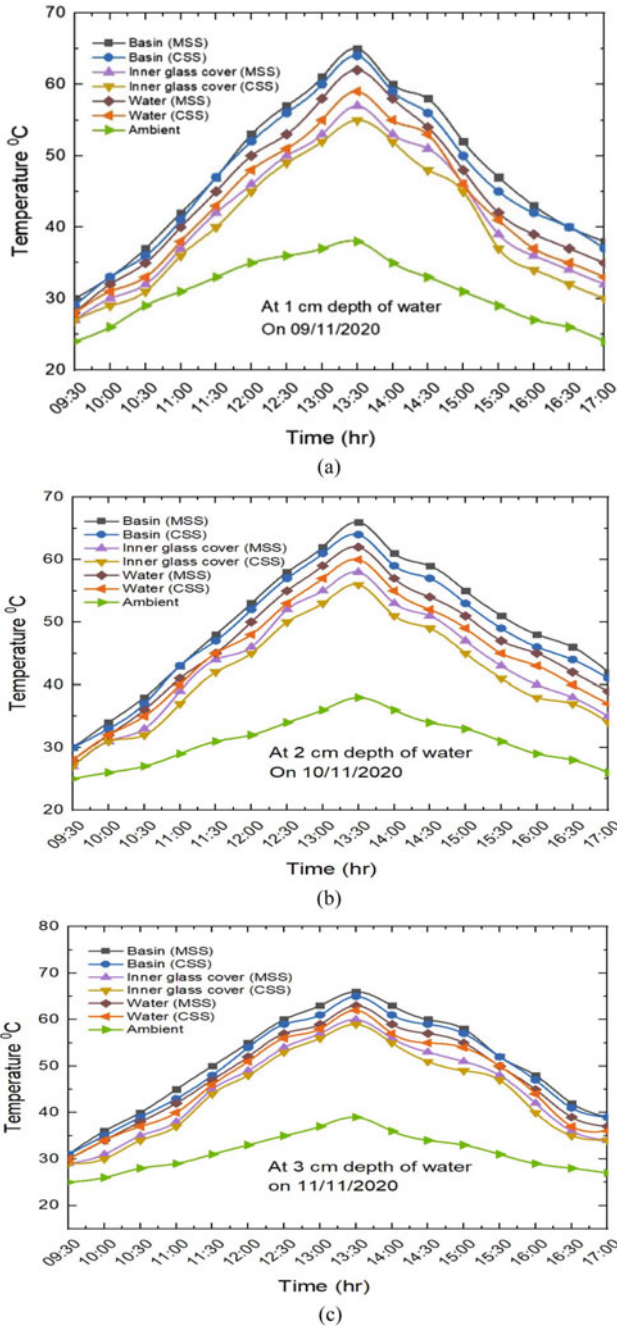


**Fig. 2** Variation of solar intensity with time for different depth of water

obtained water yield from modified still was improved by 5.93%, 6.19%, and 7.97%, respectively, compared to conventional still. This indicates that the parabolic fin-assisted base plate can receive more Sun radiation energy and enhances the pure water yield rate compared to conventional still. The still system’s potable water yield depends on the saline water and glazing cover temperature values. The remaining available basin water and glazing cover has the lesser temperature difference for the conventional still device compared to parabolic fin-assisted still device. Hence, the pure water yield of the conventional still remains lesser than the parabolic finned solar still system.

The variation of three heat transfer coefficients (like convection, radiation, and evaporation) with time from basin saltwater to glazing inside surface for the parabolic fin-assisted solar still and conventional still for different levels of water such as 1, 2, and 3 cm as shown in Fig. 5. These heat transfer coefficients reach the maximum value at around 1:30 PM for both the stills and then decreases in the evening time duration. From the experimental observation, parabolic fin-assisted still have the higher heat transfer coefficient values due to higher temperature in this still system compared to the conventional still system.

The energy efficiency variation with time for the parabolic fins modified still and normal still for the varying depths of saltwater of the basin is shown in Fig. 6. For the parabolic fin modified still, 65%, 56%, and 53% efficiencies were obtained, and for conventional still, 60%, 52%, and 49% efficiency was obtained for the different levels of water like, 1 cm, 2 cm, and 3 cm, respectively. Accordingly, 8.33%, 7.69%,



**Fig. 3** Variation of temperatures with time for still components and ambient for **a** 1-cm **b** 2-cm, and **c** 3-cm depth of water

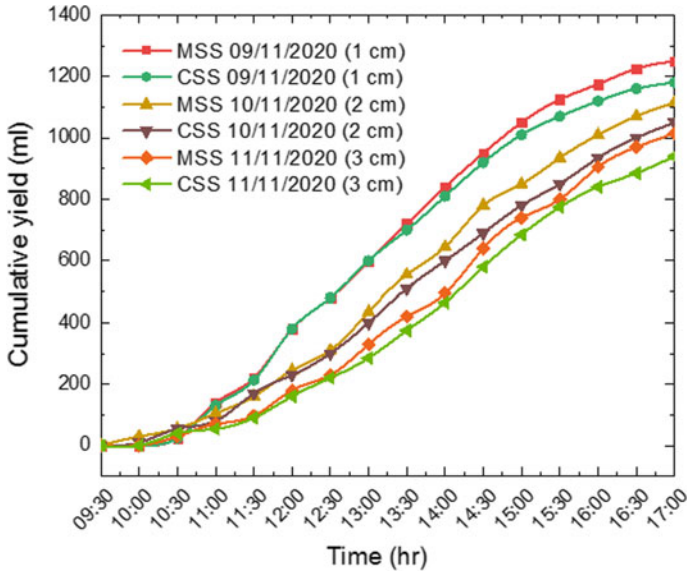
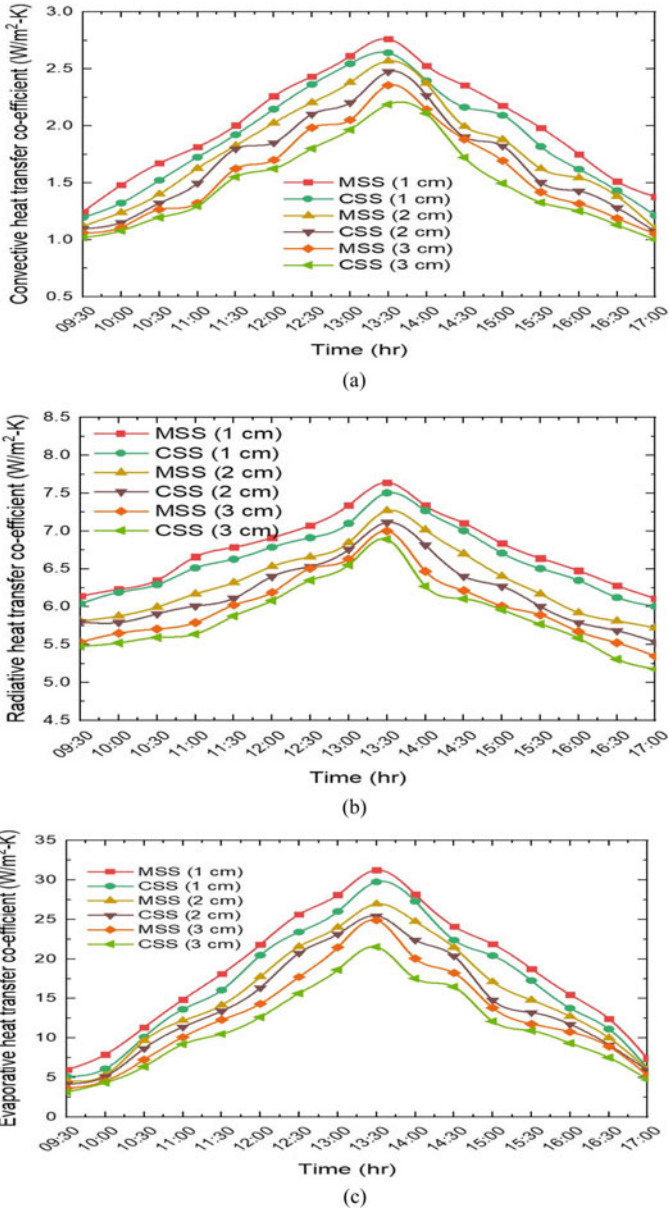


Fig. 4 Cumulative water yield variation with time for MSS and CSS at different depths of water

and 6.24% greater efficiencies were obtained for the modified still due to parabolic fins’ effect compared to conventional still.

The changes of the exergy destruction with respect to time for the parabolic fin-modified still, conventional still components like basin liner, water, and glazing cover at varying depths of saline water are shown in Fig. 7. For these still components, the exergy destruction values occurred maximum at around 1:30 PM and then reduces with evening time duration. The base plate has a higher exergy destruction value than other components for the water levels like 1, 2, and 3 cm which can observe figure. The lesser temperature difference of the still basin liner and salty water base is cause for greater destruction of exergy in the base plate. The more temperature difference can enhance the basin base plate’s exergy flow to basin saltwater and reduce the exergy destruction. In saltwater and cover of glass material, the destruction of exergy is lower compared to basin plate mainly due to the more difference in temperature between the water and glass inside area and glass outer surface and atmosphere.

The variation of efficiency of the exergy with time for both the stills for the varying depths of salty water in basin is shown in Fig. 8. The parabolic fin still and conventional still efficiencies were obtained are 3.50%, 2.90%, and 2.35% and 3.30%, 2.80%, and 2.28%, respectively, for the water levels are 1 cm, 2 cm, and 3 cm. Hence, 6.06%, 3.57%, and 3.07% greater efficiency were obtained for the parabolic fin still compared to conventional still. The reason for the degradation of energy quality is that exergy efficiency has less values than efficiency of energy values.



**Fig. 5** Variations with the time of **a** Convective **b** Radiative and **c** Evaporative Heat transfer coefficients for MSS and CSS at different water depths

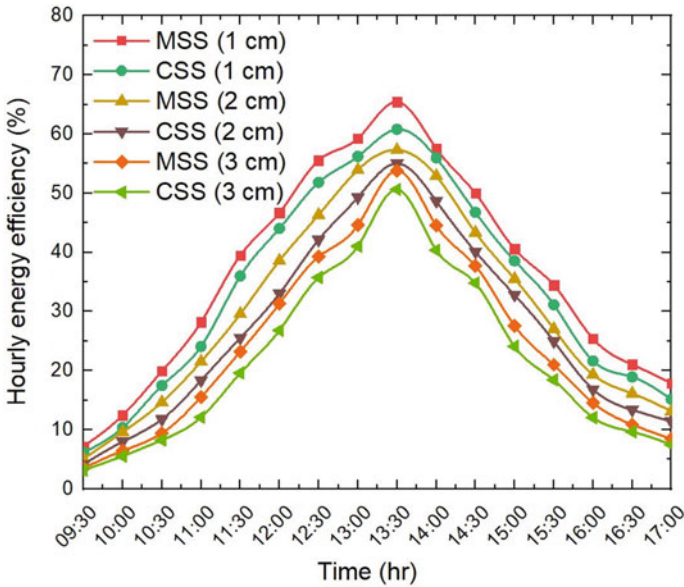
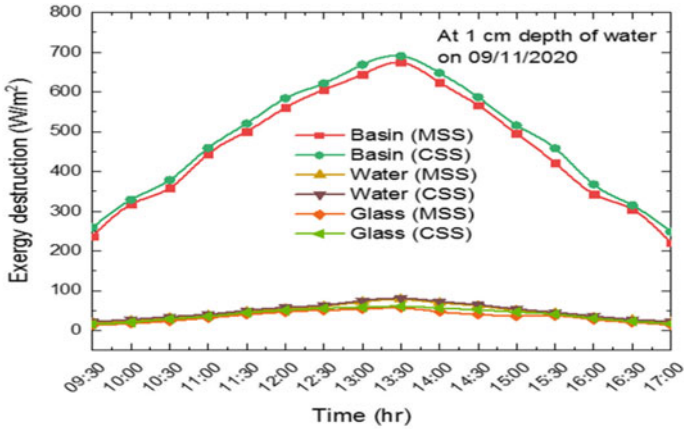


Fig. 6 MSS and CSSs energy efficiency variation with time for varying depths of water

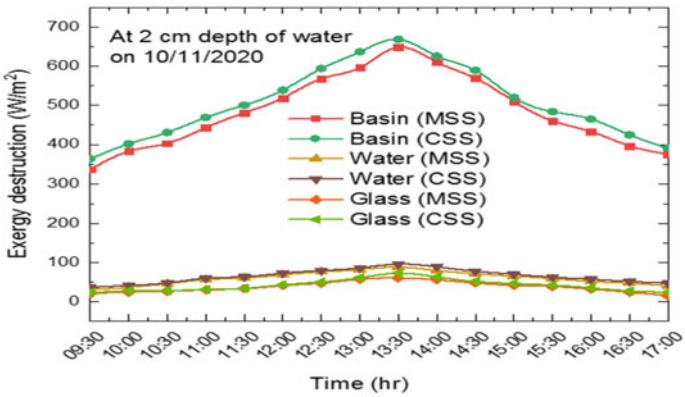
### 4 Conclusions

This study was conducted to examine the impact of parabolic fins on the performance energy and exergy of double-slope still compared with a normal still device at the same environmental situations. The main conclusions of this study are.

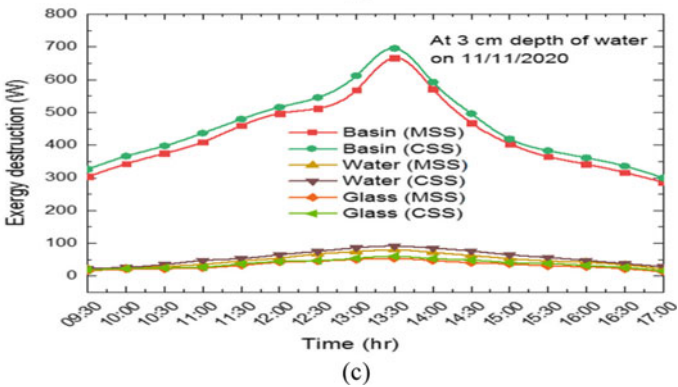
- The efficiency of energy improves with time and reaches its higher value at around 1:30 PM. The efficiency of energy obtained for parabolic fin-modified solar still is 8.33%, 7.69%, and 6.24%, respectively, higher than conventional still.
- The exergy efficiency obtained for parabolic fin-modified solar still is 6.06%, 3.57%, and 3.07%, respectively, higher due to the effect of parabolic fins compared to conventional still.
- It is examined that the attached fins on basin liner can receive higher radiation energy coming from the Sun and transfer more heat to the basin water over normal still.
- The freshwater yield was obtained for parabolic fin-modified still are 1250 ml, 1115 ml, and 1015 ml, and for conventional still, outcomes are 1180 ml, 1050 ml, and 940 ml, respectively.
- Due to the transfer of radiation energy of the Sun to heat energy compared with energy efficiency, the obtained efficiency values of exergy are less. Among the three components (basin, water, and glass cover), basin liner has higher exergy destruction.



(a)



(b)



(c)

Fig. 7 Exergy destruction variation with time from MSS and CSSs components at a 1-cm, b 2-cm and c 3-cm depth of water



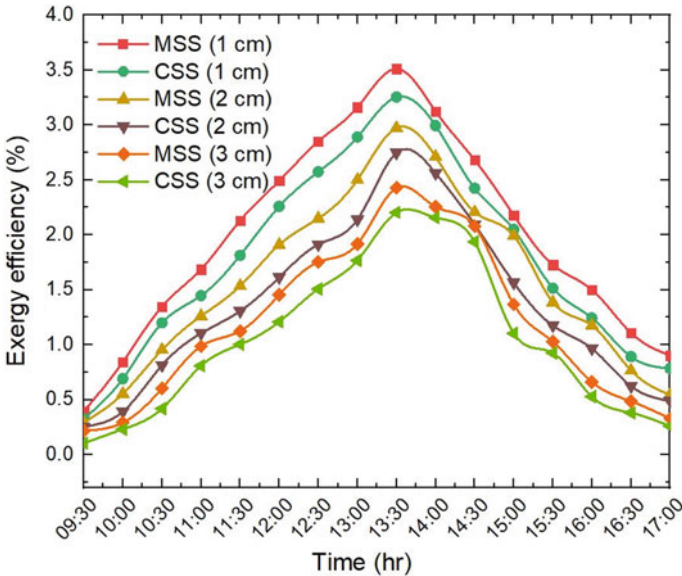


Fig. 8 MSS and CSSs exergy efficiency variation with time for varying water depths

### References

- Vishwanath Kumar P, Kumar A, Prakash O, Kaviti AK (2015) Solar stills system design: a review. *Renew Sustain Energy Rev* 51:153–181
- Kaviti AK, Yadav A, Shukla A (2016) Inclined solar still designs: a review. *Renew Sustain Energy Rev* 54:429–451
- Ram AS, Kaviti AK (2020) Effect of glass cover angles on the performance of double slope solar still. a CFD simulation analysis. *Int J Mech Prod Eng Res Dev* 10:14019–14028
- Kumar A, Siva A, Kumari AA, Hussain S (2020) Development of hierarchical structures for enhanced solar desalination. *Mater Today Proc*
- Kaviti AK, Yadav A, Shukla A (2019) Experimental investigation of solar still with opaque north triangular face. *Int J Green Energy* 1–8
- Sivakumar V, Sundaram EG, Sakthivel M (2015) Investigation on the effects of heat capacity on the theoretical analysis of single slope passive solar still. *Desalin Water Treat* 1–13
- Rosen MA, Dincer I (2007) Exergy as the confluence of energy, environment and sustainable development. *Exergy, An Int J* 1:3–13
- Layek A (2018) Exergetic analysis of basin type solar still. *Eng Sci Technol Int J* 21:99–106
- Rajaseenivasan T, Kalidasa Murugavel K, Elango T (2015) Performance and exergy analysis of a double-basin solar still with different materials in basin. *Desalin Water Treat* 55:1786–1794
- Yousef MS, Hassan H, Sekiguchi H (2019) Energy, exergy, economic and enviroeconomic (4E) analyses of solar distillation system using different absorbing materials. *Appl Therm Eng* 150:30–41
- Appadurai M, Velmurugan V (2015) Performance analysis of fin type solar still integrated with fin type mini solar pond. *Sustain Energy Technol Assessments* 9:30–36
- Velmurugan V, Gopalakrishnan M, Raghu R, Srithar K (2008) Single basin solar still with fin for enhancing productivity. *Energy Convers Manag J* 49:2602–2608
- El-Sebaïi AA, Ramadan MR, Aboul-Enein S, El-Naggar M (2015) Effect of fin configuration parameters on single basin solar still performance. *Desalination* 365:15–24

14. Alaian WM, Elnegiry EA, Hamed AM (2016) Experimental investigation on the performance of solar still augmented with pin-finned wick. *Desalination* 379:10–15
15. El-Sebaai AA, El-Naggar M (2017) Year round performance and cost analysis of a finned single basin solar still. *Appl Therm Eng* 110:787–794
16. Jani HK, Modi KV (2019) Experimental performance evaluation of single basin dual slope solar still with circular and square cross-sectional hollow fins. *Sol Energy* 179:186–194
17. Tiwari GN, Bapeshwara Rao VSV (1984) Transient performance of a single basin solar still with water flowing over the glass cover. *Desalination* 49:231–241



# Suction/Injection Effects on a Stretching Surface of the Stagnation Point Flow Through Porous Medium with Influence of Heat Generation



B. Shankar Goud, Y. Dharmendar Reddy, B. Praveen Kumar,  
and M. Anil Kumar

**Abstract** An investigation is made on steady viscous, laminar flow of fluid on stretching surface with the impact of the heat generation through porous medium in the existence of the suction and injection. The governing equations (PDEs) are converted to nonlinear ordinary differential equations (ODEs) by implementing the similarity transformations. The numerical results are achieved through the MATLAB inbuilt solver `bvp5c`. The solutions of the velocity and temperature are discussed through graphs for different non-dimensional parameters; additionally, the wall shear stress and heat transfer coefficient are presented in tabular form.

**Keywords** Stagnation point · Heat generation · Suction · Injection · Porous medium

## 1 Introduction

Several classical fluid dynamics problems, including rotating disc flows and stagnation point flows, have been used to generate similarity transformations. Heat transfer and boundary layer flow problems of viscous incompressible fluid through stretching sheet surfaces are considering a key role in different domains of engineering and sciences such as paper production, cooling of metals. Many researchers presented a different fluid problem, viz. Aziz [1] studied on thermal boundary layer over a flat plate with surface boundary conditions. Anwar et al. [2] analysed the radiation impact on MHD nanofluid stagnation point flow over an exponential stretching

---

B. Shankar Goud (✉)

Department of Mathematics, JNTUH College of Engineering, Hyderabad, Telangana 500085, India

Y. Dharmendar Reddy · M. Anil Kumar

Department of Mathematics, Anurag University, Hyderabad, Telangana 500088, India

B. Praveen Kumar

Department of Mechanical Engineering, Guru Nanak Institute of Technology, Ibrahimpatnam, R.R District 501506, India

sheet. Pal [3] studied the thermal radiation on the stretching surface, and Bhattacharya and Layek [4] analysed with the thermal radiation with suction/blowing condition. Archary et al. [5] investigated the chemical reaction effect with suction and blowing condition. Balreddy et al. [6] analysed the radiation impact on MHD fluid flow over a exponentially stretching sheet. Santhosh et al. [7] analysed an MHD stagnation point flow with heat generation over a stretching sheet in porous medium. Goud [8] investigated the MHD flow past over a oscillating plate with chemical reaction and radiation effect, and Cortell [9], Elbashbeshy and Bazid [10] studied with thermal radiation suction/blowing over a stretching surface in the occurrence of heat generation/absorption. Many of the authors studied the different fluid over various plate and surfaces, and few recent studies are cited in [11–15].

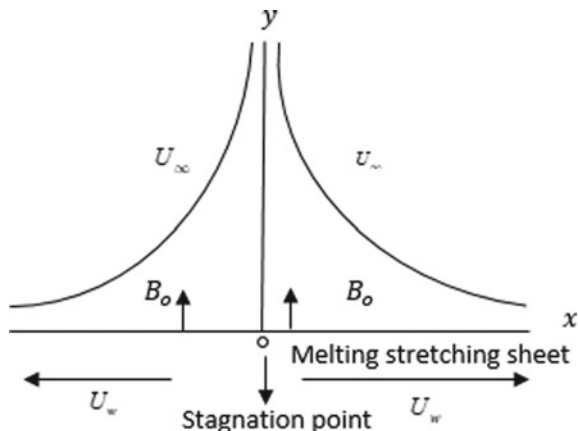
In the present article, we have deliberated the heat generation on stretching surface of the stagnation point flow through the porous medium. The main objective of the discussion is suction/injection effects on the stretching sheet.

## 2 Mathematical Formulation

Consider a steady, viscous, 2-dimensional stagnation point flow in the permeable mechanism near the stagnation point at the surface that is consistent with  $y = 0$ . The flux is in the region of  $y > 0$ , where space is filled with a porous medium over the plane sheet as seen in Fig. 1.

The  $x$ -axis is related to two equal and opposite forces, such that the surface is expanded with origin is fixed. The flow potential, which attains from the  $y$ -axis on a level wall set to “ $y = 0$ ,” splits into two flows on the wall and leaves in both ways, and the velocity transformation in the friction-free flow is known by  $U(x) = ax$ ,  $V(y) = -ay$  where the fixed ( $a > 0$ ) corresponds to the velocity for the free stream away from the stretching surface. The governing equations for 2-D stable state flow are reduced to approximations of the normal boundary layer as.

**Fig. 1** Schematic diagram of the problem



$$\frac{\partial u}{\partial x} + \frac{\partial v}{\partial y} = 0 \tag{1}$$

$$u \frac{\partial u}{\partial x} + v \frac{\partial u}{\partial y} = \nu \frac{\partial^2 u}{\partial y^2} + U \frac{\partial U}{\partial x} + \frac{\mu}{K} [U(x) - u] \tag{2}$$

$$u \frac{\partial T}{\partial x} + v \frac{\partial T}{\partial y} = \frac{k}{\rho C_p} \frac{\partial^2 T}{\partial y^2} + \frac{Q}{\rho C_p} [T - T_\infty] \tag{3}$$

The appropriate boundary conditions are specified by

$$u = u_w(x) = cx, v = -w_0, T = T_w \text{ at } y = 0 \left\{ \begin{array}{l} u \rightarrow ax, T \rightarrow T_\infty \text{ as } y \rightarrow \infty \end{array} \right. \tag{4}$$

where  $c$  is a positive constant.

Continuity equation fulfils by describing the flow functions  $u = \frac{\partial \psi}{\partial y}, v = -\frac{\partial \psi}{\partial x}$  with the help of the following similarity transformations  $\psi = \sqrt{c\nu x} f(\eta), u(x, y) = cx f'(\eta), v(x, y) = -\sqrt{c\nu} f(\eta), \eta = y\sqrt{c/\nu}$  and by introducing the dimensionless quantity  $T = T_\infty + (T_w - T_\infty)\theta(\eta)$ . Using the above functions, Eqs. (2)–(4) are reduced to

$$f''' + ff' - (f')^2 + M(C - f') + C^2 = 0 \tag{5}$$

$$\theta'' + Pr(f\theta' + B\theta) = 0 \tag{6}$$

The changed boundary conditions are:

$$f = A, f' = 1, \theta = 1 \text{ at } \eta = 0 \left\{ \begin{array}{l} f' \rightarrow C, \theta \rightarrow 0 \text{ as } \eta \rightarrow \infty \end{array} \right. \tag{7}$$

where prime refers to diff. with resp. to  $\eta, \nu = \frac{\mu}{\rho}$  is the kinematic viscosity,  $A = \frac{w_0}{\sqrt{c\nu}}$  is the suction/injection parameter,  $Pr = \frac{\mu C_p}{k}$  is Prandtl number,  $M = \frac{v}{cK}$  is magnetic parameter,  $C = \frac{a}{c}$  is stretching parameter,  $B = \frac{Q}{C_p \rho c}$  is heat generation or absorption coefficient.

### 3 Solution of the Problem

With the assistance of MATLAB method bvp5c are integrated the series of nonlinear ODEs together with boundary conditions. To do this, the cumulative ODEs are first reformed to ODEs in the first order. Using the following substitutes

$$\begin{aligned}
 f &= f_1, f' = f_2, f'' = f_3, \theta = f_4, \theta' = f_5, \&f'_1 = f_2, f'_2 = f_3 \\
 f'_3 &= ((f_2)^2 - (f_1 * f_3) - M(C - f_2) - C^2) \\
 f'_4 &= f_5, f'_5 = -Pr((f_1 * f_5) + (B * f_4))
 \end{aligned}$$

The boundary conditions take the following structure

$$\begin{aligned}
 f_1(\eta) = A, f_2(\eta) = 1, f_4(\eta) = 1 \quad \text{at } \eta \rightarrow 0 \\
 f_2(\eta) = C, f_4(\eta) = 0 \quad \text{as } \eta \rightarrow \infty
 \end{aligned}$$

In this methodology, the decision of  $\eta_\infty = 6$ , and by taking the margin of steady to  $10^{-5}$  agreements, each numerical solution approaches asymptotic characteristics closely. For different approximations of the physical constraints, the numerical approximations of  $f''(0)$  and  $-\theta'(0)$  are exhibited in Tables 1 and 2.

For changed values of stretching parameter ( $C$ ) and suction/injection parameter ( $A$ ) on  $f$  and  $f'$ , stable values of  $Pr = 0.7$ ,  $B = 0.1$  and  $M = 1.0$  are shown in Figs. 2 and 3, respectively. These figures describe the increasing the values of  $C = 0.5, 1.0, 1.5$  and  $A = 0.5$ . The result in  $f$  and  $f'$  increases. Enhanced values of  $A$  rise in  $f$ , but its influences on  $f'$  depend on  $C$ . Enhanced values of  $A$  decrease  $f'$  when  $C < 1$ . The statistic even reveals that  $C$  has an impact on  $f$  and  $f'$ , more evident for larger values of  $A$  (suction), and also the width of the velocity boundary layer enhances with raise in  $C$ .

Figure 4 illustrates the temperature distribution for varied values of  $C$  and  $A$  for a fixed of  $Pr = 0.7$ ,  $B = 0.1$  and  $M = 1.0$ . It is found that temperature enhances with an increase in  $C$ . For slighter values of  $A$  (injection case), its effect on temperature

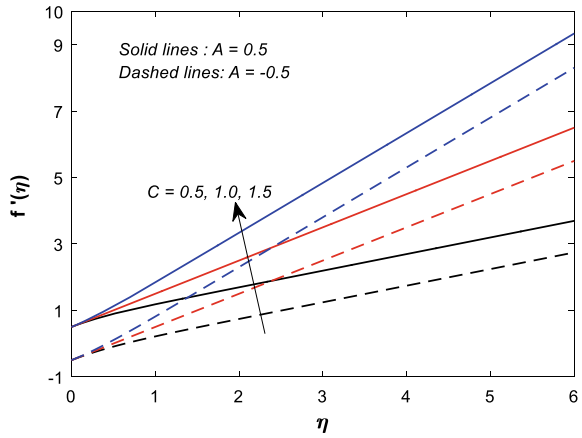
**Table 1** Variation of skin friction  $f''(0)$  with  $Pr = 0.7$

$M$	$B = 1.0, A = 0.5$			$B = 1.0, A = -0.5$		
	$C = 0.5$	$C = 1.0$	$C = 1.5$	$C = 0.5$	$C = 1.0$	$C = 1.5$
0	-0.81176	0	1.055637	-0.54533	0	0.779500
1	-0.97180	0	1.178965	-0.71083	0	0.908361
2	-1.10714	0	1.289947	-0.84896	0	1.022974
3	-1.22637	0	1.391605	-0.96987	0	1.127189

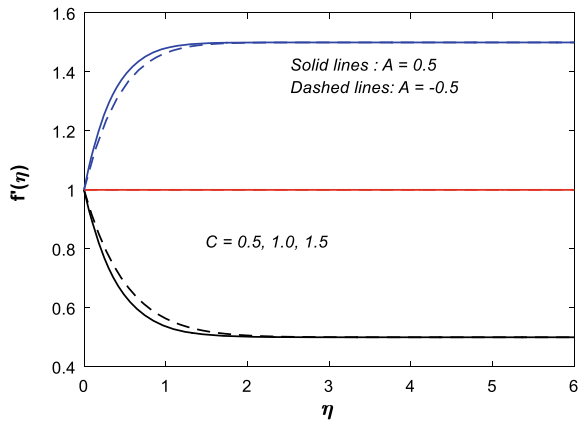
**Table 2** Variation of Nusselt number  $-\theta'(0)$  with  $Pr = 0.7$

$M$	$B = 1.0, A = 0.5$			$B = 1.0, A = -0.5$		
	$C = 0.5$	$C = 1.0$	$C = 1.5$	$C = 0.5$	$C = 1.0$	$C = 1.5$
0	0.049833	0.360008	0.549532	-0.73994	-0.27443	-0.011100
1	0.023599	0.360007	0.555098	-0.80339	-0.27443	-0.001680
2	0.004740	0.360006	0.559599	-0.84528	-0.27443	0.005515
3	-0.009710	0.360011	0.563350	-0.87521	-0.27443	0.011265

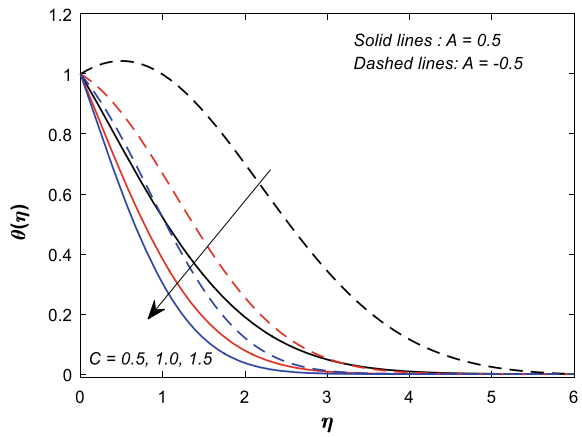
**Fig. 2** Variation of  $C$  and  $A$  versus  $f'$



**Fig. 3** Variation of  $C$  and  $A$  versus  $f'$



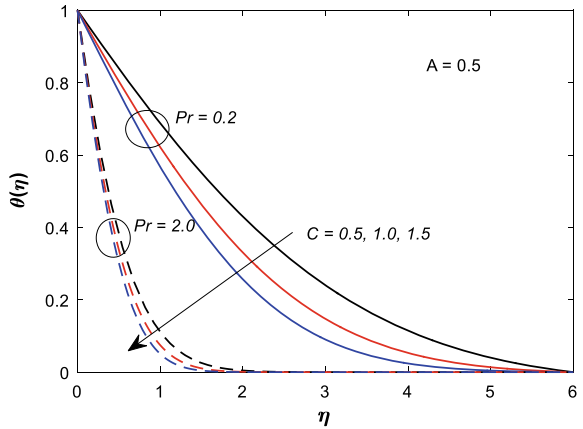
**Fig. 4** Variation of the factors  $C$  versus  $\theta$



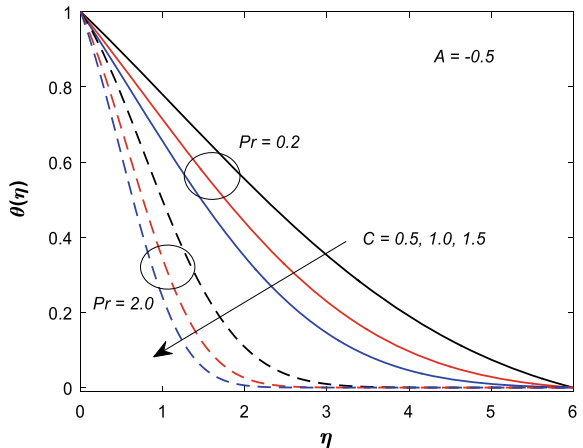
is more evident, i.e. for enhanced values of stretching sheet parameter  $C$ , the result in thermal boundary layer thickness declines also decreases for enhancing  $A$ . For injection case temperature diminishes and for a fixed values of  $B = 0.1, M = 1.0$ , the influence of the different values of  $C$  and  $Pr(0.2, 2.0)$  on velocity profile with suction ( $A = 0.5$ ) and injection ( $A = -0.5$ ) case is depicted in Figs. 5 and 6. In this situation, the temperature declines with rise in the  $C$ , whereas it increases  $Pr$  also. For a fixed  $Pr = 0.7, M = 1.0$ , the impact of heat generation/absorption factor on the temperature distribution for suction ( $A = 0.5$ ) for different values of the stretching sheet factor is described in figures. These can be shown that in both cases, the temperature profile decreases (Fig. 7).

The differences of the skin friction quantity in the existence of the suction/injection factor ( $A$ ) and heat generation/absorption constraint ( $B$ ) with different values of the porosity constraint and stretching sheet factor are described in Tables 1 and 2. For

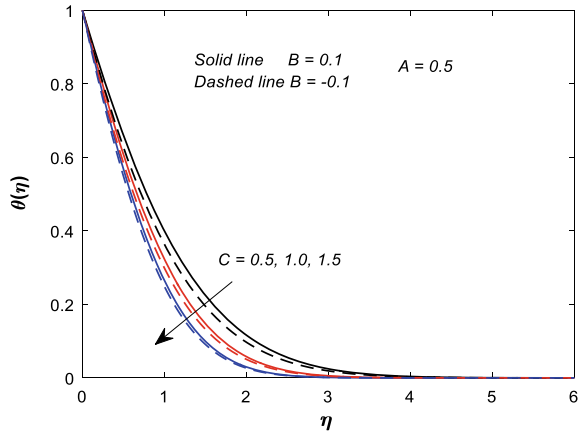
**Fig. 5** Variation  $C$  and  $M$  versus  $\theta$



**Fig. 6** Variation of  $C$  and  $B$  versus  $\theta$  ( $M = 0.5$ )



**Fig. 7** Variation  $C$  and  $B$  versus  $\theta$



$C < 1$  with different  $M$  values, the skin friction and heat transfer coefficient drop in the occurrence of suction/injection; meanwhile, for  $C = 1$ , there is no change. For  $C > 1$ , the result in  $f''(0)$  and  $-\theta'(0)$  increases in the occurrence of suction/injection.

### 4 Conclusions

In this study, an investigation is made on different flow parameters on velocity and temperature taken into account. A 2-D stagnation point flow of incompressible, viscous flow embedded on porous stretching surface is deliberate with the influence of the heat absorption/generation. The solution of the nonlinear ODE's is obtained by MATLAB inbuilt solver bvp5c tool. The findings of this analysis are:

- Velocity diminishes with an increase in stretching sheet parameter and suction/injection parameters.
- Increasing the values of  $A$ ,  $B$ ,  $Pr$  and  $C$ , the temperature profile decreases.
- Increasing the value of  $M$  for  $C < 1$  with existence of  $A$ , the skin friction and Nusselt number diminishes, and for  $C > 1$ , skin friction increases and Nusselt number declines.
- With enhance of  $Pr$  for  $C < 1$  and  $C = 1$ , Nusselt number decreases, and for  $C > 1$  with suction case, the rate of heat transfer rises, and with injection case, it decreases.

## References

1. Aziz A (2009) A similarity solution for laminar thermal boundary layer over a flat plate with a convective surface boundary condition. *Commun Nonlinear Sci Numer Simul* 14(4):1064–1068
2. Anwar I, Shafie S, Salleh MZ (2014) Radiation effect on MHD stagnation point flow of a nanofluid over an exponentially stretching sheet. *Walailak J Sci Technol* 11(7):569–591
3. Pal D (2008) Heat and mass transfer in stagnation-point flow towards a stretching surface in the presence of buoyancy force and thermal radiation. *Meccanica* 44:145–158
4. Bhattacharyya K, Layek GC (2010) Chemically reactive solute distribution in MHD boundary layer flow over a permeable stretching sheet with suction or blowing. *Chem Eng Comm* 197:1527–1540
5. Acharya M, Singh LP, Dash GC (1999) Heat and mass transfer over an accelerating surface with heat source in presence of suction and blowing. *Int J Eng Sci* 37(2):189–211
6. Bal Reddy G, Shankar Goud B, Raja Shekar MN (2018) Implicit finite difference solution of radiation effects on MHD fluid flow of a nanofluid past an exponential stretching sheet embedded in a porous medium. *J Adv Res Dyn Control Syst* 10(6):746–760
7. Santosh C, Singh S, Chaudhary S (2015) MHD flow and heat generation near stagnation point towards a stretching sheet in porous medium. *Appl Math Sci* 9(8):369–378
8. Shankar Goud B (2017) MHD flow past a vertical oscillating plate with radiation and chemical reaction in porous medium-finite difference method. *Int J Emerg Technol Eng Res* 5(11):32–35
9. Cortell R (2005) Flow and heat transfer of a fluid through a porous medium over a stretching surface with internal heat generation/absorption and suction/blowing. *Fluid Dyn Res* 37:231–235
10. Elbashareshy EMA, Bazid MAA (2004) Heat transfer in a porous medium over a stretching surface with internal heat generation and suction or injection. *Appl Math Comput* 158(315):799–807
11. Shankar Goud B, Dharmendar Reddy Y, Srinivasa Rao V, Khan ZH (2020) Thermal radiation and joule heating effects on a magnetohydrodynamic Casson nanofluid flow in the presence of chemical reaction through a non-linear inclined porous stretching sheet. *J Naval Arch Mar Eng* 7(2):143–164. <https://doi.org/10.3329/jname.v17i2.49978>
12. Shankar Goud B, Bindu P, Srilatha P, Hari Krishna Y (2020) The Joule heating effect on MHD natural convective fluid flow in a permeable medium over a semi-infinite inclined vertical plate in the presence of the chemical reaction. *IOP Conf Ser: Mater Sci Eng* 993:012111. <https://doi.org/10.1088/1757-899X/993/1/012111>
13. Shankar Goud B (2020) Heat generation/absorption influence on steady stretched permeable surface on MHD flow of a micropolar fluid through a porous medium in the presence of variable suction/injection. *Int J Thermofluids* 7–8:100044. <https://doi.org/10.1016/j.ijft.2020.100044>
14. Shankar Goud B (2020) Thermal radiation influences on MHD stagnation point stream over a stretching sheet with slip boundary conditions. *Int J Thermofluid Sci Technol* 7(2), Paper No. 070201
15. Attia HA (2006) Stagnation point flow towards a stretching surface through a porous medium with heat generation. *Turkish J Eng Env Sci* 30:299–306



# Effect of ZrB<sub>2</sub> Nano-Ingredient on Uncoated Tool Wear for Aluminum Alloys-Based Metal Matrix Composite



Seema V. Yerigeri  and Shantisagar K. Biradar 

**Abstract** The role of metal matrix composites (MMCs) has been growing significantly in engineering applications. Being scientifically and technologically advantageous, MMCs dominate important research in current times. The demand for hybrid metal matrix composites has increased due to their mechanical properties for satisfying engineering applications. Comparing particle or discontinuously reinforced MMCs and MMCs that are fiber reinforced shows that the former have isotropic characteristics which the latter do not. In the current study, fabrication of aluminum-based MMC (Al-MMC) is conducted. We have utilized zirconium diboride (ZrB<sub>2</sub>) as the reinforcement material to enhance the mechanical and tribological properties. The amount of 3% ZrB<sub>2</sub> reinforcement by weight is decided and mixed with different aluminum-based alloys to form an Al-MMC utilizing the stir casting method. The wear rate of an uncoated tool is obtained using a CNC machine and significantly impacting the tool wear while machining of Al-MMC.

**Keywords** Aluminum alloys · Aluminum matrix · ZrB<sub>2</sub> reinforcement · Wear · Stir casting

## 1 Introduction

Now a day's, aluminum alloys have wide-ranging applications in different industrial applications. There is an exceptionally wide range of physical attributes that can be

---

S. V. Yerigeri (✉)

Department of Mechanical Engineering, M.B.E. Society's College of Engineering, Ambejogai, Beed, India

e-mail: [seemayerigeri1877@gmail.com](mailto:seemayerigeri1877@gmail.com)

Department of Mechanical Engineering, G. S. Mandal's, Maharashtra Institute of Technology, Aurangabad, India

S. K. Biradar

Department of Mechanical Engineering, M.S.S. College of Engineering and Technology, Nagewadi, Aurangabad Jalna Road, Jalna, India

e-mail: [shantisagarbiradar@gmail.com](mailto:shantisagarbiradar@gmail.com)

added to these alloys. Addition of various alloying elements (Si, Zr, Cu, etc.) in the base aluminum helps to enhance properties such as wear resistance, strength, and so on. The primary goal of this study is the development of novel MMCs which are Al-based that have enhanced properties as compared to the traditional materials used in commerce and additionally to evaluate the tribological attributes of the novel alloys under various conditions, specifically dry sliding. Of all the materials used in production and commerce, aluminum along with its alloys is the third most metal to be used. Aluminum-based alloys are used most commonly in casting alloys utilized for commercial purposes specifically because of their highly valuable properties such as excellent workability, good cast ability, superior strength-to-weight ratio, and high thermal conductivity along with better wear and corrosion resistance. The role of aluminum castings has been a significant one in the evolution of the entire aluminum industry since the start of this industry in the latter part of the 19th century. In various industrial fields such as transport, auto-industry, general engineering as well as aviation, the use of these alloys has emerged dominantly. Even in the military area, these alloys are being used increasingly. In the transportation section, the use of aluminum has risen from a mere 6% in the year 1950 to an amazing 50% in the year 2018 [1]. Nevertheless, the use of aluminum alloys in the fields of aerospace, automobile, and forging industries is limited due to the very low compatibility with additives used for anti-wear lubrication in hydrocarbon oils such as zinc-dialkyldithiophosphate (ZDDP). The wear resistance of these alloys also makes them a poor choice for these industries. Researchers are putting in much effort into overcoming the shortcomings of these alloys leading to higher utilization of these aluminum alloys.

Mathan et al. [2] noted that the mechanical characteristics of Al6061 increase with the inclusion of an optimum percentage of reinforcements which leads to minimum wear rate. From the scanning electron microscopy (SEM) image analysis, porosities were not examined due to better thermal expansion coefficient of the matrix and better refinement of reinforcements as a result of using stir casting as the method of manufacturing. Gautam et al. [3] analyzed wear rate and noted that with the addition of ZrB<sub>2</sub> particles to Al<sub>3</sub>Zr/AA5052 composites it enabled the composites to be used for higher loads even though the wear regime was mild. The working load range is also enhanced with an addition of ZrB<sub>2</sub> particles. There is a decrease in the coefficient of friction on a continuous basis with load for all the composites. In a composite containing 5% volume of ZrB<sub>2</sub> particles a much lower wear rate along with a much higher wear resistance are noted. Dinaharan et al. [4] show that when the ZrB<sub>2</sub> particles are uniformly distributed they are spherical in shape, have good bonding, and clear interface. By adding more ZrB<sub>2</sub> particles to the matrix alloy, the hardness, the wear resistance as well as ultimate tensile strength (UTS) of the composites are enhanced. Moreover, by adding the ZrB<sub>2</sub> particles, there is a reduction in the elongation of the matrix alloy. Again, in similar work, Dinaharan et al. [5] came up with a mathematical model used in the prediction of the wear rate of AA6061 with 10% ZrB<sub>2</sub> in situ composites and arrived at the conclusion that the wear parameters of the normal load, the sliding velocity as well as the sliding distance exist in inverse proportion to the wear resistance. The wear rate goes up in a linear fashion when the sliding distance, the normal load, and the sliding velocity rise. Thandalam et al. [6]

compared different manufacturing processes and showed that since the process of stir casting is simple, flexible, and fairly inexpensive to be used to fabricate components that are large in size, it has been adopted extensively. The authors also arrived at the conclusion that taking into account factors based on technology and economics, zircon particles seem to show promise in their use as reinforcements for Al-MMCs. When the amount of zircon was increased along with decreasing the size of these zircon particles, the authors found that there was a significant improvement in the abrasive wear resistance of the composite. Ciftci et al. [7] undertook machining tests on Al-2014-SiC MMC utilizing carbide tools that were both, uncoated as well as coated. The authors concluded that the size of the particles as well as the weight percentage had a significant effect on the tool life. As compared to uncoated tools used for cutting, the tool wear in coated tools used for cutting is much better. The advantage of uncoated tools used in cutting is that at lower cutting speeds, the surface finish produced by uncoated tools is much better. In case of the coated carbide tools used for cutting, all MMCs the flank wear they sustained was lower compared with uncoated carbide tools used for cutting. The factors that affected the tool wear were cutting speed, particulate weight fraction, and particulate size. An increase in all of the above three factors resulted in the tool wear increasing also. Sasimurugan et al. [8] came up with a definition that every MMC be made up of a minimum of two component materials, and out of the two, one should be metal and the other a material that was ceramic or an organic compound. Such MMCs could be used in industries such as automobiles, manufacture of bicycles, aerospace, and electronic substrates. During the process of machining the MMCs, as there is a rise in the feed rate, the roughness of the surface increases, and it becomes less when the cutting speed goes up. A medium cutting speed along with a minimum feed rate as well as a decrease in the depth of cut is necessary to achieve a reduced average roughness of the surface.

Rajaneesh et al. [9] were responsible for the development of composites of zinc-Al matrix which were reinforced with SiC particles. Upon examination, the authors found that the composites that they developed exhibited a coefficient of friction that was lower during dry sliding conditions. The attributes of sliding wear improve because of the particles added to the composite to reinforce it. When the percentage of the reinforced particles goes up, the wear of the composite sample goes down. Kumar et al. [10] undertook a comparison of various methods of MMC manufacture. By making use of the in situ stir casting approach, there is a significant increase in the wear resistance. A 16% increase in the hardness of the underground specimen test (UST)-forged composite is experienced when the grain size is reduced, and the reinforcement particles are distributed homogeneously. Kumar et al. [11] were responsible for the fabrication of an AA 6351-ZrB<sub>2</sub> MMC and stated that when the weight percentage of the ZrB<sub>2</sub> was increased, there was a decrease in the wear rate. The value for the hardness of the composite goes up when there is an increase in the percentage of the ZrB<sub>2</sub> reinforcement. The authors also stated that the composite displayed maximum hardness when the ZrB<sub>2</sub> reinforcement was the highest. Kar et al. [12] came up with an estimate for the influence of reinforcement, applied load and both, the sliding speed, and distance, and noted that the wear rate of heat-treated Al/red mud and Al/TiC is lower in comparison with the same composites with no

heat treatment. The authors also noted that by increasing the red mud particles up to 6% by weight it resulted in increased hardness which led to a reduced magnitude of wear. Singla et al. [13] performed experiments by changing the weight fraction of the SiC by an increment of 5% from 5 to 30%. They discovered that by increasing the SiC in the composite there was an increase in properties such as impact strength, hardness as well as normalized displacement. They also noted the increasing trend in the specimens that were stirred manually without applying the process of stirring and with the two-step technique of stir casting, respectively. Sozhamannan et al. [14] noted that by varying the parameters used in the process of stir casting the metal matrix, an increase in the holding time was experienced with a decrease in the ultimate strength of the MMC. The authors discovered that the holding time has an effect on the viscosity of the liquid metal, along with the distribution of the particles. They also found that there is a chemical reaction that is induced between the matrix and the reinforcement. The observation was that there is a linear increase in the hardness when the processing temperature is increased from 750 to 800 °C with the holding time being 20 min. The focus of Bai et al. [15] was machinability aspects like cutting temperatures, surface topography, cutting forces, chip formation, and observed tool wear. The authors noted that the mechanism of the chip formation in ultrasonically assisted turning (UAT) confirmed an increase in the ductility of the workpiece material upon being repeatedly subjected to a process of micro-chipping. The chips that were procured in UAT were both, continuous as well as semi-continuous in nature. Upon comparing the machined surfaces of both the conventional turning (CT) and the UAT, it was noted that the surface of the CT revealed defects, whereas the surface of the UAT was of higher quality.

Bhaskar et al. [16] ran a comparison of various production methods for the manufacture of MMCs. They studied multiple techniques such as powder metallurgy, stir casting, and infiltration that were used in the manufacture of MMCs. Their primary goal was to make these methods cost-effective, productive, and efficient. Hence, to this end, researchers were in the process of development of novel methods of MMC manufacturing such as metal injection molding (MIM), mechanical alloying, and continuous binder powder coating (CBPC) to meet the requirements of multiple industries. Radhika et al. [17] utilized a machine learning approach for predicting the condition of tools during the turning of MMCs. Also, vibration analysis was performed making use of signal processing techniques for predicting the condition of tools during the process of machining. Statistical and histogram features were extracted from the signal created by the vibrations. Next, the features were sorted making use of two distinct classifiers. It was noted that by combining histogram features along with the random forest algorithm was very suitable for monitoring the conditions of the tools during the process of turning the aluminum hybrid MMCs. Udayashankar et al. [18] developed Al6061 ZrO<sub>2</sub> composite through stir casting method for 3, 6, 9%, and 12% of zirconium dioxide reinforcement. Studies of the microstructure show that it was at 9% addition of zirconia that a uniform distribution of ZrO<sub>2</sub> particles was procured in the Al matrix. The value of the tensile strength of the Al6061-ZrO<sub>2</sub> composite was higher than the base metal Al alloy. The tensile strength went up when there was an increase in the ZrO<sub>2</sub> reinforcement up to 9%.

However, it decreased after that with an increase in the percentage of ZrO<sub>2</sub>. The optimum value of UTS was obtained at 9% of Zirconia. Moona et al. [19] did a retrospective investigation of MMCs studied all available data. They concluded that the primary consideration during the process of fabrication is the final use for which the material has to be developed. Different issues like process parameters, processing route, the base metal, and the kind of reinforcements should be selected based on the final use to which the Al-MMC that has been fabricated will be put. Aruri et al. [20] looked into dry sliding wear and corrosion of the AlSiC composite in a vertical milling machine by dispersing SiC particles. The homogenous distribution of the SiC particles inside the nugget zone was done with no defect. The observation made was that the bonding of the SiC with the matrix metal that was achieved using the friction stir processing (FSP) process was excellent. Farooq et al. [21] utilized the stir casting process for the material made up of aluminum Im-6 along with fly ash, zinc, and then, the aluminum composite was formed. After the casting process was complete, the material was machined. Various tests to check out the tensility, hardness, and impact were conducted on the aluminum material. The outcome of the tests shows that there is an up-tick in the hardness and the tensile strength.

Literature survey done in this field shows that MMCs have a pivotal role in engineering applications. The demand for hybrid MMCs is increasing due to their properties which are able to satisfy engineering applications. Specimens manufactured using the process of stir casting have high hardness, and their microstructure contains finer grains as compared to other methods. The stir casting technique is used extensively because of its advantages such as a lower setup cost, ease of portability, the ability of incorporating mass production, and being able to uniformly distribute reinforcement to obtain improved mechanical properties. Of all the methods considered for fabrication, stir casting is a method that is used most extensively in the production of particle reinforced composites. Stir casting is outstanding because it is considered to be the most cost-effective technique. Therefore, the future scope of this study is the development of a novel aluminum-based MMC that has superior mechanical properties compared to the traditional commercial materials that are available and then further to conduct an analysis on how the ZrB<sub>2</sub> nano-ingredient affects uncoated tool wear during the process of machining Al-MMCs. Moreover, this study will further examine tribological behavior under dry sliding conditions in order to improve the wear resistance of both, coated as well as uncoated tools, along with Al-MMCs.

## 2 Methodology

The goal of this study is the development of a novel Al-based MMC with improved mechanical as well as wear characteristics as compared to the traditional materials available in the market. Moreover, the study also aims to conduct an analysis of these composites under dry sliding conditions. Figure 1 presents a methodology that has been adopted in the development of the novel Al-MMC. The process depicted in Fig. 2 explores estimating the cutting tool wear estimation.

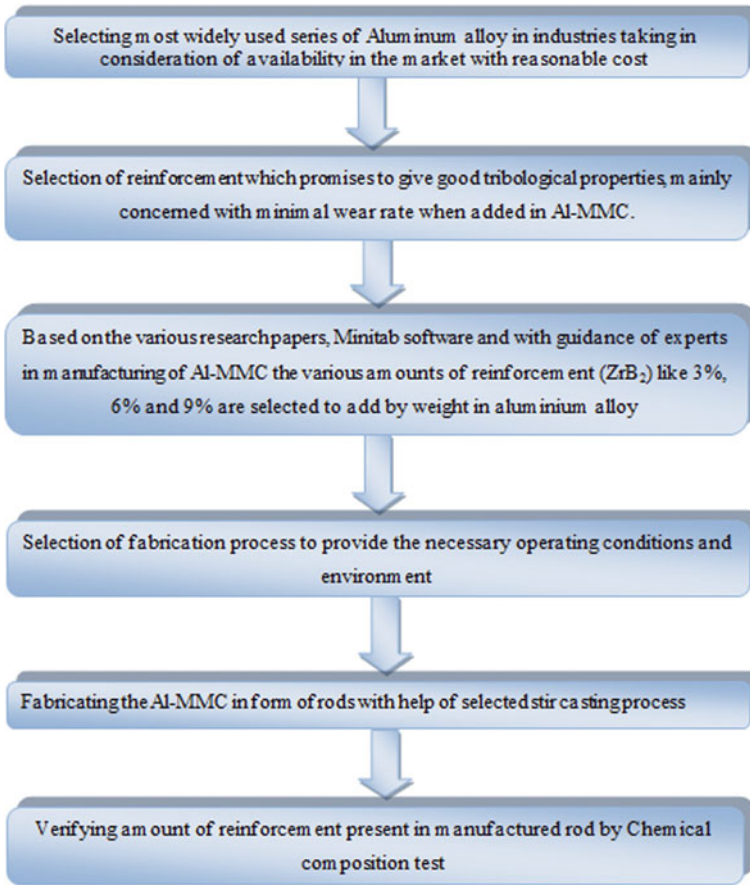
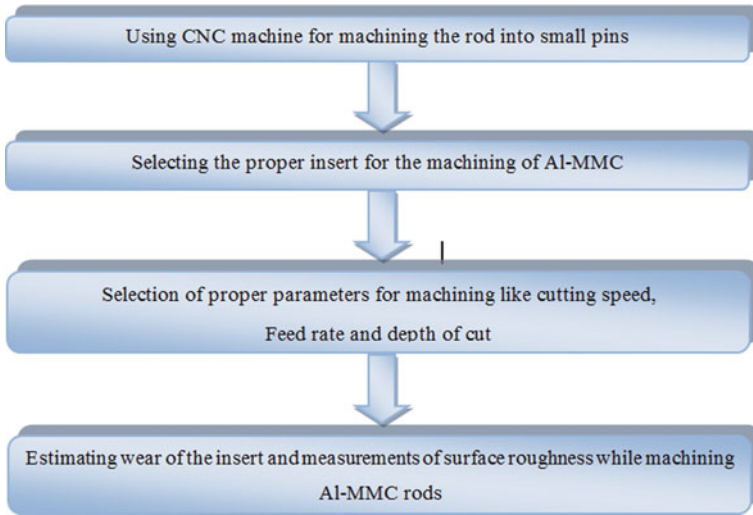


Fig. 1 Methodology

### 3 Material Selection

Composite materials are replacing monolithic materials that were used in the past to meet the global demand for cost-effective and yet high performing, high quality materials. This has resulted in researchers focusing more on composites. The evolution in the development of MMC as the promised replacement for monolithic materials is picking up momentum. More and more industries are now using MMCs for various applications. Effective attributes of MMCs like retaining high temperature strength, a higher strength-to-weight ratio, resistance to wear and fatigue, and very good creep make them excellent potential candidates for use in brakes and engines as a replacement for cast iron and other materials. Given the multiple advantages of MMCs, they became the choice of experimentation in this work. Use of MMCs that are Al based in various industries such as automobile transport, agricultural machinery, aerospace,



**Fig. 2** Tool wear estimation process

and so on is ever increasing primarily because of the multiple advantageous attributes of the MMCs. It is for this reason that we have chosen an Al-based composite as the base metal for our study. According to the availability of different alloys, wide usage of aluminum alloys in industries, and with the affordable cost, the Al 6063, Al6082, and Al7075 series of aluminum alloys are selected as the base material. As per literature review, the addition of ZrB<sub>2</sub> reinforcement to Al-based alloys results in higher wear resistance as compared to other ingredients (e.g., Al<sub>2</sub>O<sub>3</sub>, SiO<sub>2</sub>, B<sub>4</sub>C, etc.). Hence, for further analysis, ZrB<sub>2</sub> is considered as reinforcement.

Based on earlier study and statistical analysis, various amounts of reinforcements such as 3%, 6%, and 9% by weight are selected. Hence, in this paper, an in-depth fabrication process of Al as base alloy with 3% ZrB<sub>2</sub> by weight is presented with the help of the stir casting method.

## 4 Manufacturing Process and Fabrication

There are various processes to manufacture Al-based MMC's such as the liquid state fabrication method and solid state fabrication method. As an example of the liquid metal method, stir casting predominates. The reason for this is that the parameters used in the process can be easily changed as well as supervised. In cases where the quantity of the production is large, fabricating an Al alloy-based composite utilizing stir casting turns out to be the most cost-effective and most used technique. A comparison of the microstructure of samples created by using the stir casting method and other methods shows that those created using the stir casting method possess a higher

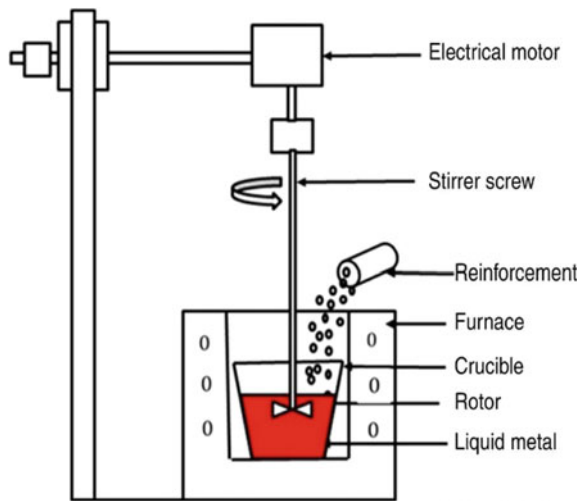


hardness as well as finer grains. There are multiple advantages to using the stir casting method such as the cost of the setup is very low; it is easily portable; it facilitates incorporation of mass production, and the distribution of the reinforcement is very uniform which in turn obtains better mechanical attributes. Figures 3 and 4 show

**Fig. 3** Used stir casting equipment



**Fig. 4** Schematic diagram of stir casting technique





a stirrer which is normally held vertically and is used in the stir casting method to agitate the molten metal mix. It can rotate at various speeds powered by a motor.

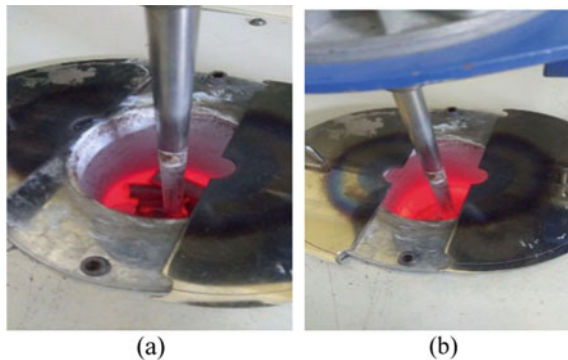
Normally, the stirrer is composed of a material that has the capacity to withstand temperatures that are higher than the melting temperature of the matrix. As a norm, a graphite stirrer is utilized in the process of stir casting. Two components, namely the cylindrical rod and an impeller, primarily make up the stirrer. The shaft of a motor is attached to one of the ends of the rod, and the other end of the rod is attached to the impeller. Composites that contain 30% volume fraction of reinforced material can be manufactured by the stir casting method. The one major consideration of the stir casting method is that the material that is used for reinforcing can be segregated. This can happen as a result of different parameters used in the process as well as the attributes of the material itself resulting in non-homogeneous distribution of the metal. The different parameters that can have an impact on the process are the settling velocity, the relative density, the wetting condition of the metal particles, and so on. The distribution of the particles that are in the molten metal matrix can be impacted by various factors such as the angle of the stirrer, the vertices cone, the speed of the stirrer, and so on. The first step in this method is that the matrix metal is heated up beyond its liquid temperature rendering it in a totally molten state. Next, it is allowed to cool down to a temperature that is in between a liquid state and a solid state. In other words, it is allowed to cool down to a semi-solid state. This is followed by the step of adding the reinforcement particles to the molten matrix. This mixture is reheated to a state where it is entirely liquid in order to mix the metal and the particles in a thorough manner. What results are a molten metal mix which can then be transferred to various dies so that it can be cast as is shown in Figs. 5 and 6.

#### A. Factors Affecting Process

There are three factors that impact the process of stir casting significantly, namely the velocity of stirring, the length of time taken to stir, and the temperature at which the process of stirring takes place.

**Velocity of Stirring:** A very significant factor for enhancing the basic attributes of the MMCs such as tensile strength, toughness, and hardness is that the reinforcement

**Fig. 5** **a** Melting of aluminum alloy by heating the crucible, **b** Using the stirrer to stir the liquid aluminum alloy and ZrB<sub>2</sub> particles



**Fig. 6** Cylindrical rod mold to form as casted Al-MMC rod



particles should be distributed uniformly in the molten matrix. If the mix is stirred at low rpms, then the shearing force that is applied on the matrix is lower, leaving no room for the particles that have been added (which is known as the dispersed phase) to be distributed in a uniform manner all over the matrix. Besides, this phase, which is the dispersed phase, has the propensity toward agglomeration resulting in formation of clusters. This can be attributed to the absence of the requisite force which is necessary to resist it. The application of a higher shearing force as a result of a faster velocity of the stirrer results in a passage being created. This allows for movement of the dispersed phase through the vortex that opens up as a result of the faster stirring. The high velocity rotation of the stirrer supplies enough energy that is strong enough to uniformly distribute the particles of the dispersed phase throughout the entire metal matrix. Researchers also discovered that higher speeds of the stirrer created an opportunity for gas particles to move around in the matrix thereby increasing the porosity of the metal matrix.

**Time duration on the stirring:** This is a factor that has a significant role in distributing the dispersed phase uniformly throughout the matrix. If the matrix is stirred for less time, it results in the particles of reinforcement forming clusters. One other possibility is that some portions of the matrix may be entirely without any particles as a result of poor distribution. Hence, it becomes obvious that with an increase in the time period of stirring, the dispersed phase also increases. This leads to the mechanical properties of the composite being enhanced.

**Stirring Temperature:** The stirring temperature is the third significant factor that greatly impacts the process of stir casting. An increase in the temperature of the matrix brings about a decrease in the viscosity of the metal matrix impacting the particle distribution. A higher temperature results in an accelerated chemical reaction that takes place between the metal matrix and the reinforcement particles.

It can be observed that a higher velocity of the process of stirring enhances the attributes of the composite material, albeit unevenly. This discontinuity is a result of increased porosity which can negatively impact the mechanical characteristics of the metal matrix. A higher rotation speed of the stirrer results in higher shear force being applied to the liquid metal. This in turn distributes the reinforcement particles uniformly through.

**Fig. 7** Casted Al-MMC rods (Al 6063, 6082, 7075 with 3% ZrB<sub>2</sub>)



## B. Production of Metal Matrix Composite

Al6063, Al6082, and Al7075 are the alloys that are utilized to form the matrix metal in the current experiments in order to fabricate a composite that has 3% of ZrB<sub>2</sub> particles weight-wise added to the base metal. The size of the ZrB<sub>2</sub> particles ranges from 10 to 15 microns. The materials that are shown in Fig. 7 have been fabricated using the liquid metal stir casting method. As shown in Fig. 5, tiny ingots of aluminum alloy are melted down in a clay graphite crucible utilizing an electrical resistance furnace.

This melted Al alloy is stirred mechanically making use of a mild steel impeller at a velocity of 400–500 rpm. The ZrB<sub>2</sub> particles are added slowly in pinches after every 5 min so that there are no lump formations in the liquid metal that has been stirred. The stirring processes are carried out for about 30 min. The melt is then poured into a cylindrical die mold (Fig. 6) to get the as-cast aluminum rods. The composite is heated to a temperature of 720 °C in order to be processed. Stir casting is shown in Figs. 3 and 4; the cylindrical rod mold is shown in Fig. 6, and final casted Al-MMC rods are shown in Fig. 7.

## 5 Test Method for Measurement of Tool Wear

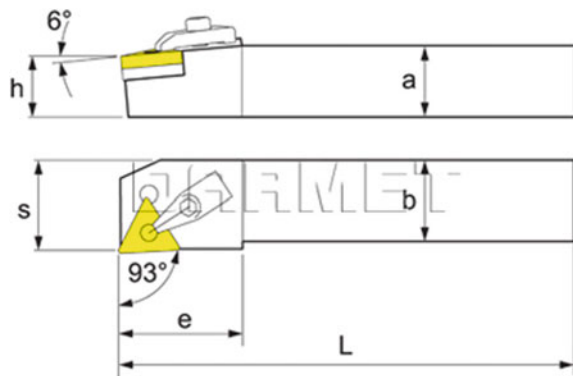
With the ever-increasing use of the composite materials in various industrial applications, machining processes to procure the requisite products are becoming more and more common. As a result of the newly added physical as well as chemical attributes, it becomes harder to machine these composite materials. The inhomogeneous as well as anisotropic type, nature and the amount of reinforcement used in the matrix make machining of these composites harder.

An additional requirement of the process of machining these composites is the appropriate choice of cutting tools and parameters since the MMCs are high-wear resistant materials. During the machining of the MMCs, the presence of the reinforcement particles exerts heavier loads on the tools when they touch the particles. As the edge of the tool comes in contact with the reinforced material, there is a rise in the cutting temperature. An analysis of the effects of the tool wear, the surface roughness, and the cutting force as well as the effect of the cutting temperature on the

machining parameters becomes necessary before undertaking the process of MMC machining. One of the most often as well as conventionally used machining process that is used in metal removal is turning. A choice of ideal machining parameters brings about advantages such as improved surface roughness, use of minimal cutting force, and cutting temperatures that are lower along with less wear on the tools that are used.

Fabricated rods of Al7075 with 3% ZrB<sub>2</sub>, each of length 210 mm and 40 mm diameter are turned on a CNC machine to make small pins of length 30 and 10 mm diameter. The machining of the rods is carried out to find out the wear rate of the insert. The selection of the insert is one of the main aspects to carry out the machining and is done taking into consideration factors like working material, type of finish required, expert suggestions, and availability of inserts. As per the objective of this research, the machining of the Al-MMC rods is intended to be carried out with both coated inserts and uncoated inserts so as to compare the wear rate and tool life of the inserts. Thus, the inserts selected are WIDIA TNMG 160408 THM (uncoated) and WIDIA TNMG160408 WS25PT (coated) with the tool holder called MTJNL 2020 K10 WIDAX. A description of the inserts and the tool holder is given below. But, in this paper, the machining of Al-MMC rod is performed with uncoated inserts. Figure 8 shows the tool and the holder geometry with specifications of tool holder as shown in Table 1. Figure 9 shows the used uncoated insert geometry. The configuration specifications of the tool holder are as shown in Table 2. Machining parameters are selected to find the wear of the uncoated insert while machining the Al-MMC. Machining tests are carried out every five minutes with the operating parameters as

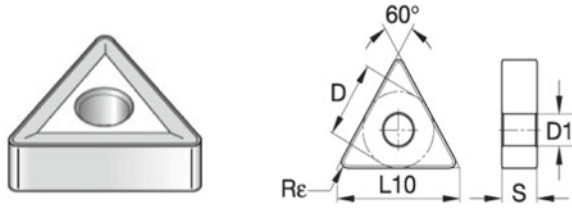
**Fig. 8** Tool and holder geometry



**Table 1** Specifications of tool holder

Tool holder	Brand name	Type	Insert	Shank dimensions	Clearance angle
MTJNL 2020 K10	WIDAX	External turning tool holder	TN_1604	20 × 20 mm	93°

**Fig. 9** Insert geometry



**GRADE:- THM (Uncoated)**

**Table 2** Specifications of insert

Name	TNMG 160408 MS
Inscribed circle diameter (D)	9.53 mm
Cutting edge length (L10)	16.5 mm
Insert thickness (S)	4.76 mm
Corner radius (Re)	0.8 mm
Fixing hole diameter (D1)	3.81 mm
Tool material	Carbide
Insert included angle	60°
Clearance angle major	0°
Insert rake angle	25°
Face land angle	25°

**Table 3** Parameters for machining on CNC

Parameters	Values
Cutting speed (Vc)	18.85 m/min
Feed rate (f)	0.167 mm/rev
Depth of cut (dp)	0.5 mm
Spindle speed (N)	150 rpm
Cycle time	5 min

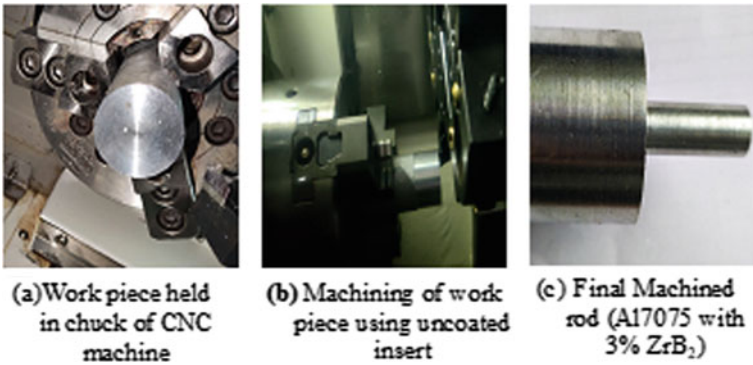
given in Table 3 with no coolant. Figure 10 shows the CNC lathe machine used to perform the machining.

## 6 Results and Discussion

To compute the wear of the insert, the weight of the insert is recorded after each machining cycle. Figure 11 explains the steps followed while machining the Al-MMC. Figure 12 shows the worn out insert after machining of the Al-MMC rod. During machining of the first sample on the CNC machine, Figure 13 shows that the weight loss of the cutting tool insert increases initially for the first 5-minute test.

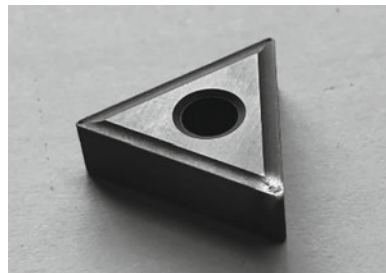


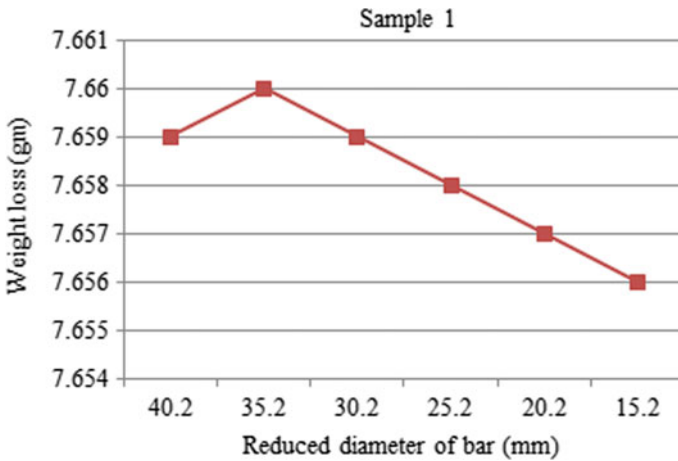
**Fig. 10** CNC lathe machine used for turning of Al-MMC



**Fig. 11** Step of machining of Al-MMC

**Fig. 12** Worn out insert after machining of Al-MMC rod

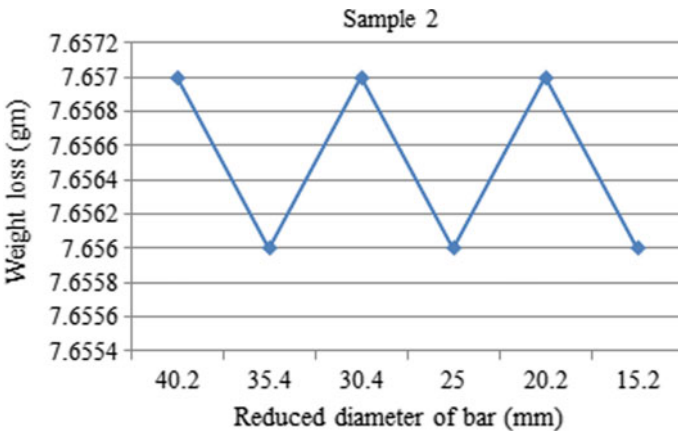




**Fig. 13** Variation of weight loss with diameter of Al-MMC bar for run 1

But, during further tests, it is seen that weight loss of the cutting tool insert decreases linearly after equal intervals.

During second run, from Fig. 14, it is observed that the weight loss of the cutting tool insert decreases initially for the first trial of the 5-min test. But, during further tests, it is seen that weight loss of the cutting tool insert is constant and varies in a zigzag pattern after equal intervals. Results of the two test runs are depicted in Table 4.



**Fig. 14** Variation of weight loss with diameter of Al-MMC bar for run 2

**Table 4** Wear loss during machining of Al-MMC rod

S. No.	Work piece	Insert type	Weight of insert (gm)		Diameter (mm)		CNC cycle time (min)
			Before machining	After machining	Before machining	After machining	
<i>Sample 1</i>							
1	7075	Uncoated	7.659	7.660	40.2	35.2	5
2	7075	Uncoated	7.660	7.659	35.2	30.2	5
3	7075	Uncoated	7.659	7.658	30.2	25.2	5
4	7075	Uncoated	7.658	7.657	25.2	20.2	5
5	7075	Uncoated	7.657	7.656	20.2	15.2	5
6	7075	Uncoated	7.656	7.657	15.2	10.2	5
<i>Sample 2</i>							
1	7075	Uncoated	7.657	7.656	40.2	35.4	5
2	7075	Uncoated	7.656	7.657	35.4	30.4	5
3	7075	Uncoated	7.657	7.656	30.4	25	5
4	7075	Uncoated	7.656	7.657	25	20.15	5
5	7075	Uncoated	7.657	7.656	20.2	15.2	5
6	7075	Uncoated	7.656	7.655	15.2	10.2	5

## 7 Conclusion

The objective of the study was to investigate the effect of the  $ZrB_2$  nano-ingredient on uncoated tool wear for an aluminum alloy-based metal matrix composite. The objective is achieved by performing extensive experimental pilot tests on a fabricated Al alloy-based MMC on a CNC lathe machine for an uncoated tool insert with 3% by weight concentration of  $ZrB_2$  nano-ingredient. In this work, an aluminum-based metal matrix composite is fabricated with  $ZrB_2$  as reinforcement material to enhance mechanical as well as tribological properties. In this paper, the machining of an Al-MMC rod is performed with an uncoated insert so as to compare the weight loss (wear rate) with the reduced diameter of Al-MMC rod. The weight loss of the cutting tool insert during machining on a CNC machine increases initially for the first 5-minute test for the considered sample during test run 1. During further tests, it is seen that the weight loss of the cutting tool insert decreases linearly after equal intervals. During run 2, it is observed that the weight loss of the cutting tool insert during machining decreases initially for first trial of the 5-minute test. Further testing shows that the weight loss of the cutting tool insert is constant and varies in a zigzag pattern after equal intervals.

**Financial and Ethical Disclosures** This work is not supported fully or partially by any funding organization or agency.

**Conflict of Interest** The authors declare that there is no conflict of interests regarding the publication of this paper.



## References

1. Hadley SW, Das S, Miller JW (1999) Aluminum R&D for automotive uses and the department of energy's role, ORNL/TM-1999/157, pp. 3
2. Mathan Kumar N, Kumarswamidhas LA (2018) Characterization and tribological analysis on AA 6061 reinforced with AlN and ZrB<sub>2</sub> in situ composites. *J Mater Res Technol* 8(1):969–980
3. Gautam GV, Kumar N, Mohan A, Mohan S, Singh D (2019) ZrB<sub>2</sub> nanoparticles transmuting tribological properties of Al<sub>3</sub>Zr/AA5052 composite. *J Braz Soc Mech Sci Eng* 41:469
4. Dinaharan I, Murugan N, Parameswaran S (2011) Influence of in situ formed ZrB<sub>2</sub> particles on microstructure and mechanical properties of AA6061 metal matrix composites. *Mater Sci Eng A* 528:5733–5740
5. Dinaharan I, Murugan N (2012) Dry sliding wear behaviour of AA6061/ZrB<sub>2</sub> in-situ composite. *Trans Nonferrous Met Soc China* 22:810–818
6. Thandalam SK, Ramanathan S, Sundarajan S (2014) Synthesis, microstructural and mechanical properties of ex situ Zircon particles (ZrSiO<sub>4</sub>) reinforced Metal Matrix Composites (MMCs): a review. *J Mater Res Technol* 4(3):333–347
7. Ciftci I, Turker M, Seker U (2004) Evaluation of tool wear when machining SiCp-reinforced Al-2014 alloy Matrix Composites. *Mater Design* 25:251–255
8. Sasimurugan T, Palanikumar K (2011) Analysis of the machining characteristics on surface roughness of a hybrid aluminium metal matrix composite (Al6061-SiC-Al<sub>2</sub>O<sub>3</sub>). *J Minerals Mater Character Eng* 10(13):1213–1224
9. Rajaneesh N, Marigoudar N, Sadashivappa K (2011) Dry sliding wear behaviour of SiC particles reinforced zinc-aluminium (ZA43) alloy metal matrix composites. *J Minerals Mater Character Eng* 10(5):419–425
10. Kumar V, Meti V, Konaraddi R, Siddhalingeswar IG (2018) Mechanical and tribological properties of AA7075 based MMC processed through ultrasound assisted casting technique. *Mater Today: Proc* 5:25677–25687
11. Kumar N, Narayanasamy G, Natarajan R, Kumaresh Babu S, Sivaprasad SP, Sivasankaran S (2010) Dry sliding wear behaviour of AA 6351-ZrB<sub>2</sub> in situ composite at room temperature. *Mater Des* 31(3):1526–1532
12. Kar C, Surekha B (2019) Effect of red mud and TiC on friction and wear characteristics of Al 7075 metal matrix composites. *Aust J Mech Eng*. <https://doi.org/10.1080/14484846.2019.1651138>
13. Singla M, Deepak Dwivedi D, Singh L, Chawla V (2009) Development of aluminium based silicon carbide particulate metal matrix composite. *J Minerals Mater Character Eng* 8(6):455–467
14. Sozhamannan GG, Balasivanandha Prabu S, Venkatagalapathy VSK (2012) Effect of processing parameters on metal matrix composites: stir casting process. *J Surface Eng Mater Adv Technol* 2:11–15
15. Bai W, Roy A, Sun R, Silberschmidt VV (2019) Enhanced machinability of SiC reinforced metal matrix composite with hybrid turning. *J Mater Process Tech* 268:149–161
16. Bhaskar CK, Kumar J, Singh H (2014) Production technologies of metal matrix composite: a review. *IJRMET* 4(2)
17. Radhika N (2015) “Prediction of tool condition during turning of aluminium/Alumina/Graphite hybrid metal matrix composites using machine learning approach”. *J Eng Sci Technol* 10(10):1310–1325
18. Udayashankar S, Ramamurthy VS (2018) Development and characterization of Al6061-Zirconium dioxide reinforced particulate composites. *Int J Eng Technol* 7(3.12):128–132
19. Moona G, Walia RS, Rastogi V, Sharma R (2018) “Aluminium metal matrix composites: A retrospective investigation”. *Indian J Pure Appl Phys* 56:164–175

20. Aruri D, Kumar A (2011) "Dry sliding wear and static immersion corrosion resistance of aluminium alloy 6061-T6/SiCp metal matrix composite prepared via friction stir processing". *Int J Appl Res Mech Eng (IJARME)*, ISSN: 2231-5950, 1(2)
21. Farooq RM, Konguraja G, Manikandan K (2019) "Fabrication and Testing of Metal Matrix Composites by Stir Casting Method", *ISSN (Online): 2319-6734, Volume 8 Issue 03 Series. II*, pp. 47-52

# Comparative Study on Dry Sliding Wear Behaviour of TiAlN, ZrAlN and ZrN/Al<sub>2</sub>O<sub>3</sub> Hard Coatings on ZA Alloys



B. Harish, K. R. Prakash, and R. Suresh

**Abstract** The objective of the paper mainly discusses on effects of coating each one of the below materials namely TiAlN, ZrAlN and ZrN + Al<sub>2</sub>O<sub>3</sub> on ZA-27 alloy specimens to understand wear resistance characteristics of such coated composite by cathodic arc coating techniques, also investigation was made on their composition, structure, hardness and wear behaviour at constant coating thickness using profilometer, EDX, SEM and pin on disc, respectively, at room temperature. The hardness of the ZrN + Al<sub>2</sub>O<sub>3</sub>, TiAlN and ZrAlN are 29.06 GPa, 24.49 GPa and 22.06 GPa, respectively, and the microstructure reveals that ZrN + Al<sub>2</sub>O<sub>3</sub> exhibited outstanding properties compared to other two because of columnar structure, dense grain size and multilayer coatings. Also, ZrN + Al<sub>2</sub>O<sub>3</sub> exhibited superior wear resistance than TiAlN and ZrAlN due to the Al<sub>2</sub>O<sub>3</sub> layer present on the upper layer of ZrN which prevents the effect of oxidation and reduces friction between tool and work piece.

**Keywords** Hard coatings · Cathodic arc coating technique · Microstructure · Wear · TEM

## 1 Introduction

The zinc-aluminium alloys (ZA27) are potential alloy to replace brass and steel for wear resistance machinery components especially used as bearing material due to lower friction coefficient [1], good wear resistance and good damping properties. The

---

B. Harish (✉)

Department of Mechanical Engineering, Maharaja Institute of Technology, Mysore, Karnataka, India

K. R. Prakash

Department of Mechanical Engineering, The National Institute of Engineering, Mysore, Karnataka, India

e-mail: [krp@nie.ac.in](mailto:krp@nie.ac.in)

R. Suresh

Department of Mechanical Engineering, VTU Center for PG Studies, Mysore, Karnataka, India

© The Author(s), under exclusive license to Springer Nature Singapore Pte Ltd. 2022

533

G. S. V. L. Narasimham et al. (eds.), *Innovations in Mechanical Engineering*,

Lecture Notes in Mechanical Engineering,

[https://doi.org/10.1007/978-981-16-7282-8\\_39](https://doi.org/10.1007/978-981-16-7282-8_39)

performance and life of the ZA bearings depends upon the surface properties and coefficient of friction between materials. However, ZA alloy material does not meet with the industrial requirements such as high speed and high load, hence they are restricted in automobile applications. Because of its good wear resistance properties of ZA-27 alloy many researchers put their effort to enhance the wear resistance of this alloy by heat treatment, addition of alloying elements, hard particle reinforcement and protective coatings [2–5]. The results have showed that the coated specimens are performing at high temperature approximately 600 °C which is generated during the wear process at high speeds and loads. Hence, the coated specimens are thermally stable at high temperature [6] and suitable as bearing materials. Nitride-based hard coatings are widely used as coating material for bearing because of outstanding hardness and wear resistance. They also provide corrosion protection in the form of a passivation layer on the components [7]. Addition of Al element into nitride material further improves wear resistance at higher temperature and these results were recorded by many researchers. However, ZrAlN coating on ZA-27 is very less explored which is the partial miscibility gap between ZrN and AlN, which makes a heterogeneous mixture than that of homogeneous materials. ZrAlN and ZrN/Al<sub>2</sub>O<sub>3</sub> are possible alternative candidates for well-established TiAlN and CrAlN hard coatings. But ZrAlN stability always depends on deposition technique and aluminium content of 0.3–0.5 based on density functional theory [8–10] so far all metal nitride and carbo-nitride coating on the surface of ferrous materials using physical vapour deposition techniques were done reported [11]. Also as per author knowledge no researchers worked on metal nitride coated on nonferrous metal like aluminium, ZA, copper, etc. there is an apparent lack of information regarding the wear resistance of nitride coating. The objective of the work is to investigate on chemical composition, morphological, micro hardness and wear properties of TiAlN, ZrAlN and ZrN/Al<sub>2</sub>O<sub>3</sub> hard coatings on ZA alloys by cathodic arc evaporation has been chosen for synthesis to present result intended to determine the best potential candidate for bearing applications.

## 2 Experimental Study

### 2.1 ZA Specimen Preparation

The present work ZA-27 alloy was selected as a base material, and its chemical composition as per ASTM standards (Al-25%, Cu-2%, Mg-0.01, Zn-balance). The specimens (12 mm diameter and 35 mm length) were prepared using liquid metallurgical technique. Wear cylindrical specimens (pin) of 8 and 20 mm were machined from the prepared casting. Then, both the circular face of the cylindrical surface was polished for a smooth surface as per standards before coating.

## **2.2 Coating on ZA Circular Surfaces**

Vaporised material impinges on the substrates and forms a thin layer of coating. The two target materials for TiAlN are Ti and Al blocks. Similarly for ZrAlN, Zr and Al blocks are used in the process and allow nitrogen and oxygen gas alternatively one after the other. Also Ar/N<sub>2</sub> gas is used to ensure high degree of ionisation, the pressure that is maintained during the process in the chamber is about 1–1.5 Pa. This process provides uniform distribution of the coatings on the substrate.

## **2.3 Surface Roughness Characterisation**

After coating of the specimens, the roughness of the samples is held in the wax mould to avoid any disturbance during the movement of stylus then they are characterised using MAP3D-25 stylus profilometer to determine the surface roughness of the deposited coatings. The six samples were selected for each condition and measured the average roughness of coatings deposited.

## **2.4 Surface Morphology Studies**

The coated specimens prior to conduct surface morphology are cleaned with acetone to remove any impurities/dust particle. For each run samples were mounted in the scanning electron microscope for the analysis, the samples are mounted in the chamber on a small carousel with small pellets using clay glue to investigate the coatings structure and grain boundaries. The coated specimen chemical compositions were determined by using Qunato FIG 600 energy dispersive spectroscopy analyser.

## **2.5 Hardness Test**

Hardness of the polished coated specimens was measured using Matsuzawa Hardness Tester MMT-X7A on Vickers hardness. The diamond pyramid type indenter was used for a load of 10 g with dwell time of 20 s. The hardness values were computed as per standard formula.

## 2.6 Wear Test

The wear test was conducted as per ASTM G99 standard at dry condition using pin on EN 24 material disc test rig diameter of 200 mm and surface roughness was  $2\ \mu\text{m}$  and its hardness of BHN 229. Before wear test both counter disc and wear specimen were cleaned by washing with acetone to remove traces of grease. The weight loss was measured using electronic balance of nearest 0.1 mg. The wear tracks were made on the pin on disc machine with normal loads of 20, 40, 60, 80 and 10 N and which was run for a total of 1000 cycles at 100 rpm in dry condition. This was done to ensure that enough particles are being generated without high rise in temperature which might alter the properties of the pin.

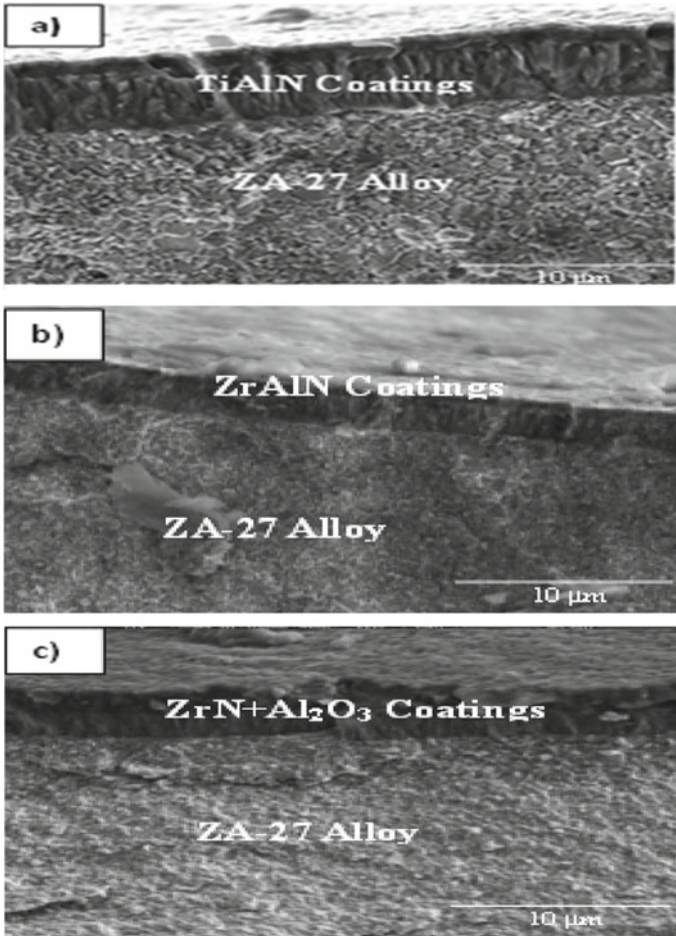
## 3 Result and Discussion

### 3.1 Microstructure

Figure 1a–c shows transfer section for TiAlN, ZrAlN and ZrN + Al<sub>2</sub>O<sub>3</sub> coated specimens on the ZA-27 alloy, respectively. The image shows the two different layers and their unevenness on the surfaces. The larger surface is ZA-27 alloy (host) and smaller layer respective coatings. All three type coating showed a columnar structure of oriented in (111) plane. At the interface between the matrix and coating material more porosity were observed in the case of TiAlN coated specimen as shown in Fig. 1a. Figure 1b shows transfer section image of ZrAlN coated specimen, which has columnar grain structure, which is similar to TiAlN with grain structure orientation of (111) direction. But some reduction in columnar structure was observed along with micro-particles on the coating surface, which promotes the roughness of the coatings. Figure 1c shows ZrN/Al<sub>2</sub>O<sub>3</sub> multi-layered coated surface images, which has two clear distinction layers such as bottom ZrN and top Al<sub>2</sub>O<sub>3</sub> layers. ZrN layer are identified by columnar structure in the direction of (111) and Al<sub>2</sub>O<sub>3</sub> layer is much denser structure. The multi-layer coating has less cavities and porosity compared to ZrAlN and TiAlN coatings and few micro-particles are observed on the surface of the coatings. Due to combined effect of multi-layer expected more hardness values.

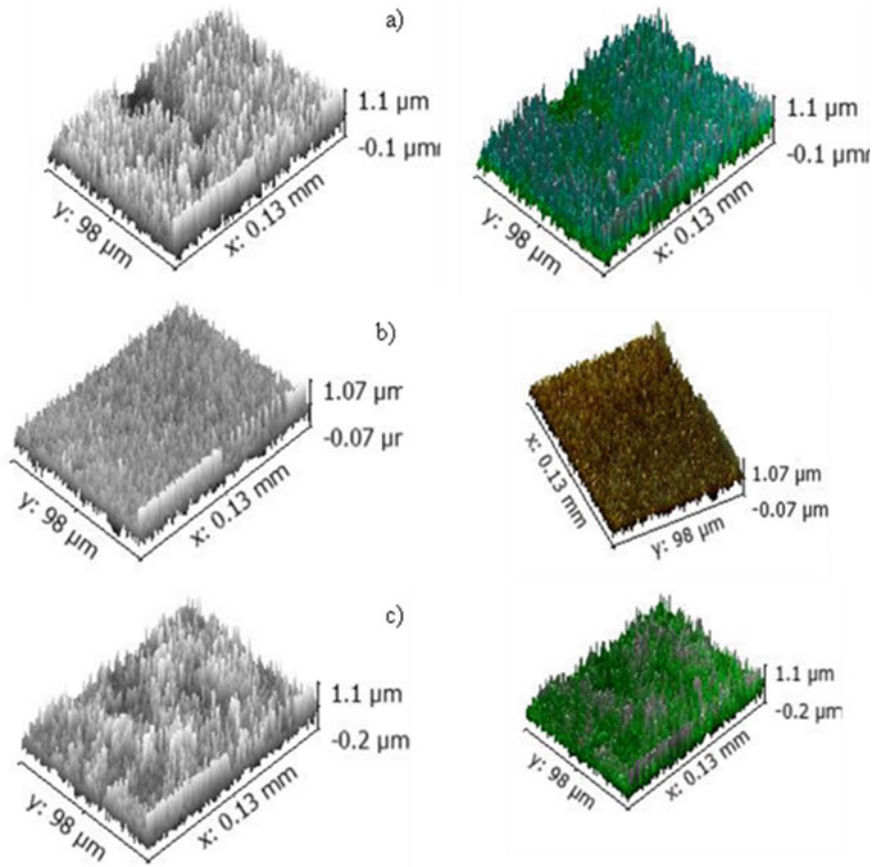
### 3.2 Surface Roughness of the Coatings

Stylus profilometer gives the surface roughness of the coated insert. The 3D image generated shows the type of surface morphology present on the coating. Figure 2a–c shows 3D representation of surface texture of TiAlN, ZrAlN and ZrN + Al<sub>2</sub>O<sub>3</sub> coated specimens on the ZA-27 alloy, respectively. Figure 2a shows the average roughness is  $0.003\ \mu\text{m}$ . Low surface roughness indicates that the bearing will have



**Fig. 1** SEM images of transfer section of coated specimens

better tribological properties and reduces the power consumption of the bearing. TiAlN and ZrN/Al<sub>2</sub>O<sub>3</sub> show the least surface roughness, whilst ZrAlN shows slightly higher surface roughness. This could be due to micro-particles deposition due to impingement of sputtered particles during the coating process. In all the coatings, some porosity in the structure is observed which could be a reason for the roughness. The porous sites are the regions where the coating deposition is uneven.

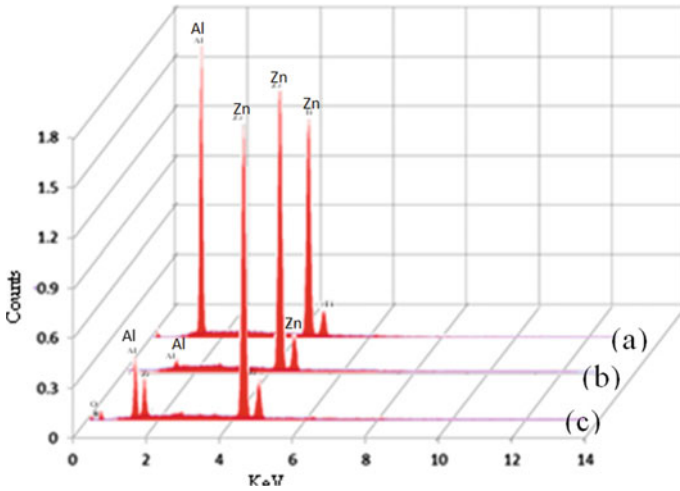


**Fig. 2** 3D images of ZA-27 coated with **a** TiAlN coating, **b** ZrAlN coating and **c** ZrN + Al<sub>2</sub>O<sub>3</sub> coating

### 3.3 Energy Dispersive Spectrometry

Figure 3 (curve a) shows the EDS mapping of elements present in TiAlN coated specimen. It is found that the coating has 60.35% of Ti, 25.84% of Al and 13.81% of N. Excess Al content is not found in the coating. The EDS mapping (curve b) of elements present in ZrAlN coated specimen. The percentage composition in Zr is the highest in ZrAlN (53.71%) coatings, followed by Al (28.67%). The EDS mapping (curve c) of elements present in ZrN + Al<sub>2</sub>O<sub>3</sub> coating. It is found Zr is the highest in proportion relative to all the elements. In all the three cases the percentage of oxygen is not detected as the atomic number, Z for oxygen is less than 11 and it is extremely difficult to detect any such element by EDS technique. Since all the coatings show very less proportion of nitrogen there could be a possible contamination by oxygen





**Fig. 3** Spectrum showing percentage of different elements present in **a** TiAlN coating, **b** ZrAlN coating and **c** ZrN + Al<sub>2</sub>O<sub>3</sub> coating

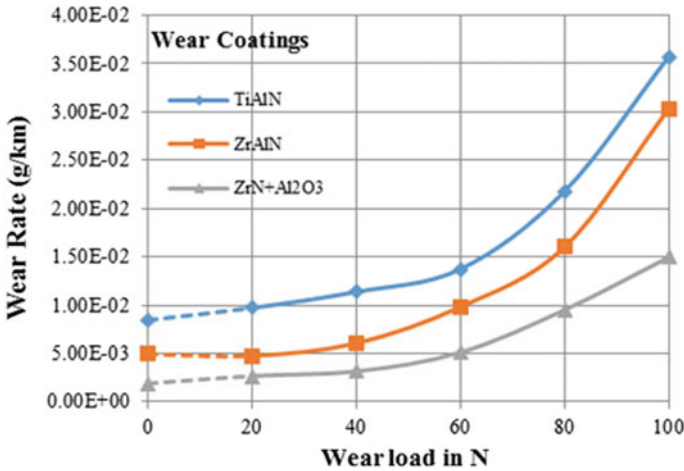
(more than 3%) in all coatings. Similar findings are reported by Veprek and Veprek in Ref. [12].

### 3.4 Micro Hardness

Table 1 gives the results of Vickers microhardness test results performed on all the three coatings. It is observed that ZrN/Al<sub>2</sub>O<sub>3</sub> coating showed the highest hardness among all the three types of coating. The increase in the hardness can be attributed to the Al<sub>2</sub>O<sub>3</sub> layer which is known to improve the hardness of the ZrN coatings as suggested by many researchers [13, 14]. It has been found that Al<sub>2</sub>O<sub>3</sub> layers have better hardness, high melting points. Hence, it can be concluded that Al<sub>2</sub>O<sub>3</sub> acts as a beneficial layer in increasing the density and hardness of the coating. Further ZrAlN shows the second highest hardness compared to TiAlN, this is because Zr has larger lattice parameter compared to Ti and also the self-organising structure of ZrAlN into c-ZrN and w-AlN is known to improve its hardness.

**Table 1** Hardness of the different coatings on ZA-27 alloy

Type of coating	Hadness (Hv 0.1)	Hardness (GPa)
TiAlN	2349	23.04
ZrAlN	2497	24.39
ZrN + Al <sub>2</sub> O <sub>3</sub>	2786	27.36



**Fig. 4** The variation of wear rate plotted against wear load for three different coatings (dotted lines are extrapolated values)

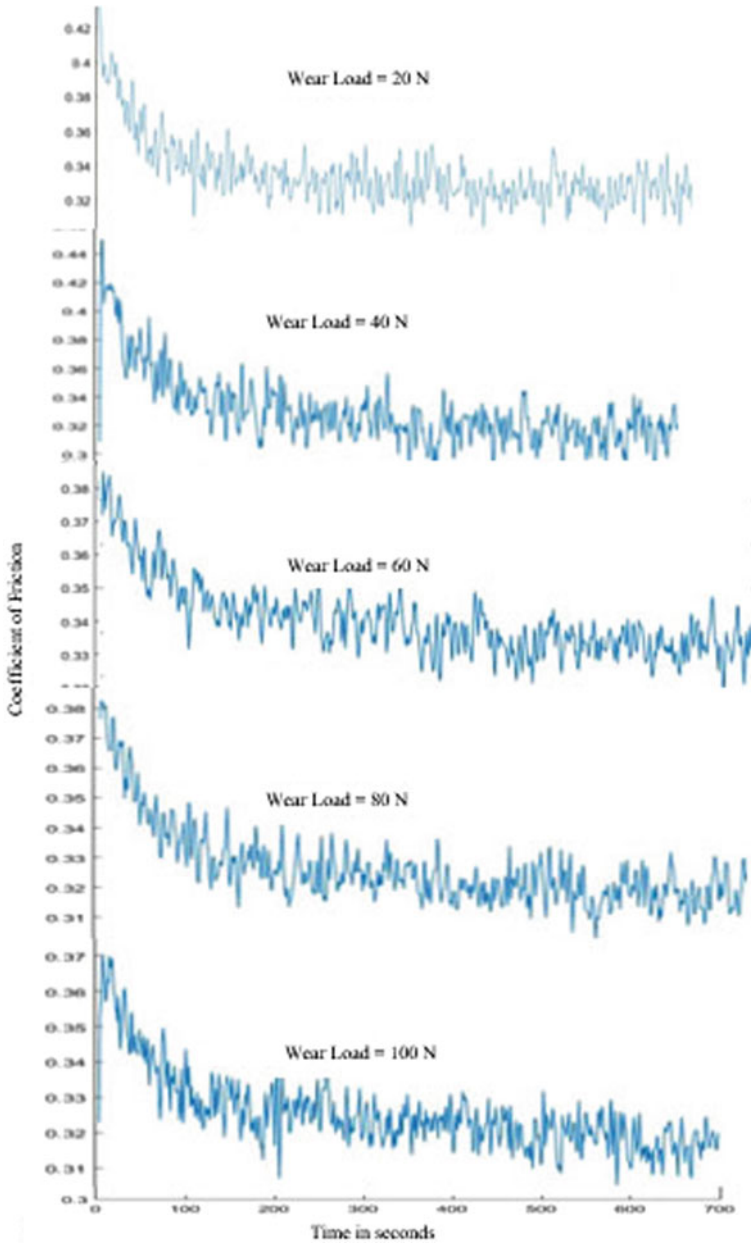
### 3.5 Wear Rates

Figure 4 shows the variation of wear rates of the three coatings such as TiAlN, ZrAlN and ZrN + Al<sub>2</sub>O<sub>3</sub> with wear loads of 20, 40, 60, 80 and 100 N. The wear rates are increasing with increasing wear loads in nonlinearly. The same trend was observed in all three coatings but the effect is more severe for TiAlN and ZrAlN coatings and less severe for ZrN + Al<sub>2</sub>O<sub>3</sub> coating. The wear rate from 20 to 60 N almost linear in all three cases but wear transition occurs at 60 N then it is exponentially increased with loads. TiAlN and ZrAlN coatings were subjected to wear transition from mild wear to severe wear because of surface hardness, roughness and porosity in the coatings. Due to multi-layer coating of ZrN + Al<sub>2</sub>O<sub>3</sub> increases hardness and reduces the porosity which leads to reduce the wear resistance.

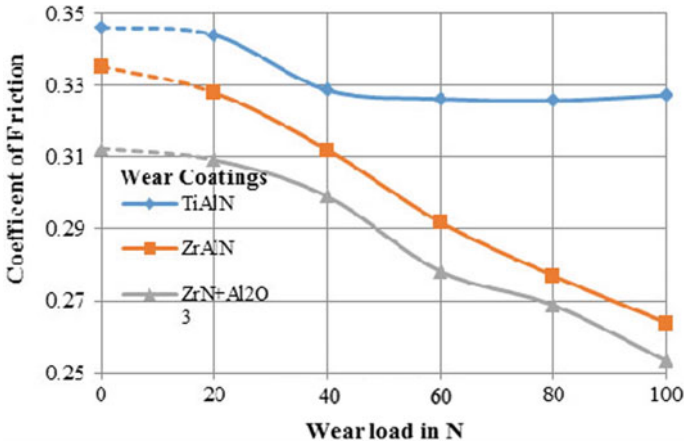
### 3.6 Coefficient of Friction

Figure 5 shows a typical coefficient of friction results obtained on a pin on disc machine. This was done to obtain maximum frictional force thereby ensuring significant coating material transfer and particle generation.

From Fig. 5, it can be observed that the frictional force increases when the normal load increases irrespective of coatings. It is observed that the coefficient of friction is initially very high and then reduces steeply within 5–8 s, this is due to the change of static friction to dynamic friction and also wear track formation. It can also be observed that the coefficient of friction gradually reduces further down to a lower



**Fig. 5** A typical graph of coefficient of friction as a function for various loads of 20 N, 40 N, 60 N, 80 N and 100 N for TiAlN coated ZA-27 alloy



**Fig. 6** Coefficient of friction as a function for various loads for TiAlN, ZrAlN and ZrN + Al<sub>2</sub>O<sub>3</sub> coated ZA-27 alloy (dotted lines are extrapolated values)

level before obtaining a saturated value, this is due to the phenomena of adhesive wear. Initially, the friction is between the coating and the metal but later the coating degenerated from the pin gets adhered to the plate and gradually the friction between metal and coating becomes friction between coating to coating there by reducing.

As the coefficient of friction values determined are found to fluctuate about average values in all the cases for the selected ranges of sliding time of 700 s, the average coefficient of friction has been considered and its variation with wear load is shown in Fig. 6 for all three types of coatings. The coefficient of friction of all three type of coating decreases with increasing load but TiAlN coating specimens decreases up to 40 N then it maintained steady state coefficient of friction which may be metal to metal contact after the complete removal of coating on the surface.

## 4 Conclusion

1. ZrN/Al<sub>2</sub>O<sub>3</sub> has the highest hardness of 27.32 GPa when compared to other two coatings. The dense grain structure and reduced grain size improves the coating hardness. Due to multilayer coating, the hardness improves.
2. EDS test shows the percentage of composition of the coatings. Percentage of Al is between 25 and 28% which helps in better hardness of the coating. Less percentage of nitrogen is present in all the coatings. The surface roughness of the coatings Ra, value between 0.02 and 0.03 μm.
3. SEM images show the columnar structure in TiAlN and ZrAlN. ZrN regions are identified by columnar grain in (111) direction and the Al<sub>2</sub>O<sub>3</sub> layer is somewhat dense in its structure very less porosity and cavities are observed.

4. Wear rate of ZrN + Al<sub>2</sub>O<sub>3</sub> coated specimen is significantly lower than the other two coating specimens
5. The average coefficient of friction of ZrN + Al<sub>2</sub>O<sub>3</sub> multilayer coated samples is less than that of the other coatings and decrease with increasing wear load is observed.

## References

1. Babic M, Stojanovic B, Dzunic D, Pantic M (2019) Micro/nanoscale structural, mechanical and tribological characterization of ZA-27/SiC nanocomposites. *J Composite Mater* pp 1–17
2. Sastry S, Krishna M, Uchil J (2001) A study on damping behaviour of aluminite particulate reinforced ZA-27 alloy metal matrix composites. *J Alloys Compounds* 314(1–2):268–274
3. Miroslav B, Vencel A, Mitrović S, Bobić I (2009) Influence of T4 heat treatment on tribological behavior of ZA27 alloy under lubricated sliding condition. *Tribol Lett* 36:125–134
4. Türk A, Durman M, Kayali ES (2007) The effect of manganese on the microstructure and mechanical properties of zinc–aluminium based ZA-8 alloy. *J Mater Sci* 42:8298–8305
5. Bobić B, Vencel A, Ružić J, Bobić I, Damjanović Z (2019) Microstructural and basic mechanical characteristics of ZA27 alloy-based nanocomposites synthesized by mechanical milling and compocasting. *J Composite Mater* 53(15):2033–2046
6. Ramanauskas R, Juškėnas R, Kaliničenko A (2004) Microstructure and corrosion resistance of electrodeposited zinc alloy coatings. *J Solid State Electrochem* 8:416–421
7. Selvakumar N, Barshilia HC (2012) Review of physical vapor deposited (PVD) spectrally selective coatings for mid-and high-temperature solar thermal applications. *Solar Energy Mater Solar Cells* 98:1–23
8. Bertrand G, Mahdjoub H, Meunier C (2000) A study of the corrosion behaviour and protective quality of sputtered chromium nitride coatings. *Surface Coat Technol* 126 (2–3):199–209
9. Rogström L, Johansson-Jöesaar MP, Landälv L, Ahlgren M, Odén M (2015) Wear behavior of ZrAlN coated cutting tools during turning. *Surface Coat Technol* 282:180–187
10. Singh A, Kuppusami P, Thirumurugesan R, Ramaseshan R, Dash S, Mohandas E (2013) Characterisation of ZrAl and ZrAlN thin films prepared by pulsed DC magnetron sputtering. *Trans Indian Inst Met* 66(4):363–367
11. Araiza JJ, Sánchez JMA (2009) Influence of the aluminum incorporation on the structure of sputtered ZrN<sub>x</sub> films deposited at low temperatures. *Vacuum* 83(10):1236–1239
12. Zhang JJ, Wang MX, Yang J, Liu QX, Li DJ (2007) Enhancing mechanical and tribological performance of multilayered CrN/ZrN coatings. *Surface Coat Technol* 201(9–11):5186–5189
13. Vepřek S, Vepřek-Heijman MGJ, Karvankova P, Prochazka J (2005) Different approaches to superhard coatings and nanocomposites. *Thin Solid Films* 476(1):1–29
14. He XD, Dong L, Wu J, Li DJ (2019) The influence of varied modulation ratios on crystallization and mechanical properties of nanoscale TiB<sub>2</sub>/Al<sub>2</sub>O<sub>3</sub> multilayers. *Surface Coat Technol* 365:65–69
15. Vepřek S, Reiprich S, Shizhi L (1995) Superhard nanocrystalline composite materials: the TiN/Si<sub>3</sub>N<sub>4</sub> system. *Appl Phys Lett* 66:2640–2642

# Failure Load of Jute–Coir Fiber Reinforced Epoxy Matrix Composites Using Micromechanics and Finite Element Method



Jami Sai Revanth, G. Pavan Kumar, P. Phani Prasanthi, K. Sai Phani Teja, A. Rama Satyanaryana, and G. Ashok Kumar

**Abstract** The usage of natural fiber reinforced composites is increasing in the present decade as these materials showing good mechanical properties and promoting biodegradability. In this work, two different natural fibers such as jute and coir fibers reinforced in epoxy matrix in different proportions are considered and elastic properties are estimated with the combination of micromechanics and finite element method. Further, using analytical and simulation methods, the safe load of the considered combination of composite materials are predicted and failure load of the composite also estimated. The finite element models are verified with analytical results, and good relation is observed between them. The present work is used for effective design of natural hybrid composite with the perspective of failure load.

**Keywords** Jute fiber · Coir fiber · Hybrid composite · Failure load · Micromechanics · Finite Element method

## 1 Introduction

Fiber reinforced laminated composites are used in many applications due to their higher specific strength-to-stiffness ratio, better corrosion and fatigue resistance compared to steel and aluminum, which are majorly used in structural and engineering applications [1]. Composites used in structural elements must be able to sustain high impact loads, shock loads; these are more durable and better alternatives for steel and concrete [2].

Composite materials have good tailorable properties so that it had been used in many precision industries [3]. As a fundamental issue, fiber–matrix interfacial properties extraordinarily influence on the mechanical behavior and load transferring phenomenon of composite structures, the failure of composite materials is catastrophic in nature [4]. Failure of composite materials had been reviewed broadly

---

J. S. Revanth (✉) · G. Pavan Kumar · P. Phani Prasanthi · K. Sai Phani Teja · A. Rama Satyanaryana · G. Ashok Kumar  
Department of Mechanical Engineering, PVP Siddhartha Institute of Technology, Vijayawada, India

using mathematical and phenomenological techniques in micromechanical scale, initiation of failure and mechanisms of failure varies with type of loading and are secretly related to the physical, mechanical and geometric properties of the ingredient phases [5].

As composites show nonlinear and rate-dependent behavior, testing them would be a difficult task and costly too. To promote and hasten the process of advancing, estimating and adopting unique composite materials, it is significant to rivet comprehend and program the characterization, modeling and failure estimation of structural laminates based on the properties of the constituent materials has to be done [6].

When uniaxial stress applied in a particular direction excluding the principal material axes produces multi-axial strains along the principal material axes of orthotropic material [7]. Therefore, the strengths of isotropic materials must be predicted through a desired failure criterion. Many failure theories are not general but are applicable only to some specific types of composites [6]. To use the theories, applied stresses to strains are transformed into the corresponding stresses to strains along the principal material directions. It is concluded that the fiber volume fraction of the epoxy section needs to be higher than that of the epoxy section in order to achieve positive hybrid. In extension to unidirectional composites, in a study on the hybrid composites made of fiber and coir woven fabrics has shown that the tensile and compressive strengths showed Effects in a positive way. In an exploration of fiber composites, Miwa and Horiba came to know that the tensile strength of hybrid composite can be estimated by using the additive rule of hybrid mixtures, using the tensile strength of both composites. Besides coir and fibers, hybrid composites reinforced by other fiber types are also can be developed. The positive or negative deviation from a particular mechanical property from the rule of mixtures behavior indicates the presence of positive or negative hybrid effect [8].

As many studies focus on material properties of hybrid composites using micromechanics and finite element method for synthetic fiber composite. In this work, natural fiber reinforced composites and their hybridization effect on failure strength estimates from finite element models with analytical validation.

## **2 Finite Element Method for Hybrid Composite:**

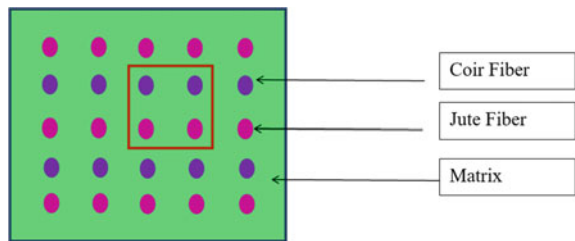
Micromechanics approach for hybrid composites—In this work, two natural fibers such as jute and coir fibers are selected and theses fibers are assumed to be distributed uniformly in the polymer matrix. Using the square array and selecting one unit cell, the properties of the jute–coir combined epoxy matrix is estimated at different combinations of natural fibers.

### 3 Methodology

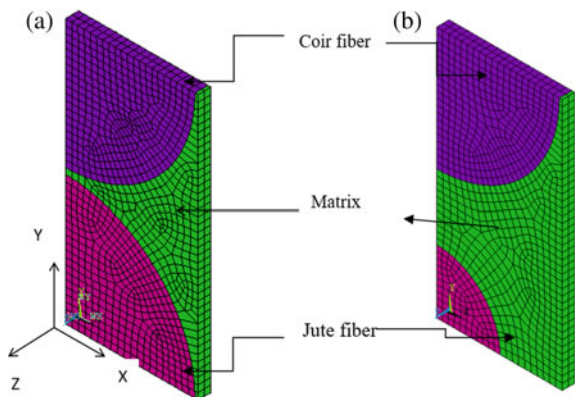
As shown in Fig. 1, the jute and coir fibers are uniformly placed in the matrix material and considering the analysis of one unit cell gives the entire composite properties. Owing the conditions of symmetry of the geometrical model for finite element analysis, loading and boundary conditions, one eighth portion which includes jute, coir fiber, matrix materials was taken for the analysis.

The symmetric unit cell which representing the hybrid composite is presented in Fig. 2. Applying unit pressure in the direction of fiber ( $Z$ ), the deformations will be attained in the model based on respective Young’s modulus, and composite Young’s modulus is determined from the deformations, load using Hook’s law. Figure 2 shows the  $H1$  and  $H7$  models; in the  $H1$  model, the jute and coir volume fractions are 37.5% and in the  $H7$  model the jute and coir volume fractions are 10% and 37.5% respectively. Table 1 presents the volume fraction of each constituent of hybrid composite. By changing the direction of loading to  $X$  or  $Y$ , the transverse modulus  $E2$  and  $E3$  is estimated. The breaking load of the composite is calculated from the ultimate strength and strain of the each constituent. The breaking load is obtained from analytical result. First strain ( $\epsilon$ ) in the composite and every composite is computed by using ultimate strength to Young’s modulus of respective constituent. From the calculated strain ( $\epsilon$ ), the smallest percentage of strain is taken for breaking strength

**Fig. 1** Representation of jute and coir fiber in the matrix and representation of unit cell



**Fig. 2** FE model of  $H1$  combination, **b** FE model of  $H7$  combination





**Table 1** Volume fraction of jute, coir fiber and matrix material

<i>vf1</i>	<i>vf2</i>	<i>vm</i>
0.375	0.375	0.25

**Table 2** First safe load of jute, coir and matrix material

$\sigma_u$ of jute (MPa)	473
$\sigma_u$ of coir (MPa)	144.6
$\sigma_u$ of matrix (MPa)	7.4
<i>E</i> of jute (MPa)	19,500
<i>E</i> of coir (MPa)	3101.2
<i>E</i> of epoxy (MPa)	176
<i>em</i>	4.20E-02
<i>ef1</i>	2.43E-02
<i>ef2</i>	4.66E-02
$\sigma_m$ (MPa)	4.26
$\sigma_j$ (MPa)	473
$\sigma$ coir (MPa)	75.22398

and multiplied with respective ultimate strength to get composite stress ( $\sigma_c$ ) which is equal to  $\sigma_{1f} v_{1f} + \sigma_{2f} v_{2f} + \sigma_{mv}$ , *1f* stands for jute, *2f* for coir, *m* for matrix. For sample calculations, taking *H1* specimen which had volume fractions fiber and matrix are as presented in Table 1 and the calculation procedure and first, second and third safe load are presented from (Table 2-4).

Now by calculating  $\sigma_c = 206.65$  MPa and the corresponding load is

$$206.65 * 100 * 200 = 4133000 \text{ N} = 4133 \text{ KN}$$

See Table 3.

Now by calculating excluding failed jute fiber

$$\sigma_c = 374 \text{ MPa the corresponding load is } 206.65 * 100 * 200 = 7.49E + 06 \text{ N} = 7489 \text{ KN}$$

See Table 4.

**Table 3** Second safe load of jute, coir and matrix material

$\sigma_u$ of jute (MPa)	473
$\sigma_u$ of coir (MPa)	144.6
$\sigma_u$ of matrix (MPa)	7.4
<i>E</i> of jute (MPa)	19,500
<i>E</i> of epoxy (MPa)	3101.2
<i>em</i>	4.20E-02
<i>ef2</i>	4.66E-02
$\sigma_m$ (MPa)	1302.4
$\sigma$ coir (MPa)	130

**Table 4** Third safe load of jute, coir and matrix material

$\sigma u$ of jute (MPa)	473
$\sigma u$ of coir (MPa)	144.6
$\sigma u$ of matrix (MPa)	7.4
$E$ of jute (MPa)	19,500
$E$ of epoxy (MPa)	3101.2
$ef^2$	4.66E-02
$\sigma$ coir (MPa)	6.74

**Table 5** Volume fraction of jute, coir and matrix material

Specimen	Volume fraction of jute fiber $vf_1$ (Jute)	Volume fraction of coir fiber $vf_2$ (Coir)	Volume fraction of epoxy matrix ( $V_m$ )
H1	0.375	0.375	0.25
H2	0.375	0.3	0.325
H3	0.375	0.2	0.425
H4	0.375	0.1	0.525
H5	0.3	0.375	0.325
H6	0.2	0.375	0.425
H7	0.1	0.375	0.525

**Table 6** Material properties for FE Analysis [9]

Property	Jute fiber	Coir fiber	Epoxy matrix
Tensile strength (MPa)	473	146.6	7.4
Young’s modulus (MPa)	19,500	3101.2	176

Final breaking load is  $\sigma_c = 2.53$  MPa (excluding jute and coir fiber) the corresponding load is  $2.53 * 100 * 200 = 5.06E + 04$  N = 50.57 KN.

See Table 4. The volume fraction of different models are presented in Table 5.

**Material Properties:** The finite element simulation studies are performed by the material properties as mentioned in Table 6. Using these properties, simulation and analytical results are framed.

The finite element models are validated with analytical result, such as the rule of mixture for longitudinal modulus and transverse modulus with Bettie’s reciprocal theorem.

### 4 Results and discussion

Figure 3 shows the variation of Young’s modulus of jute–coir fiber reinforced epoxy composite. The longitudinal modulus ( $E_1$ ) of hybrid composite is more than the transverse modulus ( $E_2$  and  $E_3$ ) and perfect closeness between the finite element results and analytical results also observed from the same Fig. 3.

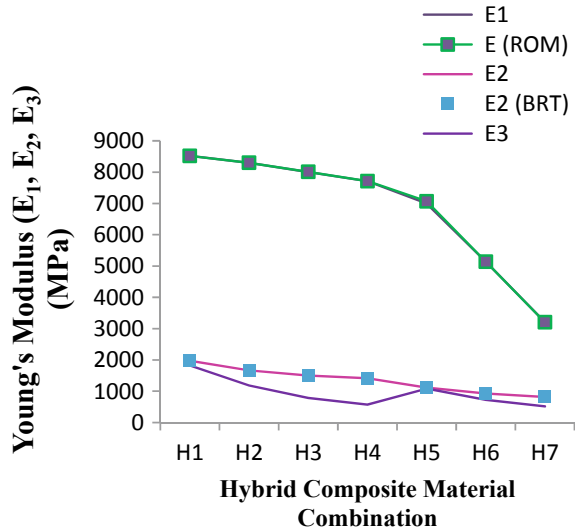
The longitudinal modulus ( $E_1$ ) is decreasing from  $H1$  model to  $H7$  models. In the  $H1$  model, the jute and coir fibers are sharing equal volume fractions and at the end of the Fe model  $H7$  having highest volume fraction of coir and minimum volume fraction of jute fiber. Up to  $H4$  model, good longitudinal modulus is observed that is due to the more contribution of jute fiber in the composite material after  $H4$  model, fall in the property is observed; this is due to the more contribution of coir and less percentage of jute fiber. From these results, it is found that the longitudinal modulus of the composite will be better enhanced by the jute fiber contribution than coir fiber.

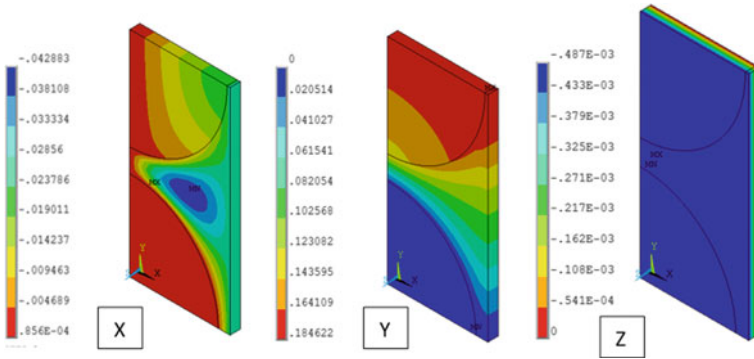
The transverse modulus ( $E_2$  and  $E_3$ ) also slightly decreases with increasing the model number. No considerable changes in the property are observed with the variation of fiber percentage combinations in these properties.

The deformation followed by strain is controlled by major and minor Poisson’s ratios. The major Poisson’s ratio of hybrid composite in different combination of fiber fraction is plotted in Fig. 5. From this Fig. 5, it is observed that the Poisson’s ratio is not changing significantly with jute and coir combination. The major Poisson’s ratio ( $\nu_{12}$ ) is increasing from  $H4$  to  $H7$  due to increasing the lateral strain of the composite with coir fiber enhancement (Fig. 5).

Figure 6 shows the minor Poisson’s ratio of natural hybrid composite for different composite specimen models of  $H1$  to  $H7$ .

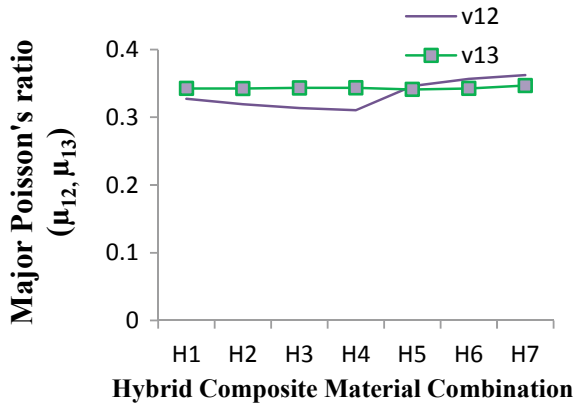
Fig. 3 Young’s modulus of jute–coir hybrid composites



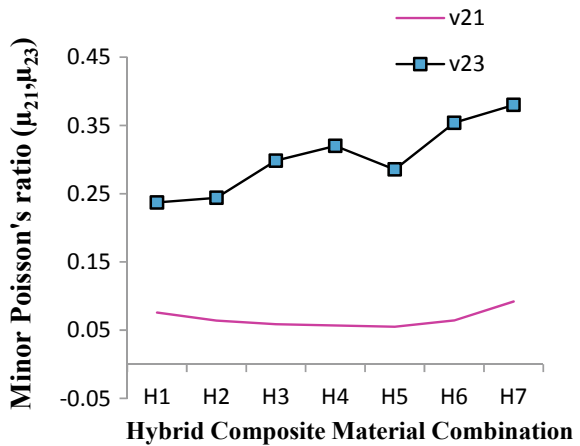


**Fig. 4** Finite element contours represent X, Y and Z directional displacement

**Fig. 5** Major Poisson’s ratio of jute–coir hybrid composites



**Fig. 6** Minor Poisson’s ratio of jute–coir hybrid composites



**Fig. 7** First failure load of hybrid composite

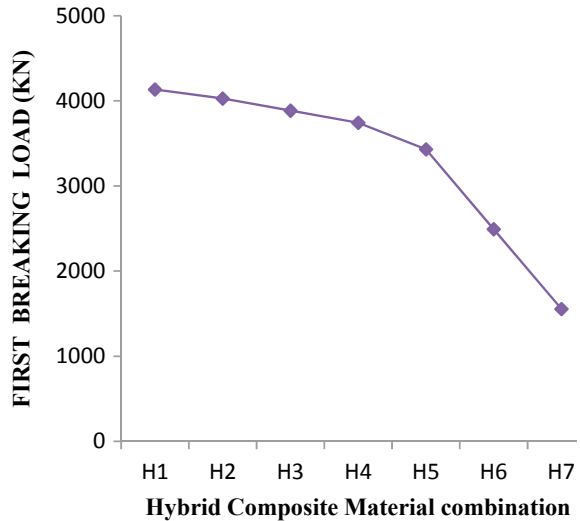
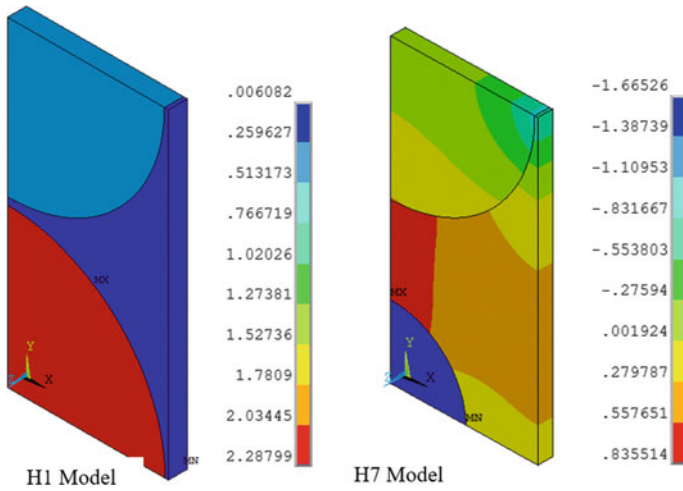


Figure 7 shows the first failure load of hybrid composite. This load is obtained from analytical equations. The first failure is obtained from the ultimate load of the each constituent. From the present work, the first load of the composite is high for *H1* model and this load is decreasing from *H1* to *H7* models. That is for composite with 37.5% of jute and coir fiber and 25% of matrix is having better strength under longitudinal load. The first failure in the hybrid composite is observed in jute fiber under longitudinal loading. This is due to more strength contribution of jute fiber to the applied load; this fiber protected the core fiber and matrix material because of that reason the failure is observed first in jute fiber. Figure 8 shows the stress contours in the fiber direction for *H1* and *H7* model. In the *H1* specimen, the jute fiber volume fractions more and experienced more stress, whereas in *H7* model, the coir fiber percentage is more the jute fiber at in this specimen (*H7*) the interface of jute and matrix got more stress (Fig. 8).

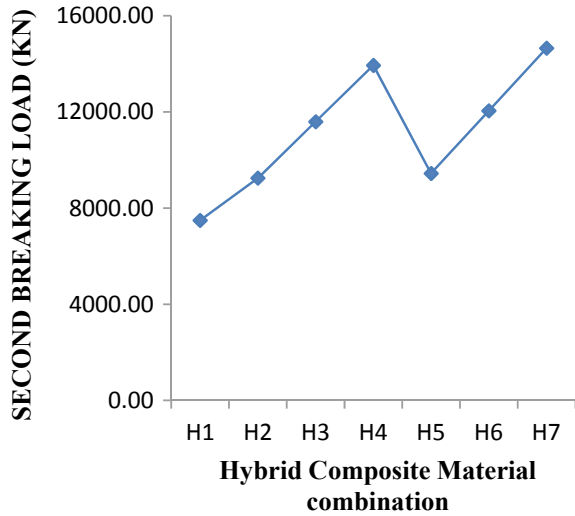
Figure 9 shows the second safe breaking load of the hybrid composite. In this case, no particular trend is observed, this is load is calculated by omitting the jute fiber contribution because the jute fiber is already reached failure strength. The second breaking load is increasing from *H1* to *H4* and showed less strength for *H1* model that is the specimen having more coir fiber. In this case, the coir fiber got failed than matrix material under longitudinal loading. The strength required for second failure is more due to the participation of coir fiber and matrix material.

The magnitude of third breaking load is very less compared to first and second failure loads. This is due to the contribution of only matrix to the applied load. This is clearly shown in Fig. 10.



**Fig. 8** Fiber directional stresses in *H1* model and *H7* model

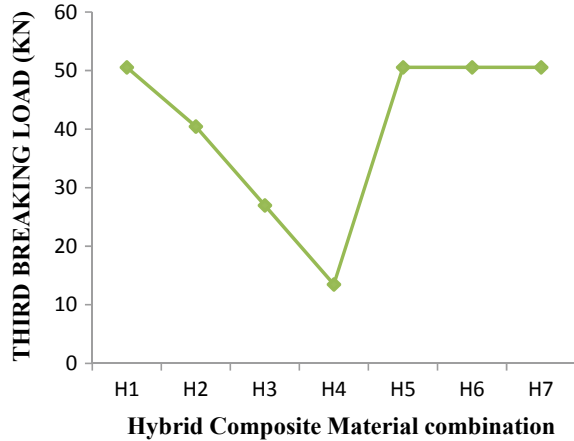
**Fig. 9** Second breaking load of hybrid composite



## 5 Conclusion

The natural fiber reinforced composite such as jute and coir fiber reinforced epoxy composite elastic properties, breaking load of the composite at different volume fraction of natural fibers has been identified from micromechanics approach using finite element method.

**Fig. 10** Third breaking load of hybrid composite



The following observations are made from the present work.

- The longitudinal modulus of jute–coir fiber reinforced epoxy matrix is effectively controlled by jute fiber volume fraction.
- The transverse modulus of hybrid composite is very less and slightly decreasing with decreasing the jute fiber volume fraction
- The first breaking load of the hybrid composite high for higher volume fraction of jute and coir fiber and the first failure is observed in jute fiber.
- The second failure load is effectively controlled by coir fiber in the hybrid composite.
- The third breaking load is very small compared to first and second breaking loads.

## References

1. Beylgeril B (2020) Multi-objective optimal design of hybrid composite laminates under eccentric loading. Mechanical Engineering Department, Alanya Alaaddin Keykubat University, Alanya, Antalya 07450, Turkey. Alexandria Engineering Journal (2020), accepted on 12th September 2020
2. Hayes MD, Lesko JJ (2007) Failure analysis of a hybrid composite structural beam. Compos: Part A 38:691–698
3. Azmi NN, Nasir MFM, Ayoub G, Hussain AK, Mahmud J (2019) The study of hybrid composite plates under transverse sinusoidal load using ANSYS. J Phys: Conf Ser. <https://doi.org/10.1088/1742-6596/1349/1/012030>
4. Malekimoghadam R, Icardi U (2019) Prediction of mechanical properties of carbon nanotube–carbon fiber reinforced hybrid composites using multi-scale finite element modelling. Compos Part B 177:107405
5. Ahmed W, Al-Rifaie W, Zaneldin E, Mathematical modeling and simulation of interfaces between fiber and its matrix. In: Engineering requirements unit (Chap. 4). United Arab Emirates University, Al Ain, United Arab Emirates

6. Dong C, Davies IJ (2013) Flexural and tensile moduli of unidirectional hybrid epoxy composites reinforced by S-2 glass and T700S carbon fibres. *Mater Des.* <https://doi.org/10.1016/j.matdes.2013.08.086>
7. Lei H, Wang Z, Tong L, Zhou B, Fu J (2013) Experimental and numerical investigation on the macroscopic mechanical behavior of shape memory alloy hybrid composite with weak interface. *Compos Struct* 101:301–312
8. Dong C, Davies IJ (2015) Flexural strength of bidirectional hybrid epoxy composites reinforced by E glass and T700S carbon fibres. *Compos: Part B* 72:65–71
9. Saw SK, Akhtar K, Yadav N, Singh AK (2014) Hybrid composites made from Jute/Coir fibers: water absorption, thickness swelling, density, morphology, and mechanical properties. *J. Nat. Fibers* 11(1):39–53. <https://doi.org/10.1080/15440478.2013.825067>
10. Mehar K, Panda SK, Dewangana HC (2020). Multiscale finite element prediction of thermo mechanical flexural strength of nanotube-reinforced hybrid smart composite panel bonded with SMA *fiber*. *Structures* 28:2300–2310



# Experimental Investigation of Mechanical and Tribological Properties of ABS-Barium Sulfate Polymer Composite by Taguchi Technique



S. Sreenivasulu and A. Chennakesava Reddy

**Abstract** In this present work, it found that there is an impact of Barium Sulfate ( $\text{BaSO}_4$ ) on the mechanical & tribological properties of ABS based composites. ABS is prepared with Barium Sulfate ( $\text{BaSO}_4$ ) by changing weights proportions. The experiments are administrated as per Taguchi design, Rockwell hardness, used to observe the hardness number and pin-on-disk wear test (ASTM G99) conducted with different combinations of reinforcement, sliding speed, sliding distance, and normal load. The outcomes show the material hardness & a toughness increase from 12 to 20% composition. Utilizing  $\text{BaSO}_4$  as filler material to ABS, the properties improved, which achieves a more broad application.

**Keywords** ABS ·  $\text{BaSO}_4$  · Pin-on-disk · Filler content · Normal load · Sliding distance

## 1 Introduction

Most of the studies made in the aerospace and automotive field show that material should possess good tribological and mechanical properties [1]. It can enhance thermal stability to the maximum extent by interaction with the nano alumina particles [2]. The fragile, breaking side effects in the ABS/BN (acrylonitrile-butadiene-styrene/ Barium Sulfate) polymer composite are drastically engendering break development directional lines [3]. Using injection molding machine ABS/  $\text{MgO}$  composite prepared. It shows the input process parameter load shows the percentage contribution (81.7%). Micro-cracks are high when the load is high [4]. The stir casting method is used to prepare a hybrid aluminum-mica reinforced metal matrix. There is good bonding between the matrix material and the reinforced material in the micrograph [5].

The friction and specific wear rate coefficient are influenced by a parameter such as filler content, load, and speed. The load is the most influencing process parameter,

---

S. Sreenivasulu (✉) · A. Chennakesava Reddy  
Department of Mechanical Engineering, JNTUH College of Engineering, Hyderabad, India

followed by speed and content [6]. The presence of exfoliated graphite decreases the electrical resistivity of the composite [7]. The addition of Teflon nanofiller particles to Nylon 6 polymer composite increases the tensile strength, hardness, and brittleness [8]. Epoxy/glass/PTW (A2) composite mechanical properties are enhanced by (2.5 wt.%) of graphite as a filler [9]. The thermal analysis reveals that nano composite particles are thermally stable. Graphene inclusion influenced both the weight and crystallinity of the polymer [10]. Microstructure analysis of the impact-fractured reveals that crack forking, plastic deformation of the matrix, and rubber voiding are primary reasons for toughening mechanisms [11]. Material with abrasive has wear mechanism and longitudinal grooves caused by micro-cutting effect [12]. The addition of filler nanoparticles, as an example, nanosilica into polypropylene composite (PP) by methods for grafting polymerization, makes both hardening and strengthening impact.

The tensile strength of composites increases with the load parameter [13]. By adding the second stage, nanoparticles are used to improve tribological properties (for example, wear and coefficient of rubbing) of the thermoplastic polyamides (PA). This outcome the smooth surface of nanocomposites, showing great working tribological properties [14, 15]. During curing, tensile strength also increases, which is due to better interfacial adhesion. Performance application glass fiber is a significant reinforcement for epoxy resin. There is a large increment in mechanical properties [16, 17]. Strategy untreated and surface-treated  $\text{TiO}_2$  produced using Anionic ring-opening polymerization of  $\epsilon$ -caprolactam by rotational molding method. Melting temperature, average molecular weight, water observation, and conversion degree decreases from actual value [18]. The addition of iron oxide to the Nylon 6/Teflon grid improves tensile strength and hardness, while reducing the ductility of the Nylon/Teflon polymer composites [19, 20]. The metal hydroxide nanorods 1-D (MHR) and their blend with two-dimensional graphene nanosheets (2-D GNS) are utilized to ABS composites.

Development of the 3-D nanohybrids network within the ABS grid. At the purpose when 2 wt.% GNS and 4 wt.% Co(OH) 2 mixed, and mechanical properties improved [21]. The submicron particles and microparticles can improve mechanically and wear opposition of the chemosphere filled vinyl ester composites. The submicron-sized particles are more successful in improving the wear opposition than the micro-sized particles [22]. Short fiber-fortified polymers (SFRPs), the tribological execution of SFRPs, can improve by using nanoparticles due to their grating diminishing capacities, especially under silly stacking conditions [23]. The wear behavior of ABS filled with Barium Sulfate ( $\text{BaSO}_4$ ) has been investigated for varying filler content, normal load, sliding speed, and sliding distance with three levels of every parameter as per Taguchi design of experiments. The morphology of wear crack also calculated and optimum circumstances of the parameters after the tribological test utilizing SEM microstructures.

## 2 Materials and Methods

ABS polymer (acrylonitrile–butadiene–styrene) taken as the major component of the composite. The ABS material composite has a good surface finish and high-impact strength; it is widely used in the industrial application BaSO<sub>4</sub> particles used as the filler material in ABS matrix composite to increase the composite’s binding properties. In the present research, BaSO<sub>4</sub> added to the ABS in various proportions to study the mechanical properties such as tensile strength and hardness. Other parameters (Table 1) are considered during fabrication and testing, such as load and speed. To know the most important influencing parameter & to archive better mechanical properties taguchi (L<sub>9</sub>) design of experiments taken and experiments conducted as slowly within the (Table 2) below.

To determine the hardness o the ABS/BaSO<sub>4</sub>, a composite Rockwell hardness test was conducted.

### 2.1 Fabrication of the Composites

The matrix material was the ABS thermoplastic powder. The filler material was BaSO<sub>4</sub>, the Barium Sulfate was added to ABS in various percentages such as 4, 8,

**Table 1** Different levels of design factors

Factor	BaSO <sub>4</sub> , (%wt)	Normal Load (N)	Sliding Speed (rpm)	Sliding distance (m)
Symbol	A	B	C	D
Level-1	4	10	100	500
Level-2	12	15	200	750
Level-3	20	20	300	1000

**Table 2** Orthogonal array (L<sub>9</sub>) and control parameters

Treat No.	A	B	C	D
1	1	1	1	1
2	1	2	2	2
3	1	3	3	3
4	2	1	2	3
5	2	2	3	1
6	2	3	1	2
7	3	1	3	2
8	3	2	1	3
9	3	3	2	1



**Fig. 1** Tensometer for testing the specimens

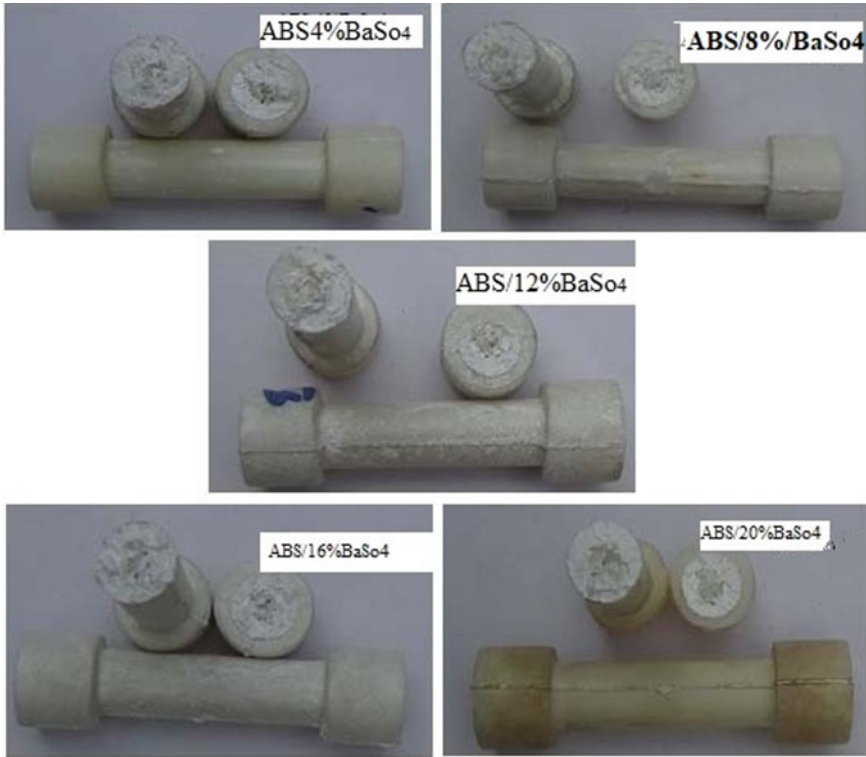
12, 16, and 20% by weight in order to improve the wear resistance of the polymer composite. The  $\text{BaSO}_4$  microparticles were mixed with the ABS in a the ME100LA mixer maintained the primary stage at 190 °C temperature, with 200 rpm, mixing blades to mix ABS/ $\text{BaSO}_4$  composite at different proportions for 20 min. The major purpose of heating to make material smooth with homogeneity all over the composite. Secondary stage, molten material injected into an injection molding at high pressure. The major reason for high pressure is to release internal stress. The material slowly cooled after material gets solidified, later ejected out from the molding.

Standard tensile specimens were fabricated under different pressures and packing pressures. Tensometer Model PC-2000 (Fig. 1) utilized for tensile tests. The dimensions of tensile specimens are shown in Fig. 2 was used to carry tensile tests specimens were then tested to determine the mechanical and wear properties, maintaining different normal load and speed. Using Rockwell indenter (Fig. 4), the hardness of the polymer composite investigated. With a scanning electron microscope (S-3000 N Toshiba SEM) fracture morphology of the specimen examined. For determining the wear rate, the wear monitor (ASTM G99) was used, which is a pin-on-disk type (Fig. 3). Further, emery paper of grade size 400 was also used for determining the wear rate.

### **3 Results and Discussions**

#### ***3.1 Effect of Filler Content on Tensile Properties***

The composites' characterization reveals that  $\text{BaSO}_4$  features a significant effect on the tensile strength of the material. The ultimate strength increases with an increase in the filler content (Fig. 5), and also, the percentage of strain values are increasing; it



**Fig. 2** Tensile tested specimens of ABS/BaSO<sub>4</sub> by varying weight percentage

means material toughness increased, and modulus of resilience increase. The curves show slope is decreasing, so the material is changing from brittle to ductile.

### ***3.2 Effect of Filler Content on the Hardness***

In this investigation, there is a change in hardness with a variation of BaSO<sub>4</sub> filler content from Fig. 6 to show that filler content increased from 4 to 12% wt. There is a decrease in the material hardness when the filler content increased from 12 to 20%. There is an increase in hardness. The maximum hardness value is 62 HRM for 20% BaSO<sub>4</sub> filler content.



**Fig. 3** Wear and friction monitor

### ***3.3 Effect of Filler Content on Sliding Wear***

The wear rate of all the specimens determined using the Taguchi orthogonal L9 array of experiments. Figure 7, with an increase in the filler content wear rate, also increasing. Wt.% of BaSO<sub>4</sub> shows a major contribution to other input process parameters. 42.39% contribution (Table 3) is major because of the percentage of filler content added into the composite (Table 4).

When load increased from 10 to 15 N, there is an increase in the wear rate, and later there is a decrease in the wear rate. The load has a percentage contribution of 37.38%. Similarly, when the speed increased wear rate increased to 200 rpm, there is a decrease in wear rate. But speed is not the most influencing factor; it shows only 9.76% of the contribution. Load and filler material major influencing parameters counter and surface plot generated (Fig. 8).



Fig. 4 Rockwell hardness Tester

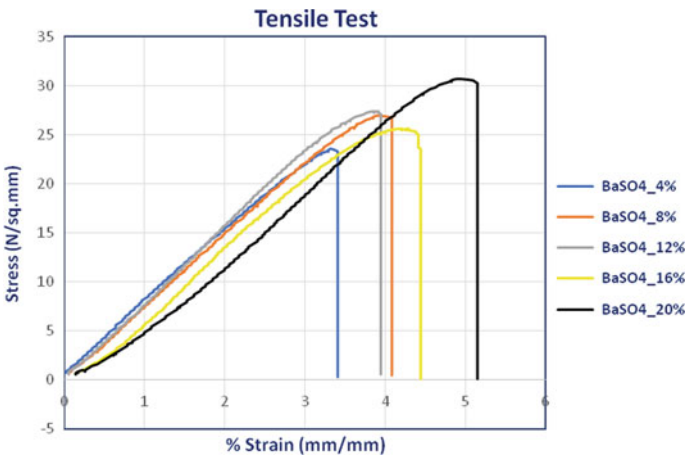
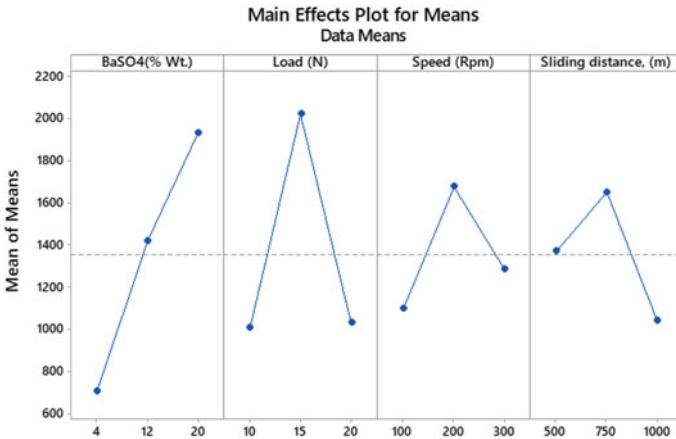
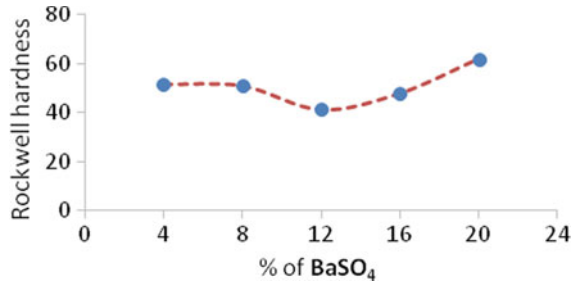


Fig. 5 Stress–strain curves of BASO<sub>4</sub>/ABS polymer composites

### 3.4 Surface Morphology of the Composites

SEM pictures were taken for each Taguchi L9 array experiment varying the load and composition, and speed. All the images were taken at 20 micro-meter magnification. From tests 1 to 3, the sample filler content kept constant load continuously increased; there is an increase in the intensity of micro-cracks. For tests 1, 2, and 3 with 4%

**Fig. 6** Hardness is a function of BaSO<sub>4</sub>



**Fig. 7** Variation of wear rate vs design factors

BaSO<sub>4</sub> particles (Fig. 9), the worn surface appears small grooves at trail 1 start-up conditions. As the load increase, large deformation was observed. For tests 4, 5, and 6 to 12% BaSO<sub>4</sub> particles, the micro-cracks observed at trail 4 and 6 were almost the same, but worn surfaces are uniform and highly intense. This worn surface is because of the load applied to the specimen. As the load increases, the worn surface cracks are more for brittle material.

For trials 7, 8, and 9 with 20% BaSO<sub>4</sub> particles, particle clustering was observed in the specimens because of an increase in the BaSO<sub>4</sub> filler material’s content.

### 4 Conclusion

The wear behavior of acrylonitrile–butadiene–styrene (ABS) filled with micro-sized BaSO<sub>4</sub> composites were investigated for varying sliding distance, filler content, normal load and speed with three levels of each parameter as per Taguchi’s design of experiments. Material toughness and modulus of resilience increase with an increase



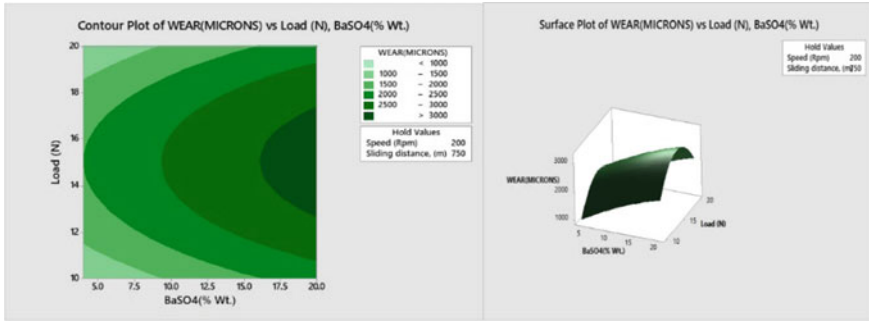
**Table 3** ANOVA summary of the wear rate

Source	DF	Sum1	Sum2	Sum3	Adj. SS	Adj. MS	F-Value	P-Value	Percentage contribution (%)
BaSO4 (% Wt.)	2	708	1423.7	1934.7	2,278,011	1,139,005	2.21	0.191	42.39
Load (N)	2	1007.3	2023.3	1035.7	2,008,544	1,004,272	1.79	0.246	37.38
Speed (rpm)	2	1100.7	1679.7	1286	524,563	262,281	0.32	0.735	9.76
Sliding distance (m)	2	1371.3	1653.3	1041.7	562,340	281,170	0.35	0.718	10.47
Error	0				0				0.00
Total	8				5,373,458				100.00

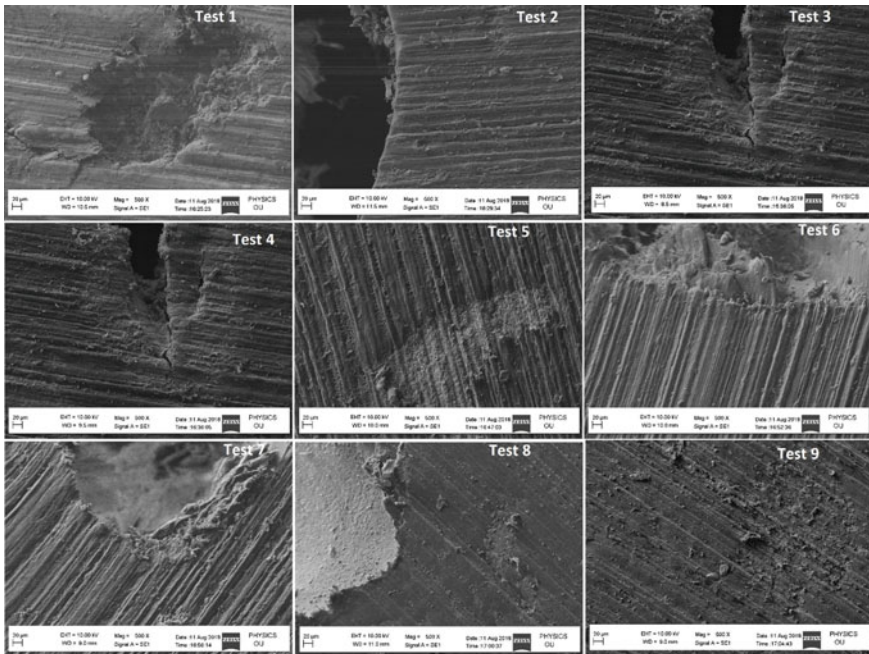
*DOF* Degree of freedom, *SS* sum of squares, *MSS* means of squares)

**Table 4** Optimum process parameter to maximize and minimize the wear

	BaSO <sub>4</sub> (% wt)	Load (N)	Speed (rpm)	Sliding distance (m)
Maximum wear (microns)	20	15	200	750
Minimum wear (microns)	4	10	100	1000



**Fig. 8** Counter and surface plot of wear versus Load (N) and speed (rpm)



**Fig. 9** SEM images of specimens for trial conditions of 1 to 9

in the filler content (4% to 20%) of the composite. When filler content increased from 4 to 12% by weight, there was a decrease in the material hardness when the filler content increased from 12 to 20%, there is an increase in the hardness. Among all design factors the percentage of BaSO<sub>4</sub> shows a major contribution (42.39%) than other input process parameters. From the SEM picture, it clears that as the load increases; the worn surface cracks are more.

## References

1. Baradeswaran A et al (2014) Experimental investigation on mechanical behavior, modelling, and optimization of wear parameters of B4C and graphite reinforced aluminum hybrid composites. *Mater Des* 63:620–632
2. Kumar V et al (2010) Fabrication and characterization of ABS nanocomposite reinforced by nano-sized alumina particulates. *Int J Plastics Technol* 13(2):133–149
3. Kumar KS, Reddy AC (2018) Mechanical, and wear behavior of ABS/BN polymer composites. *Int J Eng Sci Technol* 10(5):172–180
4. Kumar KS, Reddy AC (2020) Experimental investigation on mechanical and tribological properties of MGO/ABS polymer composites. *Int J Mech Prod Eng Res Dev*
5. Rajmohan T, Palanikumar K, Ranganathan S (2013) Evaluation of mechanical and wear properties of hybrid aluminum matrix composites. *Trans Nonferrous Metals Soc China* 23(9):2509–2517
6. Sudeepan J et al (2014) Study of friction and wear of ABS/ZnO polymer composite using Taguchi technique. *Proc Mater Sci* 6:391–400
7. Neha B et al (2012) Synthesis and characterization of exfoliated graphite/ABS composites. *Open J Organic Polym Mater* 02(04):75–79
8. Reddy AC (2015) Characterization of mechanical behavior of nylon/teflon nano particulate composites. *Int J Adv Res* 3(5):1241–1246
9. Sudheer M et al (2014) Enhanced mechanical and wear performance of epoxy/glass composites with PTW/graphite hybrid fillers. *Proc Mater Sci* 6:975–987
10. O'Neill A, Bakirtzis D, Dixon D (2014) Polyamide 6/Graphene composites: The effect of in situ polymerization on the structure and properties of graphene oxide and reduced graphene oxide. *Eur Polym J* 59:353–362
11. Ren J et al (2009) Study on the morphological and mechanical properties of nylon 6/ABS/Nano-SiO<sub>2</sub> Composites. *J Macromol Sci Part B* 48(6):1069–1080
12. Sudeepan J et al (2015) Study of mechanical and tribological properties of Abs/ZnO polymer composites. *Int J Adv Mater Manuf Character* 5(1)
13. Wu CL, Min Zhi Rong MQZ, Friedrich K (2002) Tensile performance improvement of low nanoparticle-filled-polypropylene composite. *Elsevier-Compos Sci Technol* 62:1327–1340
14. Garcia M et al (2004) Friction and wear studies on Nylon-6/SiO<sub>2</sub> nanocomposites. *J Appl Polym Sci* 92:1855–1862
15. Gebretsadik DW, Hardell J, Prakash B (2020) Friction and wear characteristics of PA 66 polymer composite/316L stainless steel tribo pair in aqueous solution with different salt levels. *Tribol Int* 141
16. Hameed N et al (2008) Mechanical properties of poly(styrene-co-acrylonitrile)-modified epoxy resin/glass fiber composites. *J Appl Polym Sci* 110(6):3431–3438
17. Rajaa VL, Kumaravel A (2015) Studies on physical and mechanical properties of silica fume-filled nylon 66 polymer composites for mechanical components. *Polym Polym Compos* 23(6):427–432
18. Rusu G, Rusu E (2011) Nylon 6/TiO<sub>2</sub> composites by in situ anionic ring-opening polymerization of ε-caprolactam: synthesis, characterization, and properties. *Int J Polym Anal Charact* 16(8):561–583

19. Agarwal K et al (2015) Enhancement in mechanical behavior of nylon/teflon composites by addition of nano iron oxide ( $\gamma$ -Fe<sub>2</sub>O<sub>3</sub>). *Int J Sci Res (IJSR)* 4(5)
20. Shiva Kumar K, Chennakesava Reddy A (2020) Investigation on mechanical properties and wear performance of Nylon-6/Boron Nitride polymer composites using the Taguchi Technique. *Results Mater* 5
21. Hong N et al (2014) Enhanced mechanical, thermal, and flame retardant properties by combining graphene nanosheets and metal hydroxide nanorods for Acrylonitrile–Butadiene–Styrene copolymer composite. *Compos A Appl Sci Manuf* 64:203–210
22. Chauhan SR, Thakur S (2013) Effects of particle size, particle loading, and sliding distance on the friction and wear properties of cenosphere particulate filled vinyl ester composites. *Mater Des* 51:398–408
23. Chang L, Friedrich K (2010) Enhancement effect of nanoparticles on the sliding wear of short fiber-reinforced polymer composites: a critical discussion of wear mechanisms. *Tribol Int* 43(12):2355–2364

# Development of Carbon and Glass Fiber-Reinforced Composites with the Addition of Nano-Egg-Shell Powder



T. Prasad, Barmavatu Praveen, Yalagandala Akshay Kumar, and Kunchala Krishna

**Abstract** Fiber-reinforced polymer-composite materials are the most advanced preferable materials used in the development and manufacturing of aircraft and spacecraft. Specifically, their utilization as essential structural materials as of late in a few technology demonstrator bleeding-edge aviation ventures worldwide has given confidence leading their acknowledgment as supreme materials for aviation vehicles. This project reviews few of these developments discussing the problems with the present generation composites and prospects for additional products. The review emphasizes composites applications as constructional materials where they are having significant growth in utilization. The research focus is mainly on the Indian aerospace industrial developments—a brief study and investigation of composites usage applications in the field of aerospace sector. The type of composite materials characteristics and unique difficulties in designing development and working with the above materials are then spotlighted. The issues deliberated relate to the impact influence of damage and damage allowances in general, ecological debasement and long-term durability. Current arrangements are quickly portrayed, and the extension for new betterment level in the plot. In this project, we have used carbon and glass fiber and their difference in strength when fabricated with 1% & 2% of the nano-egg-shell powder with 28.9 nm size.

**Keywords** Fiber-reinforced polymer · Composite materials · Aviation vehicles · Carbon and glass fiber · Nano-egg-shell powder

## 1 Introduction

Composite materials are designed or commonly occurring materials produced using at least two constituent materials with fundamentally unique physical or chemical properties that stay discrete and distinct within the completed structure. Most composites have concrete, firm fibers in the matrix that is more fragile and less

---

T. Prasad (✉) · B. Praveen · Y. A. Kumar · K. Krishna  
Department of Mechanical Engineering, Anurag University, Venkatapur, Ghatkesar 500088, India  
e-mail: [prasadmech@cvsr.ac.in](mailto:prasadmech@cvsr.ac.in)

© The Author(s), under exclusive license to Springer Nature Singapore Pte Ltd. 2022  
G. S. V. L. Narasimham et al. (eds.), *Innovations in Mechanical Engineering*,  
Lecture Notes in Mechanical Engineering,  
[https://doi.org/10.1007/978-981-16-7282-8\\_42](https://doi.org/10.1007/978-981-16-7282-8_42)

569

hardened [1]. The main objective is typically to make a rigid and robust component, frequently with low density [2]. Commercial materials usually have glass or carbon fibers in grids dependent on thermos-setting polymers, for example, epoxy and polyester resins [3]. In some cases, thermoplastic polymers might be liked hence; they are moldable after beginning creation. There are various types and grades of composite in which, the matrix may be a metal, or a ceramic. Generally, above-mentioned are still formative, with high assembling costs yet to be survived [4].

Moreover, in these composites, the explanations behind addition of fibers (or, in certain cases, particles) are regularly somewhat intricate; for instance, enhancements might be looked for in creep, wear, rupture strength and thermal stability [5]. Fiber-reinforced polymer (FRP) are composites mainly used in almost each type of the advanced and sophisticated engineering structure [6]. Their usage ranges from aircraft, helicopters and spacecraft to sports products, boats, ships, offshore platforms, automobiles parts, chemical processing equipment and civil infrastructures like bridges and buildings. FRP composites' utilization keeps developing at a great rate particularly as these materials are utilized more in their current business sectors and become set up in moderately new business sectors, like biomedical devices and civil structures [7]. A key factor aspects driving composites' expanded utilization over late years is growing new progressed types of FRP materials. This material includes high-performance resin systems and contemporary reinforcement styles, for example, carbon nanotubes and nanoparticles [8]. This research had given a latest original record of the fabrication of composites along with mechanical properties and impact tolerance, delamination resistance of composites and the utilization of 3D FRP composites.

## 2 Material Considered for Manufacturing

See Table 1.

### 2.1 *Fabrication of Composite Material*

#### **The Hand lay-up Process**

Hand lay-up is an open molding method reasonable for making a wide variety of composites variety from exceptionally little to enormous. Production volume per shape is low; however, it is possible to create significant production amounts utilizing various or multiple molds. Hand lay-up is the easiest composites shaping method, offering minimal effort tooling, basic handling and a wide scope of part measures. Design changes are promptly made. There is a base investment in design changes.

**Table 1** Material considered for manufacturing

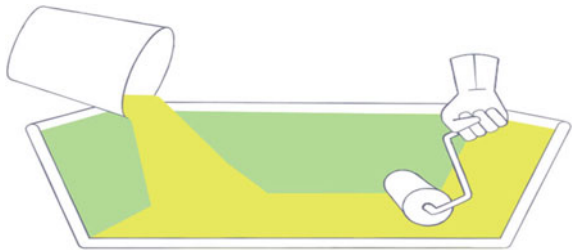
S. No.	Materials	Quantity
1	Carbon fiber	4 m
2	Glass fiber	4 m
3	Epoxy resin LY-556	2000gms
4	Hardener HY-556	200gms
5	Egg-shell powder	30 g
6	Teflon sheets	10
7	Measuring jar	1
8	Stirring rod	1
9	Gloves	4
10	Portable weighing machine	1
11	Scissors	1

With skilled operators, sensible production rates and reliable quality are possible (Fig. 1).

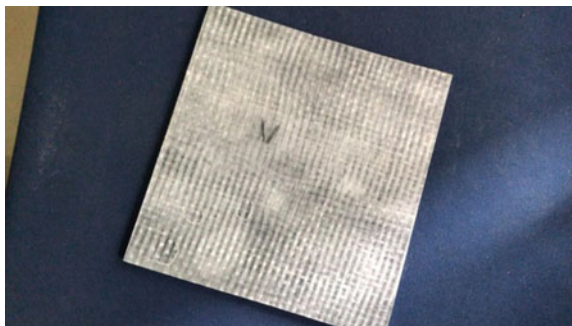
**Fabrication**

See Figs. 2 and 3.

**Fig. 1** Hand lay-up process



**Fig. 2** Composite material after cutting



**Fig. 3** Composite material before cutting



### 3 Calculations

#### 3.1 Determination Assurance of Required Epoxy Resin and Carbon Fiber

Generally, we require an electronically weighing scale for measuring exactly the required quantity of materials for the development composite laminate, which measures precisely in grams. Two different proportional ratios quantity of glass fiber to epoxy resin, ratios of carbon fiber to epoxy resin and egg-shell powder (Table 2).

For determining the weight of the material, we need to look for the density of the carbon and glass fiber. Density formulae as

$$d = \frac{m}{v}$$

where  $d$  = density,  $m$  = mass,  $v$  = volume

$$\text{Density of fiber} = 1.75 \text{ g/cm}^3,$$

$$\text{Density of matrix} = 1.2 \text{ g/cm}^3,$$

$$\text{Density of eggshell} = 1.2 \text{ g/cm}^3,$$

$$\text{Volume of composite(mold)} = 300 \times 300 \times 5 \text{ mm}$$

$$= 30 \times 30 \times 5 \text{ cm} = 450 \text{ cm}^3$$

**Table 2** Ratios of carbon fiber to epoxy resin and egg-shell powder

S. No.	The ratio of glass fiber	The ratio of carbon fiber	The ratio of epoxy resin	The ratio of egg-shell powder
1	40	40	20	0
2	40	40	19	1
3	40	40	18	2



Volume of composite = Volume of fiber + Volume of matrix

$$\begin{aligned}\text{Vol. of fiber} &= 40\% \text{ of vol. of composite} \\ &= 40 \times (450/100) = 180 \text{ cm}^3\end{aligned}$$

We know the density of fiber = Mass of fiber/volume of fiber

$$\text{Hence mass of fiber} = \text{vol. of fiber} \times \text{density of fiber} = 180 \times 1.75 = 315 \text{ g}$$

Similarly vol. of matrix = 20% of vol. of composite

$$= 20 \times (450/100) = 90 \text{ cm}^3$$

Density of matrix = mass of matrix/vol of matrix

$$\begin{aligned}\text{Hence mass of matrix} &= \text{vol. of matrix} \times \text{density of matrix} \\ &= 90 \times 1.20 = 108 \text{ g}\end{aligned}$$

For ratio of 40:19:1 of fiber: resin: eggshell,

$$\text{Vol. of matrix} = 19 \times (90/100) = 81 \text{ cm}^3$$

$$\text{Mass of matrix} = 1.175 \times 81 = 95.175 \text{ g}$$

$$\text{Vol. of eggshell} = 1 \times (90/100) = 0.9 \text{ cm}^3$$

$$\text{Mass of eggshell} = \text{density of eggshell} \times \text{Vol. of eggshell} = 1.2 \times 0.9 = 1.08 \text{ g}$$

Similarly for other ratios, i.e., 40:18:1

Resin and the hardener are added in the ratio of 10:1, i.e., if we require 100 gms of epoxy resin, ten gms of hardener are added. After calculating the required material weights, we need to cut the fiber according to the dimensions.

### 3.2 Estimation of Weights

See Table 3.

## 4 Results

The compositions ggccgg, cccggg, ccggcc and cgcgcg, where *c* = carbon fiber *g* = glass fiber, were tested for tensile strength, compression test and impact of strength for both egg-shell compositions of 1% and 2%. The below Table 4 shows the tensile

**Table 3** Estimation of weights

S. No.	% of egg-shell powder	Value of carbon fiber in gms	Weight of glass fiber in gms	Weight of resin in gms	Weight of egg-shell powder in gms
1	0	100	140	140	0
2	1	120	160	133.2	3
3	2	140	180	126	5

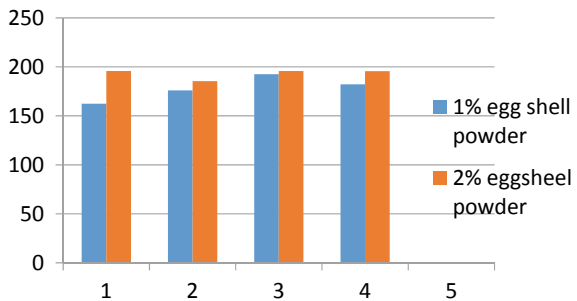
**Table 4** Tensile strength results

S. No.	Composition	% of eggshell	Tensile in N/mm <sup>2</sup>
1	Ggccgg	1	162.376
2	Cccggg	1	176.068
3	Ccggcc	1	192.376
4	Cgcgcg	1	182.176
5	Ggccgg	2	195.752
6	Cccggg	2	185.427
7	Ccggcc	2	195.752
8	Cgcgcg	2	195.606

where C = Carbon fiber G = Glass fiber

strength results, and Fig. 4 indicates bar diagram, where y-axis indicates tensile strength and x-axis various compositions. The below Table 5 shows the compression strength results, and Fig. 5 indicates bar diagram, where y-axis indicates tensile strength and x-axis various compositions. The below Table 6 shows the impact of strength results, and Fig. 6 indicates bar diagram, where y-axis indicates tensile strength and x-axis various compositions.

**Fig. 4** Tensile strength versus different compositions

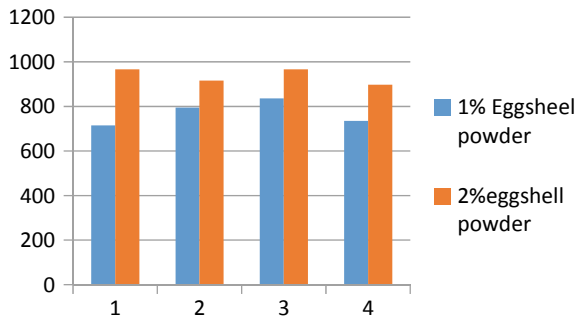


**Table 5** Compression strength results

S. No.	Composition	% of eggshell	Compression in N
1	Ggccgg	1	715.00
2	Cccggg	1	795.00
3	Ccggcc	1	836.00
4	Cgcgcg	1	735.00
5	Ggccgg	2	966.800
6	Cccggg	2	916.00
7	Ccggcc	2	966.860
8	Cgcgcg	2	898.00

where, C = Carbon Fiber, G = Glass fiber

**Fig. 5** Compression strength versus different composition



**Table 6** Impact strength results

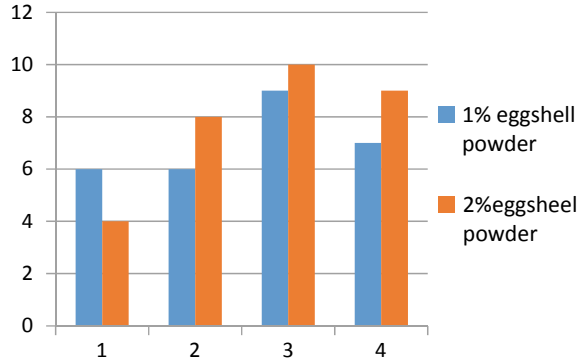
S. No.	Composition	% of eggshell	Impact in joules
1	Ggccgg	1	6
2	Cccggg	1	6
3	Ccggcc	1	9
4	Cgcgcg	1	7
5	Ggccgg	2	4
6	Cccggg	2	8
7	Ccggcc	2	10
8	Cgcgcg	2	9

where C = Carbon fiber, G = Glass fiber

### 4.1 Tensile Strength

See Fig. 4 and Table 4.

**Fig. 6** Impact versus different composition



## 4.2 Compression Strength

See Fig. 5 and Table 5.

## 4.3 Impact of Strength

See Fig. 6 and Table 6.

## 5 Conclusions

- The project gives a conclusion that the carbon and glass-reinforced composite material with 2% egg-shell powder with 28.9 nm size have more tensile, compression and impact strength than that of composite material with 1% of the egg-shell powder with 28.9 nm size.
- Fiber-reinforced composites are found useful in mechanical, automobile and construction fields. The cost of egg-shell powder is significantly less and can be extensively used to make composite materials stronger with less weight.
- In the present work, the fiber-reinforced composites with modified epoxy matrix were manufactured. The addition of egg-shell powder at low quantities has improved the mechanical properties of fiber-reinforced composites.
- Tensile, compression and impact tests are performed on fiber-reinforced composites development showed improvement in tensile strength, compression and impact strength.
- A minimal quantity of egg-shell powder mixed in epoxy resulted in significant improvements in mechanical properties.

**Acknowledgements** The authors are thankful for the facilities, and the mechanical engineering department and management give technical support.

## References

1. Pathania D, Singh D (2009) A review-on electrical properties of fiber-reinforced polymer composites. *Int J Theor Appl Sci's* 1(2):34–37
2. Hinrichsen J (2000) The material down-selection process for A3XX. CAES. 19th Eurosurveillance conference on materials for aerospace applications, Munich, pp. 6–8
3. Karthikeyan B, Ramanathan S, Ramakrishnan V (2010) Thermophysical property measurement of metal-matrix composites. *Mater Design* 82–86
4. Obilade IO (2014) use of rice husk-ash as a partial replacement for cement in concrete. *Int J Eng App Sci's* 5(4):11–16
5. Prabhakaran S, Senthil Kumar M (July 2012) Development of glass fiber-reinforced polymer-composite ceiling fan blade. *Int J Eng Res Dev* 2(3):59–64
6. Jolly SS (Nov 2012) Advancements in composite-materials and their application's in engineering and technology. *GRA—Global Res Anal* 1(5):42–44
7. Gururaja MN, Hari Rao AN (Jan 2012) A review on—recent applications and future prospectus of hybrid composites. *Int J Soft Comput Eng* 1(6):352–355
8. Thori P et al (2013) An approach of composite material's in industrial machinery: advantages, disadvantages and applications. *Int J Res Eng Tech* 2(12):350–355
9. David et al (2011) Mechanical & thermal analysis of microvascular networks in structural composite panels. *Compos Part A* 42:1609–1619
10. Mallick PK (2008) Fiber-reinforced composites. Materials, manufacturing and design, (3rd edn). CRC Press: Boca Raton, FL, USA
11. Jain R, Lee L (2012) Fiber reinforced polymer (FRP) composites for infrastructure applications. Springer, Berlin/Heidelberg, Germany
12. Bai J (2013) Advanced fibre-reinforced polymer (FRP) composites for structural applications. Woodhead Publishing, Cambridge, UK
13. Ozgur Seydibeyoglu M, Mohanty AK, Misra M (2017) Fiber technology for fiber-reinforced composites. Woodhead Publishing, Cambridge, UK
14. Corradi M, Borri A, Righetti L, Speranzini E (2017) Uncertainty analysis of FRP reinforced timber beams. *Compos Part B* 113:174–184
15. González C, LLorca J (2007) Mechanical behavior of unidirectional fiber-reinforced polymers under transverse compression: microscopic mechanism and modeling. *Compos Sci Technol* 67(13):2795–2806. <https://doi.org/10.1016/j.compscitech.2007>
16. Agarwal A, Garg S, Rakesh PK, Singh I, Mishra BK (2010) Tensile behaviour of glass fiber reinforced plastics subjected to different environmental conditions. *Indian J Eng Mater Sci* 17:471–476
17. Abdullah ET (2013) A study of bending properties of unsaturated polyester/glass fiberreinforced composites. *J Al-Nahrain Univ*

# Investigation on Nitriding and Microstructure Evolution of M50 NiL Steel: A Review



B. Venkatesh and C. Anil Kumar Reddy

**Abstract** M50 NiL steel is low carbon high alloy steel with high strength and toughness. It enhanced wear and corrosion resistance at high speed and elevated temperature; because of this unique property, it is widely used in aerospace industry. The detection methods of SEM, XPS, AES, X-Ray Diffraction and TEM are used to find out corrosion resistance, residual stress and its microstructure. The purpose of the paper is to know the importance of advanced bearing steels in satisfying the requirements of aerospace industry by considering the research contributions of previous researchers and enhance the scope of proposed material in aerospace field. M50 NiL steel has major importance in manufacturing bearing components for aerospace applications because of its good wear and corrosion resistance. Commonly, AISI 52100 and M50 hardened steel materials are used in aerospace bearing applications and M50 NiL is a M50 Alloy variant with much less initial carbon concentration and a high nickel content to help carburization, M50 NiL steel is an unique material for aerospace industrial applications as it exhibits high structure strength, as we aware of that marine components undergo corrosion failures, so M50 NiL is a kind of case-hardened steel designed to full fill the requirements. After carburization, M50 NiL steel gets good properties of fracture toughness and high-rolling contact fatigue and tough core.

**Keywords** M50 NiL · RE atoms · Plasma nitro-carburizing · Forging · TEM and SEM

---

B. Venkatesh (✉) · C. A. K. Reddy  
Mechanical Engineering Department, Vardhaman College of Engineering, Hyderabad, India  
e-mail: [b.venkatesh@vardhaman.org](mailto:b.venkatesh@vardhaman.org)

C. A. K. Reddy  
e-mail: [c.anilkumar.jrf@vardhaman.org](mailto:c.anilkumar.jrf@vardhaman.org)

© The Author(s), under exclusive license to Springer Nature Singapore Pte Ltd. 2022  
G. S. V. L. Narasimham et al. (eds.), *Innovations in Mechanical Engineering*,  
Lecture Notes in Mechanical Engineering,  
[https://doi.org/10.1007/978-981-16-7282-8\\_43](https://doi.org/10.1007/978-981-16-7282-8_43)

579

## 1 Introduction

In the view of recent developments in aerospace industry, requirements components should withstand to high rotation speeds and high temperatures. So for this, M50 NiL steel is a best solution because of its wear resistance and corrosion properties which satisfies engine requirements like bearings and gear components. M50 NiL is a type of case hardened steel with high mechanical properties like strength, toughness and fatigue, and it has a wide role in aerospace industry for special transmission components because of these properties [1]. These characteristics of material can serve the purpose even in critical conditions like heavy load and high temperature [2]. So microstructure has a major role to improve the properties of material for this few heat treatment methods like carburizing, plasma nitriding and plasma nitrocarburizing are used efficiently to treat the surface of the material, and this paper deals with three major heat treatments like plasma nitrocarburizing, forging and plasma nitriding to enhance the mechanical properties of M50 NiL steel. Plasma nitrocarburizing is one of the surface treatment process assisted by plasma which promotes diffusion of carbon and nitrogen into the surface of steel and forms iron carbides and nitrides to improve the surface properties. Wang et al. [3]. In multi-directional impact forging [MDIF] studies are done by investigating the effect of varying temperature on M50 NiL steel, and in this process, it is shown that gradual enhancement in grain size with respect to the increase in temperature from 1050 to 1180 °C for 1 h. Jiang et al. [4]. And in plasma nitriding, it is studied that the surface hardness increased  $\alpha$ -Fe and  $\gamma$ -Fe<sub>4</sub>N phases on the surface layer formed at low nitriding temperature between 460 and 560 °C, and when the temperature is increased at 575 °C, it is shown that nitride layer thickness is also increased [5]. So by this surface treatment method, wear resistance can be improved. Wang et al. [6]. Nitriding for heat-treatable steels provide compressive residual stresses and hardened cases, and this relates with phase transformation during diffusion of nitrogen and co-diffusion of carbon, and hardness is related to formation of nitride smaller than carbide, but stress gradients are not directly related [7]. Fatigue property can be enhanced by minimizing the crack propagation in the case by enhancing intrinsic property in the nitrided layer. The temperature of nitrided layer formation is nearly 500 °C with stability and limited mechanical relaxation, so surface treatment is required to enhance performance of the material under critical loads and temperatures [8].

### 1.1 Salt Bath Nitrocarburization

This process shows that the nitrogen comes from molten salt mixture of cyanide and cyanate, and this compound decomposes on the steel surface at the temperature ranges from 550 to 590 °C to produce cyanide [9]. Surface becomes rich in nitrogen even though both carbon and nitrogen are diffused in to the steel surface and the

remaining white coloured layer can be known as brittle phase and limitation of this process is toxic nature of salt [10].

## ***1.2 Gas Nitrocarburization***

This is performed in ammonia gas stream in the furnace, and the catalytic decomposition of  $\text{NH}_3$  provides required nitrogen which can be able to diffuse in to the surface of the steel. In this, hydrogen and nitrogen are used as additives, and methane and carbon dioxides are used as source of carbon, and this process can be done for selected material. The formation of white layers near the grain boundaries can be avoided by doing short treatment time 16 h at 524 °C, during this diffusion layer thickness can be observed [10].

## ***1.3 Plasma Nitrocarburizing Treatment***

This treatment requires 30 kW plasma unit, and the glow discharge was created by DC impulse source with 650 V, before performing the glow discharge treatment evacuate the furnace chamber with help of mechanical pump [11]. Then, treatment was conducted in the presence of mixed gases and RE atoms in the 480 °C temperature range up to 4 h with pressure of 280 Pa, and after this cycle, the specimen models are allowed to cool down inside the furnace itself in the presence of nitrogen so that surface oxidation can be avoided [12]. The RE atoms are mixed with ethanol and kept into the furnace with  $\text{N}_2$  and  $\text{H}_2$ . Once the cycle was completed, the specimen models are finished and cleaned with 4 %vol nital solution. Later, they are inspected with optical microscope, SEM coupled with X Ray spectrometer, chemical composition and surface morphologies can be observed. Vickers hardness test is done to know the surface hardness of the nitrided layer [3].

## ***1.4 Carburizing and Nitriding (Duplex) Treatment***

Dual treatments are done for 10 h with nitriding temperature ranges from 460 to 540 °C, and this shows that by enhancing the nitriding temperature, thickness of the nitride layer has effective growth, but it recent investigations has proved that by further enhancement in the nitriding temperature above 540 °C won't obtain deeper nitrided layer [13]. And it has observed that by increasing the nitriding temperature dissolution of grainy carbides and creates precipitation, earlier existing carbides can easily transformed at low nitriding temperature, and by increasing the nitriding temperature, the residual compressive stresses will decrease and surface roughness will increase, so nitriding at 500 °C range gives good wear resistance under heavy



load because of thick compound layer [14]. In M50 NiL, the reduction carbon leads decrease in carbide size which shows enhanced fracture toughness in core. The carburized layer provides high hardness and favourable compressive stresses on it after carburizing treatment and because of the alloys present, this material shows high temperature resistance to suit the requirements of aerospace industry. Thermochemical treatments of surface provides good improvement in mechanical and tribological properties, majorly gas carburizing, plasma carburizing, plasma nitrocarburizing because these conventional treatments satisfy the industry requirements. Combination of nitriding and carburizing was preferable, and in this, nitriding process gives the formation of compound and diffusion layer where the compound layer consists mixture of  $\gamma'$  and  $\epsilon$ , and the diffusion layer consists of nitrides and supersaturated matrix of nitrogen. The nitriding temperature has major impact on composition and structure of compound and diffusion layers, and this compound layer has effect on wear properties of the material [15]. However, M50 NiL contains huge amount of alloy elements which can easily combine with nitrogen and form alloy nitrides when the nitrogen diffuses in to the material surface during the treatment. And this type of steel has an effect of diffusion layer thickness on fatigue properties, and when it comes to carburization, the carbon leads precipitation of carbides into the material surface layer and the remaining carbides after solid solution treatment will precipitate during tempering and gradually transformed in to nitrides as N atoms. So it is required to know the effect of nitriding temperature on the considered material, and it is recommended that in duplex treatment, with temperature ranges from 460 to 540 °C and effect of nitriding temperature on carbides and effect of compound layer on wear properties is studied for better performance [16].

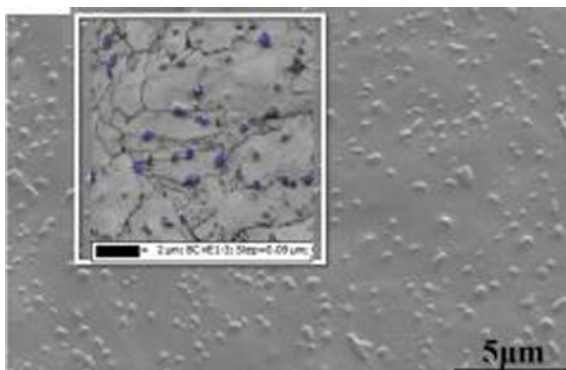
### 1.5 M50 NiL Steel Microstructure (Standard)

The sample microstructure of M50 NiL steel is shown in Fig. 1, and in this, the initial grains are rough and dispersed matrix and during second phase, they are almost in

**Fig. 1** Metallurgical micrograph of M50 NiL [16]



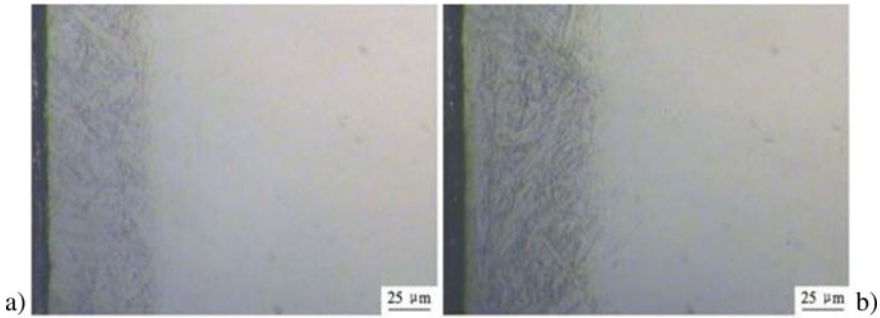
**Fig. 2** EBSD (electron backscatter diffraction) micrograph [16]



the size of nanometre range. In the electron backscatter diffraction phase, the shapes and sizes of carbides are little bit different and most of the carbides are in  $0.4 \mu\text{m}$  size (Fig. 2).

## 2 Rare Earth Addition on Plasma Nitrocarburized M50 NiL Steel

Nitrocarburizing was done at  $480^\circ\text{C}$  for selected M50 NiL steel with addition and without adding of rare earth (RE) elements like lanthanum and cerium, and this surface microstructure layer is investigated by the X-Ray diffraction and scanning electron microscopy. However, the mechanical characteristics are studied through Vickers hardness test. Wang et al. [3] conducted an investigation on M50 NiL steel by adding RE (lanthanide metals) in this. It was founded that rear earth (RE) atoms can diffuse into steel surface and inhabit the  $\epsilon\text{-Fe}_2\text{-3(N, C)}$  phase formation. During investigation, it is observed that there is a difference in microstructure when it is treated without rear earth atom addition, and later. rear earth addition further increases and hardness for surface at this stage is 143 HV0.1, and later enhanced for  $39 \mu\text{m}$  thickness on nitrocarburized layer. It has been proved that nitrocarburized sample models with and without rear earth atom addition was enhanced when they are related with quenched steel [17]. Specifically, with RE addition shown good and high corrosion resistance was observed in plasma nitrocarburized (PNC) samples. Initially, the raw material has a standard chemical composition as per the standards, and it is observed with X-Ray fluorescence spectroscopy (XRF) detection method. Before PNC treatment, M50 NiL steel has to be treated at temperature of  $1150^\circ\text{C}$  for one hour, and later, it has to be cooled in oil, then it is observed that microstructure of M50 NiL steel is martensite with 436HV0.1 hardness, the sample models are sized into  $11 \text{ mm} \times 11 \text{ mm} \times 4 \text{ mm}$  dimensions, and it has been finished with 240–800 grade silicon carbide papers and later cleaned in the presence of alcohol and acetone before performing PNC process, where 30 kW plasma unit are used and the glow



**Fig. 3** Micrographs of M50 NiL steel samples plasma nitrocarburized **a** without and **b** with RE [3]

discharge which was generated by DC impulse sourcing at 650 V, and before glow discharge furnace chamber has to be evacuated at 10 Pa. PNC treatment are conducted in the presence of mixed gases ( $N_2$ ,  $H_2$ ,  $C_2H_5OH$ ) at 480 °C up to 4 h under pressure of 280 Pa. Later, the specimen models are cooled gradually inside the chamber because surface oxidation can be avoided in the presence of nitrogen. The RE agents are dissolved in ethanol and later kept in the furnace along with  $N_2$ ,  $H_2$  [18]. Rare earth reagent is a solution mixture of  $LaCl_3 + CeCl_3 +$  isomeric-acid + isomeric-alcohol in this 8–20 wt% of  $LaCl_3 + CeCl_3$  will be there, and RE reagent in ethanol is about 10 to 16 g/l. Once PNC treatment was done the specimen models are to be polished and etched with 4 ml  $HNO_3 + 96$  ml alcohol (4 %vol nital) solution. Then, the models are inspected through optical microscope like SEM coupled with EDS (energy dispersive X-Ray spectrometer setup and later these specimen models are measured with Vickers hardness test for various loads to make the process accurate (Fig. 3).

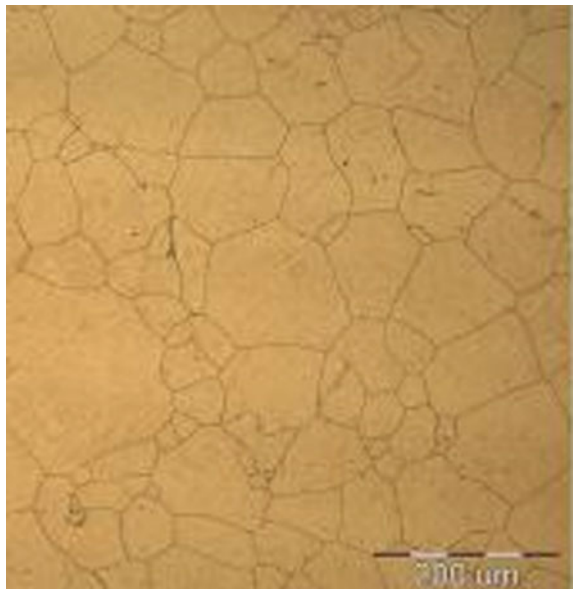
### 3 Microstructure Changes in M50 NiL Steel Under Forging Operation

Multi-directional impact forging process (MDIF) is similar to severe plastic deformation (SPD) in which refine grains and forms nanocrystals, relative to other methods [19]. This method has few advantages like less cost and flexible equipment which plays vital role in refining the crystal grains, so this process has major impact on grain refinement and macrostructural changes which has impact on mechanical properties. Jiang et al. [4] performed MDIF process in which pneumatic hammer is used for forging by changing the loads, altering the temperature and overall strain and then M50 NiL Steel microstructure was analysed [20]. After heating the steel in vacuum induction furnace, it has to be sent for forging process later annealed treatment, and then it has to be inspected through optical microscope (OM); there it is observed that it consists carbide and ferrite. To analyse macrostructural characteristics of this

specimen models after multi-directional impact forging loading direction planes are observed for different zones in specimen (Figs. 4 and 5).

In the above figure it is shown that microstructure of specimen steel has varied based on forging temperature and loads with respect to time and the grain size observed is between 72 and 182  $\mu\text{m}$ , and it is observed that when the temperature is increased gradually the grain size also increased and Jiang et al. [4] observed that the grain size is increasing slowly when the temperature is below 1100  $^{\circ}\text{C}$  and later grain size was effective [21]. Further in SEM detection method deformable zones at various forging temperature can be easily identified [22]. And in sample models it is observed that more equiaxed grains have been formed so this situation suggests dynamic recrystallization (DRX) during the forging process later at 1050

**Fig. 4** OM micrograph for unforged steel



**Fig. 5** OM micrograph for forged steel [4]



°C grain fragmentation has taken place and small DRX has occurred in some region due to this the average grain size is reduced to 4  $\mu\text{m}$ , and it can be observed from SEM detection method where granular carbides are precipitated near grain boundary and remaining are distributed inside the grain [23]. It can be clearly observed that increase in temperature has impact on grain reformation and size. If the forging temperature increases than 1180 °C some large grains are near to 23 and 6.5  $\mu\text{m}$  is the average grain size.

#### **4 Evolution of Microstructure in Plasma Nitrided M50 NiL Steel**

M50 NiL specimen models are plasma nitrided at 460–590 °C for four hours in the presence of constant supply of mixture gas  $0.05\text{N}_2\text{--}0.4\text{H}_2$   $\text{L min}^{-1}$ , and it is observed that temperature has effect on microstructure, microhardness and wear resistance on nitrided layers [24]. By enhancing nitriding temperature, nitrided layer and wear resistance increases and microhardness gets decreased on specimen models after plasma nitriding [25]. We are aware that thermochemical surface treatments such as carburising, nitriding, plasma nitriding and ion implantation are best methods to improve mechanical properties of steels. But among all of these methods, plasma nitriding is the best surface treatment process which involves diffusion of nitrogen in to the surface of steel and in this process. Wang et al. [6] observed that this process improves surface hardness and fatigue, corrosion and wear resistance of model steels as it is done at low temperature deformation of work piece and losses are effectively reduced. And it is also observed that surface hardness is increased relative to low nitriding temperatures about 460–560 °C and when nitriding temperature is beyond 575 °C, then low nitrogen phases may form [26]. When it comes to the experimental procedure, the nitrided specimen models are polished and etched in the presence of 4 vol% nital solution, and later, microstructure is observed by using optical microscope. The phase formation of nitrided models was analysed by using X-Ray diffraction method and features can be identified by using transmission electron microscope equipment. Later, the specimens have to be tested for hardness with various loads [27]. And from the study, it is known that if nitriding temperature increases from 460 to 490 °C particle size will also increase, and it is also observed flower structured shapes with the 0.3  $\mu\text{m}$  has formed on model surface, and this size will increase when the temperature is increased to 590 °C. And due to continuous sputtering and redeposition of surface atoms, the flower shape particles are formed and increase in nitriding temperature may also increase the KE of sputtered atoms.

## 5 Concluding Remarks

By considering various research contributions on this work, it is known that it has practical and economical applications. Few observations related to current research work are mentioned. They are, in plasma nitrocarburization process, it is observed that thickness of layer in nitrocarburized samples with rare earth addition was thicker than the samples which are without rare earth addition, because there is difference between nitrogen and carbon expansion which incorporates RE atoms and leads to formation of improved phase. During MDIF process, the average grain size of the specimen steel ranges from 72 to 182  $\mu\text{m}$  at the temperature ranges from 1050 to 1180  $^{\circ}\text{C}$  with basic time limit of 1 h, and if the temperature was beyond 1100 C, then grain size will be increased, respectively, during the given temperature range and grain refinement was observed with grain size ranges from 4 to 6.5  $\mu\text{m}$ . In plasma nitriding, quenched M50 NiL steel is altered as basic specimen model which has diffusion layer without compound layer. If temperature of nitrided samples are increased to 460–560  $^{\circ}\text{C}$ , then surface thickness increased, which include  $\alpha\text{-Fe}$ ,  $\gamma\text{-Fe}_4\text{N}$ , and sometimes low nitrogen phases  $\text{FeN}_{0.076}$  may form if the temperature is above 575  $^{\circ}\text{C}$ . By this study, it is known that the specimen model steel nitride at 560 C has good wear resistance in the nitride layer. M50 NiL Steel has wide scope in aerospace bearings because of its efficient response to the nitriding treatments which ensures better hardness and wear resistance after forging and nitriding treatments, so these characteristics justify for present requirements of aerospace bearings.

## References

1. Tang LN, Yan MF (2013) Influence of plasma nitriding on the microstructure, wear, and corrosion properties of quenched 30CrMnSiA steel. *J Mater Eng Perf JMEPEG* 1059–9495
2. Jiang H, Yanran SO, Yucheng WU, Debin SH, Yingying ZO (2020) Microstructure evolution and mechanical anisotropy of M50 steel ball bearing rings during multi-stage hot forging. *Chin J Aeronaut CJA* 1647: 15–18
3. Wang X, Yan M, Liu R, Zhang Y (2016) Effect of rare earth addition on microstructure and corrosion behavior of plasma nitrocarburized M50NiL steel. *J Rare Earths* 34(11):1148
4. Jiang H, Liu Y, Wu Y, Zhao K, Shan D, Zong Y (2019) Grain refinement mechanism and microstructural evolution of M50NiL steel during multi-directional impact forging. *J Mater Eng Perf JMEPEG* 28(6):3505–3516
5. Paulson KR (2014) Investigation of microstructural alterations in M50 and 52100 steel using nano indentation. Purdue University
6. Klecka MA, Subhash G, Arakere NK (2004) Microstructure–property relationships in M50-NiL and P675 case-hardened bearing steels. *Tribol Trans.* ISSN: 1040–2004 print/1547-397X online
7. Abhay K. Jha, M. Swathi Kiranmayee, P. Ramesh Narayanan, K. Sreekumar, and P.P. Sinha, Metallurgical Analysis of Ball Bearing Seized During Operation, *Journal of Materials Engineering and Performance*, 1059–9495 ,1076—Volume 21(6) June 2012.
8. Barrallier L (2015) Thermochemical surface engineering of steels, Elsevier Ltd, France, pp 393–412

9. Wang XA, Yan MF, Zhang CS, Zhang YX (2014) Microstructure and mechanical properties of surface layer of M50NiL steel plasma nitride. *Surf Eng* 30(3). Institute of Materials, Minerals and Mining
10. Steve OOI, Bhadeshia HKDH (2012) Duplex hardening of steels for aeroengine bearings. *ISIJ Int* 52(11):1927–1934
11. Wang XA, Yan MF, Zhang CS, Zhang YX, Bai B, Chen L, Long Z, Li RW (2014) Insights into plasma nitriding behaviour of M50NiL steel with different initial microstructures. *Mater Sci Technol* 30(10)
12. Basso RL, Pastore HO, Schmidt V, Baumvol IJ, Abarca SA, de Souza FS, Spinelli A, Figueroa CA, Giacomelli C (2010) Microstructure and corrosion behaviour of pulsed plasma-nitrided AISI H13 tool steel. *Corros Sci* 52(9):3133–3139
13. Jin J, Chen YB, Gao KW, Huang XL (2014) A study of the corrosion resistance of M50NiL bearing steel by ion implantation. In: *Advanced materials research*, vol 936. Trans Tech Publications, Switzerland, pp 1132–1137
14. Ji G, Li L, Qin F, Zhu L, Li Q (2016) Comparative study of phenomenological constitutive equations for an as-rolled M50NiL steel during hot deformation. *J Alloys Compd* 0925-8388/© 2016 Elsevier
15. Arakere NK, Subhash G (2012) Work hardening response of M50-NiL case hardened bearing steel during shakedown in rolling contact fatigue. *Mater Sci Technol* 28. Institute of Materials, Minerals and Mining
16. Li GM, Liang YL, Zhang XF, Sun H, Cao YG (2019) Effect of the carburized layer on the plasma nitriding behavior of duplex treated M50NiL steel. *Mater Res Express* 6:096550. © 2019 IOP Publishing Ltd.
17. Wang F, Zhou C, Zheng L, Zhang H (2017) Corrosion resistance of carbon ion-implanted M50NiL aerospace bearing steel. *Progr Nat Sci Mater Int*, 1002–0071/ 2017 Published by Elsevier B.V. on behalf of Chinese Materials Research Society
18. Carey S, Herring D (2007) Low-pressure carburizing process development of M50 Nil. *Heat Treating Progr. New Hampshire Ball Bearings Inc*
19. Babu PN, Satyanarayana MVNV, Balusu SB (2017) Study of plasma nitriding and nitrocarburizing with respect to bearing applications on M50 Nil. *Int J Res Appl Sci Eng Technol* 5(IX). ISSN: 2321-9653
20. Lian J-L, Zheng L-J, Wang F-F, Zhang H (2018) Evolution of carbides on surface of carburized M50NiL bearing steel. *J Iron Steel Res Int* 25(11):1198–1211. China Iron and Steel Research Institute Group
21. Yan MF, Wang XA, Liu RL, Zhang YX, Yang Y (2016) Kinetics and wear behaviour of M50NiL steel plasma nitrided at low temperature. *Mater Sci Technol*. Published by Taylor & Francis on behalf of the Institute of Materials, Minerals and Mining. ISSN: 0267-0836 (Print) 1743-2847 (Online). 27 July 2016
22. Li G-M, Liang Y-L, Yin C-H, Sun H, Zhu Z-L (2019) Study of M50NiL steel under carburizing and nitriding duplex treatment. *Surf Coatings Technol* 375:132–142. Available online 09 July 2019 0257–8972/ © 2019 Elsevier
23. Klecka MA, Subhash G, Arakere NK (2013) Microstructure–property relationships in M50-NiL and P675 case-hardened bearing steels. *Tribol Trans* 56:1046–1059. ISSN: 1040-2004 print/1547–397X online. C Society of Tribologists and Lubrication Engineers. Taylor & Francis
24. Venkatesh B, Anil Kumar Reddy C (2020) Experimental study on heat treatment and mechanical behaviour of M50 NiL bearing steel—a review. *Mater Today Proc*. In: *ICMMSE-2020*, Hyderabad. ISSN: 2214-7853
25. Rosado L, Forster NH, Thompson KL, Cooke JW (2009) Rolling contact fatigue life and spall propagation characteristics Of Aisi M50, M50 Nil, And Aisi 52100, Part I—Experimental Results, AFRL-RZ-WP-TP-2009-2208

26. Roy M (2013) Surface engineering for enhanced performance against wear. Springer Wien Heidelberg New York Dordrecht London, ISBN 978-3-7091-0100-1, ISBN 978-3-7091-0101-8 (eBook)
27. Venkatesh B, Sriker K, Prabhakar VS (2015) Wear characteristics of hardfacing alloys: state-of-the-art. In: 2nd International conference on nanomaterials and technologies (CNT 2014), Procedia Mater Sci 10:527–532



# Experimental Investigation of Plydrop Behavior in FRP Composites



G. Likhitha, N. Kiran Kumar, M. Manzoor Hussain, and S. N. S. Sai Hari

**Abstract** The tapered laminate is mostly used in many structural components. Plydrop is the technique used in fabrication of tapered laminate. This technique has received many researchers attention. Although there are some difficulties in dropping some of the plies because the strength of the laminate may affect due to the discontinuity in the laminate. So, the drop must be done such that the strength of the laminate should not affect. In this paper, the two configurations of the tapered laminates are introduced with symmetry along the center such that the laminate is covered with a layer of fiber at above and below of the plate. The tapered composite with two different configurations is fabricated with unidirectional glass fiber and epoxy by using hand layup vacuum bagging process. The mechanical tests such as tensile and flexural tests were done accordingly, and the obtained results indicate that configuration II show better tensile and flexural properties than configuration I.

**Keywords** Tapered composite · Plydrop · Glass fiber · Epoxy · Vacuum bag

## 1 Introduction

Fiber reinforced polymer (FRP) composites are broadly used in the construction of structural components such as fins and wings of an aircraft, helicopter blades and yoke, robot arms, and satellites. The recent fabrication of airframes is built with the 50% of FRPs. With their high structural tailoring capabilities and high stiffness, the airframe applications are very attractive. The tapered composite structures are usually formed by terminating one or more plies at different locations within the laminate. As the plies are dropped, it leads to the discontinuity in the laminate. These terminated plies give a triangular resin pockets and makes the misalignment of the plies within

---

G. Likhitha · N. K. Kumar (✉) · S. N. S. Hari  
VNR Vignana Jyothi Institute of Engineering and Technology, Bachupally, Hyderabad, Telangana 500090, India  
e-mail: [kirankumar\\_n@vnrvjiet.in](mailto:kirankumar_n@vnrvjiet.in)

M. M. Hussain  
Jawaharlal Nehru Technological University, Hyderabad, Telangana 500090, India

© The Author(s), under exclusive license to Springer Nature Singapore Pte Ltd. 2022  
G. S. V. L. Narasimham et al. (eds.), *Innovations in Mechanical Engineering*,  
Lecture Notes in Mechanical Engineering,  
[https://doi.org/10.1007/978-981-16-7282-8\\_44](https://doi.org/10.1007/978-981-16-7282-8_44)

591

the laminate. This leads to structural difficulties like stress concentration at the drop section that makes the initiation and propagation of delamination growth or resin failure. Also, interlaminar stresses are formed at drop-off location that results in initiating failure before ultimate load carrying capacity.

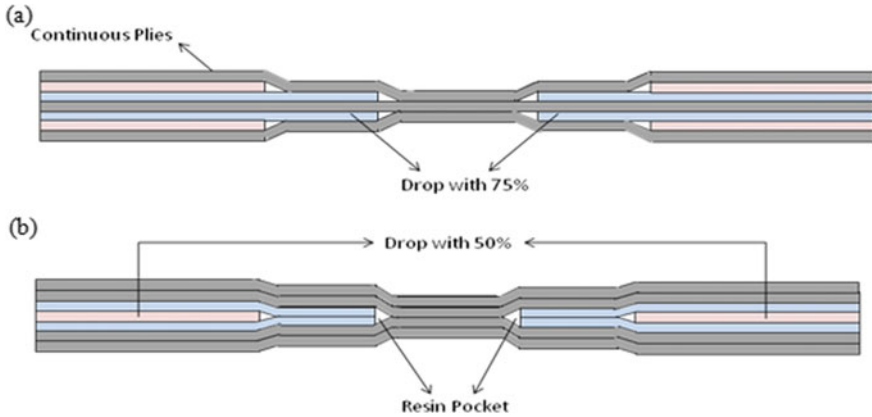
Several researchers were worked on plydrop; the optimal designs, design considerations and the guidelines have been developed [1–4]. The layup and patch-wise layup designs are optimized using genetic algorithm (GA) [5, 6]. The studies that are analyzed previously are categorized into two divisions. In the first division, they worked and investigated on different parameters that affect the properties of the tapered composite [7–16]. Some of them are as follows: The different types of resins and several fabrics are introduced and tested. So, the variation in the properties of the laminate may be varied [17]. The plydrop effect is considered in the honey comb sandwich panels. The samples are fabricated and investigated experimentally to know the behavior of the plydrop in the honeycomb core cells [18, 19]. An adhesive layer is added to improve the strength of the tapered laminate and to reduce the delamination in the composite [20]. The second divisions were focused on identifying the failure mechanisms.

This paper introduces plydrop positions of two different configurations and maintained the symmetry along the mid-plane of the composite. The specimens were fabricated using hand layup vacuum bagging process. The investigations of these specimens were done experimentally after the static tests carried on the specimen. The static tests such as tensile and flexural tests were conducted according to the ASTM standards. The two configurations were compared in each aspect, and the results were noted accordingly.

## 2 Experimental Process

The tapered composites are composed of continuous plies and some dropped plies. There are two different dropped positions such as, if the continuous fiber is 100%, the drop is at 75% and the other is at 50%. There are two different configurations of the tapered laminates as shown in Fig. 1. The laminates contain seven layers each and are symmetric. All these fibers are in same direction and their order is shown in Table 1.

In the configuration I, there is increment in the fiber and has continuous ply in the mid-plane, where as in configuration II there is decrease in the fiber and mid-plane has dropped plies. Figure 1a, b show the schematic representation of the tapered composites of configuration I and configuration II. The triangular section represents resin rich area usually known as resin pocket.



**Fig. 1** a Tapered composite of configuration I, b Tapered composite of configuration II

**Table 1** Different sample configurations and fiber order

Fiber configuration	Fiber order (%)
Configuration I	[100/50/75/100/75/50/100]
Configuration II	[100/100/75/50/75/100/100]

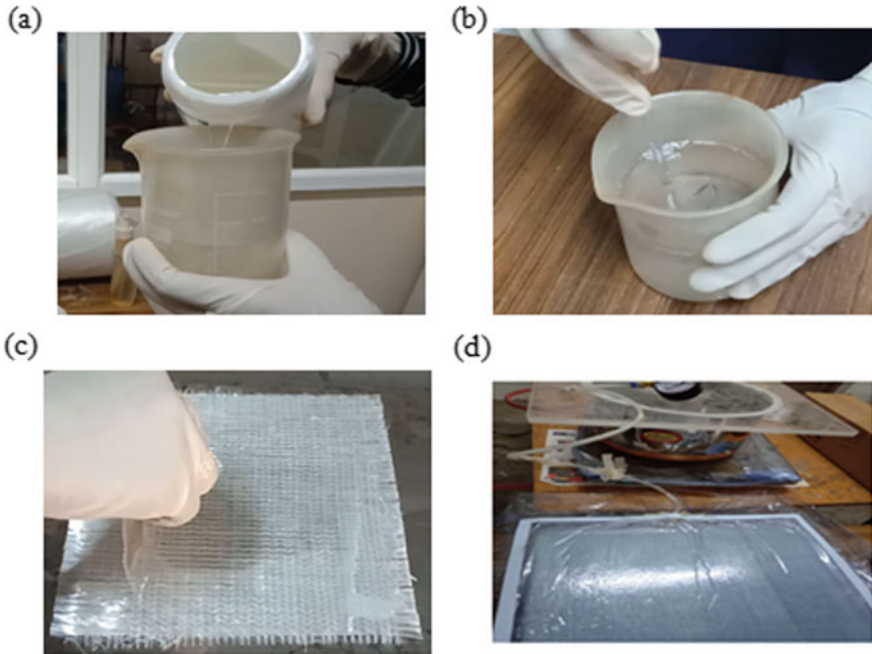
### 2.1 Materials and Fabrication Method

The laminates were fabricated from the unidirectional e-glass fiber, supplied by SAERTEX. The epoxy resin and hardener are C-51 and K-6, respectively, supplied by LAPOX. The technical specifications of the LAPOX C-51 are shown in Table 2.

The laminates were fabricated by hand layup vacuum bagging process. The unidirectional glass fibers are cut according to the dimensions. The resin is prepared by the following procedure. The epoxy is taken into a beaker (see Fig. 2a), and the hardener is added into a neat epoxy with the ratio of 1:10. The mixture is mixed slowly with the glass rod for about 5 min (see Fig. 2b). The vacuum bag and hand layup mold are prepared on the table. All the fibers are placed according to the order, and resin is spread throughout the fibers (see Fig. 2c). The tapered laminate is then placed in the

**Table 2** LAPOX C's technical specifications

Properties	Unit	Test method	Values
Appearance	–	Visual	Clear, pale-yellow liquid
Color	GS	ASTM D1544	Pale-yellow liquid
Viscosity at 25 °C	m Pas	ASTM D2196	1300–1700
Epoxy content	Eq/kg	ASTM D1652	4.15–4.4
Specific gravity at 25 °C	–	ASTM D792	1.10–1.15



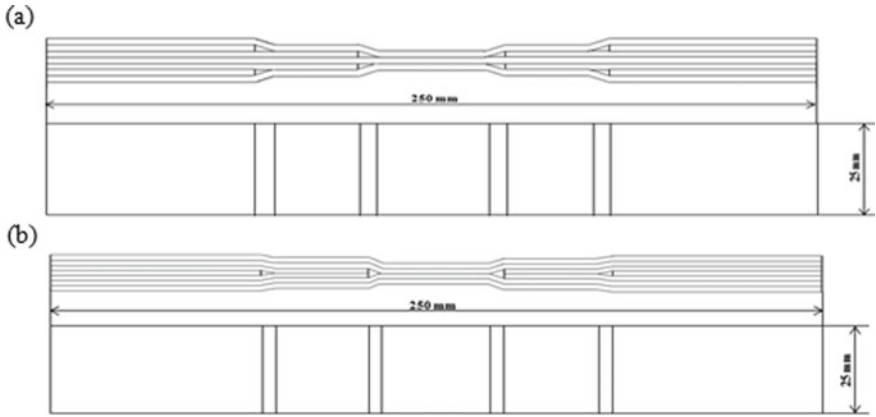
**Fig. 2** **a** Adding resin in beaker, **b** mixing resin and hardener, **c** spreading the resin, **d** placing into vacuum bag to cure the composite

vacuum bag to create additional pressure on the laminate during the cure cycle (see Fig. 2d). The main advantage of the vacuum bagging technique is as it optimizes the fiber-to-resin ratio in the composite part. Hence, the two configurations are fabricated with this process. The square laminate for tensile test is 250 mm x 250 mm and for the flexural test is 125 mm x 125 mm in size.

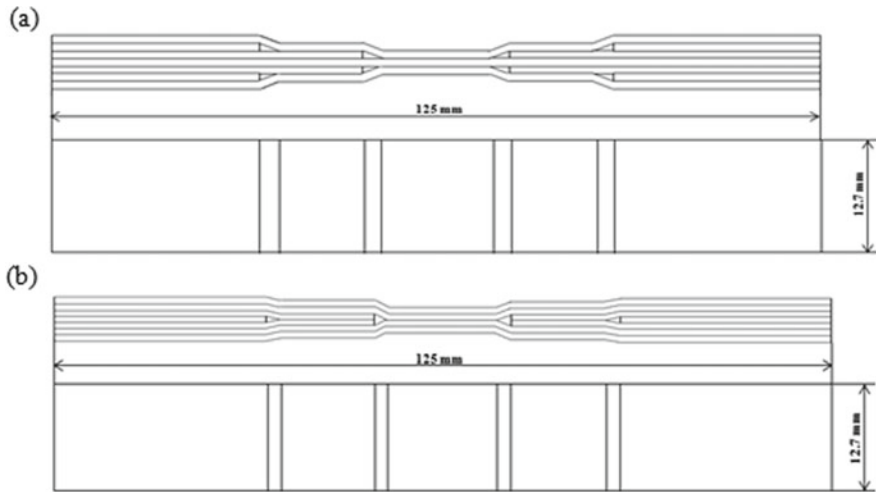
## 2.2 Specimen Preparation

The specimens were cut with high-speed vertical band saw. The dimensions of the specimens according to their tests are varied. The specimen size of tensile test of both configurations is according to the ASTM D3039 standard. Figure 3a, b show the dimensions of the specimens for testing tensile behavior of configuration I and configuration II, respectively. The flexural test for both configurations, the specimen size is shown in Fig. 4a, b according to the standard ASTM D790.

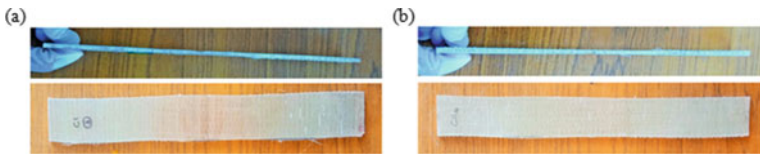
The fabricated tapered composite specimen of configuration I and configuration II for the tensile test are shown in Fig. 5a, b, respectively, and for the flexural test are shown in Fig. 6a, b. The top view along with side view is shown in the figure. These finished specimens along with five samples are tested and analyzed.



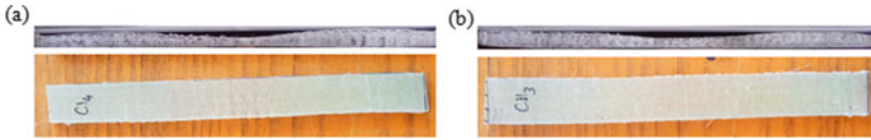
**Fig. 3** **a** Tensile test specimen size dimensions of configuration I, **b** tensile test specimen size dimensions of configuration II



**Fig. 4** **a** Flexural test specimen size dimensions of configuration I, **b** flexural test specimen size dimensions of configuration II



**Fig. 5** **a** Finished tapered specimen of configuration I for tensile test, **b** finished tapered of configuration II for tensile test



**Fig. 6** **a** Finished tapered specimen for flexural test for configuration I, **b** finished tapered specimen for flexural test for configuration II

**Table 3** Thickness measurement of configuration I and configuration II (in mm)

Points	Configuration I		Configuration II	
	Tensile	Flexural	Tensile	Flexural
A	3.90	4.61	4.10	4.42
A <sup>1</sup>	3.81	4.65	4.09	4.38
B	2.63	1.98	3.08	2.23
B <sup>1</sup>	2.87	1.92	2.84	2.19
C	3.90	4.52	4.08	4.25
C <sup>1</sup>	3.93	4.45	4.12	4.33

Specimens with the variation in thickness that are fabricated are measured and tabulated. Table 3 shows the measurement of the thickness in each specimen of tensile and flexural of configuration I and configuration II.

### 2.3 Testing

**Tensile Testing.** The tension test is performed on flat specimens. The tensile test specimen size according to the standard ASTM D3039 with the length 250 mm and width 25 mm is used. The specimen is first clamped in the chucks of the UTM machine. Both ends are clamped in an appropriate position. The test machine is started; the first load is done very slowly and evenly. The yield value is recorded then the speed of the loading is made faster to reach the maximum until the specimen reaches the failure point. All the values are recorded until the specimen reaches the maximum displacement.

The tensile test is performed in computerized servo control universal testing machine MCS UTE20T. Figure 7a shows the machine used for the testing, and Fig. 7b shows the specimen loading condition.

**Flexural Testing.** Flexural test is conducted on UTM MCS TNE-1 T machine with the specimen size of length 125 mm and width 12.7 mm as per the standard ASTM D790. A three-point bending loading where the specimen is placed at two points, and the load is added at third point. The test is done in an UTM machine with three-point bend fixture. The specimen is placed on two parallel supporting pins, and

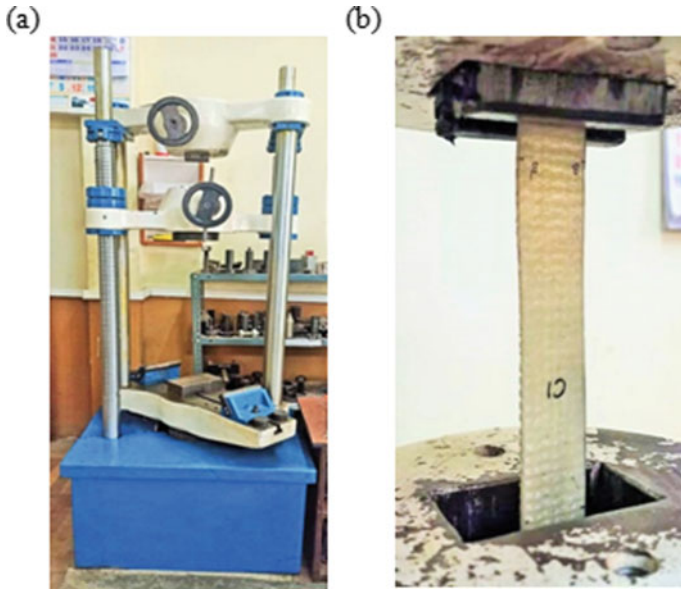


Fig. 7 a Computerized servo control UTM, b specimen loading in the machine

the loading is done at the middle of the specimen by a loading pin. Starting with a small load and increasing the loading evenly, the points are recorded. The loading is done until the specimen reaches the maximum point. The line representation of the three-point bending is shown in Fig. 8. The machine used for the flexural test and the specimens loaded in a three-point bending fixture as shown in Fig. 9.

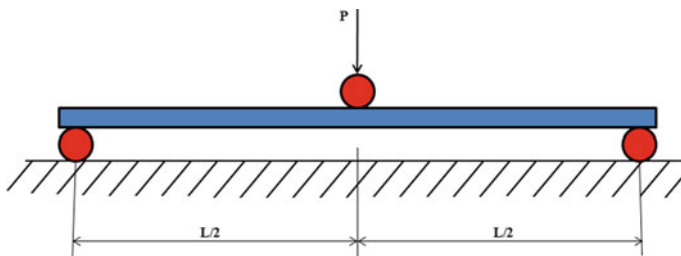


Fig. 8 Line diagram of three-point bending

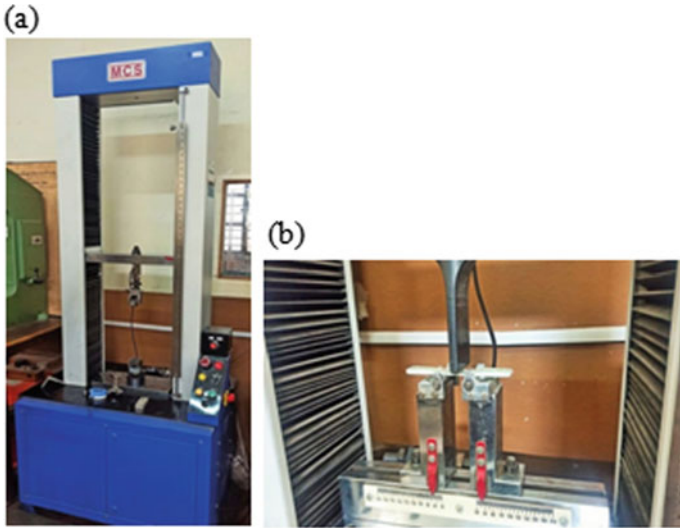


Fig. 9 a UTM, b Three-point bending fixture specimen loading

### 3 Results and Discussion

#### 3.1 Tensile Loading Tests

The fabricated specimens were loaded in tension. Figure 10 shows the configuration I of all the five samples before and after the tensile loading. The specimens were failed

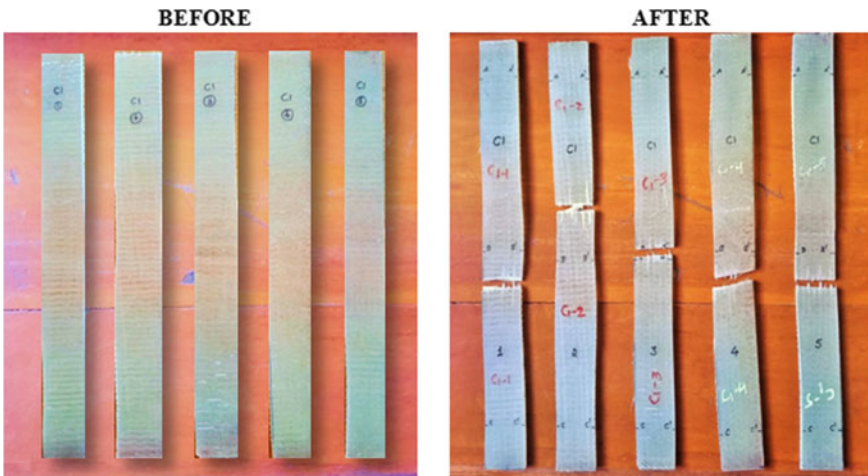


Fig. 10 Tensile specimens of configuration I before and after testing



at the thin section. The tensile stress shows high in specimen 3 among all the samples with the value of 25.6 MPa. The maximum of 2.14 kN load is applied so that the maximum displacement obtained is up to 3.4 mm. All the samples were completely failed at the thinner section except sample 2; here, the fibers are still bonded in the specimen. It displaces 2.9 mm with the load of 1.94 kN.

Figure 11 shows the tensile specimens of configuration II of all five samples before and after testing. The specimens were failed at the thin section where some part of the fibers are still bonded within the specimen except sample 1. It is completely failed with the breakage in fiber. The stress found in this sample is 45.8 MPa by applying the load of 3.76 kN and displaces up to 3.7 mm.

**Load–Displacement.** Figure 12 shows the tensile load versus displacement for the configuration I with all the samples. These samples were loaded in tension. The result

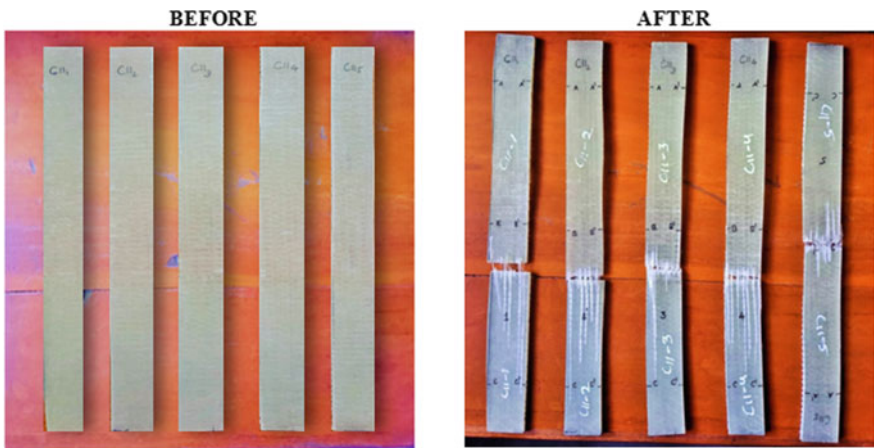


Fig. 11 Tensile specimens of configuration II before and after testing

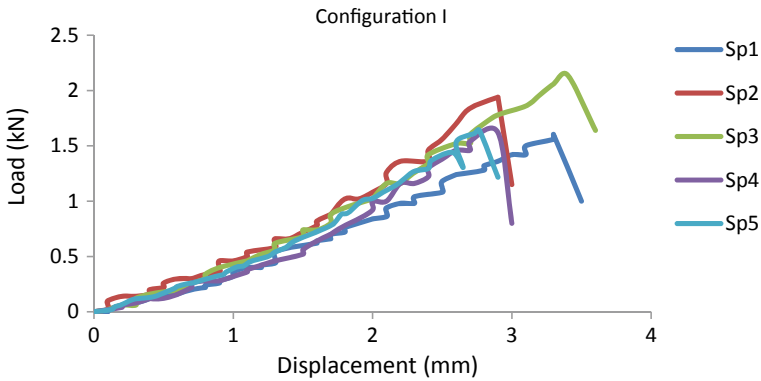


Fig. 12 Tensile load versus displacement curves of all samples of configuration I

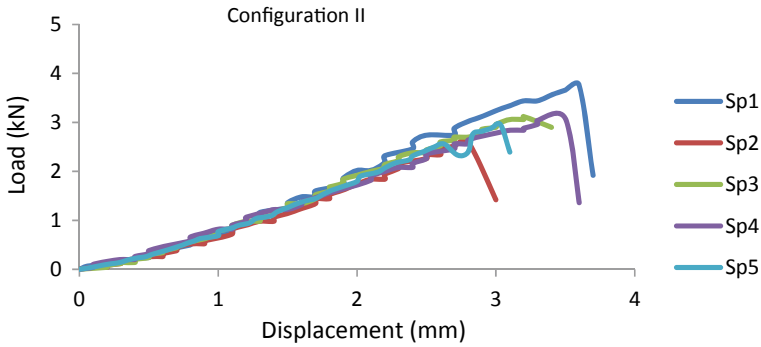


Fig. 13 Tensile load versus displacement curves of all samples of configuration II

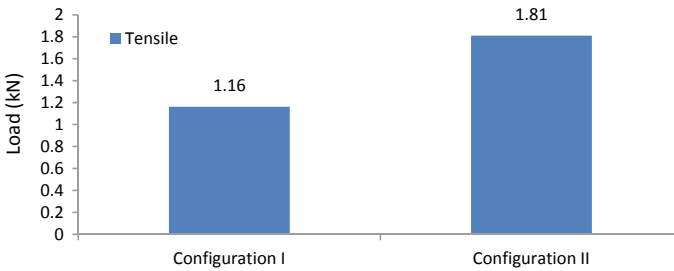


Fig. 14 Comparison of configuration I and configuration II in tension

shows by comparing all the samples of this configuration I. With the comparison, the sample 3 has displaced long with high load than other samples. Figure 13 shows the graph of tensile load versus displacement for the configuration II considering all samples. Among them, sample 1 shows the longest displacement with the high load.

The tensile tests are done for configuration I and configuration II. By the obtained results, the comparison can be made among them. Figure 14 shows the graph that compares both the configurations in tensile behavior.

### 3.2 Flexural Loading Tests

The specimens that are fabricated are loaded in a three-point bending fixture. Figure 15 shows the flexural specimens of configuration I before and after testing. After completing the bending test of all the samples, they are physically observed where fibers are displaced but not completely failed. Clearly, all the samples are failed at the thin section where the white area in Fig. 15 after shows the crack part in the specimens.

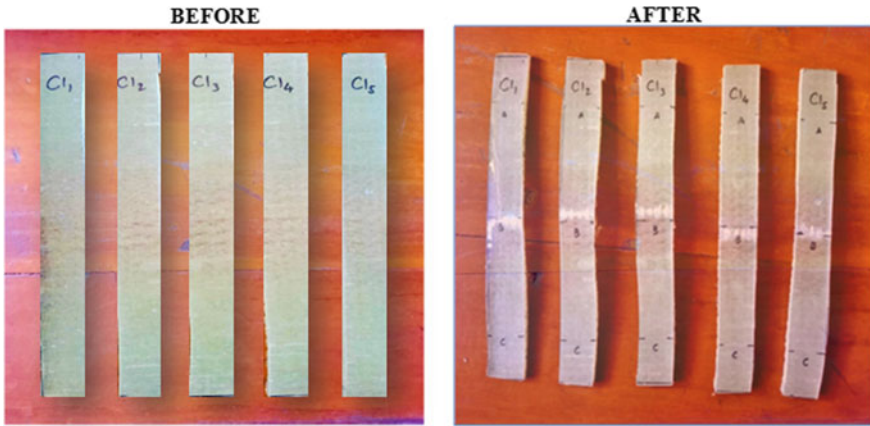


Fig. 15 Flexure specimens of configuration I before and after testing

Figure 16 shows the specimens of the flexure of configuration II before the testing and after the testing. All the samples are loading in a three-point bending fixture, and test was conducted by increasing the load every second. After the test, each sample is examined physically. All the samples are failed at the thinner section, and small amount of the fibers are displaced to crack but completely failed. The area where the crack is occurred is seen as white section in the after image.

**Load-Displacement.** The graph is plotted for configuration I considering all the five samples. Figure 17 shows the load versus displacement curves of all the samples of configuration I. The sample 2 displaces with high load, whereas the sample 5 displaces more with less load. Figure 18 gives the graph of load versus displacement

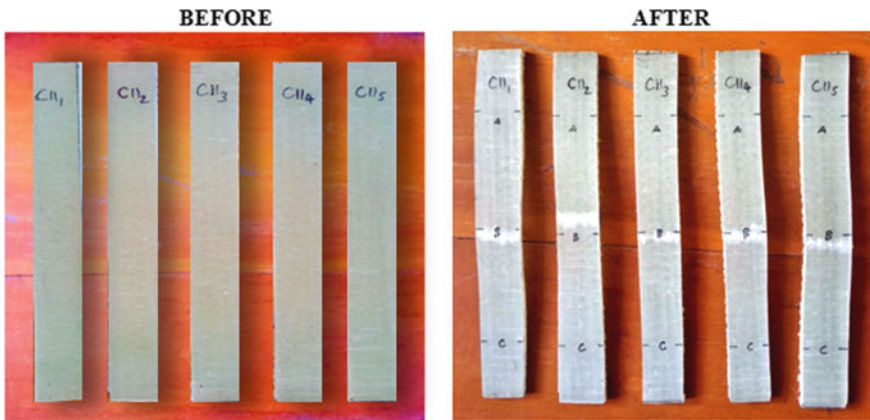


Fig. 16 Flexure specimens of configuration II before and after testing

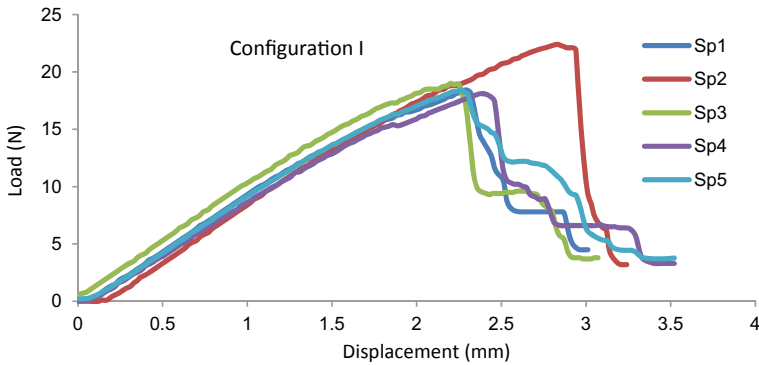


Fig. 17 Load versus displacement curves of all samples of configuration I

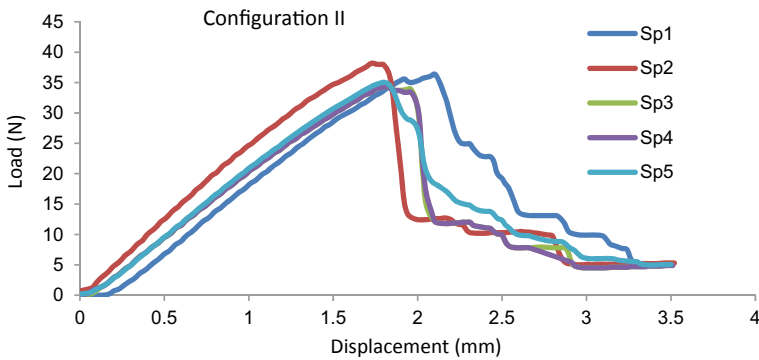


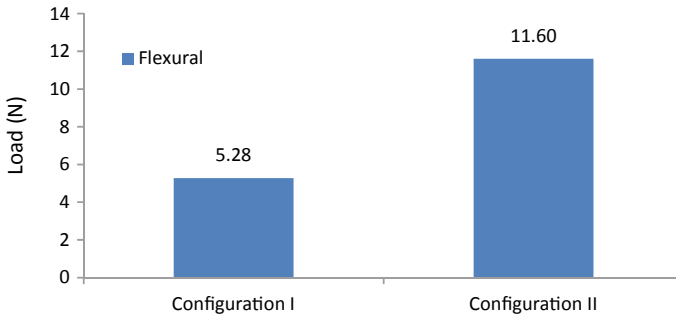
Fig. 18 Load versus displacement curves of all samples of configuration II

of all the samples of configuration II. Among them, sample 2 displaces with high load, but the sample 5 displacement is more with fewer loads.

The flexural tests are done for configuration I and configuration II. By the obtained results, the comparison can be made among them. Figure 19 shows the graph that compares both the configurations in flexural behavior.

### 4 Conclusions

This paper presents the results of the study of tensile and flexural behavior of e-glass/epoxy plydrop composite with two different configurations. The tapered laminates maintained the symmetry at the center; the configurations with plydrop and without plydrop in the mid-plane of the laminate are fabricated. The following are the conclusions obtained:



**Fig. 19** Comparison of configuration I and configuration II in bending

1. The tapered laminate with the plydrop in the mid-plane is showing good tensile and flexural properties than the tapered laminate without plydrop in the mid-plane, i.e., configuration II is effective.
2. The plydrop is maintained such that the plies that covered the tapered composite given an additional strength to the laminate. Here, the covered layer acts as an additional layer in the configuration II.
3. The plies dropped in configuration II (firstly decreased and then increased in the fiber percentage) is showing better strength than the plies dropped in configuration I (firstly increased and then decreased in the fiber percentage).

**Acknowledgements** The authors like to mention thanks to TEQIP-III, JNTUH for the support in the current project under CRS. Furthermore, authors like to thank VNRVJIET management for giving access to laboratories during the pandemic.

## References

1. Mukherjee AB, Varughese B (2001) Design guidelines for ply drop-off in laminated composite structures. *Compos Part B Eng* 32(2):153–164
2. Manne PM, Tsai SW (1997) Plydrops for tapered design optimization of composite plates. In: *Proceedings of the 11th international conference on composite materials*, vol 1, pp 762–771
3. Cairns DS, Mandell JF, Scott ME, Maccagnano JZ (1999) Design and manufacturing considerations for plydrops in composite structures. *Compos Part B Eng* 30(5):523–534
4. Irisarri FX, Lasseigne A, Leroy FH, Le Riche R (2014) Optimal design of laminated composite structures with ply drops using stacking sequence tables. *Compos Struct* (107):559–569
5. Rhee SY, Cho M, Kim HS (2006) Layup optimization with GA for tapered laminates with internal plydrops. *Int J Solids Struct* 43:4757–4776
6. Kim J-S, Kim C-G, Hong C-S (1999) Optimum design of composite structures with ply drop using genetic algorithm and expert system shell. *Compos Struct* 42:171–187
7. Vidyashankar BR, Krishna Murty AV (2001) Analysis of laminates with plydrops. *Compos Sci Technol* 61(5):749–758
8. Cui W, Wisnom MR, Jones M (1994) Effect of step spacing on delamination of tapered laminates. *Compos Sci Technol* 52(1):39–46

9. Dhurvey P, Mittal ND (2013) Study the effect of externally and internally ply drop-off in composite laminate analysis. *ARNP J Eng Appl Sci* 8(4):595–605
10. Albanesi A, Bre F, Fachinotti V, Gebhardt C (2018) Simultaneous ply-order, ply-number and ply-drop optimization of laminate wind turbine blades using the inverse finite element method. *Compos Struct* (184):894–903
11. Daoust J, Hoa SV (1989) Parameters affecting Interlaminar stresses in tapered laminates under static loading conditions. *Polymer Compos* 10(5):374–383
12. Weiss A, Michel L, Mahdi S, Cros E, Barrau JJ (2009) Influence of ply-drop position in thickness direction on static and fatigue behaviour of carbon fibre epoxy laminates
13. Wisnom MR, Atkinson JW (1997) Reduction in tensile and flexural strength of unidirectional glass fibre-epoxy with increasing specimen size. *Compos Struct* 38(1–4):405–411
14. Weiss A, Trabelsi W, Michel L, Barrau JJ, Mahdi S (2010) Influence of ply-drop location on the fatigue behaviour of tapered composites laminates. *Procedia Eng* 2(1):1105–1114
15. Hegde A, Darshan RS, Mulla F, Shoeb M, Rajanish M (2015) Tensile properties of unidirectional glass/epoxy composites at different orientations of fibres. *Int J Eng Res Appl* 5(3):150–153
16. Khan B, Potter K, Wisnom MR (2006) Suppression of delamination at plydrops in tapered composites by ply chamfering. *J Compos Mater* 40(2):157–174
17. Agastra P, Mandell JF (2010) Testing and simulation of damage growth at ply drops in wind turbine blade laminates. In: *Proceedings of society of the advancement of materials and process engineering*
18. Thomsen OT, Rits W, Eaton DCG, Brown S (1996) Ply drop-off effects in CFRP/Honeycomb sandwich panels-theory. *Compos Sci Technol* 56(4):407–422
19. Thomsen OT, Rits W, Eaton DCG, Dupont O, Queekers P (1996) Ply drop-off effects in CFRP/Honeycomb sandwich panels-experimental results. *Compos Sci Technol* 56(4):423–437
20. Llanos AS, Vizzini AJ (1992) The effect of film adhesive on the delamination strength of tapered composites. *J Compos Mater* 26(13):1968–1983

# Influence of Coating on Micro Stress Distribution in Cylindrical FRP Composites



Namala Kiran Kumar, G. Srinivasa Gupta, K. Ajay Kumar,  
and M. Manzoor Hussain

**Abstract** Composite materials have boundless applications in engineering as these exhibit high specific strength and stiffness properties. In order to achieve high stiffness each constituent present in the material play a significant role. It has been observed through literature survey that coating properties influence more than other constituents since it is acting as a bonding agent between fiber and matrix and also transfer load from the matrix to the fiber. In this work an attempt has been made to analyze extensively the influence of HM and LM coating on micro stress distribution for cylindrical composites under thermal and mechanical loadings applied individually and also simultaneously. The stress distribution in intra and inter laminar regions for composites made of carbon and S glass fiber has been estimated for low and high modulus epoxy coating and matrix. Similar stress distribution from an existing analytical model has been used and a comparative study on stress distribution is carried with numerical analysis using a four phase cylindrical composite assembly model. Both analytical and numerical stress distribution patterns under thermal and mechanical loadings have been compared in this analysis. Also a comparison has been made while thermal and mechanical loadings are applied simultaneously.

**Keywords** Cylindrical composite assembly · Coating · Inter laminar · Thermal loading · Micro stress · Hygrothermal

## 1 Introduction

Composite materials have limitless building applications where strength to weight proportion, minimal effort and simplicity of fabrication are required. For specific applications, the utilization of composite materials when contrasted with metals

---

N. Kiran Kumar (✉) · G. S. Gupta · K. A. Kumar  
VNR Vignana Jyothi Institute of Engineering and Technology, Bachupally, Nizampet (S.O.),  
Hyderabad 500090, India  
e-mail: [kirankumar\\_n@vnrvjiet.in](mailto:kirankumar_n@vnrvjiet.in)

M. M. Hussain  
Jawaharlal Nehru Technological University Hyderabad, Hyderabad, India

© The Author(s), under exclusive license to Springer Nature Singapore Pte Ltd. 2022  
G. S. V. L. Narasimham et al. (eds.), *Innovations in Mechanical Engineering*,  
Lecture Notes in Mechanical Engineering,  
[https://doi.org/10.1007/978-981-16-7282-8\\_45](https://doi.org/10.1007/978-981-16-7282-8_45)

have in reality brought about reserve funds of both weight and cost. Fiber reinforced composite materials comprises of fibers of genuine quality and stiffness implanted a matrix with particular limits between them. The two fibers and matrix keep up their physical and chemical identities, yet their combination plays out a capacity which is not possible by every constituent acting independently. Fiber reinforced plastics might be short and consistent. It seems evident that FRP having ceaseless fibers is to be indeed more efficient.

Carbon fiber is superior fiber accessible in designing and manufacturing field. It is also called graphite fiber or carbon graphite. It has high elasticity and great strength of their size. Contrast with glass fiber the carbon fiber has high young's modulus and repetitive loads. The durability life of a carbon fiber strengthened polymer has more potential than that of agamid and glass fiber. These fibers are highly safe, have high temperature resilience with warm extension low and destructive obstruction. The two important point of carbon fiber are level of carbonization (carbon content in the fiber is more noteworthy than or equivalent to 92% by weight) and direction of the layered carbon planes.

Significant utilization of these strands is in creation of airplane and shuttle parts, sport vehicle bodies, fishing rods, springs, etc.,. Major application of these fibers is in making of aircraft and spacecraft parts, racing car bodies, fishing rods, automobile springs, etc.

S Glass fiber is comprised of a few fine fibers of glass. It is most flexible mechanical material known today. Compare with polymers and carbon fiber this fiber is utilized as reinforcing agent for some polymer items, to shape an entirely tough and a lightweight material. This S Glass fiber is otherwise called fiber glass. This fiber offers interesting focal points because of thickness, weight and quality. At lower weight S Glass fiber had higher elasticity. Elongation in the fiber when load acts is normally 3% or less along these lines, this is dimensionally stabile. This fiber has good thermally insulated due higher proportion of surface area to weight. It is also chemically safe. Protected from sunlight, fungi and other microorganism. S Glass is more technically important glasses. It has the highest strength, stiffness and softening point of any commercial reinforcement glass fiber. This glass is used as FRP lightweight armor which is a very demanding product. Major application of S Glass fiber is exterior ornamentation, interior details, landscape furnishings, architectural projects, airfields runways and rocket launch pads.

Epoxy resin are referred to a group of broad reactive compounds that are characterized by the presence of an epoxy ring or oxirane. The three-member ring contains an oxygen atom that is bonded with carbon already untitled in some other way. Further epoxy resin can be combined with varied curing agents, modifiers to achieve the properties required for a specific application.

Epoxies offers some key properties:

- High strength
- Low shrinkage
- Excellent adhesion to various substrates
- Effective electrical insulation



- Chemical and solvent resistance and
- Low cost and low toxicity.

Some of the most important application of the epoxies are in aerospace and recreation industries where resins and fibers are combined for producing a strong and complex composite. Epoxy resins satisfy a various variety of non-metallic composite design in commercial and military aerospace application including flooring panels, ducting, vertical and horizontal stabilizers and wings.

Hence, the object of the present work involves selection of two types of epoxy coating materials which are different modulus values and also glass and carbon fibers for carbon fiber reinforced and glass fiber reinforced composites each with high and low modulus coating for proper bonding of fibers with matrix material and transfer of load from matrix to fiber.

## 2 Numerical Analysis

### 2.1 Mechanical Properties of the Constituent Phases

Graphite-epoxy composite was selected for the study, because it is a composite of significant technical interest [1], and also due to the fact that the properties of graphite are transversely isotropic. For isotropic fibers equations becomes simplified and, as an example of this case, some results were obtained for using AS Graphite and S Glass, epoxy composite also. Since in practice, both soft and hard kinds of fiber coatings are used depending on the nature of application of the composite, both low modulus (LM) and high modulus (HM) coatings have been considered. All the results are based on the properties of the constituent phase materials such as Graphite fiber, S Glass and epoxy matrix listed in Table 1.

### 2.2 Volume Fraction

In our project, the volume fraction help in finding the dimensions of the fiber, coating and matrix. The volume ratio taken for 4-phase model is 0.69, 0.01, 0.3, respectively, which decide the radius of the individual constituents. For the project the initial assumption is taken first for the composite material, i.e., radius of the composite is 50 mm.

After assuming the radius of composite, the dimension (radius) of fiber, coating and matrix is found. The obtained areas are again equated to its area with equivalent hollow radius.

$$V_f = \frac{A_{\text{fiber}}}{A_{\text{composite}}}, V_c = \frac{A_{\text{coating}}}{A_{\text{composite}}}, V_m = \frac{A_{\text{matrix}}}{A_{\text{composite}}}$$

**Table 1** Properties of constituent materials [2]

Properties	AS graphite fiber	S glass fiber	Epoxy matrix	Coating LM	Coating HM
Longitudinal modulus (GPa)	220	86.2	3.45	2.2	5.2
Transverse modulus (GPa)	13.8	86.2	3.45	2.2	5.2
Longitudinal shear modulus (GPa)	13.8	35.7	1.27	0.8	1.93
Transverse shear modulus (GPa)	5.5	35.7	1.27	0.8	1.93
Major Poisson's ratio	0.2	0.22	0.35	0.43	0.35
Longitudinal tensile strength (MPa)	3100	4825	103.5	55.2	138
Transverse tensile strength (MPa)	345	4825	103.5	55.2	138
Longitudinal shear strength (MPa)	1550	2410	89.7	55.2	103.5
Transverse shear strength (MPa)	172	2410	64.8	55.2	103.5
Density (gm/cc)	2.26	2.485	1.14	0.25	0.35
Thermal conductivity $k$ (W/Mk)	900	1.275	0.25	1.299	2.25

### 2.3 Rule of Mixtures

After selecting the suitable volume fraction and obtaining the dimension the composite the next is to find the mechanical property of the FRP composite using rule of mixture.

Rule of mixtures is used to know the various properties of a composite material made up of continuous and unidirectional fibers, matrix of different materials. It provides a theoretical upper-bound and lower-bound on properties. It is a method to deal with inexact estimation of composite material properties, in view of an assumption that a necessary composite property is the volume weighed average of the phases (say fiber, matrix, coating) properties.

According to Rule of Mixtures properties of composite materials are estimated as follows:

- Density
- Coefficient of Thermal Expansion
- Modulus of Elasticity
- Shear Modulus
- Poisson’s ratio
- Tensile Strength.

The following are the formulae for various mechanical properties for the composite material

**Density:**  $d_{\text{composite}} = d_f V_f + d_m V_m + d_c V_c .$

where

$d_f, d_m, d_c$ —densities of fiber, matrix and coating respectively.

**Coefficient of Thermal Expansion:**

Coefficient of Thermal Expansion (CTE) in longitudinal direction (along the fibers).

$$\alpha_{\text{composite}} = \frac{\alpha_m E_m V_m + \alpha_f E_f V_f + \alpha_c E_c V_c}{E_m V_m + E_f V_f + E_c V_c}$$

where

$\alpha_m, \alpha_f, \alpha_c$ —coefficient of thermal expansion of matrix, fiber, coating, respectively

$E_m, E_f, E$ —modulus of elasticity of matrix, fiber, coating, respectively.

$V_m, V_f, V_c$ —Volume fraction of matrix, fiber, coating, respectively.

**Modulus of Elasticity:**

Composites have their different microstructure designed in terms of their constituents in macroscopic level like we have taken fiber, matrix and coating. To obtain the modulus of elasticity of the composite the volume fraction of the above material, and alignment and their mechanical properties may be tailored to meet specific design requirement [3].

Modulus of Elasticity in longitudinal direction:

$$E_{\text{composite}} = E_m V_m + E_f V_f + E_c V_c$$

Modulus of Elasticity in transverse direction

$$\frac{1}{E_{\text{composite}}} = \frac{V_m}{E_m} + \frac{V_f}{E_f} + \frac{V_c}{E_c}$$

$E_f, E_m, E_c$ —modulus of elasticity of fiber, matrix and coating material.

**Shear modulus:**

$$G_{\text{composite}} = \frac{G_f G_m G_c}{G_f G_m V_c + G_f G_c V_m + G_c G_m V_f}$$

where:

$G_f, G_m, G_c$ —shear modulus of fiber, matrix and coating material.

**Poisson's ratio:**

Poisson's ratio is the ratio of transverse contraction strain to longitudinal extension strain in the direction of applied force.

$$v_{\text{composite}} = v_f V_f + v_m V_m + v_c V_c$$

where:

$v_f, v_m, v_c$ —Poisson ratio of fiber, matrix and coating material.

**Tensile Strength:**

Tensile strength of long-fiber reinforced composite in longitudinal direction is given by,

$$\sigma_{\text{composite}} = \sigma_f V_f + \sigma_m V_m + \sigma_c V_c$$

where

$\sigma_f, \sigma_m, \sigma_c$ —tensile strength of the fiber, matrix, coating, respectively.

**2.4 Mechanical Properties of an FRP Composite Material**

As per the “Rule of Mixture”, the calculation of the fiber reinforced polymer composite material's mechanical properties is founded. The values like density, modulus of elasticity in longitudinal and transverse direction, poisson ratio, modulus of rigidity, thermal coefficient of expansion, tensile strength is calculated by assuming the diameter of the composites as 100 mm.

And the volume ratio is taken as 0.69, 0.3, 0.01 for fiber, matrix, coating, respectively. The calculation done separately, considering the LM coating and HM coating for both AS Graphite fiber and S Glass fiber individually (Table 2).

**Table 2** Properties of composite materials [4]

Parameters	AS graphite (LM coating)	AS graphite (HM coating)	S glass (LM coating)	S glass (HM coating)
Longitudinal modulus (GPa)	152.83	152.887	60.535	60.568
Transverse modulus (GPa)	7.067	7.20	4.6017	2.0196
Longitudinal shear modulus (GPa)	3.347	3.4316	3.89	3.905
Major Poisson's ratio	0.2713	0.2473	0.2611	0.2603
Density (gm/cc)	1.9016	1.9017	2.0591	2.0601
Thermal conductivity <i>k</i> (W/Mk)	0.0079	0.01207	0.007	0.0106
Tensile strength (MPa)	2170.602	2171.43	3360	3361.6

### 3 Modeling of Cylindrical FRP Composite

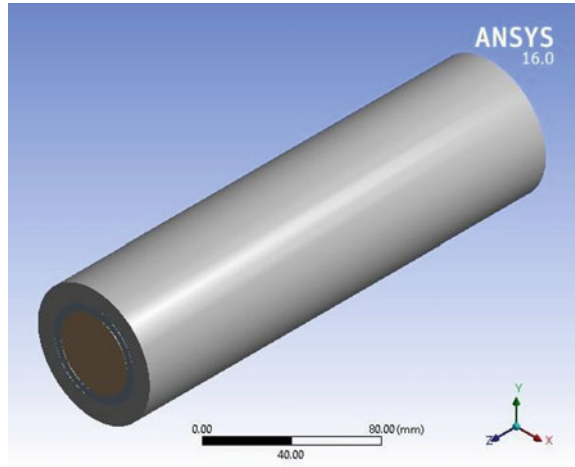
#### 3.1 Introduction to ANSYS

Ansys creates and showcases engineering simulation programming for the utilization across life cycle. Ansys mechanical finite element analysis software is utilized to simulate the desktop models of structures, electronics, or machine parts for analyzing the quality, strength, flexibility, temperature appropriation, electromagnetism, liquid stream and different characteristics. Ansys is utilized to decide the working of an item with various determinations, without building the test product or leading accident tests [5].

Ansys Workbench and APDL are for the most part utilized for performing out the Ansys simulation. These are the organization's fundamental items. Ansys users separate bigger structures into small segments that are each displayed and tried exclusively. Normally a user begins by characterizing the components of an article, and afterward including weight, temperature and other physical properties. At last, the Ansys program simulates and breaks down development, fatigue, cracks, liquid stream, temperature profile, electromagnetic effectiveness and different impacts over time.

Simulation technology is predominantly utilized during the advancement of another product or another variation. But, another significant utilization of simulation comes as effectively and rapidly correcting defective design components of an product that were missed in the underlying structure stage. One more part of simulation that shows its significance is in the way that engineer can envision their product

**Fig. 1** Four phase model on the ANSYS



better, and in this way keep their product within the standards. Physical testing has its own breaking point in showing the capability of a product, and this can be extended by the utilization of simulation. Better expectations of value and perception further lead to better advancements, and for most manufacturers, the genuine significance of development is in exploring the plan space. This is because simulation is the response for the physical restrictions that a design can be gotten through in reality.

### 3.2 ANSYS Model

See Fig. 1.

## 4 Geometry for ANSYS Model

See Table 3.

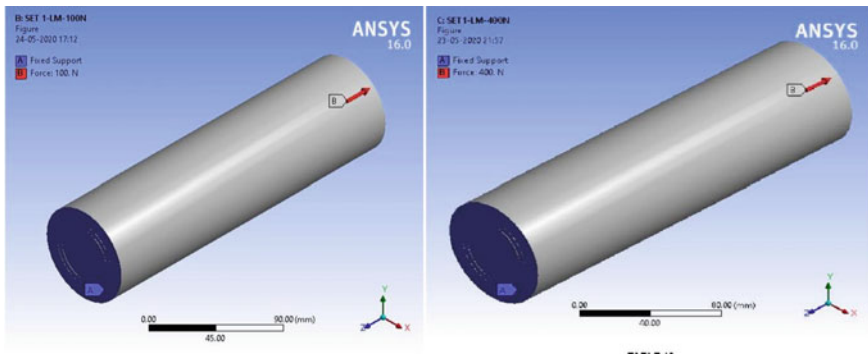
### 4.1 Loading Conditions

#### 4.1.1 Mechanical Loads: 100 N, 400 N

See Fig. 2 and Table 4.

**Table 3** Geometry for individual constituents of ANSYS model

Properties	Composite	Epoxy matrix	Coating	AS carbon fiber	S glass
Length X (mm)	70.749	50.055	41.899	41.52	41.52
Length Y (mm)	70.749	50.055	41.899	41.52	41.52
Length Z (mm)	250	250	250	250	250
Volume (mm <sup>3</sup> )	4.908e + 005	1.4726e + 005	6207.7	3.3849e + 005	3.3849e + 005
Mass (kg)	0.1277	0.16787	2.1727e-003	0.76499	0.84115
Centroid X (mm)	-2.0596e-0.15	-2.71e--0.16	-1.0658e-003	4.0609e-0.16	4.0609e-0.16
Centroid Y (mm)	-2.8907e-016	-1.1555e-0.15	1.26e-014	7.8598e-017	7.8598e-017
Centroid Z (mm)	125	125	125	125	125
Moment of inertia IP1 (kg-mm <sup>2</sup> )	721.47	914.17	11.727	4045.7	4448.5
Moment of inertia IP2(kg-mm <sup>2</sup> )	721.47	914.17	11.727	4045.7	4448.5
Moment of inertia IP3(kg-mm <sup>2</sup> )	118.75	88.511	0.93542	163.18	179.43



**Fig. 2** ANSYS model under loading with 100 and 400 N

**Table 4** Details of mechanical loading

Object name	Fixed support	Force
State	Fully defined	
<i>Scope</i>		
Scoping method	Geometry selection	
Geometry	4 Faces	1 Face
<i>Definition</i>		
Type	Fixed support	Force
Suppressed	No	
Define by		Vector
Magnitude		100 N (ramped) and 400 N (ramped)
Direction		Defined

**4.1.2 Thermal Loading (Convection Load)**

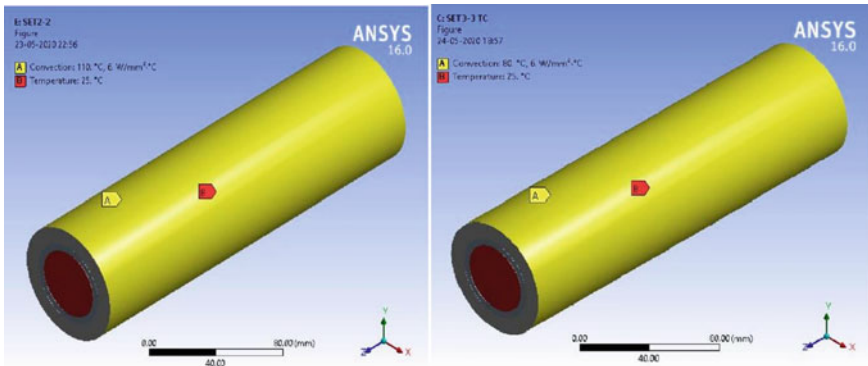
See Table 5.

Thermal Loads:

Component temperature: 22 °C, Surrounding temperature: 80 and 110 °C (Fig. 3).

**Table 5** Details of thermal loading

Steps	Times (s)	Convection coefficient (W/mm <sup>2</sup> °C)	Temperature ( °C)
	0	0	22
1	1	6	80
2	1	6	110



**Fig. 3** ANSYS model with 58 and 88 °C Temperature limits



### 4.1.3 Combination of Thermal and Mechanical Load

For this set the loading condition are combination of all the above.

- Mechanical load: 100 N  
Thermal load:  
Body temperature: 22 °C  
Surrounding temperature: 80 °C
- Mechanical load: 400 N  
Thermal load:  
Body temperature: 22 °C  
Surrounding temperature: 80 °C
- Mechanical load: 100 N  
Thermal load:  
Body temperature: 22 °C  
Surrounding temperature: 110 °C
- Mechanical load: 400 N  
Thermal load:  
Body temperature: 22 °C  
Surrounding temperature: 110 °C.

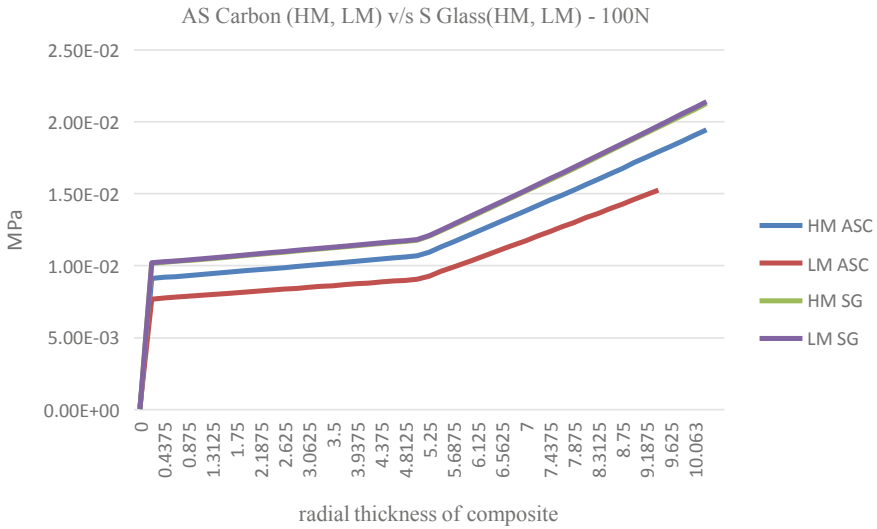
The above loading conditions are applied for both as carbon fiber and S Glass fiber with LM and HM coating.

## 4.2 Results and Discussion

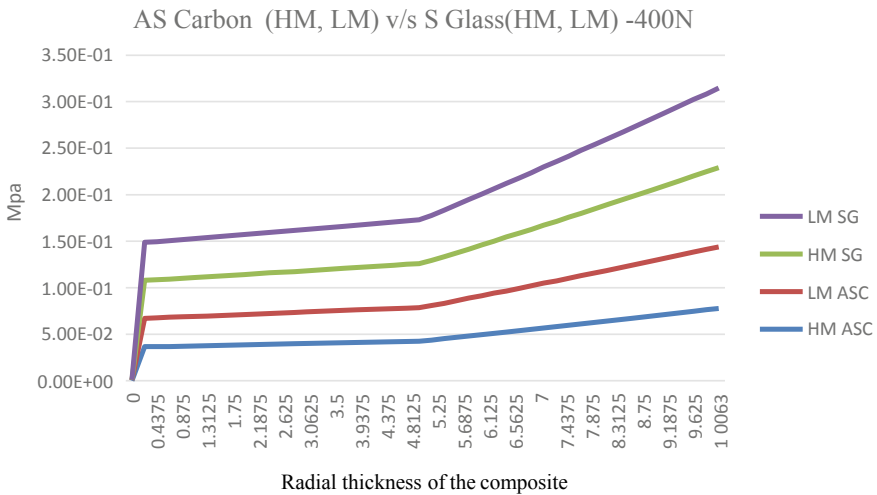
### 4.2.1 Radial Stress Variation in Composite

Figure 4 gives the information about the stress variation in composite when AS Carbon fiber and S Glass fiber are used with low and high modulus coatings. The x-axis gives the divisions of the composite thickness and y-axis represents stress values in MPa. As we can observe the stress in composite is more when S Glass is used as fiber. And when S Glass is used with low and high modulus coating the stress curve lie upon each other, i.e., the variation of the composite with low modulus coating and high modulus coating with S Glass as fiber is same. And with AS Carbon fiber the stress variation in composite seems to be equal graphically till 0.65625 mm but there is a variation in the numerical value and after certain thickness of the composite the stress variation increases gradually. But comparing AS Carbon fiber and S Glass the stress induced in composite is more when S Glass fiber is used.

Figure 5 shows the stress variation of a composite for 400 N varies from that of 100 N. The difference between the stress variation for both AS Carbon fiber and S Glass.



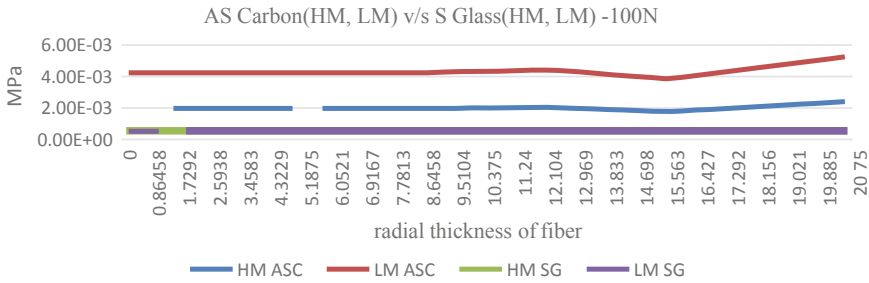
**Fig. 4** Stress variation of a composite with AS Carbon and S Glass as fiber for both LM and HM coating for 100 N loading



**Fig. 5** Stress variation of a composite with AS Carbon and S Glass as fiber for both LM and HM coating for 400 N loading

### 4.3 Radial Stress Variation in Fiber

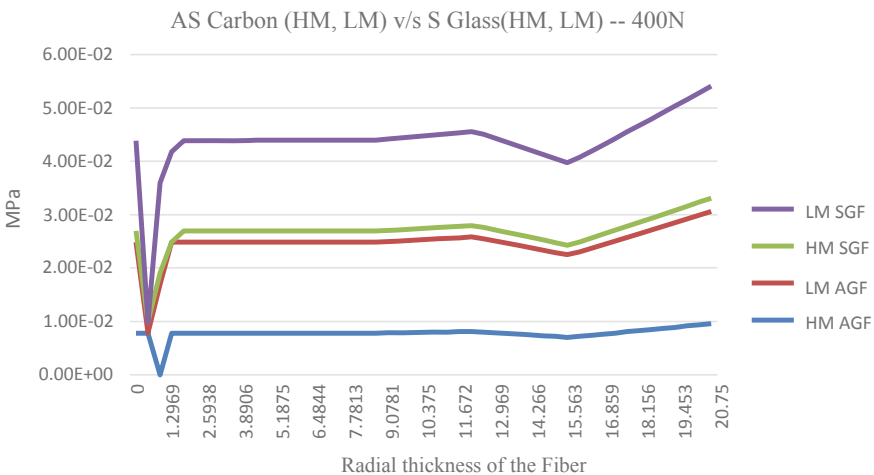
In Fig. 6, the *x*-axis gives the radial divisions of the fiber and *y*-axis gives the stress induced due to the mechanical loading conditions. The curve of a fiber is same for



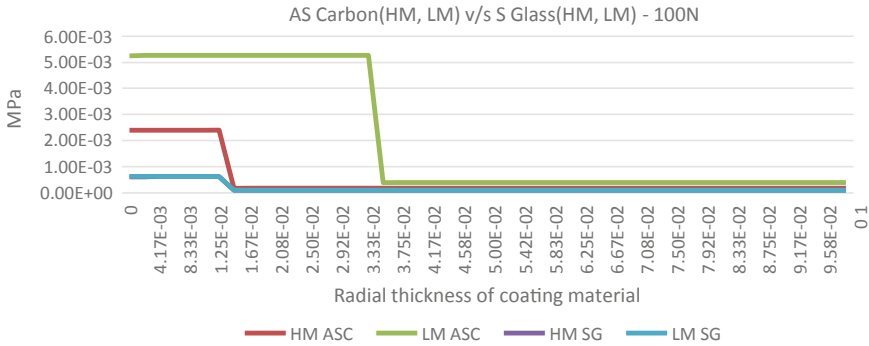
**Fig. 6** Radial stress variation of fiber with AS Carbon and S Glass for both LM and HM coating for 100 N loading

both low and high modulus coating when S Glass is used as a fiber. As we can observe the curve of low modulus and high modulus lie on each other. But the variation of stress in fiber is more in AS Carbon fiber. And the difference in stress variation in AS Carbon fiber is more between low and high modulus coating. The graph function for high modulus coating with AS Carbon fiber and low modulus coating with S Glass fiber shown discontinuous the material property at that location seems to turbulent. And amongst all the stress distribution the stress induced is high in low modulus coating of AS Carbon fiber.

The stress variation of fiber for higher load is shown in Fig. 7. From the center of the fiber the stress gradually decreases later on further the stress remains constant and then again, the stress decrease and increases. And the stress distribution values for low modulus coating with AS Carbon fiber and high modulus coating with S Glass are approximate near the center and then differs radially.



**Fig. 7** Radial stress variation of fiber with AS Carbon and S Glass for both LM and HM coating for 400 N loading



**Fig. 8** Stress variation of coating with AS Carbon and S Glass as fiber for both LM and HM coating for 100 N loading

### 4.4 Radial Stress Distribution for Coating

In Fig. 8 shows the stress distribution for a coating material. Though the thickness of the coating material very small which has a volume ratio of 0.01 to that of cross section of the composite, there is stress pattern for differing loading condition. The stress distribution for both the loading conditions are same in case of low and high modulus coating of S Glass throughout the length. But for AS Carbon fiber the stress distribution for both low and high modulus coating changes. For certain distance the stress distribution remains constant the decreases gradually and then remain constant throughout the remaining thickness in both loading condition. And from the graphical observation, the stress distribution for both loadings is for low modulus coating with AS Carbon fiber [6].

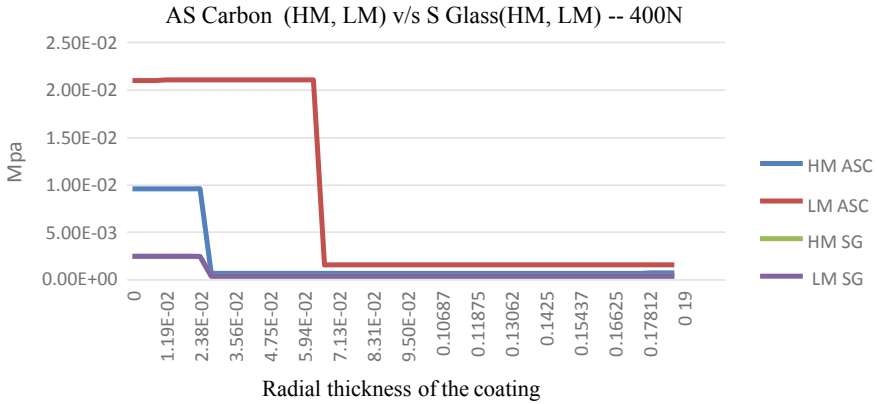
From Fig. 9, we can see that the stress distribution of high modulus coating with AS Carbon as a fiber gradually linear with all other materials and after certain thickness the stress values are almost equal to that of values of S Glass [7].

The graphical representation of the stress distribution of composite, fiber and coating for both the loading conditions of mechanical loading and combination of mechanical and thermal loadings.

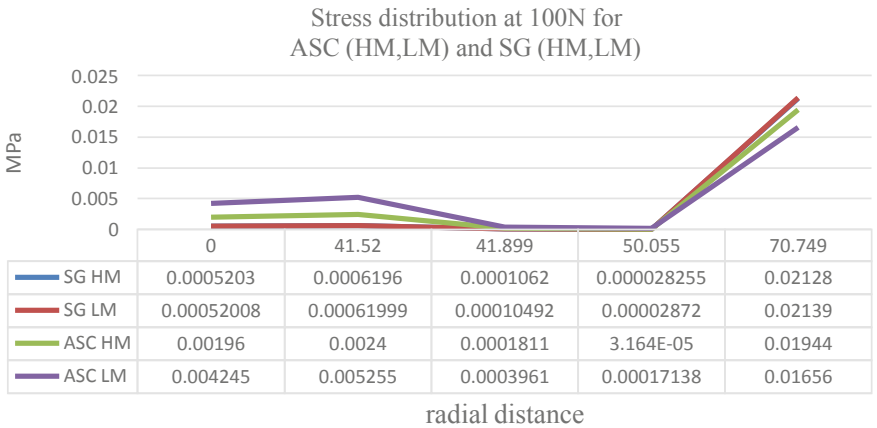
### 4.5 Radial Stress Distribution of the Four Phase Model

The stress distribution of a four phase model is shown in Fig. 10.

The stress along the radial direction is same for both S Glass fiber with low and high modulus, but for AS Carbon fiber the stress distribution from center of the fiber to coating is more for low modulus coating and stress distribution from coating to matrix is same for both low and high modulus coating. From matrix to composite the stress distribution is more for high modulus coating.



**Fig. 9** Stress variation of a composite with AS Carbon and S Glass as fiber for both LM and HM coating for 400 N loading



**Fig. 10** Stress distribution of four phase model with 100 N loading

Figure 11 gives the information of the stress distribution for four phase model with 400 N.

From the graph we can say that the stress value is same at a location till matrix. From the matrix the stress value increase in order of S Glass with low and high modulus and AS Carbon fiber with low modulus and high modulus.

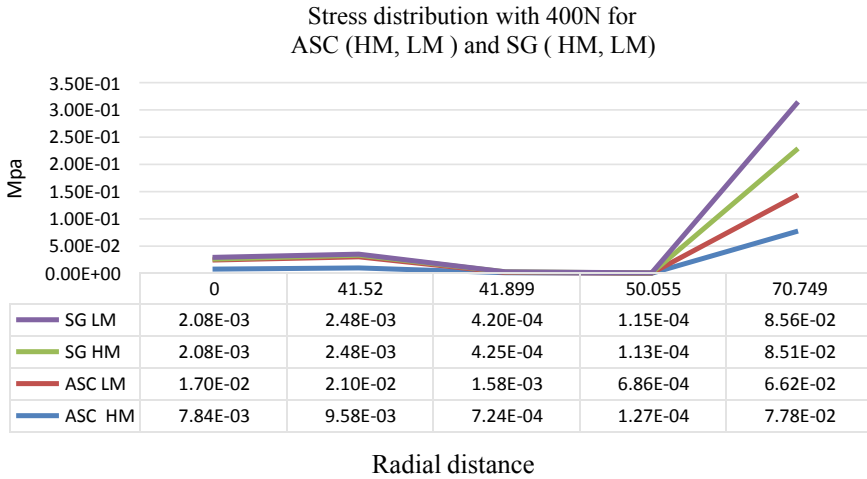


Fig. 11 Stress distribution of four phase model with 400 N loading

### 4.6 Hoop Stress Distribution of the Four Phase Model

Figure 12 shows the Hoop stress distribution of the four phase model at the interface between the layers for 100 N load.

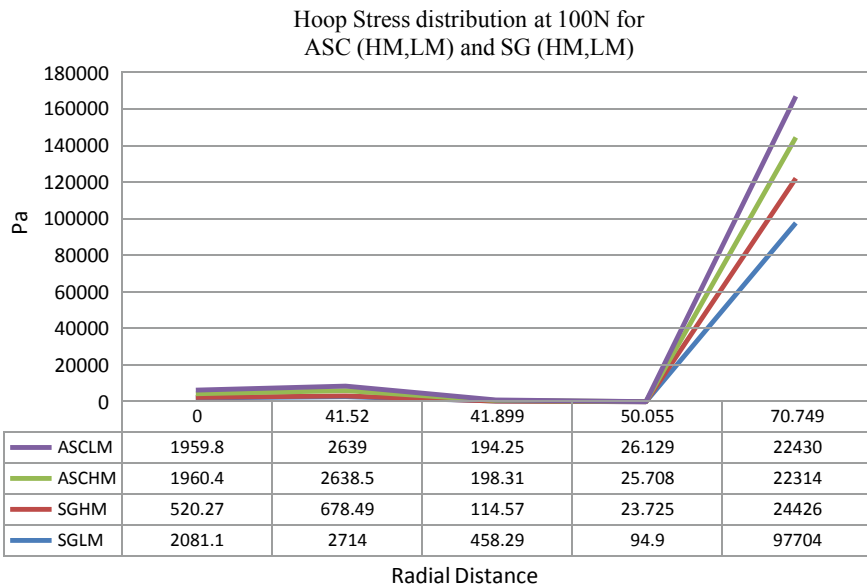
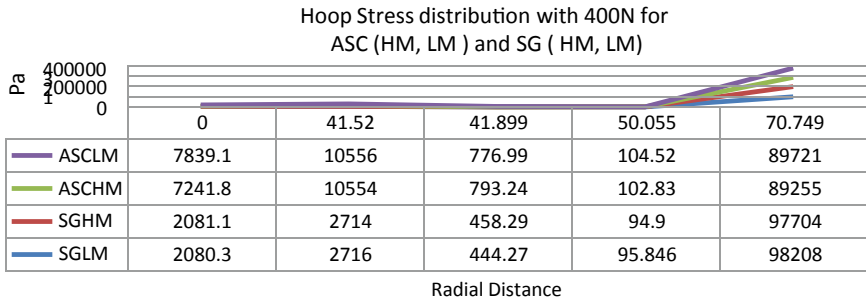


Fig. 12 Hoop stress distribution of four phase model with 100 N loading



**Fig. 13** Hoop stress distribution of four phase model with 400 N loading

Figure 13 gives the Hoop stress distribution of the four phase model at the interface between the layers with 400 N load.

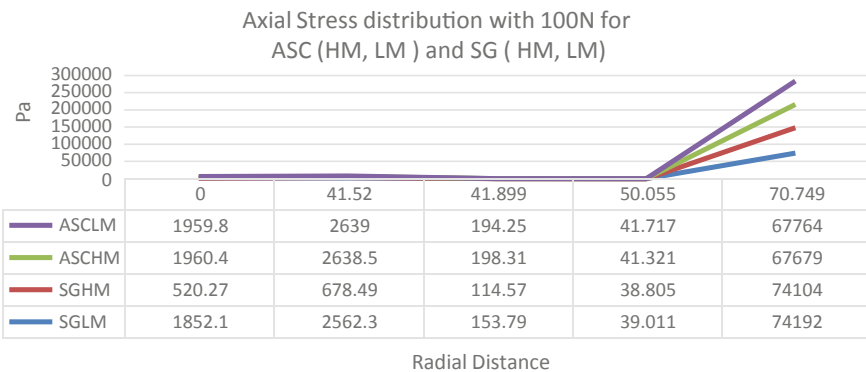
The stress level variation in the both loadings are similar. But with increase in the loadings the magnitude of the stress increases. And the stress distribution from fiber to matrix is less compare to the stress distribution in composite material.

### 4.7 Axial Stress Distribution of the Four Phase Model

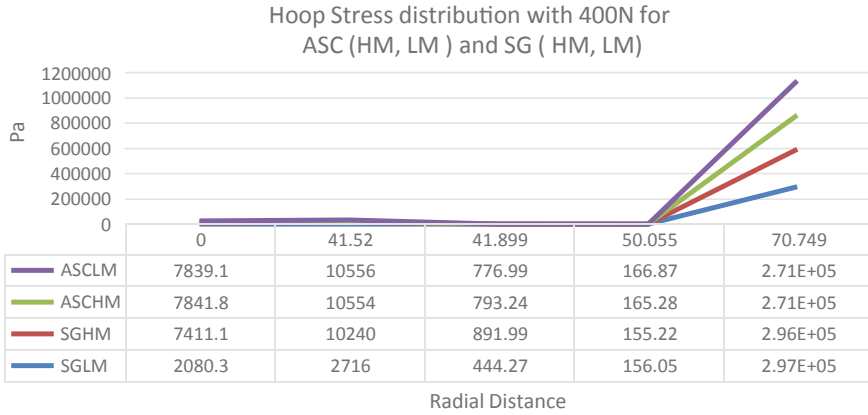
Figure 14 gives the Axial stress distribution of the four phase model at the interface between the layers for 100 N load.

Axial stress distribution of the four phase model at the interface between the layers for 400 N load (Fig. 15).

As the axial stress gives the stress about length wise the stress variation can be observed in length wise. Figure gives the similar stress variation for both 100 and



**Fig. 14** Axial stress distribution of four phase model with 100 N loading

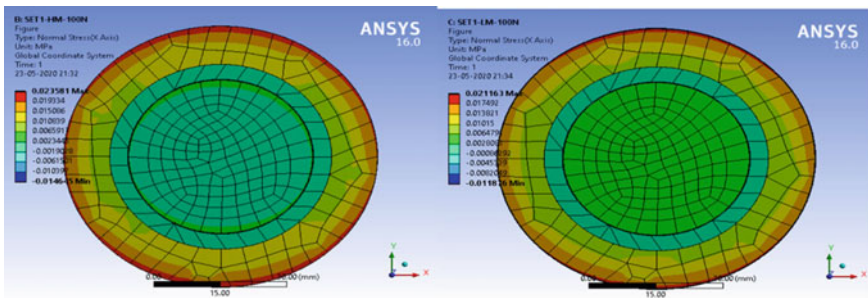


**Fig. 15** Axial stress distribution of four phase model with 400 N loading

400 N loads. Again the stress variation is small from fiber to matrix the major stress distribution is from matrix to composite.

### 4.8 Stress Variation in Four Phase Model with Combined Loading (Mechanical and Thermal Loadings)

See Figs. 16, 17, 18 and 19.



**Fig. 16** AS Carbon-HM and LM coating with 100 N load



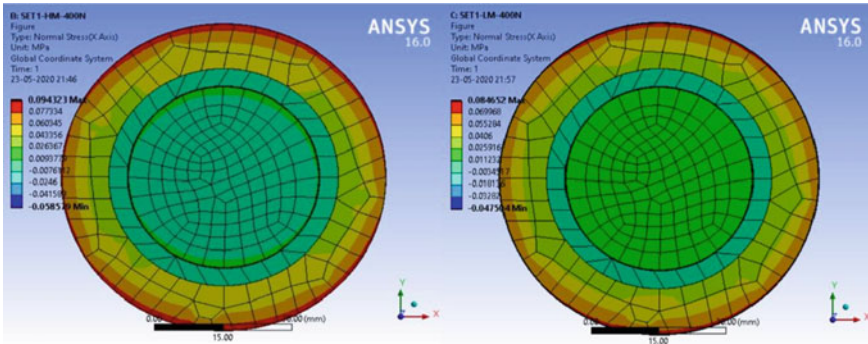


Fig. 17 AS Carbon-HM and LM coating with 400 N load

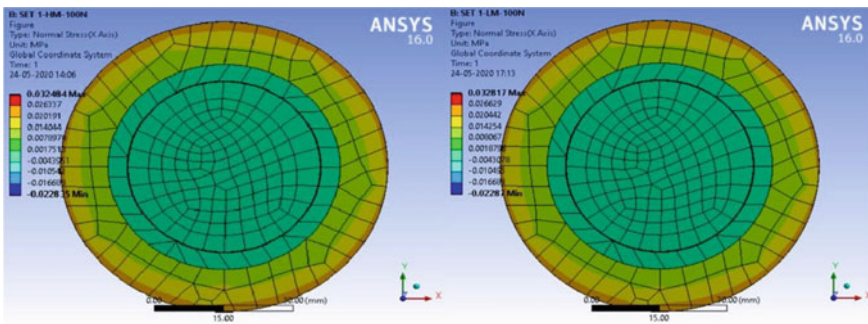


Fig. 18 S Glass-HM and LM coating with 100 N load

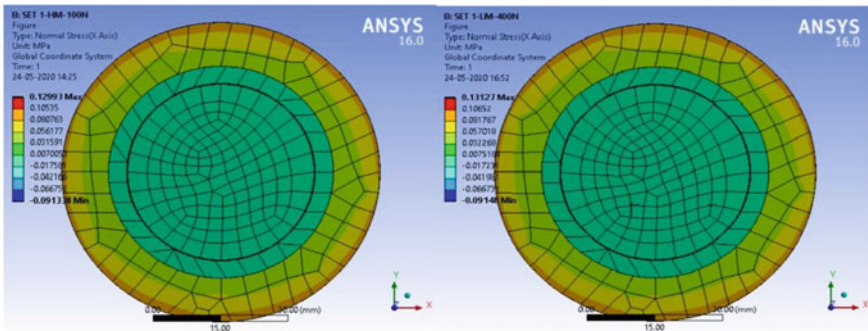


Fig. 19 S Glass-HM and LM coating with 400 N load

## 5 Conclusions

Analysis of thick fiber reinforced polymer matrix (FRP) composites under cylindrical composite assemblage model has been studied in the present work. It is concluded that

1. The Radial stress induced in fiber is more when AS Carbon fiber is used compare to S Glass for minimum loads. But the Radial stress in S Glass fiber is same in both coating condition, i.e., low modulus and high modulus coating. But when the load increases the stress variation of S Glass is more in high modulus and low modulus coating.
2. The Radial stress in composite is more when S Glass is used as fiber with both the loads. But the stress level variation for lower load in S Glass is almost same. In higher loads the stress level variation is more. For AS Carbon fiber the stress distribution is appreciable.
3. The Radial stress for coating for both low and high modulus is same, i.e., level of variation is same, for both loading for S Glass fiber. And for AS Carbon fiber the stress variation shows gap at the entry thickness of the coating later on for the further thickness of the coating the stress distribution is same for low and high modulus coating.
4. The difference between the stress levels developed in low and high coating results out to be significant.
5. From Table no. 01-04, the maximum Hoop stress and Axial stress are observed in matrix and fiber, respectively, for lower loads with high modulus ASC fiber and S Glass for both low and high modulus coating. But these stresses are maximum in composite when low modulus coating is used with AS carbon as a fiber.
6. From Table no. 05-08, the maximum Hoop stress is observed in the interface of fiber and coating with high and low modulus of AS Carbon fiber and high modulus of S Glass. The maximum Hoop stress for low modulus coating with S Glass as fiber is observed in fiber (S Glass itself). The maximum Axial stress is observed in HM coating with AS Carbon as coating. For others the Axial stress is maximum in fiber.
7. From Table 01-0.8, the minimum Hoop stress and Axial stress is observed in between the interface the fiber and coating for all the four phase models.
8. The stress distribution in composite for both 100 and 400 N is more when S Glass is used as a fiber. For minimum loads the stress distribution in composite with S Glass as fiber are same for low and high modulus coating the stress level varies with increase in the load.
9. The stress distribution from intermittent distance of coating to radial thickness of the matrix is same for all the loads and fibers.
10. The stress induced S Glass is more compare to AS Carbon fiber. And the stress value is same for both low and high modulus coating at small loads. And the stress levels develop and varies in increase order of the loads. For AS Carbon fiber the variation of stress with respect to loads.

11. The Hoop stress and Axial stress variation in the four phase model are more in composite layer. The stress variation is lesser in the layer from fiber to matrix for all the coating the condition and for both fibers say., AS Carbon fiber and S Glass fiber.
12. The stress level variation of Hoop stress and Axial stress is same for both the loadings. i.e., the magnitude with 100 and 400 N. The magnitude of the stress increases with increase in the load in the four phase fiber.

## References

1. Upadhyay PC, Guru Murthy K, Lyons DW (1996) Stress field in coated continuous Fiber reinforced polymeric composite due to hygrothermal loading. *J Reinf Plast Compos* 15
2. Ibrahim A, Ryu Y, Saidpour M (2015) Stress analysis of thin walled pressure vessels 5
3. Mali MA, Bhosale MH, Bedi MD, Modasara MA (2014) A review paper on study of pressure vessel, design and analysis. *IRJET* 4
4. Babu KN, Naresh H, Gupta GS (2018) Design and analysis of bolted joint for rocket motor casing. *Mater Today Proc* 5
5. Srinivasa Gupta G, Kiran Kumar N, Ajay Kumar K (2018) Micro stress evaluation and analysis in FRP composites for rocket motor casing. *Mater Today Proc* 5
6. Adams DF, Berglund LA (1987) A micromechanics analysis of the influence of polymer matrix composites. *J Reinf Plast Compos* 6
7. Miller AK, Adams DF (1978) Inelastic micromechanical analysis of graphite/epoxy composites subjected to hygrothermal cycling. In: *Advanced composite materials environmental effects*, ASTM STP 658

# A Review on Carbon Reinforcements in Glass Fiber Polymer Matrix Composites



N. Kiran Kumar, B. Chandra Kiran, B. Chennakesava Rao,  
and M. Manzoor Hussain

**Abstract** Hybrid reinforced composites are contrived to meet mechanical, thermal, and damping properties in contrast to the composites reinforced with single fiber. Composites which are made from polymer matrix with glass fiber alone cannot contribute to the desired properties. In this review paper, it is discussed about how carbon constituents in the form of fiber, particle or fillers when added into glass fiber composite can increase a lot of useful mechanical properties. During loading conditions like fatigue loading, carbon reinforced composites perform better when compared to glass fiber composites due to low-stress generation in carbon fiber composites. Carbon fillers increase damping characteristics. This paper mainly focuses on general fabrication methods, methodology and analysis of these hybrid reinforced composites of carbon when added to glass fiber composites to achieve better loading stability. Also, this paper focuses on the applications and future scope of work of these types of composites depending upon the properties exhibited when carbon reinforcements are added.

**Keywords** Hybrid reinforced composites · Glass fiber · Fiber reinforcement · Particle reinforcement · Fillers · Damping · Mechanical properties

## 1 Introduction

Hybrid fiber reinforced composites serves the purpose of mechanical properties such as strength, toughness, stiffness, elasticity, plasticity, ductility, brittleness and hardness ensuring these composites are light in weight but show user desired properties. These reinforced composites contain two or more materials with different properties

---

N. Kiran Kumar (✉) · B. C. Kiran · B. C. Rao  
Department of Mechanical Engineering, VNR Vignana Jyothi Institute of Engineering and  
Technology, Hyderabad, India  
e-mail: [kirankumar\\_n@vnrvjiet.in](mailto:kirankumar_n@vnrvjiet.in)

M. M. Hussain  
Department of Mechanical Engineering, Jawaharlal Nehru Technological University Hyderabad,  
Hyderabad, India

which make them transfer the stress more effectively because of the fiber matrix interfacial area. There are two constituents called phases in these hybrid composites which are discontinuous and continuous phases. The discontinuous phases are hybrid reinforcements which are harder and stronger. Continuous phases are the matrix which is further divided into the metallic, polymeric and ceramic matrix.

These fibers can bear and tolerate higher loads when compared to single fiber reinforcements. The load bearing capacity varies in different directions depending upon on the arrangement of reinforcement and matrix of the composite [1]. The uniqueness of metallic matrix type is that it has the ability to undergo plastic deformation with the thermal stresses. Ceramic materials in general are very famous for their properties. These material's strength and stiffness are considerably high at great temperatures, do not react with chemicals easily, low density, and many more. Matrix micro cracking is a significant feature in CMCs. Their ratio of modulus of fiber to the modulus of fiber determines the micro cracking.

### ***1.1 Properties of PMC's***

Polymer matrix composites (PMC) are built such that the reinforcement in the composite supports the load carrying capacity. The relative weak matrix helps in bonding fibers together and also helps in transferring loads between fibers. PMCs are further divided into reinforced plastics and advanced composites. Reinforced plastics are made of polyester resin and glass fiber which have low stiffness (E-glass), whereas advanced composites are made of matrix and fiber composition. The properties of PMCs are given below:

- High stiffness.
- High strength.
- Light weight.
- Superior corrosion resistance and fatigue resistance due to high matrix decomposition temperature.
- Depends upon matrix, reinforcement and interface proportion and geometry.
- When stressed along the direction of fibers, PMCs are stronger and when stressed in perpendicular direction, PMCs are weaker.
- Mechanical properties are highly interdependent.
- During impacts, strength of PMC is reduced.
- Compressive and shear proportions are strong.

Poor wear resistance in glass fiber reinforced PMCs are due to brittle nature of reinforced fibers which increases friction [2, 3]. There is an increment in the mechanical properties when a carbon constituent as a fiber when added to glass fiber reinforced polymeric composites [4, 5]. Carbon reinforcement as a filler also improves the mechanical and damping characteristics for a hybrid composite. Carbon constituent as particles acting as reinforcement significantly improves mechanical properties depending upon the particle size.

## 2 Reinforcement as Fiber

Developing composite materials will improve performance of the composite depending upon the reinforcement of various fibers in a single polymer matrix. These are the advanced materials called hybrid composites. Hybrid composites have a huge diversity of material properties. These hybrid materials can replace many applications in our daily life. Prosthetics that are being used in our daily life, are made of polyethylene (PE) and polypropylene (PP) [6–9]. Hybrid glass fiber-carbon fiber polymer matrix composite can serve better properties when compared to PP and PE. Prosthetics used in foot amputations are stable and they meet the purposes to replace a limb [10–13].

### 2.1 Fabrication Process

For this process, the hybrid glass fiber-carbon fiber PMC is fabricated by the process lamination. In this process, 8 layers are kept one over the other and we pull out the PVA which is present outside ensuring that the relatively smaller end is placed on the value area [14]. This process is conducted in a vacuum. This helps in developing a strong interface [15, 16]. For studying the values under tensile loading, this experiment was conducted using Universal Testing Machine.

### 2.2 Methodology and Analysis

Taking five specimens for each component of PP, PE, and Gf-Cf matrix composite subjected to mechanical loading, the tensile strengths are measured. The mechanical properties under tensile loading are shown in Table 1. Hybrid Gf-Cf polymer matrix composite showed an increment in the yield strength, ultimate tensile strengths, and modulus of elasticity has increased more than 250% when compared to polypropylene and polyethylene. From the stress values obtained for each material, we observe that hybrid glass fiber-carbon fiber polymer matrix composite can withstand higher tensile loads [17–21].

The flexibility of the material is also an important property for any composite. Fiber-reinforced matrixes are more prominent than the other composite materials as

**Table 1** Mechanical properties under tensile loading [6]

Material	$\sigma_b$ (MPa)	$\sigma_{ult}$ (MPa)	$E$ (GPa)
Polypropylene	16	24	0.602
Polyethylene	21	32.5	0.875
Gf-Cf	56.6	112.8	2.314

**Table 2** Mechanical properties under tensile loading for the hybrid case [6]

Material	$\sigma_b$ (MPa)	$\sigma_{\text{Flexural}}$ (MPa)
Polypropylene	50.65	1.7
Polyethylene	51.8	2.33
Gf-Cf	103.1	4.15

these fibers show relatively high strength and stiffness in their fibrous forms. Boron, Carbon, Alumina, Silicon, and carbide are used as reinforced matrices. As fibers are used for high performances, the following conditions provide optimistic results for a composite.

- Small diameter w.r.t the grain size (size effect)
- High aspect ratio ( $L/D$  ratio)
- High degree of flexibility.

Flexibility is a function of stiffness. The inverse of flexural rigidity is the flexibility of the matrix. This can be given by the equation given below. Flexibility depends only upon shape and diameter of the object.

$$Mr = EI = E \frac{\pi d^4}{64} \quad (1)$$

This determines that if the modulus of stiffness is low it means that the fiber has high flexibility. For the flexural tests, we use a 3-point bending test machine for the experiment. The major areas where we concentrate during the flexural analysis is the bending stress and flexural modulus [22, 23]. Table 2 mentioned shows that they requires a large magnitude of bending stress due to the inclusion of laminated layers which caused fewer magnitudes of deflections with an increase in applied load. This change in the mechanical properties due to the hybrid glass fiber and carbon fiber will make the failure aspects of the prosthetics low when compared to the plastics [24].

### 3 Reinforcement as Particle

Carbon material as a particle reinforcement has attained an influencing position in showing a better property which is added during the process of composite fabrication. Carbon constituent in the particles of SiC significantly increases the strength and properties like modulus and wear resistance of a polymer matrix composite. Better mechanical strength with easy accessibility and viability are important requirements for the polymer to consider as matrix. The SiC particles have good wettability with the polymer matrix. Energy dispersive spectroscopy was used for analyzing the presence of SiC particles in hybrid PMC [25–29].

### 3.1 Fabrication Process

The fabrication method that is used in order to make this hybrid composite consisting of carbon particles as reinforcement is a hand lay-up method. Araldite resin and hardener mixed in a certain ratio were used for polymer matrix. Araldite resin and hardener provide good resistance to static loads as well as dynamic loads [30]. Normal polymer matrix composites basically have these resins as reinforcement. SiC particles are an additional reinforcement that is added in different weights and sizes to form into hybrid polymer matrix composite. In this process, the SiC particles are mixed into the matrix by stirring.

### 3.2 Methodology and Analysis

When seen under the scanning electron microscope (SEM), the images clearly show that SiC particles have reduced the gap to a large extent between the matrix and reinforcement when cut in transverse in the direction of the fiber. This decrease in the interparticle distance will increase the bond strength which ultimately increases the overall strength of hybrid polymer matrix composite. This property also improves the resistance to failure and fracture as well.

When subjected to mechanical loadings, tensile, flexural, and compressive strengths are studied for the hybrid polymer matrix composite consisting of carbon particles as a reinforcement with normal PMCs, hybrid composite shows better mechanical properties. These are tested by using UTE 40 for tensile strength and a 3-point bending test machine for flexural analysis. The strength of composites was tested in composite with absence of SiC and composites having SiC as reinforcement. The results for the tensile tests depict that there was an increase in strength by 25% with an increase in weight fraction. On the other hand, the strength decreased to 18% when the particle size of SiC is increased. Fiber volume fraction ( $v_f$ ) plays a decisive role in the mechanical strength of a polymer matrix composite and calculated from the density of the matrix ( $\rho_m$ ), the density of fiber ( $\rho_f$ ), the weight fraction of fiber and weight fraction of matrix are represented as ( $w_f$ ) and ( $w_m$ ), respectively.

$$v_f = \frac{(\rho_m \times w_f)}{(\rho_m \times w_f) + (\rho_f \times w_m)} \quad (2)$$

The influence of the factors such as weight fraction and size in the particles of SiC in composite results in the mechanical properties of the composite material. From the study conducted by Parvesh et al. [27], on the composites containing SiC and no SiC it was found that the main aspects which influence the effect of strength are interparticle gap and interfacial area.

These two factors further depend upon size and volume fractions of the reinforced particles [31–33]. The small size of the particles reinforced enables to increase the



interfacial area. This is because a higher number of smaller particles of SiC can accommodate in the area available. This results in an increase in the interfacial area. As a result of this, the interparticle distance decreases which lead to the improvement of the bond strength between the matrix and reinforcement that helps in resistance against loading. The particles with a higher size of the particles lead to failure in the composite as these particles have only less space to occupy the region in the interfacial area. This explains to us that higher size particle reinforcements show less resistance and cavities leading to fractures when stresses are generated in the hybrid polymer matrix reinforced composite.

Besides the decrease in the size of particles increases the strength, the decrease in the weight ratio leads to debonding in the matrix. This is because the interfacial area in the hybrid reinforced composite is not occupied by particles properly and increase in the interparticle distance is also another factor. This addition of low weight fraction decreases the strength which leads to low resistance and causes cracks [32, 34]. The decrease in the strength can also occur in the process of curing where internal stresses that are generated cause micro-cracks.

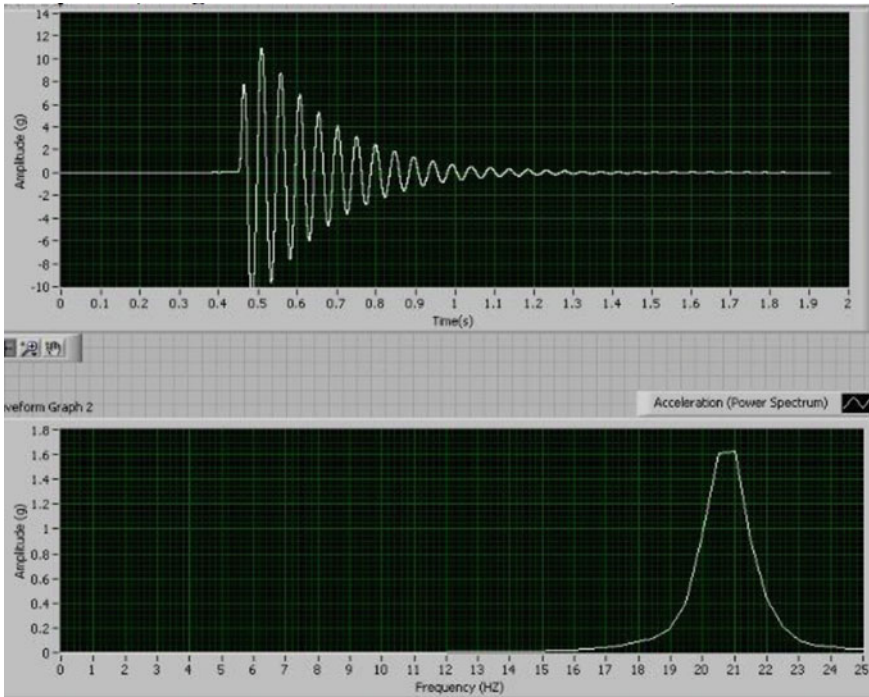
## **4 Reinforcement as Filler**

### ***4.1 Fabrication Process***

The process used in the fabrication of this composite is vacuum bag molding. Different volume fractions of carbon particles and glass–epoxy material are mixed. Stirring is done manually. Mixed particles are poured into the mold and the bag is evacuated. This helps pressure eliminating voids and allows air and resin from the mold [35, 36]. The laminate is heated for an hour with 100 °C temperature for complete curing. Parvesh Antil et al., tested for different amounts of specimens those consisting of the mentioned materials and made sure that for the same dimensions of all the study specimens the increase in carbon percentage is maintained [30].

### ***4.2 Methodology and Analysis***

The material's properties are then studied from the software. It precisely portrays that with an increase in the carbon fillers the composite shows better damping properties. The graphs shown in Fig. 1 represents the behavior of the composite under the vibration analysis. When compared to the composites that are made of only volume fractions of matrix and fiber content with the matrix that containing volume fractions of both fiber and matrix along with volume fractions of carbon, the composite that is containing carbon fillers as reinforcement decrease the vibrations that are generated within the composite.



**Fig. 1** Amplitude versus frequency analysis [38]

The graphs were plotted between amplitude and frequency. The graph that shows a higher amplitude represents the composite without carbon content. This absence of carbon reinforcement led to higher amplitudes during vibrations. When carbon filler reinforcement of 5% is added to the same composite and for the same vibration analysis, the amplitude has a change when compared to the previous readings. The amplitude of vibration decreased in this case. Increasing the volume fraction of carbon filler for the composite has also brought down the amplitude when compared to the carbon filler added 5%. This shows depicts that the increase in the carbon content in the form of filler as a reinforcement increases the damping characteristics which helps the composite to withstand vibrations generated [37, 38]. This carbon content increases the bond strength in the hybrid polymer matrix composite. This makes the hybrid polymer matrix composite to withstand higher vibrations.

### 4.3 Damping Characteristics

One of the important features for the composites that are made is to show good damping characteristics. If the damping characteristics are good for a hybrid

composite, it automatically reduces the vibrations that are generated in the composite. Vibrations are undesirable for material because higher vibrations in a material disturb the orientation and the structure of a composite. This leads to less resistance capacity and ultimately leads to the failure of the composite.

The reduction of the oscillations that are generated due to sudden and abnormal stresses due to different types of loading such as impact load is called damping. The properties which help in reducing the oscillations which are leading to cause vibrations are known as damping properties. This property depends upon the proportion of fiber and reinforcement and also the orientation of reinforcement in axial loading. Aramid is a good example that shows good damping characteristics.

The defects in the composite such as dislocations, phase boundaries, grain boundaries also determine the damping properties for a hybrid composite. In addition to these features which determine damping characteristics, viscoelastic behavior also plays an important role in improving the damping characteristics. Rubber is a commonly used material for vibration damping but rubber itself cannot contribute all the user desired properties. Since rubber has high flexibility, it has a low modulus of stiffness as shown in fiber reinforcement. The interface in the composite plays an important role between the matrix and reinforcement by increasing the stiffness and also damping characteristics for a hybrid composite [39–41]. Viscoelastic materials like rubber are used in applications where there are low oscillations taking place such as sound transmission. But for bigger applications like bearings in automobiles, these are made with conventional metals like cast iron, gun metal, etc.

Polymer matrix composites with carbon reinforcement as the filler have the ability to show better damping characteristics and also shows a better reduction of dynamic loading during high-speed processes when compared to conventional metals. Fillers make the composite less costly and at the same time, they reach the criteria of being showing good mechanical and user desired properties throughout the hybrid polymer matrix composite. In recent times, the use of inorganic fillers in hybrid polymer matrix composites has increased. These fillers also improve the friction and wear resistance properties of the composite. P. S. Senthil et al., has conducted an experiment in which carbon fillers are added to glass and carbon epoxy polymer composite and observed the behavior and properties of the composite [39].

## 5 Applications and Future Scope

For exhibiting great mechanical properties, these hybrid carbon reinforced composites are used in many applications and also can replace many existing polymers. The blades of wind turbines that generate wind energy are made of hybrid glass fiber reinforced with carbon fiber.

FRP is always best material for constructing bridges due to their impeccable mechanical properties in longitudinal directions. Conventional steels show sag effect at a point under load applications. Orthotics and prosthetics field has started using the hybrid polymer matrix composites to retain stability and maintain support. In the

aerospace industry, most components are made to increase applications of hybrid composites to withstand stresses and to offer safety of material [42].

Hybrid carbon fiber-synthetic fiber are replacing highly expensive Kevlar synthetic fiber in aircraft parts [43]. These can also be used as furniture, storage devices like cans, electrical appliances, suitcases etc. One of the future research areas in HFRP is studying the behavior of Hybrid glass fiber and carbon constituent reinforced composites. Beam members especially in constructions like bridges are expected to resist bending moments, hogging moments particularly when external loads like heavy winds and earthquakes. Thus, research on Hybrid glass fiber and carbon constituent reinforced composites subjected to cyclic loadings are required.

## 6 Concluding Remarks

- Hybrid glass fiber reinforced with carbon constituents are made in order to increase the mechanical properties and life of a composite to replace existing plastics.
- Hybrid glass fiber reinforced with carbon fiber shows better mechanical properties when compared with polypropylene and polyethylene which are used in making of prosthetics.
- Addition of SiC particles into the fiber matrix as a reinforcement increase the bond strength of the composite depending upon the size of the particles.
- Carbon fillers increases the damping property of the composite which ultimately reduces the vibrations that are generated and internal stresses within the composite.
- Hybrid glass fiber reinforced with carbon constituents are used in many applications like prosthetics, furniture, electrical appliances, etc.

## References

1. Nguyen H, Zatar W, Mutsuyoshi H (2017) Mechanical properties of hybrid polymer composite. *Hybrid Polym Compos Mater*, pp 83–113
2. Burks B, Middleton J, Kumosa M (2012) Micromechanics modeling of fatigue failure mechanisms in a hybrid polymer matrix composite. *Compos Sci Technol* 72(15):1863–1869
3. Poyyathappan K, Bhaskar GB, Pazhanivel K, Venkatesan N (2014) Tensile and flexural studies on glass-carbon hybrid composites subjected to low frequency cyclic loading. *Int J Eng Technol* 6(1):83–90
4. Fu S-Y, Lauke B (1998) Characterization of tensile behaviour of hybrid short glass fibre/calcite particle/ABS composites. *Compos A Appl Sci Manuf* 29(5–6):575–583
5. Daniyan IA, Mpofu K, Adeodu AO, Adesina O (2020) Development of carbon fibre reinforced polymer matrix composites and optimization of the process parameters for railcar applications. *Mater Today Proc*
6. Hussain HS, Takhakh AM (2017) Mechanical properties of hybrid and polymer matrix composites that used to manufacture partial foot prosthetic. *Al-Nahrain J Eng Sci* 20(4):887–893

7. Berry DA (1987) Composite-materials for orthotics and prosthetics. *Orthot Prosthet* 40(4):35–43
8. Thirumalai DP, Madsen B, Toftegaard HL, Markussen CM (2012) Flexural properties of hybrid natural composite-micromechanics and experimental assessment. In: 3rd Asian conference on mechanics of functional materials and structures (ACMFMS 2012). Indian Institute of Technology, pp 469–472
9. Wooley DP (1987) Dear Sir, Re: Angliss VE, “Holte revisited—a review of the quality of prosthetic treatment” *Prosthetics and Orthotics International*, Vol 10, No 1, April 1986 The Australian Orthotic Prosthetic Association whilst agreeing in principle to the thrust and recommendations of the article, consider that some inaccuracies need to be addressed. *Prosthet Orthot Int* 11:46–47
10. Jweeg MJ, Hasan SS, Chiad JS (2009) Effects of lamination layers on the mechanical properties for above knee prosthetic socket. *Eng Tech J* 27(4)
11. Varga C, Miskolczi N, Bartha L, Lipóczy G (2010) Improving the mechanical properties of glass-fibre-reinforced polyester composites by modification of fibre surface. *Mater Des* 31(1):185–193
12. Wichmann MH, Sumfleth J, Gojny FH, Quaresimin M, Fiedler B, Schulte K (2006) Glass-fibre-reinforced composites with enhanced mechanical and electrical properties—benefits and limitations of a nanoparticle modified matrix. *Eng Fract Mech* 73(16):2346–2359
13. Chen CH, Cheng S (1967) Mechanical properties of fiber reinforced composites. *J Compos Mater* 1(1):30–41
14. Hasan SS, Chiad JS (2009) Effects of lamination layers on the mechanical properties for above knee prosthetic socket. *Eng Technol J* 27(4)
15. Maier C, Calafut T (1998) *Polypropylene: the definitive user’s guide and databook*. William Andrew
16. Dong C, Ranaweera-Jayawardena HA, Davies IJ (2012) Flexural properties of hybrid composites reinforced by S-2 glass and T700S carbon fibres. *Compos B Eng* 43(2):573–581
17. Sathishkumar TP, Naveen J, Satheshkumar S (2014) Hybrid fiber reinforced polymer composites—a review. *J Reinf Plast Compos* 33(5):454–471
18. Rakesh PK, Singh I, Kumar D (2012) Compressive behavior of glass fiber reinforced plastic laminates with drilled hole. In: *Advanced materials research*, vol 410. Trans Tech Publications Ltd, pp 349–352
19. Burks B, Armentrout D, Kumosa M (2011) Characterization of the fatigue properties of a hybrid composite utilized in high voltage electric transmission. *Compos A Appl Sci Manuf* 42(9):1138–1147
20. Tanimoto T, Amijima S (1975) Progressive nature of fatigue damage of glass fiber reinforced plastics. *J Compos Mater* 9(4):380–390
21. Zhang Y, Xia Z, Ellyin F (2005) Nonlinear viscoelastic micromechanical analysis of fibre-reinforced polymer laminates with damage evolution. *Int J Solids Struct* 42(2):591–604
22. Dinesh T, Kadirvel A, Vincent A (2019) Effect of silane modified E-glass fibre/iron (III) oxide reinforcements on UP blended epoxy resin hybrid composite. *Silicon* 11(5):2487–2498
23. Amuthakkannan P, Manikandan V, Winowlin Jappes JT, Uthayakumar M (2013) Effect of fibre length and fibre content on mechanical properties of short basalt fibre reinforced polymer matrix composites. *Mater Phys Mech* 16(2):107–117
24. Arpitha GR, Sanjay MR, Yogesha B (2014) Review on comparative evaluation of fiber reinforced polymer matrix composites. *Carbon* 4000:30
25. Ghoneim AM, Mahani RM (2001) Electrical and mechanical properties of some composites with polymeric matrix. *Int J Polym Mater* 50(2):141–161
26. Shin S-G (2001) Retracted article: self-diagnosis of GFRP composites containing carbon powder and fiber as electrically conductive phases. *Met Mater Int* 7(6):605–611
27. Antil P, Singh S, Manna A (2018) SiC p/glass fibers reinforced epoxy composites: wear and erosion behavior
28. Finot M, Shen YL, Needleman A, Suresh S (1994) Micromechanical modeling of reinforcement fracture in particle-reinforced metal-matrix composites. *Metall Mater Trans A* 25(11):2403–2420

29. Barre S, Chotard T, Benzeggagh ML (1996) Comparative study of strain rate effects on mechanical properties of glass fibre-reinforced thermoset matrix composite. *Compos A Appl Sci Manuf* 27(12):1169–1181
30. Antil P, Singh S, Singh M (2019) Hybrid glass fiber reinforced polymer matrix composites: mechanical strength characterization and life assessment. In: *Reinforced polymer composites: processing, characterization and post life cycle assessment*
31. Felipe RCTS, Felipe RN, Batista AC, Aquino EM (2017) Polymer composites reinforced with hybrid fiber fabrics. *Mater Res* 20(2):555–567
32. Shahzad A (2019) Investigation into fatigue strength of natural/synthetic fiber-based composite materials. In: *Mechanical and physical testing of biocomposites, fibre-reinforced composites and hybrid composites*. Woodhead Publishing, pp 215–239
33. Huh Y-H, Lee J-H, Kim D-J, Lee Y-S (2012) Effect of stress ratio on fatigue life of GFRP composites for WT blade. *J Mech Sci Technol* 26(7):2117–2120
34. Deepa KS, Sebastian MT, James J (2007) Effect of interparticle distance and interfacial area on the properties of insulator-conductor composites. *Appl Phys Lett* 91(20):202904
35. Yadav BP (2008) Vibration damping using four-layer sandwich. *J Sound Vib* 317(3–5):576–590
36. Martinez-Agirre M, Elejabarrieta MJ (2011) Dynamic characterization of high damping viscoelastic materials from vibration test data. *J Sound Vib* 330(16):3930–3943
37. Sarlin E, Liu Y, Vippola M, Zogg M, Ermanni P, Vuorinen J, Lepistö T (2012) Vibration damping properties of steel/rubber/composite hybrid structures. *Compos Struct* 94(11):3327–3335
38. Senthil Kumar PS, Karthik K, Raja T (2015) Vibration damping characteristics of hybrid polymer matrix composite. *Int J Mech Mech Eng IJMME-IJENS* 15(1)
39. Gupta N, Brar BS, Woldesenbet E (2001) Effect of filler addition on the compressive and impact properties of glass fibre reinforced epoxy. *Bull Mater Sci* 24(2):219–23
40. Yuvaraja M, Senthilkumar M (2013) Comparative study on vibration characteristics of a flexible GFRP composite beam using SMA and PZT actuators. *Procedia Eng* 64:571–581
41. Khan SU, Li CY, Siddiqui NA, Kim JK (2011) Vibration damping characteristics of carbon fiber-reinforced composites containing multi-walled carbon nanotubes. *Compos Sci Technol* 71(12):1486–1494
42. Razali N, Sultan MT, Jawaid M (2019) Impact damage analysis of hybrid composite materials. In: *Durability and life prediction in biocomposites, fibre-reinforced composites and hybrid composites*. Woodhead Publishing, pp 121–132
43. Lau D (2013) Hybrid fiber-reinforced polymer (FRP) composites for structural applications. In: *Developments in fiber-reinforced polymer (FRP) composites for civil engineering*. Woodhead Publishing, pp 205–225

# Influences of Functionalized Multiwalled Carbon Nanotube on the Tensile and Flexural Properties of Okra Cellulose Nanofibers/Epoxy Nanocomposites



Ajmeera Ramesh, N. V. Srinivasulu, and M. Indira Rani

**Abstract** In recent times, demand has been increasing for lightweight, high strength, high stiffed and eco-friendly composites in many engineering applications like aerospace, automobile, marine and medical applications. Polymer nanocomposites are best suitable for making of lightweight, high strength, stiffness and eco-friendly composites. Many engineers and researchers are working for the development and improvement of nanofiller-reinforced polymer nanocomposites. The objective of this study is to investigate the effect of functionalized multiwall carbon nanotube (MWCNT) on the tensile and flexural properties of epoxy resin nanocomposites reinforced with okra cellulose nanofibers. The nanocomposite laminates were subjected to experimental investigation to evaluate tensile and flexural properties. It is desirable to improve the tensile and flexural strength properties of this polymer to enhance its current applicability and to widen its scope for variety of advanced applications. In this research work, we have prepared nanocomposite of CNFs with functionalized multiwalled carbon nanotubes (f-MWCNT) as nanofiller materials. The tensile and flexural properties of nanocomposites are tested as per the ASTM standards. The weight of functionalized MWCNT in CNFs was varied from 0.25 to 1 wt%. The distribution and confirmation of functionalized multiwalled carbon nanotubes (f-MWCNT) in CNFs were analyzed. Mechanical characterization using nanoindentation techniques also showed significant enhancement in tensile and flexural properties of with multiwalled carbon nanotubes on okra cellulose nanofibers epoxy resin nanocomposites nanocomposite in comparison to okra cellulose nanofibers epoxy resin nanocomposites. The preliminary studies of the nanofillers revealed that the nanofillers can be used as reinforcement for nanofiller composites. The

---

A. Ramesh (✉)

Department of Mechanical Engineering, CMR Technical Campus, JNTUH, Hyderabad, Telangana, India

N. V. Srinivasulu

Department of Mechanical Engineering, Chaitanya Bharathi Institute of Technology, Hyderabad, Telangana, India

M. I. Rani

Department of Mechanical Engineering, JNTUH College of Engineering, Hyderabad, Telangana, India

results revealed that the tensile and flexural properties of the proposed CNFs were enhanced considerably after the incorporation of functionalized multiwall carbon nanotube (f-MWCNT) nanofillers into the epoxy matrix. These types of nanocomposites materials CNFs and MWCNT could be used as body components in aerospace, automotive, marine and medical applications.

**Keywords** Cellulose nanofibers (CNFs) · Multiwalled carbon nanotube (MWCNT) · Epoxy nanocomposites · Tensile and flexural properties

## 1 Introduction

In recent years, nanoparticles and their nanocomposites have attracted in the field of composite materials. Engineers are searching for advanced materials, which are light in weight, low density, high specific stiffness and high specific strength. Thermosetting polymer matrix reinforcement with nanofiller leads to the development of nanocomposite [1]. The nanoparticle is an exciting candidate for the modification of epoxy nanocomposites materials and offers excellent mechanical properties [2, 3]. The research work on nanocomposite dramatically increased with the discovery of the cellulose nanofibers (CNFs) with the nanoparticles. The reinforcement of polymer epoxy nanocomposites has been extensively used in structural components as well as in aeronautical, automotive, marine and sporting industries for a wide range of applications because of their enhance mechanical performance are tensile, flexural, compression and impact properties [4–6]. The nanoscale dimensions of nanofiller provide them with a very high aspect ratio, thus providing a large reinforcement surface area in the nanocomposites [7]. Natural CNFs have shown excellent mechanical properties compared to other natural fibers. Cellulose nanocomposite is manufactured from using different processes, and these processes affect the features of the nanocomposites: dispersion distribution and alignment of the reinforcement material [8, 9]. Cellulose material significant in low environmental impact, and element for water filtration, due to their high surface area and volume ratio, high strength and sustainability [10–12]. CNF nanomaterial is a sustainable substitute for MWCNTs in water treatment technologies [12]. CNF nanofillers are taking with structural, mechanical and optical properties. While the packaging and paper, automotive, aerospace, textile industries and construction have recognized cellulose nanomaterials potential. CNF nanomaterials have significant untapped potential in water treatment technologies [13, 14]. The carbon nanotube (CNT) can be classified based on the number of cylindrical shells, a single-walled carbon nanotube (SWCNT), double-walled carbon nanotubes (DWCNT) and multiwalled carbon nanotubes (MWCNTs). As the MWCNTs exhibit excellent electrical, mechanical and thermal properties, they have become promising nanoparticles for automotive, aerospace, defense, electronics and medical sectors [15–18]. It was found that the mechanical properties of multi-walled carbon nanotubes to epoxy resin composites included strong interfacial bonding with the matrix [19]. The nucleation effect of



CNTs and the phase separation behavior of NFCs in the other filler mechanical performance of the nanocomposite scaffolds with different morphologies were investigated [20]. Nanocomposites based on epoxy resin and weight percentages of functionalized MWCNT were prepared by resin cast molding method, and the mechanical properties decreased when the MWCNT content exceeded 0.2wt% due to the agglomeration of MWCNT. Carbon/epoxy woven composites and MWCNT/epoxy composites were prepared by incorporating woven-type carbon fibers into epoxy polymer matrices modified with 2wt% acid-treated and silane-treated MWCNT [21]. The effects of functionalized MWCNT on mechanical thermal and morphological properties of an epoxy-based nanocomposite material were investigated and utilizing different techniques of polymerization [22]. In addition to 1wt%, MWCNT was used to fabricate epoxy nanocomposite.

Biopolymer MWCNT/chitosan nanocomposites have been made by an evaporation method [23, 24]. The mechanical and morphology properties of the MWNT/chitosan nanocomposites have been characterized by SEM. The obtained values showed that different type of functionalized MWCNT would have different effects on the thermal and mechanical properties of the epoxy nanocomposites [25]. The reinforcement mechanism of amino-functionalized MWCNT in epoxy resin was discussed [26]. MWCNT/CNF nanocomposites have been extensively studied for their mechanical and thermal properties of CNW films, and their composites may not be thoroughly investigated. In this research work, the effects of the different weight percentage of functionalized MWCNT in CNFs varied from 0.25 to 1 wt % of the epoxy resin have been investigated. Mechanical stirring and ultra-sonication techniques were used to disperse nanotubes in the matrix. This research work has focused on investigating, manufacturing and characterization of a newly developed biodegradable composite materials by using low cost, abundant agrowaste natural resources and epoxy resin matrix materials, and study of the effect of the addition of MWCNT on the mechanical properties of epoxy resin, tensile, flexural, compression, impact and water absorption tests was conducted. Moreover, scanning electron microscopy (SEM) was used to determine the properties of fractured surfaces and flexural properties.

## 2 Materials and Experimental Work

### 2.1 Materials

In this study, the nanocomposite material was prepared by using Araldite LY 556 epoxy resin and HY 951 hardener. The features of LY556 epoxy resin and HY 951 are the most widely used catalyst at room temperature. The epoxy resin and hardener mixing ratio were 10:1. The PVA and wax were used to release agent for easy removal of the specimen. Araldite LY556 epoxy resin and HY951 hardener were purchased from dealers in Hyderabad, India. The MWCNT is purchased from

Sigma-Aldrich Chemicals used in this study produced by the catalytic CVD method and functionalized with COOH group. The average diameter and length of MWCNT were range between 15 and 25 nm and 10 and 20  $\mu\text{m}$ .

### **3 Fabrication of Nanocomposites**

In this study, the samples were fabricated into nanocomposites by the resin casting method; epoxy resin, cellulose nanofibers (CNFs) and multiwall carbon nanotube (MWCNT) were carefully mixed. The MWCNT/CNF suspensions had solvents exchanged from water to acetone. LY556 epoxy resin was added to different amounts of the MWCNT suspensions for the preparation of 0.25, 0.50, 0.75 and 1 wt % of MWCNT/CNFs epoxy nanocomposites. Multicarbon nanotube-based epoxy grouts were prepared by dispersing specified weight percentage of MWCNT nanoparticles in hardener and thoroughly mixed using mixer for 15–20 min to get a homogeneous suspension. The ratios were chosen to make a gel time of roughly 20 minutes. This time was enough to impregnate the samples with the epoxy resin. The resultant mixture was stirred by using a magnetic stirrer at 900 rpm for per one hour at room temperature and sonicated to remove air trapped bubbles in the ultrasonic ice bath. The molds released wax polish, which was also applied to the inner surface of the aluminum metal molds wall to smooth light separation of the CNFs nanocomposites specimen. The samples were cured at room temperature for 24 h and then post-cured at 70 °C for 30 min.

## **4 Characterization and Testing**

### ***4.1 Tensile Test***

The tensile test was conducted using Universal Testing Machine (UTM), Instron 4505 with 100 KN load cell capacity and cross-head speed of 5 mm/min as per the ASTM D638 Type IV standard. Tensile load was applied to gauge length until fracture occurs. Three specimens were tested from each sample. The tensile test was performed until each sample failed.

### ***4.2 Flexural Test***

The test was conducted using Instron 4505 machine under position control with the constant cross-head movement of 5 mm/min and a load cell of 10 KN. As per the ASTM standard D790, the specimens were cut with a length of 150 mm and tested

from each sample. The span length between the two supports was set at 65 mm and the loading rate at 5 mm/min. Three specimens were tested from each sample.

### 4.3 Microstructure Study of Fractured Surfaces

The ruptured surface and the reduced diameter of the fibers helped the effective removal of non-cellulosic constituents of the untreated fibers. Further reduction in the cellulose diameter helped the transformation of cellulose into CNFs. Figure 1 shows the SEM micrographs of the okra fibers from the extraction procedure. The diameter of okra cellulose nanofibers was 40 nm as shown in Figs. 1 and 2 shows the SEM image of functionalized multiwall carbon nanotube (f-MWCNT).

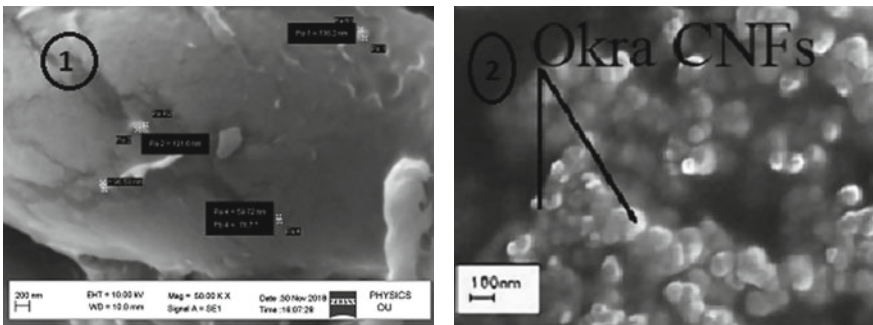


Fig. 1 SEM image of okra cellulose nanofibers

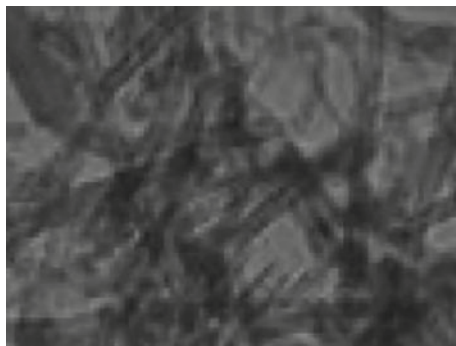


Fig. 2 SEM image of MWCNT

## 5 Results and Discussion

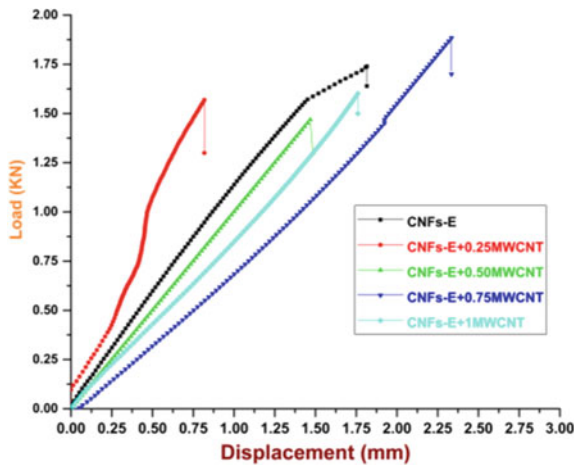
See Table 1.

### 5.1 Tensile Test

Figure 3 shows the tensile load and displacement curve of CNFs and the addition of MWCNT in CNF epoxy nanocomposites. The tensile test was carried out on the CNFs and CNFs/MWCNT epoxy nanocomposite specimen to evaluate their tensile strength and tensile modulus, and the following results were obtained. Specimen

**Table 1** Table tensile and flexural properties of nanocomposites

Nanocomposite samples	Tensile strength (MPa)	Tensile modulus (GPa)	Flexural strength (MPa)	Flexural modulus (GPa)
CNFs—E	32.83 ± 0.90	3.43 ± 0.40	52.20 ± 1.01	3.10 ± 0.17
CNFs—E + 0.25% MWCNT	34.43 ± 0.90	3.43 ± 0.90	54.2 ± 1.45	3.1 ± 0.30
CNFs—E + 0.50% MWCNT	37.63 ± 3.68	3.44 ± 3.68	58.4 ± 0.35	3.19 ± 0.12
CNFs—E + 0.75% MWCNT	42.77 ± 2.92	3.53 ± 2.92	66.37 ± 0.95	3.3 ± 0.26
CNFs—E + 1% MWCNT	35.00 ± 0.10	3.38 ± 0.10	58.85 ± 0.78	3.27 ± 0.31



**Fig. 3** Typical tensile load and displacement curves of nanocomposites

with designation CNFs-E > CNFs—E + 0.25MWCNT > CNFs – E + 0.5MWCNT > CNFs – E + 0.75MWCNT > CNFs –E + 1MWCNT possessed tensile strength of  $32.83 \pm 0.90$  MPa,  $34.43 \pm 0.90$  MPa,  $37.63 \pm 3.68$  MPa,  $42.77 \pm 2.92$  MPa and  $35 \pm 0.10$  MPa and tensile modulus of  $3.43 \pm 0.40$  GPa,  $3.43 \pm 0.25$  GPa,  $3.44 \pm 0.37$  GPa,  $3.53 \pm 0.45$  GPa and  $3.38 \pm 0.19$  GPa, respectively.

Figures 4 and 5 show the typical tensile strength and tensile modulus of the CNFs as be  $32.83 \pm 0.90$  MPa and  $3.43 \pm 0.31$  GPa, respectively. The addition of MWCNT in CNFs up to 0.75 wt% caused an increase in the tensile strength and tensile modulus of the CNFs by  $42.77 \pm 0.44$  MPa and 57.09% and  $3.53 \pm 2.92$

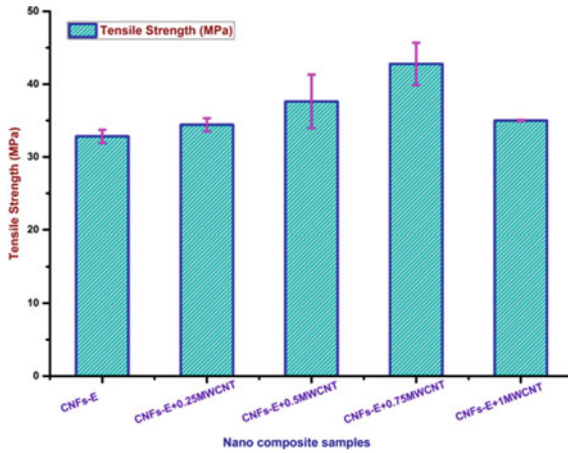


Fig. 4 Tensile strength of the CNFs and epoxy/MWNT composites containing 0.25, 0.5, 0.75 and 1 wt% MWCNT

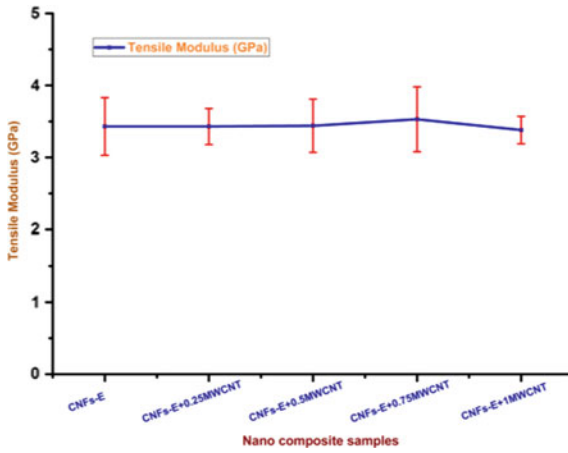


Fig. 5 Tensile modulus of the CNFs and epoxy/MWNT composites containing 0.25, 0.5, 0.75 and 1 wt% MWCNT

GPa and 3.3%, respectively. The addition of functionalized MWCNT in CNFs to the epoxy polymer matrix has improved tensile strength and tensile modulus.

Further, for given functionalized MWCNT loading in CNFs, the effect of functionalized MWCNT alignment on the tensile strength and tensile modulus is significant than the randomly dispersed epoxy polymer nanocomposites. It is observed that tensile strength and tensile modulus of epoxy polymer nanocomposites with lesser functionalized MWCNT loading in CNFs are higher than the epoxy polymer nanocomposites with random dispersion, which indicates the effect of functionalized MWCNT alignment. It can be seen from Figs. 4 and 5, the tensile strength and tensile modulus were improved for 0.75 wt % MWCNT/CNFs/epoxy polymer nanocomposite compared to all the other nanocomposite. Poor dispersion of MWCNT at 1 wt% loading in CNFs/epoxy nanocomposites caused agglomeration in MWCNT/CNFs in MWCNT agglomerate in the epoxy resin nanocomposite leading to a reduction in load transfer between MWCNT/CNFs and epoxy polymer nanocomposites. Tensile strength and stiffness enhancements were the results of a functional interaction between MWCNT/CNFs epoxy nanocomposites. On the other hand, there was a decrease in deformation at the break following an increase in the functionalized MWCNT concentrations content 1 wt% in CNFs/epoxy nanocomposite. At functionalized MWCNT loading higher than 0.75 wt% in CNFs/epoxy nanocomposite, the tensile strength and tensile modulus decrease were seen, following an increase in deformation at the break [27]. At MWCNT weight percentage concentrations higher than 0.75 wt% in CNFs/ epoxy nanocomposite, there was a decrease in tensile strength and tensile modulus of the epoxy nanocomposites as against an increase in the elongation at break [28].

## 5.2 Flexural Test

Figure 6 shows the flexural load and displacement curve of both CNFs and the addition of MWCNT in CNFs epoxy nanocomposites. The flexural test was carried out on the nanocomposite specimen to evaluate their strength, and the following result was obtained. Specimen with designation CNFs-E > CNFs – E + 0.25MWCNT > CNFs – E + 0.5MWCNT > CNFs – E + 0.75MWCNT > CNFs – E + 1MWCNT possessed flexural strength of  $52.20 \pm 1.01$  MPa,  $54.20 \pm 0.95$  MPa,  $58.40 \pm 0.78$  MPa,  $66.37 \pm 0.25$  MPa and  $58.85 \pm 0.90$  MPa and flexural modulus of  $3.10 \pm 0.17$  GPa,  $3.11 \pm 0.26$  GPa,  $3.13 \pm 0.35$  GPa,  $3.30 \pm 0.53$  GPa and  $3.27 \pm 0.40$  GPa, respectively. Figures 7 and 8 show the typical flexural strength and flexural modulus of the CNFs as be  $52.20 \pm 1.01$  MPa and  $3.10 \pm 0.17$  GPa, respectively. The addition of MWCNT in CNFs up to 0.75 wt% caused an increase in the flexural strength and flexural modulus of the CNFs by  $66.37 \pm 0.25$  MPa and 57.09% and  $3.30 \pm 0.53$  GPa and 3.3%, respectively. The addition of functionalized MWCNT in CNFs to the epoxy polymer matrix has improved flexural strength and flexural modulus.

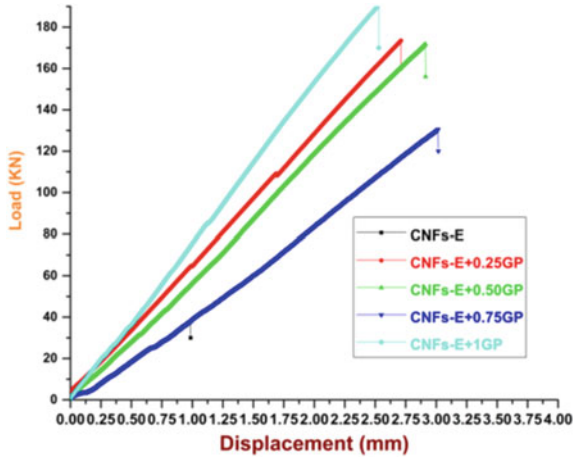


Fig. 6 Typical flexural load and displacement curves of nanocomposites

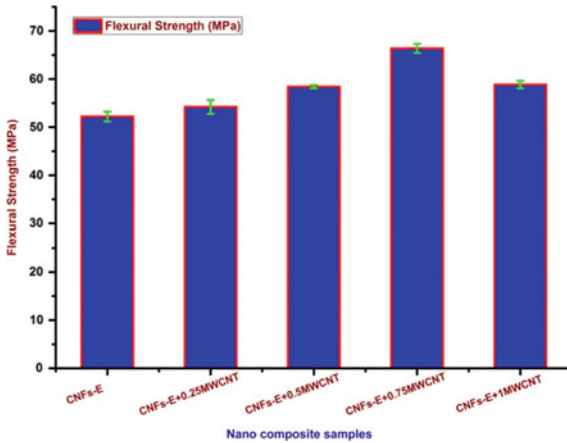
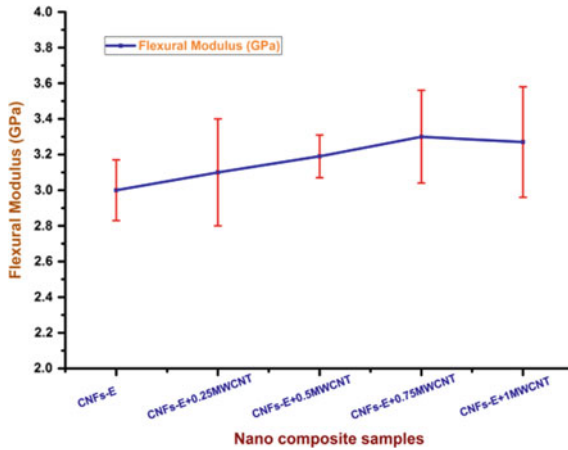


Fig. 7 Flexural strength of the CNFs and epoxy/MWNT composites containing 0.25, 0.5, 0.75 and 1 wt% MWCNT

Further, for given functionalized MWCNT loading in CNFs, the effect of functionalized MWCNT alignment on the flexural strength and flexural modulus is significant than the randomly dispersed epoxy polymer nanocomposites. It is observed that flexural strength and flexural modulus of epoxy polymer nanocomposites with lesser functionalized MWCNT loading in CNFs are higher than the epoxy polymer nanocomposites with random dispersion, which indicates the effect of functionalized MWCNT alignment. It can be seen from Fig. 2, the flexural strength and flexural modulus were improved for 0.75 wt% MWCNT/CNFs/epoxy polymer nanocomposite compared to all the other nanocomposite. Poor dispersion of MWCNT at 1 wt%



**Fig. 8** Flexural modulus of the CNFs and epoxy/MWNT composites containing 0.25, 0.5, 0.75 and 1 wt% MWCNT

loading in CNFs/epoxy nanocomposites caused agglomeration in MWCNT/CNFs in MWCNT agglomerate in the epoxy resin nanocomposite leading to a reduction in load transfer between MWCNT/CNFs and epoxy polymer nanocomposites. Tensile strength and stiffness enhancements were the results of a functional interaction between MWCNT/CNFs epoxy nanocomposites. On the other hand, there was a decrease in deformation at the break following an increase in the functionalized MWCNT concentrations content 0.75 wt% in CNFs/epoxy nanocomposite. At functionalized MWCNT loading higher than 0.75 wt% in CNFs/epoxy nanocomposite, the tensile strength and tensile modulus decrease was seen, following an increase in deformation at the break [29]. At MWCNT weight percentage concentrations higher than 0.75 wt% in CNFs/epoxy nanocomposite, there was a decrease in tensile strength and tensile modulus of the epoxy nanocomposites as against an increase in the elongation at break [30]. These results suggest an interaction between the CNFs/epoxy resin matrix and the reinforcement following an increase in MWCNT coating with an increase in MWCNT content.

### 5.3 Morphological (SEM) Studies of Tensile Specimens

Analysis of failure behavior through scanning electron microscopy of cellulose nanofibers (CNFs) and functionalized multiwall carbon nanotube (MWCNT) epoxy nanocomposite was investigated by SEM as shown in Fig. 9. The fracture surface of CNFs epoxy nanocomposite shows the smooth surface with crack propagation. The formation of agglomeration of MWCNT/CNFs restricts the flow of matrix into the agglomerated MWCNT and forms holes and void between MWCNT/CNFs and epoxy polymer matrix. The poor adhesion and compatibility between the



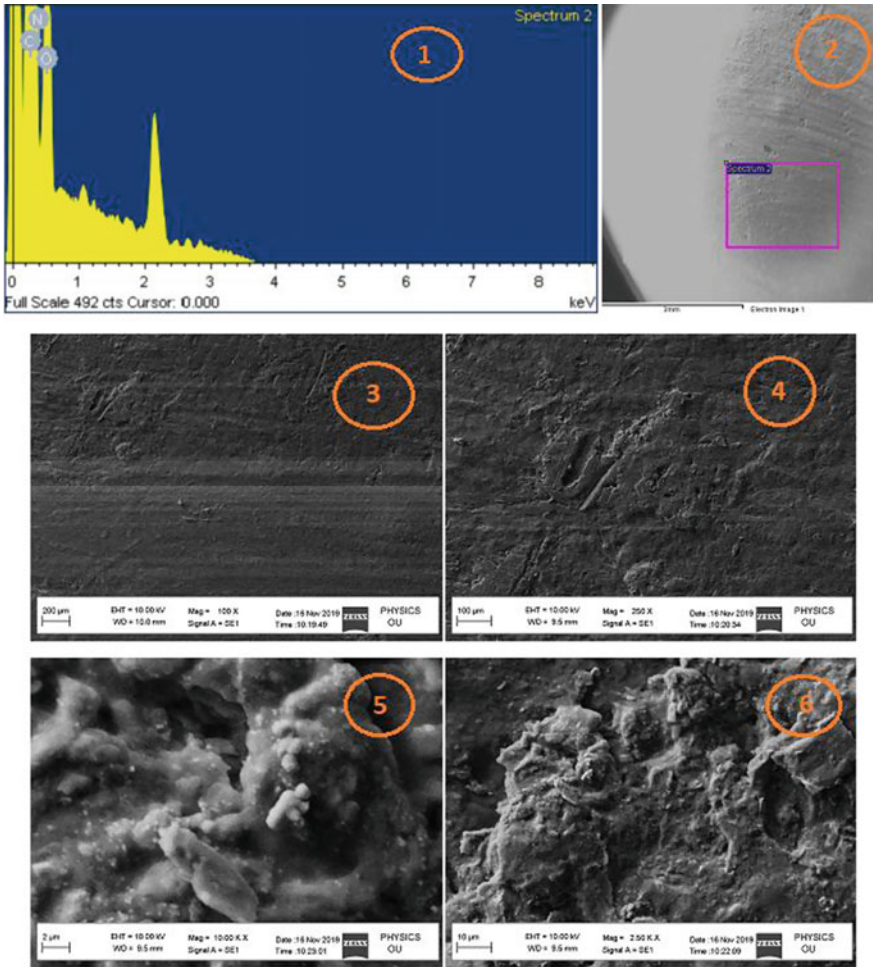


Fig. 9 SEM image of nanocomposites

MWCNT and CNFs fillers and matrix resulted in poor mechanical properties. For the micrographs of MWCNT and CNFs, nanofiller-reinforced epoxy nanocomposite agglomeration of MWCNT and CNFs could be observed when added 0.75 wt% MWCNT/CNFs/epoxy polymer nanocomposite. These results suggest an interaction between the CNFs/epoxy resin matrix and the reinforcement following an increase in MWCNT coating with an increase in MWCNT content.

## 6 Conclusions

This work investigated epoxy nanocomposites with different combination of nanofillers (MWCNT and CNFs) to find out the effect of MWCNT/CNFs on tensile and flexural properties of nanocomposites. The laminates were made using MWCNT/CNFs and epoxy resin. The tensile and flexural properties are increased with increasing functionalized MWCNT/CNFs loading up to 0.75 wt% as against a decrease in the deformation at the break with a higher MWCNT/CNFs addition, and there was a decrease in the tensile and flexural properties. As a substitute for MWCNT/CNFs/epoxy resin nanocomposites, the 0.75 wt% of MWCNT nanofiller nanocomposite laminate was a stronger substitute where the tensile and flexural properties were projected. The morphological (SEM) studies confirmed the strength of MWCNT/CNFs, and there was an increase in CNFs/epoxy resin composites with the addition of 0.75 wt% of MWCNT/CNFs composite fillers. The failure modes of nanofillers are MWCNT/CNFs nanocomposites samples were investigated to enable a study of the crack propagations CNFs nanocomposite of each sample. Epoxy nanocomposite sample containing 0.75 wt% MWCNT/CNFs showed rougher surfaces. This degradation might result due to the agglomeration of MWCNT/CNFs. It can be concluded from this research that the addition of CNFs can promote the interaction between the MWCNT and epoxy polymer matrix.

## References

1. Njuguna J, Pielichowski K, Desai S (2008) Nanofiller-reinforced polymer nanocomposites. *Polym Adv Technol* 19:947–959
2. Nuruddin M, Hosur M, Gupta R, Hosur G, Tcherbi-Narteh A, Jeelani S (2017) Cellulose nanofibers-graphene nanoplatelets hybrids nanofillers as high-performance multifunctional reinforcements in epoxy composites. *Polym Polym Compos* 25(4):273–284
3. Wetzel B, Hauptert F, Zhang M (2003) Epoxy nanocomposites with high mechanical and tribological performance. *Compos Sci Technol* 63:2055–2067
4. Rahmandoust M, Ayatollahi MR (2016) CNT-based nanocomposites, pp 117–175
5. Fu S, Sun Z, Huang P, Li Y, Hu N (2019) Some basic aspects of polymer nanocomposites: a critical review. *Nano Mater Sci* 1(1):2–30
6. Srivastava I, Rafiee M, Yavari F, Rafiee J, Koratkar N (2012) Epoxy nanocomposites, pp 315–352
7. Al-Mosawi A, Abbas Abdulsada S, Rijab M (2015) Mechanical properties of epoxy nanocomposite. *Int J Adv Res* 3:1468–1472
8. HPS AK, Saurabh CK, Asniza M, Tye YY, Fazita MR, Syakir MI, Fizree HM, Yusra AF, Haafiz MK, Kassim MA, Suraya NL (2017) Nanofibrillated cellulose reinforcement in thermoset polymer composites. In: Jawaid M, Boufi S, HPS AK (eds) *Cellulose-reinforced nanofibre composites*, Woodhead Publishing, pp 1–24
9. Oksman K, Aitomäki Y, Mathew AP, Siqueira G, Zhou Q, Butylina S, Tanpichai S, Zhou X, Hooshmand S (2016) Review of the recent developments in cellulose nanocomposite processing. *Compos A Appl Sci Manuf* 83:2–18
10. Mohammed N, Grishkewich N, Tam K (2018) Cellulose nanomaterials: promising sustainable nanomaterials for application in water/wastewater treatment processes. *Environ Sci Nano* 5

11. Mohammed N, Grishkewich N, Tam KC (2018) Cellulose nanomaterials: promising sustainable nanomaterials for application in water/wastewater treatment processes. *Environ Sci Nano* 5(3):623–658
12. Carpenter AW, de Lannoy C-F, Wiesner MR (2015) Cellulose nanomaterials in water treatment technologies. *Environ Sci Technol* 49(9):5277–5287
13. Larsson PA, Berglund LA, Wagberg L (2014) Ductile all-cellulose nanocomposite films fabricated from core-shell structured cellulose nanofibrils. *Biomacromol* 15(6):2218–2223
14. Dufresne A (2013) Nanocellulose: a new ageless bionanomaterial. *Mater Today* 16(6):220–227
15. Mi H-Y, Jing X, Salick MR, Cordie TM, Turng L-S (2016) Carbon nanotube (CNT) and nanofibrillated cellulose (NFC) reinforcement effect on thermoplastic polyurethane (TPU) scaffolds fabricated via phase separation using dimethyl sulfoxide (DMSO) as solvent. *J Mech Behav Biomed Mater* 62:417–427
16. Rathod VT, Kumar JS, Jain A (2017) Polymer and ceramic nanocomposites for aerospace applications. *Appl Nanosci* 7(8):519–548
17. Veličković Gajević S, Stojanovic B, Ivanovic L, Miladinović S, Milojević S (2018) Application of nanocomposites in the automotive industry
18. Camargo PHC, Satyanarayana KG, Wypych F (2009) Nanocomposites: synthesis, structure, properties and new application opportunities. *Mater Res* 12:1–39
19. Satish G, Prasad VVS, Ramji K (2018) Effect on mechanical properties of carbon nanotube based composite. *Mater Today Proc* 5(2, Part 2):7725–7734
20. Mi H-Y, Jing X, Salick M, Cordie T, Turng L-S (2016) Carbon nanotube (CNT) and nanofibrillated cellulose (NFC) reinforcement effect on thermoplastic polyurethane (TPU) scaffolds fabricated via phase separation using dimethyl sulfoxide (DMSO) as solvent. *J Mech Behav Biomed Mater* 62
21. Kathi J, Rhee K-Y, Lee JH (2009) Effect of chemical functionalization of multi-walled carbon nanotubes with 3-aminopropyltriethoxysilane on mechanical and morphological properties of epoxy nanocomposites. *Compos A Appl Sci Manuf* 40(6):800–809
22. Roy S, Petrova RS, Mitra S (2018) Effect of carbon nanotube (CNT) functionalization in Epoxy-CNT composites. *Nanotechnol Rev* 7(6):475–485
23. Marroquin J, Rhee KY, Park S-J (2013) Chitosan nanocomposite films: Enhanced electrical conductivity, thermal stability, and mechanical properties. *Carbohydr Polym* 92:1783–1791
24. Kim MT, Rhee KY, Lee J, Hui D, Lau KT (2011) Property enhancement of a carbon fiber/epoxy composite by using carbon nanotubes. *Compos Part B-Eng* 42:1257–1261
25. Theodore M, Hosur M, Thomas J, Jeelani S (2011) Influence of functionalization on properties of MWCNT–epoxy nanocomposites. *Mater Sci Eng A-Struct Mater Prop Microstructure Process* 528:1192–1200
26. Chen X, Wang J, Lin M, Zhong W, Feng T, Chen X, Chen J, Xue F (2008) Mechanical and thermal properties of epoxy nanocomposites reinforced with amino-functionalized multi-walled carbon nanotubes. *Mater Sci Eng. A* 492:236–242
27. Nuruddin M, Hosur M, Mahdi T, Jeelani S (2017) Flexural, viscoelastic and thermal properties of epoxy polymer composites modified with cellulose nanofibers extracted from wheat straw. *Sens Transducers* 210
28. Ireana Yusra AF, Abdul Khalil HPS, Hossain MS, Davoudpour Y, Astimar AA, Zaidon A, Dungani R, Mohd Omar AK (2015) Characterization of plant nanofiber-reinforced epoxy composites. *BioResources* 10(4):13
29. Wongjaiyen T, Brostow W, Chonkaew W (2018) Tensile properties and wear resistance of epoxy nanocomposites reinforced with cellulose nanofibers. *Polym Bull* 75(5):2039–2051
30. Hosur M, Barua R, Zainuddin S, Jeelani S, Kumar A, Trovillion J, Perez Y (2010) Processing and characterization of epoxy nanocomposites with Mwcnt's/Cnf's using thinky and 3-roll shear mixing techniques. *Matéria (Rio de Janeiro)* 15:247–253

# Virtual Instrumentation System Design for a Secured Chemical Process Industry Automation



S. G. Rahul , R. Chitra , Manasa Madabhushi , M. Kavya , and Sraya 

**Abstract** With the development and popularization of technology, virtual instruments are mostly replacing analog device gradually. The measurement and control technology plays an important role in the process of manufacturing industry and scientific research. As time advances, the conventional instruments are emerging in shortage. This study involves the development of virtual instrumentation for process industry automation. In this work, a supervisory monitoring system is developed using LabVIEW software. In today's world, the industrial applications are carried out by controlling remotely. LabVIEW is one of the useful tools for real-time monitoring and controlling of industrial systems. The system fed with having with controllers is used to perform process parameter control, and industry personals can visualize the parameters without visiting the site. Therefore, this system reduces maintenance cost and enhances easy access. Temperature and tank level are key parameters to be monitored in chemical process industries which is considered as an example in this study. Lack of control over any of them will not only affect the component and equipment but also the manpower and, therefore, ultimately resulting in equipment and life loss. Also, to the monitoring and controlling the system, this study also provides an additional security system for the users with e-mail report generation to convey the user about the parametric status.

**Keywords** LabVIEW · Monitor · Control · Chemical

## 1 Introduction

Presently, automation is one of the important and useful in many industrial applications. The main problem arises during the designation of engineering systems demanding substantial amounts of hardware circuits leading to more wiring connections [1]. At that case, it is tedious to space the system elements, and the space planning needs improvement. As the technology is improving day by day, the LabVIEW

---

S. G. Rahul (✉) · R. Chitra · M. Madabhushi · M. Kavya · Sraya  
Vel Tech Rangarajan Dr. Sagunthala R&D Institute of Science and Technology, Chennai, Tamil Nadu 600062, India

© The Author(s), under exclusive license to Springer Nature Singapore Pte Ltd. 2022  
G. S. V. L. Narasimham et al. (eds.), *Innovations in Mechanical Engineering*,  
Lecture Notes in Mechanical Engineering,  
[https://doi.org/10.1007/978-981-16-7282-8\\_48](https://doi.org/10.1007/978-981-16-7282-8_48)

653

software made the engineering design easy, and therefore, the hardware equipment required is decreased since most of the instrumentation system can be designed using software [2]. Process parameter control in chemical industries is always a challenge when the involved process consists of some synthesis of useful and powerful liquid. Any deviation in the process variable is so hazardous leading to substantial loss to life and property [3]. Utilization for process automation and control by wireless means between the LabVIEW and base station has been tremendously growing. Studies have indicated the enhanced performance of plant and machinery without the rise in the reaction time of the function [4]. Various studies are carried out involving LabVIEW in-process monitoring and controlling, and some of the literature studies are discussed as follows. Jianying Liu et al. studied on the position control of a DC servo motor using PID control algorithms. PID controllers are designed and supported by LabVIEW program, and therefore, the real-time position control of the DC servo motor was realized by using DAQ device. All codes are developed on the LabVIEW real-time development system, then download applications to run on the real-time controller of national instruments [5]. Rohit Agrawal et al. carried out their study on temperature and humidity parameters in manufacturing plants and particularly that of electronic assemblies. They have concluded that lack of control over any of them will damage the components resulting in a loss in production. Their work proposed a system to provide remote monitoring of the temperature and humidity at various parts of the plant with the assistance of the wireless sensor network and LabVIEW software platform [6].

In this project, it is aimed to reduce the manual monitoring and control by integrating LabVIEW with the chemical process where the engineer can enable the process of the tank to be controlled at their place [7, 8]. LabVIEW being a graphical programming language, it is easy to design a control system with security-enabled features with a multiple login user to secure the plant access from the unknown users. Temperature and level are key parameters to be taken care of in chemical plants and particularly that of electronic assemblies [9]. Lack of monitoring over any of them will not only affect the components but also the method and the operators' comfort, all ultimately resulting in production loss. This work aims to provide a solution for temperature monitoring in a chemical plant, a chemical tank-level controller followed by a security access system. The study is initially implemented as a software phase due to lack of access to hardware features owing to COVID-19 conditions. The successful results of the software will be enhancing as a hardware phase in the future scope.

## 2 Temperature Monitoring System

As we know that the temperature is the most crucial parameter in most of the chemical industry, so monitoring the temperature is the most important. Excessive process temperature damages the entire process loop and affects the electronic system leading to hazards. Figure 1 depicts the graphical user interface of the temperature monitoring

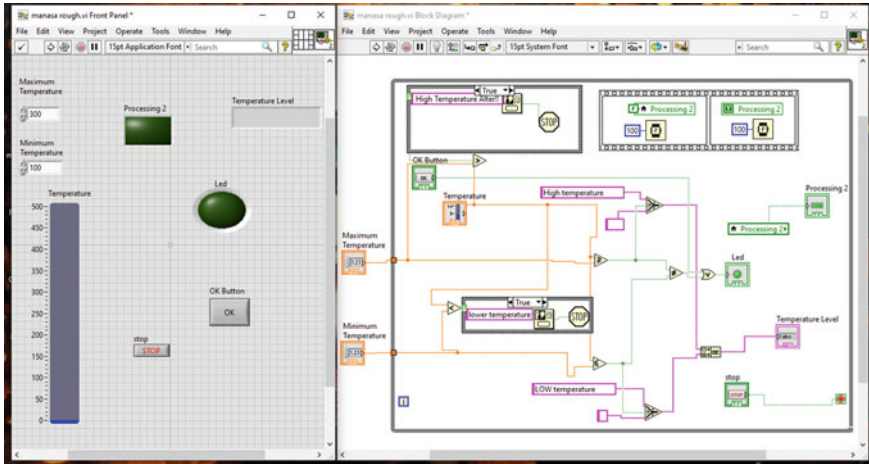


Fig. 1 GUI temperature monitoring system (left) and the block diagram logic (right)

system in the industry which helps to remotely monitor the system.

In the temperature monitoring system, a temperature indicator of certain chemical liquid is presented with the maximum and minimum temperature values. If the temperature is below the required level, a pop-up message indicates as the lower temperature, and if the temperature is greater than the required level, then the engineer gets the pop-up message as a higher temperature indication as shown in Fig. 2. The flowchart depicting in Fig. 3 presents the logic of the temperature monitoring system.

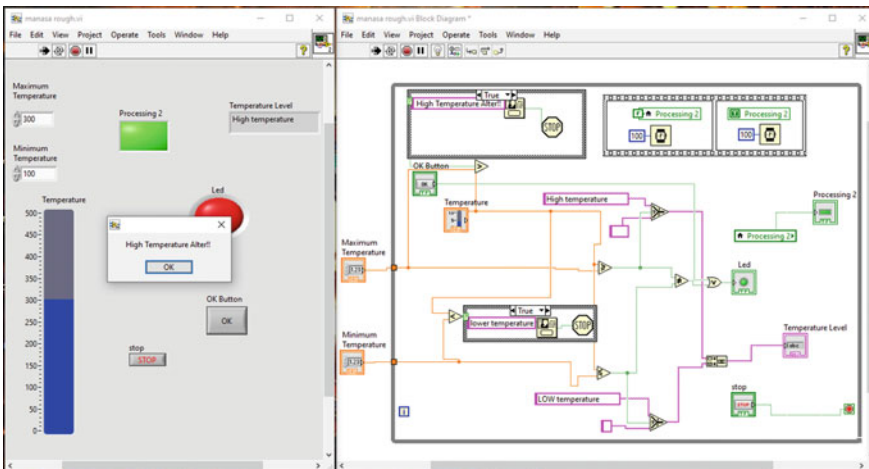
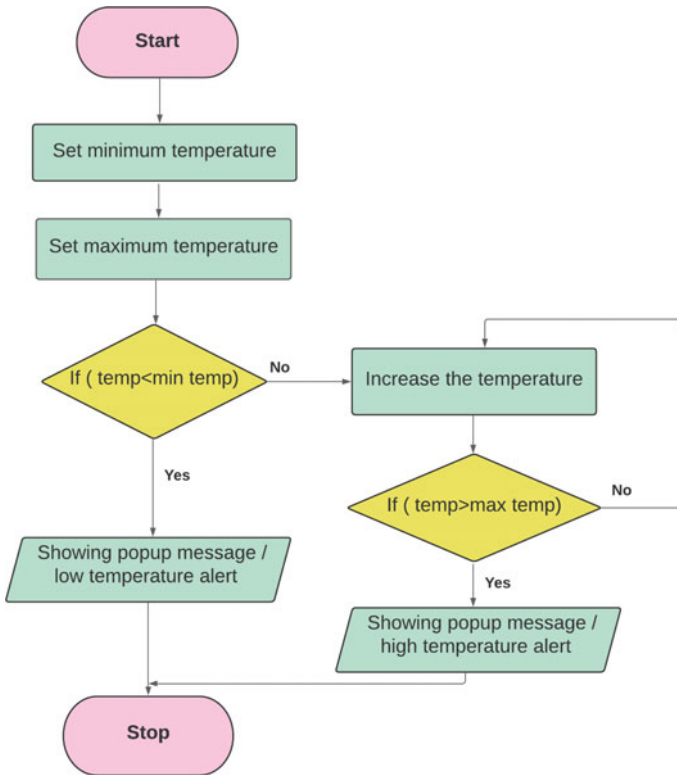


Fig. 2 GUI temperature monitoring system indicating high-temperature warning



**Fig. 3** Flowchart of the temperature monitoring

### 3 Tank-Level Controller

A tank-level control using PID controller describes the liquid-level control system deployed in many process control applications. The conventional proportional-integral-derivative (PID) controller is more reliable for single parameter control. The responses of the PID controller are verified through LabVIEW simulation [10]. From the simulation and various study results, it is observed that the PID controller gives superior performance than other controllers. Most times, the chemicals will be processed by mixing treatment within the tanks, but always the tank level must be controlled and regulated. Plant engineers need to understand the functioning of the control system. The design and analysis of conventional control systems are supported by their mathematical PID models [11].

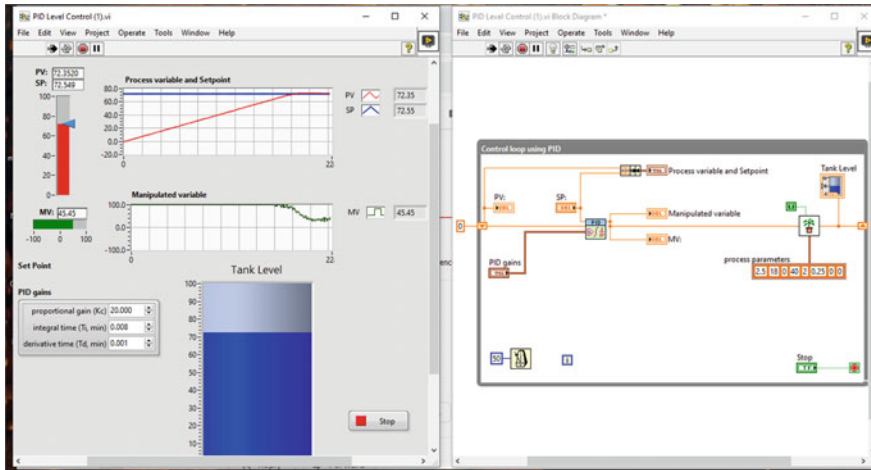


Fig. 4 PID for chemical plant-level control

### 3.1 Tank-Level Controller

A PID controller usually called a three-term controller is a control loop scheme which deploys a feedback unit and is preferred in industrial control systems. A PID controller continuously computes error value  $e(t)$  as the difference between the desired setpoint and measured process variable (say, tank level). The PID tank-level control scheme is depicted in Fig. 4. The controller is tuned by Zeigler-Nichols tuning method, and it follows the desired setpoint.

### 3.2 Security Using Username and Password

Security plays a major role in the industries as it safeguards the industry from the external user who tries to hack. In this work, a security-based system which is designed using 2-D array which contains the username and password of the certain users who frequently come to the industry and in order to check whether the person’s username and password are correct or not. If the login credential of the user matches, then the user gets the authentication to tank parameters which are depicted in. Else, no access is provided (Fig. 6).



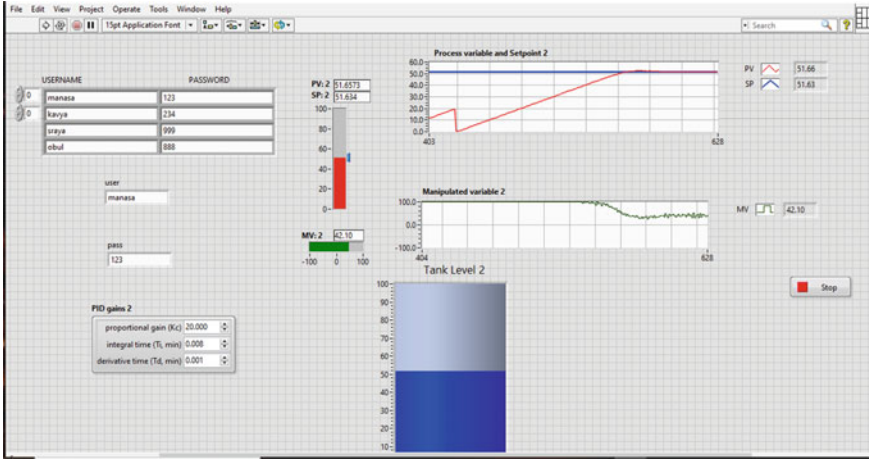


Fig. 5 Block diagram of the username and password for security

### 3.3 E-mail Alert Generation

When the tank level is greater than the required level, the higher authority gets the intimation regarding the high alert, and it helps the user to know that danger that takes places. The port number SMTP server to whom the e-mail is to be sent can be configured. After configuration, email reports can be viewed as shown in Figs. 6 and 7.

The logic of the concept discussed above is depicted in Fig. 8.

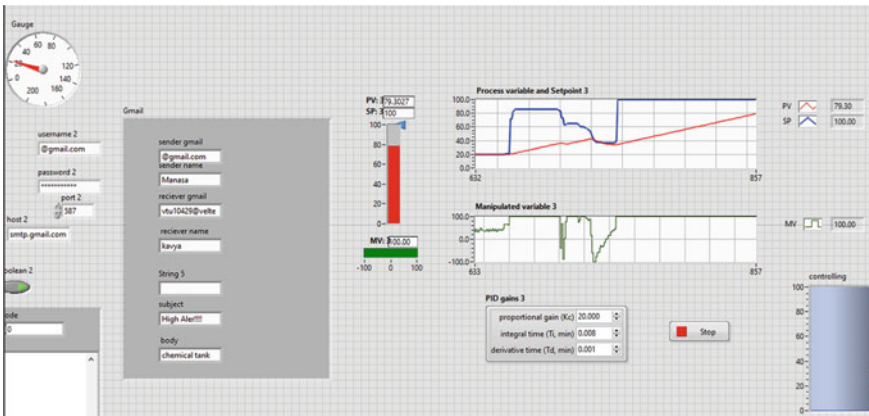


Fig. 6 Updated secured tank-level control using PID

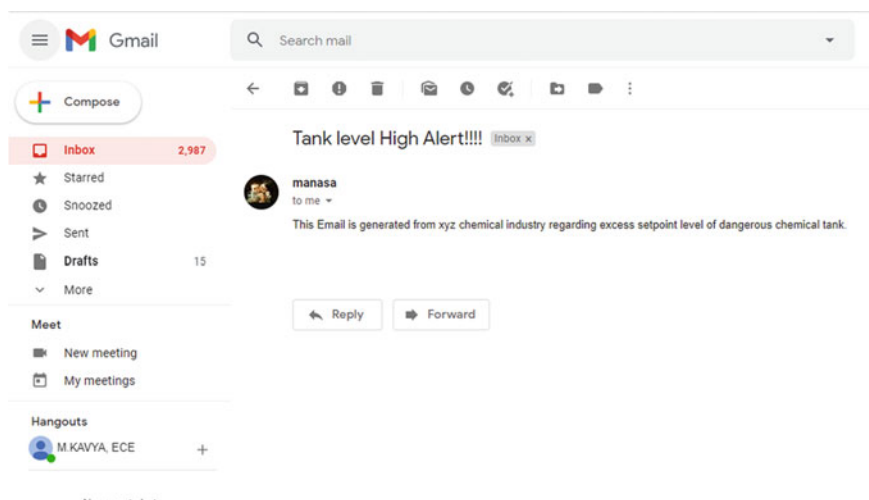


Fig. 7 E-mail alert to the industry personnel

## 4 Conclusions

Nowadays, most of the process industries are computerized. Earlier monitoring was done manually, and with the advancement in instrumentation system, technology has moved toward computerized supervisory monitoring and control. In this study, LabVIEW is implemented to simulate a level control of a chemical process industry and inform the industry personnel to take appropriate measures when there is any parameter over-limit which can prevent any harm to property and life. In this project, it is mainly aimed to control the level of the tank for the excess chemical and provide a security system to grant access to the user by restricting with username and password credentials thereby preventing the access to unknown users. This system also provides an email report to the safety team to notify regarding the excess and uncontrollable process parameters in the industry, so it helps engineers to and rescue from the industry hazards. This study is initially implemented as a software phase owing to hardware accessibility issues due to COVID-19, and in the future scope, it is to be developed into a hardware project.

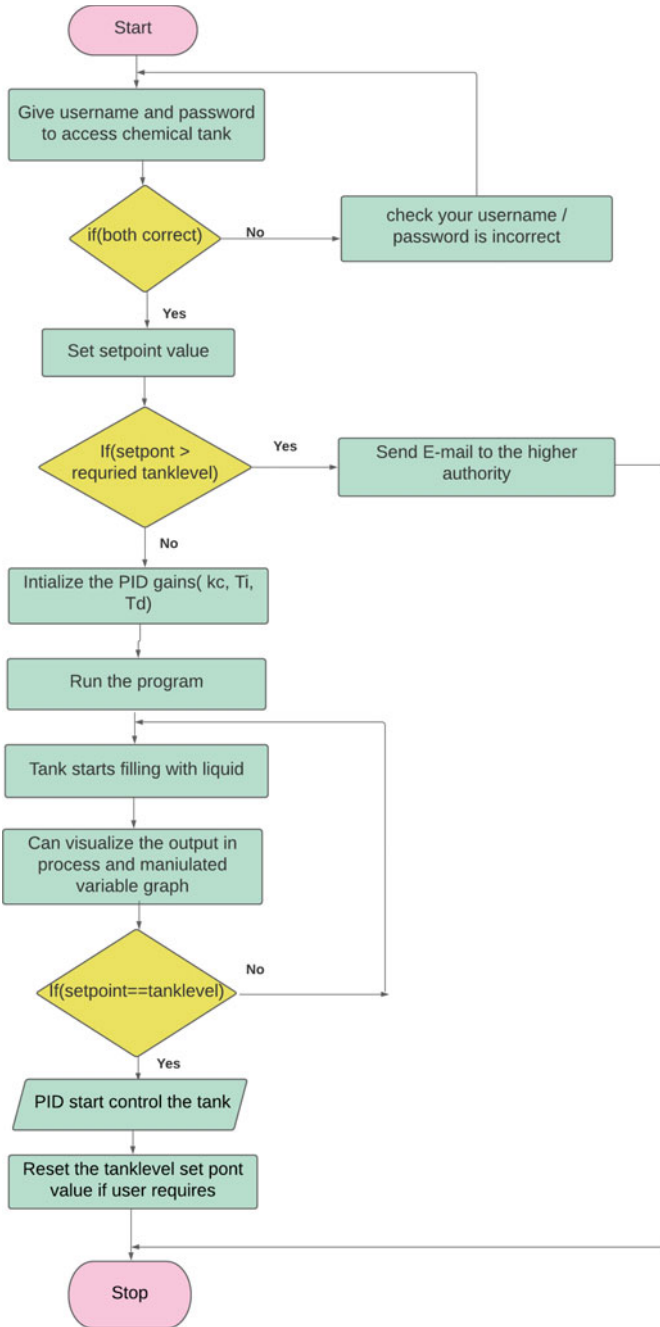


Fig. 8 Flowchart depicting secured tank-level control scheme

## References

1. Rahul SG, Dhivyasri G, Kavitha P, Vendan SA, Kumar KR, Garg A, Gao L (2018) Model reference adaptive controller for enhancing the depth of penetration and bead width during cold metal transfer joining process. *Rob Comput Integr Manuf* 53:122–134
2. Buzduga C, Ciufudean C (2020) Automation systems in LabVIEW. *Int J Educ Learn Syst* 5
3. Padhee S, Singh Y (2011) Data logging and supervisory control of process using LabVIEW. In: IEEE technology students' symposium. IEEE, pp 329–334
4. Morarum CM, Stefan I, Bucur C, Balteanu O (2020) Survey about the data acquisition system used for cryogenic process with configuration of the simulation system in LabVIEW software. *Int J Circ Electron* 5
5. Liu J, Zhang P, Wang F (2009) Real-time dc servo motor position control by PID controller using labview. In: International conference on intelligent human-machine systems and cybernetics, vol 1. IEEE, pp 206–209
6. Agrawal R, Mohan S (2012) Complete industrial solution for automation in temperature and humidity monitoring using labview. In: 2012 Ninth international conference on wireless and optical communications networks (WOCN). IEEE, pp 1–5
7. Gomez Quintero MP, Zabala Dominguez GA, Davila Rincon JA (2011) Use of LabVIEW to control systems in chemical engineering. *Dyna* 78(169):150–157
8. Chattal M, Bhan V, Madiha H, Shaikh SA (2019) Industrial automation & control trough PLC and LabVIEW. In: 2nd International conference on computing, mathematics and engineering technologies (iCoMET). IEEE, pp 1–5
9. Alia MA, Younes TM, Alsabbah SA (2011) A design of a PID self-tuning controller using LabVIEW. *J Softw Eng Appl* 4(3):161
10. Yu J, Liu C (2015) Design of self-tuning PID controller with fuzzy variable parameters based on LabView. In: IEEE International conference on information and automation. IEEE, pp 2586–2591
11. Sundaram SM (2017) Design of virtual process control laboratory (VPCL) using first principal method and interactive PID control toolkit using LabVIEW. In: 2017 9th International conference on information technology and electrical engineering (ICITEE). IEEE, pp 1–5

# Multi-robot SLAM: Challenges and Solutions



Nishad Kulkarni, Saket Yeolekar, and Prakash Mainkar

**Abstract** Simultaneous localization and mapping (SLAM) is central to the foundation of robotic exploration. Over the decades, numerous advancements have been made in the field of SLAM. Currently, most of the applications based on SLAM are implemented using a single robot. In practical applications like search and rescue operations, there is a need to implement SLAM at a multi-robot level. This paper conducts a review on SLAM at a multi-robot level.

**Keywords** Multi-robot SLAM · Extended Kalman filters · Robotic exploration · Multi-robot systems

## 1 Introduction

SLAM is one of mobile robotics' foundational problem statements. SLAM itself is a few decades old concept [1, 2]; emerging hardware solutions with increasingly better computational power in recent times have caused SLAM to gain significant momentum in practical applications.

However, most of these applications are based on a single mobile agent [3]. For applications where one needs to consider factors like time constraints, '*Kidnapped Robot Problem*,' robot's on-board processing power and storage, range of robot sensors, range of robot control, etc., there is a need to implement SLAM on a system

---

N. Kulkarni (✉)

Department of Electronics & Telecommunication, Maharashtra Institute of Technology, Pune  
Navi Mumbai, India

S. Yeolekar

School of Electrical Engineering, Dr. Vishwanath karad MIT World Peace University, Pune, India  
e-mail: [saket.yeolekar@mitwpu.edu.in](mailto:saket.yeolekar@mitwpu.edu.in)

P. Mainkar

School of Electronics & Communication Engineering, Dr. Vishwanath karad MIT World Peace University, Pune, India  
e-mail: [prakash.mainkar@mitwpu.edu.in](mailto:prakash.mainkar@mitwpu.edu.in)

of multiple robots or a swarm of robots. One of the best examples of an implemented system is [4].

There exist quite a few algorithms that address this problem. The idea of multi-robot SLAM gives rise to even more challenges that may not exist in single robot SLAM. There are various algorithms and methods to deal with these problems. This paper reviews some problems and their solutions by looking at various algorithms and implemented systems.

## 2 The SLAM Problem

### 2.1 Probabilistic Definition of SLAM in Single Robot Systems

The SLAM problem consists of two sections, viz. localization and mapping. However, they are interdependent. For localizing an agent in a certain environment, the map of the environment must be known to that agent. At the same time, if the agent's location is not known, then it becomes impossible to generate the map of the said environment. Hence, the whole process must be performed simultaneously.

The general definition of the SLAM problem is done probabilistically.

The observation model [1] is defined by:

$$p(z_t | x_t, m) \quad (1)$$

Here,  $z_t$  = observation at time instant 't'.

$x_t$  = agent state at time instant 't'.

$m$  = map space.

Similarly, the motion model [1] is defined by:

$$p(x_t | x_{t-1}, u_t) \quad (2)$$

All the notations hold the same meaning as before.

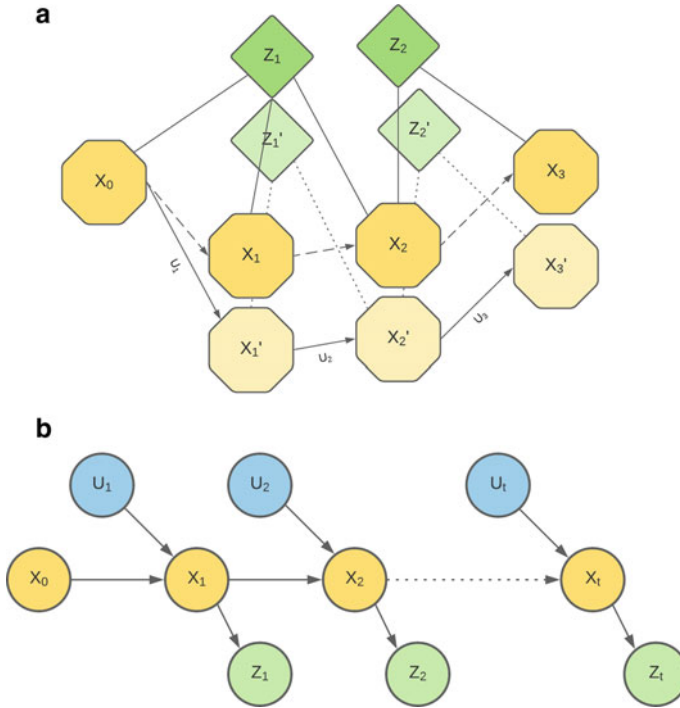
Equations (1) and (2) are combined to give:

$$p(x_{1:t}, m | z_{1:t}, u_{0:t-1}, x_0) \quad (3)$$

Here,  $x_0$  is the initial state of the agent. Figure 1a shows how a robot performs SLAM, and Fig. 1b shows the Bayesian network for a single robot SLAM.

There exist two ways of processing this data, namely full SLAM and online SLAM. The above method is that of full SLAM. Online SLAM is done as follows:

$$p(x_t, m | z_{1:t}, u_{1:t}) = \int \int \int \dots \int p(x_{1:t}, m | z_{1:t}, u_{1:t}) dx_1 dx_2 \dots dx_{t-1} \quad (4)$$



**Fig. 1** **a** Robot performing SLAM. The diagram shows errors in estimated locations of robot and landmarks. The transparent locations are the estimated location. **b** Bayesian network for single robot SLAM

### 2.2 Extension of SLAM to Multiple Robot Systems

The above equation can be extended into multi-agent systems using their individual trajectories ( $x^i_{1:t}$ ), controls ( $u^i_{1:t}$ ), and observations ( $z^i_{1:t}$ ) for ‘n’ agents as follows:

$$\begin{aligned}
 & p(x^a_{1:t}, x^b_{1:t}, \dots, x^n_{1:t}, m_t | z^a_{1:t}, z^b_{1:t}, \dots, z^n_{1:t}, u^a_{1:t}, u^b_{1:t}, \dots, u^n_{1:t}, x^a_0, x^b_0, \dots, x^n_0) \\
 &= p(x^a_{1:t}, m | z^a_{1:t}, u^a_{1:t}, x^a_0) \times p(x^b_{1:t}, m | z^b_{1:t}, u^b_{1:t}, x^b_0) \\
 & \times \dots \times p(x^n_{1:t}, m | z^n_{1:t}, u^n_{1:t}, x^n_0) \tag{5}
 \end{aligned}$$

Equation (5) shows that a multi-robot SLAM system can be created by combining multiple single robot SLAM systems. In practical applications, this becomes difficult to implement. All of the problems that arise in these multi-robot SLAM systems are in addition to the few other problems that already exist in single robot SLAM systems like the ‘loop closure’ problem.

### 3 A Few Popular Approaches to SLAM

There exist numerous algorithms to solve the SLAM problem in robotic applications which can be classified on various bases like data processing, map representation, etc. [5]. This paper will look at some popularly used and implemented algorithms.

#### 3.1 Filtering Approaches

- **The Extended Kalman Filter (EKF) SLAM** was and, in some applications, is still the most popular approach to SLAM. It is based on the recursive Bayes' filter and is a parametric filter. Other algorithms have been developed that are based on this such as extended information form (EIF) algorithm, unscented Kalman filter, and sparse extended information form (SEIF) algorithm.
- **Particle Filter (PF) SLAM:** in PF SLAM, the sample space is decomposed into individual discrete samples called 'particles.' These particles are discrete instantiations in the sample space. There are three steps in this process, sampling of particles, calculation of the importance weights, and resampling using the calculated importance weights. Rao-Blackwellized particle filters are a variant of particle filters that provide greater accuracy than traditional particle filters. The FastSLAM algorithm [6] and its successor FastSLAM 2.0 [7] are two of the most popular applications of Rao-Blackwellized particle filters.

#### 3.2 Occupancy Grid Mapping

**Occupancy grid mapping** also uses discretization, but here, the whole map is decomposed into smaller cells which hold binary values. This means that a cell is either occupied ( $p_z = 1$ ) or unoccupied ( $p_z = 0$ ). The larger the resolution, larger is the accuracy of the map and greater is the dataset to be processed. In the paper [8], grid maps are used with Rao-Blackwellized filters for a SLAM method.

#### 3.3 GraphSLAM

**GraphSLAM** algorithm is a modern approach to the SLAM problem. In this algorithm, every node represents the pose of the robot in the environment, i.e.,  $x_t$  and the edges connecting these nodes are the spatial constraints which are found using the observations  $z_t$  and odometry measurements  $u_t$ . GraphSLAM algorithm consists of two main steps—it takes the raw sensor measurements and constructs a graph, and then the edges of the formed graph are used to find the optimum configuration of the graph [9].



## 4 SLAM Devices

For implementing SLAM in practice, there are three main types of devices that are generally used—LIDAR, stereo cameras, and RGB-D cameras.

- **LIDAR** stands for ‘Light Detection And Ranging.’ LIDAR sensors are very commonly used in applications that require 2D SLAM models. Recently though, there has been a significant increase in 3D LIDARs [10] which are also used in self-driving vehicles.
- **Stereo cameras** are actually multi-camera setups in which the differences between the cameras are used to calculate the depth information.
- **RGB-D cameras** use an RGB image combined with a depth image found using infrared sensors. The XBox Kinect is the most famous of all RGB-D sensors. There has been a significant increase in RGB-D technology with the subsequent release of devices like the Asus Xtion Pro series Intel’s D400 series, etc. A review on RGB-D cameras can be found on [11]. The only problem with RGB-D cameras is their low range, making them useless in large open outdoor spaces.

There are methods that also use monocular cameras for SLAM such as ORB-SLAM [12] and ORB-SLAM2.0 [13] (ORB—oriented FAST and rotated brief). However, maps generated by monocular cameras alone are not of great quality. Some methods involve using monocular cameras with LIDAR to implement SLAM.

## 5 Challenges in Implementing a Multi-Robot SLAM System

The very first problem that instantly pops-up when implementing multi-robot SLAM systems is that of local and global reference frames for generating the final map. In this section, we inspect some of the most important problems in multi-robot SLAM.

### 5.1 *Relative Poses*

When using a single robot for implementing a SLAM system, there exists one frame of reference—the robot’s own—this is by default considered to be the global frame of reference. In multi-robot SLAM, a robot operates in its own local frame of reference. For combining the data and maps from all the robots, we need a global frame of reference with respect to which they can be transformed. In cases where of preexisting initial correspondence, this is not a problem. But in cases of no initial correspondence, this presents a major problem. Also, if the robots never meet, the accuracy of the map is greatly challenged.

## **5.2 *Dynamic Environments***

It is a straightforward task, relatively speaking, to map an environment with absolutely stationary elements. When dynamic elements like people, animals, or vehicles are introduced into this environment, they contribute to the error of estimating the map as they become obstructions in the line of sight of the robot. For multi-robot SLAM, other robots may themselves become obstructions for each other when observed. For avoiding this, they must be capable of detecting each other. And if they can, this may actually turn into an advantage while working cooperatively.

## **5.3 *Loop Closure***

While mapping an environment a robot tends to visit the same location. When this happens, the robot must be able to recognize it. In simpler words, it means that the robot must be able to understand that it has circumnavigated an area. This is a problem that is central to and challenging not just in multi-robot SLAM but to the whole problem of SLAM. Errors in odometry and dynamic environments make this quite a challenging problem.

## **5.4 *Complexity***

A multi-robot SLAM algorithm should be efficient and use minimum memory and minimum time. This is because most robotic systems are in real-time. In addition to this, the algorithm should be flexible enough to be scaled on a number of robots, which may be variable.

## **5.5 *Heterogeneous Robots***

A multi-robot SLAM system may not necessarily have a uniform design for all the member robots. There may be differences in sensors, resolutions, or even operation regions like terrestrial or aerial. There may also be differences in locally implemented algorithms; e.g., a terrestrial robot may be using LIDAR to implement grid mapping, while a UAV equipped with a camera may be performing 3D visual SLAM.

## 5.6 *Communications*

This is a subject with a very wide scope. Communication is not just limited to sharing raw data but may also include sharing locally processed datasets. What type of data and how it is sent are also a part of the communications design. In addition, robot coordination [14] is also an important subset of communications. While designing a communications system, there are interdependencies between the algorithm used for SLAM, network architecture, network topology, and computation capabilities of the components involved. The network topology may be centralized, decentralized, or even in the form of a nearest-neighbor type of network where data is only shared among nearby neighbor robots [15].

## 5.7 *Synchronization*

As we notice in Eqs. (1)–(5), SLAM algorithms are state based. This means that every single point of data captured must be labeled with the time stamp at which it was acquired. In multi-robot SLAM, the clocks must be as perfectly synced as possible. Chrony may be useful when using robot operating system (ROS). For decentralized online systems, network time protocol may be used.

## 5.8 *Performance Measure*

As the absolute and exact model of the environment may not usually be available, it is a difficult task to assess the accuracy of the developed algorithm. A workaround may be to use benchmarking datasets and comparing them with other models.

# 6 **Solutions to the Multi-robot SLAM Problem**

Multi-robot SLAM has various unique solutions [5], all of which have some basic way to deal with multi-robot SLAM. We understand a few of these basic ideas in this section to analyze how various algorithms approach this problem. As we progress, we will see the interdependency of some of these methods.

## 6.1 *Robot Rendezvous*

As we see in the previous section for successfully acquiring multi-robot SLAM-based SLAM maps, it is imperative to know the relative poses of robots. In a case where there is no initial correspondence, the two ideal solutions of calculating relative poses are—(1) to either look for overlaps or common landmarks and computing transformations accordingly for the global map or (2) to physically calculate the relative poses when the robots are in each other's line of sights. When the robots meet and detect each other, the situation is called a robot rendezvous. A number of algorithms use robot rendezvous to their advantage. Howard presents a way of using particle filters and robot rendezvous for solving the unknown initial correspondence problem. The combination of both the above stated methods is used in combination to improve the accuracy of maps generated by Zhou and Roumeliotis [16]. By doing so, they also account for the uncertainty caused while measuring relative distances and while updating maps and poses. For this project, they used two Pioneer 3-DX robots and performed EKF SLAM.

## 6.2 *Known Initial Positions*

For systems with initial coordination among the robots, the problem of correspondence is relatively decreased. Still, when robots go exploring on their own, this correspondence is prone to some error. To avoid this, rendezvous is used recursively in [17]. Another popular publication by Thrun et al. [18] uses location hypothesis using SEIF along with known initial correspondence.

## 6.3 *Map Merging*

Map merging is the most obvious solution to the multi-robot SLAM problem. In a map merging system, smaller local maps are combined to form the whole global map. Map merging, in layman's terms, may be thought to be similar to solving a jigsaw puzzle. The process involves searching for the proper alignment and then merging them. The proper transformation matrices are required to perform this process, meaning that we also require the relative poses between the robots. The relative poses may be known, found out during the process, or unknown. We have already understood how robot rendezvous and relative localization may be useful for the first two of these cases. Birk and Carpin proposed a method [19] in which relative localization is not required, and similarities between maps are located to find certain regions of overlaps. Map merging in cases of no relative localization between robots becomes a problem related to computer vision. Romero and Costa in their paper [20] compared map merging methods using FastSLAM.

## 6.4 Solutions to Loop Closure

Loop closure, as we previously understood, is one of the prime problems in the whole research area of SLAM. Loop closure is mainly a data association problem. There exist multiple solutions like using particle filters [21], intra-robot loop closure [17], pose graph methods [22], and manifold representations [23]. Manifold representations work in an ingenious way. If, while mapping, robots fail to detect each other, then the algorithm forms double spirals and keeps on forming them. As soon as the robots meet each other, the spirals are made to collapse into a single loop.

## 6.5 Heterogeneous Robots

Uniformity among robots may not always be practically viable. The most common application would be to use combinations of aerial and ground robots. An example of one such application is given in [24]. For the SLAM part of the ground, a robot named Kenaf developed 3D maps using a 3D iterative closest point algorithm [25] to generate a 3D map and also generated 2D occupancy grid maps. Similarly, their aerial vehicle named Pelican used a separate method [26, 27] to develop 3D maps while again generating a 2D occupancy grid map. These maps are then combined using initial knowledge from the takeoff point and further refined using ICP.

## 7 Future Work

Although there exist a lot of proposed methods and projects on SLAM, the likes of which have been seen in the RoboCupRescue competition, the industrial implementations of multi-robot is very limited. The applications of SLAM using multiple robots are limitless.

With the advent in the field of AI, there is significant research being carried out in using AI for SLAM [28] which could lead to robots having intuitions about the locations they would work in.

SLAM is not just limited to terrestrial applications but is now being extended to underwater applications also [29].

There is also a need to fully automate the multi-robot SLAM process.

Finally, some challenges like unavailability of some specific resources also cause a problem in conducting SLAM research as it is pointed out by Kuzmin [30].

We are currently trying to implement single robot SLAM using open-sourced SLAM projects and will work to further expand it to multiple robot systems.

## 8 Conclusion

In this paper, we conducted a review on multi-robot SLAM by first understanding its mathematical form, which was expanded from the mathematical model of a single robot SLAM. We also took a short look at a few popular approaches to SLAM and devices used for practically implementing it. Finally, an understanding of the main problems in implementing multi-robot SLAM was done. This was followed with possible solutions to these challenges.

## References

1. Durrant-Whyte H, Bailey T (2006) Simultaneous localization and mapping: part I. *IEEE Robot Autom Mag* 13(2):99–110. <https://doi.org/10.1109/MRA.2006.1638022>
2. Bailey T, Durrant-Whyte H (2006) Simultaneous localization and mapping (SLAM): part II. *IEEE Robot Autom Mag* 13(3):108–117. <https://doi.org/10.1109/MRA.2006.1678144>
3. Thrun S, Burgard W, Fox D (2005) *Probabilistic robotics*. MIT Press
4. Pfingsthorn M, Slamet B, Visser A (2008) A scalable hybrid multi-robot SLAM method for highly detailed maps. In: Visser U, Ribeiro F, Ohashi T, Dellaert F (eds) *RoboCup 2007: robot soccer world cup XI. RoboCup 2007. Lecture Notes in Computer Science, vol 5001*. Springer, Berlin, Heidelberg. [https://doi.org/10.1007/978-3-540-68847-1\\_48](https://doi.org/10.1007/978-3-540-68847-1_48)
5. Saeedi S, Trentini M, Seto M, Li H (2016) Multiple-robot simultaneous localization and mapping: a review. *J Field Rob* 33:3–46. <https://doi.org/10.1002/rob.21620>
6. Montemerlo M, Thrun S, Koller D, Wegbreit B (2002) FastSLAM: a factored solution to the simultaneous localization and mapping problem. In: *Eighteenth national conference on Artificial intelligence*. American Association for Artificial Intelligence, USA, pp 593–598
7. Montemerlo M, Thrun S, Koller D, Wegbreit B (2003) FastSLAM 2.0: an improved particle filtering algorithm for simultaneous localization and mapping that provably converges. In: *Proceedings of the 18th international joint conference on Artificial intelligence (IJCAI'03)*. Morgan Kaufmann Publishers Inc., San Francisco, CA, USA, pp 1151–1156
8. Grisetti G, Stachniss C, Burgard W (2007) Improved techniques for grid mapping with rao-blackwellized particle filters. *IEEE Trans Rob* 23(1):34–46. <https://doi.org/10.1109/TRO.2006.889486>
9. Grisetti G, Kümmerle R, Stachniss C, Burgard W (2010) A tutorial on graph-based SLAM. *IEEE Intell Transp Syst Mag* 2(4):31–43. <https://doi.org/10.1109/MITS.2010.939925>
10. Debeunne C, Vivet D (2020) A review of Visual-LiDAR fusion based simultaneous localization and mapping. *Sensors* 20:2068
11. 3D Camera Survey. <https://rosindustrial.org/3d-camera-survey>
12. Mur-Artal R, Montiel J, Tardos J (2015) ORB-SLAM: a versatile and accurate monocular SLAM system. *IEEE Trans Robot* 31(5):1147–1163
13. Mur-Artal R, Tardos J (2017) ORB-SLAM2: an open-source SLAM system for monocular, stereo, and RGB-D cameras. *IEEE Trans Robot* 33(5):1255–1262
14. Yan Z, Jouandeau N, Cherif AA (2013) A survey and analysis of multi-robot coordination. *Int J Adv Rob Syst*. <https://doi.org/10.5772/57313>
15. Zou D, Tan P, Yu W (2019) Collaborative visual SLAM for multiple agents: a brief survey. *Virtual Reality Intell Hardware* 1(5):461–482
16. Zhou XS, Roumeliotis SI (2006) Multi-robot SLAM with unknown initial correspondence: the robot rendezvous case. In: *2006 IEEE/RSJ international conference on intelligent robots and systems*, Beijing, pp 1785–1792. <https://doi.org/10.1109/IROS.2006.282219>

17. Dubé R, Gaweł A, Sommer H, Nieto J, Siegwart R, Cadena C (2017) An online multi-robot SLAM system for 3D LiDARs. In: 2017 IEEE/RSJ international conference on intelligent robots and systems (IROS), Vancouver, BC, pp 1004–1011. <https://doi.org/10.1109/IROS.2017.8202268>
18. Thrun S, Liu Y (2005) Multi-robot SLAM with sparse extended information filters. In: Dario P, Chatila R (eds) Robotics research. The eleventh international symposium. Springer tracts in advanced robotics, vol 15. Springer, Berlin, Heidelberg. [https://doi.org/10.1007/11008941\\_27](https://doi.org/10.1007/11008941_27)
19. Birk A, Carpin S (2006) Merging occupancy grid maps from multiple robots. Proc IEEE 94(7):1384–1397. <https://doi.org/10.1109/JPROC.2006.876965>
20. Romero VA, Costa OLV (2010) Map merging strategies for multi-robot FastSLAM: a comparative survey. In: 2010 Latin American robotics symposium and intelligent robotics meeting, Sao Bernardo do Campo, pp 61–66. <https://doi.org/10.1109/LARS.2010.20>
21. Howard A (2006) Multi-robot simultaneous localization and mapping using particle filters. Int J Robot Res 25(12):1243–1256. <https://doi.org/10.1177/0278364906072250>
22. Latif Y, Cadena C, Neira J (2013) Robust loop closing over time for pose graph SLAM. Int J Robot Res 32(14):1611–1626. <https://doi.org/10.1177/0278364913498910>
23. Howard A (2004) Multi-robot mapping using manifold representations. In: IEEE international conference on robotics and automation, 2004. Proceedings. ICRA '04, vol 4, New Orleans, LA, USA, pp 4198–4203. <https://doi.org/10.1109/ROBOT.2004.1308933>
24. Michael N et al (2014) Collaborative mapping of an earthquake damaged building via ground and aerial robots. In: Yoshida K, Tadokoro S (eds) Field and service robotics. Springer tracts in advanced robotics, vol 92. Springer, Berlin, Heidelberg. [https://doi.org/10.1007/978-3-642-40686-7\\_3](https://doi.org/10.1007/978-3-642-40686-7_3)
25. Ohno K, Tadokoro S, Nagatani K, Koyanagi E, Yoshida T (2009) 3-D mapping of an underground mall using a tracked vehicle with four sub-tracks. In: 2009 IEEE international workshop on safety, security & rescue robotics (SSRR 2009), Denver, CO, pp 1–6. <https://doi.org/10.1109/SSRR.2009.5424150>
26. Shen S, Michael N, Kumar V (2011) Autonomous multi-floor indoor navigation with a computationally constrained MAV. In: 2011 IEEE international conference on robotics and automation, Shanghai, pp 20–25. <https://doi.org/10.1109/ICRA.2011.5980357>
27. Shen S, Michael N, Kumar V (2012) Autonomous indoor 3D exploration with a micro-aerial vehicle. In: 2012 IEEE international conference on robotics and automation, Saint Paul, MN, pp 9–15. <https://doi.org/10.1109/ICRA.2012.6225146>
28. Vedaraj IS, Ganesh J, Swarup N, Kumar M, Tirumalapudi R (2020) Artificial intelligence using in visual slam methods—a review
29. Guth F, Silveira L, Botelho S, Drews P, Ballester P (2014) Underwater SLAM: challenges, state of the art, algorithms and a new biologically-inspired approach. In: Proceedings of the IEEE RAS and EMBS international conference on biomedical robotics and biomechatronics, pp 981–986. <https://doi.org/10.1109/BIOROB.2014.6913908>
30. Kuzmin M (2018) Review. Classification and comparison of the existing SLAM methods for groups of robots. In: 2018 22nd Conference of open innovations association (FRUCT), Jyväskylä, pp 115–120. <https://doi.org/10.23919/FRUCT.2018.8468281>

# Design and Development of a Prototype Agribot



Mohd. Firasath Ali and P. Venkata Ramana

**Abstract** In India, even in the current times where high technological development is claimed, 60% of population have employment in the agricultural sector. Agriculture sector contributes about 17% to the total GDP. As of now, because of the lack of labour, enthusiasm for the advancement of self-ruling vehicles such as robots in the rural area is expanding. Robots called agribots are intended to diminish the workforce of farmers notwithstanding speeding up and exactness of work. Existing agricultural robots are equipped with either seeding mechanism using conventional tools or ploughing with one tool which are not very reliable and have less speed. The use of irrigation is also not attained with integration of seeding mechanism. The objective of this work is to design and develop profoundly talented rural robot in work, which can perform furrowing, planting and watering tasks. A battery run, Bluetooth-controlled multi-class self-ruling agrarian vehicle was designed and developed to perform successfully the intended tasks. This independent vehicle is utilized to decrease human mediation, guaranteeing exceptional returns and proficient utilization of assets.

**Keywords** Agribot · Prototype · Automation · Multitasking

## 1 Introduction

The increase in technological inventions bring easier, sophisticated and cheaper techniques for the utilization of available equipment. The growth of a nation like India mostly relies upon the agricultural production. The main purpose of technical growth is to decrease humanistic struggles. Precision agriculture by farming robots is the present-day developing technology in the agriculture area to protect and retrieve exhausting time and energy in repeated farming jobs. Traditional methods of sowing seeds manually and other activities like ploughing, water pouring, pesticide spraying, etc., consume a lot of time and are not accurate due to human errors. Agricultural

---

Mohd. Firasath Ali · P. Venkata Ramana (✉)  
Department of Mechanical Engineering (Mechatronics), Mahatma Gandhi Institute of  
Technology, Hyderabad, Telangana 500075, India

© The Author(s), under exclusive license to Springer Nature Singapore Pte Ltd. 2022  
G. S. V. L. Narasimham et al. (eds.), *Innovations in Mechanical Engineering*,  
Lecture Notes in Mechanical Engineering,  
[https://doi.org/10.1007/978-981-16-7282-8\\_50](https://doi.org/10.1007/978-981-16-7282-8_50)

675



automation and artificial intelligence accomplishments offer the methods associated with seeding, harvesting, weed control, grove supervision, chemical applications, etc., in precision agriculture to gain production and capability [1, 2].

The ingenious use of farm power and land accessibility will certainly raise the productivity of farmers. Agricultural robots gain the yield of land and labour by meeting set points of farm tasks and elevate work output per unit time. Apart from the high importance given to agricultural robots, mechanization of existing systems also makes possible the efficient utilization of system inputs like seeding, fertilization and showering water [3].

Automation brings rise to the yield of agricultural machinery by expanding efficiency, reliability, precision and decreasing the necessity for human intervention; this is often achieved through the addition of sensors and control mechanisms. Field industrialization, often related to “smart farming”, a technology that promote farms is efficient and able to automate the crop or livestock production period. There are a lot of technologies used in the field of agriculture in modern days. It utilizes IoT, various sensors, actuators, software and to program the hardware system to work accordingly. Mechatronics is applied in automating the manual agricultural tasks. To allow the advances, agricultural automation and the mechanization of the agricultural role have been started since the industrial revolution and different methods are integrated. Mechatronics and computer science innovations are currently being used for updating agricultural equipment nowadays. Simple mechanized tools for agricultural purposes are often produced by simple mechanical means such as a paddle-driven cycle fitted with agricultural tools is mounted and can be controlled in an environmentally friendly manner [4]. Mutharasu et al. described about the lack of automation of agribusiness in many parts of India [5]. Prakash et al. developed a robot for ploughing in the agricultural farms which helped farmers increase the quality of operations at their farms sector [6]. Xue et al. developed the route following robot and the guiding method using computer vision technology in the maize field to navigate the agricultural robot along these lines using symbolic logic control [7]. Sajjad Yaghoobi et al. highlighted future trends of agrirobots for agricultural tasks and farm assignment [8].

Abirami et al. [9] did the research on agricultural robot for automatic ploughing, seeding and described concept of humidity measurement, fruit picking and pesticide spraying. Manohar Sambandam [10] in his work, created a 3D profile of the plant and created robot, to avoid its arm running into the plant’s branches. Indian Agricultural Research Institute has started Agricultural and Food Engineering Department, IIT Kharagpur [11] that monitors autonomous robot continuously by use of different sensing technologies that have the potential to figure on precision agriculture providing different crop status parameters like micronutrient availability, biomass index, status of pest and disease, water stress and thermal stress for better remedies of crops. In a single system, mechatronics, machine vision and image processing technologies assembled often acknowledging autonomous agricultural operations.

The different spraying mechanisms for crop pesticides are elaborated and explained by Chaudhary et al. [12]. Anandavelu et al. [13] designed and fabricated low-cost wheel-driven sprayer operated mechanically. The precision seed sowing

techniques of Manoharan [14] produced actual formulation for the space between seeds on the farm. Another precision technique for seed plantation is described by Ramesh Kumar et al. [15]. The system is provided with an ultrasonic sensor, which helps in detecting the obstacles and its avoidance. An automated agricultural system which runs on embedded system for multipurpose activities of the farm has been designed, developed and fabricated. DC motors were used to drive the four-wheel-based system and L293D driver to drive DC motors controlled by Renesas 64 pin microcontroller [16, 17].

The mechatronic application in the agricultural industry is explained by Azeta et al. [18]. Durga Sowjanya et al. [19] concluded various helpful consequences by the application and integration of mechatronics in agriculture. Farmers are reducing their efforts by the automation as agribots intend to take out human work essentials from planting seeds and completing various errands [20–25].

Keeping in view of the existing technologies, in this present work, an attempt is made to design and fabricate a multitasking robot planned for increasing the profitability and lessening the work of the farmers. This robot is designed for carrying out the necessary operations needed to be done in ranches. The robot begins its function by furrowing the field, at that point plants the seeds in the furrowed area and closures the cycle with covering the seeds planted with soil. To play out the capacity of furrowing, it is outfitted with three plough-like structures which are fixed in the foremost part of the robot, to plant seeds it has a compartment with seeds and its base contains a hole to drop the seed in a row. The water spraying system activates as the soil moisture sensor indicates Arduino for the dryness of the land. The vital parts such as humidity sensor, DC motors, stepper motors, motor drivers, Bluetooth module and ATMEGA 2560 Arduino as the master microcontroller has been utilized by this robot. It is a wheeled vehicle which is resistant to shocks caused by carrying the load on uneven land. A belt drive connects all the wheels to the driving wheel. The driving mechanism is designed with the two geared DC motors and NEMA 17 stepper motors. The chassis of the robot is made with 6061 T6 aluminium. 6061 precipitation-hardened aluminium alloy has lightweight, good strength and corrosion resistance.

The primary task has been to build up a sun-oriented working machine for agricultural purposes. It utilizes a sun-powered board to catch and convert sun-oriented power into electrical power in order to charge a 5 V battery powering DC motor. A Bluetooth module associates all the orders through cell phone making the electrical and mechanical frameworks in proficient manner. Ranchers can work this robot through advanced cell by sitting at a place. It is sans hands and controlled with remotely. In the field of farming, an idea been created to utilize different little machines which could be more effective than conventional enormous work vehicles and human powers.

## 2 Design of Multitasking Agribot

### 2.1 Design Parameters

**Seed sowing.** This is carried in three different rows which are in line with the plough tool. This has been designed keeping the rate at which the seed drops. One wheel is attached to the seeder rod, and it rotates the seeder rollers. One complete rotation of the wheel drops one seed.

Rate of seed drop ( $R$ ) = one per rotation of wheel, i.e.  $360^\circ$ .

Wheel radius ( $r$ ) = 0.03 m; Rotation angle ( $\theta$ ) =  $360^\circ$  or  $2\pi$ ;

Circumference of wheel ( $l$ ) =  $r \times \theta$ .

$l = 0.03 \times 2\pi = 0.188$  m, hence for every 0.188 m or 188 mm one seed drops.

$\therefore$  Rate of seed drop ( $R$ ) = 5.32 seeds per metre.

**Discharge of water and pesticides.** For watering and spraying of pesticides, a pump is used. The pump takes upto 120 L per hour with current consumption of 130–200 mA, which is very low.

Discharge ( $Q$ ) = 120 lps

**Field covered.** The prototype agribot is designed to cover field of  $2 \times 2$  m.

**Dimensions of agribot.** Dimensions of base body or chassis are as follows:

Length ( $L$ ) = 0.036 m; Breadth ( $B$ ) = 0.028 m.

Height at free suspension ( $H$ ) = 0.012 m.

Maximum length when seeder is attached ( $L_{\max}$ ) = 0.057 m.

Maximum breadth taking side wheels accounted ( $B_{\max}$ ) = 0.034 m.

Maximum height from the ground ( $H_{\max}$ ) = 0.026 m.

Total working volume ( $V$ ) =  $L_{\max} \times H_{\max} \times B_{\max} = 5.0388 \times 10^{-5} \text{ m}^3$ .

$$\therefore V = 50388 \text{ mm}^3.$$

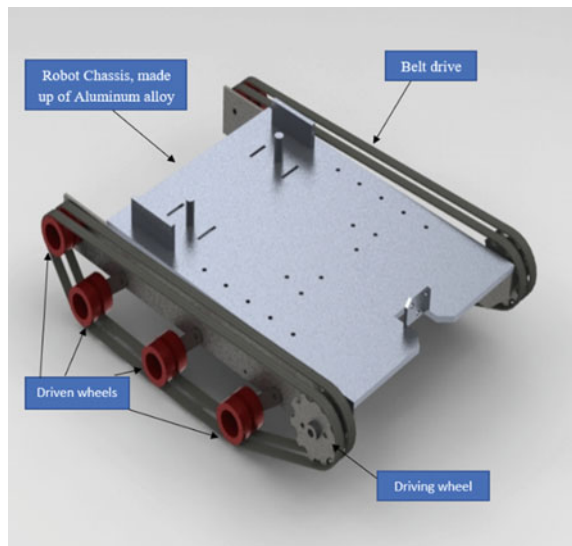
**Material.** The durability of any device rests on the type of the material of which it made up of. The higher the quality, the longer is the life of product. Also, the frequency of the device usage also alters the lifespan. Keeping these requisites, this agribot had been made by Aluminium 6061 T6 alloy for chassis and stainless steel (SS) 06 grade for ploughing tool.

### 3 Fabrication of the Agribot

3D CAD model of the agribot and 2D drawing of the chassis, shown in Figs. 1 and 2, are designed through CATIA V5 software. Prototype of the agribot is fabricated with by assembling various components, with the help of the drawings. The assembly of the parts is done manually.

The driver wheel connects four small-driven wheels by means of belt drive to ensure all wheels rotate with same speed. This locomotive action lacks in robots driving only front wheels, occurring power loss in rear wheels, and resulting in unequal speeds. The driven wheels are attached to the base by means of brackets which rests on the springs for ease absorption of shocks at uneven surfaces. The geared DC motors or stepper motors are fitted in the mountings provided adjacent to the driver wheels for rotating the wheels.

**Fig. 1** CAD model of agribot



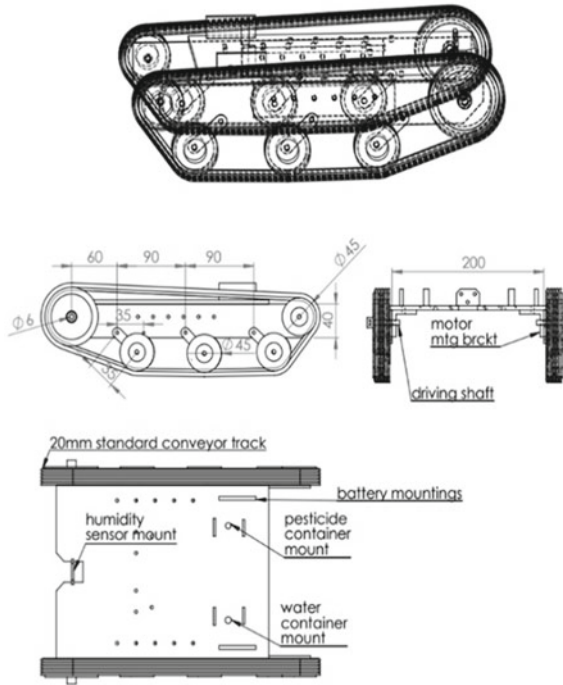


Fig. 2 The robot body (chassis) drawing

The seeder made up of aluminium sheets is shown in Fig. 3. Three wheels in line with ploughing tool have V-shaped grooves provides the way for dropping of seeds and rotate with the aid of an outer wheel attached adjacent to rod connecting three of them. The groove takes a seed on every turn to drop in precise manner row wisely. The outer wheel rotates due to inertia of robot body and power transmits through shaft connecting this wheel and the seeder wheels.



Fig. 3 Seeder—top view and front view

### 3.1 Hardware Components

Arduino Mega 2560, Stepper motors, Motor driver module (L298N), Robot body or chassis, Ultrasonic sensor module (HC—08), 16 × 2 LCD display, Soil moisture sensor, DC motor, Bluetooth module, Connecting wires or Jumper wire, Capacitor, Electronic Breadboard, Power supply (12 V DC). And Other Mechanical Components such as Rollers of 35 mm diameter, 6 mm thick Aluminium 300 × 100 sheet, Nylon flats 10 × 2 × 30, M4 bolts of Allen type, M4 nuts, washers and lock nuts, Belt drive 200 × 8, Sprocket diameter 40 × 20, Mtg plates, Fulcrum seat are the various components used to fabricate the agribot.

**Arduino Mega 2560.** The Arduino is hardware- and software-oriented prototype platform that includes a circuit board and ready-made applications that can be programmed. Arduino IDE software is used to write and upload programming code to it. A board based on the ATMEGA 2560 microcontroller is the Arduino Mega 2560. The Arduino Mega 2560 is used as master controller in current work, as shown in Fig. 4.

**Stepper motor.** A stepper motor is something like an electromechanical device, changing electrical power into mechanical power. It is also a brushless, synchronous electric motor splits into many phases in a full rotation. A DC motor is linked to a stepper motor configuration comprising permanent rotor-like magnet. A4988 or L298N driver IC is used to reduce the current intake as the stepper motors consume more amount of current.

**L298N motor driver.** It is a high-power driver module having advantage of DC and stepper motor driving arrangement mechanism. It incorporates L298 motor driver IC and a 78M05 5 V regulator, power LED, resistors, 5 V jumper, capacitor in the

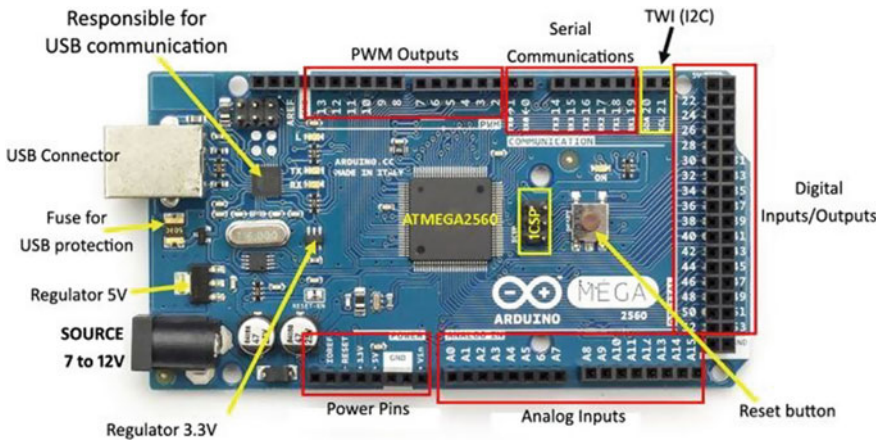


Fig. 4 Arduino Mega 2560

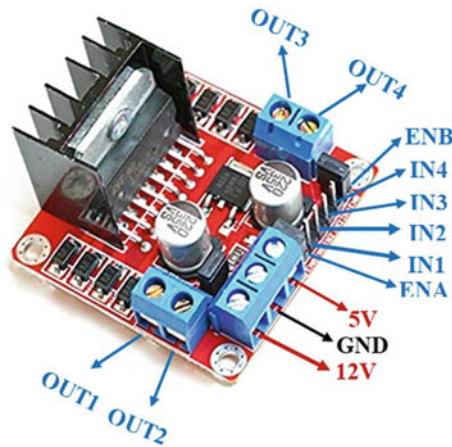


Fig. 5 L298N Driver module—Pin Out

form of an integrated circuit, current sense for each motor and heat sinks for greater conduct of the controlling action (Fig. 5).

**Ultrasonic sensor module.** Figure 6 displays the HC-SR04 module of an ultrasonic sensor. It measures the distance by travel time and the speed of sound from which the target is located by emitting a 40000 Hz (40 kHz) ultrasound via air, and it rebound back to the module when an object or obstacle hindered its way.

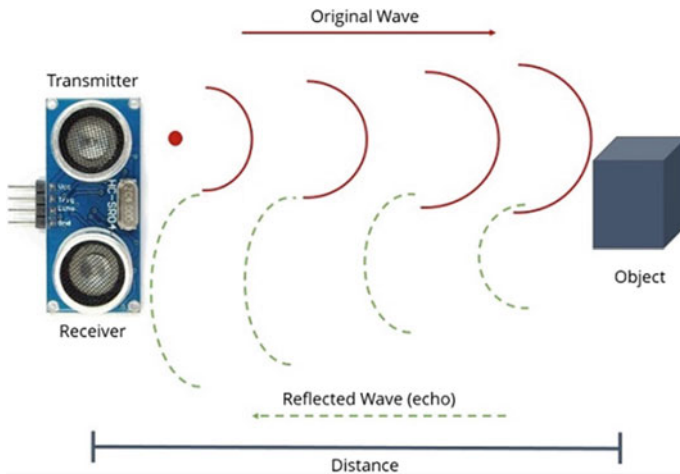
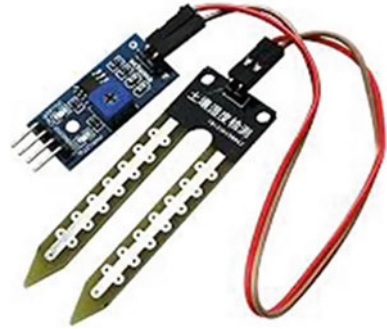


Fig. 6 Ultrasonic HC-SR04 module and principle

**Fig. 7** Soil moisture sensor



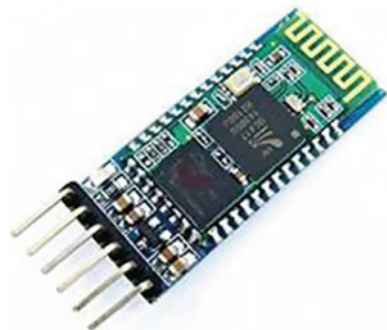
**Soil moisture sensor.** Soil moisture sensors or soil humidity sensors calculate water’s volumetric content present in the soil by dipping the two leads in the soil. Figure 7 depicts the soil moisture sensor used.

**Battery management system (BMS).** A 12 V and 10 A BMS are used to regulate the power supply. The main advantage is preventing the reversal of current flow when there is a back emf in the circuitry and when charging the cell pack from solar energy. Control amount of power induced in the cells through BMS when charging is done.

**Bluetooth module.** It aids in wireless communication of serial data as shown in Fig. 8; a reduction in wired serial link replacement allows for two directions of transparent data communication.

**Software requirements.** Arduino IDE from Arduino. It is powered by Linux, Mac OS X and Windows. Java is used for the writing of Arduino IDE environment, based on processing and other open-source tools.

**Fig. 8** Bluetooth module  
HC-05





### 3.2 Programming of the System (Coding)

The programming of the agribot is done in the C/C++ language. Stepper motor and DC motor libraries are used for program precompiled routines.

## 4 Working of the Agribot

The multitasking autonomous agribot shown in Fig. 9 performs tasks with power supply of 12 V DC. The substructure or the bedframe consisting two wheels and arms each is driven by DC or stepper motors. Two containers are like bottle storing water and liquid pesticide, respectively. Separate pumps for irrigation and pesticide spray are provided as per the requirements. Water is provided when soil moisture sensor gives dryness signal to the Arduino. The V-shaped tools (three in no.) attached at front end start ploughing when it lowered by the help of the stepper motor. The linear actuating mechanism of the cylinder governed the ploughing tool's movement. Stepper motor drives the cylinder rod connected to timer pulley by means of timer belt. An LCD panel depicts the readings of humidity sensor and distance.



**Fig. 9** Multitasking autonomous agribot

### 4.1 Working Stages of Proposed System

- Stage 1 User chooses choice of functionalities in the versatile application.
- Stage 2 These orders are given through Bluetooth module which further sends it to microcontroller for additional preparing.
- Stage 3 Based on the order, microcontroller actuates the segments identified with the chose functionalities (ploughing, seeding, watering, pesticide spraying).
- Stage 4 Obstacle identification occurs simultaneously, agribot stops for any distinguishing snag.
- Stage 5 Finally, the agribot plays out the chosen exercises.

Figures 10 and 11 are the flowcharts that describe the agribot working and function selection.

The functional view of the agribot is shown in Fig. 12.

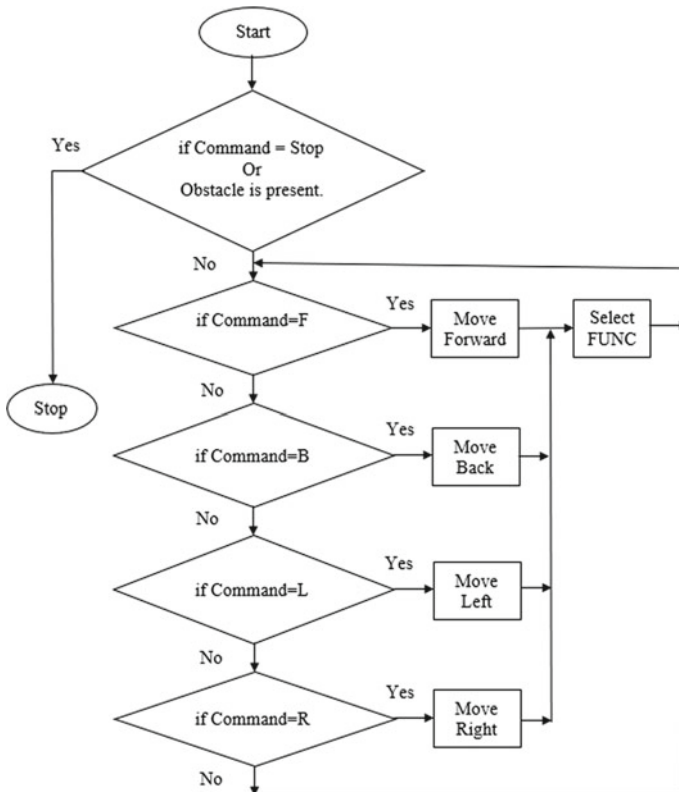


Fig. 10 Flowchart of agribot

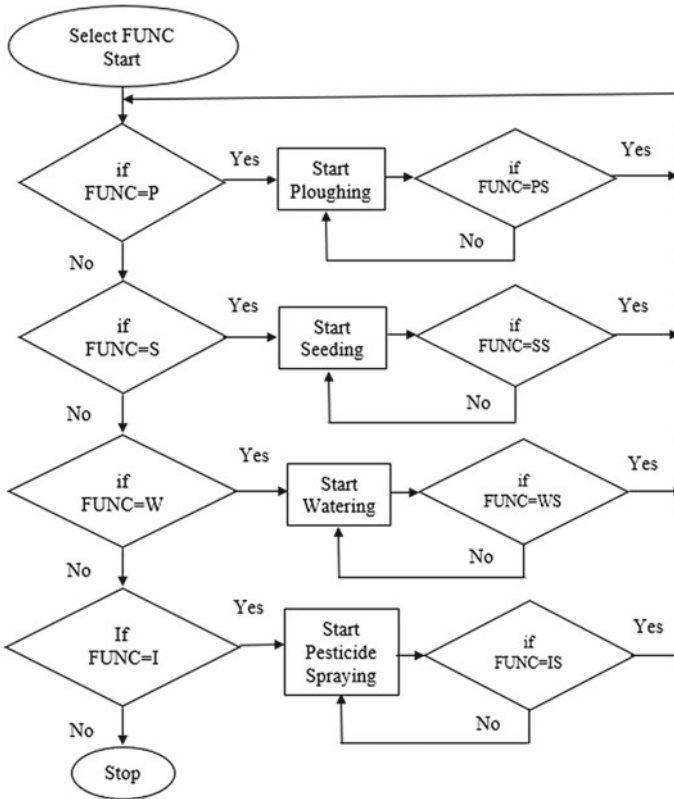


Fig. 11 Flowchart of select function

### 5 Conclusions

The aim of this work is to design and fabricate a multitasking agricultural robot. A prototype was fabricated as per the design to perform the multiple operations of agriculture, viz. ploughing, seeding, soil moisture detecting, water spraying and pesticide spraying. The developed robot was tested for the various parameters, and the following are observed: The agribot was able to perform various functions as per the design and requirements. The robot was capable to plough in three equidistant guided ways. The seeding was done in the same row lines at a particular distance, i.e. equal to the circumference of the driving wheel of the seeder. The water pump is provided irrigation to the field based on the soil condition, i.e. watering of the field at times of less moisture. Spraying of pesticides for the preset timely duration and as per the requirement was done. The robot sensed the minimum distance with the obstacle when it comes in path and sends the signal to the Arduino to stop the driving motors by the ultrasonic sensor module's aid.

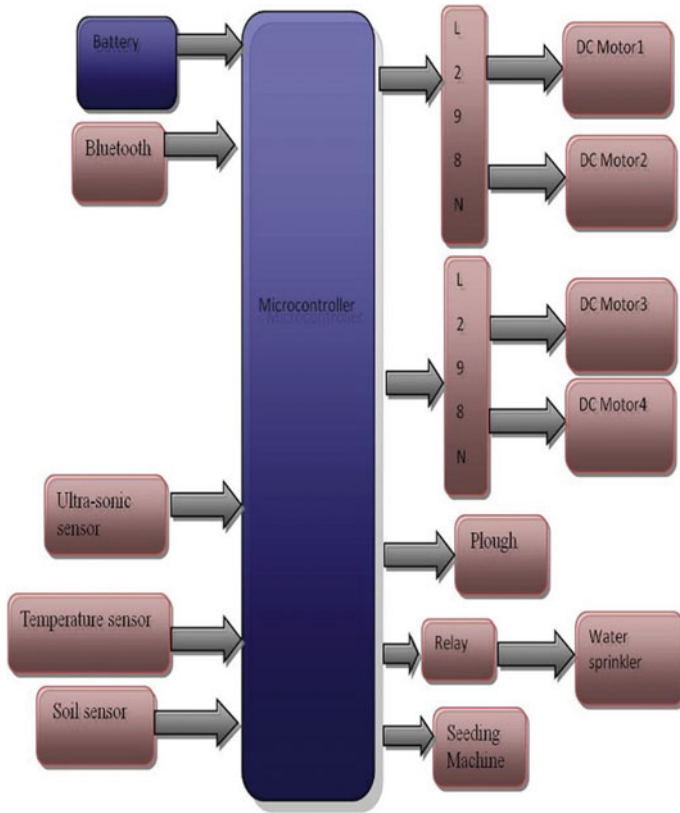


Fig. 12 Functional view of the agribot

**Acknowledgements** The authors thank the Management, Principal and Head of the Department of Mechanical Engineering (Mechatronics), Mahatma Gandhi Institute of Technology, Hyderabad, for the support in carrying out this work.

## References

1. Lalwani A, Bhide M, Shah SK (2015) A review: autonomous agribot for smart farming. *Int J Ind Electron Electr Eng* 4(2):12–15
2. Kumar AAA, Deepak RS, Kusuma S, Sreekanth DV (2020) Review on multipurpose agriculture robot. *Int J Res Appl Sci Eng Technol* 8(5):1314–1319
3. Sundaram PK, Singh SS, Sharma SC, Rahman A (2012) Prospects of farm mechanization. In: Bhatt BP, Sikka AK, Mukherjee J, Islam A, Dey A (eds) *Status of agricultural development in eastern India*, Chapter 3.9, pp 279–292
4. Kamaraj M, Chhabria AK, Kumar K, Kumar N (2017) Design and fabrication of multi-purpose farming tools equipped mobility cycle. *Int J Innov Res Adv Eng* 4(5):15–20

5. Mutharasu S, Divya V, Elakkiya MV, Dhivya BK, Janani E (2019) Design and implementation of agribot by using IoT. *Int J Adv Res Ideas Innov Technol* 5(2):10–13
6. Prakash P, Priyadarshini B, Thiriveni G, Gowrishankar V (2018) Precision agriculture using agribot for the welfare of farmers. *Asian J Appl Sci Technol* 2(2):730–736
7. Xue J, Zhang L, Grift TE (2012) Variable field-of-view machine vision based row guidance of an agricultural robot. *Comput Electron Agric* 84:85–91
8. Sajjad Yaghoubi NA, Akbarzadeh SS, Bazargani SS, Bazargani MB, Asl MI (2013) Autonomous robots for agricultural tasks and farm assignment and future trends in agro robots. *Int J Mech Mechatron Eng* 13(3):1–6
9. Amrita SA, Abirami E, Ankita A, Praveena R, Srimeena R (2015) Agricultural robot for automatic ploughing and seeding. In: *IEEE international conference on technological innovations in ICT for agriculture and rural development*, pp 17–23
10. <https://factordaily.com/agritech-cotton-picking-robot-india/> (2017)
11. Kushwaha HL, Sinha JP, Khura T, Kushwaha DK (2016) Status and scope of robotics in agriculture. at: agricultural and food engineering department, IIT Kharagpur. *Int Conf Emerg Technol Agric Food Eng* 12:264–277
12. Das N, Maske N, Khawas V, Chaudhary SK (2015) Agricultural fertilizers and pesticides sprayers—a review. *Int J Innov Res Sci Technol* 1(11):44–47
13. Pranavamoorthi V, Pravinayadav R, Sivaramakrishnan D, Tamilarasan V, Mahabubadsha A, Anandavelu K (2017) Design and fabrication of wheel driven sprayer. *Int J Adv Res* 5(4):836–843
14. Manoharan M (2018) An optimization of machine and operational parameters on seed placement index for precision sowing of black gram. *Int J Agric Sci Res* 8(6):75–84
15. Ramesh Kumar S, Sriram Kalyan H, Dhananjaya Kumar K, Dilip S (2018) Design and fabrication of autonomous robot for precision agriculture. *Int J Mech Prod Eng Res Dev* 8(3):385–392
16. Ramesh B, Tejaswini CN, Anisha MG, Ateeq S, Satyam V (2017) Automated agricultural system for multipurpose activities of farmers. *Int J Recent Innov Trends Comput Commun* 5(12):171–175
17. Srivastava A, Vijay S, Negi A, Shrivastava P, Singh A (2014) DTMF based intelligent farming robotic vehicle an ease to farmers. In: *International conference on embedded systems*, published by Bonfiring, pp 206–210
18. Azeta J, Bolu CA, Alele F, Daranijo EO, Onyeubani P, Abioye AA (2019) Application of mechatronics in agriculture: a review. In: *International conference on engineering for sustainable world*, journal of physics: conference series, vol 1378, issue 3. IOP Publishing, pp 1–10
19. Durga Sowjanya K, Sindhu R, Parijatham M, Srikanth K, Bhargav P (2017) Multipurpose autonomous agricultural robot. In: *International conference on electronics, communication and aerospace technology IEEE*, pp 696–699
20. Goyal MR (2017) *Emerging technologies in agricultural engineering*. Apple, Academic Press Inc., *Innovations in Agricultural and Biological Engineering*
21. Lowenberg-DeBoer J, Huang I, Grigoriadis V, Blackmore S (2019) *Economics of robots and automation in field crop production*. Precision Agriculture
22. Butler S (1863) *Darwin among the machines*. The Press, New Zealand
23. Tillett ND, Hague T, Marchant JA (1998) A robotic system for plant-scale husbandry. *J Agric Eng Res* 69(2):169–178
24. James Mitchell Crow (2012) *Food from machines: rise of the agribots*. *New Sci* 216(2888):42–45
25. Brian Bacher Pedersen (2001) *Weed density estimation from digital images in spring barley*. Department of agricultural sciences, section of agro technology, The Royal Veterinary and Agricultural University. DK-2630 Taastrup, Denmark

# Analysis of Breathalyzer Effect on a Passenger Vehicle



R. Dhanasekaran, S. Sreenatha Reddy, Kandadi Sai Praneeth Reddy, Pathireddy Kowshik Reddy, and Rangaraju Rohan

**Abstract** The main aim of this paper is breathalyzer connectivity with speed lock that is to reduce the drunk and drive accidents to some extent. An idea is created to introduce a mechanical component, i.e., breathalyzer and have a connection with speed lock. In literature review, many of the authors have noticed that, most of the accidents were occurred due to over speed and while drunk and drive. This component reduces the vehicle speed if the driver is drunk while drive, subsequently, the accidents also get reduced to some extent. Breathalyzer is updated and mounted in car steering. By that one can save his/her life. As per the newspaper's report of Central Ministry of Transport's Accidents' statistical information and data, every year, the graph of drunk and drive accidents is getting increased. So, this project aims at reducing accidents to some extent. The main component used in this project is MQ-3 alcohol detector to detect whether alcohol is consumed or not. Arduino-central unit will be maintained all connections such as speed lock for the maintenance of speed, reduce the speed, and the activation of speed lock. The breathalyzer is fixed at the top of steering wheel in order to grasp the alcoholic level if the driving person consumes alcohol. There will be activation of speed lock, only if the driver consumes alcohol above the permissible limit and according to the bylaws. After the activation of speed lock, the vehicle reduces its speed automatically to less than 10 kmph. Ultimately, breathalyzer controls and reduces the drunk and drive accidents to some extent.

**Keywords** Speed lock · MQ-3 alcohol detector · Central unit Arduino

## 1 Introduction

India is the second largest country with its population and faces with innumerable problems. There are many issues where the governments are taking initiatives in tackling them. Road accidents are one of the major issues which India faces. India

---

R. Dhanasekaran · S. Sreenatha Reddy · K. Sai Praneeth Reddy (✉) · P. Kowshik Reddy · R. Rohan  
Department of Mechanical Engineering, Guru Nanak Institute of Technology, Hyderabad, Telangana, India

© The Author(s), under exclusive license to Springer Nature Singapore Pte Ltd. 2022  
G. S. V. L. Narasimham et al. (eds.), *Innovations in Mechanical Engineering*,  
Lecture Notes in Mechanical Engineering,  
[https://doi.org/10.1007/978-981-16-7282-8\\_51](https://doi.org/10.1007/978-981-16-7282-8_51)

689

ranks 1st in the number of road accident deaths across the 199 countries reported in the World Road Statistics, 2018 followed by China and US [1]. As per the WHO Global Report on road safety 2018, India accounts for almost 11% of the accidents related deaths in the world. Driving under the influence of alcohol is leading to the cause of accidents. As stated in the report of Transport of Ministry, approximately, after every 30 min, a person dies due to the influence of the alcohol while driving. Every day, on an average of 4–5 accidents in Hyderabad, 5 in Mumbai, and 6–10 in Delhi is taking place.

All over India, out of overall accidents statistics information 6.2% are due to drunk and drive and more specifically 28% in Hyderabad. Drunk driving led to over 38,000 road accidents over the last three years and thus, despite the central government passing a stringent law last year to increase punishment and penalty for drunk driving. The data provided by the Ministry of Road Transport and Highways to the Rajya Sabha highlight that cases of drunk and driving increased in 2019 compared to 2018. The National Crime Records Bureau (NCRB) data also show that around 2% of the total road accidents that happen in India are due to drunk driving. In 2019, around 3000 people lost their lives in road accidents that were related to drunk driving, while 6675 people were left injured in road accidents. Keeping the above points in view, the implementation of breathalyzer gadget technology in motor vehicles, for controlling speed is necessary.

## 2 Literature Review

The mechanical component breathalyzer is an analysis machine, which analyzes the toxic level of a person. It is a device for estimating blood alcohol content [BAC] from the breath sample. In 1953 Robert Borkenstein, a former Indian Police captain and University Professor Harger had collaborated with on the drunk meter and proposed this breathalyzer. This helps us to detect the alcoholic level that a person has consumed.

Speed lock is also known as cruise control of the car. This technology was adopted by Matthew Boulton and James Watt in 1788 for steam engine. The modern speed lock is invented in the year 1948 by Ralph Teetor, a mechanical engineer. In 1965, American motors, a corporation has got an update on modern speed lock and to avoid the disadvantage and to have a low-priced automatic speed control, in 1968, Daniel Aaron Wisner invented automatic electronic speed lock.

The authors have worked on “drunken driven protection system” in 2011 and have discussed about the two wheeler driving. If driver is drunk and wearing helmet, then by the sensor in bike and helmet connected to central unit will be activated and will not allow the bike to be started. Sensors are placed at the earlobe region. If driver meets with an accident then by the use of central unit which is fixed on bike will send a SMS to driver’s family or friends [2]. The behavior of driver is one of the major reasons for the accidents and it is necessary to alert the driver when they are drowsy or under the influence of alcohol. So to reduce this type of accidents, some

authors have worked and introduced a system of self-driving, steering wheel control system, and GPS or GSM tracking system in 2014. The control of car is by assistive technology as software program that is used to maintain functional capabilities of persons with disabilities. By this process, they control the vehicle when the driver is intoxicated or drowsy [3, 4]. In 2015, authors have been proposed an innovation regarding alcohol detection. It has got an update that, if the driver consumes alcohol, then the intelligent system of vehicle transfers the data, location, and toxic level of the driver to nearby emergency system and by that they can easily detect the car location. So, they have a plan to reduce the drunk and drive accidents. Future scope of their system is to control the accidents and providing useful details about the vehicle, thereby reducing the rate of accidents taking place due to drunk and driving. Their system brings innovation to the existing technology in the vehicles and also improves the safety features by using modern technology [5].

An ignition interlock and car breathalyzer prevent drunk drivers from driving their vehicle. The device is connected to your vehicle, and it can determine the level of blood alcohol concentration (BAC). In 2016, authors have worked on “ARM-based drunk driver identification with tracking system” because of violating the rules, due to driving after taking alcohol. In this project, they have introduced a system. If driver is intoxicated, then vehicle ignition will disabled and a message is sent in the form of vehicle location to driver’s relatives and family members and nearby emergency services, by this system, they want to reduce the drunk and drive accidents to some extent [6, 7]. In 2017, authors have worked on alcohol detector and engine lock. They stated that the engine gets lock if driver consumes alcohol. For engine locking system, they used MQ-3 alcohol detector and connected engine with locking system. The present project is different from the earlier ones, which found in 2017. This project is about to introduce breathalyzer with MQ-3 alcohol detector which is connected with speed lock. It helps in reducing the speed in order to avoid the drunk and drive accidents [8].

In some states, you may be asked to blow into the car breathalyzer when the vehicle is in motion or for a “rolling retest.” If you fail the rolling retest, the vehicle will sound its alarm or horn and the lights will flash for certain time and even the engine does not get off. The guardian interlock is small, compact, and easy to use, and although it looks like a simple device, there is software built in to prevent cheating the ignition interlock. When you blow into your car breathalyzer, all information will be sent wirelessly to the court on a weekly or daily basis.

MQ-3 alcohol detector, speed lock, connecting circuit, connecting wires, resistor, indicating unit, red and green light beepers, and Arduino-central unit are the mechanical component used in this project.



**Fig. 1** Arduino-central unit

### 3 Arduino-Central Unit

Arduino-central unit is one of the major components used to apply in this project. As shown in Fig. 1, central unit works like a mother board, all the connections is fixed to the central unit. It has mother boards and performs respective and specific work. The central unit is as same as Duemilanove but has a different USB-to-serial chip [8].

### 4 Vehicle Speed Limiter

A speed lock is an intelligent speed assistant which slows down the vehicle when it crosses the limit of speed. Even, there are many auto speed lock systems which control the car speed according to the traffic and road speed limits. Here, this mechanical component is useful to slow the vehicle when the driver is under the influence of alcohol. It is also called as speed lock [8, 9] (Fig. 2).

### 5 MQ-3 Alcohol Detector

The alcohol sensor practically referred as a MQ-3 sensor which detects toxic (alcohol limit) around it. When a drunk person release breath near the alcohol sensor, it detects the toxic level according to breath and provides an output based on alcohol concentration [10]. If there is more alcohol concentration, the RED LED will glow, if the driver consumed less alcohol concentration, the GREEN LED will glow [8] (Fig. 3).

Fig. 2 Vehicle speed limiter



Fig. 3 Alcohol detector



## 6 Description About the Breathalyzer Connectivity with Speed Lock

The connectivity of breathalyzer is most efficient nowadays, in India, there is 6% of accidents is only because of drunk and drive, so to reduce these kinds of accidents, we are using breathalyzer, the working mechanism is as per follow: There will be a connection between breathalyzer and car battery. When we turn on the car battery, then the mechanical component breathalyzer will turn on and starts working for first 5 min. It will work and grasp the breath essence of the driver. If driver consumes alcohol above the permit limit, the red beeper will beep for 2 s and there will be activation of speed lock. If driver not consumed alcohol, then there will be no change. When the speed lock gets activated, then the maximum speed of the car is less than 10 km per hour. So by reducing the speed, we can reduce the accidents to some extent due to drunk and drive. This is the way the breathalyzer connectivity with speed lock will work.

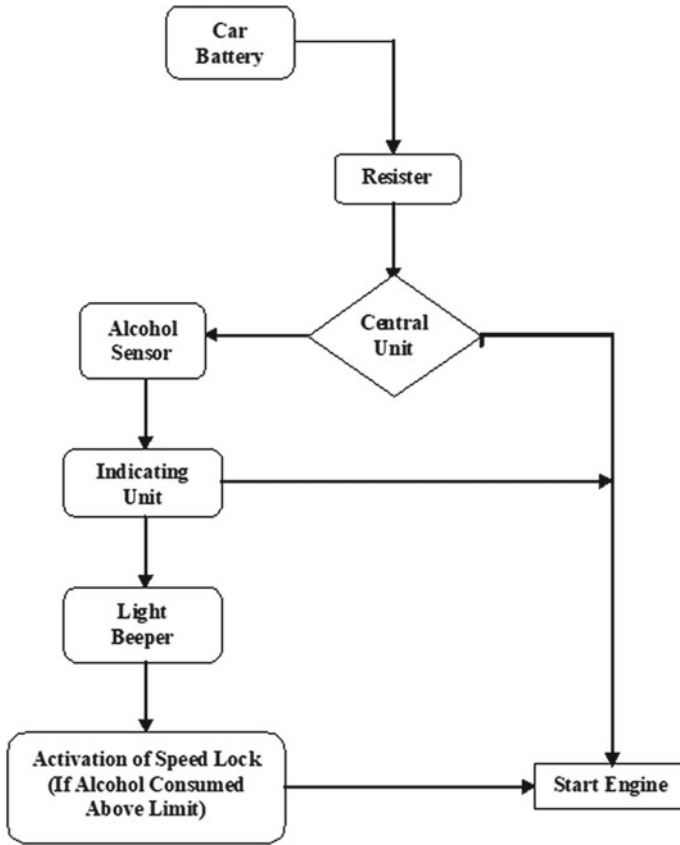


Fig. 4 Block diagram regarding breathalyzer connectivity with speed lock

The Fig. 4 describes how the breathalyzer connectivity with speed lock will work. It will start with car battery and end with the engine. This explains that all connections and instructions are given by central unit (Arduino). This process begins with the car battery. When we turn on car battery, then there will be supply of current to the central unit Arduino. Then, central unit Arduino will instruct alcohol sensor to grasp the alcoholic level of driver. After grasping, the sensor passes information to indicating unit. Here, the main work begins, if driver consume alcohol above the permissible limit set by law, then red beeper beeps for two seconds. Then, speed lock gets activated, engine will not start. If driver not consumed alcohol above, the permissible limit set by law, then there will be no change and engine gets started.

In Fig. 5, the working principle of breathalyzer connectivity with speed locks. This process begins with the car battery, then there will be supply of power to breathalyzer, then it will measure the alcoholic (toxic) level of the driver after measuring, there will be two divisions. One is alcohol consumption is not-permissible limit according to law. Then, red beeper beeps for two seconds, and then there will be activation

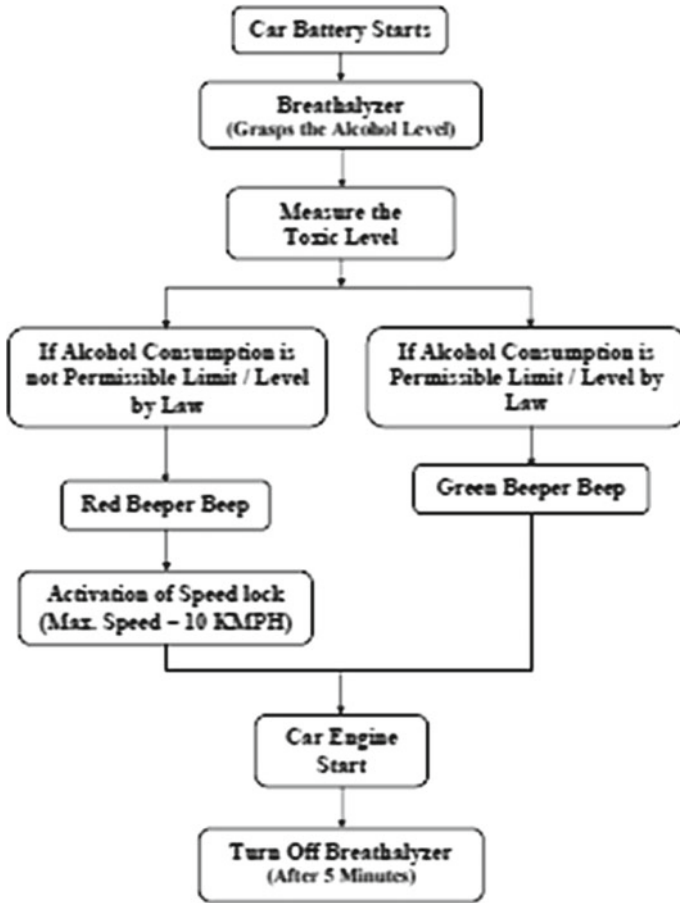


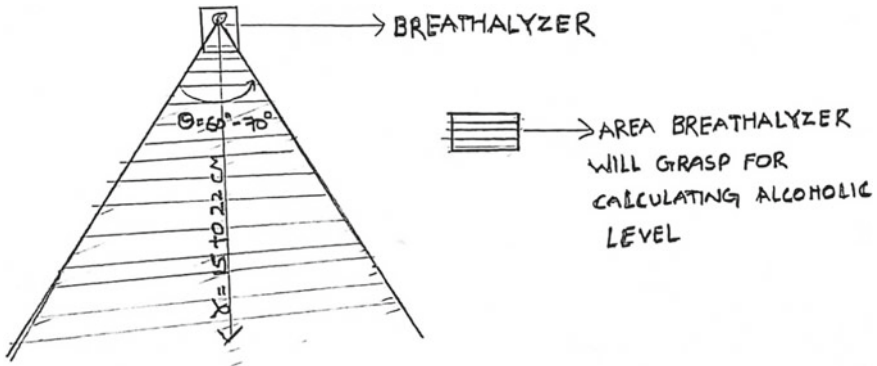
Fig. 5 Flowchart of working principle of breathalyzer connectivity with speed lock

of speed lock. Engine gets started. Another one is that if alcohol (toxic) level is permissible limit according to law, then green beeper beeps for two seconds, then engine will not start.

### 7 Functioning Area of Breathalyzer

In Fig. 6, it shows about the working space of the breathalyzer. And at certain part of the place, only the breathalyzer can grasp the breath essence (alcoholic level) of the driver.

1. The Fig. 6 describes the area covered by breathalyzer to grasp the alcoholic level of driver.



**Fig. 6** Area covered by breathalyzer to grasp alcoholic level of driver

2. If we fix breathalyzer directly to steering, it will get a problem in grasping the toxic level of drive.
3. If side passenger came near to the steering, it can grasp that too.
4. So to avoid that problem, we have adjusted and set a certain distance.
5. The max length covered is 45–49 cm.
6. The max angle between the areas covered is  $60^\circ$ – $70^\circ$ .
7. The area covered by breathalyzer is shown in Fig. 6.

At this particular area, the breathalyzer will be grasping the toxic level of driver. Then, maximum speed is less than 10 kmph. For developing, the following points tell about the effects of breathalyzer. It is a kind of development that the sensor will work only on driver.

1. After grasping the breath, the reading of breath goes to central unit.
2. In central unit, it will read a driver breathe and goes to indicator unit.
3. It will read according to limit which was set and it judge the beeps.
4. If the alcohol consumption is above the limit, then indicator unit goes to red beep.
5. If the alcohol consumption is in the limit, then it goes to green beep.
6. If the driver took more alcohol, red beeper will beeps after that the speed lock will get activated.

According to the “transport research wing of ministry of transport” here, the few of accidents in every year here; the observation in 2011 and 2012, the accident rate was decreasing and when we compare the year 2016 and 2017, in the year 2017, the percentage decreased by 0.8% [11].

To avoid these kind of accidents, United States government introduced fourth amendment in 1954. what is meant by fourth amendment? It is a kind of search done by police in house, cars, and so on, to find weather the unisexual things are using like drugs, over reacted alcohols, if cops find the criminals, there is a no warrant given to them and the place will be seized. Drunk and drive is very common and

risky behavior all over the world. Commonly, 11–17% accidents are due to driving under influence of alcohol. Drug driving is frequently less than alcohol driving but in Africa, North America, and Asia/Oceania, drug driving is reported as much or even more frequently [12, 13].

## 8 Conclusion

With help of this device in cars, we can reduce the accidents which are causing due to drink and drive. Nowadays in cars, wired breathalyzers are been used but our breathalyzer is different from that. The mechanical components used in this device can be fixed on the steering wheel of car so that there will be no problem, and the driver cannot be able to remove the device from steering. Our main theme to make this device is many of the families are losing their loved one by driving under the influence of alcohol. So by using this device, we can save many lives that will be driving under the influence of alcohol. For example, when a driver wants to drive car after drinking alcohol, the alcohol detector will sense the alcoholic percentage, if the alcoholic level extends the permissible limit set by law, then the device will start beeping and speed lock gets activated then engine starts. Finally, we conclude that by this device, we can save many lives that drive under the influence of alcohol. So by help of this device, we can make people life secure even they are under the influence of alcohol while driving.

## References

1. Road safety annual report 2019: Chile; International Transport Forum: Paris, France (2019)
2. Vijay J, Saritha B, Priyadarshini B, Deepika S, Laxmi R (2011) Drunken driven protection system. *Int J Sci Eng Res* 2(12):1–4
3. Prashanth KP, Padiyar K, Naveen KPH, Kumar KS (2014) Road accident avoiding system using drunken sensing technique. *Int J Eng Res Technol* 3(10):818–823
4. Geeta BS, Marur DR (2015) Smart drunken driver detection and speed monitoring system for vehicles. *Int J Adv Technol Eng Sci* 3(3):67–74
5. Bhuta P, Desai K, Keni A, Badre V, Rahmad IF, Nababan EB, Tanti L, Fragastia VA (2019) Application of the alcohol sensor MQ-303A to detect alcohol levels on car driver. In: 7th international conference on cyber and IT service management (CITSM)
6. Altaf SV, Abhinay S, Ansari E, Kaunain M, Anwer R (2017) Alcohol detection and motor locking system. *Int J Adv Res Electr Electron Instrum Eng* 6(2):989–993
7. Travis M (2013) ANDREWS DC for New Orleans. *The Washingtonian*, *The Washington Post Express*, Salon
8. Gbenga DE, Hamed HI, Lateefa AA, Opeyemi AE (2017) Alcohol detection of drunk drivers with automatic car engine locking system. *Nova J Eng Appl Sci* 6(1):1–15
9. Mandalkar RB, Pandore RN, Shinde MB, Godse VD (2015) Alcohol detection and accident avoidance using locking with tracking. *Int J Adv Res Comput Sci Manag Stud* 3(9):142–147
10. Das R, Chattopadhyay O, Biswas P, Das M, Chatterjee S, Paul A (2020) Intelligent alcohol detection system for car drivers. In: *Proceedings of industry interactive innovations in science, engineering & technology*

11. Kopczyński K, Kubicki J, Młyńczak J, Mierczyk J, Hackiewicz K (2016) Stand-off detection of alcohol vapours in moving cars. In: *Laser technology 2016: progress and applications of lasers*, vol 10159, pp 101590Z 1–9
12. Kousikan M, Sundaraj M (2014) Automatic drunken drive prevention system. *Int J Stud Res Technol Manag* 2(2):75–77
13. *Anuario Estadístico de Accidentes en el Tránsito y Ferroviarios Ocurredos en Chile Durante el Año 2019* (2019). Carabineros de Chile, Valparaíso, Chile

# Design and Evaluation of a Microsensor for a Bionic Hand with Metamaterials



M. Sreedhar and Y. Kalyana Chakravarthy

**Abstract** Prosthetics are the electro-mechanical frameworks which are an incredible assistance in helping the physical difficulties experienced by amputees. These are impelled in various ways, for example, wired associations, pneumatic systems, mechanical systems, and shape memory alloys. Mechanical and pneumatic frameworks that are at present utilized in prosthetics needs exactness, scholarly control and are not exceptionally light in weight. Transducers can be used in which the recognizing components have less weight with closed loop feedback system and precision of the prosthetics can be extended when differentiated with mechanical and pneumatic systems. Metamaterials and shape memory compounds are the activation innovation identified which can be a gamechanger for downsizing the structure of the transducer. These metamaterials can be used in the form of muscle actuators with the end goal that it chips away at the premise of constriction and extension of the prosthetics. This paper is an attempt to develop an idea of bionic hand with an integrated sensory system. The bionic hand is modelled with integrated microsensor system and evaluated the total heat flux of  $1.2275e^{-2}$  W/mm<sup>2</sup> and Joule heat  $3.2713e^{-23}$  W/mm<sup>3</sup>, respectively, using thermo electric analysis with sensor functional conditions. It is found analytically that these parameters are within the functional range when embedded with the structure of bionic hand with proper cladding materials.

**Keywords** Prosthetics · Bionic hand · Metamaterials · Shape memory alloys

## 1 Introduction

A sensor is a gadget which detects the environment and gives the data. There are various sorts of sensors accessible and utilized in different applications. Sensors are broadly utilized in a wide range of uses, and sensor innovation has become an essential empowering innovation in numerous cases. The fast increment in the enthusiasm for sensors has been driven by various applications, for example, smart assembling

---

M. Sreedhar (✉) · Y. Kalyana Chakravarthy  
Department of Mechanical Engineering, KL University, Guntur, Andhra Pradesh, India



handling, in which sensors can give an enormous advantage. Every sensor-type model depicts the physical marvels being detected, a scientific classification of the distinctive sensor types, and sensor materials issues identified with the application. Of need, these cases are disentanglements of the real world. For example, sensor needs are presented as though every sensor were a free element, in spite of the fact that in all actuality numerous applications require varieties of sensors or combination of data got from a wide range of sorts of sensors. New sorts of sensors are made conceivable with new materials that are created utilizing propelled preparing advances. To a more noteworthy degree than this innovation push, showcase pull is driving expanded action in sensors. Significant financial driver is the improvement and fuse of sensors into items that guide in broadening usable life.

Considering the assorted variety of sensor advancements and applications and the subsequent decent variety of materials requirements for sensors, it is as often as possible conceivable to fulfil a given need with more than one sort of sensor. A key finding of this board of trustees is that a “perfect” sensor material does not exist separated from the setting of an application. This reality significantly affects arranging R and D of sensor materials and frameworks. To quicken sensor improvement, a R and D technique that keeps up an expansive applications-driven research base is vital. This requires the recognizable proof and backing of basic centre abilities. The different idea of sensor innovation improvement requires an interdisciplinary culture. It further requires an application centre around chosen sensor advancements and materials. Hazard, logical and mechanical effect, and headway of an information base for sensors must be considered so as to recognize the most encouraging open-door territories that can have a significant effect and lead to an enormous quantifiable profit.

## 2 Literature Review

**Kaushal Gangwar et al.** in their work on metamaterials characteristics, process and applications concluded that the metamaterial is accepted to have an impact across the entire range of technologies where electromagnetic radiation is used will provide a flexible platform for technological advancement and a negative refractive index material has drawn special interest in microwaves. The properties that which will allow for the decrease in size as compared to that of the other materials for the multiband operation and reconfigurability of microwave devices and antennas. It is also known that no advancement in metamaterials research will be not possible without any further development in the fabrication. The growth and significance in this field is clear that the future of metamaterial lies in the field of optics and medical [1].

**Shridhar E. Mendhe et al.** in their research on metamaterial properties and applications, a short survey of history of metamaterials, some of quiet highlights and thoughts for metamaterial, different sorts of metamaterials, different utilizations of metamaterials have been examined. Electromagnetic reaction works that

can offer energizing potential outcomes of future structure of gadgets and segments are assessed. Some quiet properties of metamaterial have been surveyed [2].

**Gurwinder Singh et al.** in their review of metamaterials and its applications found that metamaterials are the new field of research, most assuredly it turns into an incredibly energizing examination territory. The analysts from numerous orders are being pulled in towards metamaterials due to its remarkable electromagnetic properties. The metamaterials have brought about astounding upgrades in electromagnetic reaction works that can offer energizing conceivable outcomes of future structure of gadgets, segments and notable properties of metamaterials [3].

**Subimal Deb et al.** in their work on absorption and dispersion in metamaterials: Feasibility of device applications where they have considered three potential gadget utilizations of MMs thinking about their assimilation and scattering in the structure of a full causal reaction [4].

**Ya-Fen Ge et al.** in their work on comparison of active and passive metamaterials from equivalent lumped elements modes found that the EM material parameters conditions for general dynamic and uninvolved metamaterial are determined and thought about from proportional lumped components modes. In the correlation investigation of adjusted and unequal lossless ( $R = G = 0$ ), latent lossy ( $R > 0$ ) and dynamic lossy ( $R < 0$ ) cases, various misfortunes impact (from the progressions of opposition right now) a few consequences for stage consistent and the genuine piece of trademark impedance, just as a major effect on lessening steady and the fanciful piece of trademark impedance. One can utilize included dynamic component to metamaterial to improve the weakening qualities and afterwards to defeat the significant downside of misfortunes impacts in metamaterials [5].

**Shuang Chen et al.** in their review of tuneable acoustic metamaterials revealed that the controlling acoustic waves with metamaterials as well as meta-surfaces is useful in acknowledging subwavelength acoustic gadgets and frameworks. Notwithstanding, the thin working band of most of the created metamaterials because of the nearby resounding nature of acoustic metamaterials may restrict their functional application. Creating tuneable acoustic metamaterials dependent on different balance systems, incorporating acoustic metamaterials with piezoelectric materials, precisely controllable segments, and with electric and attractive biasing. Such dynamic AMMs are promising competitors in numerous applications, including the weakening of acoustic waves, imperceptibility shrouding, and acoustic wave front building. It is significant that escalated endeavours on tuneable AMMs have been proposed to effectively adjust sound transmission/reflection in sonic, infrasonic, and ultrasonic fields. These investigations are just centred around hypothetical and numerical displaying, just as test show, there is as yet far to go in the common-sense utilization of AMMs [6].

**Jiangyi Zhang et al.** in their work on acoustic transmission line metamaterials, hypothetically, and numerically considered envelope dull (dark and dim) solitons in 1D nonlinear acoustic metamaterial made out of a waveguide with an intermittent exhibit of side openings, highlighting viscos warm, and radiation misfortunes. In view of the electro-acoustic similarity and transmission line approach, a nonlinear grid model is determined. Also, examined the straight scattering connection of framework, which was in great concurrence with the one got by utilizing the exchange network

strategy and utilized a numerous scale annoyance technique to diagnostically treat the issue and inferred a compelling NLS model depicting the advancement of the weight. Also researched the interaction between scattering, nonlinearity, and scattering, as depicted by relevant trademark length scales, on account of a water-filled acoustic metamaterial with a little sweep of side gaps. The numerical outcomes were in great concurrence with the explanatory expectations. The outcomes and approach prepare for considers on nonlinear marvels in twofold negative acoustic metamaterials, model wave directs intermittently stacked with side gaps and clipped versatile plates. As per the properties of the solitons, i.e. engendering with no twisting of high plentifulness waves, investigations could likewise make ready to plan new gadgets in therapeutic applications or to structuring non-damaging sensors [7].

**Jiawen Xu et al.** in their work on broadening bandgap width of piezoelectric metamaterial by introducing cavity found that, metamaterial comprising of piezoelectric transducers coordinated to have substrate with inductive circuits was contemplated. A lumped-parameter, semi-explanatory model of piezoelectric metamaterial was figured dependent on continuum mechanics portrayal. The identical unit cell mass, solidness, and electro-mechanical coupling parameter were inferred, which were wavenumber-subordinate. The job of the framework level electro-mechanical coupling was identified and broke down in detail. While the recurrence scope of the bandgap is controlled by the LC circuit resounding recurrence, the transmission capacity of the bandgap is principally dictated by the electro-mechanical coupling. At that point, a technique for data transfer capacity expanding through joining depression in the substrate of the unit cell was displayed. On a very basic level, the pit presented could build the framework level electro-mechanical coupling, accordingly benefiting the bandgap conduct. It was shown that the bandgap width of the piezoelectric metamaterial could be extended from 45 Hz to 126.7 Hz. The expository definition and cavity amalgamation can be utilized to control the structure advancement of the piezoelectric metamaterial [8].

**Morteza Karami et al.** in their work on polarization-independent negative index metamaterial found that another polarization-heartless left-gave metamaterial is exhibited dependent on S-formed resonators. Numerical outcomes exhibit polarization properties and compelling refractive records. These structures can be manufactured for microwave use utilizing 3D printing strategies and exploratory outcomes will be introduced [9].

**Neelam Singh et al.** in survey on techniques and design for metamaterial absorber gave an overview of methods and plan for the structuring of metamaterial absorber. The helpful arrangement is still less and experience the ill effects of various issues like intricacy of structure, improved data transmission, decrease of addition and so on [10].

**Richard W. Ziolkowski et al.** in their work on metamaterials based Antennas: Research and developments found that the metamaterials explore region has advanced into conspicuousness without a doubt, as of late. Regardless, it is now large affecting the universal electromagnetics network. Metamaterials have rejuvenated our inclinations in complex media; their fascinating properties; their examination and numerical demonstrating, and; their potential applications. There have been

enormous walks in our comprehension of their odd practices and of their conceivable usage in numerous electromagnetic applications from the microwave to the optical system. This survey has just briefly addressed some particular research efforts related with metamaterials and their receiving wire applications. Metamaterials, due to their guarantee to give engineerable permittivity's and permeabilities, have fascinating properties for the plan of cutting edge structures for emanating and dispersing applications. Artificial attractive conductors have been accomplished with high impedance and recurrence specific surface builds just as with volumetric consideration-based media. Resonances emerging in electrically little locales of room where single and twofold negative materials are matched with basic twofold positive materials were appeared to have an incredible potential for beating the breaking points for the most part connected with a few electromagnetic issues by giving a way to build the general reactions of the frameworks. Zero-list metamaterials, media with permittivity and permeabilities with zero or approach zero qualities, may have solid effect in certain applications regardless of their non-full character, since they join strange wave connections with generally bigger transfer speed and lower misfortunes. Metamaterials have been considered as a way to control the size, efficiency, transfer speed, and directivity of a few essential transmitting and dissipating frameworks. Metamaterials and their receiving wire applications is an extremely rich research territory wherein there is a lot of premium. The underlying seed material science efforts are just presently starting to hold up under some building applications natural product. There stay many testing and conceivably remunerating issues left to settle; we as a whole anticipate sharing these arrangements sooner rather than later [11].

**Milan Secujski et al.** in their work on density near-zero acoustic metamaterials proposed a novel way to deal with accomplishing thickness close to zero spread of acoustic waves. A full unit cell recently utilized for acquiring a twofold negative metamaterial is utilized to accomplish spread of acoustic waves with for all intents and purposes no adjustment in stage over genuinely long separations. Right now, acoustic vitality does not spread but instead burrows through a NZ metamaterial. Having as a main priority the wide scope of use of NZ metamaterial structures, including vitality burrowing, vitality parting, and ideal transmission through waveguides with sharp twists just as different kinds of wave front control, this exploration without a doubt offers a significant commitment right now. Our future work will incorporate the manufacture of the proposed unit cell and test check of thickness close to zero engendering, just as examination of progressively complex structures dependent on the showed wonder [12].

**Zan Lu et al.** in their work on design and analysis of a THz metamaterial structure with high refractive index at two frequencies show that the metamaterial, designed with gold structures embedded with polyimide film, effectively exhibits a high refractive index at two frequency bands and in the second frequency band, the high refractive index is of relatively smaller value than the main effective band. It is expected that through modifications in geometry and design, improvement in the electric and magnetic resonant frequency and the refractive index value can be enhanced for the second frequency band. Since polyimide has good flexibility and isolation property, the designed structure can be used in a variety of applications [13].

**Yu Guo et al.** in their review on applications of hyperbolic metamaterial substrates and found that in the most recent decade there has been gigantic improvement in the material science and nanofabrication of different classes of metamaterials. For gadgets in the obvious and close IR wavelength ranges, hyperbolic metamaterials are relied upon to lead the route because of their differed properties and appropriateness. One significant heading of use will be quantum nanophotonic. This work will assist experimentalists with social occasion a unified perspective on the different uses of hyperbolic metamaterials for structuring gadgets [14].

**Jeremiah P. Turpin et al.** in their survey on reconfigurable and tuneable metamaterials have broadly reported the condition of the metamaterials field as it applies to the age and use of tuneable or reconfigurable electromagnetic reactions. In spite of the fact that metamaterials are themselves in the beginning periods of advancement, it has delineated that the investigation of tuneable metamaterials is a lively and dynamic subfield, in light of the expansiveness and profundity of the applications and strategies that have been accounted for on in the writing. By arranging the tuning instruments and applications into bunches dependent on usefulness and capacity, as opposed to operational recurrence, as the main objective is to give an extensive outline of the cutting edge in tuneable and reconfigurable metamaterials. New tuning strategies and investigation systems might be applied to existing static metamaterial plans to significantly build their capacity and viability. In spite of the fact that there is more advancement that must be made before a considerable lot of the procedures talked about here might be for all intents and purposes applied, quick improvements in tuneable metamaterials hold incredible guarantee for future usage [15].

**Ke Chen et al.** in their work on broadband microwave metamaterial absorber with lumped resistor loading concluded that an elite meagre thickness, polarization-cold hearted, and broadband microwave metamaterial safeguard stacked with lumped components has been structured, mimicked, and tentatively verified. The working band of the proposed metamaterial safeguard can cover the entire X- and Ku-groups, with generally stable precise execution for occurrence point up to about 60°. The structure guideline of the proposed metamaterial safeguard is reliant on the stacking of lossy materials, which can be conceivably stretched out to other recurrence band or even scaled at a lot of high frequencies, for example, milli-metre wave band and terahertz. Furthermore, our proposition may find potential uses in military applications, for example, electromagnetic similarity, target shrouding, and so forth. This work is halfway bolstered by National Key Research and Development Programme of China (Grant No. 2017YFA0700201), the National Nature Science Foundation of China venture subsidized by China Postdoctoral Science Foundation, and incompletely upheld by Fundamental Research Funds for the Central Universities, PAPD of Jiangsu Higher Education Institutions, and Jiangsu Key Laboratory of Advanced Techniques for controlling electro-magnetic waves [16].

**Mr. Tj Brown et al.** in their work on a new low-cost bionic hand with the mechanical parts that make up the hand are structured utilizing 3D CAD programming and afterwards made on a 3D-printer. Utilizing 3Dprinting, the hand can undoubtedly be scaled to any measure considerably more economically than utilizing customary

techniques. The undertaking additionally brings down expense by structuring and making its own EMG circuit. This is the most significant part of the entire framework since it gives the client power over the hand. Without it, the hand is simply for looks. The EMG circuit estimates voltage over an arm muscle. At the point when the muscle contracts, the circuit imparts signs into a microcontroller that works the 3D-printed hand with the assistance of a couple of servos [17].

**Kiran kumar B. Balavalad et al.** designed MEMS capacitive sensor array simulated in the COMSOL and MATLAB Simulink software's. Each sensor having diaphragm side length of 60  $\mu\text{m}$  and a depth of 3  $\mu\text{m}$ . The diaphragm thicknesses are varied in the order of 1.5, 2, 2.5, 3  $\mu\text{m}$ . The linearity of each pressure sensor in the array have been studied and the output is read out by using combinational switching mechanism available in COSMOL and MATLAB Simulink. The work done is possible to measure pressure over a range of about 0–33.25 MPa. The pressure can be varied by varying the diaphragm thickness of the sensor [18].

**Jinkai Xu et al.** designed and simulated a piezoelectric transducer based on longitudinal vibration which can be used for precision machining, medical, and other fields. The front cover of the transducer as a horn which amplifies the output amplitude. The design frequency of the transducer is 20 kHz and the error between the theoretical and finite element results is found to be less than 5% that is 19250 Hz. The application of this designed transducer is that it transforms electric energy into vibration and the vibration can be used to process hard or brittle materials to get good results [19].

**Jing Jing Yang et al.** in his paper titled “Metamaterial Sensors” concluded that with the improvement of metamaterial science, detecting use of metamaterials has pulled in increasingly more consideration. The intensification of transitory wave at the limit among positive and negative refractive record materials not just takes into consideration subwavelength goals in optical imaging, yet additionally expands the affectability of the planar wave control sensors and the murmuring exhibition mode sensors because of the upgrade of the association among wave and matter. Sensors-based metamaterial exhibits, and particle(s) use the nearby field improvement and resounding qualities of metamaterials to accomplish exceptionally delicate identification. Also, just rescaling the size of metamaterial particles takes into consideration the structure of sensors from microwave to optics. In spite of the fact that metamaterials can not be wiped out, lessening the size of metamaterial clusters and utilizing the stereo particles rather than the planar ones are on the whole compelling measures for decreasing the effect of misfortunes on sensor execution. We accept that with the improvement of the examination of transitory wave and the attending impacts, sensors with phenomenal affectability and sub-wavelength goals may be brought by metamaterials later on [20].

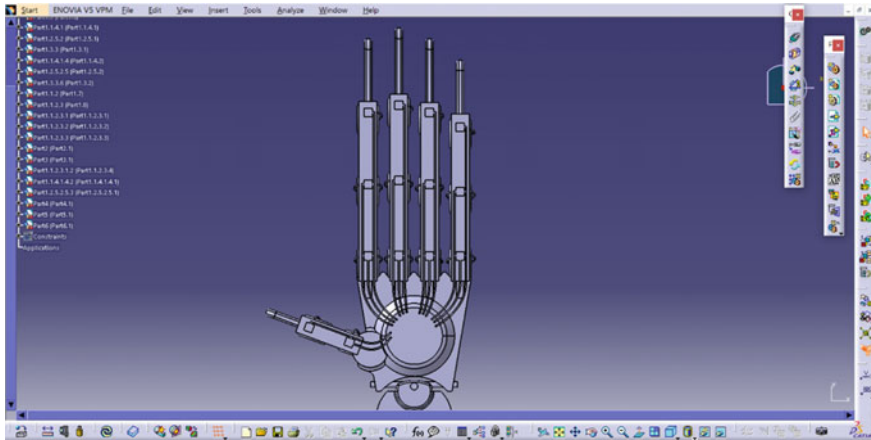


Fig. 1 Hand model with integrated metamaterial as the structural material

### 3 Methodology

The generation of 3D model consists of mathematical and computer modeling. Based on the application the geometrical parameters of the prosthetics (hand) are obtained by anthropometric analysis and sensors are designed as integrated part of the hand model by making small variations to the anthropometric data as shown in Fig. 1. The developed skeletal hand model is then used in Ansys for evaluating the performance when the metamaterial-based sensor is incorporated as an integrated part.

### 4 Results and Discussion

The metamaterial combination considered in the analysis is silver-copper alloy (thermo optic metamaterial) with the material properties listed in Table 1. A thermo electric analysis is done to find the distribution of heat flux at the time of flow of

Table 1 Themo optical metamaterial properties [21]

Name	Silver–Copper Engineered Alloy
Density	9.7–10.4 g/cm <sup>3</sup>
Current Density	0 to 1.3 mA/mm <sup>2</sup>
Electrical Resistivity	1.8–2.1 μΩcm
Poisson’s Ratio	0.34
Tensile Yield Strength	207 MPa
Thermal Conductivity	420 W/m–K



current through the integrated sensory system for the sensory structure of hand model as shown in Fig. 2.

In this analysis Voltage 20 mV, Current density 0 mA/mm<sup>2</sup> to 1.5 mA/mm<sup>2</sup> are considered as the boundary conditions for which the maximum heat flux distribution is found at the palm junction which is around 0.278 W/mm<sup>2</sup> and 1.2275e<sup>-2</sup> W/mm<sup>2</sup> in rest of the part as shown in Fig. 3 for skeletal sensory hand model.

In the analysis the maximum heat flux 0.278 W/mm<sup>2</sup> is generated in the palm region which is because of the base leads of the finger sensory systems are attached

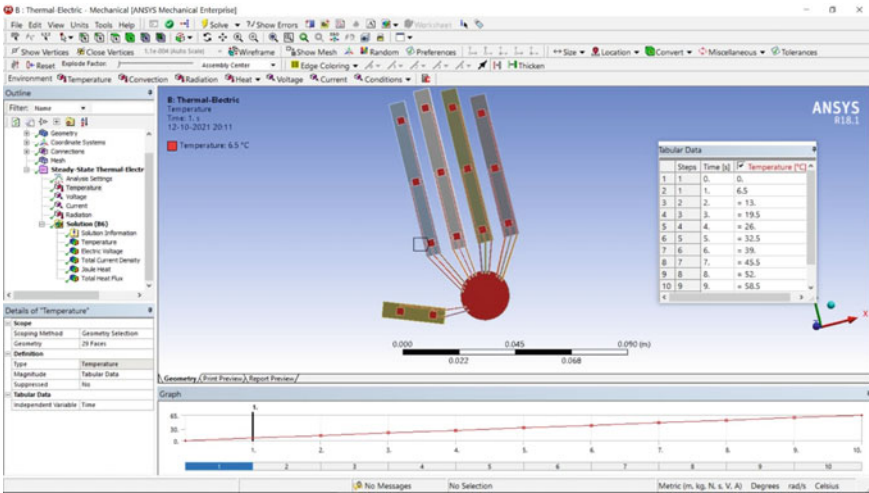


Fig. 2 Thermo electrical analysis of the sensory structure of the hand model

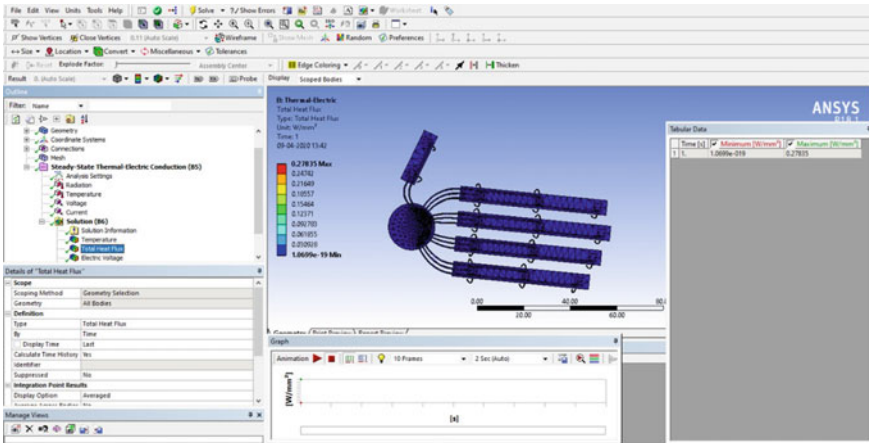


Fig. 3 Heat flux variations in the sensory hand model for thermo electric analysis



which acts as junction. As the idea is to integrate this sensory system with some 3D printing material as the cladding surface as an integrated structure the maximum heat flux generated is very negligible for the 3D printing materials like ABS plastics etc. for which the heat transfer coefficient is around  $2000 \text{ W/m}^2\text{K}$  [22]. So it is very much easy and safe to integrate this sensory system with these kind of cladding material.

## 5 Conclusion

Bionics are the electromechanical devices which are useful for the humans at different aspects of life. The advancement of the bionics from its origin has lot of changes in it. The usage of sensors in the bionics made reliable to the user. In general, the bionics with sensors are made with the common available materials. With the above combination the bionics are analysed with different techniques which provide errors in the working. Through this, the material wastage and cost of manufacturing will increase. Somehow bionics with sensors were analytically and theoretically analysed in which some of the results are not validated appropriately. In this project, one of our team members made as subject and the hand dimensions are used as reference and designed the bionic hand with the sensory system. The model is analysed by considering material as metamaterial using FEM tools like ANSYS. By considering, Voltage 20 mV, Current density  $0 \text{ mA/mm}^2$  to  $1.5 \text{ mA/mm}^2$  as boundary conditions in thermal-electric analysis, the results obtained are total heat flux and joule heat are  $1.2275e^{-2} \text{ W/mm}^2$  and  $3.2713e^{-23} \text{ W/mm}^3$ , respectively, and also it is found that the maximum heat flux of  $0.278 \text{ W/mm}^2$  present at the palm junction which is because of the finger sensory strip distribution start at this area. The variation of this flux rage is within the functional range of bionic hand and this heat flux will not damage if this is integrated with better cladding material.

## References

1. Gangwar K et al Metamaterials: characteristics, process and applications, vol 4. ISSN 2231–1297
2. Mendhe SE et al Metamaterial properties and applications, vol 4, no 1, pp 85–89
3. Singh G et al (2015) A review of metamaterials and its applications, vol 19, no 6
4. Deb S et al (2010) Absorption and dispersion in metamaterials: feasibility of device applications. Indian Acad Sci 75
5. Ge Y-F et al A comparison of active and passive metamaterials from equivalent lumped elements modes. <https://doi.org/10.4236/opj.2013.32B061>
6. Chen S et al (2018) A review of tuneable acoustic metamaterials, published on 28 Aug 2018. <https://doi.org/10.3390/app8091480>
7. Zhang J et al (2018) Dark solitons in acoustic transmission line metamaterials, published on 20 July 2018. <https://doi.org/10.3390/app8071186>
8. Xu J et al (2018) Broadening bandgap width of piezoelectric metamaterial by introducing cavity, published on 10 Sept 2018. <https://doi.org/10.3390/app8091606>

9. Karami M et al Polarization-independent negative index metamaterial
10. Singh N et al (2015) A review paper on techniques and design for metamaterial Absorber, vol 6, issue 10, Oct 2015. ISSN 2229–5518
11. Ziolkowski RW et al (2006) Metamaterials based antennas: research and developments, Sept 2006. <https://doi.org/10.1093/ietele/e89-c.9.1267>
12. Secujski M et al A novel approach to density near-zero acoustic metamaterials. *Adv Mater Sci Eng* 2015(626593) <https://doi.org/10.1155/2015/626593>
13. Lu Z et al Design and analysis of a THz metamaterial structure with high refractive index at two frequencies. *Phys Res Int* 2012(206879). <https://doi.org/10.1155/2012/206879>
14. Guo Y et al Applications of hyperbolic metamaterial substrates. *Adv Optoelectron* 2012(452502). <https://doi.org/10.1155/2012/452502>
15. Turpin JP et al Reconfigurable and tuneable metamaterials: a review of the theory and applications. *Int J Antennas Propag* 2014(429837). <https://doi.org/10.1155/2014/429837>
16. Chen K et al (2019) Broadband Microwave metamaterial absorber with lumped resistor loading, published by EDP sciences. <https://doi.org/10.1051/epjam/2018011>
17. Brown T et al (2010) A new low-cost bionic hand. *Progress Electromag Res* 108:37–49
18. Balavalad KB et al (2017) Design and simulation of MEMS capacitive pressure sensor array for wide range pressure measurement. *Int J Comput Appl* (0975–8887) 163(6)
19. Xu J et al Design and finite element simulation of an ultrasonic transducer of two piezoelectric discs. <https://doi.org/10.21595/jme.2017.19396>
20. Yang J et al Metamaterial sensors. *Int J Antennas Propag* 2013(637270). <https://doi.org/10.1155/2013/637270>
21. Prins TJ (2019) UCLA UCLA electronic theses and dissertations title [Online]. <https://escholarship.org/uc/item/0th2s0ss>.
22. Rahman M, Schott NR, Sadhu LK (2016) Glass transition of ABS in 3D printing. *Comsol Bost* 2016:3

# Ergonomic Analysis of Mouse Holding Position of Humanoids



Chelamban Kalaiselvan and Lokavarapu Bhaskara Rao

**Abstract** This paper deals with theoretical ergonomic analysis of mouse holding position of humanoids of various age limits. Ergonomic analysis plays a vital role in of the design and evaluation of the jobs, products, machines, tools and environments for safe, comfortable human functioning. The analysis is done for various angles of forearm and elbow (widening the elbow angle, lowering the forearm away from the upper arm). The ergonomic analysis of mouse holding position which reduces error, increased of use, increased productivity and to enhance the effectiveness and efficiency of human beings.

**Keywords** Ergonomics · Forearm and elbow · Mouse holding position

## 1 Introduction

The human factors/ergonomics (HFE) research faces when it attempts to increase its contribution to design of complex work stations. Figure 1 shows that how human beings and their interaction with equipment, products, procedures, facilities and environments used in work stations and everyday living. The human-machine system is the combination of one or more humans and one or more physical components interacting to convert given input to desired output.

The human-machine system is to enhance efficiency and effectiveness of certain desirable human values, including reduced stress, improved safety, increased comfort, increased job satisfaction and improved quality of life. Nowadays, different occupation causes musculoskeletal disorders and one of these occupations is frequent computer usage [1]. The continuous computer usage leads to work related extremity disorder (WRUED) and Carpal Tunnel Syndrome (CTS). WRUED causes hand and

---

C. Kalaiselvan

Tata Consultancy Services Ltd, SIPCOT IT Park, Navalur, Chennai, Tamil Nadu 603103, India

L. Bhaskara Rao (✉)

School of Mechanical Engineering, Vellore Institute of Technology, Chennai Campus, Vandalur-Kelambakkam Road, Chennai, Tamil Nadu 600127, India

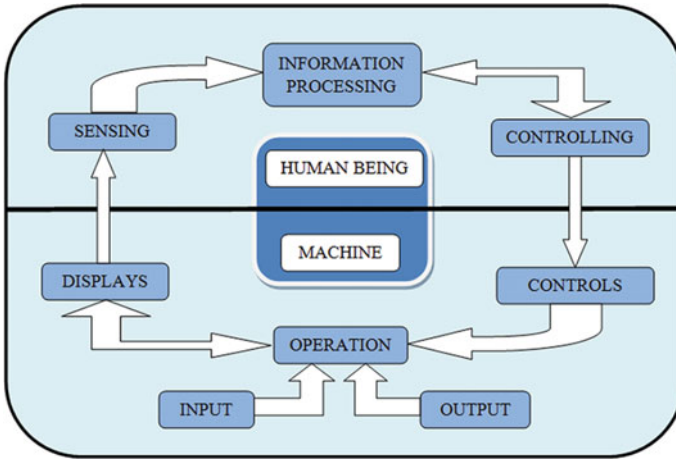


Fig. 1 Human-machine system

arm pain. CTS causes external pressure over the palmar wrist region, when the wrist supported during computer use or a wrist is positioned on the Table [2, 3]. Figure 2 shows the causes of WRUED and CTS. This complaint, amongst other factor, is associated with inappropriate positions and repetitive movement that cause injuries to muscles, tendons and joints. This includes long duration of computer usage [4, 5].

Generally, computer operators do not have any induction manual or guidance to assist them with correct hand positions, movements and the force exerted by

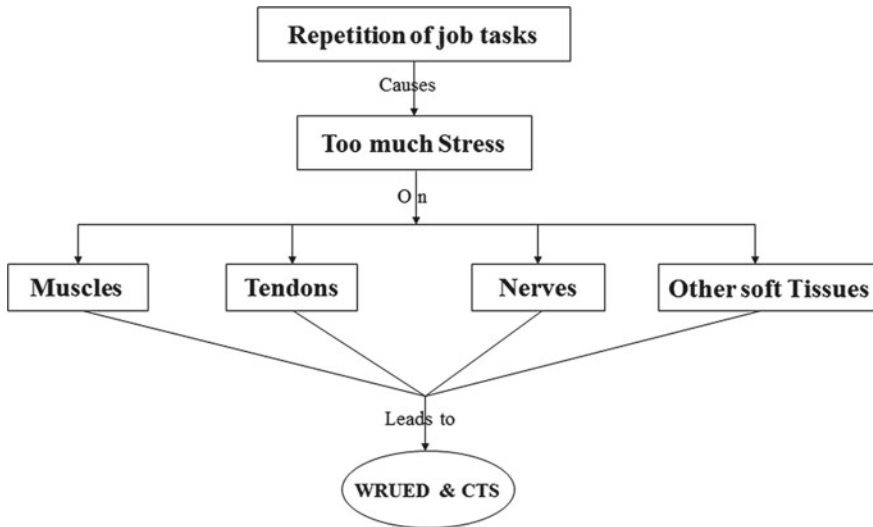
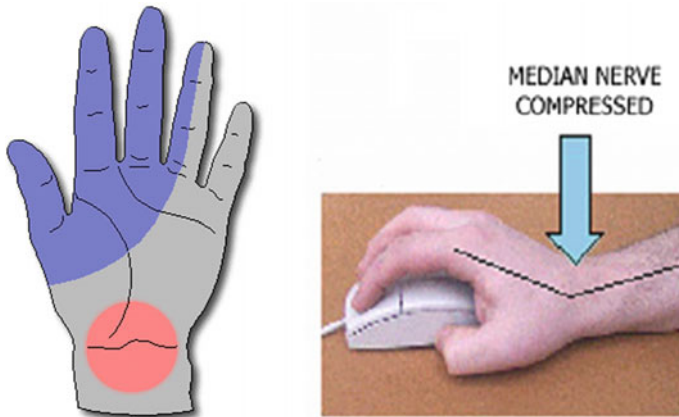


Fig. 2 Causes of WRUED and CTS



**Fig. 3** Carpel tunnel syndrome

their fingers [6]. Figure 3 shows the carpel tunnel syndrome. The musculotendinous injuries, which result from performing forceful and/or repetitive tasks, are due to compression, friction, overstretch and over-exertion. Sometimes, the key switch design and finger posture make it worse [7, 8]. Individual with severe impairment of hand. Several risk factors are associated with the development of musculoskeletal disorder in the workplace, including biomechanical factors and individual predisposition [9]. Wrist in an extreme position is dangerous for the musculoskeletal structure and tendons [10]. There is a correlation between finger joint and wrist movement, and it is possible to use minimum muscle tension. Range of finger movement can affect the carpel tunnel [11].

## 2 Biostatic Musculoskeletal System

The human factors engineering application, in specific anatomical system, the musculoskeletal system is the main focuses of biostatic mechanics. In order to analyze this anatomical system, we will use the biomechanical (biostatic) model such a model proceeds through three levels of development. The anatomical model and the approximate model are the first two models. Generally speaking, at least four of the five essential element of the system is included in each model. The third and final level are the analytical model. The approximate model is further simplified so that it may be represented by an engineering drawing.

Human factors engineers employ biostatic analytical models in two different ways. In the first (and most common) application, external forces act upon the human body. These forces represent inputs to the biostatic model of the musculoskeletal system of interest. The outputs of the biostatic model are the internal forces that are reactive in nature. In actuality, the biostatic model represents the inverse solution of what

actually happens. In the second (less common) application, a more realistic scenario is constructed. Internal forces are actively generated by contracting muscle (as well as internal reactive forces at joints). These internal forces are the inputs to the biostatic model of the musculoskeletal system of interest. The outputs of the model are the forces that act upon the external environment. In this case, this model represents a forward solution of what the human being is actually doing.

Having defined the anatomical system of interest and having developed a suitable analytical model, the human factors engineer must then identify a suitable application in order to obtain useful information for the design and development process. The human factors engineering identified for the theoretical static analysis is arm and shoulder of human body. The task of the human body is the human using computer keyboard and key. The human system involved in work is shoulder bone, arm bone and shoulder joint.

### 3 Theoretical Analysis of Human Body

#### 3.1 Upper Extremity and Hand

##### Arm and Shoulder.

The anatomical system for an arm and shoulder is as follows

Proximal segment: scapula (shoulder bone).

Distal segment: humerus (arm bone).

Joint: shoulder joint.

Muscle (action): Deltoid (abduction of the arm: when viewing a person from the front, raising the arm from the side of the body outward from the side of the body as in flapping the arms). The approximate model for the arm and shoulder is presented (see Fig. 4), and the free body diagram for the arm and shoulder is presented (see Fig. 5).

Human factor engineering application: The human skeletal muscles perform a demanding task over a long time, the muscle undergoes continuous fatigue. The biophysical and/or biochemical basis for skeletal muscle fatigue remain uncertain. However, muscle fatigue is physically characterized as a progressive decrease in its ability to generate force. Modifying the human body task to reduce muscle force can increase endurance.

- (a) A volunteer emergency worker must continuously extend his arm straight out so that the arm is at a right angle ( $\theta = 90^\circ$ ) to the side of the body. You may neglect the elbow angle. The worker is holding a 'DETOUR RIGHT' sign that represents a load weight, WL. Figure 4 shows the model of arm and shoulder, and the arm is at right angle ( $\theta = 90^\circ$ ). Figure 5 represented the free body diagrams of arm and shoulder.

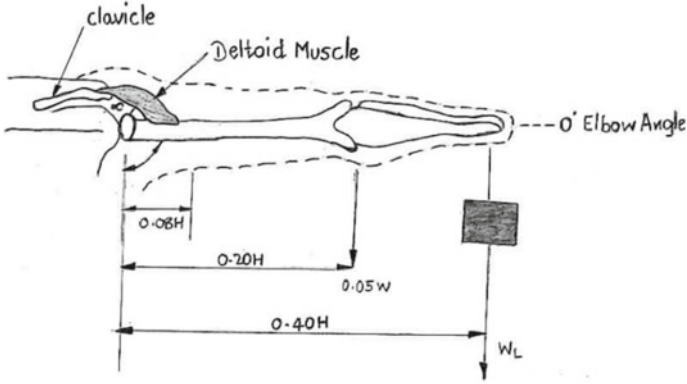


Fig. 4 Model of arm and shoulder

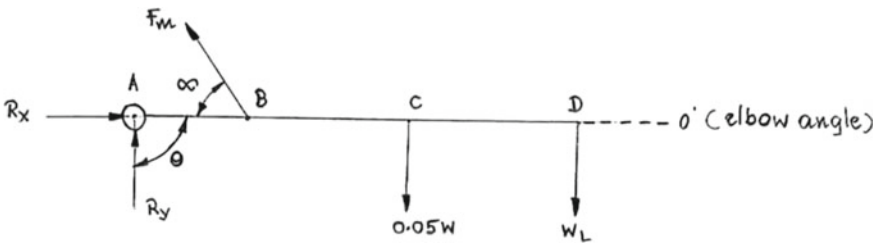


Fig. 5 Free body diagrams of arm and shoulder

$$\sum F_y = 0$$

$$F_m \cdot \sin(30^\circ) + R_y - 0.05W - W_L = 0 \tag{1}$$

$$\sum F_x = 0$$

$$-F_m \cdot \cos(30^\circ) + R_x = 0 \tag{2}$$

$$\sum M_A = 0$$

$$F_m \cdot \sin(30^\circ) * AB - 0.05W * AC - W_L * AD = 0 \tag{3}$$

$$F_m = \_\_N \tag{4}$$

The force exerted by the deltoid muscle is one-half of the body weight.

Sub Eq. (4) in (2) gives the following

$$-F_m \cdot (0.866) + R_x = 0 \tag{5}$$

$$R_x = \_\_ N \text{ (rightward)} \tag{6}$$

Sub Eq. (4) in (1) yields the following

$$F_m \cdot \sin(30^\circ) + R_y - 0.05W - W_L = 0 \tag{7}$$

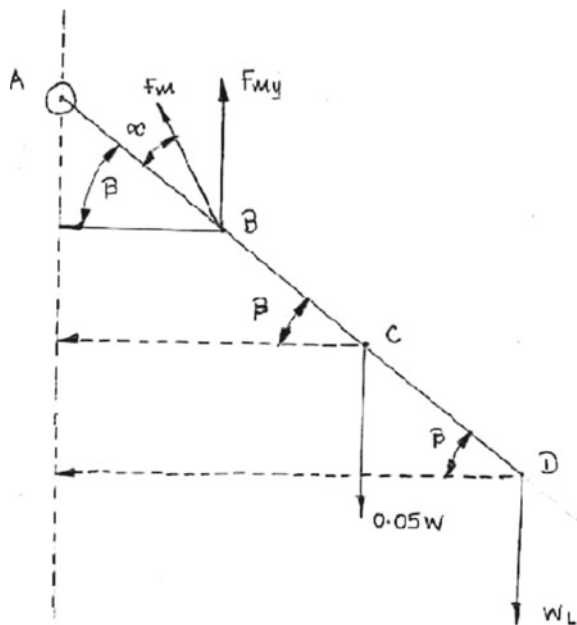
$$R_y = \_\_ N \text{ (Downward)} \tag{8}$$

- (b) As time passes by and fatigue sets in, the extended arm sags (to an angle,  $\theta = 65^\circ$ , with respect to the side of the body). Figure 6 shows the free body diagram of arm and shoulder at  $\beta = 25^\circ$ .

$$\beta = 90^\circ - \theta = 90^\circ - 65^\circ = 25^\circ$$

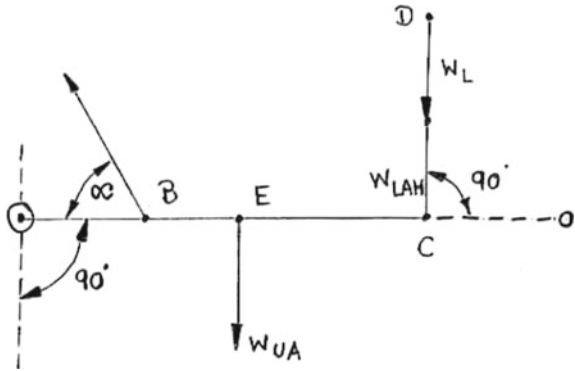
$$F_{my}[ABC\cos(\beta)] - F_{mx}[ABS\sin(\beta)] - 0.05W[ACC\cos(\beta)] - W_L[ADC\cos(\beta)] \tag{9}$$

**Fig. 6** Free body diagram of arm and shoulder at  $\beta = 25^\circ$





**Fig. 7** Free body diagram of arm and shoulder at  $\theta = 30^\circ$



$$F_m[\text{Sin}(\alpha + \beta)](AB)(0.906) - F_m[\text{Cos}(\alpha + \beta)](AB)(0.423) - 0.05W(AC)(0.906) - W_L(AD)(0.906) = 0$$

(iii) The hand right angle to the upper arm

Arm is sagging, the volunteer bends the elbow and also extends the upper arm straight outwards so that  $\theta = 90^\circ$ . The sign, hand and lower arm are now held vertically upward at a  $90^\circ$  right angle to the upper arm. Figure 7 shows the free body diagram of arm and shoulder at  $\theta = 30^\circ$ .

$$\theta = 90^\circ \quad \alpha = 30^\circ$$

From anthropometry Table 1, we divide the total arm weight in to

$$W_{UA} = W(\text{Upper arm}) = 0.03W$$

$H^a$  = Total body height, erect and standing (metres)

$W^b$  = Total body weight (Newton)

$$W_{LAH} = W(\text{lowerarm and hand}) = 0.02W$$

The new load weight ( $W_{Lx}$ ):

$$W_L = W_{LAH} + W_L \tag{10}$$

$$\sum M_A = 0$$

$$F_m \cdot \text{Sin}(30^\circ) * AB - W_{UA} * AE - W_L * AC = 0 \tag{11}$$

Modifying the task by bending the elbow upright, reduce the deltoid muscle force by 40%.

**Table 1** Anthropometric modelling data

Body segment (used in the work examples)	Segment length (fraction of H <sup>a</sup> )	Segment weight (fraction of W <sup>b</sup> )
Head and neck	0.17	0.08
Forearm and hand	0.2	0.02
Upper arm	0.2	0.03
Arm	0.4	0.05
Head, neck and both arms	–	0.18
Thorax and abdomen	0.3	0.36
Pelvis	–	0.16
Foot and foreleg	0.29	0.05
Upper leg	0.24	0.1
Leg	0.53	0.15
Head, neck, both arms, thorax, abdomen and three-eighths pelvis	–	0.6
One leg and five-eighths pelvis	–	0.25

**Forearm and Elbow**

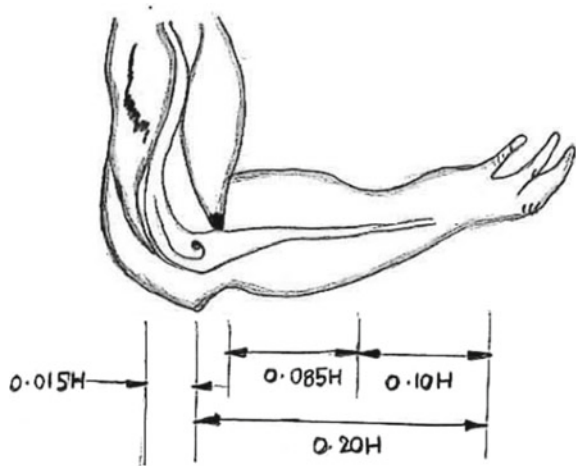
The anatomical system for the forearm and elbow is as follows.

Proximal segment: humerus (arm bone).

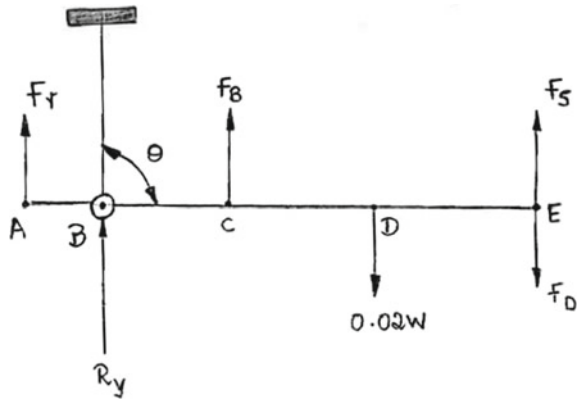
Distal segment: radius and ulna (forearm bones).

Joint: elbow joint.

**Fig. 8** Model of forearm and elbow



**Fig. 9** Free-body diagram of the forearm and elbow



The approximate model for the forearm and elbow are represented in Fig. 8 and the free body diagram for the forearm and elbow (see Fig. 9).

Agonist muscle (action): Triceps (extension of forearm: widening the elbow angle, lowering the forearm away from the upper arm).

HFE application although many biomechanical models of the musculoskeletal system depict only a functional agonist, real muscle always acts in agonist–antagonist pairs. Many tasks require the interplay of these agonist–antagonist muscle pairs. During motion in one direction, the agonist is (by definition) the prime mover in that direction. However, the muscle generating the predominant force may alternate between the actual agonist and its opposing antagonist depending on the nature of this task performed.

## 4 Case Study

### Numerical Example

A person with  $H = 1.67$  M and  $W = 550$  N is standing directly in front of the overhead roller and pulling its lower edge downward with the forearm and hand, whilst the upper arm is straight along the person’s side [12].

If the angle at the elbow between the upper arm and the forearm is  $\theta = 25^\circ$  when the vertical door drop ( $h$ ) is  $0.78$  M, then for a door weight (WD) of  $120$  N.

$$H = 1.67 \text{ M}, W = 550 \text{ N}$$

$$\theta = 25^\circ, h = 0.78 \text{ M}, W = 120 \text{ N}$$

Using the free body diagram (see Fig. 7) and the

$$AB = 0.025 \text{ M}$$

$$BC = 0.025 \text{ M}$$

$$BD = 0.167 \text{ M}$$

$$BE = 0.334 \text{ M}$$

By inspection,

$$F_s = -\left(\frac{120N}{2.1M}\right)h + 120N$$

For  $h = 0.78 \text{ M}$ ,

$$F_s = -(57.1)(0.78) + 120 = 75.4N$$

By inspection,

$$F_D = \left(\frac{120N}{2.1M}\right)h$$

$$F_D = (57.1)(0.78) = 44.5N$$

Calculate Net Force:

$$F_N = F_s - F_D = 75.4 - 44.5 = 309N(\text{upward})$$

Modify the free body diagram for  $F_N$  Upward

$$\sum F_y = 0$$

$$F_T - R_e - 11 + 30.9 = 0$$

$$R_e = F_T + 19.9 = 0$$

$$\sum M_B = 0$$

$$-(F_T)[AB\sin(25)] - (11)[BD\sin(25)] + (30.9)[BE\sin(25)] = 0$$

$$-(F_T)(0.025)(0.423) - (11)(0.167)(0.423) + (30.9)(0.334)(0.423) = 0$$

$$-(F_T)(0.0106) - (0.7771) + 4.3656 = 0$$

$$F_T = \left( \frac{3.5885}{0.0106} \right) = 339 \text{ N (upward)}$$

The net force is exerted by the triceps muscle and is slightly over 60% of the body weight

$$R_e = 339 + 19.9 = 359 \text{ N (downward)}$$

## 5 Conclusions

In this study, the theoretical approach is carried to identify the human body position and their task by bending the elbow upright, reduce the deltoid muscle force by 40%. It is designed to assess operators who may be exposed to musculoskeletal loading which is known to contribute to arm and shoulder disorders. It is used as a theoretical screening tool or incorporated into a wider ergonomics assessment of environmental, physical, mental and organizational factors. The research is continued for simulation of static and dynamic load acting in complex work stations and in human-machine system.

## References

1. Cury HJCG, Porcatti IA, Leo AJ, Kumar S (2000) Effects of progressive level of industrial automation on force and repetitive movement of the wrist. *Int J Ind Ergon* 25:587–595
2. Lundborg G, Gelberman RH, Minter-Convery M (1982) Median nerve compression in the carpal tunnel-functional response to experimental induced controlled pressure. *J Hand Surg Am* 7:252–259
3. Wigley RD (2004) Desk-edge syndrome: median nerve injury proximal to the carpal tunnel. *APLAR J Rheumatol* 7:215–218
4. Douwes M, Kraker H, Blatte BM (2007) Validity of two methods to assess computer use: self-report by questionnaire and computer use software. *Int J Ind Ergon* 37:425–431
5. Schmid AB, Kubler PA, Johnston V, Coppieters MW (2015) A vertical mouse and ergonomic mouse pads alter wrist position but do not reduce carpal tunnel pressure in patients with carpal tunnel syndrome. *Appl Ergon* 47:151–156
6. Liu CW, Chen TW, Wang MC, Chen CH, Lee CL, Huang MH (2003) Relationship between carpal tunnel syndrome and wrist angle in computer workers. *Kaohsiung J Med Sci* 19:617–622
7. Jindrich DL, Balakrishnan AD, Dennerlein JT (2004) Effects of Keyswitch design and finger joint kinematics and dynamics during tapping on computers keyswitches. *Clin Biomech* 19:600–608
8. De Lima Machado GA, Vilaverde AJB (2011) Design of an electronic instrumentation for measuring repetitive hand movement during computer use to help prevent work related upper extremity disorder. *Int J Ind Ergon* 41:1–9
9. Barbe MF, Barr AE (2006) Inflammation and the pathophysiology of work-related musculoskeletal disorders. *Brain Behav Immun* 20:423–429

10. Su FC, Chou YL, Yang CS, Lin GT, An KN (2005) Movement of finger joints induced by synergistic wrist motion. *Clin Biomech* 20:491–497
11. Ugbolue UC, Hsu WH, Goitz RJ, Li ZM (2005) Tendon and nerve displacement at the wrist during finger movements. *Clin Biomech* 20:50–56
12. Sanders M, McCormick E (1992) *Human factors in engineering and design*, 7 edn. McHill Publications

# Energy Optimization by Using Low Life Cycle Cost Analysis Method in Split Casing Pump



Ramesh. S. Gavade and Suresh M. Sawant

**Abstract** Many engineering applications of this era required low cost and high efficiency products. The life cycle cost is most important technique for analyzing the impact of a manufactured article in the process of design and development, manufacturing, services, and disposal. The requirement is generated to calculate the cost details connect to these impacts. Life cycle cost estimation is a method for evaluating the whole cost of capacity ownership. It includes all costs of obtaining, owning, and disposing of a pump or pumping scheme. This paper presents the implementation of LCCA on manufacturing of centrifugal split casing pump made and implemented by Kirloskar Brother Limited (KBL), Kirloskarwadi. The pumping systems consume one third of total energy generation. The clients are now concentrating on power consumption cost and maintenance cost than initial investment. The data presented in current research work are real-time data.

**Keywords** LCC · Split casing pump · Impeller · Coating

## 1 Introduction

The focus of a company to participate efficiently on the gradually competitive worldwide market is influenced the expense and nature of its items. Capacity to put up items for sale to the public in a convenient way. It has been demonstrated that the life-power designing way to deal with item configuration can possibly accomplish these objectives. General resource investigation can incorporate expenses of arranging, innovative work, creation, activity, upkeep, and removal. Life cycle cost examination is significant when settling on choices about gear (substitution or new securing) [1]. Finally, further improvement in support the executives (Section 8) will be conceivable because of the utilization of arising methodologies and advancements in the regions viable to have a high effect because of the past strides of our administration

---

Ramesh. S. Gavade · S. M. Sawant (✉)  
Mechanical Engineering, RIT, Rajaramnagar, Shivaji University, Kolhapur, India

cycle. With respect to the utilization of new innovations utilized for care, the idea of “e-remedy” is organized as a component of the e-creation idea [2].

The support board cycle can be separated into two sections: the system portrayal, and the execution of the technique. The idea of life cycle costs (LCC) was initially utilized by the US Department of Defense (DoD). Its significance in self-protection was provoked by the examination that the working and backing expenses of ordinary weapons frameworks represented 75% of complete expenses [3]. The item life cycle speaks to the different stages related with time, during which any framework, gadget or item should pass. All frameworks and hardware experience four significant stages during their activity, for example, idea and definition, securing, activity and capacity, and removal [4].

In the initial segment, the adequacy of upkeep decides the utilization of the idea of ease of living in an association. The adequacy of upkeep takes into account a decrease in backhanded support costs [5]. With an end goal to improve item plan and decrease configuration changes and showcasing time, corresponding designing or life cycle designing has arisen as a successful method to address these issues in the present worldwide serious market. A critical element of the existence cycle designing is that the total item life cycle is kept up and overseen at each phase of item creation [6].

Life cycle costs look at the cost adequacy of different speculations or business choices from the perspective of a monetary chief, for example, an assembling firm or shopper. For an item to be economically suitable and exceptionally serious in this worldwide commercial center, it is significant that specialists should comprehend and configuration each stage in the item life cycle. Life cycle costs allude to all costs caused in the lifetime of a solitary item [7] Pumps are the biggest customer of energy in the car business and work over 25% of power utilization. The expense of a day-to-day existence pattern of a pump is the absolute average cost for basic items related with the buy, establishment, activity, upkeep, and removal. The pump LCC is firmly connected to its dependability and upkeep (accessibility). The expense of the existence cycle can be separated into the expense of appropriation and the expense of support. The expense of procurement is something that is effortlessly reflected in the existence pattern of any framework [8]. Nesbitt et al. [9] give the basic thought of savvy pump units (IPU) and its life cycle cost. The IPU may require extra impending capital utilize anyway the presence cycle cost speculation assets can be gigantic. Improved pump decision methodology, and better structure and line work plans, would similarly fundamentally influence pump LCC, possibly with no extra basic utilization. Stavale et al. [10] took a gander at the presence cycle cost of an astute pumping structure with a normal pumping system. Insightful pumping systems can arrange pump yield correctly to structure conditions and can perceive and make sure about the pump and structure against exceptional working conditions. The use of a sagacious variable speed controller out and out decreases pump working costs by shedding the use of energy consuming control valves. The assessment of smart pumping systems to the customer is in diminished life cycle costs. It has been shown that up to 35% of saving in life cycle cost can be gotten using a canny pumping structure over fifteen years of pump life as differentiated and a standard pumping system.



## 2 Life Cycle Cost Model

The pumping scheme represents almost 20% of the world’s electrical energy interest and reach from 25 to 50% of pump energy use in certain modern plant activity. The LLC cycle is an approach to anticipate the most savvy arrangement; it doesn’t ensure specific outcome, however permits the plant director to make sensible examination between substitute arrangements inside the constraints of the accessible information. The cost segments related with life cycle cost set have been sorted are shown in Fig. 1.

The overall cycle cost of a repairable and non-repairable framework from the client’s point of view can be communicated in the most broadest exhaustive structure as shown in Fig. 2.

$$LCC = \sum_{i=1}^6 C_i \tag{1}$$

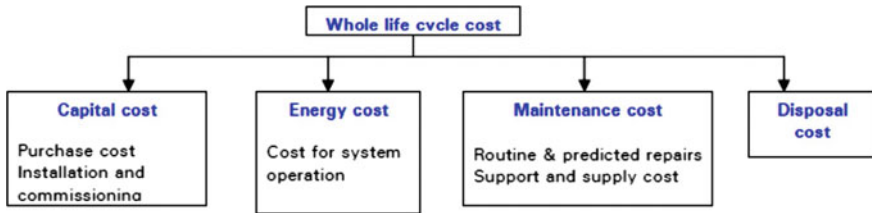


Fig. 1 Life cycle cost tree

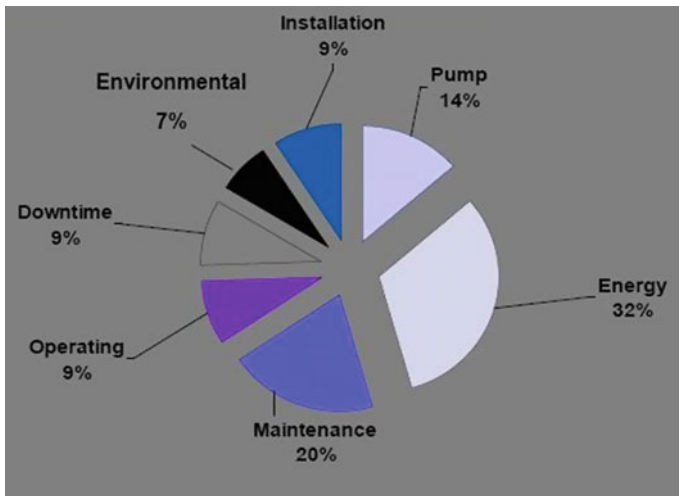


Fig. 2 Product life cycle cost analysis

where

LCC	Life cycle cost of a centrifugal pump.
$C_1$	Cost on account of manufacturing of the pump initial cost.
$C_2$	Cost on account of installation and commissioning cost.
$C_3$	Cost on account of energy consumption.
$C_4$	Cost of maintenance.
$C_5$	Cost on account of down time .
$C_6$	Cost on account of disposal.

Energy cost for pump is nearly 32% of whole life cost. Therefore, emphasis is given to post-installation cost of the impeller. High energy cost needs to reduce by designing more and more efficient pumps and also to reduce the maintenance costs. Energy saving opportunities are available both in pumps and pumping schemes.

## ***2.1 Need of Life Cycle Cost Analysis and LLC Products***

The various companies simply consider the underlying expense and foundation cost of the pump. In the current market, continually search for cost saving which will increase their efficiency. LCC examination is an incredible device for assessment of energy cost similarly as starting cost. LLC things support in conservation of energy by keeping up the total effectiveness of the product over time as difference with normal product where efficiency reduction is critical alarm. The advanced countries have effect of its energy wastage, and the overview of obligations on CO<sub>2</sub> releases at present direct expenses the ineffective of energy.

## ***2.2 Horizontal Split Case Pumps with LLC Features:***

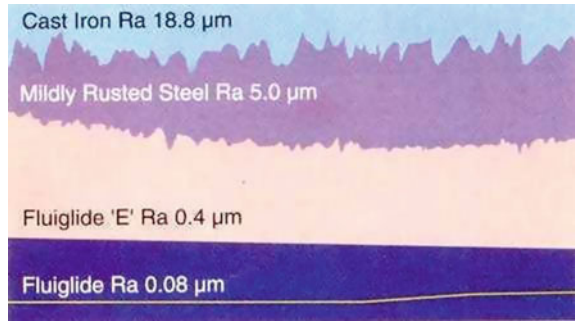
The horizontal split casing LLC pumps having medium range of flow which is commonly required for various applications such as water works, small and big lift irrigation schemes, cooling towers, air conditioning, water circulation, and water sprinkler systems. These are also used in paper, sugar, textile industries, in process plants for slightly corrosive liquid and for turbid water with special material of construction, in power stations for critical water application, in wastewater, etc.

### **2.2.1 Features Adopted in the LLC Pump:**

#### **1. Coating**

The loss in the casing is because of the friction problem, so the erosion loss is diminished by proving the pump casing with corrocoat fluiglidle coating. Due to fluiglidle coating, the frictional loss in the entries of casing is decreased definitely.

**Fig. 3** Coating



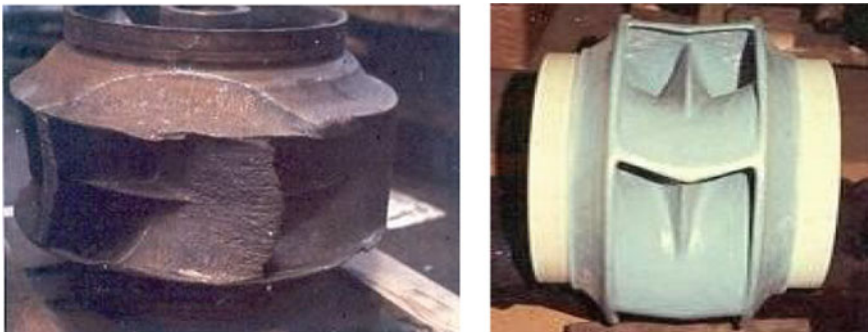
The surface harshness estimation of fluiglides covering is most minimal when contrasted with different coatings accessible on the lookout. It upgrades bearing life moreover. The coating structure is shown in Fig. 3

2. **Impeller**

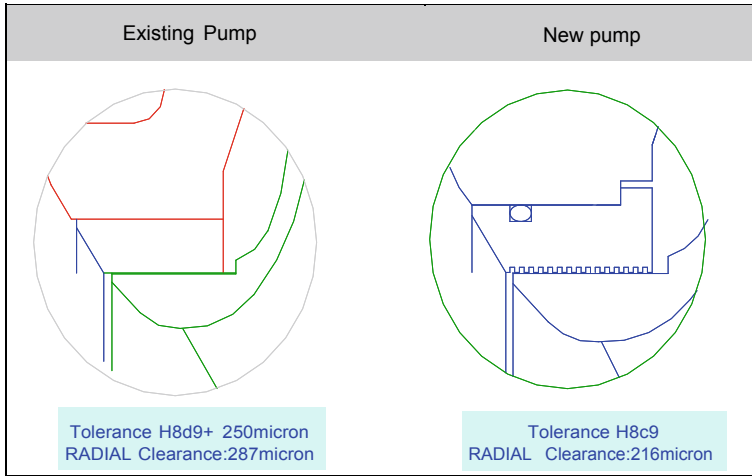
Casting in stainless steel cast grade is standard scope of supply. Double-suction impeller is shown in Fig. 4 will improve the axial thrust generated inside the pump, which also improves productivity, axial thrust is limited to extraordinary degree and upgrades bearing life. Axial thrust is generated due to difference in pressure at suction and delivery side. Pivoting congregations are progressively adjusted according to ISO 1940 Grade 2.5 limiting vibrations. Customer gets the benefit like increased impeller life, increased cavitation resistance, improved hydraulic performance, increase in bearing, and parts life. This results in reduction in overall maintenance costs.

3. **Wear Rings**

Casing wear rings shown in Fig. 5 are used to maintain the clearance between impeller and casing. Smaller the clearance, improve the efficiency as leakage reduced starting high pressure to low pressure side. When clearance between the casing ring and impeller increases, fluid moving from delivery volute to pull



**Fig. 4** Impeller design



**Fig. 5** Wear rings

chamber. Finally, it achieves loss of proficiency. These impellers are considered with closer gap. Due to the same, fluid moving from conveyance to pull. O ring is given among casing and wear ring to keep an essential separation from spillage through fixed parts.

#### 4. Mechanical Seal

The mechanical shaft seal is basically a choke around the shaft. It decreases spillage between the pump and the environmental factors to an outright least. The delivery between the fixed and turning a piece of the seal should be little to diminish spillage. They, as well, notwithstanding, are controlled spillage gadgets. The fixing faces can't be allowed to contact in a dry climate. Some fluid should pass between the turnings and fixed face to limit grinding and to divert the warmth created. Couple and twofold seals just as gas-cleansed seals have been utilized in troublesome or risky fixing administrations. These courses of action can be intricate and costly. Disappointment of the mechanical shaft seal is the most widely recognized reason for pump personal time. To beat these cartridge type mechanical seal is utilized. It offers advantages to client like zero spillage, low grinding, and simplicity of expulsion. Schematic arrangement of mechanical seal is shown in Fig. 6

#### 5. Throttle Bush

The use of throttle bush shown in Fig. 7 reduces the consumption of energy which leads to the facilitates with single mechanical seal. A throat bush covers the pump shaft and is coupled to the casing. The throat bush has an inside surface that gives a fluid passageway between the inside surface of throat bush and the shaft. The throat bush is placed on the shaft at an axial space from the mechanical seal, thus form a restriction to the fluid path.

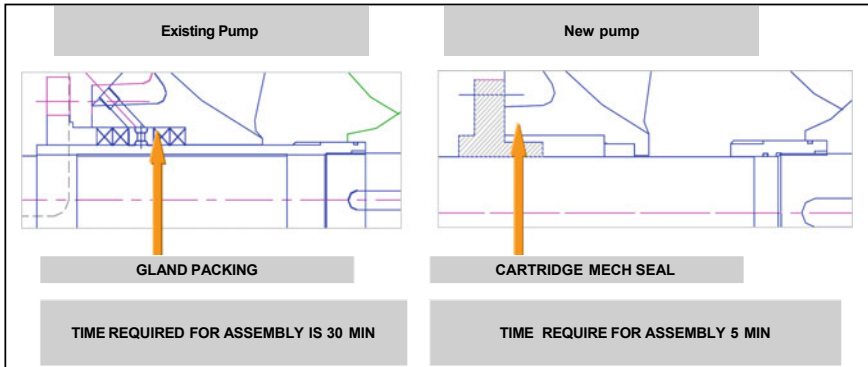


Fig. 6 Mechanical Seal

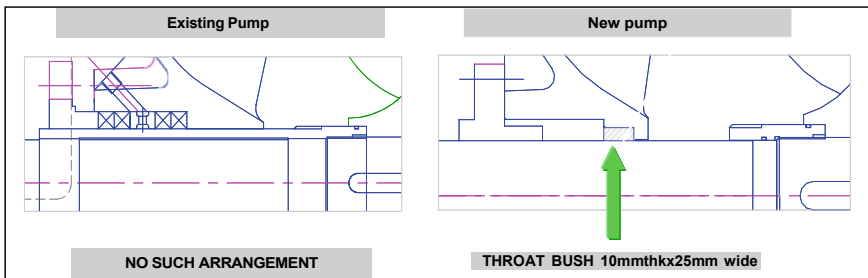


Fig. 7 Throttle Bush

6. **Double volute casings**

Double volute rib in the casing minimizes the radial force and resulting equal distribution of pressure and velocity inside the casing. This characteristic is just consolidated where vital, as double rib design will in general reduces the efficiency of the pump slightly. It gives the benefits to low energy costs, also gives intermediate support to shaft results in arresting the shaft deflection and rubbing of wear ring, and impeller is avoided. Figure 8 shows the double volute casing pump.

7. **Energy Consumption:**

The energy consumption is one of the important parameter in designing of pump. During development of pump on performance basis, energy consumption is considered as one of the top aspect. It is calculated considering the efficiency of pump and energy input of pump. In this section, comparison of energy consumption and cost saving is discussed and interpreted through graph. The energy consumption is calculated considering pump set is running by 16 hours per day and 180 days in a year. Energy cost is calculated by considering per unit rate as Rs. 12. The energy consumption is calculated year-wise, and

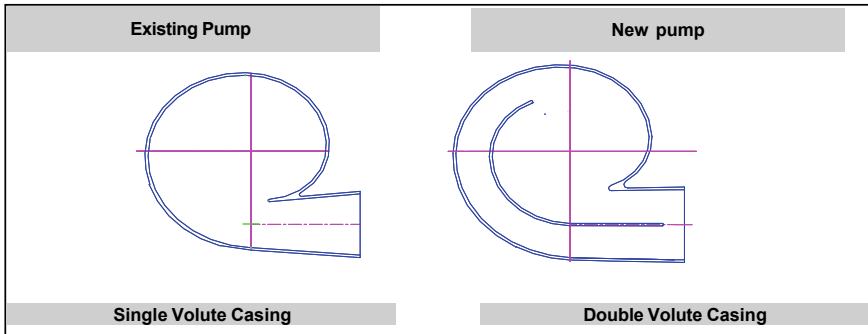


Fig. 8 Double volute casing pump

Table 1 Energy consumption (conventional pump)

Regular	1st year	2nd Year	3rd Year	20th Year
D	800	800	800	800
H	60	60	60	60
E	82	81	80	62
Input	159.4	161.4	163.4	210.8
Energy consumption	459,110	464,779	470,588	607,211
Energy cost	5,509,326	5,577,342	5,647,059	7,286,528

required data are provided by company which is mentioned in Table 1. The general life of centrifugal pump is 20 years considering running of pump 16 hours per day and 180 days in a year. Considering 20 years life of pump, energy consumption is calculated by using the Eqs. (2, 3, and 4) given below.

$$\text{Input power (Kw)} = \frac{\left(\frac{\text{Discharge}}{3.6} * \text{Head}\right)}{102 * \left(\frac{\text{Efficiency}}{100}\right)} \tag{2}$$

$$\text{Energy consumption (Kw – hr)} = \text{Input power} * \text{Hr/Day} * \text{Number of days in a year} \tag{3}$$

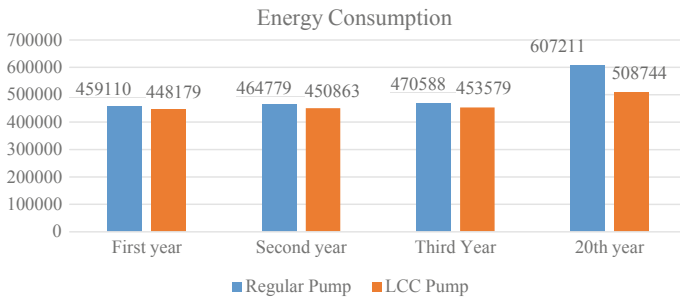
$$\text{Energy Cost} = \text{Energy consumption} * \text{per unit charge} \tag{4}$$

The energy consumption and there expenses for regular pump and LCC model is summarized in Tables 1 and 2, respectively.

Figure 9 shows the energy consumption of conventional and experimental pump. It shows that energy consumption decreases continuously after applying LCC model. It shows that approximately 16.21% less energy consumption after 20 years.

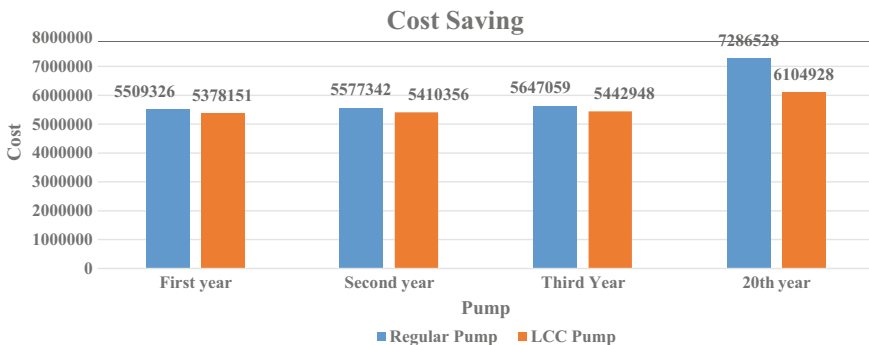
**Table 2** Energy consumption (LCC pump)

Experimental	1st	2nd	3rd	20th
D	800	800	800	800
H	60	60	60	60
E	84	83.5	83	74
Input	155.6	156.5	157.5	176.6
Energy consumption	448,179	450,863	453,579	508,744
Energy cost	5,378,151	5,410,356	5,442,948	6,104,928



**Fig. 9** Energy consumption

Figure 10 shows the energy cost saving in first, second, third, and 20 years. The energy consumption is decreased by 16.21% which directly gives commercial benefits to customer. The single pump saves Rs. 5,96,253 after 20 years. This percentage may vary depending upon the running hours of pump and application, for which pump is used.



**Fig. 10** Energy cost saving

### 3 Conclusion

As developed countries become more aware of the effects of energy wastage, the importance of energy efficiency becomes apparent. Increased pump efficiency means reduced overall power consumption. This translates directly into reducing pollution and conserving natural resources by effectively reducing the carbon footprint. Low-cost cycle pumps by Kirloskar Brothers Limited effectively reduce power consumption and thus increase the efficiency of pumps. The above percentages of energy saving may vary depending on the operating hours of the pump and the use, which is used for the pump. The LCC pump user will drive the benefit of guaranteed performance in a sustainable manner over the life of the pump.

Life cycle cost is an exceptionally useful device for the clients which can be successfully used to assess and analyze any machine, especially for complex pumping frameworks to settle on buy choice from the accessible other options and defend own advantages.

### References

1. Gupta AK (1996) Reliability engineering and terotechnology. Macmillan India Ltd, pp 409–419
2. Xu X, Chen Q, Xie SQ (2006) Framework of a product lifecycle costing system. *J Comput Inf Sci Eng ASME* 6:69–77
3. Sandborn P, Myers J (2008) Handbook of performability engineering, Misra KB (ed). Springer, London, pp 81–103
4. Dhillon S (1989) Life cycle costing: techniques, models and applications. Gordon and Breach Science Publishers
5. Castagne S et al (2008) A generic tool for cost estimating in aircraft design. *Res Eng Design* 18(4):149–162
6. Barringer PH, Weber DP (1996) Life cycle cost tutorial. In: Fifth international conference on process plant reliability. Houston, Texas
7. World Pumps (1998) Life cycle cost analysis of pumping systems, issue 383, pages 28–32
8. Foster R, Hanley C (1998) Life cycle cost analysis for photovoltaic water pumping systems in Mexico. In: 2nd world conference on photovoltaic solar energy conversion, Vienna, Austria
9. Nesbitt B (2001) Intelligent pump units and life cycle costs. *World Pumps* 415:20–25
10. Stavale AE, Lorenc JA, Sabini EP (2001) Development of a smart pumping system. In: Proceedings of eighteenth international pump users symposium, Houston, Texas



# Identification of Fault Severity of Rolling Element Bearing Using Image Augmentation and Mobile Net V\_2 Convolutional Neural Network



P. Akhenia, H. Jamani, and V. Vakharia 

**Abstract** The rolling bearing is one of the most important parts of any rotating machinery. A bearing operating condition determines the safety during working condition. So it is very important to do condition monitoring in real time and diagnosis of rolling bearing for preventing failure. The main challenges in traditional method of fault diagnosis are finding good fault features. To address this problem, author have used data augmentation technique for bearing fault diagnosis. This proposed method converts 1-D time domain vibration signals into 2-D time frequency image by using short-term fourier transformation (STFT). However, a major problem in deep convolution neural network (CNN) is that in CNN large number of samples data is required to obtain well trained model. Proposed method introduces data augmentation for generating 2-D time frequency image for preparing large number of data set, and Deep Neural Network is used for rolling bearing fault classification. Major purpose of this study is to identify and successfully classify the different severity level faults of rolling bearing. Author apply this approach on rolling bearing dataset of Case Western Reserve University to verify the effectiveness of the proposed method. Results show that proposed methodology give higher accuracy and is fast to train the model. Also this method achieve better accuracy with different fault conditions as compare to other traditional method of fault classification.

**Keywords** Rolling bearing · Fault diagnosis · Data augmentation · Deep transfer learning

## 1 Introduction

With the recent advancement in Big Data Analysis, Cyber Physical System (CPS) internet of thing (IOT), Smart Manufacturing and Intelligent, fault diagnosis have grown rapidly. Main purpose of intelligent fault diagnosis is to provide better control of production process and improve the condition awareness of machine [1]. In many

---

P. Akhenia · H. Jamani · V. Vakharia (✉)  
Pandit Deendayal Petroleum University, Gandhinagar 382355, India  
e-mail: [Vinay.Vakharia@sot.pdpu.ac.in](mailto:Vinay.Vakharia@sot.pdpu.ac.in)

© The Author(s), under exclusive license to Springer Nature Singapore Pte Ltd. 2022  
G. S. V. L. Narasimham et al. (eds.), *Innovations in Mechanical Engineering*,  
Lecture Notes in Mechanical Engineering,  
[https://doi.org/10.1007/978-981-16-7282-8\\_55](https://doi.org/10.1007/978-981-16-7282-8_55)

733

automotive industry, bearing is key component of rolling machinery and plays a vital role in maintaining normal working condition. Failure of bearing can cause sudden break down of rotating machinery and increase operating and maintenance cost. Over last few year many intelligent diagnosis method are designed to perform fault diagnosis. Condition monitoring and fault diagnosis method include acoustic analysis, vibration analysis and temperature analysis [2–4]. From the above methods, vibration method provides most accurate result and is widely used for bearing fault diagnosis. Vibration based fault classification can be divided in to three part: (1) Data collection, (2) Feature extraction, (3) Fault classification. Feature extraction is important to reduce the input dimension by extracting meaningful feature, based on time frequency analysis [5].

Traditional fault diagnosis methods are generally dependent on signal processing and signal Analysis which is relying on prior experience and field expertise. This methods do not involve any advance use of data analysis. The feature extraction technique that is used widely are Artificial Neural Networks (ANNs), Support Vector Machines (SVMs) and k-NN as Classifier for performing fault diagnosis process [6–8] V. Vakha-ria. et Al. proposed a traditional method using multiscale permutation entropy based approach to select wavelet for fault diagnosis of ball bearing [9]. However, traditional method have some limitations: Being limited to their shallow architectures. The diagnosis performance strongly depend on the diagnostic feature quality and feature selection. In real life, bearing works under different environment so to obtain original signals, noise has to be removed from it. Therefore, one requires advance knowledge of signal processing and high expertise in feature selection. In addition, traditional classifiers have simple architecture as a reason they are unable to classify complex nonlinear relationship of fault diagnosis. So instead of manually extracting feature and manually selecting important feature, more emphasis should be given on automatic feature extracting and feature selection by using deep learning architecture.

Since 2016, Deep learning method was introduced for image classification, and it was successfully applied for fault diagnosis and classification task of rolling element [10–13]. Deep learning can automatically extract valuable feature from measured data and also avoid the dependence on prior knowledge about signal processing and high expertise on feature selection. Various deep network architectures are used in recent times which includes, Auto Encoders (AE) [14], Deep Belief Networks (DBN) [15], long short-term memory (LSTM) networks [16], and Convolutional Neural Networks (CNN) [17] have been adopted for solving different diagnosis tasks. Jia et al. proposed a normalized CNN for imbalanced fault diagnosis of machinery. Although studies indicate that deep learning still has to achieve high accuracy and precision. As we know that bearing is a continuously moving part and works in different environment, fault signal is often merged with heavy noise. In such condition, considering only one dimension signal can decrease the fault diagnosis accuracy.

In this paper, CWRU bearing dataset is used for fault diagnosis model. First step is to convert time domain one-dimensional raw signal data in to two dimension time frequency image. Then, author has used short-term fourier transformation (STFT)

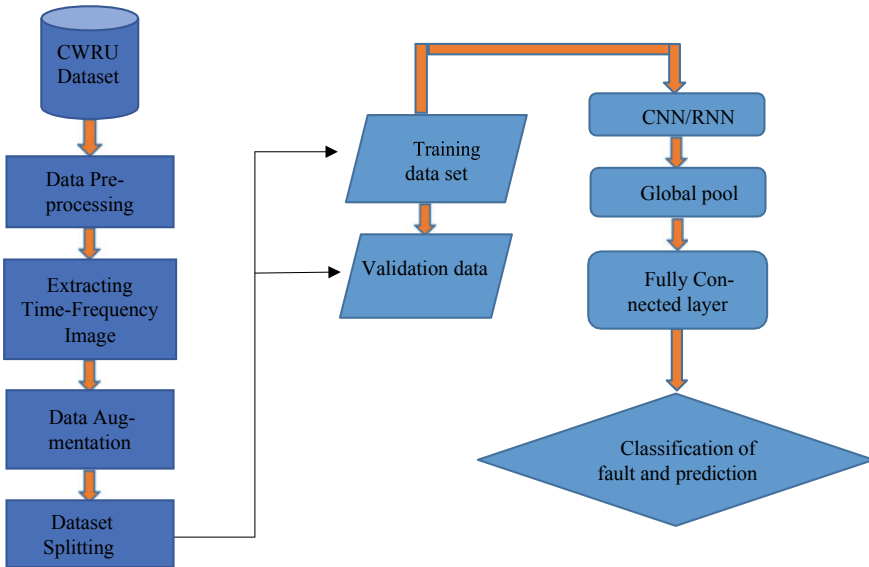


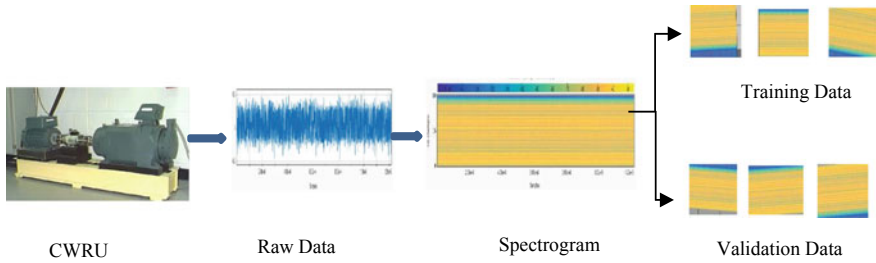
Fig. 1 Flow chart of proposed method

for generating spectrogram image of vibration signal. Two-dimensional image has been sent as input in residual neural network for extracting useful feature and to identify different fault severity level. Results show the potential of this method for identification of fault severity. Flow chart of proposed method is described below in Fig. 1.

Rest of the paper is constructed as follows (2) Details of proposed method (3) Experimental setup and data description (4) Diagnosis results and analysis (5) Conclusion.

## 2 Details of Proposed Method

For machine fault monitoring, vibration data obtained is generally in one-dimensional time series signal. To apply deep learning model for automatic extracting fault feature, one-dimensional vibration signals are used. The original vibration signals collected from bearing are transformed into time frequency 2-D image by using STFT. Then, this fault images are used for generating other images by using data augmentation. After that the data set of images is split in to two part: training dataset and testing data and is set according to certain proportionate generated image samples. Validation set is inputted in CNN model to carry out the failure detection of rotating machinery. Generally, fault signal are non-stationary and non-linear in nature, so



**Fig. 2** CWRU experiment setup and data generation process

analysis method needs to accurately identify local time varying spectrum of characteristic of signal. The change rule of the signal spectrum cannot be analyzed using global transformation and only be done using fourier transform instead.

### 2.1 Single Processing and Spectrogram Generation

In this method, STFT is used to convert vibration signal obtained from the setup, to 2-D spectrogram of time and frequency. The signals obtained from the setup is shown in Fig. 2. For smoothening the data points, we need to do signal modification so that the individual points with higher values than their adjacent points are reduced, and the values of adjacent points are changed for getting a smooth data with less irregularities and fluctuations. The smoothening of the signals does not affect true signals as we have only reduced the noise at higher frequencies. Let us consider an example, there is a three point curve ( $n = 3$ ) for  $i=2$  to  $n - 1$ , where  $R_i$  the  $i$ th point in the smoothed signal,  $X_i$  the  $i$ th point in the original signal, and  $t$  is the total number of points in the signal.

$$S_j = \frac{Y_{j-1} + Y_j + Y_{j+1}}{3}$$

### 2.2 Spectrogram Generation

As mentioned earlier, authors have used short-time frequency fourier transform for converting one dimensional time series signals to two dimensional time frequency graph. Time frequency distribution highlights the amplitude versus time and frequency distribution from the given signal. This type of transformation is widely used for the processing of acoustic signals. The plot that is generated from the coefficients of STFT is known as spectrogram. It can be represented mathematically as

$$X[k \ l] = \text{DFT}\{[x[l]w[0], \dots, x[l + N - 1]w[N - 1]]\} \quad k = 0, \dots, N - 1$$

where  $K$  denotes frequency and  $l$  denotes times.

Here spectrogram represents STFT signal's visual representation and different color scale of spectrogram indicates amplitude of the frequency. Spectrogram also includes time for the analysis of FFT which enables for the localization of time as well as frequency. The given figure shows the spectrogram of the faulty bearing.

### 2.3 Data Augmentation

Since CWRU vibration data is collected under different working conditions, it has different characteristics. So if the model is trained directly using spectrogram (time frequency graph) then fault diagnosis accuracy of model for different fault condition would be poor. In order to avoid this problem, author has proposed data augmentation method using python. Data augmentation is used for generating synthetic image data set. In this process, various changes like vertical flipping, horizontal flipping, shearing, zooming, rotation and other operation are done on the image for generating data, and thus increasing size of dataset, to improve the generalization of CNN model.

Data augmentation increases the size of data and avoid the influence of data biasness on the accuracy of the model. In rotation operation random rotation of image of around 10 degree is applied where as in zooming operation random zooming in both horizontal and vertical direction is applied. Shorten et al. studied the effects of image data enhancement on deep learning in detail [18]. Experimental studies give enough evidence that data augmentation reduce over fitting of the model and provide better data set for the model. Flow chart of experimental setup and data generation process is shown below in Fig. 2.

## 3 Experimental Setup

### 3.1 Bearing Data Description

Bearing data set from Case Western Reserve University (CWRU) [19] is used to verify the performance of the proposed method. Vibration data used in experiment is obtained from fault injection test of 6205-SKF deeply grooved ball bearing with sampling frequency of 12 kHz. Experimental setup consists of four units from left to right: 2HP motor, a torque sensor, a dynamometer, and control electronic equipment. The accelerometer is mounted on a housing with a magnetic base and uses a 16 channel DAT recorder to collect vibration signals.

In this study, author has used different vibration signals with outer race fault, inner race fault and ball fault, signal take under four different operating condition:-

1797 rpm (Load 0), 1772 rpm (Load 1), 1750 rpm (Load 2), 1730 rpm (Load 3). For each load Condition 150 time frequency images are generated by data augmentation method. Three types of single-point faults including inner-race faults (IFs), outer-race faults (OFs) and ball faults (BFs) have been introduced into SKF deep-groove ball bearings using electro-discharge machining (EDM). For the faulty bearings, each fault type has three levels of severity with fault diameters of 7 mils, 14 mils and 21 mils (1 mil = 0.001 inches), respectively. Data set consists STFT image of different type of faults size. Training and validation data set are established for rolling bearing fault data under each load condition. Training data set consists a total of 1250 images of spectrogram, while for validation set there is a total of 540 image of spectrogram.

## 4 Diagnosis Result and Analysis

In this section, author need to mention that the proposed method under different conditions of bearing fault and motor speed gives better accuracy for the prediction. Proposed methodology is able to classify different severity level of fault (0.007 0.014, 0.021 mils) with a very high accuracy. As mentioned for each type of faults, time frequency images are generated using data augmentation. Trained model is used for classification and prediction of the bearing faults. Image data set is sent as an input to trained model and the data set is split in to train and validation set in ratio of 7:3 (70% for Training and 30% for Testing). Proposed methodology shows that the deep learning model is fast and effective than the traditional methods of machine learning in terms of computation and accuracy. It requires less data for higher prediction accuracy and time taken for the computation is also less as compared to traditional methods.

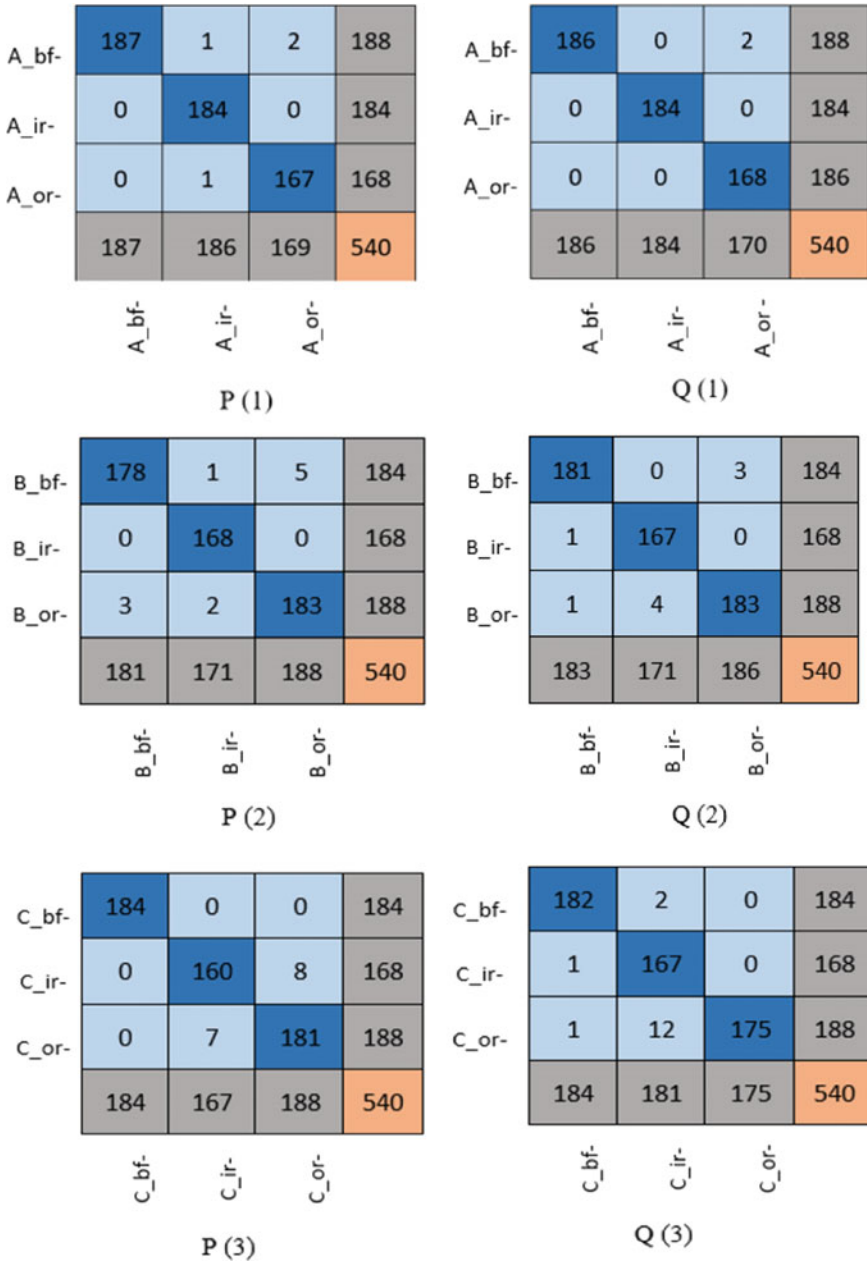
Here in this study, a comparison is also done between different pre trained deep learning model with each other for better justification. Author compared ResNet-34, VGG-16, Mobile Net and SqueezeNet1\_1 for classifying different severity level of faults. Comparison between the accuracy of different algorithm is shown in Table 1. For severity classification, each fault size consists of 3 classes (BF, IR, OR) with 1260 train images and 540 image for validation. Confusion matrix is used to visualize the diagnostic result of different fault prediction. Confusion matrix of different fault size shown in Figs. 3 and 4, where a represent 0.007 mils fault, B represents 0.014 mils fault, C represent 0.021 mils fault. Diagonal elements represents the number of correctly predicted faults, while other elements represents the number of incorrectly predicted faults. Diagonal of confusion matrix shows the right prediction and accuracy of model. Each row of the matrix represents the instances in output class, while each column represents the instances in actual class. Figure 3 shows confusion matrix of fault severity of ResNet-34 and VGG-16 model where as Fig. 4 shows confusion matrix of fault severity of MobileNet\_v2 and SqueezeNet1\_1 model and Fig. 5 shows the classification accuracy achieved from Deep Learning models.

**Table 1** Comparison of different deep learning Architecture

CNN Model	Fault Severity	Accuracy	Precision	Recall	F_Beta
ResNet-34	0.007	99.62	0.99	0.99	0.99
	0.014	97.96	0.97	0.98	0.98
	0.021	97.22	0.97	0.97	0.97
VGG-16	0.007	99.62	0.99	0.99	0.99
	0.014	98.33	0.98	0.98	0.98
	0.021	97.03	0.97	0.97	0.97
SqueezeNet1_1	0.007	99.62	0.99	0.99	0.99
	0.014	99.25	0.99	0.99	0.99
	0.021	97.22	0.97	0.97	0.97
MobileNet_V2	0.007	99.07	0.99	0.99	0.99
	0.014	99.44	0.99	0.99	0.99
	0.021	98.33	0.98	0.98	0.97

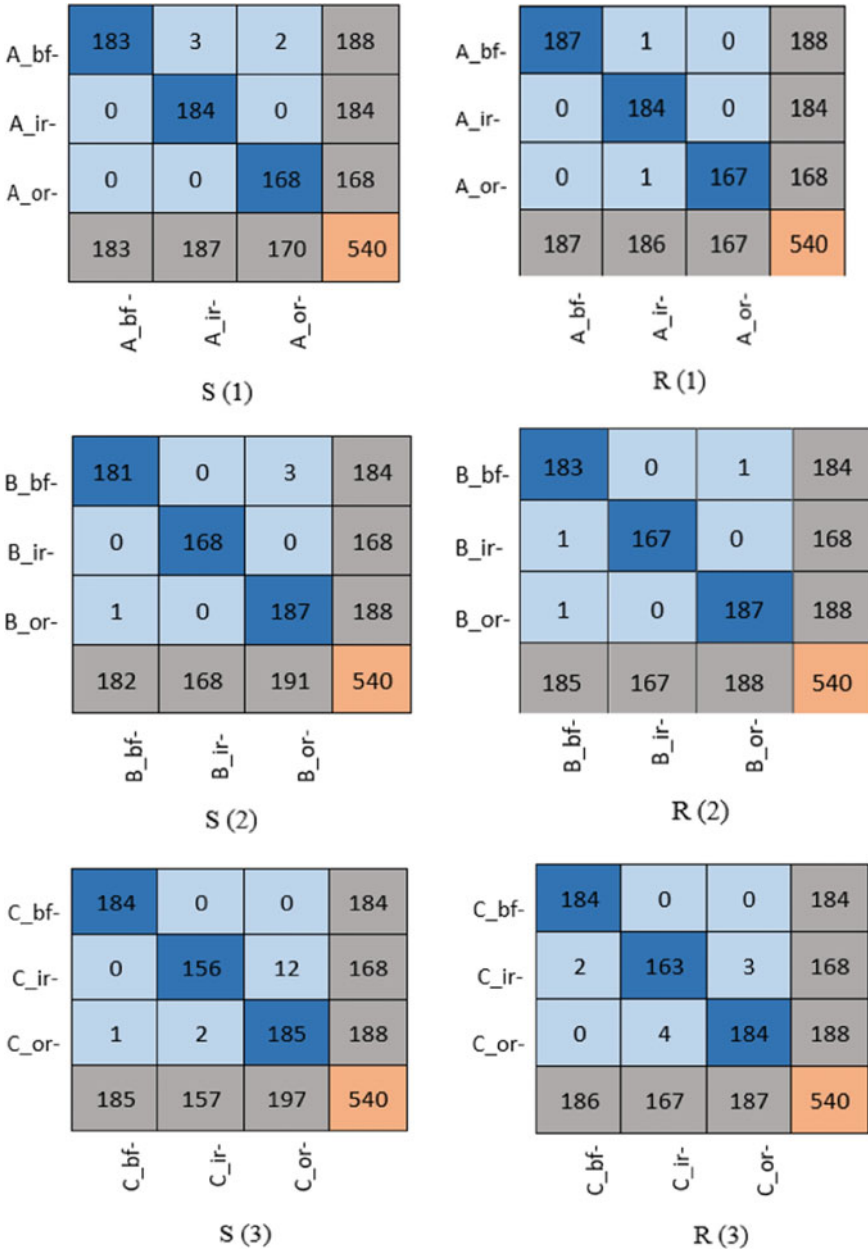
## 5 Conclusion

Traditional method for fault diagnosis and detection requires extraction of features so as to describe the faulty signal characteristic which requires much expertise and prior knowledge. In this proposed method, novel fault severity and rolling bearing fault diagnosis analysis based on residual neural network and data augmentation is presented. In this study, various CNN model are applied for fault severity classification. Time frequency images are used as input to the deep learning model. CWRU bearing fault data sets were used to verify the effectiveness of proposed methodology. In this study, a brief comparison is made between various deep learning model and as shown in diagnosis result, accuracy for different fault severity are up to 99.9%. Proposed method is also quite effective in various environment and various operating condition. Diagnosis results shows that the proposed method has achieved high classification accuracy and also better generalization performance as compared to other rolling bearing fault diagnosis method reported in literature.

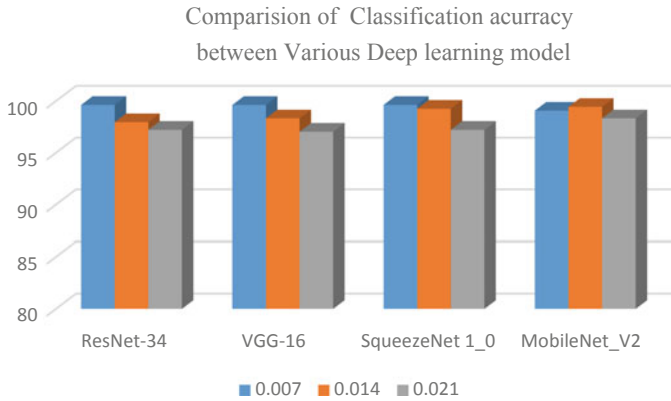


**Fig. 3** P(1), P(2), P(3) represent fault severity by ResNet-34, Q(1), Q(2), Q(3) represent fault severity by VGG-16





**Fig. 4** S(1), S(2), S(3) represent fault severity by SqueezeNet1\_1, R(1), R(2), R(3) represent fault severity by MobileNet\_v2



**Fig. 5** Comparison of classification accuracy between various deep learning models

## References

1. Wang XV, Wang L (2019) Digital twin-based WEEE recycling, recovery and remanufacturing in the background of Industry 4.0. *Int J Prod Res* 57:3892–3902. <https://doi.org/10.1080/00207543.2018.1497819>
2. Zhang D, Entezami M, Stewart E, Roberts C, Yu D (2018) Adaptive fault feature extraction from wayside acoustic signals from train bearings. *J Sound Vib* 425:221–238. <https://doi.org/10.1016/j.jsv.2018.04.004>
3. Sikora EA (2016) Detection of bearing damage by statistic vibration analysis. *IOP Conf Ser Mater Sci Eng* 124. <https://doi.org/10.1088/1757-899X/124/1/012167>
4. Zhou X, Zhang H, Hao X, Liao X, Han Q (2019) Investigation on thermal behavior and temperature distribution of bearing inner and outer rings. *Tribol Int* 130:289–298. <https://doi.org/10.1016/j.triboint.2018.09.031>
5. Li Y, Ding K, He G, Jiao X (2018) Non-stationary vibration feature extraction method based on sparse decomposition and order tracking for gearbox fault diagnosis. *Meas J Int Meas Confed* 124:453–469. <https://doi.org/10.1016/j.measurement.2018.04.063>
6. Ben Ali J, Fnaiech N, Saidi L, Chebel-Morello B, Fnaiech F (2015) Application of empirical mode decomposition and artificial neural network for automatic bearing fault diagnosis based on vibration signals. *Appl Acoust* 89:16–27. <https://doi.org/10.1016/j.apacoust.2014.08.016>
7. Muruganatham B, Sanjith MA, Krishnakumar B, Satya Murthy SAV (2013) Roller element bearing fault diagnosis using singular spectrum analysis. *Mech Syst Signal Process* 35:150–166. <https://doi.org/10.1016/j.ymsp.2012.08.019>
8. Yan X, Jia M (2018) A novel optimized SVM classification algorithm with multi-domain feature and its application to fault diagnosis of rolling bearing. *Neurocomputing* 313:47–64. <https://doi.org/10.1016/j.neucom.2018.05.002>
9. Vakharia V, Gupta VK, Kankar PK (2015) A multiscale permutation entropy based approach to select wavelet for fault diagnosis of ball bearings. *JVC/Journal Vib Control* 21:3123–3131. <https://doi.org/10.1177/1077546314520830>
10. Zhang S, Zhang S, Wang B, Habetler TG (2020) Deep learning algorithms for bearing fault diagnostics—a comprehensive review. *IEEE Access* 1–1. <https://doi.org/10.1109/access.2020.2972859>
11. Deutsch J, He D (2017) Using deep learning-based approach to predict remaining useful life of rotating components. *IEEE Trans Syst Man Cybern Syst* 1–10. <https://doi.org/10.1109/TSMC.2017.2697842>

12. Krishnamurthi M, Phillips DONT (2017) Deep learning based approach for bearing fault diagnosis. *IEEE Trans Ind Appl* 53:67–84
13. Guo S, Yang T, Gao W, Zhang C, Zhang Y (2018) An intelligent fault diagnosis method for bearings with variable rotating speed based on pythagorean spatial pyramid pooling CNN. *Sensors (Switzerland)* 18. <https://doi.org/10.3390/s18113857>
14. Shao H, Jiang H, Zhao H, Wang F (2017) A novel deep autoencoder feature learning method for rotating machinery fault diagnosis. *Mech Syst Signal Process* 95:187–204. <https://doi.org/10.1016/j.ymsp.2017.03.034>
15. Tran VT, Althobiani F, Ball A (2014) An approach to fault diagnosis of reciprocating compressor valves using Teager-Kaiser energy operator and deep belief networks. *Expert Syst Appl* 41:4113–4122. <https://doi.org/10.1016/j.eswa.2013.12.026>
16. Zhang B, Zhang S, Li W (2019) Bearing performance degradation assessment using long short-term memory recurrent network. *Comput Ind* 106:14–29. <https://doi.org/10.1016/j.compind.2018.12.016>
17. Yang Y, Zheng H, Li Y, Xu M, Chen Y (2019) A fault diagnosis scheme for rotating machinery using hierarchical symbolic analysis and convolutional neural network. *ISA Trans* 91:235–252. <https://doi.org/10.1016/j.isatra.2019.01.018>
18. Shorten C, Khoshgoftaar TM (2019) A survey on image data augmentation for deep learning. *J Big Data* 6. <https://doi.org/10.1186/s40537-019-0197-0>
19. Bearing Data Center, Case Western Reserve University. <http://csegroups.case.edu/bearingdatacenter/pages/12k-drive-end-bearing-fault-data> [dataset]

# Study of Isomorphism Among Kinematic Chains of Group-IVC



Ali Hasan

**Abstract** In this paper, author checked the isomorphism among 95 kinematic chains of group-IVC with the application of joint-joint matrix [M]. All the 95 kinematic chains have been sketched along with their identification numbers such as “absolute sum” [AS] and “absolute maximum” [AM] calculated from matrix [M] with the help of MATLAB. This study has been explained with the help of two illustrative examples and beneficial to the researchers during the initial stage of design of their research work.

**Keywords** Kinematic chain · Mobility · Characteristic polynomial

## 1 Introduction

Elimination of duplicate mechanism is extremely important in the design conceptual stage, and for this, a number of researchers have invented several theories. Mruthyunjaya [1] published a computer program applicable for mechanism identification among kinematic chains. The proposed technique was based on algebraic formulas for generation of computer program. They applied the developed technique in the design of KCs having simple kinematic pairs. They applied this program for KCs having mobility greater than zero. Mruthyunjaya [2] confirmed the trueness of computer program published by him in [1] that was developed for the design of KCs with simple kinematic pairs. He applied that technique to many other chains having no solutions in the literature at that time. He worked on seven bars with zero mobility, eight, ten, and twelve bar binary KCs with one mobility as well as nine bar having two mobility. He found some error in his results with those already was available in the literature. Mruthyunjaya [3] applied the already developed computer program by him in [1] for the invention of 97 ten bar KCs having three mobility. He published that total 676 distinct mechanisms can be derived from 97 KCs of ten bar of three mobility. Mruthyunjaya [4] tested his own work later and found that the design of

---

A. Hasan (✉)

Faculty of Engineering & Technology, Jamia Millia Islamia, New Delhi, India  
e-mail: [ahasan@jmi.ac.in](mailto:ahasan@jmi.ac.in)

mechanisms kinematic chains based on the basis of two identification numbers of adjacency matrices for checking the isomorphism purpose failed in several cases. He presented the merits and demerits of all the techniques already available in the literature. He proposed a new technique for isomorphism checking based on degree matrix. Sohn and Freudenstein [5] developed a new technique with the application of dual graphs for synthesis analysis. Their developed program was based on automatic method with highest efficiency in selecting kinematic structure of mechanisms.

Rao [6] applied fuzzy logic for the solution of isomorphism problems for inversions and kinematic chains. They defined the required conditions for the isomorphism. He demonstrated the application with several examples. P. R. He, Zhang et al. [7] developed a new technique to check isomorphism among the graphs of kinematic chains with the application of quadric form. They converted the two kinematic chains into quadratic form and reduced the both for matching purpose. They proposed that the same semi-axis of both the graph represents the isomorphism. They suggested a method using this concept. Chang et al. [8] proposed a new method with the help of eigenvectors and eigenvalues for the purpose of checking isomorphism among KCs. The KCs are converted into adjacent matrices. They matched the eigenvalues and eigenvectors of the developed matrices. In this way, the task of checking isomorphism became easier. The authors have provided the proof of their developed method. Cubillo and Wan [9] revised already published techniques for isomorphism checking purpose. They found the error in the original method and suggested the necessary corrections. They developed a new method to verify isomorphism among KCs by matching eigenvalues and eigenvectors of the adjacent matrices. He and Zhang [10] studied the various difficulties encountered in isomorphism verification among kinematic chains. The authors suggested an eigensystem technique with the application of eigenvalue and eigenvector for the adjusted adjacency matrix.

Ding and Huang [11] suggested several new basic ideas on the topological graph. They developed the characteristic adjacency matrix for any graph or mechanism. Then, they applied the synthetic degree sequence to the newly developed matrix for the verification of isomorphism in mechanism kinematic chains. Ding and Huang [12] presented two primary loop operations, " $\ominus$ " and " $\oplus$ " for the synthesis of mechanism kinematic chains. They suggested the independent loop set and an algorithm based on it. Finally, they gave a loop theory for isomorphism determination purpose. Rao [13] invented a genetic algorithm for checking isomorphism in KCs. He suggested the identification of best link to make the frame as well as the input link. It is a unique study that fulfills all the requirements of the isomorphism. Prasadraju and Rao [14] suggested the design isomorphism verification among epicyclic gear trains. Their proposed technique is efficient with the application of loop concept and hamming number concept for checking isomorphism among epicyclic gear trains. Rizvi et al. [15] suggested a method with the application of instantaneous center for mechanism design. Rizvi et al. [16] presented a isomorphism mechanism checking technique with the help of a unique matrix to represent the bars of KCS. Kong et al. [17] proposed a new method with the application of artificial neural network for isomorphism checking among KCs. They represented the KCs by graph.

## 2 The Joint-Joint Matrix [M]

This is joint-based matrix square symmetric matrix of size  $n \times n$ , where  $n$  is the number of kinematic pairs in a KC.

$$[M] = \{a_{ij}\}_{n \times n} \quad (1)$$

where

$a_{ij}$  { = 2 for binary, 3 for ternary, 4 for quaternary, —,  $n$  for  $n$ -nary link between  $i$ th and  $j$ th pairs if they are connected directly else zero including diagonal elements }.

## 3 Methodology

Each kinematic chain is converted into a joint-joint matrix [M]. We determine two identification numbers from this developed matrix [M] with help of MATLAB. These two identification numbers are “absolute sum” [AS] and “absolute maximum” [AM] of polynomials for every kinematic chain for the purpose of isomorphism checking. These two numbers are unique for every mechanism kinematic chain, and if these two numerical values are same, then the corresponding chains are isomorphic. It has been explained with the help of following illustrative examples.

## 4 Illustrative Example-1

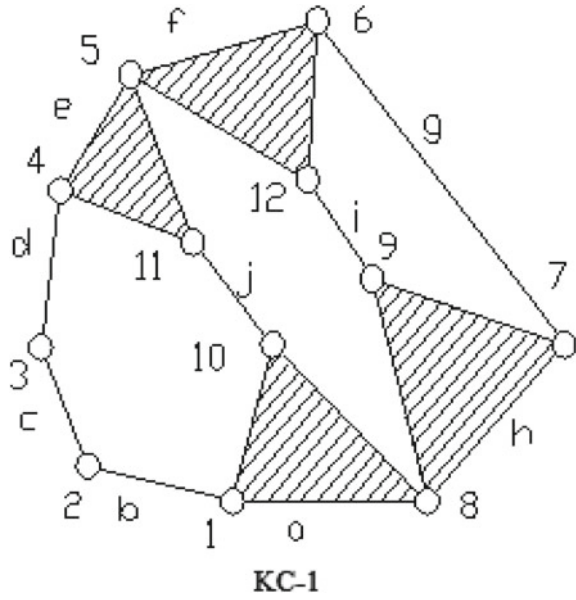
We are considering 2 KCs of 10 bars, 12 pairs, 3 degree of freedom as shown in Figs. 1 and 2. We have to check the isomorphism between these two KCs. The developed matrices from Figs. 1 and 2 are represented by [M1] and [M2], respectively. The identification numbers for both the KCs are

For KC-1 shown in Fig. 1: [AS] = 8.3734e + 006, [AM] = 3.5938e + 006

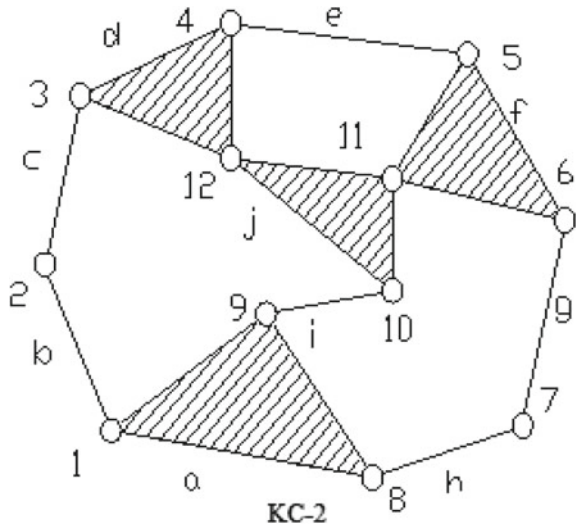
For KC-2 shown in Fig. 1 [AS] = 7.0147e + 006, [AM] = 2.9393e + 006

We see that both the identification numbers of both the KCs are different. Therefore, both the KCs are not isomorphic. We get the same result by using other proposed technique Cubillo and Wan [9] in the literature.

**Fig. 1** KC-1 of 10 bars, 12 pairs



**Fig. 2** KC-2 of 10 bars, 12 pairs



$$M1 = \begin{bmatrix} 0 & 2 & 0 & 0 & 0 & 0 & 0 & 3 & 0 & 3 & 0 & 0 \\ 2 & 0 & 2 & 0 & 0 & 0 & 0 & 0 & 0 & 0 & 0 & 0 \\ 0 & 2 & 0 & 2 & 0 & 0 & 0 & 0 & 0 & 0 & 0 & 0 \\ 0 & 0 & 2 & 0 & 3 & 0 & 0 & 0 & 0 & 0 & 3 & 0 \\ 0 & 0 & 0 & 3 & 0 & 3 & 0 & 0 & 0 & 0 & 3 & 3 \\ 0 & 0 & 0 & 0 & 3 & 0 & 3 & 0 & 0 & 0 & 0 & 3 \\ 0 & 0 & 0 & 0 & 0 & 3 & 0 & 3 & 3 & 0 & 0 & 0 \\ 3 & 0 & 0 & 0 & 0 & 0 & 3 & 0 & 3 & 3 & 0 & 0 \\ 0 & 0 & 0 & 0 & 0 & 3 & 3 & 0 & 0 & 0 & 0 & 2 \\ 3 & 0 & 0 & 0 & 0 & 0 & 0 & 3 & 0 & 0 & 2 & 0 \\ 0 & 0 & 0 & 3 & 3 & 0 & 0 & 0 & 2 & 0 & 0 & 0 \\ 0 & 0 & 0 & 3 & 3 & 0 & 2 & 0 & 0 & 0 & 0 & 0 \end{bmatrix}$$

$$M2 = \begin{bmatrix} 0 & 2 & 0 & 0 & 0 & 0 & 0 & 3 & 3 & 0 & 0 & 0 \\ 2 & 0 & 2 & 0 & 0 & 0 & 0 & 0 & 0 & 0 & 0 & 0 \\ 0 & 2 & 0 & 3 & 0 & 0 & 0 & 0 & 0 & 0 & 0 & 3 \\ 0 & 0 & 3 & 0 & 2 & 0 & 0 & 0 & 0 & 0 & 0 & 3 \\ 0 & 0 & 0 & 2 & 0 & 3 & 0 & 0 & 0 & 0 & 3 & 0 \\ 0 & 0 & 0 & 0 & 3 & 0 & 2 & 0 & 0 & 0 & 3 & 0 \\ 0 & 0 & 0 & 0 & 0 & 2 & 0 & 2 & 0 & 0 & 0 & 0 \\ 3 & 0 & 0 & 0 & 0 & 0 & 2 & 0 & 3 & 0 & 0 & 0 \\ 3 & 0 & 0 & 0 & 0 & 0 & 3 & 0 & 2 & 0 & 0 & 0 \\ 0 & 0 & 0 & 0 & 0 & 0 & 0 & 2 & 0 & 3 & 3 \\ 0 & 0 & 0 & 0 & 3 & 3 & 0 & 0 & 0 & 3 & 0 & 3 \\ 0 & 0 & 3 & 3 & 0 & 0 & 0 & 0 & 3 & 3 & 0 & 0 \end{bmatrix}$$

### 5 Illustrative Example-2

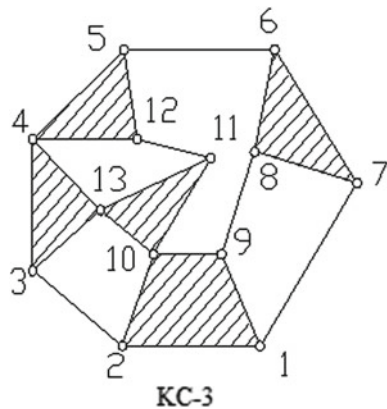
We are considering a pair of isomorphic KCs of 10 bars, 13 pairs, 1 degree of freedom as shown in Fig. 3 and Fig. 4. We have to check the isomorphism between these two KCs. The developed matrices from KC-3 shown in Fig. 3, and KC-4 Fig. 4 is by [M3] and [M4], respectively. The identification numbers for both the KCs are

For KC-3 shown in Fig. 3: [AS] = 7.5562e + 007, [AM] = 3.5648e + 007.

For KC-4 shown in Fig. 4: [AS] = 7.5562e + 007, [AM] = 3.5648e + 007.

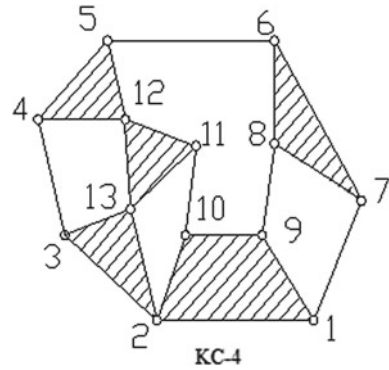
We see that both the identification numbers of both the KCs are same. Therefore, both the KCs are isomorphic. We get the same result by using other proposed technique Cubillo and Wan [9], Rizvi et al. [15, 16], Kong et al. [17] available in the literature.

**Fig. 3** KC-3 of 10 bars, 13 pairs





**Fig. 4** 2 KC-4 of 10 bars, 13 pairs



Joint	1	2	3	4	5	6	7	8	9	10	11	12	13
1	0	4	0	0	0	0	2	0	4	0	0	0	0
2	4	0	2	0	0	0	0	0	0	4	0	0	0
3	0	2	0	3	0	0	0	0	0	0	0	0	3
4	0	0	3	0	3	0	0	0	0	0	0	3	0
5	0	0	0	3	0	2	0	0	0	0	0	3	0
6	0	0	0	0	2	0	3	3	0	0	0	0	0
7	2	0	0	0	0	3	0	3	0	0	0	0	0
8	0	0	0	0	0	3	3	0	2	0	0	0	0
9	4	0	0	0	0	0	0	2	0	2	0	0	0
10	0	4	0	0	0	0	0	2	0	3	0	3	0
11	0	0	0	0	0	0	0	0	3	0	2	0	0
12	0	0	0	3	3	0	0	0	0	2	0	0	0
13	0	0	3	0	0	0	0	0	3	0	0	0	0

Joint	1	2	3	4	5	6	7	8	9	10	11	12	13
1	0	4	0	0	0	0	2	0	4	0	0	0	0
2	4	0	3	0	0	0	0	0	0	4	0	0	3
3	0	3	0	2	0	0	0	0	0	0	0	0	3
4	0	0	2	0	3	0	0	0	0	0	0	3	0
5	0	0	0	3	0	2	0	0	0	0	0	3	0
6	0	0	0	0	2	0	3	3	0	0	0	0	0
7	2	0	0	0	0	3	0	3	0	0	0	0	0
8	0	0	0	0	0	3	3	0	2	0	0	0	0
9	4	0	0	0	0	0	0	2	0	4	0	0	0
10	0	4	0	0	0	0	0	2	0	4	0	2	0
11	0	0	0	0	0	0	0	0	2	0	3	3	0
12	0	0	0	3	3	0	0	0	0	3	0	3	0
13	0	3	3	0	0	0	0	0	0	3	3	0	0

## 6 Results and Conclusions

All the 95 kinematic chains of 10 bars, 13 pairs, and single mobility group-IVC are represented from Jensen [18] in Fig. 5, and their identification numbers [AS] and [AM] are listed in Table 1. We observe that all identification numbers [AS] and [AM] are unique as well as different for every kinematic chain. We can check the isomorphism among other kinematic chains having single or multiple mobility as well as multiple kinematic pairs. This is a very simple, easy, and graspable study for the purpose of checking isomorphism among mechanism kinematic chains. This proposed study may be applied for similar of different mechanism identification. Earlier, this study has been used successfully in checking the isomorphism among sixteen known kinematic chains of eight bars. The benefit of this study is that the isomorphism checking is not difficult or confusing but very simple and easier with the application of MATLAB. It is to be noted that during the study, if [AS] is not similar for any two KCs then study may be terminated as the two are non-isomorphic in the first stage itself. But [AS] are similar, then it is necessary to check the second identification number [AM] also for both the kinematic chains.

**Fig. 5** KCs of 10 bars, 13 pairs group-IVC

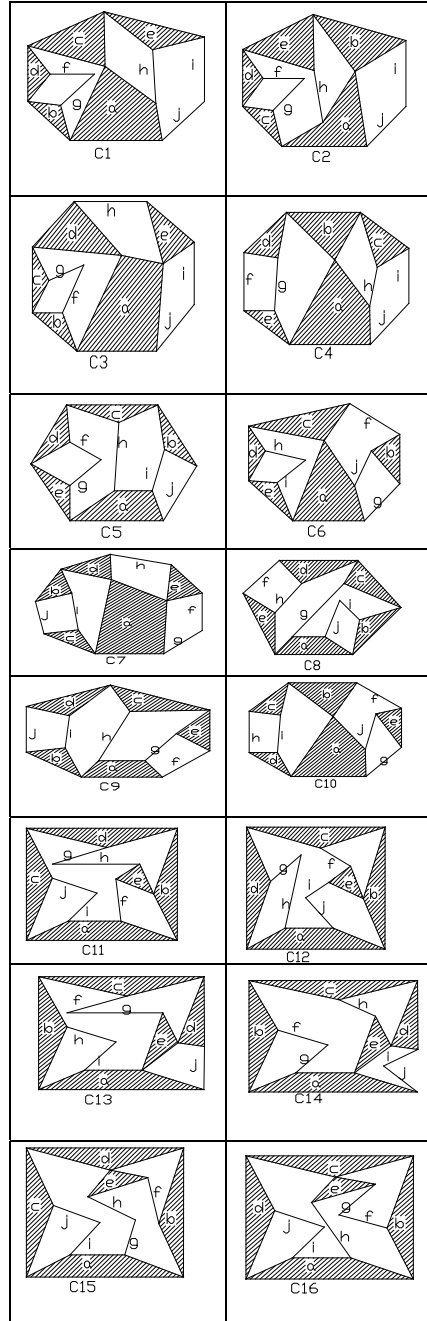


Fig. 5 (continued)

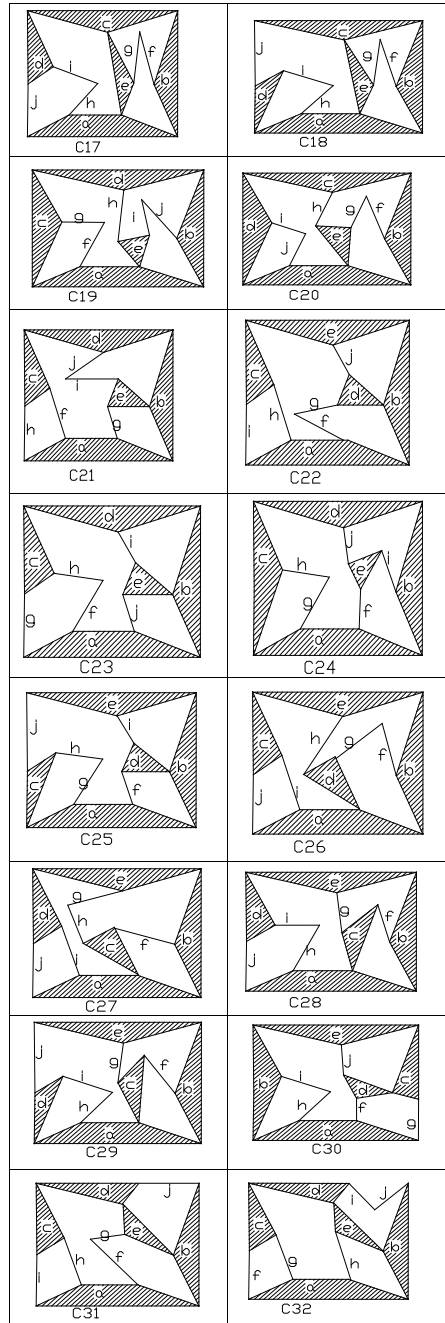


Fig. 5 (continued)

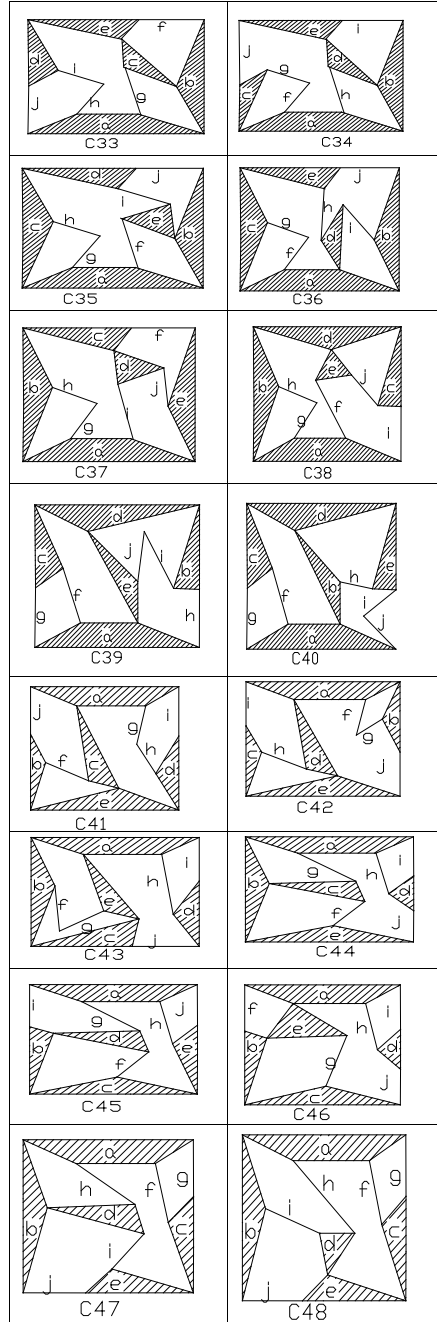


Fig. 5 (continued)

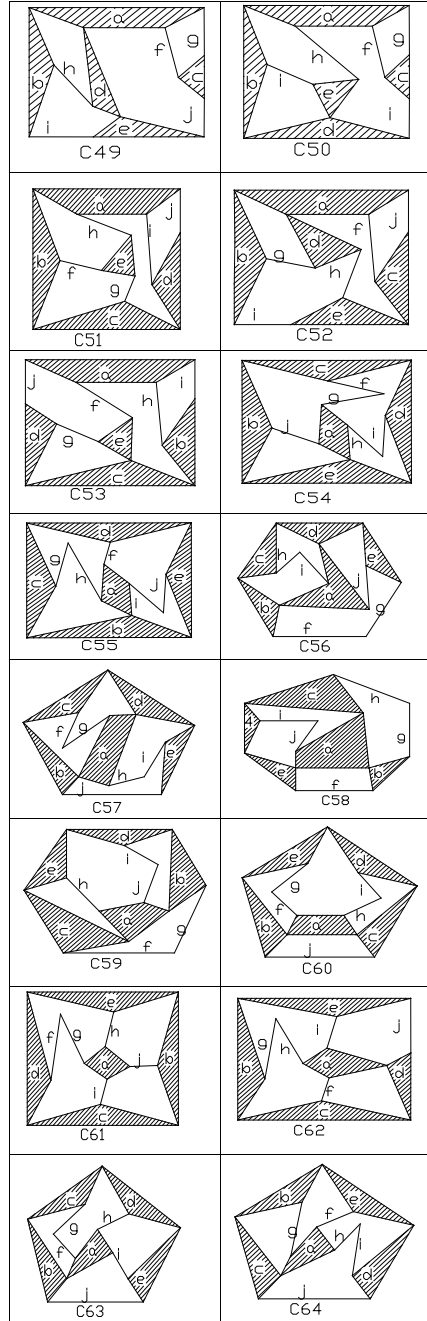


Fig. 5 (continued)

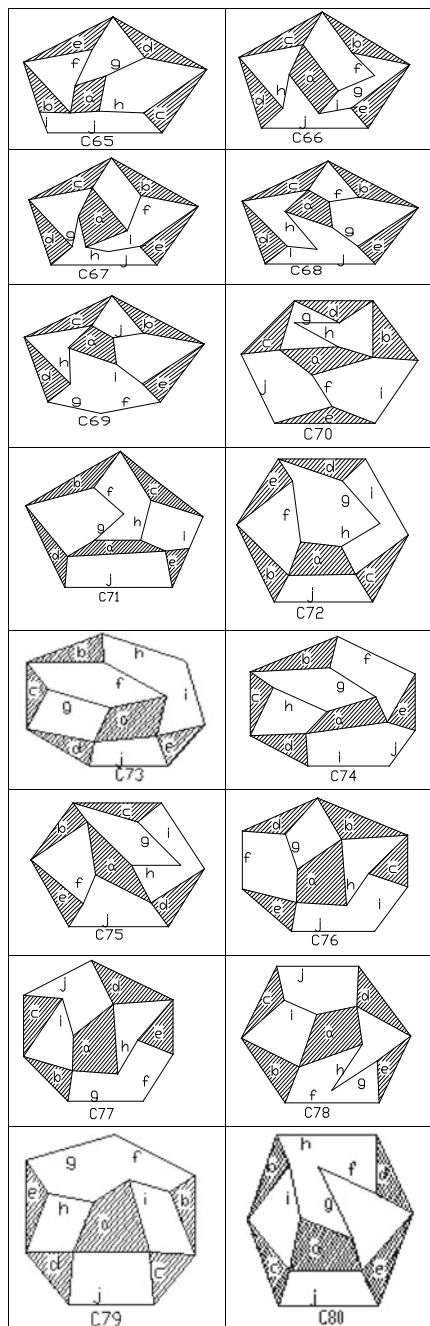
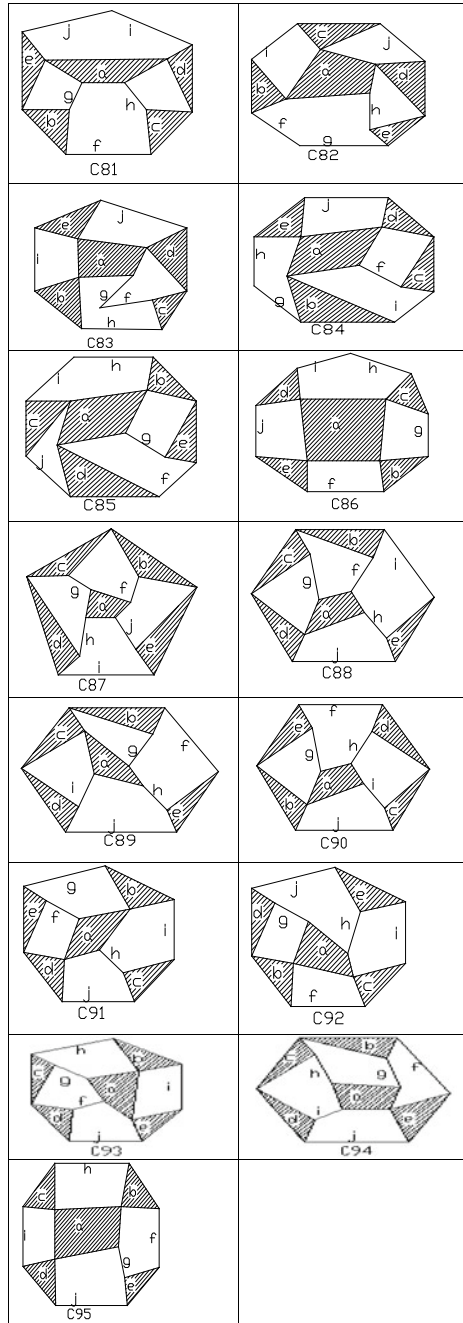


Fig. 5 (continued)



**Table 1** Identification numbers of 10 bars, 13 pairs group-IVC

KC	AS, AM of KCs
C1	5.1241e + 007, 1.5955e + 007
C2	2.5039e + 007, 6.7785e + 006
C3	2.6591e + 007, 8.2536e + 006
C4	7.6474e + 007, 3.4328e + 007
C5	5.2006e + 007, 1.9050e + 007
C6	5.4448e + 007, 2.5421e + 007
C7	4.9901e + 007, 2.1688e + 007
C8	7.0683e + 007, 3.1605e + 007
C9	8.3236e + 007, 3.7614e + 007
C10	1.3609e + 008, 5.3201e + 007
C11	3.6196e + 007, 1.4249e + 007
C12	4.2106e + 007, 1.2586e + 007
C13	3.6830e + 007, 1.1559e + 007
C14	3.3545e + 007, 3.3545e + 007
C15	3.0288e + 007, 1.0123e + 007
C16	5.1630e + 007, 2.3310e + 007
C17	7.4362e + 007, 2.7960e + 007
C18	7.3618e + 007, 2.6779e + 007
C19	4.9944e + 007, 2.2660e + 007
C20	4.9944e + 007, 2.2660e + 007
C21	7.7428e + 007, 3.2519e + 007
C22	5.9574e + 007, 2.5231e + 007
C23	6.1611e + 007, 1.8626e + 007
C24	6.3643e + 007, 2.7516e + 007
C25	6.0522e + 007, 2.7627e + 007
C26	8.4621e + 007, 3.5662e + 007
C27	6.9496e + 007, 2.9939e + 007
C28	7.9799e + 007, 3.2417e + 007
C29	7.1698e + 007, 3.0100e + 007
C30	8.1614e + 007, 2.4749e + 007
C31	4.6026e + 007, 1.6534e + 007
C32	4.8139e + 007, 2.2530e + 007
C33	5.9165e + 007, 1.8862e + 007
C34	6.8404e + 007, 2.8332e + 007
C35	7.4201e + 007, 3.2098e + 007
C36	6.6482e + 007, 2.4333e + 007
C37	7.7108e + 007, 3.3319e + 007

(continued)



**Table 1** (continued)

KC	AS, AM of KCs
C38	5.3887e + 007, 24,818,544
C39	6.8622e + 007, 3.2265e + 007
C40	38,407,512, 1.9254e + 007
C41	5.3863e + 007, 2.5888e + 007
C42	72,413,144, 2.7405e + 007
C43	8.9986e + 007, 8.9986e + 007
C44	8.3010e + 007, 3.4414e + 007
C45	6.0223e + 007, 2.4320e + 007
C46	7.5562e + 007, 3.5648e + 007
C47	9.2448e + 007, 4.1367e + 007
C48	7.4302e + 007, 3.4086e + 007
C49	1.4236e + 008, 5.7178e + 007
C50	75,906,968, 3.5030e + 007
C51	8.6384e + 007, 3.8623e + 007
C52	1.2955e + 008, 5.1812e + 007
C53	4.2068e + 007, 1.7110e + 007
C54	3.7911e + 007, 1.0651e + 007
C55	1.1483e + 008, 3.9938e + 007
C56	7.0682e + 007, 2.5383e + 007
C57	1.4607e + 008, 5.3981e + 007
C58	8.1326e + 007, 2.8634e + 007
C59	5.8727e + 007, 2.3158e + 007
C60	4.2010e + 007, 1.7779e + 007
C61	6.1092e + 007, 1.8438e + 007
C62	4.8245e + 007, 2.1863e + 007
C63	9.1824e + 007, 3.8725e + 007
C64	8.2080e + 007, 3.2376e + 007
C65	6.5048e + 007, 2.5513e + 007
C66	8.4104e + 007, 3.5349e + 007
C67	3.9441e + 007, 1.4054e + 007
C68	7.1056e + 007, 2.9579e + 007
C69	4.4065e + 007, 1.8554e + 007
C70	114,418,928, 4.6763e + 007
C71	4.1341e + 007, 1.7494e + 007
C72	5.6326e + 007, 2.3151e + 007
C73	6.4010e + 007, 2.6334e + 007
C74	6.6894e + 007, 3.0495e + 007

(continued)

**Table 1** (continued)

KC	AS, AM of KCs
C75	8.9103e + 007, 3.5719e + 007
C76	3.4951e + 007, 1.6205e + 007
C77	6.0070e + 007, 2.4295e + 007
C78	1.0487e + 008, 4.0989e + 007
C79	4.8658e + 007, 2.0524e + 007
C80	5.8731e + 007, 2.5124e + 007
C81	6.8152e + 007, 2.9501e + 007
C82	5.5425e + 007, 2.3242e + 007
C83	7.4218e + 007, 3.1764e + 007
C84	7.3512e + 007, 3.1025e + 007
C85	7.4272e + 007, 3.3845e + 007
C86	6.7669e + 007, 2.8252e + 007
C87	6.8593e + 007, 2.8961e + 007
C88	7.7662e + 007, 3.5463e + 007
C89	7.5850e + 007, 2.3156e + 007
C90	9.0486e + 007, 3.9732e + 007
C91	96,823,536, 3.9590e + 007
C92	1.3348e + 008, 5.2954e + 007
C93	1.4884e + 008, 5.8095e + 007
C94	8.6040e + 007, 3.6810e + 007

## References

1. Mruthunjaya TS (1984) A computerized methodology for structural synthesis of kinematic chains. Part 1. Formulation. *Mech Mach Theory* 19(6):487–495. [https://doi.org/10.1016/0094-114X\(84\)90055-7](https://doi.org/10.1016/0094-114X(84)90055-7)
2. Mruthunjaya TS (1984) A computerized methodology for structural synthesis of kinematic chains: part 2—application to several fully or partially known cases. *Mech Mach Theory* 19(6):497–505. [https://doi.org/10.1016/0094-114X\(84\)90056-9](https://doi.org/10.1016/0094-114X(84)90056-9)
3. Mruthunjaya TS (1984) A computerized methodology for structural synthesis of kinematic chains: part 3—application to the new case of 10-link, three- freedom chains. *Mech Mach Theory* 19(6):507–530. [https://doi.org/10.1016/0094-114X\(84\)90057-0](https://doi.org/10.1016/0094-114X(84)90057-0)
4. Mruthunjaya TS, Balasubramanian HR (1987) In quest of a reliable and efficient computational test for detection of isomorphism in kinematic chains. *Mech Mach Theory* 22(2):131–139. [https://doi.org/10.1016/0094-114X\(87\)90036-X](https://doi.org/10.1016/0094-114X(87)90036-X)
5. Sohn WJ, Freudenstein F (1986) An application of dual graphs to the automatic generation of the kinematic structures of mechanisms. *J Mech Transm Autom* 108(3):392–398. <https://doi.org/10.1115/1.3258745>
6. Rao AC (2000) Application of fuzzy logic for the study of isomorphism, inversions, symmetry, parallelism and mobility in kinematic chains. *Mech Mach Theory* 35(8):1103–1116. [https://doi.org/10.1016/S0094-114X\(99\)00060-9](https://doi.org/10.1016/S0094-114X(99)00060-9)
7. He PR, Zhang WJ, Li Q, Wu FX (2003) A new method for detection of graph isomorphism based on the quadratic form. *J Mech Des* 125(3):640–642. <https://doi.org/10.1115/1.1564574>

8. Chang ZY, Zhang C, Yang YH, Wang Y (2002) A new method to mechanism kinematic chain isomorphism identification. *Mech Mach Theor* 37(4):411–417. [https://doi.org/10.1016/S0094-114X\(01\)00084-2](https://doi.org/10.1016/S0094-114X(01)00084-2)Getrights and content
9. Cubillo JP, Wan JB (2005) Comments on mechanism kinematic chain isomorphism identification using adjacent matrices. *Mech Mach Theor* 40(2): 131–139. <https://doi.org/10.1016/j.mechmachtheory.2004.07.004>Getrights and content
10. He PR, Zhang WJ, Li Q (2000) Some further development on the eigensystem approach for graph isomorphism detection. *J Franklin Inst* 342(6):657–673. <https://doi.org/10.1016/j.jfranklin.2005.04.006>Getrightsandcontent
11. Ding HF, Huang Z (2007) A unique representation of the kinematic chain and the atlas database. *Mech Mach Theor* 42(6):637–651. <https://doi.org/10.1016/j.mechmachtheory.2006.06.010>Getrightsandcontent
12. Ding HF, Huang Z (2007) A new theory for the topological structure analysis of kinematic chains and its applications. *Mech Mach Theor* 42(10):1264–1279. <https://doi.org/10.1016/j.mechmachtheory.2006.11.007>Getrights and content
13. Rao AC (2000) A genetic algorithm for topological characteristics of kinematic chains. *J Mech Des* 122(2):228–231. <https://doi.org/10.1115/1.533569>
14. Prasadraju VVNR, Rao AC (2002) A new technique based on loops to investigate displacement isomorphism in planetary gear trains. *J Mech Des* 12:666–675. <https://doi.org/10.1115/1.1503373>
15. Rizvi SSH, Hasan A, Khan RA (2014) A new method based on the comparison of the unique chain code to detect isomorphism among kinematic chains. *Int J Modern Eng Res* 4(1):16–21
16. Rizvi SSH, Hasan A, Khan RA (2016) A new method for distinct inversions and isomorphism detection in kinematic chains. *Int J Mech Rob Syst* 3(1):48–59. Inderscience Enterprises Ltd
17. Kong FG, Li QZ, Zhang WJ (2002) An artificial neural network approach to mechanism kinematic chain isomorphism identification. *J Mech Mach Theor* 34(2):271–283. [https://doi.org/10.1016/S0094-114X\(98\)00035-4](https://doi.org/10.1016/S0094-114X(98)00035-4)
18. Jensen PW (1991) *Classical and modern mechanism for engineers and inventors*. Marcel Decker Inc., New York

# Flower Pollination Algorithm for Solving Single-Row Facility Layout Problems



R. Sanjeev Kumar, K. Vetrivel Kumar, and M. Francis Luther King

**Abstract** Linear machine sequence is the arrangement of machines for processing a variety of products in a single-row layout. The objective of this paper is to design a best linear machine sequence with the objective of minimizing the total flow distance of the products and the total length of the flow line in a single-row facility layout problem. It is a non-polynomial hard problem. A heuristic method is complicated to solve the problem when the products and machines are increased. Hence, the flower pollination metaheuristic algorithm is proposed to solve benchmark single-row facility problem. Computational result shows that the proposed flower pollination algorithm produced an improved solution. The performance of the proposed algorithm is compared with other methods in the literature.

**Keywords** Facility layout · Linear machine sequence · Flow line length · Flow distance and Flower pollination algorithm

## 1 Introduction

The design of the facility row layout is essential for arranging the facilities in a proper sequence so that the products flow line length and the flow distance are reduced. Hence, there is a consequential impact on production cost. Material handling charges are raised if the facilities are not organized in the correct sequence. Chen et al. [1] developed an adapted simulated annealing algorithm to minimize the product flow distance. They constructed a feasible flow network and the products flow in only one direction. They tested simulated annealing algorithm with several problems reported in the literature. Finally, they reported the simulated annealing algorithm produced improved solutions. Adel [2] applied a genetic algorithm to reduce material handling

---

R. S. Kumar (✉) · M. F. L. King  
Department of Mechanical Engineering, Swarnandhra College of Engineering & Technology,  
Narsapur, Andhra Pradesh, India

K. V. Kumar  
Department of Mechanical Engineering, Dhanalakshmi Srinivasan College of Engineering,  
Coimbatore, Tamil Nadu 641105, India

costs. He solved various material flow patterns facility layout problem and compared the results with previous approaches.

Jannat et al. [3] used GA for minimizing material movement cost and maximization of the proximity ranking score in the facility layout problem. The authors minimized these objectives separately. They produced a Pareto solution. Sahin [4] considered material movement and the closeness rating scores objectives. The author applied a simulated annealing algorithm to test the problems and compare the previous work results. Kumar et al. [5] developed a heuristic method to the minimization of the flow distance for different products with product sequences in a single-row facility layout. The author compared the result with previous work. Lenin et al. [6] applied the Genetic Algorithm to solve facility layout problems with the objective of machine investment cost, number of machines and product flow distance. They explained the benchmark problems and randomly generated problems. Lenin et al. [7] minimized the product flow distance, the number of machines in the layout, material movement cost and machine investment cost using a heuristic-based Tabu Search algorithm. They produced a better result when compared to the previous heuristic methods.

Keller and Buscher [8] prepared review articles for single-row facility layout problems. They discussed various objective functions, solution methods and future research opportunities. Guan and Geng [9] developed hybrid VNS and ant colony optimization to avoid local convergence in the computational result. They tested the algorithm with facility layout benchmark problems. Palubeckis [10] developed multistart simulated annealing to minimize the total products flow cost and the flow line length. He applied two types of operators to generate new facilities. It produced a better result when compared to the previous work. Ning and Pingke [11] applied a cross-entropy method to minimize the product flow distances in a single-row facility layout. They tested a cross-entropy algorithm with several benchmark problems. Finally, they reported the cross-entropy algorithm performed well. Lenin et al. [12] applied an artificial bee colony algorithm to solve single-row facility layout problems with the objective of product flow distance and flow line length. They compared ABC results with other heuristic algorithms.

Cravo and Amaral [13] proposed the GRASP algorithm for minimizing product flow distances in facility layout problems. They improved the effectiveness of the algorithm when compared to the previous approaches.

Most of the researchers considered the material movement cost, product flow distance, machine investment cost and facility closeness rating objectives. Only a few of them considered the flow line length. In this paper, the flower pollination algorithm (FPA) is applied to solve facility layout problems with the objectives of product flow distances and total flow length.

## 2 Problem Statements

All the machines are positioned in a straight line. The product flow in one direction only. The aim is to determine the linear machine sequence so that the product flow distances and the flow line length of the products are minimized. The assumptions are products demand and its variety is known, unity distance between the machines, machine availability and its duplicates are known, Machine sequence for each product is known and no backtracking. The objective is to minimize the total product flow distance ( $D$ ) and complete product flow line length ( $L$ ).

$$\text{Total Flow Distance } D = \sum_{i=1}^n d_i (P_{il} - P_{if})$$

$$P_{i(j+1)} > P_{ij}$$

$$m_k \leq dm_k$$

where,

- $n$ —Number of products,
- $i$ —Product catalog;  $i = 1, 2, 3, \dots, n$ ,
- $j$ —Machine catalog;  $j = 1, 2, 3, \dots, tm$ ,
- $d_i$ —flow distance of the products,
- $P_{il}$ — $i$ th product’s last machine position in the lms,
- $P_{if}$ — $i$ th product’s first machine position in the lms,

$$\text{Total Flow Line Length } L = \sum_{k=1}^t l_k m_k$$

where,

- $L$ —Total flow line length,
- $t$ —Number of machine types,
- $k$ —Machine type catalog;  $k = 1, 2, 3, \dots, t$ ,
- $l_k$ — $k$ th machine type Length.

## 3 Proposed Methodology

Yang [14] developed a flower pollination algorithm. It is based on the flowering plant’s pollination principle. In the pollination process, the pollen transferred from the male parts of a flower to the female part of a flower. The objective is to produce the optimal reproduction of plants by existing the fittest flowers in the flowering

plants. Two types of pollinations involved. There are biotic (or) cross-pollination and abiotic (or) self-pollination. Cross-pollination process is also called as global pollination or (global search). Self-pollination process is also called as local pollination or (local search). In cross-pollination, the pollen transferred between the flowers of the different plants with the help of Pollinators. Cross-pollination pollinators are bees, bats, birds and flies. In the self-pollination process, the pollen transferred between the flowers of the same plant with the help of pollinators. Pollination pollinators are wind or diffusion in water. Self-pollination pollinators are wind or diffusion in water. It is applied to solve multi-objective optimization problems (Yang et al. [15]), Sudoku puzzles (Osama Abdel-Raouf et al. [16]), Assembly problems (Mishra and Deb [17]), Estimate the transportation Energy Demand (Korkmaz and Payıdar [18]).

### 3.1 Procedure

Step 1: Generate the initial population randomly, the number of sequences equal to the number of flowers.

Step 2: Calculate the objective value of each sequence.

Step 3: Compute the fitness value of the sequence and find g best value.

$$\text{Fitness value} = \frac{1}{\text{Objective function}}$$

Step 4: Calculate the probability of each sequence.

Step 5: If the calculated probability value is greater than the random number, then cross-pollination takes place (global pollination). If not, then do local pollination (self-pollination).

Step 6: Evaluate the new solution.

Step 7: Update and store the best solution.

Step 8: The process is repeated until the termination criteria reached. The flowchart is represented in Fig. 1.

## 4 Results and Discussion

The proposed flower pollination algorithm is coded in java environment, and it is tested with various benchmark problems. Input data are the number of products, number of machines and their replicas, machine sequences for each product and demand. Output results are the best machine sequence, product sequence, total flow distance ( $D$ ) and full flow line length ( $L$ ) in Table 1. The recital of the flower pollination algorithm is represented interms of the average improvement rate (AIR). The concert of the flower pollination algorithm is compared with the ABC algorithm [12], Lenin et al. [6] method and Kumar et al. [5] method. Product flow distance and

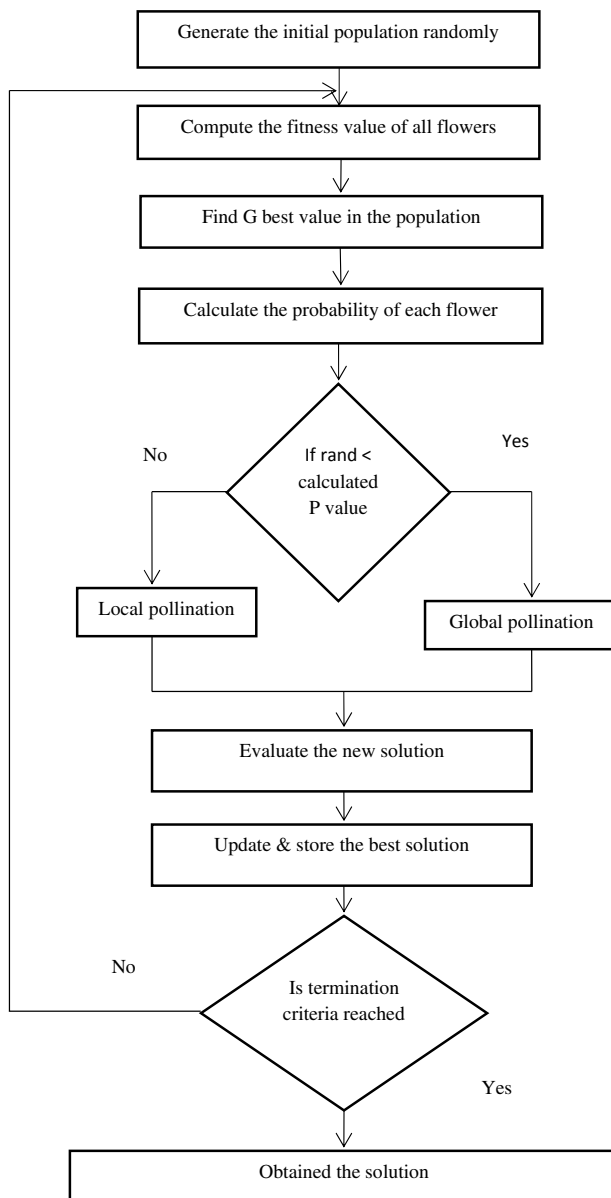


Fig. 1 Flow chart for FPA



**Table 1** Computational results for various size problems with different approaches

Problem no.	Size	Methods	Product sequence	LMS	D	L	DIS
1	13 × 5	FPA	1-5-3-4-2	12-3-7-1-11-4-5-8-2-10-9-6-5-7-2	588	140.79	604.62
		PrABC	1-5-2-3-4	12-3-7-1-11-4-8-6-5-82-10-9-6-5-7-2	640	123.39	651.78
		Le	5-4-1-3-2	4-8-6-1-11-4-5-8-2-12-3-7-1-10-9-5-7-2-6	776	136.05	787.83
		Ku	1-5-3-2-4	12-3-7-1-4-8-6-1-11-4-5-8-2-10-9-6-5-7-2	586	136.05	<b>601.58</b>
2	7 × 7	FPA	2-3-5-1-4-6-7	4-2-1-3-5-7-1-2-4-6-7-5-6	558	96.36	<b>566.26</b>
		PrABC	2-3-5-1-4-6-7	4-2-1-3-5-7-1-2-4-6-7-5-6	558	96.36	<b>566.26</b>
		Le	2-3-5-1-4-6-7	4-2-1-3-5-7-1-2-4-6-7-5-6	558	96.36	<b>566.26</b>
		Ku	Infeasible solution				
3	10 × 5	FPA	1-5-2-3-4	5-3-2-7-1-8-9-6-4-10	12,800	67.18	<b>12,800.17</b>
		PrABC	1-5-2-3-4	5-3-2-7-1-8-9-6-4-10	12,800	67.18	<b>12,800.17</b>
		Le	2-3-1-4-5	1-8-5-3-2-7-9-6-4-10	13,200	67.18	13,200.17
		Ku	1-5-2-3-4	5-3-2-7-1-8-9-6-4-10	12,800	67.18	<b>12,800.17</b>
4	10 × 5	FPA	5-2-1-4-3	6-10-8-3-1-2-7-9-2-4-8-5-4-9	707	92.02	<b>712.96</b>
		PrABC	2-1-5-4-3	7-6-10-3-10-8-1-9-2-7-4-8-5-9	763	82.77	767.39
		Le	5-1-2-4-3	7-6-10-8-3-1-2-7-4-8-5-9-2	780	89.21	785.08
		Ku	1-2-5-4-3	6-10-8-1-7-4-8-5-9-2-7-4-9	1070	90.45	1073.81
5	12 × 6	FPA	4-6-5-3-1-2	11-12-5-9-12-8-10-7-6-3-8-9-1-3-2-4-5-6-1-2-7	1621	121.77	<b>1625.56</b>
		PrABC	5-3-4-6-1-2	11-12-8-5-10-7-6-3-1-2-8-9-1-3-4-5-6-7	2655	102.75	2656.9
		Le	5-4-3-6-1-2	11-12-8-5-10-7-6-3-2-8-9-1-3-4-5-6-2-7	2900	100.22	2901.73
		Ku	Infeasible solution				

(continued)

**Table 1** (continued)

Problem no.	Size	Methods	Product sequence	LMS	D	L	DIS
6	15 × 4	FPA	3-1-4-2	7-10-11-12-2-1-10-12-13-14-7-3-4-8-9-15-8-5-11-6-4	544	135.54	560.63
		Pr <sub>ABC</sub>	3-1-2-4	3-4-8-9-15-9-8-5-11-6-4-10-12-13-14-7-10-11-12-2-1	532	140.09	<b>550.13</b>
		Le	1-4-3-2	9-8-5-11-6-4-7-10-11-12-2-1-3-4-8-9-15-10-12-13-14-7	532	147.08	551.93
		Ku	3-4-1-2	9-8-5-11-6-4-10-12-13-14-7-3-4-8-9-15-7-10-11-12-2-1	532	147.01	551.93
7	11 × 5	FPA	2-4-1-5-3	1-3-8-7-4-5-9-7-5-10-2-4-6-7-9-10-8-11-6	1647	120.95	<b>1651.43</b>
		Pr <sub>ABC</sub>	2-1-4-5-3	1-3-8-7-4-5-4-6-7-9-10-8-11-6-9-7-5-10-2	1647	120.95	<b>1651.43</b>
		Le	4-1-2-5-3	1-3-8-7-4-5-9-7-5-10-2-10-8-11-6-4-6-7-9-10	1647	124.6	<b>1651.66</b>
		Ku	5-2-4-1-3	1-3-8-10-8-11-6-4-6-7-9-10-9-7-5-10-2-8-7-4-5	2637	130.92	2640.24
8	10 × 7	FPA	1-6-5-4-7-3-2	10-7-8-9-8-6-7-9-5-1-2-3-9-4-3-1-2-7-8-4-3-2-1	1611	167.76	<b>1619.71</b>
		Pr <sub>ABC</sub>	7-5-4-2-6-3-1	10-7-8-6-7-9-8-4-3-1-2-5-1-2-3-9-4-3-2	1875	139.16	1880.15
		Le	6-7-5-4-2-3-1	10-7-8-4-3-1-2-5-1-2-3-9-4-3-2-8-6-7-9	2279	139.16	2283.24
		Ku	-Infeasible solution-				

Bolded numbers in the table last column represent the optimum value for each problem

**Table 2** Average improvement rate for Euclidean distance

Approaches	1	2	3	4	5	6	7	8	AIR
FPA	30.30	<b>0</b>	<b>3.13</b>	<b>50.61</b>	<b>78.51</b>	0	<b>59.85</b>	<b>40.96</b>	<b>32.92</b>
ABC	20.88	<b>0</b>	<b>3.13</b>	39.915	9.21	1.908	<b>59.83</b>	21.43	19.54
Le	0	<b>0</b>	<b>0</b>	36.77	0	<b>1.58</b>	<b>59.85</b>	0	12.28
Ku	<b>30.96</b>	–	<b>3.13</b>	0	–	<b>1.58</b>	0	–	4.46

Bolded numbers in the table last column represent the optimum value for each problem

flow line length objectives are conflicting nature. So using distance method (Lenin Nagarajan [12]) to find the best machine sequence.

$$dis = \sqrt{D^2 + L^2}$$

The average improvement rate is calculated by using the formula (Sayadi et al. [19]).

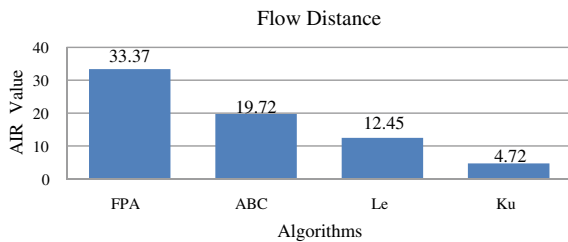
$$AIR = (C_{MAX}(UB) - C_{MAX}(H)) / C_{MAX}(H) \times 100 \tag{1}$$

$C_{MAX}(UB)$ —upper bound objective function value,  
 $C_{MAX}(H)$ —the objective value of metaheuristic algorithms.

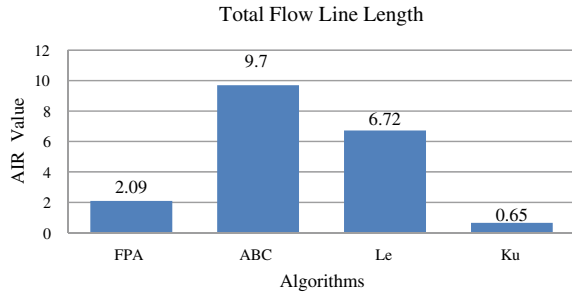
The average improvement rate of FPA is high when compared to other approaches in Table 2. It is produced better results in 5 problems. ABC produced two results, Le produced two results and Ku produced three results. The total flow distance ( $D$ ) AIR value is calculated using Eq. 1. FPA produced better average improvement rates than other approaches. FPA produced six best results, ABC produced three best results, Le produced two best results and Ku produced three best results. It is represented in a graphical manner in Fig. 2.

The total flow line length ( $L$ ) AIR value is calculated using Eq. 1. The average improvement rate of ABC is high. FPA produced two better results, ABC produced five best results, Le produced two best results and Ku produced one best results. It is represented graphically in Fig. 3.

**Fig. 2** Average improvement rate for flow distance



**Fig. 3** Average improvement rate for total flow line length



## 5 Conclusion

The average improvement rate of flower pollination algorithm is high and produced a better solution. Hence, the performance of the FPA is high when compared to other approaches. This algorithm is suitable to solve other objectives such as closeness score, material handling cost and uncertain movement. In future, flower pollination algorithm can also apply to solve unequal area facility layout problems, facility location problems, machine layout problems, scheduling problems and supply chain management problems.

## References

1. Chen DS, Wang Q, Chen HC (2001) Linear sequencing for machine layouts by modified simulated annealing. *Int J Prod Res* 39(8):1721–1732
2. Adel EM (2004) A genetic algorithm for facility layout problems of different manufacturing environments. *Comput Ind Eng* 47(1–3):233–246
3. Jannat S, Khaled AA, Sanjoy KP (2010) Optimal solution for multi-objective facility layout problem using a genetic algorithm. In: *Proceedings of the international conference on industrial engineering and operations management, Dhaka, Bangladesh*
4. Sahin R (2011) A simulated annealing algorithm for solving the bi-objective facility layout Problem. *Expert Syst Appl* 38(4):4460–4465
5. Kumar MS, Islam MN, Lenin N, Kumar DV, Ravindran D (2011) A simple heuristic for linear sequencing of machines in layout design. *Int J Prod Res* 49(2):6749–6768
6. Lenin N, Kumar MS, Ravindran D, Islam MN (2013) Multi-objective optimization in single-row layout design using a genetic algorithm. *Int J Adv Manuf Technol* 67(5–8):1777–1790
7. Lenin N, Kumar MS, Ravindran D, Islam MN (2014) A Tabu search for multi-objective single row facility layout problem. *J Adv Manuf Syst* 13(1):17–40
8. Keller B, Buscher U (2015) Single row layout models. *Eur J Oper Res* 245(3):629–644
9. Guan J, Geng L (2016) Hybridizing variable neighborhood search with ant colony optimization for solving the single row facility layout problem. *Eur J Oper Res* 248(3):899–909
10. Palubeckis G (2017) Fast simulated annealing for single row equidistant facility layout. *Appl Math Comput* 263(1):287–301
11. Ning X, Pingke L (2018) A cross-entropy approach to the single row facility layout problem. *J Int J Prod Res* 56(11):3781–3794

12. Lenin N, Siva Kumar M, Selvakumar G, Vignesh Kumar D (2018) Solution for bi-objective single row facility layout problem using artificial bee colony algorithm. *Eur J Ind Eng* 12(2):252–275
13. Cravo GL, Amaral ARS (2019) A GRASP algorithm for solving large scale single row facility layout problems. *Comput Oper Res.* <https://doi.org/10.1016/j.cor.2019.02.009>
14. Yang XS (2010) *Nature inspired metaheuristic algorithms*. Luniver Press, UK
15. Yang X-S, Karamanoglu M, He X (2013) Flower pollination algorithm: a novel approach for multi-objective optimization. *Procedia Comput Sci* 18:861–868
16. Abdel-Raouf O, El-Henawy I, Abdel-Baset M (2014) A novel hybrid flower pollination algorithm with chaotic harmony search for solving sudoku puzzles. *Int J Modern Educ Comput Sci* (3):38–44
17. Mishra A, Deb S (2016) Assembly sequence optimization using flower pollination algorithm based approach. *J Intell Manuf* 30(2):461–482
18. Korkmaz E, Payidar A (2018) Flower pollination algorithm approach for the transportation energy demand estimation in Turkey: model development and application. *Energy Sources Part B* 13:429–447
19. Sayadi MK, Ramezani R, Ghaffari-Nasab N (2010) A discrete firefly meta-heuristic with local search for makespan minimization in permutation flow shop scheduling problems. *Int J Ind Eng Comput* 1(1):1–10

# Microwaves in Healthcare Systems for Cancer Detection



R. Chitra, G. Srinivasa Sudharsan, S. G. Rahul, Seeram Sai Sudheer, and Archakam Amruthavalli

**Abstract** Cancer detection using microwaves is one of the most promising and attractive screening techniques which is currently under research. This technique offers several advantages such as low cost, better patient comfort, non-ionizing and non-invasive compared to diagnostic imaging modalities which have been available more than a decade to detect the breast cancer like X-ray mammography, ultrasound and MRI. In this work, an optimized circular patch antenna is designed in CST Microwave Studio to achieve the better trade-off between the depth of penetration and spatial resolution. The proposed patch antenna resonates from 1.5 to 7.1 GHz with the voltage wave standing ratio (VSWR) value less than 2. Other parameters like gain, directivity and specific absorption rate (SAR) are evaluated to check the performance of the antenna. The designed antenna and breast phantom with tumor of 5 mm are simulated in the CST environment. The reflected signal from the phantom is then processed to identify the presence and location of the tumor using scattering parameter ( $S_{11}$ ).

**Keywords** CST microwave studio · Patch antenna · Specific absorption rate · VSWR · Scattering parameter

## 1 Introduction

Breast cancer is the most common form of cancer among women [1]. In the year 2019–2020, American Cancer Society estimated that 1 out of 8 women are diagnosed with invasive breast cancer in their lifetime and 1 out of 39 women (3%) lost their lives due to breast cancer. To reduce the morality of this disease, it is to be detected early when the cancer is relatively small and has not spread to other parts of the body [1]. Nowadays, breast cancer is detected through various diagnostic techniques such as X-ray mammography, ultrasound and magnetic resonance imaging (MRI).

---

R. Chitra (✉) · G. S. Sudharsan · S. G. Rahul · S. S. Sudheer · A. Amruthavalli  
Department of Electronics and Communication Engineering, Vel Tech Rangarajan Dr. Sagunthala  
R&D Institute of Science and Technology, Chennai, India  
e-mail: [vtu14649@veltechuniv.edu.in](mailto:vtu14649@veltechuniv.edu.in); [vtu14615@veltechuniv.edu.in](mailto:vtu14615@veltechuniv.edu.in)

The techniques used in the clinical environment to detect breast cancer have some drawbacks.

### ***1.1 Limitations of Existing Breast Cancer Diagnostic Techniques***

X-ray mammography is currently the most recommended method utilized by doctors for breast cancer examination. Diagnosis of breast cancer using X-ray mammography involves X-ray which causes the patient to be subjected to ionization which further increases the risk of cancer development. The breast is subjected to compression while screening which causes a pain to the patient who undergoes mammography. Also, it faces a difficulty in locating tumor in dense breast [2]. It does not have enough sensitivity for patients having dense (thick) breast tissue, and it cannot detect tumors whose size is less than a 1–2 cm. Ultrasound is a safe screening tool because there is no harmful radiation, but it lacks enough spatial resolution. It could not be used to detect solid masses and the deeper lesions. Results produced by ultrasound are not always reliable since it is equipment and operator dependent [3]. MRI is not popular like other imaging techniques for breast cancer diagnosis since it is expensive. MRI is a time-consuming screening process for diagnosis of breast tumor on comparison with other diagnostic techniques [4]. The machine produces loud pounding and buzzing noises during the operation and calcification cannot be detected.

### ***1.2 Microwaves in Cancer Detection***

The requirement of a diagnostic technique which is non-ionizing, non-invasive, low cost, less time-consuming and accurate result producing has been increased. Many researchers have found that microwaves can be used for the detection of the breast tumor. Basically, microwave imaging is termed as "seeing" the internal structure of an object by means of electromagnetic fields at microwave frequencies (300 MHz–300 GHz) [5]. From a technical point of view, microwave breast tumor detection has the potential to detect small tumors [6]. The applications of microwave technology were increasing in the field of biomedical engineering for diagnostic purposes. The proposed technique employs the electrical property contrast. Microwave interaction with the human body tissues cause the electromagnetic wave's amplitude to change as it propagates through it or disperses throughout the body tissues. Tissues electrical properties are represented in terms of relative permittivity ( $\epsilon_r$ ) and conductivity ( $\sigma$ ). Studies revealed that tissues permittivity are highly dependent on the water content. Low water content tissues (such as fat) have lower permittivity than high water content tissues like muscle, skin, heart, and cancer tissues while permittivity gives us the information of the tissues ability to store microwave energy, conductivity is related

to the loss (dissipation) or attenuation (absorption) the signal suffers as it propagates through the tissue [7]. Therefore, as the microwave signal travels through different tissues on the breast it suffers both attenuation (amplitude loss) and reflection as it encounters discontinuity.

In this technique, a transmitter is used to illuminate the breast phantom with microwaves, which travel through the breast and may be detected at receivers located on the opposite side of the breast [8]. Alternatively, reflections may be recorded at the transmitting antenna. With a tumor present, waves traveling through the breast encounter a change in electrical properties, causing the incident wave to scatter. This scattering changes the amounts of energy detected at the receivers and the transmitter. The objective of the proposed system is to identify the presence and location of tumor in breast phantom with the help of reflected signal by using a monostatic antenna (single antenna for both transmission and reception). This antenna transmits UWB pulses, which propagates into the breast, where it is reflected off significant electrical discontinuities, and is received by the same antenna. To achieve a better trade-off between spatial resolution and depth of penetration, an optimized ultra-wide band antenna is proposed. By comparing the reflected signal with the transmitted signal, the presence of tumor is identified. Some of the literature reports on breast cancer detection are discussed as follows. Çalışkan et al. modeled a 3D breast structure with different permittivity and conductivity in HFSS by using finite element method (FEM). The authors initially designed a microstrip patch antenna and then modified the patch and ground plane to increase the image quality. Parameters like electric field, magnetic field distribution and current density on the antenna were evaluated [9]. Rafat Raihan et al. designed a wearable pentagon-shaped microstrip patch antenna which resonates from 2.4 to 2.4835 GHz to detect brain cancer. They embedded a 5 mm tumor in the phantom and compared the radiation pattern of both normal tissue and cancerous tissue [10]. Afyf et al. proposed a compact ultra-wideband (UWB) planar antenna for microwave thermography system. The authors performed simulation using two commercial software, CST Microwave Studio and HFSS simulators. The simulated antenna exhibits the UWB characteristics from 1.3 to 6 GHz in HFSS software and from 2.01 to 4.4 GHz in CST [11]. Ouerghi et al. presented a comparative study of five microstrip patch antennas for microwave imaging at 2.45 GHz frequency to select the suitable antenna for tumor detection. The choice was made by putting each antenna on the breast phantom to study the electric field, magnetic fields and current density in Ansoft high frequency simulation software (HFSS) [12]. From the literature review, it is understood that the techniques for tumor detection in skin, head and breast tissues using patch antenna with design equations were mostly available. In this work, an optimized circular patch antenna with wideband characteristics is investigated to identify the presence of tumor at different depth based on various parametric analysis.



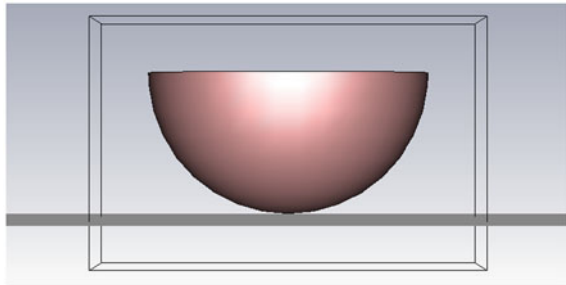
## 2 Phantom Design

The breast phantom is designed in such a way that it must replicate the natural breast both in shape and the dielectric properties. First the phantom is designed in homogeneous manner without any abnormality. Next, the phantom is developed with the tumor within the homogeneous material. The tumor varies with the normal tissue by the dielectric values like permittivity, electrical conductance, thermal conductivity, etc. [13]. Properties of the materials used for skin, fat and tumor are depicted in Table 1. The breast phantom model with and without tumor created in CST environment is shown in Figs. 1 and 2, respectively. Initially, the phantom is designed with radius of 50 mm with 5 mm tumor centered at  $x = 0$ ,  $y = 0$  and  $z = 20$  mm.

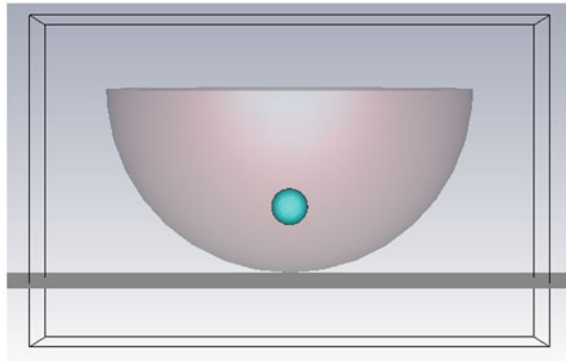
**Table 1** Dielectric values of materials used in phantom

Phantom layers	Permittivity (F/m)	Conductivity (S/m)
Skin	36.7	2.34
Fatty tissue	4.6023	0.5852
Tumor	67	49

**Fig. 1** Breast phantom without tumor



**Fig. 2** Breast phantom with tumor



### 3 Antenna Design

The most important part of the microwave-based tumor detection system is the antenna which is used [14]. Generally, the radar-based microwave detection is of two types—multistatic and monostatic. Multistatic is the one which uses two different antennas for transmission and reception purpose, whereas the monostatic type uses a single antenna for both purposes. To have less complexity, a monostatic antenna is designed. This antenna should act as a transceiver, i.e., it should transmit as well as receive the microwave signal. The microstrip antennas are popular in a wide variety of applications due to their lightweight, simple structure, low cost and ease of fabrication [15]. It consists of a conducting patch and a ground plane on both side of the substrate. The radiating patch can be square, rectangular, circular or any other shape. Antenna design is carried out using Computer Simulation Technology (CST) Microwave Studio software. Different types of antennas are designed to check whether it can fulfill the basic initial requirements like directivity, gain, impedance matching, reflection coefficient and voltage standing wave ratio (VSWR) so that it can be used for further simulation with breast phantom.

#### 3.1 Narrowband Antenna

Initially, a rectangular antenna is designed to resonate at a frequency of 2.5 GHz in which the length and width of the antenna are calculated using the below formulas. These two parameters will decide the characteristics of the designed antenna. Patch is the radiating element, where its feed is designed to have 50 ohms impedance for efficient energy transfer between source and antenna. Table 2 shows the design parameter of the narrowband antenna which are calculated using the above design equations. The perspective view of the narrowband antenna designed in CST environment is shown in Fig. 3.

**Table 2** Design parameters of narrowband antenna

Parameters	Notation	Values (mm)
Patch width	$W_p$	36
Patch length	$L_p$	28
Ground width	$W_g$	$2*W$
Ground length	$L_g$	$2*L$
Substrate thickness	$t_s$	0.035
Substrate height	$h_s$	1.6
Feed width	$W_f$	3.137
Inset feed length in patch	$F_i$	8.85
Gap between feed and patch	$G_{fp}$	1

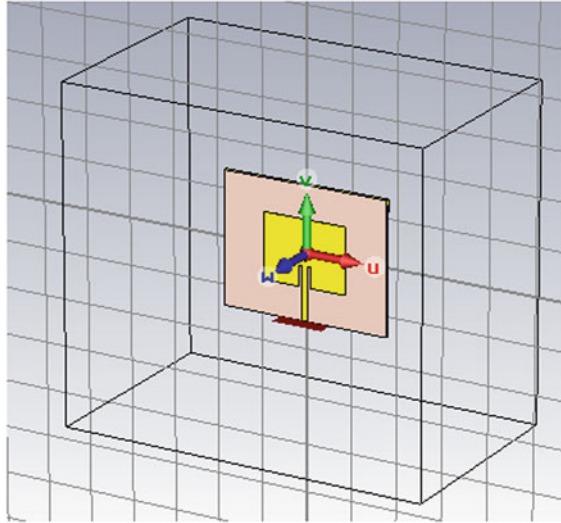


Fig. 3 Perspective view of narrowband antenna designed in CST

The scattering parameter of designed narrowband antenna is shown in Fig. 4. It is understood that the antenna is resonating at 2.5 GHz with a  $S_{11}$  value of  $-22.73$  dB. Far-field results like directivity of 6.9 dB and gain of 4.5 dB are also observed in the antenna. But there are some limitations in the narrowband antenna. When an antenna is designed to resonate at a higher frequency (e.g., 7 GHz), it could not be able to find the deeply seated tumor since the frequency is inversely proportional to the depth of penetration. And, similarly in the case of lower frequencies, the penetration will be more with low spatial resolution which makes the antenna less efficient for tumor detection.

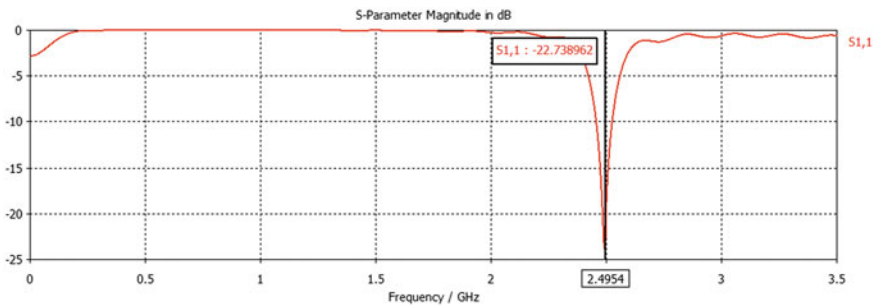


Fig. 4 S parameter of narrowband antenna

### 3.2 Ultra-wideband antenna

An ultra-wideband antenna is designed to achieve a better trade-off between spatial resolution and depth of penetration with the resonating frequency of 1.5–7.1 GHz. In order to have the sufficient bandwidth, circular patch is used in this section. Length of the ground is also changed to get the desired range of frequencies. The design and selection of suitable ultra-wide band antenna involve some optimization of antenna parameters which affects the bandwidth and radiation pattern. Figure 5 shows the effect of return loss for the patch radius which varies from 14 to 17 mm. It is understood that the radiation pattern is not having wideband characteristics for the patch radius 14 mm and 15 mm, respectively. Similarly, the radius 17 mm is not used because of the higher edge frequency which will give side effects to the human body. So, the radius 16 mm is chosen for the design of wideband antenna.

The ground structure is modified for various length as shown in Fig. 6. It is clear that the antenna exhibits UWB characteristics as the ground length decreases. The ground length of value of 28.36 mm shows the wideband frequency range in the graph which is suitable to find the deeply seated tumors and to achieve better spatial resolution. Table 3 shows the design parameters of the optimized wideband antenna.

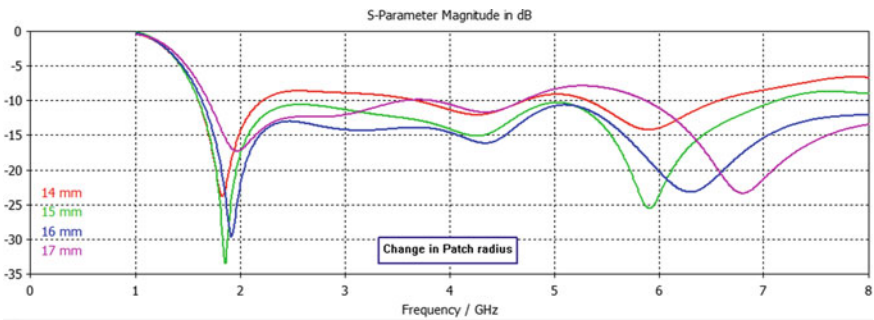


Fig. 5 Return loss for varying patch radius

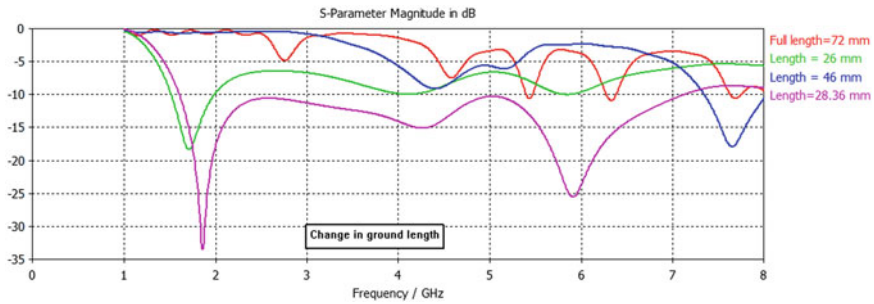
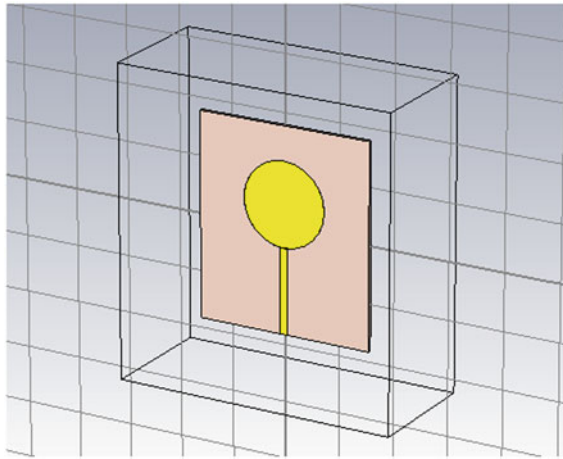


Fig. 6 S parameter for different ground length

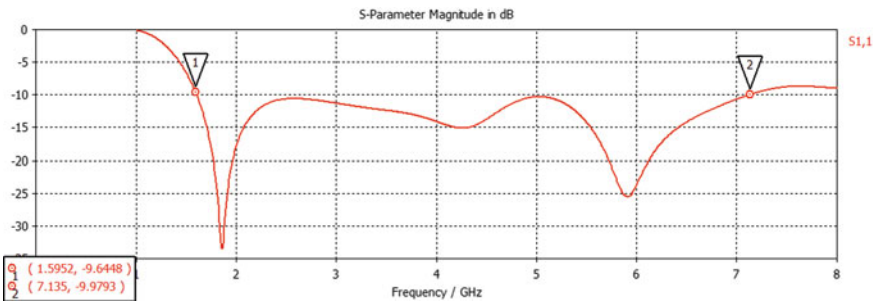
**Table 3** Design parameters of the optimized wideband antenna

Parameters	Notation	Unit (mm)
Patch radius	$R$	18
Ground length	$L_g$	28.36
Ground width	$W_g$	58.5
Substrate length	$L_s$	72
Substrate width	$W_s$	63
Substrate thickness	$h_t$	0.035
Substrate height	$h_s$	1.6

Figure 7 shows the perspective view of the proposed circular antenna designed in CST Microwave Studio. To check the suitability of the antenna, both  $S_{11}$  and VSWR are plotted as shown in Figs. 8 and 9, respectively. From the various parametric



**Fig. 7** Perspective view of circular wideband antenna



**Fig. 8** S parameter of circular wideband antenna

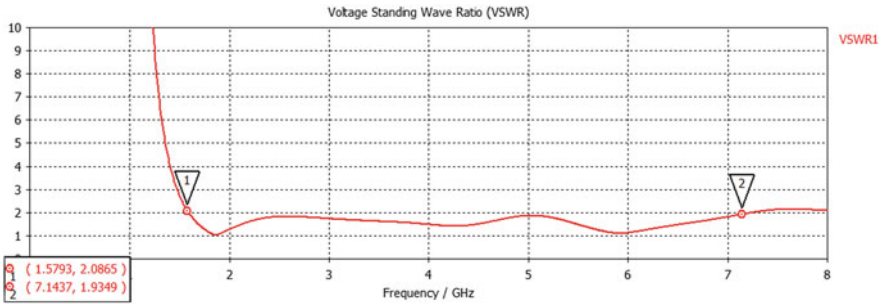


Fig. 9 VSWR of circular wideband antenna

analysis of antenna, it is understood that the proposed antenna is suitable for further simulation with the breast phantom.

### 4 Parametric Analysis of Antenna with Phantom

Once the antenna and phantom are designed separately, the simulation of antenna with phantom is carried out in CST environment. The input signal used in the antenna for simulation is a Gaussian pulse with the time in the range of nanosecond. When the antenna is simulated with the phantom having tumor, some variation is observed in the output port signal which is depicted in Fig. 10. It is understood that a tissue with different dielectric value is present in the normal tissue. Due to this change in dielectric values, the variation in output signal is occurred, and the presence of tumor is confirmed.

The presence of tumor in a normal tissue is identified by the absorption and reflection of the excited signal. When there is a healthy tissue without any malignant tumor, the absorption and reflection of the signal are less. If a tumor is present in the normal tissue, the absorbed and reflected power is more due to the change

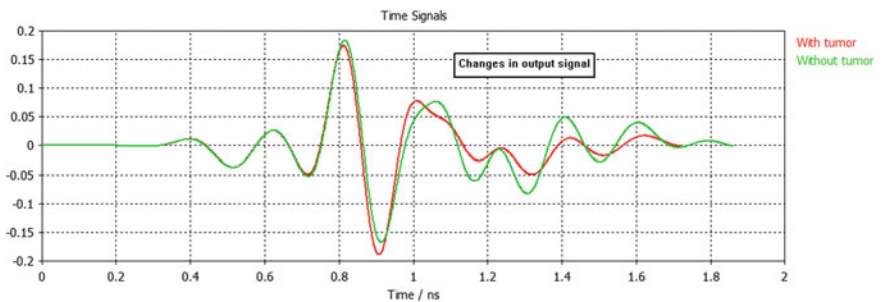
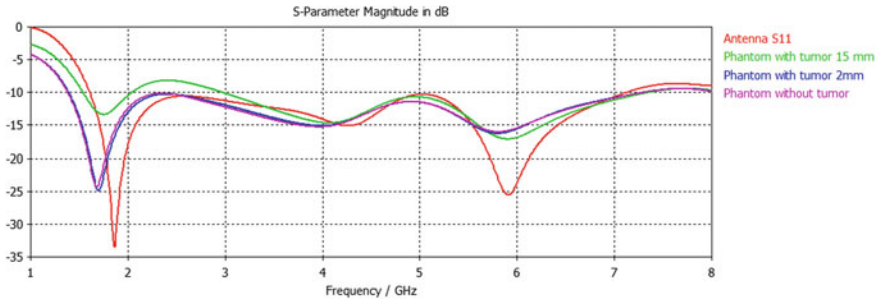


Fig. 10 Output signal for phantom without and with tumor



**Fig. 11** S parameter for different tumor size

**Table 4** Absorption rate for phantom with and without tumor for UWB range

UWB frequency range (GHz)	Absorption rate (W/Kg)	
	Phantom without tumor	Phantom with tumor
2	5.21	5.33
3	5.90	6.00
4	6.01	6.31
5	4.05	4.07
6	4.76	4.80
7	5.02	4.80

in dielectric values. Similarly, the comparison for various tumor size in terms of reflection is carried out in this work. From Fig. 11, it is understood that, as the tumor size increases, the reflection is more.

The SAR values are calculated at the frequency of 6 GHz using CST SAR calculation tool. Parameters like total SAR in W/kg, maximum SAR in W/kg, coordinate of the maximum SAR (X, Y, Z), and absorbed power in W are used for the analysis. Table 4 summarizes the value of absorption rate for phantom without tumor and for phantom with tumor of radius of 5 mm embedded in 50 mm breast phantom. From the table, it is observed that the absorption rate is high for the phantom with tumor.

Table 5 shows the power absorbed by the tumor of different radius. It is observed that when the mass of the breast increases, the absorbed power also increases for different frequencies.

## 5 Conclusion

In this study, the antenna is designed with an objective of detecting a tumor at its early stage, so a tumor of diameter 5 in a 50 mm phantom is used during the simulation. The antenna is simulated with breast phantom for measuring the various

**Table 5** Absorption rate for different tumor size in UWB range

Tumor size (mm)	Absorption rate (W/Kg) at various frequency (GHz)			
	3	4	5	6
2	3.59	3.90	3.87	4.04
3	3.81	3.92	3.94	4.08
4	3.97	4.12	4.31	4.12
5	4.41	4.97	4.33	4.21
8	4.58	4.91	4.71	4.68
10	4.67	5.89	5.52	4.90

antenna parameters. The antenna designed with single frequency is not suitable to find the tumors which are located at different depth. Optimization of some antenna parameters is carried out in this work to achieve the wideband frequency range. The resonant frequency of the proposed antenna varies from 1.5 to 7.1 GHz and the voltage standing wave ratio (VSWR), a measure for the purpose of compatibility of any antenna, is measured to be below 2. The return loss is found different for a tumor affected breast phantom than a normal breast phantom. The shift of resonant frequency during the simulation of antenna with phantom indicates the existence of tumor inside brain. Other parameters such as gain, directivity specific absorption rate (SAR) are also taken into consideration for the tumor detection. The simulation is carried out for various tumor size and different depth of tumor to identify the presence and location of the tumor. Also, the effect of the antenna parameters is observed for the above-mentioned cases. In future, the simulation can be carried out to find the exact location of tumors using the absorbed power for multiple tumor cases.

## References

1. Mohebian MR, Marateb HR, Mansourian M, Mañanas MA, Mokarian F (2017) A hybrid computer-aided-diagnosis system for prediction of breast cancer recurrence (HPBCR) using optimized ensemble learning. *Comput Struct Biotechnol J* 15:75–85
2. Curry SJ, Byers T, Hewitt M (2003) Potential of screening to reduce the burden of cancer. In: Fulfilling the potential of cancer prevention and early detection. National Academies Press (US)
3. Hellquist BN, Czene K, Hjälm A, Nyström L, Jonsson H (2015) Effectiveness of population-based service screening with mammography for women ages 40 to 49 years with a high or low risk of breast cancer: Socioeconomic status, parity, and age at birth of first child. *Cancer* 121(2):251–258
4. Ozmen N, Dapp R, Zapf M, Gemmeke H, Ruiter NV, van Dongen KW (2015) Comparing different ultrasound imaging methods for breast cancer detection. *IEEE Trans Ultrason Ferroelectr Freq Control* 62(4):637–646
5. Roganovic D, Djilas D, Vujnovic S, Pavic D, Stojanov D (2015) Breast MRI, digital mammography and breast tomosynthesis: comparison of three methods for early detection of breast cancer. *Bosn J Basic Med Sci* 15(4):64
6. Alvarez-Berdugo D, Jiménez M, Clavé P, Rofes L (2014) *Sci World J* 2014:Article ID 184526



7. Hassan AM, El-Shenawee M (2011) Review of electromagnetic techniques for breast cancer detection. *IEEE Rev Biomed Eng* 4:103–118
8. Chandra R, Zhou H, Balasingham I, Narayanan RM, De Azevedo-Marques PM, Mencattini A, Salmeri M, Rangayyan RM (2018) Medical microwave imaging and analysis. In: *Medical image analysis and informatics: computer-aided diagnosis and therapy*. CRC Press, pp 451–466
9. Sill JM, Fear EC (2005) Tissue sensing adaptive radar for breast cancer detection—Experimental investigation of simple tumor models. *IEEE Trans Microw Theory Tech* 53(11):3312–3319
10. Çalıřkan R, Gültekin SS, Uzer D, Dünder Ö (2015) A microstrip patch antenna design for breast cancer detection. *Procedia Soc Behav Sci* 195:2905–2911
11. Raihan R, Bhuiyan MSA, Hasan RR, Chowdhury T, Farhin R (2017) A wearable microstrip patch antenna for detecting brain cancer. In: *IEEE 2nd International conference on signal and image processing (ICSIP)*. IEEE, pp 432–436
12. Afyf A, Bellarbi L, Achour A, Riouch F, Errachid A (2015) A novel low cost UWB antenna for early breast cancer detection. *Am J Electromagn Appl* 3(5):31–37
13. Ouerghi K, Fadlallah N, Smida A, Ghayoula R, Fattahi J, Boulejfen N (2017) Circular antenna array design for breast cancer detection. In: *Sensors networks smart and emerging technologies (SENSET)*. IEEE, pp 1–4
14. Karli R, Ammor H, Shubair RM, AlHajri MI, Alkurd R, Hakam A (2016) Miniature planar ultra-wide-band microstrip antenna for breast cancer detection. In: *16th Mediterranean microwave symposium (MMS)*. IEEE, pp 1–4
15. Gupta H, Maheshwari V, Thakery VV (2016) Brain tumor detection by microwave imaging using planner antenna. *Int J Bio-sci Bio-Technol* 8(5):201–210

# Virtual Instrumentation Based Graphical User Interface for Fermentation Bioprocess Monitoring Using LabVIEW



S. G. Rahul , R. Chitra , Vulichi Puneeth Kumar ,  
Palla Hima Sai Abhishek , and Boggula Obula Reddy 

**Abstract** This work presents the development of a Graphical User Interface for Bioprocess parameters monitoring such as temperature, pH, and dissolved oxygen for a Fermentation process using LabVIEW. Monitoring bioprocesses is highly essential because low time intervals do not cause many variations in the values of the bioprocess. Bioprocesses play a vital role in the field of biotechnology and are widely preferred in many industrial sectors. Control schemes are being implemented to enhance productivity and product outcome without compromising process efficiency. It becomes crucial to utilize a real-time process analysis system to result in a high-quality yield for any bioprocess. Insight on the bio-parameters affecting the formation of essential biomolecules and nutrient concentration, along with a monitoring and measurements system is of high demand. The application presented in this study illustrates the usefulness of an automated monitoring system developed using LabVIEW. This study aims to demonstrate the possibility to monitor key variables in bioethanol fermentation for parameters such as temperature, pH and, dissolved oxygen. This project also illustrates the usefulness of an automated monitoring system through a graphical programming environment.

**Keywords** Graphical user interface · Temperature · pH · Oxygen · Bioprocess · Control

## 1 Introduction

Graphical User Interface (GUI) is helpful to virtually automate hardware systems. LabVIEW has an abundant in-built library of functions that need not necessitate coding and are used for most of the Graphical programming. Application-specific libraries are present for data acquisition, serial instrument, data processing, analysis presentation. LabVIEW is a programming tool to create graphical programs using drag and drop blocks with predefined functionalities. P. Thirumurugan et al.

---

S. G. Rahul (✉) · R. Chitra · V. P. Kumar · P. H. S. Abhishek · B. O. Reddy  
Vel Tech Rangarajan Dr. Sagunthala R&D Institute of Science and Technology, Chennai, Tamil Nadu 600062, India

© The Author(s), under exclusive license to Springer Nature Singapore Pte Ltd. 2022  
G. S. V. L. Narasimham et al. (eds.), *Innovations in Mechanical Engineering*,  
Lecture Notes in Mechanical Engineering,  
[https://doi.org/10.1007/978-981-16-7282-8\\_59](https://doi.org/10.1007/978-981-16-7282-8_59)

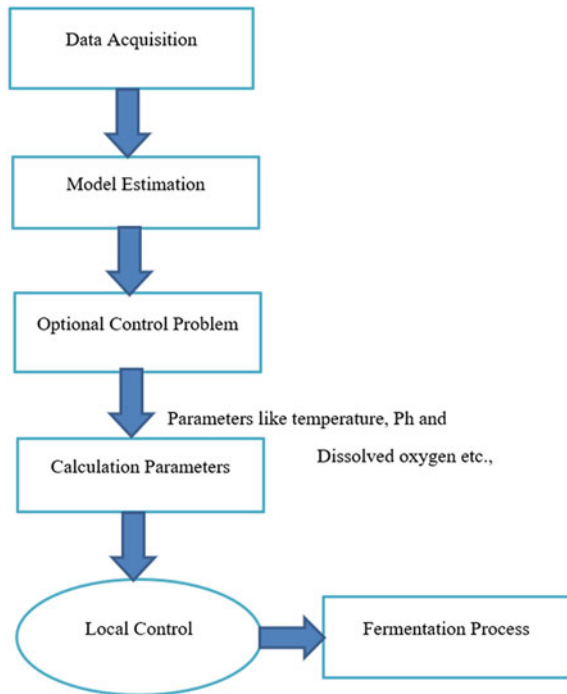
783

presented LabVIEW-based simulation design of a Proportional-Integral-Derivative (PID) controller for temperature control. Temperature control of a liquid in a heating tank was achieved by a PID controller through switching a heater on and off [1]. A graphical notation is a process where functional nodes are connected using wires to form the flow of data, unlike conventional programming like C, C++, or Java, involving long textual codes. While LabVIEW paves much more flexibilities in system design when compared to the traditional coding tools. Sankalpa Kuma et al. introduced the concept of a temperature control system which is a PC-based virtual instrument application [2]. It was identified to be an interactive program for scientists and engineers. The programs that are created using the LabVIEW environment are executed on various platforms like Pocket PC, Digital Signal Processors (DSPs), palmtops, and Field-programmable Gate Arrays (FPGAs). Dr. Channappa Bhyri and Aditya Govind developed a prototype to monitor and control temperature, liquid level and smoke in real-time [3]. Microbial fermentation is the basis of biochemical engineering. The fermentation process involves the aerobic or anaerobic reproduction of the microorganisms to reproduce themselves or simply called conversion from primary metabolites to secondary metabolites. To improve the efficiency of this biological process the control strategies are used that is to control the temperature, pH, and another related parameter that directly involves in the fermentation process. By altering the parameters and their conditions we can improve the levels of output of fermentation technology. Thus, in this project, the biological fermentation monitoring system based on LabVIEW is designed and developed as presented in Fig. 1.

### ***1.1 Common Bioprocess Parameters***

In this project, a bioprocess monitoring GUI is developed in the LabVIEW environment. Bioprocess parameters such as temperature, pH, and dissolved oxygen are crucial problems to be taken care of in the fermentation process. Lack of control on any of the parameter will affect the component and equipment along with the process and engineering personnel, leading to production loss. This study focusses on monitoring the temperature, pH, and dissolved oxygen levels of a fermentation process using the LabVIEW software platform. Besides, it offers flexibility with easy reconfiguring features, safety features like alarm and report generation with parametric limit variations. Jie Li et al. focused on the commonly used glass fermentation tank in biological fermentation and had improved and optimized the current monitoring process of biological fermentation [4]. Maintaining an ideal temperature range during the fermentation process becomes challenging which most of the ethanol plants suffer, in the summer months. The optimal temperature range for yeast fermentation is from 32 °C–35 °C. Any change in this limit suppresses the process of fermentation. Higher temperatures affect the sensitivity of yeast to acetic and lactic acids, resulting in reduced ethanol yields. The yeast cells in a fermentation process withstand a pH between 4.0 to 8.5 but the optimal pH required is between 4.0 and

**Fig. 1** Flowchart of fermentation process



6.0. It is inferred that yeast requires a mildly acidic environment for fermentation to occur. The dissolved oxygen of the fermentation is also an essential parameter for fermentation that influences cell growth. The rate at which oxygen is supplied to the cell is usually limited due to the low solubility of oxygen in the process. Therefore, monitoring and control of dissolved oxygen in a bioreactor poses a challenge.

## ***1.2 Meritorious Features of LabVIEW in Bioprocess Parameters Monitoring***

Our country has a significant improvement in the fermentation procedure where most of the countries using the traditional control method that has some limitation that affects the fermentation process. However, microorganism fermentation is the biological chemical reaction process, with non-linear and lag. It is very difficult to build an authentic model for the fermentation process because of the present technology. Within a few years with the rapid development of the technology in the different fields i.e., detection technology, Automation, microbial study etc., the fermentation process will also develop toward automation which makes it to analyze and control the process. We have set up the LabVIEW to monitor the growth of yeast and its cultural development. Now LabVIEW is the ongoing trend that is used for Graphical

User Interface where it limits the texts and uses the icons as its programming language so that is accepted worldwide. It has excellent efficiency where we cannot detect any other noise. The difficult algorithms like fuzzy, BP neural network, Support Vector Machine, etc., can be implemented in the easiest way possible in the LabVIEW. Even though automation companies are labor intensive the production of yeast is low because of the design and operations. Instead, we use LabVIEW that gives a prominent production within a short time. Yusuf Ayuba presented an automatic and manual control system for modern data acquisition processes of temperature [5]. Janani Rajaraman and K Saraswath worked to demonstrate the monitoring and control of process parameters such as temperature, pressure, flow and level using LabVIEW [6]. Kanwal Sachdev et al. proposed a system to collect information on polyhouse environment and crop status and generate a control action depending on the acquired data to act on situations based on climatic conditions [7]. Salim et al. controlled the speed of the DC motor to design a PID temperature control system for an electromagnetic oven using LabVIEW [8, 9]. N.D. Agham and V.R. Thool developed a monitoring system for continuous measurement of patient's several physiological parameters [10]. Likewise, LabVIEW provides substantial solutions for real-time monitoring of process parameters.

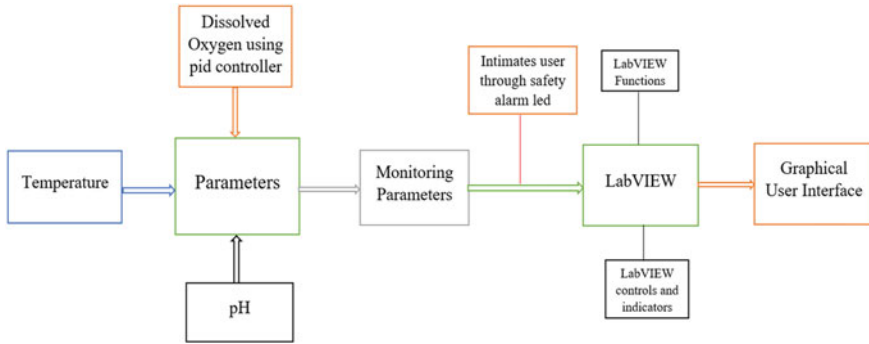
## **2 Methodology–Bioprocess Parameters Monitoring in LabVIEW**

As discussed in previous chapters, the monitoring of the bioprocess parameter is very important for the quality of the product. This chapter presents the proposed bioprocess parameters monitoring in LabVIEW as two segments:

- Design and Development of Graphical User Interface to monitor the bioprocess parameters such as temperature, pH, and dissolved oxygen using LabVIEW.
- Sending an Email on the monitored Bioprocess parameters and intimating the user through safety alarm/pop-up message.

### ***2.1 Design of Proposed System***

The proposed bioprocess parameter monitoring in LabVIEW monitors the parameters such as temperature, pH, and dissolved oxygen. At first, we have to set the parameters minimum and maximum range in LabVIEW using LabVIEW functions such as controls and indicators. After setting the range of parameters, run the G-code. If the parameters monitored is above the maximum or minimum range, it intimates the user by safety alarm/pop-up message. After intimating the user by safety alarm/pop-up message, sending an email to the user using the SMTP function in LabVIEW. All this process is carried out in the Graphical User Interface of LabVIEW. We have



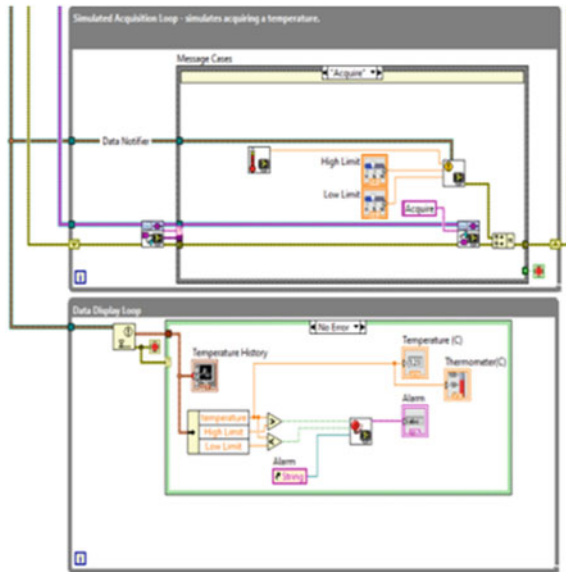
**Fig. 2** Block diagram of bioprocess parameter monitoring

developed the Graphical User Interface in this project by sending email to the user and creating event structures to start and stop the process. And we have developed it as real-time monitoring parameters using sub VI's. A sub VI enables us to use the same G-code in different circumstances and make the main VI compact. The proposed system of this study is shown in Fig. 2.

## 2.2 Temperature Monitoring

Maintaining the ideal temperature for the perfect example of fermentation is a difficult process. The optimal temperature for yeast fermentation is between 32 °C–35 °C. The algorithm for monitoring the temperature in LabVIEW: First create four while loop blocks. The first block refers to the start and stops of the process using an event structure palette. In that first block, create start and stop buttons using event structure, these will control the second while loop block. In second while loop block, it will show the processing of the system as a message. When we run the code it shows the indication message as “Ready”, after clicking the start button it changes to “simulating temperature”, and after pressing the stop button it will come back again to the “Ready...” indication. These two while loop blocks will connect to the other two while loop blocks, which are a major part of the process. In the third while loop block, create two slides (numeric controls) as a higher limit and lower limit. Create two sub VI's, in that first sub VI automatic temperature ranges, will be created. The ranges of the temperature will look like real-time monitoring. In the fourth while loop block, create a waveform graph, one numeric control and thermometer for visual digit value appearance. Third block functions are connected to the waveform graph for setting a higher and lower limit in the waveform graph. From that waveform, the graph creates a comparison logic for higher and lower temperature. These are connected to sub VI and in that sub VI, created a case structure and in that two cases were created as True and False. In True condition created a String with led

**Fig. 3** Block diagram of temperature monitoring in LabVIEW



color indication, when the temperature range reaches the higher limit it indicates HIGHER TEMPERATURE and in False condition created a String with Led color indication, when the temperature range reaches the lower limit it indicates LOWER TEMPERATURE. The acquired result will be shown via led with a strong message. Now, run the VI. While running the G-Code, if the temperature is greater than the setpoint temperature, the red LED glows indicating that the temperature is high. If the temperature is less than setpoint temperature, a blue LED glows indicating that the temperature is low. The block diagram for temperature monitoring in LabVIEW is shown in below Fig. 3.

### 2.3 PH Monitoring

The yeast cells in fermentation withstand a pH of 4.0 to 8.5 but the optimal pH is in the range of 4.0 and 6.0. The algorithm for monitoring the pH in LabVIEW: create one sub VI for manual monitoring of pH values and name it as pH scale. And take two numeric controls and name them as the pH upper limit and pH lower limit and fix the pH range as 8 and 4. Now take the numeric indicator as a meter and name it as a pH scale for seeing the pH monitoring. Now take a led from the boolean pallet and name it as a pH alarm lamp. Now on the block diagram panel take a greater than, less than and in-range operator from the comparison palletete, connect the higher limit and lower limit to the inputs of the in-range operator and other input as pH scale. Connect the inputs of these two operators as one from pH scale and other inputs as pH upper limit and pH lower limit, the output of these comparison operators to the inputs of

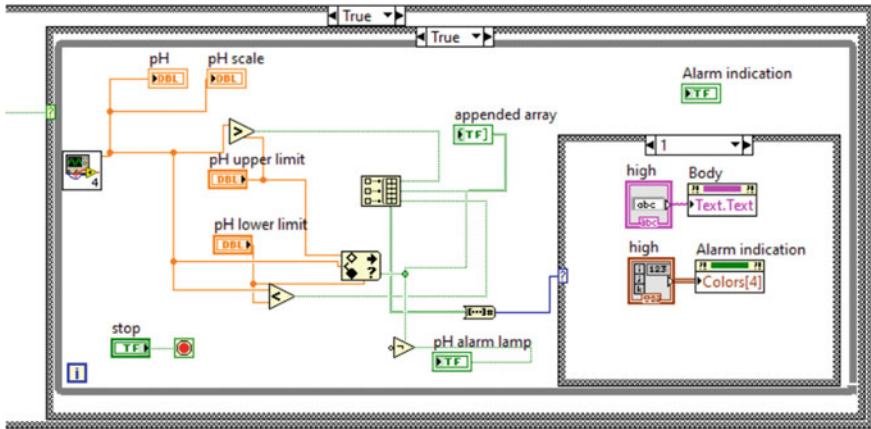


Fig. 4 Block diagram of pH monitoring in LabVIEW

build array and other input from the in-range operator output. And the output of the built array to the boolean indicator as an appended array and the boolean to a number input. Now create a case structure, connect the input of the case structure from the output of boolean to the number function. And create a not operator, the input of not operator is connected from output of in-range operator and output of not operator is connected to the pH alarm lamp. Now in case, the structure creates three cases. And create a local variable and make it as boolean and in property options make it as an array with the change to write and replace it as numeric color. Make three local variables to each case and colors like blue, skin, and red. In the first case, create a Boolean led for a normal pH range. In the second case, create a boolean led for the high pH range. In the third case, create a boolean led for the low pH range. For keeping the process to be secure, create log in credentials using appended array and string palette. When we enter the username and password correctly it will run the process otherwise it will terminate the process. Now, run the VI. While running the G-Code, if the pH is above the user’s given pH level, it shows a pop-up alert message and led will glow indicating that the pH level is high. If the pH is below the user’s given pH level, it shows a pop-up alert message and the led will glow indicating that the pH level is low. The block diagram for pH monitoring in LabVIEW is shown in Fig. 4.

### 2.4 Security System for Monitoring pH

We know that security plays a major role in the industries as it safeguards the industry from the external user who tries to enter the industry in this project we have designed a security-based system which is designed using a 2-D Array which contains the user name and password of the certain users who frequently comes to the industry



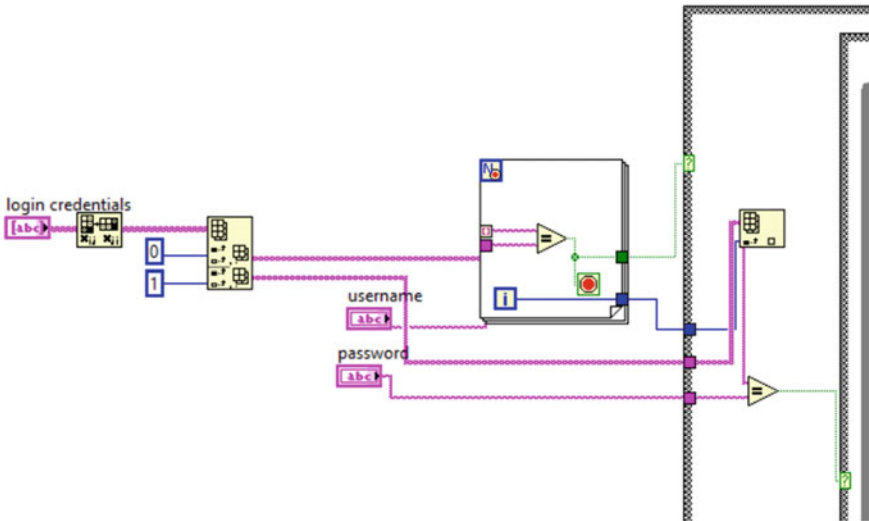


Fig. 5 Block diagram of mail alert through SMTP

and in order check whether the person entered username and password is correct or not if the user name of the person and the password of the person is matched then the user gets the authentication to access the tank level and when the username does not match with the list the user gets invalid username and when the password does not match with the username then the user gets the invalid password as shown in Fig. 5. When the user gets the authentication, the user can monitor the pH levels with the help of the comparison symbol it compares with the adequate level of the pH if the pH level is less than the required level and when the pH level is greater than the adequate level then the user sends an automatic mail to management regarding the disaster that going to take place in the monitoring of pH. We have created the cluster which contains the sender, receiver emails, and names and it contains the body and subject for the specific application and creates the SMTP. We have created the cluster which contains the sender, receiver emails, and names and it contains the body and subject for the specific application and creates the SMTP. Add the Send Email Express from .Net platelet VI to the block diagram. The Configure Send Email dialogue box automatically opens. Specify your email address or the email address from which you want to send the email in the Sender's Email Address text box located in the User Information section. Specify the hostname or IP address of the SMTP server, such as my.mailserver.com, you want to use to send the email in the Outgoing Mail Server (SMTP) text box as shown in Fig. 5.

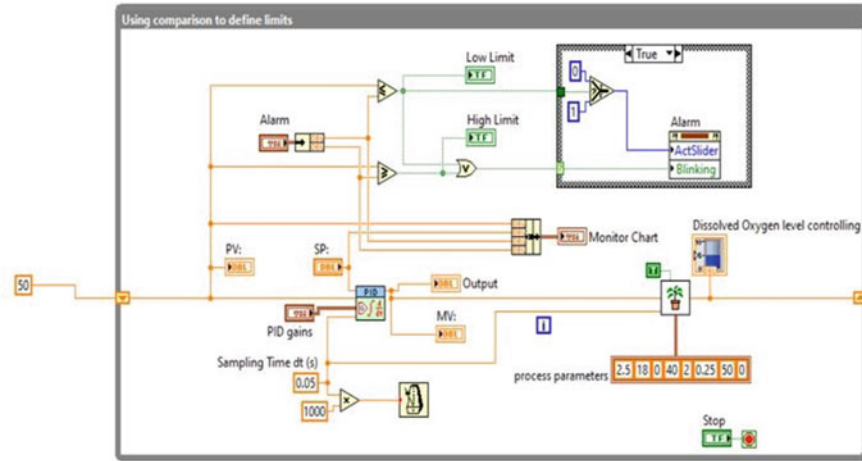


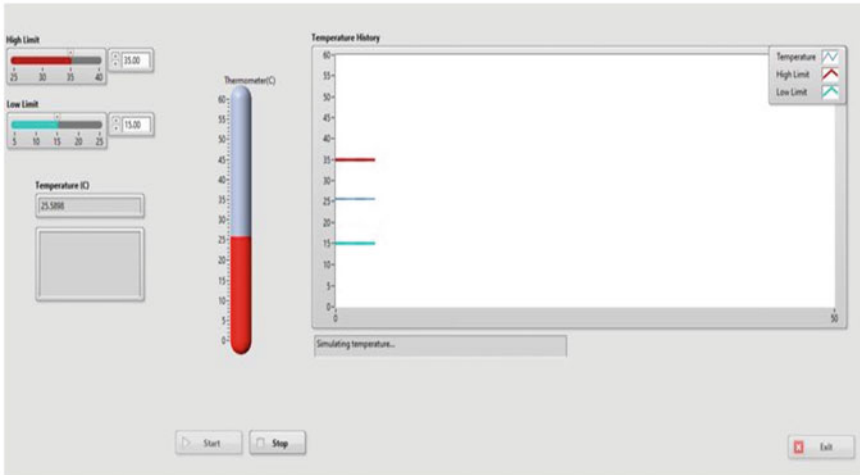
Fig. 6 Block diagram of dissolved oxygen level controlling using PID

### 2.5 Dissolved Oxygen Level Controlling Using PID

Dissolved oxygen (DO) is a relative measure of the oxygen dissolved in water. Oxygen dissolves in water by a diffusion process. The algorithm for monitoring the dissolved oxygen in LabVIEW; Proportional-Integral-Derivative (PID) controller is a common feedback scheme. In PID control, you specify a process variable and a set point. Run the VI and observe the Process variable (PV) following the Setpoint (SP) value while the output of the controller, also called Manipulated variable (MV), changes to keep both values near each other. After it settles down (the value of PV and SP are near each other), change SP. You can just move the “blue” arrow on the indicator. The MV will change to drive PV to SP again. Use the DBL instance of this VI to implement a single control loop. Use the DBL Array instance to implement parallel multi-loop control. To maintain a secured process, create login credentials using appended array and string palette. When we enter the username and password correctly it will run the process otherwise it will terminate the process. The block diagram for dissolved oxygen level monitoring using PID in LabVIEW is shown below Fig. 6.

### 2.6 PID Controller

A PID controller also called the three-term controller is a control loop mechanism deploying feedback and commonly utilized in industrial control systems and a variety of other applications involving good control. A PID controller calculates error signal  $e(t)$  continuously as a difference between the desired setpoint (SP) and measured



**Fig. 7** Temperature monitoring system when input is less than the lower limit

process variable (PV). In PID control, we mention a process variable and a setpoint. error signal behaves as in input to the controller, and the actuator input behaves like a controller output.

### 3 Simulation and Results for Bioprocess Parameter Monitoring in LabVIEW

#### 3.1 Simulation and Results of a Temperature Monitoring System

So, this is the simulation of the block diagram of temperature monitoring when the temperature range is less than the lower temperature of the temperature control. If the temperature is in this range, there will be a LED ALARM WITH STRING indicates as “Low temperature” and is indicated as LED display message as “LOW TEMPERATURE” as shown in Fig. 7. So the user can increase the average temperature in this condition until or unless the temperature range comes to the average set value.

#### 3.2 Simulation and Results of the pH Monitoring System

So, this is the simulation of the block diagram of the pH monitoring system, will produce the username and password so the best way to checking is to compare the

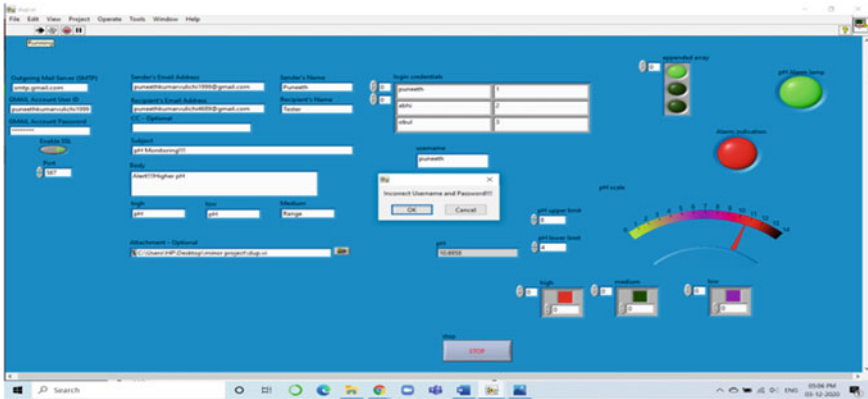
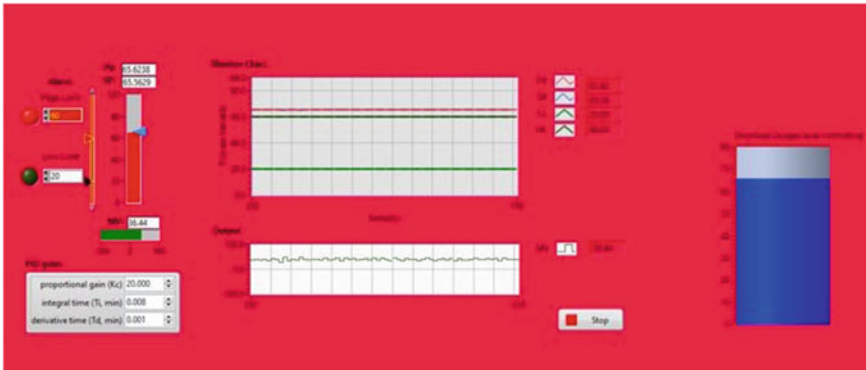


Fig. 8 pH monitoring system if username and password is incorrect

username and password, in the beginning, we going to get each of the usernames and password one at a time and compare it with the username and password. If the username and password do not match it deny the access for the user and prompt it as “WRONG USERNAME and PASSWORD” as shown in Fig. 8. When both the username and password exist then we can check whether the pH is less than or higher than the optimum limit, if it is less than, then we will get the LED Alarm blinking as blue color as shown in Fig. 9. If the pH is less than the optimum limit level, the mail will automatically send to the higher authority for security purpose. This is designed in such a way that if the input is less than the optimum limit, the mail will be sent as “Alert!!!! Lower pH”. When both the username and password exist then we can check whether the pH is less than or higher than the optimum limit, if it is in between the optimum range, then the LED Alarm will be OFF. If the pH is in between the optimum limit level, the mail will automatically send to the higher authority for security purpose. This is designed in such a way that if the input is higher than the optimum limit, the mail will be sent as “Don’t Worry!!! pH is in Optimum Range”.

Fig. 9 pH monitoring system when both username password is correct and input is less than optimum limit





**Fig. 10** PID tank level dissolved oxygen control system

### 3.3 *Simulation and Results of Dissolved Oxygen Level Controlling Using PID*

So, this is the simulation of the block diagram of the PID tank level dissolved oxygen control system. As shown in below Fig. 10 once the tank reaches the setpoint value the PID starts controlling the tank level. Observe the Process variable (PV) following the Setpoint (SP) value while the output of the controller also called Manipulated variable (MV), changes to keep both values near each other. After it settles down (the value of PV and SP are near each other), change SP. You can just move the “blue” arrow on the indicator. The MV will change to drive PV to SP again. Click Stop to stop the VI. If the setpoint is decreased to less than the lower limit, the setpoint will be controlled at what setpoint we have fixed now, and the LED Alarm will blink and indicates a text message with blinking as “LOWER LIMIT”.

## 4 Conclusions

Nowadays the trend is like most of the things done in computerized. Earlier monitoring of situations conditions was carried out only with the assistance of cameras. In this bioprocess system of the fermentation process, to scale back manual overhead, LabVIEW is implemented to this process to monitor and control as well as to inform the responsible personnel to take require appropriate measures. This project, it is aimed to monitor the bioprocess parameters such as temperature to say within the limit of 32 °C–35 °C, pH between 4.0 to 6.0 and dissolved oxygen. A security system is provided as it enables the user when the username and password match with the list of the user and does not provide security for the unknown users. This system also provides email intimation to the engineering team notifying them regarding the excess and uncontrollable level of parameters, so it helps and rescues the bioprocess

from not getting ruined. A PID controller is simulated to control the level of the tank for the excess dissolved oxygen to the required limit and the engineering personnel can the same which reduces the steady-state error using LabVIEW. This project is implemented as a software phase due to restricted access to hardware units owing to COVID-19 restrictions. The same will be extended as a hardware version in the future scope.

## References

1. Thirumurugan P, Arshad Alam Mohammed M, Karthikeyan S, Marimuthu D, Vijay PS (Mar–Apr 2019) Temperature process monitoring and control using LabVIEW. *J Instrum Control Eng, Int J Eng Tech* 5(2)
2. Kumar S, Bhattacharyya J, Bhattacharyya M (Dec 2016) Design of a PID auto tuning controller using LabVIEW. *Sch Electr Electr Eng IRJET* 3(12)
3. Bhyri C, Govind A (June 2017) Monitoring and controlling of process parameters using LabVIEW. *Int J Innovative Res Comput Commun Eng* 5(4)
4. Li J, Cui J-Y, Zhang C-T (2016) Design of fermentation process monitoring and control system based on LabVIEW. *College Control Eng, Northeast Univ Qinhuangdao, Advan Comput Sci Res* 44
5. Ayuba Y (March–April 2016) Temperature control and data acquisition method for factory using LabVIEW. (*IJCET*) 7(2)
6. Rajaraman J, Saraswathi K (Oct 2014) A LabVIEW based monitoring and controlling of various process variables. *Int J Advan Res Electr, Electron Instrum Eng*
7. Sachdeva K, Kumar N, Kumar R, Verma R (Sep 2015) Monitoring and controlling environmental parameters of polyhouse based on LabVIEW. *Int J Innovative Res Sci, Eng Technol*
8. Salim SK, Ohri J (May 2013) LabVIEW based DC motor and temperature control using PID controller. *Int J Advan Res Comput Sci Softw Eng* 3(5)
9. Kavitha S, Chinthamani B, Ponnmalar SJ (6 Dec 2012) Fuzzy based control using lab view for temperature process. *Int J Advan Comput Res* 2(4)
10. Agham ND, Thool VR (Feb 2014) LabVIEW-based physiological parameters monitoring system for patient healthcare. *Int J Eng Res Technol (IJERT)* 3(2)

# Analysis of a Multi-channel Closed Loop Green Supply Chain Using Modified Particle Swarm Optimization Algorithm



T. Niranjan, R. Thanigaivelan, and B. Singaravel

**Abstract** Conventional firms have to adapt online as well as offline chains in a multi-channel (MC) technique by making new supply chain and operating models. Because of the rise of e-commerce on the web and the micro division of customer groups, multi-channel frameworks are being adopted by numerous firms to explore newer markets and to bring down distribution costs. In this paper, the concept of multiple channels has been considered for the traditional offline supply chain of battery manufacturer in the southern part of India. The main aim of this paper is to develop the mathematical model for this multi-channel closed loop supply chain by taking into consideration the economic and environmental objectives. Chaotic initial population generation PSO with levy flight distribution has been applied for solving the model. It is concluded that this modified PSO (MPSO) gives superior results. The results indicate how the multi-channel framework optimizing the battery manufacturer's supply chain network.

**Keywords** Multi-channel · Closed loop supply chain · PSO · Levy flight · Chaotic

## 1 Introduction

Multi-channel supply network utilizes multiple channels to supply their customers with products rather than a single and strict channel. This provides choice, flexibility and better responsiveness for firms. Firms have to balance their supply chain properly. The store-only time has gone, so firms require a proper vision all through their

---

T. Niranjan (✉)

Mahatma Gandhi Institute of Technology, Kokapet, Gandipet, Hyderabad, Telangana, India  
e-mail: [tniranjan\\_mct@mgit.ac.in](mailto:tniranjan_mct@mgit.ac.in)

R. Thanigaivelan

Department of Mechanical Engineering, Muthayammal Engineering College Rasipuram, Rasipuram, Tamil Nadu, India

B. Singaravel

Department of Mechanical Engineering, Vignan Institute of Technology and Science, Deshmukhi, Hyderabad, Telangana, India

inventory network to adapt to the numerous strategies and ways customers shop—at the same time, building customer loyalty. Multi-channel (MC) concept is changing supply chain concepts. Today, new supply chain models are coming up to incorporate these changes. Operations, processes and supply chain are needed to be understood thoroughly for it. The extending scope of online supply channel is essentially creating a change in retail marketing.

### ***1.1 Metaheuristics***

Metaheuristics mimicked natural phenomenon, behaviour of species, etc., to efficiently find acceptable solutions to complex problems. Some of the recently developed techniques are Harmony Search, Firefly algorithm, Cuckoo Search, Bat Algorithm, krill Herd, Fruit fly Optimization Algorithm (FOA), Biogeography-Based Optimization (BBO), Glow-worm Swarm Optimization (GSO), particle Swarm Optimization (PSO), artificial bee colony (ABC), Genetic Algorithm (GA), Invasive Weed Optimization (IWO), Differential Evolution (DE), Ant Colony optimization (ACO), Artificial immune system (AIS), Grey Wolf Optimizer (GWO), etc.

Functioning of most of these algorithms are similar. They all starts by creating a random pool of potential solutions and iterates it over and over, trying to refine them at each step. This process is controlled by selection, reproduction, mutation and recombination operators. In the first phase of the search, namely, the exploration phase, the algorithm searches for and selects those solutions from the population which are expected to give optimum results. Next phase, namely, the exploitation phase, deals with converging towards the best possible solution rapidly.

### ***1.2 Levy Flight Distribution***

Conflicts may occur between exploration and exploitation phases of metaheuristic algorithm as clear cut boundary between the phases don't exist. These problems can lead the algorithm to be stuck in local optima instead of closing in on global optima. A better convergence speed can be attained and stagnation at local optima can be avoided by introduction of levy flight distribution in the metaheuristic algorithm.

### ***1.3 Chaotic Maps***

The final solution obtained by convergence in any metaheuristic algorithm has a strong relation to the parameter initialization. Executing algorithm by using some random sequences yields different results at different executions. To converge to a global optimum, the generated random variables should be properly spread out.



A drawback of Random Number Generators (RNGs) is that the generated random numbers are not well distributed because they do not follow any particular distribution. Many studies had been trying to find a solution to these problems as well as trying to increase the accuracy as well as speed of convergence. As a result, recently, researchers are focussing on chaotic sequences instead of RNGs as they prove to be a solution to these problems. The biggest advantage provided by chaotic sequence being proper distribution of random numbers generated. Chaotic sequence produces random and unpredictable numbers, which, on the other hand, has a level of regularity with it. It had proved itself efficient in terms of avoiding long optima and moving towards global solutions. Chaotic maps are used for selection, emigration and mutation probabilities. Exploration phase is improved by chaotic selection and emigration operators, whilst exploitation phase is enhanced by chaotic mutation operator. Recently, chaos is finding increasing applications in varied fields including secure transmission, modelling of natural phenomena, neural networks, and nonlinear circuits, etc.

This paper tries to develop Mixed Integer Linear Programming (MILP) model for the multi-channel closed loop supply chain network and to solve the model, a novel metaheuristic approach like chaotic PSO with levy flight algorithm is used.

## 2 Literature Review

Many studies have put forward the role of distribution cost in channel selection. If channel selection perfectly matches the firm's business, then the cost of transportation in channels can be minimized as proposed by Kabadayi [1]. Hakli et al. [2] studied PSO algorithm's problem of getting caught into the local optima and not being able to perform global search because of the early convergence. PSO was used along with levy flight for investigative purpose. The resulting technique seems to give better outcomes in practically every tested benchmark functions, and for being more robust in almost all cases. Kumar et al. [3] in his study, used DE along with levy flight search which resulted in OLFDE. Shan et al. [4] in his paper, proposed ABC with levy flight in order to select the best parameter settings. Various initial comparative experiments were done and after evaluating the performance of both the algorithms having the dimension sizes of 10, 30, and 50, ABC with levy showed better results compared with standard ABC. Pakzad-Moghaddam [5] put forwarded in their study, the requirement of some low order algorithms like levy flight distribution to blend with PSO for optimizing NP-hard problems.

Coelho et al. [6] proposed that Chaotic Firefly algorithms (FAC) is effective, efficient and robust in optimizing redundancy as well as reliability as proved by some of the benchmark problem simulation outcomes. FAC has a slight advantage with respect to the solution quality over other solvers. Jothiprakash et al. [7] proposed that chaos algorithms can be utilized in cases like complex nonlinear water resource systems because of its proficiency in enhancing general optimization algorithms and showed that the chaotic differential evolution (CDE) algorithm outperforms

other methods considering annual power produced in the plant. Saremi et al. [8] put forward in their study that chaotic maps are very good at avoiding localized solutions and provide higher convergence speeds when combined with evolutionary algorithms. Chaotic maps especially the mouse/Gauss map enhances the quality of results of biogeography Based Optimization. In addition, emigration operators in chaotic selection result in the highest performance. Jordehi [9] proposed chaotic artificial immune system algorithm which applied to a variety benchmark functions showed that it offers very good solutions. It has an upper hand over the conventional artificial immune system algorithm and the gravitational search algorithm. The upper hand is due to the result accurate as well as the stability in finding accurate solutions. Mitić et al. [10] proposed that chaotic fruit fly algorithms are prone to have very fast convergence rate when compared with basic Fruit fly algorithm, Levy flight distribution incorporated FOA, and different chaotic algorithms proposed recently. Chebyshev map incorporated fruit fly shows an upper hand with respect to quality of the global optimum results obtained as well as the algorithm success rate compared to the recently developed chaos enhanced algorithms. Wang et al. [11] put forward in their study that efficiency and effectiveness of cuckoo search has improved by chaotic maps. The upper hand which chaotic cuckoo search have over normal cuckoo search is that the global stability is maintained when the dimensionality of the problem is increased as shown by the scalability study.

Zhang et al. [12] proposed a novel vital model for planning inventory network systems with numerous dispersion channels. Coordination of three parts, i.e. the need based encoding plan, the Pareto optimality and the ABC calculation, includes the tackling philosophy, in a spearheading approach. It was a multi-target advancement for supportable production network arrange configuration considering different appropriation channels. In their paper, Barzinpour [13] distinguishes areas of preparations and shipment amount by abusing the exchange off amongst expenses, and emanations for a double channel production network organize. A shut circle store network (closed loop supply chain network) with numerous levels, different items, and various periods, deciding every one of the segments and crude materials of the items, was examined by Soleimani et al. [14], where they fused fluffy rationale into Fuzzy multi-objective feasible and green shut circle production network organize plan. Sensible model to adapt to dubious circumstances was presented by embracing the fluffy approach by Mohajeri [15]. To maintain a strategic distance from the deficiencies of utilizing level cuts capricious arrangements, the interim programming come nearer from the idea of the possibility mean was presented with the goal that all data on level slices could be incorporated to give a powerful arrangement. To contemplate the shut circle inventory network issue, an incorporated improvement display, is created and a true contextual analysis of a battery maker considering new and reconditioned items by Gaur et al. [16].

From the literature, it is found that the studies conducted in the field of partner selection in supply chain network with the application of advanced metaheuristic algorithms like TLBO, BAT, Cuckoo search, ABC, DE and Firefly algorithms has not been widely explored. These metaheuristics have been successfully applied to many engineering problems like job shop scheduling, colour image segmentation

problems for obtaining optimum results in minimum time. Research work with practical optimization models in line with industry requirements provides great potential and opportunities for industrial applications. The objective of this paper is to model a mixed integer linear programming which uses tangible parameters and constraints to get order quantity allocations for a company to minimize the total logistics cost for its supply chain partners of a multi-channel supply chain network.

### 3 Model Description

#### 3.1 Problem Formulation

Battery manufacturer follows a single-channel closed loop supply chain network with all the elements sequentially arranged. The initial optimal allocation and minimized cost of production, transportation and distribution were found out using the existing positions of the various supply chain entities. It was considered to be a good approximation for the purpose of a comparison between a multi-channel supply chain networks that is proposed in this work. So, in the proposed network, six retailers were short listed based on geographic proximity to plants to directly receive products from the plants. Thus, a new channel in the supply chain is created, making it a multi-channel supply chain. Because of this, it is found that the overall distance covered is reduced and an intermediate distribution centres are also eliminated, thus not only reducing the transportation cost, but also the maintenance cost and other overheads associated with these.

To analyze the effects of implementing closed loop supply chain, multi-channel supply chain and green (recycling) supply chain, we took a case study which satisfies all requirements to implement all of the above mentioned types of supply chain. In this case study we find the overall cost involved in designing and operation of the supply chain. The product flows from plant to distribution centre and to retailers (customer market zone) and automobile manufacturers directly and also from distribution centre to customer market zone as traditional supply chain fashion shown in Fig. 1. From

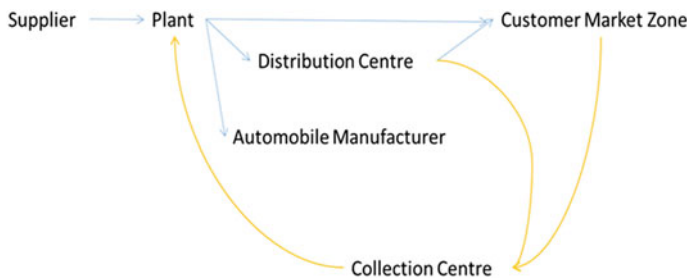


Fig. 1 Proposed supply chain network for batteries manufacturer

there, the used-up batteries are collected from the customers and sent to retailers and then they send it to the plant for recycling of the same. This reduces in raw material cost for recycling products and also reduces environment pollution. The ultimate aim of this problem is to reduce overall cost and to leave minimum carbon footprint in the environment. The proposed model is used to investigate trade-offs between cost and environmental degradation (carbon emissions).

### 3.2 *Mathematical Model for Closed Loop Battery Manufacturer*

Model Assumptions:

1. The raw materials are transported by the supplier itself to the plant.
2. The transportation cost per product from each plant to all distributors, from each distributor to all retailers, from all collection centres to plant fixed for all the periods and varies only proportionally by the distance travelled.
3. No wastage occurs during manufacturing, transportation.
4. No bottle necks are present in the entire supply chain.
5. Inventory cost is not considered at any point of supply chain.
6. All the batteries collected from customer are recycled.
7. Vehicles used for transportation are identical.
8. Routes travelled by vehicles are assumed to be identical in condition.
9. Rework and recycling are indifferent. A new part which is rejected by the customer due to a defect can be sent to either.
10. Cost of processing is uniform across products.

#### Sets

- I*: set of plants  
*J*: set of distribution centres  
*K*: set of customer market zones  
*L*: set of collection centres  
*H*: set of automobile manufacturer  
*P*: set of products  
*X*: no. of new product  
*R*: no. of recycled products.

#### Parameters

- CR<sub>p</sub>*: Cost of raw material for product *p*  
*X<sub>ijp</sub>*: no. of units transported from plant *I* to distribution centre *j* for product *p*  
*X<sub>ihp</sub>*: no. of units transported from plant *I* to automobile manufacturer *h* for product *p*

$R_{ijp}$ :	no. of recycled units transported from plant $I$ to distribution centre $j$ for product $p$
$R_{ihp}$ :	no. of recycled units transported from plant $I$ to automobile manufacturer $h$ for product $p$
$X_{jkp}$ :	no. of units transported from distribution centre $j$ to customer market zone $k$ for product $p$
$R_{jkp}$ :	no. of recycled units transported from distribution centre $j$ to customer market zone $k$ for product $p$
$B_{klp}$ :	no. of units transported from customer market zone $k$ to collection centre $l$ for recycling for product $p$
$B_{lip}$ :	no. of units transported from collection centre $l$ to plant $I$ for recycling for product $p$
$C_{ijp}$ :	cost of transportation from plant $I$ to distribution centre $j$ for product $p$
$C_{jkp}$ :	cost of transportation from distribution centre $j$ to customer market zone $k$ for product $p$
$C_{ihp}$ :	cost of transportation from plant $I$ to automobile manufacturer $h$ for product $p$
$C_{klp}$ :	cost of transportation from customer market zone $k$ to collection centre $l$ for product $p$
$C_{lip}$ :	cost of transportation from collection centre $l$ to plant $i$ for product $p$
$E_{ihp}, E_{ijp}, E_{jkp}$ :	emission rate
$t$ :	government tax rate for emission
$V_{ip}$ :	variable cost at plant $I$ for product $p$ .

### 3.2.1 Carbon Tax Model

#### Objective Function

$$\begin{aligned}
 \text{Minimize} = & \sum_p CR_p * (\sum_j X_{ijp} + \sum_h X_{ihp} + \sum_j R_{ijp} + \sum_h R_{ihp}) \\
 & + \sum_i \sum_j \sum_p C_{ijp} * (X_{ijp} + R_{ijp}) + \sum_i \sum_h \sum_p C_{ihp} * (X_{ihp} + R_{ihp}) \\
 & + \sum_j \sum_k \sum_p C_{jkp} * (X_{jkp} + R_{jkp}) \\
 & + \sum_i (\sum_j \sum_p (X_{ijp} + R_{ijp} + X_{ihp} + R_{ihp}) * V_{ip}) \\
 & + \sum_k \sum_l \sum_p (C_{klp} * B_{klp}) + \sum_l \sum_i \sum_p (C_{lip} * B_{lip}) \\
 & + \sum_i \sum_j \sum_p E_{ijp} * t * (X_{ijp} + R_{ijp}) \\
 & + \sum_i \sum_h \sum_p E_{ihp} * t * (X_{ihp} + R_{ihp}) \\
 & + \sum_j \sum_k \sum_p E_{jkp} * t * (X_{jkp} + R_{jkp})
 \end{aligned} \tag{1}$$

Constraints

$$\sum_j X_{ijp} + \sum_h X_{ihp} + \sum_j R_{ijp} + \sum_h R_{ihp} = S_{ip} \text{ for all } i \text{ belongs to } I, \tag{2}$$

$p$  belongs to  $P$  (Plant capacity constraint for each product)

$$\sum_j \sum_p X_{ijp} + \sum_j \sum_p R_{ijp} + \sum_h \sum_p X_{ihp} + \sum_i \sum_h R_{ihp} = S_i \text{ for all } i \text{ belongs to } I \text{ (Plant capacity constraint)} \tag{3}$$

$$\sum_i X_{ijp} + \sum_j R_{ijp} \leq C_j \text{ for all } j \text{ belongs to } J \text{ (Distribution centre capacity constraint)} \tag{4}$$

$$\sum_k X_{jkp} + \sum_k R_{jkp} \leq C_k \text{ for all } k \text{ belongs to } K \text{ (Retailer capacity constraint)} \tag{5}$$

$$\sum_i X_{ijp} - \sum_j X_{jkp} = 0 \text{ for all } j \text{ (No loss at distribution centre for new products)} \tag{6}$$

$$\sum_i R_{ijp} - \sum_j R_{jkp} = 0 \text{ for all } j \text{ (No loss at distribution centre for recycled products)} \tag{7}$$

$$\sum_i R_{ijp} - \sum_j B_{lip} = 0 \text{ for all } i \text{ (No wastage of recycled products at plant)} \tag{8}$$

$$\sum \sum B_{klp} \leq \sum_j R_{ijp} + \sum_h R_{ihp} + \sum_k R_{ikp} \text{ for all } k \text{ (No. of recycled products constraint)} \tag{9}$$

$$X_{ijp} \geq 0, X_{kjp} \geq 0, R_{ijp} \geq 0, R_{jkp} \geq 0, R_{ihp} \geq 0, B_{klp} \geq 0, B_{lip} \geq 0 \text{ (Non zero constraint)}$$

### 3.3 Chaotic PSO Algorithm with Levy Distribution

Particle swarm optimization is an evolutionary algorithm. It is based on the methods adopted by the swarm (group) to identify the food source. Usually, two types memory of is observed in them. One is individual memory, and other is group memory. Individual memory stores the best source that the particular individual has observed and the group memory contains the best source position observed from the entire group. Thus, the position of each particle is influenced both by its individual memory and the group memory. The weightage is distributed between them by the factors  $c1$ ,  $r1$ ,  $c2$  and  $r2$ , where  $r1$  and  $r2$  are random numbers generated in the range  $[0, 1]$ .  $C1$  and  $c2$  are the acceleration coefficients. The following steps are involved in finding an effective solution

1. Initialize the population of particles using upper and lower bound values using chaotic maps.
2. Calculation the fitness values for the particles.  
 $f[X1(i)], F[X2(i)], \dots, F[XN(i)].$

3. Calculate Pbest and store it.
4. Find the global best value using levy distribution.
5. Give the initial velocity as zero for all the particles. For the subsequent iterations, use the formula given below.
6. Update the particles using the following formula.

$$\begin{aligned}
 V_j(i) &= V_j(i - 1) + c1 * r1 * [Pbest, j - X_j(i - 1)] \\
 &\quad + c2 * r2 * [Gbest - X_j(i - 1)]; j = 1, 2, \dots, N \\
 X_j(i) &= X_j(i - 1) + V_j(i); j = 1, 2, \dots, N
 \end{aligned}$$

7. Continue the iteration several times until a proper convergence is achieved.

### 4 Results and Discussion

A new channel in the supply chain is created, making it a multi-channel supply chain. The overall distance covered is reduced and an intermediate distribution centre is also eliminated (D2) as shown in Table 1. Thus, not only reducing the transportation cost, but also the maintenance cost and other overheads associated with D2.

Six retailers were short listed based on geographic proximity for the multi-channel supply chain and receive batteries from the plants as shown in Table 2.

**Table 1** Product flow from plant to distribution centre

Product	D1	D2	D3	D4	Automobile manufacturer 1	Automobile manufacturer 2
P1	840	0	0	809	0	0
P2	840	0	821	0	1270	0
P3	840	0	701	0	0	0
P4	840	0	0	259	0	515
P5	840	0	236	465	0	0
P6	840	0	0	616	0	0

**Table 2** Product flow from plant to retailer (customer zone)

Product	R1	R2	R3	R4	R5	R6
P1	170	150	170	155	180	165
P2	175	170	170	150	170	170
P3	170	170	175	170	170	170
P4	190	170	150	180	170	165
P5	160	185	165	170	175	170
P6	150	175	170	185	190	170

**Fig. 2** Convergence graph for green model

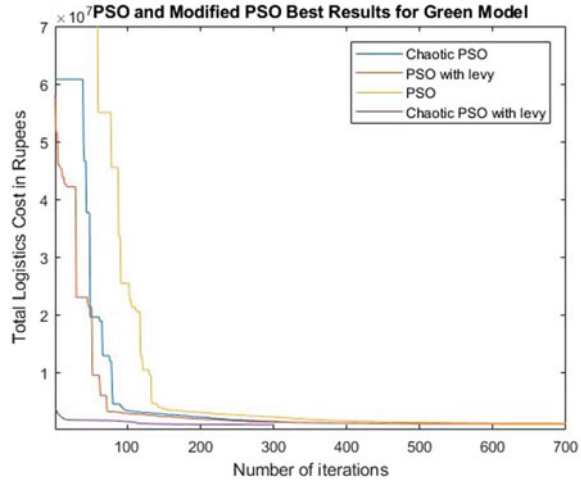


Figure 2 shows the convergence graph for the best results obtained for all four approaches for the proposed multi-channel model. From these, it is observed that total supply chain cost for carbon tax model is perceptibly less through the modified PSO approach compared with other three approaches.

## 5 Conclusion

In this study, a mathematical model for a multi-channel closed loop sustainable supply chain was proposed which considered multiple products. The model was applied on a case problem of a battery manufacturer’s supply chain network and it was solved using traditional and modified PSO. The results show that the model yields least total supply chain cost when the model is made as multi-channel supply chain, i.e. when the outlet to customer zone was delivered not only through distribution centres, also directly from plant. The result shows that this could reduce the transportation, delivery and maintenance costs for the firm. The concept of multi-channel can be applied for every industry because competitive markets require multiple channels to operate to provide consumers with flexibility and comfort of multiple channels. Further, chaotic PSO with levy giving better result comparing with traditional particle swarm optimization algorithm. This work can be taken forward by considering a better channel network, taking into account factors other than distance that are also influenced by the change in the design of the supply chain network. As the next step, a global organization can be considered to make the logistics network more complex, involving more distribution centres and retailers. The barriers to switching over to the proposed network can also be explored.



## References

1. Kabadayi S (2011) Choosing the right multiple channel system to minimize transaction costs. *Ind Mark Manage* 40:763–773
2. Haklı H, Uğuz H (2014) A novel particle swarm optimization algorithm with Levy flight. *Appl Soft Comput* 23:333–345
3. Kumar S, Sharma VK, Kumari R, Sharma VP, Sharma H (2014) Opposition based levy flight search in differential evolution algorithm. In: *International conference on signal propagation and computer technology*, pp 361–367
4. Shan H, Yasuda T, Ohkura K (2014) A Lévy flight-based hybrid artificial bee colony algorithm for solving numerical optimization problems. In: *IEEE congress on evolutionary computation*, pp 2656–2663
5. Pakzad-Moghaddam SH (2016) A Lévy flight embedded particle swarm optimization for multi-objective parallel-machine scheduling with learning and adapting considerations. *Comput Industr Eng* 109–128
6. Dos Santos Coelho L, de Andrade Bernert DL, Mariani VC (2011) A chaotic firefly algorithm applied to reliability-redundancy optimization. *IEEE Congress Evol Comput* 517–521
7. Jothiprakash V, Arunkumar R (2013) Optimization of hydropower reservoir using evolutionary algorithms coupled with chaos. *Water Res Manage* 27:1963–1979
8. Saremi S, Mirjalili S, Lewis A (2014) Biogeography-based optimisation with chaos. *Neural Comput Appl* 25(5):1077–1097
9. Jordehi AR (2015) A chaotic artificial immune system optimisation algorithm for solving global continuous optimisation problems. *Neural Comput Appl* 26:827–833
10. Mitić M, Vuković N, Petrović M, Miljković Z (2015) Chaotic fruit fly optimization algorithm. *Knowl-Based Syst* 89:446–458
11. Wang L, Zhong Y (2015) Cuckoo search algorithm with chaotic maps. *Math Probl Eng*
12. Zhang S, Lee CKM, Wu K, Choy KL (2016) Multi-objective optimization for sustainable supply chain network design considering multiple distribution channels. *Expert Syst Appl* 65:87–99
13. Barzinpour F, Taki P (2018) A dual-channel network design model in a green supply chain considering pricing and transportation mode choice. *J Intell Manuf* 29:1465–1483
14. Soleimani H, Govindan K, Saghafi H, Jafari H (2017) Fuzzy multi-objective sustainable and green closed-loop supply chain network design. *Comput Ind Eng* 109:191–203
15. Mohajeri A, Fallah M (2016) A carbon footprint-based closed-loop supply chain model under uncertainty with risk analysis: a case study. *Transp Res Part D Transp Environ* 48:425–450
16. Gaur J, Amini M, Rao AK (2017) Closed-loop supply chain configuration for new and reconditioned products: an integrated optimization model. *Omega* 66:212–223

# Wireless Electrical Impedance Tomography (EIT) Instrumentation: Progress and Limitations



Tushar Kanti Bera

**Abstract** Electrical impedance tomography (EIT) is a fast and portable radiation-free tomographic imaging modality which has been found promising in a number of applications in engineering and applied science fields. In EIT, a constant-amplitude sinusoidal current signal is applied to an object under test, and the potentials at object-boundary are measured through an array of surface electrodes surrounding the object. The voltage and current data are collected for different current injection projections to collect the data sets for a complete electrical scanning. A computer program called image reconstruction algorithm (IRA) is applied to get the conductivity distribution within the domain under test as the tomographic image by solving the forward and inverse problems. A PC-based dedicated instrumentation is required for current injection and voltage measurement from the object. In recent times, wireless instrumentation is being studied to obtain the wireless EIT (WL-EIT) systems as the wireless devices have many advantages. In wireless EIT, the current injection and data collection through wireless instrumentation suffer from some technical limitations, and hence, the scientific research investigations are required to overcome the hurdles and to explore the technology. The structural health monitoring (SHM) is required to assess the quality, durability and performance of the structure. Continuous or regular SHM is beneficial for the material assessment for longer period of time. Wireless EIT may provide an excellent opportunity for impedance imaging based SHM of any mechanical structure from remote area. In this paper, the benefits of the wireless EIT have been discussed with its possible applications for SHM of mechanical structures. The technology and instrumentation are studied, followed by a few case studies on wireless EIT. The advantages and limitations are discussed along with a highlight on future trends.

**Keywords** Electrical impedance tomography (EIT) · Structural health monitoring (SHM) · Wireless EIT (WL-EIT) · WL-EIT instrumentation · Constant current source · Data acquisition · Image reconstruction · Conductivity distribution

---

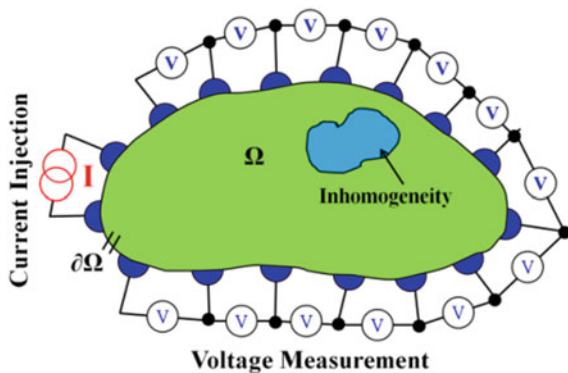
T. K. Bera (✉)

Department of Electrical Engineering, National Institute of Technology Durgapur (NITDgp), Mahatma Gandhi Avenue, A-Zone, Durgapur, West Bengal 713209, India

## 1 Introduction

Electrical impedance tomography (EIT) [1–6] is a computed tomography scanning (CT-Scanning) [7] technique what produces computed tomograms (cross-sectional images) of the body under test by calculating the conductivity or resistivity of the material from the voltage (V) and current (I) measurements conducted on the object-boundary. In EIT, the voltage-current data are acquired with an EIT-instrumentation [8–12] which consists of a constant current injector (CCI) [13–16], signal conditioner circuit (SCC) [8, 10], voltage measuring device and an electrode switching module (ESM) [8, 10, 17–19]. EIT-instrumentation injects a constant-amplitude sinusoidal AC current signal to the object under test and the developed voltage signals are measured (Fig. 1) at the object boundary. The voltage (V) and current (I) data are collected for a specific number of current projections by switching the electrodes used for current injection which are called the current electrodes (C-Electrodes) and the electrodes used to measure the voltage signals which are called the voltage-electrodes (V-Electrodes). As wireless instrumentation [20–22] has many advantages over wired systems, the wireless EIT (WL-EIT) systems are being proposed by developing the wireless instrumentation for EIT scanning. In the WL-EIT systems, current injection and voltage-collection are conducted through a wireless instrumentation and the image reconstruction is made in a similar way what is done in a wired EIT system. Like other wireless systems, WL-EIT also faces few challenges and limitations, and hence, more scientific research investigations are required to be conducted for crossing the hurdles and to explore the technology. The structural health monitoring (SHM) of mechanical materials and material structures is conducted to assess their quality, durability and performance. Structural analysis throughout the service or operational period needs either continuous or regular inspection. WL-EIT may provide an excellent opportunity for impedance imaging based SHM of any mechanical structure from remote area. In this direction, the benefits of the WL-EIT have been discussed with its possible applications in mechanical engineering domain for

**Fig. 1** Current injection and boundary voltage measurement in EIT



SHM of materials and mechanical structures. The WL-EIT technology and instrumentation are studied followed by a few case studies on wireless EIT. The technical aspects of WL-EIT-instrumentation have been discussed along with the advantages, limitations and the future trends.

## 2 Materials and Methods

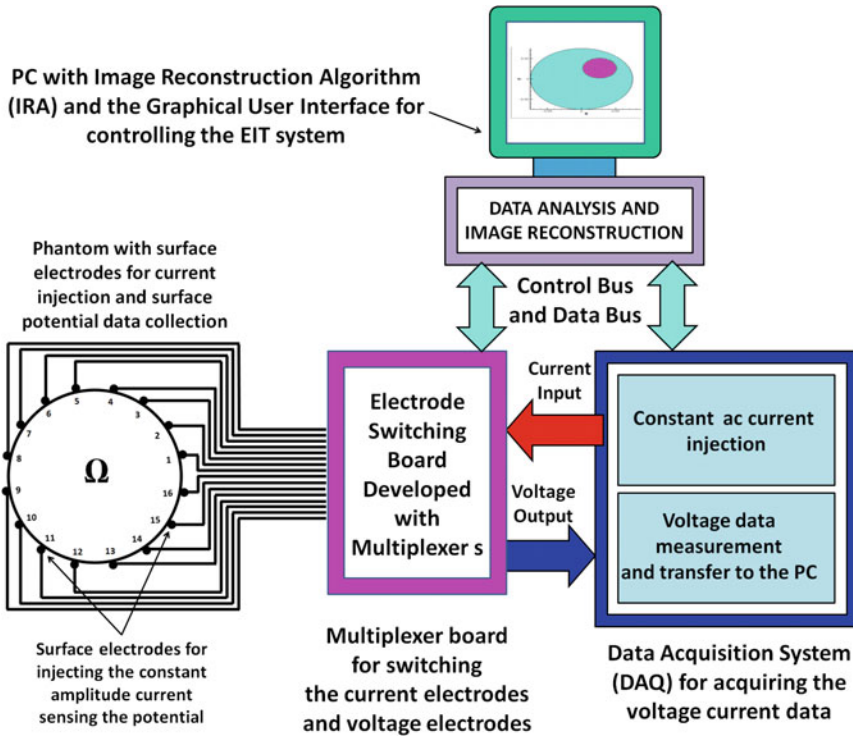
### 2.1 *The Physics of EIT*

EIT is an electrical signal based computed tomography (CT) which reconstructs the conductivity or resistivity of the material under test from the boundary voltage-current data collected by EIT-instrumentation. The EIT which is an ill-posed [23, 24] inverse problem (IP) technique [23, 24], is found very fast, portable, radiation-free tomographic imaging modality. Along with a very high-temporal resolution, EIT is also found with many other advantages over other CT techniques [25]. Therefore, EIT has been found efficient and promising in a number of applications [26–29] in engineering and applied science fields through the spatial resolution of the method is still low [30] compared to the conventional imaging modalities. In EIT, the electrical conductivity or the resistivity is calculated from the boundary voltage-current data using a mathematical algorithm written as a computer program called EIT image reconstruction algorithm (IRA) [31–34]. EIT-instrumentation (Fig. 2) injects a constant-amplitude sinusoidal current signal to the object under test and the boundary potentials are collected through an array of surface electrodes surrounding the object boundary.

The voltage-current data are collected for the current injections made with different independent current injection sets called current projections [35, 36] utilizing the maximum possible pairs of electrode pairs. After collecting the complete voltage-current data sets obtained from a complete EIT-scanning process called current injection protocol, the data are fed to the IRA for computation. The IRA tries to reconstruct the conductivity/resistivity distribution of the domain under test in the form of tomographic image called EIT tomograms by solving the forward problem (FP) and inverse problem (IP).

### 2.2 *EIT-Instrumentation*

An EIT system needs a PC-based dedicated instrumentation to collect the voltage (V) and current (I) data through the EIT sensor or EIT electrodes which must be attaching to the object-boundary. The current injection and voltage measurement is conducted using a dedicated electronic instrumentation [13, 15] using the surface electrode array [37–39]. The dedicated EIT-instrumentation not only applies the sinusoidal current



**Fig. 2** EIT-instrumentation schematic (wired instrumentation) showing CCI, ESM and data acquisition system

signal of constant amplitudes but also measures the surface potentials available on the electrodes. The collection of surface voltage data degenerated by current injection is performed preferably with a 4-probe method to avoid the contact impedance problem [39, 40]. The current signal is injected through a pair of electrodes and the voltage data are measured on the other possible independent electrode pairs excluding the pairs containing one or more current electrodes [37]. The current injection and the voltage measurement are conducted for a certain number of independent current electrode pairs. To get a complete scanning producing a set of independent voltage data (V) and current data (I) the electrodes are switched with a multiplexing unit controlled by the data acquisition system (DAS) controlled by a graphical user interface (GUI) developed in LabVIEW software. In most of the cases, the signals generated are processed to reduce the noise signals from the targeted signal.

### 2.3 C. EIT Phantom

Like any other instrumentation system, the EIT systems are also required to be studied, tested and calibrated before using it in the practical applications. To test and assess, an EIT system models of real objects are developed by mimicking the material properties of the real objects. The mimic models used for EIT system testing are known as the practical phantoms or EIT phantoms [41–44]. If the EIT system is developed for medical imaging purpose the EIT phantom must be developed with the properties of the biological tissues present in the real human body. Also, if a particular body parts are targeted to be imaged by EIT systems, the phantoms are essential to be developed by mimicking that particular body part so that the EIT system is evaluated and calibrated for practical applications.

### 2.4 EIT Reconstruction Algorithm

In EIT, the voltage data (V) and current data (I) are collected using an instrumentation and sent to the PC for process. The PC uses a computer program called image reconstruction algorithm to extract the conductivity data from the boundary voltage-current data. The image reconstruction algorithm or IRA has two parts: forward solver (FS) [24, 32, 33, 44] and inverse solver (IS) [24, 32, 33, 44]. The FS solves the forward problem in which the current data and the conductivity data are known and the voltage data are unknown (required to be calculated). On the other hand, the IS solves the inverse problem [24, 32, 33, 44] in which the current data and the voltage data are known but the conductivity data are unknown (required to be calculated). The forward solver solves the following EIT governing equation which can be obtained as a partial-differential-equation (PDE) derived from the Maxwell's equations. For, a closed domain ( $\Omega$ ) containing a homogeneous and isotropic medium if a low frequency sinusoidal current of constant-amplitude is injected at the domain boundary ( $\partial\Omega$ ), the electrical potential distribution is represented as [32, 33]:

$$\nabla \cdot \sigma \Delta \phi = 0 \tag{1}$$

Equation 1 represents the relationship between the conductivity ( $\sigma$ ) distribution of the domain and the potential distribution developed due to a constant-amplitude current injection. The solution of the PDE is conducted by utilizing numerical techniques like finite element method (FEM) [24, 32, 33, 44, 45] or else, by applying some boundary conditions [24, 32, 33, 44] such as the Dirichlet (or first-type) boundary conditions [24, 32, 33, 44] or the Neumann (or second-type) boundary conditions [24, 32, 33, 44].

## 2.5 Wireless Electrical Impedance Tomography (WL-EIT)

Wired EIT-instrumentation is interfaced with the object under test with connecting wires which are made up of highly conducting electrical wires. In wireless EIT systems, the instrumentation will have no or minimum wire connections. As the EIT system needs to generate and acquire the analog and digital data the wireless EIT systems should have capability of transferring both the analog and digital signals wirelessly. For the digital data, the data can be transmitted through Radio Frequency (RF) transmission by generating the high-frequency RF pulses.

## 2.6 WL-EIT for Structural Health Monitoring (SHM)

The structural health monitoring (SHM) is found beneficial to assess the quality, durability and performance of the material structures either their after manufacturing or during their operational life. Continuous or frequent health monitoring is beneficial for the material assessment for longer period of time. WL-EIT has the potential to provide the opportunity to apply the impedance imaging technique to conduct the SHM on any mechanical structure even from remote area. As the WL-EIT collects the data and provide the cross-sectional images of the materials under test through a wireless instrumentation (Fig. 3), the WL-EIT could be found very useful for condition monitoring of the mechanical structures remotely. As the EIT is an ill-posed inverse problem and produces an error in the output with its amplified amplitude for a particular error present at the input side. Therefore, the noise level of the data collected through the WL-EIT would be crucial point which should be studied in

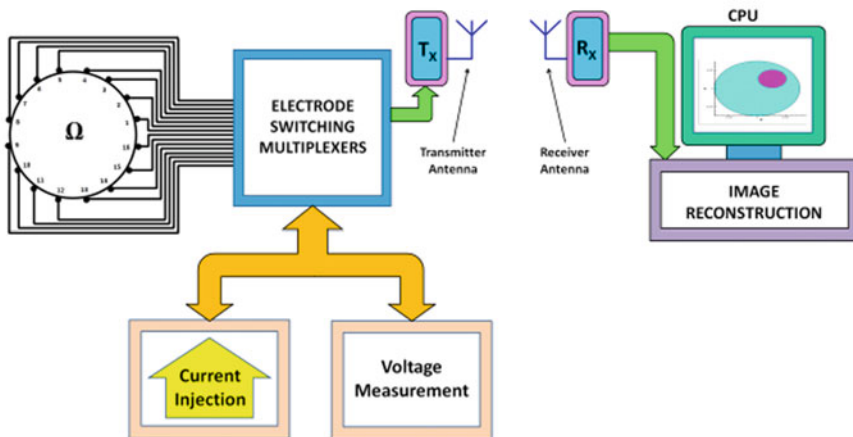


Fig. 3 Schematic of a wireless EIT system showing CCI, ESM and DAS

detail. Also the electrode connection need to be designed to achieve a reliable, durable and efficient contacts providing constant contact impedance over time.

### 3 Results and Discussion

Due to advantages of wireless technology, the EIT systems are also being developed with wireless mode and the data are collected wirelessly. The instrumentation could be developed in several ways and will have many advantages and limitations. In the following section, few case studies on wireless EIT have been discussed.

#### 3.1 Case Study 1

Bera and Nagaraju [19] developed wireless instrumentation for digital data transmission required for the electrode switching, and constant current injection. In the paper, the authors the switching of surface electrodes for a wireless EIT system developed with 16-electrode geometry. The digital data required for switching the multiplexers have been generated (at the transmitter-side) and studied are transferred wirelessly to the multiplexer side (receiver-side) with is studied using a RF-based digital data transmission system which was developed with 8 channel encoder IC and 8 channel decoder IC. An electrode switching module (ESM) is developed the CD4067BE IC [46] based analog multiplexer board to switch the EIT electrodes using the digital data transmitted through the RF transmitter ( $T_x$ )–receiver ( $R_x$ ) system. The 8-bit parallel digital data ( $D_7D_6D_5D_4D_3D_2D_1D_0$ ) generated by NIUSB6251 DAQ [47] under a LabVIEW (Laboratory Virtual Instrument Engineering Workbench) [48] based graphical user interface (GUI) card is transferred by transmitter/receiver module developed with 433 MHz ASK (Amplitude Shift Keying) RF-based transmitter ( $T_x$ )/receiver ( $R_x$ ) modules [19]. 8-bit parallel digital data is converted to 8-bit serial data by 8-bit encoder IC (HT640) [19] and transmitted by RF-based transmitter-module (TM). The 8-bit data in serial format are collected by the RF-based receiver module (RM) and then decoded by a decoder IC (HT648L) [19] to get back the parallel data ( $D_7D_6D_5D_4D_3D_2D_1D_0$ ). The 8-bit digital data are collected from the decoder output in parallel format ( $D_7D_6D_5D_4D_3D_2D_1D_0$ ) and fed to a binary adder circuit which converts the 8-bit digital data to 16-bit parallel data ( $D_{15}D_{14}D_{13}D_{12}D_{11}D_{10}D_9D_8D_7D_6D_5D_4D_3D_2D_1D_0$ ). The 16-bit parallel digital data are segmented in four parts and then fed to the multiplexer board in parallel format to operate the multiplexers ICs for electrode switching. In the proposed study, the authors studied the electrode switching for the EIT system by applying 1 mA (constant amplitude), 50 kHz AC (sinusoidal) current signal to the phantom and the boundary potentials are collected with opposite current-pattern. Digital data and the generated electrode the voltage data are studied to test and evaluate the digital data transmission wirelessly for the for the proposed EIT system.



### 3.2 Case Study 2

Huang et al. (2016) [49] proposed a wearable and wireless EIT system for reconstructing EIT images wirelessly. The wireless electrical impedance tomography system proposed by the authors consisted of a front-end amplifier circuit, a constant-amplitude current source data acquisition system circuit (CSC), a demodulation circuit (AD630, Analog Devices, U.S.), an analog multiplexer circuit, a micro-processor (MSP430, Texas Instruments, U.S.), and a circuit required for wireless-communication. To validate the performance of the proposed EIT system, EIT phantom experiments were conducted, and the EIT images were reconstructed using the back-projection algorithm. The practical phantom experiments results demonstrated that for the EIT images obtained by the proposed wireless EIT system, the average blur radius (BR) [50] value and the averaged location error ratio [49] were about  $1.3 \pm 0.2$  and  $6.27 \pm 3.14\%$ , respectively. The authors concluded that the advantages of the compact wireless EIT module could be found advantageous to acquire the EIT images in an embedded device on the clothes which could help us for impedance imaging under motion. The proposed wireless EIT system was found portable and could be made wearable which could be found as a suitable imaging device for applying it to many practical problems.

### 3.3 Case Study 3

McEwan and Holder [51] proposed a battery powered wireless electrical impedance tomography spectroscopy (EITS) system using Bluetooth technology. The proposed work modified the UCL Mk2.5 [52] to replace the RS232 cable communication system by connecting the PC with a Bluetooth radio. The system prototype system was connected to a 12 V DC battery to completely isolate the system from AC mains to increase the safety of the system and to improve the freedom to move the subject to get the advantages of getting reduced movement artifact as well as improved electrode contact [51]. Authors reported that the developed wireless EIT system was more robust to variation in contact impedance during multi-frequency time difference EIT imaging.

### 3.4 Case Study 4

Bilal et al. [53] reported their research studies conducted on an wireless Sussex MK4 system for electrical impedance mammography which was found as a low cost, reliable, accurate and efficient system. The proposed wireless planar array EIM system consisted of wireless nodes, a gateway and a computer. By the proposed system, the limitation of using fixed number of electrodes in the current planar EIM

system's is improved by increasing the number of electrodes as by the quality of information is enhanced. Using the wireless nodes for transmitting and receiving the measurements, the practical difficulties in applying large number of electrodes due to the space limitation can be solved. Also, the wireless system can isolate the system by receiving and transmitting the measurements and the control signals through a radio link. Authors reported that investigation they made with the wireless Sussex MK4 system is successful; accurate and optimized for the current planar EIM system. The authors claimed that their system aimed to reduce or eliminate the artifacts introduced by the patient during scanning and also to reduce or eliminate the frequency dependent noise, contact impedance error and the hardware limitations imposed by the cable connections in a wire EIT system.

### 3.5 Case Study 5

Peng et al. [54] proposed a wireless EIT system containing a distributed electrical impedance tomography (EIT) data acquisition system (DAS) using the IEEE 802.15.4 as the wireless transmission protocol. The authors studied both the traditional parallel EIT system and the wireless distributed EIT system. The parallel data acquisition system (DAS) consisted of two dynamic signal acquisition devices (PCI-4472, 8-channel, National Instrument Inc., USA) which was controlled by a software written in NI LabVIEW. For the wireless EIT system all the nodes were developed to provide constant-amplitude current signal to generate the voltage data. All of the nodes were equipped with the 24 bits high-precision A/D converters. The measured analog signals were filtered and then digitized for transmission. The EIT images are reconstructed from the voltage (V) and current (I) data using an improved Newton–Raphson algorithm. Authors reported that the experimental result they obtained demonstrated that the system and algorithm were successful, accurate for EIT studies. Authors reported that the wireless EIT they developed was found as a low cost, reliable, accurate and efficient.

## 4 Conclusion

Electrical impedance tomography (EIT) is found as a fast, portable, cost-effective and radiation-free imaging technique which could be applied in many practical applications in several engineering and technology fields. Wireless EIT has many advantages like any other wireless instrumentation. A number of wireless EIT systems have been developed and few of them are reviewed in this paper. The review on the wireless EIT conducted in this paper summarized that the wireless EIT systems reduce the noises produced by the connecting wire and associated stray capacitance. Also the motional artifacts contact impedance errors are minimized in a wireless ET system. Also, in few cases, the cost of the system is found reduced for wireless EIT

systems. The limitations of the wireless EIT system are the distance through which the transmission can be maintained. With the increase in distance, the noise may be introduced. WL-EIT can also be utilized for structural health monitoring (SHM) of mechanical structures. Continuous or frequency inspection through a longer period could be made possible by WL-EIT based SHM. Implementing the instrumentation, electrode connection and noise filtering, the WL-EIT could be made beneficial in future for the material assessment for longer period of time even from the remote area.

## References


1. Webster JG (ed) (1990) *Electrical impedance tomography*. Taylor & Francis Group
2. Borcea L (2002) *Electrical impedance tomography*. *Inverse Prob* 18(6):R99
3. Bera TK, Nagaraju J, Lubineau G (2016) *Electrical impedance spectroscopy (EIS)-based evaluation of biological tissue phantoms to study multifrequency electrical impedance tomography (Mf-EIT) systems*. *J Visualization* 19(4):691–713
4. Bayford RH (2006) *Bioimpedance tomography (electrical impedance tomography)*. *Annu Rev Biomed Eng* 8:63–91
5. Brown BH (2003) *Electrical impedance tomography (EIT): a review*. *J Med Eng Technol* 27(3):97–108
6. Bera TK, Nagaraju J (2017) *Electrical impedance tomography (EIT): a harmless medical imaging modality*. In: *Medical imaging: concepts, methodologies, tools, and applications*. IGI Global, pp 71–114
7. Kak AC, Slaney M, Wang G (2002) *Principles of computerized tomographic imaging*
8. Bera TK, Nagaraju J (2014) *A Low Cost Electrical Impedance tomography (EIT) instrumentation for impedance imaging of practical phantoms: a laboratory study*. In: *Proceedings of the third international conference on soft computing for problem solving*. Springer, New Delhi, pp 689–701
9. Boone KG, Holder DS (1996) *Current approaches to analogue instrumentation design in electrical impedance tomography*. *Physiol Meas* 17(4):229
10. Bera TK, Nagaraju J (2009) *A simple instrumentation calibration technique for electrical impedance tomography (EIT) using a 16-electrode phantom*. In: *2009 IEEE international conference on automation science and engineering*. IEEE, pp 347–352
11. McEwan A, Cusick G, Holder DS (2007) *A review of errors in multi-frequency EIT instrumentation*. *Physiol Meas* 28(7):S197
12. Avery J, Dowrick T, Faulkner M, Goren N, Holder D (2017) *A versatile and reproducible multi-frequency electrical impedance tomography system*. *Sensors* 17(2):280
13. Bera TK, Jampana N (2010) *A multifrequency constant current source suitable for electrical impedance tomography (EIT)*. In: *2010 international conference on systems in medicine and biology*. IEEE, pp 278–283
14. Lee JW, Oh TI, Paek SM, Lee JS, Woo EJ (2003) *Precision constant current source for electrical impedance tomography*. In: *Proceedings of the 25th annual international conference of the IEEE engineering in medicine and biology society (IEEE Cat. No. 03CH37439)*, vol 2. IEEE, pp 1066–1069
15. Bera TK, Saikia M, Nagaraju J (2013) *A battery-based constant current source (Bb-CCS) for biomedical applications*. In: *2013 fourth international conference on computing, communications and networking technologies (ICCCNT)*. IEEE, pp 1–5
16. Ross AS, Saulnier GJ, Newell JC, Isaacson D (2003) *Current source design for electrical impedance tomography*. *Physiol Meas* 24(2):509

17. Bera TK, Nagaraju J (2014) Studying the surface electrode switching of a sixteen electrode EIT system using a LabVIEW-based electrode switching module (LV-ESM). In: International conference on circuits, communication, control and computing. IEEE, pp 122–127
18. Bera TK (2015) Wireless electrical impedance tomography: LabVIEW-based automatic electrode switching. In: Telehealth and mobile health. CRC Press, pp 679–706
19. Bera TK, Nagaraju J (2011) Switching of a sixteen electrode array for wireless EIT system using a RF-based 8-bit digital data transmission technique. In: International conference on computing and communication systems Springer, Berlin, Heidelberg, pp 202–211
20. Dias NS, Carmo JP, Mendes PM, Correia JH (2012) Wireless instrumentation system based on dry electrodes for acquiring EEG signals. *Med Eng Phys* 34(7):972–981
21. Lynch JP, Loh KJ (2006) A summary review of wireless sensors and sensor networks for structural health monitoring. *Shock Vib Digest* 38(2):91–130
22. Lee S, Shin Y, Woo S, Kim K, Lee HN (2013) Review of wireless brain-computer interface systems. In: Brain-computer interface systems-recent progress and future prospects, pp 215–238
23. Lionheart WR (2004) EIT reconstruction algorithms: pitfalls, challenges and recent developments. *Physiol Meas* 25(1):125
24. Bera TK, Biswas SK, Rajan K, Nagaraju J (2011) A model based iterative image reconstruction (MoBIIR) algorithm for conductivity imaging in EIT using simulated boundary data. In: AIP conference proceedings, vol 1391, No 1. American Institute of Physics, pp 489–491
25. Bushberg JT, Boone JM (2011) The essential physics of medical imaging. Lippincott Williams & Wilkins
26. Bera TK (2018) Applications of electrical impedance tomography (EIT): a short review. In: 3rd international conference on communication systems (ICCS-2017), vol 331
27. Harikumar R, Prabu R, Raghavan S (2013) Electrical impedance tomography (EIT) and its medical applications: a review. *Int J Soft Comput Eng* 3(4):193–198
28. Dijkstra AM, Brown BH, Leathard AD, Harris ND, Barber DC, Edbrooke DL (1993) Review clinical applications of electrical impedance tomography. *J Med Eng Technol* 17(3):89–98
29. Lee K, Yoo M, Jargal A, Kwon H (2020) Electrical impedance tomography-based abdominal subcutaneous fat estimation method using deep learning. *Comput Math Methods Med*
30. Chitturi V, Farrukh N (2017) Spatial resolution in electrical impedance tomography: a topical review. *J Electric Bioimped* 8(1):66–78
31. Grychtol B, Müller B, Adler A (2016) 3D EIT image reconstruction with GREIT. *Physiol Meas* 37(6):785
32. Bera TK, Biswas SK, Rajan K, Nagaraju J (2011) Image reconstruction in electrical impedance tomography (EIT) with projection error propagation-based regularization (PEPR): a practical phantom study. In: International conference on advanced computing, networking and security. Springer, Berlin, Heidelberg, pp 95–105
33. Bera TK, Biswas SK, Rajan K, Jampana N (2011) Improving the image reconstruction in electrical impedance tomography (EIT) with block matrix-based multiple regularization (BMMR): a practical phantom study. In: 2011 world congress on information and communication technologies. IEEE, pp 1346–1351
34. Adler A, Dai T, Lionheart WR (2007) Temporal image reconstruction in electrical impedance tomography. *Physiol Meas* 28(7):S1
35. Bera TK, Nagaraju J (2012) Studying the resistivity imaging of chicken tissue phantoms with different current patterns in electrical impedance tomography (EIT). *Measurement* 45(4):663–682
36. Kolehmainen V, Vauhkonen M, Karjalainen PA, Kaipio JP (1997) Assessment of errors in static electrical impedance tomography with adjacent and trigonometric current patterns. *Physiol Meas* 18(4):289
37. Bera TK, Nagaraju J (2017) Sensors for electrical impedance tomography. In: Measurement, instrumentation, and sensors handbook. CRC Press, pp 61-1
38. McAdams ET, Jossinet J, Lackermeier A, Risacher F (1996) Factors affecting electrode-gel-skin interface impedance in electrical impedance tomography. *Med Biol Eng Comput* 34(6):397–408

39. Boyle A, Adler A (2011) The impact of electrode area, contact impedance and boundary shape on EIT images. *Physiol Meas* 32(7):745
40. Hua P, Woo EJ, Webster JG, Tompkins WJ (1993) Finite element modeling of electrode-skin contact impedance in electrical impedance tomography. *IEEE Trans Biomed Eng* 40(4):335–343
41. Bera TK, Nagaraju J (2011) Resistivity imaging of a reconfigurable phantom with circular inhomogeneities in 2D-electrical impedance tomography. *Measurement* 44(3):518–526
42. Bera TK, Nagaraju J (2009) A study of practical biological phantoms with simple instrumentation for electrical impedance tomography (EIT). In: 2009 IEEE instrumentation and measurement technology conference. IEEE, pp 511–516
43. Bera TK, Nagaraju J (2011) A chicken tissue phantom for studying an electrical impedance tomography (EIT) system suitable for clinical imaging. *Sens Imaging Int J* 12(3–4):95–116
44. Bera TK, Nagaraju J (2009) A FEM-based forward solver for studying the forward problem of electrical impedance tomography (EIT) with a practical biological phantom. In: 2009 IEEE international advance computing conference. IEEE, pp 1375–1381
45. Soni NK, Paulsen KD, Dehghani H, Hartov A (2005) Finite element implementation of Maxwell's equations for image reconstruction in electrical impedance tomography. *IEEE Trans Med Imaging* 25(1):55–61
46. Data Sheet, CD4067BE, Texas Instruments Inc., USA
47. Data Sheet, NI USB6251, National Instruments Inc., USA
48. Travis J (2009) LabVIEW for everyone. Pearson Education India
49. Huang JJ, Hung YH, Wang JJ, Lin BS (2016) Design of wearable and wireless electrical impedance tomography system. *Measurement* 78:9–17
50. Adler A, Guardo R (1996) Electrical impedance tomography: regularized imaging and contrast detection. *IEEE Trans Med Imaging* 15(2):170–179
51. McEwan A, Holder DS (2007) Battery powered and wireless electrical impedance tomography spectroscopy imaging using Bluetooth. In: 11th mediterranean conference on medical and biomedical engineering and computing. Springer, Berlin, Heidelberg, pp 798–801
52. McEwan A, Romsauerova A, Horesh L, Holder DS (2007) Performance improvements in a MF-EIT system for acute stroke: the UCL Mk2. 5. In: World congress on medical physics and biomedical engineering 2006. Springer, Berlin, Heidelberg, pp 3886–3889
53. Bilal R, Khan BM, Young R, Chatwin C (2017) A feasibility study of wireless Sussex MK4 system for electrical impedance mammography. *Int J Appl Eng* 12(12):3275–3281
54. Peng L, Xi F, Xiaoyu Z, Zhuoqiu L (2014) Reconstruction of electrical impedance tomography using improved Newton-Raphson algorithm based on wireless distributed system. *Comput Model New Technol* 18(12D):14–23

# Effect of Nano-rice Husk Ash Reinforcement on the Hardness of Al6061 Using Taguchi Method



Subrahmanyam Vasamsetti , Lingaraju Dumpala, and V. V. Subbarao

**Abstract** Metal matrix composites are getting much attraction in the automobile, aeronautical, and aerospace applications. Researchers are focusing on organic reinforcement materials such as red mud and fly ash. Rice husk ash is an industrial waste and has least applications. Surprisingly, it possess very rich silica content. The hardest metallic structures can be developed by reinforcing it with metals. In this research work, it is intended to develop nanometal matrix composites using rice husk ash. For this, rice husk ash was ground into nano-size particles and successfully reinforced in Al6061 using ultrasonic-assisted stir casting. The weight percentage of nano-rice husk ash is varied such as 1, 2, 3, 4, and 5 wt.% which are reinforced successfully. The process parameters of casting, such as casting temperature of 700, 750, and 800 °C, stirring speed 400, 500, and 600 rpm, and stirring time 60, 90, and 120 s, were optimized using the Taguchi method. Finally, 2 wt.% of reinforcement, at 800 °C of melting temperature, 600 rpm stirring speed, and for 90 s of stirring were found optimum. The result is validated with a confirmation test. The effect of each parameter on the hardness of developed composite material is analyzed using analysis of variance and found that 2 wt.% of nano-rice husk ash yielded better hardness, and there is not much difference between, stirring speeds of 500–600 rpm, and also not much difference for stirring times of 90–120 s.

**Keywords** Nanocomposites · Rice husk ash · Hardness studies · Optimization

---

S. Vasamsetti (✉) · L. Dumpala · V. V. Subbarao  
JNTU Kakinada, Kakinada, Andhra Pradesh, India

S. Vasamsetti  
Godavari Institute of Engineering & Technology, Rajahmundry, Andhra Pradesh, India

© The Author(s), under exclusive license to Springer Nature Singapore Pte Ltd. 2022  
G. S. V. L. Narasimham et al. (eds.), *Innovations in Mechanical Engineering*,  
Lecture Notes in Mechanical Engineering,  
[https://doi.org/10.1007/978-981-16-7282-8\\_62](https://doi.org/10.1007/978-981-16-7282-8_62)

821

## 1 Introduction

### 1.1 Nanocomposites and Rice Husk Ash

Nanocomposites are gaining much importance in the fields of aero/automobile fields due to their superior properties. In this research work, an effort was made to make use the industrial waste into useful product. Rice husk ash (RHA) is the industrial waste abundantly produced in the highly populated countries in Asia and also around the world. RHA has very limited applications such as raw material in fly ash bricks.

### 1.2 Present Trends

Several researchers already fabricated nanocomposites via stir casting route [1–8]. Some other researchers fabricated RHA reinforced composites in lightweight alloys such as aluminum [9–17]. RHA is rich in silica content and is about 91% by weight [18, 19]. The past research is focused on adding ceramic materials to lightweight materials and got good improvement in properties. So in this research, RHA is chosen as reinforcement material.

## 2 Materials and Methodology

RHA is produced in the laboratory using muffle furnace by combusting rice husk (RH) at 600 °C. The produced RHA is in whitish color and is ground to nanoparticle size using planetary ball mill [20]. The produced nano-rice husk ash (RHA) was reinforced in Al6061 metal pool in sonicator-assisted stir casting furnace by varying parameters at different levels.

The investigation has been made the effect of casting parameters, viz. percentage of reinforcement (wt.%), stirring time (time), stirring speed (N), and casting temperature (T) of Al6061/NRHA metal matrix composite manufactured by sonicated stir casting method on the hardness of the casting produced. An empirical model has been developed for predicting the hardness of Al6061/NRHA metal matrix composite. ANOVA is used in order to study the effects of casting parameters. The influences of different casting parameters on the hardness of Al6061/NRHA composite have been analyzed in detail. The experiment flowchart is shown in Fig. 1.

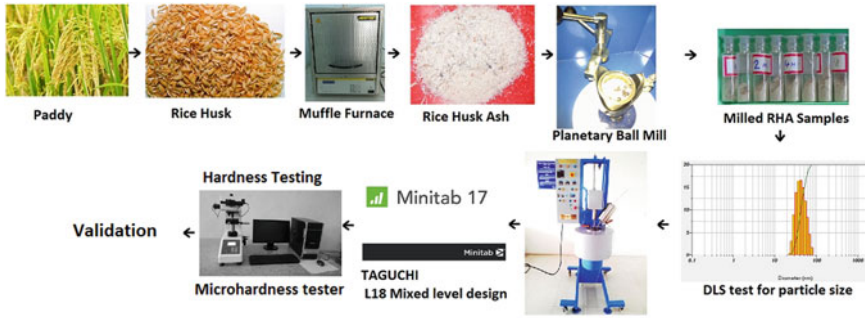


Fig. 1 Process flowchart of the experimentation

### 3 Experimentation

#### 3.1 Fabrication of NRHA Reinforced Composite and Taguchi Design

In order to fabricate the composites, different parameters were selected such as melting temperature, stirring time, stirring speed including percentage of reinforcement. Initially, weight percentage of reinforcement such as 1, 2, 3, 4, and 5 wt.% were pre-heated at the temperatures of 450 °C, Aluminum alloy was melted at selected temperatures such as 700, 750, 800 °C. Stirring is carried out for 1, 1½, 2 min for all different levels of experiment at different selected speeds of 400, 500, 600 rpm. After stirring for predetermined time, reinforcement particles were added and ultrasonicated to avoid clustering and agglomeration. The resultant molten metal was then cast into the metallic mold to form the composite specimens.

Taguchi’s orthogonal array helps in reducing the number of experiments. The specimens were prepared by choosing selective levels of parameters based on L18 array of experiments. The hardness, S/N ratios, and means for all experiments were given as shown in Table 1. The influence of different parameters chosen was analyzed, and their ranks were presented in Table 2.

i.e., at 2 wt.%, 800 °C, 600 rpm, and 90 s.

The predicted value,  $Y_p = 124.95$  HV at (3 3 3 3) Levels.

i.e., at 2 wt.%, 800 °C, 600 rpm, 120 s.

With these levels of parameters, a confirmation test was conducted and the results were displayed in Table 3. The confirmation test is very much closure to the predicted value and is satisfactory.

The main effects of plots and signal-to-noise ratios were given in Fig. 2. The graphs displayed that the increase in the percentage of NRHA reinforcement improved the hardness of the material up to 2 wt.% and then decayed. But, the values are still superior than bare material properties. The casting parameters also showed their



**Table 1** Taguchi orthogonal array design with responses, S/N ratios, and means

Ex. no.	wt.% of reinforcement	Temp (°C)	Stirring speed (rpm)	Stirring time (s)	HV	SNRA	MEAN
1	0	700	400	60	75.2	37.52436	75.2
2	0	750	500	90	78.4	37.88632	78.4
3	0	800	600	120	79.5	38.00734	79.5
4	1	700	400	90	108.2	40.68455	108.2
5	1	750	500	120	114.2	41.15332	114.2
6	1	800	600	60	115.2	41.22905	115.2
7	2	700	500	60	118.2	41.45235	118.2
8	2	750	600	90	123.9	41.86143	123.9
9	2	800	400	120	124.6	41.91036	124.6
10	3	700	600	120	111.3	40.9299	111.3
11	3	750	400	60	113.8	41.12285	113.8
12	3	800	500	90	114.3	41.16092	114.3
13	4	700	500	120	79.2	37.9745	79.2
14	4	750	600	60	81.5	38.22315	81.5
15	4	800	400	90	82.7	38.35011	82.7
16	5	700	600	90	78.8	37.93052	78.8
17	5	750	400	120	79.6	38.01826	79.6
18	5	800	500	60	80.9	38.15897	80.9

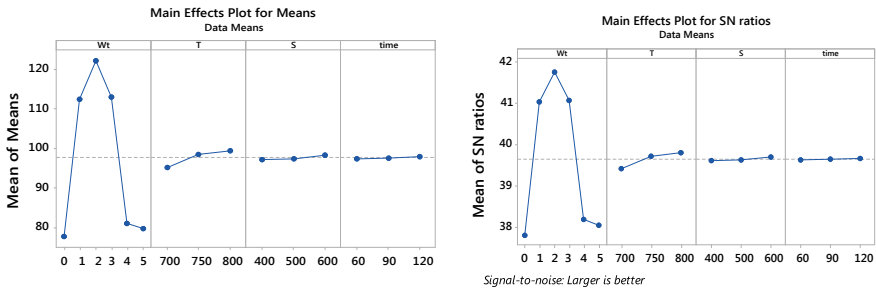
**Table 2** Response table for signal-to-noise ratios. Larger is better

Ex. no.	wt.% of reinforcement	Temp (°C)	Stirring speed (rpm)	Stirring time (s)
1	37.81	39.42	39.60	39.62
2	41.02	39.71	39.63	39.65
3	41.74	39.80	39.70	39.67
4	41.07	–	–	–
5	38.18	–	–	–
6	38.04	–	–	–
Delta	3.94	0.39	0.10	0.05
Rank	1	2	3	4
Max levels	L3	L3	L3	L3

effect on the hardness of the fabricated casting. The casting temperature played main role in the improvement of the casting superiority. The other parameters have less effect, but this is due to choosing the proven optimum values available in the literature.

**Table 3** Confirmation test

Predicted value	Practical value		Error
	Experimental values of 2 wt.% composite at 800 °C, 600 rpm, 120 s	Average experimental values	
124.95 HV	123.3 HV	123.58 HV	1.09%
	124.1 HV		
	123.8 HV		
	122.9 HV		
	123.8 HV		



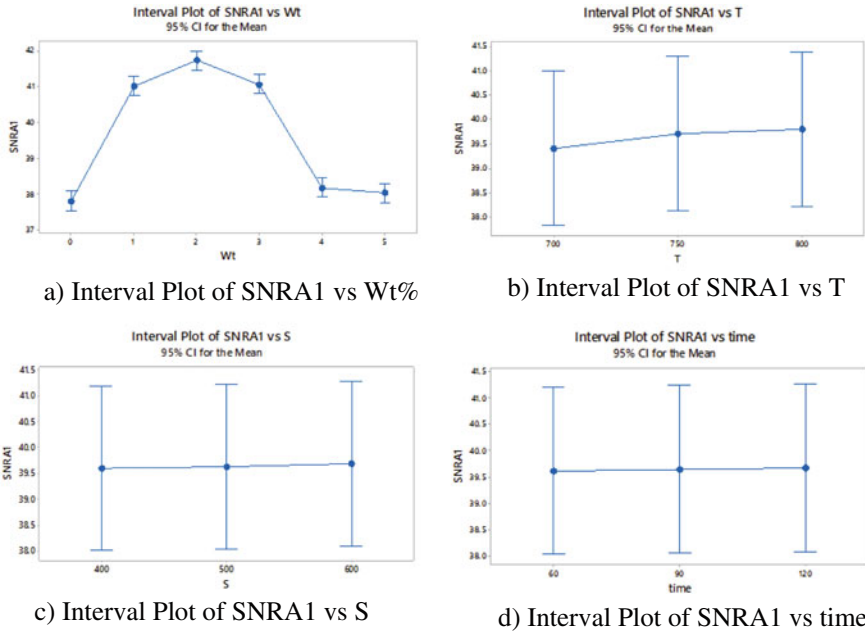
**Fig. 2** a Main effects plot for means. b Main effects plot for SN ratios

### 3.2 Analysis of Variance

Analysis of variance (ANOVA) on the hardness for the NRHA/Al6061 is presented in Table 4. The ANOVA is conducted at 5% significance level up to 95% confidence level. The fourth column in the table indicates percentage of contribution (P) of the parameters chosen. From Table 4, it can be found that the wt.% of reinforcement is playing a major role in the strength of resultant composite. But, it does not indicate that the influence of the other parameters is negligible, because the levels of these parameters were chosen based on the literature available [5–8]. So the range of parameters is closure to optimum values.

**Table 4** One-way ANOVA: SNRA1 versus Wt, T, S, and time

Source	DF	Seq SS	Contribution (%)	Adj SS	Adj MS	F-value	P-value
Wt	5	49.3067	98.88	49.3067	9.86133	212.43	0.000
T	2	0.4899	0.98	0.4899	0.2450	0.07	0.929
S	2	0.0285	0.06	0.0285	0.01425	0.00	0.996
Time	2	0.0067	0.01	0.0067	0.00336	0.00	0.999
		Error	0.07				



**Fig. 3** Interval plots of SNRA versus NRHA wt.%, temp, stirring speed, and time

The interval plots of S/N ratio versus wt.% of NRHA in Al6061, temperature of the furnace, stirrer speed, and stirring time were presented in Fig. 3.

### 3.3 General Linear Model: HV Versus NRHA wt.%, Melting Temperature, Stirring Speed, and Stirring Time

General linear regression equation was developed using Minitab 17. This developed model gives the relationship between predicted values and response variables by fitting a linear equation to the measured data.

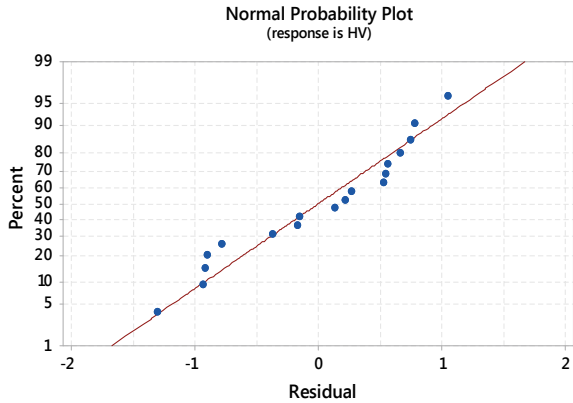
The following terms cannot be estimated and were removed:

Wt \* T, Wt \* S, Wt \* time, T \* S, T \* time, S \* time

Regression Equation:

$$\begin{aligned}
 HV = & 97.750 - 20.050 Wt\_0 + 14.783 Wt\_1 \\
 & + 24.483 Wt\_2 + 15.383 Wt\_3 - 16.617 Wt\_4 \\
 & - 17.983 Wt\_5 - 2.600 T\_700 + 0.817 T\_750 \\
 & + 1.783 T\_800 - 0.400 S\_400 - 0.217 S\_500 \\
 & + 0.617 S\_600 - 0.283 time\_60 - 0.033 time\_90 \\
 & + 0.317 time\_120
 \end{aligned}
 \tag{1}$$

**Fig. 4** Normal plot of residuals for HV



The normal plot of residuals as shown in Fig. 4 shows that the experimental values are closely following straight line and accurate.

## 4 Conclusions

From this work, the following conclusions were drawn:

1. The weight percent of nano-rice husk ash reinforcement is very much improving the hardness of the composite developed. The hardness is improving up to 2 weight percent of the NRHA and then the hardness deteriorated. But the results were superior to the hardness of Al6061 bare material.
2. In the process parameters, the melting temperature is occupying higher rank than other parameters within the chosen ranges.
3. The stirring speed and stirring time are less influential than melting temperature. It does not indicate that the stirring is not necessary. It may be due to the values closure to optimum values in the available literature.
4. The confirmation test was conducted at optimum levels, i.e., 2 wt.%, 800 °C, 600 rpm, 120 s of all the factors, and the average result is found satisfactory.
5. The influence of the process parameters, viz. melting temperature, stirring speed, and stirring time, is analyzed using ANOVA and found that the increase in all these parameters improved the hardness value. It may be due to the proper mixing of metal and reinforcement.
6. The normal plot of residuals revealed that the experimental values are closely following straight line and are accurate.

## References

1. Saravanan SD, Senthilkumar M (2015) Prediction of tribological behaviour of rice husk ash reinforced aluminum alloy matrix composites using artificial neural network. *Russian J Non-Ferrous Metals* 56:97–106
2. Gladston JAK, Dinaharan I, Sheriff NM, Selva JDR (2018) Dry sliding wear behavior of AA6061 aluminum alloy composites reinforced rice husk ash particulates produced using compocasting. Alloy matrix composites using artificial neural network. *J Asian Ceramic Soc* 5:127–135
3. Shaikh MBN, Raja S, Ahmed M, Zubair M, Khan A, Ali M (2019) Rice husk ash reinforced aluminium matrix composites: fabrication, characterization, statistical analysis and artificial neural network modelling. *Mat Res Express* 6:1–37
4. Dinaharan I, Kalaiselvan K, Murugan N (2017) Influence of rice husk ash particles on microstructure and tensile behavior of AA6061 aluminum matrix composites produced using friction stir processing. *Comp Commun* 3:42–46
5. Yang Y, Lan J, Li X (2004) Study on bulk aluminum matrix nano-composite fabricated by ultrasonic dispersion of nano-sized SiC particles in molten aluminum alloy. *Mat Sci Eng A Elsevier* 380(1):378–383
6. Cao G, Konishi H, Li X (2008) Mechanical properties and microstructure of SiC-reinforced Mg-(2–4)Al-1 Si nanocomposites fabricated by ultrasonic cavitation based solidification processing. *Mater Sci Eng A Elsevier* 486(1):357–362
7. Eskin GI, Eskin DG (2003) Production of natural and synthesized Al-based composite materials with the aid of ultrasonic (cavitation) treatment of the melt. *Ultrasonics Sonochem Elsevier* 10(4–5):297–301
8. Idrisi AH, Mourad A-HI (2019) Conventional stir casting versus ultrasonic assisted stir casting process: mechanical and physical characteristics of AMCs. *J Alloys Compd Elsevier* 805(1):502–508
9. Prasad DS, Shoba C, Ramanaiah N (2014) Investigations on mechanical properties of aluminum hybrid composites. *J Market Res* 3(1):79–85
10. Shoba C, Ramanaiah N, Rao DN (2015) Optimizing the machining parameters for minimum surface roughness in turning Al/6% SiC/6% RHA hybrid composites. *Proc Mat Sci* 10:220–229
11. Prasad DS, Shoba C (2014) Hybrid composites-a better choice for high wear resistant materials. *J Market Res* 3(2):172–178
12. Prasad DS, Shoba C (2016) Experimental evaluation onto the damping behavior of Al/SiC/RHA hybrid composites. *J Market Res* 5(2):123–130
13. Shoba C, Ramanaiah N, Rao DN (2015) Influence of dislocation density on the residual stresses induced while machining Al/SiC/RHA hybrid composites. *J Market Res* 4(3):273–277
14. Alaname KK, Adewale TM, Olubambi PA (2015) Corrosion and wear behavior of Al-Mg-Si alloy matrix hybrid composites reinforced with RHA and SiC. *J Market Res* 3(1):9–16
15. Alaname KK, Olubambi PA (2013) Corrosion and wear behavior of RHA-alumina reinforced Al-Mg-Si alloy matrix hybrid composites. *J Market Res* 2(2):188–194
16. Bodurin MO, Alaname KK, Chown LH (2015) Aluminum matrix hybrid composites: a review of reinforcement philosophies; mechanical, corrosion and tribological characteristics. *J Market Res* 4(4):434–445
17. Saravanan SD, Kumar MS (2013) Effect of mechanical properties on RHA reinforced AlSi10Mg matrix composites. *Procedia Eng* 64:1505–1513
18. Subrahmanyam V, Lingaraju D, Subbarao VV (2015) Synthesis and Raman scattering characterization of NRHA for nanocomposite applications. *Mater Today Proc* 2:4317–4322
19. Subrahmanyam V, Lingaraju D, Subbarao VV (2018) Synthesis, characterization and hardness studies of NRHA reinforced Al6061 nanocomposites. *J Eng Sci Technol* 13:2916–2929
20. Subrahmanyam V, Lingaraju D, Subbarao VV (2018) Optimization of milling parameters of planetary ball mill for synthesizing nano particles. *Int J Mech Eng Technol* 9:1579–1589